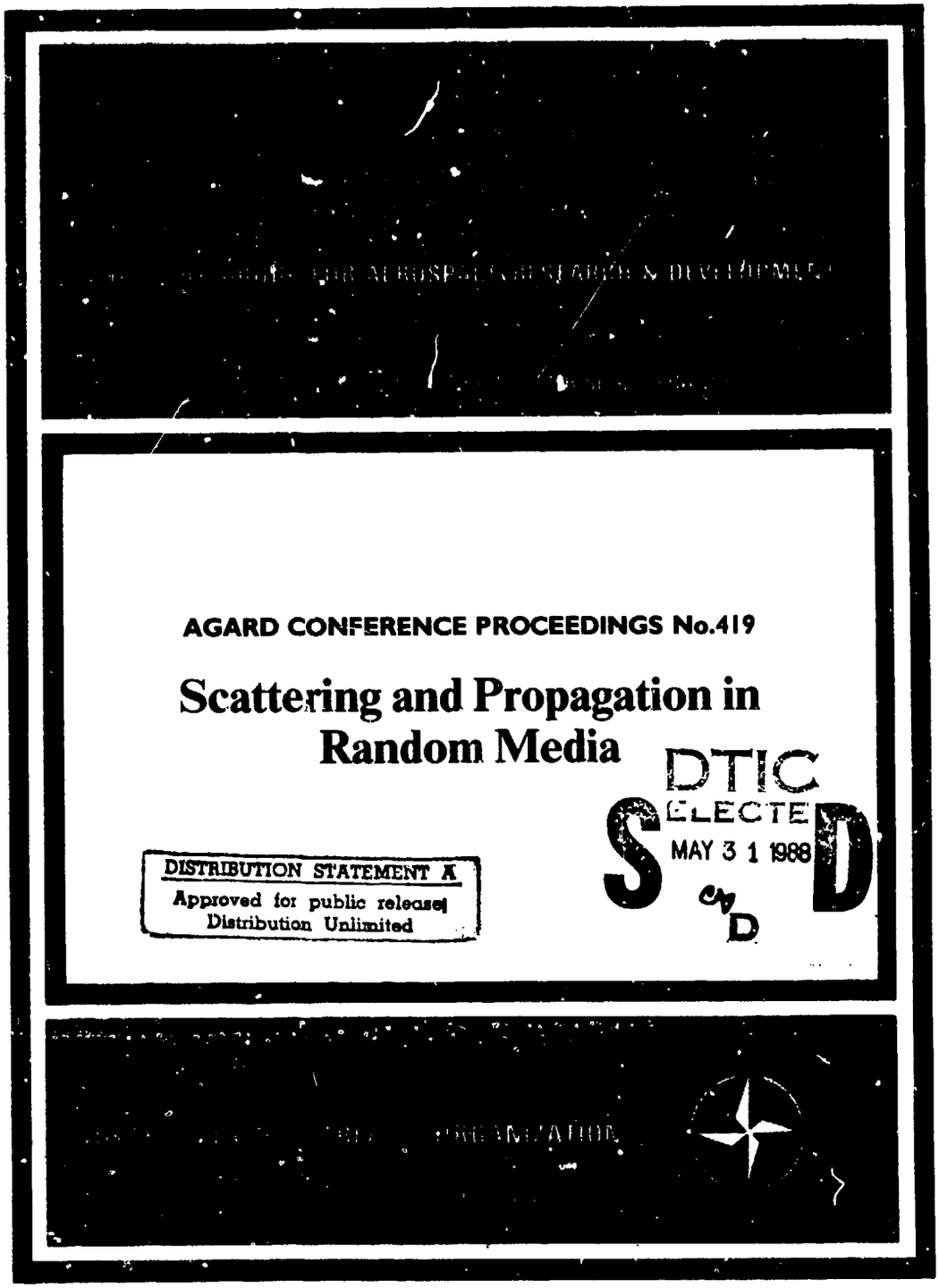
AD-A194 694 DTIC FILE COPY

(2)

AGARD-CP-419

AGARD-CP-419



AGARD CONFERENCE PROCEEDINGS No.419

Scattering and Propagation in Random Media

DTIC ELECTE MAY 3 1 1988 S D CD

DISTRIBUTION STATEMENT A
Approved for public release
Distribution Unlimited

DISTRIBUTION AND AVAILABILITY ON BACK COVER

88 5 27 018

AGARD-CP-419

NORTH ATLANTIC TREATY ORGANIZATION

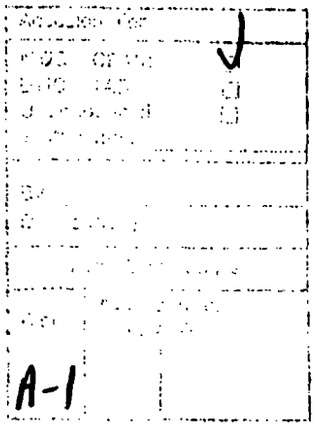
ADVISORY GROUP FOR AEROSPACE RESEARCH AND DEVELOPMENT

(ORGANISATION DU TRAITE DE L'ATLANTIQUE NORD)



AGARD Conference Proceedings No.419

SCATTERING AND PROPAGATION IN RANDOM MEDIA



Papers presented at the Electromagnetic Wave Propagation Panel Specialists' Meeting held in Rome, Italy, 18—22 May 1987.

THE MISSION OF AGARD

According to its Charter, the mission of AGARD is to bring together the leading personalities of the NATO nations in the fields of science and technology relating to aerospace for the following purposes:

- Recommending effective ways for the member nations to use their research and development capabilities for the common benefit of the NATO community;
- Providing scientific and technical advice and assistance to the Military Committee in the field of aerospace research and development (with particular regard to its military application);
- Continuously stimulating advances in the aerospace sciences relevant to strengthening the common defence posture;
- Improving the co-operation among member nations in aerospace research and development;
- Exchange of scientific and technical information;
- Providing assistance to member nations for the purpose of increasing their scientific and technical potential;
- Rendering scientific and technical assistance, as requested, to other NATO bodies and to member nations in connection with research and development problems in the aerospace field.

The highest authority within AGARD is the National Delegates Board consisting of officially appointed senior representatives from each member nation. The mission of AGARD is carried out through the Panels which are composed of experts appointed by the National Delegates, the Consultant and Exchange Programme and the Aerospace Applications Studies Programme. The results of AGARD work are reported to the member nations and the NATO Authorities through the AGARD series of publications of which this is one.

Participation in AGARD activities is by invitation only and is normally limited to citizens of the NATO nations.

The content of this publication has been reproduced
directly from material supplied by AGARD or the authors.

Published March 1988

Copyright © AGARD 1988
All Rights Reserved

ISBN 92-835-0444-5



Printed by Specialised Printing Services Limited
40 Chigwell Lane, Loughton, Essex IG10 3TZ

THEME

The topic of scattering and propagation in random media is one that has implications for the design, development and operation of most military systems that radiate energy as a means of accomplishing their function. Primary emphasis was on scattering and transmission in the atmosphere; however, other related random medium effects were not excluded.

The meeting covered modern methods of characterizing random media, mathematical methods and their applicability, effects on electromagnetic waves and the interpretation of these effects to specific system applications.

The region of the spectrum considered was essentially unlimited and ranged from very long waves to optics.

The performance of existing surveillance communication and navigation systems as well as the design of future systems is influenced by the propagation of energy via random media. An understanding of the nature of the medium and its impact on system design and performance is essential to the NATO community.

* * *

La diffusion et la propagation des ondes dans un milieu aléatoire est un sujet intéressant la conception, le développement et le fonctionnement de la plupart des systèmes militaires qui émettent de l'énergie pour accomplir leur fonction. On a étudié principalement la diffusion et la transmission dans l'atmosphère; mais les effets dans d'autres milieux aléatoires ne furent pas exclus.

La réunion a couvert les méthodes modernes de caractérisation des milieux aléatoires, les méthodes mathématiques et leurs domaines d'application, les effets sur les ondes électromagnétiques et l'interprétation de ces effets pour des applications de systèmes spécifiques.

L'intervalle du spectre étudié n'est pratiquement pas limité et va des ondes très longues aux ondes lumineuses.

Les performances des systèmes actuels de surveillance, de communication et de navigation, ainsi que la conception des futurs systèmes, dépendent de la propagation de l'énergie à travers un milieu aléatoire, et l'influence de celle-ci sur la conception et les performances d'un système présente une importance essentielle pour l'OTAN.

TECHNICAL PROGRAMME COMMITTEE

PROGRAMME CO-CHAIRMEN

Dr K.C.Yeh
Department of Electrical and Computer Engineering
University of Illinois
1406 W. Green St.
Urbana, IL 61801-2991
United States

Prof. Dr A.N.Ince
Science and Engineering Research Council
TUBITAK
Ataturk Bulvari 221
Ankara
Turkey

COMMITTEE MEMBERS

Prof. A.M.Scheggi
Istituto di Richerca sulle Onde Elettromagnetiche
del C.N.R.
Via Panciatchi, 64
50127 Firenze
Italy

Prof. C.Goutelard
Laboratoire d'Etude de Transmissions Ionosphériques
Université Paris-Sud
9, Av. de la Division Leclerc
94230 Cachan
France

Dr J.H.Blythe
GEC Research Centre
Great Baddow
Chelmsford, CM2 8HN
United Kingdom

Ing. Général L.Boithias
C.N.E.T.
38, 40, rue due Général Leclerc
92131 Issy-les-Moulineaux
France

Dr Walter A.Flood
Geoscience Division
US Army Research Office
P.O. Box 12211
Research Triangle Park NC 27709
United States

Mr Barry Uscinski
Department of Applied Mathematics and Theoretical
Physics
University of Cambridge
Silver Street
Cambridge, CB3 9EW
United Kingdom

CONTENTS

	Page
THEME	iii
TECHNICAL PROGRAMME COMMITTEE	iv
EDITOR'S COMMENTS by K.C.Yeh	ix
RANDOMIZED YET CIVILIZED by L.B.Felsen	x
	Reference
SESSION I – GENERAL	
SESSION CHAIRMAN'S SUMMARY	S1
COUPLED MODE THEORY APPROACH TO DEPOLARIZATION ASSOCIATED WITH PROPAGATION IN TURBULENT MEDIA by B.Crosignani and P.Di Porto	1
EXPERIMENT AND THEORY FOR BACKSCATTERING ENHANCEMENT AND IMAGING IN RANDOM MEDIA by A.Ishimaru and Y.Kuga	2
GEOMETRICAL THEORY OF DIFFRACTION FOR HIGH FREQUENCY COHERENCE FUNCTIONS IN A WEAKLY RANDOM MEDIUM WITH INHOMOGENEOUS BACKGROUND PROFILE by R.Mazar and L.B.Felsen	3
SESSION II: SURFACE SCATTERING	
SESSION CHAIRMAN'S SUMMARY	S2
MULTIPLE SCATTERING FROM ROUGH SURFACES by J.A.DeSanto	4
REGIONS OF VALIDITY FOR SOME ROUGH SURFACE SCATTERING MODELS by R.J.Papa and J.F.Lennon	5
Paper 6 withdrawn	
MARKOV RANDOM FIELDS: A STRATEGY FOR CLUTTER MODELLING by S.P.Luttrell	7
A SCATTERING MODEL FOR FORESTED AREA by M.A.Karam and A.K.Fung	8
COHERENT SCATTERING FROM RANDOM MEDIA by C.J.Oliver	9
SESSION III : MULTIPLE SCATTERING EFFECTS	
SESSION CHAIRMAN'S SUMMARY	S3
Paper 10 withdrawn	
THE ENHANCEMENT EFFECT OF THE BACKSCATTERED INTENSITY IN A RANDOM MEDIUM by C.C.Yang and K.C.Yeh	11
MULTIPLE SCATTERING EFFECTS OF RANDOM DISTRIBUTIONS OF IRREGULARLY SHAPED PARTICLES ON INFRARED AND OPTICAL PROPAGATION by E.Bahar and M.A.Fitzwater	12

Reference

HEIRARCHICAL SCATTERING MODELS
by E.Jakeman 13

GENERATION AND PROPERTIES OF SELF-SIMILAR STOCHASTIC PROCESSES WITH APPLICATION TO RAY PROPAGATION IN RANDOM MEDIA
by J.H.Jefferson and J.D.Anderson 14

SPACE-TIME STATISTICS OF WAVES PROPAGATING THROUGH A DEEP PHASE SCREEN
by S.J.Franke and C.H.Liu 15

SESSION IV: ATMOSPHERIC EFFECTS

SESSION CHAIRMAN'S SUMMARY S4

LINE-OF-SIGHT MILLIMETER WAVE PROPAGATION CHARACTERISTICS
by S.F.Clifford, R.J.Hill, R.B.Fritz, R.A.Bohlande, and R.W.McMillan 16

IMAGERIE OPTIQUE A TRAVERS LA TURBULENCE ATMOSPHERIQUE
par G.Rousset, J.C.Fontanella, J.Primot et A.Sève 17

INFRARED ATMOSPHERIC TRANSMISSION/EMISSION MEASUREMENT IN A MARITIME ENVIRONMENT
by G.J.Bishop and I.W.Larkin 18

A PRECIPITATION SCATTER EXPERIMENT AT 30 GHz
by H.Schmiedel and A.Ochs 19

OBSERVED PHASE DELAY THROUGH RAIN AT 96 GHz
by K.C.Allen 20

FM-CW RADAR REMOTE SENSING OF HYDROMETERS
by L.P.Ligthart and J.S.van Sinttruyen 21

SESSION V: OCEAN SURFACE EFFECTS

SESSION CHAIRMAN'S SUMMARY S5

MODELISATION DE L'INTERACTION ENTRE UNE ONDE ELECTROMAGNETIQUE ET LA SURFACE DE LA MER
par M.Fournier 22

ROUGH SURFACE PROPAGATION AND SCATTER WITH APPLICATIONS TO GROUND WAVE REMOTE SENSING IN AN OCEAN ENVIRONMENT
by J.Walsh and S.K.Srivastava 23

WAVE-TILT SOUNDING OF TROPOSPHERIC DUCTS ABOVE THE SEA
by D.P.Chrissoulidis and E.E.Kriezis 24

I-BAND MULTIPATH PROPAGATION OVER THE SEA SURFACE
by C.J.Baker and K.D.Ward 25

ETUDE EXPERIMENTALE ET MODELISATION DU PHENOMENE DE REFLEXION SUR LA MER A 36 GHz
par Y.Hurtaud, C.Terret, J.P.Daniel et A.Junchat 26

SESSION VI: IMPACT ON SYSTEMS

SESSION CHAIRMAN'S SUMMARY S6

RANDOM PROPAGATION THROUGH THE LONGWAVE CHANNEL
by F.J.Kelly, F.J.Rhoads and M.D.Andrews 27

MODELING OF WIDEBAND HF CHANNELS
by M.Nesenbergs 28

Reference

Paper 29 withdrawn

PROPAGATION AND PERFORMANCE MEASUREMENTS OVER A DIGITAL TROPOSCATTER COMMUNICATIONS LINK
by J.J.Lemmon 30

MEASUREMENT, MODELING, AND SIMULATION OF LOS MICROWAVE CHANNELS
by J.A.Hoffmeyer and L.E.Vogler 31

STRUCTURES OF DENSITY AND VELOCITY FLUCTUATIONS IN THE AURORAL OVAL AND THEIR IMPACT ON COMMUNICATION AND RADAR SYSTEMS
by Sunanda Basu, Santimay Basu, W.R.Coley and N.C.Maynard 32

IMPULSE RESPONSE MEASUREMENTS AND CHARACTERIZATION OF WIDEBAND VHF RADIO LINKS
by P.Lo Muzio, G.Guidotti, N.Benvenuto and S.Pupolin 33

SESSION VII: THEORY

SESSION CHAIRMAN'S SUMMARY S7

INTENSITY FLUCTUATIONS DUE TO MOVING POINT SOURCES
by B.J.Uscinski 34

CROSS-FREQUENCY CORRELATION OF INTENSITY FLUCTUATIONS IN PHASE-CHANGING MEDIA
by S.J.Miller 35

MODELE DE PROPAGATION D'UNE ONDE ELECTROMAGNETIQUE DANS UN MILIEU IONISE A FORTES FLUCTUATIONS PAR LA METHODE DES ECRANS DE PHASE
par Y.Beniguel et B.Gibert 36

ON THE APPLICABILITY OF CONTINUOUS SCATTERING METHODS TO DISCRETE SCATTERING PROBLEMS
by I.M.Besieris 37

ON FUNCTIONAL APPROACH TO RANDOM WAVE PROPAGATION PROBLEMS
by P.L.Chow 38

NUMERICAL SIMULATION OF WAVE PROPAGATION IN RANDOM MEDIA
by M.Spivack 39

SESSION VIII: DISCRETE RANDOM MEDIUM

SELECTIVE EXTINCTION OF A DISPERSION OF SINGLE AND AGGREGATED LAYERED SPHERES
by F.Borghese, P.Denti, R.Saija, G.Toscano and O.I.Sindoni 40

REFLECTIVITE ELECTROMAGNETIQUE D'UN MILIEU ALEATOIRE INHOMOGENE CONTINU A SYMETRIE CYLINDRIQUE
par G.Muller et F.Molinet 41

MULTIPLE SCATTERING OF WAVES IN RANDOM MEDIA CONTAINING NON-SPHERICAL SCATTERERS
by V.V.Varadan, V.K.Varadan and Y.Ma 42

NON-LINEAR EFFECTS ON THE ATMOSPHERIC TRANSMISSION OF HIGH-FLUX ELECTROMAGNETIC BEAMS
by R.L.Armstrong 43

A STATISTICAL ANALYSIS OF POLAR METEOR SCATTER PROPAGATION IN THE 45-104 MHz BAND
by M.Sowa, J.M.Quinn, J.E.Rasmussen, P.A.Kossey and J.C.Ostergaard 44

	Reference
MONTE CARLO SIMULATION OF MULTIPLE SCATTERING EFFECTS OF MILLIMETER WAVES FROM RAIN FOR A BISTATIC RADAR by P.H.Voss and H.Jeske	45
SESSION IX: IONIZED MEDIUM	
SESSION CHAIRMAN'S SUMMARY	S9
REMOTE SENSING OF INTERPLANETARY SHOCKS USING A SCINTILLATION METHOD by A.Hewish	46
Paper 47 withdrawn	
MAGNETIC STORM EFFECTS ON F LAYER IRREGULARITIES NEAR THE AURORAL OVAL by J.Aarons and A.S.Rodger	48
SPECULAR SCATTER: A NEW MECHANISM FOR IONOSPHERIC BACKSCATTER by G.S.Sales	49
IONOSPHERIC SCINTILLATIONS AND IN-SITU MEASUREMENTS AT AN AURORAL LOCATION IN THE EUROPEAN SECTOR by Santimay Basu, Sunanda Basu, E.McKenzie and D.Weimer	50
ROUND TABLE DISCUSSION	RTD
LIST OF PARTICIPANTS	P

EDITOR'S COMMENTS

The subject of wave scattering and propagation in random media is old. It can be traced back at least to the time of Rayleigh in 1892. Over this long period of nearly one hundred years, there have been periodic revivals of interest in this field. The continued interest in this subject matter stems from the realization that the propagation medium occurring naturally is invariably highly complex and a possible and successful way of describing such a complex medium is to apply notions of the stochastic theory. Recent impetus on investigations of such problems comes from remote sensing and communications. It is therefore felt useful for AGARD to revisit this area and to have on record the most up-to-date information.

The response to the Call for Papers was overwhelming. The papers covered a wide spectrum of random media, such as rough surfaces, forest, atmospheric turbulence and precipitation, ocean environment, ionosphere and interplanetary shocks. In over forty papers presented at the meeting, their effects on waves were discussed and investigated. The frequency at which the effects were reported was as low as 300 kHz or as high as optical frequencies, and in many cases at some frequency between these two extremes. The papers were organized into nine sessions, lasting four and one-half days.

The papers appearing in these proceedings have been printed by a photographic process from camera-ready manuscripts supplied by each author. The questions and answers on each paper were prepared in written form by the discussers involved. Some minor editing has been made for clarity and uniformity. I apologize to some discussers for making these minor revisions without first obtaining their approval.

Considerable help from members of the Technical Programme Committee has been provided. I want especially to thank Dr Barry Uscinski of the United Kingdom and Dr Walter A.Flood of the United States for their assistance. Each Session Chairman was asked to prepare a summary of papers presented in his session. I would like to thank them all, not only for keeping the presentations running at a smooth pace, but also for their cooperation in writing the summaries. Dr L.B.Felsen has agreed to have his piece "Randomized, Yet Civilized" included in these proceedings. He has expressed well the sentiments of all participants toward our Italian hosts.

These proceedings are a record of this symposium. I would like to thank all the participants, many of them very distinguished, for making it a success. It is a pleasure to acknowledge the interest and support of the EPP Chairman and Deputy Chairman. The EPP Executive and his staff have been most helpful. At Illinois, Mrs Belva Edwards has assisted me in editorial matters and Mr Jean-Frederic Wagen has helped on language matters.

Urbana, Illinois
September, 1987

K.C.Yeh

RANDOMIZED, YET CIVILIZED

by

L.B.Felsen

Waves travel here, waves travel there,
Some travel to, some travel fro.
The EM Propagation Panel
Is much concerned where these waves go.

Since AGARD is in NATO's fold,
Its meetings move from state to state.
Their route in this way simulates
The paths on which waves propagate.

Paths can be straight, they can be curved,
Yet start and end are well in hand.
Choosing the meeting site this way,
Permits the sequence to be planned.

But this Spring's Meeting, one may note,
Has propagation *randomized*.
Has impact on the meeting site
From this been fully realized?

The ones who with this problem coped
Are our kind Italian friends.
Just how they reasoned their way through
May indicate new future trends.

They chose *hotel* sites inside Rome,
But this is far from where we *meet*.
Yet both locales are really close
By rationale that's hard to beat.

Ingenious concepts, as is known,
Provide the Latin Logic's strength:
You can relate two distant points
By stretching correlation length.

That's what was done. Statistics helped
To implement this clever scheme.
Thus, the logistics as arranged
Accommodate the random theme.

Within this framework, all runs well.
Each bus trip the ensemble fills.
Each sample follows strict routine,
Which military thought instills.

Vigna de Valle — outside Rome —
Here nature offers views serene.
Gone is polluted city air.
What we breathe in is fresh and clean.

History also gets its due
From aviation's early days.
In the museum, we observe
Old planes and pilots' cocky ways?

The Air Force has its discipline.
Yet, there is also grace and charm
In typically Italian style,
Which does rigidity disarm.

So let us thank our Air Force hosts
For having welcomed us on base,
For having bent established rules
To cater to civilian ways.

You have prepared a banquet feast
With choice of delicacies vast.
We put our diet plans aside
And tasted all from first to last.

Your hospitality has launched
The meeting to a splendid start.
It all bodes well for what's to come
Before, at last, we all depart.

The AGARD spirit has prevailed.
Let us salute you. You've been kind.
We've come from many different lands,
Yet friendship here is what we find.

GRAZIE

Presented at the banquet on the first day of the Electromagnetic Wave Propagation Panel on "Scattering and Propagation in Random Media" held in Rome, Italy, from 18—22 May 1987.

SUMMARY OF SESSION I

GENERAL

by

A.N.Ince, Session Chairman
(The following material was supplied by the Editor)

This session contains three papers. The first paper (by Crosignani and Di Porto) is concerned with the depolarization of a vector wave propagating in a random continuum. The problem is formulated by means of the coupled-mode theory. The depolarization ratio of an initially linearly polarized wave has been obtained for the case of a Gaussian correlation. It is very small in the terrestrial atmosphere.

In the second paper, Ishimaru and Kuga review the phenomenon of backscattering enhancement and the imaging through a random medium. The backscattering enhancement is shown to be related to the weak Anderson localization in the study of transport of electrons in strongly disordered material. They first review the experimental results and then propose a diffusion theory which predicts an angular width that is in agreement with experimental observations. The image transmission characteristics are expressed by the modulation transfer function. Under the small-angle approximation, the agreement between theory and experiment has been obtained.

A general mathematical framework in treating the problem of reflection, diffraction and scattering that can occur in a random medium is constructed by Mazer and Felsen (the third paper) under the high frequency approximation. The major building block in this construction is the propagator which is provided by the geometrical theory of diffraction. The two-point coherence function is obtained formally for some general problems.

COUPLED-MODE THEORY APPROACH TO DEPOLARIZATION ASSOCIATED WITH PROPAGATION IN TURBULENT MEDIA

B. Crosignani and P. Di Porto
Fondazione Ugo Bordoni, Via Baldassarre Castiglione 59, 00142 Roma, Italy
and
Dipartimento di Fisica dell'Università dell'Aquila, Piazza dell'Annunziata 1, 67100 L'Aquila, Italy

SUMMARY

The problem of light depolarization in a turbulent atmosphere is revisited by means of coupled-mode theory.[1] This allows in particular to evaluate the depolarization ratio for a plane wave and to compare its expression with the one obtained in the frame of two distinct approaches predicting different behaviors.[2,3]

1. INTRODUCTION

The analysis of depolarization induced on a light beam propagating in a turbulent medium has been the object of theoretical and experimental investigation about twenty years ago. Since then, the subject has received little attention, also in view of the fact that depolarization effects turn out to be extremely small for the relevant case of terrestrial atmosphere. However, this topic has never been completely clarified from a theoretical point of view, since the two employed approaches[2,3] give rise to completely different expressions for the depolarization ratio as a function of the physical parameters of the problem (path length, wavelength, and refractive-index fluctuations). While Ref.2 hinges upon a direct generalization of the simple physical model first introduced by Hodara[4] in the frame of geometrical optics, in Ref.3 the calculations are based on Rytov's method. In order to settle the argument, we have reconsidered the problem by adopting a third procedure which takes advantage of coupled-mode theory, a formalism we have already employed to describe propagation of a scalar field in a turbulent medium.[5] In particular, our approach, which generalizes the scalar theory developed in Ref.5 to include depolarization effects, turns out to provide a depolarization ratio coincident with that worked out in Ref.2. The limits of validity of the result found in Ref.3 are also discussed in some detail.

2. COUPLED-MODE FORMALISM

Let us assume the turbulent medium to be characterized by a fluctuating refractive index of the form

$$n(x,y,z) = n_1 + \delta n(x,y,z) \quad , \tag{1}$$

with $|\delta n| \ll 1$ ($n_1 \simeq 1$ and $|\delta n| \simeq 10^{-6}$ for terrestrial atmosphere). The coupled-mode approach consists in expanding the propagating field in terms of the modes pertaining to the ideal medium characterized by $n = n_1$ and to look for the evolution of the expansion coefficients as functions of the z-coordinate coinciding with the (average) propagation direction. This can be formalized[6] by introducing the ideal modes

$$\underline{E}(\underline{\xi},1;\underline{r}) = N_1 \exp(-i\underline{\xi}\cdot\underline{r})\{\hat{x} - (\xi_x/\beta_\xi)\hat{z}\} \quad ,$$

$$\underline{E}(\underline{\xi},2;\underline{r}) = N_2 \exp(-i\underline{\xi}\cdot\underline{r})\{(\xi_x\xi_y/\beta_\xi)\hat{x} - (\beta_\xi + \xi_x^2/\beta_\xi)\hat{y} + \xi_y\hat{z}\} \quad , \tag{2}$$

where $\underline{r} = (x,y)$, $\beta_\xi = (k^2-\xi^2)^{\frac{1}{2}}$ with $k=2\pi/\lambda=\omega n_1/c$, the transverse wave-vector $\underline{\xi}$ is restricted to $0 \le \xi \le k$ and

$$N_1 = (1/2\pi)\{\beta_\xi \omega\mu_0/(\beta_\xi^2+\xi_x^2)\}^{\frac{1}{2}} \quad , \quad N_2 = (1/2\pi)\{\beta_\xi/\omega\varepsilon_1(\beta_\xi^2+\xi_x^2)\}^{\frac{1}{2}} \quad . \tag{3}$$

The electric field is then expressed as

$$\underline{E}(\underline{r},z,t) = \sum_{\sigma=1}^{2} \iint d\underline{\xi}\, \underline{E}(\underline{\xi},\sigma;\underline{r})\, c(\underline{\xi},\sigma;z) \exp(i\omega t - i\beta_\xi z) \quad , \tag{4}$$

where the expansion coefficients $c(\underline{\xi},\sigma;z)$ obey the set of coupled differential equations

$$\frac{dc}{dz}(\underline{\xi},\sigma;z) = \sum_{\sigma'}\iint d\underline{\xi}'\{K(\underline{\xi},\sigma;\underline{\xi}',\sigma';z)\exp\{i(\beta_{\xi} - \beta_{\xi'})z\}c(\underline{\xi}',\sigma';z)\} \quad , \tag{5}$$

with

$$K(\underline{\xi},\sigma;\underline{\xi}',\sigma';z) = (\omega\varepsilon_0/2i)\int_{-\infty}^{+\infty}\iint d\underline{r}\{n^2(\underline{r},z) - n_1^2\}\underline{E}^*(\underline{\xi},\sigma;\underline{r})\cdot\underline{E}(\underline{\xi}',\sigma';\underline{r}) \quad , \tag{6}$$

whose solution is equivalent to that of Maxwell's equations. From Eqs.(5) we derive, by means of standard iteration procedure,

$$\begin{aligned}
\frac{d}{dz}\{c_2(\underline{\xi},2;z)c_2^*(\underline{\xi}',2;z)\} = \int_0^z dz'\iint d\underline{\xi}''\iint d\underline{\xi}'''\{&\exp\{i(\beta_{\xi} - \beta_{\xi''})z + i(\beta_{\xi''} - \beta_{\xi'''})z'\} \\
&\{K(\underline{\xi},2;\underline{\xi}'',2;z)K(\underline{\xi}'',2;\underline{\xi}''',2;z')c(\underline{\xi}''',2;z')c^*(\underline{\xi}',2;z') \\
&+K(\underline{\xi},2;\underline{\xi}'',2;z)K(\underline{\xi}'',2;\underline{\xi}''',1;z')c(\underline{\xi}''',1;z')c^*(\underline{\xi}',2;z') \\
&+K(\underline{\xi},2;\underline{\xi}'',1;z)K(\underline{\xi}'',1;\underline{\xi}''',1;z')c(\underline{\xi}''',1;z')c^*(\underline{\xi}',2;z') \\
&+K(\underline{\xi},2;\underline{\xi}'',1;z)K(\underline{\xi}'',1;\underline{\xi}''',2;z')c(\underline{\xi}''',2;z')c^*(\underline{\xi}',2;z')\} \\
&+ \exp\{i(\beta_{\xi} - \beta_{\xi''})z - i(\beta_{\xi'} - \beta_{\xi'''})z'\} \\
&\{K(\underline{\xi},2;\underline{\xi}'',1;z)K^*(\underline{\xi}',2;\underline{\xi}''',2;z')c(\underline{\xi}'',2;z')c^*(\underline{\xi}''',2;z') \\
&+K(\underline{\xi},2;\underline{\xi}'',2;z)K^*(\underline{\xi}',2;\underline{\xi}''',2;z')c(\underline{\xi}'',2;z')c^*(\underline{\xi}''',1;z') \\
&+K(\underline{\xi},2;\underline{\xi}'',1;z)K^*(\underline{\xi}',2;\underline{\xi}''',2;z')c(\underline{\xi}'',2;z')c^*(\underline{\xi}''',2;z') \\
&+K(\underline{\xi},2;\underline{\xi}'',1;z)K^*(\underline{\xi}',2;\underline{\xi}''',1;z')c(\underline{\xi}'',1;z')c^*(\underline{\xi}''',1;z')\}\}
\end{aligned}$$

$$+ \text{ complex conjugate terms with the substitution } \underline{\xi} \leftrightarrow \underline{\xi}' . \tag{7}$$

If we now assume the field to be initially polarized along the 1-direction (practically coincident with the x-direction) and take advantage of the small depolarization induced by the atmosphere, we can neglect on the R.H.S. of Eq.(7) all the terms but the one containing $c(\underline{\xi}'',1;z')c^*(\underline{\xi}''',1;z')$. By taking the ensemble average of the resulting equation over the possible realizations of the system, we obtain, under the hypothesis of negligible variation of $\langle c(\underline{\xi}'',1;z')c^*(\underline{\xi}''',1;z')\rangle$ over a scale of the order of the correlation length of the refractive index fluctuations,

$$\begin{aligned}
\frac{d}{dz}\langle c(\underline{\xi},2;z)c^*(\underline{\xi}',2;z)\rangle = \int_0^z dz'\iint d\underline{\xi}''\iint d\underline{\xi}''' &\langle K(\underline{\xi},2;\underline{\xi}'',1;z)K^*(\underline{\xi}',2;\underline{\xi}''',1;z')\rangle \\
&\times \langle c(\underline{\xi}'',1;z')c^*(\underline{\xi}''',1;z')\rangle \\
&\times \exp\{i(\beta_{\xi} - \beta_{\xi''})z - i(\beta_{\xi'} - \beta_{\xi'''})z'\} \\
&+ \text{c.c. with the substitution } \underline{\xi} \leftrightarrow \underline{\xi}' .
\end{aligned} \tag{8}$$

If we assume $\langle c(\underline{\xi}'',1;z')c^*(\underline{\xi}''',1;,z')\rangle$ to be given (due to small depolarization), by the expression already worked out for a linearly polarized field,[5] Eq.(8) can be directly integrated. The amount of power transferred to the y-polarized component is then evaluated as[5]

$$\langle|E_2(\underline{r},z,t)|^2\rangle = \frac{1}{(2\pi)^2}\iint d\underline{\xi}\iint d\underline{\xi}'\exp\{i(\underline{\xi}'-\underline{\xi})\cdot\underline{r} + i\beta_{\xi'}z - i\beta_{\xi}z\}\langle c(\underline{\xi},2;z)c^*(\underline{\xi}',2;z)\rangle . \tag{9}$$

3. EVALUATION OF THE DEPOLARIZATION RATIO

Let us first evaluate the expression of $\langle K(\underline{\xi},2;\underline{\xi}'',1;z)K^*(\underline{\xi}';2,\underline{\xi}''',1;z')\rangle$ appearing in Eq.(8). Recalling Eq.(6), we have

$$K(\underline{\xi},z;\underline{\xi}'',1;z) = -(ik/4\pi^2\beta_{\xi}) \int_{-\infty}^{+\infty} d\underline{r} \exp(i(\underline{\xi}-\underline{\xi}'')\cdot\underline{r})(\xi''_x\xi''_y/\beta_{\xi''} - \xi_x\xi''_y/\beta_{\xi})\delta n(\underline{r},z) \quad , \tag{10}$$

where we have written, according to Eq.(1), $n^2-n_1^2 \simeq 2n_1\delta n$ and $n_1^2/n^2 \simeq 1$, so that

$$\langle K(\underline{\xi},z;\underline{\xi}'',1;z')K^*(\underline{\xi}',z;\underline{\xi}''',1;z'')\rangle = (k^2/4\pi^2\beta_{\xi}\beta_{\xi'})(\xi''_x\xi''_y/\beta_{\xi''} - \xi_x\xi''_y/\beta_{\xi})$$
$$\times (\xi'''_x\xi'''_y/\beta_{\xi'''} - \xi'_x\xi'''_y/\beta_{\xi'})\delta^{(2)}(\underline{\xi}-\underline{\xi}''+\underline{\xi}'''-\underline{\xi}')G(\underline{\xi}'-\underline{\xi}'',|z'-z''|) \tag{11}$$

where $\delta^{(2)}$ is the two-dimensional delta-function and

$$G(\underline{\xi}'-\underline{\xi}'',|z'-z''|) = (1/4\pi^2)\int_{-\infty}^{+\infty} d\underline{\rho} \exp(i(\underline{\xi}'-\underline{\xi}'')\cdot\underline{\rho})\langle \delta n(\underline{\rho},|z'-z''|)\delta n(0,0)\rangle \tag{12}$$

is the spatial Fourier transform of the correlation function $\langle \delta n(\underline{r},z)\delta n(\underline{r}',z')\rangle$ of the refractive-index fluctuations associated with the turbulence field, assumed to be homogeneous and isotropic.

The expression of $\langle c(\underline{\xi}'',1;z)c^*(\underline{\xi}''',1;z)\rangle$ can be found in Ref.5 and reads, for an incident plane wave

$$\langle c(\underline{\xi}'',1;z)c^*(\underline{\xi}''',1;z)\rangle = |E_0|^2\delta^{(2)}(\underline{\xi}''-\underline{\xi}''')\pi A \exp\{-A(\xi''^2_x+\xi''^2_y)/4\} \quad , \tag{13}$$

with

$$A = 1/Dz \quad , \tag{14}$$

D being a diffusion coefficient associated with the presence of turbulence ($=\pi^{\frac{1}{2}}k^2\langle\delta n^2\rangle/d$).

We can now substitute Eqs.(11) and (13) into Eq.(8), integrate over z, and insert the result into Eq.(9), thus getting

$$\langle |E_2(\underline{r},z,t)|^2\rangle = \frac{1}{4\pi}|E_0|^2k^2\int_0^z dz' \int_0^z dz'' \iint d\underline{\xi} \iint d\underline{\xi}'' \exp\{i(\beta_{\xi}-\beta_{\xi''})(z'-z'')\}\frac{1}{\beta_{\xi}\beta_{\xi'}}$$
$$\times \{\frac{\xi''_x\xi''_y}{\beta_{\xi''}} - \frac{\xi_x\xi''_y}{\beta_{\xi}}\}\{\frac{\xi''_x\xi''_y}{\beta_{\xi''}} - \frac{\xi_x\xi''_y}{\beta_{\xi}}\}G(\underline{\xi}-\underline{\xi}'',|z'-z''|)\frac{1}{Dz''}\exp\{-(\xi''^2_x+\xi''^2_y)/4Dz''\} \quad . \tag{15}$$

Equation (15) can be approximately rewritten as

$$\langle |E_2(\underline{r},z,t)|^2\rangle = \frac{1}{4\pi k^2}|E_0|^2\int dz' \iint d\underline{\xi} \iint d\underline{\xi}'' \; \xi''^2_y(\xi''_x-\xi_x)^2\hat{G}(\underline{\xi}-\underline{\xi}'')\frac{1}{Dz'}\exp\{-(\xi''^2_x+\xi''^2_y)/4Dz'\}, \tag{16}$$

where

$$\hat{G}(\underline{\xi}-\underline{\xi}'') = \int_0^{\infty} G(\underline{\xi}-\underline{\xi}'',\zeta)d\zeta \quad , \tag{17}$$

having taken advantage of the fact that $G(\underline{\xi}'-\underline{\xi}'',\zeta)$ is a short-range correlation function, which goes to zero for $\zeta \geq d >> \lambda$ (d being of the order of magnitude of the typical scale of turbulence) and that, for small angular divergence of the beam, $\beta_{\xi} \simeq \beta_{\xi'} \simeq k$.

The integrals appearing in Eq.(16) can be performed after assuming a Gaussian shape for the correlation function of the refractive-index fluctuations, that is

$$\langle \delta n(\underline{\rho},\zeta)\delta n(0,0)\rangle = \langle\delta n^2\rangle \exp\{-(\rho^2+\zeta^2)/d^2\} \quad , \tag{18}$$

thus getting for the depolarization ratio $R=\langle|E_2|^2\rangle/|E_0|^2$ the final expression

$$R = 2\pi\langle\delta n^2\rangle^2(z^2/d^2) \quad , \tag{19}$$

which coincides with that worked out in Ref.2.

4. DISCUSSION

The dependence on $\langle\delta n^2\rangle$, z and d furnished by Eq.(19) is different from that worked out in Ref.3 which reads

$$R = 4\pi^{\frac{1}{2}}\langle\delta n^2\rangle(z/d)(1/k^2d^2) \quad , \tag{20}$$

also if, for terrestrial atmosphere, both approaches imply an extremely small depolarisation.

In order to explain this discrepancy, we recort to the Luneburg-Kline asymptotic expansion[7] in 1/k,

$$\underline{E}(\underline{r},z) \sim \exp(-ikS(\underline{r},z))\sum_{m=0}^{\infty} \underline{E}_m(\underline{r},z)/(-ik)^m \quad , \tag{21}$$

whose zero-th order term corresponds to geometrical-optics approximation. In particular, the eikonal S and $\underline{E}_0$ obey the relations

$$(\underline{\nabla}S)^2 - n^2(\underline{r},z) = 0 \quad , \tag{22}$$

$$(\nabla^2 S + 2\underline{\nabla}S\cdot\underline{\nabla})\underline{E}_0 + 2\{\underline{E}_0\cdot\underline{\nabla}(\ln n)\}\underline{\nabla}S = 0 \quad . \tag{23}$$

Since Eq.(23) does not contain k and, for line-of-sight propagation of an initially plane wave S is a real quantity, the lowest-order amplitude does not contain k either, which in turn implies (if we neglect $\underline{E}_1/k$ compared to $\underline{E}_0$) a depolarization ratio independent from k, in agreement with our result.

Conversely, the result of Ref.3 corresponds to neglecting $\underline{E}_0$ with respect to $\underline{E}_1/k$, which in fact yields a depolarization ratio proportional to $1/k^2$, as in Eq.(20). The range of validity of the two approaches can be easily obtained by comparing the magnitude of the two depolarization ratios. By doing this, it is immediate to check that our result is valid for traveled distances z larger than the length z_c given by

$$z_c = \frac{1}{\pi^3 <\delta n^2> k^2 d} \quad . \tag{24}$$

For typical values of the turbulence parameters ($<\delta n^2> \approx 10^{-12}$ and d of the order of few centimeters), z_c turns out to be, at optical frequencies ($k \approx 10^5$ cm^{-1}), of the order of 1 meter.

5. CONCLUSIONS

We have developed a formalism which, as a generalization of a previous one based on coupled-mode theory and dealing with scalar propagation in a turbulent medium, allows us to describe vector propagation. In particular, our method is employed to evaluate the depolarization undergone by an initially linearly polarized plane wave and to compare the corresponding depolarization ratio with the results worked out in the frame of other approaches. Also if the depolarization effects are in practice very small, this comparison turns out to be very useful for checking the range of validity of the different approaches, respectively based on Rytov's method and coupled-mode theory. While in the scalar case the two formalisms yield the same results, in the vector case they possess different ranges of validity according to the relevant propagation parameters.

REFERENCES

1. D. Marcuse, "Theory of Dielectric Optical Waveguides", N.Y., Academic Press, 1974.

2. A.A.M. Saleh, "An investigation of laser wave depolarization due to atmospheric transmission", IEEE J. Quantum Electron., QE-3, No.11, 1967, 540-543.

3. J.W. Strohbehn and S.F. Clifford, "Polarization and angle-of-arrival fluctuations for a plane wave propagated through a turbulent medium", IEEE J. Trans. on Antennas and Propagation, AP-15, No.3, 1967, 416-421.

4. H. Hodara, "Laser wave propagation through the atmosphere", Proc. IEEE, 54, No.3, 1966, 368-375.

5. B. Crosignani and P. Di Porto, "Electromagnetic propagation in a turbulent medium: a new approach", J. Opt. Soc. Am., 73, No.11, 1983, 1581-1584.

6. B. Crosignani and A. Yariv, "Degenerate four-wave mixing in the presence of nonuniform pump wave fronts", J. Opt Soc. Am. A, 1, No. 10, 1984, 1034-1039.

7. S. Solimeno, B. Crosignani, and P. Di Porto, "Guiding, Diffraction, and Confinement of Optical Radiation", N.Y., Academic Press, 1986, p. 67.

DISCUSSION

I.M. Besieris, US

You showed an equation for the correlation function of the coupling coefficients. If I heard you correctly, you referred to that equation as an exact one. Would you please comment on the validity of your statement?

Author's Reply

The equation is an approximate one, the approximation basically consisting of 1) assuming the evolution of the strong polarization component to be that described by scalar theory, and 2) assuming negligible variation of the correlation function of the coupling coefficients over a scale of the order of d.

L.B. Felsen, US

You say that you know the result from Strohbehn and Clifford by assuming that the second term in the Luneberg-Kline asymptotic expansion overpowers the leading term. But this contradicts the concept of asymptotic expansions. Can you explain?

Author's Reply

It turns out that there are actually two smallness parameters, that is (1/kd) and $\langle \delta u^2 \rangle$. The zero-order term $\underline{E}_0$ in (1/kd) of the L-K asymptotic expansion is actually of the order $\langle \delta u^2 \rangle^2$ while $\underline{E}_1$ is of the order $\langle \delta u^2 \rangle$, so that there is a range of values of (1/kd) and $\langle \delta u^2 \rangle$ over which $\underline{E}_1/k$ can become larger than $\underline{E}_0$. Our result is valid for (1/kd) → 0 and is of the order $\langle \delta u^2 \rangle^2$; the Strohbehn and Clifford result is valid to the order $\langle \delta u^2 \rangle$ only, and therefore gives a zero depolarization for (1/kd) → 0.

EXPERIMENT AND THEORY FOR BACKSCATTERING ENHANCEMENT AND IMAGING IN RANDOM MEDIA

by
Akira Ishimaru
Yasuo Kuga
Department of Electrical Engineering, FT-10
University of Washington
Seattle, Washington 98195
USA

SUMMARY

When a wave is incident on a dense distribution of discrete scatterers, turbulent media, or rough surfaces, the backscattering is enhanced under certain conditions giving a sharp peak in the backward direction. We show experimentally and theoretically that the angular width of the peak is related to the transport coefficient and that the enhancement is caused by the constructive interference of two waves traveling through the same particles in opposite directions. This phenomenon is identified as the weak Anderson localization. The backscattering enhancement can occur from turbulence or rough surfaces which are caused by several mechanisms. A measure of the quality of the image transmission is expressed by the modulation transfer function (MTF). We show experimental and theoretical studies on MTF and speckle interferometry based on the fourth order and short-exposure MTF which can produce diffraction-limited images through random scatterers.

I. INTRODUCTION

It has been known that the backscattering from several media and surfaces exhibits a strong enhancement with a sharp peak in the backward direction [1]-[3]. In 1984 we reported on an optical experiment which shows this enhancement [4]. Subsequently, we reported on the theoretical explanation that the enhancement is caused by the constructive interference of two waves traversing through the same particles in opposite directions [5]. This idea is consistent with our earlier crude explanation (Reference 1, p. 312). We have also reported on the depolarization experiment and further theoretical studies [6]-[8]. Meanwhile, physicists have recognized that the transport of electrons in a strongly disordered material is governed by multiple scattering and that multiple scattering leads to "weak Anderson localization" caused by "coherent backscattering" [9],[10]. It is then shown that both electron localization in disordered material and photon localization in disordered dielectrics are governed by coherent backscattering which is caused by the constructive interference of two waves traversing in opposite directions. Our experimental work in 1984 was followed by several independent optical experiments showing that the backscattering enhancement is a weak localization phenomenon [11],[12],[13]. Theoretical studies on the backscattering enhancement by rough surfaces [14]-[16] and some experimental studies [17] have been reported. In this paper, we present experimental work on backscattering enhancement and a theory based on diffusion approximation [1]. We also present our recent experimental and theoretical studies on image transmission through discrete scatterers [18], which have attracted considerable attention in recent years [19]-[21]. We will also show our recent study on the use of speckle interferometry for imaging through scatterers which may give improved resolution.

2. EXPERIMENTAL RESULTS ON BACKSCATTERING ENHANCEMENT

Our experiments are described in our paper [4] and are given below The experimental setup is shown in Fig. 1. A He-Ne laser with an expanded beam diameter of 30 mm is used as the light source. The beam splitter (BS) reflects approximately 25% of the incident beam, and this reflected beam has fine interference patterns because of the surface coating of the BS. In order to eliminate the effect of the interference patterns, the incident-beam diameter and the input aperture of the detector are adjusted to be much larger than the spacing of the interference patterns.

The transmittance of the BS varies at different angles if the beam is linearly polarized. However, if the incident beam is circularly polarized, the transmittance becomes almost constant within about 60° measured from the normal direction of the BS. Therefore the phase of the incident beam is adjusted such that the beam at the spectrophotometer cell (SC) is circularly polarized. This ensures that the backscattered light, which may retain a part of the incident polarization, receives the same attenuation when it goes through the BS at different angles.

The detector, which consists of a 5-mm-input aperture, a lens, and a 100-μm-core optical-fiber cable, has a field of view (FOV) of 0.195°, and it is mounted on the computer-controlled rotational stage. The light output of the optical-fiber cable is focused onto a low-noise photodiode.

Uniform latex microspheres manufactured by Dow Chemical are used as scatterers; they are suspended in an SC with a 50-mm diameter. The path length of the SC is either 10 or 20 mm, depending on the density. In order to minimize the reflection from the SC glass wall, the SC is tilted about 5° from the vertical direction. The noise level from the water-filled SC is less than -75 dB at all angles.

At the beginning of the experiment, the SC is filled with deionized water, and then the detector is moved to position A in Fig. 1. This output is used as a reference, and each measurement is normalized by this value. Then the detector is moved to $\theta_3 = -10°$, and the backscattered intensity is measured from $\theta_3 = -10°$ to 50° at 0.1°, 0.2°, or 0.5° intervals, depending on the position of the detector. Because of the difference between the indices of refraction of water and of air, the angle θ_1 inside the SC is less than the scan angle θ_3. Therefore the scan range from $\theta_3 = -10°$ to 50° corresponds to θ_1 from -7.5° to 35°.

Since the incident-beam diameter is larger than the input aperture of the detector, the area that the detector sees changes by $1/\cos(\theta_3)$ as the detector moves. Therefore, if a medium is a perfect diffuser and if the incident beam is uniform, the output of the detector should be constant. Except for the sharp peak around $\theta_3 = 0°$, the backscattered intensity from a dense solution of small particles is close to a constant within the angle of -7.5° to 8°.

Experimental results are shown within the angle of -7.5° to 8°. Fig. 2 shows the experimental data for a particle size of 1.101 μm. The data are obtained for four different particle sizes ranging from an average diameter of 0.091 to 5.7 μm and at least seven different densities, up to 40% in some cases. In all cases, the peak of the reflectivity at 0° is observed at high densities, and we found the following results: (1) when the particle size is smaller than the wavelength ($\lambda_w = 0.475$ μm in water), the peak at 0° is small and appears at densities higher than a few percent; (2) when the particle size is 2-4 times greater than λ_w, a sharp peak appears at 0°, and it becomes larger as the density increases; and (3) when the particle size is many times greater than λ_w, the effect of the Mie-scattering pattern becomes apparent even in a dense medium, and the sharp peak at 0° is superimposed upon the Mie-scattering pattern.

3. THEORY OF BACKSCATTERING ENHANCEMENT BASED ON DIFFUSION THEORY

Let us consider a plane wave normally incident on a semi-infinite random medium as shown in Figure 3. The observed scattered wave consists of the first-order scattering I_1 and the multiple scattering I_m. The first-order scattering I_1 is created by the reduced incident intensity, attenuated through the medium, and observed outside the medium. The multiple scattering term I_m contains all orders of the scattering inside the medium including the first-order scattering and this is approximated by the diffusion approximation. Therefore this term inside the medium should be valid far from the incident wave.

The reduced incident specific intensity is given by (see Ref. 1, p. 181)

$$I_{ri}(z') = I_0 \exp(-\rho\sigma_t z') \, \delta(\hat{s} - \hat{s}_i) \quad . \tag{1}$$

The first-order scattering specific intensity I_1 and the bistatic cross section σ_1^o per unit area of the random medium (bistatic scattering coefficient) is given by

$$\sigma_1^o = \frac{4\pi I_1}{I_0} = p(\theta,0) \, \frac{\mu}{\mu+1} \quad , \qquad \mu = \cos\theta \quad , \tag{2}$$

where $p(\theta,0)$ is the phase function in the direction of θ measured from the backward direction when the incident wave is in the direction $\hat{z}$. (See Fig. 3.)

Next consider the multiple scattering I_m. This consists of two terms I_{m1} and I_{m2}. One corresponds to the wave multiply-scattered through many

particles. This is also called the ladder term. We describe this wave by the diffusion approximation. We write the bistatic cross section per unit area of the random medium (bistatic scattering cross coefficient) σ^o_{m1} as follows:

$$\sigma^o_{m1} = \int dV_2 F \quad , \tag{3}$$

$$F = \rho\sigma_s[U - \frac{\bar{\mu}}{\rho\sigma_{tr}} \nabla U\cdot\hat{s}]\, e^{-\rho\sigma_t z/\mu} \quad ,$$

where $\bar{\mu}$ is the mean cosine of the scattering angle, σ_{tr} is the transport cross section of a single particle, and $\hat{s}$ is the unit vector in the scattering direction.

$$\sigma_{tr} = \sigma_t(1 - W_o\bar{\mu}) \quad , \tag{4}$$

where $W_o = \sigma_s/\sigma_t$ is the albedo of a single particle.

The function U is given by

$$U = \int_o^\infty dz' G(\rho,z;z')Q(z') + \frac{1}{2\pi h} G(\rho,z;o)Q_1(o) \quad , \tag{5}$$

$$Q(z') = 3\rho\sigma_s[\rho\sigma_{tr} + \rho\sigma_t\bar{\mu}] \frac{I_o}{4\pi} \exp(-\rho\sigma_t z') \quad ,$$

$$Q_1(o) = \frac{\sigma_s\bar{\mu}}{\sigma_{tr}} I_o \quad , \quad h = \frac{2}{3\rho\sigma_{tr}} \quad .$$

Green's function G is given by (Ref. 1, p. 184)

$$G = \frac{1}{4\pi} \int_o^\infty \frac{\lambda d\lambda}{\gamma} J_o(\lambda\rho) \left[e^{-\gamma|z-z'|} + \frac{h\gamma-1}{h\gamma+1} e^{-\gamma(z+z')}\right] \quad , \tag{6}$$

where $\gamma^2 = \lambda^2 + k_d^2$. Now we note that the integral in (3) is

$$\int dV_2 = 2\pi \int_o^\infty \rho d\rho \int_o^\infty dz \quad . \tag{7}$$

Therefore, noting that

$$\int_o^\infty \rho d\rho\, J_o(\lambda\rho) = \frac{\delta(\lambda)}{\lambda} \quad , \tag{8}$$

we can perform the integration in (3) by evaluating the integrand at $\lambda = 0$.

Next we consider the term corresponding to two waves traversing through the same particles in opposite directions. This is also called the "cyclical term" or the "maximally crossed term." To express this term, we note that the difference between this term I_{m2} and the previous term I_{m1} is that in this case, there is a phase difference given by

$$[e^{i\vec{K}_1\cdot\vec{\rho}_1 - i\vec{K}_s\cdot\vec{\rho}_2}][e^{i\vec{K}_1\cdot\vec{\rho}_2 - i\vec{K}_s\cdot\vec{\rho}_1}]^* = e^{i(\vec{K}_1+\vec{K}_s)\cdot(\vec{\rho}_1-\vec{\rho}_2)} \quad . \tag{9}$$

Therefore, the bistatic scattering coefficient is given by

$$\sigma^o_{m2} = \int dV_2\, e^{-i(\vec{K}_1+\vec{K}_s)\cdot\vec{\rho}} F = (2\pi) \int_o^\infty \rho d\rho\, J_o(K\rho)\, F \quad , \tag{10}$$

where $K = |\vec{K}_1+\vec{K}_s| = k\ 2\sin(\theta/2)$.

Now noting that

$$\int_o^\infty \rho d\rho\, J_o(K\rho)\, J_o(\lambda\rho) = \frac{\delta(\lambda-K)}{\lambda} \quad , \tag{11}$$

we can easily evaluate the integral (10) with the Fourier Bessel transform (6).

Noting that $K \ll \rho\sigma_t$, we get approximately

$$\sigma_{m1}^{o} = A\, f[\theta, \gamma = K_{\ell}]\cos\theta \quad ,$$

$$\sigma_{m2}^{o} = A\, f[\theta, \gamma = (K_d^2 + K^2)^{1/2}]\cos\theta \quad , \tag{12}$$

where

$$A = \frac{\sigma_s^*}{2\pi\sigma_t^* a_{tr}} \left[\frac{\sigma_{tr}}{\sigma_t} + 2\bar{\mu}\right] \quad ,$$

$$f(\theta,\gamma) = \frac{\rho\sigma_{tr} - \bar{\mu}\gamma\cos\theta}{\rho\sigma_{tr} + (2\gamma)^2} \quad ,$$

$$K_d^2 = 3\,\rho\sigma_a \rho\sigma_{tr} \quad ,$$

$$K = k\,2\sin(\theta/2) \quad .$$

The second term in the numerator of $f(\theta,\gamma)$ represents the gradient term of the diffusion approximation and Eq. (12) is valid when this second term is smaller than the first term. Eq. (12) shows that σ_{m2}^{o} has a sharp peak in the backward direction $\theta = 0$. For lossless scatterers, $K_d = 0$ and σ_{m2}^{o} becomes a half of σ_{m1}^{o} when the angle is approximately equal to

$$\theta = \frac{3\rho\sigma_{tr}\lambda}{4\pi(1+3\bar{\mu})} \quad . \tag{13}$$

This angular width is consistent with our experimental data and it shows that the above diffusion theory correctly explains the backscattering enhancement phenomena.

4. IMAGE TRANSMISSION THROUGH RANDOM MEDIA

The quality of an image as observed through a random medium often deteriorates since the high spatial frequency components are usually attenuated. The image transmission characteristics are conveniently expressed by the modulation transfer function (MTF), which represents the ratio of the modulation in the image to that in the object as a function of the spatial frequency (cycles per millimeter cycles per radian) [18]-[21]. The MTF for turbulent media and discrete scatterers has been studied theoretically. In this section, we present our recent experimental work on the MTF and the comparison with the small-angle approximation formula.

The experimental results for the MTF of randomly distributed spherical particles suspended in water were obtained (Fig. 4). The results were measured by using an array detector and black and white strip patterns as an object. According to our study, if the relative index of refraction is 1.2, the error in the small-angle approximation is < 6% for $ka > 10$ and $\tau < 5$. Many of our experimental results of MTF satisfy these conditions. However, in this experiment, because of the use of particles suspended in water, it is necessary to obtain the MTF of a layered medium with different indices of refraction.

We derive an expression of MTF for a layered random medium using the small-angle approximation. As applications of this formula, we considered the shower curtain effect and the MTF for an inhomogeneous medium. Finally, we will obtain numerical results for several different particle sizes and compare them with experimental results [18].

We consider a situation in which four different layers are located between the object and detector as shown in Figure 4. Each layer has its own index of refraction n_j and function H_j which describes the characteristics of a layer and is related to the wave structure function. The object is illuminated by an incoherent light source, and the imaging system satisfies the lens law $1/L + 1/d = 1/f_o$, where L is the air equivalent length between the object and the lens and f_o is the focal length of the lens.

Using the small-angle approximation, the MTF of this medium can be written as the following.

$$M(f) = \exp(-H) \quad ,$$

$$H = \sum_{j=1}^{4} H_j \quad ,$$

$$H_j = \int_o^{L_j} \rho_{n_j} \sigma_{a_j} dx' + \int_o^{L_j} dx' \rho_{n_j} \sigma_{s_j} \frac{1}{2} \int_o^2 p(a_j)[1 - J_o(A_j)]\, a_j da_j \quad . \tag{14}$$

$$A_j = \frac{k_0 n_j \sigma_{s_j} \left(\sum_{i=1}^{j} \frac{\delta_i}{n_i} + \frac{s'}{n_j} \right) \lambda f d}{L} \qquad \text{for } j > 1 \ ,$$

$$A_j = \frac{k_0 \sigma_{s_1} s' f d \lambda}{L} \qquad \text{for } j = 1 \ ,$$

$$L = \frac{\delta_1}{n_1} + \frac{\delta_2}{n_2} + \frac{\delta_3}{n_3} + \frac{\delta_4}{n_4} \ ,$$

where f is the spatial frequency in cycles/mm, λ is the wavelength of the light in the medium (λ(0.6328 μm), k_0 is the free space wave number, and d is the distance between the lens and image detector (68.5 mm). The phase function $p(s_j)$, the absorption cross section σ_{a_j}, the scattering cross section σ_{s_j}, and the number density ρ_{n_j} are those of the layer j. The quantity $s_j = 2 \sin(\theta_j/2)$ is used to include the scattering pattern from 0 to 180° and to reduce error in the small-ang approximation.

The shower curtain effect in which the image of a person close to the shower curtain can be seen clearly, whereas a person farther from the shower curtain is difficult to see, can be explained using Eq. (14). If layer 2 is the shower curtain and δ_1 is the distance between a person and the shower curtain, M(f) of the short δ_1 has a higher cutoff frequency (the spatial frequency at which MTF becomes constant) than the one of the long δ_1. This is because when the argument of the Bessel function J_0 is large, the case for a long δ_1, M_2 becomes close to τ_2 even though the spatial frequency is small. The decrease of the MTF at a high spatial frequency results in the loss of detailed features in the image.

We conducted experimental and numerical studies for 1.101-, 2-02-, 5.7-, and 11.9-μm particles corresponding to ka of 7.3, 13.7, 36.2, and 82.8. Fig. 5 shows the comparison between the experimental data and the calculations for 1.101-μm particles. In calculating M(f), the phase function p(s) is obtained by using the size distribution data supplied by Dow Chemical, and τ is the calculated value. The agreement between experimental and numerical results is good showing the applicability of the small-angle approximation for these cases. However, the differences tend to increase as τ increases. When τ is 10, the expected error in the small-angle approximation is ~20% for ka > 10. We also compared the results for 0.109 and 0.46 μm with the small-angle approximation, but the results are quite different showing the limitation of the small-angle approximation for small ka.

We have also investigated the use of the short-exposure MTF to improve the image resolution. However, this requires the use of the fourth-order moment.

5. CONCLUSIONS

In this paper, we have presented our experimental data and theoretical studies on backscattering enhancement and image transmission. The backscattering enhancement is shown to be caused by two waves traversing the same particles in opposite directions, and the diffusion theory is used to explain the sharp peak in the backward direction. The image transmission is expressed by the modulation transfer function, and the small-angle approximation is used to explain the experimental data.

6. REFERENCES

[1] A. Ishimaru, Wave Propagation and Scattering in Random Media, Volume 1: Single Scattering and Transport Theory and Volume II: Multiple Scattering, Turbulence, Rough Surfaces and Remote-Sensing, Academic Press, New York, 1978.

[2] A. Ishimaru, editor, feature issue on "Wave Propagation and Scattering in Random Media," J. Opt. Soc. Am. A, 2:12, 1985.

[3] Y. A. Kravtsov and A. I. Saichev, "Effects of Double Passage of Waves in Randomly Inhomogeneous Media," Sov. Phys. Usp., 25:7, 494-508, 1982.

[4] Y. Kuga and A. Ishimaru, "Retroreflectance From a Dense Distribution of Spherical Particles," J. Opt. Soc. Am. A, 1:8, 831-835, 1984.

[5] L. Tsang and and A. Ishimaru, "Backscattering Enhancement of Random Discrete Scatterers," J. Opt. Soc. Am. A, 1:8, 836-839, 1984.

[6] Y. Kuga, L. Tsang, and A. Ishimaru, "Depolarization Effects of the Enhanced Retroreflectance From a Dense Distribution of Spherical Particles," J. Opt. Soc. Am. A, 2:4, 616-618, 1985.

[7] L. Tsang and A. Ishimaru, "Theory of Backscattering Enhancement of Random Discrete Isotropic Scatterers Based on the Summation of All Ladder and Cyclical Terms," J. Opt. Soc. Am. A, 2:8, 1331-1338, 1985.

[8] L. Tsang and A. Ishimaru, "Radiative Wave and Cyclical Transfer Equations for Dense Nontenuous Media," J. Opt. Soc. Am. A, 2:12, 2187-2194, 1985.

[9] D. E. Khmel'nitskii, "Localization and Coherent Scattering of Electrons," Physica, 126B, North-Holland, Amsterdam, 235-241, 1985.

[10] P. W. Anderson, "The Question of Classical Localization: A Theory of White Paint?" Philosophical B (magazine), 52:3, 505-509, 1985.

[11] M. P. Van Albada and A. Lagendijk, "Observation of Weak Localization of Light in a Random Medium," Phys. Rev. Lett., 55:24, 2692-2695, 1985.

[12] E. Akkermans, P. E. Wolf, and R. Maynard, "Coherent Backscattering of Light by Disordered Media," Phys. Rev. Lett., 1986.

[13] P. E. Wolf and G. Maret, "Weak Localization and Coherent Backscattering of Photons in Disordered Media," Phys. Rev. Lett., 55:24, 2696-2699, 1985.

[14] A. R. McGurn, A. A. Maradudin, and V. Celli, "Localization Effects in the Scattering of Light from a Randomly Rough Grating," Phys. Rev. B, 31:8, 4866-4871, 1985.

[15] V. Celli, A. A. Maradudin, A. M. Marvin, A. R. McGurn, "Some Aspects of Light Scattering From a Randomly Rough Metal Surface," J. Opt. Soc. Am. A, 2:12, 2225-2239, 1985.

[16] N. Garcia and E. Stoll, "Near-field Effects and Scattered Intensities of Electromagnetic Waves from Random Rough Surfaces," J. Opt. Soc. Am. A, 2:12, 2240-2243, 1985.

[17] E. R. Mendez, K. A. O'Donnell, A. S. Harley, "Scattering From Rough Conducting Surfaces," preprint.

[18] Y. Kuga and A. Ishimaru, "Modulation Transfer Function of Layered Inhomogeneous Random Media Using the Small-Angle Approximation," Appl. Opt., 25:23, 4382-4385, 1986.

[19] N. S. Kopeika, "Spatial-Frequency- and Wavelength-Dependent Effects of Aerosols on the Atmospheric Modulation Transfer Function," J. Opt. Soc. Am., 72:8, 1092-1094, 1982.

[20] A. Zardecki, S. A. W. Gerstl, and J. F. Embury, "Multiple Scattering Effects in Spatial Frequency Filtering," Appl. Opt., 23:22, 4124-4131, 1984.

[21] A. Zardecki, S. A. W. Gerstl, W. C. Tam, and J. F. Embury, "Image-Quality Degradation in a Turbid Medium Under Partially Coherent Illumination," J. Opt. Soc. Am. A, 3:4, 393-400, 1986.

ACKNOWLEDGMENT

This work was supported by the U.S. Army Research Office and the National Science Foundation.

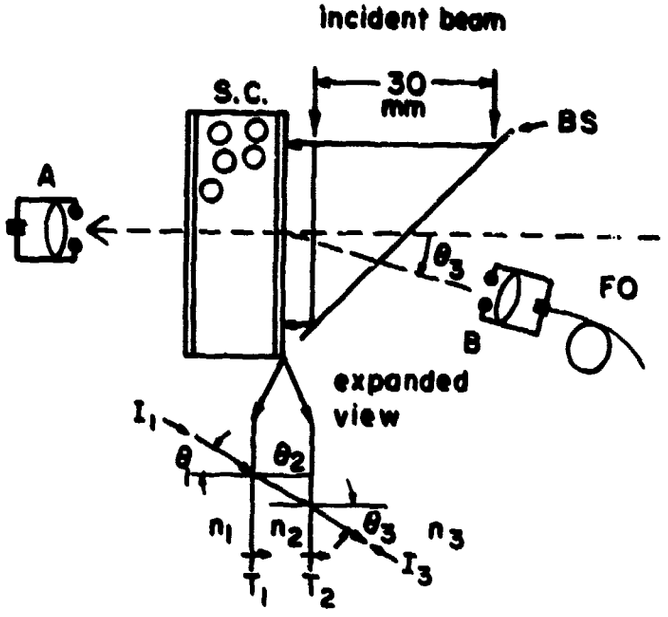


Fig. 1. Schematic diagram of the experimental apparatus (Ref. 4).

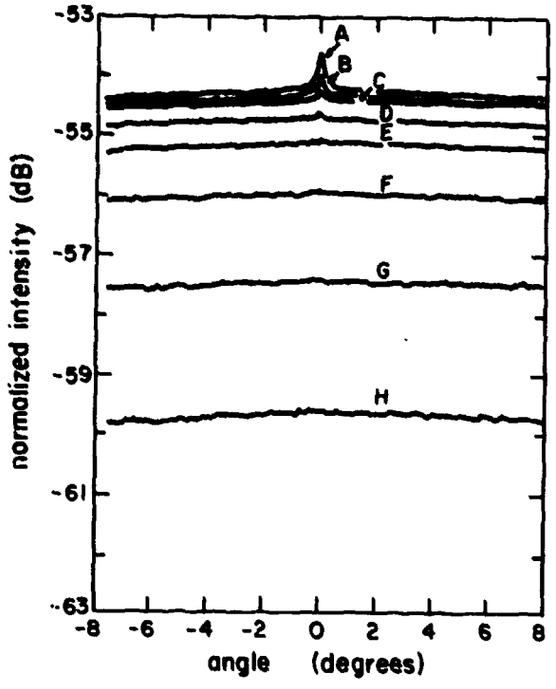


Fig. 2. Backscattered intensity versus angle. Particle size is 1.101 μm. A, experimental data for the volume density 9.55%; B, 4.78%; C, 2.39%, D, 1.19%, E, 0.597%; F, 0.299%, G, 0.149%; H, 0.075%.

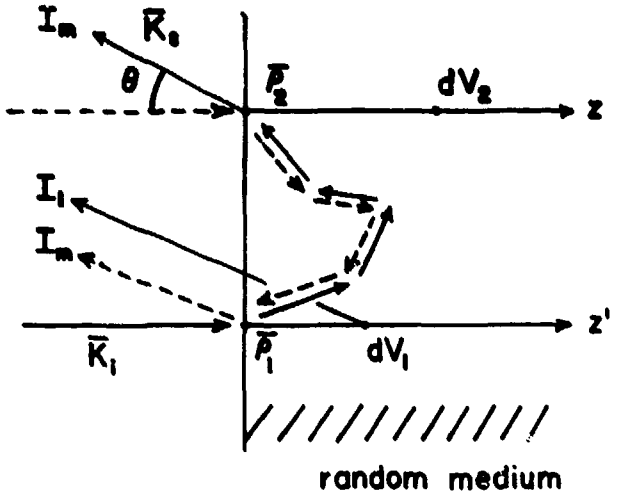


Fig. 3. First-order scattering I_1 and multiple scattering I_m.

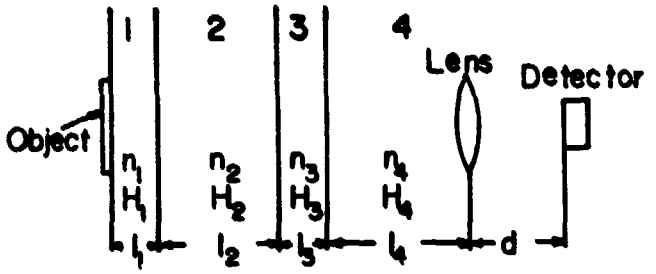


Fig. 4. Imaging through a layered medium. n_1, n_2, n_3, and n_4 are the indices of refraction of layers 1, 2, 3, and 4, respectively. H_1 to H_4 are given by Eq. (14).

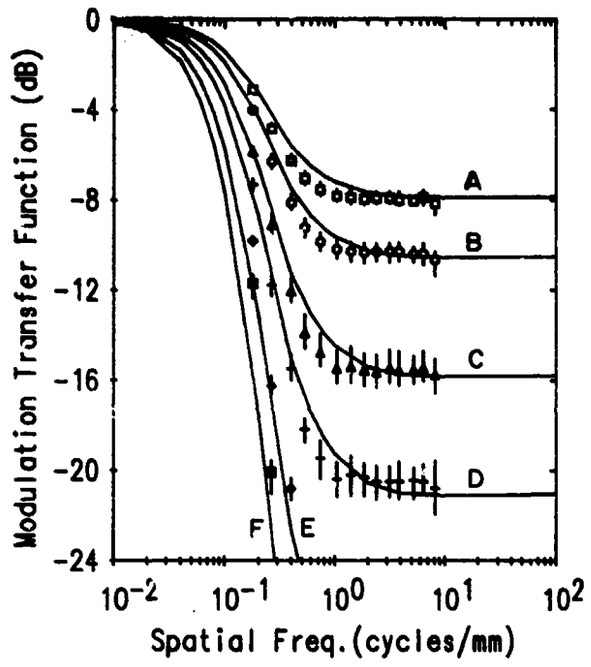


Fig. 5. MTF for 1.101-μm particles. ka = 7.3. Solid lines are small-angle approximation. A, τ = 1.81; B, τ = 2.42; C, τ = 3.63; D, τ = 4.84; E, τ = 7.26; F, τ = 9.68.

DISCUSSION

I.M. Besieris, US

You made a brief reference to the backscattering phenomenon associated with the fourth statistical moment. Could you comment on the differences of this phenomenon with the ordinary one arising in connection with the second moment?

Author's Reply

It appears that there is some experimental and theoretical evidence that the intensity fluctuations are considerably enhanced in the backward direction. This is the area which needs more study, both experimentally and theoretically.

J.A.DeSanto, US

Your work has an equation which appears to be similar to a Bragg condition. What is the relation of your backscatter enhancement to Bragg resonant backscatter?

Author's Reply

Both the enhancement and Bragg scatter are due to constructive interference. However, there are differences. Bragg scatter is created by the scattering from points separated by one correlation distance away. But the enhancement is created by scattering from points which are the mean free path away, or the mean diffusion path length away. The more fundamental difference is that the enhancements are due to two waves multiply scattered in opposite directions and occur only in the backward direction, while Bragg scatter is due to two waves singly scattered and can occur in all angles.

A.N. Ince, TU

How could the cross-polarized component (attributed to multiple scattering in the volume) of the backscattered wave vary with increasing density of the medium? What would then be the contribution by the surface?

Author's Reply

For spherical particles, the backscatter cross polarization is zero for single scatter which is dominant at low density. At higher densities, multiple scattering becomes dominant and we expect the backscatter cross polarization. For a very dense medium, we made an experiment using a sample containing particles with water completely removed (dried) and we observed some backscattering enhancement. This may correspond to a rough surface, but we do not have a good theory.

Geometrical Theory of Diffraction for High-Frequency Coherence Functions in a Weakly Random Medium With Inhomogeneous Background Profile

R. Mazar and L.B. Felsen
Department of Electrical Engineering and Computer Science/Weber Research Institute
Polytechnic University, Farmingdale, NY 11735 USA

Abstract

The localization of high-frequency wave propagation around ray trajectories, and the reflection and (or) diffraction of these local plane wave fields by boundaries, inhomogeneities and (or) scattering centers has been combined via the Geometrical Theory of Diffraction (GTD) into one of the most effective means of analyzing high-frequency wave phenomena in complex deterministic environments. These constructs are here incorporated into a stochastic propagation and diffraction theory for statistical moments of the high-frequency field in a weakly fluctuating medium with inhomogeneous background profile, provided that the correlation length ℓ_n of the fluctuations is small compared with the scale of variation, but large compared with the local wavelength $\lambda = 2\pi/k = 2\pi c/\omega$, in the fluctuation-free background, with k being the local wavenumber, c the local wave speed and ω the radian frequency. Canonical problems of deterministic GTD furnish the propagators and the local reflection, refraction and diffraction coefficients that relate incoming to outgoing wavefields. The major analytical building blocks include propagators described in local coordinates centered on the curved GTD ray trajectories in the deterministic inhomogeneous background environment; multiscale expansions in these coordinates, to chart and solve for the propagation properties of statistical measures of the parabolically formulated ray fields; Kirchoff or physical optics (PO) approximations, generated by GTD incident fields, to establish initial conditions for fields reflected from extended smooth surfaces; and "point scatterer" solutions to establish GTD initial conditions for small scatterers and edges. In addition to the conventional second and higher order coherence functions, there are introduced as appropriate statistical objects two-point random functions and corresponding higher order functions which are useful in treating correlation of incident and backward reflected or diffracted fields that traverse the same propagation volume. By this solution strategy, one gains access to a much larger class of high frequency problems in a random medium than at present. Results for the average field and higher moments have been obtained for forward propagation in a fluctuating medium with inhomogeneous and caustic-forming background, for reflection and refraction due to a plane or smoothly curved interface in such a medium, and for diffraction due to a wedge and a small scatterer.

I. Introduction and Summary

Ray theory, as formalized by the geometrical theory of diffraction (GTD), is one of the well established methods for treating high frequency propagation and diffraction in complicated environments. Shortcomings of ray theory in convergence zones near caustics, in refraction shadows, structural diffraction regions, etc., have been repaired by local uniformization, and the relation between ray fields and modal fields in guiding channels has been given a quantitative foundation [1], leading to a hybrid format that can combine rays and modes systematically to exploit the best features of each, both phenomenologically and computationally. A review of these recent developments may be found in reference [2].

It has long been tempting to incorporate into ray theory the effects of random medium fluctuations and boundary perturbations to permit more realistic modeling of propagation channels encountered in practice. Some recent efforts have been aimed at describing the transport properties of the statistical moments of the field directly through deterministic partial differential equations based on parabolically approximated wavefields [3-5]. For high frequency fields in a weakly fluctuating medium with correlation length of the random fluctuations much larger than the local wavelength, it is suggestive to structure the transport of these moments around the ray trajectories in the deterministic background. Carrying these considerations further, one is led to explore whether the entire machinery of deterministic GTD can be employed to account also for phenomena of reflection, refraction, diffraction by edges or due to shadowing on smooth surfaces, etc. The foundation of deterministic GTD is the concept of localization of high frequency fields around ray trajectories, and the consequent ability to model the local effects of an arbitrary propagation or diffraction environment by a global canonical configuration that is analytically tractable and assumes in the relevant local region the features of the actual structure. The task is to extend this scheme to the mean field and higher order moments when sources, media, interfaces, boundaries, etc., introduce weak random fluctuations. If successful, this will make accessible a whole new class of phenomena, which are presently beyond reach by rigorous methods.

The strategy outlined above is being implemented on a systematic sequence of canonical problems. The first generalization has been concerned with extending to curved rays in an arbitrary inhomogeneous background profile results in the literature developed around straight rays. As in these earlier studies, we have dealt with reduced wave fields that are defined approximately by a parabolic equation, thereby removing from the full wave function a phase term that accounts for the dominant propagation phenomena along the "preferred" coordinate. However, instead of extracting this term in the conventional form exp(iks), which describes a plane wave with reference wavenumber k propagating along the preferred straight coordinate s and thereby restricts the resulting parabolic approximation solutions to the paraxial narrow angular domain around the s-axis, we formulate the parabolic equation for the coherence function and higher moments, and extract the phase in a ray-centered coordinate system, along an arbitrarily directed ray (see also [3-5]); this yields in a small angular domain around that ray in an arbitrary refracting background the solution for the two-point coherence function by extending the multiscale expansion method employed previously for the s-directed propagation function [6-9] to arbitrarily propagated single and multiple ray contributions that may reach an observer. For single ray contributions, a single scale paraxial (quadratic) expansion around the central ray is adequate and is found to reduce in the absence of fluctuations to the familiar ray intensity variation inversely proportional to the ray tube cross section. Multiple ray contributions reaching an observer along vastly different propagation paths in the fluctuating environment are treated individually in view of the previously noted lack of phase coherence between them. Multiple ray contributions near caustics and foci in the background are treated collectively because of their almost coincident trajectories. For two ray fields near a simple caustic, this is achieved by cubic expansion around the caustic contact point of the central ray. In the absence of fluctuations, the resulting expansion for the intensity is shown to be reducible to the Airy function solution derived from uniformized ray theory. It

has thereby been confirmed that propagation of the coherence function can be localized around the ray paths in a generally refracting medium, and that tractable approximations can be made to retain the necessary unfamiliar diffractive spectra near a caustic.

Proceeding to the next step in the GTD strategy, it is necessary to introduce ray fields caused by reflection, refraction and diffraction. If a ray in this category reaches the observer along a trajectory that, on the scale of the correlation lengths of the fluctuations, is widely separated from all other rays, the statistical measures of the corresponding random wavefields can be treated in isolation. However, if such a ray passes near the trajectory of the incident ray (backscattering domain), the incident and back-scattered events must be correlated. It is then appropriate to explore the transport properties not of the two-point coherence function (TPCF) but of a more general two-point random function (TPRF) constructed by pairing random fields without ensemble averaging. The TPCF is obtained by averaging the TPRF after its construction. The propagation equation for the parabolically approximated TPRF differs from that for the TPCF in that in contains random functions. We have confirmed that for forward propagation, construct-ing the solution for the TPCF from the solution for the TPRF yields the same result as the direct solution described above. This circumstance demonstrates the versatility of the TPRF approach.

With the necessary propagators in hand to account for the whole hierarchy of GTD rays, the next task has been to establish the appropriate initial conditions for the stochastic wavefields along these rays. This has been implemented so far for two-dimensional reflection and refraction due to smooth boundaries and interfaces embedded in the random medium, and for diffraction by small scatterers and by a wedge-shaped obstacle. As noted above, a distinction is made depending on whether the reflected and(or) diffracted ray fields in the background reach the observer along vastly different or along closely adjacent paths. The GTD strategy is implemented either in the configurational or spectral domains, and by canonical or physical optics solutions for reflection, transmission and diffraction coefficients, to furnish for the mean field and coherence functions a variety of alternative representations of solutions with presumably different ranges of utility. These results are summarized below. Taken in their entirety, they suggest that the GTD-based strategy for high frequency propagation and diffraction in a randomly fluctuating medium with the stated properties holds considerable promise and deserves to be further explored and extended.

II. Propagation Equation for the Two-Point Coherence Function and Two-Point Random Function in Ray-Centered Coordinates

To develop the equations governing the propagation of statistical measures of the field $U(\underline{R})$ in a randomly fluctuating medium, we begin with the time-harmonic wave equation

$$\nabla^2 U + k^2 N^2(\underline{R}) U = 0 \tag{1}$$

which $U(\underline{R})$ must satisfy at any observation point $\underline{R}$. Here, k is a reference wavenumber, and $N(\underline{R})$ is the index of refraction, which is assumed to be comprised of a spatially varying regular (background) portion $n(\underline{R})$ and a normalized weak random portion $\tilde{n}(\underline{R})$, with $|\tilde{n}| << 1$ and $\langle \tilde{n} \rangle = 0$. The brackets $\langle\rangle$ denote the ensemble average. We shall approximate

$$N^2(\underline{R}) = n^2(\underline{R})[1+\tilde{n}(\underline{R})]^2 \simeq n^2(\underline{R})[1+2\tilde{n}(\underline{R})] \quad . \tag{2}$$

As in previous studies [6]-[12] our analysis of the transport properties of the statistical moments of the high-frequency field is based on the parabolic approximation, but is extended here by performing the parabolic expansion around the actual ray trajectories in the inhomogeneous background (see references [3-5], [13-16], [18,19]) instead of the straight coordinate z. This removes the narrow angle restriction around the z-axis, and grants access to regions that were previously inaccessible. The implementation involves ray-centered coordinates $(\underline{r},\sigma)$ for a typical ray, with extraction, from the expression for the field, of the phase accumulation along that ray,

$$U(\underline{r},\sigma) = u(\underline{r},\sigma)\exp\{ik\int_0^\sigma d\zeta n_0(\zeta)\} \quad . \tag{3}$$

Here,

$$n_0(\sigma) = n(0,\sigma) \tag{4}$$

is the deterministic (background) part of the variable refractive index at any length σ measured along the ray, while $\underline{r} = (q_1\, q_2)$ is the vector coordinate to a point located in a rectangular (q_1,q_2) coordinate system perpendicular to the ray. The ray centered coordinate system $\underline{R}(\underline{r},\sigma)$ is shown in Fig. 1, which also includes a sketch of the source region, wherein originates the ray at S that reaches the observation point M. The derivation of the parabolic equation involves the usual restrictions

$$\left|\frac{\partial u}{\partial \sigma}\right| << k|u| \quad , \quad \left|\frac{\partial^2 u}{\partial \sigma^2}\right| << k\left|\frac{\partial u}{\partial \sigma}\right| \quad , \tag{5}$$

which justify omission of "slow" σ-derivatives of u. While the formulation has been carried out for the three-dimensional case [3], we restrict ourselves for simplicity to the two-dimensional problem, independent of q_2, and denote the single transverse coordinate q_1 by r. Then, the metric coefficient $h(r,\sigma)$ for the ray-centered coordinate is

$$h(r,\sigma) = 1 + \frac{r}{R(\sigma)} \quad , \tag{6a}$$

where

$$R(\sigma) = \left(\frac{1}{n_0(\sigma)} \; \frac{\partial n(r,\sigma)}{\partial r}\right)^{-1}_{r=0} \tag{6b}$$

is the local radius of curvature of the reference ray. We also define functions

$$H(r,\sigma) \equiv \frac{1}{2}\left[\frac{1}{n_0(\sigma)}\frac{\partial n_0(\sigma)}{\partial\sigma} - \frac{1}{h(r,\sigma)}\frac{\partial h(r,\sigma)}{\partial\sigma}\right], \tag{7a}$$

$$\mu_D(r,\sigma) \equiv \frac{1}{2} n_0(\sigma)\left[h^2(r,\sigma)\frac{n^2(r,\sigma)}{n^2(\sigma)} - 1\right] . \tag{7b}$$

The average intensity distribution of the fluctuating field $U(\underline{r},\sigma)$ observed along one of the rays described above can be obtained from the two point coherence function (TPCF) Γ_2 defined at the range plane σ as the ensemble average of the two point random function (TPRF) Γ,

$$\Gamma(\underline{r}_1,\underline{r}_2,\sigma) = U(r_1,\sigma)U^*(r_2,\sigma) = u(r_1,\sigma)u(r_2,\sigma) \tag{8a}$$

$$\Gamma_2(r_1,r_2,\sigma) = \langle\Gamma(r_1,r_2,\sigma)\rangle \quad , \tag{8b}$$

where $\langle\ \rangle$ denotes the ensemble average and the asterisk the complex conjugate. The resulting equations governing the propagation of the TPCF are similar in basic structure but differ through the presence of averaged terms in the former but random terms in the latter. We consider them in turn.

A. Two-Point Coherence Function

We begin with the TPCF because this is the most familiar case. In a statistically homogeneous, isotropic random medium with variable background refractive index, the following equation governs the propagation of the TPCF Γ_2 (see [3]):

$$\frac{\partial\Gamma_2}{\partial\sigma} = \frac{i}{2kn_0(\sigma)}\left\{h^2(r_1,\sigma)\frac{\partial^2\Gamma_2}{\partial r_1^2} - h^2(r_2,\sigma)\frac{\partial^2\Gamma_2}{\partial r_2^2}\right\} + \frac{i}{2kn_0(\sigma)R(\sigma)}\left\{h(r_1,\sigma)\frac{\partial\Gamma_2}{\partial r_1} - h(r_2,\sigma)\frac{\partial\Gamma_2}{\partial r_2}\right\}$$

$$+ ik[\mu_D(r_1,\sigma) - \mu_D(r_2,\sigma)]\Gamma_2 + [H(r_1,\sigma) + H(r_2,\sigma)]\Gamma_2 - \frac{k^2}{2}V(r_1,r_2,\sigma)\Gamma_2, \tag{9}$$

where the function $V(r_1,r_2,\ )$ describing the effects of random scattering is given by

$$V(r_1,r_2,\sigma) = \{[h^4(r_1,\sigma)n^4(r_1,\sigma) + h^4(r_2,\sigma)n^4(r_2,\sigma)]A_n(0)$$

$$- 2h^2(r_1,\sigma)h^2(r_2,\sigma)n^2(r_1,\sigma)n^2(r_2,\sigma)A_n(r_1 - r_2)\}/n_0^2(\sigma) \quad . \tag{10}$$

Here, $A_n(r_1 - r_2)$ represents the correlation function for the refractive index in the plane transverse to the ray, it having been assumed that the fluctuations along the ray are delta correlated [10-12].

To solve (9), it is convenient to convert to the sum and difference coordinates

$$p = \frac{r_1 + r_2}{2} \ ; \quad s = r_1 - r_2 \quad , \tag{11a}$$

$$r_1 = p + \frac{s}{2} \ ; \quad r_2 = p - \frac{s}{2} \quad . \tag{11b}$$

Next, it is appropriate to scale these coordinates with respect to the various perturbation scales that characterize the problem. We identify in addition to a reference wavelength $\lambda = 2\pi/k$ the characteristic length ℓ, over which the background refractive index variation becomes appreciable, and the characteristic length ℓ_n, beyond which the refractive index fluctuations are uncorrelated, with the ordering $\lambda << \ell_n << \ell$, that is consistent with the high frequency assumption. The new coordinates $\bar{p}$, $\bar{s}$ and $\bar{\sigma}$ scaled over the relevant characteristic lengths are taken to be

$$p = \ell\bar{p} \ , \quad s = \frac{\bar{s}}{k} \ , \quad \sigma = \ell\bar{\sigma} \quad , \tag{12}$$

which leads to the introduction of modified and scaled functions defined as follows:

$$\mu_D(r,\sigma) = \mu(\frac{r}{\ell},\frac{\sigma}{\ell}) \ , \ A_n(s) = A_n(0)\bar{A}_n(\frac{s}{\ell_n}) \ , \ R(\ell\bar{\sigma}) = \ell\bar{R}(\bar{\sigma}) \ , \ n_0(\ell\bar{\sigma}) = \bar{n}_0(\bar{\sigma}) \ , \ h(\ell\bar{r},\ell\bar{\sigma}) = \bar{h}(\bar{r},\bar{\sigma}) \ ,$$

$$H(\ell\bar{r},\ell\bar{\sigma}) = \ell^{-1}\bar{H}(\bar{r},\bar{\sigma}) \ , \ V(\ell\bar{p} + \frac{\bar{s}}{2k} \ , \ \ell\bar{p} - \frac{\bar{s}}{2k} \ , \ \ell\bar{\sigma}) = A_n(0)\bar{V}(\bar{p} + \frac{\bar{s}}{2k\ell} \ , \ \bar{p} - \frac{\bar{s}}{2k\ell} \ , \ \frac{\bar{s}}{k\ell_n} \ , \bar{\sigma}) \tag{13}$$

Finally, following [3,4], we introduce the perturbation parameters

$$\epsilon_1 = \frac{1}{(k\ell)^{2/3}} , \quad \epsilon_2 = \frac{1}{k\ell_n} \tag{14}$$

which will be used in the asymptotic analysis of (9). The form of ϵ_1 is suggested by the behavior of the expansion of the difference term $ik[\mu_D(p+\frac{s}{2},\sigma) - \mu_D(p-\frac{s}{2},\sigma)]$ in (9) while that of ϵ_2, attributable to the fluctuations, is motivated by the measure of the spread angle for single scattering.

In the scaled variables, the propagation properties of the coherence function $\Gamma(\bar{p},\bar{s},\bar{\sigma})$ are governed by the equation

$$E\Gamma = 0 \tag{15a}$$

subject to the initial source condition (the subscript "s" used here and henceforth to identify initial conditions in the source plane should not be confused with the s coordinate in (11a)),

$$\Gamma(\bar{p},\bar{s},0) = \Gamma_s(\bar{p},\bar{s}) \tag{15b}$$

The scaled operator E is given by

$$\begin{aligned} E = \frac{\partial}{\partial\bar{\sigma}} - \frac{i}{\bar{n}_0(\bar{\sigma})}\Bigg\{&\left[\bar{h}^2(\bar{p},\bar{\sigma}) + \frac{\epsilon_1^{3-2}}{4\bar{R}^2(\bar{\sigma})}\right]\frac{\partial^2}{\partial\bar{p}\partial\bar{s}} \\ &+ \frac{\bar{h}(\bar{p},\bar{\sigma})}{R(\bar{\sigma})}\left[\frac{\epsilon_1^{3-}}{4}\frac{\partial^2}{\partial\bar{p}^2} + \bar{s}\frac{\partial^2}{\partial\bar{s}^2}\right] \\ &+ \frac{1}{\bar{R}(\bar{\sigma})}\left[\bar{h}(\bar{p},\bar{\sigma})\frac{\partial}{\partial\bar{s}} + \frac{\epsilon_1\bar{s}}{4\bar{R}(\bar{\sigma})}\frac{\partial}{\partial\bar{p}}\right]\Bigg\} \\ &- i\epsilon_1^{-3/2}\left[\mu(\bar{p}+\frac{\epsilon_1^{3/2}\bar{s}}{2},\bar{\sigma}) - \mu(\bar{p}-\frac{\epsilon_1^{3/2}\bar{s}}{2},\bar{\sigma})\right] \\ &+ \left[\bar{H}(\bar{p}+\frac{\epsilon_1^{3/2}\bar{s}}{2},\bar{\sigma}) + \bar{H}(\bar{p}-\frac{\epsilon_1^{3/2}\bar{s}}{2},\bar{\sigma})\right] \\ &+ \frac{1}{2}\beta\bar{V}(\bar{p}+\frac{\epsilon_1^{3/2}\bar{s}}{2}, \bar{p}-\frac{\epsilon_1^{3/2}\bar{s}}{2}, \epsilon_2\bar{s},\bar{\sigma}) , \end{aligned} \tag{16}$$

where

$$\beta = k^2 A_n(0)\ell \tag{17}$$

B. Two-Point Random Function

The parabolic equation for the TPRF has the same deterministic (background) portion as that for the TPCF but differs through the presence of nonaveraged stochastic functions. Again, the three-dimensional equation is available [16] but we shall be satisfied here with the two-dimensional version. As has been shown in [3], coordinate scaling can be performed either with respect to ℓ or ℓ_n. Choosing the latter, i.e., $p = \ell_n\bar{p}$, $s = \bar{s}/k$, $\sigma = \ell_n\bar{\sigma}$, one may write,

$$\begin{aligned} \frac{\partial\Gamma}{\partial\sigma} = \frac{i}{\bar{n}_0(\bar{\sigma})}\Bigg\{&\left[\bar{h}^2(\bar{p},\bar{\sigma}) + \frac{\epsilon_1^{3-2}}{4\bar{R}^2(\bar{\sigma})}\right]\frac{\partial^2\Gamma}{\partial\bar{p}\partial\bar{s}} + \frac{\bar{h}(\bar{p},\bar{\sigma})}{R(\bar{\sigma})}\left[\frac{\epsilon_1^{3-}}{4}\frac{\partial^2\Gamma}{\partial\bar{p}^2} + \bar{s}\frac{\partial^2\Gamma}{\partial\bar{s}^2}\right] + \frac{1}{\bar{R}(\bar{\sigma})}\left[\bar{h}(\bar{p},\bar{\sigma})\frac{\partial\Gamma}{\partial\bar{s}} + \frac{\epsilon_1^{3-}\bar{s}}{4\bar{R}(\bar{\sigma})}\frac{\partial\Gamma}{\partial\bar{p}}\right]\Bigg\} \\ &-i\epsilon_1^{-3/2}[\mu(\bar{r}_+,\bar{\sigma}) - \mu(\bar{r}_-,\bar{\sigma})]\Gamma + [\bar{H}(\bar{r}_+,\bar{\sigma}) + \bar{H}(\bar{r}_-,\bar{\sigma})]\Gamma + \frac{i\epsilon_2^{-1}}{\bar{n}_0(\bar{\sigma})}[\bar{h}^2(\bar{r}_+,\bar{\sigma})\bar{n}^2(\bar{r}_+,\bar{\sigma})\bar{n}(\bar{p}+\frac{\epsilon_2\bar{s}}{2},\bar{\sigma}) \\ &- h^2(\bar{r}_-,\bar{\sigma})\bar{n}^2(\bar{r}_-,\bar{\sigma})\bar{n}(\bar{p}-\frac{\epsilon_2\bar{s}}{2},\bar{\sigma})]\Gamma \end{aligned} \tag{18}$$

where $\bar{r}_\pm = \bar{p} \pm \frac{\epsilon_1^{3/2}\bar{s}}{2}$, the functions $\bar{R}(\bar{\sigma})$, $\bar{n}_0(\bar{\sigma})$, $\bar{h}(\bar{r},\bar{\sigma})$ and $\bar{\mu}(\bar{r},\bar{\sigma})$ are likewise scaled with respect to ℓ_n, and the perturbation parameters are taken as

$$\epsilon_1 = \frac{1}{(k\ell_n)^{2/3}} , \quad \epsilon_2 = \frac{1}{k\ell_n} \tag{19}$$

We note that (18) is more general than (9) because the respective index correlation function can generally be spatially dependent and also anisotropic.

III. Solution by Three-Scale Expansion

A. Two Point Coherence Function

1. The Approximated Three-Scale Propagation Equation

To solve the propagation equation (15) under conditions requiring the three length scales λ, ℓ_n, and ℓ, we have adapted to the curved trajectories here the procedure employed previously in dealing with straight background rays [6-9]. This procedure involves a succession of spectral transforms and scalings that remove nondesired variables and normalize desired ones until the transformed equation has a form that can be attacked by the method of characteristics. In addition, in transverse planes centered at various points along the relevant reference ray, one employs paraxial expansions that include up to third order (cubic) terms with respect to the central configuration or spectral coordinate; near a caustic, the reference ray is the one tangent to the caustic. It should be kept in mind that although the various Fourier transforms in this development are formally taken over an infinite transverse domain, the contributing spectral ranges are those confined to the paraxial region around the reference ray. This circumstance effectively truncates the integration interval, thereby removing formal complications that would arise from intersection of successive infinite transverse expansion planes at large distances from the (curved) ray.

The major steps are similar to those in [6-9]. The zeroth order result is [3]:

$$\tilde{E}_0\tilde{\Gamma}_0 = 0 \quad . \tag{20a}$$

$$\tilde{\Gamma}_0(\bar{\nu},\bar{\eta}_1,\bar{\eta}_2,\bar{\rho},\bar{s}_1,\bar{s}_2,0) = \tilde{\Gamma}_s(\bar{\nu},\bar{\rho}) \quad , \tag{20b}$$

where $\tilde{E}_0$ is the zeroth order operator

$$\tilde{E}_0 = \tilde{E}_g + L(\bar{\nu},\bar{\rho},\bar{s}_1,\bar{\eta}_1,\bar{\sigma})\frac{\partial}{\partial\bar{s}_1} + L(\bar{\nu},\bar{\rho},\bar{s}_2,\bar{\eta}_2,\bar{\sigma})\frac{\partial}{\partial\bar{s}_2} + M(\bar{\nu},\bar{\rho},\bar{s}_1,\bar{\eta}_1,\bar{\sigma})\frac{\partial}{\partial\bar{\eta}_1} + M(\bar{\nu},\bar{\rho},\bar{s}_2,\bar{\eta}_2,\bar{\sigma})\frac{\partial}{\partial\bar{\eta}_2}$$

$$- \frac{i}{3}P_0(\bar{\nu},\bar{\rho},\bar{s}_1,\bar{\eta}_1,\bar{\sigma}) + \beta V_0(\bar{\nu},\bar{s}_2,\bar{\sigma}). \tag{21}$$

and

$$\tilde{E}_g = \frac{\partial}{\partial\bar{\sigma}} + \frac{\bar{h}^2(\bar{\nu},\bar{\sigma})}{\bar{n}_0(\bar{\sigma})}\bar{\rho}\frac{\partial}{\partial\bar{\nu}} + \Omega(\bar{\nu},\bar{\rho},\bar{\sigma})\frac{\partial}{\partial\bar{\rho}} + Q(\bar{\nu},\bar{\rho},\bar{\sigma}) \tag{22}$$

with

$$\Omega(\bar{\nu},\bar{\rho},\bar{\sigma}) = \mu^{(1)}(\bar{\nu},\bar{\sigma}) - \frac{\bar{\rho}^{-2}}{\bar{n}_0(\bar{\sigma})\bar{R}(\bar{\sigma})}\bar{h}(\bar{\nu},\bar{\sigma}) \quad , \tag{23a}$$

$$Q(\bar{\nu},\bar{\rho},\bar{\sigma}) = H_0(\bar{\nu},\bar{\sigma}) - \frac{\bar{\rho}\bar{h}(\bar{\nu},\bar{\sigma})}{\bar{n}_0(\bar{\sigma})\bar{R}(\bar{\sigma})} \quad , \tag{23b}$$

$$H_0(\bar{\nu},\bar{\sigma}) = \frac{1}{\bar{n}_0(\bar{\sigma})}\frac{\partial\bar{n}_0(\bar{\sigma})}{\partial\bar{\sigma}} + \frac{1}{\bar{R}(\bar{\sigma})}\frac{\partial\bar{R}(\bar{\sigma})}{\partial\bar{\sigma}}\frac{\bar{\nu}}{\bar{\nu}+\bar{R}(\bar{\sigma})} \quad . \tag{23c}$$

Here, $\bar{\nu}$, $\bar{s}_1$ and $\bar{s}_2$ are coordinate-like spectral variables and $\bar{\rho}$, $\bar{\eta}_1$ and $\bar{\eta}_2$ are spectral variables obtained after several spectral transforms and embeddings of the spectral functions in a higher dimensional space according to the three-scale expansion method (see [3]). The "geometric expansion operator" $\tilde{E}_g$ which results from retaining only the zeroth order terms in ε_1 in the fluctuation-free portion of the complete operator E in (16), characterizes the isolated ray contributions in the deterministic background. The other functions are defined as follows:

$$L(\bar{\nu},\bar{\rho},\bar{s}_j,\bar{\eta}_j,\bar{\sigma}) = \frac{\bar{\eta}_j}{\bar{n}_0(\bar{\sigma})}\bar{h}^2(\bar{\nu},\bar{\sigma}) + \frac{2\bar{\rho}\bar{s}_j}{\bar{n}_0(\bar{\sigma})\bar{R}(\bar{\sigma})}\bar{h}(\bar{\nu},\bar{\sigma}) \tag{24a}$$

$$M(\bar{\nu},\bar{\rho},\bar{s}_j,\bar{\eta}_j,\bar{\sigma}) = \bar{s}_j\Omega_{\bar{\nu}}(\bar{\nu},\bar{\rho},\bar{\sigma}) - \frac{2\bar{\eta}_j\bar{\rho}}{\bar{n}_0(\bar{\sigma})\bar{R}(\bar{\sigma})}\bar{h}(\bar{\nu},\bar{\sigma}) \tag{24b}$$

$$P_0(\bar{\nu},\bar{\rho},\bar{s}_1,\bar{\eta}_1,\bar{\sigma}) = \left[\frac{\bar{s}_1^3}{8}\mu^{(3)}(\bar{\nu},\bar{\sigma}) - \frac{3\bar{\eta}_1^2\bar{s}_1}{4\bar{n}_0(\bar{\sigma})\bar{R}(\bar{\sigma})}\bar{h}(\bar{\nu},\bar{\sigma}) - \frac{3\bar{\eta}_1\bar{s}_1\bar{\rho}}{4\bar{n}_0(\bar{\sigma})\bar{R}^2(\bar{\sigma})}\right] \tag{24c}$$

where

$$\mu^{(m)}(\bar{\nu},\bar{\sigma}) = \frac{\partial^m\mu(\bar{\nu},\bar{\sigma})}{\partial\bar{\nu}^m} \quad , m=1,2\ldots, \quad \Omega_{\bar{\nu}} = \frac{\partial\Omega}{\partial\bar{\nu}} \quad . \tag{25}$$

The scattering function V_0, which incorporates the effects of the fluctuations, is given by

$$V_0(\bar{\nu},\epsilon_2\bar{s},\bar{\sigma}) = \frac{\bar{n}^4(\bar{\nu},\bar{\sigma})\bar{n}^4(\bar{\nu},\bar{\sigma})}{\bar{n}_0^2(\bar{\sigma})}\left[1-\bar{K}_n(\epsilon_2\bar{s})\right] . \tag{26}$$

The solution of (20a) subject to (20b) is simplified by normalising the initial condition. To this end, we write [6-9]

$$\bar{\Gamma}_0(\bar{\nu},\bar{\eta}_1,\bar{\eta}_2,\bar{\rho},\bar{s}_1,\bar{s}_2,\bar{\sigma}) = \bar{\Gamma}_R(\bar{\nu},\bar{\rho},\bar{\sigma})F(\bar{\nu},\bar{\eta}_1,\bar{\eta}_2,\bar{\rho},\bar{s}_1,\bar{s}_2,\bar{\sigma}) \tag{27}$$

where $\bar{\Gamma}_R(\nu,\rho,\sigma)$ is the solution of the "geometrically" approximated equations

$$\bar{E}_R\bar{\Gamma}_R = 0 \tag{28a}$$

with initial source condition

$$\bar{\Gamma}_R(\bar{\nu},\bar{\rho},0) = \bar{\Gamma}_s(\bar{\nu},\bar{\rho}) = \int_{-\infty}^{\infty} d\bar{s}\bar{\Gamma}_s(\bar{\nu},\ \bar{s})\exp(-i\bar{\rho}\bar{s}) \quad . \tag{28b}$$

The function $F(\bar{\nu},\bar{\eta}_1,\bar{\eta}_2,\bar{\rho},\bar{s}_1,\bar{s}_2,\bar{\sigma})$ now is the solution of (20) with the normalized initial condition

$$\bar{E}_0F = 0 \tag{29a}$$

$$F(\bar{\nu},\bar{\eta}_1,\bar{\eta}_2,\bar{\rho},\bar{s}_1,\bar{s}_2,0) = 1 \ . \tag{29b}$$

Knowing F and $\bar{\Gamma}_R$, we can find $\bar{\Gamma}_0$ from (27).

2. Solution of the Background (Auxiliary) Problem

The background problem posed in (28) is of interest by itself because it describes propagation of the coherence function along isolated ray paths in an arbitrarily inhomogeneous deterministic medium (see also [17]). In the present context, it may be regarded as an auxiliary problem for attacking the general case. The solution strategy is the method of characteristics built around the ray paths in the background medium. These same paths then form the basis for solving the normalized initial value problem (29a,b) in the presence of fluctuations, away from, and near, the caustic. The characteristic equations corresponding to the first order partial differential equations in (28) are

$$\frac{d\bar{\nu}}{d\bar{\sigma}} = \frac{\bar{\rho}}{\bar{n}_0(\bar{\sigma})}\bar{n}^2(\bar{\nu},\bar{\sigma}) \qquad ; \qquad \bar{\nu}(0) = \bar{\nu}_s \tag{30a}$$

$$\frac{d\bar{s}}{d\bar{\sigma}} = \Omega(\bar{\nu},\bar{\rho},\bar{\sigma}) \qquad ; \qquad \bar{\rho}(0) = \bar{\rho}_s \tag{30b}$$

$$\frac{d\bar{\Gamma}_R}{d\bar{\sigma}} = 0 \qquad ; \qquad \bar{\Gamma}_R(\bar{\sigma}=0) = \Gamma_s(\nu_s,\bar{\rho}_s) \tag{30c}$$

$$\bar{\Gamma}_R(\bar{\nu},\bar{\rho},\bar{\sigma}) = \exp\{\int_0^{\bar{\sigma}} d\zeta Q(\bar{\nu},\bar{\rho},\bar{\zeta})\}\bar{\Gamma}_R(\bar{\nu},\bar{\rho},\bar{\sigma}) \tag{30d}$$

with the parameter $\bar{\rho}$ related to the relative slope $t = \tan\phi$ of a ray as follows (see Fig. 1),

$$t(\bar{\nu},\bar{s},\bar{\sigma}) = \frac{\bar{\rho}\bar{n}(\bar{\nu},\bar{\sigma})}{\bar{n}_0(\bar{\sigma})} \quad . \tag{31}$$

Here, ϕ is the angle between the tangent to the central ray $\phi = 0 = \bar{\rho}$ and a paraxial ray described by $\bar{\nu}(\bar{\nu}_s,\bar{\rho}_s,\bar{\sigma})$, and (30d) serves to define $\bar{\Gamma}_R(\bar{\nu},\bar{s},\bar{\sigma})$.

Integrating (30a,b), we obtain $\bar{\nu}$ and $\bar{\rho}$ as functions of their initial values $\bar{\nu}_s$ and $\bar{\rho}_s$,

$$\bar{\nu} = \bar{\nu}(\bar{\nu}_s,\bar{s}_s,\bar{\sigma}) \ ; \quad \bar{\rho} = \bar{\rho}(\bar{\nu}_s,\bar{\rho}_s,\bar{\sigma}) \tag{32}$$

or inverting these equations

$$\bar{\nu}_s = \bar{\nu}_s(\bar{\nu}\bar{\rho},\bar{\sigma}) \ ; \ \bar{\rho}_s = \bar{\rho}_s(\bar{\nu},\bar{\rho},\bar{\sigma}) \quad . \tag{33}$$

Then, integrating (28) along the characteristics, we obtain for the coherence function $\bar{\Gamma}_R(\bar{\nu}\bar{\rho},\bar{\sigma})$ the following expression:

$$\bar{\Gamma}_R(\bar{\nu}\bar{\rho},\bar{\sigma}) = \bar{\Gamma}_s[\bar{\nu}_s(\bar{\nu}\bar{\rho},\bar{\sigma}),\bar{\rho}_s(\bar{\nu}\bar{\rho},\bar{\sigma})]Q_0(\bar{\nu}_s,\bar{\nu},0,\bar{\sigma}) \tag{34}$$

where

$$Q_0(\bar{\nu}_0,\bar{\nu},\bar{\sigma}_0,\bar{\sigma}) = \exp\left\{-\int_{\bar{\sigma}_0}^{\bar{\sigma}} d\zeta Q(\bar{\nu},\bar{\rho},\zeta)\right\} = \frac{\bar{n}_0(\bar{\sigma}_0)}{\bar{n}_0(\bar{\sigma})}\frac{\bar{h}(\bar{\nu},\bar{\sigma})}{\bar{h}(\bar{\nu}_0,\bar{\sigma}_0)} \quad . \tag{35}$$

The corresponding solution in configuration space is found from the inverse transform

$$\Gamma_s(\bar{p},\bar{s},\bar{\sigma}) = \frac{1}{(2\pi)^2}\iiint_{-\infty}^{\infty} d\bar{v}d\bar{\rho}d\bar{\eta}\,\bar{\Gamma}_s(\bar{v}_s,\bar{\rho}_s)Q_0(\bar{v}_s,\bar{v},0,\bar{\sigma})\,\exp(i\bar{\rho}\bar{s})\exp[i\bar{\eta}(\bar{p}-\bar{v})] \quad . \tag{36}$$

The $\bar{\eta}$ and $\bar{v}$ integrations in (36) can be performed explicitly, but we shall retain the integrals in their present form for subsequent manipulations.

For the special case of excitation by a line source, the initial condition becomes

$$\bar{\Gamma}_s(\bar{v}_s,\bar{\rho}_s) = \frac{I_s k}{i}\,\delta(\bar{v}_s) \quad , \tag{37}$$

where $\delta(\bar{v}_s)$ is the Dirac delta function, and I_s is the source strength. The general result in (36) can now be simplified, and can be shown to yield what is found from GTD [20]. This circumstance establishes confidence that the various steps leading to (28) have retained enough spectral flesh to describe geometrical ray asymptotics in a generally refracting background.

3. Solution of the Normalized General Problem

The general problem with normalized initial conditions, defined by the first order partial differential equation in (29), is also amenable to treatment by the method of characteristics. The characteristic equations, which track the variables $\bar{v}$ and $\bar{\rho}$, are the ray tracing equations in (30a,b). One may reduce the four characteristic equations for the variables $\bar{s}_1$, $\bar{s}_2$, $\bar{\eta}_1$, $\bar{\eta}_2$ to two by eliminating the dependence on $\bar{\eta}$ by defining new variables. Again, following what was done for the straight line paraxial case [6-9], we define

$$\tilde{s}_j = \tilde{s}_j = \frac{\bar{s}_j}{\varepsilon_j\bar{\eta}} \quad , \qquad \tilde{\eta}_j = \tilde{\eta} = \frac{\bar{\eta}_j}{\varepsilon_j\bar{\eta}} \quad . \tag{38}$$

These variables are tracked by the system

$$\frac{d\tilde{s}}{d\bar{\sigma}} = L(\bar{v},\bar{\rho},\tilde{s},\tilde{\eta},\bar{\sigma}) \tag{39a}$$

$$\frac{d\tilde{\eta}}{d\bar{\sigma}} = M(\bar{v},\bar{\rho},\tilde{s},\tilde{\eta},\bar{\sigma}) \tag{39b}$$

together with (43a,b), subject to the following boundary conditions at the range plane $\bar{\sigma}$,

$$\tilde{s}(\bar{\sigma}) = \frac{\bar{s}}{\bar{\eta}} \quad , \qquad \tilde{\eta}(\bar{\sigma}) = 1 \quad . \tag{40}$$

Next, we define the function

$$\bar{\alpha}(\bar{v},\bar{\rho},\bar{\sigma}_0,\bar{\sigma}) = -\frac{3i}{(\varepsilon_1\bar{\eta})^3}\left\{\ln\frac{F(\bar{\sigma})}{F(\bar{\sigma}_0)} - i\ln Q_0(\bar{v}_s,\bar{v},\bar{\sigma}_0,\bar{\sigma}) + \beta\int_{\bar{\sigma}_0}^{\bar{\sigma}} d\zeta V_0(\bar{v},\varepsilon_2\bar{\eta}\tilde{s},\zeta)\right\} \equiv \bar{\alpha}_s^3(\bar{v},\bar{\rho},\bar{\sigma}) \tag{41}$$

which is a solution of the equation

$$\frac{d\bar{\alpha}}{d\bar{\sigma}} = P_0(\bar{v},\bar{\rho},\tilde{s},\tilde{\eta},\bar{\sigma}) \quad . \tag{42}$$

This has to be solved together with (43a,b) and (60a,b) subject to the boundary condition

$$\bar{\alpha}(\bar{v},\bar{\rho},\bar{\sigma},\bar{\sigma}) = 0 \tag{43}$$

that is a direct consequence of the definition given by (41). Setting $\bar{\sigma}_0 = 0$ in Eq. (41), we can express the function $F(\bar{\sigma})$ as

$$F(\bar{\sigma}) = Q_0(\bar{v}_s,\bar{v},0,\bar{\sigma})\exp\left\{\frac{i(\varepsilon_1\alpha_s\bar{\eta})^3}{3} - \beta\int_0^{\bar{\sigma}} d\zeta V_0(\bar{v},\varepsilon_2\bar{\eta}\tilde{s},\zeta)\right\} \quad . \tag{44}$$

4. Solution of the Complete Problem

The solution of the complete problem can be synthesized from the product decomposition in (27), using the results in (39) and (44). Transforming into configuration space,

$$\Gamma(\bar{p},\bar{s},\bar{\sigma}) = \frac{1}{(2\pi)^2}\iint_{-\infty}^{\infty} d\bar{v}_s d\bar{\delta}\, \tilde{\Gamma}_s(\bar{v}_s,\bar{\delta}_s) Q_0(\bar{v}_s,\bar{v},0,\bar{\sigma}) \exp(i\bar{\rho}\bar{s}) \int_{-\infty}^{\infty} d\bar{\eta} \exp[i\bar{\eta}(\bar{p}-\bar{v})]$$

$$\times \exp\left\{\frac{i(c_1 a_s \bar{\eta})^3}{3} - s\int_0^{\bar{\sigma}} d\zeta V_0(\bar{v},c_2\bar{\eta}\bar{a},\zeta)\right\} \tag{45}$$

This result for the two-point coherence function in a weakly fluctuating medium with inhomogeneous refractive index background, which has been derived from the three-scale zeroth order operator developed in Sec. IIIA, incorporates effects accurate to third order terms in the paraxial expansion around the reference ray in the background medium. It can, therefore, accommodate phenomena ascribed to isolated ray regimes as well as transitional regimes near a caustic. We have confirmed that the spectral content of the solution in (45) is enough to reproduce independently generated results in the following limiting situations: uniform (Airy type) and nonuniform (GTD) solutions near and far from caustics when fluctuations are omitted; isolated and nonisolated solutions with fluctuations present.

B. Two-Point Random Function

The development for the TPRF follows closely the one pursued for the TPCF in Section A. We write the solution formally as,

$$\Gamma(\bar{p},\bar{s},\bar{\sigma}) = \iint_{-\infty}^{\infty} d\bar{v}_s d\bar{q}_s \Gamma_s(\bar{v}_s,\bar{q}_s) G(\bar{p},\bar{s},\bar{\sigma}|\bar{v}_s,\bar{q}_s,0) \tag{46a}$$

$$= \frac{1}{2\pi}\iiint_{-\infty}^{\infty} d\bar{v}_s d\bar{q}_s d\bar{\rho}_s \Gamma_s(\bar{v}_s,\bar{\rho}_s) G(\bar{p},\bar{s},\bar{\sigma}|\bar{v}_s,\bar{q}_s,0)\exp(i\bar{\rho}_s\bar{q}_s), \tag{46b}$$

where

$$\Gamma_s(\bar{v}_s,\bar{q}_s) = (1/2\pi)\int_{-\infty}^{\infty} d\bar{\rho}_s \tilde{\Gamma}_s(\bar{v}_s,\rho_s)\exp(i\bar{\rho}_s q_s), \tag{46c}$$

and G is the two-point random propagator (TPRP)

$$G(\bar{p}_s,\bar{s}_2,\bar{\sigma}_2|\bar{p}_1,\bar{s}_1,\bar{\sigma}_1) = \frac{1}{(2\pi)^2}\iint_{-\infty}^{\infty} d\bar{\rho}_1 d\bar{\eta}\, \frac{\bar{u}_0(\bar{\sigma}_1)}{\bar{u}_0(\bar{\sigma}_2)}\frac{\bar{h}(\bar{v},\bar{\sigma}_2)}{\bar{h}(\bar{p}_1,\bar{\sigma}_1)}$$

$$\times \exp[i\bar{\rho}\bar{s}_2 - \bar{p}_1\bar{s}_1)]\exp[i\bar{\eta}(\bar{p}-\bar{v})]C(\bar{\eta},\bar{p}_1,\bar{\rho}_1,\bar{\sigma}_1,\bar{\sigma}_2)\ \exp\left\{is_2^{-1}\int_{\bar{\sigma}_1}^{\bar{\sigma}_2} d\zeta\, \frac{\bar{h}^2(\bar{v},\zeta)\bar{n}^2(\bar{v},\zeta)}{n_0(\bar{\zeta})}\right.$$

$$\left.\times [\bar{n}(\bar{v}(\zeta) + \frac{c_2\bar{\eta}\bar{a}(\zeta)}{2},\zeta) - \bar{n}(\bar{v}(\zeta) - \frac{c_2\bar{\eta}\bar{a}(\zeta)}{2},\zeta)]\right\} . \tag{47}$$

The function $C(\bar{\eta},\bar{p}_1,\bar{\rho}_1,\bar{\sigma}_1,\bar{\sigma}_2) = \exp[i(c_1\bar{\eta})^3\bar{\alpha}/3]$, which describes effects in the vicinity of a smooth caustic formed by the confluence of two adjacent background rays, can be replaced by unity (i.e. $c_1 = 0$) when a ray is isolated. For higher order caustics and cusps, additional perturbation scales must be introduced to find the appropriate C-function. The variables $\bar{v},\bar{q},\bar{a}$ and $\bar{\alpha}$ are tracked along the reference ray by the system (30a,b), (35a,b) and (12), noting that the scaling is made with respect to ℓ_n. We shall apply this solution in the next section to reflection, transmission and diffraction problems.

IV. Reflection, Transmission and Diffraction

A. Reflection and Transmission

With the propagation problem solved (see Secs. II and III), we now consider the case when the ray field is incident on a curved boundary segment across which the background refractive index is discontinuous, being denoted by n_- on the incident side and by n_+ on the transmitted side. The TPRF corresponding to the resulting reflected and transmitted waves is obtained by propagating from the source S to the point $B(0,\bar{q}_i)$ on the interface. This propagation takes place in the ray-centered coordinates $(\bar{r},\bar{\sigma})$, assuming for the moment that the interface is absent, and yields the incident TPRF Γ as in (46) with $\bar{\sigma}$ replaced by $\bar{\sigma}_i$ and $\bar{r}$ by the coordinate $\bar{r}_i$ in the plane W_i transverse to the incident ray (see Fig. 2). At $\bar{q}_i$, the transverse plane $W_i(\bar{p}_i,\bar{s}_i)$ is rotated into the plane $W_b(\bar{p}_b,\bar{s}_b)$ tangent to the boundary and Γ_i is evaluated on W_b. This establishes the Kirchoff initial condition

$$\Gamma_b(\bar{p}_b,\bar{s}_b,\bar{\sigma}_i) = \Gamma_i(\bar{p}_b\cos\theta_i,\bar{s}_b\cos\theta_i,\bar{\sigma}_i)\exp(in_{b-}\bar{s}_b\sin\theta_i), \tag{48}$$

where θ_i is the incidence angle and $\exp(in_{b-}\bar{s}_b\sin\theta_i)$ accounts for the phase change due to rotation. Because the transverse coordinates are confined to the vicinity of the reference ray, the variable refractive indeces n_- and n_+ near the intersection point B of that ray with the interface may be replaced locally by the constant values n_{b-} and n_{b+}.

To find the transmitted field, we combine the rules of GTD with the format for tracking the TPRF. First, the initial conditions on W_b are translated across the curved interface, which is assumed to be described by the function $\kappa = \kappa(\bar{r}_b)$ (see Fig. 2). Shifting from W_b in (48) to the curved boundary, one has

$$\hat{\Gamma}_b(\bar{p}_b,\bar{s}_b,\bar{\sigma}_i) = \Gamma_b(\bar{p}_b,\bar{s}_b,\bar{\sigma}_i)\exp(-ik_n n_{b-}\phi(p_b,\bar{s}_b)) \ , \tag{49a}$$

$$\phi(\bar{\rho}_b,\bar{\sigma}_b) = \kappa(\bar{\rho}_b + \frac{c_2\bar{\sigma}_b}{2}) - \kappa(\bar{\rho}_b - \frac{c_2\bar{\sigma}_b}{2}) \quad . \tag{49b}$$

Passing to the transmitted side requires multiplication by the local Fresnel plane wave transmission coefficient $K_t(\bar{r}_b,\theta_i)$. Next, we refer the transmitted field back to the tangent plane W_b, which is now assumed to lie in the exterior medium in absence of the boundary. Finally, this reference plane is rotated into the transverse plane of the ray-centered coordinates of the transmitted ray. When all of these operations are combined, one finds for the initial condition for the transmitted TPRF,

$$\Gamma_{ts}(\bar{\rho}_t,\bar{\sigma}_t) = \hat{\Gamma}_b(\bar{\rho}_b,\bar{\sigma}_b,\bar{\sigma}_i)K_t(\bar{\rho}_b + \frac{c_2\bar{\sigma}_b}{2},\theta_i)K_t^*(\rho_b - \frac{c_2\bar{\sigma}_b}{2},\theta_i)$$

$$\times\exp\{ik\hat{s}_n n_{b+}\phi(\bar{\rho}_b,\bar{\sigma}_b) - in_{b+}\bar{\sigma}_t\tan\theta_t\} \quad , \tag{50}$$

where $\bar{\rho}_b = \bar{\rho}_t/\cos\theta_t$, $\bar{\sigma}_b = \bar{\sigma}_t/\cos\theta_t$ and θ_t is the angle of transmission according to Snell's law. The transmitted TPRF Γ_t then follows from (46), with (47), on replacing Γ_s by Γ_{ts} and (ρ,s,σ) by (ρ_t,s_t,σ_t); the TPCF is obtained by taking $<\Gamma_t>$.

For the reflected TPRF, the procedure is similar, except that the Kirchoff initial condition is stated in the ray-centered system of the reflected ray with reflection angle $\theta_r = \theta_i$, and the amplitude is modified by the local Fresnel plane wave reflection coefficient $K_r(\bar{r}_b,\theta_i)$. Thus, one obtains for the initial condition

$$\Gamma_{rs}(\bar{\rho}_r,\bar{\sigma}_r) = \Gamma_i(\bar{\rho}_r,\bar{s}_r,\bar{\sigma}_i)K_r[(\bar{\rho}_r + \frac{c_2\bar{\sigma}_r}{2})/\cos\theta_i,\theta_i]K_r^*[(\bar{\rho}_r - \frac{c_2\bar{\sigma}_r}{2})/\cos\theta_i,\theta_i]$$

$$\times\exp\{-2ik\hat{s}_n n_{b-}\phi(\bar{\rho}_r/\cos\theta_i,\ \bar{\sigma}_r/\cos\theta)\} \quad . \tag{51}$$

The reflected TPRF Γ_r follows again from (2), with (3), and the TPCF by taking $<\Gamma_r>$. If the incident and reflected background rays are separated far enough to decorrelate the corresponding fields, the product $<\Gamma_{rs}G>$ appearing in the integral for $<\Gamma_r>$ can be reduced to the product of averages. The expression in (51) is valid also for a perfectly reflecting boundary described by $K_r = 1$.

At normal incidence, the reflected ray traverses the same path as the incident ray, passing through the same inhomogeneities in the opposite direction. Now, the reference plane tangent to the interface at the point $B(\bar{r}=0,\bar{\sigma}_b)$ is in the ray-centered coordinates of both the incident and reflected rays. The initial condition for the reflected TPRF is accordingly,

$$\Gamma_{rs}(\bar{\rho},\bar{s},\bar{\sigma}_b) = \chi(\bar{\rho},\bar{s},\bar{\sigma}_b)\Gamma_i(\bar{\rho},\bar{s},\bar{\sigma}_b) \quad , \tag{52a}$$

where

$$\chi(\bar{\rho},\bar{s},\bar{\sigma}_b) = K_r(\bar{\rho} + \frac{c_2\bar{\sigma}_b}{2})K_r^*(\bar{\rho} - \frac{c_2\bar{\sigma}_b}{2})\exp\left\{-ik\hat{s}_n[\psi_r(\rho + \frac{c_2\bar{\sigma}}{2}) - \psi_r(\rho - \frac{c_2\bar{\sigma}}{2})]\right\} , \tag{52b}$$

$$\psi_r(\bar{r}) = 2\int_{\bar{\sigma}_b}^{\bar{\sigma}_b+\kappa(\bar{r})} d\tau n(\bar{r},t)[1+\tilde{n}(\bar{r},t)] . \tag{52c}$$

The average reflected intensity in the plane $\bar{r}_0$ at the range coordinate $\bar{\sigma}_0$ is then found from the formal expression derived previously[7-9],

$$I(\bar{r}_0,\bar{\sigma}_0) = \int_{-\infty}^{\infty}\cdots\int d\bar{v}_s dq_s d\bar{\rho}ds\,\Gamma_s(\bar{v}_s,q_s) < \chi(\bar{\rho},\bar{s},\bar{\sigma}_b)G(\bar{\rho},\bar{s},\bar{\sigma}_b|\bar{v}_s,q_s,0)G^*(\bar{r}_0,0,\bar{\sigma}_0|\bar{\rho},\bar{s},\bar{\sigma}_b)> , \tag{53}$$

where generally all of the factors in the averaging operation must be kept intact.

B. Diffraction by a Small Scattering Center

Next, we consider a scatterer which is small with respect to the local wavelength and has a nonisotropic radiation pattern so that it can serve as a canonical prototype for small obstacle scattering as well as edge diffraction. The previous results [18,19] obtained when the background medium is homogeneous are generalized readily to accommodate inhomogeneity. Invoking the GTD assumption of local homogeneity in a constant background whose value equals that at the scatterer location, one may express the initial condition for the diffracted TPRF in the spectral domain (see Sec. V),

$$\tilde{\Gamma}_{rs}(\bar{v}_s,\bar{\rho}_s) = \frac{I_{inc}}{I_n}\frac{k}{\delta(\bar{v}_s)}|D_0(\bar{\rho}_s,\theta_i;k)|^2, \tag{54a}$$

$$D_0(\bar{\rho}_s,\theta_i;k) \equiv D(\theta_d+\phi,\theta_i;k),\ \phi = \tan^{-1}\left[\frac{\bar{\rho}_s}{n_0(0)}\right] \quad , \tag{54b}$$

where $I_{inc}(0,\bar{\sigma}_1) = \Gamma_1(0,0,\bar{\sigma}_1)$, the intensity of the incident field at the scatterer, can be obtained by propagating the incident TPCF along the ray from the source to the scatterer location ($\bar{r}=0,\bar{\sigma}_1$). The diffraction coefficient $D(\theta_d,\theta_i;k)$ depends on the incidence and diffraction angles θ_i and θ_d, respectively [20], and the spectral parameter $\rho_s = k_0(0)\tan\phi$ spans the vicinity of the diffracted central ray. If the diffracted ray does not traverse the same path as the incident ray, the average intensity distribution at the range plane σ_d of the diffracted ray can be obtained by using (46b), with (54). For backscattering, with I_{inc} produced by a line source,

$$I(\bar{r}_0,\bar{\sigma}_0) = \frac{I_s k^2}{2\pi\lambda_n^2}\iint_{-\infty}^{\infty} d\bar{q}_s d\bar{\rho}_s |D_0(\bar{\rho}_s,\theta_i;k)|^2 \exp(i\bar{\rho}_s\bar{q}_s) \; < G(0,0,\bar{\sigma}_1|0,0,0)G^*(\bar{r}_0,0,\bar{\sigma}_0|0,\bar{q}_s,\bar{\sigma}_1)> \; , \qquad (55)$$

with the inhomogeneous background propagator G taken from (3). The above spectral formulation can also be applied to the smoothly curved boundary by relating the reflected spectra to the specularly reflected ray paths instead of the diffracted paths emanating from the fixed scattering center in (54), and replacing the diffraction coefficient in (54) and (55) by the appropriate spectral reflection coefficients.

V. Two-Point Coherence Function for Line Source Excited Edge Diffraction

In a final example, we deal with two-dimensional edge diffraction, which can be modeled in canonical form by an infinitely extended wedge that contains as a special case (for zero wedge angle) a semi-infinite thin screen. For simplicity, we take the background medium to be homogeneous, but the extension to inhomogeneous backgrounds has also been established [16]. A high frequency time harmonic line source is assumed to be positioned as in Fig. 3 in the presence of a perfectly reflecting wedge embedded in a random medium. The illuminated wedge face occupies the half plane $r>0$, $z=z_r$, and the source is located at the point $r=0$, $z=0$, with the z axis passing through the edge, but arbitrary source locations (not treated here) can also be accommodated.

The solution strategy in regions 3,4,5 of Fig. 3, wherein the various ray fields are uncorrelated, is based directly on the GTD background fields evaluated individually along each ray. In the transitional domains, where various ray fields are correlated, we employ the physical optics (PO) approximation along the aperture half plane $r<0$, $z=z_r$, for the forward region 1 and along the obstacle half plane $r>0$, $z=z_r$, for the reflected region 2. The PO fields are known to generate the correct transitional behavior that connects smoothly in an overlapping region at the edges of the transition zone to the GTD field elsewhere. The difference between the PO fields and GTD fields manifests itself at large diffraction angles where the PO edge diffraction coefficient is inaccurate. All results involve far field approximations that require observation distances from the edge to exceed the correlation length ℓ_n.

We begin with the forward transition region 1 (see Fig. 3) and the Kirchoff (PO) approximation to establish the corresponding initial conditions in the aperture plane at $z=z_r$. In the statistically isotropic random medium with homogeneous background, the solution for the TPCF with initial source condition $\Gamma_2(\bar{\rho},\bar{s},\bar{\sigma}_0) = \Gamma_{2s}(\bar{\rho},\bar{s})$, and scaled transverse sum and difference coordinates $\bar{\rho} = (r_1+r_2)/(2\ell_n)$, $\bar{s} = k(r_1-r_2)\ell_n$, as well as range coordinate $\bar{\sigma} = \sigma/\ell_n$, is (see Sec. III),

$$\Gamma_2(\bar{\rho},\bar{s},\bar{\sigma}) = \frac{1}{(2\pi)^2}\iint_{-\infty}^{\infty} d\bar{v}d\bar{\rho}\,\tilde{\Gamma}_{2s}[\bar{v}+\bar{\rho}(\bar{\sigma}_0-\bar{\sigma}),\bar{\rho}]\exp(i\bar{\rho}\bar{m})\int_{-\infty}^{\infty} d\bar{\eta}\,\exp\left\{-k^2\ell_n\int_{\bar{\sigma}_0}^{\bar{\sigma}} d\bar{\alpha}\,[\bar{\Lambda}_n(0)-\bar{\Lambda}_n(\frac{\bar{s}+\bar{\eta}(\bar{\sigma}-\bar{\sigma}_0)}{k\ell_n})]\right\}$$
$$\times \exp[i\bar{\Gamma}(\bar{p}-\bar{v})], \qquad (56)$$

where $\tilde{\Gamma}_{2s}(\bar{v},\bar{\rho}) = \int_{-\infty}^{\infty} d\bar{s}\,\Gamma_{2s}(\bar{v},\bar{s})\exp(-i\bar{\rho}\bar{s})$. For line source excitation at $\bar{\sigma}_0=\bar{z}_0=\bar{0}$, $\Gamma_s(\bar{v},\bar{\rho}) = I_s(k/\ell_n)\delta(\bar{v})$, I_s being the source strength. Using the solution $\Gamma_2(\bar{\rho},\bar{s},\bar{z}_r)$ in the plane $\bar{z}=\bar{z}_r$ allows us to establish the Kirchoff initial conditions $\Gamma_{2ts}(\bar{\rho},\bar{s},\bar{z}_r)$ for Region 1,

$$\Gamma_{2ts}(\bar{\rho},\bar{s},\bar{z}_r) = \bar{t}(\bar{\rho}+\frac{\bar{s}}{2k\ell_n})\bar{t}(\bar{\rho}-\frac{\bar{s}}{2k\ell_n})\,\Gamma_2(\bar{\rho},\bar{s},\bar{z}_r) \; , \qquad (57)$$

where the transmission function in the presence of the half plane is $\bar{t}(\bar{r})=0$ or 1 for $\bar{r}>0$ and $\bar{r}<0$, respectively. Then, the solution $\Gamma_2(\bar{\rho},\bar{s},\bar{z})$ for $\bar{z}>\bar{z}_r$ in Region 1 is given by (2) with $\tilde{\Gamma}_{2s}(\bar{v},\bar{s})$ replaced by $\tilde{\Gamma}_{2ts}(\bar{\rho},\bar{s},\bar{z}_r)$ at $\bar{\sigma}_0=\bar{z}_r$. This yields the transverse average intensity distribution $I(\bar{r},\bar{z}) = \Gamma_2(\bar{\rho}=\bar{r},\bar{s}=0,\bar{z})$ in Region 1. When the refractive index fluctuations are omitted, the intensity can be shown to reduce to what is predicted by deterministic edge diffraction. The deterministic transition function, a squared Fresnel integral [21], is generated from (56) to (57), because of the truncated integrations. At the edges of Region 1, this solution connects smoothly onto those in Regions 3 and 4.

In the backward transition region 2, the reflected and incident fields traverse the same inhomogeneities so that we must deal with the random fields and the two-point random function (see [18,19] to effect the corresponding correlation. The total field $U(r,z)$ at the observation distance $z<z_r$ in region 2 is expressed in terms of parabolically approximated incident (u_i) and reflected (u_r) fields as

$$U(r,z) = u_i(r,z)\exp(ikz) + u_r(r,z)\exp[ik(2z_r-z)] \; . \qquad (58)$$

Then with $\epsilon = (k\ell_n)^{-1}$ and the notation $u(r,\sigma) \equiv \bar{u}(\bar{r},\bar{\sigma})$, the total TPCF is given by

$$\Gamma_2(\bar{\rho},\bar{s},\bar{z}) = \Gamma_{2i}(\bar{\rho},\bar{s},\bar{z}) + \Gamma_{2r}(\bar{\rho},\bar{s},\bar{z}) + \langle \bar{u}_i(\bar{\rho} + \frac{k\bar{s}}{2}, \bar{z})\bar{u}_r^*(\bar{\rho} - \frac{k\bar{s}}{2}, \bar{z})\rangle$$
$$\times \exp[\tfrac{2i}{c}(\bar{s} - \bar{s}_r)] + \langle \bar{u}_r(\bar{\rho} + \frac{k\bar{s}}{2}, \bar{z})\bar{u}_i^*(\bar{\rho} - \frac{k\bar{s}}{2}, \bar{z})\rangle \exp[\tfrac{2i}{c}(\bar{s}_r - \bar{s})] \quad . \tag{39}$$

Setting $\bar{\rho} = \bar{r}$, $\bar{s} = 0$, yields the average intensity distribution

$$I(\bar{r},\bar{z}) = I_i(\bar{r},\bar{z}) + I_r(\bar{r},\bar{z}) + \langle \bar{u}_i(\bar{r},\bar{z})\bar{u}_r^*(\bar{r},\bar{z})\rangle \exp[\tfrac{2i}{c}(\bar{z} - \bar{z}_r)] + \langle \bar{u}_r(\bar{r},\bar{z})\bar{u}_i^*(\bar{r},\bar{z})\rangle \exp[\tfrac{2i}{c}(\bar{z}_r - \bar{z})] \quad . \tag{60}$$

The incident field intensity in (60) can be taken directly from the TPCF $\Gamma_2(\bar{\rho},\bar{s},\bar{z})$ in (56). For the reflected field, the Kirchoff initial conditions are conveniently expressed in terms of the reflection function $\bar{h}(\bar{r}) = 1 - \bar{t}(\bar{r})$. Then the reflected field u_r and the reflected field intensity I_r for line source excitation can be obtained using the formal solutions of Refs. [22,23],

$$\bar{u}_r(\bar{r},\bar{z}) = \frac{I_0^{1/2}}{k_n} \int_{-\infty}^{\infty} d\bar{r}_0 \bar{h}(\bar{r}_0) G_u(\bar{r}_0,\bar{z}_r|0,0) G_u(\bar{r}_0,\bar{z}_r|\bar{r},\bar{z}) \quad , \tag{61a}$$

$$I(\bar{r},\bar{z}) = \frac{I_0 k}{k_n} \iint_{-\infty}^{\infty} d\bar{\rho} d\bar{s} \bar{h}(\bar{\rho} + \tfrac{k\bar{s}}{2}) \bar{h}(\bar{\rho} - \tfrac{k\bar{s}}{2}) G(\bar{\rho},\bar{s},\bar{z}_r|0,0,0) G(\bar{\rho},\bar{s},\bar{z}_r|\bar{r},0,\bar{z}_r) \quad , \tag{62b}$$

and the explicit geometric solutions of the random field propagator G_u as well as the two-scale expansion solution of the two-point random field propagator G (Refs. [18], [19]).

Outside regions 1 and 2, the incident field striking the edge creates a diffracted field, which at a "far zone" observation point (σ,θ) (several wavelengths from the edge) in the forward shadow region 3, has the form

$$u_d(P_3) = (\frac{k}{2\pi i\sigma})^{1/2} u_i D(\theta_d,\theta_i;\alpha,k)\exp(ik\sigma) \quad . \tag{62}$$

Here, u_i is the incident field value at the edge ($r = 0$, $z = z_r$), and $D(\theta_d,\theta_i;\alpha,k)$ is the edge diffraction coefficient [20], with θ_i, θ_d and α describing the incidence, observation, and wedge angles, respectively (see Fig. 3). The form of $D(\theta_d,\theta_i;\alpha,k)$ is obtained from the canonical solution of wedge diffraction [20]. To calculate the average intensity, we propagate the TPCF Γ_2 (see (1)) from the edge to (σ,θ) along the single edge diffracted ray. In the angular spectral domain defined by $\Gamma_2(\bar{\rho},\bar{\rho},\bar{\sigma}) = \int_{-\infty}^{\infty} d\bar{s}\,\Gamma_2(\bar{\rho},\bar{s},\bar{\sigma})\exp(-i\bar{\rho}\bar{s})$, where the spectral variable $\bar{\rho}$ can be interpreted as a "slope parameter" (see Figs. 1,3) with respect to the reference ray, we express the initial condition at $\bar{\sigma} = 0$ as follows

$$\bar{\Gamma}_{2s}(\bar{\rho},\bar{\rho}) = \frac{I_i k}{k_n} \delta(\bar{\rho})\tilde{D}(\bar{\rho}), \quad \tilde{D}(\bar{\rho}) = |D(\theta_d,\theta_i+\phi;\alpha,k)|^2, \ \phi = \tan^{-1}\bar{\rho} \quad , \tag{63}$$

where $I_i = \langle \bar{u}_i\bar{u}_i^* \rangle$ is the intensity of the incident wave. Substituting (11) into (2) and setting $\bar{\rho} = \bar{r}$, $\bar{s} = 0$, we obtain for the intensity distribution in region 3,

$$I(\bar{r},\bar{\sigma}) = \frac{I_i k}{(2\pi)^2 k_n} \iint_{-\infty}^{\infty} d\bar{\rho} d\bar{n} \tilde{D}(\bar{\rho}) \exp\left\{-k^2 k_n \int_0^{\bar{\sigma}} d\zeta [\bar{A}_n(0) - \bar{A}_n(\frac{\bar{n}(\zeta-\bar{\sigma})}{k k_n})]\right\} \exp[i\bar{n}(\bar{r} - \bar{\rho}\bar{\sigma})]. \tag{64}$$

This result reduces in the absence of refractive index fluctuations ($\bar{A}_n \equiv 0$) to $I(\bar{r},\bar{\sigma}) = I_i k\tilde{D}(\bar{\rho} = \bar{r}/\bar{\sigma})/(2\pi k_n\bar{\sigma})$, which is in agreement with what one finds from deterministic GTD.

The field in region 4 differs from that in region 3 only through the additional presence of the incident ray field (see Fig. 1). Since the two ray fields are uncorrelated because their propagation paths sample different portions of the medium, they can be treated individually (individual treatment here and in regions 2 and 5 applies directly when use of a pulsed source or directional receiver allows isolation of distinct ray arrivals). The intensity at the observation point is accordingly

$$\begin{aligned} I(P_4) &= \{u_i(P_4)\exp(ik\sigma_1) + u_d(P_4)\exp[ik(s_r + \sigma_2)]\} \\ &\times \{u_i^*(P_4)\exp(-ik\sigma_1) + u_d^*(P_4)\exp[-ik(s_r + \sigma_2)]\} \\ &= I_i(P_4) + I_d(P_4) + \langle u_i(P_4)\rangle\langle u_d^*(P_4)\rangle \exp(ik(\sigma_1 - \sigma_2 - s_r)] \\ &+ \langle u_d(P_4)\rangle\langle u_i^*(P_4)\rangle \exp[ik(s_r + \sigma_2 - \sigma_1)] \end{aligned} \tag{65}$$

The direct and diffracted field intensities can be calculated by propagating the direct and diffracted coherence functions along each ray with corresponding initial conditions. The average fields take the form [10-12]

$$\langle u(\mathbf{r},\sigma_t)\rangle = u(\mathbf{r},\sigma_t)\exp\left[-\tfrac{1}{2}k^2\chi_n(0)\sigma_t\right], \qquad (66)$$

where $u(\mathbf{r},\sigma)$ is the solution for the field in the absence of fluctuations, and σ_t is the total distance traversed by the ray from source to observer. The same considerations apply to the field in region 3 provided that one includes the reflected ray field, which looks like an incident field originating at the image source location $\mathbf{r}=0$, $z=2z_T$.

In a more comprehensive treatment by the authors, which also illustrates various general considerations that will play a role in other propagation and diffraction problems, the analysis summarized here has been generalized to arbitrary source location.

References

1. L.B. Felsen, "Progressing and Oscillatory Waves for Hybrid Synthesis of Source Excited Propagation and Diffraction", IEEE Trans. on Antennas and Propagation, AP-32 (1984), pp. 775-796.

2. L.B. Felsen, "Novel Ways for Tracking Rays", J. Opt. Soc. Am. A, 2 (1985), pp. 934-963.

3. R. Mazar and L.B. Felsen, "High-Frequency Coherence Functions Propagated Along Ray Paths in the Inhomogeneous Background of a Weakly Random Medium: I-Formulations and Evaluation of the Second Moment", to be published in J. Acoust. Soc. Am.

4. R. Mazar and L.B. Felsen, "High-Frequency Coherence Functions Propagated Along Ray Paths in the Inhomogeneous Background of a Weakly Random Medium: II-Higher Moments", to be published in J. Acoust. Soc. Am.

5. R.J. Hill, "A Stochastic Parabolic Wave Equation and Field-Moment Equations for Random Media having Spatial Variations of Mean Refractive Index", J. Acoust. Soc. Am., 77 (5), (1985), pp-1742-1752.

6. S. Frankenthal, M.J. Beran and A.M. Whitman, "Caustic Corrections Using Coherence Theory", J. Acoust. Soc. Am. 71(2), (1982), pp. 348-358.

7. M.J. Beran, A.M. Whitman and S. Frankenthal, "Scattering Calculations Using the Characteristic Rays of the Coherence Function", J. Acoust. Soc. Am., 71(5), (1982), pp. 1124-1130.

8. R. Mazar and M.J. Beran, "Intensity Corrections in a Random Medium in the Neighborhood of a Caustic", J. Acoust. Soc. Am., 72(4), (1982), pp. 1269-1275.

9. R. Mazar and M.J. Beran, "Intensity in Stratified Random Media", J. Acoust. Soc. Am., 75(6), (1984), pp. 1748-1759.

10. V.I. Tatarskii and V.U. Zavorotnyi, "Strong Fluctuations in Light Propagation in Randomly Inhomogeneous Medium", in "Progress in Optics", Vol. XVIII, E. Wolf (Ed.), (North-Holland Publishing Co., Amsterdam, 1980).

11. S.M. Rytov, Y.A. Kravtsov and V.I. Tatarskii, "Introduction to Statistical Radiophysics, Vol. 2, Random Fields" (translated from the Russian by Springer-Verlag, forthcoming).

12. A. Ishimaru, "Wave Propagation and Scattering in Random Media", Vol. 1, 2 (Academic Press, New York, 1978).

13. V.M. Babich and V.S. Buldyrev, "Asymptotic Methods in Short Wave Diffraction Problems" (in Russian, Nauka, Moscow, 1972).

14. V.M. Babich and N.J. Kirpichnikova, "Boundary Layer Method in Diffraction Problems" (translated from the Russian by Springer-Verlag, 1980).

15. V. Červeny, M.M. Popov and I. Pšenčik, "Computation of Wave Fields in Inhomogeneous Media-Gaussian Beam Approach", Geophys. J. R. Astr. Soc. 70, (1982), pp. 109-128.

16. R. Mazar and L.B. Felsen, "Stochastic Geometrical Diffraction Theory in a Random Medium with Inhomogeneous Background", Optics Letters, Vol, 12(to be published).

17. D.M. Berman and J.J. McCoy, "Coherence Propagation and Geometric Acoustics", J. Acoust. Soc. Am., 79 (3), (1986), pp. 635-643.

18. R. Mazar and L.B. Felsen, "Geometrical Theory of Diffraction for High-Frequency Coherence Functions in a Weakly Random Medium", Optics Letters, 12(3), (1987), pp. 146-148.

19. R. Mazar and L.B. Felsen, "Edge Diffraction of High Frequency Coherence Functions in a Random Medium", Optics Letters, 12, (1987), pp. 4-6.

20. J.B. Keller, "Geometrical Theory of Diffraction", J. Opt. Soc. Am., 52(2), (1962), pp. 116-130.

21. M. Born and E. Wolf, "Principles of Optics", Pergamon Press, Oxford, 1964.

22. V.P. Aksenov, V.A. Banakh and V.L. Mironov, "Fluctuations of Retroreflected Laser Radiation in a Turbulent Atmosphere", J. Opt. Soc. Am., A1, (1984), pp. 263-274.

23. V.I. Klyatskin, ""Stochastic Equations and Waves in Randomly Inhomogeneous Media", (in Russian, Nauka, Moscow, 1980).

Acknowledgement

This work has been sponsored by the Rome Air Development Center, Hanscom AFB, through a grant administered by the Joint Services Electronics Program under Contract No. F-49620-85-C-0028.

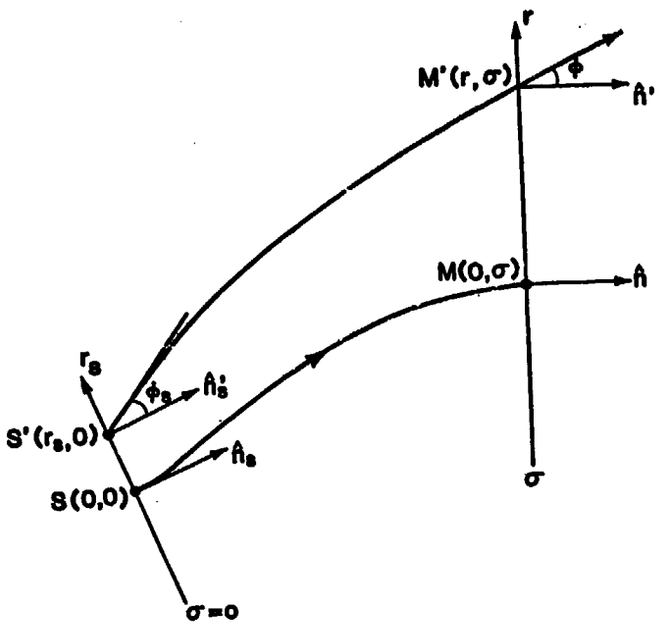


Fig. 1

Fig. 1 - Ray-centered coordinate system.

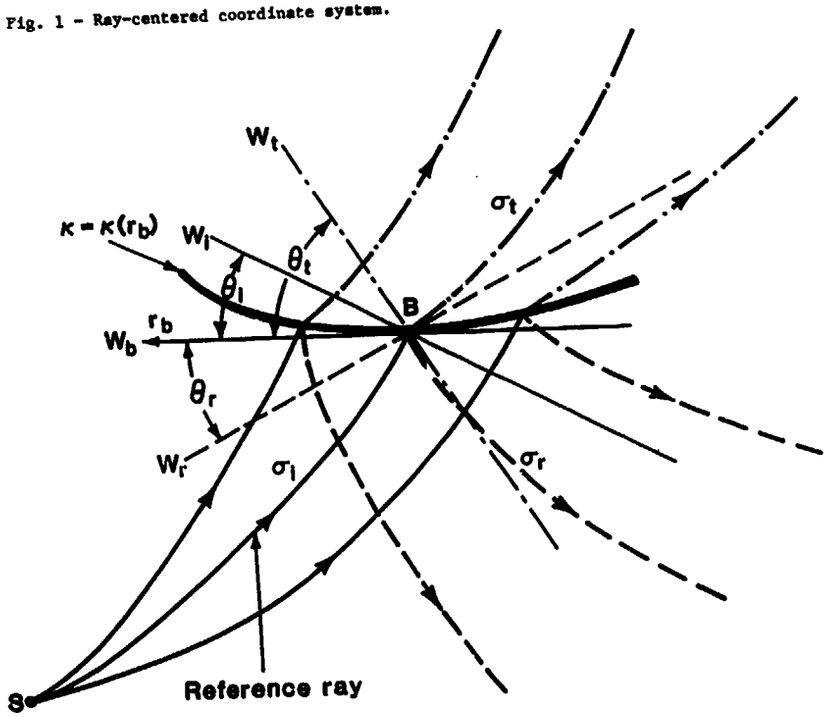


Fig. 2

Fig. 2 - Ray Reflection-Transmission Diagram. Solid lines - incident rays, dot-dashed lines - transmitted rays, dashed lines - reflected rays.

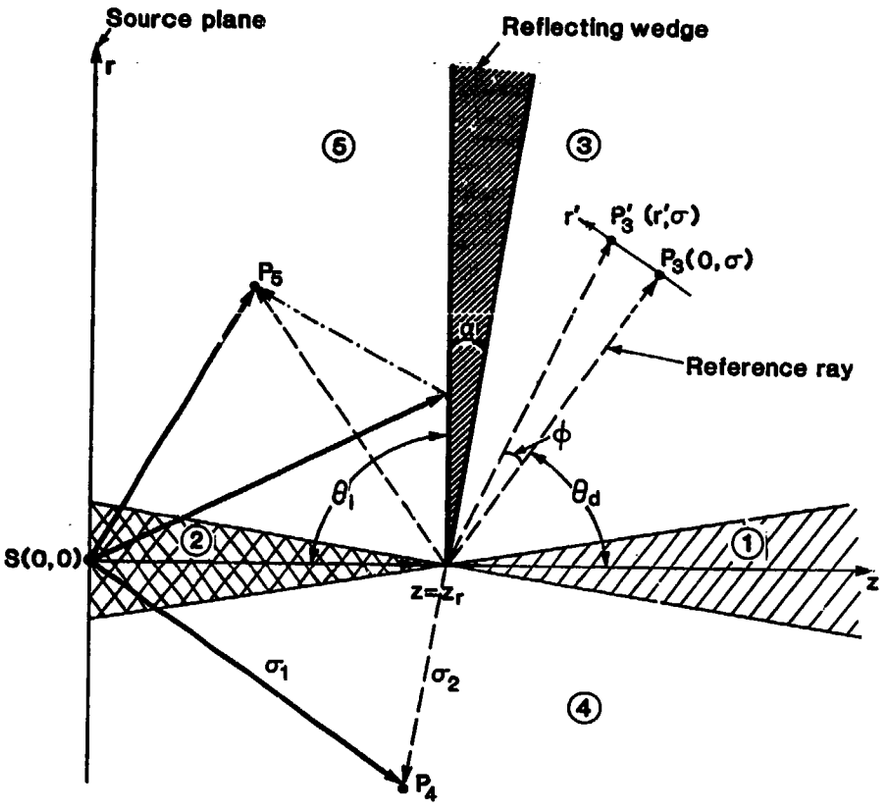


Fig. 3

Fig. 3. Physical configuration, ray-optical and transitional (shaded) domains for line source excited wedge. —— direct rays; -·- reflected rays; -- edge diffracted rays.

DISCUSSION

A.N. Ince, TU

As one increases the complexity of the GTD by, for instance, combining rays and modes in guiding channels, does one not come quickly to the point where GTD loses its validity? How can one be certain of the validity of the solution obtained in complicated environments?

Author's Reply

The reason for GTD is to cope with complicated environments. In its range of validity ("high" frequency, etc.), GTD is probably the most versatile computation intensive algorithm, which is based on a cogent physical parameterization of the scattering properties of complex shapes. When an environment contains waveguide-like features, local modes are the natural physical observables that describe propagation within it. If very many modes are required, then the most effective description involves a self-consistent combination of rays and modes. Just as for conventional GTD, one must establish the validity of hybrid ray-mode schemes by comparing with well computable canonical test problems. If the test problem is properly parameterized, the solution can be extended away from the canonical structure into a more general domain. The key is the choice of the relevant canonical problem. The task is not easy, but neither are the problems themselves.

A. Ishimaru, US

Some years ago, we made a study of fluctuations of radio waves from a spacecraft when the ray path went through the Venus atmosphere where considerable ray bending took place because of the large gradient of the refractive index. The turbulence of the Venus atmosphere then created a change in the equivalent Fresnel size and a change in the temporal frequency spectra. We used the weak fluctuation theory to explain this; however, your theory may be able to explain this in the strong fluctuation region.

Author's Reply

We do not know, at present, to what extent our theory can account for strong fluctuations. Test calculations will have to be performed to assess the range of validity of what we have done so far for strongly refracting background media.

SUMMARY OF SESSION II

SURFACE SCATTERING

by

A.Ishimaru, Session Chairman

The first paper of this session was presented by S.A.DeSanto who gave a review of multiple scattering theories for rough surface scattering. He presented a summary of the conventional perturbation and Kirchhoff methods and then proceeded to give an overview of several modern techniques, pointing out a need to consider larger height variations and smaller correlation distances. It was pointed out that while coherent scattering is fairly well understood, incoherent scattering needs further study.

The regions of validity of several rough surface scattering models were discussed by R.J.Papa in the second paper. Physical optics and geometric optics were considered as well as perturbation theory.

Models of image texture were discussed by Luttrell in the third paper. Certain statistics of the image and synthetic images were generated by the Monte Carlo method.

A.K.Fung presented a scattering model for forested areas by means of a circular disk model for leaves, and a finite cylinder model for branches which compare favourably with measured data.

The representation and simulation of clutter textures were given by Oliver in the last paper. A correlated gamma-distributed cross section model and a simulation of correlated random textures were then compared with data.

MULTIPLE SCATTERING FROM ROUGH SURFACES

by
John A. DeSanto
Center for Wave Phenomena
Mathematics Department
Colorado School of Mines
Golden, CO
80401
USA

SUMMARY

A review of multiple scattering theories will be presented with specific application to scattering from rough surfaces. This will include the limitations, advantages and range of validity of both traditional methods such as the Kirchhoff and perturbation methods as well as a discussion of modern methods. The latter include the connected diagram method (integral equations), the smoothing method, the stochastic Fourier transform approach and the spectral method. The former two methods have an analogue in the theory of wave propagation in random media. The latter method is analogous to a method developed by us for scattering from periodic surfaces.

We stress what we term the modern mathematical approach to these problems. In this approach the exact stochastic integral equations are used to develop equations on averages of the field quantities. The two most prominent equations are the Dyson equation on the first moment of the field, and the Bethe-Salpeter equation on the second moment. For homogeneous surface statistics, the former yields the coherent specular scattering, and the latter yields the incoherent scattering. Formally, both can be expressed exactly in the sense that all orders of multiple scattering are included, but, in order to be solved, must be approximated. The Dyson equation has been solved in lowest order approximation and illustrates the necessity of using multiple scattering techniques to describe coherent scattering. The situation with the Bethe-Salpeter equation, however, is not nearly so well understood, and the difficulty of finding approximation techniques for this equation will be discussed.

1. SINGLE SCATTERING THEORIES

When acoustic, electromagnetic or elastic waves impinge on a rough surface, several effects can possibly take place. One is reflection, which manifests itself in a specular return of some or all of the incident energy. A second is scattering, which can include reflection and refers to the presence of energy in other than specular directions, but still existing on the same side of the surface as the incident energy. A third is transmission, which is scattered energy occurring on the side of the surface opposite to that of the incident energy. A fourth is the creation of waves which travel along the surface, i.e. surface waves, and decay in a direction orthogonal to the mean surface. This is true whether the surfaces are the ocean, terrain, metals or rocks. On yet another dimensional scale, it is true for atomic beams scattering from crystals. The reason it is true is that the roughness or surface height h scales to wavelength λ. The parameter kh where $k = 2\pi/\lambda$ is the wavenumber occurs as one of the important dimensionless parameters of the scattering problem. Roughness, therefore, depends on wavelength. A simple geometrical argument can confirm this and also describe what happens when a plane wave incident at angle θ interacts once with a rough surface and scatters in the specular direction from it [1]. For example, a ray or plane wave incident at angle θ (from the normal) strikes a roughened surface. If it scatters only once the additional path length it experiences (as opposed to a wave striking the flat surface) is expressed as a phase difference

$$\Delta\phi = 2hk\cos\theta \quad , \tag{1}$$

corresponding to the vertical (z-direction) projections of the down- and up-going transit of the wave in the surface well of height h. The z-component of the field which is single scattered from this surface can be expressed as

$$\psi^s(z) = R \exp(izk\cos\theta + i\Delta\phi) \quad , \tag{2}$$

where R is the Rayleigh-Fresnel reflection coefficient [2]. If h is a stochastic quantity so is this scattered field in Eq.(2). Its average over the ensemble of surface realizations, denoted by the symbol E is formed by multiplying Eq.(2) by p(h), the probability distribution of h, and integrating from $-\infty$ to ∞. Since R and the phase term in z are deterministic quantities the average or what is termed the coherent scattered field is

$$E\psi^s(z) = R \exp(izk\cos\theta)\, E \exp(i\Delta\phi) \quad . \tag{3}$$

The average of the phase term depends on p(h). For example, if p(h) is a Gaussian, the average is just the two-way Fourier transform of p(h), which is a Gaussian,

$$E \exp(i\Delta\phi) = \exp(-2\Sigma^2) \quad , \tag{4}$$

where $\Sigma = k\sigma\cos\theta$ is the Rayleigh roughness parameter with σ the rms height. The result can be interpreted as an effective reflection coefficient $R \exp(-2\Sigma^2)$ for the coherent scattered field, or as an additional decay of the coherent field due to surface roughness [3,4]. The remaining energy scatters into other than specular angles, or into what is termed the incoherent field which we discuss later. To compute the latter involves multiplying the random quantities together and then averaging to construct higher order field moments.

The preceeding example is one of the simplest which can be done for rough surface scattering. The reason it is so simple, and that averages can be directly performed, is that it is a local field representation. This is obvious if the incident field is a ray since only a local surface area is illuminated. In fact it is just point scattering. For an infinite plane wave incident on an unbounded flat surface the locality is a result of the degeneration of the scattered (spherical) Huygens wavelets all recombining into a single plane wave propagating at the specular angle. When we discuss more realistic scattering models, the locality property in the deterministic sense is lost.

There are three important scale lengths for surface scattering, λ (or k), σ (or h) which is a vertical scale, and a horizontal scale L. For a deterministic periodic surface, L is the period. For a statistical surface, L is the correlation distance, that distance over which the surface becomes statistically significantly different. It is usually taken as the 1/e value of the correlation function defined below. Strictly speaking, we have assumed that the surface is isotropic, so that we only have a single horizontal scale length. The second important dimensionless parameter which then arises is the slope, σ/L, which is a purely geometrical quantity, independent of wavelength. For surfaces with shallow slopes, which appear to the eye as gently undulating or having a large radius of curvature, single scattering theories can apply although they may not be local theories. The Kirchhoff theory discussed below is an example of a non-local single scatter theory. The intuitive reason for this is that for a gently undulating surface, locally specularly reflecting waves traversing a geometrical path will most likely not reflect off another surface point. Nonlocality is necessary to take into account the fact that the full scattering consists of many local areas distributed across the surface. These must be added together to yield the total scattered field. For surfaces with large slopes or heights (kσ) on the order of one, waves are trapped in the wells and are multiply scattered. In these limits a purely geometrical theory becomes intractable and nonlocal wave theoretical methods such as integral equations are used.

A further stochastic description of the surface uses the correlation function $C(x_t)$ where $x_t = (x,y)$ is the transverse coordinate two-vector. It is defined as

$$\sigma^2 C(x_t) = E\, h(x_t')\, h(x_t + x_t') \quad , \tag{5}$$

where the statistical averaging indicated by E operates on everything to its right. It is expressed as a function only of the difference of coordinate dependences of the height terms. The assumption is that the surface is statistically homogeneous or statistically translationally invariant. Not all surfaces satisfy this property, but nonhomogeneous statistics complicate the description considerably and we do not consider them here. The Fourier transform of the correlation function, the spectral function, often appears. It is defined by

$$S(k_t) = \sigma^2 \iint C(x_t) \exp(-ik_t \cdot x_t)\, dx_t \quad . \tag{6}$$

For isotropic surface statistics, analytical correlation functions such as a Gaussian

$$C(x_t) = \exp(-x_t^2/L^2) \quad . \tag{7}$$

are often used for theoretical purposes. Practical spectra however have both a lower and upper cutoff, an angular dependence (anisotropy) and often appear to fall off as a power of the wavenumber.

2. PERTURBATION THEORY

For small height values, the boundary condition on the rough surface can be expanded in a power series in h [5]. For example the Dirichlet boundary condition (for a perfect conductor) is

$$\bar{s}(x_h) = 0 \quad ; \quad x_h = (x,y,h) \quad . \tag{8}$$

Expanding this condition in a Taylor series about h = 0 and dropping terms of order h^2 and higher yields

$$\bar{s}(x_t,0) + h \frac{\partial \bar{s}}{\partial z}(x_t,0) = 0 \quad . \tag{9}$$

where to this order of approximation, the normal derivative is approximated by the z-derivative. If h is a random quantity, we expand the field into a mean (coherent) part $E\bar{s}$ and a stochastic (incoherent) part u

$$\bar{s} = E\,\bar{s} + u \quad . \tag{10}$$

Averaging and some algebraic manipulations yield a boundary condition relating the coherent and incoherent fields

$$E\,\bar{s} = -E\, h\, \partial u/\partial z \quad , \tag{11}$$

and a second boundary condition on the incoherent field given by

$$u = -h \frac{\partial}{\partial z} E\,\bar{s} \quad . \tag{12}$$

These boundary conditions reflect the interrelationship between coherent and incoherent fields which is also present off the boundary. We have already mentioned the decay of the coherent field, and the fact that the energy couples into the incoherent field.

The suppression of the incoherent field using a Rayleigh diffraction formula can be used to derive a non-local boundary condition on the coherent field. The boundary condition is of impedance type in that it involves both the field and its z-derivative. Since the perturbation analysis yields effective coherent boundary conditions on the flat surface a coherent field expansion in terms of plane incident and scattered waves can be written as

$$\mathbb{E}\,\bar{\psi}(\underline{x}) = \exp(i\underline{k}_t\cdot\underline{x}_t)\left[\exp(-ik_z z) + R\exp(ik_z z)\right] \quad . \tag{13}$$

where the effective reflection coefficient R can be written as

$$R = \frac{I(k_t)\cos\theta - 1}{I(k_t)\cos\theta + 1} \quad . \tag{14}$$

with I non-locally related to the correlation function as

$$I(k_t) = \frac{ik_0 e^{ik_0 z}}{2\pi} \lim_{z\to 0} \iint \frac{\exp\left[ik_0(x_t^2 + z^2)^{1/2}\right]}{(x_t^2 + z^2)^{1/2}} C(x_t)\exp(i\underline{k}_t\cdot\underline{x}_t)\,d\underline{x}_t \quad . \tag{15}$$

The theory is non-local and involves some multiple scattering due to the perturbation analysis. The form of the correlation function limits the domain of the integrand in Eq.(15) to the region about $x_t = 0$.

The incoherent intensity at the field point $\underline{x} = (x_t, z)$ is given by

$$\mathbb{E}\,|\psi(\underline{x})|^2 = \bar{A}\,k_0^4 z^2 z_0^2 \left[R_0' R'\right]^{-4} S(k_t^s - k_t^i) \quad , \tag{16}$$

where $\bar{A}$ is the ratio of surface area illuminated divided by $16\pi^2$, $z_0(z)$ is the source (receiver) height above a mean plane, $R_0'(R')$ the radial distance from source (receiver) position to some mean point x_t within the illuminated area, S is the spectral function defined in Eq.(6), and k_t^s and k_t^i the horizontal components of the scattered and incident wave vectors defined by

$$k_t^s = k_0(x_t - x_t')\left[(x_t - x_t')^2 + z^2\right]^{-1/2} \quad , \tag{17}$$

and

$$k_t^i = k_0\, x_t'\left[x_t'^2 + z_0^2\right]^{-1/2} \quad . \tag{18}$$

It can be seen from Eq.(16) that in this approximation the incoherent intensity is sensitive to only a single spectral component given by the difference between incident and scattered wave vectors. Bragg scattering can be derived from this result [6].

As we previously stated, perturbation theory involves some multiple scattering. This is obvious since in perturbation theory we can count the interactions with the surface by counting the number of times h occurs in the formalism. The incoherent intensity for example is related to the spectral function, which itself is expressed using second order terms in h. This means that the theory is restricted to small values of k_0 on the order of 0.6 [7]. Renormalization methods can be used to extend this somewhat [8].

3. GREEN'S THEOREM AND MULTIPLE SCATTERING

In order to express the multiple interactions which can occur at a very rough surface we must resort to more rigorous mathematics using Green's theorem. The procedure is to use Green's theorem to write integral representations of the field in terms of surface values, and then to find the surface values using integral equations. The method can be used for both perfectly reflecting problems (which we illustrate here) as well as transmission problems. We illustrate the method briefly as a scalar problem [9] since it is simpler. The electromagnetic results are presented in [10]. The field quantity above the surface $z = h$ can be written for spherical wave incidence from a source point $\underline{x}_0$ also located above the surface as

$$\bar{\psi}(\underline{x}) - \psi^0(\underline{x},\underline{x}_0) = \int\!\!\int \left[G^0(\underline{x},\underline{x}_h')\frac{\partial}{\partial n'}\bar{\psi}(\underline{x}_h') - \bar{\psi}(\underline{x}_h')\frac{\partial}{\partial n'}G^0(\underline{x},\underline{x}_h') \right] ds' \quad , \tag{19}$$

where

$$G^0(\underline{x},\underline{x}_0) = \exp\left[ik_0\,|\underline{x} - \underline{x}_0|\right] \Big/ 4\pi\,|\underline{x} - \underline{x}_0| \quad . \tag{20}$$

is the free space Green's function. Integration is confined to the rough surface, and $\underline{n}'$ is the surface normal. If both $\bar{\psi}$ and its normal derivative on the surface were known quantities, the relation Eq.(19) would serve to fix the value at point $\underline{x}$ in the field since G^0 is explicitly known. These are in general not known and must be found using integral equations discussed below.

Several approximate versions of this theory are useful. For a Dirichlet boundary condition (TE electromagnetic perfect conductor) we have the field vanishing on the boundary

$$\Psi(\underline{x}_h) = \Psi^0(\underline{x}_h,\underline{x}_0) + \Psi^0(\underline{x}_h) = 0 \quad . \tag{22}$$

where we've expressed Ψ as the sum of incident point source plus scattered field, and the normal derivative doubled

$$\frac{\partial}{\partial \underline{n}} \Psi(\underline{x}_h) = 2 \frac{\partial}{\partial \underline{n}} \Psi^0(\underline{x}_h,\underline{x}_0) \quad . \tag{23}$$

This is what happens at a plane interface and the generalization here is interpreted as happening on a plane with a tilt or local tangent angle and is referred to as the tangent plane approximation. Several versions of this are available with an additional approximation on the normal derivative the three main ones yield an expression for the scattered field as

$$\Psi^s(\underline{x}) = \iint K(\underline{x},\underline{x}_h') \, \Psi^0(\underline{x},\underline{x}_h') \, \Psi^0(\underline{x}_h',\underline{x}_0) \, dx_t \quad , \tag{23}$$

where

$$K(\underline{x},\underline{x}_h') = \begin{cases} 2i \, \underline{k}^i \cdot \underline{n} \\ i(\underline{k}^i - \underline{k}^s) \cdot \underline{n} \\ -2i \, \underline{k}^s \cdot \underline{n} \end{cases} \quad . \tag{24}$$

depending on the version of the theory used. The first version can be derived here using Eqs.(19), (21) and (22). The second version is due to Eckart [4] and is reciprocal under the interchange $\underline{k}^s \leftrightarrow \underline{k}^i$.

A full guess for both fields with plane wave incidence Ψ^i can be written (using the tangent plane argument above) as

$$\Psi(\underline{x}_h) = (1 + R) \, \Psi^i(\underline{x}_h) \quad . \tag{25}$$

and

$$\frac{\partial}{\partial \underline{n}} \Psi(\underline{x}_h) = i \, (1-R) \, \underline{k}^i \cdot \underline{n} \, \Psi^i(\underline{x}_h) \quad , \tag{26}$$

with R the reflection coefficient. This is referred to as the Kirchhoff approximation. In the far field, Ψ^s becomes a spherical Huygens wavelet with amplitude A ($r = |\underline{x}|$)

$$\Psi^s(\underline{x}) \sim A(\theta_i,\theta_s) \exp(ik_0 r) \; / \; 4\pi r \quad . \tag{27}$$

with θ_i and θ_s the incident and scattering angles. The amplitude can be written for a one-dimensional surface as

$$A(\theta_i,\theta_s) = ik_0 \int \exp(-ik_0 x' \alpha_0 - ik_0 h(x') \beta_0) \, (b - ah') \, dx' \quad . \tag{28}$$

where

$$\alpha_0 = \sin\theta_s - \sin\theta_i \quad , \quad \beta_0 = \cos\theta_s + \cos\theta_i \quad . \tag{29}$$

and

$$a = \sin\theta_s + \sin\theta_i + \alpha_0 R \quad , \quad b = \cos\theta_s - \cos\theta_i + \beta_0 R \quad . \tag{30}$$

The function A is also referred to as the surface interaction function. It will occur in our discussion of multiple scattering below as will techniques to average it. Here, both the tangent plane and Kirchhoff results are non-local results since they involve a single integration over the surface. However, note that, unlike perturbation theory, the surface height h occurs in the phase rather than the amplitude (as in perturbation theory). This was similar to the earlier discussion where we wrote the simple ray scattering result as a phase path variability.

We have illustrated above two ways of approximating the surface values in order to calculate the total field from Eq.(19). Rigorously, however, these surface values must be found in a self-consistent manner as solutions of integral equations on the surface. As an example of how to construct one of the equations, choose the boundary condition Eq.(21) in Eq.(19). The resulting field representation is then differentiated in a normal direction and the limit taken as the field point $\underline{x}$ approaches $\underline{x}_h$, a surface point. The normal derivative of the free space Green's function Ψ^0 has a discontinuity in this limit.

This can be treated either by classical means [11] or using distribution theory [9]. The result is the integral equation of second kind

$$\frac{\partial}{\partial n}\Psi(\underline{r}_h) = 2\,\frac{\partial}{\partial n}G^0(\underline{r}_h,\underline{r}_o) + \iint P^0(\underline{r}_h,\underline{r}_h')\,\frac{\partial}{\partial n'}\Psi(\underline{r}_h')\,ds' \quad . \tag{31}$$

where P^0 is the principal value of the normal derivative of G^0 evaluated on the surface for both variables [9]. A full solution of this or any integral equation is a multiple scattering solution. Note that if we neglect the integral term in Eq.(31) we just recover the approximation Eq.(22). In this sense the solution of the full equation builds on the approximation. Analogous integral equations can be found using the hard (TM electromagnetic) boundary condition

$$\frac{\partial}{\partial \underline{n}}\,\underline{\Psi}\,(\underline{r}_h) = 0 \quad . \tag{32}$$

In addition, if a linear combination of the field and its normal derivative vanishes on the boundary, further integral equations can be found. This is called an impedance or Leontovich boundary condition [12].

The above boundary conditions refer to perfectly reflecting problems and local boundary conditions. The above equations can also be satisfied with non-local boundary conditions. Equation (19) was derived for the field and source points above the surface. If the field point $\underline{r}$ is below the surface, the lhs of Eq.(19) vanishes and we get

$$0 = G^0(\underline{r}_L,\underline{r}_o) + \iint \left[\, G^0(\underline{r}_L,\underline{r}_h')\,\frac{\partial}{\partial n'}\Psi(\underline{r}_h') - \Psi(\underline{r}_h')\,\frac{\partial}{\partial n'}G^0(\underline{r}_L,\underline{r}_h') \,\right] ds' \quad . \tag{33}$$

where we assume that $\underline{r}_L$ is restricted to the volume below the surface. The boundary condition is a volume boundary condition, and non-local since it contains an integration over the surface. It also involves both the field and its normal derivative on the surface and is precisely that boundary condition which extinguishes the incident field below the surface. It is called an extended boundary condition or extinction theorem [13-17].

In case the rough surface is really an interface separating two different media (two fluids, two dielectrics or two elastic media for example), Green's theorem must be used separately in each medium. Surface limits are then used to find coupled integral equations for the surface values of the field and the normal derivative [18,19]. With an ansatz on the representation of the field in either region (really the full Green's function of the problem) it is possible to derive a single integral equation satisfied by the generalized reflection coefficient [20].

Electromagnetically, if the region above the surface is free space, and that below is a perfect conductor, we can represent the scattered electric and magnetic fields in terms of a quantity $\underline{J}$ related to the true surface current by the Jacobian of the transformation between the surface and the flat plane [21]. They are

$$\underline{E}^s(\underline{r}) = \underline{a} \times \iint G^0(\underline{r},\underline{r}_h')\,\underline{J}(\underline{r}_h')\,dx_t' \quad . \tag{34}$$

and

$$\underline{H}^s(\underline{r}) = i\,\eta_o\,k_o^{-1}\,\underline{\nabla} \times \underline{E}^s(\underline{r}) \quad . \tag{35}$$

where η_o is the characteristic impedance of free space. Asymptotic representations of these equations are also available [22]. In order to solve the equations exactly, the surface value of the current must be found using surface integral equations, in a direct analogy with the scalar results. Now, however, we have vector equations to solve. There are two versions of these surface integral equations [23], depending on the incident field from which they are derived. If the equation is derived from an incident electric field $\underline{E}^i$ it is called the electric field integral equation (EFIE) and is an integral equation of first kind. It is

$$\hat{n}(x_t) \times \underline{E}^i(\underline{r}_h) = (i\omega\epsilon_o)^{-1}\,\hat{n}(x_t) \times \iint (k_o^2\underline{J}(\underline{r}_h') - \partial_{t'}\cdot\underline{J}\underline{\partial})\,G^0(\underline{r}_h,\underline{r}_h')\,dx_t \quad . \tag{36}$$

where $\hat{n}$ is the unit surface normal, ω is circular frequency, and ϵ_o is the free space permittivity. The lhs of Eq.(36) is known. For an incident magnetic field $\underline{H}^i$, we get the magnetic field integral equation (MFIE), an equation of second kind. It is

$$\underline{J}(\underline{r}_h) = \underline{J}_K(\underline{r}_h) + 2\,\hat{n}(x_t) \times \iint \underline{J}(\underline{r}_h') \times \underline{\nabla}\,G^0(\underline{r}_h,\underline{r}_h')\,dx_t' \quad . \tag{37}$$

where $\underline{J}_K$ is the Kirchhoff approximation

$$\underline{J}_K(\underline{r}_h) = 2\,\hat{n}(x_t) \times \underline{H}^i(\underline{r}_h) \quad . \tag{38}$$

Alternatively, surface integral equations can be derived on the field values, for example for a perfect magnetic conductor [10]. For perfectly conducting surfaces either method of solution for the surface current may be used [24]. For non-perfect conductors, coupled surface integral equations are used to solve for the equivalent electric and magnetic currents on the surface [25].

4. [illegible]

The representations for the scattered field we have discussed up to now have been in coordinate space. An alternative representation is to express the scattered field in a Fourier-transform or spectral representation. This consists in a continuous plane wave synthesis of the scattered field. We illustrate the method for a one-dimensional surface z = h(x) for simplicity [26], and again confine the discussion to scalar problems while pointing out that the electromagnetic results are available [27]. We also illustrate the results for a rough interface separating two different fluids with densities ρ_1 and ρ_2, and sound speeds v_1 and v_2 (wave numbers k_1 and k_2) all of which are constant. Region 1 is above the surface, and region 2 below. The corresponding electromagnetic problem is an interface separating two different dielectrics.

The fields in the two regions satisfy differential equations of the form (j = 1,2)

$$(\partial_x^2 + \partial_z^2 + k_j^2)\, \psi_j(x,z) = 0 \quad . \tag{39}$$

For plane wave incidence in region 1, we can rigorously express the scattered field as a plane wave spectral synthesis of only upgoing waves above the highest surface excursion. This is because of the Rayleigh hypothesis [28]. But this is all we need. For z ≥ max h(x) (region A), the solution is

$$\psi_A(x,z) = B \exp\left[ik_1(\alpha x - \beta z) \right] + \int_{-\infty}^{\infty} A(\mu) \exp\left[ik_1(\mu x + m z) \right] d\mu \quad . \tag{40}$$

where the incident plane wave is normalized to B, $\alpha = \sin\theta_1$, $\beta = \cos\theta_1$, where θ_1 is the incident angle, and $\mu^2 + m^2 = 1$ with $\mathrm{Re}(m) \geq 0$ and $\mathrm{Im}(m) \geq 0$. The spectral amplitudes A(μ) are unknown. Below the lowest surface excursion, z ≤ min h(x) (region B), the solution is

$$\psi_B(x,z) = \int_{-\infty}^{\infty} B(\mu) \exp\left[ik_2(\mu x - q z) \right] d\mu \quad . \tag{41}$$

where $\mu^2 + q^2 = 1$ and $\mathrm{Re}(q) \geq 0$, $\mathrm{Im}(q) \geq 0$. This consists in purely down-going waves. The amplitudes B(μ) are the other unknowns of the problem.

If we introduce a continuous analogue of Bloch functions in both regions (just up- and down-going plane wave states here), carry out Green's theorem in both regions, and use continuity conditions at the interface we can derive four exact equations. The first two yield the representations of the amplitudes as

$$A(\mu) = (k_2/4m) \int_{-\infty}^{\infty} \left[\left[\alpha - \mu h'(x) \right] F(x) + N(x) \right] \exp\left[-ik_1(\alpha h(x) + \mu x) \right] dx \quad . \tag{42}$$

and

$$B(\mu) = (k_2/4q) \int_{-\infty}^{\infty} \left[\left[q + \mu h'(x) \right] \rho^{-1} F(x) - K^{-2} N(x) \right] \exp\left[ik_2(q h(x) - \mu x) \right] dx \quad . \tag{43}$$

in terms of the density ratio $\rho = \rho_2/\rho_1$, the wave number ratio $K = k_2/k_1$, and the unknown surface field F(x) and its normal derivative N(x). These latter are found from the coupled equations

$$\delta(\alpha-\mu) = (k_2/4m\beta) \int_{-\infty}^{\infty} \left[\left[\alpha + \mu h'(x) \right] F(x) - N(x) \right] \exp\left[ik_1 (\alpha h(x) - \mu x) \right] dx \quad . \tag{44}$$

and

$$0 = \int_{-\infty}^{\infty} \left[\left[q - \mu h'(x) \right] \rho^{-1} F(x) + K^{-2} N(x) \right] \exp\left[-ik_2 (q h(x) + \mu x) \right] dx \quad . \tag{45}$$

Once the surface values are known, the amplitudes can be directly computed from Eqs. (42) and (43), as can their averages (whose absolute square yields coherent intensity) or averages of products (incoherent intensity), etc. All of this presupposes we can compute or approximate the surface values.

5. STATISTICS

We have mentioned statistical averaging using the operator E briefly already. The basic problem of rough surface scattering from a random surface is to relate the statistics of the surface to the statistics of the field. For the surface, the basic quantities are the probability density of surface heights p(h), often chosen as a Gaussian, and the correlation function Eq.(3), or its Fourier transform, the spectral function, Eq.(6).

There are two approaches to finding the average properties of fields or moments of fields. One is to treat the surface scattering as proceeding from a collection of elemental events, each of which is summed to yield the scattered field. For example, the scattered field is written as

$$\Psi^s(\underline{r}) = \sum_{n=1}^{N} A_n(\underline{r}) \exp(i\,\phi_n(\underline{r})) \quad . \tag{46}$$

One proceeds by assigning various probability densities to the amplitudes A_n and phases ϕ_n, and thus tabulates the resulting probability densities for Ψ^s, its amplitude or its phase [29]. This is straightforward from a purely probabilistic sense, but it is difficult to relate the A_n and ϕ_n to actual surface properties, and the method provides little insight into the physics. A second approach is to represent the scattered field as an integral over the surface using Green's theorem as we have discussed above. The surface fields or currents then relate to the physics, and the kernel of the transform, the Green's function, serves to propagate this surface effect out to the field point. For example, we could generally write the scattered field as

$$\Psi^s(\underline{r}) = \iint K(\underline{r},\,\underline{r}_h)\; \Delta\tilde{S}(\underline{r}_h)\; d\underline{r}_t \quad . \tag{47}$$

in terms of a kernel K and a surface value $\Delta\tilde{S}$. The difficulty which arises here is then the averaging. Both K and $\Delta\tilde{S}$ are stochastic quantities, and averaging Ψ^s yields the average of the product of terms $K\Delta\tilde{S}$, when in reality what we want is just the average of some $\Delta\tilde{S}$. Since $\Delta\tilde{S}$ is related to Ψ^s on the surface, we generate a hierarchy of equations [30]. This hierarchy must be broken or avoided in some way in order to put the problem in tractable form. We discuss some schemes which do this next.

6. k-SPACE FORMALISM, DIAGRAMS, AND SMOOTHING

In addition to the spectral approach discussed in Sec. 4, a Fourier transform approach is derivable directly from the coordinate-space methods we have discussed. The scattered part G^s of the full Green's function for the rough surface scattering problem can be written as the solution of a Lippmann-Schwinger integral equation as

$$G^s(\underline{k}',\underline{k}'') = V(\underline{k}',\underline{k}'')\; A(\underline{k}'-\underline{k}'') + \iiint V(\underline{k}',\underline{k})\; A(\underline{k}'-\underline{k})\; G^s(\underline{k})\; G^s(\underline{k},\underline{k}'')\; d\underline{k} \quad , \tag{48}$$

where V is called the vertex function and is defined by

$$V(\underline{k}',\underline{k}) = -\frac{2i}{(2\pi)^3}\left[\eta\,\frac{k_t'\cdot(k_t'-k_t)}{k_z'-k_z} + (k_0^2 - k_t'^2)\,P\,\frac{1}{k_z'}\right] \quad , \tag{49}$$

where P represents the Cauchy principal value, and A is the version of Eq.(38) which arises for two-dimensional surfaces, and where a partial integration of the slope term has been performed. (For $\eta = 1$ we include all slopes, and for $\eta = 0$ the slope terms drop.) It is given by

$$A(\underline{k}) = \iint \exp(-i\underline{k}\cdot\underline{r}_h)\; d\underline{r}_t \quad . \tag{50}$$

This function A is the only function which explicitly contains the surface height, and it occurs in the phase. Of course G^s is thereby a function of h also. This is a three-dimensional integral equation but with statistical averaging (for homogeneous statistics) we can reduce the result to a one-dimensional equation. Each of the terms in Eq.(48) can be given a diagrammatic interpretation analogous to Feynman diagrams, and it was with this aid that the results below were originally derived [1,9,31].

In order to discuss the averaging, define the integral operator symbolically as

$$L = \iiint VG^s\; d\underline{k} \quad . \tag{51}$$

so that Eq.(48) can be written symbolically as

$$G^s = VA + LAG \quad , \tag{52}$$

and this has a formal solution by iteration given by

$$G^s = \sum_{n=0}^{\infty} (LA)^n\, VA \quad . \tag{53}$$

Each occurrence of the interaction term A, which contains the surface height h in the phase, can be interpreted as a single surface interaction (in a different sense than perturbation theory where the interactions could be labelled by powers of the surface height occurring in the amplitude).

To form the average of Eq.(53) (to get the coherent scattered field), or the averages of G^s times its complex conjugate (to get incoherent intensity), we must know how to form averages of products of A functions. For Gaussian height statistics, the average of a single A-function is just

$$\mathcal{E}\,A(\underline{k}_1) \equiv A_1(\underline{k}_1) = (2\pi)^3\,\delta(k_{1t})\,\tilde{p}(k_{1z}) \quad , \tag{54}$$

where $\tilde{p}$ is just the Fourier transform of the probability density function

$$\tilde{p}(k_x) = \exp(-\sigma^2 k_x^2 / 2) \quad . \tag{55}$$

For two interactions we use cluster decomposition techniques

$$\mathrm{E}\, A(\underline{k}_1)\, A(\underline{k}_2) = A_1(\underline{k}_1)\, A_1(\underline{k}_2) + A_2(\underline{k}_1, \underline{k}_2) \quad , \tag{56}$$

to find a "connected" two-interaction function A_2, which involves the correlation function. Formally the process can be done to any order. Because of the homogeneous statistics, a transverse delta function arises, as in Eq.(54). This is true for any order, and the average of the three-dimensional Eq.(48) yields a one-dimensional equation for the scattering amplitude $T(\xi)$ given by

$$T(\xi') = W(\xi', -1) + \int_{-\infty}^{\infty} W(\xi', \xi)\, K(\xi)\, T(\xi)\, d\xi \quad , \tag{57}$$

where K is the Fourier transform of the Green's function times the principal value term

$$K(\xi) = \lim_{a \to 0^+} (\pi i)^{-1} (\xi^2 - 1 - ia)^{-1} P\left(\frac{1}{\xi}\right) \quad , \tag{58}$$

and W is an infinite series of terms

$$W(\xi', \xi) = \sum_{n=1}^{\infty} w_j(\xi', \xi) = \exp\left[-\frac{1}{2} \Sigma^2 (\xi' - \xi)^2 \right] + \cdots \quad , \tag{59}$$

where we have explicitly listed only w_1. If we neglect the integral term in Eq.(57) and approximate W by w_1, the resulting intensity is

$$I = |T(1)|^2 \approx \exp(-4\, \Sigma^2) \quad , \tag{60}$$

which is just the coherent field decay we illustrated simply in Sec. 1. For W approximated by w_1 and the integral term included in Eq.(57), the resulting singular integral equation has been solved numerically [32] and the results compared to both acoustic and electromagnetic scattering data [1]. The main result is the considerable improvement in the scattering results over those of single scattering. This indicates the necessity of using multiple scattering techniques in order to account for experimental data particularly when the surface is very rough.

The Fourier transform or k-space method we have described in this section can be used for either deterministic or random surfaces. There is an alternative stochastic Fourier transform technique which has been developed to treat purely random surfaces [24]. There are two key steps in the procedure. The first is to decide which stochastic variables are important to the process and are thus going to be involved in the averaging. For example, surface height, surface slopes, curvatures, etc., are possible stochastic variables. The second step is to note that the average of a stochastic variable can be written as the convolution of the Fourier transform of the variable and its probability density function. The integral equations which are derived have dimensionality which depends on the number of important stochastic variables. The procedure is still formal. Recent progress is in [33].

An alternate method of solution of Eq.(48) is the smoothing method [30] originally developed to treat propagation through continuous random media. The method consists in writing G^0 as an average (coherent) term plus a fluctuating part

$$G^0 = \mathrm{E}G^0 + \delta G^0 \quad . \tag{61}$$

Substituting Eq.(61) into Eq.(48), taking the average of the result and subtracting it from the original equation yields the smoothing integral equation [34] on the coherent field

$$\mathrm{E}G^0 = M^0 + LEA \sum_{n=0}^{\infty} \left[LA - LEA \right]^n \mathrm{E}G^0 \quad , \tag{62}$$

using Eqs.(50) and (51), and the definition of the smoothing mass operator

$$M^0 = VEA + LEA \sum_{n=0}^{\infty} \left[LA - LEA \right]^n V\left[A - EA \right] \quad . \tag{63}$$

A term by term comparison of this mass operator with the corresponding mass operator for the connected diagram method [34] yields equality for the first two terms and inequality for the remaining terms. Formally the connected diagram terms have an advantage in that their transforms vanish asymptotically (so that they are really Fourier transformable). Practically none of the higher order terms have been evaluated, however, so it is not clear what physical consequences they describe, or what the difference between the two approximations means. The smoothing method has recently been applied to the scalar rough surface problem with a variety of boundary conditions [35] and to the electromagnetic case of a perfect conductor [36].

7. [illegible]

Up to now we have primarily discussed the computation of the coherent field. Although the integral equations describing multiple scattering were three-dimensional for the stochastic field, we were able to reduce them to one-dimensional equations using the two degrees of freedom available if we assume the surface statistics to be homogeneous. One-dimensional integral equations are computable, and approximation methods are well understood. It should be remarked however, that, if the surface statistics are not homogeneous the coherent integral equation will be three-dimensional in general and approximation methods are necessary. Even in the one-dimensional case, the infinite series of terms, Eq.(59), which comprise the Born and kernel terms of the integral equation, Eq. (57), must be truncated in order for the hierarchy of equations to be solvable.

The situation for the Bethe-Salpeter equation is much more involved. This is the equation which is formed by first multiplying the scattered field by its complex conjugate and then taking the average of the resulting product. For example from Eq.(48) we would form the quantity

$$u^s(\underline{k}', k^o) \left[u^s(\underline{k}_1', k_1^o) \right]^* .$$

which can be related to the incoherent intensity [31] when $\underline{k}_1^o = -\underline{k}^o$ (for the incident direction) and $\underline{k}_1' = -\underline{k}'$ (for the scattered direction) and when the dispersion relation is satisfied. Forming the term from Eq.(48) yields a six-dimensional integral equation. Averaging and the use of homogeneous surface statistics reduce it to a four-dimensional equation, whose Born and kernel terms are again infinite series. Even in a truncation approximation these are prohibitively complex equations to solve numerically. Approximation methods to reduce the dimensionality are difficult to define physically because they must be performed over intermediate states. Although approximation methods are being pursued, this area of research is an open problem.

8. [illegible]

There are many other approaches than the ones we have discussed in this brief review. Rather than further list them here we refer to our recent lengthy review paper where they are listed and discussed [1].

9. [illegible]

[1] J.A. DeSanto and G.S. Brown, Analytical techniques for multiple scattering for rough surfaces, Progress in Optics XXIII, ed. by E. Wolf, North Holland, Amsterdam, 1986, pp. 2-62.

[2] L. Brekhovskikh, Waves In Layered Media, Academic, New York, 1960.

[3] W.S. Ament, Toward a theory of reflection by a rough surface, Proc. I.R.E., 41, 1953, p. 142.

[4] C. Eckart, The scattering of sound from the sea surface, J. Acoust. Soc. Am., 25, 1953, p.566.

[5] P.G. Bass and I.M. Fuks, Scattering of Waves From Statistically Irregular Surfaces, Pergamon, New York, 1979.

[6] J.W. Wright, Backscattering from capillary waves with application to sea clutter, IEEE Trans. Ant. Prop. AP-14, 1966, p. 749.

[7] D. Jackson, Re-examination of convergence of rough-surface perturbation theory, J. Acoust. Soc. Am., 80, 1986, p. 2116.

[8] J.S. Watson and J.B. Keller, Reflection, scattering and absorption of acoustic waves by rough surfaces, J. Acoust. Soc. Am., 74, 1983, p. 1887.

[9] J. A. DeSanto, Coherent multiple scattering from rough surfaces, in Multiple Scattering and Waves In Random Media, ed. by P.L. Chow, W. Kohler, and G.C. Papanicolaou, North Holland, Amsterdam, 1981.

[10] J.A. DeSanto, Green's function for electromagnetic scattering from a random rough surface, J. Math. Phys., 15, 1974, p.283.

[11] O.D. Kellogg, Foundations of Potential Theory, Dover, New York, 1953.

[12] Ref. 2, p. 14.

[13] P.C. Waterman, Matrix formulation of electromagnetic scattering, Proc. IEEE, 53, 1965, p.805.

[14] P.C. Waterman, Symmetry, unitarity, and geometry in electromagnetic scattering, Phys. Rev., D3, 1971, p.825.

[15] D.N. Pattanayak and E. Wolf, Scattering states and bound states as solutions of the Schroedinger equation with nonlocal boundary conditions, Phys. Rev., B13, 1976, p. 913.

[16] G.S. Agarwal, Relation between Waterman's extended boundary condition and the generalized extinction theorem, Phys. Rev. B14, 1976, p. 1168.

[17] M. Nieto-Vesperinas, Depolarization of electromagnetic waves scattered from slightly rough random surfaces: A study by means of the extinction theorem, J. Opt. Soc. Am., 73, 1983, p. 539.

[18] R. Kittappa and R.E. Kleinman, Acoustic scattering by penetrable homogeneous objects, J. Math. Phys. 16, 1975, p. 421.

[19] R. Kress and G.F. Roach, Transmission problems for the Helmholtz equation, J. Math. Phys., 19, 1978, p. 1433.

[20] J.A. DeSanto, Scattering of scalar waves from a rough interface using a single integral equation, Wave Motion, 5, 1983, p. 125.

[21] J. Van Bladel, Electromagnetic Fields, McGraw-Hill, New York, 1964.

[22] G.S. Brown, Scattering from randomly rough surfaces and the far field approximation, Radio Sci., 18, 1983, p. 71.

[23] A.D. Yaghjian, Augmented electric- and magnetic-field integral equations, Radio Sci., 16, 1981, p. 987.

[24] G.S. Brown, A stochastic Fourier transform approach to scattering from perfectly conducting randomly rough surfaces, IEEE Trans. Ant. Prop., AP-30, 1982, p. 1135.

[25] D.S. Jones, Methods In Electromagnetic Wave Propagation, Clarendon Press, Oxford, 1979.

[26] J.A. DeSanto, Exact spectral formalism for rough-surface scattering, J. Opt. Soc. Am. A2, 1985, p. 2202.

[27] G.S. Brown, A comparison of approximate theories for scattering from rough surfaces, Wave Motion, 7, 1985, p. 195.

[28] J.A. DeSanto, Scattering from a perfectly reflecting arbitrary periodic surface, Radio Sci., 16, 1981, p. 1315.

[29] P. Beckmann and A. Spizzichino, The Scattering of Electromagnetic Waves from Rough Surfaces, Pergamon, New York, 1963.

[30] V. Frisch, in Probabilistic Methods in Applied Mathematics I, ed. A.T. Bharucha-Reid, Academic, New York, 1968.

[31] G.G. Zipfel and J.A. DeSanto, Scattering of a scalar wave from a random rough surface: A Diagrammatic approach, J. Math. Phys., 13, 1972, p. 1903.

[32] J.A. DeSanto and O. Shisha, Numerical solution of a singular integral equation in random rough surface scattering theory, J. Comp. Phys., 15, 1974, p. 286.

[33] G.S. Brown, Simplifications in the stochastic Fourier transform approach to rough surface scattering, IEEE Trans. Ant. Prop., AP-33, 1985, p. 48.

[34] J.A. DeSanto, Relation between the connected diagram and smoothing methods for rough surface scattering, J. Math. Phys., 27, 1986, p.377.

[35] J.G. Watson and J.B. Keller, Rough surface scattering via the smoothing method, J. Acoust. Soc. Am., 75, 1984, p. 1705.

[36] G.S. Brown, Application of the integral equation method of smoothing to random surface scattering, IEEE Trans. Ant. Prop., AP-32, 1984, p. 1308.

DISCUSSION

A.K. Fung, US

Would you comment on the application of the method you used in your paper for computing incoherent scattering?

Author's Reply

There were some brief remarks at the end of my paper. The basic difficulty is the same as that which occurs for any process which contains multidimensional integration, in this case the Bethe-Salpeter equation and that is the inability to find reliable approximations for the intermediate state terms over which they are integrated.

REGIONS OF VALIDITY FOR SOME ROUGH SURFACE SCATTERING MODELS

Robert J. Papa
John F. Lennon

Rome Air Development Center
Electromagnetics Directorate
Hanscom AFB, MA 01731
USA

SUMMARY

The objective of this paper is to examine the regions of validity that apply to the use of various models for describing rough surface scattering. The first area to be examined is how a small slope condition allows an integral representation of the physical optics (PO) cross section to be formed that does not require the high frequency geometric optics (GO) restriction. Next, for forward scattering, we consider the extension of the roughness dependence of the PO scattering cross section (σ°) from the case of Gaussian surface and correlation to a range of surfaces with different height statistics and correlation functions. This dependence is then examined for the small perturbation method (SPM) regime as well. Finally, the forward scattering PO results are extended to the case where the azimuthal angle, $\phi_s \neq 0^\circ$.

1. INTRODUCTION

This paper considers several topics, all related to the conditions for the validity of physical optics, geometrical optics, and small perturbation methods as applied to rough surface scattering models. Conditions are given under which the domain of validity of some PO models[1-4] can be extended. Quantitative studies are presented comparing the variation of several representations of the normalized rough surface scattering cross section, σ°, as a function of surface parameters and scattering geometry. Multiple scattering and shadowing are neglected.

The basic condition for applying PO models is that $R_c \gg \lambda$ where R_c is the average radius of curvature of the surface irregularities and λ is the em wavelength. In previous work[5], we showed that the condition $T \gg \lambda$ (T is surface correlation length) is a sufficient condition for $R_c \gg \lambda$ if the surface slopes are small, but it becomes necessary as well as sufficient if larger slopes are not excluded. That demonstration assumed Gaussian heights and correlation. In this paper, we will be concerned mainly with small slope conditions. Under the assumption $R_c \gg \lambda$, Barrick and Peake[6] have given a general expression for a PO σ° with no shadowing. This expression generally[1-4] has been evaluated by taking the high frequency limit, $k = 2\pi/\lambda \to \infty$ (GO) which allows decorrelation of the ensemble averaging over the height distribution from that of the surface slope distributions followed by an asymptotic algebraic result. In the present analyses we show that their product form representation:

$$\sigma^\circ = |\beta_{pq}|^2 J \tag{1}$$

is valid without the restriction $\lambda \to 0$, so long as the surface slopes are small ($\sigma/T < 1$) and J is kept as an integral form. Here, β_{pq} is the scattering matrix element[7], p refers to the polarization of the incident wave and q refers to the polarization of the scattered wave (horizontal or vertical), J is proportional to the probability density function of the surface slopes and σ is the standard deviation in surface height. Gaussian heights and correlation are again assumed. This result and the high frequency form are then compared with numerical evaluation of the general expression for σ° for the case of forward scattering and horizontal-horizontal polarization. For purposes of efficiency of numerical calculations, the rough surface is assumed to be random in one dimension only.

Further comparisons are made of the forward scattering PO and SPM σ° dependence on roughness for a range of statistical surface conditions. These results are presented in terms of dependence on the Rayleigh roughness parameter Σ defined as $\Sigma = (2\pi/\lambda)\sigma\,(\cos\theta_i + \cos\theta_s)$ where θ_i = elevation angle of incidence and θ_s = elevation angle of scattering. Finally, the PO results are extended to the case $\phi_s \neq 0$ where ϕ_s is the azimuthal scattering angle.

2. LIMITING FORMS FOR σ°

The application of physical optics principles to rough surface scattering analysis involves the Kirchhoff integral representation for the scattered em wave where the boundary conditions on the surface are satisfied by the use of Fresnel plane wave reflection coefficients[1-7]. Under these conditions, the Barrick and Peake[6] generalized expression for the field scattered from a rough surface (horizontal polarization) is

$$\vec{E}^s = -ik\left[e^{ikR_o}/4\pi R_o\right]\hat{E}_h^i \int_{-L/2}^{L/2}\int_{-L/2}^{L/2} \vec{F}(\xi_x, \xi_y)\, e^{ik[\hat{k}_i - \hat{k}_s]\cdot\vec{r}}\, dxdy \tag{2}$$

where

E_h^i = incident, horizontally polarized electric field,

R_o = distance from origin to observation point,

$\vec{r} = x\hat{x} + y\hat{y} + \xi(x,y)\hat{z}$ = distance from origin to point on rough surface,

$\hat{k}_i, \hat{k}_s$ = unit constant vectors pointing in direction of incidence and scattering,

ξ_x, ξ_y = local surface slopes in x and y directions at surface point $\xi(x,y)$, i.e., $\partial\xi/\partial x$ and $\partial\xi/\partial y$,

The factor $\vec{F}(\xi_x, \xi_y)$ is a function of the local normal to the surface and of the local Fresnel reflection coefficients at each surface point. Their expression for $\vec{F}$ is incorrect as printed. The correct form is that given by Sancer[4].

To form the normalized cross section of the rough surface, σ°, it is necessary to calculate

$$\sigma^\circ = \langle \vec{E}s^* \cdot \vec{E}s \rangle - \langle Es \rangle^2 \tag{3}$$

where $\langle \cdot \rangle$ denotes an ensemble average over the random variables ξ, ξ_1, ξ_x, ξ_y ξ_{1x1}, ξ_{1y1}. Here, ξ is the random height at point (x,y) and ξ_1 is the random height at point (x_1,y_1). The general PO expression (3) for σ° involves a tenfold integration over the variables x, y, x_1, y_1, ξ, ξ_1, ξ_x, ξ_y, ξ_{1x1}, ξ_{1y1}. By making use of the stationarity of the random process, this expression can be reduced to an eight-fold integral. By what is traditionally referred to as a geometrical optics assumption, this result is further reduced to a single integral form and finally evaluated as an algebraic expression. The single integral form can also be obtained by making use of a small slope condition. For that case, though, the final evaluation does not apply. In this section these two types of result will be compared with the corresponding multiple integral solution for a range of conditions.

At this point, to simplify the general expressions for σ° and to make numerical evaluations of σ° more efficient, it will be assumed that the random distribution in heights, ξ have only a one dimensional variation $\xi = \xi(x)$. It will also be assumed that the scattering takes place in the direct forward direction, so that there is no azimuthal variation ($\phi_s = 0°$) and that there is no shadowing.

Under these assumptions, and following the development given by Hagfors[8], the expression for σ° may be written as

$$\sigma^\circ = 2\pi k \int_0^\infty d\tau \cos v_x\tau \; w(\tau) \tag{4}$$

where

$$v_x = k(\sin\theta_i - \sin\theta_s)$$

$\tau = x_1 - x_2$ (separation between two points on the rough surface)

and

$$w(\tau) = G(\tau) - H.$$

$$G(\tau) = 2 \int_{-\infty}^{\infty} d\mu_1 \, F(\mu_1) \int_{-\infty}^{\infty} d\mu_2 \, F(\mu_2) \int_0^\infty d\xi \cos v_z\xi \cdot P_3(\mu_1,\mu_2, \xi, \tau) \tag{5}$$

P_3 = Trivariate distribution function in height differences and surface slopes. In addition, ξ_1, μ_1, and ξ_2,μ_2 are the heights and slopes of point 1 and point 2 respectively, with $\xi = \xi_1 - \xi_2$.

$F(\mu)$ is a complicated function of the slopes μ, and is given in the appendix, as is the form for the quantity H. It can be shown that $w(\tau) \to 0$ as $\tau \to \infty$.

There are no restrictions on the expression for σ° given by Eq. (4), other than the validity of physical optics, $T \gg \lambda$. There are singularities in the integrand of Eq. (4) but they can be shown to be integrable and the expression has been evaluated numerically, using quadrature formulas to provide a standard for the two limiting case solutions. For the two sets of assumptions considered here, the expressions in Eq. (4) and Eq. (5) reduce to the simpler form of Eq.(6) involving a single integration over τ:

$$\sigma^\circ = 2\pi k\, F^2(\mu_{sp}) \int_0^\infty d\tau\, \cos v_z\tau \cdot [\chi_2 - \chi_1^2] \qquad (6)$$

where

$$\chi_2 = \exp[-\sigma^2 v_z^2(1 - \bar{F})]$$

$$\bar{F} = \exp(-\tau^2/T^2)$$

$$\chi_1 = \exp(-v_z^2\sigma^2/2)$$

and

$$v_z = -k(\cos\theta_i + \cos\theta_s).$$

The details of the arguments in each case are presented in the appendix. Finally, for the case where $\lambda \to 0$ and $\Sigma > 1$, the integral of Eq. (6) can be explicitly evaluated for σ° using the stationary phase method[10]:

$$\sigma^\circ = \pi k F^2(\mu_{sp})(T\sqrt{\pi}/\Sigma)\exp(-v_x^2T^2/4\Sigma^2) \qquad (7)$$

As indicated, our objective here is to examine the conditions under which each of these two forms agrees with a direct numerical evaluation of Eq. (4) and Eq. (5) and to define the regions where one or the other limiting case solution would be preferred. These results are shown in the first series of figures. Figure 1 shows the variation in σ° as the Rayleigh parameter is varied. In all three methods the slope is held fixed at $\sigma/T = 0.2$. Since the slope is small, it may be seen that the single integral (PO) result is always close to the triple integral numerical evaluation (TI), which is also close to the GO result when the Rayleigh parameter is large ($\Sigma \gg 1$). However, as the Rayleigh parameter decreases, the GO result diverges from both the PO evaluation and the TI result.

Figure 2 shows the variation of σ° for the three methods of evaluation as a function of Rayleigh parameter when the slope $\sigma/T = 5.0$. Here, the values of PO and TI are not very close, because the slope is not small. Similarly, even when the Rayleigh parameter is large, the GO approximation is not accurate compared to the TI result. Further, the GO result becomes very inaccurate as Σ decreases below the value ≈ 2.

Additional parametric studies for different slope conditions confirmed that to obtain agreement between the GO result and the "exact" triple integral values, it is necessary that the condition of large Rayleigh parameter, $\Sigma > 1$, be coupled with the further condition that $\sigma/T < 1$. This is implicit in the specular point evaluation of the $\bar{F}$ terms that leads to the single integral representation for GO conditions. It should also be noted that the GO result can not be applied close to grazing incidence and scattering for the condition $\Sigma > 1$ to be satisfied.

3. FORWARD SCATTERING ROUGHNESS DEPENDENCE

In this section we discuss an extension of the well known PO result for the roughness dependence of forward scattering from Gaussian surfaces to surfaces having other statistical properties and to those satisfying perturbation regime conditions. The result for Gaussian height distributions with Gaussian correlation is given in Beckmann and Spizzichino[9]: for a smooth surface the scattering is concentrated in the specular direction and as the roughness increases the elevation plane scattering extends over wider ranges of angles.

The Gaussian surface description has been widely used for its mathematical convenience[7] but it may not always be a suitable model. Miller et al[10] have used a Bessel function correlation for sea state conditions, and other forms have been introduced as well[11]. Brown[12] has suggested that there could be a fundamental difference in the scattering from surfaces where the decorrelated heights are still statistically dependent. The dependence introduces a noncoherent scattering contribution in the specular direction in addition to the general diffuse term. The effect of such alternative conditions will be addressed.

In the discussion, we do not restrict the height variation to one dimension. Next, we make use of the previously defined product form for σ° and note that the β_{pq} terms do not change with roughness. J is a term dependent on the surface height statistics and the surface correlation function. If we restrict ourselves to consideration of the effect of roughness on σ°, the analysis reduces to a study of the behavior of the J term. In addition to the usual Gaussian correlation we also introduce a Bessel function form:

$$c(\tau) = [1 + (\tau^2/8T^2)](\tau/T)\, K_1(\tau/T) - (\tau^2/T^2)\, K_0(\tau/T) \qquad (8)$$

For the surface with Gaussian heights, we found that changing the form of the correlation function did not change the trend of the roughness dependence. These results are essentially independent of incident angle. The next aspect is the use of the exponential height characterization described by Brown[12]. For this case, he gives $J_{BX} = J_D + J_S$ where the J_S term represents the additional diffuse power in the specular direction and

$$J_D = 2k^2 \int_0^\infty J_o(v_{xy}\tau)[(1+(2/3)\Sigma^2(1-c(\tau)))^{-3/2} - (1+(2/3)\Sigma^2)^{-3/2}]\tau d\tau \qquad (9)$$

where

$$v_{xy}^2 = k^2 [(\sin\theta_i - \sin\theta_s\cos\phi_s)^2 + \sin^2\theta_s\sin^2\phi_s].$$

Brown pointed out that the term J_S, which is independent of correlation function, depends on the surface statistics while the general diffuse term is related to the slopes; this suggested that arbitrary relationships could exist between the two terms J_D and J_S. The diffuse scattering term does involve the correlation function and, in fact, for our two types of correlation function, the kernel of the integral (9) would be expected to decrease as the correlation length decreases. The behavior of J_D (specular direction) was studied as a function of Σ and T. T was decreased as far as would be consistent with the physical optics constraint $T \gg \lambda$. The J_D term in the specular direction always dominated the corresponding value of J_S. Although J_D always exceeded J_S it does show a dependence on Σ and peaks near a value $\Sigma > 1$. This behavior will be referred to again in the next section. As a result of this finding, we assumed that $J_{BX} \approx J_D$ and made our comparisons using the results for J_D. These are shown in Figures 3-5.

For surfaces with exponential height distributions, the overall angular pattern of diffuse scattering as a function of roughness is similar for the two correlation functions; no distinct difference is apparent between the behavior for this type of surface and that for a surface with Gaussian height statistics. Thus, in the physical optics regime, the roughness dependence of the diffuse scattering angular distribution is insensitive to correlation function, height statistics, and angle of incidence.

Finally, we introduce the scattering analysis that applies for the perturbation theory case. Here, the height variation, σ_s must be small compared to a wavelength ($k\sigma_s < 1$) and the rms slopes must also be small. This is equivalent to the condition, $\sigma_s/T_s < 1$, where T_s is the associated correlation length of the small scale heights. For this case the cross section σ°_{ss} is given by[7] $\sigma^\circ_{ss} = |\alpha_{pq}|^2 J_{ss}$. The α_{pq} term is the small height scattering matrix contribution and

$$J_{ss} = (2\pi)[(4k^4/\pi)\sigma_s^2\cos^2\theta_i\cos^2\theta_s]\int_0^\infty c(\tau)Jo(|vxy|\tau)\tau d\tau$$

$$= [4\pi k^4\cos^2\theta_i\cos^2\theta_s]S(|vxy|). \qquad (10)$$

Note that the value of σ°_{ss} is independent of the surface height statistics and depends only on the form of the correlation function. Thus, the question of surface dependent results does not apply here and we are concerned only with the differences for the two types of correlation function. As seen in Figures 6-7 the results are more complicated than the PO results. There is a definite dependence of the scattering patterns on incident angle as can be seen in Eq. (10). There is an explicit $\cos\theta_i$ term, in addition to implicit angle effects in the power spectra component from the Rayleigh parameter dependence. The power spectra terms have peaks in the specular direction for Gaussian correlation, but a sharp null for the Bessel form. The combination of the two effects leads to distinctly different patterns as the incident angle changes. The relative insensitivity to correlation for $\theta_i = 85°$ arises from the dominance of the cos θ_s term at that specular angle. For the perturbation theory regime, then, the diffuse scattering pattern is independent of height statistics and, except for magnitude, tends to be insensitive to roughness; however, it is strongly dependent on incident angle and correlation function.

4. GENERALIZED ROUGHNESS DEPENDENCE

In our previous discussions extending the surface and correlation conditions under which roughness effects can be analyzed, we were concerned primarily with the statistical aspects and limited ourselves to forward scattering. There is no reason to restrict the discussion of how PO cross sections vary with roughness to specular forward scattering and in this section we extend the previous results. We restrict the discussion here to Gaussian correlation. Similar results could be obtained for other cases. In addition, since we wish to conduct the analysis using the product form of σ° (considering only the J-term variation) we will limit the results to small slope values to be consistent with our previous analysis.

In Figure 8 through Figure 10 we show the dependence of J on Σ for a Gaussian and exponential surface for three azimuthal conditions, $\phi_s = 5°$, 90°, and 180°, respectively. The specific plots are calculated for the case $\theta_i = \theta_s$ but there is no restriction requiring this condition and the general case will be discussed as well. For these cases,

λ = 0.9 m and T = 5m. One point is that the curves are cut off at different values consistent with the assumption of small slopes.

In Figure 8 (ϕ_s = 5°) we see several trends as the elevation angles increase. First, the curves change with angle and then reach a limiting form. This includes both location of peak J in terms of Σ and the relative magnitude of J. Another aspect is that all the cases show that the variation for a Gaussian surface is quite similar to that for an exponential one.

The results when ϕ_s = 90° are shown in Figure 9. The same type of trends are present. The peak J values are lower and occur at larger roughness values than the ϕ_s = 0°, 5° cases. Again there is little difference in results for the two surface types.

The final set of results (ϕ_s = 180°) is shown in Figure 10. The only difference between these results and those for ϕ_s = 90° is a slight decrease in the peak J-value.

If we consider the series of figures and take J to be a measure of the likelihood of there being specular facets in the appropriate direction, we see that as the scattering direction moves from forward to backscatter the probability of such scattering contributors decreases in general and the level of roughness for peak conditions tends to increase. Except for forward scattering, where specular J values appear insensitive to elevation angle, the smooth surfaces emphasize equal angle scattering at small incidence angles and rougher surfaces tend to have equally likely values for all elevation plane angles.

For simplicity this discussion has been presented in terms of equal elevation angles. Consideration of the J-integrals indicates that the angles enter through the term v_{xy}. There is no need to limit this to $\theta_i = \theta_s$, although the result is simpler in that case.

5. CONCLUSIONS

Several areas have been addressed in which conditions for application of models can be extended or comparisons made between different models. It was pointed out that $T \gg \lambda$ is a sufficient condition for PO models for all slope regimes but that unless the slopes are small it is also a necessary condition. Continuing along this line we have shown that in the small slope regime a simplified PO integral representation can be obtained which is not subject to the GO limit. For GO cases, $\Sigma > 1$ and the conditions for specularity must be applied carefully as seen in the poor agreement with the triple integration result for large slope values, i.e., two conditions are required for the accuracy of the GO model, $\Sigma > 1$ and $\sigma/T < 1$.

The well known roughness dependence of PO scattering in the forward direction for Gaussian surfaces with Gaussian correlation has been extended to other sets of surface statistics and correlation functions. The diffuse PO scattering patterns appear to be relatively insensitive to surface statistics, incident angle and correlation function.

In contrast, for conditions where perturbation methods apply, the scattering patterns do not depend on surface statistics and are relatively insensitive to roughness (except in magnitude). However, there is a strong dependence on incident angle and correlation function.

The roughness dependence of PO scattering has been extended to cases where $\phi_s \neq 0°$. For equal angle scattering ($\theta_i = \theta_s$), smooth surfaces result in a preference for small incident angles while rougher surfaces tend toward equal likelihood of scattering at any incident angle. Also, as ϕ_s increases, the overall likelihood of scattering decreases and the level of roughness at which peak conditions occur increases.

REFERENCES

1. B.I. Semyonov, "Approximate Computation of Scattering of Electromagnetic Waves by Rough Surface Contours", Radiotekhnika i Electronika 11, pp 1179-1187, 1966.

2. D.E. Barrick, "Rough Surface Scattering Based on the Specular Point Theory", IEEE Trans. Antennas Propagat., Vol AP-16, No. 4, pp 449-454, July 1968.

3. R. Kodis, "A Note on the Theory of Scattering From an Irregular Surface", IEEE Trans. Antennas Propagat., Vol AP-14, No. 1, pp 78-82, January 1966.

4. M.I. Sancer, "Shadow-Corrected Electromagnetic Scattering From a Randomly Rough Surface", IEEE Trans. Antennas Propagat., Vol AP-17, No. 5, pp 577-585, September 1969.

5. R.J. Papa, J.F. Lennon, and R.L. Taylor, RADC Report, An Analysis of Physical Optics Models for Rough Surface Scattering, RADC-TR-84-195, ADA 154960, September 1984.

6. D.E. Barrick and W.H. Peake, Batelle Report, Scattering From Surfaces With Different Roughness Scales: Analysis and Interpretation, AD662751 (Unlimited), Nov 1967.

7. G.T. Ruck, D.E. Barrick, W.D. Stuart, and C.K. Krichbaum, Radar Cross Section Handbook, Vol. 2, New York, Plenum Press, 1970.

8. T. Hagfors, "Backscattering From an Undulating Surface With Applications to Radar Returns From the Moon", J. Geophysical Res., Vol. 69, No. 18, pp 3779-3784, Sept 1964.

9. P. Beckmann and A. Spizzichino, The Scattering of Electromagnetic Waves From Rough Surfaces, Pergamon Press, Macmillan Co., New York, 1963.

10. Miller, L.S., Brown, G.S., and Hayne, G.S., NASA Report, Analysis of Satellite Altimeter Signal Characteristics and Investigation of Sea-Truth Data Requirements, NASA-CR-137465, 1972.

11. Cosgriff, R., Peake, W., and Taylor, R., Terrain Scattering Properties For Sensor System Design (Terrain Handbook II), Ohio State University, EES Bulletin 181, 1960.

12. Brown, G.S., "Scattering From a Class of Randomly Rough Surfaces", Radio Science, 17 (No. 5), 1982, pp 1274-1280.

APPENDIX

The purpose of this appendix is to outline the details of the respective arguments by which the results of Eq. (4) and Eq. (5) can be simplified to those of Eq. (6) for both sets of assumptions. The first step is to examine the elements of the integrands in more detail.

First, the quantity H used in $w(\tau)$ in Eq. (4) is given by the expression

$$H = (T^2 e^{-v_x^2\sigma^2} / 4\tau\sigma^2) \cdot \int_{-\infty}^{\infty} e^{-(\mu_1/(2\sigma/T))^2} F(\mu_1)d\mu_1 \cdot \int_{-\infty}^{\infty} e^{-(\mu_2/(2\sigma/T))^2} F(\mu_2)d\mu_2 \tag{A1}$$

The function $F(\mu)$ used in Eq. (5) can be reduced to the form

$$F(\mu) = (1 - R_\perp(\gamma_i))(\mu\sin\theta_i + \cos\theta_i) + [1 + R_\perp(\gamma_i)](\mu\sin\theta_s - \cos\theta_s) \tag{A2}$$

where it has been assumed that there is no y variation $\partial/\partial y = 0$ and the scattering takes place in the forward direction ($\phi_s = 0°$). Here, the Fresnel reflection coefficient is given by

$$R_\perp(\gamma_i) = (\cos\gamma_i - \sqrt{\varepsilon - \sin^2\gamma_i})/(\cos\gamma_i + \sqrt{\varepsilon - \sin^2\gamma_i})$$

and

$$\cos\gamma_i = (\mu\sin\theta_i + \cos\theta_i)/(\sqrt{1+2\mu^2}).$$

The trivariate distribution funtion P_3 in Eq. (5) is given by

$$P_3 = (2\pi)^{-3/2} |R|^{-1/2} e^{-\underset{\sim}{u}^T \underline{R}^{-1} \underset{\sim}{u}}. \tag{A3}$$

$\underset{\sim}{u}^T \underline{R}^{-1} \underset{\sim}{u}$ is a positive definite quadratic form:

$$\underset{\sim}{u}^T \underline{R}^{-1} \underset{\sim}{u} = 1/(2|\underline{R}|)[M_{11}\,\xi^2 + 2M_{12}\,\xi(\mu_1 + \mu_2) + M_{22}(\mu_1^2 + \mu_2^2) + 2M_{23}\mu_1\mu_2]$$

$|R|$ is the determinant of the surface height covariance matrix $u^T = (\xi, \mu_1, \mu_2)$

$$\underline{R} = \begin{pmatrix} 2(\sigma^2 - \rho) & -\partial\rho/\partial\tau & -\partial\rho/\partial\tau \\ -\partial\rho/\partial\tau & \partial^2\rho/\partial\tau^2\,|_{\tau=0} & -\partial^2\rho/\partial\tau^2 \\ -\partial\rho/\partial\tau & -\partial^2\rho/\partial\tau^2 & \partial^2\rho/\partial\tau^2\,|_{\tau=0} \end{pmatrix} \tag{A4}$$

where

ρ = surface correlation function

$= \sigma^2 \exp(-\tau^2/T^2)$.

M_{ij} is the co-factor of the covariance matrix R_{ij}. The triple integral in Eq. (5) may be reduced to a double integral when $\tau \neq 0$ by using the known expression for the cosine transform of a Gaussian function

$$\int_0^{\infty} d\xi \cos v_z\, \xi P_3 = 1/(2\pi\sqrt{M_{11}})\, e^{-C} \cos v_z B e^{-v_z^2/4A} \tag{A5}$$

where

$$A = M_{11}/2|R|$$

$$B = (M_{12}/M_{11})(\mu_1 + \mu_2)$$

$$C = (1/2|\underline{R}|)[(M_{22} - M_{12}^2/M_{11})(\mu_1^2 + \mu_2^2) + 2(M_{23} - M_{12}^2/M_{11})\,\mu_1\,\mu_2]$$

At this point we turn to the two cases that are derived under different assumptions.

First, consider the small slope case, $\sigma/T \ll 1$. In this case, the covariance matrix $|\underline{R}|$ becomes

$$\underline{R} = \begin{pmatrix} 2(\sigma^2 - \rho) & 0 & 0 \\ 0 & 0 & 0 \\ 0 & 0 & 0 \end{pmatrix} \tag{A6}$$

so that the heights and slopes are decorrelated. Then, the integrations over μ_1 and μ_2 in Eq. (5) may be approximated by setting up $\mu_1 = \mu_2 = \text{constant} = \tan\gamma = \mu_{sp}$ where $\tan\gamma$ is the slope of a facet which will produce a reflected wave in the specular direction:

$$\tan\gamma = |\sin\theta_i - \sin\theta_s|/(\cos\theta_i + \cos\theta_s) \tag{A7}$$

Equation (4) for σ° now reduces to a single integration form as shown in Eq. (6). It should be noted that since the slopes are assumed to be small ($\sigma/T \ll 1$), then $\mu = \tan\gamma$ so that $\gamma = 0$, which implies the specular condition $\theta_s = \theta_i$.

The argument for reducing the integrals in Eq. (5) to the result in Eq. (6) is somewhat different for the high frequency case. In the GO limit the integrals over μ_1 and μ_2 may be approximated by removing $F(\mu_1)$ and $F(\mu_2)$ from the integrals and setting them equal to constants; the justification for this is the stationary phase (or specular point) argument. This argument states that for large k in the exponential (or cosine) factor, the only surface regions which contribute to the integral are those smoothly curving portions which are in a position to specularly reflect into the desired scattering direction. Then, $\mu_1 = \mu_2 = \tan\gamma = \mu_{sp}$ and Eqs. (4) and (5) reduce to Eq. (6) (see Barrick and Peake[6]).

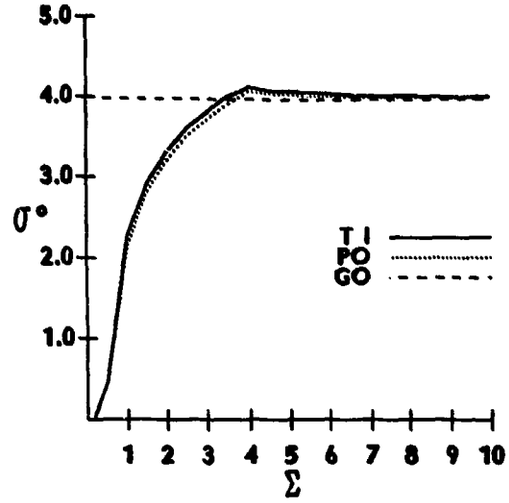


Fig. 1. σ° vs Roughness for three models, σ/T = 0.2.

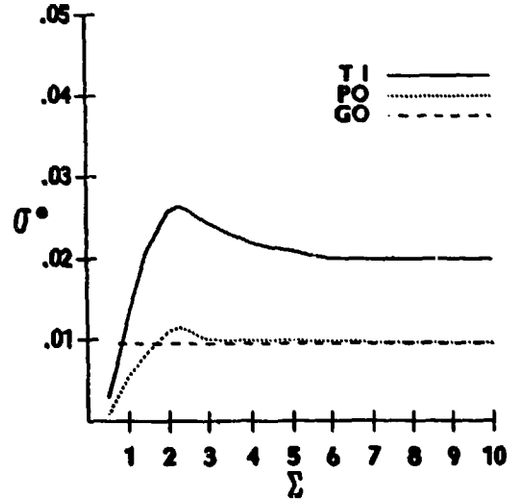


Fig. 2. σ° vs Roughness for three models, σ/T = 5.

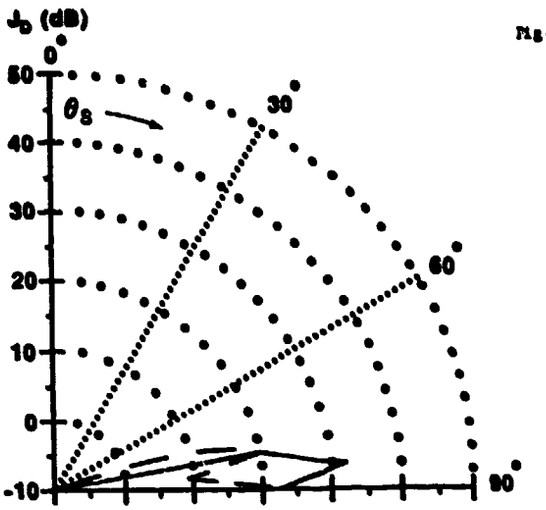


Fig. 3. Forward scatter J_D pattern smooth exponential surface $\sigma/T = 0.002$

$\lambda = 0.275$ m

$\theta_i = 85°$

Gaussian

Bessel

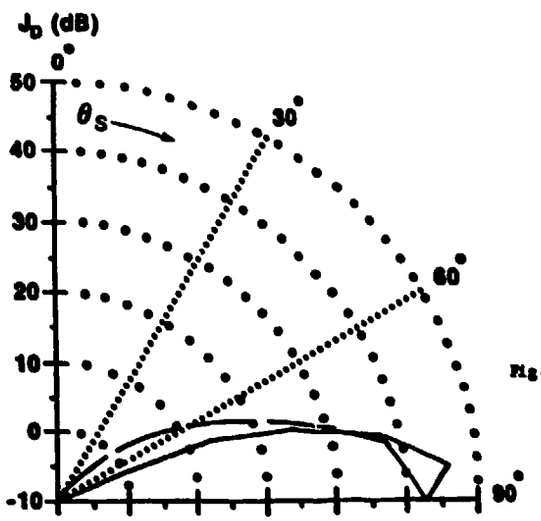


Fig. 4. Forward scatter J_D pattern, rough exponential surface. $\sigma/T = 0.02$

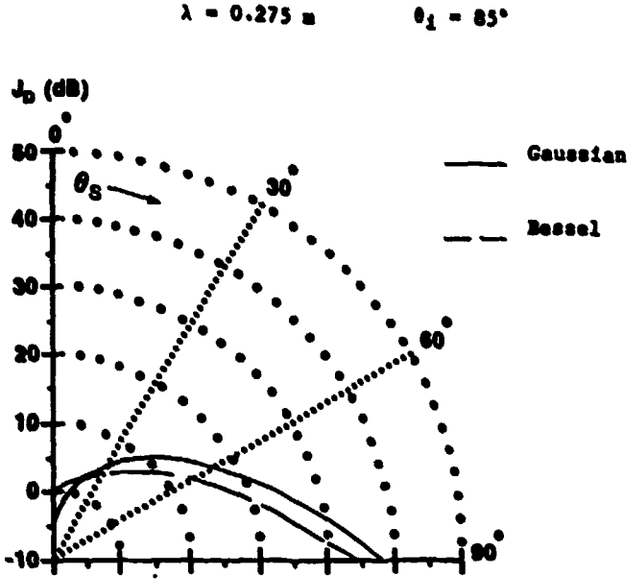


Fig. 5. Forward scatter J_p pattern, very rough exponential surface $\sigma/T = 0.2$

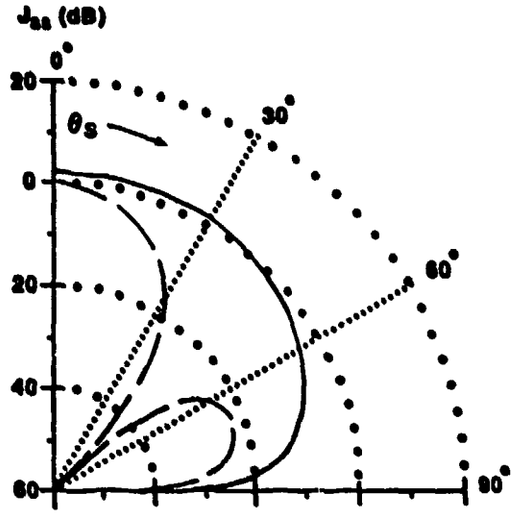
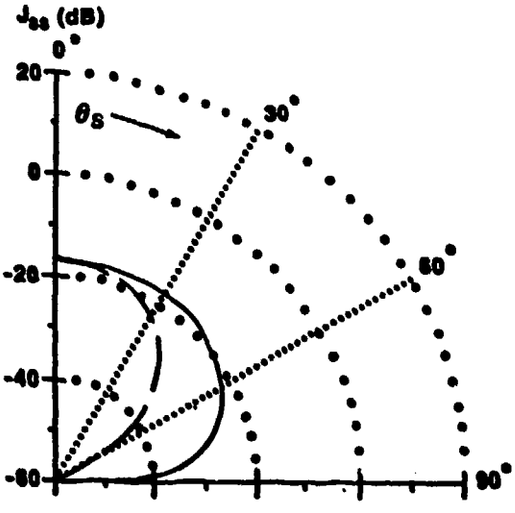


Fig. 6. Small Scale J_{ss} pattern very rough surface with $\theta_i = 45°$

$\lambda = 0.275$ m

$T_s = 0.0444$ m

$k\,\sigma_s = 0.914$



——— Gaussian

— — Bessel

Fig. 7. Small Scale J_{ss} pattern very rough surface with $\theta_i = 85°$

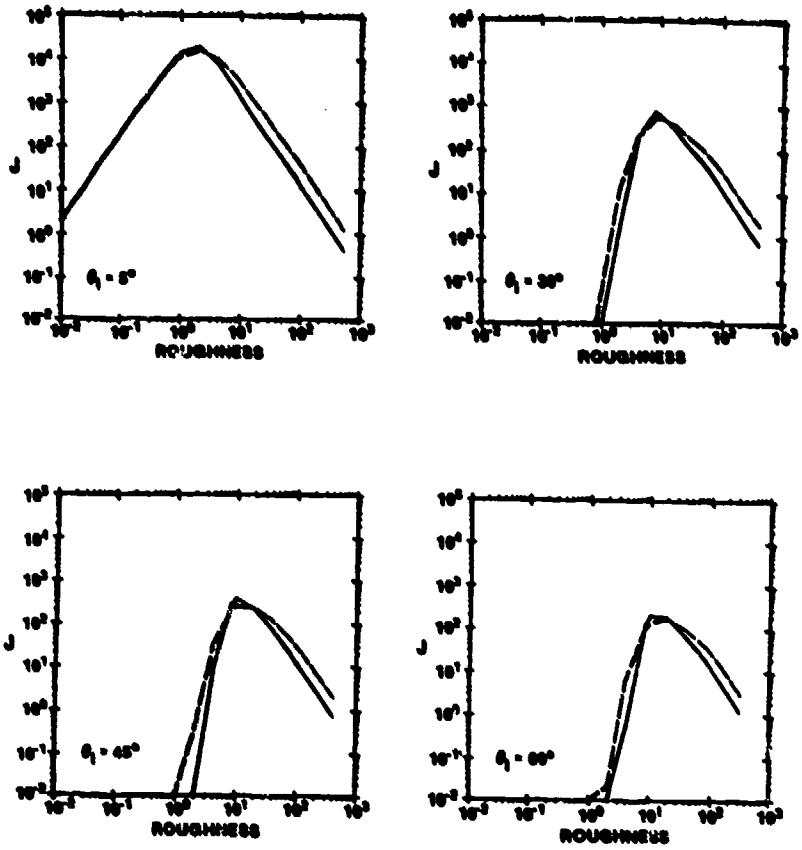


Fig. 8. Scattering dependence on Payleigh Parameter as a function of θ_i; $\phi_s = 3°$.

GAUSSIAN CORRELATION
CORR LENGTH 5.000
WAVELENGTH 0.000

AZIMUTHAL ANGLE 5.000

KEY
——— JDG. EXP SURFACE
— — — JDG. GAU SURFACE

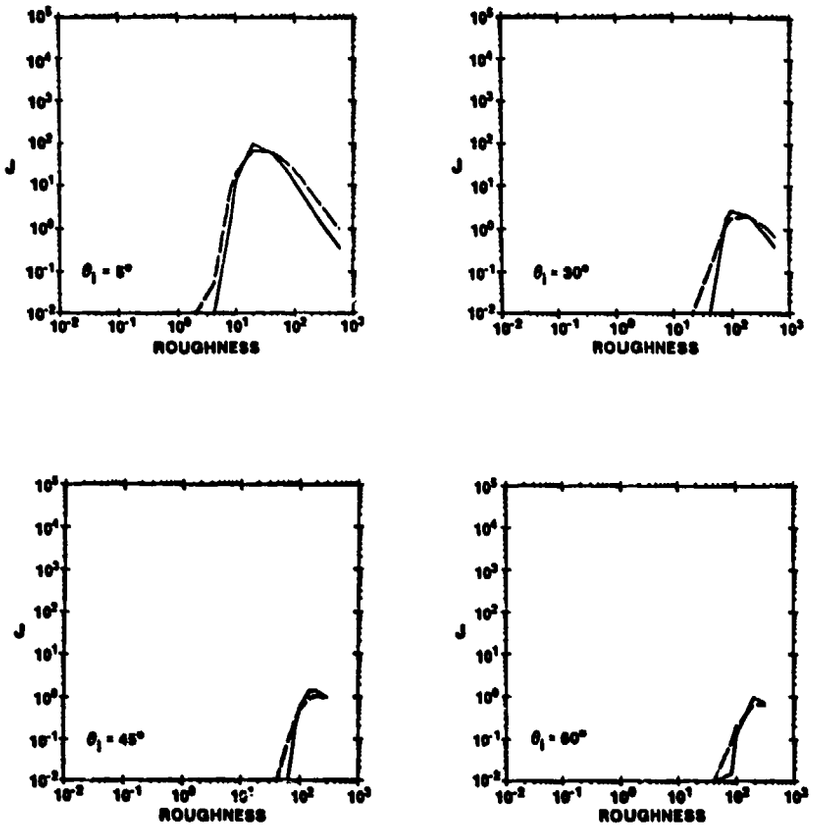


Fig. 9. Scattering dependence on Rayleigh Parameter as a function of θ_i; $\phi_s = 90°$.

GAUSSIAN CORRELATION
CORR LENGTH 5.000
WAVELENGTH 6.000

AZIMUTHAL ANGLE 90.00

KEY
——— JDE. EXP SURFACE
— — — JDG. GAU SURFACE

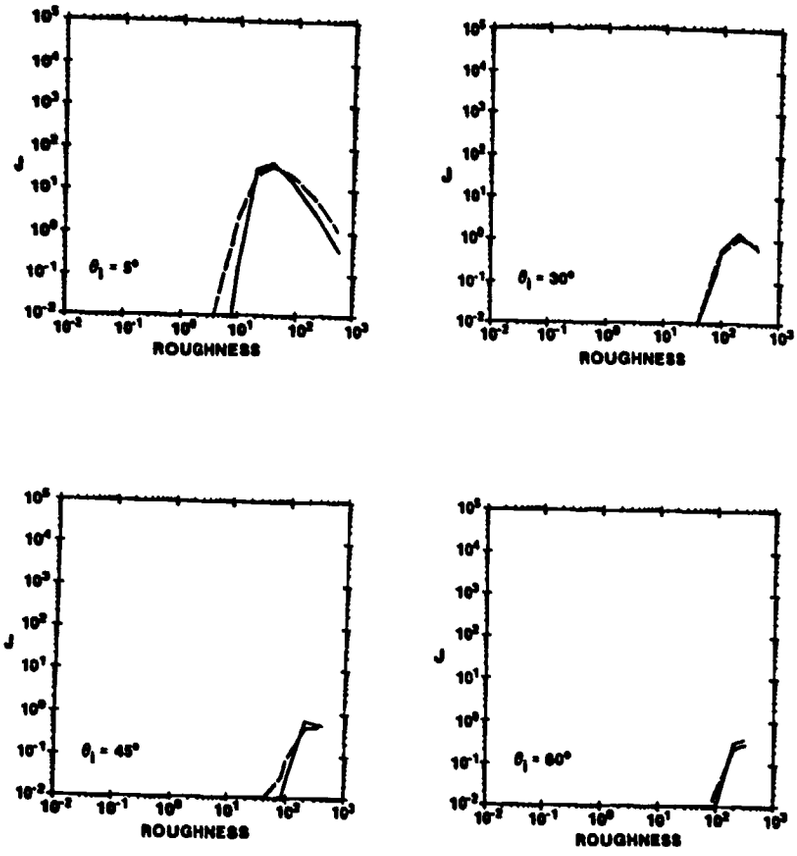


Fig. 10. Scattering dependence on Rayleigh Parameter as a function of θ_i; $\phi_s = 180°$.

GAUSSIAN CORRELATION
CORR LENGTH 5.000
WAVELENGTH 0.090
AZIMUTHAL ANGLE 180.00

KEY
——— JDE. EXP SURFACE
— — — JDG. GAU SURFACE

DISCUSSION

A.K. Fung, US

You indicated only the small slope requirement in your conclusion on the PO integral. Do you want to require a large correlation length simultaneously for the physical optics method to work?

Author's Reply

For the validity of the Kirchhoff PO representation as a single integral, without going to the high frequency GO limit, one must have small slopes. However, when the slopes are small $\sigma/T < 1$, the condition correlation length $T >> \lambda$ is a sufficient condition, but not necessary. For PO to be valid when $\sigma/T < 1$, the condition on correlation length may be relaxed to $T \gtrsim \lambda$, i.e., the correlation length may become of the order of a wavelength, but not less than a wavelength.

MARKOV RANDOM FIELDS: A STRATEGY FOR CLUTTER MODELLING

Stephen P. Luttrell
Royal Signals and Radar Establishment
St Andrews Road
Malvern
Worcestershire
WR14 3PS
UK

SUMMARY

We briefly review the need for models of image texture (or clutter). The use of detailed physical models is prohibited by the difficulty of characterising the scatterer distribution and the scattering process which cause the texture, and so we resort to phenomenological modelling. We propose that certain statistics of the image be measured, and that synthetic images which are consistent with these measurements be generated by a Monte Carlo method - this allows us to test the need for further statistics. We point out the relationship of this scheme to the well-known maximum entropy method for constructing least committal probability distributions. Furthermore we show how a Markov random field model is generated by this process. Finally we suggest some methods of selecting useful statistics, which we demonstrate by analysing a synthetic aperture radar image of a wood and a sonar image of the sea bed.

LIST OF SYMBOLS:

x	sample position in image
N	number of pixels (or samples) in image
$T[\underline{x}]$	image pixel (ie sample) value at position $\underline{x}$
$\underline{s}_j$	vector of local statistics of $T[\underline{x}]$ at pixeT j
$\underline{S}[T]$	vector of statistics of $T[\underline{x}]$
$\underline{S}_0$	the value of $\underline{S}$ for a particular image
$P[T]$	PDF over $T[\underline{x}]$
$P_{synth}[T]$	PDF over synthetic images $T[\underline{x}]$
$P[\underline{S}]$	PDF over $\underline{S}[T[\underline{x}]]$
$Z[\underline{S}]$	the number of T which map to $\underline{S}$ (Jacobian)
$\mathcal{E}$	ensemble of images
M	number of images in ensemble
$\langle \underline{S} \rangle$	ensemble average of $\underline{S}[T]$

CHARACTERISING TEXTURE IN IMAGES

We shall be concerned with building phenomenological models which describe the structure of textured coherent images. Typical examples of coherent imaging systems are synthetic aperture radar (SAR) and sonar, and such images frequently consist of well defined regions of homogeneous texture. Image texture is often called clutter because it is usually regarded as the background against which objects of interest must be detected. Therefore a good model of image texture is required before we can proceed to the detection and analysis of embedded objects.

The most important property of most of the textures of interest is that they are stochastic rather than deterministic in character, so that for a given texture the image pixel (ie sample) values are not rigidly constrained. Rather, there is a loose relationship or correlation between pixel values which produces the overall impression of texture. There are circumstances where models in which a mixture of stochastic and deterministic behaviour is desirable, such as modelling images of urban regions. Some such techniques have been described elsewhere [1], so we shall not dwell upon these.

When confronted with a textured image we must decide which statistics to measure in order to characterise the image structure. This is not a trivial problem in general, because we do not know in advance what properties of the image need to be measured. The usual approach [1] has been to measure a few simple statistics (eg moments, autocorrelation function, mean, variance, entropy, co-occurrence matrix). This method has the advantage of simplicity, but it provides no hint of the necessity or otherwise of the chosen statistics in any particular case.

TEXTURE MODELS

In information theoretic terms the probability density function (PDF) over images having a particular texture contains all the information that is required to derive the properties of images of that texture. It is very difficult (and usually impossible) to derive such a PDF entirely from first principles, so approximations are made in order to construct a physical model of the various processes which underlie the generation of the image. Image formation consists of four essential processes: arrangement of the scatterers, illumination of the scatterers, scattering of the illumination, and focussing of the scattered illumination (or beamforming). Thus a model of the scatterer distribution is used as input to a model of the scattering process, which in turn is used as input to a model of the focussing process: the result of this is a stochastic model of the image texture. We now describe these stages in more detail.

The model which is used to describe correlations in the scatterer distribution is usually highly simplified. In order to construct such a model an understanding of the processes which gives rise to scatterer correlations is required - this is usually hard to express in simple terms. For example when modelling the distribution of scatterers in a wooded area there are many length scales to consider (eg clusters of trees, trees, branches, twigs, etc), each of which has its own characteristic properties

in general. In such cases it is necessary to use a grossly simplified model of the physical processes which underlie the scatterer distribution. However the variety of textures which can be modelled with a restricted set of physical parameters is severely limited, and so phenomenology is used when constructing more realistic models.

The scattering process is usually modelled using the Born (or single scattering) approximation. The validity of this is not obvious, but it leads to a simple picture of the scattering process which allows the eventual image to be interpreted in the light of the scattering model chosen. Circumstances where this model might break down typically occur when strong specular reflections are possible. Phenomenology may be used to construct more complicated scattering models in circumstances where the single scattering approximation is invalid, but at the cost of complicating image interpretation.

The focussing process itself is well understood in most situations. The point spread function is used to describe this part of the overall imaging model, and it is provided by an independent instrumental calibration or by calibration in situ using a bright point target. Phenomenology is not usually required to model this stage of image formation.

PHENOMENOLOGICAL TEXTURE MODELS

We have seen that the difficulty of constructing realistic physical models suggests that phenomenology should be used. The trade-off which we seek here is to simplify the construction of the model at the expense of complicating the physical interpretation of the image. If a purely descriptive model of the image is all that is required then a phenomenological model alone will suffice: this occurs when we need only to discriminate between various textured regions in an image, for instance.

There are two complementary approaches to phenomenological texture modelling. Either phenomenology is included only in the model of the scatter distribution, or an entirely phenomenological model of the image itself is developed. An account of the first approach has been given at this meeting by Oliver, so we shall concentrate on the latter approach.

An advantage of the purely phenomenological approach is that it turns out to be very easy to model high order statistical properties (eg n-point moments). This is important when we wish to model textures with very complicated correlations. The corresponding disadvantage is that the physical origin of the various statistical properties is completely lost in phenomenology. However for the purposes of building a purely descriptive framework within which objects embedded in clutter might be analysed this is acceptable. We should point out that hybrid models may be developed in which physics is used to constrain the structure of some parts of the model, whilst the remainder of the model is purely phenomenological. We shall be using translational symmetry to constrain the structure of our texture models, so strictly our method is a member of the hybrid class.

THE PROPOSED PHENOMENOLOGICAL MODEL

The model which we propose for texture modelling consists of three parts: the choice and measurement of suitable statistics, the generation of synthetic textured images using the measured statistics, and the refinement of the choice of statistics based upon a comparison of the synthetic and the original textured images. The model is thus built in an iterative fashion whereby the choice of statistics is refined until a satisfactory match between the synthetic and the original images is obtained.

We shall denote position in an image by x, the image itself by $T(x)$, and the vector of statistics which is obtained from $T(x)$ by $\underline{S}[T]$. We shall assume throughout that $\underline{S}[T]$ has the form of a spatial average of some local statistic. Thus

$$\underline{S}[T] \equiv \frac{1}{N}\sum_{j=1}^{N} \underline{s}_j \qquad (1)$$

where $\underline{s}_j$ is a vector of local statistics evaluated at pixel j, and N is the number of image pixels. $\underline{S}[T]$ has a PDF which is given by

$$P[\underline{S}] = Z[\underline{S}]\, P[T] \qquad (2)$$

where $Z[\underline{S}]$ is the Jacobian of the transformation $T \rightarrow \underline{S}$ (ie the number of distinct $T(x)$ which map to a single value of $\underline{S}$), and $P[T]$ is the PDF over images $T[x]$ of a particular texture. We shall denote the particular value of $\underline{S}$ which is measured in a textured image by the symbol $\underline{S}_0$. The value of $\underline{S}_0$ usually contains insufficient information to determine $P[\underline{S}]$, but an exception to this occurs when $N \rightarrow \infty$ so that $P[\underline{S}]$ is asymptotically a delta function. $\underline{S}_0$ then completely characterises $P[\underline{S}]$, and so an inversion of Eq.(2) to obtain $P[T]$ may be attempted.

This asymptotic method relies on the crucial assumption that N is large enough that fluctuations in the value of $\underline{S}_0$ (measured from independent realisations of the same texture) are small compared to its absolute value. We shall not present a rigorous analysis of the information loss (insofar as specifying $P[T]$ is concerned) that accompanies such fluctuations, because we shall adopt the viewpoint that $\underline{S} = \underline{S}_0$ summarises all the information that we wish to preserve about the image $T[x]$. Further information can then be obtained only by measuring further statistics as we shall describe later.

$P[T]$ must satisfy the constraint

$$P[T] = 0 \qquad \underline{S} \neq \underline{S}_0 \qquad (3)$$

This does not specify what form $P[T]$ must take when $\underline{S} = \underline{S}_0$ because such information is not contained in

$\underline{S} = \underline{S}_0$. We emphasise that $\underline{S} = \underline{S}_0$ is the sole source of information about the original image, so that we have no choice but to define P[T] to be constant when $\underline{S} = \underline{S}_0$: this is the least committal way of performing the reconstruction of the PDF P[T]. Only one of the images which is permitted by such a PDF is the original image, but the set of all permitted images forms an ensemble which is representative of the actual information which is contained in $\underline{S} = \underline{S}_0$ alone.

We then generate synthetic images from the permitted set by defining an approximate P[$\underline{S}$] by

$$P[\underline{S}] \propto \exp\left\{-\frac{(\underline{S}-\underline{S}_0)^2}{2a^2}\right\} \tag{4}$$

which has the correct form in the limit $a \to 0$. We have chosen to use a Gaussian PDF purely for convenience; it has no fundamental significance. We then define a P[T] by inserting Eq.(4) into Eq.(2) ignoring the contribution of the Z[$\underline{S}$] factor which is effectively constant in the limit $a \to 0$. We then use a Monte Carlo (MC) technique to sample from P[$\underline{S}$] by repeatedly attempting to update a pixel values according to the prescription

$$T[\underline{x}] \to T'[\underline{x}] \quad \text{with probability} \quad \frac{P'}{P+P'} \tag{5}$$

$$P \equiv P[\underline{S}[T]] \qquad P' \equiv P[\underline{S}[T']]$$

The order in which we select pixels for updating is random in order to ensure that translational symmetry is preserved by the MC algorithm. We refer to a set of N such updates as a Monte Carlo cycle, because such a set will cause an average of one attempted update of each pixel in an N pixel image. The particular update $T \to T'$ which is attempted at any stage may be chosen flexibly, because the properties of the MC method guarantee convergence provided that the sequence of images generated is ergodic. In our work we have represented pixel values as integers in the range [0,255], and we have selected at random within this range new pixel values to be attempted according to Eq.(5). Other prescriptions could be used in order to enhance the ability of the MC algorithm to explore the set of allowed images.

The parameter a is steadily decreased towards zero whilst the MC algorithm proceeds, until finally $\underline{S} = \underline{S}_0$ and a sample synthetic image emerges. This particular way of using the MC is known as optimisation by simulated annealing (OSA) by analogy with the process that is used in crystal growth to remove unwanted defects [2]. The parameter a in Eq.(4) is usually referred to as the temperature, and the sequence of values of a which is used by the OSA algorithm is called the annealing schedule. We offer no simple prescription for a general annealing algorithm because the best choice is highly problem dependent. However in our work (see the results described later) we have found that 5 Monte Carlo cycles at each temperature is sufficient to allow equilibriation, and that the temperature may be reduced by a factor of 5 after each set of 5 cycles. The initial temperature was chosen to be sufficiently high that the statistics were only weakly constrained.

RELATIONSHIP TO ENTROPY MAXIMISATION

The OSA algorithm which was described above leads to a synthetic image $T_0[\underline{x}]$ which is sampled non-committally from the set of images which satisfy the constraint $\underline{S} = \underline{S}_0$, and we shall denote the PDF over synthetic images by $P_{synth}[T]$. $P_{synth}[T]$ has a very rich underlying structure which is derived as follows.

Consider an ensemble E of images defined by

$$E \equiv \{T_1, T_2, \ldots, T_M\} \tag{6}$$

where each member of E is drawn independently from P[T]. Define the average statistic

$$\langle \underline{S} \rangle \equiv \frac{1}{M}\sum_{j=1}^{M} \underline{S}[T_j] \tag{7}$$

When the number of image pixels N is large enough that the relative fluctuations of $\underline{S}_0$ are negligibly small the constraint $\langle \underline{S} \rangle = \underline{S}_0$ is equivalent to the constraint $\underline{S} = \underline{S}_0$. Now we wish to find that PDF over images T[$\underline{x}$] which maximises the number of ways in which the ensemble E can be generated (using independent samples) consistent with the constraint $\langle \underline{S} \rangle = \underline{S}_0$.

The optimisation problem posed above is easily solved, and gives rise to the familiar maximum entropy solution when M is large [3]

$$P_{synth}[T] \propto \exp\{-\underline{k}.\underline{S}[T]\} \tag{8}$$

where the constant vector $\underline{k}$ must be chosen so that $\langle \underline{S} \rangle = \underline{S}_0$. The existence of such a maximum entropy solution is not invariably guaranteed for a particular constraint $\underline{S} = \underline{S}_0$, and failure to obtain a solution indicates that the set of statistics being used is insufficient to characterise the texture fully. The converse does not hold however: an insufficient set of statistics does not preclude the existence of a maximum entropy solution.

Recall that we are considering only those statistics $\underline{S}[T]$ which have the form of a spatial average as defined in Eq.(1). Eq.(8) may now be written as

$$P_{synth}[T] \propto \prod_{j=1}^{N} \exp\{-\underline{k}.\underline{s}_j\} \tag{9}$$

The simple global constraint $\underline{S} = \underline{S}_0$ which was expressed in Eq.(3) has therefore induced a rich structure in $P_{synth}[T]$ which is expressed in Eq.(9). The jth term in the product is dependent only on the local vector of statistics $\underline{s}_j$, and so the overall probability measure is a product of factors with only local pixel dependencies.

RELATIONSHIP TO MARKOV RANDOM FIELD THEORY

The form for $P_{synth}[T]$ which was obtained in Eq.(9) defines a Markov random field (MRF) [4]. The form of the statistics vector $\underline{S}[T]$ may be chosen arbitrarily in principle, and so a correspondingly complicated MRF structure may be generated according to Eq.(9). The scalar product $\underline{k}.\underline{s}_j$ records the information which is contained in the constraint $\underline{S} = \underline{S}_0$: the form of $\underline{S}$ is recorded in the $\underline{s}_j$ vector, and the particular value $\underline{S}_0$ which is measured is recorded in the $\underline{k}$ vector.

The OSA algorithm provides a quick way of assessing the usefulness of a particular set of statistics $\underline{S}$ for modelling a textured image. Derivation of the vector $\underline{k}$ requires more extensive computation, and so the MRF formulation should only be derived if the detailed form of the $P_{synth}[T]$ which is implied by $\underline{S} = \underline{S}_0$ is required.

An advantage of the MRF formulation is that an explicit PDF is obtained, which may be used to derive explicit conditional probabilities. For instance the ratio of probabilities that a pixel can take each of two possible values whilst all other pixel values are held constant is given by

$$\frac{P[T']}{P[T]} = \prod_j \exp\{-\underline{k} \cdot (\underline{s}'_j - \underline{s}_j)\} \tag{10}$$

where the product is over only those factors in which $\underline{s}_j$ involves the pixel of interest. This expression may be used to derive the MRF formulation of the MC update scheme in Eq.(5). Another advantage of the MRF formulation which emerges from Eq.(10) if the $\underline{s}_j$ are local statistics is that the MC update scheme depends only on local computations.

CHOICE OF STATISTICS

We could adopt the assumption that nothing at all is known about the structure of the image prior to making any measurements. However in practice there are many useful strategies for designing statistics which facilitate model building. We have assumed throughout that the statistical properties of the image are translation invariant (see Eq.(1)). This is a very useful approximation, and it provides a good starting point for image analysis.

We must now make additional assumptions about which particular form of $\underline{S}$ should be chosen. We can make much progress by appealing to simple dimensional arguments. For instance if we suspect that the image structure contains certain length scales, then it is useful to construct statistics which are sensitive to structure on such length scales. A particular example of this strategy occurs when we identify the scale which corresponds to the point spread function width of the imaging system. The image will usually be locally smooth on such a scale, so a statistic which responds to the presence or absence of such local smoothness is essential. Other length scales will derive from the structure of the object which is being imaged - these are more difficult to quantify.

Another fundamentally important point to observe when constructing $\underline{S}$ is to ensure as far as possible that its various components measure independent image information. A priori this is an impossible condition to satisfy because we do not know in advance what we are measuring. An interesting case arises however when it is known in advance that the image is described by an MRF model: a necessary and sufficient set of statistics may then be constructed [5]. However more generally there is a simple rule of thumb which may be used to reduce substantially the interdependencies of the various statistics.

For simplicity we shall describe a one dimensional n pixel image $T(\underline{x})$, which is written out as a vector of pixel intensities

$$T(\underline{x}) = (I_1, I_2, \ldots, I_N) \tag{11}$$

Define a doublet of local statistics $\underline{s}_j$ thus

$$\underline{s}_j = (I_j, I_j I_{j+1}) \tag{12}$$

The first component of $\underline{s}_j$ measures the mean pixel intensity, and the second component measures the autocorrelation for a one pixel displacement. This is an example of a poor choice of statistics because $\langle I_j I_{j+1} \rangle$ implicitly contains a lot of information about $\langle I_j \rangle$. A far better choice is the doublet

$$\underline{s}_j = (I_j, I_j I_{j+1} - \langle I_j \rangle \langle I_{j+1} \rangle \tag{13}$$

where the second component is now zero when I_j and I_{j+1} have their mean values. This new component measures the degree of correlation of the intensities of adjacent pixels.

The general principle which underlies the above strategy may be written in a recursive manner. Thus define the basic image statistic by

$$s_j^{(1)} = I_j \tag{14}$$

from which all other statistics will be derived. Define a derived statistic by

$$s_j^{(2)} = f(s_j^{(1)}, s_{j+1}^{(1)}) = f(\langle s_j^{(1)} \rangle, \langle s_{j+1}^{(1)} \rangle) \tag{15}$$

where f is a suitably chosen function of two variables. Clearly when $f(z_1,z_2) = z_1 z_2$ the doublet in Eq.(13) is recovered. Eq.(15) may be generalised further by using it recursively to construct further statistics. The function f need not be the same at each stage of the recursion, nor need it be a function of two variables only. If the first term in Eq.(15) has the general form $f(z_1,z_2,\ldots,z_k)$, then the second term should have the form $f(\langle z_1 \rangle,\langle z_2 \rangle,\ldots,\langle z_k \rangle)$. This recursive method of defining new statistics has the advantage that the second term can always be obtained from existing measurements of the spatial average of simpler statistics, and so the computational overhead in producing a desirable behaviour for the new statistic is acceptable. It is important to note that this method has been justified on the grounds of simplicity alone: it is not guaranteed to produce anything more than a qualitative improvement in the independence of the statistics.

A problem may arise in the OSA algorithm when the components of S_o have widely differing absolute values. For instance this may occur when the dimensions of the various statistics are different (eg different powers of intensity). Either the statistics should be redefined so that they have similar absolute values, or Eq.(4) should be replaced by

$$P[S] = \exp\left\{-\sum_j \frac{(S_j - S_{oj})^2}{2a_j^2}\right\} \tag{16}$$

where now the a_j define different temperatures for each statistic. Typically the ratio of the various a_j should be chosen to be equal to the ratio of the corresponding $S_{o,j}$ in order to ensure that the $S_j - S_{j,o}$ are given equal weight in Eq.(16).

RESULTS

We shall now examine how a simple set of statistics can successfully model textured SAR and sonar images. For simplicity we shall restrict ourselves to using the first six moments and some local 2-point statistics. Thus we define the intensity of pixel (j,k) of an image to be $I_{j,k}$, and then we define the vector of local statistics to be of the form

$$\underline{s}_{jk} = (\underline{s}_{jk}^{(0)}, \underline{s}_{jk}^{(1)}, \underline{s}_{jk}^{(2)}, \underline{s}_{jk}^{(4)}, \underline{s}_{jk}^{(8)}) \tag{17}$$

where

$$\begin{aligned}
\underline{s}_{jk}^{(0)} &= (I_{jk}, (I_{jk})^2, \ldots, (I_{jk})^6) \\
\underline{s}_{jk}^{(1)} &= I_{jk}(I_{j+1,k}, I_{j+1,k+1}, I_{j,k+1}, I_{j-1,k+1}) \\
\underline{s}_{jk}^{(2)} &= I_{jk}(I_{j+2,k}, I_{j+2,k+1}, I_{j+2,k+2}, I_{j+1,k+2}, \\
&\qquad I_{j,k+2}, I_{j-1,k+2}, I_{j-2,k+2}, I_{j-2,k+1}) \\
\underline{s}_{jk}^{(4)} &= I_{jk}(I_{j+4,k}, \ldots\ldots, I_{j+4,k+4}, \\
&\qquad I_{j+3,k+4}, \ldots\ldots, I_{j-4,k+4}, \\
&\qquad I_{j-4,k+3}, \ldots\ldots, I_{j-4,k+1}) \\
\underline{s}_{jk}^{(8)} &= I_{jk}(I_{j+8,k}, \ldots\ldots, I_{j+8,k+8}, \\
&\qquad I_{j+7,k+8}, \ldots\ldots, I_{j-8,k+8}, \\
&\qquad I_{j-8,k+7}, \ldots\ldots, I_{j-8,k+1})
\end{aligned} \tag{18}$$

where $\underline{s}_{jk}^{(1)}$, $\underline{s}_{jk}^{(2)}$, $\underline{s}_{jk}^{(4)}$, and $\underline{s}_{jk}^{(8)}$ are understood to have the product of means subtracted out as prescribed in Eq.(15). The four components of $\underline{s}_{jk}^{(1)}$ measure the degree of correlation between I_{jk} and the nearest pixel in the east, north-east, north and north-west directions. The remaining points of the compass are contained in $\underline{s}_{j-1,k}$, $\underline{s}_{j-1,k-1}$, $\underline{s}_{j,k-1}$ and $\underline{s}_{j+1,k-1}$. The purpose of remaining statistics is to measure the analogous degrees of correlation at separations of 2, 4 and 8 pixels, where the pixel separation is the half-length of the side of a square (with sides parallel to the north-south and east-west directions) centred on one pixel and passing through the other pixel. This choice of statistics is somewhat arbitrary and possibly redundant, but it will suffice to demonstrate the power of our technique.

The image in Figure 1(a) is a 128 x 128 SAR image of a wooded region.

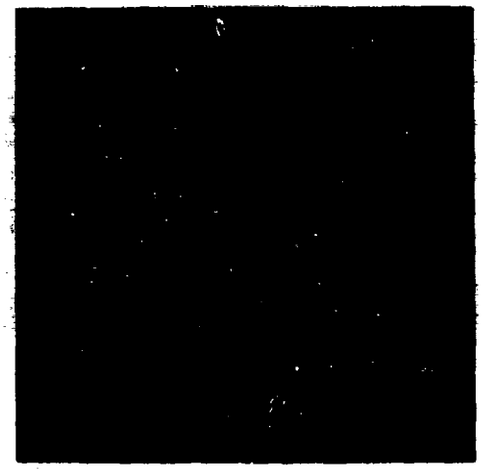


Figure 1(a)

There are several distinctive features to note in this image. Firstly there is an obvious correlation in the north-south direction which smooths the image on a length scale of about two pixels. This anisotropy is caused by the different physical means which are used to create two orthogonal components of the (factorisable) point spread function in the SAR. The image also has a clumpy structure which has a range of length scales ranging from a few pixels out to many tens of pixels. However the dominant structure is found at length scales less than of order 10-20 pixels. There are also a few much darker regions in the image: these are regions which are not illuminated by the radar (ie shadows).

The 64 x 64 synthetic images which are shown in Figures 1(b) to 1(e) correspond respectively to using $\underline{s} = (\underline{s}(0),\underline{s}(1))$ to $\underline{s} = (\underline{s}(0),\underline{s}(1),\underline{s}(2),\underline{s}(3),\underline{s}(4))$.

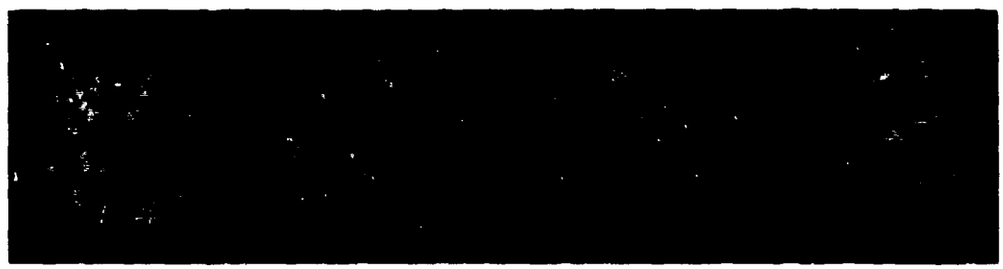


Figure 1(b) Figure 1(c) Figure 1(d) Figure 1(e)

Thus each successive image has an extra set of statistics included. There is a clear improvement in the quality of the synthetic image as longer range statistics are introduced, until finally Figure 1(e) shows a marked similarity to Figure 1(a). There are nevertheless discrepancies which remain because there are no statistics which are sensitive to structure on a scale greater than 8 pixels, nor are there any statistics which depend on more than 2 pixel values. It is interesting to note that the set of statistics which is used to produce Figure 1(e) is highly redundant. A more careful approach where a statistic is added to the existing set of statistics only when inconsistencies between the original and the synthetic images are observed gives a much more efficient representation of the textured image structure.

The 128 x 128 image in Figure 2(a) is a sonar image of the sea bed.



Figure 2(a)

It shows a completely different texture to that seen in Figure 1(a), and so it provides an independent test of our method. Figures 2(b) to 2(e) are produced in an analogous fashion to Figures 1(b) to 1(e).



Figure 2(b) Figure 2(c) Figure 2(d) Figure 2(e)

As before the synthetic image quality improves as we pass from Figure 2(b) to Figure 2(e), with the texture of Figure 2(e) showing a marked similarity to that of the original image in Figure 2(a).

The 64 x 64 image in Figure 3(a) is another sonar image of the sea bed which shows the presence of sandwaves.

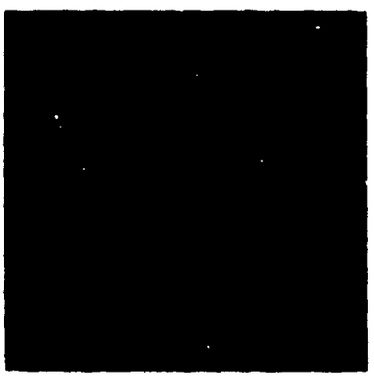


Figure 3(a)



Figure 3(b)

This image has been preprocessed to reduce its resolution by a factor of 8 in order to bring the characteristic structure within the length scale (8 pixels) measured by the statistics which we are using. This image is not ideally suited to our method because its statistical properties are not homogeneous. However the synthetic image obtained using the statistics of Eq.(17) which is shown in Figure 3(b) again has a marked similarity to the original.

This result is probably fortuitous because the statistics measured from Figure 3(a) are a spatial average over an inhomogeneous texture, and so represent no single texture within the image. To a much lesser extent this remark also applies to the images in Figures 1(a) and 2(a).

CONCLUSIONS

The results which we have presented demonstrate that our synthetic image generation method produces good results when using a limited set of simple statistics. This is even more impressive when the set is pruned to remove redundant statistics. It is interesting to note that we have produced a workable scheme for modelling textured images using only translation invariance, and simple dimensional arguments. Of course we do not pretend that all textures can be modelled using the 1-point and 2-point statistics of Eq. (18); these were used only to demonstrate how our method is used in simple cases. We have shown how it is possible to use MRF models to describe textures without actually solving explicitly for the MRF parameters. This is a great computational saving in circumstances where such parameters are not explicitly required, and it provides a significant advance over previous MRF modelling schemes for textured images [1].

An example of the type of image which will require more complicated statistics is a SAR image of a town, where there are many extended linear and angular features. We will then need high-order statistics which respond to and distinguish between such features. The power of our method is such that we can systematically design a set of such statistics which extracts only that information from the textured image $T[\underline{x}]$ which is required to describe its textural structure. It is interesting to note that the use of high-order statistics can produce models in which there is a strong deterministic element, so we see that the separation of models into stochastic and deterministic classes is somewhat artificial. The MC algorithm must be very carefully designed when high-order statistics are used because there is a real possibility that ergodicity might not be achieved during the annealing process.

The choice of statistics is not entirely arbitrary, because physical insight is available to narrow down the variety of possible statistics which might be considered. This strategy will ensure that the set of statistics represents the textural structure of $T[\underline{x}]$ economically - translational invariance is a trivial example of the use of a physical constraint to build a model. The optimum trade-off between phenomenology and physics must be chosen to match the particular type of image and prior knowledge that is available.

Finally the answer to the question "Markov random fields: a strategy for clutter modelling?" is emphatically "yes", because of their flexibility in describing a great variety of textured images, and because of the great computational saving which is offered by our technique.

REFERENCES

[1] Van Gool, L., Dewaele, P. and Oosterlinck, A., "Texture analysis anno 1983", Comp. Vis. Graph. Im. Proc., 29, 1985, 336-357.

[2] Kirkpatrick, S., Gelatt, C.D. and Vecchi, M.P., "Optimisation by simulated annealing", Science, 220, (4598), 671-680.

[3] Jaynes, E.T., "Prior probabilities", IEEE Trans. SSC, 4(3), 1968, 227-241.

[4] Kindermann, R. and Snell, J.L., "Markov random fields and their applications", Contemporary Mathematics, Volume 1, American Mathematical Society, Providence, Rhode Island, 1980, 24-33.

[5] Luttrell, S.P., "The use of Markov random field models to derive sampling schemes for inverse texture problems", Inv. Prob., to be published.

A SCATTERING MODEL FOR FORESTED AREA

M.A. Karam and A.K. Fung
Wave Scattering Research Center
Box 19016, College of Engineering
University of Texas at Arlington
Arlington, TX 76019
USA

SUMMARY

A forested area is modeled as a volume of randomly oriented and distributed disc-shaped, or needle-shaped leaves shading a distribution of branches modeled as randomly oriented finite-length, dielectric cylinders above an irregular soil surface. Since the radii of branches have a wide range of sizes, the model only requires the length of a branch to be large compared with its radius which may be any size relative to the incident wavelength. In addition, the model also assumes that the thickness of a disc-shaped leaf or the radius of a needle-shaped leaf is much smaller than the electromagnetic wavelength. The scattering phase matrices for disc, needle and cylinder are developed in terms of the scattering amplitudes of the corresponding fields which are computed by the Helmholtz integral formula. The extinction coefficients are computed by the forward scattering theorem. These quantities along with the Kirchhoff scattering model for a randomly rough surface are used in the standard radiative transfer formulation to compute the backscattering coefficient.

Numerical illustrations for the backscattering coefficient are given as a function of the shading factor, incidence angle, leaf orientation distribution, branch orientation distribution and the number density of leaves. Also illustrated are the properties of the extinction coefficient as a function of leaf and branch orientation distributions. Comparisons are made with measured backscattering coefficients from forested areas reported in the literature.

1. INTRODUCTION

Scattering of electromagnetic waves from a forested area is modeled by a layer of discrete randomly oriented and distributed scatterers over a rough interface. The discrete scatterers are the leaves and branches of the trees, the rough interface is the soil underneath. The leaves will be modeled as circular discs or needles. The branches will be modeled as randomly oriented cylinders of finite length. A shading factor will be introduced to study the shading effect of the leaves on the branches.

In the literature the scattering of electromagnetic waves from a layer of discrete scatterers had been investigated using the distorted Born approximation [1, 2], the doubling method [3, 4], and the radiative transfer method [5-7].

In this study the first order solution of the radiative transfer will be used to calculate the backscattering coefficients [5-7] in which the phase function and the extinction coefficient for each scatterer are required. For a randomly oriented, disc, needle or finite length cylinder to obtain the phase function and the extinction coefficient we will follow the technique developed in references [7-9].

Finally in Sec. 6 numerical illustrations for the backscattering coefficient will be given as a function of the shading factor, the incidence angle, the leaf orientation distribution, the branch orientation distribution and the number density of leaves. Also illustration will be given for the properties of the extinction coefficient as a function of leaf and branch orientation distributions. At the end comparisons will be made with some measured backscattering coefficients from forested areas reported in the literature [10].

2. BACKSCATTERING COEFFICIENT

Consider a forested area modeled as a layer of randomly oriented disc-shaped or needle-shaped leaves shading a distribution of branches modeled as randomly oriented finite length cylinders above a rough interface. The layer has a depth (D) and is illuminated by a plane wave in the form;

$$\bar{E}_i = (\hat{v}_i \hat{v}_i + \hat{h}_i \hat{h}_i) \cdot \bar{E}_0 \exp(-jk\hat{i}\cdot\bar{r}) \qquad (1)$$

where $\hat{i}$ is the incident direction and $\hat{v}_i$ and $\hat{h}_i$ are the unit polarization vectors defined as (see Fig. 1):

$$\begin{aligned}
\hat{i} &= \sin\theta_i \cos\phi_i \hat{x} + \sin\theta_i \sin\phi_i \hat{y} - \hat{z}\cos\theta_i \\
\hat{h}_i &= \hat{z} \times \hat{i} / |\hat{z} \times \hat{i}| = \hat{y}\cos\phi_i - \hat{x}\sin\phi_i \\
\hat{v}_i &= \cos\theta_i (\hat{x}\cos\phi_i + \hat{y}\sin\phi_i) - \hat{z}\sin\theta_i
\end{aligned} \qquad (2)$$

The backscattering coefficient from the layer can be written by using the first order solution of the radiative transfer equations as [9]

$$\sigma_{pq} = \sigma_{pq}^{s} + C\sigma_{pq}^{l} + (1 - C)\sigma_{pq}^{b} \qquad (3)$$

In (3) p stands for the polarization of the scattered wave ($p = v_s, h_s$), q stands for the polarization of the incident wave ($q = v_i, h_i$) and C stands for the shading factor ($C \leq 1$). σ_{pq}^{s}, σ_{pq}^{l}, and σ_{pq}^{b} are the backscattering coefficients from the surface, the leaves and the branches respectively.

For a Gaussian distributed random surface we can write the surface backscattering coefficient σ_{pq}^{s} as [11]

$$\sigma_{pq}^{s} = L_{pq} \begin{cases} 0 & p \neq q \\ [|R_{pp}(o)|^2 / 2\cos^3\theta_i \langle z_x^2 \rangle] \exp[-\tan^2\theta_i / 2\langle z_x^2 \rangle] & p = q \end{cases} \qquad (4)$$

where $R_{pp}(o)$ is the Fresnel reflection coefficient evaluated at normal incidence; $\langle z_x^2 \rangle$ is the surface variance and L_{pq} is the loss factor due to the leaves and the branches given by

$$L_{pq} = \exp[-(\alpha_{ep}(\hat{i}) + \alpha_{ep}(\hat{i}))\, 2 \sec\theta_i] \qquad (5)$$

$$\alpha_{ep}(\hat{i}) = n_l \alpha_{elp}(\hat{i}) + n_b \alpha_{ebp}(\hat{i})$$

where $\langle k_{ep}(\hat{i}) \rangle$ is the p-polarized extinction coefficient for both the leaves and the branches; n_l is the number density of leaves; $\langle k_{elp}(\hat{i}) \rangle$ is the extinction coefficient of a single leaf while n_b and $\langle k_{ebp}(\hat{i}) \rangle$ are the corresponding quantities for branches. The extinction coefficients can be obtained from the scattering amplitudes through the forward scattering theorem [12]. In (5) the ensemble average is taken over the scatterer orientations.

For the leaves we can write the backscattering coefficient σ_{pq}^{l} [9] as

$$\sigma_{pq}^{l} = 4\pi n_l \cos\theta_i [(1 - L_{pq}) / (\langle k_{ep}(\hat{i}) \rangle + \langle k_{eq}(\hat{i}) \rangle)] \langle |F_{pq}^{l}(-\hat{i}, \hat{i})|^2 \rangle \qquad (6)$$

where $\langle |F_{pq}^{l}(-\hat{i}, \hat{i})|^2 \rangle$ is the pq term of the phase matrix in the backward direction. $F_{pq}^{l}(-\hat{i}, \hat{i})$ is the pq term of the leaf scattering amplitude tensor in the backward direction.

Similarly, we can write the backscattering coefficient for the branches as [9]:

$$\sigma_{pq}^{b} = 4\pi n_b \cos\theta_i [(1 - L_{pq}) / (\alpha_{ep}(\hat{i}) + \alpha_{eq}(\hat{i}))] \langle |F_{pq}^{b}(-\hat{i}, \hat{i})|^2 \rangle \qquad (7)$$

where $F_{pq}^{b}(-\hat{i}, \hat{i})$ is the pq term of the scattering amplitude tensor for a branch in the backward direction.

3. THE SCATTERING AMPLITUDE TENSOR FOR A RANDOMLY ORIENTED SCATTERER

Fig. (2) depicts the geometry of a randomly oriented scatterer with its local frame $\hat{x}_1'$ ($\hat{x}_1' = \hat{x}'$, $\hat{x}_2' = \hat{y}'$, $\hat{x}_3' = \hat{z}'$) related to the reference frame $\hat{x}_i$ ($\hat{x}_1 = \hat{x}$, $\hat{x}_2 = \hat{y}$, $\hat{x}_3 = \hat{z}$) through the relation

$$\hat{s}_i' = \sum_{j=1}^{3} \lambda_{ij} \hat{s}_j \tag{9}$$

For the Tait-Bryan angles of orientation $(\alpha, \beta, \gamma)\lambda_{ij}$'s are given in [7, 8].

In the local frame the scattering amplitude tensor can be written as:

$$\bar{\bar{F}}'(\hat{s},\hat{i}) = \sum_{p} \sum_{q} F_{pq}'(\hat{s},\hat{i})\, \hat{p}_{sl}\, \hat{q}_{il} \tag{9}$$

where $F_{pq}'(\hat{s},\hat{i})$ can be computed by the Helmholtz integral equation [13], p_{sl}, and q_{il} are the polarization vectors for the scattered and the incident fields in the local frame ($p_{sl} = v_{sl}$, h_{sl} and $q_{il} = v_{il}$, h_{il}).

For a circular disc with radius, a, and thickness, 2l, (l<<a) we can write $F_{pq}'(\hat{s},\hat{i})$ as [13]

$$F_{pq}'(\hat{s},\hat{i}) = C_{pq}^{d}(\hat{s},\hat{i})\, \mu^{d}(\hat{s},\hat{i}) \tag{10}$$

where

$$C_{pq}^{d}(\hat{s},\hat{i}) = [k^2(\epsilon_r - 1)v_o/4\pi][(\hat{u}_{sl}\hat{u}_{il} + \hat{v}_{sl}\hat{v}_{il}) \cdot (\hat{u}_{il}\hat{u}_{il} + \hat{v}_{il}\hat{v}_{il})\, a_{Td} + (\hat{w}_{sl} \cdot \hat{z})\hat{u}_{il}\hat{u}_{il}(\hat{w}_{il} \cdot \hat{z})(a_{Nd} - a_{Td})] \tag{11}$$

and k is the wave number of the host medium, ϵ_r is the relative dielectric constant of the disc and v_o is the disc volume. a_{Td} and a_{Nd} are the polarizability tensor elements for the disc [14]. In (10) $\mu_d(\hat{s},\hat{i})$ is the disc pupil function and is given by

$$\mu^{d}(\hat{s},\hat{i}) = (2\pi/a_o^2) \sum_{n=-\infty}^{\infty} j^{-n} \cos[n(\phi_{sl} - \phi_{il})] \int_{0}^{a} \int_{-l}^{l} J_n(k\rho' \sin\theta_{il})\, J_n(k\rho' \sin\theta_{sl})\, \rho'\, d\rho'\, dz' \tag{12}$$

where $J_n(\,)$ is the cylinderical Bessel function. (θ_{il}, ϕ_{il}) are the local angles in the incident direction. (θ_{sl}, ϕ_{sl}) are the local angles in the scattered direction.

For a needle of radius, a, and length, 2l, (l>>a) we can write the scattering amplitude tensor in the local frame as [13]

$$F_{pq}'(\hat{s},\hat{i}) = C_{pq}^{N}(\hat{s},\hat{i})\, \mu^{N}(\hat{s},\hat{i}) \tag{13}$$

where

$$C_{pq}^{N}(\hat{s},\hat{i}) = [k^2(\epsilon_r - 1)v_o/4\pi][(\hat{u}_{sl}\hat{u}_{il} + \hat{v}_{sl}\hat{v}_{il}) \cdot (\hat{u}_{il}\hat{u}_{il} + \hat{v}_{il}\hat{v}_{il})\, a_{Tn} + (\hat{w}_{sl} \cdot \hat{z})\hat{u}_{il}\hat{u}_{il}(\hat{w}_{il} \cdot \hat{z})(a_{Nn} - a_{Tn})] \tag{14}$$

$$\mu^{N}(\hat{s},\hat{i}) = \sin\psi / \psi \tag{15}$$

and ψ can be written as

$$\psi = kl(\cos\theta_{sl} + \cos\theta_{il}) \tag{16}$$

In (14) a_{Tn} and a_{Nn} are the polarizability tensor elements for the needle [14].

For a finite length cylinder with radius, a, and length, 2ℓ, we can write the scattering amplitude tensor in the local frame as [9]

$$\bar{F}_{pq}^{\,c}(\hat{s},\hat{i}) = \zeta_{pq}^{\,c}(\hat{s},\hat{i})\,\mu^{c}(\hat{s},\hat{i})\,\bar{\bar{U}} \tag{17}$$

where

$$\begin{aligned}\zeta_{pq}^{\,c}(\hat{s},\hat{i}) = k^2\ell(\epsilon_r - 1)\Big\{&\sum_{n=-\infty}^{\infty} j\big[E_{1q}^{\,n} Z_{n+1}\exp(j\phi_{sq}) - \zeta_{2q}^{\,n} Z_{n-1}\exp(-j\phi_{sq})\big] \\ &\cdot(\hat{\phi}_{sq}\cdot\hat{x})\big[E_{1q}^{\,n} Z_{n+1}\exp(j\phi_{sq}) + \zeta_{2q}^{\,n} Z_{n-1}\exp(-j\phi_{sq})\big] \\ &\cdot(\hat{\phi}_{sq}\cdot\hat{y}) + \zeta_{nq} Z_n(\hat{\phi}_{sq}\cdot\hat{z})\Big\}\end{aligned} \tag{18}$$

where $\zeta_{1q}^{\,n}$, $\zeta_{2q}^{\,n}$ and E_{nq} are given in terms of the cylinderical Bessel and Hankel function [9]. Furthermore,

$$Z_n = \int_0^{a} J_n(\rho' k\sqrt{1-\epsilon_r\cos^2\theta_{sq}})\,J_n(\rho' k\sin\theta_{sq})\,\rho'\,d\rho' \tag{19}$$

In (17) the pupil function $\mu^{c}(\hat{s},\hat{i})$ can be written as

$$\mu^{c}(\hat{s},\hat{i}) = \sin\psi / \psi \tag{20}$$

$$\psi = k\ell(\cos\theta_{sq} + \cos\theta_{iq}) \tag{21}$$

To transfer the scattering amplitude tensor into the reference frame we write the identity tensor $\bar{\bar{U}}$ as

$$\bar{\bar{U}} = \hat{i}\hat{i} + \hat{v}_i\hat{v}_i + \hat{h}_i\hat{h}_i \tag{22}$$

and

$$\bar{\bar{U}} = \hat{s}\hat{s} + \hat{v}_s\hat{v}_s + \hat{h}_s\hat{h}_s \tag{23}$$

Then multiplying (9) from the right by (22) and from the left by (23) and after some mathematical manipulation the scattering amplitude tensor in the refrence frame can be written as

$$\bar{F}(\hat{s},\hat{i}) = \sum_p\sum_q F_{pq}(\hat{s},\hat{i})\,\hat{p}_s\,\hat{q}_i \tag{24}$$

where

$$F_{pq}(\hat{s},\hat{i}) = \sum_{p_{sq}}\sum_{q_{iq}} F_{pq}^{\,c}(\hat{s},\hat{i})\,(\hat{\phi}_{sq}\cdot\hat{p}_{sq})\,(\hat{\phi}_{iq}\cdot\hat{q}_i) \tag{25}$$

In (25) $(\hat{p}_s\cdot\hat{p}_{sq})$ and $(\hat{q}_{iq}\cdot\hat{q}_i)$ can be obtained from [7-9].

4. THE EXTINCTION COEFFICIENT

The extinction coefficient in (5) can be computed in accordance with the forward scattering theorem [12] for the leaves as:

$$k_{eq}(\hat{i}) = (4\pi/k)\,\mathrm{Im}\langle\sigma_{pq}^{\,c}(\hat{i},\hat{i})\rangle \tag{26}$$

where Im( ) is the imaginary part operator. For a needle or a disc in the forward direction the pupil function reduces to unity and consequently the extinction coefficients reduce to those corresponding to a Rayleigh scatterer as given in Ref. (5, 7). For a finite length cylinder the extinction coefficient is given in [9].

5. NUMERICAL RESULTS AND DISCUSSION

In Figs. 3 through 6 theoretical curves are shown to illustrate the backscattering behaviors of trees when the branches are assumed uniformly distributed while the leaves are taken to be either nearly horizontally or vertically distributed to provide bounds for the scattering coefficient. The disc-shaped leaves are shown in Figs. 3 and 4 and the needle-shaped leaves in Figs. 5 and 6. Fig. 7 shows the extinction coefficient for deciduous vegetation assuming a volume fraction of 0.1% for branches and 0.3% for leaves. It turns out that the branches are not the dominant attenuators so that large difference is seen when we change the leaf distribution from nearly horizontal to nearly vertical. If the volume fractions of the branches and leaves are switched, the same calculations

should produce much smaller variations of the extinction coefficient with the incidence angle. Fig. 8 shows the effect of initial shading of leaves on the branches when the antenna beam first get in contact with the vegetation. In the case of deciduous vegetation probably 80% or more of the illuminated area is covered with leaves. This percent of shading should be less for coniferous vegetation. However, the exact figure is not well known. For the purpose of illustration we consider a case of uniform distribution for the branches and nearly horizontal or vertical for disc-shaped leaves at an incidence angle of 50 degrees. In Fig. 9 a comparison of the scattering model with the measurements from forest is shown [10]. Since there is not enough ground truth for a serious comparison, only the bounds established by the theory under the assumption of nearly horizontal and vertical leaf distributions and uniform branch distributions are shown. In general, the branch distribution is probably not uniform. It is seen that the theoretical bounds do cover the measurement region.

6. CONCLUSIONS

A fairly complete scattering model for a vegetated area has been developed. The complexity of a vegetated environment requires better knowledge of leaf and branch volume fractions, their orientation distributions, their dielectric properties, the shading factor, and the size distribution of branches to realize a direct comparison. At this writing the size distribution of branches is not known and only an effective branch size is used to save computational time. Further study is clearly needed to justify or improve the model.

ACKNOWLEDGEMENTS

This work was supported by the NASA Johnson Space Center under grant NA69-115.

REFERENCES

1. R.H. Lang and J. Sidhu, "Electromagnetic backscattering from a layer of vegetation: a discrete approach," IEEE Trans. Geoscience and Remote Sensing, GE-21(1), 1983, pp.62-71

2. R.H. Lang, S. Saatchi and D.M. Levine, "Microwave backscattering from anisotropic soybean canopy," proceeding of Intr. Geoscience and Remote Sensing Syp. Ref. ESA, SP-254, 1986, pp. 1107-1112

3. H.J. Eom and A.K. Fung, "Scattering from a random layer embedded with dielectric needles," Remote Sensing of Environment, 19, 1986, pp. 139 - 149

4. H.J. Eom and W.M. Boerner, "Scattering from a layered medium connected with rough interfaces: matrix doubling method," IEEE Trans. Geoscience and Remote Sensing, GE-24(6), 1986, pp. 937 - 939

5. M.A. Karam and A.K. Fung, "Scattering from randomly oriented scatterer of arbitrary shape in the low frequency limit with application to vegetation," Digest of Intr. Geoscience and Remote Sensing Syp. vol. 2, 1983, pp. 5.1 - 5.7

6. M.A. Karam and A.K. Fung, "Scattering model for defoliated vegetation" proceeding of Intr. Geoscience and Remote Sensing Syp. Ref. ESA, SP-254, 1986, pp. 879 - 881

7. M.A. Karam, Remote Sensing of Random Media with Electromagnetic wave: A Discrete Approach, Ph.D. Dissertation, the University of Kansas, 1984

8. M.A. Karam and A.K. Fung, "Scattering from randomly oriented circular discs with application to vegetation" Radio Science, 18(4), 1983, pp. 557 - 565

9. M.A. Karam and A.K. Fung, "Electromagnetic scattering from a layer of finite-length, randomly oriented dielectric circular cylinder over rough interface with application to defoliated vegetation" Int. J. Remote Sensing, Sent for publication

10. T. Bush, F. Ulaby, T. Metzler and H. Stiles, "Seasonal variations of the microwave scattering properties of deciduous trees as measured in the 1-18GHz spectral range", Tech. Rep. 117-60, 1976

11. F.T. Ulaby, R.K. Moore and A.K. Fung, Microwave Remote Sensing, Active and Passive, voll II, Reading Massachusetts, Addison-Wesley Publishing Company, 1982, pp. 922 - 1031

12. M.A. Karam and A.K. Fung, "Vector forward scattering theorem" Radio Science, 17(4), 1982, pp. 752 - 756

13. M.A. Karam and A.K. Fung, "Scattering models for some vegetation samples" Tech. Rep. No. 445-13, 1986

14. J.A. Osborn, "Demagnetizing factors of the general ellipsoid" Physical Review, Vol. 67, 1945, pp. 351 - 357

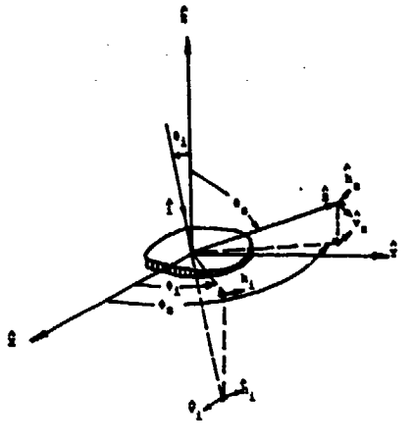


Fig. 1 The incident direction $\hat{i}$, the scattered direction $\hat{s}$, and the polarization vectors in the refrence frame

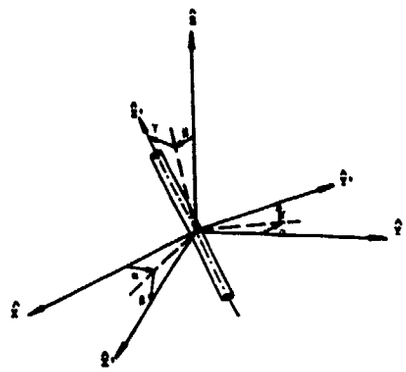


Fig. 2 The Tait-Bryan angles of orientation

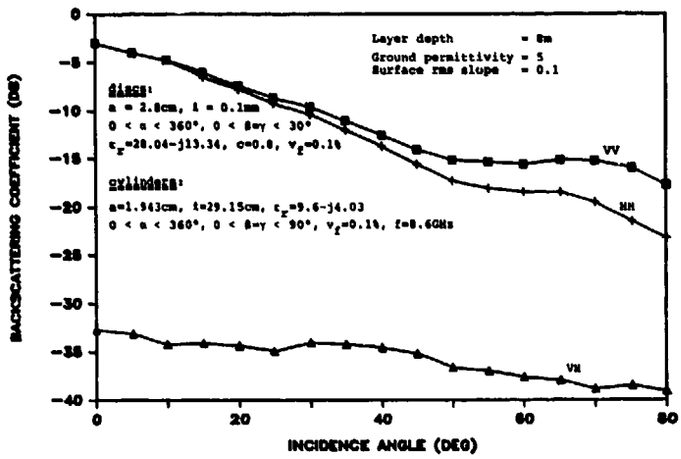


Fig. 3 Backscattering from a layer of circular discs shading finite length cylinders over rough interface

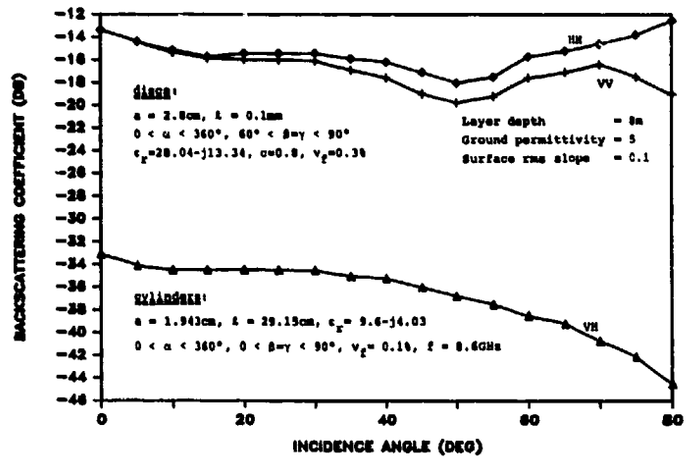


Fig. 4 Backscattering from a layer of circular discs shading finite length cylinders over rough interface

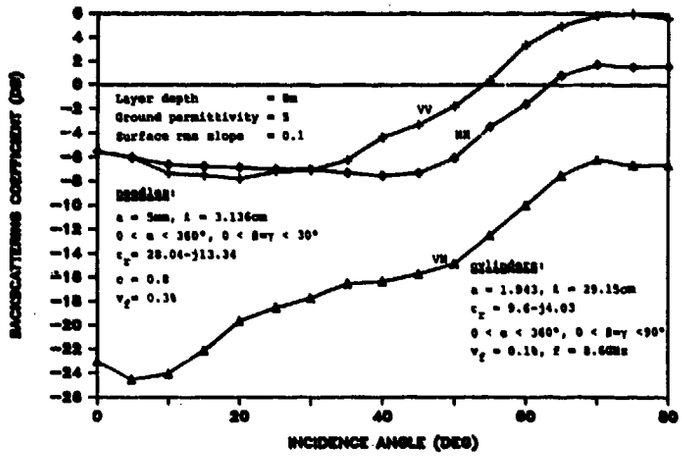


Fig. 5 Backscattering from a layer of needles shading finite length cylinders over rough interface

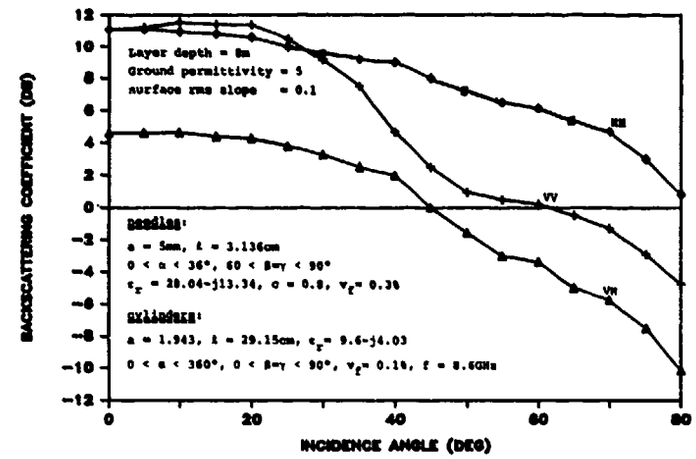


Fig. 6 Backscattering from a layer of needles shading finite length cylinders over rough interface

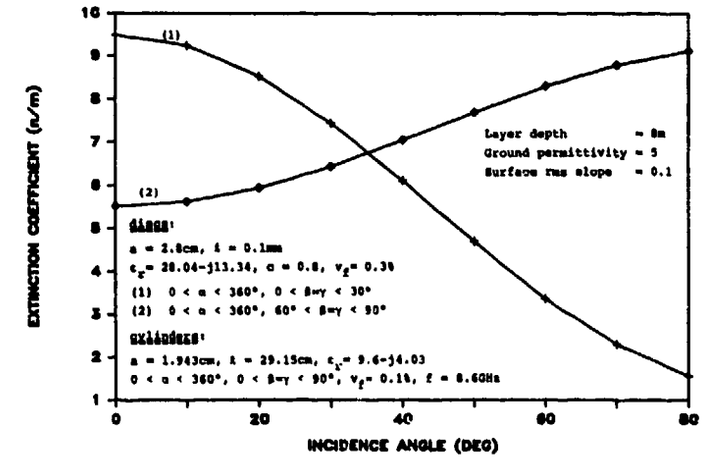


Fig. 7 The extinction of vertically polarised plane wave within a layer of discs shading finite length cylinders over rough interface

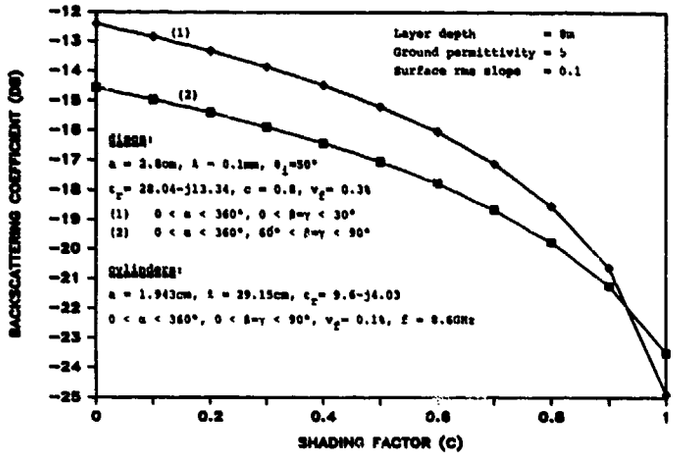


Fig. 8 Backscattering of vertically polarised plane wave from a layer of discs shading finite length cylinders over rough interface

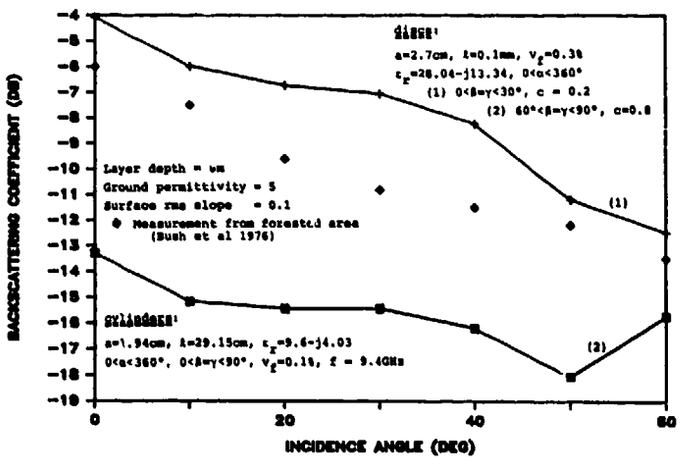


Fig. 9 Backscattering of horizontally polarised plane wave from a layer of discs shading finite length cylinders over a rough interface

DISCUSSION

R. Miller, UK

In order to obtain the cross section, it is necessary to have good estimates of the parameters in your model. The parameters are difficult to measure, and vary greatly from one type of woodland to another; some also vary with season. Is it possible to obtain meaningful estimates of the cross section without previously measuring all the parameters?

Author's Reply

It is possible to obtain meaningful estimates of σ^{o} when the bounds on the model parameters are known for a given case of interest. The value of a theoretical model is to provide the sensitivity of σ^{o} to different model parameters.

H.M. Schimpf, W.GR

For radar practice, one defines the reflectivity of σ_{o} in the hope that this parameter does not depend on the beam size of the antenna. Does your model allow any predictions whether or not there exists a relationship between reflectivity and beam size?

Author's Reply

Modeling deals only with σ^{o}. The radar beam function is used in the return power calculation which is a function of both the radar beam width and σ^{o}. No relationship should exist between the latter two quantities.

COHERENT SCATTERING FROM RANDOM MEDIA

C.J. Oliver
Royal Signals and Radar Establishment
St Andrews Road
Malvern
Worcestershire
WR14 3PS
UK

SUMMARY

This paper discusses the representation and simulation of clutter textures in coherent scattering in terms of a correlated noise model. Initially expressions for the detected intensity when coherent radiation is scattered from a surface with fluctuating cross-section are derived demonstrating how the effects of surface statistics and correlation properties interact with the imaging function. Secondly, a model for the cross-section fluctuations based on negative-binomial or gamma-distributed statistics is proposed. When coherent radiation is scattered by a surface with these properties the resulting intensity distribution can be shown to be K distributed. Having derived theoretical predictions for the correlated noise model with a variety of spectral forms a texture simulation technique is proposed based on linear filtering which duplicates the two-point correlation properties of the observed intensity. Finally, a comparison of original image data, simulated textures and the theoretical model is made for a number of examples of differing textures of both natural and manmade clutter.

LIST OF SYMBOLS

$\varepsilon(x)$	:	field at position x in the receiver
$a(x)$	:	scattering amplitude at position x in the surface
$\phi(x)$	:	random phase contribution at position x in the surface
$h(x)$	:	imaging response function
$I(x)$	:	detected intensity
$\sigma(x)$	:	surface cross-section
$\Gamma(\nu)$	:	gamma function of order ν
$K_\nu(x)$	:	modified Bessel function of order ν
W_j	:	jth coefficient of weighting function used in cross-section simulation

1. INTRODUCTION

When coherent radiation is scattered from a large number of randomly positioned scatterers the resulting field takes the form of a complex Gaussian random variable due to the random interference between contributions. This gives rise to the well-known speckle in coherent imaging. In this paper we shall discuss the interaction between this consequence of the imaging process and the statistical and correlation properties of the underlying surfaces. Central to the approach is the assumption that the surfaces to be imaged are rough. Such rough surfaces may be represented as made up of a large number of randomly-positioned scatterers per resolution cell. Provided that the mean number of scatterers per resolution cell, or local cross-section, does not vary the intensity probability density function (PDF) would be a negative exponential. Spatial fluctuations in the scatterer density or cross-section would then give rise to the excess fluctuations in the detected intensity which convey the scene content.

In the first section we derive the properties of the scattered radiation from such a rough surface for an arbitrary cross-section fluctuation demonstrating the interaction of the imaging function with the surface properties. Secondly, we consider a correlated noise model, based on the gamma or negative-binomial distributions, to describe the surface [1-3] demonstrating that this yields a correlated K-distributed intensity. In the third section a method for simulating such textures, based on a linear filter approach, is discussed [3,4]. Finally, we make a comparison of a variety of coherent image clutter textures with simulations and the predictions of the theoretical model in the fourth section. Most of these textures are taken from high resolution synthetic aperture radar (SAR) images obtained with the RSRE X-band airborne system. To indicate the generality of the approach an example of sonar clutter is also included. Throughout the paper the theory will be expressed in a one-dimensional form for simplicity. A full two-dimensional treatment is given elsewhere [2,3].

2. SCATTERING FROM ROUGH SURFACES

For the rough surface model based on a large number of randomly-positioned scatterers per resolution cell the complex field contribution from the single scatterer at a position x_1 can be separated into a scattering amplitude factor, $a(x_1)$, and a random phase factor, $\phi(x_1)$, determined by the scatterer position. The total field at the receiver at a position x is then derived by summing over all such contributions within the resolution cell, ie

$$\varepsilon(x) = B \int_{-\infty}^{+\infty} dx_1 \, a(x_1) \exp[i\phi(x_1)] \, h(x_1 - x) \qquad (1)$$

where $h(x)$ is the spatial impulse response of the imaging system and B is a constant describing the energy collection of the receiver. The spatial average over this field is zero because of the cancellation of the random phase terms. If we consider the detected intensity

$$I(x) \equiv |a(x)|^2 = |B|^2 \iint_{-\infty}^{\infty} dx_1\, dx_2\, a(x_1)\, a^*(x_2)\, \exp[i(\phi(x_1) - \phi(x_2))]$$

$$\times\, h(x_1 - x)\, h^*(x_2 - x) \qquad (2)$$

then this only has non-zero contributions to the average when pairs of positions are identical so that

$$\langle I \rangle = |B|^2 \langle \sigma \rangle \int_{-\infty}^{+\infty} dx_1\, |h(x_1)|^2 \qquad (3)$$

where $\sigma = a(x)\, a^*(x)$ is defined as the cross-section at position x. It can be shown [1-3] that all the higher-order statistical properties of the received field and intensity are subject to the same cancellation so that the only non-zero contributions are expressed in terms of the cross-section variable alone. One important measure of the properties of the detected intensity is the two-point statistics, the auto-correlation function (ACF). This may be shown to separate into four terms which combine the imaging function with the surface cross-section ACF [1-3,5]

$$\langle I(0)I(x)\rangle / \langle I\rangle^2 = 1 + \int_{-\infty}^{+\infty} dx_1\, |h(x_1)|^2 |h(x_1+x)|^2 \Big/ \left(\int_{-\infty}^{+\infty} dx_1\, |h(x_1)|^2 \right)^2$$

$$+ \iint_{-\infty}^{+\infty} dx_1 dx_2 \left(\frac{\langle \sigma(x_1)\sigma(x_2)\rangle}{\langle \sigma \rangle^2} - 1 \right) (|h(x_1)|^2 |h(x_2+x)|^2$$

$$+ h(x_1)h^*(x_1+x)h(x_2)h^*(x_2+x)) \Big/ \left(\int_{-\infty}^{+\infty} dx_1\, |h(x_1)|^2 \right)^2 \qquad (4)$$

The first of these terms is a constant flat background corresponding to uncorrelated noise. The second contains only the ACF of the imaging function. These first two terms would be observed if there were no underlying cross-section fluctuations and describe the correlation properties of the speckle. The third term can be reduced to a convolution form involving the surface covariance function and the square modulus of the imaging function [3,5]. Basically it represents the effects of incoherent imaging of the original surface and yields a detected intensity contribution proportional to original cross-section filtered by the envelope of the imaging function. It therefore contains information about the cross-section fluctuations on a scale greater than the instrumental width. The last term is due to the coherent parts of the imaging process and depends on the full complex imaging response. In practice this term only contributes for delays less than the imaging function width and indeed approximates to the form of the second term with a value at the origin of $\langle \sigma^2 \rangle / \langle \sigma \rangle^2 - 1$.

Similar analysis can be performed to derive the properties of higher-order single-point moments [1,2]. The normalised nth moment of the detected intensity can be shown to be related to that for the cross-section by the equation

$$\frac{\langle I^n \rangle}{\langle I \rangle^n} = n! \frac{\langle S^n \rangle}{\langle S \rangle^n} \qquad (5)$$

where S represents the filtered form of the cross-section [3] given by

$$\frac{\langle S^n \rangle}{\langle S \rangle^n} = \int_{-\infty}^{+\infty} \cdots \int_{-\infty}^{+\infty} dx_1 \cdots dx_n \frac{\langle \sigma(x_1) \cdots \sigma(x_n) \rangle}{\langle \sigma \rangle^n}$$

$$\times\, |h(x_1)|^2 \cdots |h(x_n)|^2 \Big/ \left(\int_{-\infty}^{+\infty} dx_1\, |h(x_1)|^2 \right)^n \qquad (6)$$

This simple relationship between the moments of the detected intensity and the filtered cross-section results from the cancellation of all but those pairs of terms in which the phases are identical in the original model for the surface.

In interpreting image data one would prefer to remove the effects of the imaging process so far as is possible to deduce the underlying behaviour. In this section we have analysed the physics of the imaging process in terms of the relationship between the properties of the detected intensity and those of the original cross-section. Let us next examine the cross-section fluctuations.

3. CORRELATED GAMMA-DISTRIBUTED CROSS-SECTION MODEL

While the physics of the imaging process is well understood the approach to representing the underlying cross-section has perforce to be largely phenomenological. Previous work [1,2,6-12] has shown that the detected intensity in a very large number of scattering situations can be represented by a K distribution of the form

$$p(I) = \frac{1}{\langle I \rangle}\left(\frac{I}{\langle I \rangle}\right)^{\frac{\nu-1}{2}} \frac{1}{\Gamma(\nu)} K_{\nu-1}\left[2\left(\frac{I}{\langle I \rangle}\right)^{\frac{1}{2}}\right] \qquad (7)$$

where $\Gamma(\nu)$ is the gamma function of order ν and $K_{\nu-1}$ is the K distribution (modified Bessel function) of order $\nu-1$. It is not possible to justify uniquely the use of this distribution; all that can strictly be said is that it is consistent with the data. Such a distribution would be obtained if coherent radiation were scattered from random scatterers which underwent spatial number fluctuations having a negative binomial distribution or a cross-section described by a gamma distribution. On the scale of the resolution cell it is not possible to distinguish between the number fluctuation and cross-section representations. The negative-binomial distribution applies to a discrete variable whereas the equivalent gamma-distribution relates to a continuous variable. These distributions occur very widely in statistical analysis. In common with the present case only a few of these situations may be uniquely physically modelled in this fashion. The model would be physically justified if the local number of scatterers, or cross-section, could be regarded as the result of a random process of birth, death and migration [13]. While this type of model is not implausible it cannot be applied rigorously in this context; as a result the approach is fundamentally phenomenological. A gamma-distribution model may be regarded as a generalised noise model in which the contrast can be varied through the order parameter ν. As can be seen from the expression for the gamma distribution

$$p(\sigma) = \frac{1}{\langle \sigma \rangle}\left(\frac{\sigma}{\langle \sigma \rangle}\right)^{\nu-1} \frac{1}{\Gamma(\nu)} \exp\left[-\frac{\sigma}{\langle \sigma \rangle}\right] \qquad (8)$$

thermal noise is a special case when $\nu = 1$.

In order to derive the detailed properties of gamma-distributed noise with varying spectral properties we may use the fact that a gamma-distribution may be generated by a random walk process in ν dimensions of a complex Gaussian variable [1,13]. Thus we may define complex Gaussian variables of defined spectral form, ie varieties of thermal noise, and then deduce the equivalent gamma-distribution results based on the known factorisation properties [1-3]. Various spectral forms have been analysed including [2,3]:

(i) noise with either Gaussian or Lorentzian spectrum
(ii) mixed with an offset local oscillator if required
(iii) mixed with a similar noise term if required

Both Gaussian [1,3] and rectangular [2] imaging functions have been treated analytically. In each case expressions for the first four single-point intensity moments and the ACF have been derived. In order to represent an arbitrary clutter texture we first select the most appropriate of these models to represent the ACF. It is not possible to perform the inverse process of deducing the cross-section ACF from the intensity ACF so the method that is employed is to iterate the forward problem of defining the cross-section in Eq.(4) and hence predicting the intensity ACF. The properties of the cross-section and the associated parameter values are then varied until a reasonable fit to the observed intensity ACF is obtained. The theoretical predictions for the single-point moments can then be compared with those of the data as a further test.

4. SIMULATION OF CORRELATED RANDOM TEXTURES

In the above discussion we have demonstrated that the texture in random clutter images can be represented in terms of correlated gamma-distributed noise. Homogeneous regions may therefore be represented as such noise processes which can be described in terms of only a few parameter values once the model is defined. It is desirable to be able to synthesise such a texture having the identical correlation and statistical properties. Let us choose to define the ACF of the surface in terms of the model. This also fixes all other correlation properties since the entire process can be derived from underlying Gaussian processes. Thus the ACF contains all the information necessary, provided that the model is correct. There is no suitable practical method for generating two-dimensional gamma-distributed surfaces with a variety of spectral forms. However, an approximate method has been developed [4] which is applicable to arbitrary spectra and is capable of representing the ACF precisely. Higher-order properties, however, are not identical to gamma statistics but in practice differ by less than the statistical fluctuations in the synthesised image. As with the gamma-distribution model all the higher-order properties are determined by the ACF so there are no remaining degrees of freedom in the process.

The essence of the simulation method is to pass white noise of appropriate statistics through a linear filter such that the ACF of the resulting correlated noise is identical to that for the surface. This determines the relationship between the white noise statistics, the weighting function and the surface ACF. As shown by Oliver and Tough [4] the normalised surface ACF at lag value r and the weighting function ACF are related by

$$\frac{\langle \sigma(o)\sigma(r) \rangle}{\langle \sigma \rangle^2} - 1 = \frac{\text{Var } x}{\langle x \rangle^2} \frac{\sum_{j=1}^{N} W_j W_{j-r}}{\left(\sum_{j=1}^{N} W_j\right)^2} \qquad (9)$$

where W_j is the jth coefficient of the resulting weighting function, N is the number of filter weights and x is the uncorrelated random noise variable. The form of the surface ACF is the same as that for the weighting function while the statistics of the input white noise are determined by the surface statistics and the properties of the weighting function. The form of the weighting function may be derived from the ACF of the surface, obtained from the model, provided that the surface may be regarded as a stationary ergodic variable. The positive square root of the power spectrum of the surface (forward Fourier Transform of the ACF) is real, positive and symmetric and corresponds to an amplitude spectrum. Though this result is only one possible form of this spectrum we are justified in using it since it has the defined ACF. On taking the inverse Fourier Transform of the amplitude spectrum the desired weighting function is obtained.

The stages of the simulation are illustrated in Figure 1 for a particular texture. This is derived from a section of SAR image obtained with the RSRE X-band system and corresponds to a segment of a plantation of young trees so that the lines of trees are visible as shown in the top left of the image. The ACF of the image intensity is then calculated (top centre) and the weighting function deduced as described above (top right). The white noise is required to have variable contrast as shown in Eq.(9). We choose an uncorrelated gamma-distribution for the input with its contribution order parameter defined appropriately. The output correlated distribution after filtering will not, in general, be gamma-distributed, as noted above. However, the discrepancy is usually much less than any statistical fluctuations [3]. Having determined the order parameter uncorrelated gamma-distributed noise is then generated (bottom left) which is then convolved with the weighting function to generate a simulated cross-section variable (bottom centre). The final stage is to simulate the scattering and imaging of coherent radiation from this correlated surface. On scattering, the field contribution in each element of the receiver is formed by the interference between the many random scatterers within each resolution cell. Thus the received field will have a complex Gaussian speckle simulated by taking Gaussian random numbers for real and imaginary parts of the field with variance proportional to the local cross-section. This field is then imaged which corresponds to convolving with the imaging function. The final received field is then envelope detected to give the intensity (bottom right). Close resemblance between this simulated texture and the original image is apparent.

5. COMPARISON OF MODEL WITH DATA

Having established the correlated gamma-distributed clutter model and the linear filter texture simulation method let us next compare the results for various examples of image texture, simulation and the theoretical model. These comparisons are given in more quantitative detail elsewhere [3]. In the present paper we shall assume that the ACF is well represented by a choice of model and parameters and make the comparison in terms of the single-point statistics and a montage of real and simulated image textures for visual comparison.

Initially we shall consider a region of texture corresponding to a field in a SAR image illustrated in Figure 2. We would expect that there should be no cross-section fluctuation so that the results are determined entirely by the imaging process and consist of speckle whose correlation properties are determined by the imaging function widths. The original image texture is the top right of Figure 2; the remaining images are obtained by simulation. Obviously the detailed position of bright speckles varies randomly from image to image, as it would between different SAR images of the same area since it would be impossible to reproduce the flight trajectory precisely. It is the two-point statistics which describe the texture which should be identical within statistical fluctuations. Visually it appears that a pure speckle simulation does indeed represent the region. A more detailed test can be performed in terms of the single-point intensity moments. A comparison of the normalised moments of the data, the theoretical predictions and a set of 10 simulations are given in Table 1. The predicted standard deviations are derived as described in [3] and show close agreement with the standard deviations obtained from the set of simulations. The original image statistics and the simulated ones are both compatible with theory.

Having demonstrated the agreement where no underlying fluctuations are obtained we next consider an image of well-developed woodland in which large well-separated trees are randomly distributed. The results of simulation are compared with the original image texture in Figure 3; as before the original image is on the top right. As one would expect not only the speckle but the underlying bright features, "trees", occur at different positions in the images since these are generated randomly. It is the texture, defined by the ACF, that should be duplicated once again. It is clear that most of the details of the texture are faithfully reproduced. Careful study suggests that the genuine texture has larger regions of dark than the simulated textures. However, the results for the simulated and original ACFs are quite consistent. It may be that two-point statistics are not adequate to represent the texture completely; in which case the fundamental model also fails since there are no remaining degrees of freedom. In any case the textures appear reasonably close to the human interpreter. On comparing the single-point moments in Table 2 the agreement is within experimental errors. It is noticeable though that the predicted errors are consistently less than those obtained from simulation. This effect was noted previously [3] and probably results from the over-simplistic assumption that pixels are either completely correlated or uncorrelated in the theoretical derivation.

Figure 4 illustrates the comparison of the original image with a set of simulations of the young plantation texture used to demonstrate the simulation technique in the previous section (Figure 1). Agreement is visually excellent; the original texture is again on the top right. On comparing the moments in Table 2 we note that the results are again consistent. However the errors in the higher moments are sufficiently large that it is impossible to detect any discrepancy between simulation and the model even though this is expected [4].

So far we have considered the representation of natural clutter observed with a SAR system. In the next example we take a region of urban clutter. It seems probable that the fundamental assumption that large regions of homogeneous noise-like texture exists in the image is unlikely to be well founded for such manmade clutter. In the first example of town texture, shown in Figure 5, the original image (top right) consists of roads lying at about 20 degrees to the vertical. In the simulations this fundamental orientation is retained but the continuous nature of streets has been partially lost. It appears that more than two-point statistics might be required to represent both the concept of "building", a local effect, and that of "street" which covers much larger scales. The comparison of single-point moments is again within statistics

though the errors are sufficiently large with scenes with such strongly-fluctuating contrast that discrepancies would not be apparent.

In the final SAR texture example a scene is chosen for which the model is not expected to apply. A single row of cottages lining a road is chosen set in a background of fields (Figure 6, top right). This obviously violates the necessary condition that the texture should be homogeneous since different parts of the image exhibit clearly differing textures. On seeking to characterise the entire segment with the ACF we are therefore averaging over these different textures and would expect to produce some averaged resultant. This is obvious in the simulated textures in Figure 6. The underlying orientation is retained but the texture is spread over the entire simulation. Comparison of the single-point moments in Table 5 shows agreement within the statistics. This indicates that these single-point moments are a poor measure of texture compared with the two-point statistics which exhibit an obvious discrepancy. Furthermore higher-order correlation properties would also be required to represent the texture which implies that the underlying model is incorrect.

For a final comparison let us consider an example from another form of coherent imaging, namely sonar. In this case the image, shown in Figure 7 is taken from sonar images of the sea bed. This example illustrates sand ripples, such as those left on a beach when the tide goes out. The original texture (top right) shows clear evidence of these ridges. The simulations appear very similar visually. Detailed comparison reveals that the "ridges" in the simulations, which are a result of the observer joining regions of high intensity, tend to be weaker than the corresponding regions of the original texture. A model which is based essentially on a point spread function, rather than any knowledge of higher level structures such as ridges, would be expected to fail with this type of image. Nevertheless, the resemblance, even in this case is close. Other sonar examples exhibit better agreement on the whole. As noted in previous examples the single-point statistics, compared in Table 6, exhibit good agreement revealing again their insensitivity to the detail of the texture.

6. DISCUSSION AND CONCLUSIONS

The importance of the correlated clutter model described here lies in the fact that it includes the effects of imaging function, surface statistics and correlation properties in a consistent manner. Various types of distribution have been used in the past to describe the statistics of the clutter in terms of the probability distribution. These may give totally misleading predictions of, for example, radar detection performance unless the correlations between image pixels are correctly treated [10,11]. In the majority of cases uncorrelated samples are assumed which may be totally erroneous. The present model combines all the important aspects in a consistent manner enabling one to predict, for example, the expected statistics for a given scene as a function of resolution which is quite beyond the scope of other methods.

From a visual comparison of the simulation results it is clear that the method is extremely successful at representing a wide range of clutter textures. Indeed the exceptions that are shown have been selected from a much larger number of good representations. Both manmade and natural clutter textures can be represented though the latter are more consistently correct. One of the problems in the method is the difficulty of selecting a form for the model which duplicates the original image ACF most closely. The task is obviously most onerous where complicated spectra are encountered, as was the case for the sonar example given. A method which circumvents this problem has been proposed [14] in which the observed ACF is treated as a perturbed version of some simple model [3]. This approach has proved capable of deducing the surface ACF such that the predicted intensity ACF is almost indistinguishable from that for the original data. Using this approach the process of simulating such textures is essentially determined by the convolution processes, performed by DFT methods, which underly so much of the analysis. In principle these could be implemented extremely fast if suitable parallel hardware were available.

In this paper we have presented an analysis of clutter textures and their simulation based on a specific model. The original theory assumes that the underlying cross-section can be described in terms of the negative binomial or gamma distribution. The simulation generates the cross-section by a linear filtering operation applied to uncorrelated gamma-distributed noise. In both cases all the higher-order single and multi-point statistics are defined once the two-point statistics are specified. This approach therefore contains a richness of detail much greater than is contained merely in the ACF. This implies that if the texture were indeed the result of scattering from a gamma-distributed surface it would be impossible to improve on a measurement of the ACF as a means of classifying or simulating such a texture. Any other classification or simulation method could only achieve the same performance when all statistical properties were defined, not just the two-point statistics. Thus this approach is very successful at handling those textures which could be represented in terms of such a model. However, the obvious corollary is that where the original texture does not fit the model the approach enforces incorrect higher-order correlation properties. This appears to be the case with some of the more intransigent clutter textures considered here. Another problem is the question of how one establishes whether the model holds in any particular case. Comparison of the three-point statistics with the model might offer a possible method. For completely arbitrary textures, however, a different approach in which one measures sets of statistical properties of increasing complexity until one can no longer distinguish the simulated and original textures is required [15]. This approach essentially uses no information other than that specifically introduced in the defined statistical measures.

REFERENCES

1. Oliver, C.J., "A model for non-Rayleigh scattering statistics", 1984, Opt. Acta, 31, No 6, 701-722.

2. Oliver, C.J., "Correlated K-distributed clutter models", 1986, Opt. Acta, 32, No 12, 1515-1547.

3. Oliver, C.J., "The interpretation and simulation of clutter textures in coherent images", 1986, Inv. Problems, 2, 481-518.

4. Oliver, C.J. and Tough, R.J.A., "On the simulation of correlated K-distributed random clutter", 1986, Opt. Acta, 33, No 3, 223-250.

5. Miller, R.J., "Correlation properties of coherently imaged non-uniform surfaces", IMA Conf. on "Mathematics and its Applications to Remote Sensing", Danbury, 1986.

6. Jakeman, E. and Pusey, P.N., "A model for non-Rayleigh sea echo", 1976, IEEE Trans. Antennas Propag., AP-24, 806-814.

7. Jakeman, E. and Pusey, P.N., "Non-Gaussian fluctuations in electromagnetic radiation scattered by a random phase screen", 1976, J. Phys. A: Math. Gen., 8, 369-410.

8. Jakeman, E. and Pusey, P.N., "Significance of K-distributions in scattering experiments", 1978, Phys. Rev. Lett., 40, No 9, 546-550.

9. Jakeman, E., Parry, G., Pike, E.R. and Pusey, P.N., "The twinkling of stars", 1978, Contemp. Phys., 19, 127-145.

10. Ward, K.D., "Compound representation of high resolution sea clutter", 1981, Electron. Lett., 17, 561-565.

11. Ward, K.D., "A radar sea-clutter model and its application to performance assessment", 1982, IEE Conf. Publ. 216 (Radar '82), 203-207.

12. Jao, J.K., "Amplitude distribution of composite terrain radar clutter and the K distribution", 1984, IEEE Trans. Antennas Propag., AP-32, 1049-1062.

13. Jakeman, E., "On the statistics of K-distributed noise", 1980, Opt. Acta, 27, 735-741.

14. Oliver, C.J., "On the simulation of coherent clutter textures with arbitrary spectra", 1987, Inv. Problems, to be published.

15. Luttrell, S.P., "Markov random field models: a strategy for clutter modelling", AGARD Symposium on "Scattering and Propagation in Random Media", Rome, 1987.

		MODEL		SIMULATION	
MOMENT	DATA	MEAN	SD	MEAN	SD
Second	1.970	2.000	.014	2.003	.015
Third	5.68	6.00	.14	6.01	.14
Fourth	21.3	24.0	1.3	23.6	1.0
Fifth	97	120	-	116	9
Sixth	520	720	-	660	80

Table 1. Comparison of the moments for the fields texture

		MODEL		SIMULATION	
MOMENT	DATA	MEAN	SD	MEAN	SD
Second	2.77	2.77	.03	2.74	.08
Third	14.3	14.8	.5	17.1	2.6
Fourth	111	130	8	219	90
Fifth	1.11(3)	-	-	4.7(3)	3.4(3)
Sixth	1.34(4)	-	-	13.9(4)	13.5(4)

Table 2. Comparison of moments for the first woods texture

		MODEL		SIMULATION	
MOMENT	DATA	MEAN	SD	MEAN	SD
Second	2.64	2.64	.04	2.55	.11
Third	13.1	13.1	.7	14	3
Fourth	100	108	10	160	90
Fifth	1.01(3)	-	-	3.2(3)	2.9(3)
Sixth	1.19(4)	-	-	8.3(4)	9.8(4)

Table 3. Comparison of moments for the second woods texture

		MODEL		SIMULATION	
MOMENT	DATA	MEAN	SD	MEAN	SD
Second	7.4	7.4	.5	6.9	1.5
Third	160	160	20	200	140
Fourth	.47(4)	.71(4)	.12(4)	1.15(4)	1.49(4)
Fifth	.16(5)	-	-	9.0 (5)	16.6 (5)
Sixth	.60(7)	-	-	8.5 (7)	18.8 (7)

Table 4. Comparison of moments for the first town texture

		MODEL		SIMULATION	
MOMENT	DATA	MEAN	SD	MEAN	SD
Second	8.5	8.5	.8	9.0	3.0
Third	270	230	50	480	520
Fourth	1.3(4)	1.5(4)	.3(4)	6.(4)	11.(4)
Fifth	6.9(5)	-	-	10.(5)	25.(5)
Sixth	3.9(7)	-	-	210.(7)	580.(7)

Table 5. Comparison of moments for the second town texture

		MODEL		SIMULATION	
MOMENT	DATA	MEAN	SD	MEAN	SD
Second	2.99	2.99	.09	2.92	.09
Third	19.6	20.0	2.7	17.0	2.1
Fourth	227	279	81	171	57
Fifth	4.0(3)	-	-	2.6(3)	1.6(3)
Sixth	9.3(4)	-	-	5.3(4)	4.7(4)

Table 6. Comparison of the moments for the texture of the sonar image of sand ripples



Figure 1. Stages in the simulation of correlated random textures

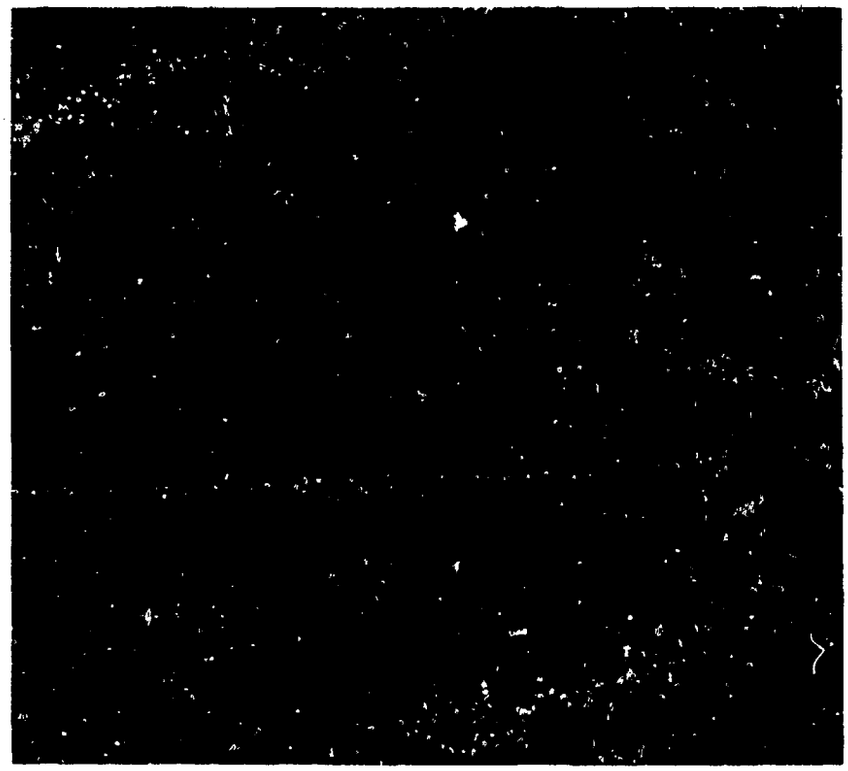


Figure 2. Comparison of a SAR image of a field texture (top right) with several simulations

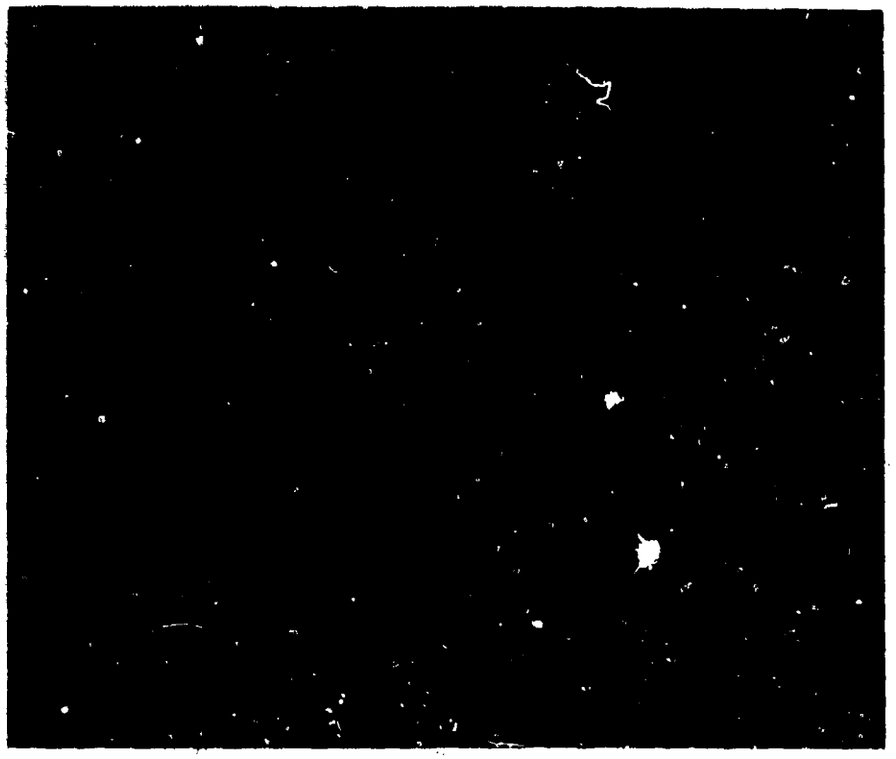


Figure 3. Comparison of a SAR image of the first wood texture (top right) with several simulations

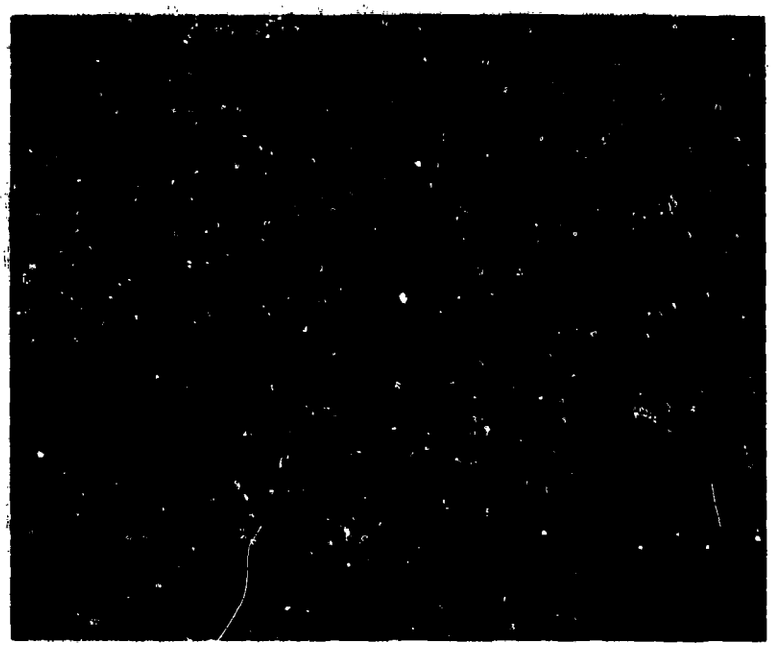


Figure 4. Comparison of a SAR image of the second wood texture (top right) with several simulations



Figure 5. Comparison of a SAR image of the first town texture (top right) with several simulations

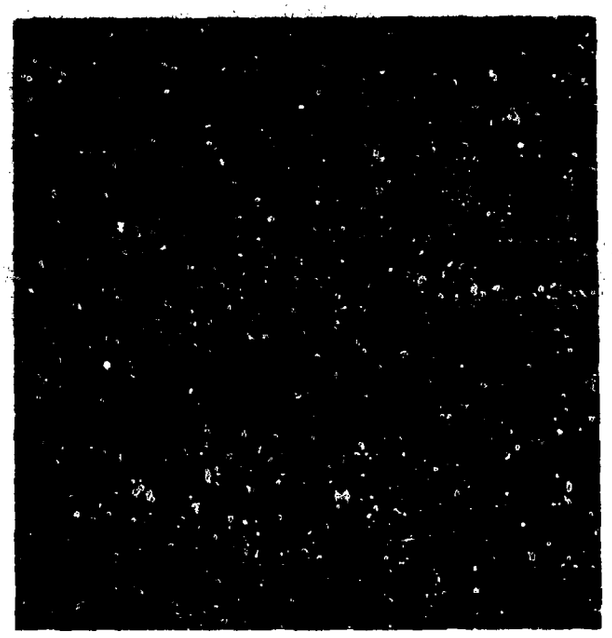


Figure 6. Comparison of a SAR image of the second town texture (top right) with several simulations



Figure 7. Comparison of a sonar image of a sand ripples texture (top right) with several simulations

SUMMARY OF SESSION III

MULTIPLE SCATTERING EFFECTS

by

I.M.Besieris, Session Chairman
(The following material was supplied by the Editor)

This session is concerned with the multiple scattering effects. Such effects can be manifested in many different ways. For example, it can result in enhanced backscattering as described by Yang and Yeh in the first paper of this session. It can also result in depolarization when scattering from rough spheres. In this regard, Bahar and Fitzwater (second paper in this session) approach the problems by using the equation of transfer. Under various conditions, the behaviour of waves after being perturbed by the random medium can be modelled by a phase-changing screen. Jakeman's paper (third paper in this session) is concerned with the statistical properties of amplitude scintillation when either the phase of the screen is a Gaussian random fractal or the phase gradient is fractal. In a fourth paper of the session, Jefferson and Anderson are concerned with the mathematical models of the multi-scale phenomena and the use of such models in the study of wave propagation and scattering. In the last paper of the session, Franke and Liu examine the statistics of the wave when the phase screen varies randomly both in time and space.

THE ENHANCEMENT EFFECT OF THE BACKSCATTERED INTENSITY IN A RANDOM MEDIUM

C. C. Yang
CSSL, Department of Electrical Engineering
The Pennsylvania State University
University Park, PA 16802

K. C. Yeh
Department of Electrical and Computer Engineering
University of Illinois
Urbana, IL 61801
USA

ABSTRACT

A wave gradually loses its coherence while propagating in a random medium. This is because the wave experiences decorrelation along a propagation path that has uncorrelated irregularities. If, however, different parts of the propagation path have correlated irregularities, the decorrelation of the wave will not proceed as rapidly as otherwise. This effect is most prominently manifested in the case of backscattering where the returned wave propagates through the same irregularities as the outgoing wave. The average backscattered intensity can be shown to be higher than that expected from a wave propagating over a path equal to the round trip distance but through uncorrelated irregularities. This phenomenon is known as the enhancement effect. This enhancement effect is clearly revealed when the receiver is moved ever closer to the transmitter. As the separation between the receiver and the transmitter is reduced, the average scattered intensity will increase and reaches a peak when the receiver is co-located with the transmitter. If the wave statistics are in the saturation regime, this maximum increase amounts to a doubling of the average intensity.

In this paper, the enhancement effect under various conditions is examined. There can be backscattering from random irregularities themselves or from a deterministic scattered. The difference between weak and strong scattering is distinguished. The effects produced by various power spectral functions from the random medium are also considered.

I. INTRODUCTION

Recently, the phenomenon of enhanced backscattering in a random medium has received some attention. It was first pointed out in [1], the coherence between the forward and backward propagating wave may lead to enhanced backscattering. Later work showed that either in continuous [2-8] or discrete [9-14] random media, the variation of the average backscattered intensity forms a narrow peak around the backward direction. In other words, for a fixed range from the scattering target, the scattered intensity is increased as the receiver is moved closer to the transmitter and reaches a maximum value when the receiver is exactly co-located with the transmitter. This effect, known as the enhancement effect, is usually attributed to the gain of coherence recovered from random decorrelation when the backward scattered ray passes through the same random structure as the incident ray. Because the decorrelation effect is important when there is strong scattering, this enhancement effect is expected only when there is significant multiple scattering.

In this paper, the enhancement effect in a turbulent medium under various conditions of scattering strength is examined. The geometry of the problem is depicted in Fig. 1. A point source is placed at $\vec{r}_T$ and a wave is propagated in a statistically homogeneous and isotropic random medium which occupies the half space above the plane denoted by the horizontal line. We are concerned with the returned wave scattered from a scattering volume V_s. This returned wave is detected by a receiver at $\vec{r}_R$. In Fig. 1, two scattering points $\vec{r}$ and $\vec{r}''$ are shown and both are inside V_s. The incident and scattered rays associated with the scatterer at $\vec{r}$ are represented by two chain lines and those associated with the scatterer at $\vec{r}''$ are represented by two dashed lines. We will consider only those cases where the distance $|\vec{r}_R - \vec{r}_T|$ is very small so that the four rays just mentioned are nearly parallel to allow the use of the paraxial or forward scattering approximation. In this context, it is convenient to use z-axis as the propagation axis. In Fig. 1, the vector $\vec{r}' = \vec{r}'' - \vec{r}$ is also shown and it, when expressed in the Cartesian coordinates, is just $\vec{r}' = (\vec{\rho}', z')$. Finally, two horizontal vectors $\vec{\rho}_T = \vec{r}_T - \vec{r}_o$ and $\vec{\rho}_R = \vec{r}_R - \vec{r}_o$ are indicated in Fig. 1.

To demonstrate the enhancement effect, the scattering cross section σ_s as a function of the distance between the transmitter and receiver, i.e., $\vec{r}_R - \vec{r}_T$, will be evaluated. Two ranges of scattering strength are to be considered: 1) weak scattering in which the supereikonal approximation [15] is valid; 2) strong scattering in which the saturation [16] has been reached. In either range, the forward scattering approximation is assumed to be applicable. The convenience of forward scattering is that the concept of propagator [17] is valid. For more concrete discussions, two kinds of power-spectrum function for random irregularities will be used, i.e., a Gaussian spectrum and a Bessel-function spectrum. A Bessel-function spectrum can be reduced to a power-law format in the initial subrange [18], i.e., between the spatial frequencies corresponding to the inner and outer scales. Therefore, it is more realistic in modeling a turbulent atmosphere [19]. However, a Gaussian spectrum, due to its mathematical simplicity, can lead to much physical insight.

The rest of this paper is organized as follows: A general derivation for the scattering cross section is presented in Section II. Here, a multiple-scattering factor is introduced. The explicit forms of this factor for the weak and strong scattering are derived in Sections III and IV, respectively. The

numerical results and discussions are presented in Sections V and VI for the cases of Gaussian and power-law spectrum functions, respectively. Finally, conclusions are drawn in Section VII.

II. BACKSCATTERING CROSS SECTION

To derive the backscattering cross section, we start with an expression for the random wave field E_s scattered from the volume V_s and received at $\vec{r}_R$: [6,20]

$$E_s = \frac{-1}{4} \iiint_{V_s} d^3r \; e^{-2jkr} \; K(\vec{r}_T, \vec{r}) \; \varepsilon_1(\vec{r}) \; K(\vec{r}, \vec{r}_R) \tag{1}$$

Since the depolarization effect is of no concern, only scalar waves are considered in Eq. (1). Here, k denotes the wavenumber in the background medium and ε_1 denotes the relative fluctuation of the dielectric permittivity. The random propagation K represents wave propagation along a designated propagation axis from the first argument to the second one under the forward scattering approximation. The expression for E_s in Eq. (1) can be obtained under the cumulative forward-scatter single-backscatter approximation [21] which has been discussed in the literature [6,20].

Let ℓ denote a characteristic scale of random irregularities. Under the condition $k^2\langle\varepsilon_1^2\rangle\ell^2\ll 1$, an approximate expression for the averaged scattered intensity $I_s = \langle E_s E_s^* \rangle$ can be obtained. In the expression for the scattered field (1), there is a product of three random functions: two propagators and one relative dielectric permittivity. The averaged scattered intensity is thus an ensemble average of six random functions: four propagators and two relative dielectric permittivities. By applying the Novikov-Furutsu theorem [19], this mixed moment of the sixth order can be factored into a product of two pure moments: the second moment of ε_1 (or the correlation function) and the fourth moment of K [6,20]. The result is

$$I_s = \frac{1}{16} \iiint_{V_s} d^3r \iiint_{V_s} d^3r'' \; e^{-2jk(r-r'')} \; B_\varepsilon(|\vec{r}'' - \vec{r}|)$$
$$\langle K(\vec{r}_T, \vec{r}) \; K(\vec{r}, \vec{r}_R) \; K^*(\vec{r}_T, \vec{r}'') \; K^*(\vec{r}'', \vec{r}_R) \rangle \tag{2}$$

Here, the scalar r'' is the distance between $\vec{r}''$ and $\vec{r}_T$ (or $\vec{r}_R$) along the propagation axis. Also, the correlation function B_ε of ε_1 is introduced to describe the turbulent structure of the medium.

In the next step, we define a multiple scattering factor M such that the fourth moment of K in Eq. (2) can be written as

$$\langle K(\vec{r}_T, \vec{r}) \; K(\vec{r}, \vec{r}_R) \; K^*(\vec{r}_T, \vec{r}'') \; K^*(\vec{r}'', \vec{r}_R) \rangle$$
$$= K_0(\vec{r}_T, \vec{r}) \; K_0(\vec{r}, \vec{r}_R) \; K_0^*(\vec{r}_T, \vec{r}'') \; K_0^*(\vec{r}'', \vec{r}_R) \; M(\vec{r}, \vec{r}'') \tag{3}$$

where the deterministic K_0 represents the propagator for the background medium and is given, for example, by

$$K_0(\vec{r}_T, \vec{r}'') = (jk/2\pi r'') \exp(-jk|\vec{\rho}' - \vec{\rho}_T|^2/2r'') \tag{4}$$

Other K_0's appearing in (3) can be similarly written down. It is apparent that when M is set to unity in (3) and substituted to (2), we get the intensity under the single scatter approximation. Multiple scattering effects can be included by letting M be an expression to be derived in the next two sections. In this regard, M is found to be functions of only $\vec{r}$ and $\vec{\rho}'$ which will be assumed in the following development. Under the condition $k\ell^3/r^2 \ll 1$, Eq. (2), with (3) inserted, becomes

$$I_s = \frac{k^4}{256\pi^4} \; \mathrm{Re} \iiint_{V_s} d^3r \; \frac{1}{r^4} \iint_{-\infty}^{\infty} d^3r' \; e^{2jkz'} \; B_\varepsilon(|\vec{r}'|) \; F(\vec{r}, \vec{\rho}') \; M(\vec{r}, \vec{\rho}') \tag{5}$$

The Fresnel factor F, that appeared in Eq. (5), is given by

$$F(\vec{r}, \vec{\rho}') = \exp\{-jk[(\vec{\rho}_T + \vec{\rho}_R) \cdot \vec{\rho}' - \rho'^2]/r\} \tag{6}$$

This Fresnel factor F will produce the effect of Fresnel diffraction around the forward scattering direction [6,20] and is not of concern in this paper.

In obtaining Eq. (5), several approximations have been made. They are: (a) The condition $k\ell^3/r^2\ll 1$ is assumed. This has already been noted previously. (b) After the integration variable $\vec{r}''$ is replaced by $\vec{r}'$, the integration limits have been extended to infinity. This is justified on the premise that the linear dimension of the scattering volume V_s is much larger than the characteristic size ℓ. (c) The notation "Re" has been added to guarantee the reality of the integral. This procedure is required because the approximations we adopt produce a slight imaginary part. (d) The approximation $z' = r'' - r$ has been used.

Having Eq. (5), we can write an expression for the scattering cross section $\sigma_s(\vec{r})$, defined as the power scattered per unit solid angle per unit incident power density and per unit scattering volume. It is given by

$$\sigma_s(\vec{r}) = \frac{k^4}{16\pi^2} \; \mathrm{Re} \iint_{-\infty}^{\infty} d^2\rho' \; \tilde{A}_\varepsilon(\vec{\rho}') \; F(\vec{r}, \vec{\rho}') \; M(\vec{r}, \vec{\rho}') \tag{7}$$

Here,

$$\tilde{A}_\varepsilon(\vec{\rho}') = \int_{-\infty}^{\infty} dz' \; e^{2jkz'} \; B_\varepsilon(|\vec{r}'|) \tag{8}$$

is the one-dimensional Fourier spectral content of B_ϵ at 2k. In the limit of single scattering, M is reduced to unity. The single scattering cross section becomes, from (7),

$$\sigma_{so}(\hat{r}) = \frac{k^4}{16\pi^2} R_1 \iint_{-\infty}^{\infty} d^2\rho' \, \tilde{A}_\epsilon(\hat{\rho}') \, F(\hat{r}, \hat{\rho}') \tag{9}$$

It is convenient to define a ratio of cross sections by the expression

$$\eta = \frac{\sigma_s}{\sigma_{so}} \tag{10}$$

This ratio reveals the importance of multiple scattering for which the enhancement effect is one manifestation.

III. WEAK SCATTERING

In the case of weak scattering, the supereikonal approximation [15] will be utilized. Having the first-order approximation in the complex phase, the supereikonal approximation is supposed to be equivalent to the Rytov approximation [19] as far as the degree of accuracy is concerned [17]. The validity of Rytov approximation has been investigated [22]. The supereikonal approximation is valid in the same range. For propagators it is more convenient to use the supereikonal approximation.

The supereikonal approximation can be expressed by the following two equations [17].

$$K(\hat{r}_T, \hat{r}) = K_o(\hat{r}_T, \hat{r}) \exp[\psi(\hat{r}_T, \hat{r})] \tag{11}$$

where

$$\psi(\hat{r}_T, \hat{r}) = jk K_o^{-1}(\hat{r}_T, \hat{r}) \int_o^r dz_1 \iint_{-\infty}^{\infty} d^2\rho_1 \, K_o(\hat{r}_T, \hat{r}_1) \, \epsilon_1(\hat{r}_1) \, K_o(\hat{r}_1, \hat{r}) \tag{12}$$

with the equality $\hat{r}_1 = (\hat{\rho}_1, z_1)$. Hence, according to Eq. (3), the multiple-scattering factor $M(\hat{r}, \hat{r}')$ becomes

$$M(\hat{r}, \hat{r}') = \exp\{\tfrac{1}{2} < [\psi(\hat{r}_T, \hat{r}) + \psi(\hat{r}, \hat{r}_R) + \psi^*(\hat{r}_T, \hat{r}') + \psi^*(\hat{r}', \hat{r}_R)]^2 >\} \tag{13}$$

In obtaining Eq. (13), the permittivity fluctuation ϵ_1 has been assumed to be statistically Gaussian distributed.

Before proceeding to compute M, we note in (13) two general forms of the second moment of ψ, i.e., $<\psi(\hat{r}_\alpha, \hat{r}_\beta)\, \psi^*(\hat{r}_\eta, \hat{r}_\xi)>$ and $<\psi(\hat{r}_\alpha, \hat{r}_\beta)\, \psi(\hat{r}_\eta, \hat{r}_\xi)>$. First, the pair of complex conjugate is

$$\begin{aligned} &<\psi(\hat{r}_\alpha, \hat{r}_\beta)\, \psi^*(\hat{r}_\eta, \hat{r}_\xi)> \\ &= k^2 [K_o(\hat{r}_\alpha, \hat{r}_\beta)\, K_o^*(\hat{r}_\eta, \hat{r}_\xi)]^{-1} \int_o^r dz_1 dz_2 \iiint_{-\infty}^{\infty} d^2\rho_1 \, d^2\rho_2 \\ &\quad K_o(\hat{r}_\alpha, \hat{r}_1)\, K_o^*(\hat{r}_\eta, \hat{r}_2)\, B_\epsilon(\hat{\rho}_1 - \hat{\rho}_2, z_1 - z_2)\, K_o(\hat{r}_1, \hat{r}_\beta)\, K_o^*(\hat{r}_2, \hat{r}_\xi) \end{aligned} \tag{14}$$

with $\hat{r}_1 = (\hat{\rho}_1, z_1)$ and $\hat{r}_2 = (\hat{\rho}_2, z_2)$. In order to complete the integrations in Eq. (14), we apply the approximation of stationary path, i.e., the arguments of the correlation B_ϵ in Eq. (14) are replaced by the stationary paths:

$$B_\epsilon(\hat{\rho}_1 - \hat{\rho}_2, z_1 - z_2) \approx B_\epsilon(\hat{\rho}_{01} - \hat{\rho}_{02}, z_1 - z_2) \tag{15}$$

Here, the transverse coordinates of the stationary paths are given by

$$\begin{aligned} \hat{\rho}_{01} &= \hat{\rho}_\alpha + (\hat{\rho}_\beta - \hat{\rho}_\alpha)\, z_1/r \\ \hat{\rho}_{02} &= \hat{\rho}_\eta + (\hat{\rho}_\xi - \hat{\rho}_\eta)\, z_2/r \end{aligned} \tag{16}$$

Notice that the approximation of stationary path has been widely used in the path integral technique [16]. By putting Eq. (15) in (14), the integrations with respect to $\hat{\rho}_1$ and $\hat{\rho}_2$ can be performed according to the composition law [17]. The result is

$$\begin{aligned} &<\psi(\hat{r}_\alpha, \hat{r}_\beta)\, \psi^*(\hat{r}_\eta, \hat{r}_\xi)> \\ &\approx k^2 \int_o^r dz_1 \, dz_2 \, B_\epsilon(\hat{\rho}_{01} - \hat{\rho}_{02}, z_1 - z_2) \end{aligned} \tag{17}$$

The expression for $<\psi(\hat{r}_\alpha, \hat{r}_\beta)\, \psi(\hat{r}_\eta, \hat{r}_\xi)>$ can be similarly derived. The result is the same as Eq. (17) except for a minus sign, i.e.,

$$\begin{aligned} &<\psi(\hat{r}_\alpha, \hat{r}_\beta)\, \psi(\hat{r}_\eta, \hat{r}_\xi)> \\ &= -k^2 \int_o^r dz_1 \, dz_2 \, B_\epsilon(\hat{\rho}_{01} - \hat{\rho}_{02}, z_1 - z_2) \end{aligned} \tag{18}$$

Having Eqs. (17) and (18), we can compute the factor M given by Eq. (13). However, this computation requires the knowledge of the correlation function B_ϵ. This will be performed in Sections V and VI for two assumed correlation functions. To conclude this section, let us mention that by noting Eqs. (16), (17) and (18), the multiple-scattering factor M does not have any dependence on z' as was assumed immediately below Eq. (4) to get (5). In the next section we turn to the strong scattering case.

IV. STRONG SCATTERING

We assume that the fluctuations are so strong that before the incident wave arrives at the scattering volume V_s, the wave statistics can be described as being saturated. In the saturation regime, the random propagator is supposed to possess a complex Gaussian distribution. Therefore, the fourth moment of the propagator K in Eq. (2) can be split into a sum of the product of two second moments as follows [16, 17]

$$\begin{aligned}
&\langle K(\vec{r}_T, \vec{r}) K(\vec{r}, \vec{r}_R) K^*(\vec{r}_T, \vec{r}'') K^*(\vec{r}'', \vec{r}_R)\rangle \\
&= \langle K(\vec{r}_T, \vec{r}) K^*(\vec{r}_T, \vec{r}'')\rangle\langle K(\vec{r}_R, \vec{r}) K^*(\vec{r}_R, \vec{r}'')\rangle \\
&+ \langle K(\vec{r}_T, \vec{r}) K^*(\vec{r}_R, \vec{r}'')\rangle\langle K(\vec{r}_k, \vec{r}) K^*(\vec{r}_T, \vec{r}'')\rangle
\end{aligned} \tag{19}$$

In some propagators on the right-hand side of Eq. (19), we have interchanged the order of two arguments because of the reciprocal property of the propagator. The second moment of the propagator has been obtained by using the path integral technique [16]. For example,

$$\begin{aligned}
&\langle K(\vec{r}_T, \vec{r}) K^*(\vec{r}_R, \vec{r}'')\rangle \\
&= K_o(\vec{r}_T, \vec{r}) K_o^*(\vec{r}_R, \vec{r}'') \exp[-\tfrac{1}{4} k^2 r D(\vec{\rho}_R - \vec{\rho}_T, \vec{\rho}')]
\end{aligned} \tag{20}$$

Here, the structure function $D(\vec{\rho}_1, \vec{\rho}_2)$ is defined by

$$D(\vec{\rho}_1, \vec{\rho}_2) = \int_0^1 [A_\varepsilon(o) - A_\varepsilon[(1-u)\vec{\rho}_2 + u\vec{\rho}_1]]\, du \tag{21}$$

with the integrated correlation function $A_\varepsilon(\vec{\rho})$ defined by

$$A_\varepsilon(\vec{\rho}) = \int_{-\infty}^{\infty} dz\, B_\varepsilon(\vec{\rho}, z) \tag{22}$$

Notice that in writing Eq. (20), we have used the propagation axis defined in the first section. Introduction of Eq. (20) and its similar in (19) produces an expression like that in Eq. (3) with the multiple scattering factor M given by

$$\begin{aligned}
M(\vec{r}, \vec{\rho}') &= \exp[-\tfrac{1}{2} k^2 r D(0, \vec{\rho}')] \\
&+ \exp[-\tfrac{1}{4} k^2 r [D(\vec{\rho}_R - \vec{\rho}_T, \vec{\rho}') + D(\vec{\rho}_T - \vec{\rho}_R, \vec{\rho}')]]
\end{aligned} \tag{23}$$

The right-hand side of Eq. (23) shows that M has no dependence on z' as assumed previously.

V. NUMERICAL RESULTS AND DISCUSSIONS -- GAUSSIAN SPECTRUM

In this section, a Gaussian spectrum will be used in computing the scattering cross section in both the weak and strong scattering limits. The Gaussian correlation function is given by

$$B_\varepsilon(\vec{r}) = \langle \varepsilon_1^2 \rangle \exp(-r^2/\ell^2) \tag{24}$$

The $\tilde{A}_\varepsilon$ given by Eq. (8) can be evaluated

$$\tilde{A}_\varepsilon(\vec{\rho}') = \sqrt{\pi}\, \ell \langle \varepsilon_1^2 \rangle \exp[-(k^2\ell^2 + \rho'^2/\ell^2)] \tag{25}$$

The cross section σ_{so} given by Eq. (10) is given by

$$\sigma_{so}(\vec{r}) = \frac{k^4}{16\sqrt{\pi}} \ell^3 \langle \varepsilon_1^2 \rangle \exp(-k^2\ell^2) \tag{26}$$

$$\mathrm{Re}(1 - jk\ell^2/r)^{-1} \exp\left[\frac{-k^2\ell^2\, |\vec{\rho}_T + \vec{\rho}_R|^2/4r^2}{1 - jk\ell^2/r}\right]$$

In the case of weak scattering, the integrals of (17) and (18) need to be done first. After some computations, we have from (17)

$$\begin{aligned}
&\langle \psi(\vec{r}_\alpha, \vec{r}_\beta)\, \psi^*(\vec{r}_\eta, \vec{r}_\xi)\rangle \\
&= \mu \int_0^1 dv \exp\{-[(\vec{\rho}_\alpha - \vec{\rho}_\eta) + (\vec{\rho}_\beta - \vec{\rho}_\alpha - \vec{\rho}_\xi + \vec{\rho}_\eta)v]^2\}
\end{aligned} \tag{27}$$

where $\mu = k^2 \langle \varepsilon_1^2 \rangle \sqrt{\pi}\, \ell\, r$. When these expressions are substituted into (13), it produces

$$M(\vec{r}, \vec{\rho}') = \exp\{-\mu[2 + \frac{\sqrt{\pi}\,\ell}{|\vec{\rho}_T - \vec{\rho}_R|} \mathrm{erf}(\frac{|\vec{\rho}_T - \vec{\rho}_R|}{\ell}) - \frac{\sqrt{\pi}\,\ell}{|\vec{\rho}'|} \mathrm{erf}(\frac{|\vec{\rho}'|}{\ell})$$

$$- \int_0^1 dv \exp[-((\hat{\rho}_R - \hat{\rho}_T - \hat{\rho}')v + \hat{\rho}')^2/\ell^2]$$

$$- \int_0^1 dv \exp[-((\hat{\rho}_T - \hat{\rho}_R - \hat{\rho}')v + \hat{\rho}')^2/\ell^2]]\} \quad (28)$$

where erf represents an error function. Without loss of generality, in numerical computations we consider a situation in which $\hat{\rho}_R = -\hat{\rho}_T = -x_T\hat{x}$. Hence, we have an expression for η ready for numerical computations:

$$\eta = \frac{1 + (k'/r')^2}{\pi} \mathrm{Re} \iint_{-\infty}^{\infty} dxdy \exp[-(x^2 + y^2) + jk'(x^2 + y^2)/r']$$

$$\exp\{-\mu [2 + \frac{\sqrt{\pi}}{d} \mathrm{erf}(d) - \frac{\sqrt{\pi}}{\sqrt{x^2 + y^2}} \mathrm{erf}(\sqrt{x^2 + y^2})$$

$$- \int_0^1 dv \exp[-(-(d+x)v + x)^2 - (1-v)^2 y^2]$$

$$- \int_0^1 dv \exp[-((d-x)v + x)^2 - (1-v)^2 y^2]]\} \quad (29)$$

Here, we have used the new dimensionless variables: $k' = k\ell$, $r' = r/\ell$, $d = 2x_T/\ell$, $x = x'/\ell$ and $y = y'/\ell$.

In numerical computations, we consider a case in which $k = 10^6 m^{-1}$, $\ell = 0.05m$ and $r = 1000m$. In Fig. 2, Curves I and II represent η values as a function of d for two $\langle \varepsilon_1^2 \rangle$ values: $\langle \varepsilon_1^2 \rangle = 0.5 \times 10^{-15}$ and 0.5×10^{-14}, respectively. These two $\langle \varepsilon_1^2 \rangle$ values correspond to $\mu = 0.0443$ and 0.443, respectively. The former, Curve I, represents a case of very weak multiple scattering. The latter, Curve II, represents a situation of medium scattering which can be regarded as the upper limit for the validity of the supereikonal approximation. From these two curves, the enhancement effect, though weak, can be clearly seen. Further discussion is postponed to a later section.

In the case of strong scattering, since the major contribution to the integral in Eq. (7) comes from the range $|\hat{\rho}'| \lesssim \ell$, the series expansion of the integrated correlation function $A_e(\hat{\rho})$ can be truncated to give [6, 20]

$$A_e(\hat{\rho}) \approx \sqrt{\pi} \langle \varepsilon_1^2 \rangle \ell (1 - \rho^2/\ell^2) \quad (30)$$

The introduction of this quadratic approximation in (23) produces

$$M(\hat{r}, \hat{\rho}') = \exp[-\mu(\rho'/\ell)^2/6]\{1 + \exp[-\mu |\hat{\rho}_R - \hat{\rho}_T|^2/6\ell^2]\} \quad (31)$$

Inserting Eq. (31) in (7), the resulting expression can be computed to give

$$\eta = \frac{(1+\mu/6)[1 + (k\ell^2/r)^2]}{(1+\mu/6)^2 + (k\ell^2/r)^2} [1 + \exp(-\mu d^2/6)] \quad (32)$$

where the assumption $\hat{\rho}_R = -\hat{\rho}_T = -x_T\hat{x}$ and the definition $d = 2x_T/\ell$ have been used.

For numerical computations, we consider a situation with parameters: $k = 10^5 m^{-1}$, $\ell = 0.05m$, $r = 1000m$. Again, two values of $\langle \varepsilon_1^2 \rangle$ are used: $\langle \varepsilon_1^2 \rangle = 2.5 \times 10^{-12}$ and 10^{-11}, corresponding to $\mu = 2.215$ and 8.86, respectively. The variations of η are also drawn as Curves III and IV in Fig. 2. A comparison between the parameter values of the weak and strong scattering cases shows that they have the same scattering geometry and a decrease in frequency by ten times. However, an increase of mean-square fluctuation by 500 times brings the scattering strength from a medium range into the saturation regime. The case with the smaller μ value, i.e., $\mu = 2.215$, represents a scattering strength at the lower limit of the saturation condition. The larger μ value describes a strong scattering situation before the forward scattering approximation becomes invalidated. In Fig. 2, Curves III and IV demonstrate prominently the enhancement effect. An enhancement by a factor of two is obtained when comparing the cross section for the exact monostatic case with that for a receiver-transmitter separation of a few correlation lengths. A comparison among these four curves in Fig. 2 gives the follow impression. In the case of very weak scattering, as shown in Curve I, η value is close to unity and little if any enhancement is shown. As the scattering gets stronger in Curve II, the enhancement peak begins to manifest. Also, the whole level of backscattering is raised. Then, in the saturation regime, the enhancement peak becomes very prominent. This peak gets narrower and the scattering cross section becomes smaller as the dielectric fluctuations intensify. This may be attributed to the decorrelation brought about by multiple scattering and the loss of coherence for waves propagating in the intensified turbulence.

VI. NUMERICAL RESULTS AND DISCUSSIONS — POWER-LAW SPECTRUM

In this section, we consider a Bessel-function power spectrum with the correlation function given by [18]

$$B_\varepsilon(\hat{r}) = \frac{\langle \varepsilon_1^2 \rangle [\kappa_0(r^2 + \ell_1^2)^{1/2}]^{(p-3)/2} K_{(p-3)/2}(\kappa_0\sqrt{r^2 + \ell_1^2})}{(\kappa_0\ell_1)^{(p-3)/2} K_{(p-3)/2}(\kappa_0\ell_1)} \quad (33)$$

Here, $K_\nu(\cdot)$ is a ν^{th} order Bessel function with an imaginary argument. The symbols ℓ_1 and $\ell_0 = 1/\kappa_0$ represent the inner and outer scales of the turbulent structure, respectively. It has been shown that after a Fourier transformation, the power spectrum follows a power law with power index p in the initial subrange. For atmospheric applications, p can be set at 11/3 in Eq. (33). Actually, when the value $\ell_1(\kappa^2 + \kappa_0^2)^{1/2}$ is not large, the power spectrum can be approximated by [18]

$$\phi_\varepsilon(\kappa) = \frac{8\langle \varepsilon_1^2 \rangle \pi^{3/2}}{\kappa_0^3} \frac{\Gamma(p/2)}{\Gamma((p-3)/2)} \frac{1}{(1+\kappa^2/\kappa_0^2)^{p/2}} \tag{34}$$

with Γ standing for a gamma function. When p is set at 11/3, Eq. (34) becomes

$$\phi_\varepsilon(\kappa) = 15.6 \frac{\langle \varepsilon_1^2 \rangle \kappa_0^{2/3}}{(\kappa^2+\kappa_0^2)^{11/6}} \tag{35}$$

This equation is compared with a power law usually used for refractive-index fluctuations in a turbulent atmosphere: [14]

$$\phi_n(\kappa) = 0.033\, C_n^2\, \kappa^{-11/3} \tag{36}$$

A comparison between Eqs. (35) and (36) in the case $\kappa^2 \gg \kappa_0^2$ leads to a relation as

$$\langle \varepsilon_1^2 \rangle = 0.00846\, \kappa_0^{-2/3}\, C_n^2 \tag{37}$$

Equation (37) provides a more concrete physical meaning for $\langle \varepsilon_1^2 \rangle$ since C_n^2 is a quantity that can be measured in experiments.

The function $\bar{A}_\varepsilon(\vec{\rho}')$ in Eq. (8) has been computed [20]:

$$A_\varepsilon(\vec{\rho}') = \frac{\sqrt{2\pi}\langle \varepsilon_1^2 \rangle (\kappa_0^2 \rho'^2 + \kappa_0^2 \ell_1^2)^{(p-2)/4} K_{(p-2)/2}\left(\sqrt{1 + 4k^2\kappa_0^{-2}}\, \sqrt{\kappa_0^2 \rho'^2 + \kappa_0^2 \ell_1^2}\right)}{\kappa_0 (\kappa_0 \ell_1)^{(p-3)/2} [1 + 4k^2 \kappa_0^{-2}]^{(p-2)/4} K_{(p-3)/2}(\kappa_0 \ell_1)} \tag{38}$$

Because for $p \geq 2$, the Bessel function $K_{(p-2)/2}$ decreases very fast as its argument becomes larger than unity, the effective range of ρ' for significant $\bar{A}$ value cannot be larger than $1/k$ in the case $p = 11/3$. Accordingly, Eq. (6) simplifies to $F(\vec{r}, \vec{\rho}') = F(\vec{r}, 0) = 1$ and Eq. (13) simplifies to $M(\vec{r}, \vec{\rho}') = M(\vec{r}, 0)$ when $\rho' \lesssim 1/k$. With these approximations, Eq. (7) becomes

$$\sigma_s(\vec{r}) = \frac{k^4}{16\pi^2} \operatorname{Re} M(\vec{r}, 0)\, \phi_\varepsilon(2k) \tag{39}$$

The ratio of the cross sections reduces to

$$\eta = \operatorname{Re} M(\vec{r}, 0) \tag{40}$$

This ratio depends only on the factor M. In the weak scatter limit, Eqs. (16), (17) and (18) can be used to yield

$$\begin{aligned} &\langle \psi(\vec{r}_T, \vec{r}')\, \psi^*(\vec{r}', \vec{r}_R) \rangle + \langle \psi(\vec{r}_T, \vec{r}')\, \psi(\vec{r}', \vec{r}_R) \rangle = 0 \\ &\langle \psi(\vec{r}', \vec{r}_R)\, \psi^*(\vec{r}_T, \vec{r}') \rangle + \langle \psi^*(\vec{r}_T, \vec{r}')\, \psi^*(\vec{r}', \vec{r}_R) \rangle = 0 \end{aligned} \tag{41}$$

These approximations lead to the conclusion that $M(r, 0) = 1$ and thus $\eta = 1$. This implies that when the supereikonal approximation is valid, multiple scattering does not produce significant effects on the backscattering cross section when the dielectric permittivity fluctuations have a power law spectrum. Actually, it has been shown [20] that in such a case, multiple scattering effects are important only in a narrow range of angle around the forward-scattering direction. Therefore, in the case of weak scattering, the enhancement effect is not important.

On the contrary, in the saturation regime, $M(\vec{r}, 0)$ is not identical to unity even for propagation in a power law environment. From Eq. (23), we have

$$\begin{aligned} \eta &= \operatorname{Re} M(\vec{r}, 0) \\ &= 1 + \exp\left[-\tfrac{1}{2} k^2 r D(d', 0)\right] \end{aligned} \tag{42}$$

with d' being defined by $d' = |\vec{\rho}_R - \vec{\rho}_T|$, the distance between the transmitter and receiver. In order to make numerical computations feasible, we consider a case with $p = 4$. Then we have an expression for η

$$\eta = 1 + \exp[-\pi' \bar{D}(d, 0)] \tag{43}$$

Here,

$$\bar{D}(d, 0) = 1 - \frac{\pi}{2} [K_1(\kappa_0 d)\, L_0(\kappa_0 d) + L_1(\kappa_0 d)\, K_0(\kappa_0 d)] \tag{44}$$

with $L_\nu(\cdot)$ representing a modified Struve function with order ν. Also, $\mu' = k^2 \langle \varepsilon_1^2 \rangle r/\pi_0$ which is similar to μ in the last section. The input parameters for numerical computations are given: $k = 10^3 m^{-1}$, $\ell_1 = 10^{-3} m$, $\ell_2 = 1m$ and $r = 1000m$. Two curves are shown in Fig. 3 corresponding to two values of $\langle \varepsilon_1^2 \rangle$: 10^{-12} (Curve I, $\mu' = 10$) and 5×10^{-12} (Curve II, $\mu' = 50$). Evidently, a factor of two can be seen in the ratio of the peak value and the flat tail in either curve. Also, as in the case of the Gaussian spectrum, in the situation of stronger scattering, i.e., μ' is larger, the enhancement range is narrower. In addition, in Fig. 3 we learn that except for the enhancement effect, the multiple scattering plays an insignificant role in backscattering. This is consistent with the conclusion in the case of weak scattering. It is unfortunate that, so far, there is no theory that can close the theoretical gap between the supereikonal approximation and saturation regime. Otherwise, we may be able to see the gradual growth of enhancement effect as the scattering strength is increased.

VII. CONCLUSIONS

In this paper, we have demonstrated the enhancement effect in turbulent media. Two ranges of scattering strength are considered. In weak scattering, the supereikonal approximation is used, while in the limit of strong multiple scattering the saturation statistics are assumed. To present numerical results, two kinds of power spectral functions are applied: a Gaussian and a power-law format.

It has been shown that the enhancement effect is completely controlled by the multiple-scattering factor M. Then, the most crucial parameter controlling M is μ in the case of Gaussian spectrum or μ' in that of power-law. For a simpler discussion, let us look into the case of Gaussian spectrum. In this case, μ can be rewritten as $\mu = k^2 \ell_c(o) r$. This parameter can be identified as one eighth of the extinction distance. The extinction distance is the distance of propagation over which the coherent field is attenuated to its 1/e value [19]. Let $\langle E \rangle$ and $\langle I \rangle$ represent the coherent field and average intensity, respectively. After a wave emitted by a point source propagates through the random medium, μ can be regarded as a parameter of coherence defined by

$$\mu = -4 \ln \frac{|\langle E \rangle|^2}{\langle I \rangle} \tag{45}$$

Apparently, $|\langle E \rangle|^2$ is the coherent intensity. The value of μ can vary from zero, corresponding to a completely coherent wave, to infinity, corresponding to a completely incoherent wave. Since the enhancement effect is attributed to the coherence recovered in the round-trip propagation, it must be controlled by this parameter of coherence μ as we showed in this paper. Although, only limited range of μ value could be considered, we did show that a larger μ value leads to a more prominent enhancement effect. This trend can be interpreted by saying that relatively more coherence is recovered in the enhancement region as the wave loses more coherence during propagation in a random medium.

REFERENCES

[1] A. G. Vinogradov, Yu. A. Kravtsov and V. I. Tatarskii, "The effect of intensification on backscattering by bodies that are situated in a medium having random inhomogeneities," Radiofizika, 16, 1973, 1064-1070.

[2] A. B. Krupnik and A. I. Saichev, "Coherent properties and focusing of wave beams reflected in a turbulent medium," Radiofizika, 24, 1981, 1234-1239.

[3] K. S. Gochelashvili and V. I. Shishov, "Propagation of reflected radiation in a randomly inhomogeneous medium," Sov. J. Quantum Electron, Eng. Transl., 11, 1981, 1182-1184.

[4] Yu. A. Kravtsov and A. I. Saichev, "Double passage wave effects in randomly inhomogeneous media," Sov. Phys. Usp., 25, 1982, 494-509.

[5] K. C. Yeh, "Mutual coherence functions and intensities of backscattered signals in a turbulent medium," Radio Science, 18, 1983, 159-165.

[6] C. C. Yang and K. C. Yeh, "Effects of multiple scattering and Fresnel diffraction on random volume scattering," IEEE Transac. Antennas Propagat., AP-32, 1984, 347-355.

[7] C. C. Yang and K. C. Yeh, "The behavior of the backscattered power from an intensely turbulent ionosphere," Radio Science, 20, 1985, 319-324.

[8] Yu. A. Kravtsov and A. I. Saichev, "Properties of coherent waves reflected in a turbulent medium," J. Opt. Soc. Am., 2, 1985, 2100-2105.

[9] L. Tsang and A. Ishimaru, "Backscattering enhancement of random discrete scatterers," J. Opt. Soc. Am. (A), 1, 1984, 836-839.

[10] Y. Kuga and A. Ishimaru, "Retroreflectance from a dense distribution of spherical particles," J. Opt. Soc. Am. (A), 1, 1984, 831-835.

[11] M. P. van Albada and A. Lagendijk, "Observation of weak localization of light in a random medium," Phys. Rev. Lett., 55, 1985, 2692-2695.

[12] P. E. Wolf and G. Maret, "Weak localization and coherent backscattering of photons in disordered media," Phys. Rev. Lett., 55, 1985, 2696-2699.

[13] P. A. Lee and A. D. Stone, "Universal conductance fluctuations in metal," Phys. Rev. Lett., 55, 1985, 1622-1623.

[14] S. Etemad, R. A. Thompson, and M. Andrejco, "Weak localization of photons: Universal fluctuations and ensemble averaging," Phys. Rev. Lett., 57, 1986, 575-578.

[15] W. H. Munk and F. Zachariasen, "Sound propagation through a fluctuating stratified ocean: Theory and observation," J. Acoust. Soc. Am., 59, 1976, 818-838.

[16] R. Dashen, "Path integrals for waves in random media," J. Math. Phys., 20, 1979, 894-920.

[17] S. Y. Lee, C. H. Liu, and K. C. Yeh, "Waves in random continuum described by path integrals," Research Topics in Electromagnetic Wave Theory, edited by J. A. Kong, New York:John Wiley & Sons, 1981, Chapter Two.

[18] I. P. Shkarofsky, "Generalized turbulence space-correlation and wave-number spectrum-function pairs," Can. J. Phys., 8, 1968, 2133-2153.

[19] V. I. Tatarskii, The Effects of the Turbulent Atmosphere on Wave Propagation, English translation, U.S. Department of Commerce, Washington, D.C., 1971.

[20] C. C. Yang, Electromagnetic Scattering from a Strongly Turbulent Medium, Ph.D. dissertation, Department of Electrical and Computer Engineering, University of Illinois at Urbana-Champaign, 1984.

[21] D. A. deWolf, "Electromagnetic reflection from an extended turbulent medium: Cumulative forward-scatter single-backscatter approximation," IEEE Trans. Ant. Propagat., AP-19, 1571, 254-262.

[22] W. P. Brown, Jr., "Validity of the Rytov approximation," J. Opt. Soc. Am., 57, 1967, 1539-1543.

ACKNOWLEDGEMENTS

This research was supported by the National Science Foundation through the grants ATM 83-12175 and ECS 83-11345.

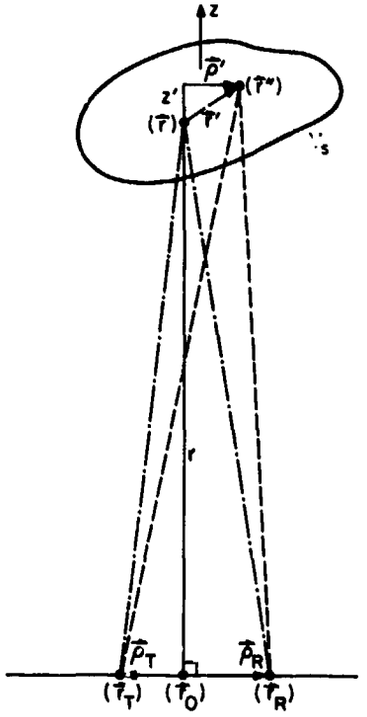


Fig. 1 Geometry of problem. The transmitter, receiver and two scatterers are respectively located at $(\vec{r}_T)$, $(\vec{r}_R)$, $(\vec{r})$ and $(\vec{r}'')$. The scattering volume V_s is far away from the transmitter and receiver in the random medium which occupies the half space above the horizontal line. The z-axis is used as the propagation axis.

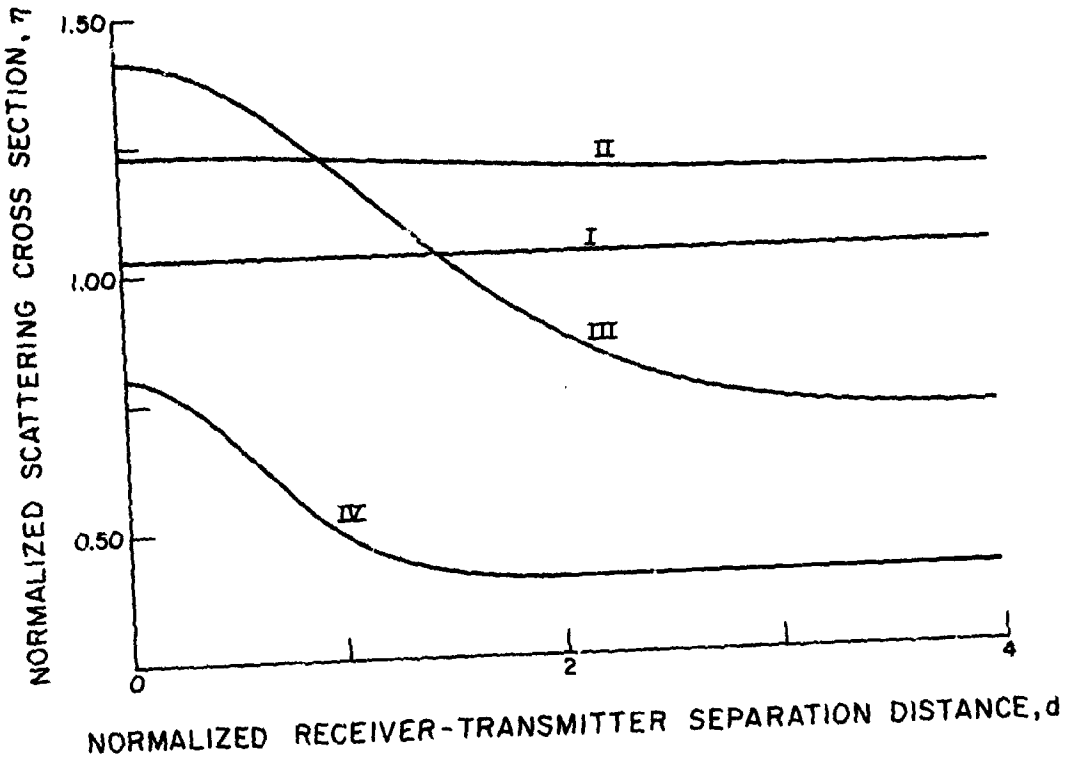


Fig. 2 Value of $\eta = \sigma_s/\sigma_{so}$ as a function of d, the distance between the transmitter and receiver normalized by the characteristic scale ℓ. A Gaussian spectrum function is used. Curves I (μ = 0.0443) and II (μ = 0.443) are plotted by using the supersational approximation. Curves III (μ = 2.215) and IV (μ = 8.86) represent two cases in the saturation regime. The enhancement effect can be clearly seen.

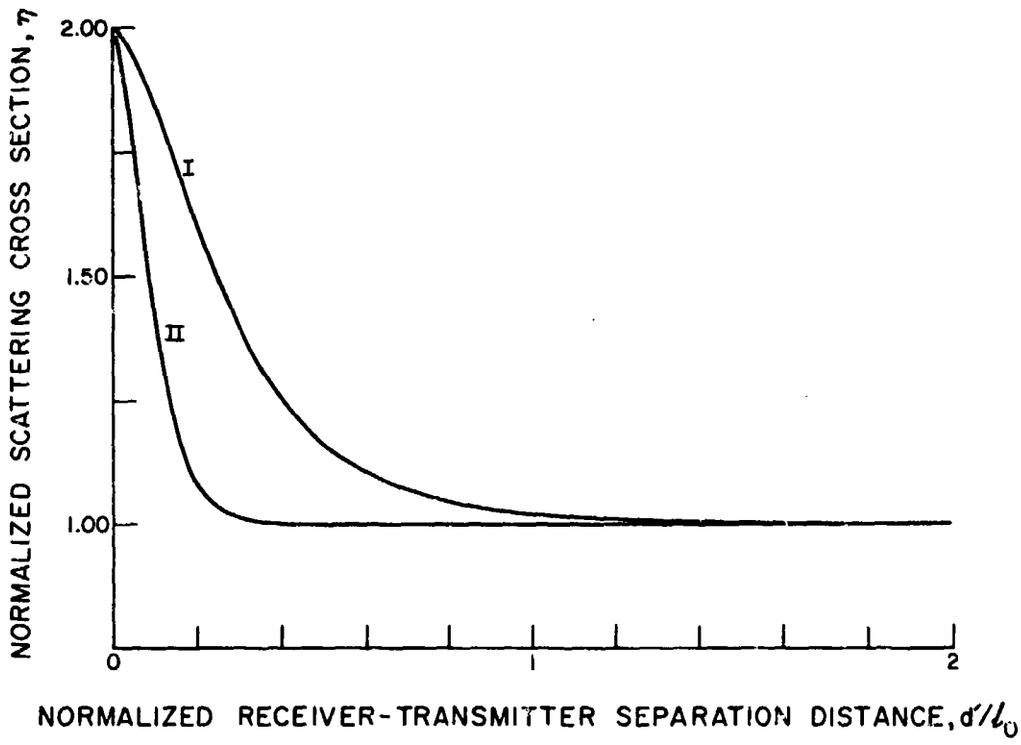


Fig. 3 Value of $\eta = \sigma_s/\sigma_{s0}$ as a function of d'/ℓ_0, the distance between the transmitter and receiver normalized by the outer scale. A power-law spectrum is used. Both Curves I ($\mu' = 10$) and II ($\mu' = 50$) describe scattering in the saturation regime. The enhancement effect can be clearly seen.

DISCUSSION

S. Clifford, US

The enhanced backscatter case (equivalent problem) has been considered in lidar scattering off a rough surface field. Enhanced backscatter occurs when transmitter/RCVR are colocated due to "tilt compensation". Is this the same effect to which you refer? If you have a tilt-only measurement (quadratic structure function) do you see enhanced backscatter? I did the same type of calculation in Applied Optics (Clifford and Wandzura, 1982; Clifford and Lasing, 1984). For the lidar problem in weak scattering, I'm curious about unifying the two problems, i.e, doing the strong scatter lidar case by following your development.

Author's Reply

The enhanced backscattering from a rough surface under an experimentally controlled environment has been observed in recent years, but a satisfactory theory that explains all aspects of the observed phenomena is still lacking. In the case of volume scattering, the enhancement is caused by the existence of two kinds of propagation paths which give rise to contributions to the scattered intensity. By "tilt compensation" if you mean the quadratic approximation to the correlation function, then this approximation alone is not the cause of enhancement.

W.A. Flood, US

In the case of the power-law spectrum, what is the angular width of the backscatter enhancement? (In the particle case discussed by Ishimaru, the angular width of the backscattered enhancement is far, far less than would be predicted by diffraction from a particle of a given radius.)

Author's Reply

For the example shown in Fig. 2, the width of enhancement is of the order of the correlation length which is 0.05 m. The scattering volume is at a distance of 1000 m from the radar. This corresponds to an angular enhancement width of 0.05 m rad which is very small indeed.

A. Consortini, IT

The power-law spectrum that you used takes into account the outer scale of the turbulence. Are you planning to take into account the effect of the inner scale?

Author's Reply

Yes. As a matter of fact some computations are made for the case when the wavelength is smaller than the inner scale.

I.M. Besieris, US

It is interesting to compare the changes in the backscattering enhancement level and angular spread when you increase the strength of the statistical fluctuations with those discussed by Akira Ishimaru in connection with scattering by large concentrations of particles.

Author's Reply

I agree. We have made some computations showing these effects. Perhaps more computations are needed.

MULTIPLE SCATTERING EFFECTS OF RANDOM DISTRIBUTIONS OF IRREGULARLY SHAPED PARTICLES ON INFRARED AND OPTICAL PROPAGATION

Ezekiel Bahar
and
Mary Ann Fitzwater

Electrical Engineering Department
University of Nebraska-Lincoln 68588-0511

ABSTRACT

Scattering and depolarization by layers of randomly distributed particles of irregular shape and finite conductivity are determined for infrared and optical electromagnetic excitations. The irregularly shaped particles considered here are spheres with random rough surfaces. They are characterized by their two dimensional surface height spectral density functions or autocorrelation functions. Circularly and linearly polarized excitations at normal incidence as well as vertically and horizontally polarized excitations at oblique incidence are considered. The co-polarized and cross-polarized incoherent diffuse specific intensities (Modified Stokes Parameters) are determined by solving the vector form of the equation of radiative transfer. To this end the full wave approach which accounts for diffuse scattering as well as specular scattering in a self-consistent manner is used to evaluate the extinction cross sections as well as the scattering (phase) matrix for the irregularly shaped particles. Both single-scatter and multiple-scatter incoherent specific intensities are evaluated for particles with smooth as well as rough surfaces. It is shown that the particle surface roughness can have a significant effect on the diffuse specific intensities. The phenomenon of enhanced backscatter is also examined.

1. INTRODUCTION

The vector form of the equation of radiative transfer is solved to determine the co-polarized and cross-polarized incoherent diffuse specific intensities (Modified Stokes Parameters) generated in layered media consisting of random distributions of irregularly shaped particles of finite conductivity. Linearly polarized and circularly polarized waves at normal incidence as well as obliquely incident vertically and horizontally polarized electromagnetic excitations at infrared and optical frequencies are considered.

The problem of electromagnetic wave scattering by random distributions of particles has been studied extensively by researchers with interests in fields such as atmospheric aerosols, smoke and dust in planetary atmospheres (Chandresekhar 1950, Ishimaru 1978). However, in most of the work on this topic, the scattered particles are assumed to be of idealized shapes such as spheres, oblate and prolate spheroids and circular cylinders for which rigorous separable solutions are known (Ruck et al. 1970). In many physical problems of interest however, the individual scatterers are of irregular shapes such as flakes, spheres and cylinders with random rough surfaces (Greenberg 1960, Chylek 1971, Scheurman 1980; Bahar and Fitzwater 1983, 1985; Bahar and Chakrabarti 1985). Several theoretical and experimental techniques used in the study of scattering and absorption by irregularly shaped particles have been reported in the proceedings of the workshop on light scattering (Scheurman 1980). A survey of several analytical and numerical techniques including their respective pros and cons has been presented by Yeh and Mei (1980). For example, if the mean square height of the surface roughness $\langle h^2 \rangle$ is small ($\beta = 4k_o^2 \langle h^2 \rangle \ll 1$, where k_o is the free space wavenumber) a perturbation approach can be used to account for diffuse scattering attributable to the rough surface (Ruck et al. 1970, Rice 1951, Kiehl et al. 1980). However, for $\beta \ll 1$ the effects of the rough surface on the scattered specific intensities are negligible. For problems of practical interest with $\beta > 1$, the perturbation solutions are not suitable and a full wave solution, which accounts for physical optics and diffuse scattering in a self-consistent manner, can be used to express the scattering cross sections as weighted sums of the physical optics and the diffuse scattering cross sections. These full wave expressions are used to determine the elements of the phase matrix as well as the extinction coefficient that appears in the equation of radiative transfer for media consisting of random distributions of irregularly shaped particles (Bahar and Fitzwater 1986a).

When equivalent spheres, spheroids or cylinders do not reasonably represent the basic scattering characteristics of irregularly shaped particles, experimental microwave techniques developed by Greenberg (1960) can be used to determine the albedo for particles for which no analytical solution yet exists (Scheurman 1980, Chylek 1977).

For the illustrative examples presented in this paper the irregularly shaped particles of finite conductivity are spheres with random rough surfaces. They are characterized by their two dimensional surface height spectral density functions or their corresponding non-Gaussian autocorrelation functions. Since it is assumed here that the roughness parameter is large ($\beta \gg 1$), in order to evaluate the extinction cross sections the full wave approach is used. In addition, judicious use is made of the forward scattering theorem (Born and Wolf 1964) and the very perceptive observation that for large scatterers (physical dimensions large compared to wavelength) the forward scattered "shadow forming" wave is the same for all surfaces which have the same shadow line (Morse and Feshbach 1953). To facilitate the analysis, it is assumed here that the radius of the sphere is not only large compared to the wavelength λ but also large compared to the rough surface height correlation length. However, the radii of curvature of the rough surface need not be large compared to the wavelength. Multiple scattering between the different elements of the surface of the same sphere is neglected.

To solve the equation of radiative transfer for the incoherent specific intensities, Gaussian quadrature and the matrix characteristic value techniques are used (Ishimaru et al. 1982). The problem is formulated in Section 2. The method used to evaluate the extinction cross section is described in Section 3. Illustrative examples are presented in Section 4. Both single scatter and multiple scatter results for the co-polarized and cross-polarized incoherent specific intensities are given for particles with smooth surfaces as well as rough surfaces. Thus the effects of particle surface roughness upon the co-polarized and cross-polarized intensities are investigated in detail. Special consideration is given to the evaluation of the degree of polarization of the incoherent specific intensities and the observed phenomenon of enhanced backscatter.

2. FORMULATION OF THE PROBLEM

A linearly polarized electromagnetic wave is assumed to be obliquely incident upon a parallel layer of randomly distributed particles of finite conductivity and irregular shape. Specificically, in this work the particles are assumed to be spheres whose surfaces are randomly perturbed (see Fig. 1). Thus, if h is the random surface height of the particle measured normal to the unperturbed sphere of radius a, the radius vector to the surface of the irregularly shaped particle is

$$\bar{r}_s = (a + h)\bar{a}_r \tag{2.1}$$

in which $\bar{a}_r$ is the unit radius vector. The mean square height of the rough surface $\langle h^2 \rangle$ is assumed to be such that the roughness parameter $\beta = 4k_o^2\langle h^2 \rangle$ (where k_o is the free space wavenumber) is large ($1 < \beta < 40$). Thus, the small perturbation method (Rice 1951; Ruck et al. 1970; Kiehl et al. 1980) cannot be used to analyze the scattering by the very rough particles considered The small perturbation method is restricted to particles with small roughness parameters $\beta \leq 0.1$, for which the incoherent diffuse specific intensities are not significantly different from those for the corresponding smooth (spherical) particles. Theoretical and exporimental techniques used in the study of scattering and absorption by irregularly shaped particles have been presented in the proceedings on the workshop on light scattering (Scheurman 1980). A survey of analytical and numerical techniques including their pros and cons has been presented by Yeh and Mei (1980).

The full wave method that accounts for specular point scattering and diffuse scattering in a unified, self-consistent manner has been used in this work to determine the scattering and depolarization by particles with rough surfaces (Bahar and Fitzwater 1983; Bahar and Chakrabarti 1985). The random rough surface height h is characterized by its surface height spectral density function W or its Fourier transform, the surface height autocorrelation function $\langle hh' \rangle$.

The incoherent diffuse specific matrix [I] satisfies the equation of transfer (Chandrasekhar 1950; Ishimaru 1978)

$$\mu \frac{d[I]}{d\tau} = -[I] + \int [S][I']d\mu\, d\phi + [I_i] \tag{2.2}$$

in which the elements of the matrix [I] are the modified Stokes parameters (Chandrasekhar 1950, Ishimaru 1978)

$$[I] = \begin{bmatrix} I_1 \\ I_2 \\ U \\ V \end{bmatrix} = \begin{bmatrix} \langle E_1 E_1^* \rangle \\ \langle E_2 E_2^* \rangle \\ 2\mathrm{Re}\langle E_1 E_2^* \rangle \\ 2\mathrm{Im}\langle E_1 E_2^* \rangle \end{bmatrix} \tag{2.3}$$

The symbol $\langle \cdot \rangle$ denotes the statistical average and * denotes the complex conjugate (a suppressed $\exp(i\omega t)$ time dependent excitation is assumed). The vertically and horizontally polarized components of the electric field are E_1 and E_2 respectively. The optical distance τ is measured in the z direction (normal to the plane of the slab, see Fig. 2).

$$\tau = z\rho[\sigma_t] \equiv z\int \sigma_t n(D)dD \tag{2.4}$$

where D is the diameter of the unperturbed spherical particle, n(D) is the particle size distribution and σ_t is the total cross section (extinction coefficient). The aymbol $\rho[\cdot]$ denotes integration over the size distribution. The effects of the particle surface roughness (which is assumed to be isotropic and homogeneous) are vanishingly small in the forward direction, thus the extinction matrix (Ishimaru and Cheung 1980; Cheung and Ishimaru 1982) for the particle with the rough surface can be represented by the scalar quantity σ_t. The matrices [I] and [I'] are the incoherent diffuse intensities for waves scattered by the particles in the direction $\theta = \cos^{-1}\mu$ and ϕ and for waves incident in the direction $\theta' = \cos^{-1}\mu'$ and ϕ' respectively. The (4x4) scattering (phase) matrix [S] in the reference coordinate system is expressed in terms of the scattering matrix [S'] in the scattering plane (that contains the incident and scatter wave normals $\bar{n}^i$ and $\bar{n}^f$ respectively see Fig. 2) through the following transformation

$$[S] = [\mathcal{L}(-\pi + \alpha)][S'][\mathcal{L}(\alpha')] \tag{2.5}$$

in which [S'] is the weighted sum of two matrices

$$[S'] = |\chi(\bar{\nu}\cdot\bar{a}_r)|^2[S_{Mie}] + [S_D] \tag{2.6}$$

In (2.6) $[S_{Mie}]$ is given by

$$[S_{Mie}] = \frac{1}{\rho[\sigma_t]} \begin{bmatrix} \rho[|f_{11}|^2] & \rho[|f_{12}|^2] & \rho\mathrm{Re}[f_{11}f_{12}^*] & -\rho\mathrm{Im}[f_{11}f_{12}^*] \\ \rho[|f_{21}|^2] & \rho[|f_{22}|^2] & \rho\mathrm{Re}[f_{21}f_{22}^*] & -\rho\mathrm{Im}[f_{21}f_{22}^*] \\ \rho 2\mathrm{Re}[f_{11}f_{21}^*] & \rho 2\mathrm{Re}[f_{12}f_{22}^*] & \rho\mathrm{Re}[f_{11}f_{22}^* + f_{12}f_{21}^*] & -\rho\mathrm{Im}[f_{11}f_{22}^* - f_{12}f_{21}^*] \\ \rho 2\mathrm{Im}[f_{11}f_{21}^*] & \rho 2\mathrm{Im}[f_{12}f_{22}^*] & \rho\mathrm{Im}[f_{11}f_{22}^* + f_{12}f_{21}^*] & \rho\mathrm{Re}[f_{11}f_{22}^* - f_{12}f_{21}^*] \end{bmatrix} \tag{2.7}$$

where f_{ij} are elements of the 2x2 scattering matrix for the unperturbed (spherical) particle

$$\begin{bmatrix} E_\ell \\ E_r \end{bmatrix} = \begin{bmatrix} f_{11} & f_{12} \\ f_{21} & f_{22} \end{bmatrix} \begin{bmatrix} E_\ell' \\ E_r' \end{bmatrix} \frac{\exp(-ik_o r)}{r} \tag{2.8}$$

In (2.8) E_ℓ', E_r' and E_ℓ, E_r are the incident and scattered vertically and horizontally polarized electric field components in the scattering plane and r is the distance to the field point from the center of the spherical particle. For a smooth sphere f_{ij} are given by the Mie solution (Ruck et al. 1970; Ishimaru 1978) and [f] is a diagonal matrix. The Mie solution contains the specularly scattered contribution as well as the contribution of the shadow forming wave (Morse and Feshbach 1953).

The transformation matrices $[\mathcal{L}]$ in (2.5) are given in terms of the angle α' between the reference plane of incidance and the scattering plane and the angle α between the scattering plane and the reference plane of scatter (see Fig. 2)

$$[\underline{f}(\alpha)] = \begin{bmatrix} \cos^2\alpha & \sin^2\alpha & \frac{1}{2}\sin 2\alpha & 0 \\ \sin^2\alpha & \cos^2\alpha & -\frac{1}{2}\sin 2\alpha & 0 \\ -\sin 2\alpha & \sin 2\alpha & \cos 2\alpha & 0 \\ 0 & 0 & 0 & 1 \end{bmatrix} \tag{2.9}$$

The quantity χ in (2.6) is the particle random rough surface characteristic function

$$\chi(\bar{\nu}\cdot\bar{a}_r) = \langle \exp(i\bar{\nu}\cdot\bar{a}_r h)\rangle \tag{2.10}$$

in which

$$\bar{\nu} = k_o(\bar{n}^f - \bar{n}^i) \tag{2.11}$$

Thus the coefficient $|\chi|^2$ in (2.6) accounts for the degradation of the specular point contributions to the scattered fields by the rough surface ($|\chi|^2 \leq 1$ and as $\beta \to 0$ $|\chi|^2 \to 1$). The diffuse scattering contribution to the matrix S' due to the particle rough surface is given by

$$[S_D] = \begin{bmatrix} [S^D_{11}] & [S^D_{12}] & 0 & 0 \\ [S^D_{21}] & [S^D_{22}] & 0 & 0 \\ 0 & 0 & [S^D_{33}] & [S^D_{34}] \\ 0 & 0 & [S^D_{43}] & [S^D_{44}] \end{bmatrix} \tag{2.12}$$

where

$$[S^D_{ij}] = \frac{A_y}{4\pi\rho[\sigma_t]}\ \rho[\langle\sigma^{ij}\rangle_D] \quad , \quad \text{for } i,j = 1,2 \tag{2.13}$$

in which $A_y = \pi a^2$ is the average cross sectional area of the unperturbed particle and $\langle\sigma^{ij}\rangle_D$ are the full wave solutions for the like (i=j) and cross polarized (i≠j) normalized scattering cross sections (Bahar and Fitzwater 1983; Bahar and Chakrabarti 1985). The first and second superscripts i,j denote the polarizations (V vertical and H horizontal) of the scattered and incident waves respectively

$$\langle\sigma^{ij}\rangle_D = \int_0^{2\pi}\int_0^{\pi} |k_o D^{ij}|^2\, P_2 Q\, \sin\gamma d\gamma d\delta/\pi^2 \tag{2.14}$$

where

$$Q = \int_{-\infty}^{\infty} (\chi_2(\bar{\nu}\cdot\bar{a}_r) - |\chi(\bar{\nu}\cdot\bar{a}_r|^2)\exp(i\bar{\nu}\cdot\bar{r}_d)dx_d ds_d \tag{2.15}$$

Since the rough surface height h is assumed to be isotropic and homogeneous, the surface height autocorrelation function $\langle hh'\rangle$ and the joint characteristic function χ_2 are only functions of the distance $r_d = (x_d^2 + s_d^2)^{\frac{1}{2}}$ measured along the surface of the unperturbed sphere. For rough surface heights with Gaussian distributions

$$|\chi(\bar{\nu}\cdot\bar{a}_r)|^2 = \exp[-(\bar{\nu}\cdot\bar{a}_r)^2\langle h^2\rangle] \tag{2.16}$$

and

$$\chi_2(\bar{\nu}\cdot\bar{a}_r) = \langle \exp i\bar{\nu}\cdot\bar{a}_r(h-h')\rangle = \exp[(\bar{\nu}\cdot\bar{a}_r)^2\langle hh'\rangle]\, e^{|(\bar{\nu}\cdot\bar{a}_r)|^2} \tag{2.17}$$

In (2.15) it is assumed that the surface height correlation length r_c is small compared to the particle circumference πD.

For i = 3 and 4

$$[S^D_{ii}] = \rho[\mathrm{Re}[\langle\sigma^{11}_{22}\rangle_D \pm \langle\sigma^{12}_{21}\rangle_D]]A_y/4\pi\rho[\sigma_t] \tag{2.18}$$

(upper and lower signs for i = 3 and 4 respectively). For i≠j

$$[S^D_{ij}] = \rho[\mathrm{Im}[\pm\langle\sigma^{11}_{22}\rangle_D + \langle\sigma^{12}_{21}\rangle_D]]A_y/4\pi\rho[\sigma_t] \tag{2.19}$$

(upper sign for i = 4, j = 3 and lower sign for i = 3, j = 4 respectively).
In the above expressions

$$\langle\sigma^{ij}_{kl}\rangle = \int_0^{2\pi}\int_0^{\pi} k_o^2\, D^{ij}\, D^{kl*}\, P_2 Q\, \sin\gamma d\gamma d\delta/\pi^2 \tag{2.20}$$

In (2.14) and (2.20), P_2, the shadow function, is the probability that a point on the surface of the particle is both illuminated and visible given the slope of the surface at the given point (Sancer 1964). The scattering coefficients D^{ij} are functions of $\bar{n}^i, \bar{n}^f$ and $\bar{n}$, the normal to the unperturbed surface of the particle, as well as its electromagnetic parameters ε, μ. The remaining eight terms of the matrix $[S_D]$ vanish since D^{ii} and D^{ij} (i≠j) are symmetric and antisymmetric respectively with respect to δ the azimuth angle for the sphere.

In this work it is assumed that a linearly polarized wave (vertical or horizontal) is obliquely incident upon a parallel layer of optical thickness τ_o containing a random distribution of particles with rough surfaces. The incident Stokes matrix at z = 0 is (see Fig. 2)

$$[I_{inc}] = [I^P_o]\delta(\mu' - \mu^i)\delta(\phi') \tag{2.21}$$

in which $\mu^i = \cos\theta^i$, the direction of the incident wave is $(\theta^i, 0)$ and

$$[I^V_o] = \begin{bmatrix}1\\0\\0\\0\end{bmatrix},\ [I^H_o] = \begin{bmatrix}0\\1\\0\\0\end{bmatrix},\ [I^R_o] = \begin{bmatrix}1\\1\\0\\-2\end{bmatrix} \text{ and } [I^L_o] = \begin{bmatrix}1\\1\\0\\2\end{bmatrix} \tag{2.22}$$

for P=V (vertical), P=H (horizontal), P=R (right), and P=L (left). In (2.21) $\delta(\cdot)$ is the Dirac delta function. Thus, the reduced incident intensity is

$$[I_{ri}] = [I_{inc}]\exp(-\tau/\mu^i) \tag{2.23}$$

and the (4x1) excitation matrix (2.2) is

$$[I_i] = \int[S][I_{ri}]d\mu'd\phi' \equiv [F]\exp(-\tau/\mu^i) \tag{2.24}$$

in which the (4x1) matrix [F] is

$$[F] = [S][I_o^p]\Big|_{\substack{\mu'=\mu^i \\ \phi'=o}} \tag{2.25}$$

and the matrix $[I_o^p]$ is defined in (2.22). The matrix [F] can be expressed as a Fourier series (Ishimaru et al. 1982)

$$[F] = \sum_{m=o}^{\infty}[F]_m^a\cos m\phi + \sum_{m=1}^{\infty}[F]_m^b\sin m\phi \tag{2.26}$$

in which

$$[F]_m^a = \begin{bmatrix} F_{m1} \\ F_{m2} \\ 0 \\ 0 \end{bmatrix}, \quad [F]_m^b = \begin{bmatrix} 0 \\ 0 \\ F_{m3} \\ F_{m4} \end{bmatrix} \tag{2.27}$$

For normally incident (θ^i=0) linearly polarized waves, the terms m=0 and m=2 are the only non-vanishing terms and for normally incident circularly polarized waves the only non-vanishing term is m=0. However, for the obliquely incident linearly polarized waves considered in this work, the number of terms of the infinite series needed to be considered depends on the desired accuracy of the numerical results (see Section 4).

From (2.26) it follows that

$$[F]_o^a = \frac{1}{2\pi}\int_0^{2\pi}[F]d\phi \tag{2.28a}$$

and for $m \geq 1$

$$[F]_m^a = \frac{1}{\pi}\int_0^{2\pi}[F]\cos m\phi d\phi, \quad [F]_m^b = \frac{1}{\pi}\int_0^{2\pi}[F]\sin m\phi d\phi \quad , \tag{2.28b}$$

The incoherent specific intensity matrix [I] can also be expressed in terms of the Fourier series

$$[I] = \sum_{m=o}^{\infty}[I]_m^a\cos m\phi + \sum_{m=1}^{\infty}[I]_m^b\sin m\phi \tag{2.29}$$

Since the elements of the scattering matrix [S] are functions of $\phi'-\phi$ it is expressed as follows

$$[S] = \frac{1}{2\pi}[S]_o^a + \frac{1}{\pi}\sum_{m=1}\left[[S]_m^a\cos m(\phi'-\phi) + [S]_m^b\sin m(\phi'-\phi)\right] \tag{2.30}$$

Furthermore, for the rough sphere f_{ii} are even functions and f_{ij} $(i\neq j)$ are odd functions of $\phi'-\phi$, for m=0,1,2 ... , thus

$$[S]_m^a = \begin{bmatrix} [S_1]_m^a & 0 \\ 0 & [S_4]_m^a \end{bmatrix}, \quad [S]_m^b = \begin{bmatrix} 0 & [S_2]_m^b \\ [S_3]_m^b & 0 \end{bmatrix} \tag{2.31}$$

where $[S_1]_m^a$, $[S_4]_m^a$, $[S_2]_m^b$ and $[S_3]_m^b$ are (2x2) matrices given by

$$[S_i]_m^a = \int_0^{2\pi}[S_i]\cos m(\phi'-\phi)d(\phi'-\phi) \quad , i=1,4 \quad , \tag{2.32a}$$

$$[S_i]_m^b = \int_0^{2\pi}[S_i]\sin m(\phi'-\phi)d(\phi'-\phi) \quad , i=2,3 \tag{2.32b}$$

and $[S_i]$ are the (2x2) matrices defined by

$$[S] = \begin{bmatrix} [S_1] & [S_2] \\ [S_3] & [S_4] \end{bmatrix} \tag{2.33}$$

It therefore follows that the first two elements of the Stokes matrix, I_1 and I_2, are even functions of $\phi'-\phi$ while the last two elements, U and V, are odd functions of $\phi'-\phi$(Ishimaru et al. 1982). Thus for m=0,1,2 ...

$$[I]_m^a = \begin{bmatrix} I_{m1} \\ I_{m2} \\ 0 \\ 0 \end{bmatrix} \text{ and } [I]_m^b = \begin{bmatrix} 0 \\ 0 \\ U_m \\ V_m \end{bmatrix} \text{ where } [I]_o^b = [0] \tag{2.34}$$

The equation of transfer for each of the Fourier components can be written as follows

$$\mu\frac{d}{d\tau}[I]_m = -[I]_m + \int_{-1}^{1}[S]_N[I']_m d\mu' + [F]_m\exp(-\tau/\mu^i) \tag{2.35}$$

in which

$$[I]_m = [I]_m^a + [I]_m^b \ , \ [F]_m = [F]_m^a + [F]_m^b \tag{2.36}$$

and

$$[S_m] = \begin{bmatrix} [S_1]_m^a & [S_2]_m^b \\ -[S_3]_m^b & [S_4]_m^a \end{bmatrix} \tag{2.37}$$

Note that since $[I]_o^b = [0]$, $[S_i]_o^b = [0]$ $(i=2,3)$ and $[F]_o^b = [0]$, the last two elements of the matrix equation (2.35) vanish for the case $m=0$.

The boundary conditions for the Stokes matrix $[I]$ are

$$[I]_m = 0 \quad \text{for } 0 \leq \mu \leq 1 \text{ at } \tau = 0 \tag{2.38a}$$

and

$$[I]_m = 0 \quad \text{for } 0 \geq \mu \geq -1 \text{ at } \tau = \tau_o \tag{2.38b}$$

Equation (2.35) together with the associated boundary conditions (2.38) are solved for $[I]_m$ using the Gaussian quadrature method (to discretize the angle θ) and the matrix characteristic value technique (Ishimaru 1978).

The diffuse scattering intensities I_1 and I_2 correspond to the vertically polarized (E_θ) and horizontally polarized (E_ϕ) waves. However, in practice, the polarization of the receiver is either parallel (E_x) or perpendicular (E_y) to the polarization of the incident wave. The corresponding specific intensities I_x and I_y are called the co-polarized and cross-polarized incoherent intensities, respectively (Cheung and Ishimaru 1980). They are related to the intensities I_1 and I_2 through the linear transformation

$$\begin{pmatrix} I_x \\ I_y \\ U_{xy} \\ V_{xy} \end{pmatrix} = \begin{pmatrix} \langle E_x E_x^* \rangle \\ \langle E_y E_y^* \rangle \\ 2\langle \mathrm{Re}(E_x E_y^*) \rangle \\ 2\langle \mathrm{Im}(E_x E_y^*) \rangle \end{pmatrix} = [R][I] \quad , \tag{2.39}$$

where

$$[R] = \begin{bmatrix} \cos^2\theta\cos^2\phi & \sin^2\phi & -\tfrac{1}{2}\sin 2\phi\cos\theta & 0 \\ \cos^2\theta\sin^2\phi & \cos^2\phi & \tfrac{1}{2}\sin 2\phi\cos\theta & 0 \\ \cos^2\theta\sin 2\phi & -\sin 2\phi & \cos 2\phi\cos\theta & 0 \\ 0 & 0 & 0 & \cos\theta \end{bmatrix} \tag{2.40}$$

The degree of polarization of scattered waves is given by

$$m = \frac{[(I_1 - I_2)^2 + U^2 + V^2]^{\frac{1}{2}}}{I_1 + I_2} \quad . \tag{2.41}$$

All the specific intensities as well as the parameter m are symmetric about the $\phi = 0, 180^\circ$ plane.

It is also necessary to determine the extinction coefficient (total cross section) σ_t in order to solve the equation of transfer (2.2). When "equivalent" spheres do not reasonably represent the basic scattering characteristics of irregularly shaped particles, Greenberg has developed experimental microwave techniques to determine the albedos of particles for which no analytical solution existed (Greenberg 1960; Chylek 1977; Scheurman 1980).

In this work (Section 3) the full wave approach (which unlike the small perturbation method is not restricted to small values of β) is used to evaluate σ_t (Table I) (Bahar et al. 1986) by making judicious use of the forward scattering theorem (Born and Wolf 1964) and the very perceptive observation that for large scatterers (compared to wavelength) the forward scatter "shadow forming wave is the same for all surfaces which have the same shadow line" (Morse and Feshbach 1953).

3. TOTAL CROSS SECTIONS AND ALBEDOS FOR SPHERICAL PARTICLES WITH ROUGH SURFACES

The albedos for particles with rough surfaces are given by

$$A = \sigma_S/\sigma_t = \sigma_S/(\sigma_S + \sigma_a) \quad , \tag{3.1}$$

in which σ_a is the normalized absorption corss section, and σ_S is the normalized scattering cross section (per unit cross-sectional area):

$$\begin{aligned} \sigma_S &= \frac{1}{\pi a^2}\int |\chi|^2 \sigma_M d\Omega + \frac{1}{4\pi}\int \sigma_D d\Omega \\ &\equiv \sigma_{S1} + \sigma_{S2}; \end{aligned} \tag{3.2}$$

the rough surface height characteristic function is χ, and σ_M is the Mie solution for the differential scattering cross section (per unit solid angle) for the smooth (unperturbed) sphere (Ruck et al. 1970; Ishimaru 1978). Thus

$$\sigma_{S1} = (k_o a)^{-2}\int |\chi|^2 [|S_1(\theta)|^2 + |S_2(\theta)|^2] \sin\theta d\theta \quad . \tag{3.3}$$

Explicit expressions for the terms S_1 and S_2 in the Mie solution are given by Ishimaru (1978). Furthermore, σ_R is the diffuse scattering contribution to the cross section. Thus (see Appendix A)

$$\sigma_{S2} = 0.25\int (\langle\sigma_D^{VV}\rangle + \langle\sigma_D^{VH}\rangle + \langle\sigma_D^{HV}\rangle + \langle\sigma_D^{HH}\rangle) \sin\theta d\theta \quad , \tag{3.4}$$

in which $\langle\sigma_D^{PQ}\rangle$ $(P,Q=V,H)$ are the like and cross-polarized diffuse differential scattering contributions to the cross sections (Bahar and Chakrabarti 1985; Bahar and Fitzwater 1986). The above full wave solution represents a weighted sum of two cross sections. The first, σ_{S1} is the modified Mie solution. The degradation of the physical optics contribution is manifested by the factor $|\chi|^2 < 1$ in the integrand of σ_{S1}. The degradation of the physical optics contribution due to the effects of the rough surface is accompanied by an increase in the diffuse scattering contribution. Note, however that since in the forward direction $|\chi|^2 \to 1$, the surface roughness has practically no effect on the shadow forming forward scattered contribution to σ_{S1}.

This term corresponds to Bragg scattering (as predicted by perturbation theory) for $\beta \ll 1$ (Rice 1951). When $\beta=0$ (smooth sphere), σ_s reduces to the Mie solution, and the integration with respect to the solid angle $d\Omega$ can be performed analytically (Ishimaru 1978).

To facilitate the solution of Eq. (3.1), it is rewritten as follows:

$$A = \frac{\sigma_s}{\sigma_t} = \frac{\sigma_s}{\sigma_{to}} \frac{\sigma_{to}}{\sigma_t} = \frac{\sigma_s}{\sigma_{to}} \left(\frac{\sigma_{to}}{\sigma_t}\right)_{P.C.} \tag{3.5}$$

In Eq. (3.5) σ_{to} is the total cross section for the smooth particle. In Eq. (3.5) use has been made of the "forward scattering theorem" (making σ_t proportional to the forward-scattered field) and the fact that for large particles ($k_o a > 1$) the forward-scattered shadow-forming wave is the same for all surfaces which have the same shadow line (Morse and Feshbach 1953). Thus the ratio (σ_{to}/σ_t) in Eq. (3.5) is approximated by the value of the ratio for perfectly conducting particles $(\sigma_{to}/\sigma_t)_{P.C.}$. Therefore, implicit in Eq. (3.5) is the approximation that for conducting particles the above ratio (related to the forward-scattered field intensities that extinguish the incident fields in the forward direction) does not critically depend on the conductivity of the particle. The expressions for σ_{to} and $(\sigma_{to})_{P.C.}$ are given by the corresponding Mie solutions (Ishimaru 1978) for finitely and perfectly conducting spherical particles. To obtain the value for $(\sigma_t)_{P.C.}$ use is made of the fact that

$$(\sigma_t)_{P.C.} = (\sigma_s)_{P.C.} \tag{3.6}$$

where $(\sigma_s)_{P.C.}$ is the normalized scattering cross section for the perfectly conducting particle with the same rough surface as the one under consideration. Thus $(\sigma_s)_{P.C.}$ is given by Eq. (3.2) for the corresponding perfectly conducting particle and Eq. (3.5) is evaluated as follows:

$$A = \left(\frac{\sigma_s}{\sigma_{to}}\right) \Big/ \left(\frac{\sigma_s}{\sigma_{to}}\right)_{P.C.} = A_1/A_2 \quad . \tag{3.7}$$

Examine Eq. (3.7) for two limiting cases of particular interest. As the conductivity of the particle increases $A_1 \to A_2$ and $A \to 1$. Furthermore, as $\beta \to 0$ (small roughness) $A_2 \to 1$, since $(\sigma_s)_{PC} = (\sigma_t)_{PC} + (\sigma_{to})_{PC}$ and $A \to A_1 = \sigma_s/\sigma_{to}$. As expected, the albedo approaches unity for highly conducting particles and approaches the corresponding value for smooth particles as $\beta \to 0$.

4. ILLUSTRATIVE EXAMPLES

For the illustrative examples considered in this work, the particle random rough surface height h (measured normal to the unperturbed surface) is assumed to be homogeneous and isotropic and the unperturbed surface is assumed to be spherical (2.1). Thus, the rough surface height autocorrelation function $\langle h(\bar{r})h(\bar{r}')\rangle$ is only a function of the distance $r_d = |\bar{r}-\bar{r}'| = (x_d^2 + z_d^2)^{\frac{1}{2}}$ measured along the surface of the (unperturbed) spherical particle of radius a. It is also assumed that the rough surface correlation distance r_c (where $\langle hh'\rangle \to \langle h^2\rangle \exp(-1)$) is smaller than the circumference of the particle. The correlation length is related to the mean square height $\langle h^2\rangle$ and the total mean square slope $\langle \sigma_s^2\rangle$ through the expression

$$r_c = 2(\langle h^2\rangle/\langle \sigma_s^2\rangle)^{\frac{1}{2}} \tag{4.1}$$

The surface height spectral density function $W(v_x, v_z)$ is the two dimensional Fourier transform of the surface height autocorrelation function $\langle hh'\rangle$. Since the rough surface is assumed to be homogeneous and isotropic the spectral density function is only a function of

$$v_T = (v_x^2 + v_z^2)^{\frac{1}{2}} \tag{4.2}$$

Thus

$$W(v_x, v_z) = \frac{1}{\pi^2} \int_{-\infty}^{\infty} \langle hh'\rangle \exp(iv_x x_d + iv_z z_d)\, dx_d\, dz_d$$

$$= \frac{2}{\pi} \int_0^{\infty} \langle hh'\rangle J_o(v_T r_d) r_d\, dr_d \tag{4.3}$$

in which $J_o(v_T r_d)$ is the zero order Bessel function of the first kind and v_x and v_z are components of the vector $\bar{v} = k_o(\bar{n}-\bar{n}')$ in the direction of the unit vectors $\bar{n}_1$ and $\bar{n}_3$ tangent to the surface of the unperturbed sphere. In view of the Fourier transform relationship between $\langle hh'\rangle$ and W

$$\langle hh'\rangle = \int_{-\infty}^{\infty} \frac{W(v_x, v_z)}{4} \exp(-iv_x x_d - iv_z z_d)\, dv_x\, dv_z$$

$$= \frac{\pi}{2} \int_0^{\infty} W(v_T) J_o(v_T r_d) v_T\, dv_T \tag{4.4}$$

The following special form is assumed in this work for the surface height spectral density function

$$W(v_T) = \frac{2c}{\pi} \left[\frac{v_T}{v_T^2 + v_m^2}\right]^6 \tag{4.5}$$

Thus the surface height autocorrelation function is

$$R(\xi) = [1 - \frac{3\xi^2}{8} + \frac{3\xi^4}{32} + \frac{\xi^6}{3072}]\xi K_1(\xi)$$

$$+ [\frac{1}{2} - \frac{\xi^2}{4} + \frac{\xi^4}{96}]\xi^2 K_o(\xi) \tag{4.6}$$

in which K_o and K_1 are the modified Bessel functions of the second kind of order zero and one respectively (Abramowitz and Stegun 1964) and the dimensionless argument is

$$\xi = v_m r_d \tag{4.7}$$

The dominant roughness scale (where $W(v_T)$ is maximum) is $v_T = v_m$ and $W(v_m) = C/128\pi v_m^4$. The mean square height is

$$\langle h^2 \rangle = \frac{\pi}{2}\int_0^\infty W(v_T)dv_T = C/210v_m^6 \tag{4.8}$$

and the total mean square slope is

$$\langle \sigma_s^2 \rangle = \frac{\pi}{2}\int_0^\infty W(v_T)v_T^3\, dv_T = C/84v_m^4 \tag{4.9}$$

Thus

$$r_c = 1.26/v_m \tag{4.10}$$

Two special cases are considered in detail at infrared and optical frequencies.

Case (a) $\lambda = 10\mu$ $D = 5\lambda$ $\epsilon_r = 1.5\text{-}i8$ (dissipative dielectric)

Case (b) $\lambda = 0.555\mu$ $D = 10\lambda$ $\epsilon_r = 1.40\text{-}i12$ (aluminum, Ehrenreich 1965)

The case which includes the effects of particle size distribution has been considered recently for vertical incidence ($\theta^i=0$) (Bahar and Fitzwater 1986b). For case (a) ($D=5\lambda$) it is necessary to use a Gaussian quadrature formula of order 20 to discretize the angle θ (Abramowitz and Stegun 1964) and for case (b) ($D=10\lambda$) since the differential scattering cross sections are very sharply peaked in the forward direction it is necessary to use a Gaussian quadrature formula of the order 32. The number of terms needed in the Fourier series expansions for the incoherent specific diffuse intensities depends on the angle of incidence θ^i. As was noted, for normal incidence all the terms of the Fourier series except m=0 and m=2 vanish. For case (a) it is necessary to account for the terms m=0,1,...16 when $\theta^i=15^\circ$ and when $\theta^i=30^\circ$ it is necessary to account for the terms m=0,1,2...24 to obtain two significant figure accuracy for the excitation matrix F (2.25).

The values of σ_{s1}, σ_{s2}, σ_s, A_1 and A_2 together with the corresponding values for the albedo A and the total cross section σ_t are given in Table I as functions of roughness parameter β for case (b) with $\langle\sigma_s^2\rangle = 0.101$. The corresponding values for the correlation length $r_c(k_0^2r_c^2=\beta/\langle\sigma_s^2\rangle)$ and v_mD are also given in the table. The values for the scattering cross section σ_{s0}, the total cross section σ_{t0} and the albedo A_0 are also given for the smooth sphere ($\beta=0$). In Fig. 3 σ_{s1}, σ_{s2} and σ_s are plotted as functions of β while the albedo A and the total cross section σ_t are plotted in Fig. 4. Since $|\epsilon_r| >>1$, σ_s, σ_t and A decrease slightly with increasing roughness while the absorption cross section σ_a increases slightly with increasing roughness. As expected σ_{s1}, which includes the specular point contribution, decreases and σ_{s2} the diffuse scattering contribution increases as the roughness increases. Note that σ_{s1} and σ_{s2} vary rapidly for small values of β, however as β becomes very large they both approach unity. This is because as β increases the specularly reflected contribution vanishes and what is left in σ_{s1} is only the contribution from the shadow forming, forward scattered wave. The specularly reflected power by the smooth sphere ($\beta=0$) essentially becomes diffusely scattered by the sphere with the rough surface for $\beta >> 1$. Thus the normalized scattering cross section σ_s remains approximately two for $1 < \beta < 10$ in agreement with the phenomenon referred to as the "extinction paradox" (Van de Hulst 1957; Ishimaru 1978).

In Figures 5 and 6 the diffuse specific intensities I_1 and I_2 are plotted as functions of the forward scatter angle $\theta(\phi=0,180^\circ)$ for a right circularly polarized infrared excitation $[I_o^R]$ (2.22) at normal incidence ($\mu^i=1$) (case a). The optical thickness of the layer of particles is $\tau_o=1$. The rough surface of the particle is given by (4.5) with $v_mD=4$. Thus the correlation length is $r_c=0.101$ mD. The roughness parameter is $\beta=10$, corresponding to a mean square slope $\langle\sigma_s^2\rangle = \beta/k_0^2r_c^2 = 1/\pi^2$. The solid curves are the single scatter results for smooth and rough spheres. Thus the particle surface roughness tends to smooth out the undulations in the specific intensities as θ, the forward scatter angle increases. The multiple scatter results for the rough and smooth spheres are given by the symbols (Δ) and (+) respectively. Thus, in the forward scatter direction there is very little difference between the multiple and single scatter results. However, away from the forward scatter direction the specific intensities for the rough particle are smaller than the corresponding results for the smooth particle because the albedos of the rough particles are slightly smaller. Note that I_1 which corresponds to the vertically polarized component is more oscillatory than I_2 which corresponds to the horizontally polarized component.

In Figures 7 and 8 the parallel I_x and perpendicular I_y diffuse specific intensities (2.39) are plotted as functions of the azimuth angle ϕ for the forward scatter direction $\theta=15.3^\circ$. The excitation is a normally incident linearly polarized wave, $[I_o^V]$ (the electric field is in the $\hat{x}$ direction) at $\lambda=0.555\mu$m (case b). The optical thickness of the layer is $\tau_o=0.1$ The rough surface of the particle is given by (4.5) with $v_mD=4$ ($r_c=0.101$mD) and $\beta=40$ ($\langle\sigma_s^2\rangle=1/\pi^2$). For the thin layers, the single (solid curves) and multiple scatter results for I_x are close, however there is a significant difference between the results for the smooth and rough spheres. In Figure 8 the sharp nulls in the single scatter results for the smooth particles are due to the fact that smooth particles do not depolarize the incident waves in the scatter plane. This is not the case for the rough particles.

In Figures 9 and 10 the diffuse specific intensities I_1 and I_2 are plotted as functions of the forward scatter angle $\theta > 0(\phi=0)$ and $\theta < 0(\phi=180^\circ)$ for an obliquely incident ($\theta^i=30^\circ$) horizontally polarized $[I_o^H]$, (2.22) infrared excitations (case a). The optical thickness of the layer is $\tau_o=1$. The rough surface of the particle is given by (4.5) with $v_mD=4$ ($r_c=0.101$mD). The roughness parameter is $\beta=10$ ($\langle\sigma_s^2\rangle=1/\pi^2$). Note that the single scatter cross-polarized results (I_1) is zero for the smooth particle. However, for the rough particle the single scatter results become very small only in the forward scatter direction ($\theta=30^\circ$). The like-polarized diffuse specific intensities are insensitive to surface roughness in the direction of the forward scattered lobe. However, the effects of surface roughness are significant away from the forward scatter direction.

In Figures 11 and 12 the diffuse specific intensities I_1 and I_2 are plotted as functions of the forward scatter angle $\theta > 0(\phi=0)$ and $\theta<0$ ($\phi=180^\circ$) for an obliquely incident ($\theta^i=15^\circ$) vertically polarized $[I_o^V]$ (2.22) excitation at $\lambda=0.555\mu$m (case b). The optical thickness of the larger is $\tau_o=1$. The rough surface of the particle is given by (4.5) with $v_mD=4$ ($r_c=0.10$mD). The roughness parameter is $\beta=40$ ($\langle\sigma_s^2\rangle=1/\pi^2$). The particle

surface roughness a little effect on the results for I_1 and I_2 for the forward scatter direction. The single and multiple scatter results for the like-polarized intensity I_1, are practically the same in the forward scatter direction. This is not so for the cross-polarized intensity I_2. Note also that except for the forward scatter direction the diffuse specific intensities for the rough particles are isotropic and the degree of polarization is very small since $I_1 \approx I_2$. Furthermore, the like-polarized intensity I_1 is smaller for the rough particles than for the smooth particles, while the cross-polarized intensity I_2 is larger for the rough particles. This is because the rough particles depolarized the incident waves even in the scatter plane and the albedos for the rough particles are slightly smaller than the albedos for the smooth particles.

In Figures 13 and 14 the degree of polarization m (2.41) is plotted as a function of the azimuth angle ϕ. The excitation at $\lambda = 0.555\mu m$ (case b) is normally incident and linearly polarized (electric field in the E_x direction). The cases shown are for the forward scatter angles $\theta = 15.3^\circ$ and $\theta = 20.8^\circ$ (Fig. 13) and the backward scatter angles $\theta = 170.3^\circ$ and $\theta = 175.8^\circ$. The optical thickness of the layer is $\tau_o=2$. The particle surface roughness is given by (4.5) with $v_m D=4$ ($r_c=0.101\pi D$). The roughness parameter is $\beta \cong 40$ ($\langle\sigma_\beta^2\rangle \approx 1/\pi^2$). The corresponding results are also shown for the smooth particles. The effect of the particle surface roughness becomes increasingly pronounced as the angle between the incident and scatter directions increases. The degree of polarization very significantly depends upon the particle surface roughness.

In Figures 15 and 16, the backward scattered specific intensities I_1 and I_2 respectively are plotted as functions of the scatter angle θ. The excitation at $\lambda = 0.555\mu m$ (case b) is normally incident and linearly polarized (the electric field is in the E_x direction). The optical thickness of the layer is $\tau_o=0.1$. The particle surface roughness is given by (4.5) with $v_m D=4$ ($r_c=0.101\pi D$). The roughness parameter is $\beta=40$ ($\langle\sigma_\beta^2\rangle = 1/\pi^2$). In Figure 15 the results are given in the $\phi = 0,180^\circ$ plane (I_1 is therefore the vertically polarized diffuse scattered intensity). In Figure 16 the results are given in the $\phi=90^\circ,270^\circ$ plane (I_2 is therefore the horizontally polarized diffuse scattered intensity). Since $\tau_o=0.1$ the single scatter (solid lines) and multiple scatter results are not very different. However, the particle surface roughness does have a significant effect on the diffuse specific intensities. Note also that for the smooth particles the vertically polarized diffuse specific intensity (Figure 15) is far more oscillatory than the corresponding horizontally polarized diffuse specific intensity. This results directly from the Mie solution for large conducting spheres. The very pronounced backscatter enhancement has been observed in the laboratory. The phenomenon of backscatter enhancement that is presented in this work is related to the effects of the roughness of the particle and/or to the scatter from moderate to large particles. The numerical results presented in Figures 15 and 16 are obtained from the solution of the unmodified equation of radiative transfer (2.2).

5. CONCLUDING REMARKS

The illustrative examples presented in Section 4 vividly describe the effects of particle surface roughness on the co-polarized and cross-polarized incoherent specific intensities for optical and infrared electromagnetic excitations at normal and oblique incidences.

It is shown that as the surface roughness increases, the specularly reflected contribution to the normalized scattering cross section σ_s decreases while the diffuse scattering term undergoes a corresponding increase. However, the contribution to the scattering cross section from the shadow forming wave is practically uneffected by the particle surface roughness. These results are shown to be consistent with the phenomenon referred to as the "extinction paradox." The albedo A, the scattering cross section σ_s as well as the total cross section σ_t, undergo a small but significant decrease as the roughness parameter β increases.

The corresponding effects of surface roughness on the scattering and total cross section σ_s and σ_t respectively at infrared frequencies as well as the effects of changing the mean square slope $\langle\sigma_\beta^2\rangle$ of the rough surface (while the correlation length r_c is fixed) have also been reported recently (Bahar et al. 1986).

Since the diffuse scattering contributions due to particle surface roughness are negligible in the near forward direction, the primary effect of the surface roughness is to smooth out the side lobe undulations of the specific intensities for the corresponding smooth particles. Furthermore, the particles with rough surfaces more strongly depolarize the incident wave. Thus, since the albedos are smaller for the particles with rough surfaces than for the smooth particles, the co-polarized specific intensities are smaller for the rough particles while the cross-polarized specific intensities are smaller for the smooth particles when the optical thickness of the layer of particles is small; $\tau_o < 1$. However, as the optical thickness of the layer increases ($\tau_o > 1$) both the co-polarized and cross-polarized specific intensities are smaller for the particles with rough surfaces.

In general as the optical thickness increases and multiple scattering effects become significant, the layer consisting of particles with rough surfaces tend to scatter the incident waves in a more isotropic manner. The sharp undulations in the specific intensities are smoothed out and the results become more polarization independent. Thus, the degree of polarization for the particles with rough surfaces is significantly smaller than for the smooth particles. When the layers of particles with rough surfaces are optically thin, the first order single scatter results and the multiple scatter results for the co-polarized and cross-polarized intensity are in very good agreement.

The phenomenon of enhanced backscatter from particles with smooth and rough surfaces has been observed in the numerical results obtained from the solution of the unmodified equation of radiative transfer.

6. REFERENCES

1. Abramowitz, M., and I. A. Stegun (1964), Handbook of Mathematical Functions with Formulas, Graphs, and Mathematical Tables, Appl. Math. Ser. 55, National Bureau of Standards, Washington, D.C.
2. Bahar, E., and S. Chakrabarti (1985), "Scattering and Depolarization by Large Conducting Spheres with Rough Surfaces," Applied Optics, 24, No. 12, p. 1820.
3. Bahar, E., S. Chakrabarti, and M. A. Fitzwater (1986), "Extinction Cross Sections and Albedos for Particles with Very Rough Surfaces," Applied Optics, 25, 2530-2536.
4. Bahar, E., and M. A. Fitzwater (1983), "Backscatter Cross Sections for Randomly Oriented Metallic Flakes at Optical Frequencies—Full Wave Approach," Applied Optics, 23, pp. 3813-3819.

5. Bahar, E., and M. A. Fitzwater (1985), "Like- and Cross-Polarized Scattering Cross Sections for Random Rough Surfaces: Theory and Experiment," Journal of the Optical Society of America A, 2, pp. 2295-2303.
6. Bahar, E., and M. Fitzwater (1986a), "Multiple Scattering by Finitely Conducting Particles with Rough Surfaces at Infrared and Optical Frequencies," Radio Science, 21, No. 4, pp. 689-706.
7. Bahar, E., and M. A. Fitzwater (1986b), "Scattering and Depolarization of Linearly Polarized Waves by Finitely Conducting Particles of Irregular Shape," Journal of Applied Physics, 60, pp. 2123-2132.
8. Born, M., and E. Wolf (1964), Principles of Optics, Pergamon Press, New York.
9. Chandrasekhar, S. (1950), Radiative Transfer. Dover, Publ., New York.
10. Cheung, R.L.-T., and A. Ishimaru (1982), "Transmission, Backscattering, and Depolarization of Waves in Randomly Distributed Spherical Particles," Applied Optics, 21, No. 20, p. 3792.
11. Chylek, Petr (1977), "Extinction Cross Sections of Arbitrarily Shaped Randomly Oriented Nonspherical Particles," Journal of the Optical Society of America, 67, No. 10, pp. 1348-1350.
12. Ehrenreich, H. (1965), "The Optical Properties of Metals," IEEE Spectrum, 8, p. 162.
13. Greenberg, J. M. (1960), "Scattering by Nonspherical Particles," Journal of Applied Physics, 31, p. 82.
14. Ishimaru, A. (1978), Wave Propagation and Scattering in Random Media, Academic, New York.
15. Ishimaru, A., and R.L.-T. Cheung (1980), "Multiple Scattering Effects in Wave Propagation Due to Rain," Ann. Telecommun., 35, p. 373.
16. Ishimaru, A., R. Woo, J. W. Armstrong, and D. C. Blackman (1982), "Multiple Scattering Calculations of Rain Effects," Radio Science, 17, No. 6, pp. 1425-1433.
17. Kiehl, J. T., M. W. Ko, A. Mugnai, and Petr Chylek (1980), Perturbation Approach to Light Scattering by Nonspherical Particles, chapter in Light Scattering by Irregular Shaped Particles (Editor D. W. Scheurman), Plenum Press, New York.
18. Morse, P. M., and H. Feshbach (1953), Methods of Theoretical Physics, McGraw-Hill, New York.
19. Rice, S. O. (1951), "Reflection of Electromagnetic Waves from a Slightly Rough Surface," Communication of Pure and Applied Math., 4, pp. 351-378.
20. Ruck, G. T., D. E. Barrick, W. D. Stuart, and C. K. Krichbaum (1970), "Radar Cross Section Handbook," Plenum, New York.
21. Sancer, M. H. (1969), "Shadow-Corrected Electromagnetic Scattering from a Randomly Rough Surface," IEEE Trans. Antennas Propag. AP-17, p. 577.
22. Scheurman, D. W. (1980), Editor, Light Scattering by Irregular Shaped Particles, Plenum Press, New York.
23. Van de Hulst, H. C. (1957), Light Scattering by Small Particles, Wiley, New York.
24. Yeh, C., and K. K. Mei (1980), On the Scattering from Arbitrarily Shaped Inhomogeneous Particles, chapter in Light Scattering by Irregular Shaped Particles, (Editor D. W. Scheurman) Plenum Press, New York.

APPENDIX A

Assume that an $\bar{a}_x$ directed electric field, propagating in the $-\bar{a}_z$ direction is incident upon the sphere with rough surfaces. For an observer in the direction $\bar{r}^s(\theta,\phi)$, the vertically and horizontally incident fields for the scatter plane normal to $\bar{r}^i \times \bar{r}^s$ are, respectively

$$E_\ell^i = E_x \cos\phi \tag{A.1}$$

$$E_r^i = -E_x \sin\phi \tag{A.2}$$

Thus using equation (2.8)

$$E_\ell^D = (f_{VV}^D E_x \cos\phi - f_{VH}^D E_x \sin\phi) \frac{\exp(-ik_o r)}{r} \tag{A.3}$$

$$E_r^D = (f_{HV}^D E_x \cos\phi - f_{HH}^D E_x \sin\phi) \frac{\exp(-ik_o r)}{r} \tag{A.4}$$

where f_{ij}^D are the diffuse scattering coefficients in the scatter plane. The diffuse scattering contribution due to the surface roughness is

$$\sigma_D = \frac{4\pi r^2}{A_y} \left[\frac{|E_\ell^D|^2 + |E_r^D|^2|}{|E_x|^2} \right] \tag{A.5}$$

Thus for normalized incident fields

$$\sigma_{s2} = \frac{1}{4\pi} \iint \frac{4\pi r^2}{A_y} (|E_\ell^D|^2 + |E_r^D|^2) \sin\theta d\theta d\phi \tag{A.6}$$

Since

$$\int_0^{2\pi} \cos^2\phi d\phi = \int_0^{2\pi} \sin^2\phi d\phi = \pi \tag{A.7}$$

and

$$\int_0^{2\pi} \sin\phi \cos\phi d\phi = 0 \tag{A.8}$$

thus equation (A.6) reduces to

$$\sigma_{s2} = \frac{\pi}{A_y} \int (|f_{VV}^D|^2 + |f_{VH}^D|^2 + |f_{HV}^D|^2 + |f_{HH}^D|^2) \sin\theta d\theta \tag{A.9}$$

The differential scattering cross sections per unit solid angle per unit cross sectional area are defined as (Bahar and Fitzwater, 1986a)

$$\langle \sigma_D^{PQ} \rangle = \frac{4\pi}{A_y} |f_{PQ}^D|^2 \tag{A.10}$$

Therefore the total diffuse scattering cross sections (per unit cross sectional area) are

$$\sigma_{s2} = \frac{1}{4} \int^{\pi} (\langle \sigma_D^{VV} \rangle + \langle \sigma_D^{VH} \rangle + \langle \sigma_D^{HV} \rangle + \langle \sigma_D^{HH} \rangle) \sin\theta d\theta \tag{A.11}$$

ACKNOWLEDGMENTS

This investigation was sponsored by the U.S. Army Research Office Contract DAAG-29-82-K-0123. The authors acknowledge the National Science Foundation Engineering Supercomputer Grant MCS 8515794/5. The manuscript was typed by Mrs. E. Everett.

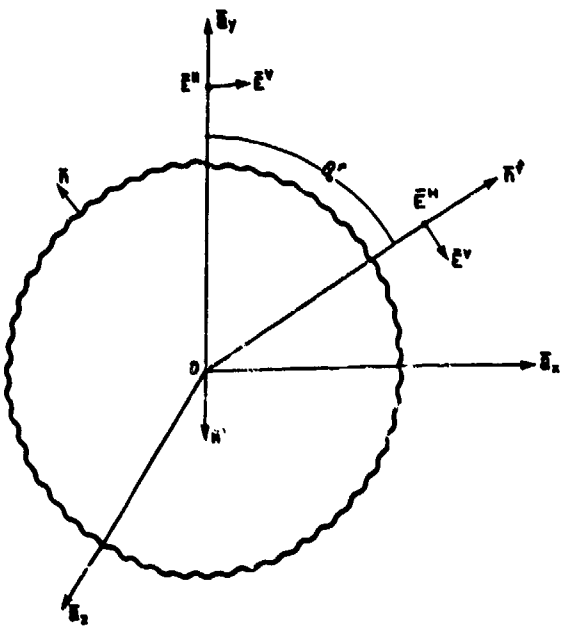
TABLE I. Extinction Cross Section and Albedos for Spheres with Rough Surfaces

β	1	5	10	15	20	40
σ_{s1}	1.747	1.306	1.190	1.142	1.112	1.047
σ_{s2}	0.3345	0.7174	0.7989	0.8241	0.8358	0.8508
σ_s	2.082	2.024	1.989	1.966	1.948	1.898
A_1	0.9214	0.8927	0.8805	0.8701	0.8621	0.8403
A_2	1.084	1.017	1.010	1.003	0.9976	0.9794
$A = A_1/A_2$	0.8999	0.8803	0.8719	0.8671	0.8642	0.8579
$\sigma_t = \sigma_s/A$	2.313	2.299	2.281	2.267	2.254	2.21
$v_m D$	25.16	11.24	7.9	6.52	5.64	
$r_c/\pi D$	0.016	0.036	0.050	0.062	0.072	0.101

$\lambda = 0.555\mu m$ $\quad D = 10\lambda$ $\quad \varepsilon_r = -40-112$

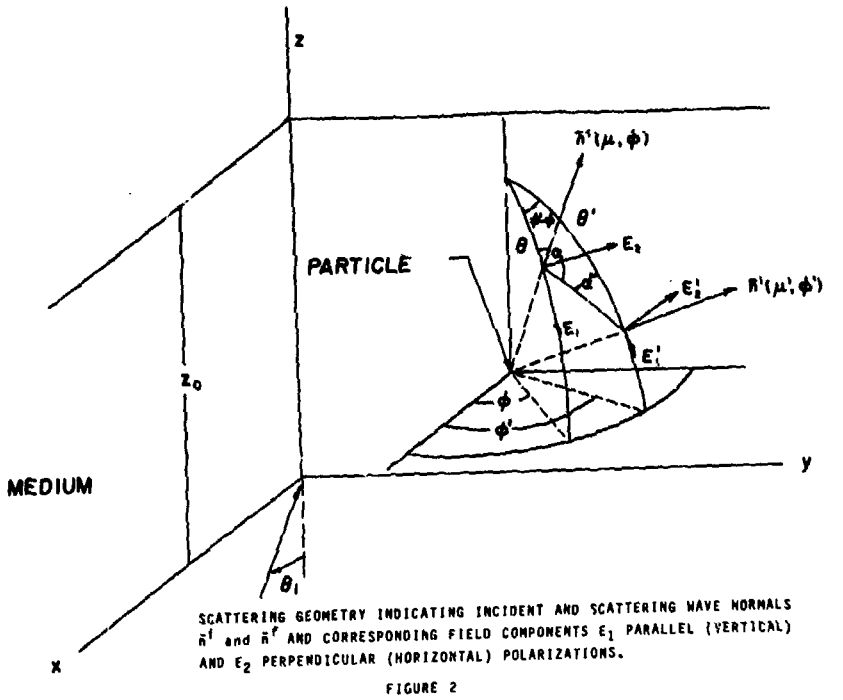
$$W = \frac{2\beta}{\pi}\left[\frac{v_T}{v_T^2 + v_m^2}\right]^8 , \quad \langle\sigma_s^2\rangle = 0.101$$

For $\beta = 0$: $\sigma_{so} = 2.114$ $\quad \sigma_{to} = 2.259$ $\quad A_o = 0.936$



SCATTERING GEOMETRY FOR A ROUGH CONDUCTING SPHERE.

FIG. 1



SCATTERING GEOMETRY INDICATING INCIDENT AND SCATTERING WAVE NORMALS $\bar{n}^i$ and $\bar{n}^r$ AND CORRESPONDING FIELD COMPONENTS E_1 PARALLEL (VERTICAL) AND E_2 PERPENDICULAR (HORIZONTAL) POLARIZATIONS.

FIGURE 2

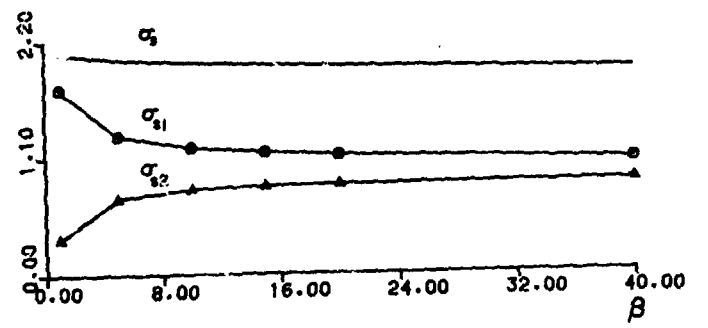


Fig. 3. Scattering cross sections σ_{s1}, σ_{s2} and σ_s versus the roughness parameter β (Table I), case (b).

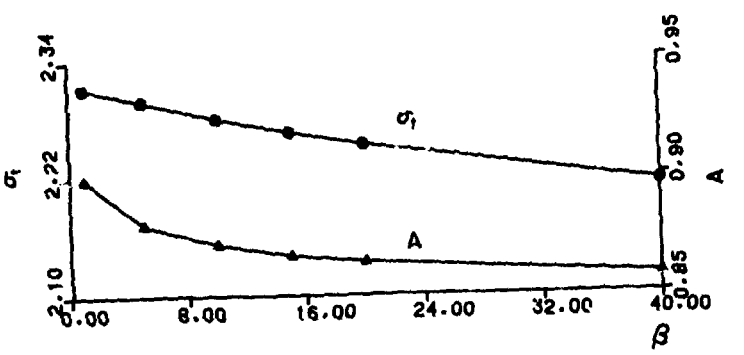


Fig. 4. Extinction cross sections σ_t and albedo A versus the roughness parameter β (Table I), case (b).

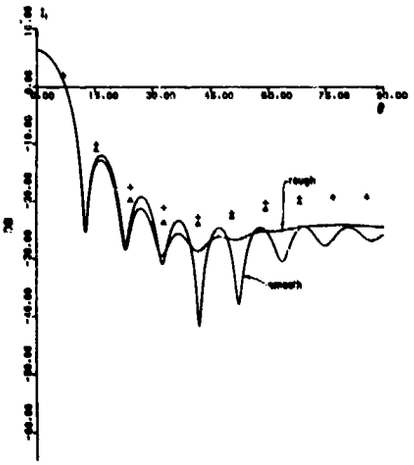


Fig. 5. Specific incoherent intensity I_1 for a right circularly polarized wave, normal incidence, case (a), β=10, $v_m D$=4, τ_o=1, ϕ=0°,180°. First order (—), smooth and rough particles. Multiple scatter (+) smooth, (Δ) rough.

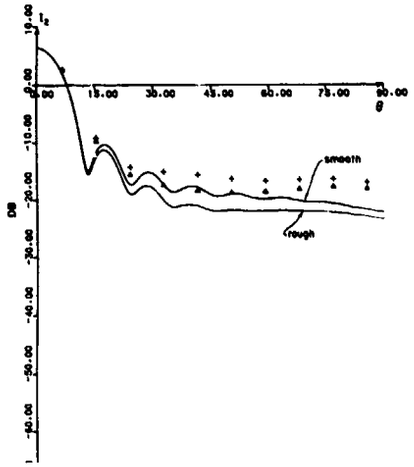


Fig. 6. Specific incoherent intensity I_2 for a right circularly polarized wave, normal incidence, case (a), β=10, $v_m D$=4, τ_o=1, ϕ=0°,180°. First order (—), smooth and rough particles. Multiple scatter (+) smooth, (Δ) rough.

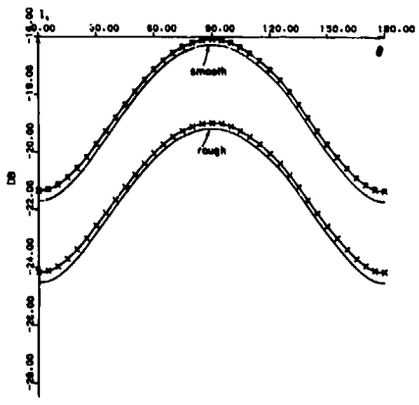


Fig. 7. Specific incoherent intensity I_x for a linearly polarized wave, normal incidence, case (b), β=40, $v_m D$=4, τ_o=.1, θ=15.3°. First order (—), smooth and rough particles. Multiple scatter (X) smooth, (X) rough.

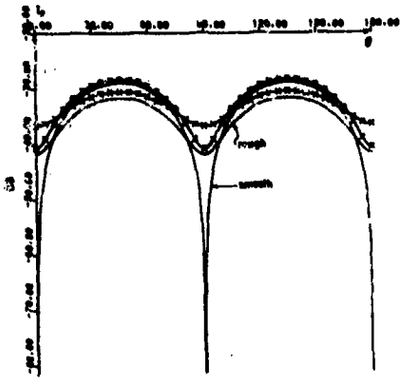


Fig. 8. Specific incoherent intensity I_y for a linearly polarized wave, normal incidence, case (b), β=10,v_mD, τ_o=.1, θ=15.3°. First order (—), smooth and rough particles. Multiple scatter (X) smooth, (X) rough.

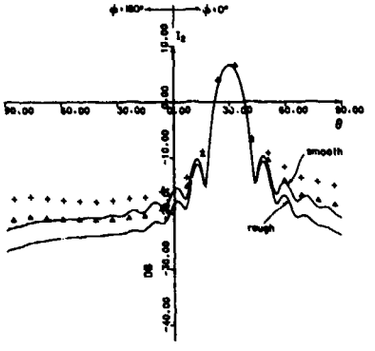


Fig. 9. Specific incoherent intensity I_1 for a horizontally polarized wave, obliquely incident, θ_o^i=30°, case (a), β=10,v_mD=4, τ_o=1, ϕ=0°,180°. First order (—), rough particles. Multiple scatter (+) smooth, (Δ) rough.

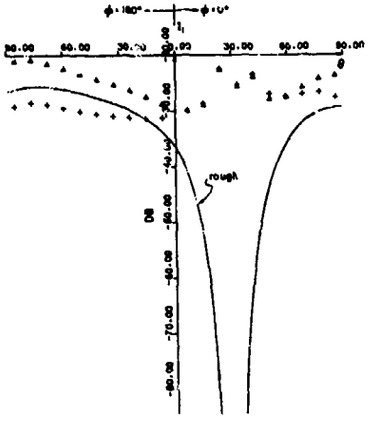


Fig. 10. Specific incoherent intensity I_2 for a horizontally polarized wave, obliquely incident, θ_o^i=30°, case (a), β=10,v_mD=4, τ_o=1, ϕ=0°,180°. First order (—), smooth and rough particles. Multiple scatter (+) smooth, (Δ) rough.

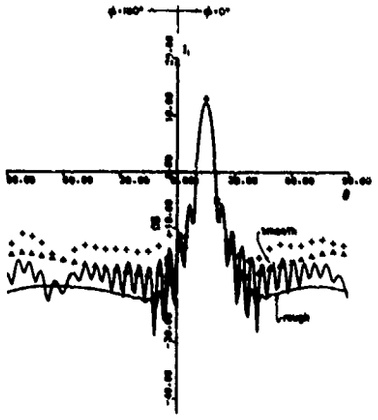


Fig. 11. Specific incoherent intensity I_1 for a vertically polarized wave, obliquely incident, θ_o^i=15°, case (b), β=40, $v_m D$=4, τ_o=1, ϕ=0°,180°. First order (—), smooth and rough particles. Multiple scatter (+) smooth, (Δ) rough.

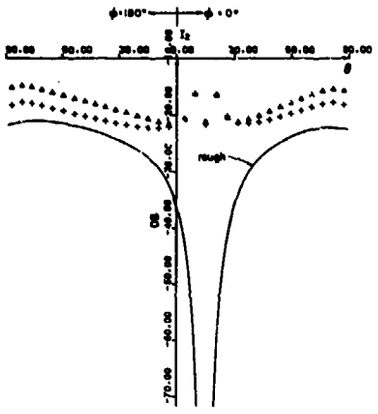


Fig. 12. Specific incoherent intensity I_2 for a vertically polarized wave, obliquely incident, θ_o^i=15°, case (b), β=40, $v_m D$=4, τ_o=1, ϕ=0°,180°. First order (—), rough particles. Multiple scatter (+) smooth, (Δ) rough.

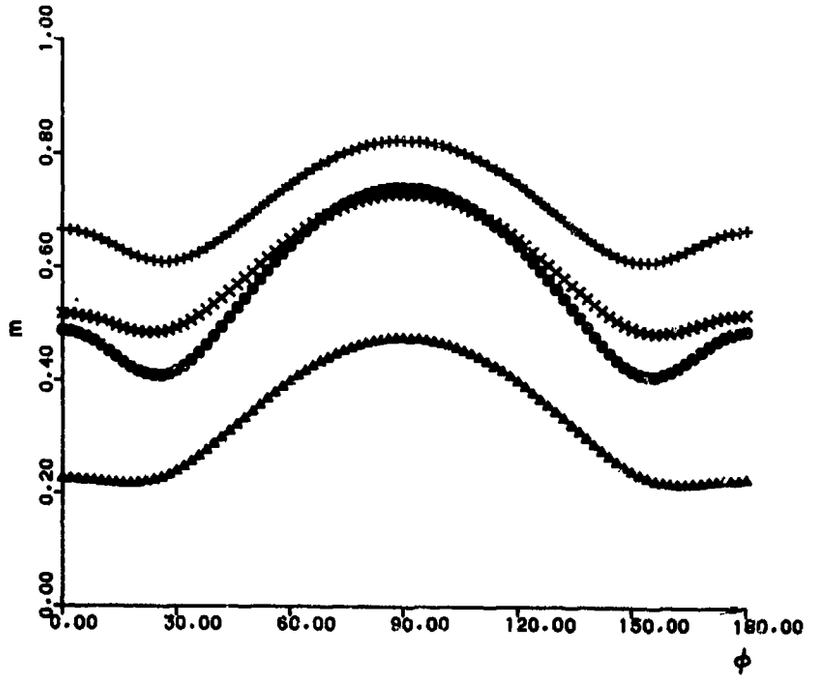


Fig. 13. Degree of polarization π. Normal incidence, linearly polarized wave, case (b), β=40, $v_m D$=4, τ_o=2.θ=15.3° (+) smooth, (X) rough; θ=20.8°, (0) smooth, (Δ) rough.

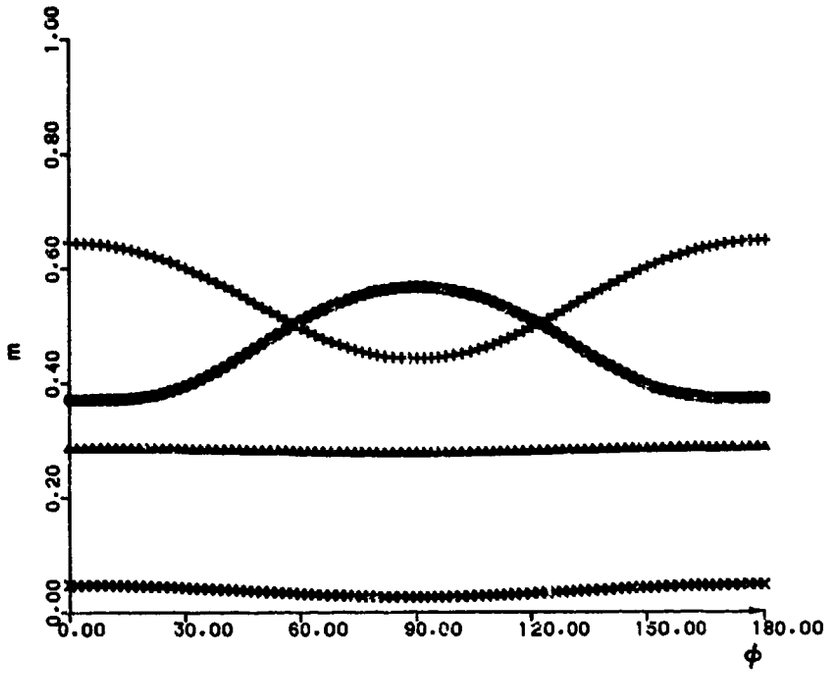


Fig. 14. Degree of polarization m. Normal incidence, linearly polarized wave, case (b), β=40, $v_m D$=4, τ_o=2.8=170.3° (+) smooth, (X) rough, θ=175.8°, (O) smooth, (Δ) rough.

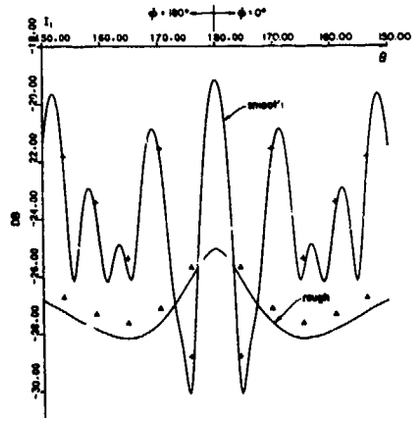


Fig. 15. Backscattered specific incoherent intensity I_1 for a vertically polarized wave, normal incidence, case (b), β=40, $v_m D$=4, τ_o=.1, ϕ=0°,180°. First order (—), smooth and rough particles. Multiple scatter (+) smooth, (Δ) rough.

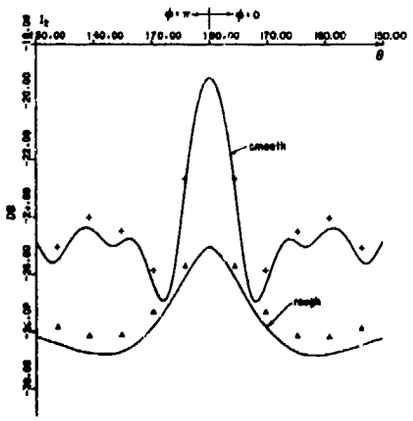


Fig. 16. Backscattered specific incoherent intensity I_2 for a vertically polarized wave, normal incidence, case (b), β=40, $v_m D$=4, τ_o=.1, ϕ=90°,270°. First order (—), smooth and rough particles. Multiple scatter (+) smooth, (Δ) rough.

HEIRARCHICAL SCATTERING MODELS

by
E Jakeman
Royal Signals and Radar Establishment
St Andrews Road
Malvern, Worcestershire WR14 3LG
United Kingdom

SUMMARY

The most familiar descriptor of multi-scale structure in continuous scattering media is the power law spectrum which characterises heirarchical or fractal behaviour. In this paper the mathematical and phenomenological implications of adopting such models in scattering calculations will be discussed with particular reference to the statistical properties of amplitude scintillation generated by a phase changing screen or diffuser. A brief summary of results obtained when the phase itself is a Gaussian random fractal will be followed by a more detailed review of the case when the phase gradient is fractal. This last model is not only more realistic for fluid systems subject to diffusive or other smoothing effects, but is also amenable to mathematical and numerical analysis. The geometrical optics contribution to the scattered intensity pattern is particularly easy to calculate and a number of new results for the statistics of ray density fluctuations will be presented.

1 INTRODUCTION

The subject matter of this paper forms part of a larger programme of work to investigate the non-Gaussian fluctuations of scattered waves which arise when the scattering region contributing at the detector is comparable to, or smaller than, the largest scale size present in the scattering medium. This programme began in the mid-seventies with an experimental and theoretical investigation of the far field scintillation of laser light scattered by small areas of turbulently convecting liquid crystal [1,2]. The realisation that this system behaved as a random phase changing screen enabled early theoretical results and developing phenomenology to be applied more widely to the scattering of electromagnetic radiation and scalar waves by rough surfaces, thin diffusing layers and extended media containing refractive index fluctuations. Probably the most important development from this early work has been that of a non-Gaussian noise model based on the class of K-distributions [3]. Although originally justified by semi-empirical arguments based on a random walk model for the scattering, together with requirements of mathematical simplicity and data fitting, the K-distribution model has been surprisingly successful not only in the original context of microwave sea echo [3,4], but also in characterising microwave land clutter [5], optical atmospheric propagation effects [6,7], optical scattering by thermal plumes and mixing layers [8,9] and even underwater acoustic propagation effects [10]. It has been conjectured [11] that this is a consequence of the multiple scales present in the scattering systems, which leads to modulation of the smaller scales by larger ones. The inclusion of step number fluctuations in a random walk model for the scattering can be used to take account of the consequent variations in scatter density. It is found [11,12] that a negative binomial distribution of step number (corresponding to a gamma distributed scatterer density) is required to generate K-distributed noise, which can then be interpreted as a combination of interference effects and underlying density fluctuations ie as a Gaussian speckle pattern with locally varying mean.

Although the above arguments provide a plausible mechanism leading to K-distributed noise, they do not explain why the model should be widely applicable, because a specific model has had to be adopted for the underlying scatterer density variations. Whereas the speckle or interference contribution to the scattered wave statistics, being a consequence of the central limit theorem, is expected to be a widely observed effect, it is more difficult to explain the common occurrence of gamma distributed scatterer density fluctuations. Some progress has been made in this direction, however, by recognising that universal behaviour may follow not only as a consequence of large number limits, but also as a manifestation of the widespread occurrence in nature of heirarchical systems, ranging from phase transitions and critical phenomena at the microscopic level to turbulence and to land and sea surfaces on a geophysical scale [13]. The work to be described in this paper began with an investigation of the simplest class of heirarchical scattering systems - the Gaussian random fractal phase screens - which was undertaken in the hope that properties of the scattered wave would confirm the significance of the K-distribution model. One configuration has indeed been shown to lead to K-distributed intensity fluctuations, [14], but the investigation has in addition, and perhaps more importantly, shed new light on the physical significance of power law spectral models and on the mathematical implications of employing them in scattering calculations [15]. It has also revealed a class of scattering models which cause geometrical optics effects without singularities such as caustics. The principal part of this paper will be concerned with these "fractal slope" phase screen models [16] which generate ray density statistics that are finite and amenable to mathematical analysis. Their properties are also relatively simple to simulate numerically (a feature which will be demonstrated in the companion paper [17]) and appear to be in agreement with some experimental data [18,19].

In the next section scattering by a Gaussian random phase screen which introduces a fractal distortion into an incident wave will be discussed. Section 3 will introduce the notion of fractal slope models and show how such behaviour can follow from the inner scale smoothing of a fractal. Existing theory will be reviewed briefly, with most recent results on ray density statistics being discussed in section 4. A summary and conclusions will be presented in the final section 5.

2 SCATTERING BY A GAUSSIAN RANDOM FRACTAL PHASE SCREEN

The statistical properties of waves which have been scattered by a random phase changing screen are given in a physical optics approximation by the Huyghens-Fresnel diffraction integral at the detection point r [20].

$$\varepsilon(\underset{\sim}{r}) = F(\theta)\int_{-\infty}^{\infty} d^2r' A(\underset{\sim}{r}') \exp[ikr'^2/2z - i\underset{\sim}{k}.\underset{\sim}{r}' \sin\theta + i\phi(\underset{\sim}{r}')]. \quad (1)$$

Here r' is measured in the plane of the phase screen, z is the screen-detection plane distance, θ is the angle between the propagation and viewing directions, ϕ is the phase distortion introduced by the screen, $k = 2\pi/\lambda$ is the wave vector, A an aperture function and F an angle-dependent factor. If the phase screen is placed at the waist of a laser beam then

$$A(\underset{\sim}{r}') = \exp(-r'^2/W^2) \quad (2)$$

Assuming relation (2) often simplifies the calculations. Two scattering geometries are normally examined: (1) the far field or Fraunhofer limit where $kW^2/2z << 1$ and (2) the Fresnel limit $kW^2/2z >> 1$. In the far field it is well known that when $W >> \xi_o$, where ξ_o is the largest scale size of the phase fluctuations, then the scattered field is a complex Gaussian process so the intensity, $I = |\varepsilon|^2$, forms a "speckle" pattern with distribution

$$p(I) = \frac{1}{\langle I\rangle}\exp\left(-\frac{I}{\langle I\rangle}\right) \quad (3)$$

and moments $$\frac{\langle I^n\rangle}{\langle I\rangle^n} = n! \quad (4)$$

When W is comparable to or smaller than ξ_o the statistics are non-Gaussian and the normalised moments exceed the values given by equation (4). It is simplest to evaluate the Fresnel limit by setting $A(\underset{\sim}{r}') \equiv 1$. For sufficiently large propagation distances, such that an area of the screen which is much larger than ξ_o contributes at the detector, the field is again a complex Gaussian process, but close to the phase screen geometrical and/or diffraction effects limit the area contributing and again non-Gaussian statistics are observed. It is these non-Gaussian regimes with which this paper is concerned.

A measure of the information content of the intensity fluctuations is provided by their statistical properties. In the Fraunhofer region these depend on the illuminated area and scattering angle θ. In the Fresnel region they are a function of propagation distance. In order to calculate the statistical properties of the intensity from equation (1) a model has to be assumed for the properties of ϕ. This is usually chosen to be a Gaussian process so that only the spectrum or its Fourier transform - the phase auto-correlation function - remains to be specified. When the latter possesses an even powered expansion about the origin, the phase model is said to be "smoothly varying" since the phase function is then differentiable to all orders. It is now well-known that non-Gaussian scattering by such models is dominated by the presence of geometrical optics features such as caustics in the intensity pattern [21-23]. In the Fresnel region the second normalised intensity moment increases from unity at the screen, where there are only phase fluctuations, to a peak in the focussing region, where lens like regions of the screen generate single caustics, and then decreases slowly with increasing propagation distance to a value of two, where the overlap of effects generated by independent regions of the screen cause convergence to Gaussian speckle statistics given by equation (4). In the far field a similar shaped curve is obtained when the second normalised intensity moment is plotted against illuminated area. In this case however, the geometrical features in the pattern are masked at small values of the illuminated area by aperture diffraction. As the illuminated area is increased, geometrical features of the pattern emerge and its contrast again peaks as single caustics fall on the detector. Thereafter the fluctuations subside to Gaussian speckle as the aperture begins to include many independent scattering elements. Experimental measurements on a number of different scattering systems have confirmed the behaviour described above [24].

In the case of fractal models the phase is not stationary and the structure function is a more convenient measure of coherence than the phase autocorrelation function. It is useful to write the phase distortion in terms of a notional height $\phi(r) = kh(r)$ with structure function

$$D(\underset{\sim}{r}) = \langle(h(0) - h(\underset{\sim}{r}))^2\rangle. \quad (5)$$

For a simple corrugated fractal diffuser

$$D(x) = |x|^{\nu} L^{2-\nu} \qquad \text{with} \qquad 0 < \nu < 2 \tag{6}$$

where the "topothesy" L is a measure of the average rate of change of height [25] and ν is related to a fractal "dimension" D by $\nu = 2(2-D)$ [26]. Note that (6) possesses a certain scale invariance since the relation remains unchanged if x is multiplied by a factor k and h by a factor $k^{\nu/2}$. This shows that h is "self-affine" under magnification. Phase screen models of this type have been investigated by a number of authors over the years [20,26-35] following the pioneering work on propagation through turbulent media by Tatarski [36]. However, it was not until the concepts of fractal geometry [37] were brought to bear on the problem [26] that its physical interpretation and mathematical implications were fully clarified. Analytical work and numerical calculations have shown that the model generates only weak non-Gaussian effects by comparison with the class of smoothly varying screens [15], both in Fresnel region and far field scattering geometries. This is now attributed to the absence of geometrical optics effects in patterns generated by fractal-diffusers which follows from the fact that a profile governed by the structure function (6) is continuous but not differentiable and cannot therefore give rise to rays. Experiments on artificially constructed fractal surfaces have confirmed both the predictions of theory and their interpretation [38,39]. The observed non-Gaussian intensity patterns are qualitatively different from those generated by smoothly varying diffusers [40,24] and are characterised by combinations of powers of the parameters k, L and either W or z reflecting the self-affine geometry of the scatterer.

Because the non-Gaussian intensity fluctuations generated by fractal phase screens are relatively weak they are perhaps a less useful source of information than their smoothly varying counterparts. They also provide a less serious limitation on system performance and a more detailed analysis of their properties will therefore not be given here. It is worth noting, however, that the distribution of mean intensity as a function of angle in the far field is a sensitive signature of this kind of scatterer enabling the model parameters ν and L to be determined unambiguously from simple scattering measurements. It is found that $\langle I(\theta)\rangle$ is a "stable" distribution of argument $\sin\theta$:

$$\langle I(\theta)\rangle \propto p_{\nu}([kL]^{1-\frac{2}{\nu}} \sin\theta) \tag{7a}$$

where $$\int_{-\infty}^{\infty} p_{\nu}(x) \exp(isx)\, dx = \exp(-As^{\nu})$$

The tail of the distribution (7a) falls off like $\sin^{\nu+1}\theta$ beyond $(kL)^{1-2/\nu}$ $\sin\theta \sim 1$ and a log-log plot against $\sin\theta$ can therefore be used, in principle, to determine ν and L from experiments independent of the absolute magnitude of the scattered wave amplitude [38,41]. For a smoothly varying surface which is rough compared to the incident wavelength

$$\langle I(\theta)\rangle \propto p_{m}(\sin\theta) \tag{7b}$$

and only information regarding the slope distribution p_m can be obtained from measurements of the distribution of intensity in this case. The fact that a power law decay of the distribution of intensity with angle is inconsistent with a geometrical optics interpretation of the scattering process leading to equation (7b) was noted twenty years ago [42].

PHASE SCREENS INTRODUCING DISTORTIONS WITH FRACTAL SLOPE

The fractal height model (6) is not only somewhat uninteresting by virtue of its ability to generate only weak intensity fluctuations, but is also unrealistic in several respects. Although fractal behaviour is commonly observed in nature, it invariably extends over only a limited range of scale sizes. The raw power law behaviour defined by equation (6) therefore needs to be modified to include high and low frequency spectral cut-offs and perhaps additional regions of different power law behaviour. The effect of an outer scale or low frequency cut-off is well understood. It ensures that regions of the phase screen separated by more than the outer scale contribute independently to the scattered field at the detector and hence leads to Gaussian speckle in the appropriate scattering geometries. However, calculations show that it does not significantly modify the predictions obtained using model (6) provided the height fluctuations, h, introduced by outer-scale sized inhomogeneities exceed the wavelength of the incident radiation [20]. This "strong scattering" requirement must be satisfied in any case to obtain significant fluctuations.

The effect of an inner scale or high frequency cut-off is to produce a more smoothly varying behaviour at smaller length scales which can be revealed by magnification or equivalently by scattering incident waves of sufficiently short wavelength. In the simple forward scattering geometries governed by equation (1) this kind of modification of model (6) will be important when inner scale sized inhomogeneities introduce height fluctuations of the order of a wavelength or more. Inner scale smoothing is an important consideration in the propagation of light through the turbulently mixing atmosphere and other similar systems. It is normally assumed for these systems (and indeed there is supporting experimental evidence, for example reference [43]) that the spectrum of refractive index fluctuations closely follows the Kolmogorov spectrum of turbulence which, in the present

context, leads to $\nu = 5/3$ in equation (6). However, both detailed light scattering experiments, in which very large intensity fluctuations have been measured, and also observations with the naked eye of white light "twinkling" phenomena, indicate that geometrical optics effects due to refractive scattering are pre-eminent. This casts doubt on the relevance of the fractal height model. At the same time experimental measurements suggest that a single scale smoothly varying model is also inadequate [8] and that some multi-scale element must be included in order to predict the observed phenomena.

It is therefore interesting to investigate a scattering model which is both multi-scale and capable of generating geometrical optics effects. The simplest one is a corrugated Gaussian random phase screen which introduces a distortion h(x) whose slope is a fractal. Models of this kind were first investigated in detail by Rino [44,45] in the context of ionospheric scintillation and correspond to an inverse power law spectrum with index in the range three to five. In the present context it is instructive to show how such behaviour can, in principle, result from the smoothing of a fractal by, for example, thermal diffusion or surface tension effects. It is sufficient for present purposes to adopt a simple "top hat" integration model:

$$H(x) = \frac{1}{X}\int_{x-X/2}^{x+X/2} h(x')\,dx' \qquad (8)$$

where h is fractal with structure function (6). Although h is not differentiable, evidently H(x) is once differentiable so that the relationship between the slope structure function $S(x) = \langle (M(0)-M(x))^2 \rangle$, where $M(x) = dH/dx$, and the smoothed height structure function, $D(x) = \langle (H(0)-H(x))^2 \rangle$, namely

$$S(x) = -\frac{d^2D}{dx^2}\Big|_0^x \quad . \qquad (9a)$$

can be used to derive the result

$$S(x) = \frac{1}{X^2}\left\{2D(X) + 2D(x) - D(x+X) - D(x-X)\right\} \qquad (9b)$$

where D(x) is given by equation (6). Thus

$$S(x) = |x|^\nu \left(\frac{2L^{2-\nu}}{X^2}\right)\left[1 - \frac{\nu(\nu-1)}{2}\left(\frac{x}{X}\right)^{2-\nu} + \ldots\right] \qquad x \ll X \qquad (10a)$$

$$= 2\left(\frac{L}{X}\right)^{2-\nu}\left[1 - \frac{\nu(\nu-1)}{2}\left(\frac{X}{x}\right)^{2-\nu} + \ldots\right] \qquad x \gg X \qquad (10b)$$

whilst for the special "Brownian" case $\nu = 1$ (9) reduces exactly to

$$S(x) = |x|\left(\frac{2L}{X^2}\right) \qquad \text{for } x \leqslant X \qquad (11)$$

$$= 2\,\frac{L}{X} \qquad \text{for } x > X \ .$$

The slope structure function (9) is plotted in figure 1 for various values of ν lying between zero and two. The curves show that the slope, M, exhibits fractal behaviour of the form (10a) for sufficiently small arguments but that smoothing has introduced a scale size X beyond which M is either totally decorrelated ($\nu = 1$, equation (11)) or decorrelates according to an inverse power law (equation 10b). The implications of this low frequency spectral truncation will be considered later; for the present the unmodified fractal slope or "sub fractal" model

$$S(x) = |x|^\nu/L^\nu \qquad 0 < \nu < 2 \qquad (12)$$

will be adopted. Note that L has been redefined here in line with previous publications [14] and that the value of ν in equation (12) is only the same as that for the unsmoothed quantity, h, in the case of the top hat smoothing (8).

It is inappropriate here to review earlier results obtained using the sub-fractal model (12) in great detail and only the more significant features of this kind of scattering system will be mentioned. These derive from the ability of the sub-fractal diffuser to generate highly correlated ray effects without geometrical singularities such as caustics. As a direct consequence, the fluctuations of intensity in the Fresnel region fail to saturate at the Gaussian speckle value at large distances [45,14]. In fact it has been shown [14] that for plane wave illumination of an infinite corrugated sub-fractal diffuser

$$\lim_{z\to\infty} \frac{\langle I^2\rangle}{\langle I\rangle^2} = \frac{4}{2-\nu} \qquad (13)$$

In this asymptotic regime the expected interference phenomena are modulated by underlying geometrical optics effects which persist because the directions of rays leaving the phase screen are correlated from whatever distance they are viewed (in the absence of an outer scale). According to equation (13) very large fluctuations in intensity will be generated near $\gamma = 2$ unlike the weak non-Gaussian effects generated by the fractal height model (6). In the case $\gamma = 1$ the asymptotic distribution is a member of the K-distribution class [14]

$$p(I) = 2K_0(2\sqrt{I}) \tag{14}$$

and the underlying ray density defined by the formula

$$R(y,z) = \frac{1}{z}\int_{-\infty}^{\infty} \delta(M(x) - \frac{x-y}{z})\, dx \tag{15}$$

is a gamma variate

$$p(R) = \exp(-R) \tag{16}$$

Investigation of the moments of R show that this quantity is approximately gamma distributed for a range of values of ν [14]. Thus the sub-fractal phase screen scattering model not only generates intensity fluctuations in the asymptotic regime by the mechanism suggested (see section 1) for K-distributed noise, but the heirarchical nature of the scatterer is seen to be responsible for the underlying process being approximately gamma distributed.

The spatial coherence properties of the intensity pattern in the asymptotic Fresnel region also separate into terms associated with interference and terms associated with ray density fluctuations. The former are characterised by a scale size which decreases with distance whilst the latter are characterised by a scale size which increases non-linearly with distance. This behaviour may be contrasted with that associated with a smoothly varying single scale diffuser, for which the interference scale is independent of propagation distance and the geometrical optics scale increases linearly with distance [20].

The presence of an outer scale size within a sub-fractal diffuser, beyond which the direction of emanating rays decorrelates, leads to a rapid averaging out of ray density fluctuations at large distances in the Fresnel scattering geometry, as larger areas of the scatterer contribute at the detector. The intensity fluctuations then subside from their high asymptotic values to those expected for Gaussian speckle and the plots of scintillation index versus distance assume a familiar humped appearance with saturation at unity and show good agreement with experimental data [18].

In the far field the inevitable low frequency cut-off plays a more crucial role in ensuring the finiteness of the statistics of intensity fluctuations, which requires a finite spread of rays [46]. Although superficially similar to those obtained for a smoothly varying single scale screen, plots of normalised second intensity moment against illuminated area exhibit a characteristic power law regime where, for the corrugated case (ξ_0 is the outer scale)

$$\frac{\langle I^2\rangle}{\langle I\rangle^2} \propto \left(\frac{\xi_0}{W}\right)^{\nu/2} \tag{17}$$

In this geometrical optics regime the intensity fluctuations are dominated by a "lighthouse" effect in which an incident parallel beam is deflected through a maximum angle $\sim\sqrt{S(\xi_0)}$ and spread over an angle $\sim \sqrt{S(W)}$. This regime is bounded by aperture diffraction effects for small apertures and by outer scale decorrelation when $W > \xi_0$. Result (17) is obtained by assuming, crudely, that the scattered beam has a rectangular profile so that the intensity observed by the detector is a telegraph wave. Again there is some experimental support for these predictions [19].

4 RAY DENSITY FLUCTUATIONS

The most significant feature of scattering by a random phase screen governed by the fractal slope model (12) is the dominant role played by the geometrical optics contribution to the scattered intensity pattern. This contribution relates closely to the topography of the phase distortion and can be separately investigated through a study of the ray density functional

$$R(y,z) = \frac{1}{z}\int_{-\infty}^{\infty} A(x)\, \delta(M(x) - \frac{x-y}{z})\, dx \tag{18}$$

which generalises equation (15) to include an aperture function A(x). Note that the statistical properties of this quantity are finite when the structure function of M is given by equation (12). This may be contrasted with the case of a smoothly varying diffuser for which the second and higher moments of R diverge due to the presence of caustics in the scattered intensity pattern.

A large number of analytical results have been derived for the statistical properties of the ray density (18), particularly for the case $A(x) \equiv 1$ which corresponds to the

Fresnel region scattering geometry. Confining the discussion to this case for the time being, it is not difficult to show that

$$\langle R \rangle = 1 , \qquad \langle R^2 \rangle = 2/(2-\nu) \tag{19}$$

Comparison of equation (19) with equation (13) confirms the extra factor of two required to take account of speckle or interference effects in the case of intensity fluctuations. It is interesting that the exact result (19) is independent of z whereas result (13) applies only at large propagation distances. Indeed it may be shown that the single interval statistics of ray density fluctuations are quite generally independent of z although the transverse spatial decay length of features in the ray density pattern increases like $z^{2/(2-\nu)}$ [14]. The third moment, $\langle R^3 \rangle$, cannot be evaluated exactly for all values of ν but can be expressed in the form of a simple integral which can then be evaluated numerically [14]. Comparison with the moments of a gamma distribution show that the statistics are close for values of ν ranging from zero to well in excess of unity and equal when $\langle R^2 \rangle = 2$ which corresponds to the case $\nu = 1$. Examination of this "Brownian" case has revealed that the entire scattering problem is exactly solvable [14], with R behaving like the square modulus of a zero mean circular complex Gaussian-Markov process having a negative exponential single interval distribution and coherence function

$$\langle R(0)\, R(x) \rangle = 1 + \exp(-2L|x|/z^2) \qquad (\nu = 1) \tag{20}$$

The finite aperture problem can also be formally solved for the Brownian case by noting that the joint distribution of slopes may be factorised:

$$p(M_1, M_2, M_3 \ldots) = p_0(M_1)\; p(M_2 - M_1)\; p(M_3 - M_2) \ldots \tag{21}$$

where $M_j = M(x_j)$ with $x_j > x_{j-1}$ and $p_0(M_j)$, strictly speaking, has infinite width. Noting also that both p and p_0 are Gaussian, a little algebra shows that the Nth moment of R for a hard aperture of width W can be expressed in the form

$$\langle R^N \rangle = N! \frac{z}{L} \int_0^{LW/z^2} dx\; p_0\left(\frac{N}{2z} - \frac{zx}{L} - \frac{y}{z}\right) \mathcal{L}_x^{-1} \left\{ \frac{g^{N-1}(p)}{p} \right\} \tag{22}$$

where $\mathcal{L}_x^{-1}\{f(p)\}$ is the inverse Laplace transform $\int_{c-i\infty}^{c+i\infty} \exp(px)\, f(p)\, dp$, $g(p) = 1/\sqrt{2p+1}$, $p(x) = \exp(-x^2/2)/\sqrt{2\pi}$, $p_0(x) = \exp(-x^2/2m_0^2)/\sqrt{2\pi m_0^2}$ and m_0 is a "maximum" slope related to the largest scale size present (see equation (26)). The corresponding distribution of ray density fluctuations is given by

$$\begin{aligned} P(R) = \delta(R) \Bigg[1 &+ \frac{z}{L} \int_0^{LW/z^2} dx\; p_0\left(\frac{N}{2z} - \frac{zx}{L} - \frac{y}{z}\right) \mathcal{L}_x^{-1} \left\{ \frac{1}{pg(p)} \right\} \Bigg] \\ &+ \frac{z}{L} \int_0^{LW/z^2} dx\; p_0\left(\frac{N}{2z} - \frac{zx}{L} - \frac{y}{z}\right) \mathcal{L}_x^{-1} \left\{ \frac{\exp(-R/g(p))}{p^2 g(p)} \right\} \end{aligned} \tag{23}$$

The transform in equation (22) is an incomplete γ-function and those in equation (23) can be expressed in terms of error functions. When $LW/z^2 \gg 1$ the main contribution to the integrals in (23) comes from the region where x is large and $P(R) \to \exp(-R)$, $\langle R^N \rangle \to N!$ as indicated above. However these general results allow the narrow beam limit $LW/z^2 \ll 1$ to be explored:

$$P(R) = (1 - 2\beta/\sqrt{\pi})\, \delta(R) + (\beta/\alpha)\, \mathrm{erfc}(R/2\alpha) \tag{24}$$

$$\frac{\langle R^N \rangle}{\langle R \rangle^N} = \frac{N!}{\Gamma\left(\frac{N+3}{2}\right)}\, \beta^{(1-N)}, \quad \langle R \rangle = \alpha\beta \tag{25}$$

where $\alpha = \sqrt{LW/2z^2}$ and $\beta = \sqrt{2W/L}\; p_0(x/z)$. A numerical evaluation of the normalised second moment on axis (x = 0) given by equation (25) shows how, for a finite aperture, ray density fluctuations increase with distance from the scatterer and eventually saturate as predicted by result (25). Results (24) and (25) are entirely consistent with the comments made in section 3 concerning the geometrical optics dominated far field scattering regime: the incident beam of rays is steered and broadened by the screen so that, as indicated by the delta-function term in equation (24), for some fraction of the time no energy falls on the detector.

In the above discussion the concept of maximum slope m_0 was introduced in order to obtain results in the finite aperture case. This quantity is defined by introducing an outer scale or low-frequency cut-off into the sub-fractal model. The simplest modification of equation (12) for the slope structure function is given by (see also equations (10) and (11))

$$\begin{aligned} S(x) &= |x|^\nu / L^\nu && |x| \leq \xi_0 \\ &= (\xi_0/L)^\nu = 2m_0^2 && |x| > \xi_0 \end{aligned} \tag{26}$$

and leads to the following expression for the second normalised moment of ray density fluctuations in the large aperture limit A(x) ≡ 1 (equation (18))

$$\langle R^2 \rangle = \operatorname{erfc}\left(\frac{\xi_o}{2m_o z}\right) + \frac{2}{2-\nu} \operatorname{erf}\left(\frac{\xi_o}{2m_o z}\right) \tag{27}$$

As expected, this formula predicts that for large propagation distances the directions of rays overlapping at the detector become uncorrelated and the structure of the pattern is averaged out.

As a final illustration of the mathematical tractability of the sub-fractal model it is interesting to investigate the effect of spatial integration at the detector, which will often play a significant role in real experiments. The results obtained here also shed further light on the nature of the full diffraction problem. First it should be noted that spatial averaging using a hard rectangular aperture in the Brownian case $\nu = 1$ is a well documented problem (see for example reference 47) with explicit results to be found in the literature on integrated Gaussian-Markov processes [48]. For other values of ν some simplification of the formulae can be achieved by assuming a "soft" Gaussian detector area so that

$$R(z;W) = \frac{1}{\sqrt{2\pi W^2}} \int_{-\infty}^{\infty} dx\, R(x,z) \exp(-x^2/2W^2) \tag{28}$$

The second moment of integrated ray density fluctuations, R, for the "Fresnel" geometry, when $A(x) \equiv 1$ in equation (18), is then given by the formula

$$\langle R^2 \rangle = \sqrt{\frac{2}{\pi}} \int_{-\infty}^{\infty} \frac{dx \exp(-x^2/2(z^2 S(x) + 2W^2))}{\sqrt{(z^2 S(x) + 2W^2)}} \tag{29}$$

Now, a steepest descents approximation for the second intensity moment calculated from equation (1) with model (12) leads to [18]

$$\langle I^2 \rangle = \frac{4k}{\pi z} \int_0^{\infty} dx \int_0^{x} dx' \cos\frac{kxx'}{z} \exp\left(-\frac{1}{2} k^2 x'^2 S(x')\right) \tag{30}$$

which is known to provide good agreement with more exact calculations [18]. Replacing the upper limit of the x'-integral with a smoother cut-off factor $\exp(-x'^2/x^2)$ and performing the integration obtains

$$\langle I^2 \rangle = \sqrt{\frac{2}{\pi}} \int_0^{\infty} \frac{dx \exp(-x^2/2(z^2 x S(\sqrt{x}) + 2z^2/k^2))}{\sqrt{(z^2 x S(\sqrt{x}) + 2z^2/k^2)}} \tag{31}$$

The structure of equations (29) and (31) is remarkably similar. Inspection shows that each is a function of a single parameter when S(x) is given by model (12). In the case of equation (29) the parameter is (W/ξ) where $\xi = (z^2/L^{\nu})^{\frac{1}{2-\nu}}$ is the scale size of ray density fluctuations [14] (cff equation (20) for the Brownian case). On the other hand equation (31) is a function only of the parameter (W_D/ξ) where $W_D = z/k\xi$. Now ξ is also the (z-dependent) size of the scattering region providing the dominant contribution at the detector [14] so that W_D is the scale characterising the smoothing effect of diffraction in the full intensity pattern. Thus the attenuation of intensity fluctuations as the propagation path is reduced to zero can be interpreted as a simple diffraction smoothing effect analogous to integration over a z-dependent detector area W_D.

Both equations (29) and (31) diverge in the limit $\nu \to 2$. This is associated with divergence of the scale size ξ introduced above and can be overcome by introducing a fixed outer scale as in equation (26). Equation (29) then gives

$$\langle R^2 \rangle = \operatorname{erfc}(q) + \frac{q}{\sqrt{\pi}} \exp(-q^2) \left[\ln\left(\frac{2z^2\xi_o^2}{L^2W^2}\right) + \pi \operatorname{erfi}(q) - F(q)\right] \tag{32}$$

where $F(q) = \int_0^q \exp(x^2) \operatorname{erfc}(x)\, dx$

and $q = L/z\sqrt{2}$

whilst equation (31) gives

$$\langle I^2 \rangle = 2 \operatorname{erfc}(q) + \frac{q}{\sqrt{\pi}} \exp(-q^2) \left[\ln\left(\frac{2k^2\xi_o^2}{L^2}\right) + \pi \operatorname{erfi}(q) - F(q)\right] \tag{33}$$

The last equation is virtually identical to previous analytical approximations [20]. The terms in square brackets, which arise from the region of integration $[0,\xi_o]$ in equations (29) and (31), represent the geometrical optics contribution to the pattern. These are

identical when W is identified with $z/k\xi_o$, the diffraction spread associated with the largest scale size ξ_o. The first terms on the right hand side of equations (32) and (33) arise from the region of integration $[\xi_o,\infty]$ in formulae (29) and (31). They relate to the averaging out of the geometrical optics structure at large distances, due to the presence of an outer scale, as in the formula (27) valid for more general values of ν. The additional factor 2 appearing in equation (33) reflects the presence of interference effects in the full diffraction problem. Thus, as is well known [23], diffraction serves to smooth the singular variations in ray density generated when $\nu = 2$ and so limit the degree of fluctuation according to the logarithmic term present in equations (32) and (33). However, the geometrical optics contribution to the pattern increases with z for propagation distances which are smaller than the characteristic focussing length $q \sim 1$. This is different from the situation for $\nu < 2$, when the geometrical optics contribution is independent of z, owing to the introduction of the fixed (ie z-independent) scale size ξ_o.

5 SUMMARY AND CONCLUSIONS

Experimental evidence suggests that K-distributed noise may be widely applicable as a model for amplitude fluctuations in waves scattered by multi-scale media. The work described in this paper has explored effects generated by the simplest kind of multi-scale scattering system: the Gaussian random phase screen introducing wavefront distortions with fractal slope. It has been demonstrated that in one scattering geometry this class of model generates interference effects modulated by underlying ray density fluctuations, a mechanism of the kind which has been suggested for K-distributed noise. Moreover, one member of the class leads exactly to K-distributed intensity fluctuations in this scattering configuration. It has also been shown that the fractal slope model is interesting in its own right, being analytically tractable as a result of the absence of caustics. This allows the short wave limit to be investigated through a study of ray density fluctuations which have finite statistical properties. Results have been presented for a range of properties of the scattered rays which reflect the power law behaviour of the heirarchical scattering model and help to clarify the role of geometrical optics, diffraction and interference in the full diffraction problem. However, some areas of work such as scattering by multiple screens [48] have not been covered for lack of space.

Although the results discussed here have been confined to the one-dimensional or corrugated screen, work on the isotropic two-dimensional sub-fractal diffuser is also to be found in the literature [18,44,32]. In this case the slope M(r) is the vector gradient of a distortion, $h(\underline{r})$, with structure function which can be expanded about the origin in the form

$$D(\underline{r}) = Ar^2 - B|\underline{r}|^{\nu+2} + \ldots \qquad 0 < \nu < 2 \qquad (34)$$

Several simple results can be obtained using this model. For example intensity fluctuations in the Fresnel region again saturate at a value above the Gaussian speckle value [18]

$$\lim_{z\to\infty} \frac{\langle I^2\rangle}{\langle I\rangle^2} = \frac{4\sqrt{\nu+1}}{2-\nu} \qquad (35)$$

However, the two dimensional problem is on the whole less tractable and more suited to investigation by numerical techniques. In fact, calculation of the properties of ray density fluctuations is particularly suited to the techniques of numerical simulation [49] and this approach is discussed fully in a companion paper [17].

In conclusion, the sub-fractal diffuser is an interesting intermediate scattering model which combines simple multi-scale behaviour with the ability to generate non-singular geometrical optics effects. It is amenable to both analytical and numerical investigation and is currently providing valuable new insight into the origin of non-Gaussian fluctuations of waves scattered by random media. Further studies which are currently envisaged include applications of the model to the extended medium problem and to the statistical characteristics of imaging systems.

REFERENCES

1 E Jakeman and P N Pusey, "Non-Gaussian fluctuations in electromagnetic radiation scattered by a random phase screen. I. Theory", J Phys A: Math Gen, 8 (1975) 369-391.

2 P N Pusey and E Jakeman, "Non-Gaussian fluctuations in electromagnetic radiation scattered by a random phase screen. II. Application to dynamic scattering in a liquid crystal", J Phys A: Math Gen 8 (1975) 392-410.

3 E Jakeman and P N Pusey, "A model for Non-Rayleigh Sea Echo", IEEE Trans Ant Prop AP24 (1976) 806-814.

4 K D Ward and S Watts, "Radar Sea Clutter", Microwave J 28 (1985) 109-121.

5 C J Oliver, "Clutter models based on correlated K-distributions", RSRE Memorandum No 3775 (1985).

6 G Parry and P N Pusey, "K-distributions in atmospheric propagation of laser light", J Opt Soc Am 69 (1979) 796-798.

7 G Parry, "Measurement of atmospheric turbulence induced intensity fluctuations in a laser beam", Optica Acta 28 (1981) 715-728.

8 G Parry, P N Pusey, E Jakeman and J G McWhirter, "Focussing by a random phase screen" Opt Commun 22 (1977) 195-201.

9 E Jakeman, G Parry, E R Pike and P N Pusey, "The Twinkling of Stars", Contemp Phys 19 (1978) 127-145.

10 T E Ewart, C Macaskill and B J Uscinski, "Intensity fluctuations. Part II: Comparison with the Cobb experiment", J Acoustic Soc Am 74 (1983) 1484-1499.

11 E Jakeman and P N Pusey, "Significance of K-distributions in scattering experiments", Phys Rev Letts 40 (1978) 546-550.

12 E Jakeman, "On the statistics of K-distributed noise", J Phys A 13 (1980) 31-48.

13 B B Mandelbrot, "Fractals", San Francisco: Freeman (1977).

14 E Jakeman, "Fresnel scattering by a corrugated random surface with fractal slope", J Opt Soc Am 72 (1982) 1034-1041.

15 E Jakeman, "Scattering by multi-scale systems", in "Wave Propagation and Scattering", Ed. B J Uscinski, Oxford: Clarendon Press (1986) 49-63.

16 C L Rino, "A power law phase screen model for ionospheric scintillation. I: Weak scatter", Rad Sci 14 (1979) 1135-1145.

17 J H Jefferson and J D Anderson "Generation and properties of self-similar stochastic processes with application to ray propagation in random media", this volume.

18 E Jakeman and J H Jefferson, "Scintillation in the Fresnel region behind a sub-fractal diffuser", Optica Acta 31 (1984) 853-865.

19 J G Walker and E Jakeman, "Observation of sub-fractal behaviour in a light scattering system", Optica Acta 31 (1984) 1185-1196.

20 E Jakeman and J G McWhirter, "Correlation function dependence of the scintillation behind a deep random phase screen", J Phys A: Math Gen 10 (1977) 1599-1643.

21 M V Berry and C Upstill, "Catastrophe optics: morphologies of caustics and their diffraction patterns", Progress in Optics XIII, Ed. E Wolf, Amsterdam: North Holland (1979) 610-23.

22 M V Berry, "Focussing and twinkling: critical exponents from catastrophes in non-Gaussian random short waves", J Phys A 10 (1977) 2061-2081.

23 E E Salpeter, "Interplanetary scintillations. I. Theory", Astrophys J 147 (1967) 433-48.

24 E Jakeman, "Optical scattering experiments", in "Wave Propagation and Scattering", Ed. B J Uscinski, Oxford: Clarendon Press (1986) 241-259.

25 R S Sayles and T R Thomas, "Surface topography as a non-stationary random process", Nature 271 (1978) 431-4.

26 M V Berry, "Diffractals", J Phys A 12 (1979) 781-797.

27 R Buckley, "Diffraction by a random phase screen with very large rms phase deviation", Aust J Phys 24 (1971) 351-71.

28 K S Gochelashvily and V I Shishov, "Saturation of laser irradiance fluctuations beyond a turbulent layer", Opt and Quant Electron 7 (1975) 524-536.

29 V H Rumsey, "Scintillations due to a concentrated layer with a power law turbulence spectrum", Radio Sci 10 (1975) 107-114.

30 M Marians, "Computed scintillation spectra for strong turbulence", Radio Sci 10 (1975) 115-119.

31 Y Furuhama, "Covariance of irradiance fluctuations propagating through a thin turbulent slab", Radio Sci 10 (1975) 1037-1042.

32 V I Shishov, "Dependence of the form of the scintillation spectrum on the form of the spectrum of refractive index inhomogeneities", Radiophys Quantum Electron 17 (1974) 1287-1292.

33 B J Uscinski and C Macaskill, "Intensity fluctuations due to a deeply modulated phase screen", Atm Terr Phys 45 (1983) 595-605.

34 B J Uscinski, H G Booker and M Marians, "Intensity fluctuations due to a deep phase screen with a power law spectrum", Proc Roy Soc Lond A374 (1981) 503-530.

35 H G Booker and G Majdiahi, "Theory of refractive scattering in scintillation phenomena", Atm Terr Phys 43 (1981) 1199-1214.

36 V I Tatarski, "Wave Propagation in a Turbulent Medium", New York: McGraw-Hill (1961).

37 B B Mandelbrot, "The fractal geometry of nature", San Francisco: Freeman (1982).

38 D L Jordan, R C Hollins and E Jakeman, "Experimental Measurements of Non-Gaussian scattering by a fractal diffuser", Appl Phys B 31 (1983) 179-186.

39 D L Jordan, R C Hollins and E Jakeman, "Infrared scattering by a fractal diffuser", Opt Commun 49 (1984) 1-5.

40 D L Jordan, E Jakeman and R C Hollins, "Laser scattering from multi-scale surfaces", SPIE 525 (1985) 147-153.

41 D L Jordan, R C Hollins and E Jakeman, "Scattering from thermal-imager mirrors", RSRE Memorandum 3929 (1986).

42 T Hagfors, "Relationship of geometrical optics and autocorrelation approaches to the analysis of lunar and planetary echoes", J Geophys Res 71 (1966) 379-383.

43 W A Coles and R G Frehlich, "Simultaneous measurements of angular scattering and intensity scintillation in the atmosphere", J Opt Soc Am 72 (1982) 1042-1048.

44 C L Rino, "A power law phase screen model for ionospheric scintillation. 2. Strong scatter", Rad Sci 14 (1979) 1147-1155.

45 C L Rino, "Numerical computations for a one-dimensional power law phase screen", Rad Sci 15 (1980) 41-47.

46 E Jakeman, "Fraunhofer scattering by a sub-fractal diffuser", Optica Acta 30 (1983) 1207-1212.

47 E Jakeman, "Statistics of integrated gamma-Lorentzian intensity fluctuations", Optica Acta 27 (1980) 735-741.

48 E Jakeman and J H Jefferson, "Scattering of waves by refractive layers with power law spectra", Proc Inst Acoust 8 (1986) 12-19.

49 J H Jefferson, E Jakeman and J E P Beale, "Computation of ray statistics beyond a multi-scale diffuser", Proc Inst Acoust 8 (1986) 30-35.

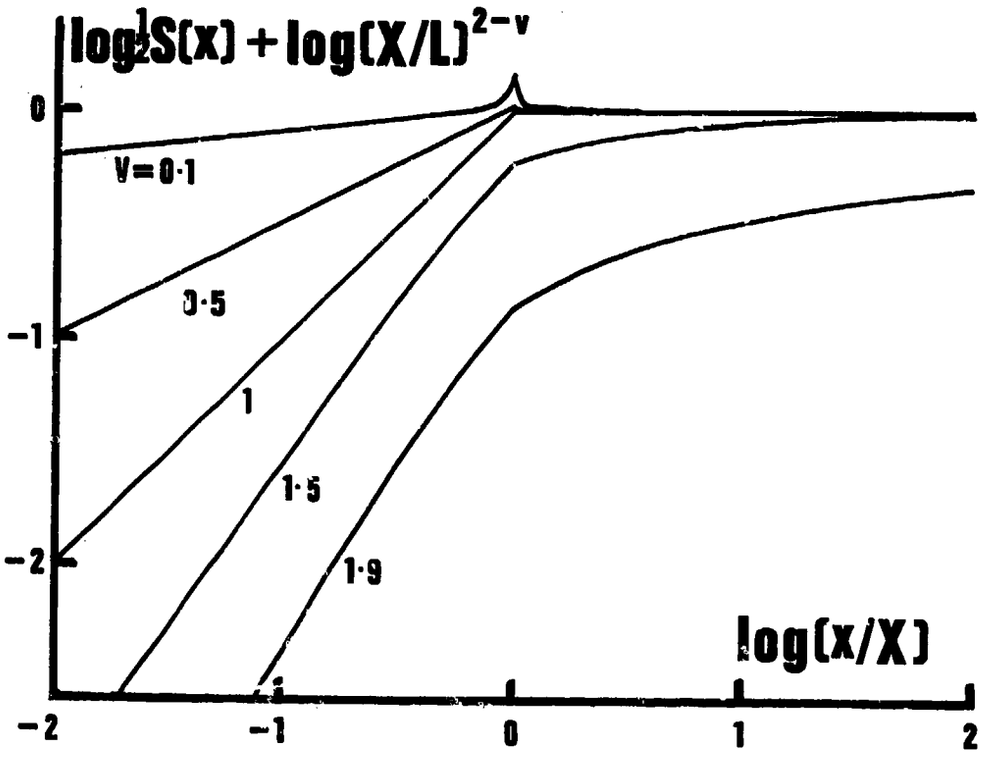


Figure 1 Slope structure function of a smoothed fractal

GENERATION AND PROPERTIES OF SELF-SIMILAR STOCHASTIC PROCESSES WITH APPLICATION TO RAY PROPAGATION IN RANDOM MEDIA

J H Jefferson and J D Anderson
Royal Signals and Radar Establishment
St Andrews Road
Malvern
Worcs
WR14 3PS
UK

SUMMARY

The importance of random media containing many length scales, and propagation of waves in such media is now widely recognised. In this paper, specific mathematical models to generate stochastic processes which have 'self-similar' properties will be analysed. Examples will be presented graphically to illustrate similarities and differences between processes with various degrees of 'roughness' and it will be shown how they are related to fractional integration and fractal dimension. Such processes are non-Markovian, in general, and both causal and non-causal models are shown to be stochastically equivalent. Their use in modelling the scattering of waves from rough surfaces, particularly in the geometrical optics limit, will be discussed and the effects of inner and outer scales investigated. Finally, the generalisation to two and three dimensions is considered together with application to ray propagation in extended random media.

LIST OF SYMBOLS

$\varepsilon(t)$, $\varepsilon(x)$	:	δ-correlated random noise
$v(t)$	:	velocity of a particle undergoing Brownian motion
$v_\nu(t)$	:	velocity of particle undergoing fractional Brownian motion
$\bar{v}_\nu(t)$	:	$v_\nu(t)$ with polynomial variation removed
$V_\nu(t)$	:	$v_\nu(t)$ with smooth inner scale
$C_\nu(t)$	:	velocity autocorrelation function
σ_v	:	standard deviation of velocity
$D_\nu(t)$	:	velocity structure function (variance of velocity increments)
τ	:	velocity correlation time
x_o	:	correlation length of Brownian sub-fractal
α	:	strength of the random driving term in Brownian motion
ℓ	:	topothesy of Brownian sub-fractal
$\phi(t)$, $\phi(x)$	:	inner-scale smoothing function
$h_\nu(x)$, $h_\nu(\underline{r})$	:	random height of fractal wavefront relative to its mean
$m_\nu(x)$, $\underline{m}_\nu(\underline{r})$	:	gradient of integrated fractal wavefront (ray gradient)
$M_\nu(x)$	:	gradient of fractal wavefront with smooth inner-scale.
$\bar{\varepsilon}(\omega)$, $\bar{v}(\omega)$ ... $\bar{\varepsilon}(k)$, $\bar{h}(k)$ ...	:	Fourier transforms of $\varepsilon(t)$, $v(t)$, ... , $\varepsilon(x)$, $h(x)$, ...
λ	:	wavelength
Δ	:	step length in numerical simulations
$\Gamma(\nu)$	:	gamma function
$K_\nu(x)$	:	modified Bessel function
$\mu(\underline{r})$	:	refractive index
$\underline{e}$	:	unit vector tangential to a ray
ds	:	elemental path length along a ray
$\langle \ldots \rangle$	:	statistical expectation, ensemble average

INTRODUCTION

Random phenomena which appear similar over many length-scales are observed in a diversity of situations. Examples include naturally occuring surfaces and boundaries (coastlines, terrain, clouds, sea surfaces, etc), the motion of particles subjected to random forces (noise in electrical circuits, Brownian motion) and fluctuations of temperature, pressure, refractive index, etc, in random media. Mandelbrot [1] has emphasised the ubiquity of multi-scale phenomena and has coined the word *fractal* to describe such objects which may be classified according to their *fractal dimension*. In this paper we shall be concerned with mathematical models which may be used to explicitly generate such stochastic processes by computer simulation and to use the resulting data to model wave scattering and propagation in the geometrical optics limit. In section 2 most of the concepts are introduced via a simple and much studied example, Brownian motion. A Brownian fractal is Brownian motion for which there are no bounds on scale-size. It is simply integrated white noise and has a fractal dimension of 1.5. Integration is, of course, a smoothing process though the Brownian fractal is still very rough in the sense that it is not differentiable, like all fractals. As such there can be no geometrical optics limit for fractal wavefronts, or *diffractals*, and they give rise to only weak intensity fluctuations as the wave propagates [2]. Progressively smoother processes may be generated by repeated integration and it is shown that these too have a hierarchical structure. They are Markovian processes and have a frequency spectrum $\sim \omega^{-2n}$, where n is the order of integration of the white noise. Rays scattered from integrated fractals produce large fluctuations in intensity (infinite for $n \geq 2$) and the ray-density pattern becomes increasingly sharp with the order of integration. However, these changes are quite abrupt as n is incremented and in section 3 we show how they can be made continuous by using fractional integration as the smoothing process, leading to the fractional Brownian process. The consequences of inner and outer scales (high and low frequency spectral cut-offs) are discussed together with how they affect the change in intensity fluctuations with distance of a propagating fractal wavefront in the geometrical optics limit. Section 4 deals with the extension to higher dimensions. Explicit examples are given for the two-dimensional propagating wavefront showing how the contrast patterns develop and also how these same two-dimensional models may be used to simulate ray-propagation in a multi-scale extended medium.

2. A SIMPLE EXAMPLE - THE BROWNIAN PROCESS

2.1 Brownian Motion

Stochastic processes may be generated by filtering δ-correlated white noise. A well known example which has received considerable attention since the turn of the century [3] is ordinary Brownian motion which may be described by the stochastic differential equation

$$\frac{dv}{dt} = -\frac{v}{\tau} + \alpha\varepsilon(t) \tag{1}$$

where $\langle\varepsilon(t)\varepsilon(t')\rangle = \delta(t-t')$, τ is the correlation time and α is a constant characterising the magnitude of the random driving force. Equation (1) describes the motion of a particle in a continuous viscous medium which is subjected to uncorrelated impulses. It may be formally integrated to give

$$v(t) = \alpha \int_{-\infty}^{t} e^{-(t-t')/\tau}\, \varepsilon(t')dt' \tag{2}$$

which is simply integrated white noise with an exponentially decaying 'memory'. Some care is needed in interpreting such derivatives and integrals since $\varepsilon(t)$ is a random function which is everywhere discontinuous. One method of giving a rigorous meaning to these quantities, which is particularly useful for simulation purposes, it to regard (1) as the limit as $\Delta t \to 0$ of the finite difference equation (or map)

$$v_{n+1} = (1 - \frac{\Delta t}{\tau})v_n + \alpha\varepsilon_n\sqrt{\Delta t} \tag{1'}$$

which has solution, for $\Delta t \to 0$,

$$v_n = \alpha\sqrt{\Delta t} \sum_{n'=1}^{n} e^{-(t_n - t_{n'})/\tau}\, \varepsilon_{n'} \tag{2'}$$

where $t_n = n\Delta t$ and $\langle\varepsilon_n\varepsilon_{n'}\rangle = \delta_{nn'}$. These equations are, of course, perfectly well defined and constitute a Markov chain by which is meant that given v_n at time t_n then $v_{n'}$ at some time $t_{n'} > t_n$ cannot independently depend on values of v at times less than t_n. The continuum limit, equation (1), is called a Markov process and is a direct consequence of the fact that the stochastic process can be described by a first-order differential equation. In general an n-th order stochastic differential equation will give rise to an n-th order Markov process meaning that given $v_1, v_2, \ldots v_n$ at times $t_1 < t_2 < \ldots t_n$ then v(t) with $t > t_n$ cannot (independently of $v_1, v_2, \ldots v_n$) depend on v at times less than t_1. In section 3 it will be shown that self-similar stochastic processes are, in general, manifestly non-Markovian in the sense that they cannot be described by finite-order stochastic differential equations.

2.2 Affine Scaling - The Brownian Fractal

The autocorrelation function of v(t) is, from equation (2),

$$C(t) = \langle v(t+t')v(t')\rangle = \frac{a^2\tau}{2} e^{-|t|/\tau} \qquad (3)$$

showing that the process is stationary with correlation length τ. In fact all stationary first-order Markov processes have exponentially decaying correlation functions and vice versa [4].

The presence of an outer scale, τ, has two important consequences. Firstly it limits the amount by which the random noise allows v to grow giving it a standard deviation $\sigma_v = \sqrt{\langle v\rangle^2} = a\sqrt{\tau/2}$ and secondly, for time separations $>>\tau$ velocities become decorrelated. This latter fact means that plots of v(t) will be statistically invariant under magnification of the time axis provided we do not resolve time scales $\leq\tau$. In this sense ordinary δ-correlated noise ($\tau = 0$) is self-similar! On the other hand, when τ is very large and we consider time separations $<< \tau$ then from equation (3)

$$C(t) \simeq \frac{a^2\tau}{2}(1 - |t|/\tau)$$

and hence

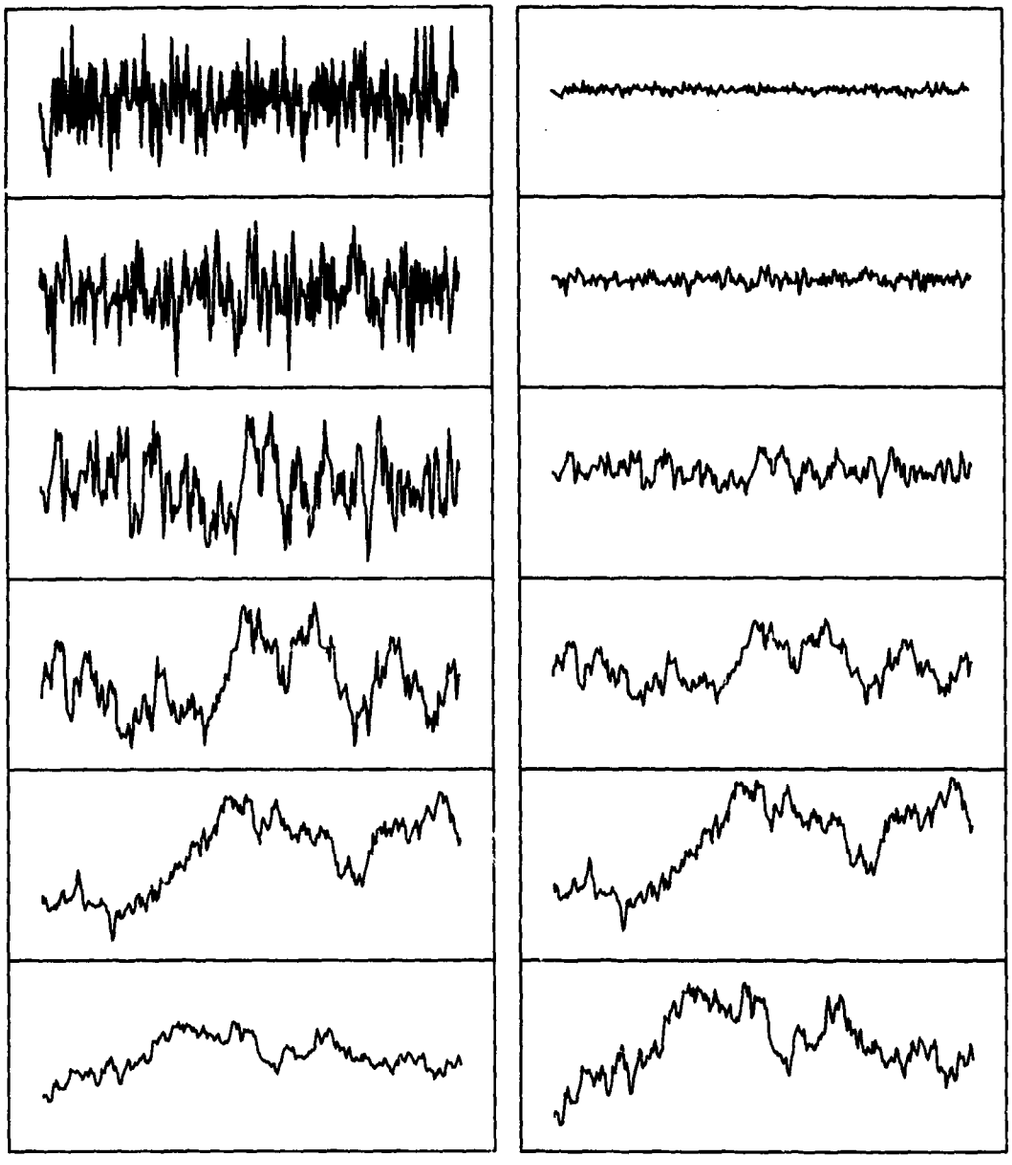
$$D(t) \equiv \langle [v(t+t') - v(t')]^2\rangle \simeq a^2|t| \qquad (4)$$

In this regime v(t) is statistically invariant under the self-affine transformation

$$t \to kt \qquad v \to k^{\frac{1}{2}}v \qquad (5)$$

in the sense that the variance of increments of v remain unchanged. These situations are depicted in figure 1 which shows successive threefold magnification (stretching) of the time-axis. In (a) the v-axis is kept constant and the graphs look similar on long time scales whereas in (b) where there is root scaling of the v-axis the graphs look similar on short time scales.

Consider the limit that $\tau \to \infty$. We see from equation (3) that the autocorrelation function diverges though the structure function (equation 4) is still well defined and varies linearly with time, satisfying the self-affine transformation (5) for all time-scales. This self-affinity is a fundamental property of all fractals which, as we shall see, will always remain statistically invariant under some power-law scaling. The scaling properties are also intimately related to the apparent 'roughness' of the graphs. δ-correlated noise (top of figure 1a) behaves as eratically as a one-dimensional curve can. This follows directly from the statistical invariance of v(t) under the scaling law $t \to kt$. If the root-mean squared change in velocity over any time interval is to be zero this can only be achieved by highly erratic fluctuations. In the limit $\tau \to 0$ the curve becomes area filling and is said to have a fractal dimension $D = 2$. On the other hand, for $t << \tau$ the curve is less rough (bottom of figure 1b) though in order that the rms change in velocity varies as $\sqrt{t}$ for any t it cannot do so smoothly. In the limit $\tau \to \infty$ it is said to be Brownian fractal with fractal dimension $D = 1.5$.



(a) (b)

Figure 1. Graphs of velocity vs time for Brownian Motion.
(a) linear scaling of the t-axis.
(b) linear scaling of the t-axis and root scaling of the v-axis.

2.3 Further Smoothing by Integration

Now the Brownian fractal is simply integrated δ-correlated white noise (equation (2) with $e^{-(t-t')/\tau} = 1$) and hence the integration acts as a smoothing process, as one would expect. This operation can, of course, be repeated to give a family of ever smoother curves:

$$v_n(t) = \int_{-\infty}^{t} dt_1 \int_{-\infty}^{t_1} dt_2 \ldots\ldots \int_{-\infty}^{t_{n-1}} dt_n \varepsilon(t_n) = \frac{1}{(n-1)!} \int_{-\infty}^{t} (t-t')^{n-1} \varepsilon(t')dt' \qquad (6)$$

which are solutions of the differential equations

$$\frac{d^n v_n}{dt^n} = \varepsilon(t) \qquad (7)$$

$v_n(t)$ is thus a simple nth-order Markov process. As has already been shown, the case $n = 1$ has inifinite variance though this singularity is of little consequence and is circumvented by considering increments, which have finite variance, ie

$$\bar{v}_1(t+t') = v_1(t+t') - v_1(t') \qquad (8)$$

has variance

$$D(t) = \langle \bar{v}_1^2 \rangle = |t|$$

even though $\langle v_1^2 \rangle = \infty$. For $n > 1$, $\langle v_n^2 \rangle$ is again infinite due to the presence of constant, linear, quadratic .... components which dominate the process. However, these are easily removed just as the constant term was in equation (8). Using equation 6 we get

$$\begin{aligned} \bar{v}_n(t+t') &\equiv v_n(t+t') - \left[v_n(t') + t \frac{dv_n}{dt'} + \frac{t^2}{2!} \frac{d^2 v_n}{dt'^2} + \ldots\ldots \frac{t^{n-1}}{(n-1)!} \frac{d^{n-1} v_n}{dt'^{n-1}} \right] \\ &= v_n(t+t') - \left[v_n(t') + t v_{n-1}(t') + \ldots\ldots \frac{t^{n-1} v_1}{(n-1)!}(t') \right] \\ &= \frac{1}{(n-1)!} \int_{t'}^{t+t'} (t + t' - \varepsilon)^{n-1} \varepsilon(s) ds \end{aligned} \qquad (9)$$

giving

$$\langle \bar{v}_n^2 \rangle = \frac{|t|^{2n-1}}{(2n-1)[(n-1)!]^2} \qquad (10)$$

and hence $\bar{v}_n(t+t')$ is statistically invariant under the affine scaling law

$$t \to kt, \quad \bar{v}_n \to k^{n-\frac{1}{2}} \bar{v}_n \qquad (11)$$

This invariance is demonstrated in figure 2 for the case $n = 2$ where we plot $\bar{v}_2$ under successive magnifications using affine scaling, at each stage rotating the section to be magnified according to equation (9), ie

$$v_2(t+t') + \bar{v}_2(t+t') = v_2(t+t') - \frac{t dv_2(t')}{dt'}$$

The important point to notice is that the degree of roughness of "waviness" of the curve at all time scales is a direct consequence of equation (10) and does not depend on the slope (which has infinite variance).

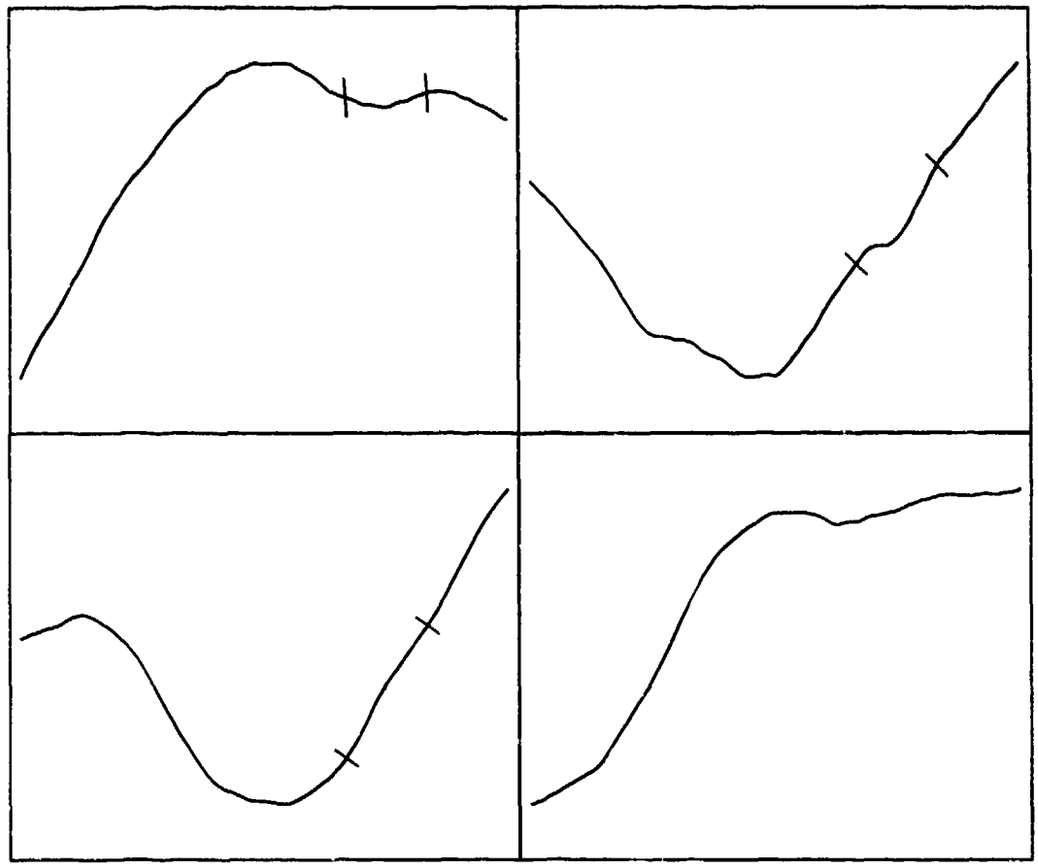


Figure 2. Affine scaling transformations of a Brownian sub-fractal. The markers denote the section to be magnified.

Figure 3 shows sections of $v_0(t)$ (δ-correlated noise) to $v_3(t)$, demonstrating how integration leads to smoothing of the stochastic process. However, this smoothing takes place in discrete jumps and one may ask whether it is possible to generalise the procedure to produce self-affine stochastic processes of any desired roughness (or smoothness).

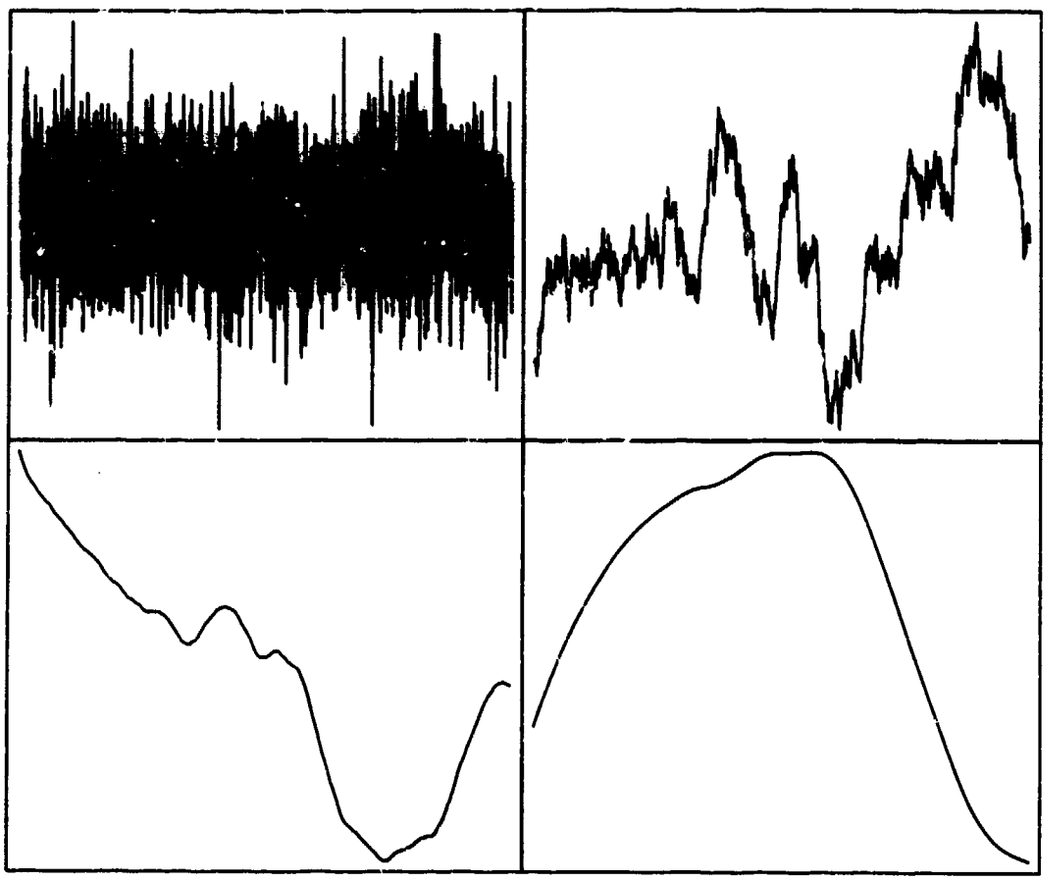


Figure 3. Smoothing by integration.

Since, as we have shown, the degree of roughness is primarily dependent on the index $2n - 1$ in equation 10, one way of making this generalisation would be to replace n by a continuous variable, leading to the concept of fractional differentiation and integration. This is indeed possible, as will be shown in section 3.

2.4 Spectrum

The spectrum of a process may be defined as the modulus squared of its Fourier transform (if it exists) which is the Fourier transform of its autocorrelation function. (Wiener-Khintchine theorem [5]). For Brownian motion this is, from equation 3,

$$\bar{C}(\omega) \equiv \int_{-\infty}^{\infty} e^{i\omega t} C(t)dt = \frac{\alpha^2}{(\tau^{-2}+\omega^2)} \tag{12}$$

Note that this quantity exists in the limit $\tau \to \infty$ even though C(t) diverges. Furthermore, any v(t) having this spectrum will have the same structure function since (cf equation 4)

$$D(t) = 2[C(o) - C(t)] = \frac{\alpha^2}{2\pi} \int_{-\infty}^{\infty} \frac{1-e^{-i\omega t}}{\omega^2} = \alpha^2|t| \tag{13}$$

In this sense the spectrum may be regarded as more fundamental than the stochastic differential equation which gave rise to it. Indeed, it is not difficult to define a number of different stochastic processes which give the same spectrum, $C(\omega) \sim \omega^{-2}$. For example, with the choice

$$\bar{v}(\omega) = \frac{\bar{\varepsilon}(\omega)}{-i\omega}$$

then

$$v(t) = \frac{1}{2\pi} \int_{-\infty}^{\infty} \frac{e^{-i\omega t}}{-i\omega} \bar{\varepsilon}(\omega) d\omega \tag{14}$$

which satisfies the differential equation

$$\frac{dv(t)}{dt} = \varepsilon(t)$$

ie equation 1 with $\tau = \infty$ and $\alpha = 1$. However the choice $\bar{v}(\omega) = |\omega|^{-1} \bar{\varepsilon}(\omega)$ gives $v(t)$ which satisfies the 'non-causal' differential equation

$$\frac{dv}{dt} = -\frac{1}{\pi} \int_{-\infty}^{\infty} \frac{dt' \varepsilon(t')}{t-t'}$$

ie $$v(t) - v(o) = -\frac{1}{\pi} \int_{-\infty}^{\infty} \ln|1 - t/t'| \varepsilon(t') dt' \tag{15}$$

This procedure is easily generalised to the multiply integrated Brownian fractal v_n (equation 6), which has a spectrum $C(\omega) = |\omega|^{-2n}$, and it is easily verified that

$$v_n(t) = \frac{1}{2\pi} \int_{-\infty}^{\infty} \frac{e^{-i\omega t}}{(-i\omega)^n} \bar{\varepsilon}(\omega) d\omega \tag{16}$$

satisfies equation 7. The process of removing the divergent constant, linear, quadratic... components described by equation (9) is particularly simple in frequency space with

$$\bar{v}_n(t) = \frac{1}{2\pi} \int_{-\infty}^{\infty} \frac{\bar{\varepsilon}(\omega)}{(-i\omega)^n} \left[e^{-i\omega t} - 1 + i\omega t + \ldots - \frac{(-i\omega t)^{n-1}}{(n-1)!} \right] \tag{17}$$

which is easily shown to have finite variance $\sim |t|^{2n-1}$.

2.5 Scattering

Waves which have encountered fractals are referred to by Berry [2] as diffractals. The one-dimensional Brownian diffractal may be modelled by equation (1) if we replace $v(t)$ by $h(x)$, the height of the wavefront relative to its mean. Such a distorted wave may result from the transmission of a plane wave through a narrow region of turbulence or from a rough surface. The restriction to one-dimension, which corresponds to a 'corrugated' wavefront, is somewhat unrealistic but is made for mathematical (and numerical) convenience. The extension to two and three dimensions will be considered in section 4. In this paper we will be concerned only with the geometrical optics limit $\lambda \to 0$. This is an important limit for a large class of scatterers where interference effects are of only secondary importance. In any case this limit is worth exploring in detail since it is usually easier to make progress both analytically and numerically, and comparison with a full wave treatment, when possible, will give insight into the relative importance of geometrical effects. For the Brownian fractal, the wavefront $h(x)$ is non-differentiable and there is, strictly speaking, no geometrical optics limit. In practice the wavefront (and the random media or surface from which the wave is scattered) in unlikely to be a fractal at all length scales amenable to experimental investigation. What is most relevant is the behaviour of $h(x)$ on scales $\gtrsim \lambda$. No geometrical effects will be observed if $h(x)$ remains fractal down to $\sim \lambda$. The resulting weak flucutations in intensity of the scattered waves are due entirely to interference and diffraction and require a full wave treatment [2]. On the other hand, if $h(x)$ is differentiable (non-fractal) on scales $\sim \lambda$ but is fractal-like on larger length scales, a geometrical optics limit is meaningful. We return to this point briefly below. The integrated fractals given by equation (7) with $n > 1$, are, ipso facto, always at least once differentiable and thus have a geometrical optics limit. The case $n = 2$, the Brownian sub-fractal, with slope $m(x) = \frac{dh}{dx}$ and outer scale x_0 satisfies the stochastic differential equation

$$\frac{dm}{dx} = -\frac{m}{x_0} + \frac{\varepsilon(x)}{\sqrt{\ell}} \tag{18}$$

ie $m(x)$ is analogous to $v(t)$ in Brownian motion with $h(x)$ analogous to $x(t)$ and ℓ, the 'topothesy', a constant length characterising the strength of the random driving term [2,6]. Rays propagating from such a wavefront are shown in figure 4. When viewed on a scale much less than the outer scale (figure 4a) the rays are highly correlated ($\langle [m(x)-m(0)]^2 \rangle \propto |x|/\ell$) though with the absence of curvature ($m(x)$ is not differentiable) no sharp focussing can occur. However, the fluctuations in intensity (ray-density) are quite large and it can in fact be shown that they have an exponential probability distribution with a scintillation index of unity [6]. At larger distances (figures 4b and 4c) the fluctuations are reduced since the pattern is now predominantly formed from

the superposition of rays whose directions are only weakly correlated until finally (figure 4d) the fluctuations virtually disappear.

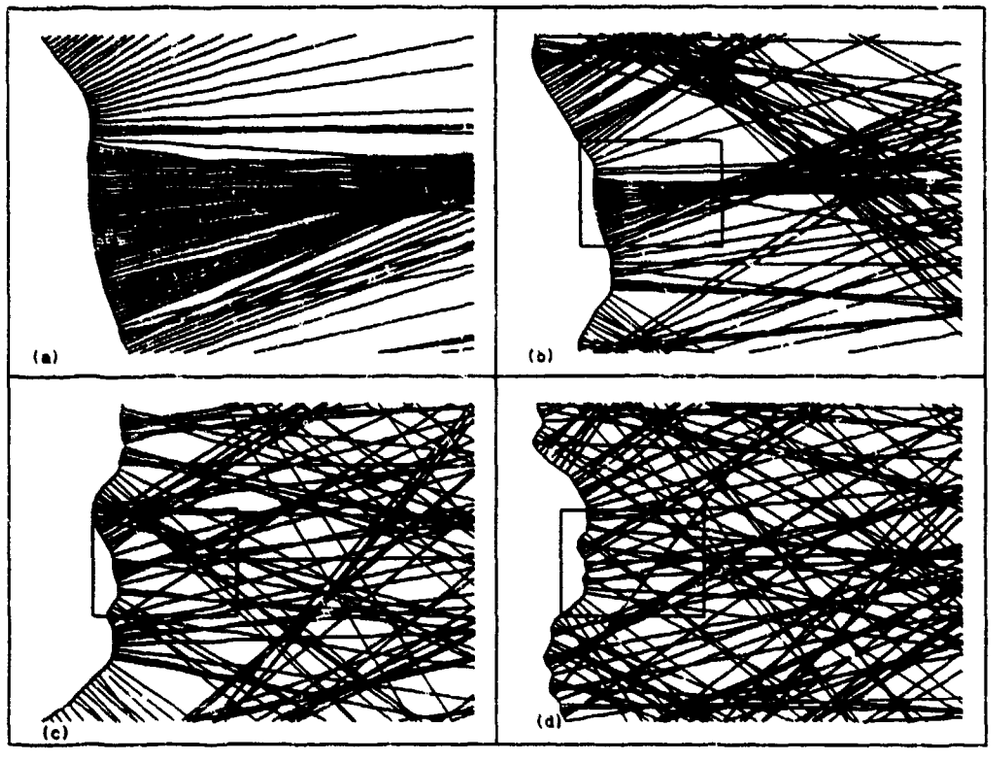


Figure 4. Rays from a Brownian sub-fractal under de-magnification. Boxes denote boundary of previous diagram.

We also see in figure 4 the effect of an inner-scale, an unavoidable consequence of discretisation. Under high magnification and close to the parent wavefront (figure 4a) the fluctuations in intensity are again weak but increase with distance with rays overlapping at distances $\geq \Delta/\delta\bar{m}$, where Δ is the discretisation length and $\delta\bar{m}$ the standard deviation of the change in slope of adjacent rays. It can be shown that covergence to asymptotic statistics is quite slow and since rays at a distance x eminate from a region of length $\sim x^2$, accurate simulations are 'expensive', requiring a large number of steps [7]. One can, of course, consider other kinds of inner-scale smoothing such as local integration [8]

$$\text{ie} \quad m(x) \rightarrow M(x) = \int_{-\infty}^{\infty} \phi(x-x')m(x')dx' \tag{19}$$

where $\phi(x)$ is peaked about $x = 0$ with $\phi(x) \rightarrow 0$ as $|x| \rightarrow \infty$. In reciprocal space

$$\bar{M}(k) = \bar{m}(k)\bar{\phi}(k) \tag{20}$$

and for $\phi(x)$ normalised, $\bar{\phi}(k) \rightarrow 1$ as $k \rightarrow 0$ showing that the low-frequency components are unaffected, as expected. Hence

$$S(x) \equiv \langle [M(x) - M(0)]^2 \rangle \xrightarrow[|x| \rightarrow \infty]{} \frac{|x|}{\Delta} \tag{21}$$

whereas, for $\phi(x)$ smooth (differentiable) and x small, S(x) is a power series in even powers of x reflecting the fact that M(x) is differentiable. It follows that under high magnification the smooth inner scale will give rise to caustics and infinite fluctuations in intensity [9]. However, at distances much greater than the inner scale, but still much less than the outer scale, the pattern is dominated by the fractal-slope behaviour (equation 21) and, provided the overlapping caustics are not resolved, will appear as in figure 4a.

Let us now return to the question of the geometrical optics limit for a Brownian fractal which should be relevant to situations where the wavelength is less than the inner scale. From equation 7, $h(x)$ satisfies $m(x) = \frac{\partial h}{\partial x} = c(x)$, ie the directions of the 'rays' are uncorrelated and the pattern would be similar to that in figure 4d. In the continuum (ray-density) limit there would be no fluctuations, ie the intensity would be constant. How this limit is approached will, of course, depend on the particular type of inner scale smoothing. Figure 4, for example, can be re-interpreted as the geometrical optics limit of a Brownian fractal with no outer scale but an inner scale such that $h(x)$ gradually changes from being a sub-fractal on small scales (figure 4a) to a fractal on large scales (figure 4d). A similar model with an abrupt change from sub-fractal to fractal has been considered by Jakeman [10]. For sufficiently smooth inner scale behaviour the fine structure will again consist of caustics which become unresolvable at large distances.

Finally, consider ray propagation from wavefronts generated from multiply integrated δ-correlated noise, shown in figure 3 and described by equations (6) and (7) with $v_n(\epsilon)$ replaced with $h_n(x)$. Examples for $n = 1 \rightarrow 4$ are shown in figure 5. The Brownian fractal and sub-fractal ($n = 1$ and 2) have been discussed above and the figure shows the disappearance of fluctuations and absence of focussing respectively. For $n = 3$, where curvature exists, caustics have formed and these become 'sharper' for the smoother curve with $n = 4$.

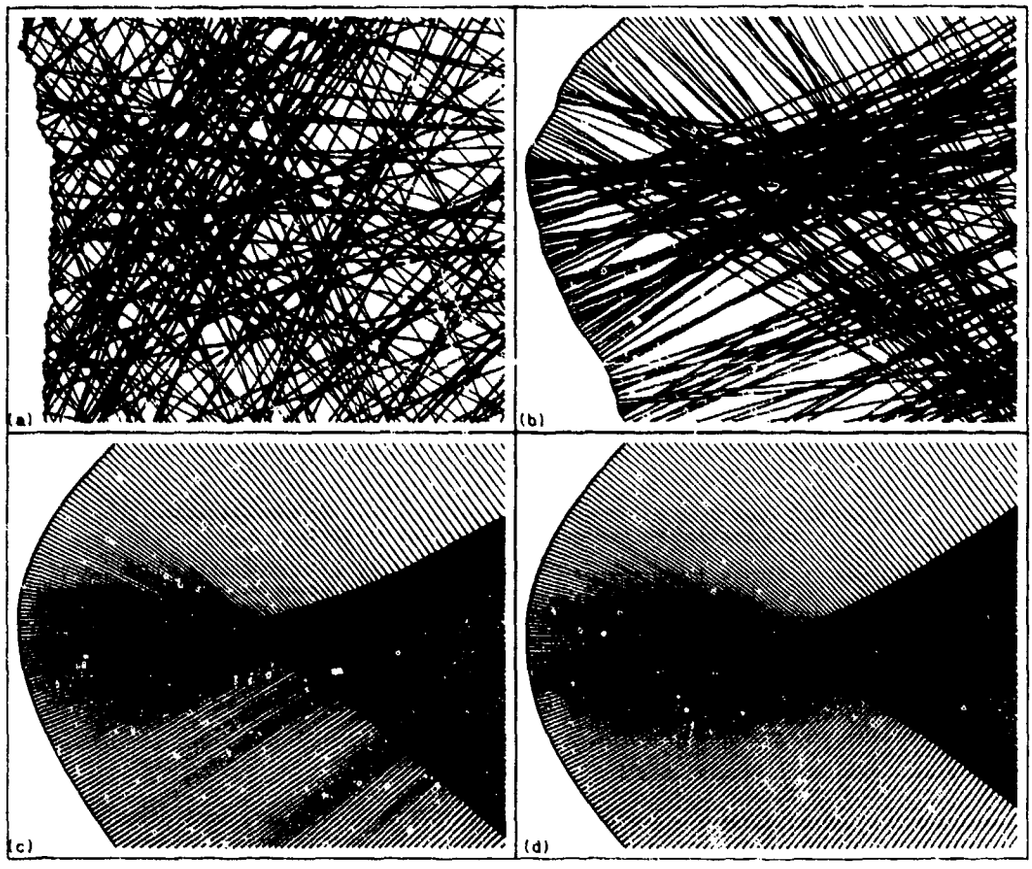


Figure 5. Ray propagation from wavefronts generated by n-th order integration of white noise with n = 1 to 4.

3. THE FRACTIONAL BROWNIAN PROCESS

3.1 Fractional calculus

In the last section we showed how repeatedly integrating δ-correlated noise led to a family of increasingly smoother stochastic processes, though smoothing occurs in discrete jumps. This procedure can be made continuous by replacing n, the order of integration, by a continuous parameter ν. Thus we are led to the concept of fractional integration and differentiation, a subject which has received a great deal of attention in the mathematics literature [11]. The stochastic processes of the last section, described by the equations 6 and 7, are now generalised to

$$v_\nu(t) = \frac{1}{\Gamma(\nu)} \int_{-\infty}^{t} (t-t')^{\nu-1} \varepsilon(t')dt' \tag{22}$$

which satisfies the fractional differential equation

$$\frac{d^\nu v_\nu(t)}{dt^\nu} = \varepsilon(t) \tag{23}$$

The form (22), often referred to as fractional Brownian motion, was first used by Mandelbrot [1] though it is at least implicit in much earlier work by Levi [12]. We see immediately from equation (22) that, for ν non-integral, the process $v_\nu(t)$ is manifestly non-Markovian, the value of the random variate $v_\nu(t)$ depending on all values in the distant past. It is only for integer values, $\nu = n$, that the process reduces to an n-th order Markov process. Since fractional differentiation satisfies the rule

$$\frac{d^\nu}{dx^\nu}\left[\frac{d^\mu f(x)}{dx^\mu}\right] = \frac{d^{\nu+\mu} f(x)}{dx^{\mu+\nu}} \tag{24}$$

then ν in equation (22) may be restricted to a range of unity and all other values outside this range may then be obtained by ordinary integration or differentiation. The choice $\frac{1}{2} < \nu < 3/2$ ensures that the increments in $v_\nu(t)$ have finite variance:

$$D_\nu(t) \equiv \langle [v_\nu(t+t') - v_\nu(t')]^2 \rangle = A_\nu |t|^{2\nu-1} \tag{25}$$

where

$$A_\nu = \frac{1}{\Gamma(\nu)^2} \left\{ \int_0^\infty [(1+x)^{\nu-1} - x^{\nu-1}]^2 dx + (2\nu-1)^{-1} \right\}$$

and $v_\nu(t)$ is referred to as fractional Brownian motion. All higher-order smoothed processes are given by integration of v_ν (cf equations 6 and 7) ie

$$v_{\nu+n} = \frac{1}{(n-1)!} \int_{-\infty}^{t} (t-t')^{n-1} v_\nu(t')dt' \tag{26}$$

satisfying

$$\frac{d^n v_{\nu+n}}{dt^n} = v_\nu(t) \tag{27}$$

Processes $\bar{v}_{\nu+n}(t)$ with finite variances may be produced in exactly the same way as described in section 2 by removing linear, quadratic ..... components from $v_{\nu+n}(t)$ (cf equations (9) and (10)).

Since $v_\nu(t)$ is non-Markovian for $\nu \neq n$ it is not practical to solve equation 23 numerically by the finite difference method, though this method is suitable for generating $v_{\nu+n}$ from v_ν (equation 27). A more general approach is to use Fourier analysis and exploit the efficiency of the FFT [12, 13]. It is easily verified that (cf equation 14)

$$v_\nu(t) = \frac{1}{2\pi} \int_{-\infty}^{\infty} \frac{e^{-i\omega t}}{(-i\omega)^\nu} \bar{\varepsilon}(\omega)d\omega \tag{28}$$

which has a spectrum

$$\bar{C}_\nu(\omega) = \omega^{-2\nu} \tag{29}$$

that is finite even though the autocorrelation function, $C_\nu(t)$, diverges. As with the Brownian case, we can find other processes which satisfy equations (25) and (29) and in this sense they are statistically equivalent. A convenient choice for numerical simulations is $\bar{v}_\nu(\omega) = |\omega|^{-\nu}\bar{\varepsilon}(\omega)$ giving the 'non-causal' process

$$v_\nu(t) = \frac{\sec(\nu\pi/2)}{2\Gamma(\nu)} \int_{-\infty}^{\infty} |t-t'|^{\nu-1} \varepsilon(t')dt' \tag{30}$$

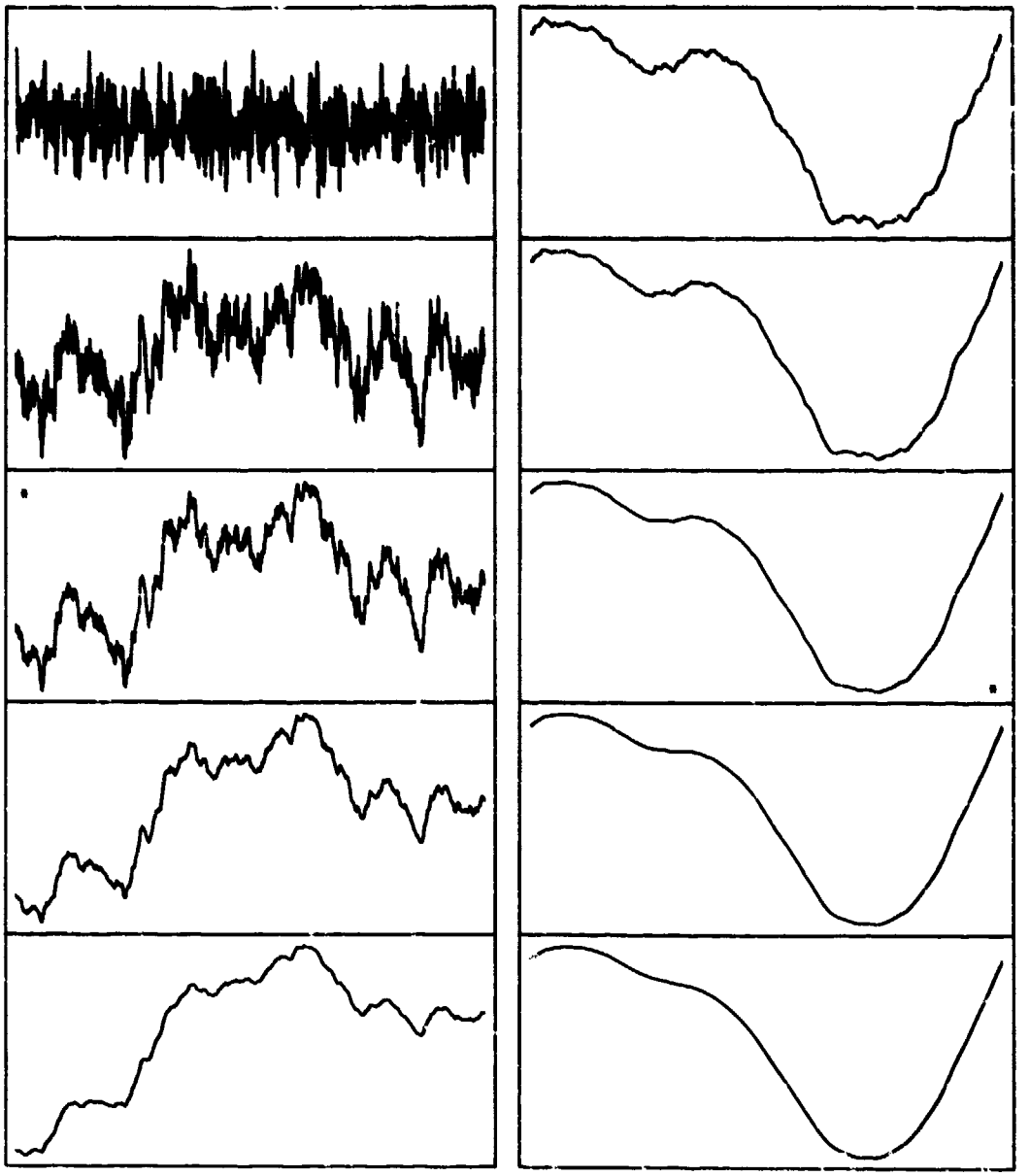
which reduces to equation (15) in the limit $\nu \to 1$.

The processes $v_\nu(t)$ in equations (22) and (30) again satisfy an affine scaling law, ie they remain statistically equivalent under the transformation $t \to kt$, $v_\nu \to k^{\nu-\frac{1}{2}} v_\nu$ in the sense that $D_\nu(t)$, equation 25, remains invariant. Processes $v_\nu(t)$ for $\nu = \frac{1}{2}$ to $\nu = 3/2$ (fractal) in steps of $\frac{1}{4}$ are shown in figure 6a, and for $\nu = 3/2$ to $\nu = 5/2$ (sub-fractal) in figure 6b. The cases of ordinary integrated white noise discussed in section 2, ie $\nu = 1$ and 2, are marked with an asterisk. This demonstrates that the procedure does indeed provide a means of generating processes with varying degrees of

roughness. It can, in fact, be shown that for the fractals (figure 6a) the 'fractional integration' index ν is related to fractal dimension by the equation [13]

$$D = \frac{5}{2} - \nu \qquad (31)$$

For $\nu > 3/2$ equation 31 is no longer applicable though ν may still be interpreted as a measure of smoothness.



(a) (b)

Figure 6. Stochastic processes produced by fractional integration of white noise. a) Fractal b) Sub-fractal.

3.2 Inner and Outer Scales

Ordinary Brownian motion, equation 1, has an exponential correlation function (equation 3) due to the presence of the correlation length or outer scale, τ. A natural way of introducing a correlation length into generalised Brownian motion is through the fractional differential equation (23) [15]:

$$\left(\frac{d}{dt} + \frac{1}{\tau}\right)^{\nu} v_{\nu}(t) = \varepsilon(t) \tag{32}$$

which has solution

$$v_{\nu}(t) = \frac{1}{\Gamma(\nu)} \int_{-\infty}^{t} e^{-(t-t')/\tau} (t-t')^{\nu-1} \varepsilon(t') dt' \tag{33}$$

ie equation (22) with an exponential damping of the integrand. The correlation function is now well defined and

$$C_{\nu}(t) \equiv \langle v_{\nu}(t) v_{\nu}(o) \rangle = \frac{(\tau t/2)^{\nu-\frac{1}{2}}}{\sqrt{\pi}\Gamma(\nu)} K_{\nu-\frac{1}{2}}(t/\tau) \xrightarrow[t>>\tau]{} (\tau/2)^{\nu} t^{\nu-1} e^{-t/\tau} \tag{34}$$

This 'non-exponential' correlation function again confirms the non-Markovian nature of the process with a power-law tail symptomatic of fractals. In fact equation (33) may be generalised by replacing the exponential factor with any smooth function peaked about the origin with a characteristic width τ and vanishing at infinity. For $t \gg \tau$, $C_{\nu}(t)$ will then be of the form $|t|^{\nu-1} f_{\nu}(t)$ where $f_{\nu}(t)$ is smooth.

Inner-scale smoothing on short time scales can again be achieved by local integration and $v_{\nu}(t)$ (equation (22) or (30)) is replaced by $V_{\nu}(t)$ where (cf equation (19))

$$V_{\nu}(t) = \int_{-\infty}^{\infty} \phi(t-t') v_{\nu}(t') dt' \tag{35}$$

where $\phi(t)$ is sharply peaked about $t = 0$ and differentiable to all orders. Hence $V_{\nu}(t)$ is also differentiable to all orders and the process is 'smooth' despite the fact that $v_{\nu}(t)$ is not differentiable and for large time scales (compared with the characteristic width of ϕ) V_{ν} and v_{ν} appear indistinguishable. This is reflected in the variance of increments of $V_{\nu}(t)$ which approximately takes the form (25) for large t but varies quadratically with t for t small ie

$$\langle [V_{\nu}(t) - V_{\nu}(o)]^2 \rangle = \frac{2}{\pi} \int_{0}^{\infty} \frac{\bar{\phi}(\omega)^2}{\omega^{2\nu}} [1 - \cos\omega t] d\omega \xrightarrow[t \to 0]{} a t^2$$

where $a = \frac{1}{\pi} \int_{0}^{\infty} \frac{\bar{\phi}(\omega)^2}{\omega^{2(\nu-1)}} d\omega$

and

$$\langle [V_{\nu}(t) - V_{\nu}(o)]^2 \rangle = |t|^{2\nu-1} \frac{2}{\pi} \int_{0}^{\infty} \frac{\phi(x/t)^2}{x^{2\nu}} [1 - \cos x] dx$$

which reduces to equation (25) for $t \to \infty$, using $\bar{\phi}(0) = 1$ for $\phi(t)$ normalised.

The correlation function is, of course, still infinite being unaffected by the inner-scale smoothing. However, since $V_{\nu}(t)$ is now differentiable, the gradient of the curve exists and we may determine its correlation properties from equation (35) ie

$$M_{\nu}(t) \equiv \frac{dV_{\nu}(t)}{dt} = \int_{-\infty}^{\infty} \phi'(t-t') v_{\nu}(t') dt' = \frac{1}{2\pi} \int_{-\infty}^{\infty} e^{-i\omega t} [-i\omega \bar{\phi}(\omega)] \bar{v}_{\nu}(\omega) d\omega$$

and

$$\langle M_{\nu}(t) M_{\nu}(o) \rangle = \frac{1}{2\pi} \int_{-\infty}^{\infty} \frac{e^{-i\omega t} \bar{\phi}(\omega)^2}{\omega^{2(\nu-1)}} d\omega \tag{36}$$

The integral obviously converges for a fractal since $2(\nu-1)$ lies between $+1$ and $\bar{\phi}(\omega)$ must decay more rapidly than ω^{-1} (otherwise $\phi(0)$ would be infinite). For large times it has the asymptotic form:

$$\langle M_{\nu}(t) M_{\nu}(o) \rangle \xrightarrow[t \to \infty]{} \frac{\Gamma(3-2\nu) \sin\pi\nu}{\pi |t|^{3-2\nu}} \tag{37}$$

Since $3-2\nu$ lies between 0 and 2 we see that the gradients tend to become decorrelated at large times [illegible] or $\nu = 1$, (37) vanishes in agreement with section 2 where it was argued that the slope [illegible]come δ-correlated as the inner-scale smoothing tends to zero. Note that (37) change[illegible]n through $\nu = 1$ and the gradients for $\nu > 1$ are said to be anti-correlated.

These results are easily extended to the integrated fractals with $\nu > 3/2$ (see equation 26) and in general the correlation properties of the process are unaffected by the inner-scale smoothing (equation 35) on sufficiently large time scales whereas the presence of an outer scale (the correlation length τ in equation 32) will mean that the process will always appear δ-correlated on time-scales $\gg\tau$.

3.3 Geometrical Optics

As with the Brownian case (section 2.5), the general one-dimensional diffractal is modelled by fractional Brownian motion (equation 22 or 30) with the replacement

$$v_\nu(t) \rightarrow h_\nu(x)$$

where $h_\nu(x)$ is the height of the wavefront relative to its mean. $h_\nu(x)$ is not differentiable as evidenced by the fact that

$$\langle\left|\frac{\Delta h}{\Delta x}\right|\rangle = \frac{\langle|h(x+\Delta x)-h(x)|\rangle}{\Delta x} \sim \frac{1}{|\Delta x|^{3/2-\nu}} \xrightarrow{\Delta x \to 0} \infty$$

and h(x) appears rough on all length scales (see, for example, figure 1b). As a consequence, there can be no geometrical optics limit and the build up of fluctuations as the wave propagates are due entirely to interference and diffraction and have been shown to be weak [2,16]. As pointed out in section 2.5, this idealised picture should be a reasonable approximation to a more realistic model in which the wavefront has a fractal form down to length scales of the order of the wavelength. On the other hand, if the fractal wavefront has inner-scale smoothing on length scales greater than the wavelength then the geometrical optics limit should be relevant. Neighbouring rays will coalesce to form caustics and large intensity fluctuations will build up on short length-scales. At greater distances the intensity (ray-density) pattern will be dominated by the overlap of rays which originate from points which are separated by distances much greater than the inner-scale. However, the directions of these rays are only weakly correlated since the correlation function varies inversely as a power of the separation (equation 37 with t replaced by x). Hence the fluctuations in ray-density will be small, provided the caustics are not resolved, tending to zero with distance. Indeed, it can be shown that the ray-density fluctuations disappear at <u>all</u> distances in the limit of vanishingly small inner-scale.

The once integrated fractal wavefront has, by definition, a fractal slope and hence the directions of the rays are correlated over all length-scales, the variance of increments in slope being

$$\langle[m_\nu(x)-m_\nu(o)]^2\rangle = \text{const}\ |x|^{2\nu-1} \qquad (38)$$

where $2\nu - 1$ varies between 0 and 2 (cf equation 25). Such strong correlations lead to large intensity fluctuations as ν increases and these scale with distance in a manner determined uniquely by the affine scaling property of $m_\nu(x)$ [17]. We have already argued that there are no ray-density fluctuations from a fractal with a vanishingly small inner scale and we might expect, from continuity, that the fluctuations from a fractal-slope wavefront would gradually increase from $\nu = \frac{1}{2}$. This is indeed the case as is demonstrated in figure 7 where we show ray propagation from sub-fractal wavefronts similar to those shown in figure 6b

Since there is no curvature to the wavefront, caustics cannot be formed, though for the 'marginal' sub-fractal, $m_{3/2}(x)$ shown in figure 7e, caustics are beginning to emerge and gradually become sharper as ν is increased (see, for example, figures 5c, 5d).

4. HIGHER DIMENSIONS

The methods for generating multi-scale stochastic processes in one-dimension may be extended to higher dimensions as follows. Let $h_\nu(\underline{r})$ be a random function in an n-dimensional space (a stochastic field) and $\bar{h}_\nu(\underline{k})$ its Fourier transform. Choosing the spectrum of $h_\nu(\underline{r})$ to be

$$\bar{C}_\nu(\underline{k}) = 1/k^{2\nu+n-1} \tag{39}$$

leads to a divergent autocorrelation function for ν in the range 1/2 to 3/2, though the variance of increments of $h_\nu(\underline{r})$ is finite.

$$\text{ie} \quad D_\nu(\underline{r}) \equiv \langle [h_\nu(\underline{r}+\underline{r}') - h_\nu(\underline{r}')]^2 \rangle = \left(\frac{1}{2\pi}\right)^n \int \frac{2}{k^{2\nu+n-1}} [1 - e^{-i\underline{k}\cdot\underline{r}}] d^n k = A_\nu r^{2\nu-1} \tag{40}$$

where

$$A_\nu = \left(\frac{1}{2\pi}\right)^n \int d\Omega_n \int_0^\infty dx \, \frac{2}{x^{2\nu}} [1 - \cos(x \cos\theta_n)]$$

(cf equations 25 and 29). Choosing

$$\bar{h}(\underline{k}) = \frac{\bar{\varepsilon}(\underline{k})}{k^{\nu+\frac{n-1}{2}}},$$

where $\bar{\varepsilon}(\underline{k})$ is the Fourier transform of δ-correlated gaussian noise, gives

$$h(\underline{r}) = \left(\frac{1}{2\pi}\right)^n \int \frac{e^{-i\underline{k}\cdot\underline{r}}}{k^{\nu+\frac{n-1}{2}}} \bar{\varepsilon}(\underline{k}) d^n k = \int |\underline{r} - \underline{r}'|^{\nu-\frac{n+1}{2}} \varepsilon(\underline{r}') d^n r' \tag{41}$$

which satisfies the fractional differential equation

$$\nabla^{\nu+\frac{n-1}{2}} h_\nu(\underline{r}) = \varepsilon(\underline{r}) \tag{42}$$

It may be shown [13] that the fractal dimension of $h_\nu(\underline{r})$ is

$$D = n + 3/2 - \nu \tag{43}$$

and hence lies in the range $n < D < n + 1$. As in one-dimension, D is a measure of roughness. In two dimensions, for example, $D = 2^+$ (marginal fractal) corresponds to a 'smooth' (ie almost differentiable) surface whereas $D = 3^-$ is very rough and virtually volume filling. Further smoothing can again be achieved by extending the range of ν as described in sections 2 and 3. The analogue of a Markov process in higher dimensions is when $\nu + (n-1)/2$ in equation (42) is integral and the equation may be solved by finite difference methods. An interesting example is the case

$$\nabla^2 h_\nu(\underline{r}) = \varepsilon(\underline{r}) \tag{44}$$

which is Poisson's equation for the potential $h_\nu(\underline{r})$ due to random δ-correlated charges. In one-dimension $h_\nu(\underline{r}) = h_2(x)$, a Brownian sub-fractal; in two dimensions $\nu = 3/2$ and $h_{3/2}(\underline{r})$ is a marginal fractal, whereas in three dimensions $\nu = 1$ and $h_1(\underline{r})$ is a Brownian fractal.

For $\nu + (n-1)/2$ fractional, equation (42) may be solved numerically using the integral form (41) and fast Fourier transforms. We have used this method to generate surfaces which are at least once differentiable ($\nu > 3/2$) from which surface gradients, $\underline{m}(\underline{r}) = \nabla h(\underline{r})$, are computed. This data has been used to simulate free propagation of a planar wavefront in the geometrical optics limit. Figure 8 shows contrast plots (cross sections through rays) at a fixed distance from the parent wavefronts for $3/2 < \nu < 7/2$ in steps of 1/4. As in one dimension (see figure 7), the fluctuations increase from virtually none (figure 8, top left) to quite large values at the end of the sub-fractal regime (centre of figure 8) where caustics are just beginning to form. These become sharper with increasing ν.

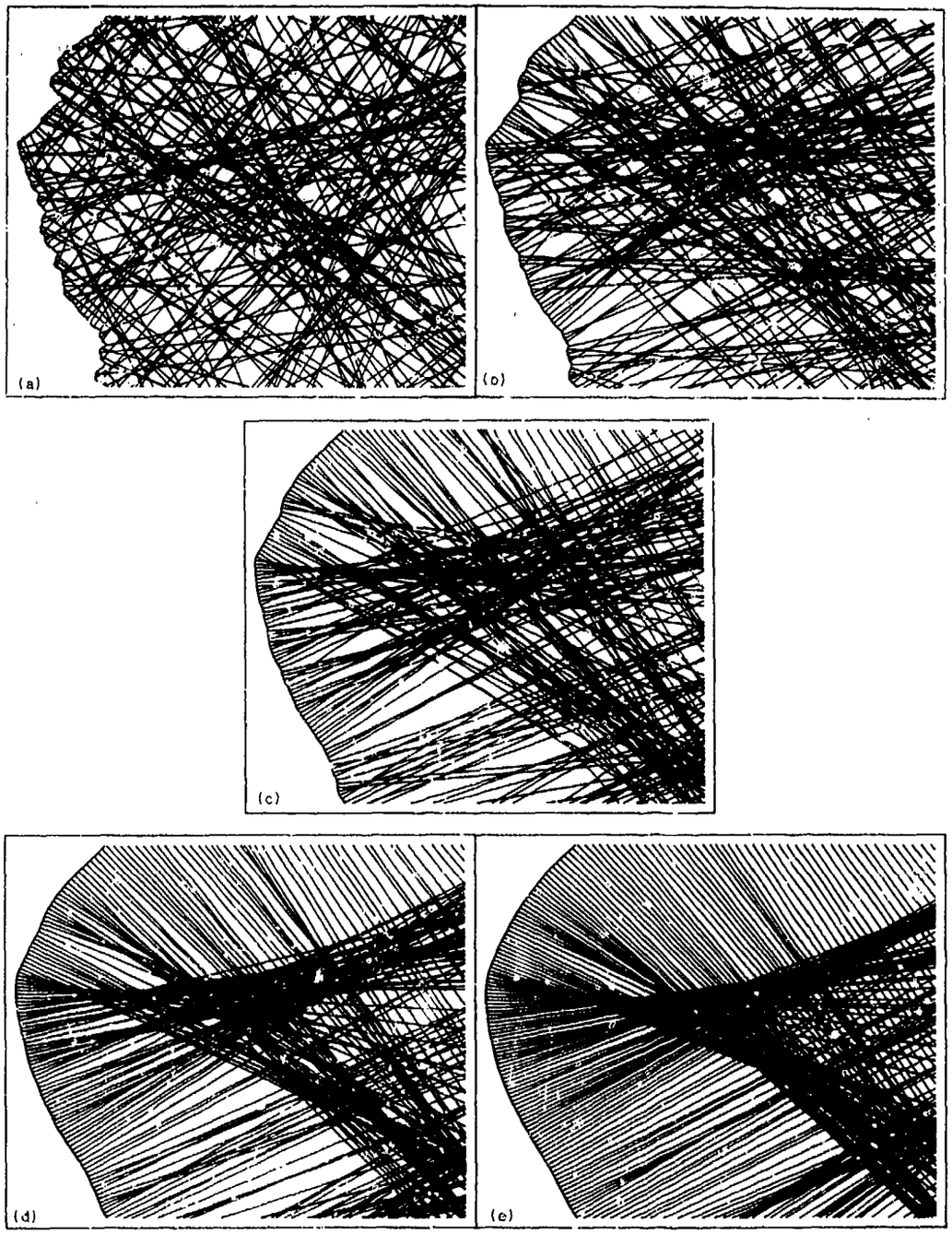


Figure 7. Ray propagation from sub-fractal wavefronts generated by fractional integration of white noise. (c) is the Brownian sub-fractal, figure 3b.

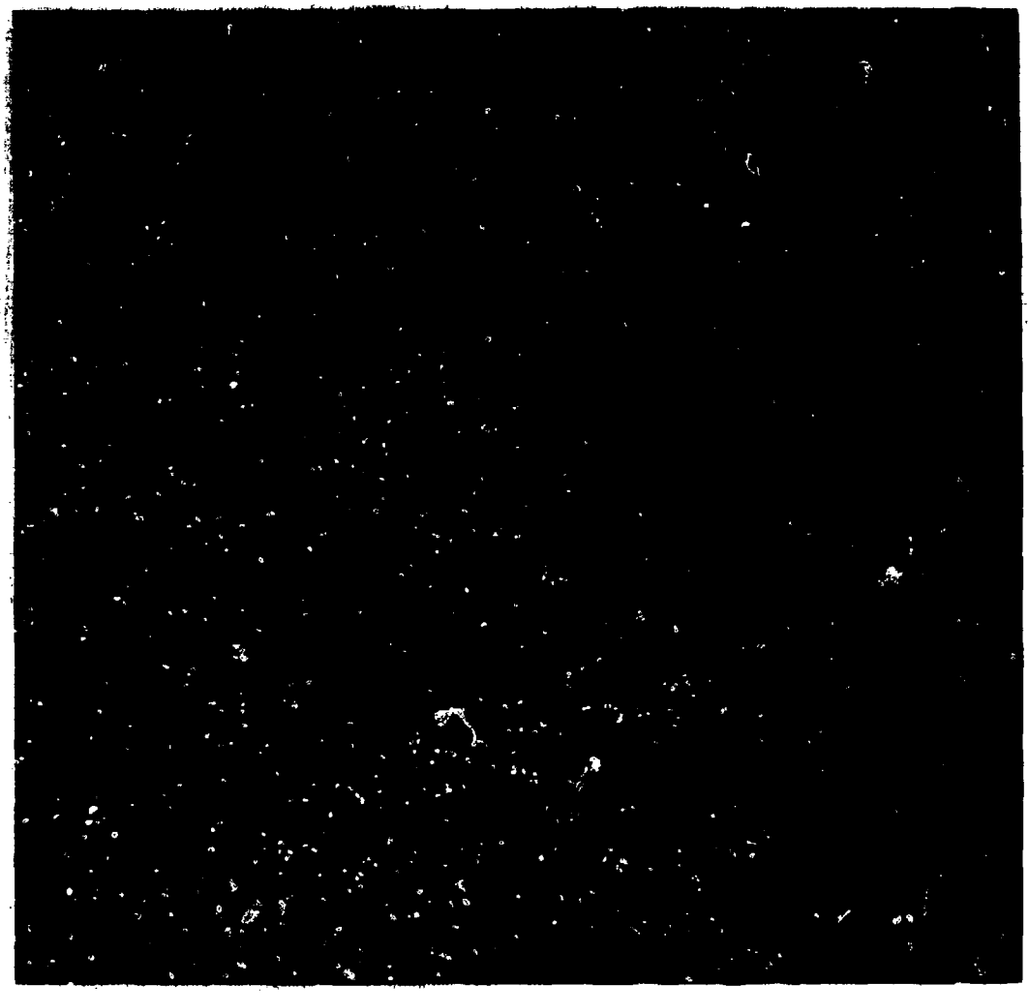


Figure 8. Contrast plots of rays from two-dimensional wavefronts after free propagation. ν = 1.5 (rays just defined) to ν = 3.5 (ν = 1.5 twice integraced) in steps of 0.25.

Finally, let us briefly consider ray-propagation in an extended medium with refractive index $\mu(\underline{r})$. As the rays propagate their directions change continuously according to the equation [18]:

$$\mu \frac{d\underline{e}}{ds} = \underline{\nabla}\mu - \underline{e}(\underline{e}.\underline{\nabla}\mu) \qquad (45)$$

where $\underline{e}$ is a unit vector along a ray and ds an element of path. Setting $\mu = \mu_o + \delta\mu$, where $\langle \delta\mu \rangle = 0$, a multi-scale stochastic field $\mu(\underline{r})$ may be simulated using equation (41) with the replacement $h(\underline{r}) \rightarrow \delta\mu(\underline{r})$ and equation (45) then solved numerically using finite difference methods. This has been done in two dimensions using essentially the same data which generated the freely propagating wavefronts whose contrast patterns were shown in figure 8. The results are plotted in figure 9 which clearly shows the progression from 'turbulent flow' to a more 'laminar flow' with greater fluctuations in ray density due to bunching and anti-bunching of bundles of rays.

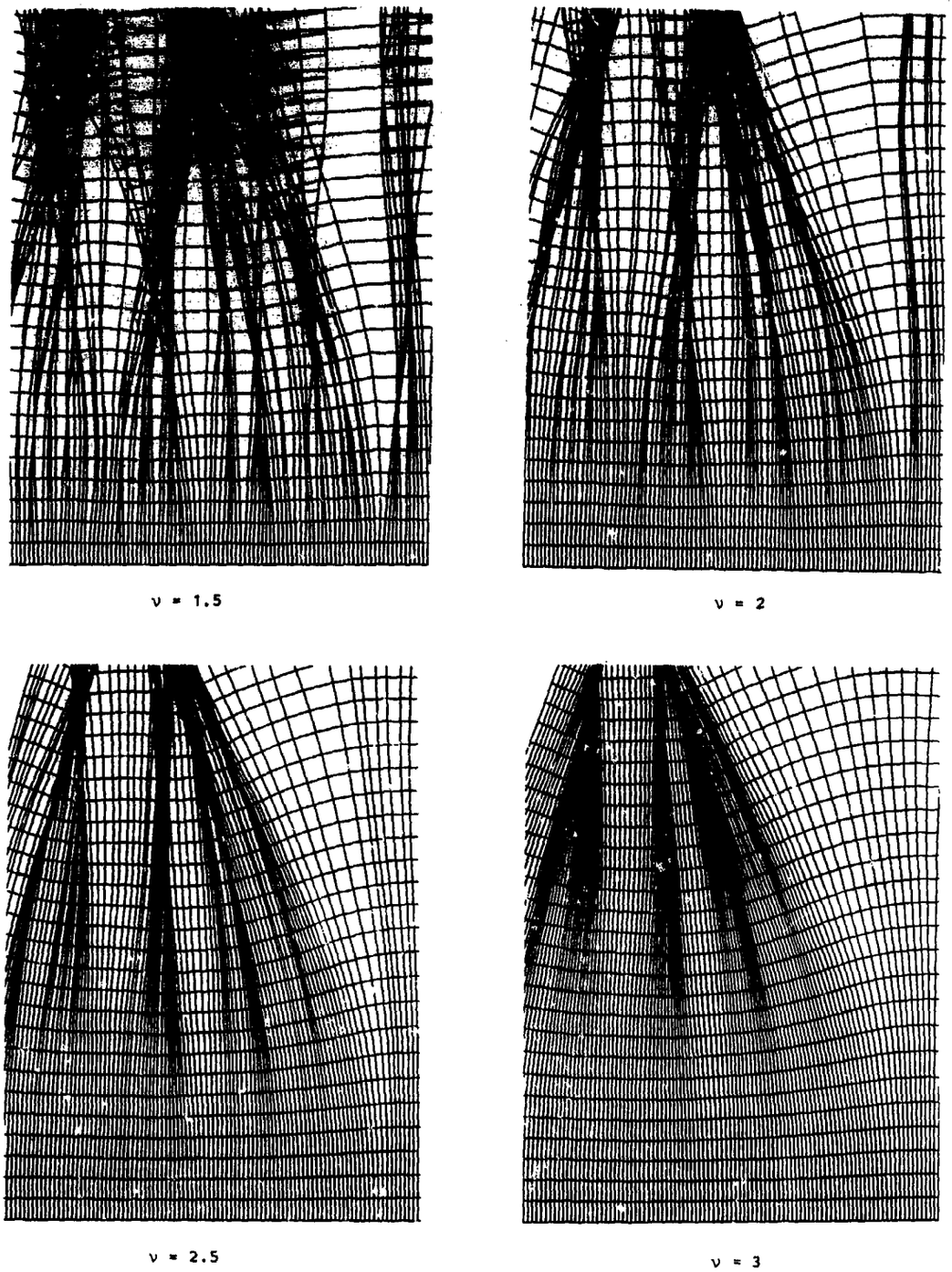


Figure 9. Ray diagrams showing geometrical wavefronts for a one-dimensional plane wave propagating through multi-scale random media.

5. SUMMARY AND CONCLUSIONS

In this paper we have analysed a class of multi-scale stochastic processes which remain statistically invariant under certain scaling transformations.

Such processes have been generated numerically from white noise using standard Fourier techniques and a wide range of examples have been presented graphically to illustrate the versatility of the model in simulating a broad spectrum of naturally occuring random phenomena. In particular, we have used the model to discuss wave propagation in the geometrical optics limit.

It is hoped that future work will concentrate on accurate determinations of the ray statistics and correlation properties, an extension of the techniques to full wave propagation, and application to the simulation of image degradation and reconstruction.

REFERENCES

1. B B Mandelbrot, "The fractal geometry of nature", San Francisco: Freeman (1982).

2. M V Berry, "Diffractals", J Phys A12 (1979) 781-797.

3. N Wax (Ed), "Selected papers on noise and stochastic processes", Dover (1954).

4. W Feller, "An introduction to probability theory and its applications", Vol 2, Wiley (1971) p97.

5. D C Champeney, "Fourier transforms and their physical applications", Academic Press (1973).

6. E Jakeman, "Scattering by a corrugated random surface with fractal slope", J Phys A 15, (1982) L55-L59.

7. J H Jefferson, E Jakeman and J E P Beale, "Computation of ray statistics beyond a multi-scale diffuser", Proc Inst Acoust 8 (1986) 30-35.

8. B B Mandelbrot and J W Van Ness, "Fractional Brownian motions, fractional noises and applications", SIAM review 10 (1968) 422.

9. M V Berry, "Focussing and twinkling: critical exponents from catastrophes in non-gaussian random short waves", J Phys A 10 (1977) 2061-2081.

10. E Jakeman, "Hierarchical scattering models", this volume.

11. A Dold and B Eckmann, "Fractional calculus and its applications", lecture notes in mathematics 457, Springer-Verlag (1975).

12. P Levi, "Random functions: General theory with special reference to Laplacian random functions", Univ California Publ Statist, 1 (1953) 357.

13. R F Voss, "Random fractal forgeries", Proc NATO ASI on fundamental algorithms in computer graphics, Ilkley, Yorkshire, UK (1985) 805-829.

14. R F Voss, "Random fractals: characterisation and measurement", Proc NATO ASI on scaling properties of disordered systems, Geilo, Norway (1985).

15. P Whittle, "Stochastic processes in several dimensions", Statistics in Physical Sciences I (1963) 974-994.

16. E Jakeman and J H Jefferson, "Scintillation in the Fresnel region behind a sub-fracal diffuser", Optica Acta 31 (1984) 853-865.

17. E Jakeman, "Fresnel scattering by a corrugated random surface with fracal slope", J Opt Soc Am 72 (1982) 1034-1041.

18. L D Landau and E M Lifshitz, "Electrodynamics of continuous media", Pergamon, New York (1960).

ACKNOWLEDGMENTS

We are grateful to Professor E Jakeman and Dr R J A Tough for helpful and stimulating discussions.

SPACE-TIME STATISTICS OF WAVES PROPAGATING THROUGH A DEEP PHASE SCREEN

S. J. Franke and C. H. Liu
University of Illinois at Urbana-Champaign
Urbana, Illinois 61801 USA

SUMMARY

In this paper, we study wave propagation through a deep phase screen in which the properties vary randomly both with time and space. Two approaches will be discussed. One is analytical, the other involves numerical simulation. In the analytical approach, asymptotic expressions for the space-time correlation functions of the wave field are derived for the case of gaussian random irregularities. For the simulation approach, general prescribed space-time random variations of irregularities are generated and used to represent a time varying phase screen. This technique can be used to model a screen with a power-law type of irregularity spectrum. Numerical propagation code is then used to compute the wave fields at the reception plane from which statistics will be calculated. The relations between the statistics of the wave fields and the space-time variations of the medium will be discussed. Applications of the results will be discussed.

INTRODUCTION

The concept of a "phase screen" is often used as a simplified model in problems involving wave propagation through a slab containing continuous random variations in refractive index. This model has been extensively used to study scintillation effects caused by the atmosphere, ionosphere and interplanetary medium (e.g. Booker and MajidiAhi, 1981; Rino, 1981;Scott et al., 1983). Most of the work has concentrated on studies of the spatial correlation function or spectrum of the intensity fluctuations that develop after a wave encounters a random phase screen. The temporal correlation or spectrum is usually obtained by invoking Taylor's frozen-in hypothesis. Notable exceptions may be found in the work of Jakeman and Pusey, (1975) and Wernik et al., (1983) where the space-time correlation was studied for models that allow for random temporal variation. These studies were restricted to the far-field of a screen with Gaussian irregularities, and a screen with power-law irregularities and small phase variance, respectively.

In this paper we consider the space-time intensity correlation function caused by a deep-phase screen with a realistic model for the random space and time variations. We first review an analytical approach based on the Huygens-Fresnel integral to study the screen with Gaussian space correlation and time variation modeled by giving the phase irregularities in the screen a distribution of velocities. Some interesting aspects of the resulting intensity correlation function will be noted and discussed. In particular, we study the case where the time variation is caused purely by rearrangement, i.e. the average drift velocity of the irregularities is zero. In the focusing, or non-Gaussian, regime of intensity fluctuations we find that the temporal correlation function exhibits peaks that are displaced symmetrically from zero time lag for spatial separations larger than width of a "focusing spike". A physical interpretation will be given for this phenomenon. The characteristic spatial and temporal scales of the intensity fluctuations in the non-Gaussian regime will be shown to yield a characteristic velocity for the intensity fluctuations that is smaller than the characteristic random velocity associated with the underlying phase screen. Then, in section 2, we describe a numerical simulation procedure that can be used to study more general types of phase correlation functions and temporal variation models. We will show that the simulation gives results that agree closely with the analytical approach. Some results for a screen with power-law irregularities will also be presented. Finally, we present a set of examples that correspond to a realistic ionospheric scintillation measurement where the irregularities have an average drift as well as random temporal rearrangement.

1. FORMULATION AND ANALYTICAL APPROACH

We consider a plane wave propagating in the +z direction incident on a one-dimensional phase screen located at z=0. The complex amplitude of the wave field in a plane at a distance z from the screen can be written under the Huygens-Fresnel approximation as:

$$u(x,z,t) = \sqrt{\frac{jk}{2\pi z}} \int_{-\infty}^{\infty} e^{-j\phi(x_1,t)} e^{-j\frac{k}{2z}(x-x_1)^2} dx_1 \qquad (1)$$

Using (1), the intensity of the wave field can be found.

$$I(x,z,t) = \frac{k}{2\pi z} \iint_{-\infty}^{\infty} \exp[-j\{\phi(x_1,t) - \phi(x_2,t) + \frac{k}{2z}((x_1-x)^2 - (x_2-x)^2)\}] dx_1 dx_2 \qquad (2)$$

The intensity correlation function in a plane at a distance z from the screen can be derived from (2) and is given by (Jakeman, 1982):

$$B_I(x,t) = \langle I(0,z,0)I(x,z,t)\rangle = \frac{k}{2\pi z}\iint_{-\infty}^{\infty} \exp[\, g(u,w,t)]\, \exp[\, -j\,\frac{k}{z}\, w(u+x)\,]\, du\,dw \qquad (3a)$$

where

$$g(u,w,t) = -2B_\phi(0,0) + 2B_\phi(-u,t) + 2B_\phi(w,0) - B_\phi(w-u,t) - B_\phi(-w-u,t) \qquad (3b)$$

where k is the free space wavenumber and $B_\phi(x,t)$ is the space-time correlation function of the phase variations in the screen which is defined as:

$$B_\phi(x,t) = \langle \phi(0,0)\phi(x,t)\rangle \qquad (4)$$

We now consider the model for the phase correlation function. We adopt the random motion model introduced by DeWolf (1975) in which the screen is built up from a superposition of individual irregularities (eddies) with a specified cross section i.e.:

$$\phi(x,t) = C \sum_{i=1}^{M} \sum_{k=1}^{N_i} a_{ki}\, f(x - x_{ki}, l_i) \qquad (5)$$

where

C = normalization constant

N_i = number of eddies with scale size l_i

M = number of scale sizes

x_{ki} = position of k'th eddy with scale size l_i

f(x,l) = profile of the eddies

a_{ki} = amplitude of k'th eddy with scale size l_i

This is a very general model for the time varying phase screen and allows for a range of scale sizes through the parameter l_i. The time variation is introduced by allowing the amplitudes and/or positions of the eddies to be functions of time. We chose to represent the screen in form given by (5) because this representation is convenient for direct numerical simulation of time varying phase screens. For this study we assume a Gaussian profile for the individual eddies, i.e.

$$f(x,l) = \exp(-\frac{x^2}{2l^2}) \qquad (6)$$

To model a phase screen with a Gaussian correlation function we can set M=1 in (5). Using (6) this model gives a spatial correlation function of the form:

$$B_\phi(x) = \sigma_\phi^2 \exp(-\frac{x^2}{l_0^2}) \qquad (7)$$

where σ_ϕ^2 is the variance of the phase fluctuations. For this study we introduce temporal rearrangement into the model by assigning a constant but random drift velocity to each eddy, i.e. in (5) we let x_{ki} depend on time through:

$$x_{ki}(t) = x_{ki0} - v_{ki}\, t \qquad (8)$$

where x_{ki0} and v_{ki} are the position at t=0, and velocity of the k'th eddy with scale size l_i, respectively. From here on, we assume that x_{ki0} is uniformly distributed over the screen and v_{ki} are independent, normally distributed random variables with mean v_0 and variance σ_v^2. We also assume that the initial position and velocity of the irregularities are independent. In this case, the space-time correlation function will have the form:

$$B_\phi(x,t) = \int B_\phi(x-vt)\, p(v)\, dv \qquad (9)$$

where

$$p(v) = \frac{1}{\sqrt{2\pi}\ \sigma_v} \exp[- \frac{(v - v_0)^2}{2\sigma_v^2}] \qquad (10)$$

For the special case where $B_\phi(x)$ is a Gaussian spatial correlation function (e.g. equation (7)) it is possible to obtain a simple closed form expression for the space-time phase correlation function:

$$B_\phi(x,t) = \frac{\sigma^2}{\sqrt{\gamma}} \exp[- \frac{(x - v_0 t)^2}{\gamma l_0^2}] \qquad (11)$$

where the time dependent parameter $\gamma(t)$ is defined by:

$$\gamma(t) = 1 + \frac{2\sigma_v^2 t^2}{l_0^2} = 1 + \frac{2t^2}{T_r^2} \qquad (12)$$

The parameter T_r may be thought of as the "rearrangement" time of the screen. Note that this model is not separable in the space and time variables. This is a consequence of the fact that the random temporal variation is introduced through convective rearrangement of the screen. A separable model would result if the amplitudes instead of the positions of the scattering centers were allowed to change randomly in time. The model described by equations (11) and (12) can be used in equation (3) to study the space-time intensity correlation function. Jakeman and McWhirter (1977) have studied the spatial intensity correlation function using a Gaussian correlation function (i.e. equation (7)). They derived an asymptotic result that is valid when $\sigma_\phi^2 >> 1$. The space-time correlation function can be studied in a similar manner. The resulting expression is somewhat lengthy and will not be repeated here. It should be noted that evaluation involves the computation of two one-fold integrals which are computed using an adaptive integration routine. The analysis is given in Franke (1987). The result can be expressed in terms of the following dimensionless parameters:

$$q = \frac{k l_0^2}{2\sqrt{6}\, z}$$

$$T_c = \frac{l_0}{v_0}$$

$$T_r = \frac{l_0}{\sigma_v}$$

$$X = \frac{x}{l_0}$$

$$Z = \frac{z}{k l_0^2}$$

Jakeman and McWhirter (1977) have identified the parameter q^{-1} as the effective number of statistically independent scatterers that contribute to the field at a point in the reception plane. When q^{-1} is large, the in-phase and quadrature components of the complex amplitude are independent and normally distributed and the statistics of the field are said to be "Gaussian". In this limit, the intensity fluctuations are Rayleigh distributed. When q^{-1} is near unity, the fluctuations are non-Gaussian, and the intensity is dominated by focusing "spikes" of width on the order of $l_0/(\sqrt{2}\sigma_\phi)$. The Gaussian limit for the space-time intensity correlation function can be obtained directly by invoking the factorization theorem for Gaussian fields (Yeh and Liu, 1982) which gives:

$$B_I(x,t) = 1 + \exp[- D_\phi(x,t)] \qquad (13)$$

where $D_\phi(x,t)$ is the phase structure function:

$$D_\phi(x,t) = 2 [B_\phi(0,0) - B_\phi(x,t)] \qquad (14)$$

Note that for times much smaller than the rearrangement time of the screen, (13) can be written (using (11)) as:

$$B_I(x,t) = 1 + \exp[- \frac{2\sigma_\phi^2}{l_0^2} \{ (x - v_0 t)^2 + \sigma_v^2 t^2 \}] \qquad (15)$$

In this case, the saturated intensity correlation function has a spatial correlation scale $l_c = l_0/(\sqrt{2}\sigma_\phi)$ and a temporal correlation scale $\tau_c = l_0/(\sqrt{2}\sigma_v\sigma_\phi)$. The intensity correlation function can be characterized by defining a characteristic rearrangement velocity for the intensity pattern $v_c = l_c/\tau_c = \sigma_v$. Note that this characteristic velocity is the same as the width of the random velocity distribution in the screen. It should be noted that Wernik et al (1983) have shown that the same relationship holds true for intensity fluctuations due to a shallow screen where $\sigma_\phi^2 << 1$. In what follows, the relationship between the velocity distribution in the screen and characteristic velocity of the intensity pattern will be examined for the deep screen in the case where the statistics are non-Gaussian.

For illustration, we consider two cases for which the space correlation was also studied by Jakeman and McWhirter (1977). In both cases the phase variance $\sigma_\phi^2 = 100$. The parameter q^{-1} is 1.38 and 2.45 for cases 1 and 2, respectively. The intensity scintillation index $S_4 = (\langle I^2 \rangle - \langle I \rangle^2)^{1/2}/\langle I \rangle$ for both cases is greater than 1, so these examples correspond to intensity fluctuations in the focusing regime. Figure 1a,b shows contour plots of the normalized intensity covariance function $C_I(x,t)$ for these two examples where:

$$C_I(x,t) = \frac{B_I(x,t) - 1.0}{B_I(0,0) - 1.0} \qquad (16)$$

In these figures, the spatial covariance function $C_I(x,0)$ corresponds to the cut along the vertical axis and the temporal covariance function $C_I(0,t)$ corresponds to the cut along the horizontal axis. The interesting shape of the contours is evidence that the intensity covariance is not separable in the space and time variables. Note that width of the space covariance is approximately the same for the two cases. This can be seen by noting that the 0.5 level contour intersects the vertical axis at a normalized space lag of approximately 0.075. Jakeman and McWhirter (1977) showed that the space covariance will be dominated by a component with characteristic scale $l_0/(\sqrt{2}\sigma_\phi)$, or in normalized coordinates, $1/(\sqrt{2}\sigma_\phi)$. For both of these examples, this scale is 0.071 in normalized coordinates. On the other hand, it is seen that the temporal coherence time is significantly different for the two examples. For case 1 where $q^{-1} = 1.38$, the 0.5 level contour intersects the normalized time axis at 0.131. For case 2 where $q^{-1} = 2.45$, the temporal covariance falls to 0.5 at normalized time 0.080. The temporal coherence time is longer for the case that corresponds to the fewest number of independent scattering contributions. It is interesting to compute a characteristic random velocity, v_c, for the intensity flucuations where v_c is the quotient of the characteristic length and time scales. For case 1 we find $v_c = 0.57\sigma_v$, and for case 2, $v_c = \sigma_v$. Note that the characteristic random velocity associated with the intensity fluctuations is smaller than that of the underlying phase screen for the case corresponding to the smaller number of independent scattering contributions.

Another interesting aspect of the temporal covariance function can be seen by examining horizontal cuts through Figure 1a,b. This is shown in Figure 2 where the temporal covariance for case 1 is shown for normalized spatial separations of 0.0, 0.05, 0.10 and 0.15. Note that for spatial separations larger than the characteristic width of the space covariance, the temporal covariance exhibits a peak that is displaced from 0 time lag. Because of the symmetry of the covariance function, a peak would also be seen at the same negative time lag. This peak suggests the following physical interpretation: In the focusing regime, the intensity is dominated by spikes of width $l_0/(\sqrt{2}\sigma_\phi)$. If two receivers are separated by more than the width of a spike, then it is likely that when receiver #1 "sees" a spike, receiver #2 will not (or vice versa). In this case, the intensity covariance will be small. Because of the temporal rearrangement, however, it is likely that some time later, a similar spike will be seen on receiver #2. Of course, by the time the spike is seen on receiver #2 it may have changed its shape appreciably, so the correlation is relatively small. It is tempting to associate this phenomenon with the fact that we have introduced time variation through convective motions of the individual scattering centers. To check this hypothesis, we also computed the intensity covariance using a separable model for the phase correlation function, i.e.:

$$B_\phi(x,t) = e^{-x^2/l_0^2} e^{-t^2/\tau_r^2} \qquad (17)$$

This model could result from a situation where temporal variation comes from random fluctuations of the amplitude (but not position) of the scattering centers. It is interesting to note that we found a similar phenomenon for this model as well. In fact, the overall shape of the intensity covariance contours were very similar to those shown in Figure 1. The reason that the intensity covariance is very similar for both separable and non-separable phase correlation models is due to the fact that the intensity covariance is appreciable only for time lags which are much smaller than the rearrangement time of the screen. For such short lags, both models have essentially the same (separable) form. In other words; whether the time variation is caused by convective rearrangement, or time varying amplitudes, the effect in the reception plane under focusing conditions is evidently to cause the focusing spikes to randomly "convect".

In the following section, we describe the results of a numerical simulation procedure that has been used to check the analytical results. The procedure will also allow us to consider more general models for the phase correlation function and temporal rearrangement mechanisms.

2. NUMERICAL SIMULATIONS

The analytical approach that was reviewed in the previous section is limited by the condition that $\sigma_\phi^2 >> 1$ and by the need for a relatively simple closed form expression for $B_\phi(x,t)$. Using the model given in equation (5) it is relatively simple to numerically

generate phase screens with prescribed space-time correlation functions. In practice, the number of eddies used is large enough so that the phase at any point in the screen is determined by the superposition of several individual eddies. This is done to ensure that the phase will be approximately normally distributed. As in the previous section, we introduce random time variation into the model by giving each eddy a random drift velocity. Since the length of the phase screen is necessarily limited, when an eddy leaves the edge of the screen, we make it wrap around and re-enter the screen on the other side. If this is not done, the number density of irregularities in the screen will decrease in time as the scattering centers "diffuse". In practice, a screen is generated for some instant in time, say t_1. A plane wave is then numerically propagated through the screen using equation (1) to some observation plane at a distance z from the screen. This step can be done very efficiently using the Fast Fourier Transform (e.g. Knapp, 1983). Then, a new screen is generated at time $t=t_1+\delta t$ by changing the position of each the irregularities in the screen by $v_{xi}\delta t$, where v_{xi} is the velocity of the i'th irregularity with scale size l_i. The propagation is then repeated for this new screen. This process is continued until a sufficiently long time sequence has been built up.

For the examples to be presented here we use 2048 points along the x-direction with a normalized increment $x/l_0 = 0.005$ to represent the screen at each instant in time. The total length of the screen is then 10 times the characteristic scale size of the irregularities. We then re-generate the screen at each of 2048 time steps with normalized time increment $t/T_r = 0.006$. The total length of the resulting time series is 12 times the rearrangement time of the screen. We therefore generate data equivalent to that which would be obtained in an experiment with 2048 individual receivers. It should be noted that care must be taken to ensure that the spatial sampling interval is small enough to avoid aliasing when the q^{-1} parameter becomes large. This calculation is carried out on a CRAY X-MP computer at the University of Illinois.

Figure 3 shows a small section of a sequence of phase screens that were generated using the simulation program. Each screen corresponds to one instant in time. In this example only a single scale size is used and the average drift velocity of the irregularities is zero. Thus, the temporal arrangement is due only to the random convective motions of the individual eddies. Because the phase at any point in the screen results from the superposition of many eddies, it is not possible to follow the motions of the individual components of the screen. The space-time correlation function for this example was computed and found to be in excellent agreement with the analytical result given in equation (11). Figure 4a,b shows the intensity covariance function computed from a simulation using the same parameters that were used in Figure 1a,b. The maximum space and time lags for the results in Figure 3 are smaller than those in Figure 1a,b. Thus, these contours correspond to the lower left-hand corners of Figures 1a and 1b. Note that the characteristic shape of the contours is also seen in the simulation results. If the characteristic random velocity of the intensity correlation function is computed from the simulation results by using the 0.52 level contour, it is found to be $0.53\sigma_v$ and $0.72\sigma_v$ for cases 1 and 2, respectively. Again, the characteristic velocity is significantly smaller than that of the underlying phase screen for the first case where the number of independent scattering contributions is small. In addition, the peak in the temporal covariance is present for space lags larger than the characteristic length scale of the intensity pattern.

The results presented so far pertain only to the phase screen with Gaussian correlation function. A more realistic model for the ionosphere and interplanetary medium would be a phase screen with a power-law type spectrum, e.g.:

$$S_\phi(\kappa_x) = \frac{C_\phi}{[\kappa_0^2 + \kappa_x^2]^{p/2}} \qquad (18)$$

where

$$\kappa_0 = \frac{2\pi}{L_0} = \text{outer scale wavenumber}$$

$$p = \text{spectral index}$$

For the ionosphere, the appropriate spectral index to use in the model is p=3 (Yeh and Liu, 1982). We have used the model given in equation (5) to simulate the power-law type phase screen. The procedure used to choose the scale size and amplitude distribution for the eddies is described in DeWolf (1975). We consider two examples using parameters appropriate for the ionospheric scintillation case. The distance from the phase screen to the reception plane is z=350 km, frequency f=250 MHz, power-law index p=3, outer scale size $L_0=2\pi/\kappa_0=10$ km. In both cases, the average drift velocity of the irregularities was set to zero, and the standard deviation of the velocity was 30 m/s. Figures 5a,b show the intensity covariance contours for cases with σ_ϕ =3 and 5 radians, respectively. These correspond to intensity scintillation indices S_4 = 0.7 and 0.9, respectively. Note that the intensity correlation scale size is approximately 120 meters and 95 meters, respectively. The characteristic random velocity for these examples is found to be v_c = 22 and 23 m/s, respectively, if the 0.5 level contours are used. Thus, as in the Gaussian case, the characteristic velocity of the intensity fluctuation pattern is significantly smaller than that of the underlying phase screen. The power-law covariance contours appear to be nearly ellipsoidal out to the maximum space and time lags that were computed. The non-separable form that was evident in the Gaussian examples could possibly appear for larger space and time lags, however.

The examples that have been presented so far pertain to the case where the mean drift velocity of the irregularities is zero. A simulation that more closely represents an actual ionospheric scintillation experiment can be performed by including a realistic average drift velocity in the model. To illustrate some of the qualitative features of the space-time statistics for this case, we ran the simulation

using a mean drift velocity of 100 m/s with a standard deviation of 30 m/s. All other parameters are the same as for the previous power-law example. This is representative of the average and fluctuating drift components that are seen in the equatorial F-region during the post-sunset to pre-midnight period. Figure 6 shows a small section of the intensity fluctuations on three receivers located at x = 0, 100, and 200 meters (bottom to top) in the reception plane for a screen with phase standard deviation σ_ϕ = 5 radians. The two upper curves have been offset by multiples of 5 intensity units. The scintillation index for this example was approximately 0.9. This example shows the rearrangement of the intensity pattern during the 1 second interval that it takes for the screen to drift the 100 meter distance between the receivers. Figure 7 a,b,c,d shows a set of temporal correlation functions for the same parameters except σ_ϕ = 1, 3, 10, and 30 radians. The receiver separations used for the first 3 cases were 100, 200 and 300 meters, while for the last case the separations were 30, 60 and 90 meters. The scintillation indices for these cases were approximately 0.3, 0.8, 1.0 and 1.0, respectively. It should be noted that the same set of phase screens was used to generate all 4 cases. Only the "depth" of the screen was changed. The results shown in Figures 7a and 7d correspond to "weak" and "saturated" scintillations, respectively. The parameters used in this simulation are typical for an ionospheric scintillation experiment. Some general characteristics of the temporal covariance can be noted from these examples. As the scintillation strength increases, the width of the covariance function decreases due to the development of narrow focusing spikes and eventually a homogeneous "fine structure" in the intensity pattern. In addition, the peak covariance decreases more rapidly with increasing receiver separation as the scintillation strength increases. This sequence illustrates that a relatively narrow distribution of velocities in the phase screen can produce very significant decorrelation in the intensity pattern for sufficiently strong intensity fluctuations. It also shows that the peak value of the normalized covariance is a sensitive indicator of the relative importance of rearrangement when the scintillation is very severe.

3. DISCUSSION AND CONCLUSIONS

The results presented in the previous sections for intensity fluctuations in the focusing and saturated regimes have been interpreted in terms of characteristic length and time scales. It is important to note that such a characterization tells only part of the story and cannot adequately represent all features of the covariance functions. In particular, the characteristic non-separable shape of the covariance functions that was seen for the Gaussian phase correlation function is one example. Further study is necessary in order to develop relatively simple models that lend physical insight into the space-time scattering process. In this regard, the "micro area" approach used by Johannes (1974) may be appropriate for studying this type of system.

Our results may have important implications for applications where one would like to estimate the velocity distribution in the screen from the intensity measurements. For example, experimental measurements of ionospheric and interplanetary scintillation are often used to estimate the average and random components of the drift velocities in the propagation medium. For cases where the random velocity is of interest, most experimentalists make use of an assumption about the form of the space time correlation function that was originally introduced by Briggs, Phillips and Shinn (1950). These authors noted that any correlation function that is twice differentiable at the origin can be written in the form:

$$B(x,t) = f\left(\frac{(x - v_0 t)^2}{l_c^2} + \frac{t^2}{\tau_c^2}\right) \qquad (19)$$

where l_c and τ_c are space, and time correlation scales, respectively. Various methods have been devised to estimate these scales from time series of intensity fluctuations measured on two or more spaced receivers. The characteristic random velocity $v_c = l_c/\tau_c$ is then taken to be a measure of the relative importance of temporal rearrangements. As noted earlier, for the case of weak scintillations, Wernik et al (1983) showed that the v_c parameter is numerically equal to the width of the random velocity distribution in the phase screen itself if the fluctuations are caused by a temporal rearrangement model like the one presented in this paper. As noted in section 1, this correspondence also holds for the case of a deep screen if the intensity fluctuations are saturated (Gaussian fluctuations). On the other hand, both the analytical and simulation results presented here show that the characteristic velocity derived from intensity fluctuations in the non-Gaussian, or focusing, regime will be smaller than the width of the phase screen velocity distribution.

4. ACKNOWLEDGMENTS

The authors wish to thank Dr. A. Bhattacharya and Professor K.C. Yeh for many helpful suggestions.

5. REFERENCES

Booker, H. G. and G. MajidiAhi, "Theory of refractive scattering in scintillation phenomenon," J. Atmos. Terr. Phys., 43, pp. 1199-1214, 1981.

Briggs, B. H., G. J. Phillips and D. H. Shinn, "The analysis of observations on spaced receivers of the fading radio signals," Proc. Phys. Soc. London, 63, pp. 106-121, 1950.

DeWolf, D. A., "A random-motion model of fluctuations in a nearly transparent medium," Radio Science, 18, pp. 138-142, 1975.

Franke,S. J., "The space-time intensity correlation function of scintillation due to a deep random phase screen," To appear in Radio Science, 1987.

Knepp, D. L., "Multiple phase screen calculation of the temporal behavior of stochastic waves," Proc. IEEE, 71, pp. 722-737, 1983.

Jakeman, E., Photon Correlation and Light Beating Spectroscopy, eds. H. Z. Cummins and E. R. Pike (New York:Plenum), 1974.

Jakeman, E. and P.N. Pusey, "Non-Gaussian fluctuations in electromagnetic radiation scattered by a random phase screen," J. Phys. A.: Math. Gen., Vol. 8, No. 3, pp. 369-391, 1975

Jakeman, E. and J. H. McWhirter, "Correlation function dependence of the scintillation behind a deep random phase screen," J. Phys. A.:Math. Gen., 10, pp. 1599-1643, 1977.

Jakeman, E., "Fresnel scattering by a corrugated random surface with fractal slope," J. Opt. Soc. Am., 72, pp. 1034-1041, 1982.

Rino, C. L., "A power law phase screen model for ionospheric scintillation 1. Weak scatter," Radio Science, 14, pp. 1135-1145, 1981.

Scott, S.L., W.A. Coles, and G. Bourgois, "Solar wind observations near the Sun using interplanetary scintillation," Astron. Astrophys., 123, pp. 207-215, 1983.

Wernik, A. W., C. H. Liu, and K. C. Yeh, "Modeling of spaced-receiver scintillation measurements," Radio Science, 18, pp. 743-763, 1983.

Yeh, K. C. and C. H. Liu, "Radio wave scintillations in the ionosphere," Proc. IEEE, 70, pp. 324-360, 1982.

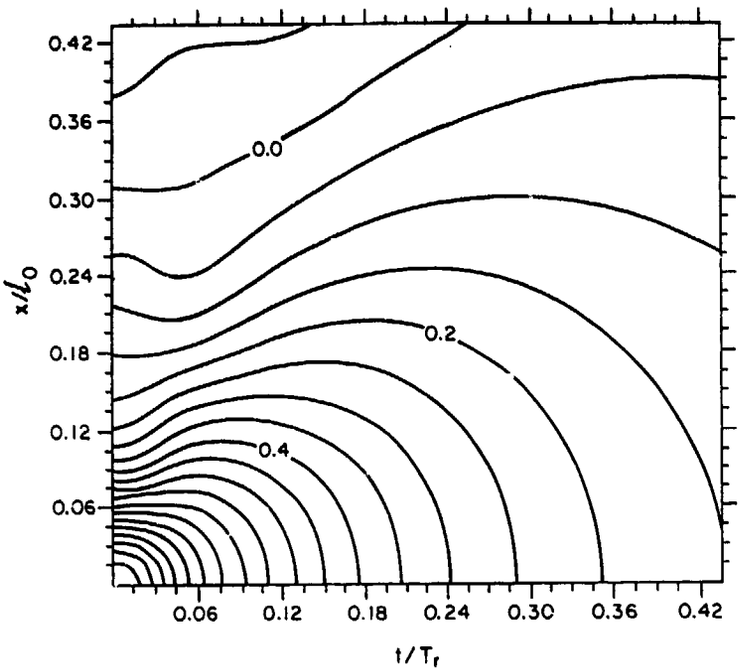


Figure 1a. Contours of constant normalized intensity covariance for a phase screen with Gaussian correlation function and $q^{-1} = 1.38$, $\sigma_\phi^2 = 100$. The average drift velocity of the irregularities was set to zero.

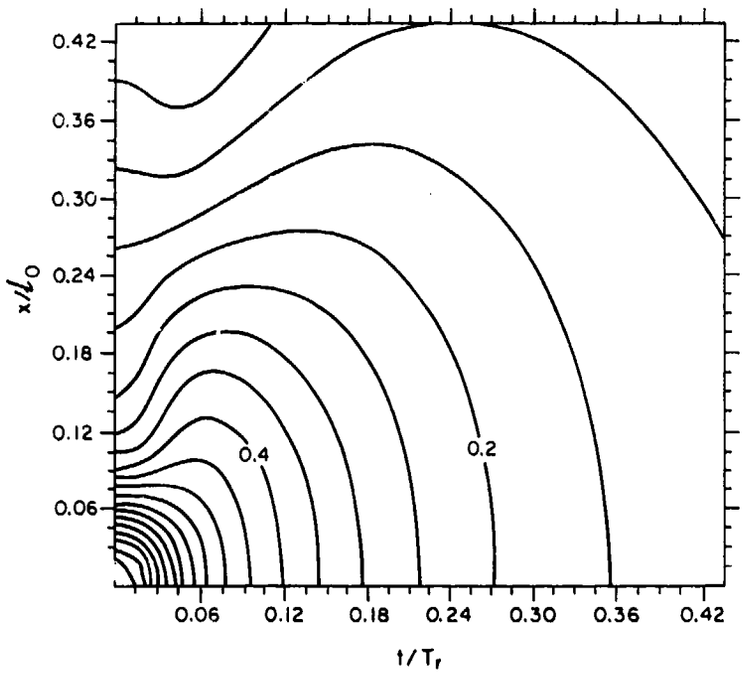


Figure 1b. Same as Figure 1a. except $q^{-1} = 2.45$.

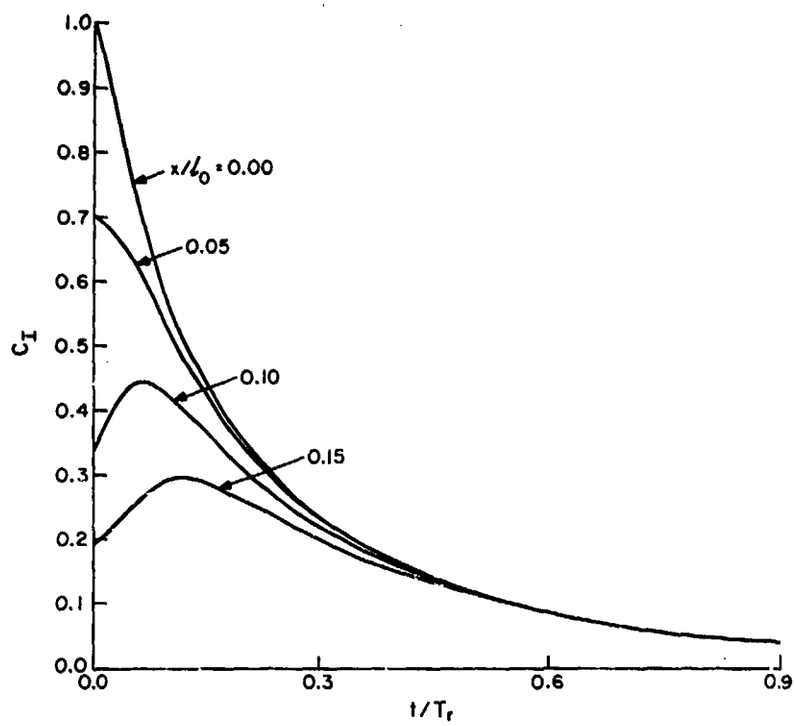


Figure 2. Temporal covariance functions corresponding to horizontal cuts through Figure 1a at normalized receiver separations of 0.0, 0.05, 0.10, and 0.15.

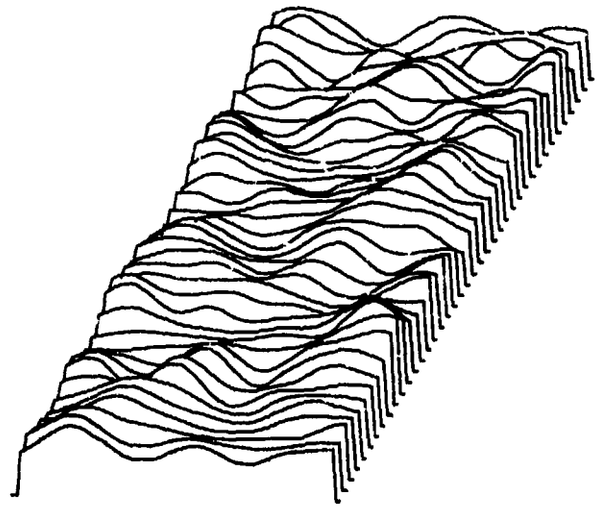


Figure 3. A section of a sequence of phase screens generated using the simulation procedure. Each screen corresponds to one instant in time. For this example, only a single irregularity scale size is used and the average drift velocity of the irregularities is set to zero.

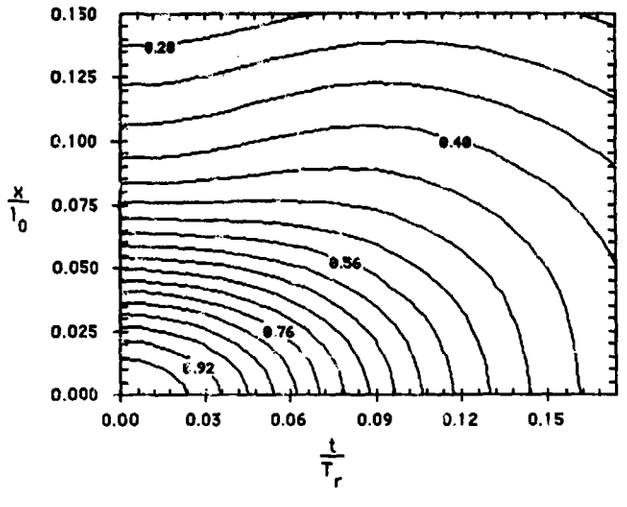


Figure 4a. Contours of constant normalized intensity covariance computed using the numerical simulation technique. The phase screen parameters are the same as those in Figure 1a. The maximum space and time lags in this Figure are smaller than those in Figure 1a.

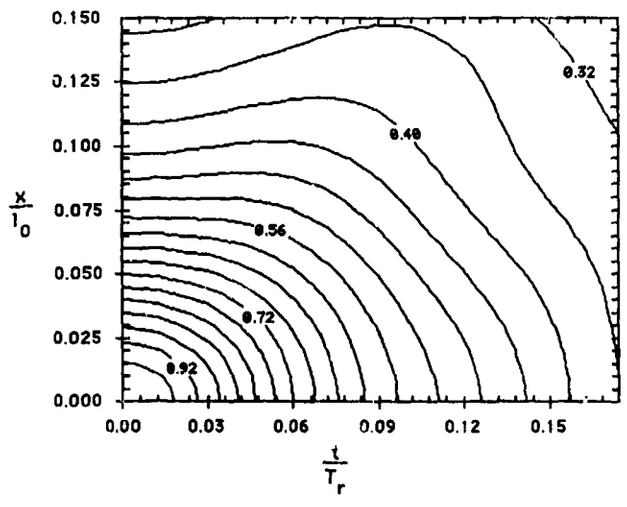


Figure 4b. Same as Figure 4a, except the parameters used in the simulation were the same as in Figure 1b.

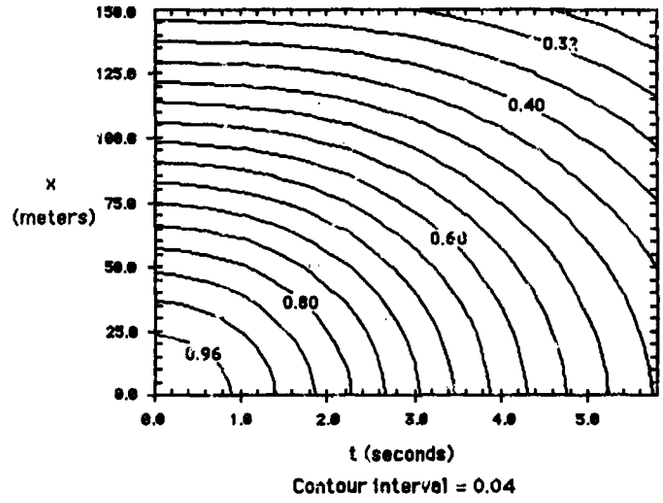


Figure 5a. Contours of constant normalized intensity covariance for a phase screen with power-law correlation function. The parameters were chosen to be appropriate for ionospheric scintillation. In this case, $\sigma_\phi = 3$, and the average irregularity drift velocity is zero..

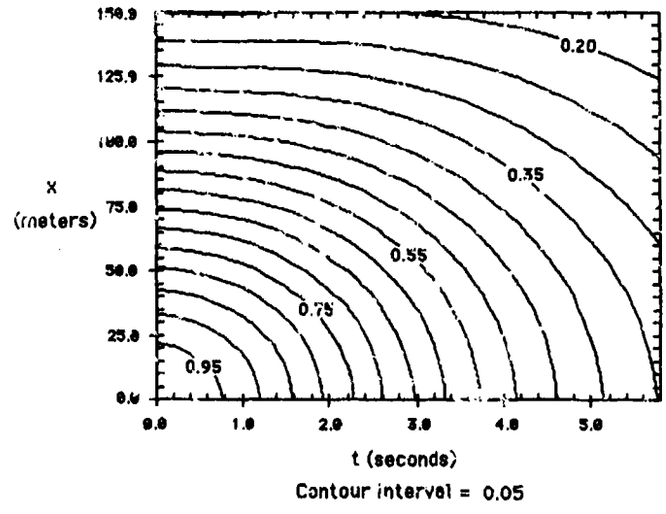


Figure 5b. Same as Figure 5a. except $\sigma_\phi = 5$.

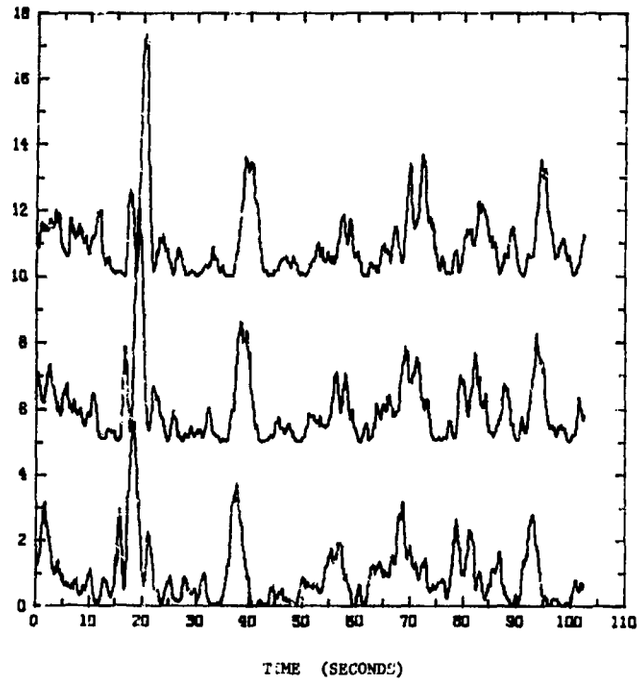


Figure 6. Time series of the intensity fluctuations on 3 receivers located at x = 0, 100, 200 meters in the reception plane generated using the numerical simulation.. For this case, the average drift velocity of the irregularities was 100 m/s, and the width of the velocity distribution was 30 m/s. The rms phase fluctuation in the screen was $\sigma_\phi = 5$ and the scintillation index was approximately 0.9.

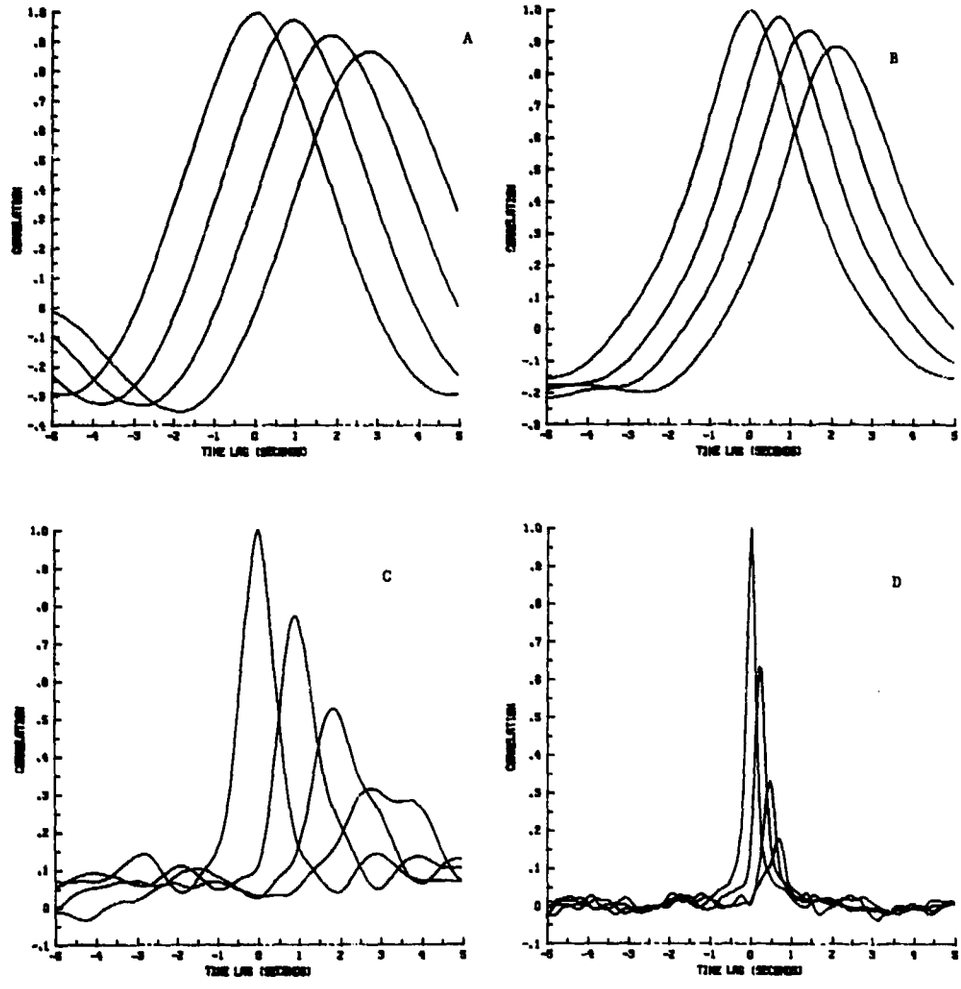


Figure 7. (a) through (d) show temporal correlation functions for the power-law example with rms phase fluctuations of 1,3,10 and 30 radians, respectively. The receiver separations are 0,100,200, and 300 meters in Figures (a)-(c) and 0,30,60, and 90 meters in Figure (d).

DISCUSSION

A. Ishimaru, US

The Gaussian phase correlation function is used. How realistic is this model? How sensitive may the results be to the assumption?

Author's Reply

The Gaussian correlation function was chosen primarily for mathematical convenience and so that we could verify the numerical simulation results. This model is not realistic for atmospheric or ionospheric applications, however. The numerical simulation technique is being used to study the more realistic power-law correlation function. We find that many of the qualitative features of the results that have been presented here are also seen when the power-law correlation function is used.

J.H. Jefferson, UK

In your simulations, do you generate $\phi(x,t)$ using two-dimensional FFTs?

Author's Reply

No, we do not.

J.H. Jefferson, UK

Then I do not understand how you bind in correlations in both x and t.

Author's Reply

We construct the random screens by superimposing many individual "eddies". Each eddy is assigned a random position and velocity. Thus, a screen can be generated at any instant in time by simply calculating the positions of the constitutive eddies and then adding them together. This avoids the computer memory problems associated with two-dimensional FFTs.

E. Jakeman, UK

In the sections of cross-correlation functions that you showed, presumably the peak at nonzero delay also occurs at both advanced and delayed times, i.e., the cross-correlation function is symmetric?

Author's Reply

Yes, it is. I've shown only the positive space and time lag quadrant.

SUMMARY OF SESSION IV

ATMOSPHERIC EFFECTS

by

L.Boithias, Session Chairman

This session contains six papers, numbered 16 through 21, which may be classified as follows:

(a) — Paper No.16, by Clifford et al., is related to millimetre waves. It describes measurements of amplitude and phase spectra on a 1 km path at frequencies between 116 and 230 GHz with simultaneous meteorological measurements. During clear air periods the results agree with the single scatter theory. During rain periods a high correlation exists between rain and attenuation fluctuations.

(b) — Two papers, No.17 by Rousset et al. and No.18 by Bishop and Larkin, are related to infrared, ultraviolet and optical wavelengths. Paper 17 studies the means of restoring the quality of an image damaged by transmission through the atmosphere. Three methods are considered: digital processing, wave front analysis, adaptive optics.

Paper 18 is divided into two parts. The first one describes some trials to measure the atmospheric transmission and emission effects on the performance of electro-optics systems. The second one studies the effects of ozone absorption on the design of a passive surveillance system working in the ultraviolet band.

(c) — Three papers, No.19 by Schmiedel and Ochs, No.20 by Allen and No.21 by Ligthart et al., are related to various effects of attenuation and scattering by rain.

Paper 19 describes a very important experiment, on precipitation scatter, to determine the practical effect of this phenomenon on telecommunications. Bistatic measurements are made on a short path (25 km) and a long path (97 km). Only the first preliminary results are presented.

Paper 20 presents observation of phase delay through rain at 96 GHz. This experiment is of great importance for radar target identification, when relative amplitude and phase information is used.

Paper 21 presents the measurements by a vertically pointed Doppler radar of the main characteristics of hydrometeors influencing the propagation of an Earth space path (number, geometry, orientation, velocity of various hydrometeor particles).

***

EFFETS DE L'ATMOSPHERE

par

L.Boithias, Session Chairman

Cette session comporte 6 exposés qui peuvent être classés comme suit:

(a) — Un exposé (No.16) est relatif aux ondes millimétriques. Il décrit des mesures des spectres d'amplitude et de phase sur un trajet de 1,4 km à des fréquences comprises entre 116 et 230 GHz, ainsi que des mesures météorologiques simultanées. Dans les périodes d'air clair les résultats sont conformes à la théorie de la diffusion simple. Dans les périodes de pluie, il existe une forte corrélation entre les fluctuations de la pluie et celles de l'affaiblissement.

(b) — Deux exposés (No.17 et 18) sont relatifs aux longueurs d'ondes infrarouges, ultraviolettes et optiques. L'exposé 17 étudie les moyens de rétablir la qualité d'une image perturbée par la transmission à travers l'atmosphère. Trois méthodes sont envisagées, le traitement numérique, l'analyse du front d'onde et l'optique adaptative.

L'exposé 18 se divise en deux parties. La première décrit quelques essais pour mesurer les effets de la transmission et de l'émission atmosphérique sur les performances des systèmes électro-optiques. La deuxième étudie les effets de l'absorption par l'ozone sur la conception de systèmes de surveillance passifs fonctionnant dans l'ultraviolet.

(c) — Trois exposés (No.19, 20 et 21) sont relatifs à divers effets d'atténuation et de diffusion par la pluie.

L'exposé 19 décrit une expérimentation très importante sur la diffusion par la pluie, pour déterminer son influence pratique en télécommunication. Des mesures bistatiques sont faites sur une base courte (25 km) et sur une base longue (97 km). On présente seulement des premiers résultats obtenus.

L'exposé 20 présente l'observation du retard de phase à travers la pluie à 96 GHz. Cette expérience est d'une grande importance pour l'identification des cibles radar lorsqu'on utilise des informations à partir de l'amplitude et de la phase.

L'exposé 21 présente les mesures, au moyen d'un radar Doppler pointé verticalement, les principales caractéristiques des hydrométéores qui influencent la propagation sur un trajet Terre-espace (nombre, géométrie, orientation, vitesse de diverses particules d'hydrométéores).

LINE-OF-SIGHT MILLIMETER WAVE PROPAGATION CHARACTERISTICS

S.F. Clifford, R.J. Hill, and R.B. Fritz
NOAA/ERL/Wave Propagation Laboratory
325 Broadway
Boulder, Colorado 80303

R.A. Bohlander and R.W. McMillan
Georgia Institute of Technology
Atlanta, Georgia 30332

ABSTRACT

From 1983 to 1985 a team of scientists from NOAA's Wave Propagation Laboratory and Georgia Institute of Technology conducted an extensive set of millimeter wave propagation measurements. In five, thirty-day sessions, chosen for the widest variety of weather conditions, we propagated millimeter wave frequencies from 116 to 230 GHz over a 1.4 km horizontal path in Flatville, Illinois. Simultaneous, extensive measurements of the meteorology allowed a detailed comparison of the propagation characteristics with the current state of the atmosphere. We report on the observations of millimeter wave propagation characteristics during clear air and severe weather. Amplitude and phase spectra for propagation in clear air are compared with theory derived using the weak refractive turbulence approximation. Excellent agreement is found. Further, probability density functions appear to be; respectively, lognormal (amplitude) and Gaussian (phase difference), as expected from application of the central limit theorem. Interesting meteorological observations and their millimeter wave signatures will also be presented.

INTRODUCTION

Over the past five years a team of scientists from the National Oceanic and Atmospheric Administration and the Georgia Institute of Technology conductd an extensive set of millimeter-wave propagation measurements. In five, thirty-day sessions, chosen for the widest variety of weather conditions, we propagated millimeter wave frequencies from 116 to 230 GHz over our 1.4 km horizontal path in Flatville, Illinois. Simultaneous, extensive measurements of the meteorology allowed detailed comparisons of the propagation effects with the state of the atmosphere.

The details of the experiment layout and data processing are contained in Reference 1. (Table 1 and Figs. 1-6 of this paper are extracted from Reference 1.) Figure 1 illustrates the propagation geometry. The beam propagated 1.4 km - 4 meters above an extremely flat terrain, chosen for its outstanding fetch in all wind directions. This enabled us to characterize the site micrometeorology with two instrumented towers using Monin-Obukov surface-layer similarity theory. The intensity fluctuations were measured at each of the four horizontally spaced antennas and phase differences were measured among all possible antenna pairs with spacings from 1.43 to a 10 m maximum. The fifth antenna was used in a limited way to test the isotropy of the different wave parameter fluctuations.

A variety of meteorological measurements were obtained simultaneously with the millimeter-wave data. Figure 1 shows the optical propagation paths which give optical refractive-index structure parameter C_n^2 as well as the cross-path component of the wind. Figure 1 also shows the optical rain gauge, optical drop size disdrometers, and the weighing bucket rain gauges. Two micrometeorological stations are shown on Fig. 1; these are 4 m high instrumented towers. At these stations the mean temperature and humidity were recorded, a prop-vane gave wind speed and direction, a three-axis sonic anemometer gave the fluctuating components of the wind vector, platinum resistance-wire thermometers gave the fluctuating temperature, and Lyman-α hygrometers recorded the humidity fluctuations. The millimeter-wave signals, resistance-wire temperature, and Lyman-α humidity were digitized at 100 Hz. The sonic anemometers were digitized at 25 Hz. The other instrument's signals were digitized at 0.39 Hz. Table 1 shows the great variety of clear-air micrometeorological statistics available from our instrumentation.

Figure 2 shows a probability density function (PDF) of the measured intensity; it is compared with lognormal and Gaussian PDFs. At such small intensity variances (0.02) there is little difference between lognormal and Gaussian PDFs, but the data definitely favors the lognormal PDF. Figure 3 shows the PDF of phase difference obtained from antennas 2 and 3, which have a separation of 2.9 m. This PDF is clearly Gaussian. In addition, we find that intensity and phase difference are uncorrelated.

Figure 4 shows the structure function of phase for each of our antenna pairs (separations). The structure function is definitely less steep than the slope of 5/3 that would be predicted by a Kolmogorov intertial-subrange model. This is caused by the outer scale. A very simple prediction that includes the effects of the outer scale is shown as a solid curve for a horizontal outer scale of 2.2 m. The mutual coherence function (second moment of the field) is shown in Fig. 5. Since the log-intensity and phase difference are both Gaussian and uncorrelated it follows from the weak turbulence

theory that the mutual coherence function should be equal to $\exp[-.5(D_\chi + D_S)]$ where D_χ and D_S are the log-amplitude and phase structure functions. We find that this formula predicts the values in Fig. 5 to within 0.5%.

In Fig. 6 we show the normalized variance of intensity versus the inertial range prediction for a spherical wave. Here the radio C_n^2 is obtained from the micrometeorological data. We see that the intensity variance is somewhat underestimated by the inertial-range prediction but consistent with the phase structure function shown in Fig. 4. This discrepancy is most probably because of difficulties in calibrating the Lyman-α hygrometer.

PHASE AND AMPLITUDE SPECTRA

Using the spherical-wave theory for propagation through refractive turbulence, Clifford[4] shows that the temporal power spectrum of log-amplitude fluctuations in the single scattering or weak turbulence limit has the form shown labeled "theory" in Fig. 7. In addition Fig. 7 contains a log-log plot of (f/f_o) times the log-amplitude spectrum W_χ versus normalized frequency (f/f_o). The spectrum W_χ is normalized to the log-amplitude variance such that the area under the curve is unity. The frequency $f_o = v/\sqrt{2\pi\lambda L}$, where v is the cross-path component of windspeed, λ is the wavelength, and L = 1.4 km is the millimeter-wave path length. The dotted (solid) fluctuating curve represents the low (high) frequency Fourier transform of 35 min of log-amplitude data taken at 142 GHz. The solid "theory" curve fits the data quite well until the high frequency tail beyond $\log(f/f_o) = 1$, where aperture averaging effects are important. The dashed curve is a plot of the theory including aperture averaging effects; overall, the fit to the data is excellent. Deviations at low frequencies above the "theory" curve are most likely due to receiver antenna drift. It is possible from the theory to estimate the cross-path velocity from the location of the peak. The peak is predicted at $\log(f/f_o) \sim 0.43$. In the case shown the cross-path velocity estimate from the millimeter wave scintillations agrees with the prop vane to within a few percent. (Note, the data were plotted with f_o calculated from prop vane-measured crosswind.)

Figure 8 illustrates the theoretical spectra for phase difference fluctuations. In contrast to the log-amplitude result phase-difference is very sensitive to the "outer scale" L_o of the refractive index fluctuations. Consequently, we have a family of curves for different values of the spacing ρ normalized to L_o. (L_o is the size of the largest eddy for which the assumption of isotropy holds, so L_o is the order of the height above the ground). The theoretical curves are plotted versus normalized frequency f/f_1 where $f_1 = v/\rho$ and v is the cross-path wind component. From our knowledge of the wind speed and the dependence of the spectra on ρ/L_o, we can estimate L_o from a spectrum measured at a known separation, e.g., $\rho_{12} = 1.43$ m, and use that derived value $L_o \sim 2.8$ m for all further comparisons.

Figures 9 and 10 show the theoretical curves superimposed over the phase-difference spectra from the data for antenna pairs (1,2) separated by $\rho_{12} = 1.43$ m and antenna pair (1,4) separated by $\rho_{14} = 10$ m. We used the value $L_o \sim 2.8$ m and selected our curves from Fig. 8 to fit the data based on the ratios $\rho_{12}/L_o = 0.51$ and $\rho_{14}/L_o = 3.5$ appropriate to each antenna pair. The resulting fit is quite good. We could also estimate crosswind from the peak of the spectrum if we knew the accurate L_o from other independent measurement.

MILLIMETER PROPAGATION THROUGH RAIN

Figures 11 and 12 illustrate a unique measurement of a rain event where the effects of oscillations in rain rate were observed simultaneously by the millimeter wave link and two laser-beam rain gauges, deployed as shown in Fig. 1. An oscillating rain rate, probably caused by a convective instability in the cloud cover, could explain the observed temporal pattern of the rain. In Fig. 12 the rain fluctuations are compared with the simultaneously measured attenuation fluctuations. As expected, a very high correlation between the two is observed. The lowest curve in Fig. 12, illustrates a simulated attenuation time curve that would result by assuming a sinusoidal convective disturbance propagating along the millimeter path. A more detailed description is available in Reference 3.

CONCLUSIONS

The Flatville data set has been analyzed to show the effects of clear air and rain on millimeter wave systems. We have reported only a minute amount of the available data and show that the results agree quite closely with the clear-air single-scatter theory for propagation in the turbulent atmosphere. We intend to make much more extensive comparisons in the future for propagation in clear air, rain, fog, and snow. We made a deliberate choice to forgo analysis of other segments of the data in order to complete a readily accessible data base for study by both NOAA/GIT and other researchers. The completed data base should be available for study in 1987.

ACKNOWLEDGMENT

This work was supported by the Army Research Office under MIPR 122-85.

REFERENCES

1. Hill, R.J., W.P. Schoenfeld, J.P. Riley, J.T. Priestley, S.F. Clifford, S.P. Eckes, R.A. Bohlander, and R.W. McMillan, "Data analysis of the NOAA/GIT millimeter wave propagation experiment near Flatville, Illinois." NOAA Technical Report. ERL 429-WPL 60, U.S. Government Printing Office, Washington, D.C., (August, 1985).

2. Clifford, S.F., "Temporal-frequency spectra for a spherical wave propagating through atmospheric turbulence." J. Opt. Soc. Am., 61, 1285, (1971).

3. Frith, R.B., R.J. Hill, J.T. Priestley, and W.P. Schoenfeld. "Evidence for oscillitory rain rate in a midwestern winter rain." (To appear in Climate and Applied Meteorology).

Table 1.--Summary of micrometeorological data from tape 24, taken at 11:30 MDT July 1983

Average Values	
Humidity	19 g/m^3
Temperature	32°C
Wind speed	5.3 m/s
Wind angle	10°
Pressure	993 mb
Solar flux	94% of full sun
Wind stress	-0.14 $(m/s)^2$
Humidity flux	0.1 $(g/m^2)/s$
Temperature flux	0.03°C m/s
Stability	-0.03
Square Roots of Variances	
Humidity	0.72 g/m^3
Temperature	0.35°C
Wind speed	1.2 m/s
Wind angle	11°
Streamwise wind component	1.1 m/s
Cross-stream wind component	1.0 m/s
Vertical wind component	0.54 m/s
Structure Parameters	
C_n^2 from optical scintillometers	2×10^{-13} $m^{-2/3}$
C_T^2 from optical C_n^2	$0.03°C^2$ $m^{-2/3}$
C_T^2 from resistance wires	$0.03°C^2$ $m^{-2/3}$
C_q^2 from Lyman-α hygrometers	0.2 $(g/m^3)^2$ $m^{-2/3}$
C_{Tq} from resistance wires and Lyman-α hygrometers	0.075°C (g/m^3) $m^{-2/3}$
C_n^2 for radio frequencies*	5.9×10^{-12} $m^{-2/3}$

*Obtained from Eq. (79) of Ref. 1, using C_T^2, C_q^2, and C_{Tq} from the resistance wire thermometer and Lyman-α hygrometer with A_T and A_q obtained from the radio refractive-index equation.

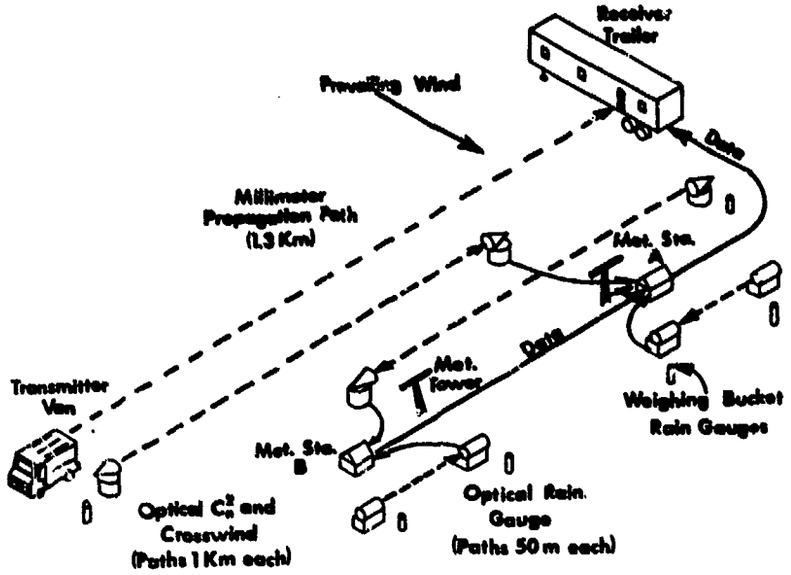


Figure 1. The instrument positions at the experiment site. The dashed and dotted line denotes mm-wave propagation path (1.4 km); the long-dashed lines, the optical propagation paths (1 km each); and the short-dashed lines, the optical rain gauge paths (50 m each). Solid lines show the flow of micrometeorological data to the data acquisition system in the receiver trailer. Antennas are numbered 1 to 5 in the receiver trailer.

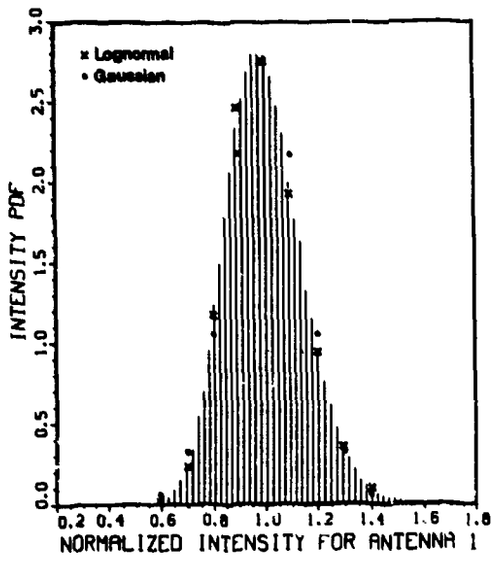


Figure 2. Probability distribution function of intensity for antenna 1. Normalized intensity is scaled to unit mean value.

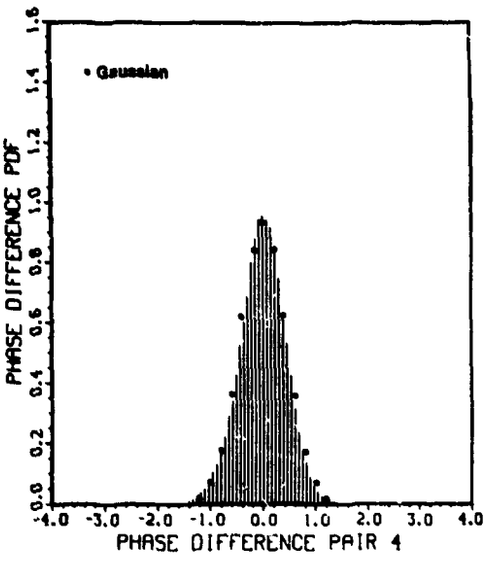


Figure 3. Probability distribution of phase difference in radians.

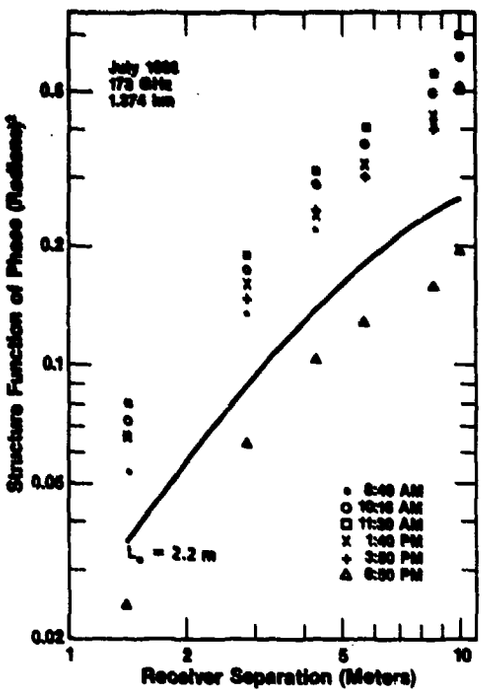


Figure 4. The structure function of phase. The solid line represents a theoretical prediction for the 6:50 p.m. data.

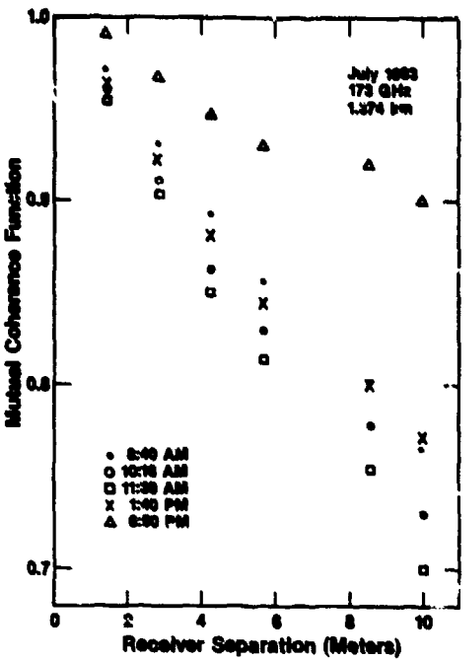


Figure 5. The modulus of the mutual coherence function.

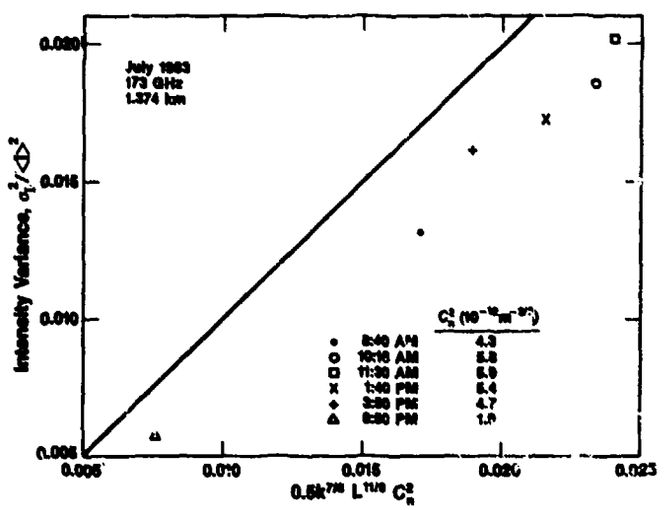


Figure 6. The normalized variance of intensity versus its inertial-range formula. The straight line shows theoretical calculations.

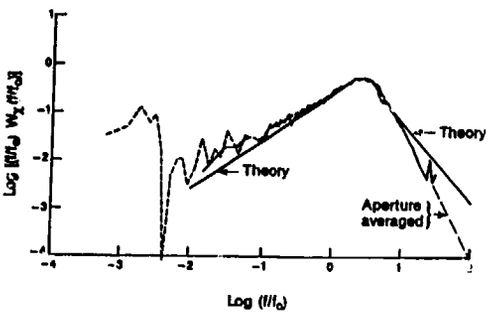


Figure 7. Theoretical and experimental power spectra of amplitude fluctuations.

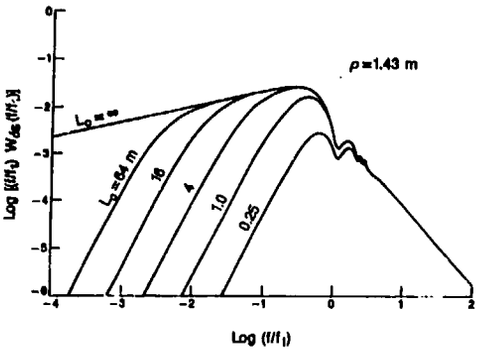


Figure 8. Theoretical power spectra or phase difference fluctuations as a function of the ratio or spacing to the outer scale ρ/L_0 and characteristic frequency $f_1 = v/\rho$ where v is the cross-path wind.

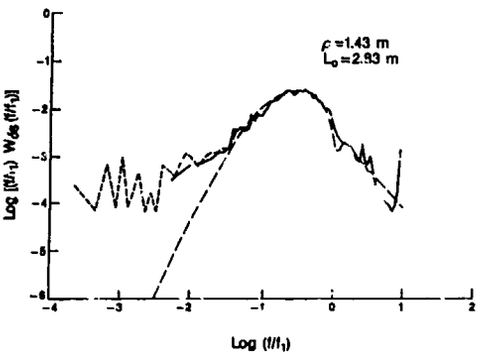


Figure 9. Comparison of theoretical and measured spectra of phase difference for spacing ρ_{12} = 1.43 m.

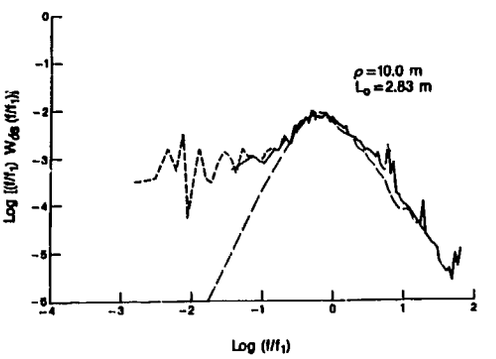


Figure 10. Comparison of theoretical and measured spectra of phase difference for spacing ρ_{14} = 10 m.

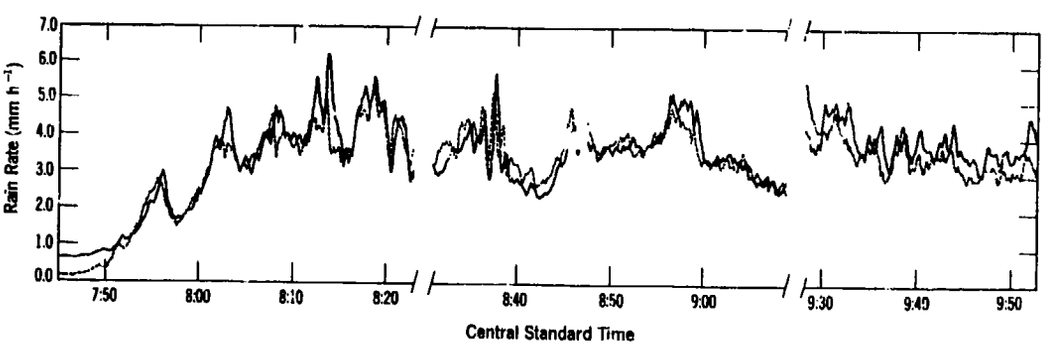


Figure 11. Time series of rain rates measured by path-averaging optical rain gauges. Note oscillatory feature at approximately 0837 CST.

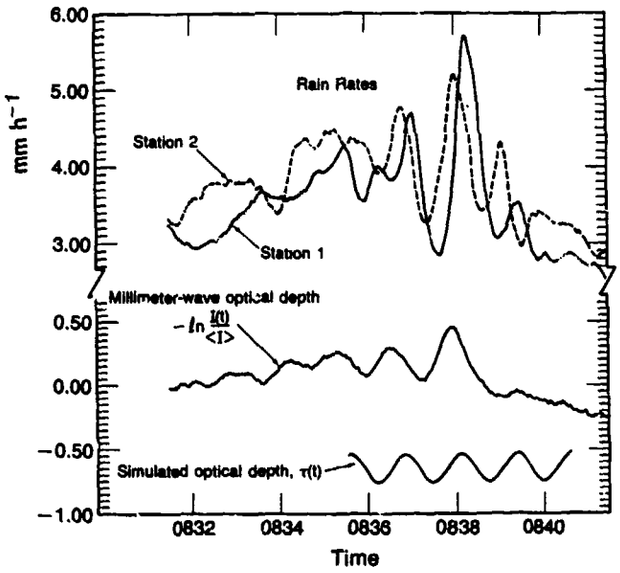


Figure 12. Detail of rain rates and millimeter-wave attenuation, 0832-0841 CST. Bottom trace is the simulated millimeter-wave path optical depth.

IMAGERIE OPTIQUE A TRAVERS LA TURBULENCE ATMOSPHERIQUE*

par G. Rousset, J.C. Fontanella, J. Primot, A. Sève
Office National d'Etudes et de Recherches Aérospatiales,
BP 72, 92322 Châtillon Cedex, FRANCE

RESUME

Une revue est faite des travaux effectués à l'ONERA en imagerie optique à travers la turbulence atmosphérique.

Plusieurs techniques proposées auparavant permettant d'obtenir des images ayant une résolution à la limite de diffraction sont comparées dans cette communication. La comparaison porte sur le champ d'application, le rapport signal à bruit espéré et les difficultés pratiques de ces méthodes qui sont :

- les techniques de traitement numérique a posteriori reposant sur une généralisation de la méthode de "speckle interferometry" proposée par A. Labeyrie ; en particulier des résultats obtenus avec l'algorithme dit de "Knox et Thompson" sont présentés.

- la "déconvolution à partir d'analyse de front d'onde" ; le principe de cette méthode est décrit en insistant sur l'importance du concept d'analyse de front d'onde dans le problème de l'imagerie à travers la turbulence ;

- l'optique adaptative qui apparaît comme une technique très prometteuse ; un système en cours de développement et destiné à l'astronomie infrarouge est présenté.

LISTE DES SYMBOLES UTILISES

$A(f,\Delta f)$	densité spectrale croisée d'image courte pose
$a_1(r)$	module du champ dans la pupille
$A_1(\alpha)$	amplitude complexe du champ dans le plan focal
$B(f)$	fonction de transfert longue pose de l'atmospnère
$C_n^2(h)$	constante de structure de l'indice de réfraction
$D_\varphi(r)$	fonction de structure de la phase
D	diamètre du télescope
F	distance focale du télescope
f	fréquence spatiale
Δf	pas de fréquence
G	gain en résolution
H	distance objet instrument
h	position sur le trajet optique
$\bar{h}$	moyenne pondérée de la distance de propagation
Im	partie imaginaire d'une quantité complexe
$I_1(\alpha)$	image instantanée
$\tilde{I}_1(f)$	transformée de Fourier de l'image instantanée
M	nombre minimum d'images à utiliser dans les algorithmes
N	nombre de tavelures présentes dans l'image courte pose
N_A	nombre de sous-pupilles de l'analyseur
$O(\alpha)$	objet observé
$\tilde{O}(f)$	transformée de Fourier de l'objet
$\tilde{O}'(f)$	transformée de Fourier de l'objet normalisée à 1 à f = 0
p	nombre de photons moyen par tavelure
p_A	nombre de photons moyen par sous-pupille de l'analyseur
r	position dans la pupille
r_0	diamètre de Fried
Re	partie réelle d'une quantité complexe
$S_1(f)$	fonction de transfert optique instantanée.
$T(f)$	fonction de transfert du télescope
$\bar{v}$	vitesse transverse moyenne des masses d'air
α	direction de l'espace observé
γ	distance zénithale
ζ	position quelconque d'un point
η	rendement quantique du détecteur
θ	angle de champ isoplanétique
λ	longueur d'onde
$\Delta\lambda$	bande spectrale
σ_φ	écart type de la phase du front d'onde
σ_{ϕ_T}	écart type de la phase de la fonction de transfert optique
τ	durée de vie des tavelures
ϕ_0	phase de la transformée de Fourier de l'objet
$\Delta\phi_0$	écart de phase de la T.F. de l'objet

*Travail soutenu en partie par contrats de la Direction des Recherches, Etudes et Techniques (DRET).

Φ_F	phase de la fonction de transfert optique
φ	phase du front d'onde
$\varphi_1(r)$	phase du champ dans la pupille
$\Delta\Psi$	écart de phase de la fonction de transfert du télescope
$\lvert\ \rvert$	module
$\langle\ \rangle$	moyenne
$\sim$	transformée de Fourier
*	quantité conjuguée.

1. INTRODUCTION

La turbulence atmosphérique limite sévèrement la résolution angulaire de tous les instruments optiques de grand diamètre observant depuis le sol : quel que soit le diamètre de leur pupille, la limite de résolution accessible est rarement inférieure à une seconde d'arc.

Toutefois, depuis une quinzaine d'années un ensemble de faits nouveaux est apparu qui permet d'espérer compenser, au moins partiellement, les effets de la turbulence atmosphérique sur les images :

- les mécanismes de dégradation des images par la turbulence atmosphérique sont maintenant bien expliqués (voir paragraphe 2),
- divers algorithmes de restauration a posteriori des images ont été proposés qui donnent des résultats encourageants (voir paragraphe 3),
- les progrès techniques dans la mise au point de miroirs déformables, d'analyseur de front d'onde, de détecteurs d'images performants, de petits calculateurs puissants font de la correction en temps réel par une optique adaptative une voie réaliste.

Dans l'état actuel des techniques numériques et expérimentales, il est difficile de trancher entre les méthodes de restauration a posteriori des images et l'optique adaptative. C'est pourquoi il est particulièrement important de s'attacher à analyser en permanence le front d'onde incident (voir paragraphe 4). Ceci répond en effet à deux impératifs :

- améliorer considérablement les possibilités de restauration d'image a posteriori (voir paragraphe 5),
- permettre de générer les signaux de commande du miroir déformable en imagerie adaptative (voir paragraphe 6).

Les techniques "temps réel" (optique adaptative) ou "a posteriori" apparaissent de plus, dans cette perspective, complémentaires plutôt que concurrentes. Elles sont comparées au paragraphe 7.

Ce travail a pour but de décrire rapidement les travaux effectués à l'ONERA dans les domaines de la restauration d'image a posteriori et de l'optique adaptative.

2. LES EFFETS DE LA TURBULENCE ATMOSPHERIQUE SUR LA FORMATION DES IMAGES

La propagation des ondes optiques à travers l'atmosphère est perturbée par les variations de l'indice de réfraction dues aux variations de température directement liées à la turbulence. Dans le domaine de fréquences spatiales intéressant, la turbulence atmosphérique obéit à la loi de Kolmogorov [1], dont découlent directement les relations ci-dessous [2]. La répartition de la turbulence d'indice le long du parcours est décrite par les valeurs de la constante de structure de l'indice de réfraction $C_n^2(h)$ où h désigne la position du point courant sur le trajet optique.

2.1. Les perturbations du front d'onde

Les variations de l'indice de réfraction génèrent des retards aléatoires entre les divers points du front d'onde. Cette perturbation de la phase s'accompagne de fluctuations de l'amplitude généralement négligées (approximation "champ proche"). L'indice de réfraction de l'atmosphère variant peu du visible à l'infrarouge thermique, il est remarquable que ces retards ne dépendent pratiquement pas de la longueur d'onde et donc que le front d'onde soit identique dans le visible et l'infrarouge.

Les variations de la phase sont caractérisées par la fonction de structure D_φ :

$$D_\varphi(r) = \left\langle |\varphi(\zeta) - \varphi(\zeta+r)|^2 \right\rangle$$

où ζ et $r + \zeta$ désignent les positions de deux points distants de r et appartenant à un plan perpendiculaire à la direction de propagation. D_φ varie comme $r^{5/3}$. La notation $\langle\ \rangle$ désigne la valeur moyenne.

2.2 Formation des images

La relation fondamentale de l'imagerie (filtrage des fréquences spatiales f) s'écrit à chaque instant, pour des images monochromatiques :

$$\tilde{I}_1(f) = \tilde{O}(f) \cdot S_1(f) \qquad (1)$$

$\tilde{I}_1(f)$ désigne la transformée de Fourier (T.F.) d'une image instantanée $I_1(\alpha)$ où α est une direction de l'espace. $\tilde{O}(f)$ est la T.F. de la répartition de l'intensité lumineuse dans l'objet et $S_1(f)$ la fonction de transfert optique (F.T.O.), instantanée (et aléatoire), de l'ensemble télescope-atmosphère turbulente.

2.2.1. Images longue pose

Dans le cas d'une pose longue (typiquement quelques secondes), les fonctions de transfert du télescope T(f) et de l'atmosphère B(f) sont séparables [2]. La valeur moyenne de $\tilde{I}_1(f)$ s'écrit alors :

$$\left\langle \tilde{I}_i(f) \right\rangle = \tilde{O}(f) \cdot T(f) \cdot B(f) \qquad (2)$$

B(f) peut s'écrire sous la forme [2,3] :

$$B(f) = \exp\left[-3{,}44\ (\lambda f / r_0)^{5/3} \right] \qquad (3)$$

r_0 est le paramètre de Fried [3], diamètre d'un télescope fictif dont la limite de résolution angulaire imposée par la diffraction serait la même que celle imposée par la turbulence. λ est la longueur d'onde. r_0 s'exprime par la relation [2,3] :

$$r_0 = 0{,}185\ \lambda^{-6/5} \left[\int_0^H (\cos\gamma)^{-1} \left(\frac{h}{H}\right)^{5/3} C_n^2(h)\ dh \right]^{-3/5} \qquad (4)$$

où H désigne la distance objet instrument (h orientée dans ce sens) et γ la distance angulaire zénithale. Dans le cas d'une observation astronomique (à la verticale, source à l'infini), r_0 vaut typiquement 10 cm (à $\lambda = 0{,}5$ µm) et 3,5 m (à $\lambda = 10$ µm). La turbulence est gênante lorsque le diamètre D de l'instrument est supérieur à r_0, c'est-à-dire pour les grands télescopes observant dans le visible ou le proche infrarouge.

2.2.2. Images courte pose : les tavelures (ou "speckles")

Lorsque l'objet comporte des hautes fréquences spatiales, une image courte pose présente de fines structures aléatoires (tavelures), résidus de ces hautes fréquences après la traversée de l'atmosphère. Pour une source ponctuelle le nombre de tavelures présentes dans une image est approximativement fixé par la relation :

$$N = 2{,}3\ (D/r_0)^2 \qquad (5)$$

Une manière simple d'exploiter l'information haute fréquence (qui disparaît lorsque l'on moyenne les images) est de considérer la densité spectrale des images qui peut se mettre sous la forme [2] :

$$\left\langle \left| \tilde{I}_i(f) \right|^2 \right\rangle = N^2 p^2 \left| \tilde{O}'(f) \right|^2 \cdot \left\langle \left| S_i(f) \right|^2 \right\rangle + Np \qquad (6)$$

où p est le nombre moyen de photons détectés dans une tavelure. Le produit Np est la densité spectrale du bruit de photons. $\tilde{O}'(\cdot)$ est la T.F. de l'objet normalisée à 1 ; elle vérifie :

$$\tilde{O}(f) = Np\ \tilde{O}'(f) \qquad (7)$$

L'allure de la densité spectrale des images est présentée sur la figure 1. Elle se caractérise par une aile haute fréquence, atténuée, qui est exploitée par les algorithmes de restauration d'images.

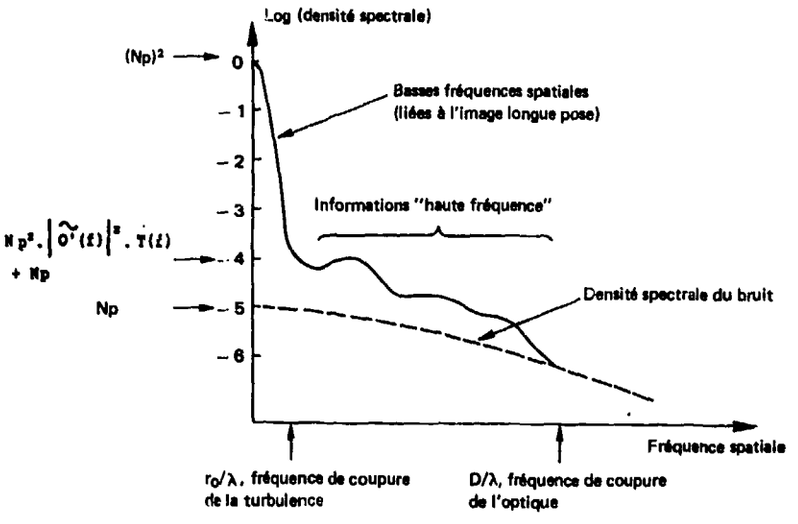


Figure 1 - Forme typique de la densité spectrale des images. Le niveau des différentes portions de la courbe est indiqué. Pour $f > r_0/\lambda$ on a $\left\langle |S_i(f)|^2 \right\rangle \simeq T(f)/N$

Cette aile haute fréquence n'apparait que si l'image est observée avec une bande spectrale étroite $\Delta\lambda$ telle que [2] :

$$\frac{\Delta\lambda}{\lambda} \simeq \pm\ 0{,}45 \left(\frac{r_0}{D}\right)^{6/5} \tag{8}$$

Il faut également que les tavelures soient figées ; leur durée de vie est typiquement :

$$\tau = \frac{r_0}{\bar{v}} \tag{9}$$

où $\bar{v}$ est la vitesse transverse moyenne des masses d'air. Avec $r_0 = 10$ cm, $\bar{v} = 10$ m/s, on trouve $\tau = 10$ ms. C'est donc le temps de pose maximal des images exploitables par les algorithmes décrits ci-dessous ; c'est aussi le délai maximum avec lequel les systèmes adaptatifs de compensation doivent réagir.

2.3 Le domaine isoplanétique

Une limitation des techniques décrites ci-dessous est introduite par le non-isoplanétisme, c'est-à-dire par le fait que la perturbation varie d'un point à l'autre du champ. Dans l'état actuel des techniques de restauration, la compensation ne se fait qu'à l'intérieur d'un champ isoplanétique. L'angle de champ θ correspondant vaut approximativement :

$$\theta \simeq \frac{r_0}{\bar{h}} \tag{10}$$

où $\bar{h}$ est une moyenne pondérée de la distance de propagation [2]. Le champ isoplanétique est limité en astronomie visible à quelques secondes d'arc. Il est d'autant plus large que la perturbation turbulente se trouve près de la pupille du télescope.

3. LES METHODES DE RESTAURATION D'IMAGE A POSTERIORI

Ces méthodes utilisent l'information haute fréquence présente dans les tavelures. Elles reposent généralement sur le calcul des densités spectrales des images ou de moments d'ordre plus élevés (technique dite "speckle masking" [4]). Elles visent à reconstituer la transformée de Fourier de l'objet. Labeyrie [5] en développant la méthode d'interférométrie de tavelures a montré que la relation (6) après correction des biais dûs au bruit permettait de calculer le module de la T.F. de l'objet par la relation :

$$\left|\widetilde{O}(f)\right|^2 = \frac{\left\langle \left|\widetilde{I_i}(f)\right|^2 \right\rangle}{\left\langle \left|S_i(f)\right|^2 \right\rangle} \tag{11}$$

La fonction $\left\langle \left|S_i(f)\right|^2 \right\rangle$ est déterminée par l'observation préliminaire d'une source ponctuelle. L'emploi de la relation (11) suppose que les propriétés statistiques de la turbulence atmosphérique sont stationnaires, ce qui n'est parfois vrai qu'à l'échelle de quelques minutes.

Knox et Thompson [6] ont généralisé la méthode d'interférométrie de tavelures et ont montré que l'on pouvait déterminer la phase Φ_0 de la T.F. de l'objet en calculant des quantités de la forme :

$$A(f,\Delta f) = \left\langle \widetilde{I_i^*}(f).\ \widetilde{I_i}(f+\Delta f) \right\rangle \tag{12}$$

où Δf est un pas de fréquence inférieur à r_0/λ, (* désigne la quantité conjuguée). Le gradient $\Delta\Phi_0$ de la phase se déduit de la quantité précédente par la relation :

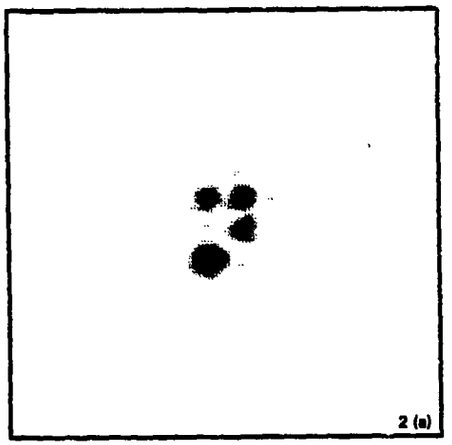
$$\Delta\Phi_0(f) + \Delta\Psi(f) = \mathrm{Arctg}\ \frac{\mathrm{Im}\ (A)}{\mathrm{Re}\ (A)} \tag{13}$$

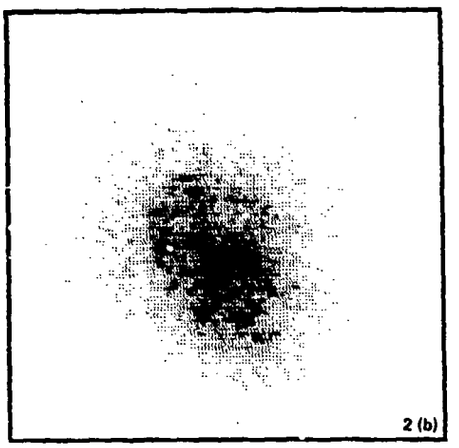
où les notations Im et Re désignent respectivement les parties réelle et imaginaire. $\Delta\Psi$ est un terme dû aux aberrations du télescope que l'on détermine à partir d'une expérience préliminaire en supposant celles-ci fixes. Là aussi, les quantités A doivent être corrigées de biais dû au bruit. La phase doit être ensuite calculée à partir de son gradient par intégration. La présence de zéros de la quantité A dans le plan de Fourier pose quelques problèmes particuliers [7].

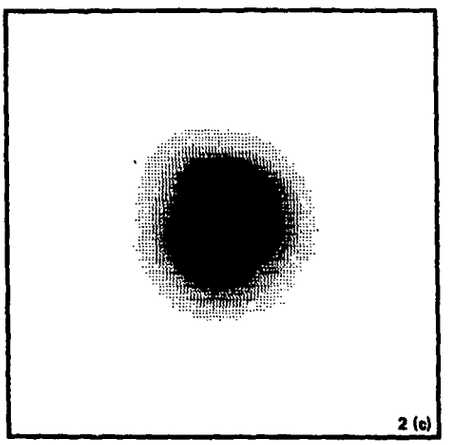
L'atténuation importante des hautes fréquences dans les images dégradées implique la sommation d'un grand nombre d'images pour obtenir une restauration du module et de la phase [6,7]. La restauration est satisfaisante si, pour chaque fréquence F, l'erreur de détermination de la phase $\Phi_0(f)$ reste inférieure à $\pm\ \pi/2$. Le nombre minimum N d'images est alors donné par la relation [7] :

$$p\ \left|\widetilde{O}(f)\right|^2\ T(f).\ \sqrt{N} > 2 \tag{14}$$

Les possibilités de la méthodes sont illustrées par deux résultats expérimentaux obtenus l'un à partir d'une série d'images dégradées produites dans une cuve de simulation de la turbulence (fig. 2a,b,c,d) et l'autre à partir de données enregistrées par D. Bonneau et R. Foy (CERGA) au foyer du télescope franco-canadien de Hawaï (fig. 3a,b,c).







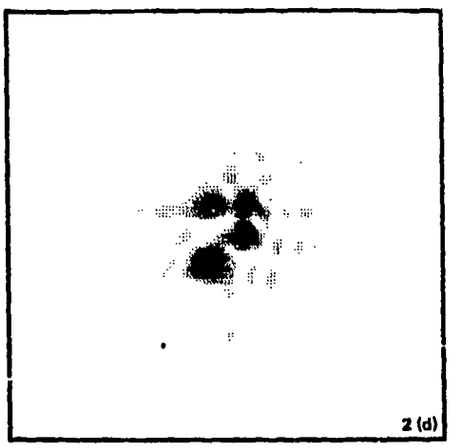


Figure 2 - Expérience de restauration d'image par la méthode de Knox et Thompson sur des images dégradées produites dans une cuve de simulation de la turbulence.
a) image originale sans turbulence (4 taches)
b) image courte pose ($D/r_0 \sim 10$)
c) image longue pose
d) reconstruction avec 170 photons/tavelure

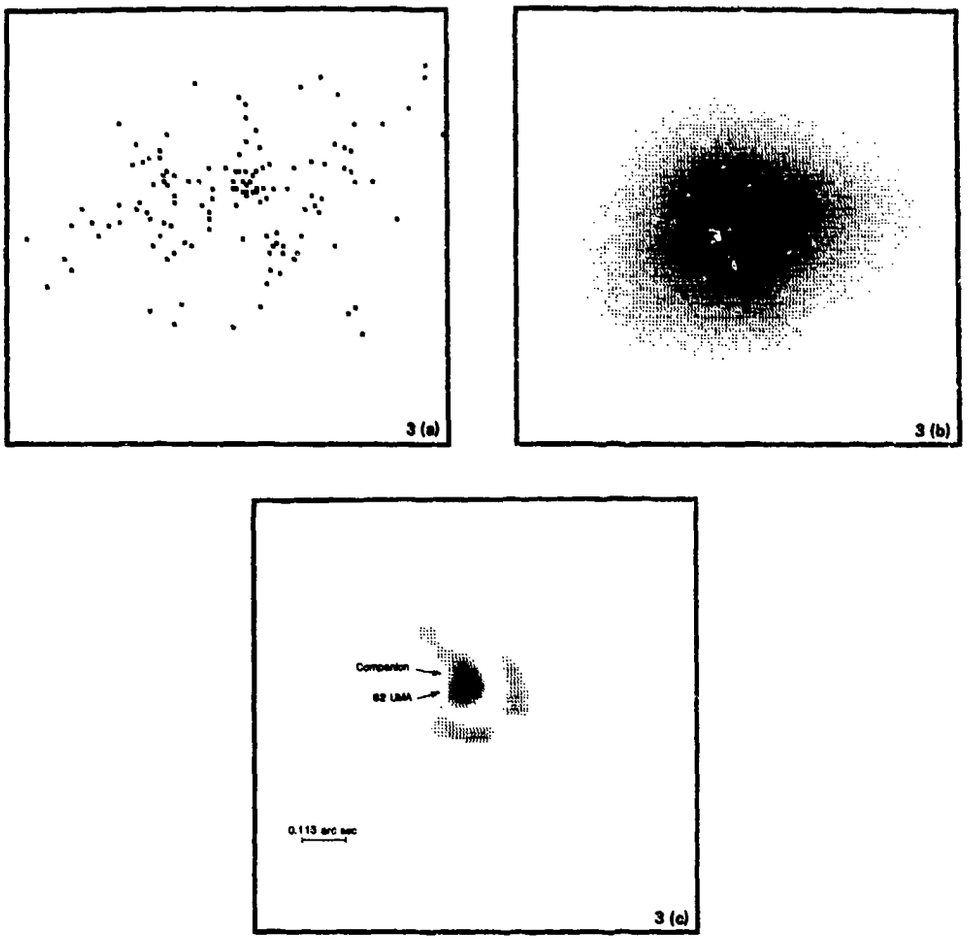


Figure 3 - Expérience de restauration d'image par la méthode de Knox et Thompson sur des images astronomiques de l'étoile double 62 UMA (données de R. Foy et D. Bonneau (CERGA)).
a) une image courte pose typique
b) une image longue pose
c) reconstruction à partir de 1800 images courte pose, séparation binaire 0,048", λ = 0,7 µm.

4. L'ANALYSE DE FRONT D'ONDE

L'analyse de front d'onde permet de déterminer les déformations du front d'onde dans la pupille de l'instrument (en pratique dans un plan conjugué). A partir de cette analyse, il est possible de corriger numériquement les images (paragraphe 5) ou de piloter une optique adaptative (paragraphe 6).

De nombreux principes permettent d'effectuer l'analyse de front d'onde [8]. Deux seulement fonctionnent avec de faibles flux et apparaissent donc bien adaptés à l'imagerie passive : les interféromètres à dédoublement latéral [9] ou les analyseurs dits de Hartmann-Shack [10].

Plusieurs analyseurs utilisant le principe de Hartmann-Shack ont été développés à l'ONERA [11]. Le fonctionnement est le suivant (figure 4) : une image de la pupille est formée par une lentille de champ sur une mosaïque de microlentilles. La dimension de chaque microlentille ramenée dans la pupille détermine la dimension d'une "sous-pupille" qui doit être de l'ordre de r_0 ; on assimile alors le front d'onde à un plan sur chaque microlentille. Ce front d'onde produit dans le plan focal de la microlentille une tache image dont le déplacement, par rapport à une position de référence déterminée à l'aide d'une onde plane, est proportionnel à la pente locale de l'onde.

La position de ces taches est mesurée à l'aide d'une matrice de détecteurs à transfert de charge (CCD) ; en face de chaque sous-pupille se trouve une zone de la matrice : le calcul de la position du barycentre des signaux délivrés par les détecteurs de cette zone fournit la position de la tache et donc la pente locale de l'onde [11,12]. Le front d'onde peut être ensuite reconstruit à partir de ses pentes (à une constante près), selon plusieurs techniques dites zonales ou modales (décomposition sur une base de fonctions appelées "modes", telles que les polynômes de Zernike) [13].

Cet appareil a deux propriétés remarquables :
- il utilise un rayonnement polychromatique,
- il fonctionne avec une source étendue qui peut être l'objet même dont on cherche à faire l'image. Chaque image de la source donnée par une sous-pupille se déplace en fonction des aberrations introduites par le trajet et le calcul de la position de son barycentre fournit la même information que si l'objet était ponctuel à un basculement près.

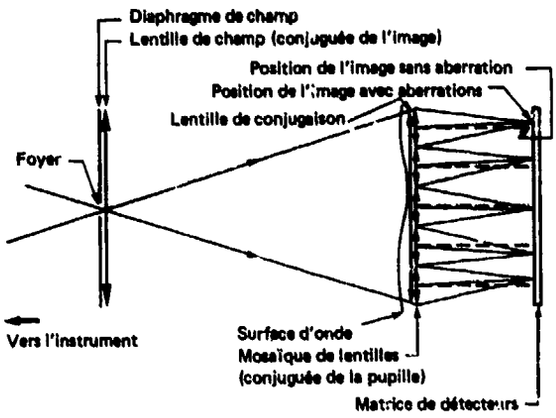


Figure 4 - Principe de l'analyseur de front d'onde de Hartmann-Shack.

Dans le cas d'un objet peu étendu l'erreur quadratique moyenne σ_φ^2 dans la reconstruction du front d'onde est [12] :

$$\sigma_\varphi^2 \simeq \frac{2\pi^2}{p_A} \tag{15}$$

où p_A est le nombre de photons détectés par sous-pupille durant le temps d'analyse. Pour reconstruire le front avec une précision crête-crête meilleure que $\lambda/4$ (c'est-à-dire $\sigma_\varphi^2 = \pi/6$) il faut collecter au moins $\frac{72}{\eta}$ photons par sous-pupille soit pour tout l'instrument :

$$N_A\, p_A \geq 72\, N_A/\eta \tag{16}$$

η est le rendement quantique du détecteur et N_A le nombre de sous-pupilles de l'analyseur de front d'onde.

5. DECONVOLUTION D'IMAGES A PARTIR DE L'ANALYSE DE FRONT D'ONDE

L'analyse de front d'onde permet de déterminer, avec une source éventuellement étendue, l'amplitude $a_1(r)$ et la phase $\varphi_1(r)$ d'un front d'onde qui serait donné par un point source situé dans le même domaine d'isoplanétisme. r est la position dans la pupille. Ainsi, le transfert optique entre l'objet et le plan focal du télescope est parfaitement caractérisé, à partir de la seule observation de l'objet, par l'utilisation d'un analyseur de front d'onde.

L'intensité $a_1^2(r)$ dans la pupille se calcule à partir des données issues d'un analyseur de Hartmann-Shack comme la moyennne des signaux reçus par les détecteurs affectés à une zone de la pupille par chaque microlentille. La phase $\varphi_1(r)$ est obtenue comme indiqué au paragraphe précédent. Ainsi, la répartition des amplitudes complexes du champ électromagnétique dans la plan de la pupille pour un point source est complètement déterminée par l'analyseur et a pour expression $a_1(r)\, e^{i\varphi_1(r)}$ (voir figure 5). L'amplitude complexe du champ $A_1(\alpha)$, que produirait un point source dans le plan focal, est alors simplement donnée par une T.F. inverse, notée $T.F.^{-1}$, permettant le passage du plan de la pupille (variable r) au plan focal (variable α) :

$$A_1(\alpha) = TF^{-1}\left(a_1(r)\, e^{i\varphi_1(r)}\right) \tag{17}$$

La fonction d'étalement de point (F.E.P.) est égale à $|A_1(\alpha)|^2$: c'est la réponse impulsionnelle du filtre spatial correspondant au transfert optique analysé. La F.T.O. est alors calculée par la relation classique suivante (voir figure 5) :

$$S_1(f) = TF\left(|A_1(\alpha)|^2\right) \tag{18}$$

La fréquence spatiale f est reliée à la dimension r mesurée dans la pupille par :

$$f = r/\lambda \tag{19}$$

Il est alors possible de déconvoluer des images suivant la relation de l'imagerie optique (Eq. 1). L'ensemble de la procédure est décrit sur le schéma de la figure 5. Ces traitements ne peuvent être faits actuellement qu'a posteriori compte tenu du temps de calcul nécessaire pour les quatre T.F.

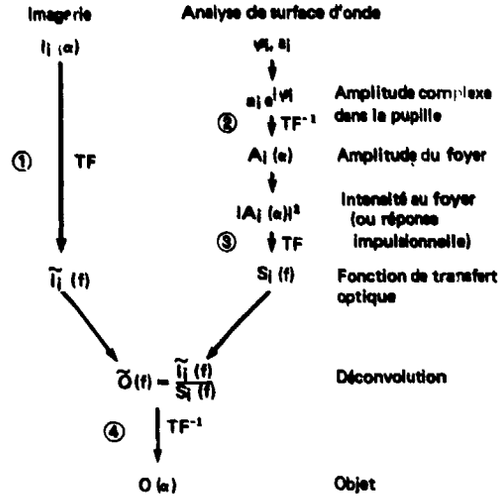


Figure 5 - Déconvolution d'images à partir d'une analyse de front d'onde. Ce processus nécessite le calcul de 4 transformées de Fourier (T.F.) numérotées de 1 à 4. La T.F. 2 porte sur les tableaux de données (32 x 32) de l'analyseur, les T.F. 1, 3 et 4 sur des tableaux (256 x 256).

Expérimentalement, les données perturbées par la turbulence sont figées et enregistrées simultanément selon deux voies parallèles (figure 6) :
- d'une part la voie analyse de front d'onde,
- d'autre part la voie imagerie fournissant des images courte pose $I_i(\alpha)$.

Une lame dichroïque sélectionne une bande spectrale étroite pour former l'image (cf paragraphe 2.3) et transmet à l'analyseur le rayonnement non utilisé. Les calculs à partir des données instantanées de l'analyseur sont évidemment exécutés pour la longueur d'onde de l'imagerie. Les caméras de prise de données sont deux matrices de détecteurs (CCD) couplées à deux amplificateurs à galette de microcanaux faisant aussi office d'obturateurs rapides synchronisés pour figer au même instant le phénomène turbulent dans le plan focal du télescope et dans le plan de la pupille. En outre, le montage inclut les éléments nécessaires à l'étalonnage de l'analyseur (front d'onde plan de référence) et au réglage des fréquences spatiales de la voie imagerie en correspondance avec celles données par l'analyseur. Ces éléments ne sont pas représentés sur la figure 6. Cet étalonnage et ce réglage sont à faire une fois pour toute avant les expériences.

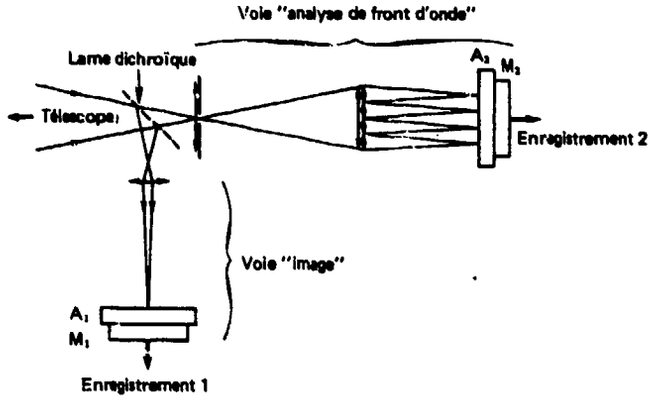


Figure 6 - Dispositif instrumental d'imagerie permettant d'obtenir les données nécessaires à la déconvolution d'images à partir d'un analyseur de front d'onde. M_1 et M_2 sont deux matrices de détecteurs, A_1 et A_2 deux amplificateurs à galette de microcanaux. A_1 et A_2 jouent aussi le rôle d'obturateur.

Dans les domaines de fréquences spatiales où le module de la F.T.O. devient plus faible que le niveau de bruit, la déconvolution ne peut pas être effectuée. Mais, du fait des perturbations de la turbulence, ces domaines changent à chaque instant aléatoirement. Ainsi en exploitant une série d'images courte pose et de F.T.O. associées (voir figure 7), on peut finalement couvrir tout le domaine de fréquences spatiales et donc restaurer l'objet. En effet, on additionne les T.F. partielles de l'objet restituées pour chaque prise de données en gardant en mémoire le nombre de fois où chaque fréquence a été déconvoluée. Lorsque la sommation des T.F. partielles de l'objet à restaurer est terminée, on divise cette somme par le nombre de déconvolutions effectuées pour chaque fréquence spatiale afin d'obtenir la T.F. de l'objet restauré $\widetilde{O}(f)$.

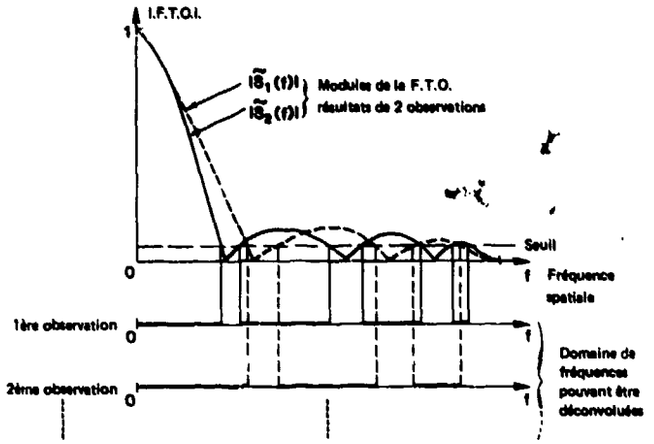


Figure 7 - Forme typique de deux fonctions de transfert instantanées de la turbulence atmosphérique et domaines associés de fréquences spatiales où la déconvolution d'image peut être calculée. Un seuil, imposé par le bruit à la FTO, délimite ces domaines.

Pour que la sommation s'effectue de manière constructive, il faut que la correction de phase effectuée sur $\widetilde{O}(f)$ par la F.T.O. n'introduise pas des valeurs aléatoires équiréparties entre 0 et 2π. C'est-à-dire que pour chaque fréquence f l'erreur de détermination de la phase de la F.T.O. ϕ_f due au bruit, reste inférieure à $+\pi/2$; on a ainsi :

$$\sigma^2_{\phi_f} < \left(\frac{\pi}{6}\right)^2 \qquad (20)$$

Par ailleurs, il est possible de relier l'erreur quadratique moyenne sur la phase de la F.T.O. à celle du front d'onde mesuré [12]. On obtient dans le cas de la turbulence atmosphérique l'égalité de ces deux erreurs quadratiques moyennes :

$$\sigma_{\phi_f} \simeq \sigma_\varphi \qquad (21)$$

Ainsi le nombre minimum de photons pour une déconvolution correcte par le processus décrit ci-dessus est égal (d'après la condition (20) et l'équation (21)) au nombre minimum de photon pour une détermination correcte du front d'onde donné au paragraphe 4 (relation 16) et vaut $72N_A/\eta$.

D'autre part, sur la voie imagerie, le bruit de photon introduit aussi une imprécision dans la restauration de l'objet. Ceci implique de moyenner un nombre minimum N d'images, donné par la relation :

$$Np \left|\widetilde{O}(f)\right|^2 T(f) > 2 \qquad (22)$$

La comparaison des implications des relations (22) et (14) est faite au paragraphe 7.

6. OPTIQUE ADAPTATIVE

Un dispositif d'optique adaptative est un système opto-électronique qui compense en temps réel les perturbations du front d'onde. Un des composants essentiels est donc un élément optique qui permet d'introduire des déphasages variables (généralement il s'agit d'un miroir déformable [14]). Un schéma général est présenté sur la figure 8. L'ensemble est placé au foyer du télescope. Il comporte d'abord un miroir déformable conjugué de la pupille et un miroir à deux axes de rotation corrigeant uniquement le basculement de l'onde qui constitue la composante la plus importante des fluctuations de phase provoquées par la turbulence atmosphérique [3]. Le flux issu de ces miroirs est séparé en deux faisceaux : l'un sert à former l'image et l'autre permet de mesurer les pentes du front d'onde au moyen d'un analyseur (voir paragraphe 4). A partir de ces pentes, un calculateur détermine les commandes à appliquer aux miroirs pour corriger le front d'onde.

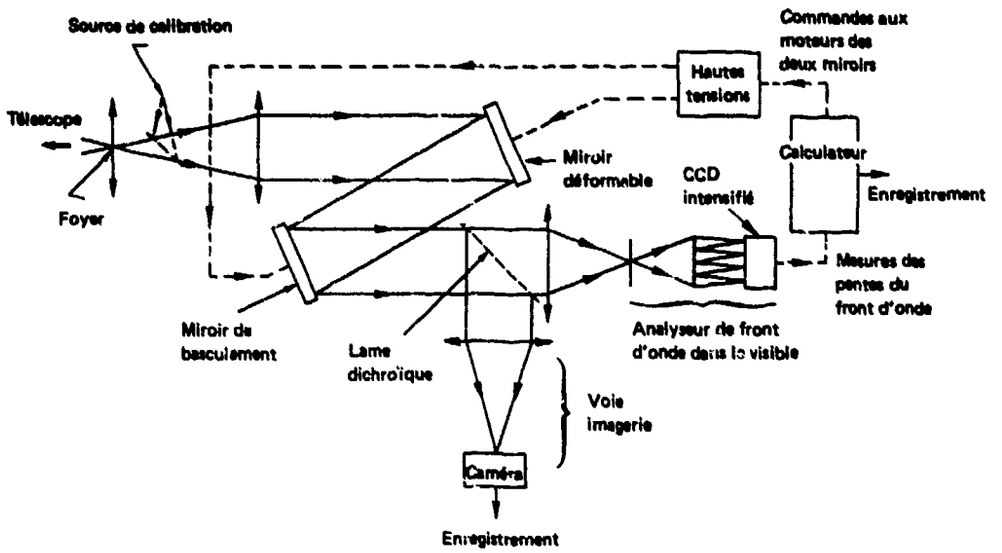


Figure 8 - Principe de montage d'un système d'optique adaptative pour correction d'image en temps réel.

Si l'optique adaptative corrige parfaitement les perturbations de phase dans la pupille, l'image sur la caméra est fixe et est limitée seulement par la diffraction. Dans le cas d'objets faibles, le nombre N d'images à intégrer pour obtenir une observation satisfaisante est donné par la relation suivante :

$$N\,N_p \left|\widetilde{O'}(f)\;T(f)\right|^2 > 2 \qquad (23)$$

Cette relation est calculée à partir du bruit de photon sur la caméra de la voie imagerie.

Pour des raisons techniques et pratiques, l'application à l'astronomie est plus facile dans le cas de l'imagerie infrarouge avec analyse de front d'onde dans le visible. Pour un télescope de diamètre D = 3,6 m, avec r_0 = 0,8 m à λ = 3µm, le nombre nécessaire d'éléments de corrections sur le miroir déformable est de l'ordre de $(D/r_0)^2$ = 20 et la bande passante requise de 20 Hz, pour obtenir une image pratiquement limitée par la diffraction du télescope. Actuellement, de telles contraintes sont relativement faciles à satisfaire. De plus, le nombre de sources astronomiques, assez lumineuses pour servir à analyser le front d'onde, est beaucoup plus grand dans le visible que dans l'infrarouge pour un domaine d'isoplanétisme donné (~ 15 secondes d'arc à λ = 3 µm).

Un projet d'optique adaptative au foyer d'un grand télescope astronomique sous la maîtrise d'oeuvre de l'ONERA est en cours de définition avec l'European Southern Observatory (ESO) réunissant aussi les laboratoires de Marcoussis (CGE) et l'Observatoire de Paris-Meudon. Il comporte 19 moteurs sur le miroir déformable avec une excursion de ± 7,5 µm, plus deux moteurs commandant le miroir de basculement de l'onde et 20 sous-pupilles utiles dans l'analyseur de front d'onde. Le calcul des commandes appliquées aux moteurs est fondé sur une relation matricielle déduite une fois pour toute par une méthode des moindres carrés de la matrice d'interaction reliant le déplacement élémentaire de chaque moteur aux mesures issues de l'analyseur. 21 commandes de moteur sont à calculer à partir de 40 mesures de pente du front d'onde.

Si l'on admet que l'optique adaptative peut corriger les 19 premiers modes dans la décomposition du front d'onde sur la base des polynômes de Zernike, l'écart quadratique moyen des fluctuations de phase résiduelles sur la pupille est alors donné par la relation [15] :

$$\sigma_\varphi^2 = .023\;(D/r_0)^{5/3} \qquad (24)$$

Ce qui correspond à une fluctuation crête à crête de π radians dans des conditions de turbulence telles que $r_0 = D/\sqrt{19}$ à la limite du dimensionnement du système. Cette erreur est due à l'ajustement imparfait des corrections au front d'onde turbulent, introduit par le nombre insuffisant de modes considérés : ici les polynômes de Zernike, dans la réalité, les modes propres du miroir déformable. Elle peut être réduite en augmentant le nombre de modes à corriger. A ce type d'erreur s'ajoutent l'erreur de mesure introduite par l'analyseur de front d'onde (voir paragraphe 4) et l'erreur temporelle introduite par la constante de temps de la boucle d'asservissement.

Même dans les cas où l'optique adaptative ne corrige pas parfaitement les effets de la turbulence atmosphérique à cause d'une bande passante insuffisante ou encore d'un nombre de moteurs trop réduit, elle apporte cependant un gain G en résolution par la réduction de la taille de la tache image (figure 9) [12]. La taille des tavelures, liée uniquement au diamètre de la pupille, reste de l'ordre de $\lambda F/D$ où F est la distance focale de l'optique et donc le nombre de tavelures est réduit d'un facteur G^2.

Ceci aboutit à une amélioration de la fonction de transfert (figure 10). La fréquence de coupure en longue pose se trouve être alors de l'ordre de Gr_o et l'aile haute fréquence de la fonction de transfert de tavelures est multipliée par G. La présence d'une optique adaptative favorise donc les méthodes d'imagerie reposant sur l'exploitation des tavelures. De plus, il est toujours possible d'exploiter les mesures de l'erreur résiduelle sur le front d'onde fournies par l'analyseur pour appliquer la déconvolution a posteriori des images enregistrées dans une telle situation, par la méthode décrite dans le paragraphe 5.

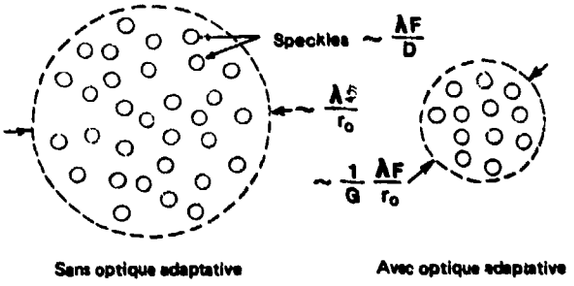


Figure 9 - Aspects des taches image instantanées.

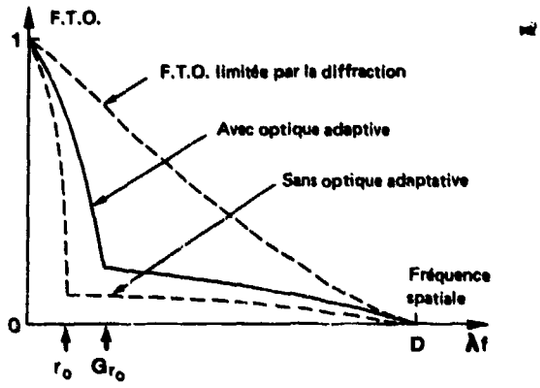


Figure 10 - Fonction de transfert de tavelures, avec et sans optique adaptative.

Méthode Elément de comparaison	Algorithme de Knox-Thompson	Déconvolution à partir de l'analyse de front d'onde	Optique adaptative
Hypothèse de la stationnarité de la turbulence	OUI	NON	NON
Nécessité d'une source brillante* dans le domaine d'isoplanétisme	NON	OUI	OUI
Variations du rapport signal à bruit	p	$\sqrt{p}$	$\sqrt{Np}$
Domaine spectral limité pour l'enregistrement de l'image	OUI	OUI	NON
Nombre N d'images à traiter**	2.10^4	2.10^2	~ 1
Complexité technique	simple	modérée	complexe
Complexité des algorithmes	complexe	modérée	pas d'algorithme

Tableau I
Comparaison des méthodes d'imagerie à travers la turbulence

* Non obligatoirement ponctuelle

** Calculs faits avec p = 1, $\left|\widetilde{O'}(f)T(f)\right| = 0,1$, N = 400 (cas du visible).

7. COMPARAISON DES METHODES

Les caractéristiques principales des trois méthodes décrites sont rassemblées dans le tableau I ; les nombres minimaux d'images à traiter pour obtenir une restauration satisfaisante y sont comparés dans le cas d'une observation de type astronomique (d'après les équations 14, 22 et 23).

La méthode la plus simple à mettre en oeuvre, l'algorithme de Knox et Thompson, présente trois inconvénients : les propriétés statistiques de la turbulence doivent être stables, le nombre d'images à traiter est très grand et l'algorithme complexe. Les deux autres méthodes ne présentent pas cet inconvénient mais requièrent la présence d'une source brillante bien que non obligatoirement ponctuelle dans le champ d'isoplanétisme pour effectuer l'analyse de front d'onde. Rappelons que cette source peut être l'objet lui-même, éventuellement utilisé dans une autre bande spectrale que celle qui sert à l'observation. L'optique adaptative est théoriquement la méthode la plus puissante mais elle nécessite une technologie complexe en cours de développement.

8. CONCLUSION

La turbulence atmosphérique constitue une aberration souvent importante, rapidement évolutive, d'autant plus gênante que la longueur d'onde est courte. Toutefois, au cours des dernières années, plusieurs méthodes sont apparues qui permettent de compenser ses effets. Elles sont complexes ; un dispositif expérimental simple s'accompagne d'un traitement numérique lourd et inversement. Certaines ont fait l'objet de démonstrations expérimentales ponctuelles mais le caractère opérationnel reste à établir.

Le problème de l'isoplanétisme limite la restauration des images à un domaine angulaire restreint quelle que soit la méthode employée. Toutefois, dans une étape future, le fractionnement du champ en une mosaïque de domaines isoplanétiques peut se concevoir.

Si l'optique adaptative apparaît comme la méthode la plus puissante, les méthodes numériques appliquées a posteriori sont probablement complémentaires : on peut imaginer que, si la compensation par l'optique adaptative n'est pas parfaite pour des raisons technologiques, la restauration soit achevée par une méthode numérique comme la déconvolution à partir de l'analyse des défauts résiduels du front d'onde.

REFERENCES

[1] - Tatarskii, V.I., Wave propagation in a turbulent medium, Dover, New York, 1961.

[2] - Roddier, F., The effects of atmospheric turbulence in optical astronomy, Progress in Optics, vol. 19, E. Wolf (Editor), North Holland Publishing Co., Amsterdam, 1981.

[3] - Fried, D.L., Statistics of a geometric representation of wavefront distorsion, J. Opt. Soc. Am., vol. 55, p. 1427, 1965.

[4] - Weigelt, G.P., Modified speckle interferometry: speckle masking, Opt. Commun., vol. 21, p. 55, 1977.

[5] - Labeyrie, A., High resolution techniques in optical astronomy, Progress in Optics, vol. 14, E. Wolf (Editor), North Holland Publishing Co., Amsterdam, 1976.

[6] - Knox, K.T., Thompson, B.J., Recovery of images from atmospherically degraded short exposure photographs, Astrophysical Journal, vol. 193, p. L45, 1974.

[7] - Fontanella, J.C., Sève, A., Turbulence degraded images reconstruction using the Knox and Thompson algorithm, J. Opt. Soc. Am. A, (à paraître, mars 87).

[8] - Wyant, J.C., Koliopoulos, C.L., Phase measurement systems for adaptative optics, AGARD Conference Proceedings n° 300, p. 48-1, 1981.

[9] - Koliopoulos, C.L., Radial grating lateral shear heterodyne interferometer, Appl. Opt., vol. 19, p. 1523, 1980.

[10] - Schmutz, L.E., Bowker, J.K., Feinleib, S., Tubbs, S., Integrated imaging irradiance (I^2) sensor: a new method for real-time wavefront mensuration, Proc. SPIE n° 179, p. 76, 1979.

[11] - Fontanella, J.C., Teron, R., Rousset, G., Image Quality evaluation from wavefront sensing, International Topical Meeting on Image Detection and Quality, Société Française d'Optique, Paris, Juillet 1986.

[12] - Fontanella, J.C., Analyse de surface d'onde, déconvolution et optique adaptative, J. Optics (Paris), vol. 16, p. 257, 1985.

[13] - Southwell, W.H., Wave-front estimation from wave-front slope measurements, J. Opt. Soc. Am., vol. 70, p. 998, 1980.

[14] - Hardy, J.W., Lefebvre, J.E., Koliopoulos, C.L., Real time atmospheric compensation, J. Opt. Soc. Am., vol. 67, p. 360, 1977.

[15] - Noll, R.J., Zernike polynomials and atmospheric turbulence, J. Opt. Soc. Am., vol. 66, p. 207, 1976.

DISCUSSION

K. Altmann, W.GR

In what regime of turbulence do you think your adaptive mirror works?

Author's Reply

English translation

The mirror is designed so that the spacing between motors measured in the pupil is of the order of r_o (Fried's diameter). For a telescope of 3.6 m, in the "COME ON" experiment, this corresponds to an $r_o \cong 90$ cm, for the viewing in the spectral domain around 4 μm (the relation r_o, C_n^2 is given by equation (4) in the text).

A. Ishimaru, US

How short is the short-exposure time? How did you take care of the signal-to-noise problem?

Author's Reply

English translation

The short exposure times are of the order of milliseconds. The recording of images are done in conditions where photon noise dominates (visible, and less than one photon per pixel). The signal-to-noise ratio is then proportional to $p\sqrt{M}$ where p is the number of photons per pixel and M is the number of images used for the restoration. So, a large number of images are necessary. Finally, the bias introduced by the camera response on the spectral densities has been calibrated and has been eliminated during the restoration.

A. Consortini, IT

How much is the value of the distance between the centers of the small lenses used for the measurements of the wavefront?

Author's Reply

English translation

The distance between the center of the microlenses is about 500 μm. It varies depending upon the situation so that it is of the order of the r_o limit (Fried's diameter) when measured in the pupil.

INFRARED ATMOSPHERIC TRANSMISSION/EMISSION MEASUREMENT IN A MARITIME ENVIRONMENT

G. J. BISHOP and I. W. LARKIN

BRITISH AEROSPACE plc,
NAVAL AND ELECTRONIC SYSTEMS DIVISION
FPC.026, P.O. BOX 5, FILTON,
BRISTOL, BS12 7QW
U.K.

ABSTRACT

This paper is divided into two parts, the first covering atmospheric measurement trials, the second describing predictions of atmospheric effects on sensor design.

In 1985 a programme of collaborative electro-optical research was agreed between ARE (Admiralty Research Establishment) and British Aerospace, co-ordinated by the Naval and Electronic Systems Division at Bristol. The object of this research was to gather trials data on the performance of electro-optical systems in a maritime environment. In order to achieve this objective, it was important to measure the atmospheric transmission/emission close to the sea surface in a variety of weather conditions.

During the course of the trial (Fraser Battery October 1985) considerable experience was gained in the operation of various imaging sensors, especially in calibration and measurement techniques. The need to obtain calibrated measurements of atmospheric transmission/emission between the electro-optic sensor and any trials target is to be emphasised. This paper describes how these measurements were made and compares the results to those predicted by the Lowtran V atmospheric model.

The second part of this paper describes how ozone absorption will affect the design of a passive surveillance system working in the ultraviolet band.

PART 1 - ATMOSPHERIC MEASUREMENT TRIALS

1.1 INTRODUCTION

MEASUREMENT OF ATMOSPHERIC DATA

In order to assess the performance of electro-optic systems, it is necessary to know the atmospheric transmission and emission effects. This trial showed the importance of measuring these, rather than simply predicting their effects from atmospheric models (unless full meterological data and aerosol measurements are available). The atmospheric transmission and emission data from the computer model will subsequently be compared to those obtained from the trial.

1.1.1. MEASUREMENT OF ATMOSPHERIC TRANSMISSION USING A SINGLE SOURCE

Knowing the source temperature it is possible to calculate the emitted radiance of the source. If the received radiance on a source pixel is measured, then the atmospheric transmission (or attenuation) is given by the following equation:

This work has been carried out with the support of the Procurement Executive, Ministry of Defence.

$$\tau = \frac{N_r - N_{air}}{N} \quad \text{.....(1.1)}$$

where:- τ = Atmospheric transmission

N_r = Measured received radiance of source pixel / W $m^{-2}sr^{-1}$

N_{air} = Near atmospheric airlight / W $m^{-2}sr^{-1}$

N = Source emitted radiance / W m^{-2} sr^{-1}

The problem with this method is that it still relies on the LOWTRAN model to produce an estimate of the near atmospheric airlight and so does not give completely independent measurements of the atmospheric characteristics. This problem can be overcome by using two sources in order to measure both the atmospheric transmission and the atmospheric airlight.

1.1.2. Measurement of Atmospheric Data using Two Sources

If the radiance received by the thermal imager is measured for two sources which are at different temperatures but at the same range, then the following two equations can be comprised using eqn (1):-

$$N_1 = \frac{N_{r1} - N_{air}}{\tau} \quad \text{.....(1.2)}$$

$$N_2 = \frac{N_{r2} - N_{air}}{\tau} \quad \text{.....(1.3)}$$

where:- N_1 = Emitted radiance from source 1 / W $m^{-2}sr^{-1}$

N_2 = Emitted radiance from source 2

N_{r1} = Received radiance of source 1

N_{r2} = Received radiance of source 2

N_{air} = Near atmospheric airlight radiance

= Atmospheric transmission

By subtracting eqn (1.3) from eqn (1.2) and rearranging the result the following equation is obtained:-

$$\tau = \frac{N_{r1} - N_{r2}}{N_1 - N_2} \quad \text{.....(1.4)}$$

Therefore from eqn (1.4) it is possible to calculate from the measurements of the received radiances of the two targets. As this equation uses the difference in received and emitted radiances of the two sources, this method of measuring atmospheric transmission can only be used with confidence where the difference in temperature of the two sources is quite high. This is necessary to ensure that the radiance differences are reasonably high, because small difference values would lead to high errors.

After the atmospheric transmission as been calculated from eqn (1.4) then the atmospheric airlight can be calculated from either eqn (1.2) or (1.3).

1.2 TRIALS CONFIGURATION

The trial at Fraser Battery in October 1985 employed two land-based far-infrared band thermal imagers and two boat-carried standard sources ($1m^2$, temperature controlled panels). The imagers and sources were between 4 to 10m above sea level and the boat-carried sources could be viewed along a near-horizontal over-water

line of sight at ranges between 2 to 5km. Calibration of the thermal imagers was achieved by viewing two or three standard sources at very short range (approximately 20 metres) and the images were recorded with non-AGC analogue video recorders. An automatic recording meteorological station was used to provide all the data (except visibility and aerosol measurements) required for atmospheric transmission and emission modelling purposes (LOWTRAN V). Measurements were taken under a range of weather conditions and visibilities.

1.2.1 Imager Calibration.

The thermal imagers can be calibrated in terms of received radiance by viewing a number of standard temperature-controlled panels (well resolved by the imagers) at very short range, where atmospheric transmission and emission effects will be negligible. In principle, the imager response curve will be piecewise linear and the temperatures of two calibration sources should be chosen appropriately (see Figure 1.1), or a larger number of sources used. For radiances close to those of the calibration sources, non-linearity effects in the recording system should also be largely self-cancelling.

1.2.2. Imager MTF Effects

As the radiance calibration was carried out using well-resolved sources, radiance measurement of longer range sources also requires that they are well resolved. This is particularly true when one considers blurring of the image due both to optical effects and to detector scanning effects (optical and modulation transfer functions). Figure 1.2 shows a digitised example of this effect, where the anticipated 'uniform image radiance' is only achieved for the central group of pixels. It is possible to apply processing to partially compensate for imager MTF-blurring effects, but the need for well-resolved sources is obvious from figure 2.

1.2.3 Received Radiance Measurements

Data reduction follows the schematic of figure 1.3, where the analogue sensor output is digitised and then compensated for sensor MTF. Following the calibration procedure, the received radiance from the source (including atmospheric 'airlight' emission) can be directly determined.

1.3 ATMOSPHERIC TRANSMISSION AND EMISSION MEASUREMENTS AND PREDICTIONS

As the measured received radiance contains both the attenuated source emissions and a contribution from atmospheric airlight emission (see Figure 1.4), a single-source measurement must rely on an estimate of this airlight contribution if atmospheric transmission 'measurements' are to be made. Tables 1.1 and 1.2 show examples of single-source transmission measurements for the two imagers used on the trial, the airlight estimates having been made using the LOWTRAN V program. The LOWTRAN V estimated transmission agrees closely with these single-source measurments, but it must be remembered that these are based on the related airlight predictions from LOWTRAN V.

The two-source differential measurement techniques, however, gives a direct measurement of both atmospheric transmission and emission in the measurement band. Examples from the 1985 trials of the measured transmission and airlight (using this two-source technique) are also given in Tables 1.1 and 1.2. It will be seen that these measurements indicate lower transmissions and higher airlight emissions than predicted by LOWTRAN V (with the model atmosphere assumed to be most appropriate for this maritime situation and latitude). As no aerosol measurements were available it would not be surprising if a low over-water line-of-sight such as this were to behave differently from the LOWTRAN V prediction.

1.4 TRIALS CONCLUSIONS

When carrying out trials, the need to measure both atmospheric transmission and emission is recommended, rather than purely relying on predictive techniques, especially for non-standard situations as far as atmospheric modelling is concerned.

Improvements to both the recording and calibrating techniques employed in 1985 are recommended as the overall measurement accuracy at that time was not as good as was hoped for. Recent experimental work indicates a considerable improvement in accuracy.

PART II - ATMOSPHERIC EFFECTS ON SENSOR DESIGN IN THE 200-300nm WAVEBAND

2.1 INTRODUCTION

Infra-red detection systems are normally designed to work within an atmospheric window, to maximise range performance. The window that the system designer will normally choose to operate in is based on a knowledge of the spectral emittance characteristics of the objects he is trying to detect (barring limitations in detector performance). As detection systems become more sensitive, the problem of rejecting background clutter becomes more acute requiring sophisticated algorithm development. The Electronic Warfare Department at British Aerospace, Bristol has recently undertaken a system study on the design of a passive detection system operating within the ozone absorption band between 200 and 300nm. The reasons for designing such a system to work within an absorption band are outlined in the following section.

2.2 OZONE ABSORPTION EFFECTS

In the Ultra-Violet spectral band there is strong absorption due to atmospheric ozone which consists of a few diffuse bands followed by a very strong continuum which extends from 200nm to 300nm.

Below 300nm the radiance from the atmosphere is negligible in comparison with the radiation arriving from the sun.

It is not normal practice, as previously described to operate a passive detection system within an atmospheric absorption band. However the ozone concentration is an order of magnitude lower at sea level than at altitudes between 15 and 20km (figure 2.1) and thus the sun's radiance at sea level is greatly reduced. If therefore the ozone continuum at sea level allows reasonable inband transmission, a detection system could work against a virtually black photon background. To calculate the optimum spectral response of a device operating within this absorption band, the solar irradiance background count at sea level has to be calculated. A simple model has been developed to predict the solar irradiance at any altitude. If it is assumed that the sun is a Lambertian surface of radius r, then the spectral irradiance H from the sun at range R is defined by:

$$H_\lambda = \pi(r/R)^2 L_\lambda \qquad (2.1)$$

where L_λ is the spectral radiance of the sphere.

If it is assumed that the sun is a blackbody with unit emissivity at a temperature (T) of 5900K, then the spectral radiance is given by

$$L_\lambda = \frac{2\pi hc^2}{\lambda^5} (\exp(hc/\lambda kT)-1)^{-1} \qquad (2.2)$$

The spectral photon irradiance N_λ is then given by:

$$N_\lambda = T_\lambda H_\lambda / E_\lambda \qquad (2.3)$$

where T_λ is the atmospheric transmission and E is the energy per photon of wavelength λ. To calculate the atmospheric transmission it is assumed that the atmospheric transmission is dominated by ozone absorption below 315nm. For a vertical path through the atmosphere from sea level to 100km that is approximately 3.2mm of ozone at STP. The maximum ozone opacity is approximately $14m^2$/gramme (255nm).

The result obtained by Tanaka and Inn (1) display a 5% variation in ozone opacity given a variation in pressure from 0.3 to 650mm Hg. An equivalent pressure variation is observed in the atmosphere as altitude varies from 500metres to 50km. The Doppler broadening of the individual transition lines will not be important in comparison with the Lorentz broadening until the atmospheric pressure is below 10mbar (WOLFE and ZISSIS(2)). Atmospheric pressure does not fall below 10mbar until the altitude exceeds 30km. Since the majority of atmospheric ozone is distributed below 30km, the largest contribution to atmospheric absorption will occur within a region of constant opacity.

If $N_\lambda(x)$ photons per second of wavelength λ are normally incident upon a section of atmosphere with unit area and thickness dx, then the number absorbed at position x is defined by

$$dN_\lambda(\underline{x}) = K_\lambda(\underline{x})\,\rho(\underline{x})\,N_\lambda(\underline{x})\,d\underline{x} \qquad (2.4)$$

where $\rho(x)$ is the ozone density at x and $k_\lambda(x)$ is the ozone opacity (or mass absorption coefficient). The optical path length at a wavelength is defined by

$$d\tau_\lambda = K_\lambda(\underline{x})\,\rho(\underline{x})\,d\underline{x} \qquad (2.5)$$

Hence the optical path length from x_1 to x_2 is given by

$$\tau_\lambda(\underline{x}_1, \underline{x}_2) = \int_{\underline{x}_1}^{\underline{x}_2} K_\lambda(\underline{x})\,\rho(\underline{x})\,d\underline{x} \qquad (2.6)$$

Given the assumption that $k_\lambda(x)$ is independent of pressure and temperature, we may write the integral as

where $$\tau_\lambda(\underline{x}_1, \underline{x}_2) = K_\lambda\,W(\underline{x}_1, \underline{x}_2) \qquad (2.7)$$

$$W(\underline{x}_1, \underline{x}_2) = \int_{x_1}^{x_2} \rho(\underline{x})\,d\underline{x} \qquad (2.8)$$

$w(x_1, X_2)$ represents the mass of absorber per unit area along the optical path. The accepted solution to this equation is $6.8 g/m^2$ (Tanaka and Inn(1), although this quantity can vary depending on the latitude and the time of the year. Obviously, the lower the mass absorber per unit area, the greater will be the solar background at any altitude.

From equation (2.4) and (2.5) we may write

$$dN_\lambda = N_\lambda\,d\tau_\lambda \qquad (2.9)$$

which has as its solution

$$N_\lambda(\tau_\lambda) = N_\lambda(0)\exp(-\tau_\lambda) \qquad (2.10)$$

where from sea level to 100km,

$$\tau_\lambda = \tau_\lambda(\underline{x}_1, \underline{x}_2) \qquad (2.11)$$

Then the transmission (T_λ) from sea level to 100km is given by:

$$T_\lambda = N_\lambda(\tau_\lambda)/N_\lambda(0) = \exp(-\tau_\lambda) \qquad (2.12)$$

As an example at λ = 255nm

K = $14 m^2/gm$
W = $6.8\ gm/m^2$
τ_λ = 95.2

Hence the transmission at λ = 255nm is approximately 10^{-42}.

The mass absorption coefficient of ozone at STP was obtained from Matthews (3); these data, reproduced in figure 2.2, show the variation of this quantity from 200 to 300nm. These data allow us to calculate the spectral transmission across this waveband due to ozone absorption.

Given that the sun is 215 solar radii from the earth, then equation (2.3) may be re-written as

$$N_\lambda d\lambda = \frac{\pi}{215^2}\,\frac{L_\lambda T_\lambda}{E_\lambda} \qquad (2.13)$$

Using equation 2.13, the solar spectral photon irradiance is plotted in figure 2.3 as a function of wavelength. This figure shows that the sea level irradiance is less than 1ph/sec/m^2/nm for wavelengths between 232 and 275nm. Hence a system with a hemispherical FOV and a $1m^2$ collecting aperture will receive less than 1 photon per second from the sun in this waveband. For a detection system to be completely solar blind, it must therefore have a filter which rolls off to a stop band with rejection greater than 10^{-18} at 315nm.

As previously described the solar irradiance at any altitude depends on the optical path length. As the major concentration of ozone is between 10 and 25km the optical path lengths will not change significantly until the receiver exceeds an altitude of 10km. Therefore the solar irradiance will not change significantly until the receiver exceeds an altitude of 10km, with it rising exponentially above this altitude. We may conclude that an operational ceiling for a UV detection system will be about 10km. When the sun is at low zenith angles, the optical path length is increased. If molecular absorption were the only mechanism, then the optical path length would increase as the cosecant of the zenith angle. However, scattering becomes increasingly important at low angles, especially at short wavelengths. Green (4) predicts that the solar irradiance at 280nms will be reduced by four orders of magnitude when the sun is at a solar angle of 5 deg compared with overhead (90^0).

Atmospheric transmission close to the earth's surface within the UV solar blind spectral region is a function of the aerosol profile. At low visibilities (high aerosol profile), transmission is dominated by aerosol effects, which in this passband are almost independent of wavelength. Molecular scattering effects are calculated as a function of the fourth power of the wavelength. Hence the molecular transmission is a monotonically increasing function of wavelength, as shown in figure 2.4 Molecular absorption in the middle UV is dominated by the strength of the ozone absorption continuum from 195 to 315nm (figure 2.2). Hence ozone is the only molecular species included in the molecular absorption calculation.

It may be concluded that a UV-band detection system will be more sensitive to aerosol concentration than a visible or infra-red system. This is a physical consequence of increased scattering with shorter wavelengths. At altitudes above sea level and up to 10km (where the atmosphere is cleaner), the detection range will increase. However, above 10km the ozone concentration increases rapidly and transmission will fall below that at sea level.

2.3 EMISSION SOURCES

In the design of any detection system, one has to consider the magnitude of the emitting sources that the system is designed to detect. The primary source of radiation in this UV waveband will arise from the hot combustion products which occur in rocket exhaust plumes. The radiation from these is primarily of molecular origin; however, electronic levels are excited and give rise to weaker emission in the visible and ultra violet.

Conversely the reaction zone of an exhaust flame may contain high concentrations of electronically excited, middle UV active species. This zone may be far from thermodynamic equilibrium, in which case the distribution of electronic states of a given radical may not be Maxwellian.

The chemical reaction that creates a true radical may create disproportionately large numbers in an excited state: for example the reaction

$$CH + O_2 \longrightarrow CO + OH^*$$

is sufficiently energetic to create electronically excited OH^* radicals. As the radical decays to the ground state, it will emit photons in the middle UV. This mechanism is called Chemiluminescence. This emission of radiation is not adequately described by the Maxwell distribution or by Planck's law for blackbody emission.

In the middle UV, the largest emissions from a hydrocarbon/air flame are due to the electronic excitations levels of OH. The most intense emissions are from the (0,0), (1,0) and (0,1) bands of the 306.4nn transition. Much weaker emissions are found at 267.7nm (3,1) band and at 260.9nm (2,0) band. Further details of the fine structure are given in references (5,6). Calculation of these emissions within the solar blind region requires detailed modelling of line/band emission for the contributing constituents within the plume structure.

2.4 ULTRA VIOLET DETECTION SYSTEMS

Given the solar radiance characteristics and the exhaust plume signature, the ideal detector should have a passband from 232nm to 275nm. Its spectral response must roll off to less than 10^{-18} counts per photon outside the passband (specifically beyond 200nm and 315nm). It is very difficult to achieve a spectral response with such fast roll off whilst maintaining a high sensitivity within the passband.

The most promising device found to perform this task is the phototube (7). A phototube consists of two electrodes within an evacuated chamber. A potential is applied between the two electrodes. When photons with sufficient energy are incident upon the cathode, it emits electrons which are attracted to the anode. A small amount of inert gas can be introduced to the tube: this results in an amplification of the initial photo-current by ionization of the gas. With the correct electrode spacing and gas pressure, avalanche ionization is caused by the emission of a single electrode, thus the tube may be configured to have a large amplification.

The short wavelength spectral response depends on the choice of window material for the phototube. Many dyes and polymers have a rapid change in absorption length with wavelength. Recent studies have revealed some promising candidates which could be used in a detection system.

The spectral response of the device at long wavelengths is dependent upon the work function of the metal that forms the photo cathode. The rate at which the response rolls off with increasing wavelength is dependent upon the distributions of valence electrons within the energy levels of the metal. At abolute zero the electrons will occupy those states up to the Fermi level. In this case an electron will not be emitted from the surface unless an incident photon has a wavelength shorter than the cut-off wavelength. Tungsten and Copper are considered the most suitable cathode metals for this passband. Factors which have to be considered in the cathode design include the effect of temperature on the spectral response and its quantum yield.

2.5 SUMMARY

In this brief description, we have outlined thebasis behind the design of a ground based detection system working in the 200-300 ozone continuum. Detailed calculation, especially on the receiver characteristics, can define the systems performance under a variety of meteorological conditions.

2.6 REFERENCES

1) INN, E and TANAKA, Y

"Absorption Coefficient of Ozone in the UV and visible Regions".
JOSA 43, 10(1953)

2) WOLFE and ZISSIS

"The infra-red Handbook"

3) M. MATTHEWS

"Atmospheric Transmission/Radiance from 0.25 to 28.5 Micrometers
Using Fortran Computer Program Lowtran V"
ST.25369 JULY 1981

4) GREEN A.E.S. AND SHETTLE E.P.

"Multiple Scattering Calculations of the Middle UV Reaching the ground".

Applied Optics 13,7(1974)

5) BRINTMANN R.T. et al

"Atomic and Molecular Species"
Chapter 2
"The middle U.V. It's Science and Technology"
Green A.E.S. (Ed) John Wiley 1966

6) PEARCE R.W.B. and GAYDEN A.G.

"The Identification of Molecular Structure"
Chapman and Hall Limited 1950

7) B. RAY

"Flame Sensing with UV Radiation Detectors"
Fire prevention Science and Technology No.17

RUN	LOWTRAN V ESTIMATED TRANS. %	LOWTRAN V ESTIMATED AIRLIGHT $Wm^{-2}sr^{-1}$	TRANS. MEASURED FROM ONE SOURCE %	TRANS. MEASURED FROM TWO SOURCES %	AIRLIGHT MEASURED FROM TWO SOURCES $Wm^{-2}sr^{-1}$
1	74	8.87	74.9	33.1	22.6
2	64	11.51	63.3	17.4	26.7
3	56	13.53	57.0	10.9	28.8
4	73	9.03	73.6	29.9	23.9
5	66	10.89	65.3	25.9	24.8
6	57	13.51	56.3	14.9	26.3

TABLE 1.1 - MEASUREMENT OF ATMOSPHERIC TRANSMISSION AND NEAR ATMOSPHERIC AIRLIGHT FROM TWO SOURCES - IMAGER (A)

RUN	LOWTRAN V ESTIMATED TRANS. %	LOWTRAN V ESTIMATED AIRLIGHT $Wm^{-2}sr^{-1}$	TRANS. MEASURED FROM ONE SOURCE %	TRANS. MEASURED FROM TWO SOURCES %	AIRLIGHT MEASURED FROM TWO SOURCES $Wm^{-2}sr^{-1}$
1	60	11.38	63.5	23.1	24.7
2	49	14.84	50.8	17.2	26.0
4	54	12.13	53.7	36.3	18.4
5	38	15.27	41.6	17.8	23.9

TABLE 1.2 - MEASUREMENT OF ATMOSPHERIC TRANSMISSION AND NEAR ATMOSPHERIC AIRLIGHT FROM TWO SOURCES - IMAGER (B)

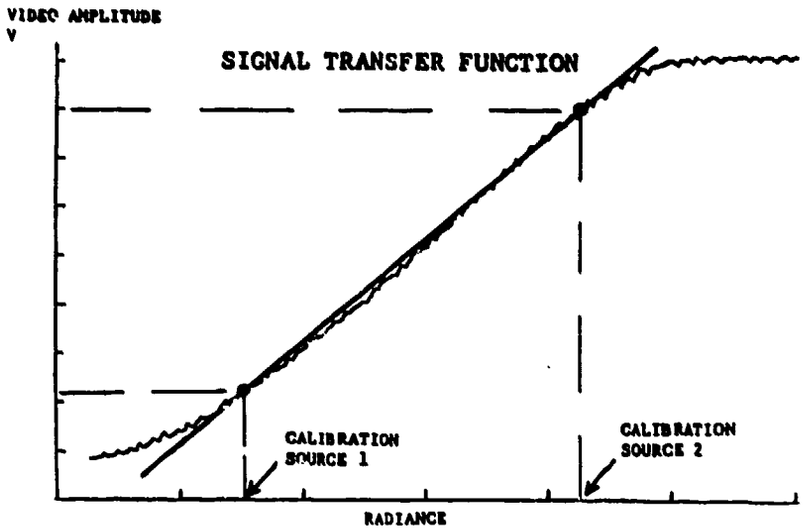


FIG 1.1

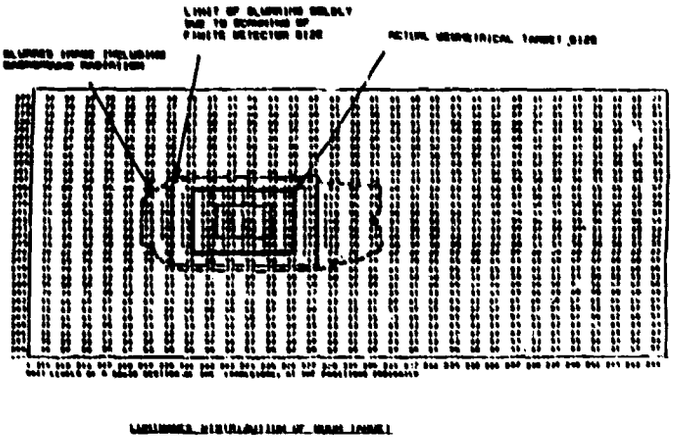


FIG 1.2 - BLURRING OF CALIBRATED TARGETS

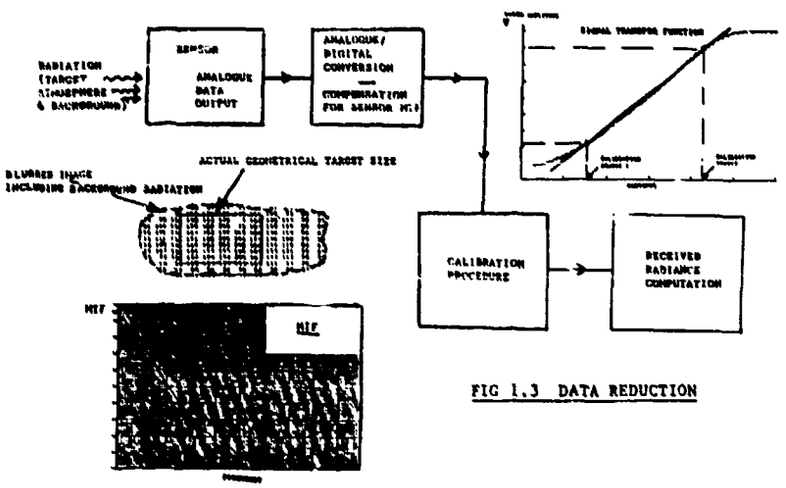


FIG 1.3 DATA REDUCTION

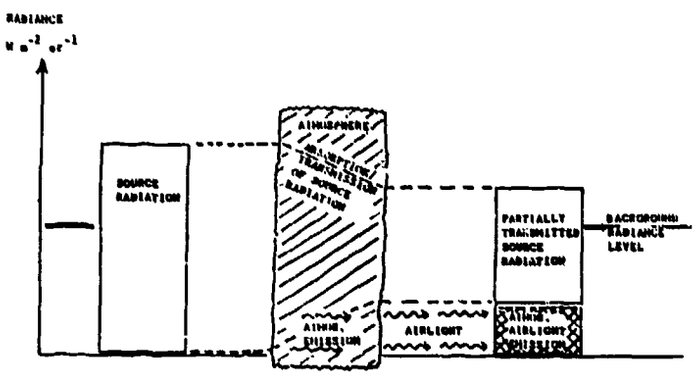


FIG 1.4 - ATMOSPHERIC EFFECTS

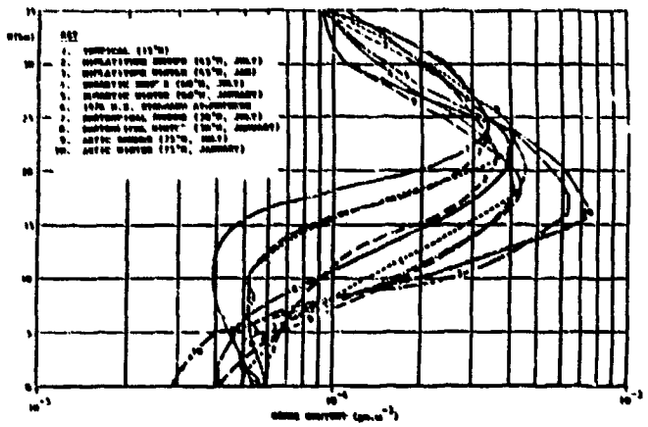


FIG 2.1 OZONE-ALTITUDE PROFILES (FOR THE STANDARD ATMOSPHERIC MODELS)

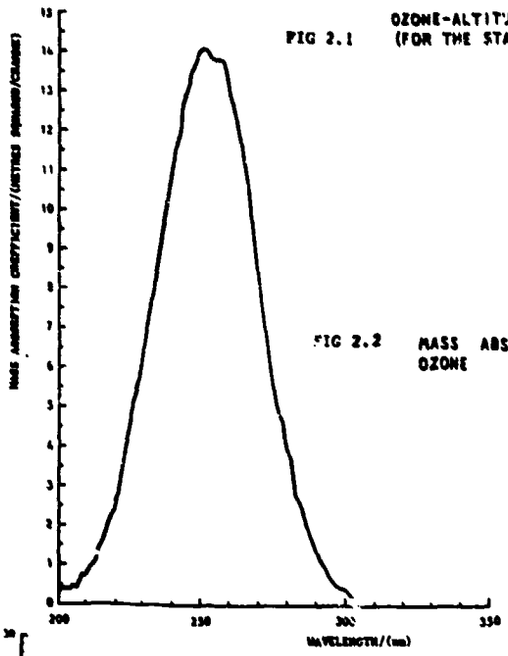


FIG 2.2 MASS ABSORPTION COEFFICIENT AGAINST WAVELENGTH FOR OZONE

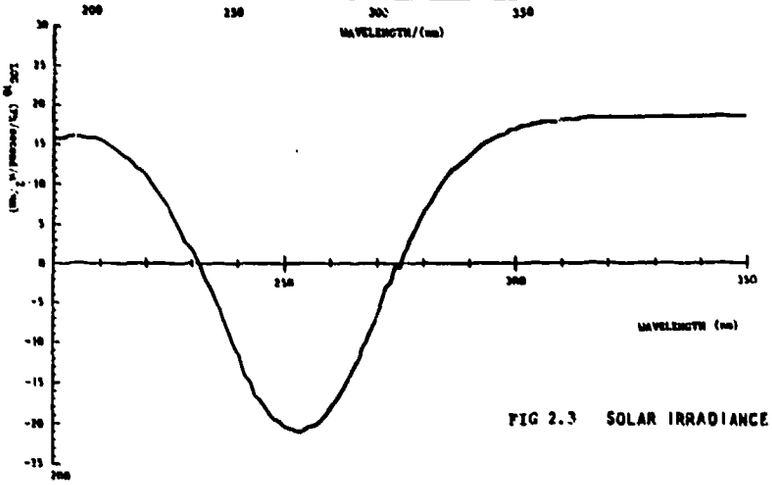


FIG 2.3 SOLAR IRRADIANCE AT SEA LEVEL

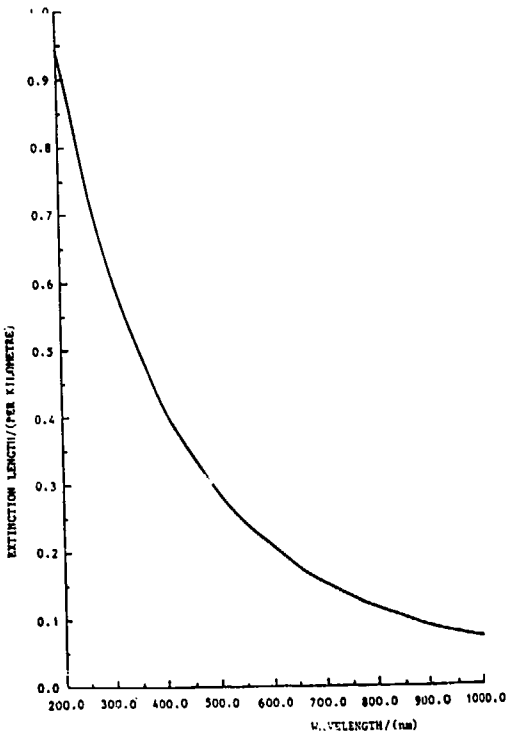


FIG 2.4 MOLECULAR EXTINCTION LENGTH AGAINST WAVELENGTH

A PRECIPTITATION SCATTER EXPERIMENT AT 30 GHZ

Heinz Schmiedel and Alfred Ochs

Forschungsinstitut der Deutschen Bundespost beim
Fernmeldetechnischen Zentralamt
D-6100 Darmstadt, Federal Republic of Germany

Abstract

The Research Institute of the German PTT Administration has initiated and put into operation an experiment to study scattering of microwaves at 30 GHz from precipitation, which is of importance in interference analysis and system coordination.

The measurements are made in a bistatic configuration with transmit and receive sites separated by some 25 km. The propagation paths are run in a vertical plane containing the two terminal sites. Four transmitters are operated at different fixed elevations, one receiver is connected to a fixed antenna, a second one to a steerable antenna. Thus a total of eight main-beam intersections are formed, from which precipitation scatter can be received under different scatter angles and at different heights up to 10 km. Both, horizontally and vertically polarised signals are measured. In addition, a line-of-sight link and a rain-scatter link are operated at 30 and 11 GHz for the purpose of comparison. To study precipitation scattering in a situation close to those of actual communication links, a further 100-km path is run at 30 GHz.

The main objectives of the experiment are:
- Studies of direct relevance to system design and coordination:
  - long-term statistics of transmission loss in various interference configurations,
  - significance of backscatter in relation to forward scatter,
  - influence of the melting layer,
  - scattering from ice crystals up to a height of 10 km,
  - power density spectra and fading rate of the scattered signal.
- Studies of physical processes relevant to precipitation scatter.

The experimental set-up is described and first results of the measurements will be given at the conference.

1 Introduction

Scattering from hydrometeors may cause interference, i.e. unwanted coupling of different microwave radio systems operating at frequencies above 10 GHz, e.g. from a transmitting terrestrial radio-relay station into a receiving earth station of a satellite system (or vice versa) whose antenna beams intersect in a precipitation area. For a proper coordination of such systems one has to consider the probability and strength of scattered signals as a function of several (meteorological and system) parameters [1-4]. Experimental investigations are necessary mainly to study the impact of microscale and mesoscale structures of precipitations, which cannot be deduced theoretically.

So far, a couple of experiments have been conducted in a bistatic configuration, i.e. with a significant separation (at least several kilometres) of the transmit and receive sites. However, only few of them have been run over at least several months to yield statistically significant results [5-11], and only one [10] at a frequency above 20 GHz.

In addition to these bistatic measurements, monostatic radars, especially dual-polarized or dual-frequency wheather radars, can be used as a tool to investigate precipitation structures with the advantage of 3-dimensional spatial resolution. It is possible, e.g. to use a database built up by a dual-polarized radar to simulate precipitation scattering and attenuation on a variety of interference paths within the area covered by the radar measurements [12].

Both, the monostatic as well as the bistatic measurements, have their merits and drawbacks. It has to be noted, however, that the derivation of signal intensities from monostatic radar data is an indirect method and it is desirable to supplement and validate the results by direct bistatic measurements.

Frequencies as high as 30 GHz become more and more interesting for satellite-to-earth links, especially for mobile and wide-band applications. Comparable antenna gain and lower sidelobes are achievable with antennas smaller than those run at lower frequencies. In contrast to lower frequencies, scatter effects at 30 GHz are more pronounced because the dimensions of the raindrops are no longer small compared with the operating wavelength. Furthermore, the attenuation in rain is much more important at 30 GHz.

The Research Institute of the German PTT Administration has initiated and put into operation an experiment to study precipitation scattering at 30 GHz on a variety of bistatic propagation paths in the vicinity of Darmstadt (FRG). This experiment is a continuation of earlier measurements at 11.5 GHz [9]. It is conducted in coordination with similar experiments in several European countries in

the framework of Action 210 of the European Cooperation in the Field of Scientific and Technical Research (COST).

2 Objectives and design considerations

The experiment has the following main objectives:
- to obtain reliable transmission loss statistics for a variety of different path geometries which may be representative of practical interference situations,
- to study physical processes relevant to precipitation scatter with the aim of improving the prediction of interference signals,
- to study characteristics of the received scattered signal (such as depolarisation, power density spectra, fading rates and Doppler shift) which will determine the impact of an interfering signal on the system.

These objectives lead to partly conflicting requirements for which, therefore, compromise solutions for the main design parameters had to be found.

2.1 Height above ground of the scattering volume

The variation with height of the scattering cross section per unit volume (expressed here as an "equivalent" reflectivity, Z_e) and the maximum height at which significant scattering can occur are important parameters in coordination calculations because they determine the maximum distances between interfering and interfered stations that must be considered.

Previous statistical observations [7, 9, 13-15] have shown, that for certain fixed percentages of time reflectivities occur which decrease with height above the freezing level by 3-6 dB/km. Scattering above the freezing level is thought to be due to ice crystals, which do not give rise to simultaneous attenuation. Moreover, significant scattering can sometimes be observed up to the tropopause during heavy thunderstorms. To study this variability it was decided to apply several transmitters and receivers with separate antennas, whose beams intersect at various heights between about 2 and 10 km. One of the receive antennas is steerable and can be directed to the zenith, thus enabling measurements from scattering volumes along a vertical profile. By staggering the transmitters in frequency it is possible to measure the signals from the different paths simultaneously and continuously, in contrast to the procedure used previously for our 11-GHz experiment, in which only one transmitter and one receiver were provided.

2.2 Scattering angle

Microwaves at 30 GHz undergo significant attenuation in rain and wet snow. This leads to a fundamental distinction between propagation paths with dominant forward scatter or back scatter. In the former case the attenuation acts along the whole path through the rainy area, thus counteracting the increasing scattering cross section per unit volume with increasing rain rate. Hence, with forward scattering the net signal will be largest for low-to-medium rain rates; at high rain rates the higher attenuation will overcompensate the increased scattering.

In the backscatter case, however, the attenuation of the scattered radiation can be lower, when the wave has to travel only through part of the rain. If an intense rain cell, with a steep gradient of the rain rate at its front approaches the receiving site in the receiver-transmitter direction, high reflectivity in the cell and low attenuation outside could combine to produce a large net signal [10]. Even with a less steep gradient the maximum scatter signal will be found at a higher rain rate than in the forward scatter case.

With the steerable receive antenna it will be possible to study both these cases (and, of course, intermediate ones, i.e. side scatter, too). A comparison of the statistics will be extremely interesting.

2.3 Distance transmitter - receiver

To study physical phenomena that depend on the spatial structure of precipitations, relatively small and well defined scatter volumes are needed. This requirement calls for highly directive antennas and moderate path lengths. Hence, an available transmit site 26 km from the receiving station at Darmstadt was selected. (A shorter distance would reduce the range over which the scattering angle can be varied for scattering volumes at greater heights.)

At the same time, this configuration might be taken as a realistic example of two small so-called business stations working with two different satellites. It is however not representative of a terrestrial radio-relay station interfering with an earth station. To simulate this latter case too, an additional transmit station at some 100 km distance was installed and provided with a horizontally radiating antenna of moderate gain.

2.4 Sensitivity

Bearing in mind the requirements of network planners and on the basis of the present knowledge of the statistics of reflectivity at great altitudes [7, 14], it was decided that the minimum detectable equivalent reflectivity (including the effect of attenuation) at 10 km above ground should be about 1 mm^6/m^3 ≙ 0 dBZ. As shown later this minimum reflectivity leads to about 160 dB transmission loss in our experiment.

2.5 Frequency dependence

Both, scattering and attenuation increase with frequency as well as with rain rate. As discussed earlier, at 30 GHz this will lead to the net signal reaching a maximum at some intermediate rain rate, additionally depending on the rain structure and path geometry. This is also true, in principle, at lower frequencies (11 GHz, e.g.) but the maximum signal then will occur at much higher rain rates.

In contrast to the above, scattering from dry ice crystals is not accompagnied by appreciable attenuation. Hence, its relative importance will be much greater at 30 than at 11 GHz.

It is evident from the foregoing discussion that marked differences are to be expected between 30 and 11 GHz effects. Probably it will not be possible to develop a simple scaling procedure. To study these dependencies and to link the 30-GHz results to the results of the earlier 11-GHz experiment, an 11-GHz scatter link with fixed antennas will be operated in parallel to one of the 26-km 30-GHz links.

3 Experimental configuration

The whole experiment is composed of a short-path experiment over about 26 km (Nordheim-Darmstadt, Fig. 1) and a long-path experiment over about 97 km (Karlsruhe-Darmstadt, Fig. 2). The two paths run over the Rhine valley and cross the river Rhine.

Besides transmission-loss statistics, the main intention of the short-path experiment is to gain information on the precipitation structure. Thus a high spatial resolution is needed. This resolution is determined by the beamwidths of the transmit and receive antennas and must be a compromise as discussed later on.

In principle it would have been possible to use steerable antennas for the transmit and receive station with the benefit of reaching any common volume of interest. The disadvantage of this concept, on the other hand, is the sophisticated synchronisation required to move the two antennas in a coordinated manner. Furthermore, it would be impossible to get signals from different scatter volumes simultaneously, using only one antenna at each site. For the short-path experiment we therefore decided to install at 30 GHz four transmitters, with separate antennas at different fixed elevation angles but all in the same vertical plane determined by the terminal sites. To distinguish the different beams, CW-signals with different frequencies spaced 1 MHz from each other are transmitted. They are picked up with one fixed and one steerable antenna at the receive site, each one provided with a receiver frontend. The different frequency channels are available after downconversion into the 1st IF.

With this arrangement the signals from eight different scatter volumes can be evaluated simultaneously. The steerable antenna can be used to receive both forward scatter and backscatter as well as scattering from the zenith. At the fixed antenna, which is mounted 40 m below the steerable antenna, low receive angles are partly shadowed by a building nearby, which gives us some site-shielding against sidelobe reception.

The following consideration deals with the determination of the elevation angles for the short-path experiment. In order to investigate backscatter effects up to a height of about 10 km the maximum transmit elevation angle is set to 17.1°, leading to heights of the common volume of 8 resp. 10 km corresponding to elevation angles ϵ_{R1} of 90.0° and 123.0° of the steerable antenna on top of the building.

Because of the antenna beamwidth, the angular spacing should be > 3.0°, to ensure a minimum decoupling of 25 dB. The lowest angle is chosen to be 3.8°, so that in the backscatter case a height of the common volume down to 2 km is obtained, which is well below the freezing level height during most of the year [13]. The other angles are spaced about 3.5° apart, leading to 7.4° and 10.9°. The azimuth angles of all the transmitters are adjusted such that all possible scatter volumes lie in the mentioned vertical plane.

To get information about the attenuation of the signal from the scatter volume to the receive antenna, the scatter experiment will later on be combined with signal measurements of the planned OLYMPUS satellite. This requires to fix the receive antenna at an elevation angle of $\epsilon_{R2} \approx 27°$.

The short-path scatter experiment is supported by a line-of-sight link to obtain additional information about the attenuation on the whole path. The precipitation structure investigation is supported by concurrent rain-gauge measurements.

The long-path experiment simulates a radio-relay interference into a satellite-earth link. This necessitates to make use of an antenna with greater beam-

width typical for radio-relay systems. Transmission-loss statistics are thus gained for both forward- and backscatter geometries.

4 Transmit and receive antennas

4.1 Antennas of the short-path experiment

The diameters of the involved antennas are the result of a compromise. On one hand, high spatial resolution is wanted for investigating the precipitation structure. Small beamwidths, on the other hand, lead to large diameters and therefore elaborate antenna mounting. Furthermore, the costs are increased as the adjustment of the antennas is more sophisticated and time consuming. As a compromise, diameters of 1.2 m and 2.0 m were chosen for the transmit and receive antennas, respectively. Of equal importance are low sidelobes to reduce unwanted sidelobe coupling.

All the transmit antennas are horizontally polarised, whereas the receive antennas are dual-polarised (horizontally and vertically). Horizontal polarisation was chosen to achieve comparable scattering-radiation patterns at different scatter angles. If wanted the transmit antennas could later on be turned around their axes to vertical polarisation.

As the antennas are not operated on a line-of-sight path, they had to be adjusted by optical means. This was done by attaching optical mirrors to the rear of the antennas, so that the mirror axes are parallel to the respective electrical antenna axes. The deviations from this theoretical alignment were measured. With the declinations being known, all antennas were adjusted in the operating position by geodetic means. The over-all alignment error is below 0.015°.

The main antenna parameters are compiled in Table 1.

For the line-of-sight link a parabolic antenna is used for the transmitter and a horn antenna for the receiver.

Table 1: Antenna parameters

Station	Nordheim (Transmit)	Karlsruhe (Transmit)	Darmstadt (Receive)
Diameter	1.2 m	0.6 m	2.0 m
Gain	47.0 dBi	40.3 dBi	51.0 dBi
Beamwidth (3dB)	0.7°	1.6°	0.4°
Sidelobe suppression			
1st sidelobe	-16 dB	-23 dB	-19 dB
$>3^{\circ}$ off axis	-25 dB	-	-33 dB
$>20^{\circ}$ off axis	-48 dB	-	-52 dB
Polarisation	horizontal	horizontal	horiz./vertic.
Crosspol. isol.(XPI)	> 30 dB	> 30 dB	> 30 dB
Azimuth direction	38.8°	9.2°	219.0° (Nordheim) 189.2° (Karlsruhe)

4.2 Antennas of the long-path experiment

The main objective of the long-path experiment is to simulate a radio-relay interference situation. Therefore, one transmit antenna is installed at Karlsruhe (97 km south of Darmstadt) at an elevation angle of 0°. The steerable receive antenna is used for the short-path experiment and for the reception of the 29.65 GHz CW signal from Karlsruhe as well.

The diameter of the transmit antenna is smaller than those at Nordheim to be comparable to that of a typical radio-relay station (0.6 m ϕ). The signal is again horizontally polarised, with the option for changing to vertical polarisation.

The size of the common scatter volume near the receive site at Darmstadt is about $8*10^{4}$ m^{3} for reception from the zenith. It varies as $1/\sin^{3}(\epsilon_{R1})$ (see Fig. 2).

5 Transmitters and receivers

5.1 General considerations

In designing the experiment, we intended to detect a minimum equivalent reflectivity of 0 dBZ for the short-path geometry (Nordheim-Darmstadt). Assuming a 0-dB signal-to-noise ratio and the antenna gains of Table 1, the maximum transmission loss to be measured is about 160 dB [1].

As a travelling wave tube with higher power for the transmitter would be extremely expensive compared to a solid-state solution, we decided to use a Gunn oscillator. State of the art is an output power of about +20 dBm at 30 GHz.

Therefore we needed high receiver sensitivity. As a compromise between perform-

ance and cost we chose a solid-state version run at a stabilised temperature of about 320 K. To achieve a noise floor of about -140 dBm the receiver bandwidth must not exeed about 1 kHz. This relatively narrow bandwidth conflicts with the received Doppler-broadened frequency spectrum.

As the scatter process is induced by precipitation particles, we have to deal with a Doppler shift of the scattered frequency due to motions of the hydrometeors.

With our geometry, a maximum wind speed of 30 m/s [16] can cause Doppler shifts up to about +/-4.5 kHz, depending on the wind direction. The falling speed of rain droplets (0 ... 10 m/s, depending on the dropsize [17]) will produce a Doppler broadening of the spectrum of about 1 kHz. Hence we chose an RF-bandwidth of 1 kHz for the detection with an additional shift of 10 kHz (+/- 5 kHz) controlled by the AFC-circuit. This requires, of course, a high-precision frequency reference. As the AFC-voltage is available for recording purpose, we have as well an information about the mean frequency shift. It must be admitted, however, that turbulent motions in the scattering volume might occasionally increase the spectral width of the received signal.

5.2 Transmitters

All 30-GHz transmitters, including the line-of-sight equipment, are identical in design to be interchangeable in case of a failure. The frequency controlled Gunn oscillators provide an output power of +22 dBm. A PLL circuit locks the frequency to an atomic frequency standard with a long-term accuracy better than 10^{-10}. The transmitters are tuned close to 29.65 GHz, with a frequency spacing of 1 MHz. High stability, especially constant output power is achieved by temperature control of the whole transmitter. In addition, the power is monitored by a detector diode. By means of a heating/cooling system the temperature of the circuit is stabilised at 45°C with a tolerance of +/-1°C within an ambient temperature range from -10°C to +30°C.

The same holds for the receiver frontends described in the following chapter.

5.3 Receivers

Each of the two parabolic receive antennas and the additional horn for the line-of-sight link are connected to a receiver frontend. Without prefiltering the signal is fed to the first mixer (see Fig. 3). The design of the local oscillator (LO) is the same as for the transmitters. Its frequency is locked to a frequency standard (10^{-10}). The signal is then amplified in the 1st IF. The receiver frontend is mounted in a temperature controlled box at the rear of the respective antenna.

The 1st IF is fed to the backends, where 5 channels are operating at different frequencies with spacings of 1 MHz each, corresponding to the transmit frequencies. Every channel consists of two subchannels for the horizontal and vertical polarisation.

The 2nd oscillator is a voltage-controlled crystal oscillator (VCXO) controlled by an automatic-frequency control unit (AFC). The input of the AFC unit is fed by the horizontally polarised signal because its level is more than some 15 dB higher than that of the vertically polarised channel. The output of the VCXO is supplied to both channels so that the two orthogonal sub-channels are synchronised in frequency. The RF-bandwidth of the 2nd IF at 10.7 MHz is 10 kHz, equal to the capture range of the AFC.

The noise temperature of the receiver was measured by cold-load calibration. According to the bandwidth of 1 kHz, the noise temperature of 567 K leads to the noise floor of -138 dBm at the antenna input port. With the 1-dB compression point at -50dBm the dynamic range of the receiver is 88 dB. The 2nd IF output voltage is amplified by a logarithmic amplifier at 10.7 MHz. Its output is available for recording purpose. The overall power accuracy is about +/- 0.5 dB.

Thus, the maximum measurable transmission loss is 160 dB.

To ensure long-term stability the whole receiver chain is calibrated including the frontend every 12 hours.

6 Additional measurements

To investigate precipitation structures, additional measurements are made. To deduce attenuation of the atmosphere, time coordinated radiometer data are evaluated. The spatial distribution of the rain rate is obtained by evaluating 4 raingauges along the path, the data of which are stored in semiconductor memories. A raingauge comprises a dropcounter and tipping bucket measuring system, so that rain rates from 0.1 mm/h to 200 mm/h with an accuracy of about 10 % and a time resolution of 15 s can be recorded.

To study the frequency dependence of scattering an additional scatter link operating at 11 GHz is installed in parallel to the 29.65 GHz links between Nordheim and Darmstadt making use of existing equipment from earlier experiments [9].

7 Conclusion

The experiment was first put into operation in November, 1986. However due to failure of the equipment, evaluation of data has been delayed. We therefore see forward to present first results during the symposium in May 1987.

References

[1] CCIR-Report 882-1:
Scattering by precipitation
Recommendations and Reports of the CCIR, Geneva 1986

[2] CCIR-Report 569-3:
The evaluation of propagation factors in interference problems between stations on the surface of the earth at frequencies above 0.5 GHz
Recommendations and Reports of the CCIR, Geneva 1986

[3] J. Awaka
A prediction method for the received power from rain scattering
Radio Science, 19 (2), 1984, pp. 643-651

[4] J. Awaka
A method of predicting the desired-to-undesired power ratio in rain scatter interference
Trans. IECE Japan, E69 (5), 1986, pp. 645-650

[5] R. K. Crane
Virginia precipitation scatter experiment: data analysis
Nasa Rep. tm-x-70457.202s zldi, 1973

[6] R. W. Hubbard
Measurement and prediction of bistatic radio scattering due to precipitation
J. Rech. Atm., 8 (1-2), 1974, pp. 365-373

[7] R. L. Olsen and U. H. W. Lammers
Bistatic radar measurements of ice-cloud reflectivities in the upper troposphere
Electron. Lett., 14 (7), 1978, pp. 219-221

[8] S. Sakagami
Some experimental results on bistatic scatter from rain
IEEE Trans. Antennas Propagat. AP-28 (2), 1980, pp. 161-165

[9] A. Ochs
Statistical analysis of the directivity of precipitation scattering at 11.5 GHz
2nd Intern. Conf. Antennas Propagat. (ICAP), IEE Conf. Publ. 195 (2), 1981, pp. 193-197

[10] J. Awaka, K. Nakamura and H. Inomata
Bistatic rain-scatter experiment at 34.8 GHz
IEEE Trans. Antennas Propagat. AP-31, 1983, pp. 693-698

[11] J. Awaka, T. Kozu, K. Nakamura and H. Inomata
Experimental results on bistatic rain scattering at 14.3 GHz
IEEE Trans. Antennas Propagat. AP-32 (12), 1984, pp. 1345-1350

[12] S. M. Cherry and J. W. F. Goddard
The use of dual-polarisation radar in rainscatter interference studies
Proc. ICAP 85, IEE Conf. Publ. 248, 1985, pp. 18-21

[13] CCIR Report 563-3:
Radiometeorological data
Recommendations and Reports of the CCIR, Geneva 1986

[14] M. P. M. Hall and J. W. F. Goddard
Variation with height of the statistics of radar reflectivity due to hydrometeors
Electron. Lett. 14 (7), 1978, pp. 224-225

[15] Y. Furuhama, T. Ihara, H. Inuki and N. Fugono
Radar reflectivity profile classified by rain types

Trans. IECE Japan E63, 1980, pp. 437-438

[16] G. Brussard
A meteorological model for rain-induced cross polarisation
IEEE Trans. Antennas Propagat., AP-24, 1976, pp. 5-11

[17] R. Gunn and G. D. Kinzer
The terminal velocity of fall for droplets in stagnant air
J. Meteorol. 6, 1949, pp. 243-248

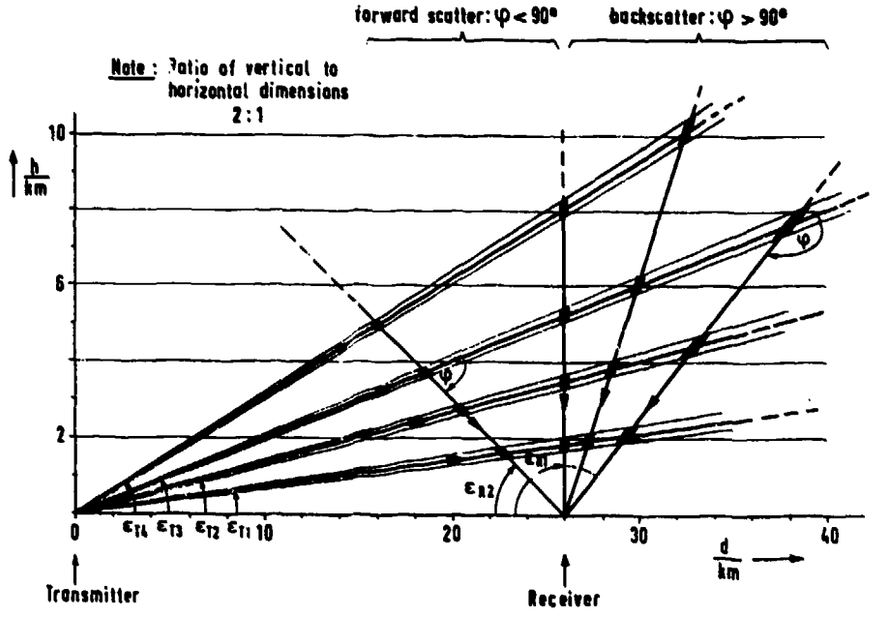


Fig.1 Geometry of the short - path experiment

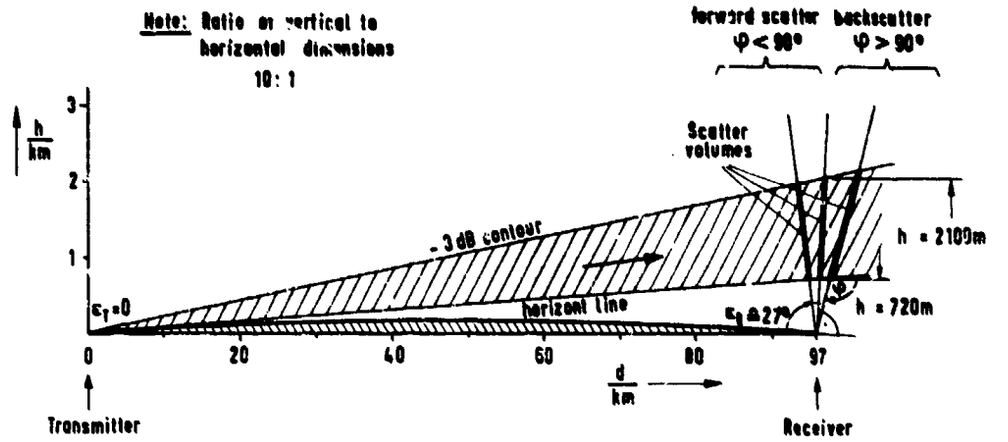


Fig.2 Geometry of the long-path experiment

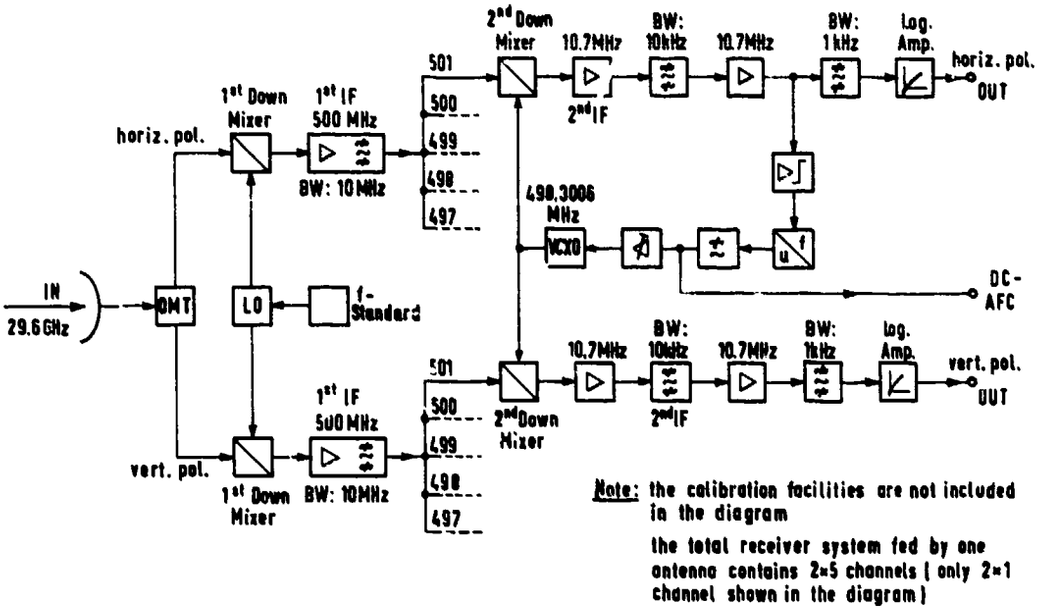


Fig.3 Receiver block diagram

OBSERVED PHASE DELAY THROUGH RAIN AT 96 GHZ

Kenneth C. Allen
U.S. Department of Commerce
NTIA/ITS.S3
325 Broadway
Boulder, CO 80303-3328
USA

SUMMARY

This paper presents observations of phase delay through rain at 96 GHz. The results are pertinent for target identification when relative amplitude and phase information are used from circularly polarized radar returns.

At the transmitter site, a 9.6 GHz source was vertically polarized and a 96.1 GHz source was right-hand circularly polarized. A single local oscillator phased locked both sources.

At the receiver site, 1050 m away, the local oscillator was phase locked to the received 9.6 GHz signal. Both left- and right-hand circular polarizations at 96.1 GHz were received using separate antennas. The phase of each polarization at 96.1 GHz was measured relative to the 9.6-GHz reference. This allowed the examination of the behavior of the differential phase delay of the circular polarizations.

1. BACKGROUND

When polarimetric radars [1] are used to identify targets [2], the effect of the atmosphere on the propagation of the radar signal must be considered. In particular, if the relative phase and amplitude of the circularly polarized components of a radar return are to be used in the identification of the target, changes in the relative phase and amplitude caused by the atmosphere are important. Measurements of the effect of rain are reported here.

Using complex valued notation and suppressing the time dependence, $\exp(j\omega t)$, a polarized plane wave at a point in space can be denoted by

$$E = E_v + E_h \tag{1}$$

where E_v and E_h are the complex vector amplitudes of the vertically and horizontally polarized components of the wave. The vertical component has the form

$$\bar{E}_v = \bar{a}_v E_v \exp(j\theta_v) \tag{2}$$

where $\bar{a}_v$ is the unit vector in the vertical direction, E_v is the real amplitude, and θ_v is the phase of the vertical component. The horizontal component is expressed in a corresponding form.

In matrix notation, a transmitted polarized plane wave can be denoted by

$$E_t = \begin{bmatrix} E_h \\ E_v \end{bmatrix}. \tag{3}$$

The effect of the propagation of the wave through a medium with polarization influencing properties (such as rain [3]) is then described by a transmission matrix, T_1. A linearly polarized wave, E, after propagation through the medium, is given by the transmission equation

$$E = T_1 E_t \tag{4}$$

where

$$T_1 = \begin{bmatrix} t_{hh} & t_{vh} \\ t_{hv} & t_{vv} \end{bmatrix}. \tag{5}$$

Each element, t_{xy}, of the transmission matrix is complex valued and gives the gain and phase shift of the transition of energy from the "x" polarized wave to the "y" polarization.

For circular polarization, the polarized plane wave can be represented by

$$E = \begin{bmatrix} E_r \\ E_l \end{bmatrix} \tag{6}$$

where the subscripts r and l denote right- and left-hand polarized components. The transmission matrix, T_c, for circular polarization is related to the transmission matrix for linear polarization by

$$T_c = C T_l C^{-1} \tag{7}$$

where

$$C = \frac{1}{\sqrt{2}} \begin{bmatrix} 1 & j \\ 1 & -j \end{bmatrix}. \tag{8}$$

Ideally, one would like to know the transmission matrix of the propagation path. Then the relative phase and amplitude of the radar echo could be corrected for the effects of propagation.

The experiment described in this paper was designed only to demonstrate the effects of rain on the relative amplitude and phase of circularly polarized waves at 96 GHz. Subsequent experiments are needed to determine the transmission matrix.

2. TEST SITE

The test site was located at the Redstone Arsenal near Huntsville, Alabama. The path was over level ground with 1050 m separation between the transmitting and receiving antennas. The antennas at one end of the path were 5 m above ground level and at the other end, 3 m. Observations were made from September 16 through November 30, 1986.

3. EQUIPMENT

All of the transmitter and receiver electronics were protected from the weather and were housed in thermally insulated, electronically shielded boxes. Thermostat controlled heaters and circulating air fans in each box provided a controlled operating environment over a wide range of ambient temperatures. A constant enclosure temperature was necessary for the proper operation of much of the radio frequency (rf) electronics. Thermal stability was especially critical for the phase measurements.

Fig. 1 illustrates the configuration of the transmitters. A single 100-MHz temperature-controlled crystal oscillator (TCXO) was used as the reference for both the 9.6- and 96.1-GHz sources. The phase of the reference is denoted as θ_t. All phases in this discussion are measured in wavelengths and constant phase offsets will be ignored.

The 9.6 GHz signal is derived from the 100 MHz reference by means of a phase-locked, cavity-tuned x96 multiplier. The multiplier provides 20 mW of rf power at 9.6 GHz to a 46-cm parabolic reflector antenna (5 degree beamwidth). The phase at the antenna is therefore 96 θ_t.

The 96.1 GHz transmitter uses the 100-MHz TCXO signal as the reference for a phase-locked IMPATT oscillator. After passing through a right-hand circular (RHC) polarizer, the IMPATT output (28 mW) feeds a 30.5-cm scalar horn lens antenna (0.7° beamwidth). The phase of this signal at the antenna is 961 θ_t.

Fig. 2 illustrates the 9.6-GHz receiver and the reconstruction of the 100-MHz transmitter reference. The phase of the 9.6-GHz signal at the receiving antenna is

$$\theta_s = 96\theta_t + 9.6\tau \tag{9}$$

where τ is the propagation delay at 9.6 GHz in nanoseconds.

The 9.6-GHz receiving antenna is identical to the one used at the transmitter and feeds a mixer. The output of the mixer feeds the phase locking electronics (PLE). A local reference oscillator at 5-MHz also feeds the phase-locking electronics (PLE). The phase of this oscillator is denoted by θ_r. The output of the PLE controls a 99.9479-MHz voltage-controlled crystal oscillator (VCXO) reference. The PLE adjusts the VCXO to match the phase of the intermediate frequency (IF) to that of the 5-MHz reference oscillator. Thus the IF output of the mixer has a phase of θ_r. This means that the phase at the local oscillator (LO) input to the mixer is adjusted to $\theta_s - \theta_r$. Since this signal is multiplied by 96, the phase at the VCXO is $(\theta_s - \theta_r)/96$.

By use of a power divider, the 9.595-GHz LO feeds another mixer which allows the phase locking of a second VCXO reference to the 100 MHz TCXO at the transmitter. Once again in this phase-locking loop the 5-MHz reference feeds by means of a power divider one input to a PLE. The output of the PLE adjusts the 100-MHz VCXO so that the 5-MHz output of the mixer into the other PLE port will have the same phase as the 5-MHz reference. The mixer 5-MHz output phase of θ_r and 9.595-GHz LO input to the mixer with phase $\theta_s - \theta_r$ then require that the VCXO controlled input have a phase of θ_s. Since the VCXO output is multiplied by 96 before feeding the mixer, the phase of the 100-MHz VCXO is $\theta_s/96$. By the use of power dividers, the 100, 99.9479, and 5-MHz oscillator outputs are fed to the 96.1-GHz receiver.

The 96.1-GHz receiver is diagrammed in Fig. 3. Antennas identical to the one used at the transmitter are used for both the RHC and LHC polarizations. Each antenna feeds a polarizer like the one used in the transmitter. A variable attenuator was used after the polarizer in the RHC channel to reduce the signal level to that received by the cross-polarized channel (LHC). This allowed the maximum

use of the dynamic range of the receiver and the isolation of the waveguide switch. A ferrite isolator then reduces the voltage standing wave ratio (VSWR) to 1.06 at the ferrite waveguide switch to increase the isolation through the switch. Separate antennas were used for the two polarizations to achieve the greatest isolation.

An aluminum plate placed over the RHC antenna reduced the signal level by 50 dB. The same plate over the LHC antenna reduced the signal level by 33 dB. Thus the isolation achieved at the waveguide switch was at least 33 dB. The overall isolation between the two polarizations was less. The variable attenuator was set at 15 dB. This value and losses due to the isolator and additional waveguide in the RHC channel indicate that the received signal levels under clear-air conditions only differed by 18 dB. This is discussed further in Section 5, below.

The phase of the 96.1-GHz signal at the receiving antenna is

$$\theta_m = 961\theta_t + 96.1\tau' \qquad (10)$$

where τ' is the propagation delay at 96.1 GHz in ns.

A 96.05-GHz LO for mixing with the received 96.1-GHz signal is generated by a Gunn oscillator phase locked by the outputs of the 99.9479 and 100-MHz VCXOs. The 100-MHz VCXO reference feeds one port of the PLE. The other port is fed by the output of the mixer generating the LO. The PLE error signal adjusts the Gunn oscillator until the phase of the output of the mixer is $\theta_s/96$. One input to the mixer is fed by the 99.9479-MHz reference after being multiplied by 960 resulting in an input of 95.95 GHz with a phase of $10(\theta_s - \theta_r)$. The other mixer input is coupled from the Gunn oscillator and is forced to have a phase of $10(\theta_s - \theta_r) + \theta_s/96$ by the PLE. The LO with this phase mixed with the received signal results in a 50 MHz IF having a phase of

$$\theta_m - 10(\theta_s - \theta_r) - \theta_s/96. \qquad (11)$$

The IF feeds an AC/DC log converter (for measuring the signal amplitude) and the phase-measuring electronics.

The phase-measuring electronics are diagrammed in Fig. 4. The output of the 5-MHz reference oscillator is multiplied by 9 to 45 MHz and with a phase of $90\theta_r$ feeds one input of a mixer. The 50-MHz IF of the 96.1-GHz receiver feeds the other mixer input so that a 5 MHz IF results with a phase of

$$\theta_m - 10\theta_s + \theta_r - \theta_s/96. \qquad (12)$$

This IF feeds a commercial phase meter that gets its reference from the 5-MHz oscillator having a phase of θ_r. The phase measured by the equipment is therefore

$$\theta = \theta_m - 10\theta_s - \theta_s/96. \qquad (13)$$

Using Equation (9) and Equation (10) to substitute for θ_s and θ_m in (13) results in

$$\theta = 96.1(\tau' - \tau). \qquad (14)$$

Thus, the phase meter is measuring the propagation delay difference between the 9.6- and 96.1-GHz signals. The output of the phase meter is an analog voltage proportional to the relative phase delay (in degrees at 96.1 GHz).

Measurements were controlled by a computer. Once each second the computer set the waveguide switch in the 96.1 GHz receiver to first one polarization and then the other. After setting the switch, the computer waited 30 ms for the commercial phase meter to settle and then read the phase and amplitude through a multichannel, analog-to-digital converter. Also, once each second the analog output of a capacitive bridge rain rate gauge was sampled. The rain gauge was located near the receiving end of the path.

4. MEASUREMENT ERROR ANALYSIS

There are several sources for error in the measurement of phase delay due to rain. For the purpose of discussion, these will be divided into long- and short-term categories. Short-term sources contribute error that varies at rates on the order of the sampling rate, i.e. a few seconds. Long-term sources contribute error that varies at rates on the order of minutes or longer.

Among the long-term sources are variability in the path delay because of changes in the refractivity of the atmosphere, temperature instabilities in the rf equipment, and the physical stability of the transmitting and receiving terminals.

The long-term variability in the refractivity of the atmosphere can be tens of N units (ppm) and for the path length used can result in phase changes of tens of wavelengths at 96.1 GHz. However, the delay at 96.1 GHz was measured relative to the delay at 9.6 GHz so that only changes in the dispersive refractivity, i.e. changes in the relative refractivity at 96.1 GHz and 9.6 GHz, contribute to changes in the phase. This has the advantage of reducing the delay variability to less than 120 degrees at 96.1 GHz as predicted by Liebe's model [4].

Temperature instabilities in the rf equipment result in phase changes that range from diurnal variations to variations taking only a few seconds. The slower variations are due to the inability to maintain a constant temperature for the equipment over a wide range of ambient temperatures.

There was no indication of vibrations in the physical stability of the equipment. Longer-term instabilities would be expected due to changes in the temperature of the vans and mounting hardware for the antennas. It is easy to see that these instabilities could result in delay changes on the order of 1 mm (100 degrees) or more.

Typically, the measured phase at 96.1 GHz would advance by two to three wavelengths as the ambient temperature increased during the day and then would decrease back to the same value as the day cooled. Since the phases of the two polarizations at 96.1 GHz were measured within a few tens of milliseconds of each other, the slow variations in the phases with respect to the 9.6-GHz signal did not contribute errors to the measurements. In addition, almost all of the slow variations resulted from temperature changes that effected the RHC and LHC polarizations equally because almost all the mounting hardware and electronics were common to both polarizations. It was the rapid variations in phase that primarily caused the phase errors in the measurements. These rapid variations were due to path delay changes caused by scintillation (refractivity), unstable phase shifts through the waveguide switch, phase-locking noise, and the limited accuracy of the commercial phase meter.

For the signal levels present, the commercial phase meter was specified to have an accuracy better than ± 10 degrees. The actual short-term phase noise was about ± 7 degrees. It is not certain that all of this measurement noise came from the phase meter.

In Fig. 5, a 1-hour sample of the recorded time series data is shown. The long-term variability can be seen before and after the rain storm. The short-term variability can be seen throughout the time series. In Fig. 6, the differential phase of the RHC and LHC signals are shown for the same time period. From the figure it can be seen that most of the long-term variability (which was common to both polarizations) is absent from the differential phase.

5. EQUIPMENT POLARIZATION ISOLATION

When measuring the effects of the atmosphere on polarized waves, it is important to consider polarization properties of the antennas and other devices in the transmitter and receiver in order to understand what is truly being measured [5].

The circular polarizers connected to the antennas discriminate by a factor greater than 35 dB between the co- and cross-polarized components according to the manufacturer. The antennas were claimed to have an axial ratio of better than 1 dB. The axial ratio (AR) [6] is given as a function of the ratio, $q < 1$, of the amplitudes of the circular polarizations by

$$AR = \frac{1 + q}{1 - q} \tag{15}$$

where AR is not in decibls. Using an axial ratio of 1.0 dB gives AR=1.122 so that q=0.0575 from Equation (15). This q corresponds to a ratio of 24.8 dB between the co- and cross-polarized waves. Thus, the antennas are the components limiting the isolation between the polarizations.

Ignoring relative phase, the normalized transmitted wave is assumed to be

$$E_t = \begin{bmatrix} 1 \\ q \end{bmatrix}. \tag{16}$$

If the antennas and polarizers at the receiver are assumed to be identical in performance to the transmitting equipment, then the received amplitude in each polarization channel can be found by multiplying E_t by the matrix

$$A = \begin{bmatrix} 1 & q \\ q & 1 \end{bmatrix} \tag{17}$$

where phase has again been ignored.

The resultant received signals, with no atmospheric effects considered, are then

$$E = AE_t = \begin{bmatrix} 1 + q^2 \\ q + q \end{bmatrix} = \begin{bmatrix} 1 \\ 2q \end{bmatrix}. \tag{18}$$

Using the value of q found from Equation (15) for an axial ratio of 1 dB results in the RHC received amplitude being 18.8 dB greater than the LHC amplitude. This is very close to the value of 18 dB actually observed under clear-air conditions.

It should be noted that the received LHC signal is composed of two parts: the RHC wave that was received LHC and the LHC wave that was also received LHC. Because of the assumed symmetry, these two parts are equal in amplitude. A relative phase shift between the RHC and LHC waves during propagation would therefore generally appear to be less since at the receiver the LHC signal contains contributions from both waves. However, in some sense the relative phase shift during propagation can be measured as shown below.

For rain on the path the received signals are given by

$$E = AT_c E_t \tag{19}$$

where T_c is the transmission matrix for the rainy medium. In practice, the matrix T_c is symmetric so that with A symmetric by assumption, $AT_c = T_cA$ giving

$$E = T_c AE_t. \qquad (20)$$

Thus, the received signals are the same as they would be for a perfect receiver with infinite isolation between polarizations and a transmitted wave AE_t. Under these conditions, the relative amplitude and phase shifts observed correspond to T_c operating on a transmitted wave AE_t as given in Equation (18).

The implication for the observations are as follows. No depolarization or change in relative amplitude will be observed if the fraction of power transferred to the opposite polarization is less than $2q$ (less than -18 dB). The differential phase shift between polarizations observed is the phase shift resulting from the rain for a wave initially polarized as AE_t.

6. RESULTS

The cumulative distributions of the attenuations of the RHC and LHC polarizations were identical. For individual rain storms, sometimes the RHC and sometimes the LHC peak attenuation was greater. However, they never differed by more than about 2 dB. As much as 30 dB attenuation was observed due to rain on the path. In Fig. 7, difference in signal amplitude is plotted against the observed rain rate. There is only a slight indication of depolarization. In Fig. 8, the difference in amplitude is plotted against the copolarized (RHC) attenuation. In this figure, there is some depolarization apparent for copolar attenuation greater than about 17 dB.

When there was rain on the path, the phase of both polarizations at 96.1 GHz was correlated with the measured rain rate. An example is shown in Fig. 5. In Fig. 9, the RHC 96.1-GHz phase (relative to the 9.6 GHz phase) is shown cross-plotted against rain rate. In the figure, the relative phase predicted from the refractivity computed by Crane [7] (for 9.35 and 94 GHz) using the Laws and Parsons drop-size distribution and a drop temperature of 0 Celsius is shown. Also shown, is the nearly identical result found from Zufferey's [8] predictions based on the Marshall-Palmer drop-size distribution and a drop temperature of 20 Celsius. In Figure 10, the same RHC 96.1 GHz phase shift data as in Figure 9 is shown cross-plotted against the RHC attenuation. It can be seen in Figures 9 and 10 that the phase shift is more correlated with attenuation than rain rate.

A differential phase shift between the RHC and LHC waves was observed that also correlated highly with rain rate. In Fig.11, the difference in the LHC and RHC phases are cross-plotted against rain rate. A curve, hand fitted to the data, given by

$$\Delta\theta = .05\ R^{1.6}, \qquad (21)$$

is also shown in the figure.

In Fig. 12, the same differential phase data are shown plotted against the copolarized (RHC) attenuation.

7. CONCLUSION

Observations of the differential phase shift through rain of right-hand and left-hand circular polarizations at 96.1 GHz have been made. The results show that rain will effect the use of phase information from polarimetric radar returns for target identification.

More generally applicable measurements are needed before techniques for mitigating the effects of rain can be evaluated. These should include measurements of all of the complex valued elements of the transmission matrix and their joint statistical dependence on rain rate.

8. REFERENCES

[1] Giuli, Dino, "Polarization diversity in radars," IEEE Proc., Vol. 74, No. 2, Feb. 1986, pp. 245-269.

[2] Chaudhuri, S.K. and Boerner, W., "A polarimetric model for the recovery of the high-frequency scattering centers from bistatic-monostatic scattering matrix data," IEEE Trans. Ant. Prop., Vol. AP-35, No. 1, Jan. 1987, pp. 87-93.

[3] Oguchi, T., "Electromagnetic wave propagation and scattering in rain and other hydrometeors." IEEE Proc., Vol. 71, No. 9, Sept. 1983, pp. 1029-1078.

[4] Liebe, H.J., "An updated model for millimeter wave propagation in moist air," Radio Sci., Vol. 20, No. 5, Sept.-Oct. 1985, p. 1078.

[5] Kaul, R.D. and R.G. Wallace, NASA, "Propagation effects handbook for satellite systems design," 1981, Ref. Pub. 1082, pp. 103-154.

[6] Mott, H., "Polarization in antennas and radar," New York, John Wiley and Sons, 1986, p. 73.

[7] Crane, R.K., MIT Lincoln Labs, "Microwave scattering parameters for New England rain," Oct. 3, 1966, Tech. Rep. 426, Table V.

[8] Zufferey, C.H., Univ. of Colorado Master of Science Thesis, "A study of rain effects on electromagnetic waves in the 1-600 GHz range," 1972, pp. 106-113.

9. ACKNOWLEDGEMENTS

The author is appreciative of the sponsorship of this work by the U.S. Army Missile Command, Redstone Arsenal, Alabama. Significant contributions were also made by Dave Jones, Ed Violette, and Dick Espeland who were responsible for the instrumentation and by Rob DeBolt who did the computer programming needed to acquire and analyze the data. An invaluable contribution was made by Dale Divis who watched over the operation of the equipment during the absence of the author and those named above.

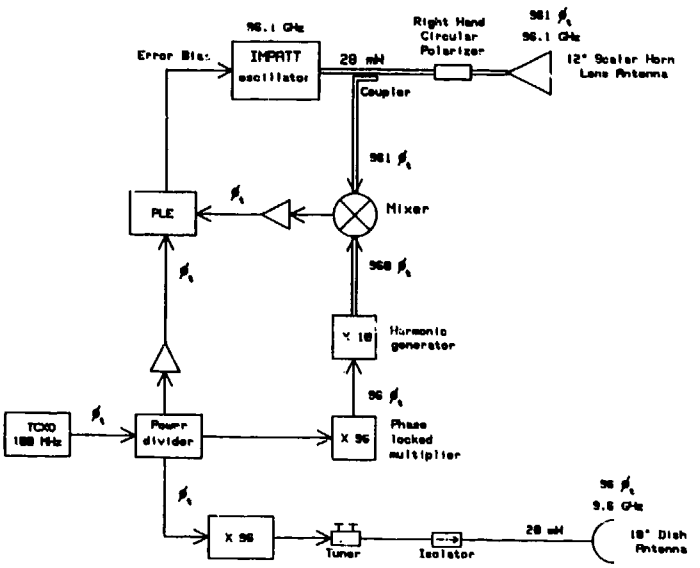


Figure 1. Diagram of transmitters.

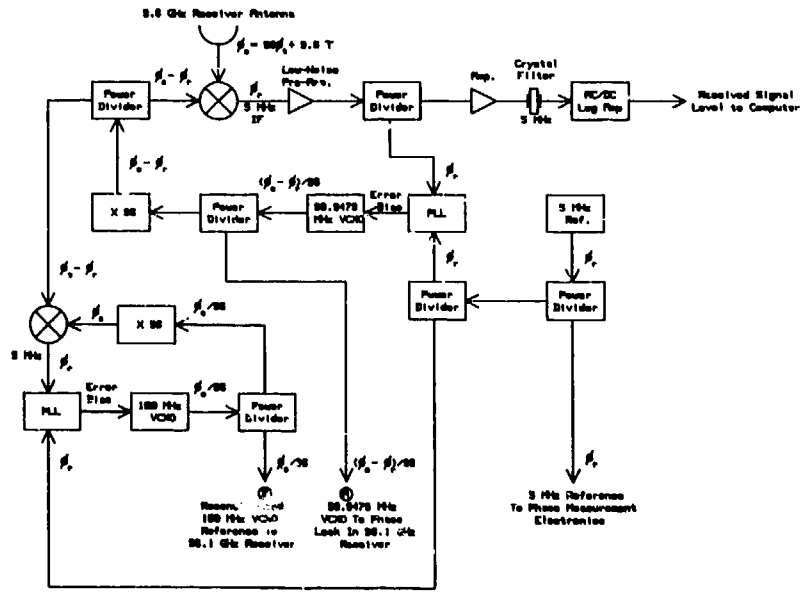


Figure 2. Diagram of 9.6 GHz receiver with reconstruction transmitter reference oscillator.

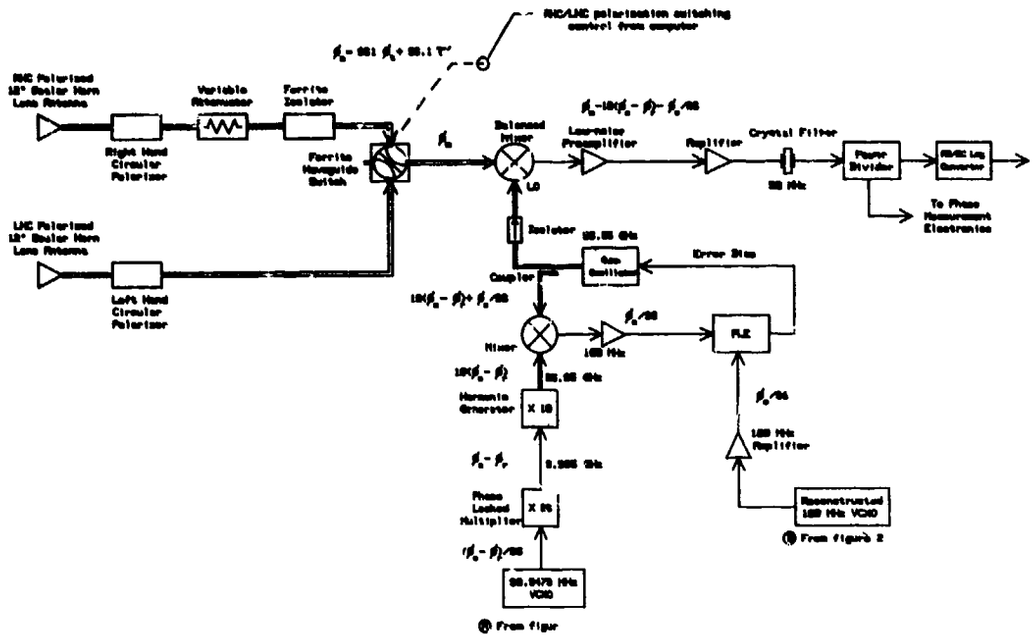


Figure 3. Diagram of 96.1 GHz receiver.

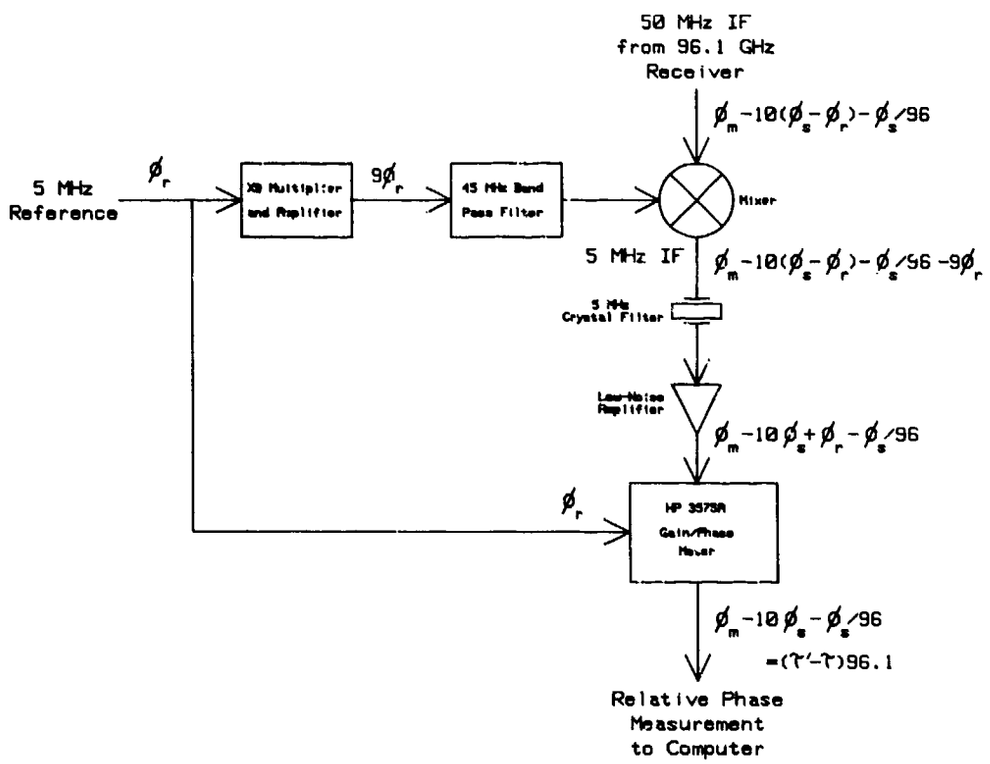


Figure 4. Diagram of phase measurement technique.

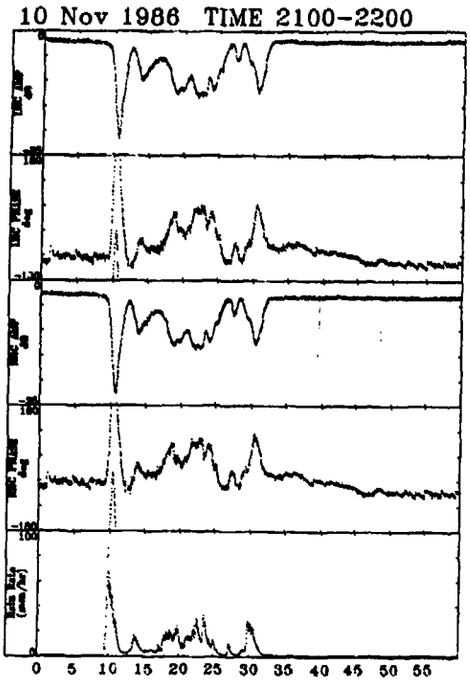


Figure 5. Time series data for a rain event.

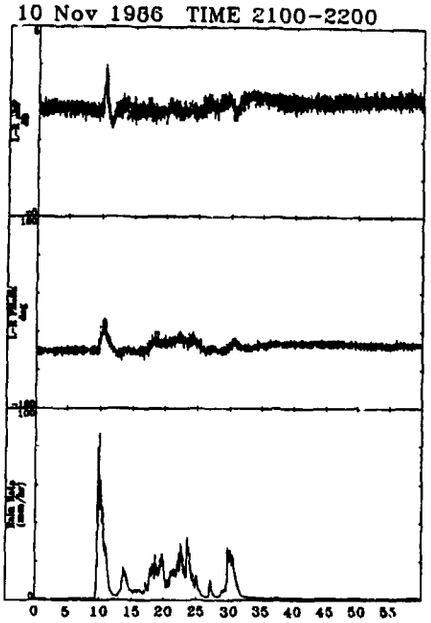


Figure 6. Differential phase and amplitude from the data shown in Figure 5.

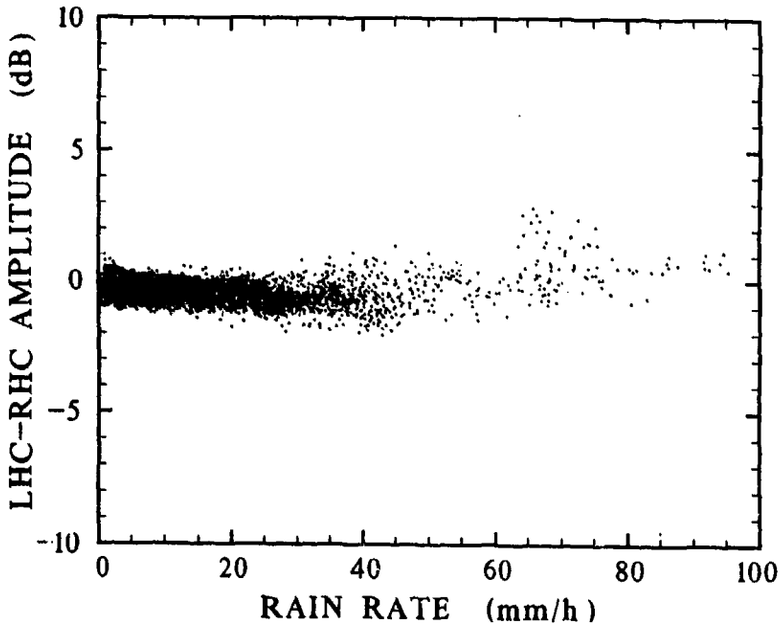


Figure 7. Scatter plot of differential amplitude at 96.1 GHz, normalized for 18 dB offset between LHC and RHC signals.

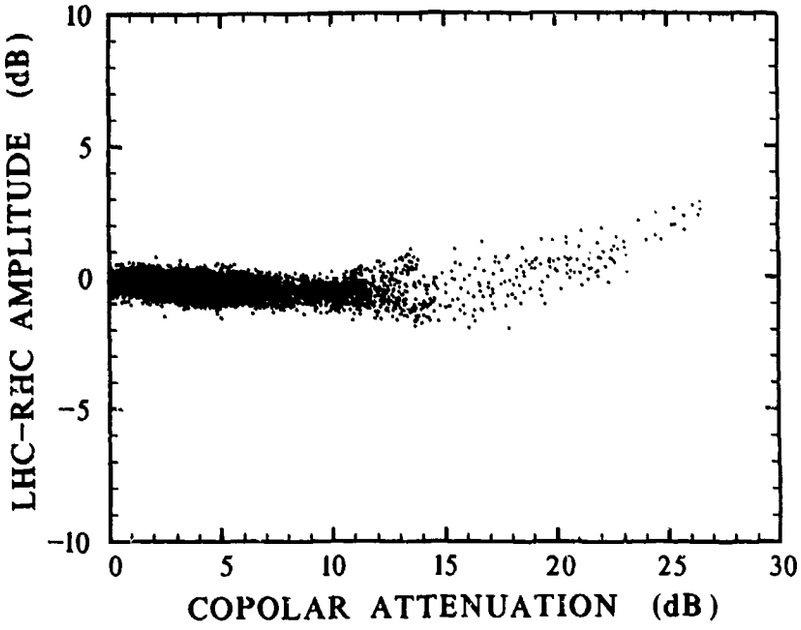


Figure 8. Scatter plot of differential amplitude at 96.1 GHz, normalized for 18 dB offset between LHC and RHC signals.

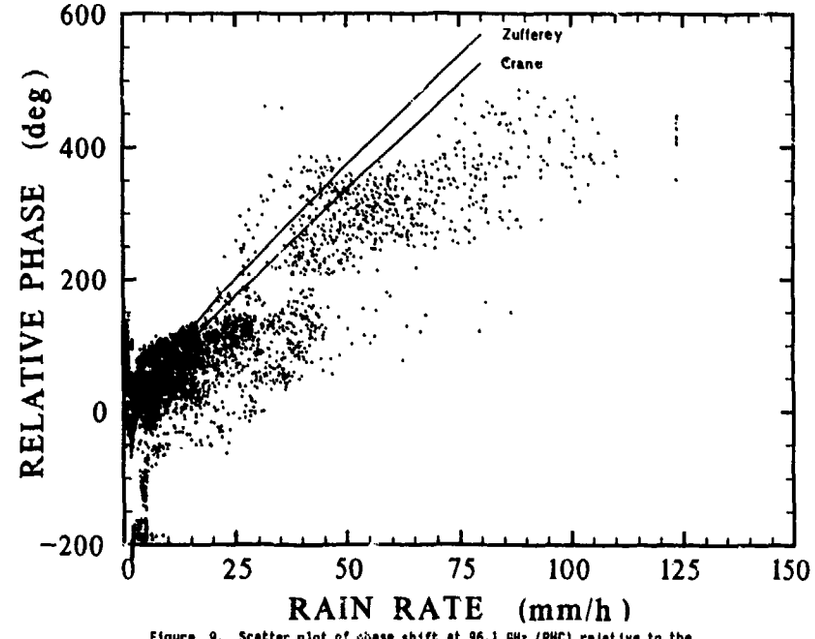


Figure 9. Scatter plot of phase shift at 96.1 GHz (RHC) relative to the 9.6 GHz reference and rain rate. Predictions based on the work of Zufferey [8] and Crane [7] are also shown.

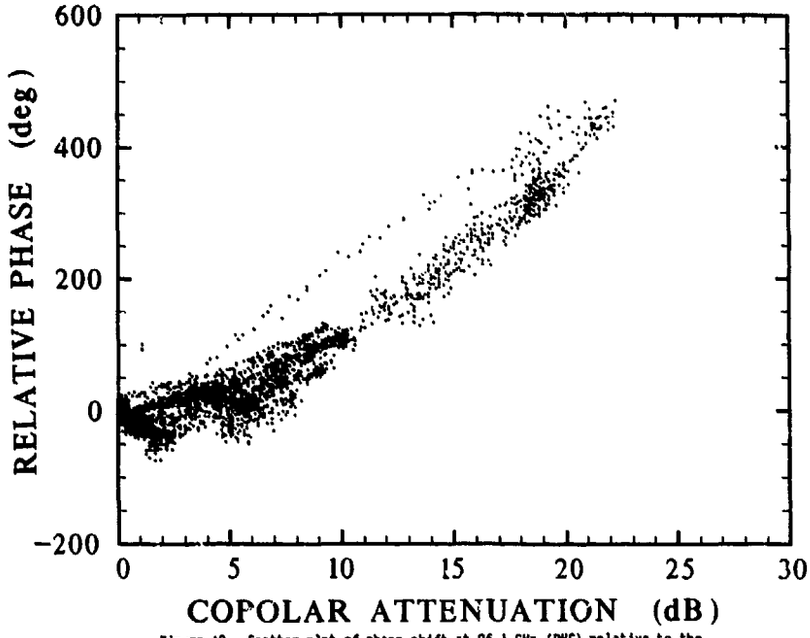


Figure 10. Scatter plot of phase shift at 96.1 GHz (RHC) relative to the 9.6 GHz reference and copolar (RHC) attenuation.

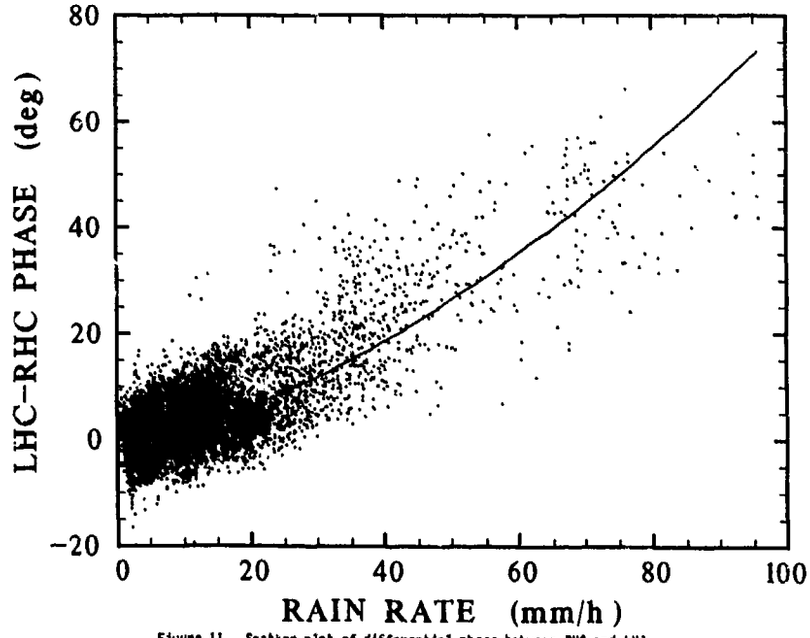


Figure 11. Scatter plot of differential phase between RHC and LHC polarizations at 96.1 GHz and rain rate for all observations.

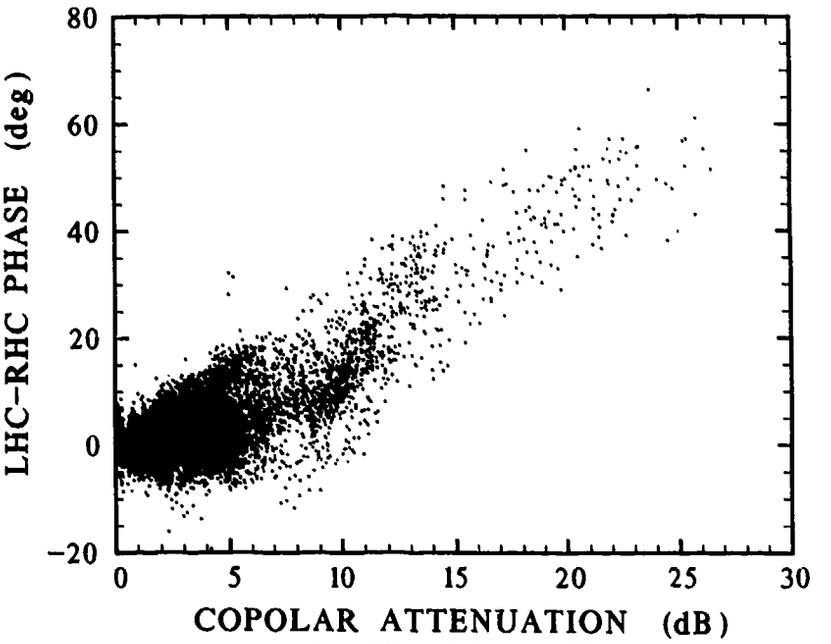


Figure 12. Scatter plot of differential phase between RHC and LHC polarizations at 96.1 GHz and copolar (RHC) attenuation for all observations.

FM-CW Radar Remote Sensing of Hydrometeors.

L.P. Ligthart, J.S. van Sinttruyen
Delft University of Technology
Faculty of Electrical Engineering
Mekelweg 4, 2628 CD Delft
The Netherlands

SUMMARY.

In order to investigate phenomena influencing co-polar attenuation and cross-polar discrimination along earth-space satellite paths and terrestrial radio links at frequencies above 10 GHz, the number density, geometry, and orientation of hydrometeors (rain, snow, hail, melting particles etc.) along the path have to be characterized. This paper describes the modelling of the melting process, the dielectric properties of melting particles, and fall velocity behavior of hydrometeors for Doppler velocity computation with vertically pointing radars.

Attention is paid to backward scattering of ellipsoidal hydrometeors for radar polarimetry computations at arbitrary elevation angles, and to forward scattering of spherical hydrometeors for attenuation computations at high frequencies.

The multi-parameter FM-CW radar system of Delft University of Technology is able to measure the polarization properties and Doppler velocity spectra of hydrometeors with high resolution in range and reflectivity level. Preliminary results obtained with this radar system are shown, indicating the capabilites of combined Doppler- and polarimetry measurements for classification of hydrometeors along a satellite path.

INTRODUCTION.

The still growing demand for larger bandwidths for satellite as well as terrestrial radio links needs a disclosure of the frequency bands above 10 GHz. The technological developments in the field of earth- and satellite-based communication systems combined with a better knowledge of the behavior of radiowaves along the radiopath have resulted in reliable satellite communication systems in the 11/14 GHz frequency band which were realised in the eighties while 20/30 GHz links have to become operational in the nineties. To reach the same reliability and availability of these future links as for the existing ones radiowave propagation studies in these frequency bands are essential. The main propagation effects at frequencies above 10 GHz, occur in the troposphere, where the radiowave "feels" the tropospheric influence by its change in the -for the radiowave characteristic- quantities : i.e. amplitude, phase, polarization and propagating direction. In particular the amplitude and polarization effects get large attention due to the fact that they are caused by the frequently occuring phenomena of appearing hydrometeors in the radiobeam, like rain, snow, hail and melting particles. These hydrometeors can all be present at the same time along a satellite path where f.e. during rainshovers raindrops exist at altitudes below the 0° C isotherm, melting particles around this 0° C level and ice- and snow particles in the clouds above.

These dominant phenomena, measured on a link as co-polar attenuation and cross-polar discrimination, can be investigated in detail by using coherent multi-parameter radar systems at non-attenuating wavelengths which are able to measure reflectivities coming from hydrometeors so that information can be obtained about the hydrometeor type, their velocity profiles and their polarization characteristics. These quantities have to be measured accurately in a calibrated mode with high resolution in range and velocity.

Such a system is the S-band FM-CW Delft Atmospheric Research Radar (DARR), which is a Doppler-Polarimetric radar system. Last years the investigations in this field concern the characterization of the melting layer processes based on DARR-Doppler measurements to be used for 20/30 GHz attenuation computations of the radiowaves. Such a melting layer often exists in stratiform rainclouds but is detected also during more convective showers. Especially during stratiform conditions the melting layer appears during radar measurements as a strong increase in the reflectivities and is therefore often called the "radar bright band".

The paper is divided into 4 sections. The backward scattering properties of spheroidal and ellipsoidal hydrometeors are summarized in Section 1. Based on these properties the radar measurement of the raindrop size distribution -derived from Doppler velocity spectra yielding for vertically pointing Doppler radar or from Polarimetric radar for elevations in accordance with the angles for satellite communication links- is discussed in Section 2. Attenuation computations at high frequencies can be performed assuming spherical hydrometeors with known dielectric properties together with known range and time dependent dropsize distributions. Theoretical results are shown in Section 3. Also some

modelling aspects of the radar bright band are described which have been supported by vertically pointing DARR Doppler measurements. Attention is given to the varying dielectric constant of melting particles, their backscattering and specific attenuation behavior. Section 4 illustrates some preliminary examples to demonstrate the capabilities of DARR as Doppler- as well as Multi-Polarization radar.

1. BACKWARD SCATTERING PROPERTIES OF SPHERICAL AND ELLIPSOIDAL HYDROMETEORS.

When an electromagnetic wave coincides on hydrometeors, it excites electric and magnetic dipoles inside the particle. These dipoles are responsible for the scattering field.

In this section we limit ourselves to the so-called Rayleigh approximation for the radar cross-section of hydrometeors i.e. the radar backward-scattering coefficients are valid for particles which are small relative to the radar wavelength. Furthermore only linear polarization of the transmitted and received signal at the radar antenna is considered. The remark is made that other polarization states can be analyzed by transformation of the scattering coefficients for linear polarizations to new polarization states under the condition that targets are characterized by their full linear polarization behavior in amplitude and phase. The geometry of hydrometeors is approximated by ellipsoides. In the limits the ellipsoides have the ability to become needles at one side to spheres at the other.

The hydrometeor type is characterized by its refractive index, its ellipsoidal geometry and the axis of revolution of the ellipsoides relative to the incident radar field with given linear polarization.

The refractive index of ice particles is strongly different from that of rain drops. In figures 1 and 2 the theoretical real and imaginary parts of the refractive index are shown for ice and water respectively, as a function of frequency with the temperature as parameter [1]. This knowledge of the permittivity is used also for the attenuation computations on communication links at frequencies above 10 GHz (Section 3).

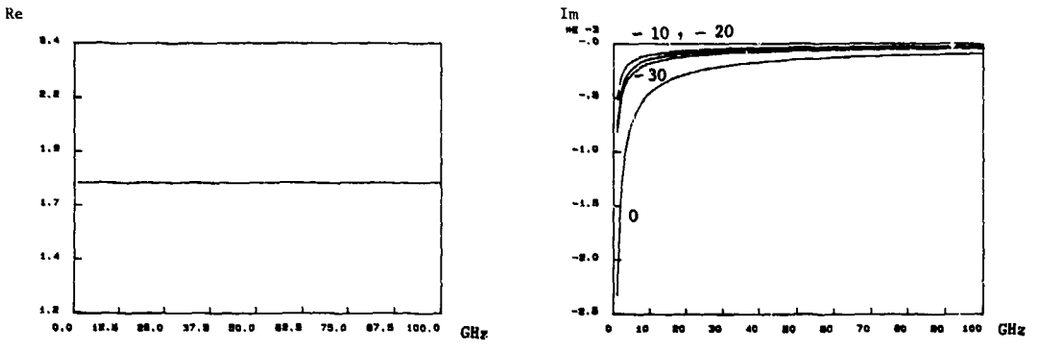


Figure 1. Real (a) and imaginary (b) part of the refractive index of ice as a function of frequency and temperature [Celcius] as parameter.

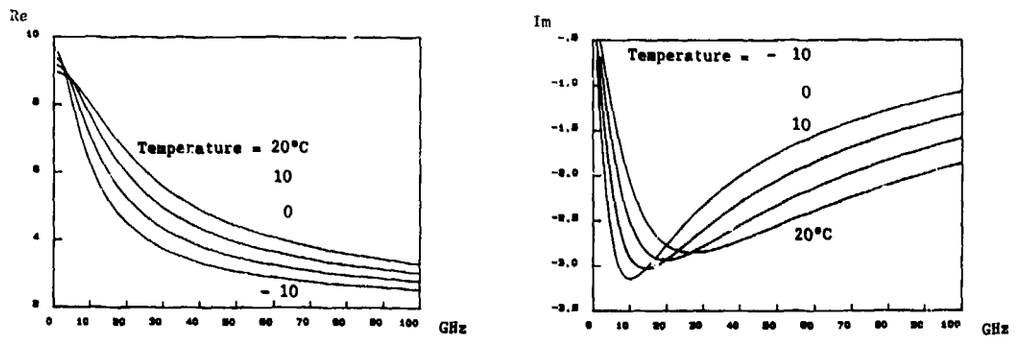


Figure 2. Real (a) and imaginary (b) part of the refractive index of water as a function of frequency and temperature [Celcius] as parameter.

Changes in the geometry are possible f.e. when melting snowflakes are falling to become raindrops. (Section 4).

Here the ellipsoidal model for a raindrop and its backscattering properties are evaluated. Examples for practical axial ratios of an ellipsoidal raindrop as function of the radius of an equi-volume "artificial-spherical" raindrop are shown in figure 3.

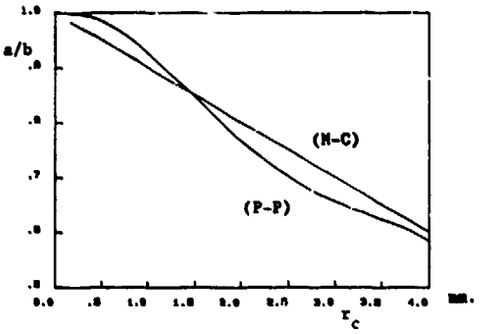


Figure 3. Axial ratios of ellipsoidal raindrops as function of the radius of an equi-volume spherical raindrop; (1) according [2]; (2) according [3].

"a" is the short axis, "b" is the long one perpendicular to the axis of revolution. These results are obtained from experiments done by Pruppacher-Pitter [2] and from approximations given by Morrison-Cross [3]. Physically the non-spherical shape of the raindrop is caused by friction during its fall in the atmosphere. For small drops the axial ratio tends to unity giving more spherical raindrops. In case the radar elevation angle = 0° (along the earth surface) and the axis of revolution is directed vertically (i.e. no canting angle of the raindrop is taken into account) the scattering coefficients S_{HH}, S_{VV} and S_{HV} are given in amplitude in figure 4a and in phase in figure 4b as function of the equivalent radius of an equi-volume raindrop.

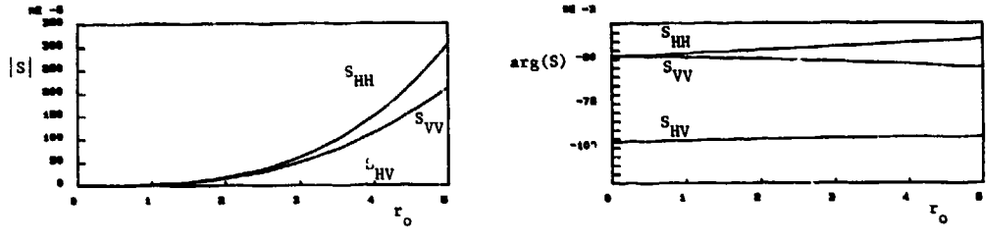


Figure 4. Scattering coefficients S_{HH}, S_{VV}, S_{HV} of ellipsoidal raindrops as function of the equivalent radius. (a) Modulus, (b) Phase. No canting. Elevation angle = 0°.

The notation S_{HH} indicates the scattering coefficient for horizontal polarization at transmitting and receiving. S_{VV} is similar for vertical polarization. S_{HV} is the scattering coefficient for horizontal polarization at transmitting and vertical at receiving. Due to reciprocity $S_{HV} = S_{VH}$.

From figure 4a differences in polarization behavior of the amplitudes of backscattering coefficients can be seen for larger raindrops. This property allows a polarization discrimination for different raindrop sizes. The phase differences in the coefficients are so small that they can be neglected. $S_{HV} = 0$, which means that in this situation no cross-polarized backscattering occurs.

For a similar orientation of such a raindrop with an equivalent radius of 4 mm but for different elevation angles the results of figure 5 are obtained.

For an elevation angle = 90° no polarization dependence exists. Also here $S_{HV} = 0$. This can be changed in case the ellipsoidal raindrop with the same size is canting as shown in figure 6.

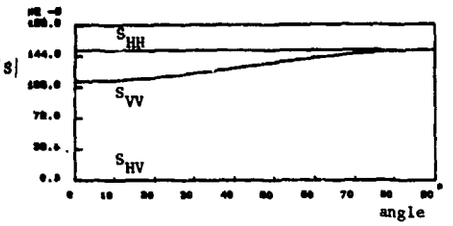


Figure 5. The magnitudes $|S_{HH}|$, $|S_{VV}|$ and $|S_{HV}|$ of raindrop with equivalent radius = 4mm as function of elevation angle. No canting.

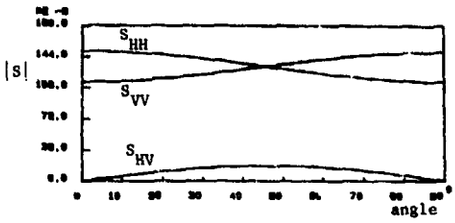


Figure 6. $|S_{HH}|$, $|S_{VV}|$ and $|S_{HV}|$ of a raindrop with equivalent radius = 4mm as function of canting angle. Elevation = 0°.

From this result it becomes clear that for arbitrary orientation of an ellipsoidal target all three coefficients have to be measured. In reality, for rain however, the canting angles due to windshears are much less than 45°. Canting angles ≠ 0 are not further considered.

For snow and melting particles it is assumed here that no preferred polarization behavior occurs despite the fact that in areas with rain-snow mixtures or in melting snow high orientation dependent effects have been measured already, proving that more investigations in this field are needed.

By the assumption that no specific information of the melting layer can be obtained from a polarimetric radar, the propagation aspects of this layer have to be derived from the backscattering properties and the Doppler velocity spectrum envelope of melting particles with varying dielectric properties during their fall through the radar bright band (Section 4). This section is ended by extending the results of "single target" scattering to volume scattering from hydrometeors with given dropsize distribution. As dropsize distribution the so-called gamma distribution is assumed according:

$$N(D) = N_0 D^e \exp(-AD^f)$$

with four unknown constants N_0, A, e and f.

N(D).ΔD gives the number of particles per unit volume [m^3] in the equivalent diameter interval D and D + dD. The often used negative exponential rain dropsize distribution is a particular case of the gamma distribution with e=0, f=1 and N_0 dependent on the type of rain and A dependent on the rain intensity. For an assumed negative exponential distribution two unknowns have to be determined from radar measurements. This means that the reflectivity

$$Z = C \int_0^{D_{max}} S(D)N(D)\, dD \qquad (C = \text{physical constant})$$

has to be measured in a calibrated radar system with sufficient geometrical and time resolution in combination with a second set of independent measurements such as Doppler fall velocity characteristics of hydrometeors as function of D or polarization dependence of the backscattering as function of D. This is done in the next section.

2. RADAR MEASUREMENT OF THE RAIN DROPSIZE DISTRIBUTION.

In case the two unknowns in the negative exponential distribution are derived from Doppler velocity measurements, optimum results are possible for vertically pointing Doppler radar. As we have seen in the previous section the reflectivity is then - as a consequence of this antenna positioning - caused by rotationally symmetrical raindrops with equivalent diameter D and, at the same time, the Doppler measurements are not influenced by horizontal windcomponents. In the diameter interval D and D+dD, by using the Rayleigh approximation, the reflectivity dZ becomes

$$dZ = N(D).D^6.dD$$

To make use of the Doppler velocity spectrum measurements it is assumed here that the fall velocity of rainparticles relative to air is dependent on height. At sea level this velocity v(D) can be approximated by [4].

$$v(D) = 9.65 - 10.3 \exp(-0.6D) \quad [m/s], \quad D \text{ in mm}.$$

At height h above the mean sea level the velocity v'(D) becomes [5].

$$v'(D) = v(D)10^{\gamma'}[1 + .0023(1.1-\rho'/\rho)(T-T')]$$

$$\gamma' = .43 \log(\rho/\rho') - .4(\log(\rho/\rho'))^{2.5}$$

where ρ is the air density and T the temperature in Kelvin. The vertical air velocity v_a has to be taken into account as well. v_a is chosen positive in the upwards direction and has to be subtracted from v'(D) to get the measured velocity spectrum at the ground-based radar. The vertical air velocity is a third unknown which has to be extracted from the Doppler measurements too. For modelling applications it is suggested to use the Marshall-Palmer (M-P) distribution i.e.

$$N(D) = N_o \exp\left(-3.67 \frac{D}{D_o}\right)$$

where $N_o = 8.10^6$ [m^{-4}] and D_o = median diameter of the distribution. In this model D_o [mm] is related to the rain intensity R [mm/hr] via

$$D_o = 0.895\ R^{0.21}$$

The Doppler velocity spectrum for this distribution has an envelope at sea level as shown in figure 7 where the reflectivity per diameter interval is given as function of the fall velocity and D_o = 1, 1.5 and 2 mm as parameter. These D_o values correspond with rain intensities from 1.7 to 47 mm/hr.

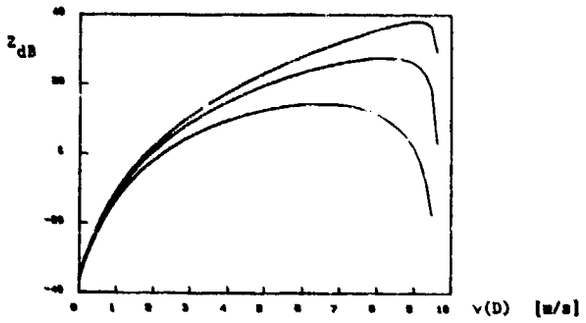


Figure 7. Normalized Doppler velocity spectra at sea level for the M-P distribution as function of fall velocity and the median diameter as parameter; v_a = 0.

Two Doppler analysis techniques have been developed for each range cell:
1. spectral moments method;
2. fitting theoretical Doppler spectra to measured Doppler data.
The spectral moments method has the following properties:
- the zero-th moment equals the average reflectivity level over the whole Doppler range and is comparable to the reflectivity measured with a single parameter radar without Doppler capabilities. This spectral moment is proportional to N_o and is dependent on A as can be seen in figure 8 for the M-P distribution but independent of v_a.

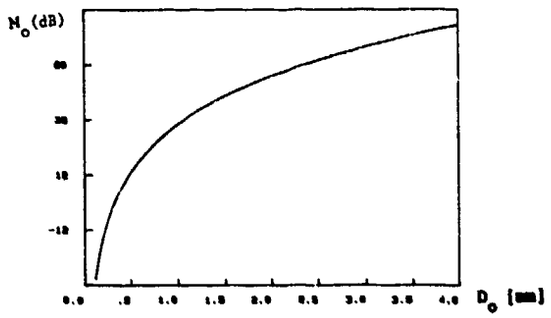


Figure 8. The zero-th spectral moment for the M-P distribution as function of D_o. $N_o = 8.10^6$ [m^{-4}].

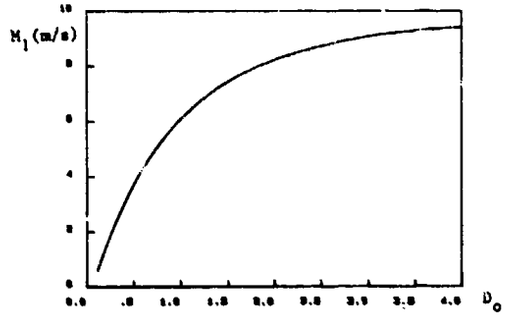


Figure 9. The first spectral moment for the negative exponential distribution as function of D_o. v_a = 0.

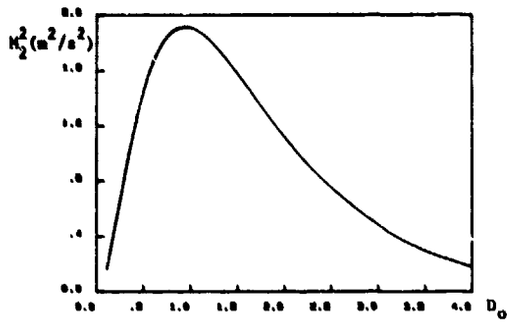


Figure 10. The second spectral moment for the negative exponential distribution as function of D_o.

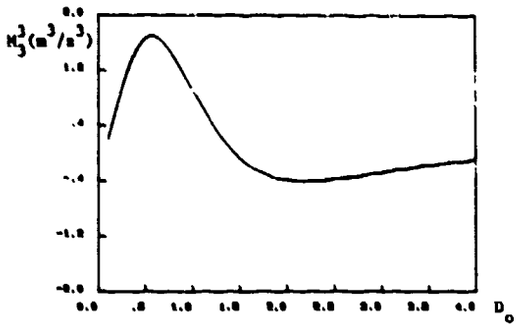


Figure 11. The third spectral moment for the negative exponential distribution as function of D_o.

- The first moment M_1 equals the mean Doppler velocity v_a. This spectral moment is independent of N_o and gets a shift equal to v_a. Figure 9 gives the results as function of D_o for $v_a = 0$ [m/s].
- The second spectral moment M_2 [m/s] is a measure for the spectral width, independent of v_a and N_o (figure 10 gives the square of the spectral moment).
- The third spectral moment M_3 [m/s] indicates peak skewness of the Doppler spectra and is also independent of v_a and N_o (figure 11 gives the third power of M_3).

The disadvantage of the spectral moments method is the limitation to distributions characterized by maximally 2 parameters. The advantage is that the method can be implemented for real-time Doppler analysis.

The technique of fitting theoretical to measured Doppler data per range cell has been set up by Dissanayake [6]. Starting from the gamma distribution, four unknown parameters of the distribution together with the vertical air velocity have to be determined. This involves a non-linear parameter estimation problem which has been solved by using the minimum least-square criterion applied to the sum of the squared differences between theoretical reflectivity and measured reflectivity within each Doppler velocity cell. For the parameter estimation problem only those spectral components were employed which were positioned around the peak reflectivity in the Doppler spectrum.

The advantage of the fitting technique is its flexible approach which can be used for distributions characterized by 2, 3 or 4 parameters. The disadvantage is that it is a computing time intensive procedure which makes a real-time Doppler analysis nearly impossible.

Examples of both Doppler-analysis techniques based on DARR measurements are given in Section 4.

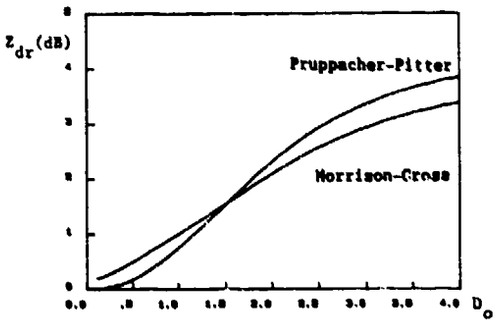


Figure 12. Z_{dr} vs the median D_o with different axial-ratio distributions.

A different way to determine the rain dropsize distribution is to make use of the polarisation dependence of the backscattering coefficients when elevation angles far from zenith are applied.

Here theoretical results are shown for the negative exponential distribution, elevation angle = 0 and where use is made of the so-called differential reflectivity technique. The differential reflectivity Z_{dr} [dB] is defined as:

$$Z_{dr} = 10 \log \left| \frac{Z_{HH}}{Z_{VV}} \right| \text{ [dB]}$$

where the reflectivities Z_{hh} and Z_{vv} are applied to volume scattering. In figure 12 Z_{dr} as function of D_o is given assuming a distribution truncated at a maximum equivalent radius R_{max} = 4 mm and a Pruppacher-Pitter (P-P) and a Morrison-Cross (M-C) axial-ratio distribution. Enlargement of R_{max} does not influence Z_{dr} results for D_o up to 2 mm.

Comparison between the Z_{dr} using P-P or M-C indicates differences of ± 0.3 dB for D_o values of interest, i.e. D_o less than 2 mm. From figure 12 it can be seen already that Z_{dr} has to be measured accurately because all independent information for the determination of the two unknown parameters in the D_o range under 2 mm has to be derived from accurate Z_{hh} and Z_{dr} measurements, where Z_{dr} is under 2.4 dB and becomes less for elevation angles $\neq 0$. A DARR polarimetric-radar measurement is worked out in Section 4.

3. COMPUTATION OF HYDROMETEOR ATTENUATION ALONG HIGH FREQUENCY LINKS

The attenuation caused by hydrometeors in a radio beam can be calculated using the expression of the specific attenuation γ [dB/km]

$$\gamma = 4.343 \int_{r_{min}}^{r_{max}} N(r)\, Q_t(r) dr .10^3$$

where N(r) = distribution [m^{-4}] of hydrometeors with equivalent radius r;
$Q_t(r)$ = attenuation cross-section [m^2] of a spherical particle with radius r.

To get this expression, spherical particles with homogeneous density per unit length along the radio path are assumed. $Q_t(r)$ is defined as the relation between the total power sum of the scattered power at the surface of the spherical particle + the absorbed power inside the particle relative to the power density of the incident field.

For the analysis of scattering properties the scattering cross-section $Q_s(r)$ is introduced in a similar way but dealing with the scattered power only. For particles which are no longer small relative to the radio wavelength the Rayleigh approximation is invalid and the cross-section computations have to be performed according to the theory initially described by Mie [7]. The temperature dependent refractive index is taken into account by using the refractive index model-set up by Ray [1]- for water and ice as indicated in the Section 1.

3.1 Attenuation computations due to rain.

In figures 13 and 14 theoretical results for $Q_t(r)$ and $Q_s(r)$ of a spherical water droplet are given as function of the radius. The frequencies are 3 GHz and 30 GHz respectively. The temperature equals 20°C.

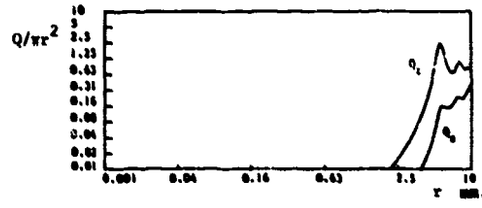


Figure 13. Normalized cross-sections Q_t and Q_s of a spherical raindrop as function of its radius. Frequency = 3 GHz. Temperature = 20°C.

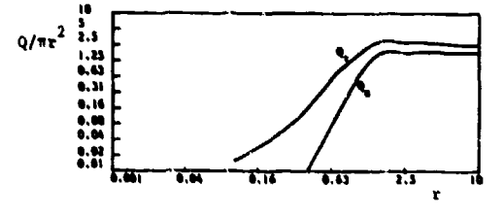


Figure 14. Normalized cross-sections Q_t and Q_s of a spherical raindrop as function of its radius. Frequency = 30 GHz. Temperature = 20°C.

Based on the M-P distribution figure 15 shows the specific attenuation as function of rain intensity for 3 frequencies: 12, 20 and 30 GHz.

The frequencies selected are the frequencies of the beacons in the Olympus Satellite. This ESA satellite (launch planned in 1988) has these beacons to perform propagation experiments. Co-polar attenuation and cross-polar discrimination measurements along the earth-space path are possible by the availability of this satellite. In a collaboration with the Dr. Neher Laboratory (PTT) Delft University has the opportunity to verify the DARR reflectivity profiles with experimental co-polar attenuation and cross-polarization data measured along the same path with a 12-30 GHz groundstation placed aside the radar.

For a fixed rain intensity of 25 mm/hr, a maximum radius of 4 mm in the M-P distribution and a temperature of 0°C, a specific attenuation envelope as function of frequency is obtained shown in figure 16.

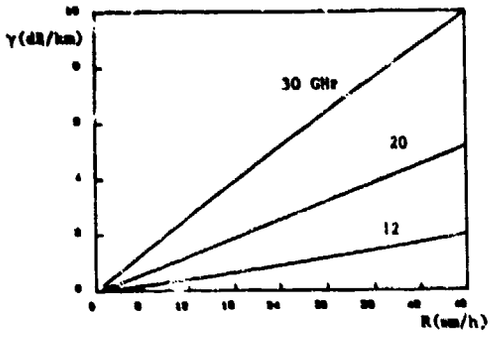


Figure 15. Specific attenuation as function of rain intensity. Temperature = 20°C. Frequencies = 12, 20, 30 GHz.

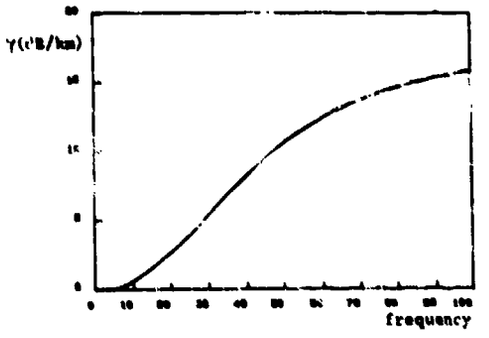


Figure 16. Specific attenuation as function of frequency. Temperature = 0°C. r_{max} = 4 mm. R = 25 mm/hr.

3.2 Attenuation computations due to ice particles.

For non-melting ice particles the attenuation due to absorption can be neglected at nearly all frequencies so that attenuation due to scattering remains. In figure 17 Q_s results of spherical ice particles are shown as function of the normalized radius i.e. the radius relative to wavelength. The temperature is assumed to be - 10°C.

Using the results of figure 17 it is remarked that r is the radius of an equivalent spherical ice particle with always a constant mass density of 1 gram/cm^3. To get computational results for the specific attenuation a maximum for the dropsize distribution of ice particles is assumed according [8]

$$N(r) = N_0' \exp(-0.618\ r)$$

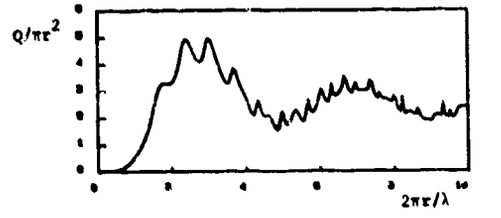


Figure 17. Normalized attenuation cross-section of a spherical ice particle as function of the radius relative to wavelength. Temperature = - 10°C.

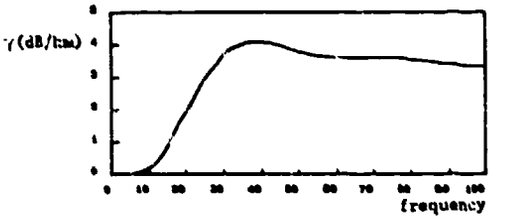


Figure 18. Specific attenuation as function of frequency for ice particles. Temperature = 0°C.

where N_0' = 9.10^3 [m^{-4}], r in mm and r_{max} = 5mm. In figure 18 the specific attenuation curve at 0°C as function of frequency is given, illustrating that in these circumstances attenuation due to ice particles can still be significant at frequencies of 20 and 30 GHz.

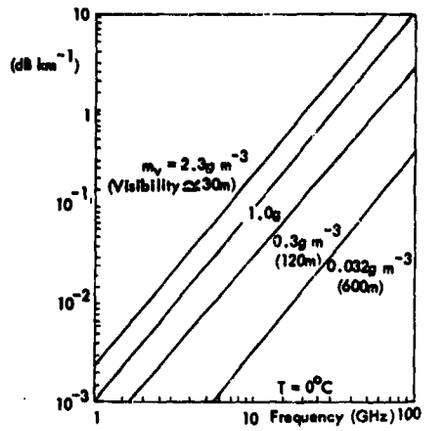
A consequence of the assumed constant mass density is that hail particles which have such densities can contribute to the attenuation. Snow however has a much lower density and will therefore have much less contribution.

Melting hail and snow give an increase in the real and imaginary part of the refractive index. Because of their contribution to the attenuation on radio links, these phenomena are of particular interest.

Water clouds with different water content m_v per unit volume give specific attenuation envelopes as shown in figure 19 [9] and is based on empirical data.

Special attention is given to mixtures of water and ice which exist in the radar bright band. Melting particles have to be considered as hydrometeors which have a strongly height-, time- and temperature gradient dependent refractive index profile. Studies in this field are still underway. Our present view based on DARR measurements suggest

- a water shell at the boundary of a melting hail particle with ice inside;
- concentrations of ice-water bounded mixtures with small sizes, homogeneously distributed over a melting snow particle.



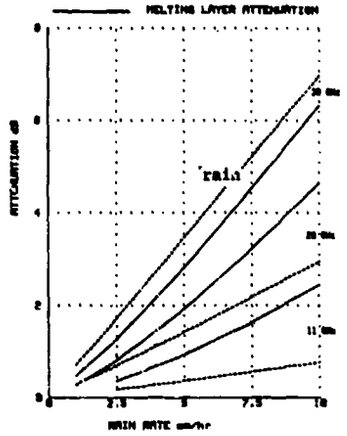


Figure 19. Specific cloud attenuation as function of frequency and the water content per unit volume as parameter.

Figure 20. Melting layer and rain attenuation along a slant path as function of rain intensity with the frequencies 11, 20 and 30 GHz as parameter. Melting layer width = 500 m. Rain height = 1500 m. Elevation = 30°.

Especially variations in models of melting snow indicate large influences on specific attenuation computations.

The dynamics in the melting process as function of height and time is dependent on the drag resistance of the atmosphere, fall velocity relative to air, temperature and density difference between the particle and surrounding air.

The dropsize distribution of snow at the top of the melting layer is selected so that at the lower height where melting is complete, a raindrop size distribution exists which is comparable with the M-P distribution.

Using a water shell model for melting snow, a radar bright band model as described by Dissanayake et al. [10] with varying snow densities, attenuation computations have been carried out as shown in figure 20 for a slant path through the melting layer. The width of this melting layer - defined as the height interval in which the reflectivity is above the rain reflectivity just below the layer - is calculated to be 500 m. The rain height is chosen 1500 m; the elevation angle is 30°. These theoretical results show that in this case for frequencies up to 25 GHz the attenuation in the melting layer is dominant above attenuation due to rain. This means that in nearly all cases melting layer attenuation can not be neglected.

4. THE MULTI-PARAMETER FM-CW DELFT ATMOSPHERIC RESEARCH RADAR (DARR).

Since 1980 the Delft Atmospheric Research S-band Radar has been operational for hydrometeor studies. While initially target reflectivity and Doppler properties could be determined with high resolution, recently polarization measurement capabilities have been added to the DARR system.

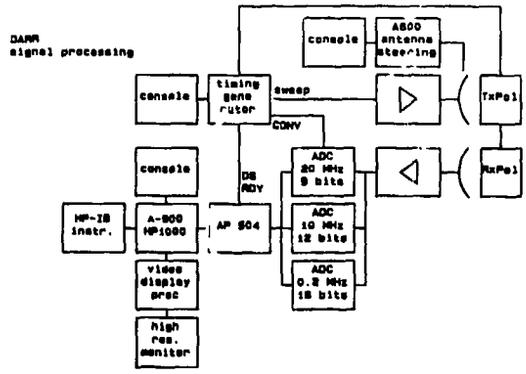


Figure 21. DARR signal processing scheme.

In figure 21 a simplified block diagram of the DARR signal processing scheme is given (for a detailed description of the DARR system and its parameters reference is made to [11], [12] and [13]).

The transmitted signal of a FM-CW radar consists of a linearly frequency-modulated wave of constant envelope during a measuring time T_m. The received signal is delayed over $\tau = 2r/c$ seconds (r-target distance, c-velocity of light). Mixing of transmitted and received signal delivers a difference signal (called beat signal) whose amplitude is proportional to the target reflectivity and whose frequency is proportional to the target distance. After AD conversion a Fast Fourier Transform (FFT) can then be applied in order to measure target reflectivity as a function of range.

The range resolution is inversely proportional to the frequency excursion of the transmitted signal. The maximum frequency excursion used in the DARR system is 50 MHz, corresponding to a minimum range resolution of 3m.

For the determination of Doppler spectra a number of consecutive measuring periods is used, requiring a coherent system. As the beat signal phase is linearly dependent on the target distance, in the observed range interval the FFT spectral line argument will be proportional to the beat signal phase. Due to the target velocity, the target distance will accumulate over consecutive measurement periods, resulting in corresponding argument changes in the FFT spectral line. If a second FFT is applied to these consecutive values of the spectral line a Doppler spectrum will result for the observed range interval. Under the condition that measurements are taken within the target decorrelation time, the resolution in the Doppler domain will be proportional to the number of measurements. The maximum unambiguous Doppler velocity is inversely proportional to the measurement period T_m ($\approx 11.10^{-3}/T_m$ [ms^{-1}]). The minimum measurement period of 0.625 ms corresponds to a maximum unambiguous Doppler velocity of approximately +/- 18 ms^{-1}. Moreover, when the consecutive beat signals or corresponding Fourier spectra are stored, the possibility exists to adjust the Doppler resolution in off-line signal processing.

The timing generator assures system coherency in controlling the generation of the linearly frequency-modulated signal over consecutive measuring periods, the analog to digital conversion of the beat sgnal, the synchronization with the AP504 array processor in which real-time signal pre-processing takes place and the generation of steering signals for the polarizers (figure 22).

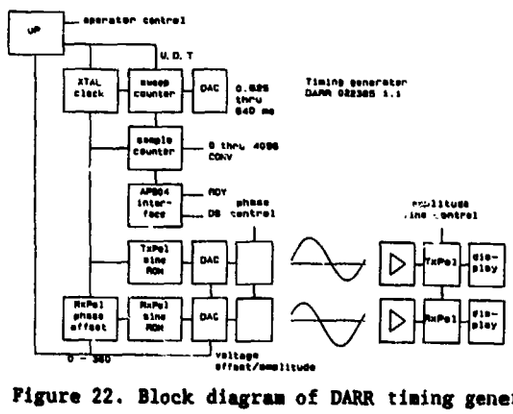


Figure 22. Block diagram of DARR timing generator.

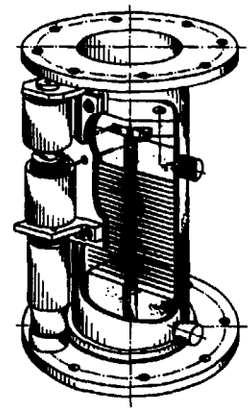


Figure 23. Exploded view of the polarizer.

Polarization measurement capabilities were added to the DARR system by the inclusion of separate polarizers in both the transmitting and receiving channels. As the polarizers have the ability to rotate the polarization continuously, the full polarization matrix can be measured using one receiver only, excluding the need for dual orthogonal matched polarization channels.

In figure 23 an exploded view of the polarizer is given. Essential for its operation is a number of small electrically conducting vanes that are held together by two wires in the middle of the vanes. As the vanes are electrically conductive the transversal electrical field is perpendicular to the direction of each vane. At the top the vanes are mechanically driven by a motor, at the bottom no rotation is possible, so the polarization of the outgoing electromagnetic wave is gradually rotated by a helix of vanes.

By using a mechanically resonant structure the polarization angle varies sinusoidally as a function of time with a period T_p of 40 ms and maximum polarization angles of $\pm$ 90 degrees.

In figure 24 a typical example of the transmitted and received polarization angles over 32 measurement periods of 1.25 ms is shown.

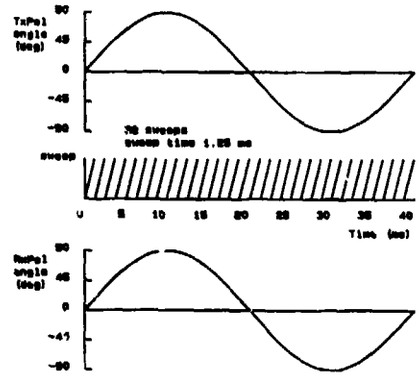


Figure 24.

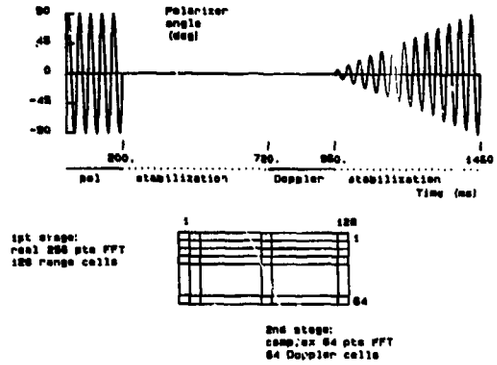


Figure 25. Practical measurement for alternate polarimetry/Doppler determination.

Generally, the transmitted and received polarization angles, apart from their repetition period, can be chosen independently from each other as required.

For a single point target the beat signal u(t) can be written as:

$$u(t) = \mathrm{Re}\ \{(\underline{Sa}.\underline{b})e^{j(\omega+\omega_d)t}\} \qquad (1)$$

in which:

$\underline{S}$ - scattering matrix $\underline{S} = \begin{bmatrix} S_{HH} & S_{HV} \\ S_{HV} & S_{VV} \end{bmatrix}$; $S_{HH} = |S_{HH}|e^{j\phi_{HH}}$ etc.

$\underline{a}$ - polarization of transmitting antenna

$\theta_t(t)$ - transmitted polarization angle

θ_o - polarization angle for non-activated polarizers, dependent on elevation

$\underline{a} = \begin{bmatrix} \cos\{\theta_t(t)\} \\ \sin\{\theta_t(t)\} \end{bmatrix}$; $\theta_t(t) = \theta_o + \theta_{tt}\sin(2\pi \frac{t}{T_p} - \alpha_t)$

$\underline{b}$ - polarization of receiving antenna

$\theta_r(t)$ - received polarization angle

$\underline{b} = \begin{bmatrix} \cos\{\theta_r(t)\} \\ \sin\{\theta_r(t)\} \end{bmatrix}$; $\theta_r(t) = \theta_o + \theta_{rr}\sin(2\pi \frac{t}{T_p} - \alpha_r)$

ω - radian frequency of beat signal

ω_d - Doppler radian frequency offset of beatsignal.

(1) can be re-written as:

$$\mathrm{Re}[\{S_{HH}\cos\{\theta_t(t)\}\cos\{\theta_r(t)\}+S_{HV}\sin\{\theta_t(t)+\theta_r(t)\}+S_{VV}\sin\{\theta_t(t)\}\sin\{\theta_r(t)\}\}e^{j(\omega+\omega_d)t}]$$

For the absolute scattering matrix 6 parameters have to be determined for each range interval under observation. When the Doppler velocity has also to be determined a total of 7 parameters results. Thus 4 measurement periods are required within the target decorrelation time in which magnitude and phase have to be measured.

Although, in principle, a system of 4 complex non-linear equations can be solved, it is beyond our present real-time processing capabilities to do so. Therefore, in practice, a separation is made between the measurements for the Doppler velocity and for the determination of the scattering matrix.

For polarimetry the Doppler components can be excluded by taking the absolute value of the spectral lines as a basis for further processing. Consequently this means that instead of the absolute scattering matrix only the relative scattering matrix can be determined, requiring 5 parameters (or 3 measurement periods). For Doppler velocity determination a separate measurement is done with non-rotating polarizers (figure 25).

In the first period at least 5 independent measurements are taken for determination of the relative polarization matrix. In the second period the polarizers are switched off. Taking the mechanical bandwidth of the polarizers into account, a stabilization period of about 0.5 s is needed for the polarizers to come to rest. In the next period, for each observed range interval, 64 measurements are taken for determination of the Doppler spectra, whereafter the polarizers are switched on again. In this combined polarization/Doppler mode the assumption is made that the decorrelation time in hydrometeor velocity is sufficiently high.

Mostly the polarizer angles are chosen such that $\theta_t(t) = \theta_r(t)$, the co-phase mode, so that canting angle data becomes easily available in the time dependency of spectral lines over consecutive measurements. Although, in principle, the relative polarization matrix can be determined with other modes, i.i. the anti-phase mode in which $\theta_t(t)+\theta_r(t) = 2\theta_0$, such modes are especially attractive when combinations of S-parameters are of particular interest. A summary of the specifications of the DARR, including polarizer data, is given in table 1.

DARR specifications (after processing)		DARR specifications (hardware)	
Range R	0.4 - 30 km	Radar type	linear FM,
Analyzer bandwidth B	1/Ta		triangular, sawtooth
Min. detectable signal	-150 + 10.log(B)	Transmitted power	50 dBm (max)
	(S/N = 12 dB)	Centre frequency	3.315 GHz
Min. detectable reflectivity	8.10^{-18} km^2/h cm^{-1}	Frequency excursion F	1 - 80 MHz
Fixed target suppression	26 - 32 dB	Range resolution h	2 - 150 m
Max. unambiguous Doppler	+/- 16 m/s	Sweep time Ta	0.625 - 340 ms
Doppler resolution cell	0.25 m/s (minimum)	Beat frequencies	0.4 - 1000 kHz
Polarizer angles	+/- 90 degrees,	Receiver noise figure	2.5 dB
	transmitter, receiver	Antenna gain	32.7 dB receiver
period	40 ms		40.3 dB transmitter
steering	co-phase, anti-phase	Antenna beamwidth	4.6 degrees receiver
accuracy	1.5 degrees		1.8 degrees transmitter
		Antenna isolation	> 90 dB

Table 1.

A first example of a Doppler reflectivity profile as function of height and measured with a vertically pointing DARR during stratiform rain is given in figure 26. The radar is capable to measure not only the effective reflectivity factor and Doppler fall velocity but also the higher order (2nd and 3rd) spectral moments with high resolution in range (30 m) and in velocity (0.1 m/s).

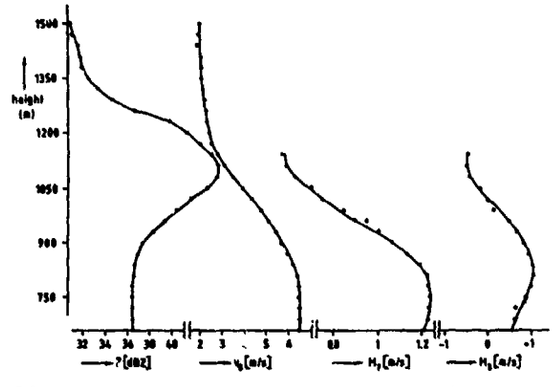


Figure 26. Spectral moments of rain measured with DARR [13].

The physical phenomena can be analyzed and studied based on this type of Doppler measurements. Above the so-called 0°C isotherm ice particles and snov exist. The mean Doppler velocity at this height is low. Around the 0°C isotherm snowflakes melt. The radar detects this process by an increase in reflectivity due to dielectric changes in the melting snowflakes. The melted snowflakes - first the small ones and with decreasing altitude also the larger ones - fall as raindrops with an inherent increase in fall velocity. The reflectivity, below the height where the peak reflectivity occurs, decreases drastically due to the reduced dimensions of a raindrop relative to the size of the

snowflake from which the raindrop originates. When all snowflakes have melted the reflectivity in this rain area is nearly constant showing no dominant changes in the dropsize distribution with height.

The 2nd and 3rd spectral moments are shown below the peak reflectivity. Above the peak reflectivity these higher spectral moments give a large scatter due to the narrow Doppler profile combined with a large sensitivity in the computation of these moments forreflectivity fluctuations far away from the mean Doppler velocity. Based on this type of measurements the melting process is modelled.

At the bottom of the melting layer the rain dropsize distribution is determined. Comparing M_0 (o th moment) and M_3 (3rd moment) with figures 8 and 11 leads for this rain event to $N_0 = 75\ 10^6$ [m^{-4}], $D_0 = 1.0$ mm.
From M_2 (2nd moment) it becomes clear that the measured number of small raindrops is less than can be explained from the M-P distribution. This reduction in the measured M_2 can be analyzed in more detail by using a gamma raindropsize distribution [14].

At last the measured mean Doppler fall velocity in rain (1 st spectral moment) indicates a vertical air velocity of around 0.8 m/s upwards.

A second rain-Doppler measurement with DARR is shown in figure 27. The non-linear parameter estimation routine has been used for fitting a modified gamma distribution with the vertical air velocity as fifth parameter and applied to a measured Doppler velocity spectrum within a range cell. Not the whole Doppler velocity range is used in the fitting routine as can be seen in the figure. In this case only 12 Doppler velocity cells have been considered with each velocity cell equalling 9/17 m/s. Using this technique a second indication has been found for a more narrow raindropsize distribution relative to the negative exponential distribution.

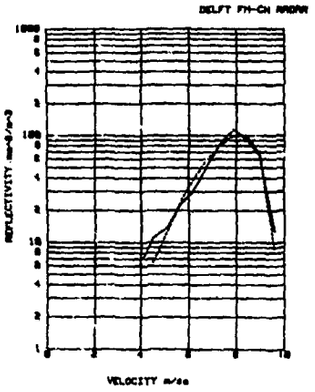


Figure 27. Observed and fitted Doppler velocity spectrum of rain within a range cell of 30 meters.

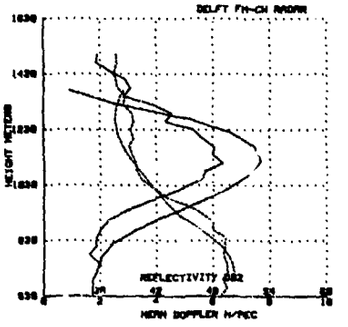


Figure 28. Observed and predicted reflectivity and Doppler velocity profiles through the melting layer.

Figure 28 is derived from the melting layer model with a water shell around dry snow particles [10] combined with DARR measurements of the 0 th and the 1 st spectral moments.

Doppler fall velocity envelopes show good agreement; the profile of the envelope of the mean reflectivity is correct except that the peak value in the model is overestimated. Lowering the peak reflectivity in the model is possible by introducing a more sophisticated refractive index characterization of the melting particles.

A last example of DARR-Doppler results is given as part of the Doppler measurement campaign in 1985. Special interest is given to DARR detection capabilities during convective rainshowers. During these events no distinct radar bright band is detected and in case of hail peak reflectivities even do not occur within the melting process. Based on the mean-reflectivity and mean-Doppler envelope as function of height and time, the top and the bottom of the radar bright band is determined together with the height of maximum reflectivity in between. Even when detection difficulties exist to characterize the melting process at some instant, the time dependence gives more insight into the characteristic heights mentioned above (figure 29).

DARR polarimetric measurements have been carried out in a measurement campaign with 30° elevation. During the measurements the azimuth angle has been selected so that perpendicular to the horizontal wind the polarization dependence of the reflectivity can be measured with minimum Doppler disturbance. The polarisers are steered in co-phase mode in such a way that the minimum and maximum polarization angles equal -41° and 49° respectively, relative to horizontal polarization. The range resolution is 30 meters. The

sweep time is 2.5 ms. Within a range cell at 900 m. distance the polarimetric data in figure 30 as function of time has been derived for 8 up-going sweeps per polarization period. The polarization-time dependence indicates that windshears are responsible for strong variations in canting of a few large raindrops. So far only preliminary DARR-polarimetric measurements have been executed. This type of measurement has to be carried out in future to get more detailed polarization information of hydrometeors.

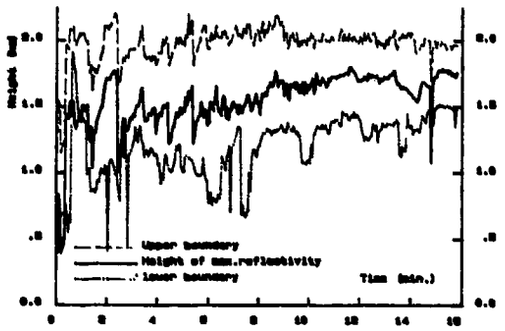


Figure 29. Top and bottom of the melting layer and the peak-reflectivity within the layer during convective showers as function of time.

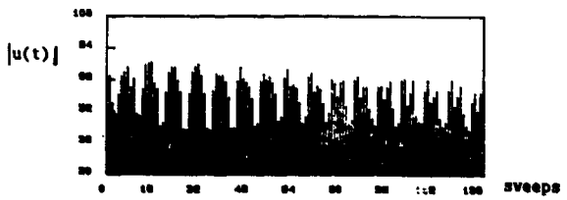


Figure 30. Polarimetric data as function of time, within a 30 m range cell.

References

1. P.S. Ray, "Broadband Complex Refractive Index of Ice and Water", Applied Optics, Vol. 2, No. 8, pp. 1836-1844, 1972.
2. H.R. Pruppacher, R.L. Pitter, "A Semi-Empirical Determination of the Shape of Clouds and Raindrops", Journ. of Atm. Sci., Vol. 28, pp. 86-94, 1971.
3. J.A. Morrison, M.J. Cross, "Scattering of a Plane Electromagnetic Wave by Axisymmetric Raindrops", Bell Syst. Tech. J., Vol. 53, No. 6, pp. 955-1019, 1974.
4. R. Gunn, G.D. Kinzer, "The Terminal Velocity of Fall for Water Droplets in Stagnant Air", J. Meteor., Vol. 6, pp. 243-248, 1949.
5. G.B. Foot, P.S. du Toit, "Terminal Velocity of Raindrops Aloft", J. Appl. Meteor., Vol. 8, pp. 249-253, 1969.
6. L.P. Ligthart, L.R. Nieuwkerk, A.W. Dissanayake, "Radar Study of the Melting Layer", Final Rep. ESTEC Contract 5482/83/NL/GM(SC), 1983.
7. G. Mie, "Beiträge zur Optik Trüber Medien, Speziell Kolloidaler Metallösingen", Ann. Phys., Vol. 25, pp. 377-445, 1908.
8. L.J. Battan, "Radar Observation of the Atmosphere", The Univ. of Chicago Press, Chicago, 1973.
9. F.T. Ulaby, R.K. Moore, A.K. Fung, "Microwave Remote Sensing", Vol. I, Addison-Wesley Publ. Comp., London, 1981.
10. A.W. Dissanayake, N.J. McEvan, "Radar and Attenuation Properties of Rain and Bright-Band", Ant. and Prop., Pt. 2, IEE Conf. Proc. 169, pp. 125-129, 1978.
11. L.P. Ligthart, L.R. Nieuwkerk, "FM-CW Delft Atmospheric Research Radar", IEE Proc., Part F, Vol. 127, No. 6, pp. 421-426, 1980.
12. L.P. Ligthart, L.R. Nieuwkerk, "Review of Capabilities of the Delft FM-CW Radar for Measurements of Precipitation", URSI-IEE Conf. Bournemouth, pp. 102-109, August 1982.
13. L.P. Ligthart, L.R. Nieuwkerk, J.S. v. Sinttruyen, "Basic Characteristics of FM-CW Radar Systems", AGARD Conf. Proc., No. 381, pp. 33.1-33.11, October 1985.
14. C.W. Ulbrich, "Natural Variations in the Analytical Form of the Raindrop Size Distribution", J of Climate and Applied Meteor., Vol. 22, pp. 1764-1775, 1983.

DISCUSSION

A. Ishimaru, US

Why did you choose M-P and gamma distribution? Did you consider ice particles?

Author's Reply

The M-P distribution was selected to make comparisons in the radio drop sizes derived from polarimetric measurements and from Doppler measurements. The gamma distribution was used to get an optimum fit between the measured Doppler spectrum and the theoretical Doppler spectrum derived from the gamma distribution. The vertical air velocity was taken into account in the fitting routines as an additional unknown parameter. Ice particles were only considered at the top of the melting layer to investigate in detail the melting process in the radar bright band.

F.J. Kelly, US

Are there any effects on rain or snow particles detected coincident with lightning events?

Author's Reply

No.

SUMMARY OF SESSION V

OCEAN SURFACE EFFECTS

by

J.H.Richter, Session Chairman

The Ocean Surface Effects Session consisted of an overview paper of theoretical modelling techniques followed by four other papers which are concerned with applications in the HF, VHF, microwave and millimetre regions, respectively. The overview paper by M.Fournier entitled "Modelling of EM Wave and Sea Surface Interaction" reviews EM systems parameters and signal characteristics used in connection with ocean surface effects. It then covers hydrodynamic and statistical properties of the sea surface, including various spectral representations. Finally, the paper reviews available models of EM wave and ocean surface interactions. These models consist of perturbation theory for EM waves which are large with respect to ocean waves, physical optics techniques for small EM wavelengths and a combination of both when EM and ocean wavelengths are of the same order.

The second paper, by J.Walsh and S.Srivastava entitled "Rough Surface Propagation and Scatter with Applications to Ground Wave Remote Sensing in an Ocean Environment", addresses HF radar for surface or low altitude target detection. The authors use a general formulation for rough surface propagation and scattering problems based on the concept of generalized functions. Their technique uses a spatial and temporal three-dimensional Fourier transform representation for the field quantities and requires, in the most general case, the solution of a pair of coupled vector integral equations for surface field quantities. For their application, this general solution reduces to a single vector integral equation for the electric field intensity, which is the primary quantity of interest for ground wave propagation and scattering. This equation may be further reduced to a Volterra equation of the second kind. With this approach, the backscattered field solutions at ground wave frequencies and resulting radar cross section solutions derived previously are presented and discussed. The second-order cross section contains new terms in addition to those provided by existing theories. These terms may be important, for example, for detection of stationary surface targets.

The third paper by D.Chrissoulidis and E.Kriezis, entitled "Wave-Tilt Sounding of Tropospheric Ducts above the Sea", is an interesting proposal to extend wave-tilt measurements, used successfully at lower frequencies, to the 100—200 MHz frequency band in order to sense atmospheric ducts above the ocean. A numerical study relates wave tilt (as measured by an airborne platform) and trapping refractivity gradients above the sea. The effect of ducts on wave tilt is shown through frequency shifts in a wave tilt versus frequency diagram. This shift is rather insensitive to duct thickness variations and even sea state. Whether this idea can be practically realized remains to be demonstrated experimentally.

The fourth paper by C.Baker and K.Ward, is entitled "I-Band Multipath Propagation over the Sea Surface". A 3-cm wavelength radar was used to measure target fluctuations over a line-of-sight path and interpret the results as a function of sea surface roughness. They find a good fit of their data to the Rice model provided that the measurements are made over a sufficient duration to include low frequency sea surface components. Observed effects of large scale ocean structures on the resulting multipath lobing structure suggest that two relatively similar sea states can result in very different multipath properties, with swell destroying the multipath lobing pattern by increasing the total roughness of the sea surface.

The last paper, by Y.Hurtaud, D.Terret, J.Daniel and A.Junchat, is entitled "Measurement and Modelling of 36 GHz Sea Reflection Phenomena". Extensive line-of-sight measurements were taken over a 9.6-km path. Tidal changes caused interference pattern variations of the received signal for a fixed receiving antenna. The receiving antenna could be moved vertically to create steady-state conditions which enabled the measurement of forward specular reflection coefficients. Good agreement between theory and measurement was obtained. Effects of atmospheric refractive structure on the data were also observed.

MODELISATION DE L'INTERACTION ENTRE UNE ONDE ELECTROMAGNETIQUE ET LA SURFACE DE LA MER

Michel Fournier
Le Centre Thomson d'Applications Radars
18-20 rue Grange Dame Rose, 78143 Vélizy-Villacoublay FRANCE

RESUME

Cet exposé a pour but de présenter une synthèse sur les moyens théoriques dont peut disposer un concepteur de systèmes électromagnétiques fonctionnant au voisinage de la mer.

L'interaction entre l'onde électromagnétique et la surface de la mer apporte de profondes modifications au fonctionnement de ces systèmes qu'il convient de prendre en compte.

Trois aspects sont présentés :

- Cerner les besoins de l'utilisateur en dégageant les exigences sur le nombre et la nature des paramètres qu'il est nécessaire de connaître pour atteindre l'objectif qu'il s'est fixé. Ces exigences sont fonction de la fréquence d'émission, de la disposition géométrique des aériens vis-à-vis de l'interface mer-atmosphère, du type d'émission ainsi que du contexte opérationnel envisagé.

Dans tous les cas, il est nécessaire de pouvoir estimer les caractéristiques statistiques spatiales et temporelles des signaux radioélectriques reçus.

- description appropriée de la surface de la mer comportant, en particulier, un examen de la compatibilité entre les lois de l'hydrodynamique et celles de la statistique. D'un point de vue théorique, le problème est de décrire la surface de la mer comme un processus stochastique à deux dimensions. Les différentes formes de représentation spectrale de la surface sont exposées ainsi que les liens qui existent entre elles,

- examen des différents modèles disponibles pour décrire l'interaction entre l'onde électromagnétique et la surface de la mer. Ces modèles peuvent être classés en trois principaux groupes :

  . la théorie des perturbations qui s'applique bien lorsque la longueur d'onde électromagnétique est plus grande que la hauteur moyenne des vagues,

  . théories basées sur l'optique physique qui s'appliquent à des fréquences plus élevées,

  . théories mixtes qui cherchent à concilier les deux aspects précédents.

Dans chaque cas, on s'efforce de mettre en évidence les avantages et les limites d'emploi du modèle.

1. INTRODUCTION

Les caractéristiques des signaux recueillis par un récepteur radioélectrique se trouvent profondément modifiées lorsque celui-ci est situé au voisinage de la surface de la mer. En effet outre le signal direct identique à celui qu'il recevrait en espace libre viennent s'ajouter un certain nombre de signaux perturbateurs résultant de réflexions multiples sur la surface de la mer.

De nombreuses études ont montré que ces signaux peuvent se décomposer en deux termes :

- un signal réfléchi d'une manière cohérente,
- un signal réfléchi d'une manière diffuse.

Le signal direct et le signal réfléchi cohérent sont deux signaux déterministes. Ils s'additionnent vectoriellement en tenant compte du déphasage lié à la différence entre les deux trajets fonction de la géométrie de la liaison. Il en résulte des interférences pouvant donner lieu, soit à un renforcement du signal, soit à des atténuations pouvant aller pratiquement jusqu'à l'extinction. Ces effets doivent être évalués et pris en compte lors de la conception de matériels.

Le signal diffus est un signal aléatoire qui fluctue dans le temps et dont l'origine provient des différentes réflexions qui se produisent sur la surface de la mer.

Ces fluctuations jouent un rôle important dans les performances globales des systèmes et leur influence doit également être prise en compte lors de la conception de ces systèmes.

Dans la plupart des cas, qu'il s'agisse :

- de radars,
- de systèmes de télécommunications,
- d'autodirecteurs d'engins.

le capteur électromagnétique est composé de plusieurs aériens élémentaires constituant l'antenne principale. Il convient en vue de concevoir un traitement du signal adapté d'évaluer, d'une part les fluctuations à la sortie de chaque récepteur élémentaire mais aussi d'évaluer les termes de corrélation entre deux capteurs voisins.

Pour analyser le problème d'une manière théorique la disposition la plus simple est de considérer un récepteur composé de deux aériens voisins, les résultats obtenus pourront être facilement étendus au cas de plusieurs antennes élémentaires. Une antenne réceptrice peut être considérée comme un opérateur linéaire ; la tension en sortie est donnée par :

$$v = \int_{\mathcal{D}} G(\vec{\alpha}.\vec{E_H} + \vec{\beta}.\vec{E_V})\, ds$$

expression où $\vec{E_V}$ et $\vec{E_H}$ sont respectivement les composantes verticale et horizontale du champ électrique incident dans la direction considérée, $G(\vec{\alpha};\vec{\beta})$ est le gain généralisé de l'antenne de réception dans cette même direction, $\mathcal{D}$ correspond au domaine dans lequel le phénomène de diffusion est significatif (ce domaine est selon les cas limité par le gain de l'antenne ou bien au contraire par les caractéristiques de diffusion de la surface).

les <u>fluctuations temporelles</u> du signal diffus peuvent être évaluées en cherchant sa statistique du second ordre, c'est-à-dire, la fonction d'autocorrélation du processus stochastique associé qui est définie par :

$$R(\tau) = E\left[v(t)\, v(t+\tau)\right]$$

De la même façon le <u>couplage spatial</u> entre composantes diffuses du signal à la sortie des deux capteurs élémentaires considérés et notés A et B peut être évalué par la matrice :

$$\Lambda_s = E\left[y^T y\right] \qquad \text{où :}$$
$$y = \left| v_A(t)\ v_B(t) \right|$$

On ne s'intéresse ici qu'à la corrélation du signal au même instant et en deux points séparés.

D'une manière plus générale la matrice :

$$\Lambda_{ts} = E\left[y^T y\right] \qquad \text{où :}$$
$$y = \left| v_A(t)\ v_B(t)\ v_A(t+\tau)\ v_B(t+\tau) \right|$$

caractérise complètement la <u>corrélation spatio-temporelle</u> entre la sortie des capteurs placés aux points A et B.

En utilisant la notation matricielle une formulation simple permet en reliant les caractéristiques géométriques de la liaison, les caractéristiques des récepteurs et les caractéristiques de diffusion de la surface de déterminer les paramètres statistiques du second ordre à la sortie des récepteurs. Ces paramètres statistiques permettent de tenir compte du canal propagation dans un traitement du signal adapté. Cette formulation met en évidence que pour effectuer ce calcul il est nécessaire de connaître d'une part la matrice de covariance des termes de diffusion au même instant mais aussi la matrice de cross-covariance de ces même termes entre deux instants décalés t et $t+\tau$.

La matrice de covariance des termes de diffusion à un même instant est définie par :

$$\Lambda_D(0) = E\left[\mathcal{D}^T \mathcal{D}^*\right] \qquad \text{où :}$$
$$\mathcal{D} = \left| d_{HH}\ d_{VH}\ d_{HV}\ d_{VV} \right|$$

Les composantes du vecteur $\mathcal{D}$ sont les termes de la matrice de diffusion définie d'une manière classique. La matrice de cross-covariance entre deux instants décalés est définie de la même façon par :

$$\Lambda_2(\tau) = E\left[\mathcal{D}^T(t)\,\mathcal{D}^{\#}(t+\tau)\right]$$

Le problème qui se pose au concepteur de matériel utilisant une liaison radioélectrique au voisinage de la surface de la mer est donc d'avoir accès à ces matrices caractérisant la diffusion et ses fluctuations temporelles.

L'obtention des éléments de la matrice $\Lambda_2(0)$ peut se faire en appliquant les lois de l'électromagnétisme à la surface de la mer supposée figée. En revanche l'obtention des éléments de la matrice $\Lambda_2(\tau)$ fait intervenir à la fois les lois de l'électromagnétisme et les lois de l'hydrodynamique et ne peut se faire sans une bonne connaissance préalable des phénomènes permettant de décrire correctement la surface et incluant l'aspect temporel.

Une méthode théorique idéale devrait donc dans tous les cas de figures être capable de fournir les deux matrices $\Lambda_2(0)$ et $\Lambda_2(\tau)$ en n'utilisant que les seuls lois de l'électromagnétisme et de l'hydrodynamique et ne faire appel qu'à un minimum d'hypothèses simplificatrices.

2. MODELISATION DE LA SURFACE DE LA MER

L'objet de cette partie de l'exposé est de mettre en relief les paramètres essentiels permettant une modélisation de la surface de la mer pouvant servir de matériau de base pour une étude des propriétés de diffusion en vue de fournir les éléments nécessaire à la résolution du problème théorique posé ci-dessus.

La surface de la mer peut être considérée comme constituée par la superposition de trois phénomènes distincts :

- la mer du vent,
- les ondes de capillarité,
- la houle.

La mer du vent est caractérisée par des vagues qui se forment sous l'action du vent soufflant sur une certaine étendue de mer. Ce sont des ondes de gravité mettant en mouvement des masses d'eau plus ou moins importantes et dont la vitesse est contrôlée par l'action de la pesanteur. Cette agitation continue même après que le vent ait cessé pour s'amortir progressivement.

Les ondes de capillarité sont des ondes de courte longueur d'onde dont la vitesse est contrôlée par les phénomènes de tension superficielle sur la surface. Elles ne mettant pas en mouvement des masses d'eau importantes et cessent dès que le vent tombe. Par vent fort, elles se superposent à la mer du vent et par vent faible elles constituent la risée.

La houle est constituée par des vagues se propageant loin de leur lieu de formation. Elle se caractérise par une grande régularité et des crêtes plus longues que la mer du vent. Elle peut exister en l'absence de tout vent sur la zone où elle est observée.

La mer du vent et la houle correspondent à des vagues dont les crêtes sont séparées par des distances de l'ordre du mètre à quelques centaines de mètres, alors que les ondes de capillarité sont de l'ordre du centimètre.

2.1) Lien entre l'aspect hydrodynamique et l'aspect statistique

Du point de vue hydrodynamique la linéarisation des équations rigoureuses de la mécanique des fluides conduit au résultat que les mouvements de la surface correspondent à une superposition d'ondes dispersives, c'est-à-dire que leur vitesse de propagation dépend de la longueur d'onde.

Dans le cas des ondes de gravité, c'est-à-dire lorsque le mouvement de la surface peut être considéré comme régi par les seules forces liées à la pesanteur la relation de dispersion s'écrit :

$$\Omega^2(\vec{K}) = g\,K$$

Ω est la pulsation de l'onde de gravité,
$\vec{K}$ est le nombre d'onde et $K = |\vec{K}|$,
g est l'accélération de la pesanteur.

Dans le domaine où seules interviennent les forces liées à la tension superficielle, la relation de dispersion s'écrit :

$$\Omega^2(\vec{K}) = \frac{T_1}{\rho+\rho'} K^3$$

T_1 est le coefficient de tension superficielle de l'eau de mer ρ et ρ' sont respectivement les densités de l'air et de l'eau.

Dans la zone de transition entre ces deux domaines la relation de dispersion peut s'écrire :

$$\Omega^2(\vec{K}) = gK + \frac{T_1}{\rho+\rho'} K^3$$

Les équations de l'hydrodynamique conduisent très facilement aux relations de dispersion mais ne donnent pas de renseignements sur la hauteur des dénivellations. En effet pour avoir accès à la hauteur des vagues il est nécessaire de faire intervenir, outre les forces de gravité ou de capillarité, le couplage énergétique entre le vent et les vagues et de tenir compte des turbulences de l'air au voisinage de la surface. Les théories qui ont été développées dans ce sens conduisent à des résultats qui sont difficilement utilisables dans le problème de l'interaction d'une onde électromagnétique et la surface de la mer. C'est pourquoi d'un point de vue beaucoup plus pratique a été introduite une description statistique de la surface. Cette approche est cohérente avec l'approche hydrodynamique. En considérant la surface comme spatialement et temporellement stationnaire, il est possible de définir un spectre et l'on peut montrer qu'il existe une analogie formelle entre la solution linéarisée des équations de l'hydrodynamique et le théorème de la représentation spectrale de Wiener-Khintchine que l'on généralise ainsi à une surface constituée par une superposition d'ondes dispersives. Cette représentation conduit donc à une surface qui est stationnaire par rapport aux coordonnées du temps et de l'espace et qui vérifie les lois de l'hydrodynamique.

2.2) Spectre de la surface

Cette notion de spectre liée à une surface en mouvement avec une loi dispersive est approfondie ici sur trois points importants :

- lien entre les différentes définitions du spectre selon que l'on considère le spectre mono, bi ou tridimensionnel,

- étude de la zone spectrale correspondant au domaine des ondes de capillarité,

- obtention pratique d'un spectre directif.

La surface étant considérée comme spatialement et temporellement stationnaire, il est légitime d'écrire :

$$E[\zeta(\vec{\pi}, t)] = 0$$

$$E[\zeta(\vec{\pi}_1, t_1)\,\zeta(\vec{\pi}_2, t_2)] = R(\vec{\pi}_2 - \vec{\pi}_1, t_2 - t_1)$$

$$= R(\vec{\pi}, \tau)$$

$\zeta(\vec{\pi}, t)$ correspond à la dénivellation par rapport au niveau moyen au point défini spatialement par le vecteur $\vec{\pi}$ et à l'instant t. La fonction d'autocorrélation de la surface est obtenue en se plaçant en deux points de l'espace séparés définis par $\vec{\pi}_1$ et $\vec{\pi}_2$ et à deux instants décalés t_1 et $t_2 = t_1 + \tau$.

On peut dans ces conditions définir le spectre tridimensionnel par :

$$S(\vec{K}, \Omega) = \frac{1}{(2\pi)^3} \int_{-\infty}^{+\infty} R(\vec{\pi}, \tau)\, e^{-j(\vec{K}\cdot\vec{\pi} + \Omega\tau)}\, d\vec{\pi}\, d\tau$$

La surface étant réelle ce spectre est symétrique, c'est-à-dire que :

$$S(-\vec{K}, -\Omega) = S(\vec{K}, \Omega)$$

La hauteur quadratique moyenne des vagues s'exprime en fonction de ce spectre par la relation :

$$\sigma_s^2 = \int_{-\infty}^{+\infty} S(\vec{K}, \Omega)\, d\vec{K}\, d\Omega$$

La généralisation du théorème de Wiener-Khintchine appliquée à la surface amène à introduire d'une manière naturelle le spectre $S_+(\vec{K})$ qui correspond à l'énergie qui se propage dans le sens du vecteur $\vec{K}$ ainsi que le spectre $S_-(\vec{K})$ qui correspond à une propagation dans le sens contraire.

Ces deux spectres sont dissymétriques. Il est plus commode pour les applications d'introduire deux autres spectres qui eux sont symétriques. Ces spectres sont définis par :

$$\begin{cases} S_1(\vec{K}) = S_+(\vec{K}) & \text{si} \quad \vec{K}.\vec{V} \geq 0 \\ S_1(\vec{K}) = S_-(\vec{K}) & \text{si} \quad \vec{K}.\vec{V} < 0 \end{cases}$$

$$\begin{cases} S_2(\vec{K}) = S_-(\vec{K}) & \text{si} \quad \vec{K}.\vec{V} \geq 0 \\ S_2(\vec{K}) = S_+(\vec{K}) & \text{si} \quad \vec{K}.\vec{V} < 0 \end{cases}$$

$\vec{V}$ est un vecteur correspondant à la direction du vent. A ces deux spectres sont attachés deux processus dY_1 et dY_2 correspondant respectivement à des ondes se propageant dans le sens du vecteur $\vec{V}$ (direction du vent) et dans le sens rétrograde. Ces deux processus sont à incréments orthogonaux et orthogonaux entre eux et permettant une représentation de la surface sous la forme :

$$\zeta(\vec{x}, t) = \int_{-\infty}^{+\infty} \Big\{ e^{j\left[\mathrm{signe}(\vec{K}.\vec{V})\,\Omega(\vec{K})\,t - \vec{K}.\vec{x}\right]} dY_1(\vec{K}) + e^{j\left[\mathrm{signe}(\vec{K}.\vec{V})\,\Omega(\vec{K})\,t + \vec{K}.\vec{x}\right]} dY_2(\vec{K}) \Big\}$$

En fonction de $S_1(\vec{K})$ et $S_2(\vec{K})$ la fonction d'autocorrélation spatio-temporelle de la surface s'écrit :

$$R(\vec{x}, \tau) = \int_{-\infty}^{+\infty} e^{j\left[-\mathrm{signe}(\vec{K}.\vec{V})\,\Omega(\vec{K})\,\tau + \vec{K}.\vec{x}\right]} S_1(\vec{K})\, d\vec{K} + \int_{-\infty}^{+\infty} e^{j\left[\mathrm{signe}(\vec{K}.\vec{V})\,\Omega(\vec{K})\,\tau + \vec{K}.\vec{x}\right]} S_2(\vec{K})\, d\vec{K}$$

ce qui conduit à une autre expression du spectre tridimensionnel :

$$S(\vec{K}, \Omega) = S_1(\vec{K})\, \delta\left[\Omega + \mathrm{signe}(\vec{K}.\vec{V})\,\Omega(\vec{K})\right] + S_2(\vec{K})\, \delta\left[\Omega - \mathrm{signe}(\vec{K}.\vec{V})\,\Omega(\vec{K})\right]$$

(δ est la fonction de Dirac)

Cette dernière relation permet d'écrire la hauteur quadratique moyenne des vagues sous la forme :

$$\sigma_\zeta^2 = \int_{-\infty}^{+\infty} [S_1(\vec{K}) + S_2(\vec{K})]\, d\vec{K}$$

Le spectre bidimensionnel est obtenu en se plaçant au même instant en deux points différents de la surface, c'est-à-dire en considérant celle-ci comme figée.

Par définition, la fonction d'autocorrélation de cette surface figée est égale à :

$$R(\vec{R}) = E[\zeta(\vec{R}_1, t)\, \zeta(\vec{R}_2, t)]$$

Le spectre bidimensionnel qui est la transformé de Fourier de cette fonction d'autocorrélation est donné par :

$$S(K) = \frac{1}{(2\pi)^2} \int_{-\infty}^{+\infty} R(\vec{R})\, e^{-j\vec{K}.\vec{R}}\, d\vec{R}$$

Par construction ce spectre est symétrique :

$$S(-\vec{K}) = S(\vec{K})$$

La hauteur quadratique moyenne des vagues s'exprime en fonction de ce spectre par :

$$\sigma_\zeta^2 = \int_{-\infty}^{+\infty} S(\vec{K})\, d\vec{K}$$

Ce qui conduit à la relation :

$$S(\vec{K}) = S_1(\vec{K}) + S_2(\vec{K})$$

Le spectre bidimensionnel se déduit du spectre tridimensionnel par :

$$S(\vec{K}) = \int_{-\infty}^{+\infty} S(\vec{K}, \Omega)\, d\Omega$$

Le spectre unidimensionnel (ou spectre temporel) est obtenu en se plaçant en un point de la surface et en considérant la statistique temporelle des dénivellations. Ce spectre est directement accessible par l'expérience. La fonction d'autocorrélation de la hauteur des vagues est donnée par :

$$R(\tau) = E[\zeta(\vec{R}_1, t_1)\, \zeta(\vec{R}_1, t_2)]$$

$$(t_2 = t_1 + \tau)$$

Le spectre unidimensionnel s'écrit par définition :

$$S(\Omega) = \frac{1}{2\pi} \int_{-\infty}^{+\infty} R(\tau)\, e^{-j\Omega\tau}\, d\tau$$

Ce spectre est bien entendu symétrique : $S(-\Omega) = S(\Omega)$. La hauteur quadratique moyenne des vagues est donnée par :

$$\sigma_\zeta^2 = \int_{-\infty}^{+\infty} S(\Omega)\, d\Omega$$

On peut passer du spectre tridimensionnel au spectre temporel par la relation :

$$S(\Omega) = \int_{-\infty}^{+\infty} S(\vec{K}, \Omega)\, d\vec{K}$$

Cette expression peut se transformer en introduisant les spectres $S_1(\vec{K})$ et $S_2(\vec{K})$ des deux processus dV_1 et dV_2 permettant la représentation spectrale de la surface.

On a vu que :

$$S(\vec{K}, \Omega) = S_1(\vec{K})\, \delta\left[\Omega + \text{signe}(\vec{K}.\vec{V})\, \Omega(\vec{K})\right] + S_2(\vec{K})\, \delta\left[\Omega - \text{signe}(\vec{K}.\vec{V})\, \Omega(\vec{K})\right]$$

La fonction de Dirac qui apparaît dans cette formule signifie qu'une onde de nombre d'onde spatial K ne se propage que si la relation de dispersion :

$$\Omega = \pm\, \Omega(\vec{K}) = f(K)$$

est vérifiée. En introduisant la fonction inverse de la relation de dispersion : $K = g(\Omega)$ et en passant en coordonnées polaires dans le plan des vecteurs d'onde spatiaux, on peut écrire :

$$\begin{cases} K_x = g(\Omega) \cos\theta \\ K_y = g(\Omega) \sin\theta \end{cases}$$

Il existe une correspondance biunivoque entre les variables (K, θ) et les variables (Ω, θ), transformation dont le Jacobien s'écrit :

$$J' = \frac{dg(\Omega)}{d\Omega}\, g(\Omega)$$

d'où la relation :

$$S(\Omega) = g(\Omega)\, \frac{dg(\Omega)}{d\Omega} \int_{-\pi}^{\pi} \left[S_1(K) + S_2(K)\right] d\theta$$

Relation qui établit un lien entre le spectre temporel et le spectre directif. Par ailleurs le spectre temporel peut s'exprimer en fonction du module du vecteur d'onde K . En utilisant la relation de dispersion $\Omega = f(K)$ on obtient une relation qui s'écrit :

$$S(K) = S(\Omega) \frac{d\Omega}{dK}$$

Le modèle pratique de spectre le mieux confirmé par l'expérience est celui de Pierson-Moskowitz [1] qui est actuellement universellement adopté. Il permet de relier $S(\Omega)$ à la vitesse du vent par une formulation simple. Cependant il présente le défaut de ne bien s'appliquer qu'au domaine des ondes de gravité et traduit mal la réalité dans le domaine des courtes longueurs d'onde en particulier dans le domaine correspondant à la capillarité.

En effet le spectre permet de calculer la pente quadratique moyenne des vagues. Dans le cas du spectre de Pierson-Moskowitz ce calcul conduit à une pente quadratique moyenne infinie [2] ; ceci est dû au fait que la décroissance du spectre (en $1/\Omega^5$) n'est pas assez rapide pour assurer la convergence de l'intégrale donnant la pente des vagues. Or certaines théories de l'interaction entre une onde électromagnétique et la surface de la mer font intervenir la pente quadratique moyenne comme un paramètre essentiel dans les calculs, dans ce cas le spectre de Pierson-Moskowitz est inutilisable et l'on fait souvent appel aux formules empiriques de Cox et Munk [3] qui expriment directement la pente quadratique moyenne des vagues en fonction de vitesse du vent. Cependant une telle démarche n'est pas satisfaisante sur le plan théorique et il est bien préférable de disposer d'un spectre donc la décroissance en fonction de la fréquence conduit à une estimation correcte de la pente des vagues.

Des travaux basés sur un grand nombre de mesures expérimentales se sont efforcés de combler cette lacune. Il est actuellement établi que dans le domaine des ondes capillaires [4-5-6] le spectre peut s'exprimer sous la forme :

$$S(\Omega) = \left(\frac{0.875}{2\pi}\right)\left(\frac{2\pi}{\Omega}\right)^{p}$$

où Ω est en radians par seconde et $p = 5 - \log_{10} U_*$

U_* est la vitesse de friction (cm/s).

Cette vitesse introduite en théorie de la turbulence peut être reliée à la vitesse du vent mesurée par un anémomètre à l'altitude z (cm) au-dessus du niveau moyen de la surface par les relations :

$$U = (U_* / 0.4) \log (z / z_0) \qquad \text{(cm/s)}$$

$$z_0 = (0.684/ U_*) + 4.28 \times 10^{-5} U_*^2 - 0.0443 \text{ (cm)}$$

Formulation valable pour $U_* > 12$ cm/s.

Cette théorie conduit à un spectre qui dépend pour son calcul, de deux paramètres :
la vitesse du vent et la hauteur de l'anémomètre, elle nécessite la détermination de la vitesse de friction en inversant les formules donnant U en fonction de U_* .
En utilisant cette méthode il a été établi un spectre couvrant toute la gamme des fréquences [7].
Ce spectre est défini par morceaux à l'aide de formules qui se raccordent aux frontières de chaque domaine de validité. Dans le domaine des basses fréquences régies par la gravité, ce spectre est identique à celui de Pierson-Moskowitz.
Dans le domaine des ondes de capillarité il correspond à la formulation décrite ci-dessus. Le raccord entre ces deux zones se fait en divisant la plage intermédiaire en deux parties distinctes.
Par ailleurs une cinquième zone couvrant le domaine allant de la frontière supérieur des ondes capillaires jusqu'aux fréquences très élevées assure une décroissance spectrale telle que l'ensemble du spectre conduit à une pente quadratique moyenne des vagues finie et conforme aux mesures expérimentales de Cox et Munk.

Pour résoudre le problème lié au traitement du signal qui se pose au concepteur de matériel, la connaissance du seul spectre temporel est insuffisante et il est nécessaire pour mettre en oeuvre les théories permettant de déterminer la corrélation spatio-temporelle du signal, de disposer du spectre tridimensionnel ou tout au moins du spectre bidimensionnel de la surface de la mer.

L'examen des formules permettant de relier entre eux les différents spectres montrent qu'il est facile de passer du spectre tridimensionnel au spectre bidimensionnel et du spectre bidimensionnel au spectre temporel, mais ce passage se fait d'une manière irréversible et il est impossible de passer par exemple du spectre temporel au spectre bidimensionnel par une formulation purement analytique, il est nécessaire à ce stade de faire des hypothèses physique supplémentaires.

Pour obtenir un spectre directionnel compatible avec le spectre temporel, le principe de la démarche est le suivant :

- comme $S(-\Omega) = S(\Omega)$ il est commode de définir un nouveau spectre dans lequel n'interviennent que des fréquences positives :

$$S^{*}(\Omega) = 2\,S(\Omega) \qquad \Omega \geq 0$$

- le spectre directif peut s'écrire :

$$S(\Omega,\theta) = g(\Omega)\,\frac{dg(\Omega)}{d\Omega}\,S^{*}(\vec{K})$$

$S^{*}(\vec{K})$ est ici le spectre directif non symétrique :

$$S^{*}(\vec{K}) = 2\left[\,S_{+}(\vec{K}) + S_{+}(-\vec{K})\,\right]$$

- dans ces conditions :

$$S^{*}(\Omega) = \int_{-\pi}^{\pi} S(\Omega,\theta)\,d\theta$$

- d'une manière formelle on peut toujours écrire :

$$S(\Omega,\theta) = S^{*}(\Omega)\,f(\theta,\Omega)$$

La relation écrite précédemment montre que $f(\theta,\Omega)$ doit obéir à :

$$\int_{-\pi}^{\pi} f(\theta,\Omega) = 1$$

aussi le problème de la détermination du spectre directif revient à trouver un modèle pour la fonction $f(\theta,\Omega)$ qui caractérise la répartition angulaire des vagues. La fonction $f(\theta,\Omega)$ est l'objet de modélisations que l'on peut répartir en deux classes : celles où f est indépendant de Ω et celles où f en dépend.

Dans la première classe le modèle le plus simple est le modèle semi-isotrope :

$$f(\theta,\Omega) = \frac{1}{\pi} \qquad -\frac{\pi}{2} \leq \theta \leq \frac{\pi}{2}$$
$$= 0 \qquad \text{ailleurs}$$

Un autre modèle couramment employé est :

$$f(\theta,\Omega) = \frac{2\cos^{2}\theta}{\pi} \qquad -\frac{\pi}{2} \leq \theta \leq \frac{\pi}{2}$$
$$= 0 \qquad \text{ailleurs}$$

Dans la deuxième catégorie on rencontre des modèles du type :

$$f(\theta,\Omega) = \frac{\cos^{s}\left(\frac{\theta}{2}\right)}{\int_{-\pi}^{\pi}\cos^{s}\left(\frac{u}{2}\right)du}$$

expression où s est une fonction plus ou moins compliquée de Ω. L'obtention de tels modèles a fait l'objet de nombreux travaux de la part des océanographes dont le détail dépasse le cadre du présent exposé qui ne vise qu'à indiquer les principes. On peut trouver dans [8] et [9] une discussion extrêmement complète de ces modèles.

3. MODELISATION DE L'INTERACTION ENTRE L'ONDE ELECTROMAGNETIQUE ET LA SURFACE DE LA MER

Il est nécessaire pour répondre à l'objectif fixé, de connaître les deux matrices $\Lambda_D(0)$ et $\Lambda_D(\tau)$ correspondant respectivement à la matrice de covariance des éléments de diffraction $\begin{vmatrix} d_{HH} & d_{HV} \\ d_{VH} & d_{VV} \end{vmatrix}$ à un même instant et à leur matrice de cross-covariance à deux instants décalés t et $t+\tau$.
L'obtention des éléments de la matrice $\Lambda_D(0)$ peut se faire en appliquant les lois de l'électromagnétisme à la surface supposée figée, alors que les éléments de la matrice $\Lambda_D(\tau)$ font intervenir à la fois les lois de l'électromagnétisme et les lois de l'hydrodynamique.

Nous examinons ici, ce que l'on peut attendre des modèles théoriques existants pour aborder ces deux problèmes. La méthode théorique idéale devrait pour tous les cas de figures être capable de calculer les deux matrices $\Lambda_D(0)$ et $\Lambda_D(\tau)$, en se s'aidant que des seules lois de l'électromagnétisme et de l'hydrodynamique en ne faisant appel qu'à un minimum d'hypothèses simplificatrices. La pratique montre qu'il s'avère en fait nécessaire de faire dès le départ des hypothèses simplificatrices pour écrire les conditions aux limites qui sont difficiles à formuler d'une manière rigoureuse dans le cas d'une surface aléatoire.

3.1) Méthode des perturbations [8-11]

Cette théorie pose comme hypothèse de départ que le champ total peut s'écrire sous forme d'une somme infinie d'ondes planes et que cette description est valable en tout point au-dessus de la surface.

En écrivant des conditions aux limites exactes et en utilisant les équations de Maxwell, on aboutit à un système linéaire qui permet d'identifier les coefficients de la somme d'ondes planes décrivant le champ diffusé par la surface. Pour ce faire, on décompose la surface en harmoniques spatiaux et l'on suppose dans les calculs que la rugosité de la surface est inférieure à la longueur d'onde du champ électromagnétique incident. La méthode conduit à décomposer le champ total résultant en deux termes :

- une composante cohérente correspondant à ce que donnerait la réflexion spéculaire sur le plan non perturbé,
- une composante non cohérente correspondant à la diffusion liée à l'influence des perturbations de la surface de la mer.

Les calculs développés au départ pour une surface figée sont aisément généralisés à une surface en mouvement.

La méthode met en relief le résultat remarquable que la diffusion de l'onde électromagnétique peut être interprétée comme l'interaction entre deux phénomènes ondulatoires, l'un de nature électromagnétique et l'autre de nature mécanique, seule la composante spectrale de la surface de la mer qui a la même longueur d'onde que l'onde électromagnétique incidente interagit avec celle-ci.

On aboutit donc à un phénomène assez semblable à ce qui se passe en cristallographie pour la diffraction des rayons X par un réseau cristallin (diffraction de Bragg).

La méthode des perturbations permet d'accéder par le calcul aux matrices $\Lambda_D(0)$ et $\Lambda_D(\tau)$ en tenant compte de tous les aspects du problème, en particulier la polarisation est prise en compte d'une manière rigoureuse et l'effet d'ombre pour les incidences rasantes est implicitement inclus dans la méthode. Dans le calcul des termes du premier ordre le spectre de la surface intervient seul et aucune hypothèse n'est faite sur la loi de probabilité des dénivellations. Si l'on cherche les termes d'interaction du deuxième ordre l'hypothèse Gaussienne doit être faite pour pouvoir effectuer les calculs analytiquement.

La méthode des perturbations a malheureusement l'inconvénient de ne bien s'appliquer qu'à une surface rugueuse (en termes de longueur d'onde du rayonnement incident), son domaine d'application ne couvre donc pas les hyperfréquences pour lesquelles la hauteur quadratique moyenne des vagues (ondes de gravité) est en général supérieure à la longueur d'onde électromagnétique. En revanche, elle s'applique bien pour les fréquences utilisées dans le domaine des télécommunications.

3.2) Méthodes de l'optique physique et de l'optique géométrique

Les méthodes de l'optique physique sont basées sur l'approximation par l'intégrale de Kirchhoff [12]. Les calculs utilisent des conditions aux limites approximatives, grâce à l'approximation dite du plan tangent : les conditions aux limites sont celles qui seraient déduites relativement au champ électromagnétique incident pour un plan localement tangent à la surface considérée.

Cette approximation n'est valable que si les rayons de courbure principaux de la surface sont plus grands que la longueur d'onde et si l'incidence n'est pas trop rasante.
Ces méthodes sont beaucoup moins rigoureuses que la méthode des perturbations, car elles dissocient l'aspect polarisation du calcul du champ rerayonné par la surface. L'intégrale de Kirchhoff est appliquée à un champ scalaire et la polarisation du champ réémis est assimilée à celle résultant du plan tangent moyen à la surface [13-14].

En incidence rasante, il est évident que seulement une partie de la surface se trouve illuminée par la source, l'autre partie se trouvant dans l'ombre. La mise en oeuvre correcte de la méthode de calcul supposerait que l'on connaisse la partie éclairée puisque le champ réémis est obtenu en intégrant dans cette zone les courants induits par le champ électromagnétique incident. En fait, on suppose toute la surface éclairée dans un premier temps du calcul, puis l'on introduit un coefficient numérique qui tient compte de l'ombre [15-18]. Il s'agit là d'une méthode extrêmement artificielle, dont le résultat devient de plus en plus douteux vers les incidences rasantes.

Les méthodes de l'optique physique peuvent être généralisées à des surfaces anisotropes en mouvement. l'hypothèse d'une surface Gaussienne est alors nécessaire pour effectuer les calculs [19].

Deux aspects intéressants, car faciles à mettre en oeuvre et bien vérifiés par l'expérience, sont à retenir dans cette méthode.

Il s'agit :

- de l'influence de la rugosité de la mer sur l'amplitude du signal réfléchi cohérent [20-21],

- de la possibilité de définir d'une manière précise la notion intuitive de surface scintillante qui est reliée à la pente quadratique moyenne des vagues [12].

Dans les méthodes de l'optique physique, on calcule la composante diffuse en moyennant le champ par rapport à toutes les réalisations statistiques de la surface.
Au contraire, dans les méthodes de l'optique géométrique, on développe le calcul avant d'effectuer la moyenne statistique en faisant apparaître les caractéristiques géométriques locales à travers l'orientation de la normale et les rayons de courbure de la surface au point considéré. Le champ diffus est finalement calculé en considérant un ensemble de points brillants ayant une courbure dont on a calculé la moyenne à l'aide de la description statistique de cette surface [22-25].

Ces méthodes s'appliquent bien pour une surface très rugueuse ; elles présentent cependant le défaut de se prêter difficilement au calcul des corrélations temporelles entre deux éléments de surface, le calcul statistique étant introduit d'une manière beaucoup plus artificielle que dans le cadre des méthodes basées sur l'optique physique.

3.3) Méthodes mixtes

Elles cherchent à concilier les deux approches précédentes : pour les petites ondulations (capillarité) on utilise la méthode des perturbations et une autre méthode pour les grandes ondulations (vagues et houle).

La méthode de Semenov [26-27] est la plus simple : elle utilise la méthode de l'intégrale de Kirchhoff pour les grandes ondulations. La méthode de Wright [26-29] est plus élaborée. Elle met en oeuvre un repère principal dans lequel sont décrits les grandes ondulations et un repère local dont l'orientation est donnée par la normale à la surface correspondant à l'ondulation de grande amplitude. Dans le repère local, le champ électromagnétique rediffusé est calculé en considérant les petites ondulations comme venant se juxtaposer à une surface localement plane et en appliquant la théorie des perturbations. Le résultat obtenu est moyenné par rapport aux orientations aléatoires du repère local dans le repère principal. Cette théorie fait actuellement l'objet de nombreuses investigations et donne des résultats qui cadrent bien avec l'expérience [6-30].

Elle est cependant limitée au cas monostatique. En effet, l'examen des formules fournies par la théorie des perturbations montre que dans ce cas, ce sont les composantes les plus hautes du spectre hydrodynamique qui interagissent avec l'onde électromagnétique incidente, en revanche, dans le cas de trajets multiples, on peut voir que ce sont les composantes les plus basses qui interagissent, or ces composantes correspondent aux ondes de gravité qui sont de grande amplitude et pour lesquelles l'hypothèse de perturbations petites par rapport à la longueur d'onde n'est plus valable. Cette méthode n'est donc pas applicable au cas de trajets multiples.

Toutes les méthodes mixtes font appel pour leur mise en oeuvre à l'hypothèse que la surface est Gaussienne de plus le problème de l'ombre se pose pour les grandes ondulations de la même manière que dans le cas des méthodes de l'optique physique.

4. CONCLUSION

La présence de l'interface mer-atmosphère apporte des perturbations importantes aux matériels radioélectriques fonctionnant dans son voisinage. En effet les réflexions multiples sur la surface interfèrent avec le signal direct ce qui produit des fluctuations de l'amplitude et de la phase du signal résultant. Dans certains cas, on peut observer une quasi-extinction du signal. Pour lutter contre ces influences néfastes et prendre en compte le canal de propagation, le concepteur de matériel doit utiliser un traitement du signal approprié.

Ce traitement est basé sur une connaissance des caractéristiques temporelles ou spatiales du signal ou sur une combinaison des deux. Il est donc important au niveau de la conception de ces matériels de pouvoir disposer d'un moyen d'évaluation des caractéristiques statistiques du signal reçu.

On peut montrer que les termes du second ordre : fonction d'auto-corrélation ou spectre à la sortie du récepteur et matrice de corrélation spatiale peuvent être déduits de la géométrie de la liaison, du gain des aériens constituant le récepteur et des paramètres caractérisant la diffusion de l'onde électromagnétique par la surface de la mer : $\Lambda_p(0)$ matrice de covariance de termes de diffusion et $\Lambda_p(\tau)$ matrice de cross-covariance entre deux instants décalés.

L'évaluation de ces éléments caractérisant la diffusion nécessite une description appropriée de la surface de la mer. Un point important est que les ondes mécaniques qui engendrent cette surface sont dispersives.

La notion de spectre permet de décrire statistiquement la surface en regroupant sous une forme accessible un très grand nombre de mesures effectuées par les océanographes :

- le spectre de Pierson-Moskowitz décrit les ondes de gravité,
- le domaine des ondes capillaires peut être actuellement appréhendé d'une manière correcte,
- il existe des modèles de décroissance spectrale conduisant à une estimation de la pente des vagues conforme à l'expérience.

Par ailleurs il est possible par une formulation appropriée de passer du spectre temporel facilement accessible à l'expérience et dont on dispose de bons modèles, à un spectre directif qui traduise d'une manière réaliste les propriétés physiques de la surface.

Disposant d'une description convenable de la surface les caractéristiques de diffusion peuvent être obtenues à partir d'une modélisation de l'interaction entre l'onde électromagnétique et la surface de la mer.

Les modèles disponibles peuvent être classés en trois principaux groupes :

- la théorie des perturbations qui s'applique lorsque la longueur d'onde électromagnétique est plus grande que la hauteur quadratique moyenne des vagues,

- les théories basées sur l'optique physique qui s'appliquent à des fréquences plus élevées,

- les théories mixtes qui cherchent à concilier les deux aspects précédants.

Les méthodes des perturbations permet d'atteindre l'objectif fixé qui est d'accéder aux termes caractérisant la diffusion en se servant que des équations de Maxwell et d'une description de la surface incluant les équations de la mécanique des fluides. Malheureusement cette méthode est limitée en fréquence. Les autres méthodes pour leur part ne répondent qu'imparfaitement à l'objectif décrit.

Le choix d'un modèle doit donc se faire sur la base d'un certain nombre de compromis en fonction des besoins correspondant au problème posé au concepteur.

Dans beaucoup de cas un modèle semi-empirique peut donner des résultats satisfaisants dans le cadre d'un problème particulier. Par exemple la théorie de l'optique physique permet de calculer les termes de diffraction de la surface supposée figée alors que les fluctuations du signal sont obtenues par des considérations empiriques qui ne sont pas incluses dans la méthode théorique mise en oeuvre pour décrire l'interaction entre l'onde électromagnétique et la surface de la mer [31-32] .

D'un point de vue pratique il convient aussi de prendre en considération la complexité de mise en oeuvre d'une théorie dans le choix de celle-ci en vue d'une application.

Un aspect important qui est négligé par les théories existantes est l'influence des fluctuations du signal dues à l'hétérogénéité des basses couches de l'atmosphère au voisinage du dioptre constitué par la surface de la mer. Il est donc illusoire pour le praticien de mettre en oeuvre des théories trop complexes de l'interaction entre onde électromagnétique et la surface de la mer qui conduiraient à des résultats négligeant un facteur qui peut se révéler important.

REFERENCES

1 W.J. PIERSON, L. MOSKOWITZ, A proposed spectral form for fully developed wind seas based on the similarity theory of S.A. KITAIGORODSKI, Journal of Geophysical Research, Vol. 69, n° 24, pp. 5181-5190, December 15, 1964.

2 P.J. WELTON, On the connection between the surface characteristics and the frequency dependance of the back-scattered field, Colloque sur la diffusion des ondes ultrasonores, 5-9 mars 1979, Paris, Revue du CETHEDEC (Rouge) 16ème année, 3ème trimestre 1979, n° 60, pp. 125-133.

3 C. COX, W. MUNK, Measurement of the roughness of the sea surface from phtographs of the sun's glitter, Journal of the Optical Society of America, Vol. 44, n° 11, pp. 838-850, November 1954.

4 W.J. PIERSON, The theory and applications of ocean wave measuring systems at and below the sea surface on the land, from aircraft, and from spacecraft, NASA, Contrat Rep. CR-2646, N76-17775, 1976.

5 A.K. FUNK, K.K. LEE, A semi-empirical sea spectrum model for scattering coefficient estimation, IEEE, Journal of Oceanic Engineering, Vol. OE-7, n° 4, October 1982.

6 R.T. LAWNER, R.K. MOORE, Short gravity and capillary wave spectra from tower-based radar, IEEE, Journal of Oceanic Engeneering, Vol. OE-9, n° 5, December 1984.

7 R.K. MOORE, Radar sensing of the ocean, IEEE, Journal of Oceanic Engeneering, Vol. OE-10, n°2, April 1985.

8 PH. FORGET, Observation des vagues par radar décamétrique en ondes de sol, Modélisation et résultats expérimentaux, Thèse présentée à l'Université Pierre et Marie Curie, Paris VI, 2 mars 1979.

9 D.L. JOHNSTONE, Second order electromagnetic and hydrodynamic effects in highfrequency radio-wave scattering from sea, Technical Report n° 3615-3, March 1975, Center for radar Astronomy, Stanford Electronics Laboratories, Stanford University, Stanford California.

10 S.O. RICE, Reflection of electromagnetic waves from slightly rough surfaces, Communication on Pure and Applied Mathematics, Vol. 4, p. 351, August 1951.

11 A. ISHIMARU, Wave propagation and scattering in random media, Academic Press, New-York, San Francisco, London, Vol. 2, 1978.

12 P. BECKMANN, A. SPIZZICHINO, The scattering of electromagnetic waves from rough surfaces, Pergamon Press, Oxford, London, New-York, Paris 1963.

13 K.M. MITZNER, Change in polarisation on reflection from a tilted plane Radio-Science, Vol. 1, n° 1, January 1966.

14 P. BECKMANN, The depolarization of electromagnetic waves Golem Press, Boulder, Colorado, 1968.

15 P. BECKMANN, Shadowing of random rough surfaces, IEEE Transactions on Antennas and Propagation, AP-13, pp. 384-388, May 1965.

16 R.J. WAGNER, Shadowing of randomly rough surfaces, Journal of the Acoustical Society of America, Vol. 41, n° 1, pp. 138-147, 1967.

17 R.A BROCKELMAN, T. HAGFORS, Note on the effect of shadowing on the backscattering of waves from a random rough surface, IEEE, Transactions on Antennas and Propagation, Vol. AP-14, n° 5, pp. 621-629, September 1966.

18 B.G. SMITH, Geometrical shadowing of a random rough surface, IEEE, Transactions on Antennas and Propagation, Vol, AP-15, n° 5, pp. 668-671, September 1967.

19 E. MEDWIN, C.S. CLAY, Dependance of spatial and temporal correlation of forward scattered underwater sound on the surface statistics, Part I theory, Part II experiment, The Journal of the Acoustical Society of America, Vol. 47, Number 5 (part 2), pp. 1412-1429, 1970.

20 A.R. MULLER, R.M. BROWN, E. VEGH, New derivation for the rough surface reflection coefficient and for the destribution of sea-wave elevations, IEE, Proceeding, Vol. 131, Pt.H, n° 2, April 1984.

21 CCIR, Données sur la propagation nécessaires pour les services mobiles maritimes par satellite à des fréquences supérieures à 100 MHz (programme d'études 7C/5), CCIR XVIè assemblée plénière Dubrovnik, 1986, Document 5/1042-F, 14 janvier 1986.

22 R.D. KODIS, A note on the theory of scattering from an irregular surface, IEEE, Transactions on Antennas and Propagation, Vol. AP-14, n°1, pp. 77-82, January 1966.

23 J.E. SELTZER, Spatial densities for specular points on a Gaussian surface, IEEE, Transactions on Antennas on Propagation, Vol. AP-20, n° 6, pp. 723-731, November 1972.

24 D.E. BARRICK, Rough surface scattering based on the specular point theory, IEEE, Transactions on Antennas and Propagation, Vol. AP-16, n°4, pp. 449-454, July 1968.

25 M.S. LONGUET-HIGGINS, Reflection and refraction at a random moving surface, Part I Pattern and paths of specular points, Part II Number of specular point on a Gaussian surface, Journal of the Optical Society of America, Volume 50, NUmber 9, pp. 838-850, September 1960.

26 B.I. SEMENOV, An approximate calculation of electromagnetic wave from a slightly rough surface, Radiotekhnika i Electronika, Vol. 11, p. 1351, 1966.

27 B.I. SEMENOV, Computation of scattering of electromagnetic waves by a rough surface for arbitrary angles of observations, Radio Engeneering and Electronic Physics, Volume 15, n° 3, pp. 505-508, 1970.

28 J.W. WRIGHT, Backscattering from capillary wave with application to sea clutter, IEEE, Transactions on Antennas an Propagation, Vol. AP-14, n° 6, pp. 749-754, November 1966.

29 J.W. WRIGHT, A new model for sea clutter, IEEE, Transaction on Antennas and Propagation, Vol. AP-16 n° 2, pp. 217-223, March 1968.

30 D. DE STAERKE, Contribution expérimentale à l'interprétation des images de radar latéral en mer ; utilisation des données de scatteramètre sur plate-forme, Thèse, Université Pierre et Marie Curie, Paris, Décembre 1981.

31 M. FOURNIER, Trajets multiples sur la surface de la mer, AGARD, Conference Proceeding n° 345, Propagation factors affecting remote sensing by radio waves, Oberammergau 24-28, May 1983, AGARD, 7 rue Ancelle, 92200 Neuilly sur Seine, FRANCE.

32 D. BEGUIN, F. AURADON, M. FOURNIER, G. DUBIEN, Dispositifs de trajectographie à très basse altitude, Colloque international sur le radar, 21-24 mai 1934, Paris.

ROUGH SURFACE PROPAGATION AND SCATTER WITH APPLICATIONS TO GROUND WAVE REMOTE SENSING IN AN OCEAN ENVIRONMENT

John Walsh and Satish K. Srivastava
Faculty of Engineering and Applied Science
Memorial University of Newfoundland
St. John's, Newfoundland, Canada, A1B 3X5

SUMMARY

Some properties of the vector integral equation representing a general formulation for propagation and scattering from rough surfaces are discussed. It is shown that under certain conditions the equation may be reduced to a Volterra equation of the second kind in the normal component of the surface field for an initially unexcited surface, and hence some confidence may be had in a Neumann series or successive approximation solution. Using the formulation, the backscattered field solutions at ground wave frequencies and resulting radar cross section solutions derived previously for a model of the ocean surface are presented and discussed. The source assumed is a vertical pulsed dipole. The choice of receiving antenna is left arbitrary. The second-order cross section contains new terms in addition to those provided by existing theories. The additional terms may become very significant in certain Doppler frequency regions and hence required for ocean clutter estimation in the detection of certain types of surface targets. Some of the new predictions have been verified experimentally.

1. INTRODUCTION

The interaction of electromagnetic waves with the ocean surface has been a topic of investigation for many years. In particular, the analytical models of this interaction are used in the interpretation of ground wave Doppler returns in order to estimate ocean surface parameters, such as surface current and directional wave height spectra. Also these models are useful in understanding and prediction of contending ocean clutter, when using these radars for surface or low altitude target detection. The analytic models for ground wave radars have in the past been obtained largely by Rice's [1] perturbation method. Of particular interest is the work of Barrick [2], who has derived an average first- and second-order backscattered radar cross section for a patch of the ocean surface.

In a different approach, the authors have presented a general formulation for rough surface propagation and scattering problems based on the concept of generalized functions [3]. The technique utilizes a three dimensional (spatial and temporal) Fourier transform representation for the field quantities and requires in the most general case the solution of a pair of coupled vector integral equations for surface field quantities. However, under certain assumptions, (reasonable for the ocean at ground wave frequencies), on the refractive index and spatial frequency spectrum of surface and fields these equations may be reduced to a single vector integral equation in one unknown, which happens to be the electric surface field intensity. This, of course, is the primary quantity of interest for ground wave propagation and scattering. Using the integral equation for periodic surfaces, a Neumann series solution is derived for the surface field in the transform domain. As an application of the series solution in ground wave propagation and scattering, the source is taken to be an elementary vertical pulsed electric dipole. For this source, the first- and second-order expressions for the backscattered surface field for a model of the ocean surface have been developed elsewhere [4,5]. Consequently, the two orders of the backscattered radar cross section are derived. In this paper some properties of the above vector integral equation are discussed. It is shown that this equation for the normal component of the field may be reduced to a Volterra equation of the second kind when considering it in the time domain for an initially unexcited surface such as using a time pulsed source. This automatically brings the convergence properties of the Volterra equation into effect when generating a Neumann series or successive approximation solution. The field and cross section results derived in [4] and [5] are also presented and discussed.

2. ONE VIEW OF ROUGH SURFACE SCATTER

The starting point in the present discussion is the equation,

$$2\,\underline{\overset{+}{E}}_{s}^{z^-}\, e^{-z^- U_o} = \int_{x'} \left[|\overset{+}{n}(x')|^2\, \overset{++}{E}(x') - \frac{\overset{+}{R}^{+}(x')}{U_o} \right] e^{-f(x')U_o}\, e^{-j\overset{+}{x}' \cdot \overset{+}{K}}\, dx' . \qquad (1)$$

This equation is equation (64) in Walsh and Srivastava [3]. In Eq. (1) the function $f(x') = f(x,y)$ is the rough surface profile. $\overset{++}{E}$ is the electric field immediately

above the surface, i.e., the surface field. $\overset{+}{R}^{+}$ is a vector function related to $\overset{+}{E}^{+}$ and the normal derivatives of the field at the surface. The expression $\underline{\overset{+}{E}}_s^{z^-}$ refers to the electric source field (assumed to be above the surface) in a plane $z=z^- < f(x,y)$. The underbar denotes two dimensional $\underline{x} = (x,y)$ Fourier transform while $\underline{K} = (K_x, K_y)$ is the transform variable or spatial wavenumber. The vector $\overset{+}{n}$ is given by

$$\overset{+}{n}(x,y) = -f_x \hat{x} - f_y \hat{y} + \hat{z}$$

and is a vector normal to the surface. $U_o = (K^2 - k^2)^{1/2}$ where $k = \omega(\mu_o \varepsilon_o)^{1/2}$ is the free space radio wavenumber. The geometry is illustrated in figure 1.

In the most general case Eq. (1) is one of a pair of integral equations relating the source $\overset{+}{E}_s$ and the vector fields $\overset{++}{E}$ and $\overset{++}{R}$. A simultaneous solution of those two equations for $\overset{++}{E}$ and $\overset{++}{R}$ allows calculation of the scattering above and below and on the surface. In the case of a good conducting surface satisfying reasonable roughness conditions, relative to the source frequency, e.g., the interaction of high frequency (3-30 MHz) radio waves with ocean gravity waves, one integral equation may be approximately solved to give

$$\overset{++}{R}(x,y) = -\frac{n_1^2 - 1}{n_1^2} \overset{+}{\nabla}_{xy} (\overset{+}{n} \cdot \overset{++}{E}) - jkn_1 |\overset{+}{n}|^2 \overset{++}{E}_t - jk \left(\frac{1}{n_1}\right) |\overset{+}{n}|^2 \overset{++}{E}_n . \qquad (2)$$

Where $n_1^2 = \varepsilon_r - j\sigma/(\omega\varepsilon_o)$ is the square of the refractive index, $\overset{+}{\nabla}_{xy}$ denotes the two dimensional (x,y) gradient and the subscripts t and n denote tangential and normal components respectively. It should be mentioned that for many cases of interest, e.g. ground wave propagation and scatter the $\overset{++}{E}$ is the quantity of interest. Details of the formulation as well as the assumptions in arriving at Eq. (2) may be found in Walsh and Srivastava [3].

Also, in the above referenced paper, a series solution of Eqs. (1) and (2) is provided for a general periodic surface and for arbitrary source. This solution is given in the Fourier transform or spatial wavenumber domain and in terms of the surface Fourier coefficients. For this reason some of its properties are not immediately apparent, in particular when it is applied to problems involving time pulsed ground wave radar systems.

We note Eq. (1) may be written as,

$$2 \underline{\overset{+}{E}_s}^{z^-} e^{-z^- U_o} = (\underline{|\overset{+}{n}|^2 \overset{++}{E}} - \frac{1}{U_o} \underline{\overset{+}{R}^{+}}) - [\underline{|\overset{+}{n}|^2 \overset{++}{E} (1 - e^{-fU_o})} - \frac{1}{U_o} \underline{\overset{++}{R} (1 - e^{-fU_o})}]. \qquad (3)$$

Noting from Eq. (2) that $\overset{++}{R}$ is a linear function of $\overset{++}{E}$, then Eq. (3) may be interpreted as,

$$2 \underline{\overset{+}{E}_s}^{z^-} e^{-z^- U_o} = T_1 (\overset{++}{E}) - T_2 (\overset{++}{E}) , \qquad (4)$$

where the linear operators T_1 and T_2 have obvious definitions from Eq. (3). Assuming T_1 is invertable Eq. (4) may be rewritten as

$$T_1^{-1} (F_{xy}^{-1} (2 \underline{\overset{+}{E}_s}^{z^-} e^{-z^- U_o})) = \overset{++}{E} - T_1^{-1} T_2 (\overset{++}{E}) \qquad (5)$$

where F_{xy}^{-1} denotes inverse (x,y) Fourier transformation. Also recall underbars denote forward (x,y) Fourier transformation. The general formal solution of Eq. (5) is,

$$\overset{++}{E} = T_1^{-1} (F_{xy}^{-1} (2 \underline{\overset{+}{E}_s}^{z^-} e^{-z^- U_o})) + T_1^{-1} T_2 T_1^{-1} (F_{xy}^{-1} (2 \underline{\overset{+}{E}_s}^{z^-} e^{-z^- U_o})) + \ldots \qquad (6)$$

The evaluation of Eq. (6) requires initially the inversion of

$$2 \underline{\overset{+}{E}_s}^{z^-} e^{-z^- U_o} = \underline{|\overset{+}{n}|^2 \overset{++}{E}_o} - \frac{1}{U_o} \underline{\overset{++}{R}_o} , \qquad (7)$$

where $\overset{++}{E}_o$ and $\overset{++}{R}_o$ satisfy Eq. (2). Physically, Eq. (7) ignores the height effect e^{-fU_o}, this being accounted for in the subsequent terms in Eq. (6).

When Eq. (2) is inserted into Eq. (7) then the result may be written in two forms;

$$\frac{2U_o \overset{+z^-}{E_s} e^{-z^- U_o}}{U_o + jk\Delta} = \underline{|\hat{n}|^2 \overset{++}{E_{no}}} + \underline{|\hat{n}|^2 \overset{++}{E_{to}}} + \frac{1}{U_o + jk\Delta}\left[\underline{\vec{\nabla}_{xy}(|\hat{n}| E^+_{no})} + jk(n_1 - \Delta)\,\underline{|\hat{n}|^2 \overset{++}{E_{to}}}\right] \tag{8a}$$

$$\frac{2U_o \overset{+z^-}{E_s} e^{-z^- U_o}}{U_o + jkn_1} = \underline{|\hat{n}|^2 \overset{++}{E_{no}}} + \underline{|\hat{n}|^2 \overset{++}{E_{to}}} + \frac{1}{U_o + jkn_1}\left[\underline{\vec{\nabla}_{xy}(|\hat{n}| E^+_{no})} + jk(\Delta - n_1)\,\underline{|\hat{n}|^2 \overset{++}{E_{no}}}\right] \tag{8b}$$

In Eq. (8) we have set $\Delta = 1/n_1$ to conform with established notation. The vector projection operators,

$$\overset{+}{N} F_{xy}^{-1}(\overset{+}{E}) = \hat{n}\,\hat{n} \cdot F_{xy}^{-1}(\overset{+}{E})$$

$$\overset{+}{T} F_{xy}^{-1}(\overset{+}{E}) = F_{xy}^{-1}(\overset{+}{E}) - \overset{+}{N} F_{xy}^{-1}(\overset{+}{E})$$

may now be defined, where $\hat{n}$ is the outward unit normal to the surface. Applying $\overset{+}{N} F_{xy}^{-1}$ to Eq. (8a) and $\overset{+}{T} F_{xy}^{-1}$ to Eq. (8b) results in the two independent, but coupled, equations,

$$\overset{+}{N} F_{xy}^{-1}\left(\frac{2U_o \overset{+z^-}{E_s} e^{-z^- U_o}}{U_o + jk\Delta}\right) = |\hat{n}|^2 \overset{++}{E_{no}} + \overset{+}{N} F_{xy}^{-1}\left[\frac{1}{U_o + jk\Delta}\left\{\underline{\vec{\nabla}_{xy}(|\hat{n}| E^+_{no})} + jk(n_1 - \Delta)\underline{|\hat{n}|^2 \overset{++}{E_{to}}}\right\}\right] \tag{9a}$$

$$\overset{+}{T} F_{xy}^{-1}\left(\frac{2U_o \overset{+z^-}{E_s} e^{-z^- U_o}}{U_o + jkn_1}\right) = |\hat{n}|^2 \overset{++}{E_{to}} + \overset{+}{T} F_{xy}^{-1}\left[\frac{1}{U_o + jkn_1}\left\{\underline{\vec{\nabla}_{xy}|\hat{n}| E^+_{no})} - jk(n_1 - \Delta)\,\underline{|\hat{n}|^2 \overset{++}{E_{no}}}\right\}\right]. \tag{9b}$$

If the "good" conducting assumptions $U_o + jkn_1 \sim jkn_1$ and $jk(n_1 - \Delta) \sim jkn_1$ are made Eq. (9b) may be written as

$$jkn_1 |\hat{n}|^2 \overset{+}{E_{to}} \sim \overset{+}{T} F_{xy}^{-1}(2U_o \overset{+z^-}{E_s} e^{-z^- U_o} - \underline{\vec{\nabla}_{xy}(|\hat{n}| E^+_{no})}). \tag{10}$$

When Eq. (10) is substituted into Eq. (9a) and the result simplified the following equation relates the normal component of the surface field E^+_{no} and the source,

$$|\hat{n}|^2 E^+_{no} + \hat{n} \cdot F_{xy}^{-1}\left[\frac{\hat{n}\,\hat{n} \cdot \vec{\nabla}_{xy}(|\hat{n}| E^+_{no})}{U_o + jk\Delta}\right] = \hat{n} \cdot F_{xy}^{-1}\left[\frac{\hat{n}\,\hat{n} \cdot F_{xy}^{-1}(2U_o \overset{+z^-}{E_s} e^{-z^- U_o})}{U_o + jk\Delta}\right]. \tag{11}$$

If we now accept the asymptotic expression

$$F_{xy}^{-1}\left(\frac{1}{U_o + jk\Delta}\right) \sim F(\rho)\,\frac{e^{-jk\rho}}{2\pi\rho}$$

where F is the Sommerfeld attenuation function and $\rho = (x^2 + y^2)^{1/2}$ is the plane polar distance variable, then Eq. (11) takes the form,

$$E^+_{no} + \frac{\hat{n}}{|\hat{n}|^2} \cdot \left(\hat{n}\,\hat{n} \cdot \vec{\nabla}_{xy}(|\hat{n}| E^+_{no}) \underset{xy}{*} F(\rho)\,\frac{e^{-jk\rho}}{2\pi\rho}\right)$$

$$= \frac{\hat{n}}{|\hat{n}|^2} \cdot \left(\hat{n}\,\hat{n} \cdot F_{xy}^{-1}(2U_o \overset{+z^-}{E_s} e^{-z^- U_o}) \underset{xy}{*} F(\rho)\,\frac{e^{-jk\rho}}{2\pi\rho}\right), \tag{12}$$

where $\underset{xy}{*}$ denotes two dimensional (x,y) convolution.

3. QUASI-TIME DOMAIN EQUATION (TIME PULSE RADAR)

We now wish to interpret Eq. (12) in a time domain sense, in particular, for time pulsed ground wave radars in which periodic (assumed long compared with propagation times), single frequency (say ω_o) dominated pulses are transmitted. We assume that the following is valid:

1) the surface, hence $\hat{n}$, $\hat{n}$ etc., is considered time invariant (slowly varying with respect to propagation times, significant changes occurring only between pulses);

2) the surface is relaxed before excitation, which is assumed to occur at t = 0 for each pulse by time shifting, this requires

$$\overset{+}{E}^{+}(x,y,t) = h(t)\,\overset{+}{E}^{+}(x,y,t),$$

where h(t) is the Heaviside or unit step function;

3) $F_t^{-1}\left(F(\rho)\,\frac{e^{-jk\rho}}{2\pi\rho}\right) \sim F(\rho)\,\frac{\delta(t-\rho/c)}{2\pi\rho}$.

It is understood that the attenuation function F is now evaluated at $\omega = \omega_o$, where ω_o is the dominant pulse frequency. c is the vacuum velocity of light. $\delta(t)$ is the Dirac delta function. This assumption neglects the natural transient effects of the surface. An improvement on this may be found in Walsh [6].

A more detailed discussion of these assumptions is available in Srivastava's thesis [4].

By using the above Eq. (12) may be rewritten as,

$$E_{no}^{+}(x,y,t) + \frac{\hat{n}}{|\overset{+}{n}|^2}\cdot\left[\hat{n}\,\hat{n}\cdot\vec{\nabla}_{xy}\left(|\overset{+}{n}|\,E_{no}^{+}(x,y,t)\right) \underset{xyt}{*} F(\rho)\,\frac{\delta(t-\rho/c)}{2\pi\rho}\right]$$

$$= \frac{\hat{n}}{|\overset{+}{n}|^2}\cdot\left[\hat{n}\,\hat{n}\cdot F_{xyt}^{-1}\left(2U_o\,\overset{+z^-}{E_s}\,e^{-z^-U_o}\right) \underset{xyt}{*} F(\rho)\,\frac{\delta(t-\rho/c)}{2\pi\rho}\right], \qquad (13)$$

where $\underset{xyt}{*}$ denotes three dimensional (x,y,t) convolution. By changing variables and carrying out the t convolution on the left hand side of Eq. (13) an equation equivalent to Eq. (13) is,

$$E_{no}^{+}(x,y,t) + \frac{1}{2\pi}\int_0^t\int_0^{2\pi} F(ct')\left[\left(\frac{\hat{n}}{|\overset{+}{n}|^2}\,(x,y)\right)\cdot\left\{\left(\cos\theta_a\,(|\overset{+}{n}|\,\hat{n}\,n_x\,(u,v))\right.\right.\right.$$

$$\left. + \sin\theta_a\,(|\overset{+}{n}|\,\hat{n}\,n_y\,(u,v))\right)\overset{+}{E}_{no}^{+}(u,v,\,t-t')$$

$$\left.\left. - c\left(\left(|\overset{+}{n}|\,\overset{+}{\nabla}_{uv}\cdot\hat{n}\,\hat{n}\,(u,v)\right)E_{no}^{+}(u,v,\,t-t')\right)\right\}\right]\,d\theta_a\,dt'$$

$$= \left[\frac{\hat{n}}{|\overset{+}{n}|^2}\cdot\left\{\hat{n}\,\hat{n}\cdot F_{xyt}^{-1}\left(2U_o\,\overset{+z^-}{E_s}\,e^{-z^-U_o}\right) \underset{xyt}{*} F(\rho)\,\frac{\delta(t-\rho/c)}{2\pi\rho}\right\}\right], \qquad (14)$$

where, $u = x + ct'\cos\theta_a$, $v = y + ct'\sin\theta_a$

$$\overset{+}{\nabla}_{uv}\cdot\hat{n}\,\hat{n} = \frac{\partial}{\partial u}(n_x\,\hat{n}) + \frac{\partial}{\partial v}(n_y\,\hat{n})\ ,\ n_x = \hat{x}\cdot\hat{n},\ n_y = \hat{y}\cdot\hat{n}\ ,\ \overset{+}{E}_{no}^{+}(t) = \frac{\partial}{\partial t}E_{no}^{+}(t)$$

Equation (14) is clearly a Volterra type integral equation, hence, some confidence may be had in a Neumann series or successive approximations type solution. The smoothness of the kernel is not evident for a surface such as the ocean, however, even in this case, a generalized function or distribution interpretation should be possible. Eq. (14) also implies the Volterra nature of the more general Eq. (5) when interpreted as above.

4. BACKSCATTERED SURFACE FIELD FOR THE OCEAN SURFACE

The ocean surface, z = f(x,y,t), may be described by a three dimensional Fourier series in the sense of Rice [1] and Barrick [2] with random Fourier coefficients;

$$f(x,y,t) = \sum_{m,n,\ell} P_{m,n,\ell}\,\exp\left[j(mNx + nNy + \ell Wt)\right] \qquad (15)$$

where N is the fundamental wave number and W is the fundamental frequency. The symbol $\sum_{m,n,\ell}$ indicates a triple summation over the integers m,n and ℓ from $-\infty$ to ∞. The mean level of the surface is taken to be the z = 0 plane. Assuming ocean waves are, statistically, spatially homogeneous and temporally stationary, the following ensemble average may be defined [4,5]

$$\langle P_{m,n,\ell}\,P_{p,q,i}^{*}\rangle = \begin{cases} N^2W(2\pi)^{-3}\,S(mN,\,nN,\,\ell W)\ ,\ p = m,\ q = n,\ i = \ell \\ 0\ ,\ \text{otherwise} \end{cases}$$

where the asterisk (*) as a superscript denotes the complex conjugate. $S(mN, nN, \ell W)$ may be referred to as a three dimensional waveheight spectrum. It is symmetric in the sense that $S(mN, nN, \ell W) = S(-mN, -nN, -\ell W)$. Considering only deep water ocean gravity waves, in the limit N and W → 0, the three dimensional spectrum may be reduced to a non-symmetric two dimensional or directional waveheight spectrum as [5]

$$S(\vec{K},\Omega) = \pi[S(\vec{K})\ \delta\{\Omega + (g\,K)^{1/2}\} + S(-\vec{K})\ \delta\{\Omega - (g\,K)^{1/2}\}] \tag{16}$$

where $\vec{K} = K_x\,\hat{x} + K_y\,\hat{y}$ is the ocean wavenumber vector with magnitude K and Ω is the frequency. g is acceleration due to gravity. From these spectra the mean square surface displacement (h^2) may be given as

$$h^2 = \langle f^2(x,y,t)\rangle = \frac{1}{8\pi^3}\int_{K_x}\int_{K_y}\int_{\Omega} S(\vec{K},\Omega)\,d\Omega\,dK_y\,dK_x$$

$$= \frac{1}{4\pi^2}\int_{K_x}\int_{K_y} S(\vec{K})\,dK_y\,dK_x\ . \tag{17}$$

Using the series solution presented in Walsh and Srivastava [3], the first and second-order approximations of the vertical component of the backscattered surface field for the above ocean surface model have been derived. The mathematical details may be found in [4] and [5]. The source assumed is an elementary vertical electric dipole located close to the surface along the z-axis. It is excited by a pulsed sinusoidal current of peak value I_o and frequency ω_o with pulse duration τ_o. The expression for the first-order backscattered surface field, E_{sf}, is as follows;

$$E_{sf}(t_o,\ t') = \frac{2C_a\Delta_\rho}{(2\pi\rho_o)^{3/2}}\sum_{m,n,\ell} P_{m,n,\ell}\,F_o^2(\rho_o,\phi_m)\,g_r(\phi_m)\,(K_m)^{1/2}$$

$$\cdot\,(K_m - k_o)\,Sa[\Delta_\rho\,(K_m - 2k_o)]\,\exp[j(\rho_o K_m + \ell W t' - \tfrac{\pi}{4})] \tag{18}$$

where

$$\vec{K}_m = mN\,\hat{x} + nN\,\hat{y},\ K_m = |\vec{K}_m|,\ \phi_m = \tan^{-1}\left(\frac{n}{m}\right),\ Sa(x) = \frac{\sin x}{x} \tag{19}$$

$C_a = (-j\ 120\ \pi k_o)$ is the dipole constant for the transmitting antenna with $k_o = \omega_o/c$ as the transmitted wavenumber. $g_r(\theta)$ represents the free space field or voltage gain of the receiving antenna in a direction θ in azimuth with x-axis taken as the reference. t_o is the time delay between transmitted and received signals. This field is received from an angular section of a circular annulus of the surface located at a radial distance $\rho_o = ct_o/2$ from the antenna. The radial width of the angular section is $2\Delta_\rho = cr_o/2$. The angular width equals the beam width of the receiving antenna. For omnidirectional reception, the first order scattering region is the complete annulus. If the receiving antenna is narrow beam, the angular section reduces to a patch [5]. The variable t' in Eq. (18) refers to the temporal variation of the surface and hence the temporal variation of the received field from one pulse to another for a fixed t_o.

The function $F_o(\rho_o,\ \theta)$ in Eq. (18) is the same as the Sommerfeld attenuation function except the numerical distance contains $\Delta_o(\theta)$ instead of the normalized surface impedance Δ. $\Delta_o(\theta)$ is an average modified surface impedance and it takes into account the surface roughness also. It is dependent on the direction of propagation θ as the surface roughness may not necessarily be the same in all directions. The expression may be given as [5],

$$\Delta_o(\theta) = \Delta + \frac{1}{8\pi^2}\int_{K_x}\int_{K_y}\left[\frac{K^2\cos^2(\phi-\theta)}{(d+\Delta)} - \Delta\left\{\frac{k_o K\,d\,\cos(\phi-\theta)}{d+\Delta}\right.\right.$$

$$\left.\left. + \frac{1}{2}\,K^2\sin 2\phi\,\sin 2\theta\right\}\right]\,[S(\vec{K}) + S(-\vec{K})]\,dK_y\,dK_x \tag{20}$$

where

$$\vec{K} = K_x\,\hat{x} + K_y\,\hat{y}\ ,\ K = |\vec{K}|\ ,\ \phi = \tan^{-1}\left(\frac{K_y}{K_x}\right)$$

$$d = \begin{cases} \dfrac{1}{k_o}\,|K^2 + 2k_oK\cos(\phi-\theta)|^{1/2}\ ,\ \cos(\phi-\theta) < -\dfrac{K}{2k_o} \\ -\dfrac{j}{k_o}\,|K^2 + 2k_oK\cos(\phi-\theta)|^{1/2}\ ,\ \cos(\phi-\theta) > -\dfrac{K}{2k_o} \end{cases} \tag{21}$$

By using a surface wave formulation in Rice's [1] perturbation technique, Barrick [ ] has derived an expression for the average modified surface impedance. The above

expression appears somewhat different when compared with his expression. However, Dawe [8] has computed the surface impedance using both expressions for different sea conditions and at different frequencies and good numerical agreement is found.

In order to use the relatively simpler and more transparent solution given by Eq. (14), then the previous series solution given in [3] an expression for the first-order backscattered surface field has been recently derived, using the same source. The field derived in this way is denoted as E^1_{sf}.

$$E^1_{sf}(t_o,t') = \frac{2C_a\Delta_\rho}{(2\pi\rho_o)^{3/2}} F^2(\rho_o) \sum_{m,n,\lambda} g_r(\phi_m)\ (K_m)^{1/2}$$

$$\cdot\ (K_m-k_o)\ Sa[\Delta_\rho\ (K_m-2k_o)]\ \exp[j(\rho_o K_m + \lambda\omega t' - \tfrac{\pi}{4})]$$

$$\cdot\ [P_{m,n,\lambda} + \frac{2}{K_m(K_m-k_o)} \sum_{p,q,i} \sum_{u,v,w} P_{m-p,n-q,\lambda-i}\ P_{p-u,q-v,i-w}$$

$$\cdot\ P_{u,v,w}\ [(\vec{K}_{m-p}\cdot\vec{K}_{p-u})\ (K_u^2 - k_o\hat{K}_m\cdot\vec{K}_u) + (\vec{K}_{m-p}\cdot\vec{K}_u)\ (\vec{K}_{p-u}\cdot\vec{K}_u)]] \qquad (22)$$

where

$$\vec{K}_u = u\mathrm{N}\,\hat{x} + v\mathrm{N}\,\hat{y}\ ,\quad K_u = |\vec{K}_u|\ ,\quad \vec{K}_p = p\mathrm{N}\,\hat{x} + q\mathrm{N}\,\hat{y}\ ,\quad K_p = |\vec{K}_p|$$

$$\vec{K}_{m-p} = \vec{K}_m - \vec{K}_p\ ,\quad \vec{K}_{p-u} = \vec{K}_p - \vec{K}_u \qquad (23)$$

When comparing Eqs. (20) and (22), the two results appear to be somewhat different. The attenuation function in Eq. (20) contains the modified surface impedance Δ_o whereas it contains Δ in Eq. (22). On the otherhand there is a third order correction to the first order field in Eq. (22) whereas no such correction is there in Eq. (20). It is suspected that the change in the first order field caused indirectly by the modified surface impedance in Eq. (20) is equivalent to some extent to that produced by the third order effect in Eq. (22). However, this requires further investigation.

The second-order backscattered surface field derived from the series solution given in [3] consists of three parts,

$$E_{ss}(t_o,t') = E_{ss1}(t_o,t') + E_{ss2}(t_o,t') + E_{ss3}(t_o,t') \qquad (24)$$

The corresponding expressions are as follows [5];

$$E_{ss1}(t_o,t') = \frac{2C_a\Delta_\rho}{(2\pi\rho_o)^{3/2}} \sum_{p,q,i} \sum_{\substack{m,n,\lambda \\ (m,n)\neq(0,0)}} P_{p,q,i}\ P_{m-p,n-q,\lambda-i}\ g_r(\phi_m)$$

$$\cdot\ F_o^2\ (\rho_o,\phi_m)\ Sa[\Delta_\rho(K_m-2k_o)]\ \exp[j(\rho_o K_m + \lambda\omega t' - \tfrac{\pi}{4})]$$

$$\cdot\ [\frac{Q(m,n,p,q,\phi_m)}{\{K_m(K^2_{m-p} - \vec{K}_m\cdot\vec{K}_{m-p})\}^{1/2}} + H(m,n,\lambda,p,q,i)\ (K_m-k_o)\ (K_m)^{1/2}] \qquad (25)$$

$$E_{ss2}(t_o,t') = \frac{2C_a\Delta_\rho}{(2\pi\rho_o)^{3/2}} \sum_{p,q,i} \sum_{\substack{m,n,\lambda \\ (m,n)\neq(0,0)}} P_{p,q,i}\ P_{m-p,n-q,\lambda-i}\ g_r(\phi_p)\ F_o^2\ (\rho_o,\phi_p)$$

$$\cdot\ Sa[\Delta_\rho(K_p-2k_o)]\ \exp[j(\rho_o K_p + \lambda\omega t' - \tfrac{\pi}{4})]\ \frac{Q(m,n,p,q,\phi_p)}{\{K_p(K^2_{m-p} + \vec{K}_p\cdot\vec{K}_{m-p})\}^{1/2}} \qquad (26)$$

$$E_{ss3}(t_o,t') = \frac{C_a\Delta_\rho}{\pi^2\rho_o} \sum_{p,q,i} \sum_{\substack{m,n,\lambda \\ (m,n)\neq(0,0)}} P_{p,q,i}\ P_{m-p,n-q,\lambda-i} \int_{-\pi}^{\pi} F_o(r_b,\phi_b+\theta)$$

$$\cdot\ F_o(r_a,\phi_o+\theta+\pi)\ F_o(r_a,\theta+\pi)\ g_r(\theta)\ Sa[\Delta_\rho\{\xi(\beta_o,\alpha_o,\theta) - 2k_o\}]$$

$$\cdot\ \exp[j\rho_o\xi(\beta_o,\alpha_o,\theta)]\ \exp[j(\lambda\omega t' + \tfrac{\pi}{4}\,\mathrm{sig}\,A)]\ \frac{Q(m,n,p,q,\theta)}{(1+\cosh\beta_o)|\det A|^{1/2}}\,d\theta \qquad (27)$$

where the restriction $(m,n) \neq (0,0)$ means the summation indices m and n cannot be simultaneously equal to zero. ϕ_m and ϕ_p are the directions of the wavenumber vectors $\vec{K}_m$ and $\vec{K}_p$. K_{m-p} and ϕ_{m-p} are the magnitude and direction respectively of $\vec{K}_{m-p}$. Other functions and symbols are defined below.

$$Q(m,n,p,q,\theta) = (p\cos\theta + q\sin\theta)\,[(m+p)(k_o\cos\theta - mN) + (n+q)\,(k_o\sin\theta - nN)]\,N^2k_o - (p^2+q^2)\,[m(k_o\cos\theta - mN) + n(k_o\sin\theta - nN)]\,N^3$$

$$H(m,n,\ell,p,q,i) = \frac{1}{2}\left[K_p + K_{m-p} + (K_pK_{m-p} - \vec{K}_p \cdot \vec{K}_{m-p})\left(\frac{g\,K_m + \ell^2W^2}{g\,K_m - \ell^2W^2}\right)\left(\frac{g}{i(\ell-i)W^2}\right)\right] \tag{28}$$

$$r_a = \frac{2\rho_o}{(1+\cosh\beta_o)}$$

$$r_b = \frac{\rho_o(\cosh\beta_o + \cos\alpha_o)}{(1+\cosh\beta_o)}\ , \quad \phi_b = \tan^{-1}\left[\frac{\sinh\beta_o\sin\alpha_o}{\cosh\beta_o\cos\alpha_o + 1}\right]$$

$$r_c = \frac{\rho_o(\cosh\beta_o - \cos\alpha_o)}{(1+\cosh\beta_o)}\ , \quad \phi_c = \tan^{-1}\left[\frac{\sinh\beta_o\sin\alpha_o}{\cosh\beta_o\cos\alpha_o - 1}\right]$$

$$\xi(\beta,\alpha,\theta) = \frac{1}{(1+\cosh\beta)}\,[2K_p\cos(\phi_p-\theta) + K_{m-p}\sinh\beta\sin\alpha\sin(\phi_{m-p}-\theta) + K_{m-p}\,(1+\cosh\beta\cos\alpha)\cos(\phi_{m-p}-\theta)] \tag{29}$$

det A and sig A are the determinant and signature of the matrix A, where A is given as

$$A = \begin{bmatrix} \frac{\partial^2\xi}{\partial\beta^2} & \frac{\partial^2\xi}{\partial\alpha\partial\beta} \\ \frac{\partial^2\xi}{\partial\beta\partial\alpha} & \frac{\partial^2\xi}{\partial\alpha^2} \end{bmatrix} \tag{30}$$

Both det A and sig A should be evaluated at $\beta = \beta_o$ and $\alpha = \alpha_o$. β_o is the solution of the equation,

$$a_1\cosh^2\beta + a_2\cosh\beta + a_3 = 0\ , \tag{31}$$

where

$$a_1 = 4\,K_p^2\cos^2(\phi_p-\theta) + 4K_p\,K_{m-p}\cos(\phi_p-\theta)\cos(\phi_{m-p}-\theta) + \frac{a_2}{2}$$

$$a_2 = -2\,K_{m-p}^2\sin^2(\phi_{m-p}-\theta)$$

$$a_3 = -\sin^2(\phi_{m-p}-\theta)\,(K_{m-p}^2 + a_1 - \frac{a_2}{2})\ , \tag{32}$$

such that β_o is real, non-zero and it satisfies the following equation,

$$[2K_p\cos(\phi_p-\theta) + K_{m-p}\cos(\phi_{m-p}-\theta)]\cos(\phi_{m-p}-\theta)\cosh\beta_o\,[1+\tanh^2\beta_o \cdot \tan^2(\phi_{m-p}-\theta)]^{1/2} = K_{m-p}\,\mathrm{sgn}[\beta_o\tan(\phi_{m-p}-\theta)]\,[\sin^2(\phi_{m-p}-\theta) + \cosh\beta_o]. \tag{33}$$

sgn(x) is the sign function defined as

$$\mathrm{sgn}(x) = \begin{cases} 1\ , & x > 0 \\ -1\ , & x < 0\ . \end{cases} \tag{34}$$

Having obtained β_o, α_o may be derived from

$$\tan\alpha_o = \tanh\beta_o\,\tan(\phi_{m-p}-\theta) \tag{35}$$

such that $0 < \alpha_o < \pi$. It may be seen that β_o and α_o are functions of wavenumber vectors $\vec{K}_m$, $\vec{K}_p$ and the integration variable θ.

The first part (E_{zs1}) represents the case where the two scatterings occur on the angular section of the annulus defined by the first-order scattering. This part also includes the second order hydrodynamic term derived by Weber and Barrick [9], which is represented by the function H in Eq. (25). The second part (E_{zs2}) represents the case where a first scattering occurs at the source point and the second scattering occurs on the angular section. Lastly, the third part (E_{zs3}) represents the case where the two scatterings occur off the annulus. r_b is the distance between the source and a first scattering point. r_c is the distance between the first and a second scattering points. r_a represents the distance between the second scattering point and the receiving (or source) point. The corresponding three directions measured with respect to the x-axis are $(\phi_b + \theta)$, $(\phi_c + \theta + \pi)$ and $(\theta + \pi)$. It should be mentioned that Eqs. (25) to (27)

are valid provided the respective square root term in the denominator is not zero. However, these expressions are used in deriving the cross section with due regard to the regions of their validity.

Thus it may be seen that for a given time delay t_o between transmitted and received signals, the first-order field is received from an angular section of the surface. On the other hand the second-order field is received from the angular section as well as from other regions of the surface, all arriving at the same time. The additional two second-order parts (E_{zs2} and E_{zs3}) may be viewed as the effect of interaction of the source with the surrounding surface and the multipathing effect respectively.

5. BACKSCATTERED RADAR CROSS SECTION

In deriving an average backscattered ground wave radar cross section for the model of the ocean surface it is assumed: (i) the three parts of the second-order field given above are uncorrelated, (ii) the probability distribution of the surface displacement is Gaussian with zero mean. In this event cross power spectra are zero and hence the average power spectrum of the received signal may be given as

$$P_r(\omega_d) = P_f(\omega_d) + P_{s1}(\omega_d) + P_{s2}(\omega_d) + P_{s3}(\omega_d), \tag{36}$$

where $\omega_d = (\omega - \omega_o)$ is the Doppler frequency. P_f is the first-order spectrum corresponding to first-order field (E_{zf}). P_{s1}, P_{s2} and P_{s3} are the three parts of the second-order spectrum corresponding to the three parts of the second-order field.

For convenience we introduce the standard radar range equation for the average backscattered power spectrum (P_{rp}) received from a small patch of the ocean surface located at a distance ρ_o in a direction θ_o [2,5],

$$P_{rp}(\omega_d) = \frac{P_t G_{tp} G_{rp} \lambda_o^2}{(4\pi)^3 \rho_o^4} |F_p|^4 \sigma_p(\omega_d) \qquad \text{(W/Hz)} \tag{37}$$

where P_t is the average transmitted power. G_{tp} and G_{rp} are the free space power gains of transmitting and receiving antennas in the direction θ_o. λ_o is the radar wavelength. $F_p = F_o(\rho_o, \theta_o)$ is the one way ground wave attenuation function between the radar and the patch. $\sigma_p(\omega_d)$ is the average Doppler frequency dependent backscattered cross-section (spectrum in m^2/Hz) of the patch. Also,

$$\sigma_p^o = \frac{1}{2\pi} \int_{\omega_d} \sigma_p(\omega_d)\, d\omega_d \qquad (m^2) \tag{38}$$

where σ_p^o is the backscattered cross section of the patch for ground wave radars. Although the backscattered signal for a narrow or wide beam receiving antenna is not just received from the patch only, we may treat it as if it was for determining the cross section. In other words both first- and second-order scattering regions may be taken equivalent to the patch for this purpose. In this sense we may say $P_r(\omega_d) = P_{rp}(\omega_d)$. This in turn implies from Eq. (36)

$$\sigma_p(\omega_d) = \sigma_f(\omega_d) + \sigma_{s1}(\omega_d) + \sigma_{s2}(\omega_d) + \sigma_{s3}(\omega_d) \tag{39}$$

where σ_f is the first-order cross section. σ_{s1}, σ_{s2} and σ_{s3} are the respective three parts of the second-order cross section. These cross sections have been derived in [5]. The results are presented here.

First-Order

The first-order cross section may be given as

$$\sigma_f(\omega_d) = \frac{8 A_a \Delta_\rho |\omega_d|^5}{|F_p|^4 G_{rp} \pi g^3 (\theta_2 - \theta_1)} \left(\frac{\omega_d^2}{g} - k_o\right)^2 Sa^2\left[\Delta_\rho \left(\frac{\omega_d^2}{g} - 2k_o\right)\right] \cdot \int_{\theta_1}^{\theta_2} G_r(\phi) |F_o(\rho_o, \phi)|^4 S(-2\nu^2 \operatorname{sgn}(\nu) \vec{k}_o)\, d\phi \tag{40}$$

where $\nu = \omega_d/\omega_B$, $\omega_B = (2gk_o)^{1/2}$ is the well known Bragg frequency [2]. $\vec{k}_o = k_o \cos\phi\, \hat{x} + k_o \sin\phi\, \hat{y}$ is the incident radar wavenumber vector. $A_a = 2\rho_o \Delta_\rho (\theta_2 - \theta_1)$ is the area of the angular section responsible for first-order scattering. $G_r(\phi)$ is the free space power gain of the receiving antenna with $\theta_1 < \phi < \theta_2$. The angular range of the

receive beam is arbitrarily taken from θ_1 to θ_2. Assuming a large Δ_ρ, the limit of the squared sampling function $[Sa^2(x)]$ may be taken to be the Dirac delta function. In this event Eq. (40) reduces to

$$\sigma_f(\omega_d) = \frac{16\, k_o^4\, A_a}{|F_p|^4\, G_{rp}\, (\theta_2 - \theta_1)} \sum_{m=\pm 1} \delta(\omega_d + m\omega_B) \int_{\theta_1}^{\theta_2} G_r(\phi)\, |F_o(\rho_o, \phi)|^4 S(2m\, \vec{k}_o)\, d\phi \tag{41}$$

where m = 1 and -1 for summation.

A comparison of the above two equations shows that Eq. (40) contains two peaks at $\pm\omega_B$ and around the peaks the cross section is a continuum but rapidly decaying due to the squared sampling function. Whereas Eq. (41) gives two spikes or impulses at $\pm\omega_B$. For narrow beam reception, θ_1 and θ_2 reduce to $(\theta_o - \Delta_\theta)$ and $(\theta_o + \Delta_\theta)$, where θ_o is the look direction and $2\Delta_\theta$ is the beam width of the receiving antenna. The first-order scattering region then reduces to the patch. Under this condition the integral in Eq. (40) or (41) may be easily evaluated by approximating the integrand at $\phi = \theta_o$. Proceeding with Eq. (41) the result would then be the same as that derived by Barrick [2] when interpreted in our notation.

In deriving Eq. (40) the field equation used is (20). If Eq. (22) is used instead, the first-order cross section (σ_f') is given as follows:

$$\sigma_f'(\omega_d) = \frac{8\, A_a \Delta_\rho\, |\omega_d|^5}{|F_p|^4\, G_{rp}\, \pi g^3 (\theta_2 - \theta_1)} \frac{|F(\rho_o)|^4}{} \left(\frac{\omega_d^2}{g} - k_o\right)^2 Sa^2\left[\Delta_\rho \left(\frac{\omega_d^2}{g} - 2k_o\right)\right]$$

$$\cdot \int_{\theta_1}^{\theta_2} G_r(\phi)\, S(-2v^2\, \mathrm{sgn}(v)\, \vec{k}_o)\, C^2(v,\phi)\, d\phi \tag{42}$$

where

$$C(v,\phi) = 1 - \frac{1}{2\pi^2} \int_{K'=0}^{\infty} \int_{\phi=-\pi}^{\pi} K'^3\, S(\vec{K}')\, \left[1 + \left(\frac{v^2-1}{v^2-0.5}\right) \cos^2(\phi - \phi')\right] d\phi' dK' \tag{43}$$

$$\vec{K}' = K' \cos\phi'\, \hat{x} + K' \sin\phi'\, \hat{y}.$$

If the effect of surface roughness on the attenuation function is ignored in Eq. (40), the two expressions σ_f and σ_f' for the first-order cross section are the same except σ_f' contains a modifying factor $C^2(v,\phi)$. For estimating its effect on the first order peaks (v = 1), the integral in Eq. (43) is evaluated using the Neumann-Pierson model for one dimensional waveheight or frequency spectrum [4]. The factor C simplifies to $[1 - C_n U g^{-3} (\pi/2)^{3/2}]$, where U is the wind speed in m/s and $C_n = 3.05\ m^2/s^5$ is a constant. At a typical wind speed of 30 knots, C^2 gives a reduction in the first order peaks by 0.9 dB. Eq. (42) may also be reduced in the form of (41) containing two impulses at $\pm\omega_B$. In that case the factor C^2 would give the reduction in the weights of delta functions, e.g., 0.9 dB at 30 knots wind speed.

Second-Order

(i) The first part of the second-order cross section may be given as [5],

$$\sigma_{s1}(\omega_d) = \frac{4k_o^4\, A_a}{|F_p|^4\, G_{rp}\, \pi^2 (\theta_2 - \theta_1)} \sum_{m,m'=\pm 1} \int_{\phi=\theta_1}^{\theta_2} G_r(\phi)\, |F_o(\rho_c, \phi)|^4$$

$$\cdot \int_p \int_q |C_e + C_h|^2\, S(m\, \vec{K}_1)\, S(m'\vec{K}_2)\, \delta[\omega_d - m(g\, K_1)^{1/2} - m'(g\, K_2)^{1/2}]\, dq\, dp\, d\phi \tag{44}$$

where m = 1, -1 and m' = 1, -1 for summation.

$$\vec{K}_1 = (p - k_o \cos\phi)\, \hat{x} + (q - k_o \sin\phi)\, \hat{y}, \qquad K_1 = |\vec{K}_1|$$

$$\vec{K}_2 = -(p + k_o \cos\phi)\, \hat{x} - (q + k_o \sin\phi)\, \hat{y}, \qquad K_2 = |\vec{K}_2|$$

$$C_e = \frac{1}{2} \frac{[k_o^2 - (p\cos\phi + q\sin\phi)^2 - 2\vec{K}_1 \cdot \vec{K}_2]}{(\vec{K}_1 \cdot \vec{K}_2)^{1/2}} \tag{45}$$

$$C_h = -\frac{j}{2} \left[K_1 + K_2 + \frac{(K_1 K_2 - \vec{K}_1 \cdot \vec{K}_2)\, (\omega_B^2 + \omega_d^2)}{m\, m' (K_1 K_2)^{1/2}\, (\omega_B^2 - \omega_d^2)}\right]$$

C_e and C_h are the second-order electromagnetic and hydrodynamic contributions, respectively. The part containing C_e in Eq. (44) is valid provided C_e is not singular. This singularity corresponds to the square root term in the denominator becoming zero in the field expression (25).

(ii) The second part of the second-order cross section may be given as [5],

$$\sigma_{s2}(\omega_d) = \frac{2k_o^4 A_s}{|F_p|^4 G_{rp} \pi^2(\theta_2 - \theta_1)} \sum_{m,m'=\pm 1} \int_{\phi=\theta_1}^{\theta_2} G_r(\phi) |F_o(\rho_o,\phi)|^4 \cdot \int\int_{p\,q} \frac{[(\vec{K}_1 + \vec{k}_o) \cdot \vec{K}_1]^2}{|(\vec{K}_1 + 2\vec{k}_o) \cdot \vec{K}_1|} S(m\vec{K}_1)\, S(2m'\vec{k}_o)\, \delta[\omega_d + m(g K_1)^{1/2} + m'\omega_B]\, dq\, dp\, d\phi \quad (46)$$

where

$$\vec{K}_1 = p\,\hat{x} + q\,\hat{y}, \qquad K_1 = |\vec{K}_1|, \qquad \vec{k}_o = k_o \cos\phi\,\hat{x} + k_o \sin\phi\,\hat{y}. \quad (47)$$

Again, Eq. (46) is valid provided the integrand is not singular. This singularity corresponds to the square root term in the denominator becoming zero in the field expression (26).

(iii) The third part of the second-order cross section is as follows [5]:

$$\sigma_{s3}(\omega_d) = \frac{A_s \rho_o \Delta_\rho}{|F_p|^4 G_{rp} \pi^4(\theta_2 - \theta_1)} \sum_{m,m'=\pm 1} \int_{\theta=\theta_1}^{\theta_2} \int_{\theta'=\theta_1}^{\theta_2} [G_r(\theta)\, G_r(\theta')]^{1/2} \cdot \int_{K_1=0}^{\infty} \int_{\phi_1=-\pi}^{\pi} \int_{K_2=0}^{\infty} \int_{\phi_2=-\pi}^{\pi} F_r(r_{ts}, \Phi_{bs} + \theta)\, F_o^*(r'_{bs}, \Phi'_{bs} + \theta')\, F_o(r_{cs}, \Phi_{cs} + \theta + \pi)$$

$$\cdot F_o^*(r'_{cs}, \Phi'_{cs} + \theta' + \pi)\, F_o(r_{as}, \theta + \pi)\, F_o^*(r_{as}, \theta' + \pi)\, Q_s\, Q'_s\, K_1\, K_2\, \mathrm{Sa}[\Delta_\rho (\xi_s - 2k_o)]$$

$$\cdot \mathrm{Sa}[\Delta_\rho(\xi'_s - 2k_o)]\, \frac{\exp[j\rho_o(r_s - r'_s) + j\frac{\pi}{4}(\mathrm{sig}\, A_s - \mathrm{sig}\, A'_s)]}{(1 + \cos h\beta_s)(1 + \cos h\beta'_s)\,|\det A_s \det A'_s|^{1/2}} S(\pi\vec{K}_1)\, S(m'\vec{K}_2)$$

$$\cdot \delta[\omega_d + m(g K_1)^{1/2} + m'(g K_2)^{1/2}]\, d\phi_2\, dK_2\, d\phi_1\, dK_1\, d\theta'\, d\theta \quad (48)$$

where

$$\vec{K}_1 = K_{1x}\,\hat{x} + K_{1y}\,\hat{y}, \qquad K_1 = |\vec{K}_1|, \qquad \phi_1 = \tan^{-1}(K_{1y}/K_{1x})$$

$$\vec{K}_2 = K_{2x}\,\hat{x} + K_{2y}\,\hat{y}, \qquad K_2 = |\vec{K}_2|, \qquad \phi_2 = \tan^{-1}(K_{2y}/K_{2x}). \quad (49)$$

Other symbols and functions may be defined with the help of Eqs. (28) to (35) associated with the corresponding field expression (27) by first substituting $K_{1x} = pN$, $K_{1y} = qN$, $K_{2x} = (m-p)N$ and $K_{2y} = (n-q)N$ in those equations. r_{bs}, r_{cs}, r_{as}, Φ_{bs}, Φ_{cs}, Q_s, ξ_s, sig A_s, det A_s, β_s and α_s are then, respectively, equivalent to r_b, r_c, r_a, Φ_b, Φ_c, Q, ξ, sig A, det A, β_o and α_o appearing in Eq. (27). By replacing θ with θ' we similarly obtain r'_{bs}, r'_{cs}, r'_{as}, Φ'_{bs}, Φ'_{cs}, Q'_s, ξ'_s, sig A'_s, det A'_s, β'_s and α'_s. Again, Eq. (48) is valid provided the integrand is not singular. The singularity corresponds to the square root term in the denominator becoming zero in the field equation (27).

The equations (44), (46) and (48) thus represent three parts of the second-order Doppler frequency dependent backscattered cross section of the ocean surface. The expressions are applicable to any receiving antenna configuration, e.g., narrow beam or wide beam. The transmitting antenna is assumed to be omnidirectional. It may be again mentioned that strictly speaking these three equations do not represent the second-order cross section of the patch. However, they have been derived as if the total scattering region is equivalent to the patch in the sense $P_r(\omega_d) = P_{rp}(\omega_d)$. On the other hand σ_{s1} represents the case where both first and second scatterings occur on the angular section of the circular annulus. The section which is also the scattering region for the first-order is bounded by $(\rho_o - \Delta_\rho) < \rho < (\rho_o + \Delta_\rho)$ and $\theta_1 < \theta < \theta_2$. σ_{s2} represents the case where the first scattering occurs at the source point and the second scattering falls on the angular section. σ_{s3} represents the case where the two scatterings occur off the angular section.

Consider now the case of narrow beam reception. The angular section reduces to the patch with $\theta_1 = (\theta_o - \Delta_\theta)$ and $\theta_2 = (\theta_o + \Delta_\theta)$, where θ_o is the look direction. Under this condition, the ϕ integral in Eqs. (44) and (46) may be easily evaluated by approximating the integrand at $\phi = \theta_o$. A problem remains with σ_{s3}. An inspection of

Eq. (48) shows that the approximation $\theta = \theta' = \theta_0$ in the integrand may not be justified due to the highly oscillatory exponential term present in the integrand. However, we may approximate β_s, α_s, β_s' and α_s' at $\theta = \theta' = \theta_0$ and then perform the stationary phase integrations with respect to θ and θ' treating ρ_0 as the large parameter. This approximation for β_s to α_s' simplifies the solution for stationary points with respect to θ and θ'. As a result the arguments of the two sampling functions become equal. Assuming a large Δ_ρ the limit of the squared sampling function may then be taken as the Dirac delta function. In this way the number of integrals in Eq. (48) may be reduced significantly and thus provide a relatively easy computation of σ_{s3} as given in [10].

For the above narrow beam conditions, Barrick [2] (also [11]) has previously derived an expression for the second-order cross section using a different technique. His cross section result corresponds to σ_{s1}. A comparison of our result for σ_{s1} with that derived by Barrick shows that both solutions are the same except for one difference. In his result, when interpreted in our notation, the denominator for C_e contains $[(\vec{K}_1 \cdot \vec{K}_2)^{1/2} + k_0\Delta^*]$ instead of $(\vec{K}_1 \cdot \vec{K}_2)^{1/2}$, where Δ^* is the complex conjugate of the normalized surface impedance. Since $|k_0\Delta^*|$ is very small for the ocean surface at HF or lower radio frequencies, the effect of $(k_0\Delta^*)$ on C_e is negligible except when $(\vec{K}_1 \cdot \vec{K}_2)^{1/2}$ is almost zero. But then our result is not valid when $(\vec{K}_1 \cdot \vec{K}_2) = 0$ as mentioned before. A new analytic estimate of σ_{s1} shows no such singularity. However, the expression is not given here because of its complexity. Hence it may be said that the apparent singularity in the present σ_{s1} is the result of the approximate integration technique. A plane wave incidence is used in Barrick's analysis which accounts for the double scattering occuring on the patch only and hence his result does not contain the two additional second-order cross section terms, σ_{s2} and σ_{s3}. In the present work a pulsed dipole source is used which does not limit the scattering region to the patch only. A discussion on the additional second-order cross section terms is given in Srivastava and Walsh [12,13].

To show the individual effects of the three parts of the second-order cross section some examples have been presented here. For computational ease, especially for σ_{s3}, only narrow beam reception is considered. Also, for computational purposes Δ is used instead of the modified surface impedance (Δ_0) for evaluating the attenuation functions in σ_{s3}. The oceanographic model used for the directional wave height spectrum is the Pierson-Moskowitz frequency spectrum with a cardioid directional distribution [4]. Figure 2 shows the individual spectrum of σ_{s1}, σ_{s2} and σ_{s3} normalized to the patch area for a 10 MHz radar frequency and figure 3 at 25.4 MHz. The wind velocity is assumed to be 30 knots at 45° with reference to the direction of the patch. Figures 4 and 5 show similiar plots at 90° wind condition (cross wind). Not shown in the plots are the two first-order peaks at $\pm\omega_B$, which lie in the null regions of σ_{s1}. It may be mentioned that these plots are based on the assumption that the sea is fully developed in the total scattering region including the region surrounding the radar, e.g., a ship or an offshore platform based radar.

The shape of the second-order spectrum given by σ_{s1} is well known [2,11]. The spectrum of σ_{s2} is produced by all ocean waves present at the transmitting antenna but by only two waves on the patch, with wavenumbers $2k_0$, one moving towards and the other away from radar. The resulting spectrum has a much slower cutoff than that of σ_{s1}. It has peaks at zero Doppler and at $\omega_d = \pm 2\omega_B$. A study of Eq. (46) shows that these peaks may be viewed as a repeated first-order phenomenon, first at the source, then on the patch. Figures 6 and 7 show Doppler spectra measured by Barrick [14] in the North Sea with an offshore platform based radar operating at 25.4 MHz. The second-order peaks predicted by σ_{s2} are clearly present in the measured spectra in addition to the standard peaks produced by σ_{s1} and the two first-order peaks. Referring again to figures 2 to 5 the spectrum of σ_{s3} is now considered. The spectrum is significantly lower than that of σ_{s1} at all Dopplers except at $\omega_d = 0$ and near $\pm 2^{3/4}\,\omega_B$, but not at $\pm 2^{3/4}\omega_B$ (corner reflector point). In these regions it is higher than or comparable to σ_{s1}. Based on the plots it may be inferred that the contribution to the second-order cross section by σ_{s2} is very significant around zero Doppler and in the region $|\omega_d| > 2^{3/4}\,\omega_B$. The contribution of σ_{s3} is small in comparison to σ_{s1} plus σ_{s2} except near $\pm 2^{3/4}\,\omega_B$. Also, the Doppler regions near $\pm\,\omega_B$, which are commonly used for estimating ocean wave parameters [11], are relatively unaffected by the additional terms. Therefore, in these regions the second-order cross section may be adequately described by σ_{s1} alone. On the other hand in target detection σ_{s2} and σ_{s3} may be very important in modelling the contending ocean clutter when the target Doppler frequency is around zero (for sea ice, icebergs and ships) or greater than $2^{3/4}\omega_B$ (for ships).

Consideration is now given to land based radars. In this case the antennas are generally located on the beach or near the shore. σ_{s2} may not be wholly present in this case. Also, a reduction in σ_{s3} may be expected as it does not account for any scattering occurring on the land. No change may be expected in σ_{s1}. Figure 8 shows spectra of σ_{s1} and σ_{s3} for such a condition at 10 MHz and figure 9 at 25.4 MHz. The wind velocity is taken as 30 knots at 45°. The shore line required for σ_{s3} is assumed to be perpendicular to the look direction. Compared to σ_{s1}, σ_{s3} is only effective near $|\omega_d| = 2^{3/4}\,\omega_B$. If there is a part of the sea behind the radar, σ_{s3} may be significant at zero Doppler also. It may be mentioned that another additional term in the second-order scattering has recently emerged from the analysis with sole contribution at the zero Doppler frequency. This contribution is presently under investigation.

6. CONCLUSIONS

A formulation for electromagnetic propagation and scattering from rough surfaces has been presented by the authors elsewhere [3]. It consists of a vector integral equation in the spatial and temporal Fourier transform domain some properties of which are discussed in this paper. It is shown that under certain conditions the equation may be effectively reduced to a single scalar integral equation for the normal component of the surface electric field. Further, when interpreted in the time domain for an initially unexcited surface, the integral equation is a Volterra equation of the second kind. This immediately provides a basis for convergence when solving the equation in the form of a Neumann series or successive approximation solution for a time pulsed source. Hence, some confidence may be had in the Neumann series solution generated in [3] for periodic surfaces.

As an application of the series solution in ground wave remote sensing in an ocean environment, first- and second-order expressions of the surface electric field for a model of the ocean surface are derived [4,5]. The source assumed is a vertical pulsed electric dipole located close to the surface. The choice of receiving antenna is kept open, e.g. a wide beam or narrow beam. Using the field results, the two orders of the average Doppler frequency dependent backscattered cross section are obtained [5]. In order to demonstrate the relatively simpler solution given by Eq. (14) than the previous series solution used in [4] and [5] an expression for the first-order field and the corresponding cross section solution are derived. It is interesting to note that the result derived this way estimates a slightly lower first-order cross section than predicted by the well known expression [2,11]. The reduction is due to interaction of primary scattering ocean waves with other ocean waves. This may be interpreted as a reduction in the coherency of return from the primary waves. If the effect of surface roughness on the attenuation function is ignored, a reduction in the first-order peaks by about 1 dB at 30 knots wind speed may be expected.

The second-order cross section consists of three parts, σ_{s1}, σ_{s2} and σ_{s3}, corresponding to three parts of the second-order field. The first part σ_{s1} is equivalent to the well known second-order cross section [2,11]. The additional two parts may be viewed as the effect of interaction of the source with the surrounding surface and multipathing effect on radar return respectively. The second part σ_{s2} gives peaks at zero Doppler and at $\pm 2\omega_B$, where ω_B is the Bragg frequency. These peaks may be viewed as a repeated first-order phenomenon, first at the source, then on the patch. This part also causes a slower cutoff of the total second-order spectrum. The contribution from the third part σ_{s3} is effective only at zero Doppler and at frequencies near $\pm 2^{3/4}\omega_B$. The Doppler regions near $\pm\omega_B$, which are commonly used for estimating ocean wave parameters [11], are relatively unaffected by the additional terms. Therefore, the second-order cross section may be adequately described by σ_{s1} for this purpose. On the other hand σ_{s2} and σ_{s3} may be very important in modelling the contending ocean clutter in target detection when the target Doppler frequency is around zero or greater than $2^{3/4}\omega_B$.

It may be mentioned that the above second-order discussion is based on the assumption that sea is fully developed in the scattering region including the region surrounding the radar, e.g., a ship or an offshore platform based radar. The second-order peaks predicted by σ_{s2} have been clearly observed in the Doppler spectra measured by Barrick [14] in the North Sea with an offshore platform based radar. In case the radar is located on the beach or near the shore, σ_{s2} may not be wholly present. Compared to σ_{s1}, σ_{s3} is only effective at frequencies near $\pm 2^{3/4}\omega_B$. However, depending upon the coastal topography if there is a part of the sea behind the radar σ_{s3} may be significant at the zero Doppler frequency also. Thus, this analysis constitutes a more complete model for the ground wave radar return from the ocean surface.

REFERENCES

[1] S.O. Rice, Reflection of electromagnetic waves from slightly rough surfaces, in Theory of Electromagnetic Waves, M. Kline, Ed., New York: Interscience, 1951, pp. 351-378.

[2] D.E. Barrick, Remote sensing of sea state by radar, in Remote Sensing of Troposphere, V.E. Derr, Ed., Washington, DC: U.S. Govt. Printing, 1972, ch. 12.

[3] J. Walsh and S.K. Srivastava, Rough surface propagation and scatter 1. General formulation and solution for periodic surfaces, Radio Sci., 22, 2, 1987, pp. 193-208.

[4] S.K. Srivastava, Memorial University of Newfoundland, St. John's, Canada, Scattering of high-frequency electromagnetic waves from an ocean surface: An alternative approach incorporating a dipole source, 1984, Ph.D. thesis, ch. 3 and 4 (available from Canadian theses on microform service, National Library of Canada, 395 Wellington Street, Ottawa, Canada).

[5] J. Walsh, S.K. Srivastava and B.J. Dawe, Memorial University of Newfoundland, St. John's, Canada, Analytic model development for the study of ground wave radars as remote sensors in an ocean environment, 1986, Tech. Rep. prepared for the Department of National Defence, Govt. of Canada, Ottawa, Canada (D.S.S. contract No. 25V84-00152), ch. 3.

[6] J. Walsh, Time-domain behaviour of electric field of an elevated dipole, Electron. Lett., 20, 21, 1984, pp. 889-890.

[7] D.E. Barrick, Theory of HF and VHF propagation across the rough sea, 1 and 2, Radio Sci., 6, 5, 1971, pp. 517-533.

[8] B.J. Dawe, Memorial University of Newfoundland, St. John's, Canada, Radio wave propagation over earth: Field calculations and an implementation of the roughness effect, 1987, M.Eng. thesis, ch. 3 (submitted for examination).

[9] B.L. Weber and D.E. Barrick, On the nonlinear theory for gravity waves on the ocean's surface, Part I: Derivations, J.Phys. Oceanogr., 7, 1, 1977, pp. 3-10.

[10] R. Howell, R.S. Srivastava, S.K. Srivastava and J. Walsh, Remote sensing of sea state using ground wave radars, Proc. Oceans 87 Conference, Halifax, Canada, Sept. 1987 (to appear).

[11] B.J. Lipa and D.E. Barrick, Methods for the extraction of long-period ocean wave parameters from narrow beam HF radar sea echo, Radio Sci., 15, 4, 1980, pp. 843-853.

[12] S.K. Srivastava and J. Walsh, An analysis of the second order Doppler return from the ocean surface, IEEE J. Ocean. Eng., OE-10, 4, 1985, pp. 443-445.

[13] S.K. Srivastava and J. Walsh, An analytical model for the HF backscattered Doppler spectrum for the ocean surface, IEEE J. Ocean. Eng., OE-11, 2, 1986, pp. 293-295.

[14] D.E. Barrick, Codar Ocean Sensors Ltd., 1823 Sunset Pl., Suite 6, Longmont, CO., U.S.A., private communication, 1987.

ACKNOWLEDGEMENTS

This work was supported by a research contract from the Canadian Department of National Defence and through a strategic grant from the Natural Sciences and Engineering Research Council, Govt. of Canada. The authors wish to thank D.E. Barrick of the Codar Ocean Sensors Ltd. for providing us with some of his radar data collected in the North Sea.

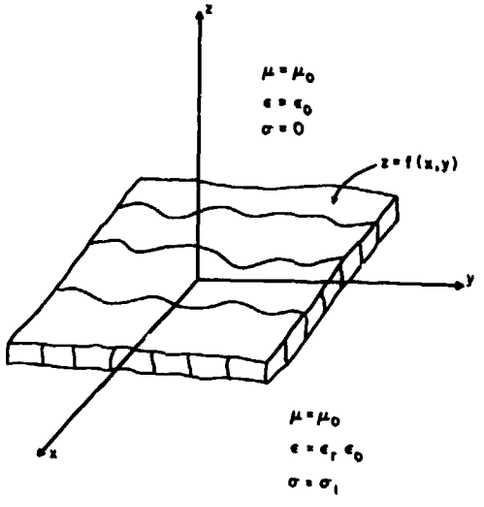


Fig. 1 Geometry of the surface

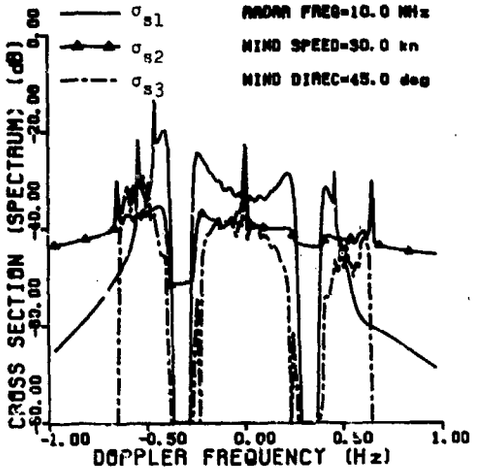


Fig. 2

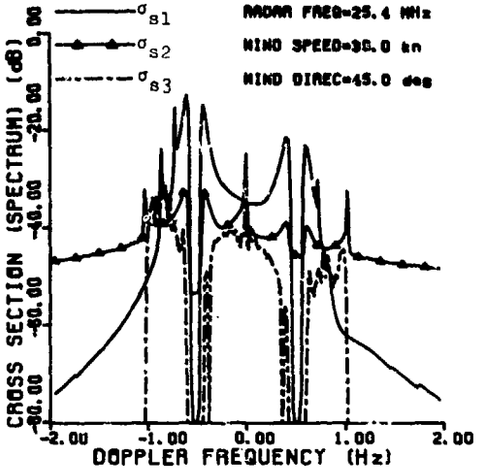


Fig. 3

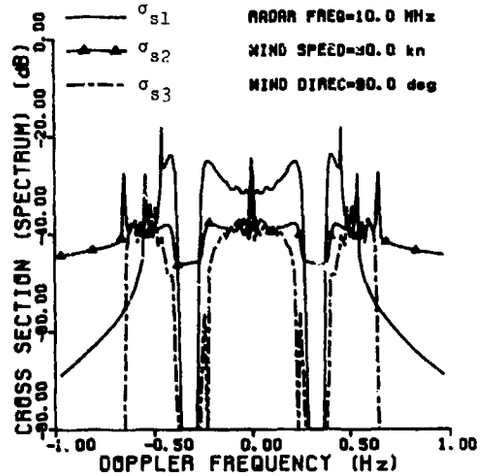


Fig. 4

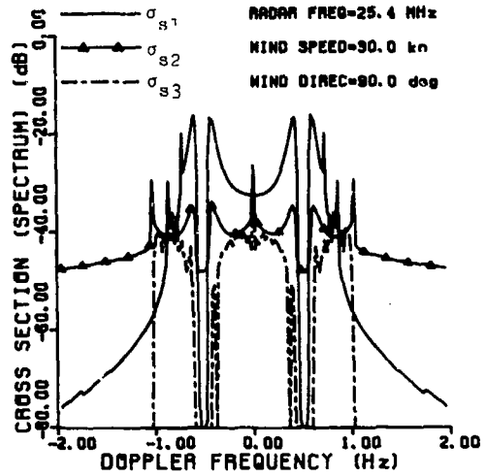


Fig. 5

Figs. 2 to 5. Three parts of the second-order backscattered cross section (spectrum) of the ocean surface patch normalized to its area at different radar frequencies and wind conditions for omnidirectional transmission and narrow beam reception (open sea condition).

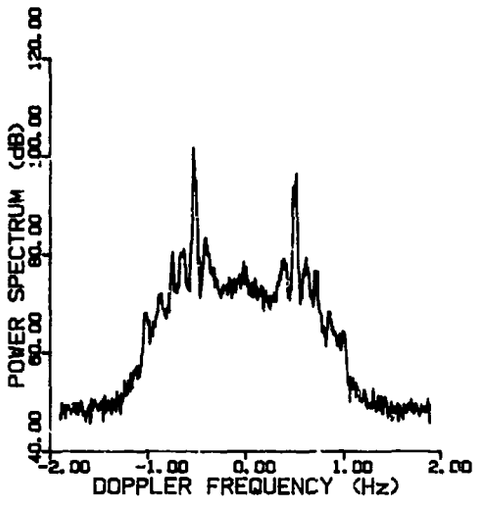


Fig. 6

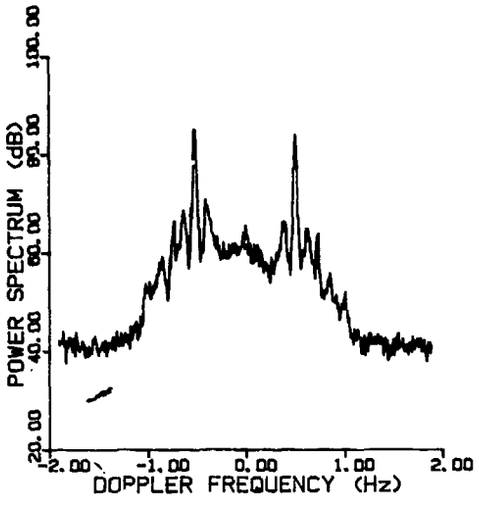


Fig. 7

Figs. 6 and 7. Measured backscattered power spectrum with an offshore platform based radar operating at 25.4 MHz (from Barrick [14]).

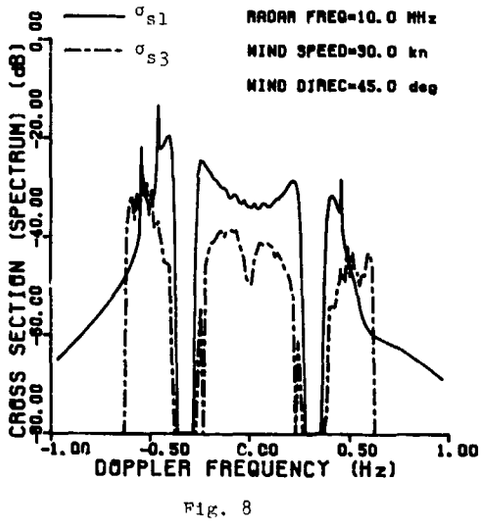


Fig. 8

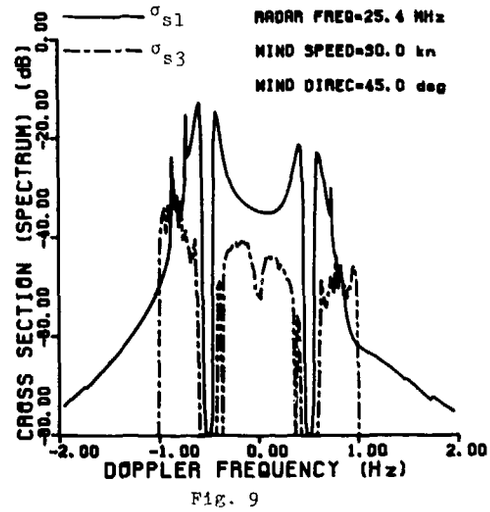


Fig. 9

Figs. 8 and 9. Two parts of the second-order backscattered cross section (spectrum) of the ocean surface patch normalized to its area at different radar frequencies for omnidirectional transmission and narrow beam reception (land based condition).

WAVE-TILT SOUNDING OF TROPOSPHERIC DUCTS ABOVE THE SEA

D.P.Chrissoulidis and E.E.Kriezis

Department of Electrical Engineering,Faculty of Technology,
Aristotle University of Thessaloniki,GR-54006 Thessaloniki,Greece.

SUMMARY

The possibility to detect tropospheric ducts above the sea through airborne wave-tilt measurements is investigated in this work. Sea roughness and tropospheric refractivity anomalies associated with the presence of ducts are incorporated in an iterative procedure resulting in wave-tilt versus frequency diagrams at some altitude above sea level. In general, the diagram corresponding to ducting conditions appears shifted by Δf with respect to the diagram of the standard troposphere. This frequency shift is rather insensitive to variations of sea state, duct thickness and optimum coupling height. It is though strongly dependent on duct intensity ΔM. The diagram Δf vs. ΔM is not far from linear in the VHF band thus offering itself for ΔM estimation through Δf measurements.

LIST OF SYMBOLS

a (m)	: earth's radius
f (Hz)	: frequency of electromagnetic wave
ε_0 (F/m)	: dielectric constant of free-space ($\approx 8.854\times10^{-12}$)
σ (mhos/m)	: conductivity of sea water (≈ 4)
N (N-units)	: refractivity of troposphere
M (M-units)	: modified refractivity of troposphere
D (m)	: duct thickness
h_{opt} (m)	: optimum coupling height
ΔM (M-units)	: duct intensity
h (m)	: height above sea level
Δf (Hz)	: frequency shift
Δ	: normalized surface impedance
Δ_{eff}	: normalized effective surface impedance
$\Delta(h)$	: normalized surface impedance at height h above sea level
$\Delta(0)$	: normalized surface impedance at sea level
W	: wave-tilt of vertically polarized electromagnetic wave
W(p,q)	: roughness spectrum

1. INTRODUCTION

Electromagnetic groundwaves present a forward tilt strongly depending on the electrical properties of the underlying medium. This dependency originates from the relationship between wave-tilt and the surface impedance of the guiding interface [1]. So far, the wave-tilt probing method has been applied to infer the electrical properties of the uppermost ground [2-4]. Potential airborne wave-tilt measurement systems for rapid geophysical prospecting of extended areas are discussed in [5].

Other factors controlling the surface impedance of the guiding interface (e.g. roughness) might be sensed from wave-tilt measurements. The possibility to apply the wave-tilt probing method for sea state estimation was indicated in [6] through a theoretical model accounting for both sea roughness [7,8] and vertical refractivity inhomogeneity in the lower troposphere. However, a standard vertical profile for the refractivity (i.e. dN/dh=-40 N-units/km) was only considered, because interest was focused on the relationship between sea state and wave-tilt. The upper boundary of a tropospheric slab overlying a rough sea surface was identified as the guiding interface. Since wave-tilt is sensitive to any anomalies of the electrical properties beneath the elevated guiding interface, tropospheric ducts might be detected through airborne wave-tilt measurements, if only ducts are below flight level. Wave-tilt calculations corresponding to standard and ducting models are compared in order to reveal the expected relationship between wave-tilt and trapping gradients in the lower troposphere above an agitated sea region.

2. MODELING

Grazing incidence of an electromagnetic wave upon the ground results in a Norton surface wave. If the guiding interface is highly conducting (e.g. sea surface up to VHF), vertical polarization is favored and the wave-tilt is equal to the normalized surface impedance:

$$W = \Delta \quad ; \ |\Delta| \ll 1 \tag{1}$$

The sensitivity of wave-tilt to the electrical properties of the underlying homogeneous medium is explained from the well-known expression for the normalized surface impedance:

$$\Delta = (1+j)(2\pi f\varepsilon_0/2\sigma)^{\frac{1}{2}} \tag{2}$$

with ε_0, σ standing for the free-space dielectric constant and the conductivity of the highly conducting ground. Eq.(2) only holds for harmonic excitation ($\exp(j2\pi ft)$) and a perfectly smooth guiding

interface. With roughness superimposed the guiding interface presents an effective normalized surface impedance:

$$\Delta_{eff} = \Delta + 0.25\iint F(p,q)W(p,q)dpdq \qquad (3)$$

where $W(p,q)$ is the spatial wavenumber spectrum of surface roughness and $F(p,q)$ is a complicated function determined in [7,8]. If Eq.(3) is used in wave-tilt calculations, the air-ground interface is in effect considered perfectly smooth and the wave-tilt will be controlled by both the electrical properties and surface roughness.

Let the guiding surface be the upper boundary of a stratified medium. In this case the normalized surface impedance is determined through an iterative procedure [9] involving all interfaces between successive layers. Rough interfaces may be considered in the model by simply applying Eq.(3) in the iterative procedure [6]. The wave-tilt is then sensitive to the electrical properties, thickness and surface roughness of all layers. Yet, electrically thick layers dominate over thin ones [1] and wave-tilt measurements at multiple frequencies are required [10] in order to estimate the dominant parameters of the underlying medium.

The model to be used herein involves a tropospheric slab of thickness h overlying an agitated sea region (Fig.1). The upper boundary of the tropospheric slab is identified as the guiding interface for a vertically polarized electromagnetic wave. The vertical inhomogeneity of refractivity in the troposphere is accounted for by subdividing the tropospheric slab below the guiding interface into a number of layers. This is a tolerable approximation, if the layer thickness is smaller than the quarter wavelength of the highest frequency used [11]. The absence of conductivity in the troposphere implies that the vertically inhomogeneous tropospheric slab above the sea is electrically thin. The underlying half space having the electrical properties of sea water may be considered highly conducting up to VHF and, therefore, it dominates over the tropospheric slab. As a consequence, the guiding interface though elevated is still highly conducting and the wave-tilt at grazing incidence may be represented by the normalized surface impedance $\Delta(h)$ (Fig.1). The latter is determined iteratively starting from the normalized surface impedance of the sea $\Delta(0)$. The sea roughness effect may be included in the expression for $\Delta(0)$ by applying Eq.(3). For simplicity only the isotropic Philips spectrum of wind waves developed on a relatively open, deep-water and swell-free sea region [12] will be used in the calculations to follow. All other interfaces of the stratified guiding structure are considered perfectly smooth.

The vertical profile of refractivity in the troposphere may be either standard or ducting. According to the International Radio Consultive Committee (CCIR), the standard profile of refractivity in the lower troposphere is approximately a straight line with $N(0)=289$ N-units and $dN/dh=-40$ N-units/km. Earth's curvature may be taken into account by introducing the modified refractivity:

$$M(h) = N(h) + 10^6(h/a) \quad ; \quad dM/dh = dN/dh + 157 \qquad (4)$$

where a is the earth's radius in meters. Evidently, the standard profile of modified refractivity is also approximately a straight line with $M(0)=N(0)$ and $dM/dh=117$ M-units/km. Considering that ducting only occurs if $dN/dh<-157$ N-units/km, it is readily realized that ducting is associated with negative gradients along the modified refractivity profile. The M-profiles presented in Fig.2 correspond to evaporation, surface-based and elevated ducts. These linearized models of M-profiles involve the parameters D (duct thickness), ΔM (duct intensity) and h_{opt} (optimum coupling height), which will be collectively referred to as duct characteristics. The standard gradient 117 M-units/km is assumed for all positive sloped portions of the M-profiles. Typical values for duct characteristics over Greek seas are used to determine wave-tilt in the VHF band at various altitudes in the troposphere and for sea states 1-3. In any case calculations are repeated for the standard M-profile so that results for ducting conditions can be compared to corresponding results for the standard troposphere.

3. NUMERICAL RESULTS AND DISCUSSIONS

The diagrams of Fig.3 correspond to a simple model involving an evaporation duct ($D=h_{opt}=15m$, $\Delta M=25$ M-units) on a calm sea surface. The wave-tilt is determined well above the duct (h=50m) throughout the HF, VHF bands. The effect of sea roughness is only temporarily suppressed in favor of the expected relationship between wave-tilt and the trapping gradient. The diagrams corresponding to standard and ducting conditions are almost identical in the HF and lower VHF bands. However, at higher frequencies an increasing frequency shift Δf is gradually introduced between the diagrams. This effect may be justified through the following expression for the period of wave-tilt oscillations with frequency [2,11]:

$$F = c_o/2h(2\langle M\rangle)^{\frac{1}{2}} \qquad (5)$$

where $\langle M\rangle$ is the average of the modified refractivity from sea level up to the height h, the latter being measured in kilometers. If a trapping gradient exists beneath the elevated guiding interface, $\langle M\rangle$ is reduced and, therefore, F is increased. Thus the (W vs. f)-diagrams corresponding to standard and ducting conditions are shifted apart by Δf. Attention will henceforth be focused on the relationship between this frequency shift and duct characteristics.

Raising the guiding interface to h=300m, the period of wave-tilt oscillations with frequency is reduced to F=20MHz and the maxima of ($|W|$ vs. f)-diagrams are sharpened. Thus Δf-resolution is improved. On the other hand, thicker evaporation ducts as well as surface-based ducts might be considered too.

The results of Fig.4 reveal that the frequency shift Δf between standard and ducting diagrams is clearly dependent on the duct intensity ΔM. The diagram (Δf vs. ΔM) is almost linear (Fig.5) and, therefore, ΔM might be estimated, if Δf were determined through wave-tilt measurements. However, it remains to be proved that the effect of duct intensity on wave-tilt is not masked by the corresponding effect of duct thickness and sea roughness.

If the duct thickness D is varied while ΔM is kept constant, the diagrams of Fig.6 are obtained. On the other hand, if sea roughness is introduced into the model, both the standard and ducting diagrams are modified as is shown in Fig.7. In all cases the ducting diagrams are shifted from the standard ones by a more or less constant amount. Hence, the frequency shift Δf is only slightly affected by duct thickness and sea roughness. It should therefore be primarily attributed to duct intensity. Similar conclusions may be drawn from the diagrams of Figs.8,9 that correspond to a surface-based duct.

The numerical results presented indicate, that detection of trapping refractivity gradients above the sea requires: (i) calculations resulting in the reference (W vs.f)-diagram, that corresponds to the standard M-profile in the lower troposphere, and (ii) multifrequency airborne wave-tilt measurements in order to determine the actual (W vs.f)-diagram that eventually carries information on existing tropospheric ducts.

In fact wave-tilt measurements involve both amplitude $|W|$ and phase argW determination. A system which can measure the complex wave-tilt comes to be rather complicated and sensitive to errors induced by aircraft rocking and wobble. The modified crossed dipoles technique proposed by King [5] seems to handle these problems at least in theory but its efficiency is not as yet verified experimentally. The simpler phase quadrature technique [5] has been successfully used for airborne wave-tilt measurements [10]. The output of the quadrature phase detector (Fig.10) is proportional to the imaginary part of the wave-tilt $|W|\sin(\arg W)$. Either $|W|$ or argW should therefore be known beforehand in order to determine the complex wave-tilt. In exchange errors due to aircraft rocking and wobble may be kept low.

Inspecting the numerical results presented in Figs.3-4,6-9 , it is realized that extrema of ($|W|$ vs. f)-diagrams correspond to roots of (argW vs. f)-diagrams. If this property is taken into account, the phase quadrature technique may be adapted for wave-tilt sounding of trapping gradients above the sea. It is evident from Eq.(5) that a complete cycle of wave-tilt oscillations with frequency may be included in the frequency band of the available transmitting/receiving devices by simply adjusting the flight height of the airborne platform. Once the height is determined according to this criterion, it is easy to calculate the reference (W vs. f)-diagram. Let f_1 be the frequency at which a maximum of the reference ($|W|$ vs. f)-diagram appears (Fig.10). According to the above-mentioned property argW will be zero at f_1. Hence, if no duct is present beneath the aircraft, the output of the quadrature phase detector, which measures $|W|\sin(\arg W)$, will only be zero at the frequencies $f_1 + mF/2$; $m \in Z$, where the extrema of the reference diagram appear. On the other hand, if a duct does exist, the actual (W vs.f)-diagram will be shifted from the reference diagram. Yet, it is not necessary to sketch the actual diagram in order to determine the frequency shift Δf. It only suffices to sweep the selected band starting from f_1. If the quadrature phase detector yields a zero output at $f_2 = f_1 + mF/2$, the frequency shift will obviously be $f_2 - f_1$ and the corresponding duct intensity may then be determined from the (Δf vs. ΔM)-diagram (Fig.5).

The effect of sea roughness is accounted for through Barrick's theory for the normalized effective surface impedance of an agitated sea. Based on a boundary perturbation technique this theory is only applicable to a slightly rough and highly conducting surface. The surface of the sea may be considered highly conducting throughout the VHF band. Yet, in the middle of the band (≈150MHz) only seas up to moderate may be considered slightly rough. Hence, a restriction concerning the upper boundary of the band to be selected for wave-tilt measurements is imposed by the highest sea states to be taken into account. On the other hand,the frequency shift of the (W vs. f)-diagram due to a trapping layer is only significant at high frequencies. A tradeoff between Δf-resolution and accuracy of sea roughness effect is therefore required and the band 80-120 MHz is considered appropriate for wave-tilt sounding of tropospheric ducts above the sea.

4. CONCLUSIONS

The relationship between wave-tilt in the lower troposphere and trapping refractivity gradients above the sea has been revealed through numerical calculations. The dominant parameter affecting wave-tilt is duct intensity. In general the effect of ducts on wave-tilt above them is a frequency shift of the wave-tilt versus frequency diagram. This shift is rather insensitive to variations of duct thickness, optimum coupling height and even sea state. Airborne wave-tilt measurements may reveal the presence of tropospheric ducts above the sea, if the phase quadrature technique is applied according to a certain procedure. Experimental work is required to assess the efficiency of the proposed method.

5. REFERENCES

1. King,R.J., Wave-tilt measurements, IEEE Trans. Ant. Prop., vol.AP-24, no.1, pp.115-119, 1976.
2. Lytle,R.J, D.L.Lager and E.F.Laine, Subsurface probing by high frequency measurements of the wave-tilt of electromagnetic waves, IEEE Trans. Geosci. Electron., vol.GE-14, no.4, pp.244-249, 1976.
3. Singh,R.P. and T.Lal, Wave-tilt characteristics of EM waves over a homogeneous earth model, IEEE Trans. Geosci. Electron., vol.GE-18, no.4, pp.285-288, 1980.
4. Thiel,D.V, K.S.Park and R.J.King, Wave tilt fluctuations near a vertical discontinuity in a flat ground plane, IEEE Trans. Geosci. Rem. Sensing, vol.GE-20, no.1, pp.131-134, 1982.
5. King,R.J., On airborne wave tilt measurements, Radio Sci., vol.12, no.3, pp.405-414, 1977.
6. Chrissoulidis,D.P. and E.E.Kriezis, Wave tilt calculations in the layered troposphere above a slightly rough sea, Radio Sci., vol.17, no.5, pp.1265-1273, 1982.
7. Barrick,D.E., Theory of HF and VHF propagation across the rough sea,1,The effective surface impedance for a slightly rough highly conducting medium at grazing incidence, Radio Sci., vol.6, no.5, pp.517-526, 1979.
8. Barrick,D.E., Theory of HF and VHF propagation across the rough sea,2,Application to HF and VHF propagation above the sea, Radio Sci., vol.6, no.5, pp.527-533, 1979.
9. Wait,R.J., Electromagnetic waves in stratified media, Oxford, Pergamon Press, 1962, pp.8-63.
10. Hockstra,P., A.Delaney and P.Sellmann, Surface impedance of radio groundwaves over stratified

earth, AGARD Conf. Proc., Vol. 144, pp.23.1-23.8 and D.14-D.15, 1974.
11. Wayne,L.D., D.L.Jaggard and C.F.Machi, Wave-tilt sounding of multilayered structures, Radio Sci., vol.14, no.6, pp.1069-1076, 1979.
12. Kinsman,B., Wind waves, Englewood Cliffs, N.J., Prentice-Hall, 676pp.

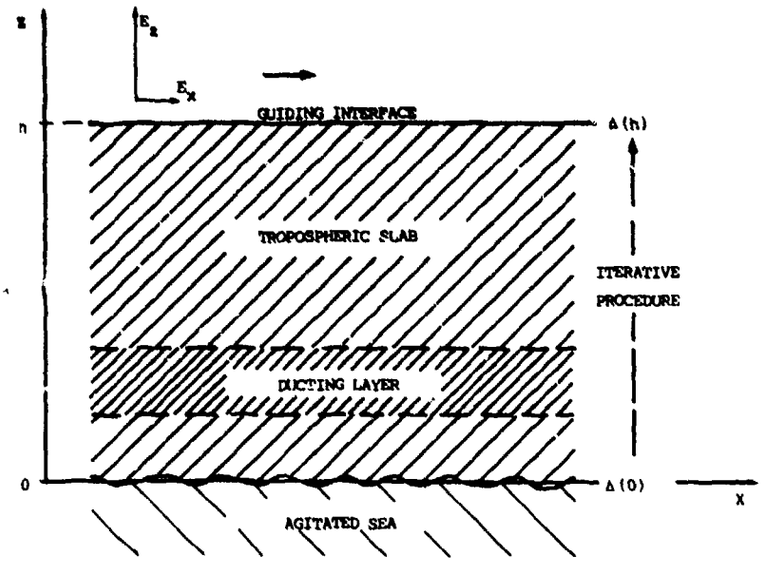


Fig.1 Geometric configuration for wave-tilt calculations.

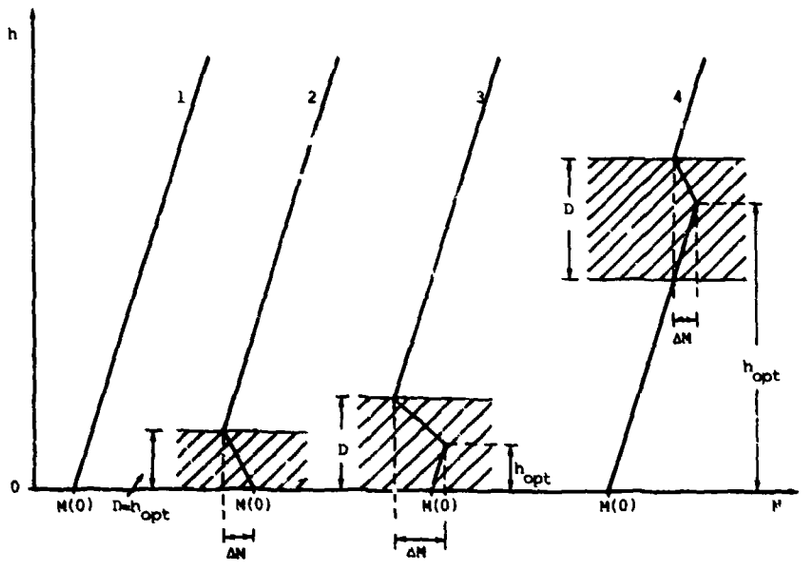


Fig.2 Vertical profiles of modified refractivity corresponding to:
(1)Standard troposphere, (2)Evaporation duct, (3)Surface-based duct, (4) Elevated duct.

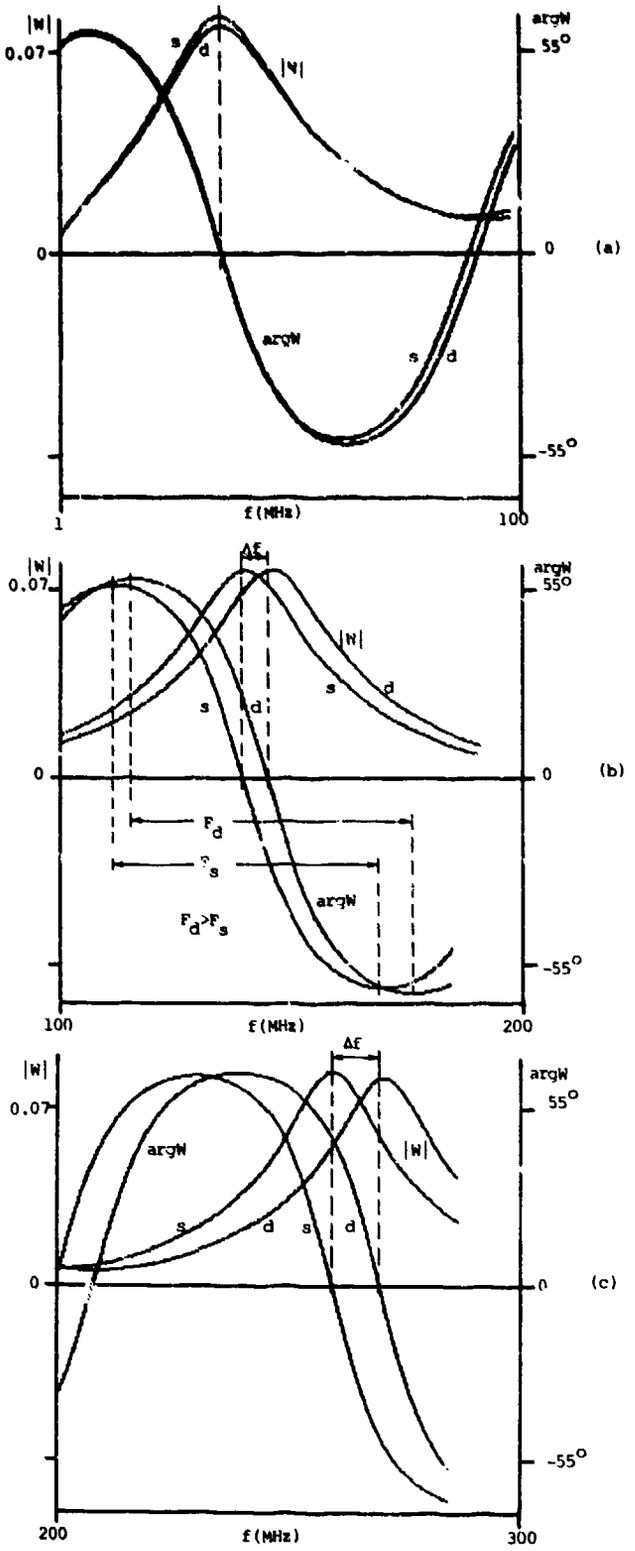


Fig.3 Wave-tilt versus frequency in HF,VHF bands at height h=50m for: (s)Standard troposphere, (d)Evaporation duct (D=15m, ΔM=25 M-units)

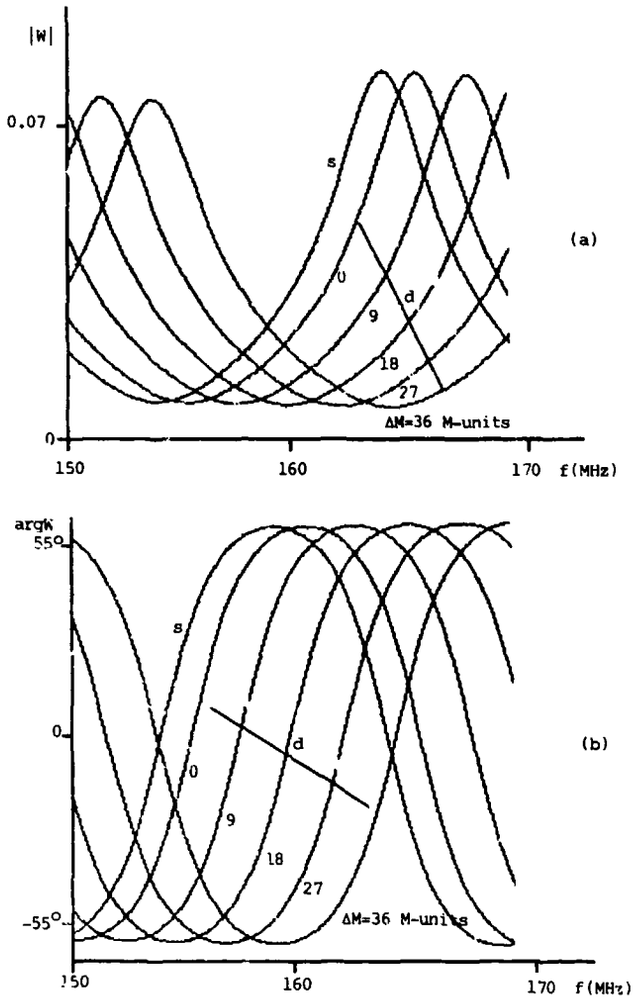


Fig.4 Wave-tilt versus frequency at height h=300m for:
(s)standard troposphere, (d)evaporation duct (D=50m, ΔM=0,9,18,27,36 M-units)

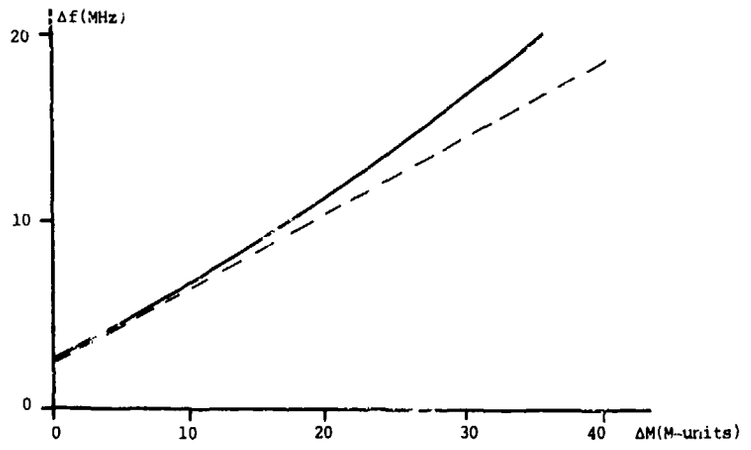


Fig.5 Relationship of frequency shift to duct intensity.

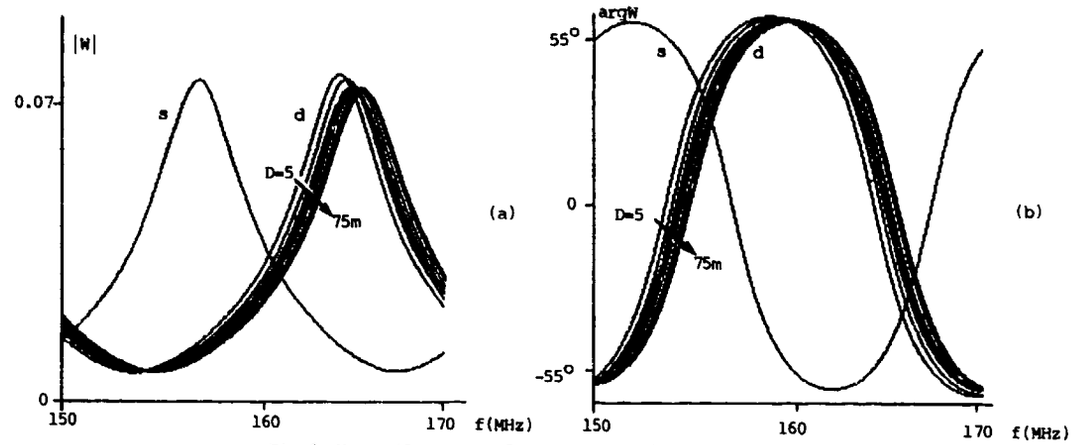


Fig.6 Wave-tilt versus frequency at height h=300m for:
(s)Standard troposphere, (d)Evaporation duct (D=5,15,25,35,45,55,65,75m, ΔM=25 M-units)

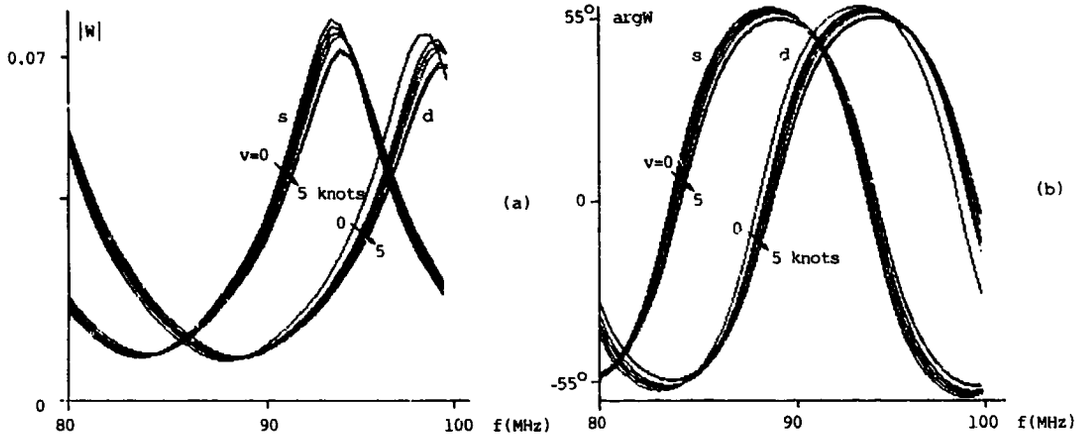


Fig.7 Wave-tilt versus frequency at height h=300m for:
(s)Standard troposphere, (d)Evaporation duct (D=50m, ΔM=25 M-units). Wind speed v=0,1,2,3,4,5 knots.

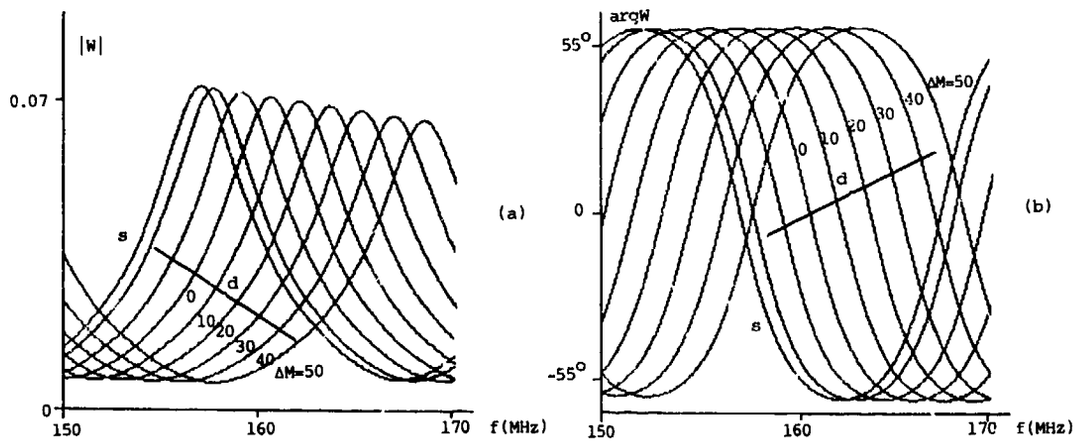


Fig.8 Wave-tilt versus frequency at height h=300m for:
(s)Standard troposphere, (d)Surface-based duct (D=250m, h_{opt} =40m, ΔM=0,10,20,30,40,50 M-units)

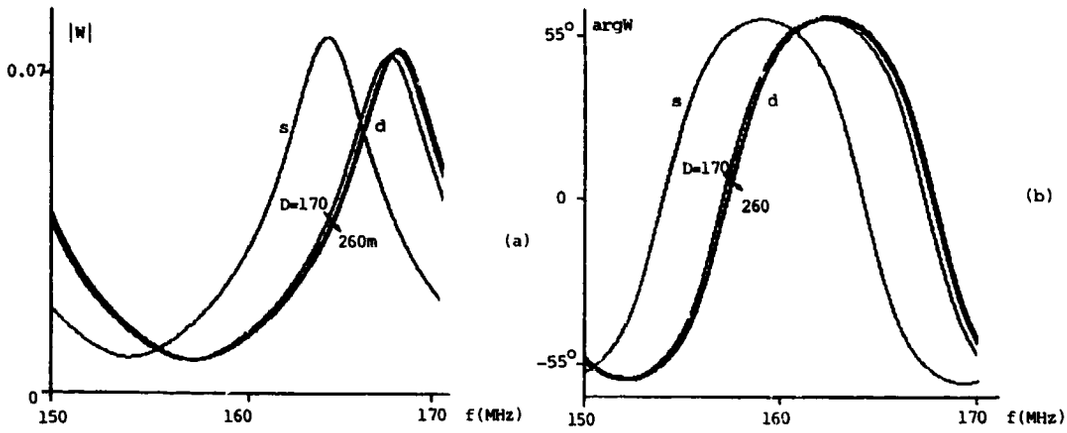
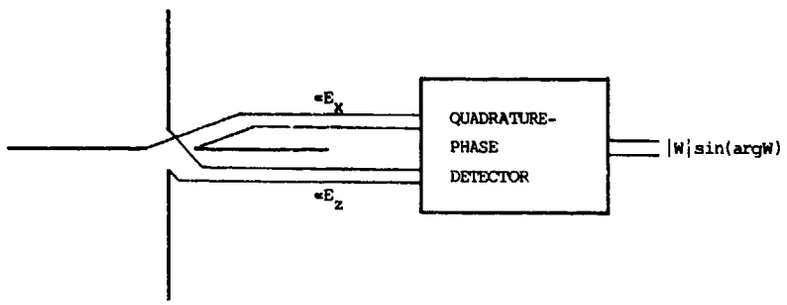


Fig.9 Wave-tilt versus frequency at height h=300m for:
(s)Standard troposphere, (d)Surface-based duct (D=170,200,230,260m, h_{opt} = 40m, ΔM=25 M-units)



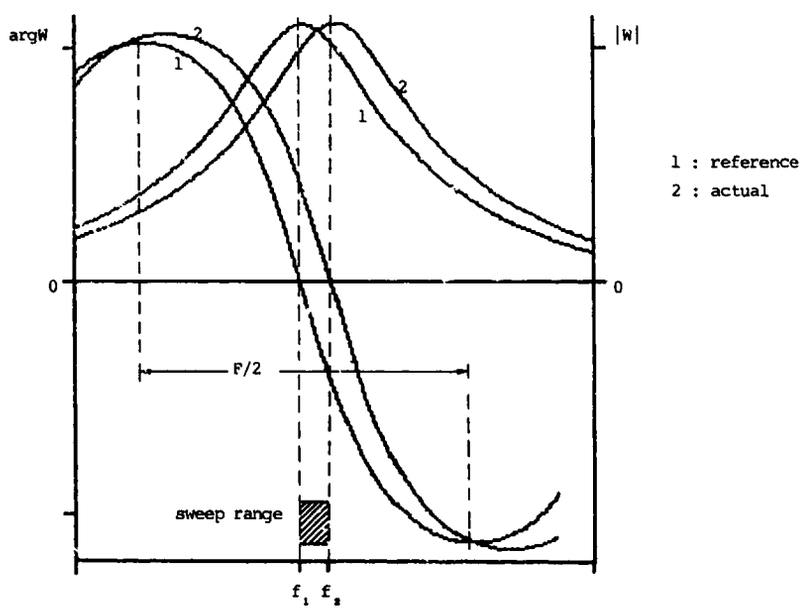


Fig.10 Measurement procedure for the phase quadrature technique.
A duct is detected if $f_2 \neq f_1 + mF/2$; $m \in Z$.

DISCUSSION

H. Vissinga, NE

Does introducing a nonphysical guiding interface and neglecting the atmosphere above it affect your predicted results?

Author's Reply

It is true that the elevated guiding interface is a fictitious one. Since the downward-looking surface impedance is quite small for the frequencies considered, an apparent conductivity may be introduced and thus the dielectric-coated conductor is replaced by a conducting half-space. Furthermore, the surface impedance looking downward is quite different from that looking upward, and, therefore, the elevated interface may be used as a guiding structure just as any other physical interface that causes a significant discontinuity of surface impedance in the upward/downward direction.

H. Vissinga, NE

Are your predicted results in agreement with the results from the theory of Dr. Rotheram for an exponential atmosphere.

Author's Reply

Both Rotheram's theory and the classical Norton's theory are macroscopical views of the propagation field. In our model the propagation field is locally treated as a guided (Zenneck-) wave, because the surface impedance is but a local boundary condition.

L.B. Felsen, US

As was pointed out in earlier discussion, your model is approximate, yet you provide detailed curves with numerical parameters. Have you checked the sensitivity of your results with respect to small changes in your parameters? If the results are strongly model dependent, they may not model reality adequately. Also, are the phenomena described by you actually measurable and therefore observable?

Author's Reply

This work has only established theoretically a promising relationship between the duct intensity and the wave-tilt at some altitude above the sea. The corresponding effect of other duct characteristics or sea roughness on the wave-tilt is weaker by an order of magnitude. The authors feel that the phenomena described are actually measurable. Yet, an accurate sensitivity study as well as experimental work are required to prove the theoretical results.

J.H. Richter, US

I would like to follow up on Dr. Felsen's questions and comment and ask if you plan any experimental verification of your technique.

Author's Reply

A project on "Tropospheric duct detection through wave-tilt measurements above the sea" will probably be initiated in collaboration with the Greek Air Force and AGARD (through the support-to-nations program).

L. Boithias, FR

Have you an idea concerning the feasibility of a possible utilization of your method?

Author's Reply

A sensitivity study should be the next step. Yet the authors can state that errors due to platform motion (rocking, wobble, altitude variation, velocity...) will not be serious problems. The optimism is based on the fact that the measurement is relative, namely, the ratio of electric field components should be determined, and therefore some errors might be finally eliminated. The success of the proposed detection method will depend on the accuracy of sea roughness/surface refractivity data to be used for the calculation of the standard wave-tilt versus frequency diagram.

I-BAND MULTIPATH PROPAGATION OVER THE SEA SURFACE

by
C J Baker and K D Ward
Royal Signals and Radar Establishment
St Andrews Road
Great Malvern
Worcs
England
WR14 3PS

SUMMARY

This paper summarises a series of measurements which were aimed at studying the phenomenon of multipath resulting from line of sight, two way, microwave propagation over the sea surface. It has been observed that the expected lobing structure, due to the interference of the direct and reflected signals is destroyed when the sea surface becomes sufficiently rough, suggesting the coherent part of the forward scattered sea reflection to be zero. Further, it has been observed that although the pulse by pulse fluctuations show deep fading characteristics they may be modelled by the "Rice-squared" distribution. However, it has been found that care must be taken in choosing the duration of the measurement when evaluating the statistical properties of the data.

LIST OF SYMBOLS

h = RMS water surface fluctuations (m)

ψ = Grazing angle (rads)

λ = Transmitted wavelength (m)

ρ_C = Coherent reflection coefficient

ρ_I = Incoherent reflection coefficient

INTRODUCTION

When a radar target is situated close to the surface of the sea there are two illumination paths from the radar to the target. One is the direct signal between the radar and the target the other is a signal reflected from the surface of the sea. These two signals sum constructively or destructively so that the energy illuminating the target may be increased or decreased as compared with free space propagation. An example of the geometry used is shown in figure 1. The multipath phenomenon is again present on the reciprocal path so that target backscatter characteristics may exhibit an enhanced or reduced mean echoing area which also fluctuates as the motion and roughness of the sea surface change the forward scatter vector. An additional facet of target behaviour is a dynamic multipath "error" in tracking caused by resultant perturbations in the received wavefront. The degradation in radar performance may be considered, in simple terms, as a result of reflections causing both the real target and its image to be detected with the consequence of erratic tracking between the two. In order for the performance of radar to be assessed in these conditions we require a thorough understanding of multipath and forward scattering from the sea surface.

The field incident on a target from an electro-magnetic wave scattered by the rough sea surface is the vector sum of wavelets with phases perturbed by the sea height roughness. These perturbations increase with the standard deviation of waveheight and decrease with electro-magnetic wavelength and incident grazing angle. From a knowledge of the amplitude and phase statistics of the contributing wavelets it is possible to evaluate the statistical properties of the total forward scattered wave and thereby the statistical properties of the multipath return.

It has been suggested [1,2] that the forward reflected signal may be described in terms of coherent and incoherent reflection coefficients. The coherent coefficient is the mean of the field (expressed as a proportion of the direct signal) and the incoherent coefficient is the root mean square amplitude of the deviation of the field about the mean.

The terms specular and diffuse, although commonly used, are not employed here as they make assumptions that the coherent term results from specular reflection, whilst the incoherent term results only from non-specular scattering. Our terminology also removes confusion introduced by fluctuations in the "specular" term [3, Chapter 12]. While the sea state and waveheight remain unchanged, the coherent coefficient is constant by definition.

If we consider electro-magnetic wave scattering from a surface with many independent height variations then the simplest assumption is that incoherent term will be Rayleigh distributed with phase varying uniformly between ϕ and 2π [3]. Therefore, having defined the coherent term to be a constant vector one would expect the Rice distribution to describe the amplitude received at the target and, assuming reciprocity to hold, a "Rice-squared" distribution at the receiver for our two way geometry. Using these concepts we examine the experimental evidence to determine the statistical

properties of electro-magnetic wave scattering in a dynamic multipath environment resulting from propagation over the sea surface.

EXPERIMENTATION

To investigate the phenomenon of forward scattering and multipath propagation in a controlled way, a series of experiments have been conducted in open sea conditions, to include the presence of large wavelength swell. Measurements have been made of radar backscatter from a corner reflector of known free space echoing area positioned at various heights above the sea surface. (In this way the forward scattering is examined under relatively controlled conditions.) The radar is located at a clifftop fixed site at a height of approximately 80 m looking across open sea to the corner reflector. Analysis of the recorded backscatter is based on the assumption that the measured amplitudes are proportional to the square of amplitude for one way propagation, the former resulting from the combined multipath of the reciprocal paths. The experimental configuration is shown in figure 1. The radar is an I-band (9.5 - 10 GHz) pulsed device with a chirp compressed pulsewidth of 28 ns (4.2 m range resolution) and a pencil beamwidth of 1.2°. It can measure in either Horizontal or Vertical polarisation modes, has frequency agility and the ability to record range profiles on a pulse by pulse basis. A number of measurements have been made over a period of approximately three years to obtain data resulting from a variety of environmental conditions. Samples of this data base are utilised here in order to investigate further the characteristics of multipath.

ANAYLSIS

Figure 3 shows a received amplitude time history of approximately 9 mins, from a measurement made over a calm sea. Each point is the average of one second of data (PRF = 1 kHz). During this measurement the corner reflector was slowly raised and lowered at a constant rate thus giving rise to the lobing structure due to the interference of the direct and reflected signals. From this plot it may be deduced that the coherent term ρ_c is close to unity owing to the deep nulls in the lobing structure. The non-coherent term ρ_i is small although not insignificant, and is due to the many small but random, phase shifts introduced by the surface roughness.

In contrast figure 4 shows a similar plot for a rougher sea state. It may be observed that there is now no discernable lobing structure, which should appear on the same time scale as figure 3. This suggests that the coherent term is close to zero. Figure 5 again shows a similar measurement made with a rough sea where the corner reflector has been held at a constant position with respect to the mean sea level (assuming this to be constant for the observation period). In figure 6 a sample of this data is presented on a pulse by pulse basis for a time history of approximately 5 seconds.

The normalised third and fourth moments are evaluated and plotted on a graph of the theoretically derived Rice-squared moments versus "noise to signal" as in figure 7. The first moment is used for normalistion and the second moment to evaluate the "noise to signal" ratio in the Ricean distribution. It is found they are in excellent agreement with those predicted. Further, if the coherent term is assumed to be zero, the square-root of the Horizontal axis yields the incoherent term. Before the interpretation of this value is considered for the rough sea case, the effect of duration of the observation period is examined. Figure 7 also shows the evaluated moments for differing lengths of observation time. This suggests a minimum time of approximately 30 seconds in order to accurately evaluate moments. The reason for this may be the presence of long wavelength structure in the sea surface which results in a modulation of the received signal. Using the method described in the introduction we may define a coherent signal of constant amplitude and phase and a fluctuating incoherent term. If the incoherent scattering obeys the central limit theorem this will lead to the Rice squared distribution that has been observed. In calculating the sea roughness the effects of swell must be included, as this may result in no lobing structure even on days when the average wind speed would suggest the sea to be calm.

For the case under consideration the value of the incoherent component is 0.29 suggesting a peak to trough wave height of approximately 1.65 m. (See figure 2) and a negligible coherent term. It should be pointed out that although the wave height was not measured, visual observations and measurements of the average wind speed would suggest that this value for the peak-trough wave height is somewhat high. It is envisaged that future measurements will be made with a wavebouy present.

Figure 7 also shows the points plotted for a calm sea case where the roughness parameter has been estimated from wavebouy measurements to be 47 and the value of the incoherent component is 0.16 which is in very good agreement with figure 2.

Thus in conclusion it has been demonstrated that, in measurements reported here, the Rice model for forward propagation provides an excellent fit to experimental observations provided that the measurement is made over a sufficient duration to include low frequency components that may be present in the sea surface. In this way the reflected signal is made up of a constant coherent signal and a Rayleigh distributed incoherent signal. Further any correlation properties of the forward scatter will be associated with the Rayleigh term and may easily be built into a statistical model for a radar target at low altitudes over the sea surface. The importance of the effects of large scale structure in the sea surface on the resulting multipath lobing structure has

also been demonstrated and it is suggested that two relatively similar sea states can result in very different multipath properties, with swell destroying the multipath lobing pattern by increasing the total roughness of the sea surface.

REFERENCES

[1] C I Beard, I Katz and L M Spetner, "Phenomenological vector model of microwave reflection from the Ocean", IRE Trans Antennas and propagation, April 1963, 162-167.

[2] C I Beard, "Coherent and Incoherent scattering of microwaves from the Ocean", IRE Trans Antennas and Propagation, September 1961, 470-483.

[3] P Beckmann and A Spizzichino, "The scattering of electromagnetic waves from rough surfaces", Pergamon press, 1963.

Copyright © Controller HMSO, London, 1987

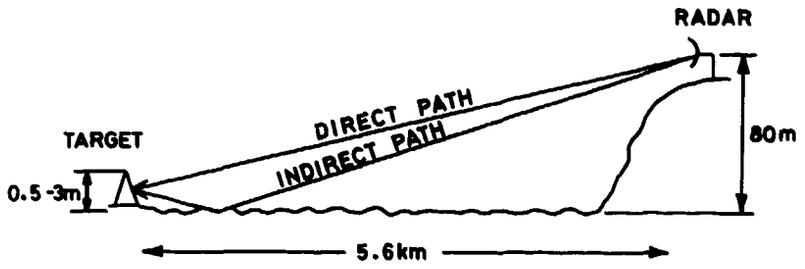


FIG 1 EXPERIMENTAL GEOMETRY

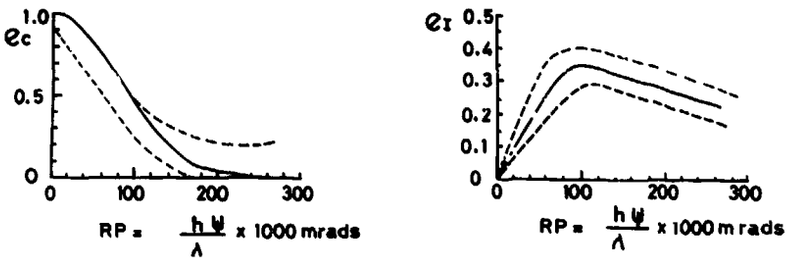


FIG 2 VARIATION OF COHERENT (ρ_c) AND INCOHERENT (ρ_I) TERMS WITH ROUGHNESS PARAMETER (RP) [2]

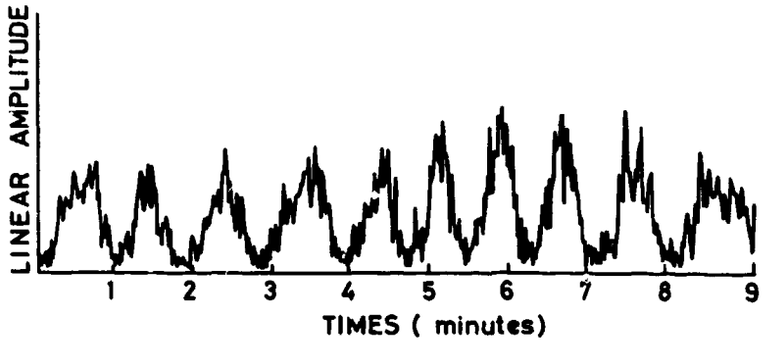


FIG 3 TIME HISTORY OF MULTIPATH SIGNAL FROM A TARGET BEING RAISED AND LOWERED (CALM SEA)

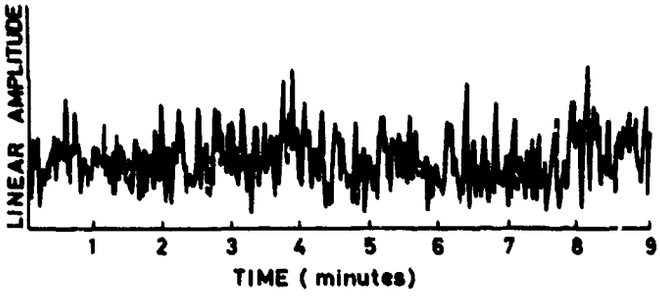


FIG 4 TIME HISTORY OF MULTIPATH SIGNAL FROM A TARGET BEING RAISED AND LOWERED (ROUGH SEA)

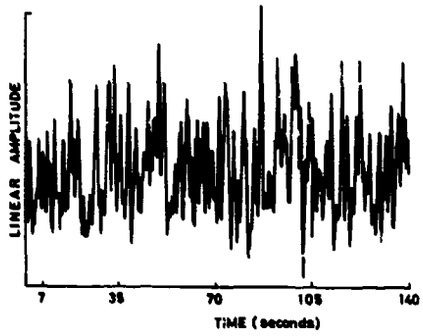


FIG 5 TIME HISTORY OF MULTIPATH SIGNAL FROM A TARGET AT A FIXED HEIGHT (ROUGH SEA)

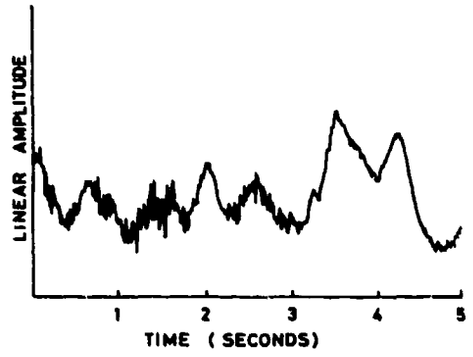


FIG 6 PULSE BY PULSE TIME HISTORY OF A MULTIPATH SIGNAL FROM A TARGET AT A FIXED HEIGHT (ROUGH SEA)

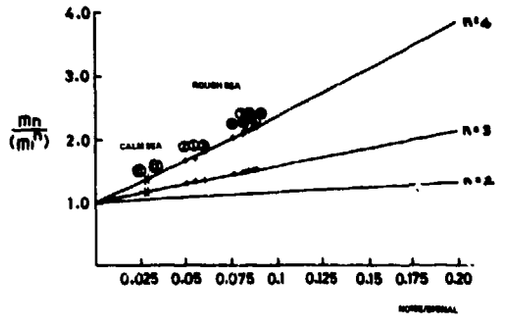


FIG 7 COMPARISON OF MOMENTS OF MEASURED DATA WITH THOSE FOR THE "RICE SQUARED" DISTRIBUTION (NORMALISED)

DISCUSSION

L. Bolthias, FR

Could you give additional information concerning the possible influence of the target characteristics on the results: size, stability with wind, etc.?

Author's Reply

The target had a free space value of 30 dB/m. It is secured to the support structure in such a way that there is negligible motion with wind. Also, when being raised and lowered, we found no evidence of vibration, etc. I would point out, however, that the orientation of the target has to be chosen carefully to avoid bistatic scatter by the reflector.

C. Goutelard, FR

English translation

You made sure that the first Fresnel zone was sufficiently free of littoral coasts? When the sea is agitated, the contribution from outside the first Fresnel zone is not negligible. Isn't this extension of the first Fresnel zone too close to the coast?

Author's Reply

During my presentation, I stated that it wasn't clear as to the dominant scattering zone. This is an area of debate. On average, it might be argued that the first Fresnel zone is the dominant contributor to the resultant perturbation in the reflected wave front. It might also be argued that the surface roughness destroys the phase relationship necessary to satisfy the Fresnel zone ideas.

C. Goutelard, FR

English translation

You said that you tried to measure the effects of multipath in deep sea on radar detection in the I band. How did you ensure yourself that your experimental conditions were representative? The proximity of the coast may enhance the Rice character of the model that you measured.

Author's Reply

The experimental conditions were such that the free space echoing area of the corner reflector needed to provide our backscatter signal was sufficiently large to provide a large enough dynamic range between the target and the background (plus target support structure) so that the effects of the interference between the free space and reflected wave fronts could always be observed.

The Rice model was actually proposed by Beard and Katz, we simply examined the single point statistical fit of our data to that description and found it to be in excellent agreement.

ÉTUDE EXPÉRIMENTALE ET MODÉLISATION DU PHÉNOMÈNE DE RÉFLEXION SUR LA MER À 36 GHZ

Yvonick HURTAUD, Claude TERRET, Jean-Pierre DANIEL
Département Antennes - UA 834 CNRS
UNIVERSITÉ de RENNES I
Avenue du général Leclerc
35042 - RENNES CEDEX

et

Alain JUNCHAT
groupe "Analyse des Signatures et Rayonnements électromagnétiques - Environnement"
CENTRE D'ÉLECTRONIQUE DE L'ARMEMENT
35170 - BRUZ

SUMMARY

During the 1984 autumn, a measurement campaign of the propagation of electromagnetic waves at 36 GHz has been led on the French Atlantic coast, near Lorient.

The length of the link between the transmitting site, located on the isle of GROIX and the receiving site at GAVRES, was 9.7 km.

Owning to the small height of the antennas, a part of the emitted energy was reflected by the sea surface. At the reception point, the fields coherent interference produced by the direct and reflected radiations, gave a signal varying periodically with the influence of tides.

In order to study the specular reflection phenomena over the sea, specific measurements have been made with the help of an elevator. It allowed the height of the receiving antenna to change on a distance of about 5 meters, maintaining that way, at the same time, steady environment conditions.

Thanks to this device, the forward specular reflection coefficient, at a frequency of 36 GHz could then be determined. The measurements which have been made, proved the good agreement between them and the Miller and al. theory, especially in case of strong roughness.

Following these results, a model of propagation based on the specular reflection has been developped to be then compared with the measurements. In some particular meteorological situations, it can be observed a distortion of the interference figures owing to variations of the atmospheric structure.

RÉSUMÉ

Durant l'automne 1984, une campagne de mesure de la propagation des ondes électromagnétiques à 36 GHz a été menée sur la côte atlantique française, près de la ville de LORIENT.

La longueur de la liaison entre le site d'émission, situé sur l'île de GROIX, et le site de réception à GAVRES était de 9,7 km.

Du fait de la faible hauteur des antennes, une partie de l'énergie émise était réfléchie par la surface de la mer. A la réception, l'interférence cohérente des champs dus aux rayonnements direct et réfléchi, procurait un signal variant périodiquement en fonction de la marée.

Afin d'étudier les phénomènes de réflexion spéculaire sur la mer, des mesures spécifiques ont été entreprises avec un élévateur. Il permettait de faire varier, sur environ 5 mètres, la hauteur de l'antenne réceptrice tout en conservant des conditions d'environnement stables pendant ce temps.

Grâce à ce dispositif le coefficient de réflexion spéculaire vers l'avant, à la fréquence de 36 GHz, a pu être déterminé. Les mesures effectuées ont montré la bonne concordance existant entre elles et la théorie de Miller and al., en particulier pour des rugosités fortes.

A la suite de ces résultats, un modèle de propagation basé sur la réflexion spéculaire a été développé et confronté avec les mesures. Il apparaît, dans certaines situations météorologiques particulières, une déformation des figures d'interférences due aux variations de la structure atmosphérique.

ÉTUDE EXPÉRIMENTALE ET MODÉLISATION DU PHÉNOMÈNE DE RÉFLEXION SUR LA MER À 36 GHZ

- - -

1 - INTRODUCTION

Afin d'accroître les performances des systèmes de télécommunication, de détection et de guidage, la propagation des ondes millimétriques dans l'atmosphère a fait l'objet, ces deux dernières décennies, d'une recherche soutenue.

Dans ce cadre, différentes expériences de propagation à basse altitude ont été conduites, y compris en ambiance maritime [1], [2], [3], [4].

Elles mettent toutes en évidence, un certain nombre de perturbations, au niveau :

- de la troposphère (en raison de l'absorption des gaz composant l'atmosphère et des variations à petite ou à grande échelle de l'indice de réfraction de l'air)
- de la surface de la mer (à cause du phénomène de réflexion)

Pour compléter ces connaissances, une série d'expériences* à la fréquence de 36 GHz, a été menée sur la côte atlantique française.

Ces expérimentations ont, entre autre, permis d'étudier la réflexion vers l'avant de la surface de la mer

Elles ont aussi permis le recueil de phénomènes anormaux de propagation d'origine atmosphérique.

2 - PRÉSENTATION GÉNÉRALE DE L'EXPÉRIMENTATION

2.1. CADRE GENERAL

A l'initiative du sous-groupe propagation de l'AC 243, commission III, RSG.8 : "Application des ondes millimétriques", une campagne d'étude de la propagation des ondes millimétriques s'est déroulée sur une période de trois mois, d'octobre 84 à janvier 85, sur la côte sud de la BRETAGNE, près de la ville de LORIENT.

Le trajet de propagation, entièrement au-dessus de la mer, s'effectuait sur une longueur de 9,7 km.

Le site d'émission (île de GROIX) était placé à 48,2 m, par rapport au niveau zéro des cartes marines, tandis que la position du récepteur (presqu'île de GAVRES), dans sa configuration la plus basse, était à 10,5 m par rapport à cette même référence.

Dans cette région, la marée est de type semi-diurne. Elle varie de façon quasiment sinusoïdale.

2.2. LE FAISCEAU HERTZIEN FONCTIONNANT A 36 GHz

Durant cette campagne, le CELAR a mis en oeuvre un faisceau hertzien T.F.H. 720 fonctionnant à 36 GHz.

Ce matériel, fabriqué par THOMSON-CSF, se caractérise par des antennes de type CASSEGRAIN de 42 dB de gain et d'ouverture à 3 dB 1,5°.

La polarisation du champ émis est linéaire, orientée à 45° par rapport au plan horizontal.

La dynamique du récepteur est d'environ 60 dB.

Pour étudier les variations de champ électrique, la tension de contrôle automatique de gain (C.A.G.) du récepteur était échantillonnée à la cadence de 1 Hz. Elle était ensuite numérisée et stockée sur bande magnétique. Grâce à une courbe d'étalonnage, ces tensions étaient alors transposées en niveaux de champ.

* Cette série d'expériences a été soutenue financièrement par le service technique des télécommunications et des équipements aéronautiques (STTE).

2.3. LES MATERIELS COMPLEMENTAIRES

2.3.1. Les appareils de mesures océanographiques et météorologiques

Afin de connaître l'agitation de la mer, une bouée de mesure des vagues était mouillée à proximité de la zone de réflexion. A partir d'un traitement effectué sur les hauteurs instantanées du niveau de la mer, enregistrées sur 10 minutes, la bouée fournissait toutes les demi-heures la hauteur significative des vagues (H 1/3).

Les hauteurs moyennes du niveau de la mer étaient mesurées toutes les heures à PORT-TUDY (île de GROIX), situé à quelques kilomètres de la zone de réflexion.

Une station météorologique fonctionnait à terre et délivrait toutes les 6 minutes les principaux paramètres classiques.

2.3.2. L'élévateur

Les récepteurs de toutes les liaisons mises en oeuvre durant cette campagne étaient montés sur un élévateur.

Cet élévateur, d'une course de 4,8 m, permettait de simuler la variation de la hauteur de la marée dans un temps suffisamment court pour s'affranchir des conditions d'environnement.

3 - PROPAGATION RASANTE DES ONDES MILLIMETRIQUES SUR LA MER

3.1. GENERALITES

Sous incidence rasante, quand l'atmosphère ne perturbe pas la propagation des ondes, le champ capté par l'antenne de réception peut être représenté par la somme d'un champ provenant du rayonnement direct et d'un champ dû au rayonnement réfléchi sur la surface de la mer. Ce champ total est développé en une composante cohérente et une composante incohérente [5], [6].

La somme vectorielle de ces deux composantes dépend fortement de la géométrie de la liaison et de l'état de la mer. Elle permet de rendre compte des fluctuations lentes et rapides des niveaux de champ reçu.

3.2. FLUCTUATIONS DE LONGUE DUREE

Ces fluctuations sont dues à la composition cohérente du champ direct et du champ réfléchi cohérent. A cause de l'amplitude de la marée, ce phénomène était particulièrement marqué dans l'expérience effectuée.

En effet, le passage d'un extrêmum à l'autre requiert une variation du niveau moyen de la mer d'environ 40 cm. Aussi, lors des fortes marées, la variation de phase du champ réfléchi atteignait-elle plus de 400° par heure.

C'est sur la première zone de FRESNEL que s'effectue principalement la réflexion spéculaire vers l'avant [7]. Du fait du faible dégagement des antennes au-dessus de la mer, cette zone, de forme elliptique est très allongée dans le sens de la propagation. Son axe principal mesure environ 1200 mètres alors que son axe secondaire n'est que de 6 mètres. L'étude de son déplacement en fonction de la hauteur du niveau de la mer montre (figure n° 1) :

- que l'ellipse est correctement éclairée par chacune des deux antennes, la variation maximum d'éclairement dans cette zone étant inférieure à 2 dB
- qu'une variation de la hauteur du récepteur de 4,8 m vers le bas translate la surface réfléchissante d'environ 500 m en direction de la côte

Pendant ce déplacement, on peut raisonnablement supposer que la mer garde les mêmes propriétés statistiques.

3.3. FLUCTUATIONS DE COURTE DUREE

Ce type de fluctuations provient des multiples surfaces élémentaires composant la mer. La distribution statistique de l'amplitude du vecteur "diffus" correspondant suit une loi de RAYLEIGH.

La distribution des fluctuations de courte période du niveau de champ reçu s'apparente donc à une loi de RICE. Ces lois limites : loi normale par mer agitée levée par le vent et loi de RAYLEIGH sur minima par mer calme, ont été mises en évidence au cours de cette expérimentation [8].

On précise à ce sujet que la durée de la période d'analyse des fluctuations est un paramètre à considérer avec précaution.

En effet, sous certaines configurations de liaisons, le champ réfléchi présente la périodicité du mouvement de la houle. De ce fait, pour accéder aux distributions statistiques des niveaux de champ, les périodes d'analyses doivent être d'une durée largement supérieure à la période du mouvement principal de la mer.

4 - CALCUL THÉORIQUE DU COEFFICIENT DE RÉFLEXION ρ_S DANS LA DIRECTION SPÉCULAIRE D'UNE SURFACE RUGUEUSE

4.1. APPROCHE THEORIQUE

C'est pendant la seconde guerre mondiale que se sont effectuées les premières études théoriques sur le sujet. Puis, en 1954, AMENT [9] proposa une théorie permettant de calculer ρ_c en prenant en compte les caractéristiques statistiques de la surface éclairée. Il suppose une onde électromagnétique polarisée linéairement éclairant une surface rugueuse mono-dimensionnelle parfaitement conductrice. En utilisant les équations de MAXWELL et en introduisant une description statistique de cette surface, il met en évidence un ensemble d'équations intégrales portant sur les courants surfaciques moyennés.

Pour aboutir à une solution, des simplifications importantes sont introduites. Elles supposent d'une part que la densité surfacique de courant est seulement une fonction de l'altitude (l'effet d'ombre n'est pas pris en compte) et, d'autre part, que le courant induit est celui du plan tangent au point considéré (le rayon de courbure de la surface doit être grand devant la longueur d'onde incidente).

Moyennant ces approximations, AMENT relie le coefficient de réflexion dans la direction spéculaire à la densité de probabilité p (h) des hauteurs de la surface :

$$\rho_S = \int_{-\infty}^{+\infty} \exp(-2i\, k\, h \sin\theta) \cdot p(h) \cdot dh \qquad (1)$$

où $k = 2\pi/\lambda i$ est le nombre d'onde

et θ = l'angle d'indicence de l'onde par rapport au plan d'altitude moyenne

L'application de l'expression précédente au cas d'une surface gaussienne conduit à :

$$\rho_S = \exp[-2(2\pi g)^2] \qquad (2)$$

où g = est la rugosité de la mer

$$g = \frac{\sigma \sin\theta}{\lambda i} \qquad (3)$$

avec σ = hauteur quadratique moyenne de la surface. (Dans le cas d'un spectre hydrodynamique étroit : $H\,1/3 = 4\,.\,\sigma$).

En s'appuyant comme AMENT sur la méthode de l'Optique physique et en utilisant des simplifications similaires (effet d'ombre et diffusion multiple négligés), BECKMAN [7] aboutit aussi à l'expression (2) par une démarche de calcul différente.

Plus récemment MILLER et AL. [10] ont déduit une nouvelle expression de ρ_S en prenant appui sur des expériences effectuées par BEARD [6].

Ils supposent que, sur une période d'observation, la surface varie comme une sinusoïde dont la distribution d'amplitude est gaussienne et dont la phase est uniformément répartie sur $[-\pi/2, \pi/2]$.

Cette représentation introduit l'aspect périodique du mouvement de la mer.

Sous ces hypothèses et en appliquant l'expression (1) le coefficient de réflexion dans la direction spéculaire s'écrit alors :

$$\rho_S = \exp[-2(2\pi g)^2] \cdot I_o[2(2\pi g)^2] \qquad (4)$$

C'est cette dernière formulation, différente de l'expression de AMENT pour les fortes rugosités que l'on se propose de vérifier expérimentalement.

4.2. DEPENDANCE DU COEFFICIENT DE REFLEXION DANS LA DIRECTION SPECULAIRE A INCIDENCE RASANTE EN FONCTION DE LA HAUTEUR DES VAGUES ET DE L'ANGLE D'INCIDENCE

Des abaques fournissant la rugosité de la mer et le coefficient de réflexion dans la direction spéculaire ont été tracés à la fréquence de 36 GHz dans le cadre de liaisons rasantes (figure n° 2). Elles illustrent les expressions (3) et (4).

Pour des hauteurs de vagues constantes, ρ_S varie faiblement et de façon linéaire en fonction de l'angle d'incidence. C'est lorsque le dégagement des antennes au-dessus de l'eau est le moins important que ρ_S est le plus élevé (la rugosité de la mer est alors plus faible).

Quand la mer passe de l'état 1 à l'état 3 sur l'échelle de DOUGLAS, ρ_S décroît fortement : l'agitation de la mer, caractérisée par sa hauteur significative ou sa hauteur quadratique moyenne apparaît comme étant le paramètre dominant pour ce type de liaison à incidence rasante.

5 - MODÈLE DE RÉFLEXION SPÉCULAIRE

La mise en place d'un modèle de réflexion spéculaire rend compte des fluctuations lentes dûes à la marée. Il se fonde sur la composante provenant du rayonnement direct (Ed) et sur la composante cohérente du rayonnement réfléchi (Er). Afin de simplifier les calculs du champ résultant, les hypothèses suivantes sont émises :

- l'atténuation atmosphérique est identique sur le trajet direct et sur le trajet indirect
- la variation de l'indice de réfraction en fonction de l'altitude est linéaire et invariante dans le temps
- l'effet de dépolarisation de l'onde réfléchie sur la surface de la mer due à la rugosité est négligé. Puisque l'onde incidente est polarisée linéairement, sa composante cohérente après réflexion sur une surface de grande conductivité et de rayons de courbure grands devant la longueur d'onde incidente n'est pas dépolarisée

En s'appuyant sur l'Optique géométrique, la norme du champ reçu prend la forme simple suivante :

$$E_T = (E_d^2 + E_r^2 + 2\, E_d\, E_r \cos\phi)^{1/2} \qquad (5)$$

où ϕ représente le déphasage du champ indirect par rapport au champ direct

Le modèle classique de la propagation sur terre sphérique permet d'exprimer les champs direct et réfléchi en fonction du champ émis E_0 :

$$E_d = \alpha \cdot F_d \cdot E_0 \qquad (6)$$

$$E_r = \alpha \cdot \rho_0 \cdot \rho_S \cdot F_r \cdot D \cdot E_0 \qquad (7)$$

relations dans lesquelles :

- α caractérise l'atténuation atmosphérique
- ρ_0 est le coefficient de réflexion de FRESNEL (proche de - 1)
- ρ_S est le coefficient de réflexion dans la direction spéculaire (expression de MILLER et AL.)
- D est le facteur de divergence du faisceau réfléchi
- F_d, F_r sont les contributions des antennes d'émission et de réception pour le rayonnement direct et pour le rayonnement indirect

A l'aide des expressions (6), (7) et (5), les variations temporelles du champ résultant E_T sont déterminées à partir des données de marée mesurée et d'agitation de la mer fournie par la bouée.

Ce type de traitement ne permet en général qu'une reconstitution approchée des figures d'interférence à cause de la méconnaissance de la structure atmosphérique et des incertitudes de mesures concernant la hauteur moyenne de la mer. Cette dernière valeur n'était disponible que toutes les heures en un point placé à quelques kilomètres de la zone de réflexion. De plus, les effets de marée, importants dans cette région induisaient des décalages temporels de hauteur moyenne de la mer entre le point de mesure et la zone de réflexion.

Aussi, en supposant que la propagation s'effectue en atmosphère standard, le profil de marée relevé a été réajusté à partir de la position des extrêma de champ reçu.

Cette procédure a permis de restituer correctement les variations de longue durée du niveau de champ reçu pour l'ensemble des périodes pour lesquelles l'influence de l'atmosphère n'apparaît pas (figure n° 3).

6 - ÉTUDE EXPÉRIMENTALE DU CALCUL DU COEFFICIENT DE RÉFLEXION DANS LA DIRECTION SPÉCULAIRE

6.1. PRINCIPE DE LA MESURE

Le calcul à partir des données expérimentales de ρ_s s'appuie sur le modèle précédemment développé au paragraphe 5. En effet, cette valeur se calcule à partir des valeurs extrêmales du niveau de champ reçu déduit de l'expression (5). Leurs formulations en sont les suivantes :

- Pour le champ minimum :

$$E_m\ (dB) = 20 \log (F_{dm} - \rho_{om}\ \rho_s\ D_m\ F_{im}) \qquad (8)$$

- Pour le champ maximum :

$$E_M\ (dB) = 20 \log (F_{dM} + \rho_{oM}\ \rho_s\ D_M\ F_{iM}) \qquad (9)$$

Elles supposent le coefficient de réflexion dans la direction spéculaire invariant entre deux extrêma successifs. Ceci est vrai pour les situations de mer établies où les conditions météorologiques et océanographiques sont stables dans le temps.

La résolution des deux équations précédentes conduit immédiatement à l'expression du coefficient de réflexion dans la direction spéculaire :

$$\rho_s = -\frac{F_{dm}\ 10^{A/20} - F_{dM}}{D_m\ F_{im}\ \rho_{om}\ 10^{A/20} + D_M\ F_{iM}\ \rho_{oM}} \qquad (10)$$

où $A = E_M - E_m > 0$ est la différence d'atténuation entre les deux extrêma successifs

Pour accéder à cette valeur par l'expérience, deux façons de procéder ont été mises en place.

- La première utilise la marée. Selon son amplitude, la période nécessaire à la détermination d'un point de mesure est alors comprise entre 20 minutes et une heure.

- Comme sur de longues périodes, les caractéristiques d'environnement peuvent changer, un élévateur supportant l'antenne de réception a été employé : les figures d'interférence sont alors reproduites en un temps beaucoup plus court (quelques minutes).

6.2. MESURE DE LA REFLEXION SPECULAIRE A PARTIR DE LA VARIATION DE LA HAUTEUR DU RECEPTEUR

Le champ reçu étant sujet à des fluctuations rapides dues principalement à la mer et dont la période principale maximale était de l'ordre de 10 secondes.

Pour réduire l'influence du terme incohérent correspondant sur les valeurs des extrêma, tout en n'émettant pas d'hypothèses a priori sur sa loi de probabilité, le champ reçu a été moyenné sur un temps largement supérieur à la période principale des vagues.

Dans ce but, la hauteur de l'élévateur variait par palier pendant la mesure. En fixant sa durée à 30 mn et en limitant les erreurs de phase, la durée d'un palier était de 30 secondes et la hauteur entre deux paliers de 10 cm.

A 36 GHz, une descente de 5 m de l'antenne de réception fait passer le champ reçu par 5 minima. La figure n° 4 présente une montée de l'élévateur par mer calme. La courbe en trait plein représente le champ moyenné sur chaque palier tandis que les mesures à 1 Hz apparaissent sous forme de points.

Onze mesures de ce type ont été effectuées sur trois jours consécutifs :

- Le matin du 17 octobre, la mer était calme (H 1/3 = 0.6 m). Les figures d'interférences, dont l'amplitude est 10 dB, sont prononcées. Puis le vent de secteur ouest forcit dans le courant de la journée et de la nuit.

- Le lendemain, sa vitesse atteint plus de 13 m/s. La mer est fortement agitée (H 1/3 > 2.5 m).

  L'amplitude des figures d'interférence, inférieure à 2 dB, a décru fortement.

- Le 19, le vent a molli et la mer est un peu moins rugueuse (H 1/3 = 1.9 m) (figure n° 5).

Puisque l'on considère l'état de la mer invariant pendant la durée du déplacement de l'élévateur, et puisque l'incidence du rayon réfléchi a peu d'influence sur la rugosité de la mer, les valeurs des coefficients de réflexion dans la direction spéculaire ont été moyennées et leurs écarts-type calculés. Ces résultats pour un certain nombre de mesures effectuées apparaissent en figure n° 6 où ont aussi été tracées les courbes théoriques de AMENT et de MILLER et AL.

On y constate une meilleure concordance de l'expression de MILLER et AL. avec les mesures. En particulier, cette expression apparaît bien adaptée quand la mer devient rugueuse.

6.3. MESURE DE LA REFLEXION DANS LA DIRECTION SPECULAIRE A ANTENNES FIXES

Pour compléter les résultats obtenus à partir des mesures effectuées avec l'élévateur, le coefficient de réflexion ρ_s dans la direction spéculaire a aussi été calculé en utilisant les données acquises lorsque les antennes étaient fixes.

Les périodes sélectionnées présentent des figures d'interférence dues au seul phénomène de marée. Les mesures météorologiques mettaient alors généralement en évidence :

- une température de l'air peu élevée
- une forte humidité relative
- la présente de vent

Pour s'abstraire des scintillations dues à la réflexion sur l'océan, les niveaux de champ reçu ont été moyennés sur deux minutes. Cette durée, grande par rapport à la période des vagues dominantes, assure une erreur acceptable sur la position des minima. L'erreur maximale commise sur la phase du signal indirect par rapport au signal direct est inférieure à 15 degrés dans les cas les plus défavorables (marées de forte amplitude).

Les données ont été, de plus, lissées sur 10 minutes, par moyenne glissante, dans le but de filtrer les variations dues à la propagation des vagues par groupe et les variations causées par les turbulences atmosphériques.

De la même façon que précédemment, le coefficient de réflexion dans la direction spéculaire a été déterminé sur une dizaine de périodes correspondant à des rugosités comprises entre 0.06 et 0.46 (figure n° 7).

Suite à ces résultats, il apparaît que la théorie de MILLER et AL. par l'introduction d'une forme sinusoïdale dans l'expression de la hauteur instantanée du niveau de la mer, permet de rendre compte de façon satisfaisante des valeurs du coefficient de réflexion ρ_S mesuré, ceci dans l'ensemble du domaine de rugosité.

7 - PROPAGATION ANORMALE : CAS DE L'ATMOSPHÈRE PERTURBÉE

Dans les paragraphes précédents, la troposphère a été modélisée en considérant une variation linéaire de l'indice de réfraction en fonction de l'altitude (- 39 N/km en atmosphère standard).

Cette modélisation était justifiée par les conditions d'environnement rencontrées car elles étaient peu propices à la suprarréfraction et aux turbulences atmosphériques.

Toutefois, elle est mise en défaut pour rendre compte du champ reçu par changement de la situation météorologique locale. En effet, des mouvements d'advection déforment les figures d'interférences comme il a été observé, pendant une campagne de mesure précédente, lors du passage d'un front chaud et humide venant de l'océan (figure n° 8). Ils conduisent à une variation du gradient d'indice de réfraction de l'air changeant la phase du rayon réfléchi par rapport au rayon direct.

Outre la déformation des figures d'interférence, des fluctuations des niveaux de champ de grandes amplitudes (plus de 25 dB) et de courtes périodes ont été relevées (figure n° 9). Durant cet événement la température de l'air était proche de son maximum journalier (environ 15° C), le vent était faible (quelques mètres par seconde) et l'humidité relative la plus basse (60 - 70 %).

Les conditions météorologiques précédentes sont celles qui permettent d'observer les conduits d'évaporation. Ces conduits, de quelques dizaines de mètres de hauteur, dépendent fortement des paramètres météorologiques au voisinage de la surface. Aussi peuvent-ils avoir des propriétés radioélectriques très fluctuantes causant des évanouissements de grandes amplitudes et de courtes périodes.

8 - CONCLUSION

Cette nouvelle campagne vient compléter la connaissance du phénomène de réflexion spéculaire, sur la surface de la mer, à 36 GHz.

Le coefficient de réflexion dans la direction spéculaire a été calculé à l'aide de mesures recueillies à hauteur fixe, et de mesures recueillies via un système mobile en hauteur, simulant le phénomène de marée.

Compte tenu des incertitudes de mesures, on remarque qu'il existe une bonne correspondance entre ces points de mesures et l'expression de MILLER et AL.

Un modèle de réflexion spéculaire, utilisant cette formulation, dans le cas d'une atmosphère stable à gradient d'indice constant, a permis de calculer les variations de longue durée du signal reçu.

Il ne permet pas néanmoins de rendre compte des phénomènes de propagation anormale observés certains jours.

En effet, des fluctuations de grande amplitude ont été observées durant des périodes non ventées et ensoleillées.

Pour lutter contre les affaiblissements dus :

- au trajet double sur une mer caractérisée par une marée de forte amplitude
- aux fluctuations de l'atmosphère

des techniques variées telle que la diversité d'espace ou le dépointage des antennes, pourraient alors améliorer de façon notable la qualité de la liaison.

BIBLIOGRAPHIE

[1] A.J. MONDLOCH "Overwater propagation of millimeter waves" IEEE Trans. on antennas and propagation, Vol. AP-17, n° 1, January 1969.

[2] J.A. VIGNALI "Overwater line-of-sight fade and diversity measurements at 37 GHz" IEEE Trans. on antennas and propagation, Vol. AP-18, n° 4, July 1970.

[3] R.J. SHERWELL "Measurements of effective sea reflectivity and attenuation due to rain at 81 GHz" Agard conference proccedings n° 245, p. 45-1, 45-8, 1979.

[4] R. MAKARUSCHKA, H.H. FUCHS "Propagation measurements at 94 GHz in a maritime environment" Agard conference proccedings n° 345, Aout 1983.

[5] C.I. BEARD, I. KATZ et L.M. SPETNER "Phenomenological vector model of microwave reflection from the ocean" IRE Trans. on antennas and propagation, Vol. AP-4, pp. 162 - 167, April 1956.

[6] C.I. BEARD "Coherent and incoherent scattering of microwaves from the ocean" IRE Trans. on antennas and propagation, Vol. AP-9, pp. 470 - 483, September 1961.

[7] P. BECKMAN, A. SPIZZICHINO "The scattering of electromagnetic waves from rough surfaces" Pergamon press, 1963.

[8] Y. HURTAUD, A. JUNCHAT "The effects of the sea surface on low level propagation at 36 GHz" Conférence AGARD n° 407, Ottawa, Octobre 1986.

[9] W.S. AMENT : "Toward a theory of reflection by a rough surface "Proccedings of the IRE", n° 41, 1953, pp. 142 - 146.

[10] A.R. MILLER, R.M. BROWN, E. VEGH : "New derivation of the rough - surface reflection coefficient and for the distribution of the sea-wave elevations" IEE Proccedings, Vol. 131, Pt. H, n° 2 April 1984, pp. 114 - 115.

REMERCIEMENTS

Les auteurs souhaitent adresser leurs remerciements au sous-groupe AC.243 commission 3 du RSG.8 pour leurs avis éclairés et leurs soutiens techniques. Leur gratitude s'adresse spécialement au Dr. J. SNIEDER, président du sous-groupe ainsi qu'à W. KEIZER (FEL - TNO), R. MAKARUSCHKA (FGAN - FHP), J.P. CHAPUIS, B. DUBOISSET (STTE/DCC/TFH). Sans le financement du service technique des télécommunications et des équipements aéronautiques (STTE), les campagnes de mesures menées près de LORIENT n'auraient pu être menées à bien.

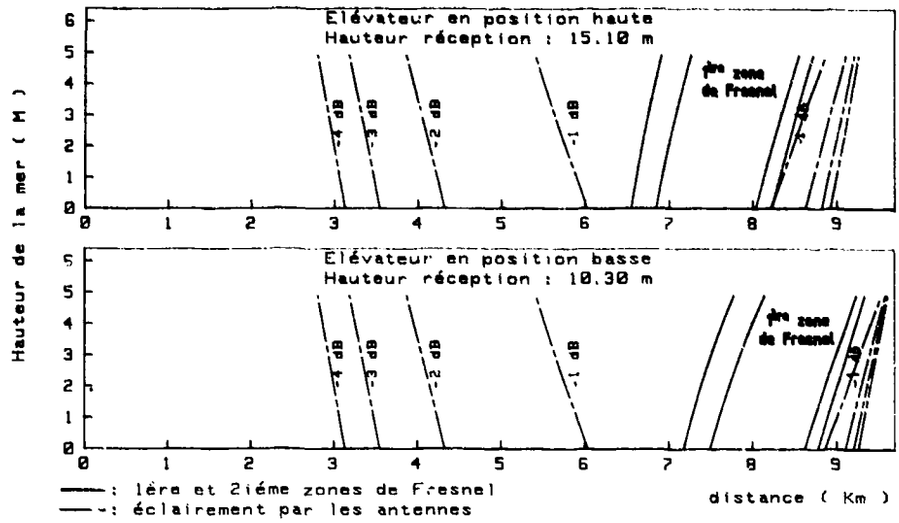


FIGURE N° 1

ECLAIREMENT PAR LES ANTENNES DES DEUX PREMIERES ZONES
DE FRESNEL EN FONCTION DU NIVEAU MOYEN DE LA MER
ET DE LA HAUTEUR DU RECEPTEUR

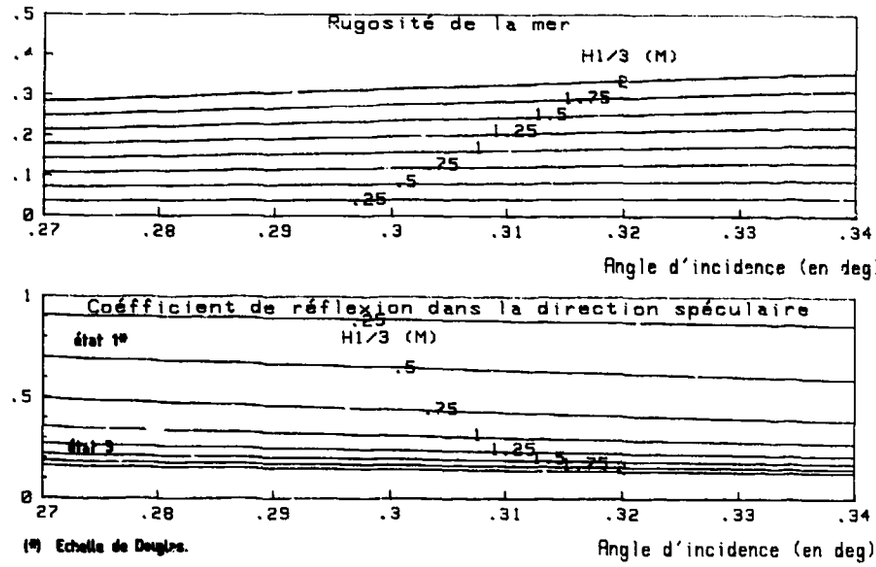


FIGURE N° 2

RUGOSITE DE LA MER ET COEFFICIENT DE REFLEXION
DANS LA DIRECTION SPECULAIRE A 36 GHz
POUR UNE LIAISON A INCIDENCE RASANTE

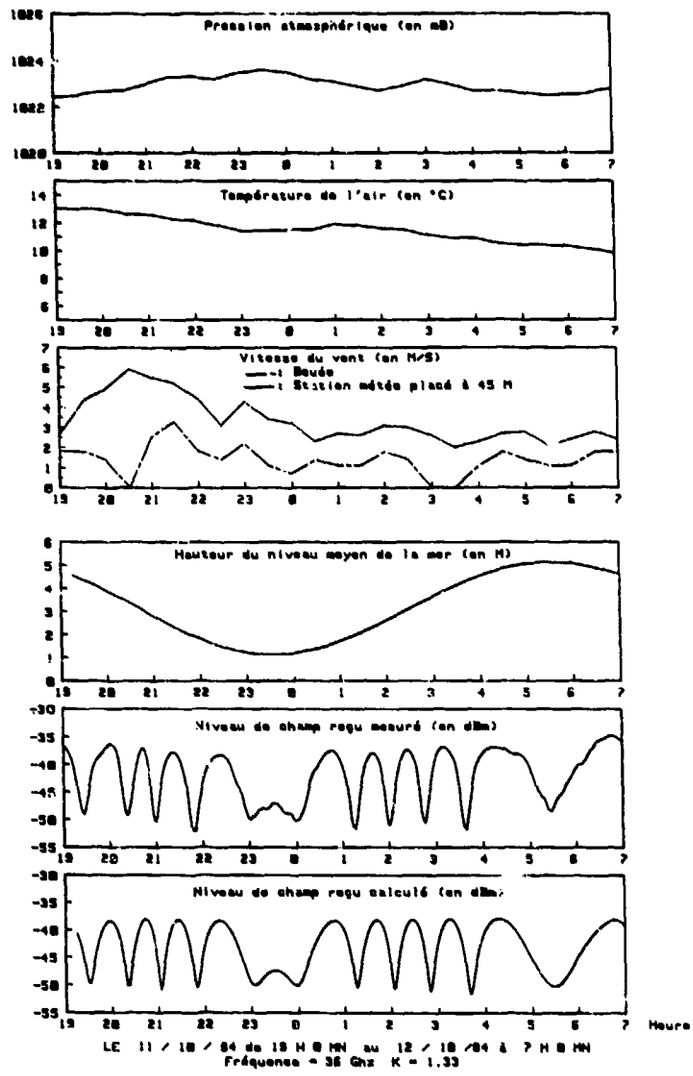


FIGURE N° 3

FIGURES D'INTERFERENCE A 36 GHz

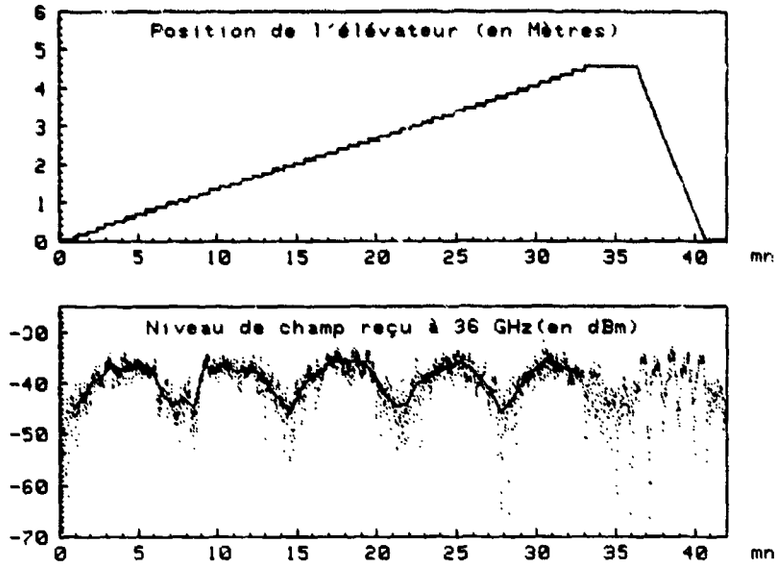


FIGURE N° 4

MESURE EFFECTUEE AVEC L'ELEVATEUR
PAR MER CALME (H 1/3 = 0.6 m)

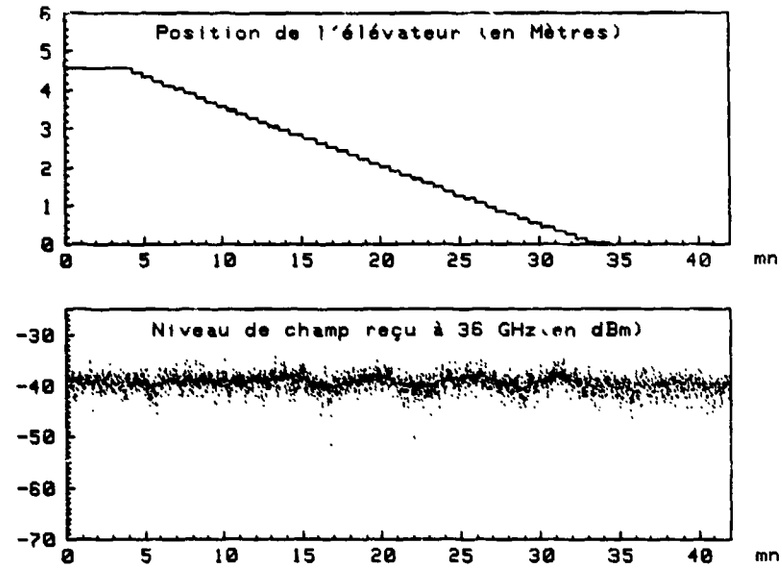


FIGURE N° 5

MESURE EFFECTUEE AVEC L'ELEVATEUR
PAR MER AGITEE (H 1/3 = 1.9 m)

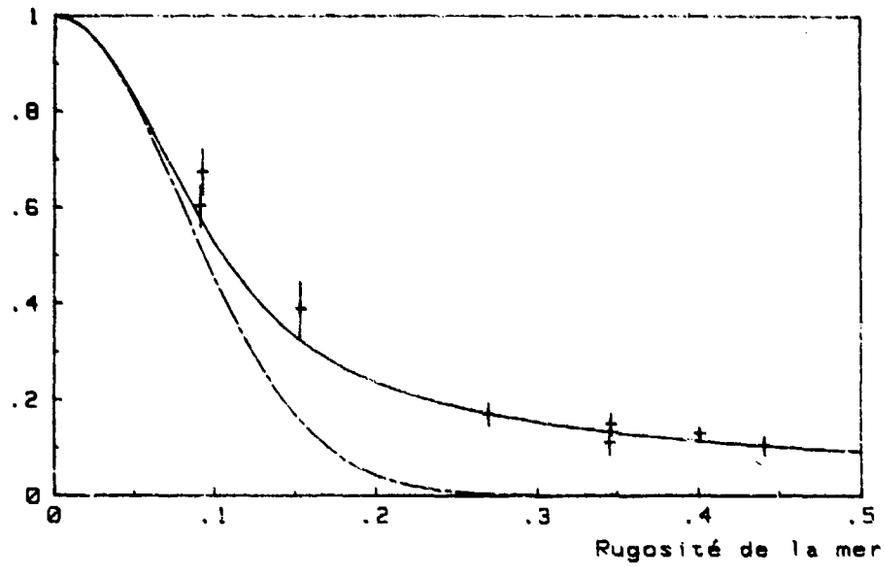


FIGURE N° 6

COEFFICIENT DE REFLEXION DANS LA DIRECTION SPECULAIRE
(MESURES EFFECTUEES AVEC L'ELEVATEUR)

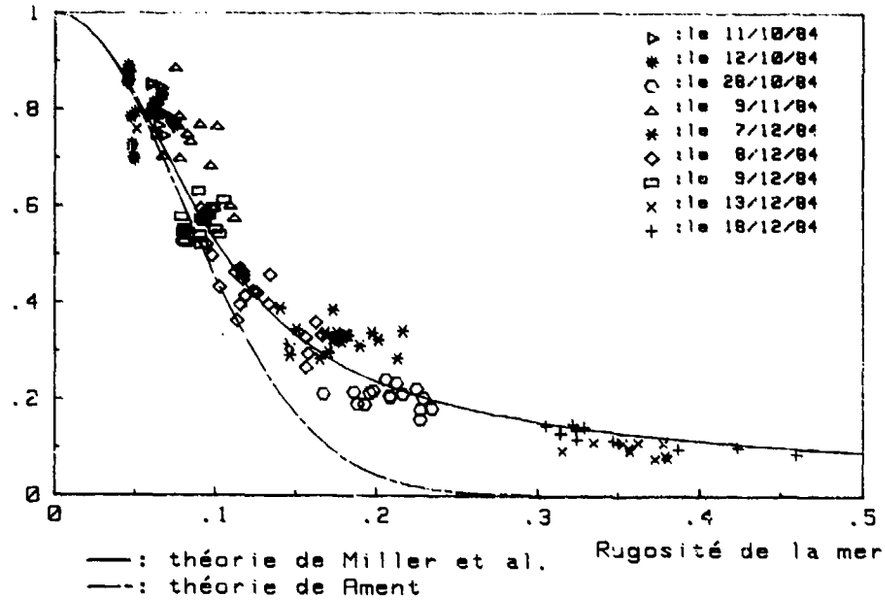


FIGURE N° 7

COEFFICIENT DE REFLEXION DANS LA DIRECTION SPECULAIRE
(MESURES EFFECTUEES A ANTENNES FIXES)

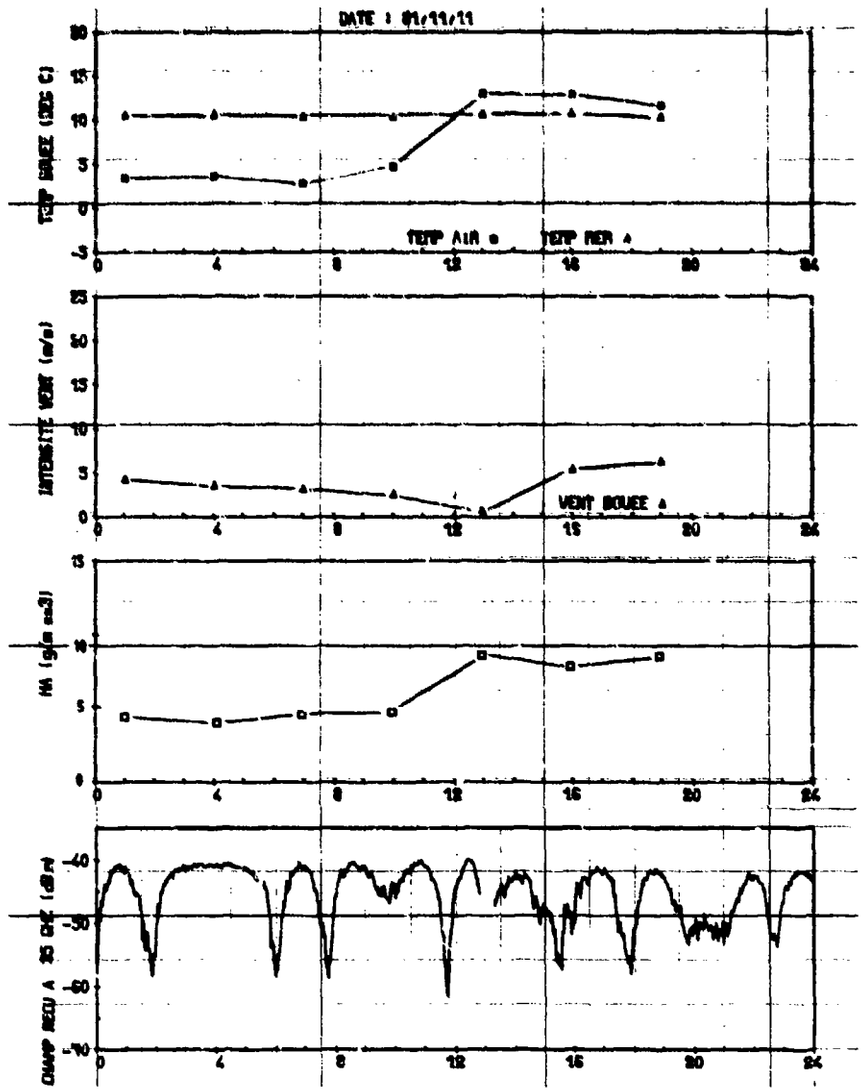


FIGURE N° 8

DEFORMATION DES FIGURES D'INTERFERENCE
LORS DU PASSAGE D'UN FRONT CHAUD ET HUMIDE

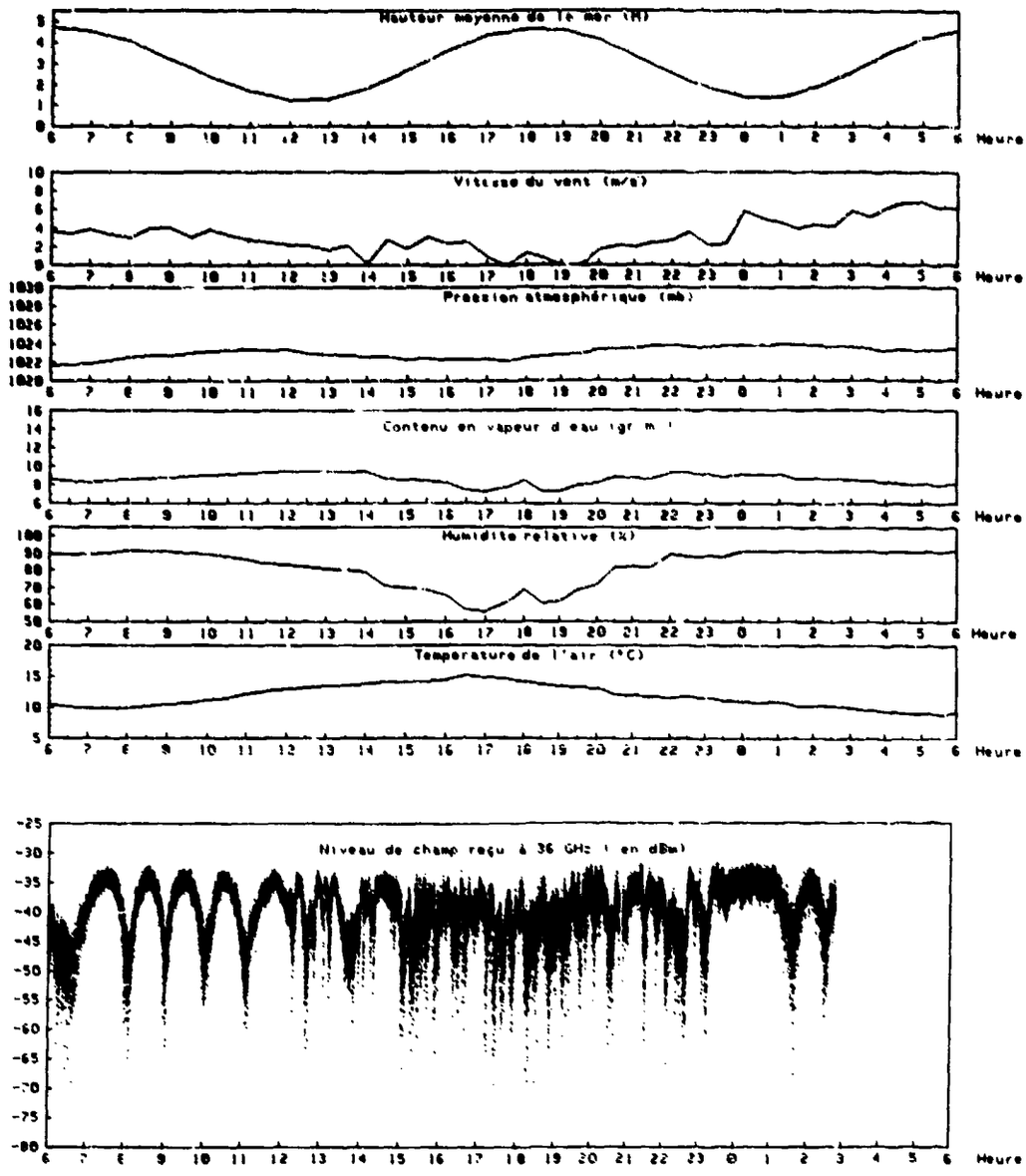


FIGURE N° 9

FLUCTUATIONS DE NIVEAUX DE CHAMP PAR TEMPS CALME
LE 13.10.1984 A LORIENT

SUMMARY OF SESSION VI

IMPACT ON SYSTEMS

by

C.Goutelard, Session Chairman

Session VI, entitled "Impact on Systems" consisted of six papers. Two main themes were addressed. The first one concerned channel modelling and simulation, the second one dealt with the influence of propagation phenomena in random media on systems reliability.

In his report, Martin Nesenbergs tackled the ticklish problem of the use of HF channels in broad band (1 MHz). He mentioned the influence of the jammers and he proposed modelling the channel through a generalisation of the Watterson model.

The report of P.Lo Muzio et al. related to an experiment consisting of measuring the impulse response of VHF links which brings out the existence of multipaths.

In his paper, John Lemmon proved that, in a tropospheric scattering link, there exist particular aspects of the impulse response of the channel. He explained this phenomenon by the dynamics of the propagation medium. A good correlation was found between the BER and the measured channel parameters.

In the next paper, J.A.Offmeyer presented a problem of microwave fading and proposed a model. He analysed the influence of the multipath on the quality of the signal received.

S.Basu et al. presented transfer phenomena occurring in the auroral zone and their effects on communication systems and radars. She described development of irregularities, in particular their drift speed and density. Their effects on clutter from HF radars and on communications were then examined.

The paper by F.Kelly et al. dealt with the worldwide propagation of long waves in the earth-ionosphere cavity. Numerous parameters were introduced in a simulator. The authors have compared the calculation results with the experimental results.

In each paper of this session, two themes, modelisation-simulation and reliability of systems, were addressed either separately or simultaneously in a very broad frequency band, extending from long waves to millimetre waves.

Every report contained, or relied on, experimental results and five of them either used or referred to simulation. These subjects raised considerable interest among the audience and there was extensive debate about the problems.

Suggestions were made by the authors on the explanation of the phenomena and on the difficult problems connected with simulation, as well as on the improvement of concepts, which must be considered for future systems.

The number and the relevance of the questions and comments coming from the audience proves the great interest they felt for the session.

* * *

IMPACT SUR LES SYSTEMES

par

C.Goutelard, Session Chairman

La session VI, dont l'intitulé est "impact on systems" comportait 6 contributions.

Deux thèmes essentiels y ont été abordés. Le premier porte sur la modélisation et la simulation des canaux, le second traite de l'influence des phénomènes de propagation dans les milieux aléatoires sur les performances des systèmes.

Dans sa communication, Martin Nesenbergs aborde le problème délicat de l'utilisation en large bande — 1 MHz — du canal ionosphérique en ondes décamétriques. L'influence des brouilleurs est signalée et une modélisation du canal par une généralisation du modèle de Watterson y est proposée.

La communication de P.Lo Muzio et autres, relate une expérimentation sur la mesure de la réponse impulsionnelle de liaisons VHF qui fait ressortir l'existence de trajets multiples.

Le Dr John Lemmon montre l'existence, dans une liaison numérique par diffusion troposphérique, d'aspects particuliers de la réponse impulsionnelle du canal, qu'il interprète par la prise en compte de la dynamique du milieu de propagation. Le BER comparé aux paramètres mesurés du canal, montre une bonne corrélation.

Le problème de l'affaiblissement des micro-ondes est abordé dans l'exposé du Dr J.Offmeyer qui en propose une modélisation et une simulation. Les trajets multiples et leur influence sur la qualité du signal reçu y sont discutés.

Les phénomènes de communication et les radars sont exposés par le Dr S.Basu et autres. Le développement des irrégularités, notamment leur vitesse de dérive et leur densité, est décrit. Les effets sur le fouillis des radars HF et sur les télécommunications sont ensuite examinés.

Les ondes longues sont considérées dans l'exposé du Dr F.Kelly et autres, qui examinent leur propagation à l'échelle mondiale dans la cavité Terre-Ionosphère. De nombreux paramètres sont introduits dans un simulateur dont les résultats de calcul sont comparés à ceux obtenus expérimentalement.

Dans cette session, les deux thèmes (modélisation-simulation et performances des systèmes) ont été abordés séparément ou simultanément dans chaque exposé mais dans un domaine de fréquences extrêmement vaste qui s'étend des ondes longues aux ondes millimétriques.

Toutes les communications présentées comportent ou s'appuient sur des résultats expérimentaux et cinq d'entre elles utilisent ou font référence à la simulation. Ces points ont d'ailleurs soulevé l'intérêt de l'auditoire qui en a longuement débattu.

Des suggestions ont été faites par les auteurs, tant sur les interprétations des phénomènes et les difficiles problèmes que soulève la simulation que sur l'amélioration des concepts à envisager pour les systèmes futurs.

Le nombre et la pertinence des questions et des commentaires émanant de l'auditoire montrent le grand intérêt qu'il y a trouvé.

RANDOM PROPAGATION THROUGH THE LONGWAVE CHANNEL

by
F.J. Kelly, ?.J. Rhoads, M.D. Andrews*
Naval Research Laboratory
E.O. Hulburt Center for Space Research
Ionospheric Effects Branch
Washington, D.C. 20375-5000

*Interferometrics, Inc.
8150 Leesburg Pike
Vienna, VA 22180

SUMMARY

The longwave propagation channel in the earth-ionosphere waveguide has many characteristics of a random medium. The lower surface of the waveguide is sometimes rough or smooth depending on the propagation path considered. The ionospheric boundary is significantly perturbed by sudden events during both daytime and nighttime. The polar-arctic regions of the world evidence these effects in a striking manner and require different statistical treatment. Recent observation of longwave fields in the arctic will be described and their degree of agreement with statistica predictions displayed.

1.0 INTRODUCTION

At low frequencies (below 300kHz) radio wavelengths are large (greater than a kilometer) in comparison to common antenna sizes. Such waves can be radiated efficiently from long wires suspended from balloons on aircraft or from high Q vertical monopole antenna structures. The change of electron density in the lower ionosphere is so rapid with height that a large change in radio refractive index takes place within a wavelength of the propagating wave. To treat this case, a true specular reflection formulation of the problem is required - rather than the WKB type of treatment that is used at high frequencies.

The ionospheric effective reflection height is typically 70-90km, which implies that the space between the ionosphere and the ground can be treated efficiently using waveguide mode theory.

The variability of the ionosphere and the earth's surface makes the earth-ionosphere waveguide a random propagation channel for long wavelength radio waves. The upper boundary of the waveguide, the ionosphere, is too large, complex and variable to be adequately predicted or sensed over an entire propagation path totalling many thousand kilometers in length. In many longwave prediction calculations this variability is suppressed and a constant ionospheric profile assumed - one profile for daytime propagation and one profile for nighttime (Refs. 1 and 2). We will discuss in greater detail attempts to treat the ionosphere statistically (Refs. 3 and 4). The lower boundary of the earth-ionosphere waveguide, the ground, is a rough and variable surface whose parameters are also not well known over the vast distances of a typical propagation path. In the Arctic there are regions of low ground conductivity caused by ice caps, perma-frost and sea ice (Refs. 5 and 6). Likewise the hills and mountains along a propagation path represent a challenging assembly of random scattering centers.

The daytime and nighttime D-region where the reflection of long radio waves normally occurs is not very well modelled (Refs. 7 through 18). In spite of hard work and large computer codes, the baffling chemistry and composition of this region have presented strong obstacles to our understanding of its behavior.

Recently, an additional complication has been added with the suggestion that the occurrence of lightning from thunderstorms is a strong causative factor in the production of the nighttime D-region through the laser-like stimulation of electron precipitation from the Van Allen Belts (Refs. 19 through 21). There has also been a strong suggestion that the water vapor molecules which are important to the D-region chemistry are supplied to the D-region by a "rain" of snowy meteors from space (Ref. 22). It will be interesting to see how these speculations affect the future development of longwave propagation predictions.

In this paper we shall treat several statistical aspects of the longwave channel. In section 2 we will present some hitherto unpublished experimental results on the stability of the longwave channel in the neighborhood of an interference null. We will also display measurements and theory for the frequency dependence of the broadcast signals strength from the NWC broadcast

transmitter in Australia measured at Japan, Alaska, the Philippines, Madagascar, and Bahrein.

In section 3 we will treat propagation in the arctic area, involving solar proton events (SPE's) and propagation over the Greenland Ice Cap. We observe that such events must be taken into account for the specification of a 99% time availability signal exceedance level prediction in the arctic.

2.0 PROPAGATION IN TEMPERATE LATITUDES

An experiment was performed to study the stability of the longwave propagation channel near multimode interference nulls in November and December 1970. Longwave measurements were made continuously as a function of distance and time in the neighborhood of the modal interference null in Florida, USA, at a range of 2.4 Megameters from the Navy VLF transmitter located in Balboa, The Canal Zone -now Panama- (see Figure 1). Figure 2 shows the predicted field strength versus distance pattern. The ionospheric profile parameters β and h were assumed to have average values of .5km^{-1} and 70km. The assumed standard deviation of height was 1km and of β was .05km^{-1}. The statistical prediction (Ref. 3) of field strength was made using a Monte Carlo technique. The data (also shown in Figure 2) indicate that the observed variability was smaller than predicted. A scatter plot of the aircraft measurements is shown in Figure 3. There is a very small variability of the observed data except for one case which probably indicates a solar flare disturbance. Diurnal plots of several days' observations at different ground stations along the propagation path are shown in Figure 4.

Measurements were also made in 1981 and 1982 using the U.S. Navy LF transmitter near Athens with reception at Naples, Italy, and La Maddalena, Sicily, (Ref. 4). These observations were compared with predictions using the following distribution function of the ionospheric parameters β and h.

$$f_{ij} = \frac{\exp - \frac{1}{2} G_{ij}}{2\pi\sigma_\beta \sigma_h (1-r^2)^{1/2}} \qquad (1)$$

The G_{ij} parameter is given by

$$G_{ij} = \frac{\frac{(\beta_i - \beta_0)^2}{\sigma_\beta} + \frac{(h_j - h_0)^2}{\sigma_h} - 2r \frac{(\beta_i - \beta_0)}{\sigma_\beta} \frac{(h_j - h_0)}{\sigma_h}}{1 - r^2} \qquad (2)$$

Here r is the correlation coefficient, σ_β is the standard deviation of β, and σ_h is that of h. From the observations, the ionospheric parameters given in Table I were deduced.

Between September and December 1967 the U.S. Navy North West Cape transmitter at Exworth, Australia, broadcast in a regular schedule which permitted measurements at six different frequencies between 15.5kHz and 26.8kHz. Field strength measurements were made in Madagascar, Japan, the Philippines, Alaska, and Bahrein (Refs. 23 and 24) during this time. Figures 5 through 9 show the results of daytime measurements. Comparisons are given with theoretical predictions. The solid prediction curve labelled 6663 refers to signal predictions extracted from the graphs in Reference 26, based on Reference 27 for a β = .5km^{-1}, h = 70km ionospheric profile. The short dashed line curve is labelled NCPP-70 (standing for Navy Coverage Prediction Program -70) is a prediction from an empirically-developed single mode propagation model. The long dashed line labelled WAVEGUIDE is based on a waveguide mode propagation prediction method taking the anisotropy of the ionosphere into account. We see that all three models predict the variation of the observed data. It is interesting to notice that the NCPP-70 model and the 6663 model are in significant disagreement (7-11dB error) with the observations for the Madagascar and Bahrein measurements at 14.7kHz. The agreement is better for these models at Japan and Alaska. The WAVEGUIDE predictions show that accounting for the ionospheric anisotropy improves the agreement between theory and observation.

Figures 10 through 14 show comparisons for nighttime propagation conditions on the same paths. For the paths shown in Figures 10 through 13, the multimode model (labelled 6663) seems to agree better with the measurements than the empirical single mode model (labelled NCPP-70). In Figure 14 the reverse is this case.

3.0 PROPAGATION IN THE ARCTIC

The arctic environment poses a special problem of the prediction of long waves because both boundaries of the earth-ionosphere waveguide are significantly different from temperate zones. The earth's surface is different because of the predominance of low conductivity areas of perma-frost, sea ice, and ice cap. The ionosphere is different because of the prevalence of aurorae and the ready access of cosmic rays and other ionising charged particle fluxes into the earth's geomagnetic polar cap area. Thus, there are large uncertainties about the behavior of long radio wavefields in this dynamic, unfamiliar environment (Refs. 28-31).

On September 20, 1985, an NRL aircraft flew from Soundrestromfjord, Greenland, to Bardufoss, Norway, via Nord, Greenland. During this flight the NAA transmitter of Cutler, Maine, was monitored using an NM-12 AT receiver which was stabilized in frequency at 24.0kHz. Figure 15 shows the behavior of the fields as a function of aircraft location. The most significant aspect of this data is the high attenuation as the aircraft flew across the ice cap. At the end of the transit of the ice cap, the fields recover in intensity above 80°N latitude. A second interesting observation is the fluctuation of the fields in the portion of the flight between 70°N and 78°N in the sea area north of Norway. The aircraft is still in the "shadow" of the Greenland Ice Cap during this portion of the flight. These deep and rapid (short range) oscillations are not predicted by the standard two-dimensional waveguide propagation models. They possibly represent an interference pattern from waves diffracting horizontally around the ice cap. Figure 16 shows a typical comparison between the observed and predicted signal and noise level for the U.S. Navy's NAA, Cutler, Maine, transmitter (NAA) on 24.0kHz and 1MW (megawatt) radiated power as measured at Isfjord Radio, Spitzbergen, Svalbard. The signal and noise are referred to a 100 Hz bandwidth. We can observe that there is good agreement during all nighttime propagation conditions, but during the daytime the observed signal is about 10dB lower than predicted.

When a solar proton event occurs, enhanced absorption is often noted on riometer and HF communications circuits. Longwave propagation is affected also. Figures 17 and 18 show the variations of Cutler's VLF field at Spitzbergen during the solar proton events of Feb. 6 and Feb. 14, 1986. The VLF fields decreased by about 5dB during daytime and 20dB at nighttime. The solar x-ray burst intensity, which precedes the arrival of the protons at the earth's orbit by a period of hours, is also displayed.

Solar proton events (Refs. 32 and 33) are fairly common occurrences at any time in the solar cycle. Figure 19 shows the observed probability of proton flux as calculated from the data given in Ref. 33. We may note that one percent of the time the flux level exceeded 2×10^4 protons m^{-2} sec^{-1} str^{-1}. Figure 20 shows the impact of these protons in reducing the reflection height of VLF waves at Thule (Ref. 31). Combining Figures 19 and 20, one can observe that one percent of the time the Arctic VLF reflection height is expected to be reduced 7km below its expected level. Thus the solar proton disturbed ionosphere must be accounted for in any 99% or higher time availability prediction.

It is interesting to note that the signal reductions of Figs. 17 and 18 correlate with the intensity of the highest energy protons which produce ionization at the lowest altitudes.

4.0 ANALYSIS OF ARCTIC PROPAGATION PROBLEMS

The propagation of long waves across icecaps and sea water were considered by Field et al (Refs. 34,35) and by Kossey et al (Ref. 36) during ambient conditions and polar cap absorption events. Figure 21 shows the electron and ion density profiles similar to those considered by Field. Field's ambient day profile has a soft or diffuse ionospheric lower boundary as exhibited by the electron density curve. Field's PCA1 and PCA2 profiles have a much sharper and lower electron density profile. This lowering of the electron density profile during a PCA causes somewhat increased attenuation because of the greater number of reflections between ionosphere and ground needed to go a specified distance. However, this is largely counterbalanced by the increase in the ionosphere reflection coefficient because of the sharpening of the ionospheric boundary. The strong absorption during a Polar Cap Absorption Event over an ice cap requires the presence of a greatly enhanced level of ionization present as positive and negative ions below the level of the electron ionosphere. The attenuation rate versus frequency curves calculated by Field for ambient day, PCA1 and PCA2 over an ice cap are shown on Figure 22 which also include the attenuation rate curves used in the empirical VLFACM program for ice cap and arctic land. We note that the attenuation rates of Field for an ice cap condition exceed those of the VLFACM program by about 5dB/Mm. Since there is approximately 1.6Mm of ice cap between NAA Cutler, Maine, and Spitzbergen, Svalbard, the increase in attenuation rate can nearly account for the 10dB discrepancy in daytime field level evidenced in Fig. 16. Replacing the ice cap attenuation rate in the VLFACM program by those of Field, we calculate the

theoretical received strength pattern shown in Fig. 23. When we replace the ice cap attenuation rate by the PCA2 attenuation rates, we get the predictions shown in Fig. 24 which are contrasted with field strength data obtained during the PCA events of February 1987. We see that the utilization of the ice cap attenuation rate curves of Field in the VLFACM program greatly improves the theoretical agreement with the September 1985 Spitzbergen ambient day measurements. The February 1986 polar cap absorption measurements are reproduced fairly well by using Field's PCA2 attenuation rate.

5.0 CONCLUSIONS

The present paper has outlined some current problems in longwave propagation predictions and points the way to some progress. The random nature of the propagation channel has been displayed for both temperate and arctic propagation conditions.

REFERENCES

1. Gardiner, R.S., "Comparison of Predicted VLF/LF Signal Levels with Propagation Data," Defense Communications Agency, 960-TP-74-5, 21 Jan 1974.

2. Reed, W.G., "Determination of Effective Ionospheric Electron Density Profiles for VLF/LF Propagation," Defense Communications Agency, C650-TP-76-4, 1 Jan 1976.

3. Kelly, F.J., F.J. Rhoads and J.P. Hauser, "On Statistical VLF Multimode Propagation Predictions," NRL Report 7239 (1971).

4. Furgeson, J.A., D.G. Morfitt and P.M. Hansen, "Statistical Model for LF Propagation," in Effects of the Ionosphere in C3I Systems, ed. by J.M. Goodman, (1984), pp. 387-394.

5. Morgan, R.R., "World-Wide VLF Effective-Conductivity Map," Westinghouse Electric Corporation Report 8013 F-1, 1968.

6. Hauser, J.P., W.E. Garner and F.J. Rhoads, "A VLF Effective Ground Conductivity Map of Canada and Greenland with Revisions Derived from Propagation Data," NRL Report 6893, 4 March 1969.

7. Heaps, M.J. and J.M. Heimserl, "The Quiet Midlatitude D-region: A Comparison Between Modeling Efforts and Experimental Measurements," J.Atmos.Terr.Phys., 42, (1980), pp. 733-742.

8. Torkar, K.M. and M. Frederich, "Tests of an Ion. Chemical Model of the D- and Lower E-region," J.Atmos.Terr.Phys., 45, (1983), pp. 369-385.

9. Swider, W. and R.S. Narcisi, "A Study of the Nighttime D Region During a PCA Event," J.Geophys.Res., 80, (1975), pp. 655-664.

10. Sears, R.D., M.G. Heaps and F.E. Niles, "Modeling the Ion Chemistry of the D Region: A Case Study Based on the 1966 Total Solar Eclipse," J.Geophys.Res., 86, (1981), pp. 10,073-10,086.

11. Swider, W., "Daytime Nitric Oxide at the Base of the Thermosphere," J.Geophys.Res., 83, (1978), pp. 4407-4410.

12. Johnson, C.Y., "Ion and Neutral Composition of the Ionosphere," Annals of the IQSY, Vol. 5, Solar Terrestrial Physics: Terrestrial Aspects, (M.I.T. Press, 1969).

13. Solomon, S., G.C. Reid, D.W. Rusch and R.J. Thomas, "Mesopheric Ozone Depletion During the Solar Proton Event of July 13, 1982: Part II. Comparison Between Theory and Measurements," Geophys.Res.Lett., 10, pp. 257-260 (1983).

14. Rusch, D.W., J.C. Gerard, S. Solomon, P.J. Crutzen and G.C. Reid, "The Effect of Particle Precipitation Events on the Neutral and Ion Chemistry of the Middle Atmosphere - I. Odd Nitrogen," Planet. Space Sci., 29, pp. 767-774 (1981).

15. Garcia, R.R. and S. Solomon, "A Numerical Model of the Zonally Averaged Dynamical and Chemical Structure of the Middle Atmosphere," J. Geophys. Res., 88, pp. 1379-1400, (1983).

16. Solomon, S., G.C. Reid, R.G. Roble and P.J. Crutzen, "Photochemical Coupling Between the Thermosphere and the Lower Atmosphere 2. D Region Ion Chemistry and the Winter Anamoly," J. Geophys. Res., 87, pp. 7221-7227, (1982).

17. Swider, W., T.J. Keneshea and C.I. Foley, "An SPE-Disturbed D-Region Model," Planet. Space Sci., 26, (1978), pp. 883-892.

18. Blekovich, V.V., Ye. A. Benediktov and M.A. Itkena, "Electron-Loss Function in the Ionospheric D Region and Dependence of Anamalous Radio-Wave Absorption on the Solar Zenith Angle During Sudden Ionospheric Disturbances," Geomag. and Aeronomy, 17, (1977), pp. 290-292.

19. Tolstoy, A., T.J. Rosenberg and D.L. Carpenter, "The Influence of Localized Precipitation-Induced D-Region Ionization Enhancements on Subionospheric VLF Propagation," Geophys. Res. Letters, 9, (1982), pp. 563-566.

20. Voss, H.D., W.L. Imhof, M. Walt, J. Mobilia, E.E. Gaines, J.B. Reagan, U.S. Inan, R.A. Helliwell, D.L. Carpenter, J.P. Katsufrakes and H.,C. Chang, "Lightning-induced Electron Precipitation," Nature, 312, (1984), pp. 740-742.

21. Leyser, T.B., U.S. Inan, D.L. Carpenter, and M.L. Trimpi, "Diurnal Variation of Burst Precipitation Effects on Subionospheric VLF/LF Signal Propagation Near L-2," J. Geophys. Res., 89, (1984), pp. 9139-9143.

22a. Frank, L.A., J.B. Sigwarth and J.D. Craven, "On the Influx of Small Comets into the Earth's Upper Atmosphere I. Observations," Geophys.Res.Letters, 13, (1986), pp. 303-306.

22b. Meier, R.R. and T.A. Chubb, "Issues Relating to 'Holes' in the Far UV Dayglow", (to be published in Geophys. Res. Letters).

23. Brookes, C.B. and J.E. Raudenbush, "Field Strength Measurements for NWC, North West Cape, Australia, from September to December 1967," NRL Report 7148, 23 Sept. 1970.

24. Lynn, K.J.W., "Frequency Dependence of VLF Modal Interference Effects Observed on East-West Propagation Paths," J. Atmos. and Terr. Phys., 33, (1971), pp. 951-958.

25. Bickel, J.A. - Private Communication.

26. Brookes, C.B., Jr., J.H. McCabe and F.J. Rhoads, "Theoretical VLF Multimode Propagation Predictions," NRL Report 6663, 1 Dec. 1967.

27. Wait, J.R. and K.P. Spies, "Characteristics of the Earth-Ionosphere Waveguide for VLF Radio Waves," NBS TN300, 30 Dec 1964.

28. Sengupta, P.R., "Solar X-ray Control of the D-region of the Ionosphere," J. Atmos. and Terr. Phys., 42, (1980), pp. 339-355.

29. Larsen, T.R., "Irregular Variations in the High Latitude Ionosphere and their Effects on Propagation," J.A. Holtet (ed.), ELF-VLF Radio Wave Propagation, pp. 171-185 (1974), D. Reidel Publishing Co. (Dordrecht, Holland).

30. Westerlund, S. and F.H. Reder, "VLF Propagation at Auroral Latitudes," J. Atmos. and Terr. Phys., 35, (1973), pp. 1453-1474.

31. Turtle, J.P., J.E. Rasmussen, W.I. Klemetti and P.A. Kossey, "VLF/LF Pulse Reflection Measurements of the Polar D-Region During Quiet and Disturbed Ionospheric Conditions," in "Medium, Long and Very Long Wave Propagation (at frequencies less than 3000kHz), AGARD Conference Proceedings No. 305 (1982), ed. by J. Belrose, pp. 3-1 to 3-12.

32. Adams, J.H. and A. Gelman, "The Effects of Solar Fluxes on Single Event Upset Rates," IEEE Trans. on Nucl. Sci., Vol. NS-31, (1984), pp. 1212-1216.

33. Adams, J.H., R. Silberberg and C.H. Tsao, "Cosmic Ray Effects on Microelectronics, Part I: The Near-Earth Particle Environment," NRL Memo Report 4506, 25 Aug. 1981.

34. Field, E.C., "The Effects of Ions on Very-Low-Frequency Propagation during Polar-Cap Absorption Events," Radio Science, 5 (1970), pp. 591-600.

35. Field, E.C., C. Greifinger and K. Schwartz, "Transpolar Propagation of Long Radio Waves," Jour. of Geophys. Res., 77 (1972), pp. 1264.

36. Kossey, P.A., J.P. Turtle, R.P. Pagliarulo, W.I. Klemetti, and J.E. Rasmussen, "VLF Reflection Properties of the Normal and Disturbed Polar Ionosphere in Northern Greenland," Radio Sci., 18 (1983), pp. 907-916.

6.0 ACKNOWLEDGMENTS

We want to thank N. Sheeley and J. Adams of NRL for help in understanding, obtaining, and plotting the solar proton data. We want to thank J. Bickel of NOSC for sharing his measured data from Alaska and the Philippines with us. We want to thank A. Kermaier, M. Lord, and P. Rodkin for their work in data analysis, and Mrs. I.P. Hansen-O'Neill and Miss L. DeBlasio for preparing the waveguide mode predictions. We want to thank Arne Gundersen of NTNF, Norway, and the Norwegian workers at Andoya, Norway, and Isfjord Radio, Spitzbergen, for their hospitality. We want to thank Major Clemmenson of the Danish Defense Establishment and the men at Nord, Greenland, for their fine support. We want to thank the air crew and officers of our NRL aircraft for their cooperation and understanding during our measurement campaign. We want to thank the Space and Naval Warfare Systems Command (T. Giaudrone and M. Deebel) and the Defense Communications Agency (Y.S. Fu and A. Blankfield) for their support and advice during these experiments. We want to thank R.A. Pappert, J. Furgeson, and D. Morfitt (deceased) for sending us copies of their prediction programs and instructing us in their use. We want to thank Herb Sauer of the Environmental Research Laboratories of NOAA for providing the solar proton data and x-ray data from the GOES satellites.

TABLE I: Optimum Distribution Parameters from Reference 4.

Month	r	β_0	$\sigma\beta$	h'	σ_h
July	0.90	0.38	0.03	69.0	0.20
January	-0.99	0.33	0.17	73.0	2.80

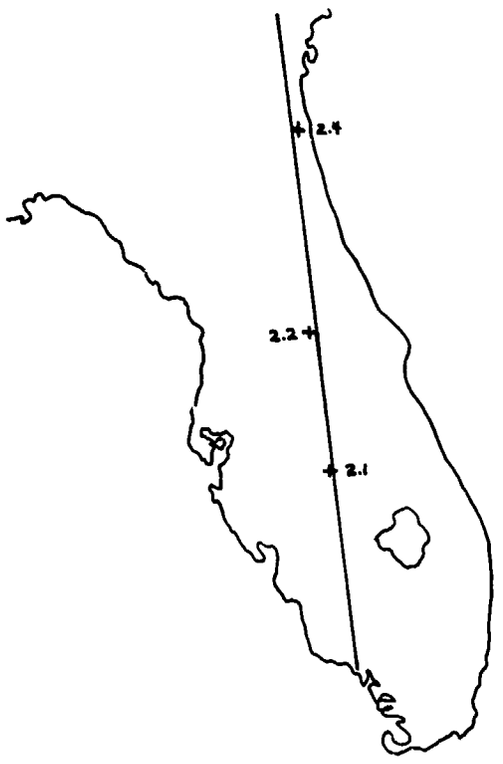


Figure 1. Map of Florida showing the great-circle paths from the NBA transmitter in Panama and the locations of the ground field sites.

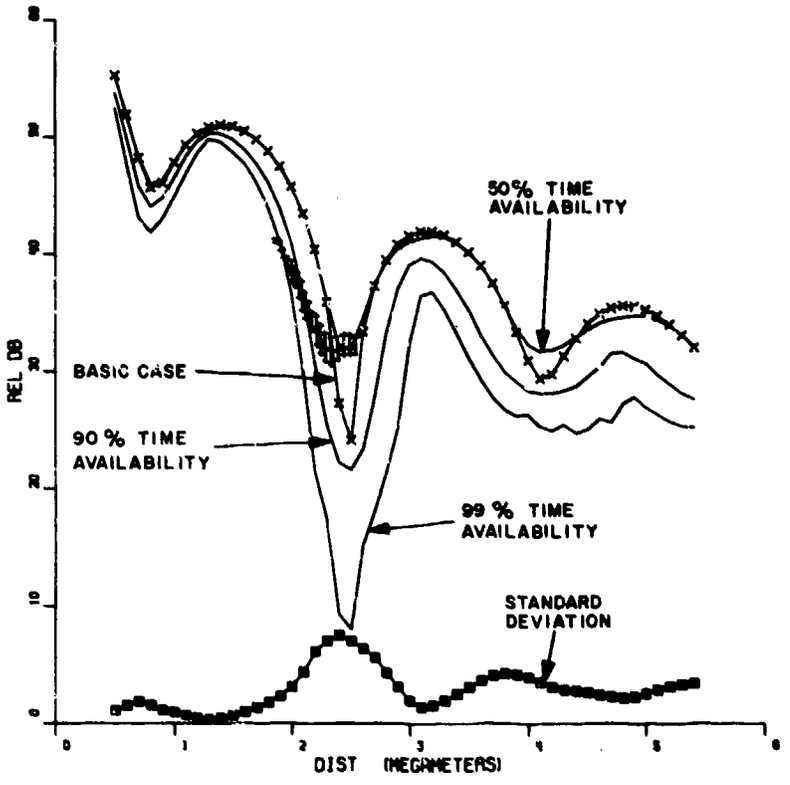


Figure 2. Statistical field strength versus distance predictions. The observed data are also shown.

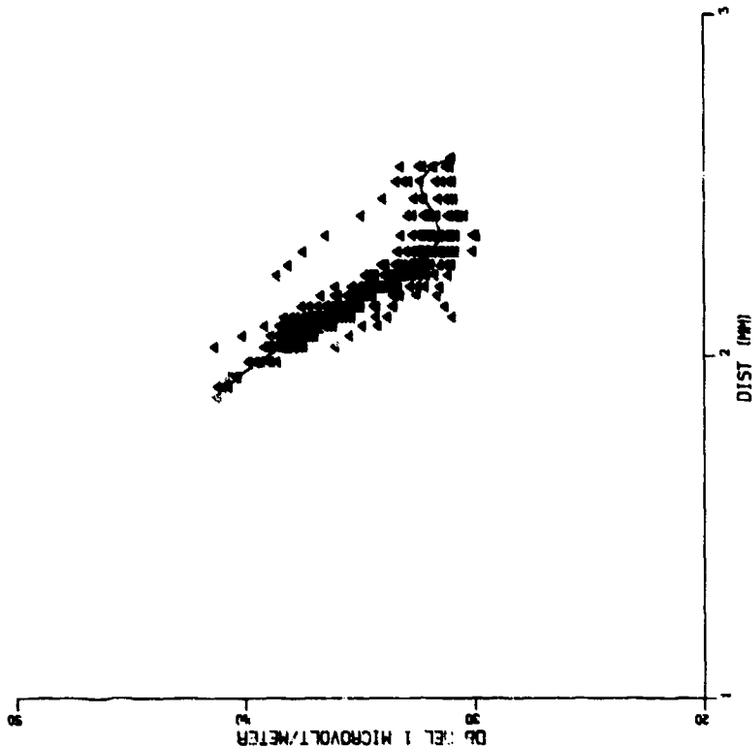


Figure 3. Scatter plot of field strengths observed on the aircraft.

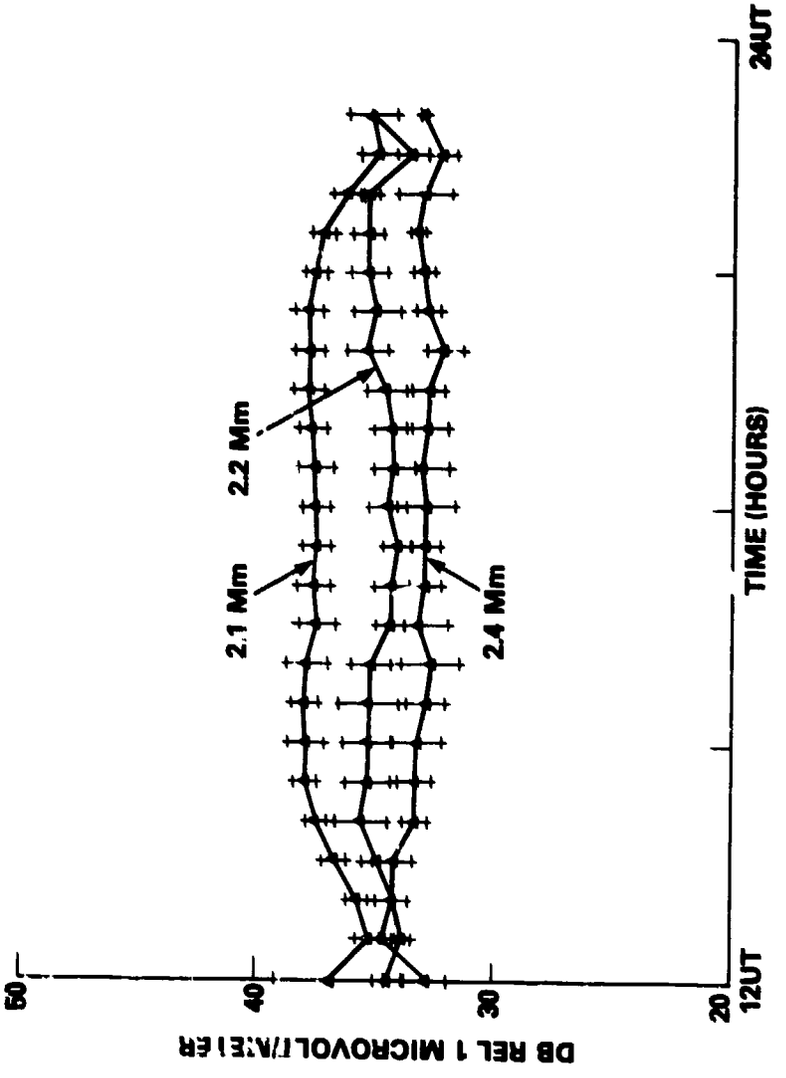


Figure 4. Daytime field strength versus time plots at the three ground sites in Florida.

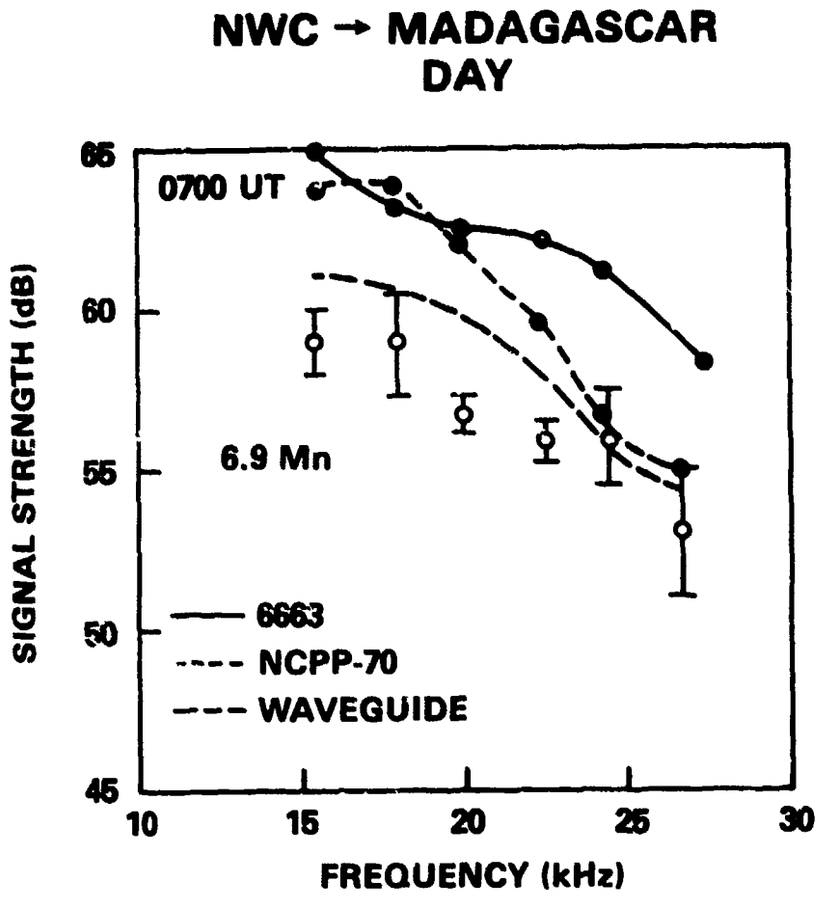


Figure 3. Observed and predicted fields at Madagascar during the 1967 multifrequency experiments of the NWC transmitter.

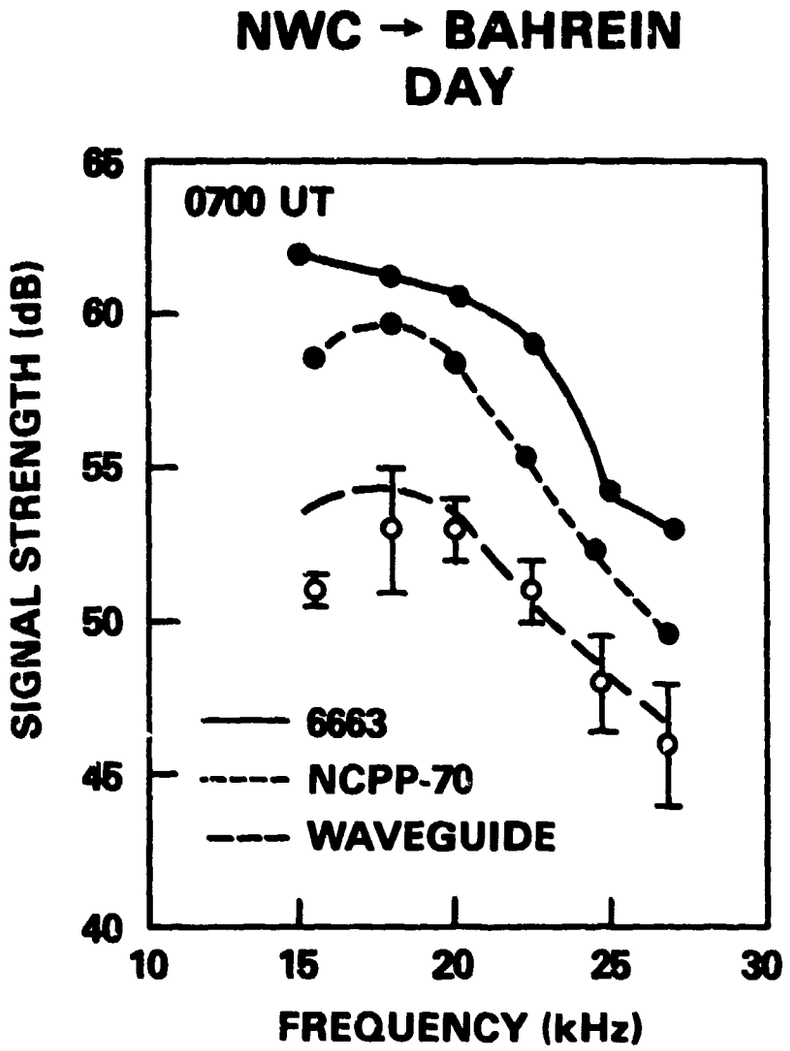


Figure 6. Observed and predicted fields at Bahrein during the 1967 multifrequency experiments of the NWC transmitter.

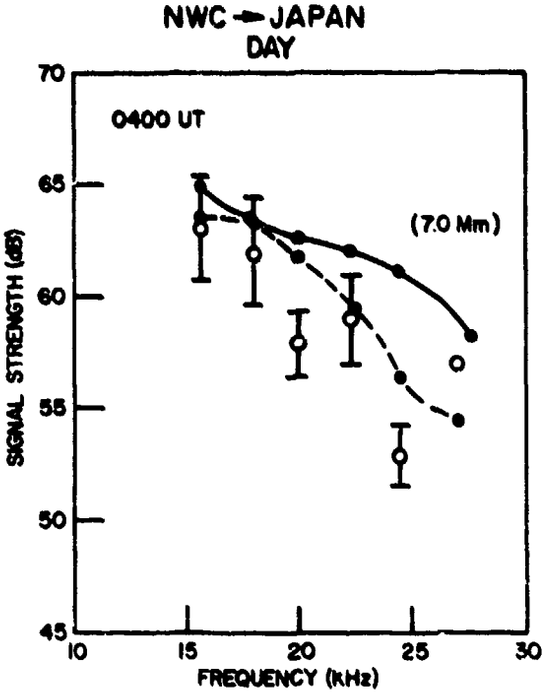


Figure 7. Observed and predicted fields at Inubo, Japan, during the 1967 multifrequenc experiments of the NWC transmitter.

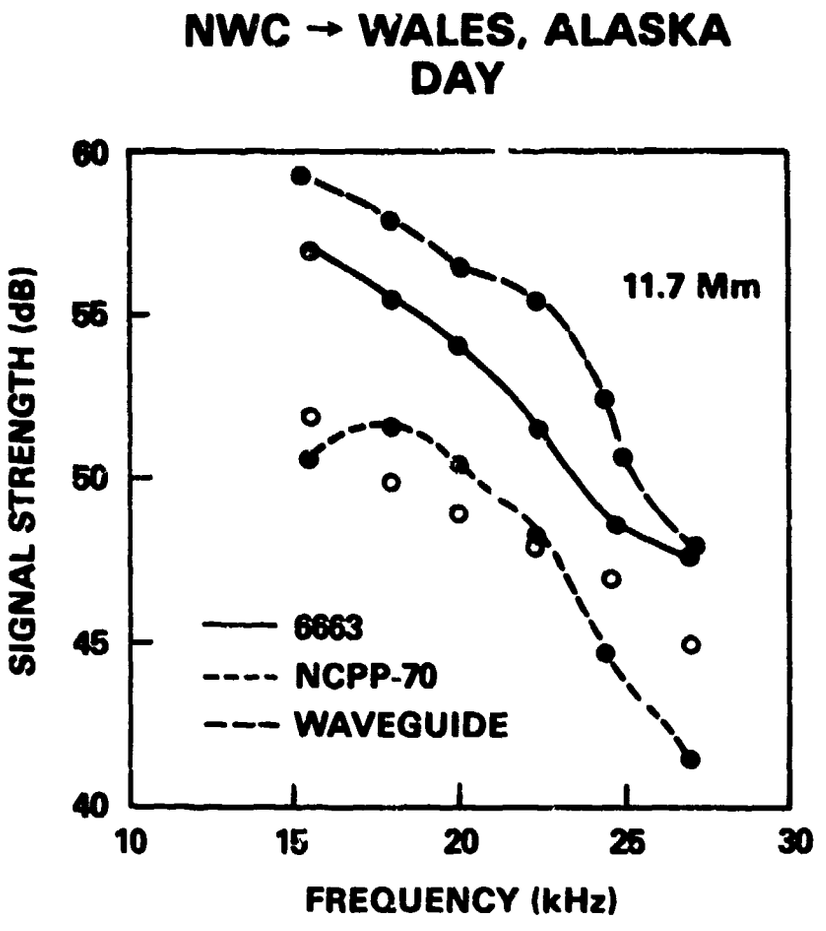


Figure 8. Observed and predicted fields at Wales, Alaska, during the 1967 multifrequency experiments of the NWC transmitter.

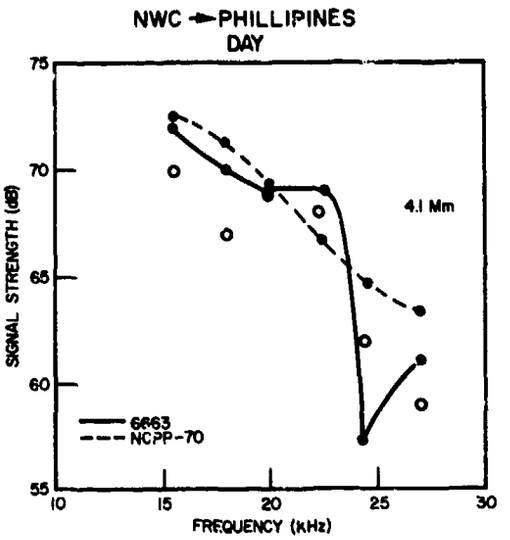


Figure 9. Observed and predicted fields at the Philippines during the 1967 multifrequency experiments of the NWC transmitter.

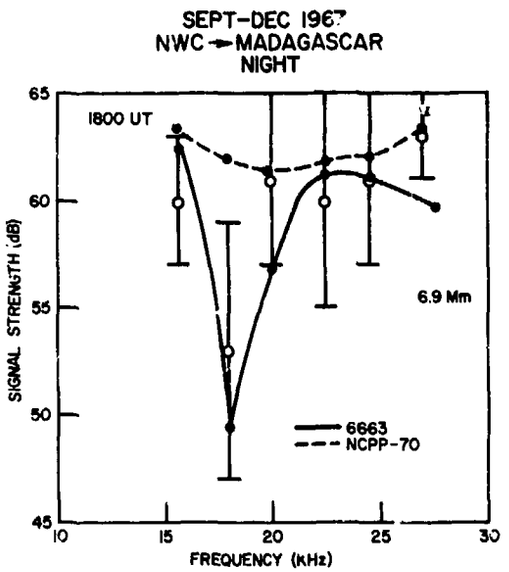


Figure 10. Observed and predicted fields at Madagascar during the 1967 multifrequency experiments of the NWC transmitter.

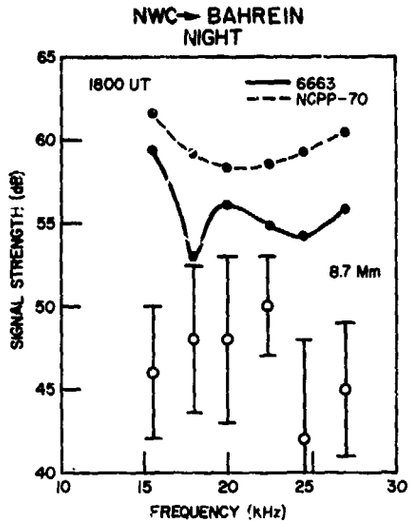


Figure 11. Observed and predicted fields at Bahrein during the 1967 multifrequency experiments of the NWC transmitter.

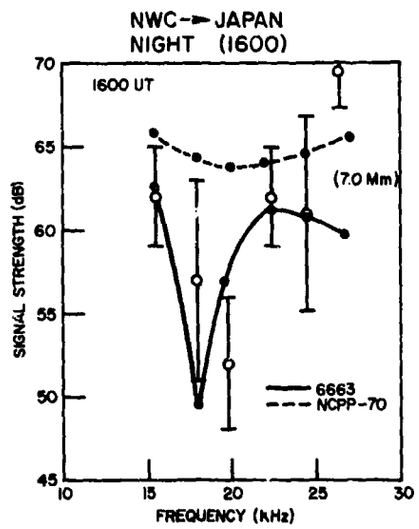


Figure 12. Observed and predicted fields at Inubo, Japan, during the 1967 multifrequency experiment of the NWC transmitter.

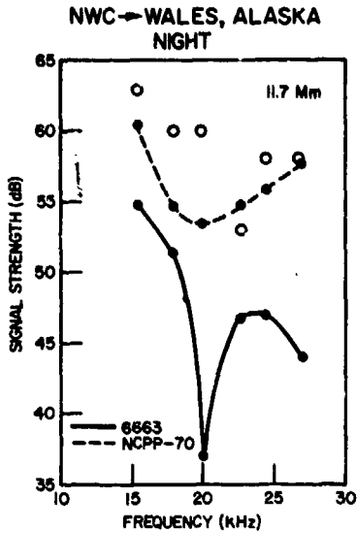


Figure 13. Observed and predicted fields at Alaska during the 1967 multifrequency experiment of the NWC transmitter.

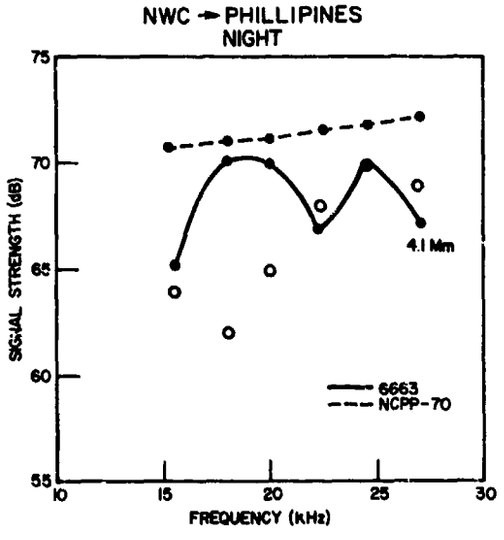


Figure 14. Observed and predicted fields at the Philippines during the 1967 multifrequency experiment of the NWC transmitter.

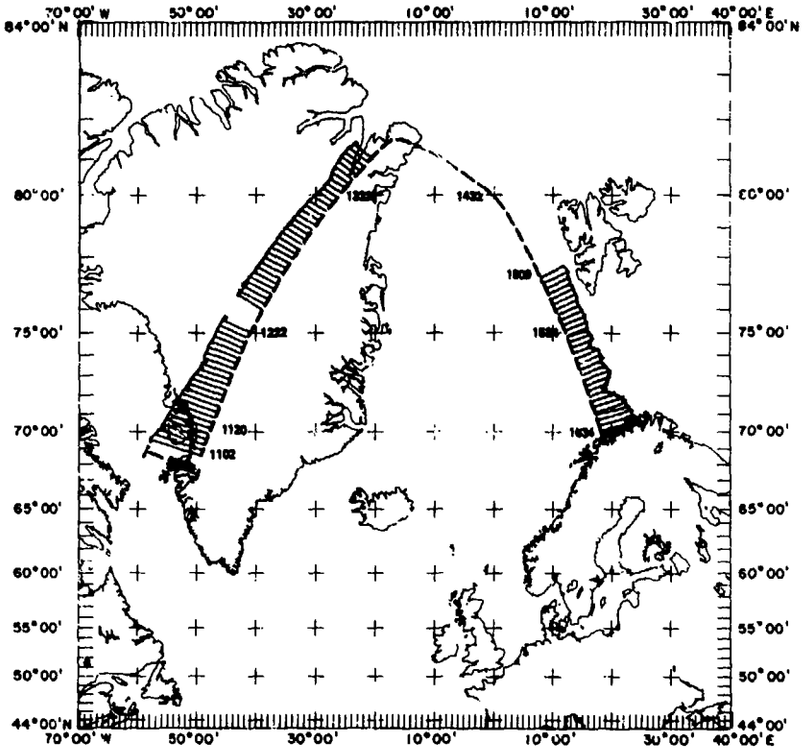


Figure 15. Relative field strength versus location measured on the Sept. 20, 1985, flight from Sondrestromfjord, Greenland via Nord, Greenland, to Bardsfoss, Norway.

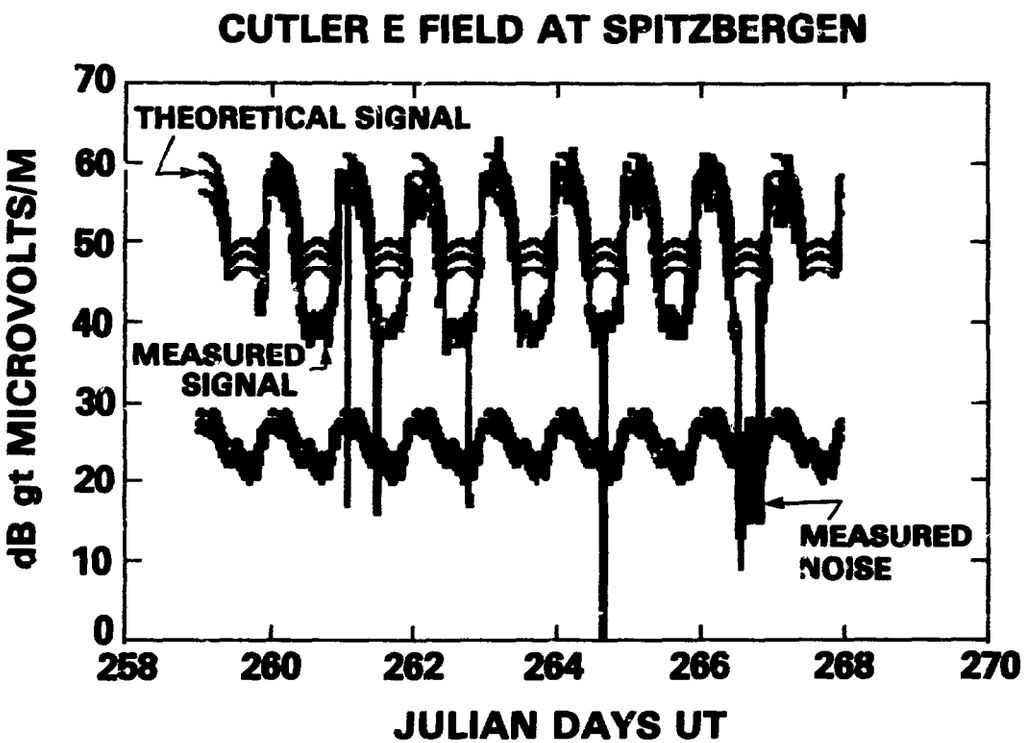


Figure 16. NAA electric fields on 24.0kHz measured from day 259 through day 266 at Isfjord Radio, Spitzbergen, Svalbard. Signal predictions are the MCPP70 model (also known as VLFACM). Noise predictions are using the NRL-WGL noise model. Signal and noise are referenced to 100Hz bandwidth.

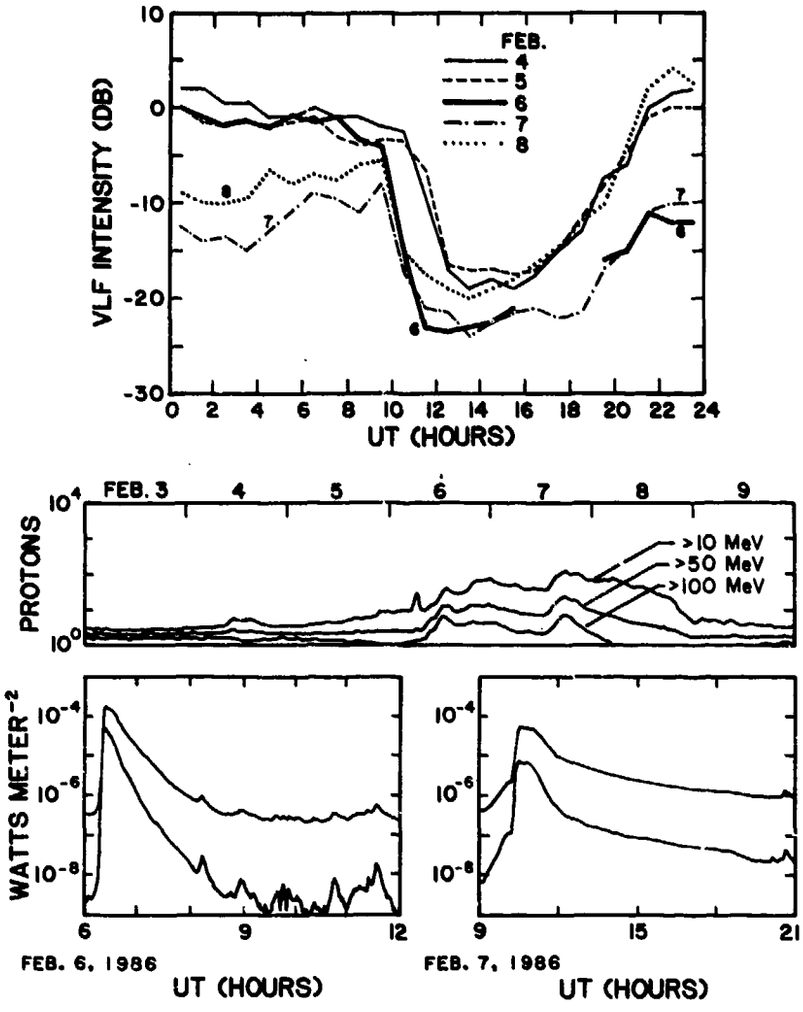


Figure 17. Plots of field strength at Isfjord Radio, Spitsbergen, Svalbard along with simultaneous solar x-ray and proton flux data. Proton flux units are protons/(cm^2 sec ster MeV). The upper x-ray flux curve is the 1 to 8 Angstrom channel. The lower x-ray flux curve is the .5 to 4 Angstrom channel of the GOES satellite data. X-ray flux in watts/m^2.

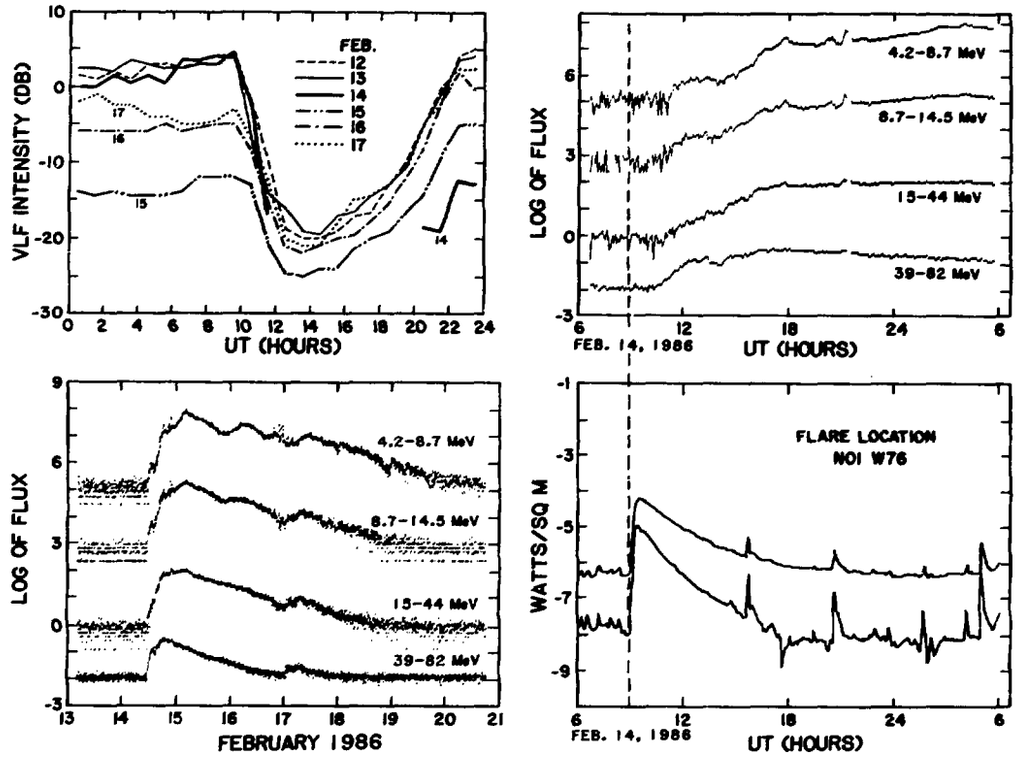


Figure 18. Plots of field strength at Isfjord Radio, Spitzbergen, Svalbard along with simultaneous solar x-ray and proton flux data. Upper solar proton flux levels are augmented by factors of 100 and 10,000 for clarity of reading. Lowest level is correct. Proton flux units are protons/(cm^2 sec ster MeV). The upper x-ray flux curve is the 1 to 8 Angstrom channel. The lower x-ray flux curve is the .5 to 4 Angstrom channel of the GOES satellite data. X-ray flux in watts/m^2.

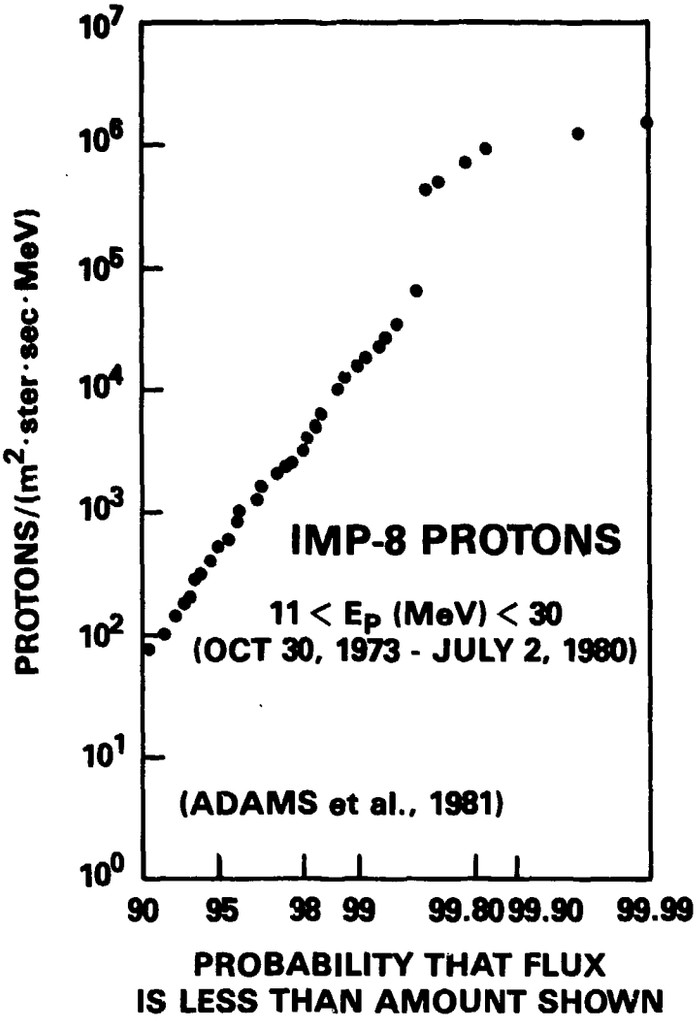


Figure 19. Probability of occurrence of solar proton flux levels in the 11 to 30 MeV channel of the IMP-8 satellite proton detector. Data taken from Oct. 30, 1973, to July 2, 1980.

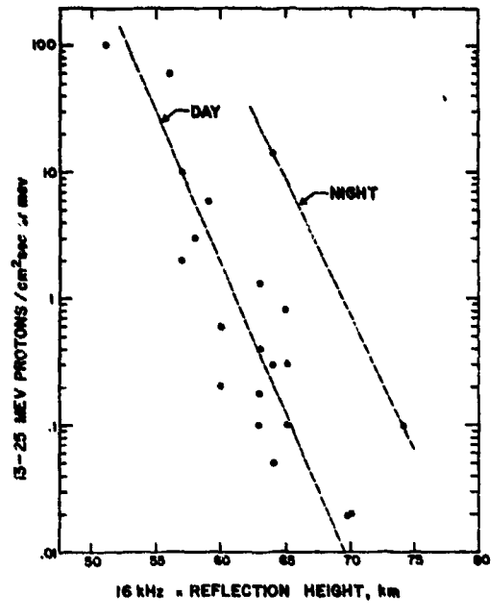


Figure 20. Scatter plot of apparent reflection height of lower ionosphere at Thule, Greenland, for 16kHz radiowaves during solar proton events plotted versus intensity of solar proton flux in 13-25 MeV energy range.

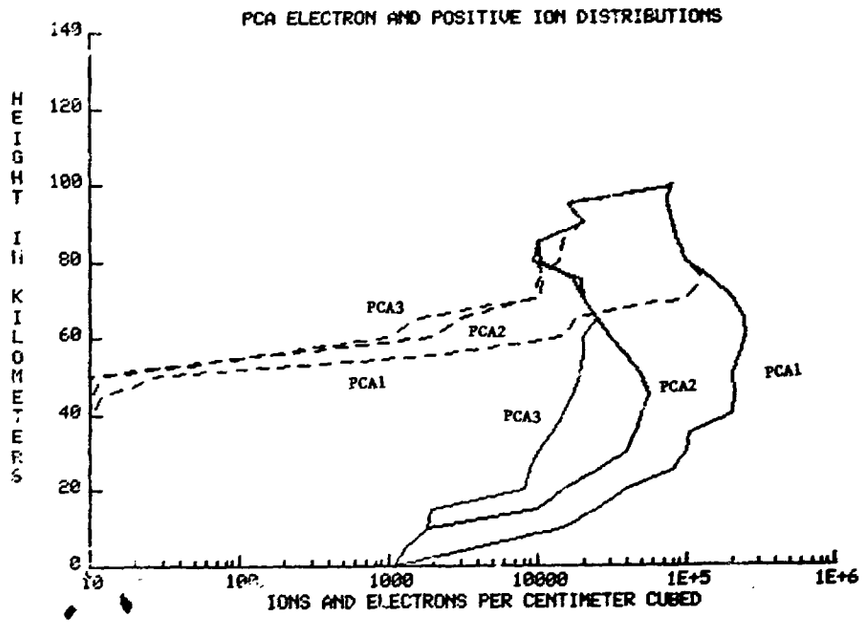


Figure 21. Daytime ionization height profiles for disturbed (PCA) and ambient conditions from Field (Ref. 34). Dashed lines are electron densities; solid lines are positive ion densities.

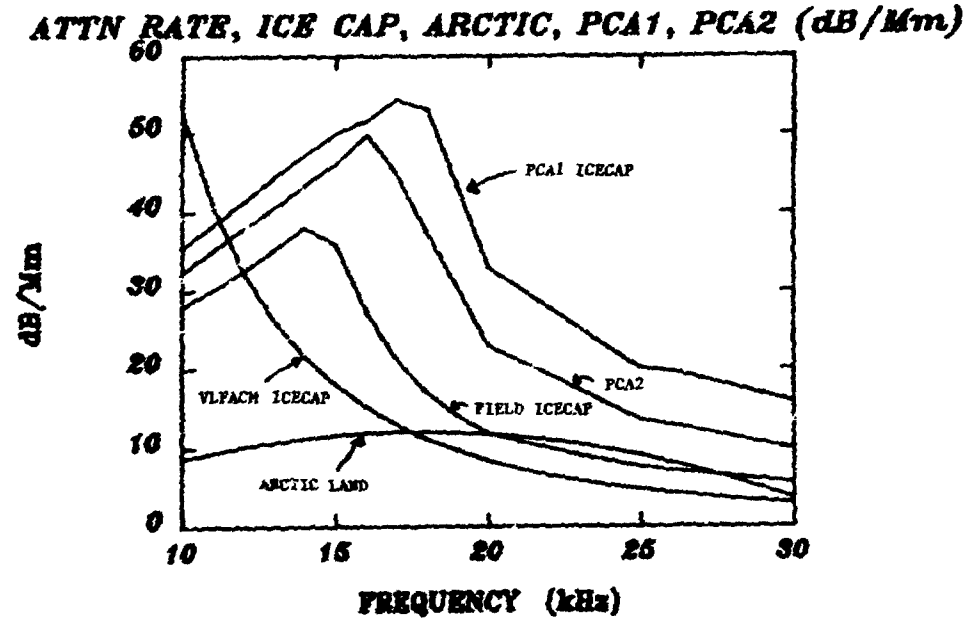


Figure 22. Attenuation rates for ice cap and arctic land during ambient and disturbed conditions.

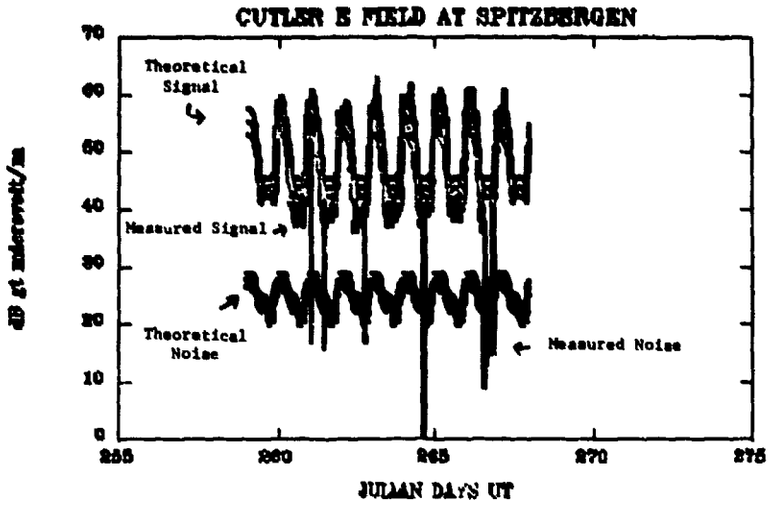


Figure 23. The same as Figure 16 except the signal level predictions are from a modified VLFACM program using Field's ice cap attenuation rates.

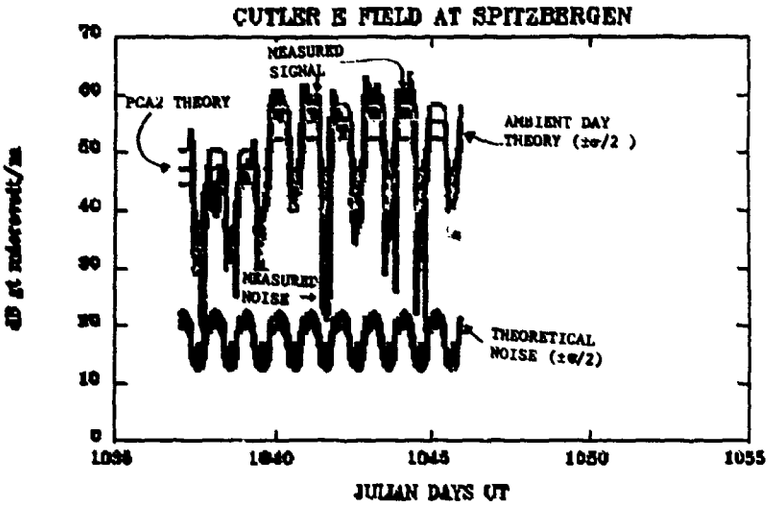


Figure 24. Comparison of theoretical and observed data during the PCA of February 1986. Theory is a modified VLFACM program using Field's PCA attenuation rate for the PCA disturbed days and a modified VLFACM program using Field's ambient day ice cap attenuation rate for the undisturbed days.

DISCUSSION

K.C. Yeh, US

You mentioned that it is desirable to introduce randomness in the analysis of long wave propagation. Can you describe just what these random parameters are? Are they the coast lines, the conductivities of the ocean versus those of the land, the ionospheric conditions or the effects of CPA on the ionosphere?

Author's Reply

We need a better understanding of the effective ground conductivity and dielectric constant as a function of frequency in land areas. We also need to understand the variability of the ground parameters caused by rain, temperature, vegetation and ice. Long waves may penetrate effectively hundreds of feet into low conductivity soil and thousands of feet through glaciers; so the parameterization of earth properties to significant depths is required. We believe that the sea surface is quite homogeneous except in bays where the salinity is decreased and in ice-covered polar seas.

We need a better understanding of the ionospheric boundary of the waveguide. For both day and night, we need a better understanding of the background composition of the neutral atmosphere from 40 km to 90 km height -- especially of the chemicals O_3, H_2O, and NO. To understand these constituents, we must take the atmospheric wind system into account. For daytime, we need a better understanding of the statistics of solar and stellar X-ray and ultraviolet radiation (especially Lyman-alpha). We also need a better understanding of the PCA process, the statistical probability of these events, and their extent in latitude and longitude as a function of magnetic time coordinates, and as a function of intensity of magnetic disturbance. The precipitation of electrons from the Van Allen belts needs better understanding to explain the variation of the long wave signal at nighttime over temperate zone paths. We also need to know the variation of scattered Lyman-alpha from the geocorona.

In the prediction of paths crossing discontinuities in the waveguide such as a land-sea boundary, or day-night terminator, improvement is certainly needed. Current models are one-dimensional and should be enlarged to take into account the focussing and defocussing of waves crossing curved (and fractal) coastlines or terminators.

So, in short, almost all of our boundary conditions are statistical in nature; and they are currently being modeled deterministically to a large extent -- except for the few studies mentioned in my paper.

J.F. Patricio, PO
English translation

There are networks in service that work at 10 kHz, 10 MHz, 100 kHz (LORAN C) and reference stations at 60 kHz, 72 kHz, etc. Was the information obtained from these installations useful for your work?

Author's Reply

We utilize field strength and voice measurements of these navigation systems whenever it is available. However, it is not often available because of the great emphasis of the navigation system developers are phase or time-of-arrival measurements. Often they do not give great emphasis on making well-calibrated signal amplitude measurements because of the extra effort required for such measurements. However, we have about 40 10.2 kHz Omega propagation paths included in our NRL long wave data base, and we would be happy to include data on Decca, Loran or Omega field strength measurements if they are well calibrated and available.

MODELING OF WIDEBAND HF CHANNELS

Martin Nesenberga
U.S. Department of Commerce
National Telecommunications and Information Administration
Institute for Telecommunication Sciences
325 Broadway
Boulder, CO 80303

USA

SUMMARY

Laboratory simulation of wideband high frequency (HF) system performance is currently not possible because such simulators do not exist. Moreover, there are no validated HF channel models for bandwidths of the order of one megahertz, on which to base the simulator design.

This paper starts with a very brief review of additive distortions, namely noise and interference, in the HF band. It presents an introduction and an appraisal of past narrowband HF models: their background, validation tests, and the NTIA/ITS development of the Watterson's simulator. That laboratory tool, judged best by many, works in real time and offers accurate representations of HF channel bandwidth up to 10 or 12 kHz. In the present study an extension to wideband models is attempted. Unfortunately, it suffers from an apparently serious shortage of measured data for the time-varying channel transfer function. A possible wideband model is hypothesized, conjectures are made, many questions are raised, but hardly any are answered. One is left faced with a requirement for an experimental program that is to ascertain the wideband (1 MHz or more) characteristics of multipath fading for digital radio transmissions in the HF band (2 to 30 MHz) and over propagation paths of interest.

1. INTRODUCTION

To help in the spread spectrum system development and laboratory testing, a real-time channel simulator can be a valuable tool. For systems in the high frequency band, the desired bandwidth of the simulator must be on the order of 1 MHz to accommodate planned direct sequence, frequency hopping, or their hybrid systems.

Given the objective to implement a convincingly realistic simulation facility, the key question concerns the structural options for the simulator. One calls this the issue of modeling. After all, every simulator is based on some conceptual model--call it mathematical, statistical, stored database, state driven, or an engineering approximation. That model must be a valid, experimentally verified, representation of the real medium. For HF, the only sufficiently verified models known to this writer (we shall return to these shortly) pertain to narrowband channels. These are channels with bandwidths on the order of, or less than, 10 kHz. For larger bandwidths, such as 100 kHz or higher, there apparently is no corresponding validated model.

One should question how and why such a state of affairs could exist. After all, HF communications have existed for most of this century. Thousands of HF circuits, analog and digital, criss-cross the globe every hour. Past reports on experimental and theoretical research abound. References to more than one thousand studies have been collected before 1960 [1]. There may be a combination of reasons for this apparent neglect of wideband HF characterization. First, nearly all working circuits at HF are quite narrowband. They occupy no more than the standard 3 kHz voice band and usually less. Second, the strategy to combat HF misbehavior has been to rely on human operator skills. Predictions and frequency switching options are in the hands of operators. Third, a large percentage of the HF propagation tests has been devised, performed, and analyzed by individuals whose main intent has been and still is to understand ionospheric physics. Fourth, the HF channel is by and large unpredictable, randomly time-varying, with sudden variations from time to time as well as from place to place. Its complex, nonstationary, nature only becomes more so as one examines wider bandwidths.

The most basic model of current relevance is the time-varying linear channel. It is graphically introduced in Figure 1. For the purposes of this study, it is assumed that the basic model of a linear time-varying filter plus additive noises or interference remains valid for the HF radio signal path between antennas, regardless of the time-and-frequency characteristics of the signal.

The fading of the time-varying HF medium is determined by the two-dimensional random function H(f,t). In electronic circuit applications one may be familiar with the fixed filter and its invariant frequency response, H(f). For the HF channel to be represented by a filter, one must permit the filter to possess an unpredictable or random variation in time. One incorporates this phenomenon into H(f,t) via the second argument "t."

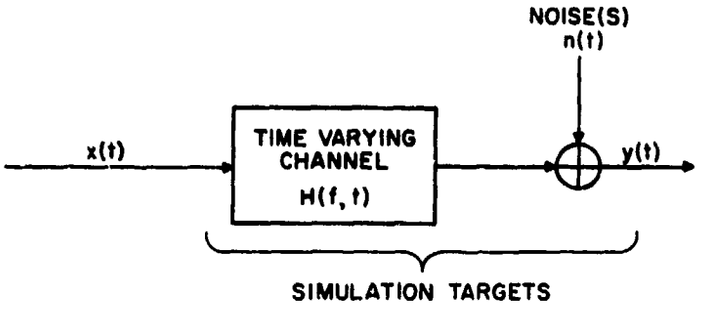


Figure 1. The linear time-varying channel model.

The transfer function, H(f,t), is a sum of all propagation modes experienced by the radio waves. Thus, one must be cognizant of the physical multimode or multipath aspects of HF propagation. At a given radio frequency, wave reflection can take place at several regions or layers in the ionosphere. These are called the D, E, F, F1, F2, and other regions. Actual layer profiles vary in intensity, in time, in space, and are subject to unpredictable solar and geophysical events. Certain layers may or may not be visible to all frequencies, or all antenna beam elevations of interest. Moreover, multihop propagation may occur over longer distances. As is well known, the number and character of received modes--while seldom completely random--nevertheless do vary in a hard-to-predict fashion. For HF paths in moderate zones the number of modes can range from zero to a half-dozen.

Radio probes, called sounders or ionosondes, have been useful to determine the presence of ionospheric layers and their return signatures [2,3,4]. Either vertical- or oblique-incidence sounders are used to transmit short pulses at different frequencies and to analyze the delays and amplitudes of their echoes. The generated plots of delay versus frequency are known as ionograms. An illustration is given in Figure 2. Several modes are present in this ionogram. However, the effective frequency range is limited between the lowest usable frequency (LUF) and the maximum usable frequency (MUF). Frequencies outside the range are lost through either total absorption or radiation that escapes into space. Within the LUF-MUF range several returns from E, F, or other layers are noted. The higher rays travel longer distances. They suffer longer delays. Furthermore, due to magneto-ionic interaction, individual modes may be split into two rays that traverse slightly different paths. These are denoted as Ordinary (O) and Extraordinary (X) rays. Usually, the more pronounced O-X splitting takes place at higher frequencies, such as near and just below the junction frequency (JF). The biggest signal distortion due to interference of delayed modes tends to occur when the delay spread between two strong modes, often between the High and the Low Ray, is the largest. This occurs at the so-called critical frequency (CF).

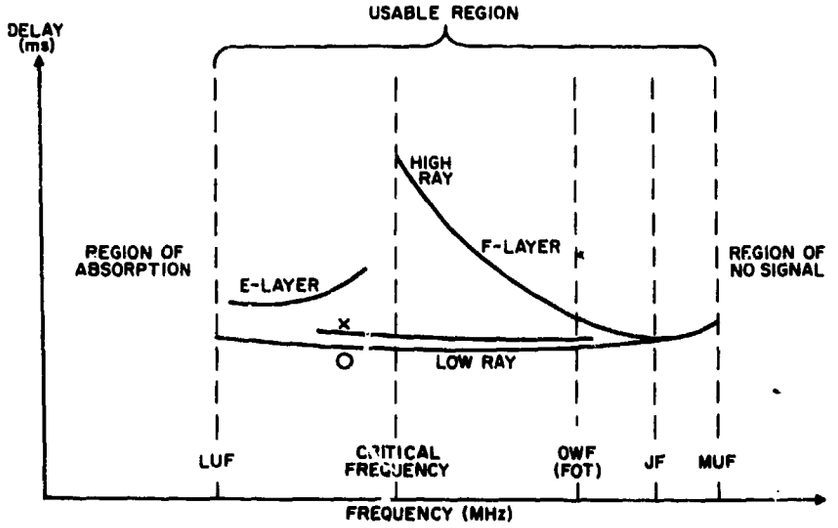


Figure 2. Ionogram terminology.

2. NOISE AND INTERFERENCE

The classical model for thermal noise is that of a random wideband process with Gaussian statistics. It exists in all narrowband and wideband HF radio systems. However, it is neither the only noise nor is it always the dominant additive disturbance. The receiving antenna is typically subjected to a group of natural and man-made noises or interferences. The relative intensities are illustrated in Fig. 3.

In many sections of the globe the dominant HF noise may be man-made [5,6,7]. It depends on the presence of electrical machinery and spark-generating devices. As seen, the emissions from solar and cosmic origins are less than those from median business areas. Their intensity decreases gradually as one goes to higher radio frequencies. That is not always the case with atmospheric or thunderstorm generated noise. The atmospheric noise can be most severe at night and at the very lowest frequencies in the HF band.

The accepted, more or less standard, model for all dominant noise emissions in the HF band is the weighted sum of Gaussian plus impulsive processes. Classifications have been done to identify and to distinguish different mixes of the two components. Another additive disturbance is radio interference. It can be intentional or unintentional, local, or propagated as long a distance as the existing HF modes would permit. Jamming is an example of intended destructive interference. It may take the form of single tone continuous wave, high power pulses, broadband modulated carrier, swept frequencies, or other intentionally harmful waveforms. Due to their unique nature, standardization of all interference--especially that of intentional interference--appears impossible. Interference should be modeled on a case-by-case basis.

3. NARROWBAND HF MODELS

Several HF channel simulators, based on different narrowband channel models, have been implemented in the United States. References to their designs and characteristics are found scattered through the technical literature of the last 20 years. As an example see [8]. We will not review them here, because 1) next we do present a discussion of the Watterson channel model, 2) the capabilities of the other known simulators are not superior to those of the Watterson scheme, 3) all the other models are inherently narrowband in that their parameter settings are constants, and 4) none of the other models appear as well validated and documented as is the Watterson model.

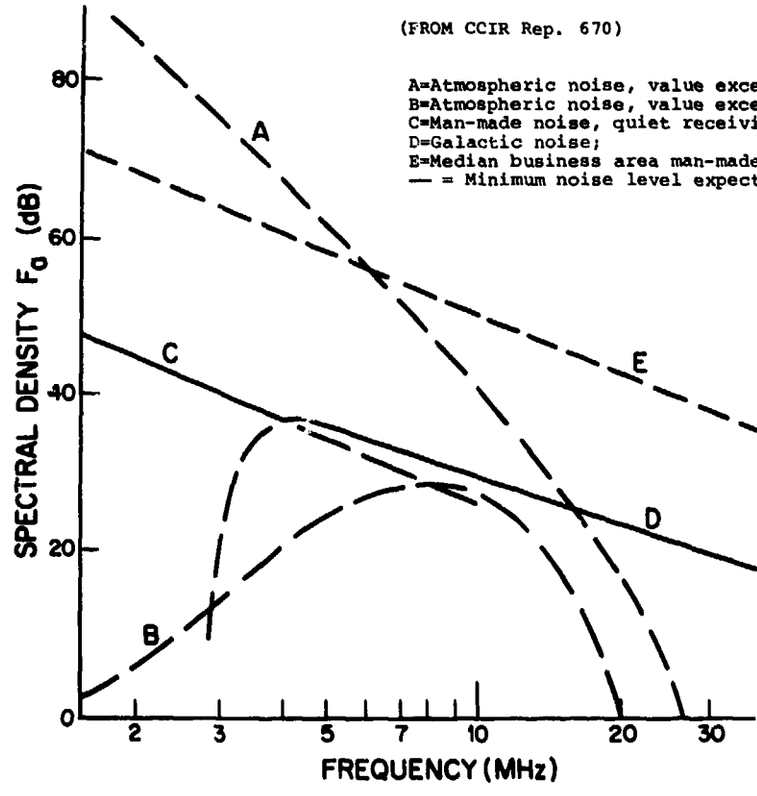


Figure 3. Relative power spectral densities of HF noise sources.

The Watterson Model

Around 1970, the Institute for Telecommunication Sciences in Boulder, Colorado, developed an HF channel model, established the validity and the accuracy of the model in extensive field tests, implemented a corresponding HF channel simulator, and used the simulator to run laboratory performance tests on digital HF modems in a controlled and repeatable manner. Since the entire program was performed by C.C. Watterson and his colleagues [9 to 12], the model and the simulator are often called the Watterson model and Watterson simulator, respectively. What follows is a brief summary of that model.

In principle, the channel model is a stationary realization of the unequal tap spaced tapped delay line (TDL) with time-function multipliers that generate the time, or t, dependence in H(f,t). The key entities of the model are included in the following expression for the time-varying channel frequency response:

$$H(f,t) = \sum_i c_i(t) \exp(-j2\pi\tau_i f). \qquad (1)$$

Here summation over i corresponds to the presence of the multiple or i=1,2,3,..., multipath signal returns. The exponential term $\exp(-j2\pi\tau_i f)$ represents the delay line function with a tap set at delay τ_i. Physically, τ_i is the constant path delay for path i. The explicit purpose of the time-variant factors $c_i(t)$, i=1,2,3,..., is to generate different time-frequency signal energy scatter for every path i through the ionosphere. When a factor is a random function, its power spectrum exhibits Doppler shifts and spreads. Multiplied onto every tapped signal, these modal spectral distortions eventually appear in the summed output signal y(t). Single modes are also known to undergo delay distortions. If the delay characteristic of a mode is a rapidly changing function of frequency, one talks of it as the differential delay spread. In other instances, delay spreading may be due to some unresolved fine structure within the mode. In both cases, at a given radio frequency, signal energy can be variously dispersed in the time-frequency plane of the Watterson model by selecting appropriate random multiplicand functions for the taps.

A block diagram implementation of H(f,t) from Eq.(1), plus appropriate noise and interference generation, is illustrated in Figure 4. There are several features to be noted in this model. First, only the desired, delayed, and scattered signal is passed through the delay line. If, for instance, the propagation path is sufficiently short for the given radio frequency, the receiver may see a significant nonfading ground wave. The nonfading component is called specular, to distinguish it from the fading scatter components that may or may not be present. Typical specular components are the earliest to arrive at the receiver. In the model, therefore, they can be realized just before the signal enters the delay line. No TDL taps are involved. Specular components by themselves also undergo insignificant amounts of fade-related distortions. Therefore a constant gain setting, instead of the complicated $c_i(t)$ function generators plus multipliers, suffices for the specular component in the Watterson model.

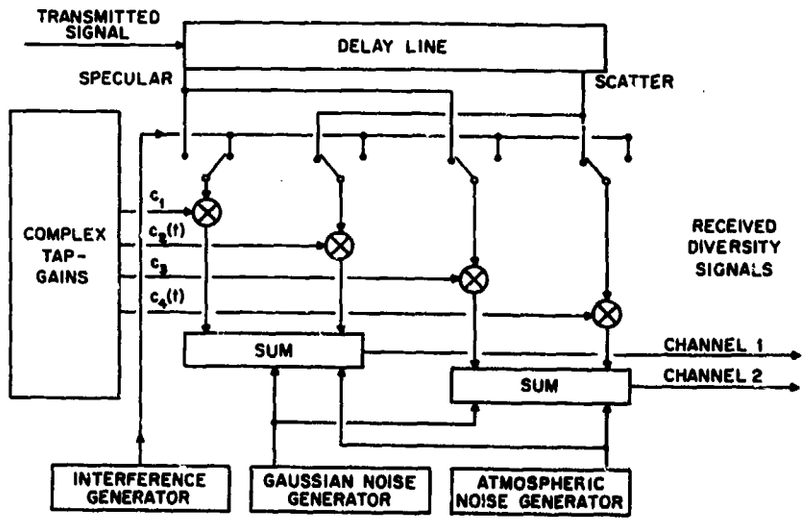


Figure 4. Block diagram for simulation of dual diversity reception of a ground- and sky-wave mix.

Each tap-gain function, $c_i(t)$, is a complex function that applies uniformly (i.e., with constant first and second moments) over the entire channel bandwidth. Otherwise, however, it is a random function of time and with certain preassigned, stationary, statistical properties. Specifically, each tap-gain function is an independent bivariate (complex) Gaussian function with zero mean and quadrature components that have identical variances. In their effect on scatter mode amplitudes, such multiplicands cause independent Rayleigh fading.

Every tap-gain function, in general, is permitted to possess a double-peaked spectrum. The peaks represent the previously mentioned O-and-X ray splitting due to magneto-ionic effects. The two spectra in question have Gaussian shapes with individually adjustable gains (amplitudes), independent frequency shifts, as well as frequency spreads. The HF channel effects on the transmitted signal phase are thus determined by the total effects of the prescribed Gaussian processes. Of course, the rapidity of phase, as well as amplitude, fluctuations is also affected by channel bandwidth assignments. Typical bandwidth filter settings for this narrowband model range up to 12 kHz.

Undesired signals, i.e., interference, also bypass the delay line, but may be subject to the time-function multiplicative effects. For sky-wave channels, the number of multipliers is nominally the same as the number of taps and also the same as the number of multipath modes, granted that the simulated receiver is to be of the nondiversity type. Any order or type of diversity is permitted by the model. However, only dual diversity has been fully implemented in the laboratory. This seems quite adequate for the majority of HF systems to be tested. If the number of available multipliers is fixed, the effect of the simplest dual diversity is to reduce the number of HF channel modes by two. Diversity combining techniques or related processing are not parts of the Watterson model. However, additive distortions consisting of Gaussian noise and impulsive components are summed into the output.

From the narrowband channel characterization point of view, the most essential features are associated with the delay taps and their processing. The model assumes that, while the number of taps (i.e., modes) can be selected and their settings (i.e., delays, etc.) adjusted, this all must be done in preparation for a simulation run. During a run the settings remain fixed, as is required by stationarity. Similar statistical principles apply to the selection of the time-varying multipliers, called tap-gain functions by many. Then, however, based on experimental evidence and theoretical conclusions, the spectral and temporal distributions must be specified through an assignment of means and variances to predetermined component types. For $c_i(t)$, these components are typically approximations of the Gaussian distribution.

Table 1 is a summary specification of the numerical values available on the Watterson HF simulator. It must be emphasized that the implementation of this unique laboratory test instrument represents conservative, moderately practical, state-of-the-art engineering circa 1970. For less resources, more can be procured now in terms of parameter ranges, accuracy, and other overall measures of performance. Many parameter inaccuracies listed in Table 1 are probably extremes, in that they are deduced from estimated largest possible equipment errors. The specular and scatter path attenuations, in decibels, have the indicated accuracies over the range normally used.

Proceeding from the top down in the Watterson's simulator specification, one finds first the three standard options for bandwidth. They are 3, 6, and 12 kHz, respectively. The maximum number of paths (viz., modes or taps) is 4. The delay settings for taps are selectable constant values in 20-μs steps over a quite realistic interval from 0 to 10 ms. Note that this would normally exclude frequency-dependent delays and associated differential delay spreads. To avoid this shortcoming for lower frequencies, the HF simulator is supplied with dispersion filters that can be inserted in any path between the delay line tap and the path gain multiplier. The dispersion filters are all-pass filters with a delay characteristic linear in frequency.

By going down row by row in Table 1, one finds numerical specification for the previously introduced parameters of the model. A more detailed explanation of their features appears unnecessary here. Interested readers will find comprehensive descriptions in the list of references [9 to 12]. However, one may note that the model admits both Gaussian and atmospheric noises at continuously preset signal-to-noise ratios, and with controlled impulsiveness coefficients. Likewise, the model permits exterior signal interference at fixed signal-to-interference levels. At the very bottom of the table one finds two possible internal distortion sources, both less than minus 70 dB relative to the signal-to-noise ratio. They appear to be due to A/D conversion and occasional clipping. However, minus 70 dF appears so minute compared with ordinary HF fluctuations as to render their detrimental effect as entirely negligible.

Model Validation

Even for narrowband HF channels, the verification of a given model's validity or accuracy of fit is considered important for ordinary data transmission. When faced with more advanced systems, especially those with designs or algorithms that depend on proposed channel simulation, the question grows in significance. After all, the substantial advantages promised by laboratory simulator tests over on-the-air experiments may be entirely erroneous, unless it is ascertained how accurately the model (on which the simulator implementation is based) represents the real HF. While

Table 1. Watterson's Channel Simulator Specifications

Parameter	Available Values	Accuracy
Bandwidth, B	3, 6, or 12 kHz	--
Number of Paths, n	4 maximum	--
Delay, τ_i	0 to 10 ms in 20-μs steps	0.5 μs
Dispersion, D_i	0, -100, -220, and -320 μs/kHz	2×10^{-2}
Specular Atten., $\bar{A}_i$	0 to 100 dB continuous	0.2 dB†
Specular Phase, $\bar{\theta}_i$	continuous (modulo 2π)	0.01 rad.
Scatter Atten., $\tilde{A}_i$	0 to 100 dB continuous	0.2 dB†
Frequency shift, ν_i	Int. Synthesizer: 0, ±1, ±2, or ±5 x .01, .1, 1, 10, or 100 Hz	1×10^{-4}
	Ext. Synthesizer: -500 to 500 Hz in 1-mHz steps	1×10^{-6}
Frequency Spread, $2\sigma_i$	Each Path: 1, 2, or 5 x .01, .1, 1, 10, or 100 Hz	2×10^{-2}
	One Path: 1.00, 1.33, 1.78, 2.37, 3.16, 4.22, 5.67, or 7.50 x .01, .1, 1, 10, or 100 Hz	2×10^{-2}
Fading Spectrum, $v_i(\nu)$	3-pole approximation of Gaussian	<0.03 dB*
Signal to Noise, E_b/N_d	-100 to +90 dB continuous, Gauss. Atmos.	0.2 dB† 0.5 dB†
Atmospheric Noise Impulsiveness, V_d	HF: 7.2 dB in 2.7 kHz LF: 10.8 dB in 2.7 kHz LF: 9.0 dB in 2.7 kHz	-- -- --
Signal to Interf., S/I	-100 to +90 dB continuous	0.2 dB†
Space Diversity	Single or independent dual	--
Internal Distortions:		
Additive	< -70 dB relative to signal+noise	--
Nonlinear	< -70 dB relative to signal+noise	--

†Over range of significance *Theoretical

measurements of the ionospheric channels, such as the ionogram generating sounders, have been made over the last 50 years, many detailed properties were not available before Watterson's work.

The model verification experiments by Watterson took place in November of 1967 [9,10]. They were preceded by preparation and testing of the equipment to support test bandwidths of 12 kHz or higher. The transmitting system was installed at Long Branch, Illinois (40°13'N, 90°01'W). The receiver was located in Boulder, Colorado (40°08'N, 105°14'W). The propagation path has a great-circle distance of 1,294 km. It is at a very moderate latitude and displays a nearly perfect east-to-west orientation. Two assigned frequencies of 5.864 MHz and 9.259 MHz were used for night and daytime operation, respectively. In both cases, the radio frequency was sufficiently below the predicted MUF to make it likely that both one- and two-hop modes would be present.

In one reported experiment the link was operated continuously in three separate test periods. Over 7 hours of recorded measurements were obtained at night (5.864 MHz) and nearly 10 hours during daytime (9.259 MHz). The recorded data were subsequently sampled, reduced, processed, and analyzed with verification of the proposed channel model being the main objective.

Data were divided into 10- to 13-minute intervals called samples. Of all the samples covering the total 17 hours of measurement, about 2 hours or 12 percent was found to be approximately stationary in terms of fading rates, modal time delays, and average powers in the modes. Three particular sample intervals, designated as I1, I2, and I3 by Watterson, received the most detailed analysis and produced the summary shown in Table 2. Note that the number of distinct modes, excluding the magneto-ionic or O-X fine structure, is either 3 or 4. In all cases the channel delay numbers remain under 1 ms, which is quite normal. The Doppler shifts and spreads are also well behaved. Their magnitudes are small fractions of a hertz. The so-called path time spread measures the effective delay smear within a mode and is observed to range from 20 to 100 μs. As claimed in the literature and verified by Watterson, this leads to definite conclusions about the maximum bandwidth over which the model is an accurate replication of the real channel behavior. This "validity bandwidth" for the model is not a fixed, forever invariant, entity on an HF circuit. The last row of Table 2 reveals that all three samples have markedly different validity bandwidths.

Table 2. Summary of the Three Samples

SAMPLE	I1	I2	I3
Frequency (MHz)	9.259	9.259	5.864
Number of Modes	3	4	3
Channel Time Delay (μs)	137	173	589
Channel Time Spread (μs)	478	520	464
Channel Doppler Shift (Hz)	.0013	.0171	.110
Channel Doppler Spread (Hz)	.123	.140	.0666
Path Time Spread (μs)	20	30	100
Validity Bandwidth for the Model (kHz)	12.5	8.3	2.5

The reasons for this distinctive behavior are found in the details of the data observed. These details, when magnified, show very different structures for the test intervals I1, I2, or I3. For brevity sake, we show only I1 in Table 3. Note how the three modes, namely E, F, and 2F, have different relative powers, time delays, Doppler shifts, and spreads. The magneto-ionic splitting into O-X components is present only in the E-mode. Of course, all of these statistics would be expected to be quite different over other different HF paths, i.e., at different frequencies, or different places, or different times, or even different antennas.

Moreover, further analysis shows that the tap-gain functions are justified as defined. It is indeed valid to take them as mutually statistically independent, complex (bivariate) Gaussian random processes at baseband. Their spectral densities are also representable as claimed. They are either single, or sums of two, Gaussian functions. To fit observations, these Gaussian peaks must be permitted arbitrary central positions (means) and different spreads (variances).

Table 3. Detail for Sample I1

Parameter Vector	Channel	Mode	O-X Split
		E	
			-4.1
			40
			.0022
		-1.2	.0073
		40	
		.0094	
Rel. Power (dB)	0*	.0272	-4.3
Time Delay (μs)	137		40
			.0170
Doppler Shift (Hz)	.0013		.0318
Doppler Spread (Hz)	.123	F	
		-7.2	
		290	
		.0089	
		.144	
		2F	
		-13.5	
		1139	
		-.167	
* By Convention		.340	

Perhaps the most noteworthy conclusion drawn from these validation tests is that under the assumed narrowband conditions certain parameters are indeed constants for workable intervals of time and over all frequencies in the band. This includes modal structures, i.e., fixed number of modes and their O-X splits, constant mode delays, constant mode amplitudes, constant delay spreads, constant Doppler shifts and spreads, and the total amount of mode dispersion, to mention the main variables. It is proper to assign to them constant numeric values over bandwidths that do not exceed 12 kHz, or roughly so. However, to presume constant values for larger bands appears unjustified. A look at the wideband properties of ionograms only strengthens this suspicion.

4. WIDEBAND HF MODELING

The Approach

The extension of narrowband (e.g., 10 kHz) channel models to wideband (e.g., 1 MHz) models cannot be substantiated by existing measured data at this time. Nevertheless, this section does attempt to present an approach to HF modeling. Based on extrapolation of narrowband results plus the latest wide bandwidth measurements [13,14,15] and other pertinent inferences, the approach is both conjectural and factual.

The HF channel is not stationary over a very long time. For the ITS simulator, Watterson's tests established a 10- to 15-minute window of apparent stationarity. What happens when the band is much wider is not too certain. However, one should expect no novel nonstationarity effects here. For 10 to 15 minutes, or thereabouts, the wideband channel structure is likely to be more or less fixed. By that one means that over the entire bandwidth of interest, the number of modes, their amplitudes, their delays, Doppler spreads, and so on, could very well retain constant profiles as functions of frequency. The situation is as illustrated in Figure 5. Over a sufficiently long sky-wave path, ionograms are observed at several 3-hour instances. When scrutinized, they show quite discernible differences from one snapshot to the next. The operating frequencies increase as the morning hours pass. The number of modes undergo changes. If one focuses only on 15 MHz, one finds no modes at 0300 and 0600 hours, five modes at 0900, and two at 1200 (noon). The intermode delays are on the order of 1 ms, but their systems effects are unclear because the relative amplitudes, Dopplers, etc., are unresolved.

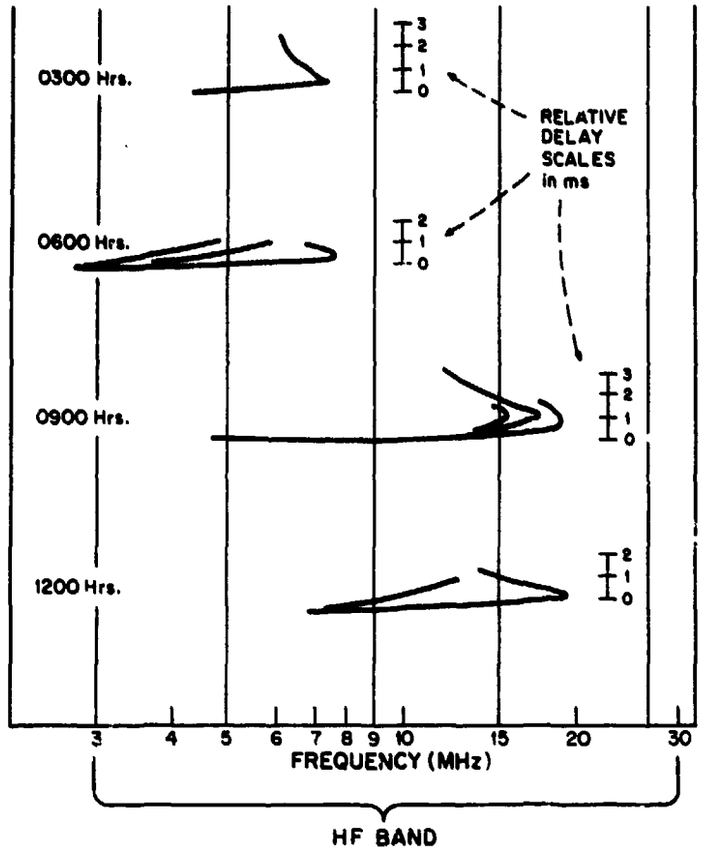


Figure 5. Ionogram snapshots of multipath variation over time and wide bandwidth.

What can the higher resolution probe hope to reveal about the wideband channel? The answer comes in many forms. For example, Figure 6 is based on the premise that the channel bandwidth is 2 MHz, but that depending on the time of day, different 2-MHz slots are utilized. In said slots, the multipath modes display a fine structure of energy (viz., amplitude) scatter versus delay that, as suggested by Figure 6, must somehow vary with frequency. The amplitudes and widths of the encountered distributions vary. Some modes expire in the middle of the band, others stretch across the band, while yet others merge or split apart at certain junction frequencies. But this is far from being the whole story. The previously mentioned Doppler effects must also be included, as must be a large matrix of mutual cross-correlations between all the above random processes or variables, as the case may be. Things would be greatly simplified if most of the entities turned out to be statistically mutually independent. However, there appears to be a genuine shortage of experimental data on this issue. And one doubts whether significant independence (or even approximate uncorrelation) could be realistic from the wave propagation point of view such large bandwidths.

To have a concise definition, and to clarify the time-varying channel transfer function, H(f,t), for this and similar ionogram cases, from now on we propose the following wideband channel model:

$$H(f,t) = \sum_i A_i(f)\, u_i(f,t)\, \exp[-j2\pi v_i(f) f]. \qquad (2)$$

This model is claimed to be one possible generalization of the model described earlier in Eq. (1). There may indeed be many other potential generalizations and extensions. However, to discern which candidate model is better and for what reasons would require experimental validation over real HF channels.

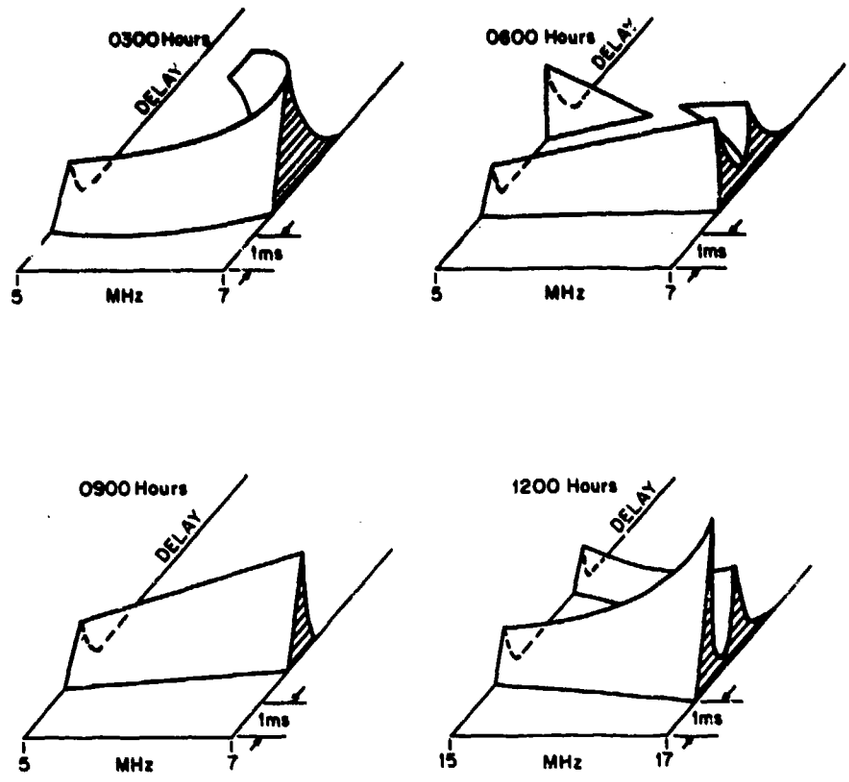


Figure 6. Relative amplitudes and delay scatter in a 2-MHz bandwidth.

The explanation of terms in the above wideband H(f,t) of Eq. (2) is given next. Gradually, as needed, it is to be followed by justification arguments that support the assumptions made. The formal transfer function nomenclatures for both narrow- and wideband models are briefly summarized in Table 4. There are more than a few similarities and differences to be stressed here.

First, the time-varying transfer functions for both are sums of all incident modes. An individual contributing mode is identified by index i. Its contribution to the transfer function is $H_i(f,t)$. So far, the two models obey the same additive and linear formalism. Returning to Figure 5, 0900 hours and 15 MHz, with its five modes, the sum would go from i=1 to i=5 and separate contributions to the transfer function would come from $H_1(f,t)$ to $H_5(f,t)$. Of course, individual modes can have a variety of properties at given frequencies. This is incorporated in the wideband model, as it was done for the narrowband, through specification of modal components, $H_i(f,t)$. See the second row of Table 4.

Next, the definition of all elements in $H_i(f,t)$:

$A_i(f)$ Real, nonnegative, amplitude for the i-th mode at frequency f. It is a constant number with respect to time and can be zero for all those frequencies where the mode vanishes. This dependence on f is unnecessary and therefore absent in all former narrowband models. However, in wideband observations that led to Figures 5 and 6, variations with f have been noted. In particular, the converging modes are known to possess high amplitude peaks just below the MUF. To complicate things further, some modes display a noticeable oscillatory behavior (viz., $A_i(f)$ as function of f). In as much as this phenomenon appears to persist in the presence and absence of O and X ray splitting, including their delay crossovers, it should be incorporated into the $A_i(f)$ properties of the model. Or else, rationale should be developed to ignore it as something of secondary importance.

Table 4. Formal Differences Between Narrow- and Wideband Models

Characteristic Description	Narrowband Model	Wideband Model	
1. Time-varying transfer function for the entire HF channel	$H(f,t) = \sum_i H_i(f,t)$		
2. Time-varying transfer function for an individual mode, $H_i(f,t)$	$C_i(t) \exp[-j2\pi\tau_i f]$	$A_i(f)\, u_i(f,t) \exp[-j2\pi\tau_i(f)f]$	
3. Time-varying multiplier factor(s) for an individual mode	$C_i(t)$	$A_i(f)$	
		$u_i(f,t)$	
4. Time delay characteristic for an individual mode	τ_i	$\tau_i(f)$	$\overline{\tau_i(f)}$
			$\tau_i(f) - \overline{\tau_i(f)}$

$u_i(f,t)$ Complex, bivariate Gaussian, random process in time t, with zero means and statistically mutually independent components. For every fixed frequency, f, this function is quite similar to the narrowband tap-gain multiplier $c_i(t)$, except that $u_i(f,t)$ is to have unity rms values for both quadrature processes. For the special narrowband case, the f-dependence can be neglected in both $u_i(f,t)$ and $A_i(f)$. Their product then is equivalent to the frequency insensitive $c_i(t)$. This correspondence is indicated in row 3 of Table 4. The wideband Doppler spreads and shifts are also generated by this $u_i(f,t)$ process. That includes the familiar spectral shaping from before, except that now the center frequencies and the spreads of the Doppler spectra can be varied across the arbitrarily wide channel bandwidths that are to be simulated. Just how small the bandwidth should be for the f-dependence to become insignificant is not at all well established. However, based on reported past work, that bandwidth should be at least 10 kHz--and perhaps much higher.

As a matter of form, one may prefer to write the magnitude $u_i(f,t)$ in front of the exponential function, and to incorporate its phase $\arg[u_i(f,t)]$ into the exponent. That would make the exponent time varying. It can, of course, be done, but the overall advantages of such a formality are unclear.

$\tau_i(f)$ Frequency-sensitive path delay encountered by the i-th mode. As illustrated in earlier ionograms of Figures 2, 5, and 6, the mode delay appears to be constant only over a relatively narrow band. Even for narrowband applications, some workers have deemed it necessary to include dispersion filters that in effect reproduce the same delay scatter as would a delay entity with a linear delay versus frequency characteristic. For wideband models, depending on the occupied spectral region, the first, second, and even higher order derivatives of $\tau_i(f)$ with respect to f may be of significance.

A final comment on this hypothetical modeling approach deals with the issue of statistical dependence versus independence, or cross-correlations versus absences thereof. Since all random elements of the wideband communications channel somehow share the same common physical medium, i.e., the ionosphere, one can argue that some mutual statistical dependence must exist. But, whatever its constitution, that dependence appears either unknown or extremely complicated. To make some progress in a practical sense and to initiate a dialogue, one could propose the following totally unsubstantiated hypothesis:

FOR ENGINEERING PURPOSES IN HF CHANNEL MODELING, AND UNLESS SHOWN OTHERWISE, ALL RANDOM VARIABLES AND PROCESSES CONTAINED IN THE TIME-VARYING CHANNEL TRANSFER FUNCTION H(f,t) ARE MUTUALLY UNCORRELATED.

It would then be up to future experimenters and statistical analysts either to prove, disprove, or to modify the above hypothesis. Or, as before, it would remain the burden of the HF system designers and communicators to carry on without an answer to this question.

Required Experimental Data

Watterson's modeling of the narrowband HF channel in terms of its time-varying transfer function was discussed in Section 3, as was the experimental verification of that model. Measured data established the validity of that model. Eventually, a simulation facility was implemented. It met the channel specifications listed in Table 1. Unfortunately, despite many old and new reported experiments, no such happy state of affairs exists for the wideband HF channels.

Only one wideband model has been emphasized here (see Section 4 and Table 4), yet the root of difficulty seems not to be associated with a shortage of models. Many wideband models can be conjectured and analyzed ad infinitum. Instead, the root of the problem appears to be tied to a genuine shortage of knowledge about this medium. Let us return to the comparison of narrow- and wideband models in Table 4 and ask for facts and numbers about the wideband model. The answer is a disappointing one. Very little is known. The number of multipath modes can by all means be deduced from ordinary ionograms. So can the delay characteristics, $\tau_i(f)$. The behavior of mode amplitudes as functions of frequency, $A_i(f)$, could be obtained with more sophisticated ionosondes. But, unfortunately, either they are not fully instrumented or the data are not processed. For delay dispersions, Doppler shifts and spreads, etc., even less is known. The existence of statistical properties and the fine structure of random multiplier functions $u_i(f,t)$ are indicated in recent Naval Research Laboratory tests [12,14]. However, useful and representative parametric summaries remain undetermined for f bands that exceed 10 kHz, or so. The bottom line is a simple conclusion that without further experimentation one has no way of ascertaining whether the proposed (or any other) H(f,t) is or is not a valid model.

Assume for a moment that the economic and technology limitations of HF measurement programs were lifted. What types of data would one seek? A way to answer this question may be to return to Tables 1 to 4 and to ask what parametric behavior is anticipated for broader ranges of frequency. The answer may be surprisingly simple. Many variables that appeared constant when viewed through a narrow spectral window show functional dependency on frequency f when viewed in the context of broader bandwidth. Eight parameters are identified below. They all were constants in Watterson's narrowband model, but to be safe, they may have to be replaced by functions of f in the wideband scenario. The eight, potentially f-dependent, quantities are:

1. Delay(s).

As discussed, every propagation mode i in the channel bandwidth has its own delay-versus-frequency characteristic. In Eq. (2) and Table 4 it is called $\tau_i(f)$. Seldom is this function a constant for bandwidths approaching 1 MHz. To simplify modeling, the function may be approximated by piecewise linear segments. It is hoped that 1, 2, or at most 3, segments will suffice in practice. For realistic HF paths, the absolute propagation delays are less than 10 ms. The differential delays between paths are usually on the order of 1 ms.

2. Dispersion Slope.

For every mode, dispersion of energy in time contains a part proportional to the magnitude of the delay derivative with respect to f. While there may be other sources that contribute to the time delay scatter in the modes, the point is that distinctly unique dispersion functions may be required by individual modes. For simplicity, step functions or piece-wise linear approximations may suffice. Per multipath mode, the dispersion slope may have to be bounded by a value yet to be determined.

3. Specular Attenuation.

In the more common situations, there is at most one specular wavefront received. Then the assumption of a constant term over all f appears justified. However, if there were two or more specular components, even relatively mild phase fluctuations can cause nulls and peaks at sufficiently separated frequencies.

4. Specular Phase.

If there is one specular term, its phase could be treated as a constant. However, in the infrequent case of more than one specular term, special adjustments (such as uniformly distributed phase differences) may be appropriate in the wideband model.

5. Scatter Attenuation.

Each received multipath mode shows some amplitude dependence on frequency f. The function has been denoted as $A_i(f)$ for the i-th path. When attenuation is total at a given f, no energy is received, and the function vanishes. For ease of representation, a small number of piece-wise linear segments may suffice to approximate the scatter attenuation function of a mode.

6. Frequency Shift.

As a function of f, the average Doppler shift of a mode i may differ from other modes. This functional dependence on index i and on frequency f must be incorporated in the complex, bivariate Gaussian, random tap multiplier function $u_i(f,t)$. A single linear function over f appears the easiest model for the Doppler shift. The magnitude of the Doppler shift should typically remain below 10 Hz.

7. Frequency Spread.

This is the standard deviation of the modal Doppler spread. Just like the Doppler shift, its functional behavior is part of the random multiplier function $u_i(f,t)$. Again, a single linear function over f should suffice for each multipath mode. The frequency spreads are normally on the order of 1 Hz or less.

8. Fading Spectrum.

This spectral shape has only one peak when there is no magneto-ionic path splitting. When splitting occurs, each of the O and X components has its own peak. In all cases, the shapes are to be Gaussian functions with relative displacements that vary linearly with frequency.

It has been stressed repeatedly that the objective of wideband HF measurements need not be to record every detail of the proposed channel model, and certainly not the complete frequency dependent characteristics of H(f,t). There are two reasons for that. First, due to the great variability of the HF channel, the entirety of traits would be incredibly difficult to establish with any degree of confidence. Second, details that are too complex may eventually be impossible to model and to simulate with the state-of-the-art technology. It appears far more expedient to seek channel representations based on simple approximations. That is the motivation for utilizing piece-wise linear segments to fit only a few selected functions of frequency, such as $A_i(f)$, $\tau_i(f)$, and so forth. Furthermore, the number of segments should be kept low, say at 1, 2, or at most 3.

5. CONCLUSIONS

There is only one dominant conclusion for this study. That is to recognize the need for pertinent measured data about the HF channel as a wideband (on the order of 1 MHz) channel. To help in the spread spectrum system development, the requirement for wideband HF simulators has been noted. However, every simulator is based on a model--and that model must be based on valid, experimental, real-world, HF numbers.

Comprehensive measurement programs are necessary to remedy this shortcoming. On a very cursory level, the programs would have to employ sufficiently high resolution channel probes to measure in detail the HF channel responses over the required large bandwidths. The detail is to include identification and estimation of transfer function characteristics for all multipath modes that are present.

To be specific, consider the wideband time-varying channel transfer function, H(f,t), of Eq. (2) in Section 4. That function is:

$$H(f,t) = \sum_i A_i(f)\, u_i(f,t)\, \exp[-j2\pi\tau_i(f)f].$$

As explained, it contains many variables or parameters that require quantitative specification.

In summary, experimental data are needed for wideband HF modeling

- to validate the overall model for H(f,t)
- to identify the most significant functional elements of H(f,t)
- to establish typical and extreme quantitative ranges for the significant functional element of H(f,t)
- to include realistic geographic and time-of-day (viz., month, year, season, solar cycle) effects on the distortion elements
- to justify simple approximations for the significant functional elements of H(f,t)

- to test the hypotheses of mutual statistical independence and/or lack of correlation between random components of the significant functional elements of H(f,t)
- to find the duration of time intervals during which these random components can be considered stationary.

The proposed model agrees with the convincingly validated Watterson model for narrowband channels. Unfortunately, without adequate verification via wideband HF measurements, the above H(f,t)--like many other such conjectures--will represent little more than a hypothesis.

6. REFERENCES

1. Nupen, W., Bibliography on ionospheric propagation of radio waves (1923-1960), (1960), NBS Technical Note 84, National Bureau of Standards, Boulder, CO.

2. Agy, V., K. Davies, and R. Salaman, An atlas of oblique-incidence ionograms, (1959), National Bureau of Standards, NBS Technical Note 31, Boulder, CO.

3. Balser, M., and W.B. Smith, Some statistical properties of pulsed oblique HF ionospheric transmissions, Radio Science 66D, (1962), pp. 721-730.

4. Davies, K., Ionospheric Radio Propagation, (1965), National Bureau of Standards Monograph No. 80, U.S. Government Printing Office, Washington, DC (NTIS Order No. PB 257-342/6ST).

5. CCIR, Recommendations and Reports of the CCIR, Volume I: Spectrum Utilization and Monitoring, (1982). Includes Report 670, Worldwide minimum external noise levels, 0.1 Hz to 100 GHz, pp. 224-229, ITU, Geneva, Switzerland.

6. CCIR, Recommendations and Reports of the CCIR, Volume VI: Propagation in ionized media, (1982). Includes Report 258-4, Man-made radio noise, pp. 177-183; Report 342-4, Radio noise within and above the ionosphere, pp. 184-196, ITU, Geneva, Switzerland.

7. CCIR, Characteristics and applications of atmospheric radio noise data, (1983), Report 322-2, ITU, Geneva, Switzerland.

8. Ehrman, L., L.B. Bates, J.F. Eschle, and J.M. Kates, Real-time software simulation of the HF radio channel, IEEE Trans. Commun. COM-30, (1982), pp. 1809-1817. [Also available as a Signatron Report to the U.S. Air Force, RADC, Signatron, Inc., Lexington, MA].

9. Watterson, C.C., J.R. Juroshek, and W.D. Bensema, Experimental verification of an ionospheric channel model, (1969), ESSA Tech. Report ERL112-ITS80, ESSA/ITS, Boulder, CO.

10. Watterson, C.C., J.R. Juroshek, and W.D. Bensema, Experimental confirmation of an HF channel model, IEEE Trans. Commun. COM-18, (1970), pp. 792-803.

11. Watterson, C.C., and C.M. Minister, HF channel-simulator measurements and performance analyses on the USC-10, ACQ-6, and MX-190 PSK modems, (1975), OT Report 75-56, OT/ITS, Boulder, CO (NTIS Order No. COM 75-11206).

12. Watterson, C.C., Methods of improving the performance of HF digital radio systems, (1979), NTIA Report 79-29, NTIA/ITS, Boulder, CO (NTIS Order No. PB 80-128606/AS).

13. Wagner, L.S., and J.A. Goldstein, Wideband HF channel prober timing and control modules, (1982), NRL Memorandum Report 4933, Naval Research Laboratory, Washington, DC.

14. Wagner, L.S., and J.A. Goldstein, High-resolution probing of the HF ionospheric skywave channel: F2 layer results, Radio Science 20, (1985), pp. 287-302.

15. Wagner, L.S., J.A. Goldstein, and E.A. Chapman, Wideband HF channel prober: System description, (1983), NRL Report 8622, Naval Research Laboratory, Washington, DC.

DISCUSSION

K.C. Yeh, US

In your proposed model, would you give the range of parameters that would be applicable to the ionospheric communication channel?

Author's Reply

The identification of key parameters and estimation of their ranges is, of course, the main substance of the wide band HF modeling program. At this time, the parameter identification has barely begun. It is therefore difficult to respond to this question. In the published paper, conjectures were made as based on the narrow band by Watterson. See Table 1. All these parameters will definitely have a role with their numerical ranges extended by a factor yet to be determined. However, other new parameters may be suggested by research programs that are being initiated in the United States.

J. Aarons, US

In developing an HF wide band model, the author has noted gaps in observations for which research studies should be developed. These should be noted in order to be addressed by the research community. Is this aspect being addressed?

Author's Reply

Research to be undertaken is being approached along theoretical and experimental lines at several organizations. Theoretical modeling work has begun at the Institute for Telecommunication Sciences and elsewhere, experimental work at the Naval Research Laboratory, Air Force (RADC), and elsewhere. Specific ordering by relative significances appears difficult at this early time.

S. Basu, US

Professor Yeh raised questions on coherence bandwidth of HF channels. In satellite-to-ground communication links at UHF, we observed coherence bandwidth of at least ± 5%. If this can be translated directly to HF, it will amount to ± 500 kHz at MHz.

Author's Reply

The proposed spread spectrum systems of bandwidths of 1 MHz, or thereabout, would, by design, extend far outside the expected HF coherence bandwidth. This will be so in most, if not all, of the channels of interest. The system aspects of this fact, however, must be faced by the specific system users through appropriate receiver designs (i.e., signal processing). The effect therefore is not of primary concern to the wide band HF channel modeling effort, as long as the model represents the medium in acceptable fashion.

G. Sales, US

Is there any a priori reason for leaving out the possible time dependence in the time delay $\tau(f)$? Is it possible to simulate the wide band channel by sampling the 1 MHz spectrum at some interval smaller than the total bandwidth?

Author's Reply

No, to the first question. However, since there may be innumerable ways of incorporating parts of time variation into modal time delays $\tau_i(f,t)$, and none appear clearly superior at this time, we have taken the simplest way out and have assumed time-invariant $\tau_i(f)$.

For the second question, the selection of unique narrower subbands (or intervals) of the 1 MHz band does not appear justified for all HF channels and all system applications. Perhaps this will change in the future as we learn more about the wide band HF structures and important system requirements (e.g, frequency hopping spread spectrum).

C. Goutelard, FR

English translation

In evaluating the systems, we have to take into account the channel transfer function, noise and jamming. In a narrow band, we can avoid them, but in a wide band context the problem can become quite critical. Don't you think that these parameters must be introduced in the simulations and taken into account in the same way as the signal? Many European and American studies have highlighted their importance.

Author's Reply

We agree that noise(s), interference, and jamming must be modeled and incorporated into wide band HF simulators. Their features, however, are sufficiently unique to permit them to be handled separately and somewhat apart form the channel transfer function modeling stressed in this paper.

DISCUSSION

K.C. Yeh, US

In your proposed model, would you give the range of parameters that would be applicable to the ionospheric communication channel?

Author's Reply

The identification of key parameters and estimation of their ranges is, of course, the main substance of the wide band HF modeling program. At this time, the parameter identification has barely begun. It is therefore difficult to respond to this question. In the published paper, conjectures were made as based on the narrow band by Watterson. See Table 1. All these parameters will definitely have a role with their numerical ranges extended by a factor yet to be determined. However, other new parameters may be suggested by research programs that are being initiated in the United States.

J. Aarons, US

In developing an HF wide band model, the author has noted gaps in observations for which research studies should be developed. These should be noted in order to be addressed by the research community. Is this aspect being addressed?

Author's Reply

Research to be undertaken is being approached along theoretical and experimental lines at several organizations. Theoretical modeling work has begun at the Institute for Telecommunication Sciences and elsewhere, experimental work at the Naval Research Laboratory, Air Force (RADC), and elsewhere. Specific ordering by relative significances appears difficult at this early time.

S. Basu, US

Professor Yeh raised questions on coherence bandwidth of HF channels. In satellite-to-ground communication links at UHF, we observed coherence bandwidth of at least ± 5%. If this can be translated directly to HF, it will amount to ± 500 kHz at MHz.

Author's Reply

The proposed spread spectrum systems of bandwidths of 1 MHz, or thereabout, would, by design, extend far outside the expected HF coherence bandwidth. This will be so in most, if not all, of the channels of interest. The system aspects of this fact, however, must be faced by the specific system users through appropriate receiver designs (i.e., signal processing). The effect therefore is not of primary concern to the wide band HF channel modeling effort, as long as the model represents the medium in acceptable fashion.

G. Sales, US

Is there any a priori reason for leaving out the possible time dependence in the time delay $\tau(f)$? Is it possible to simulate the wide band channel by sampling the 1 MHz spectrum at some interval smaller than the total bandwidth?

Author's Reply

No, to the first question. However, since there may be innumerable ways of incorporating parts of time variation into modal time delays $\tau_i(f,t)$, and none appear clearly superior at this time, we have taken the simplest way out and have assumed time-invariant $\tau_i(f)$.

For the second question, the selection of unique narrower subbands (or intervals) of the 1 MHz band does not appear justified for all HF channels and all system applications. Perhaps this will change in the future as we learn more about the wide band HF structures and important system requirements (e.g, frequency hopping spread spectrum).

C. Goutelard, FR

English translation

In evaluating the systems, we have to take into account the channel transfer function, noise and jamming. In a narrow band, we can avoid them, but in a wide band context the problem can become quite critical. Don't you think that these parameters must be introduced in the simulations and taken into account in the same way as the signal? Many European and American studies have highlighted their importance.

Author's Reply

We agree that noise(s), interference, and jamming must be modeled and incorporated into wide band HF simulators. Their features, however, are sufficiently unique to permit them to be handled separately and somewhat apart form the channel transfer function modeling stressed in this paper.

PROPAGATION AND PERFORMANCE MEASUREMENTS OVER A DIGITAL TROPOSCATTER COMMUNICATIONS LINK

John J. Lemmon
U. S. Department of Commerce
National Telecommunications and Information Administration
Institute for Telecommunication Sciences
325 Broadway
Boulder, CO 80303
USA

SUMMARY

This paper discusses propagation and performance measurements that were obtained over a digital troposcatter communications link between Bocksberg, West Germany, and West Berlin. The measurements were unusual in that three general types of data were collected simultaneously over the link: propagation data, digital performance data, and meteorological data. The propagation data include received signal level (RSL) and multipath measurements made with a channel probe, the performance data consist of bit-error data obtained from a 1.544 Mbps T1 bank, and the meteorological data (in the form of radiosonde messages) have been used to generate profiles of the radio refractive index over the link.

The basic principles and instrumentation of the channel probe and the test configurations used to obtain these data are discussed. Then the results of analyses of these data are presented and discussed. These results include the measured impulse response of the channel, delay spread, RSL, bit-error ratios, and refractive index profiles. Potential relationships among these results are investigated in order to assess the impact of various troposcatter channel conditions on digital radio performance. In particular, the paper discusses both the definition and methods of utilizing the all important parameter of delay spread. These considerations range from the simple parameter of 2σ values to a more complete evaluation of the dynamic properties of delay-spread derived from the channel probe data.

Previous studies have addressed many facets of troposcatter propagation. This paper attempts to bring all of these facets together, to present a more complete description of the troposcatter channel, and to enhance future digital upgrades of existing troposcatter links.

1. INTRODUCTION

The U.S. Army recently completed equipment installation of a digital troposcatter communication system between Bocksberg, West Germany, and West Berlin. The radio system is composed of an upgraded Army tactical troposcatter radio operating with the MD 918/GRC Digital Data Modem at a nominal bit rate of 10 Mbps. This is the first digital upgrade of an existing analog troposcatter link in the Defense Communications System in Europe, and it is, therefore, important to evaluate both the propagation factors and the digital performance over this link.

One of the most important parameters to be measured is the delay spread of the signal in the propagation path. The measurement of delay spread over the Berlin/Bocksberg link was specified as part of the test and acceptance program, conducted by GTE Government Systems Corporation, Communication System Division, Needham Heights, Massachusetts, under contract to the U.S. Army. The instrument used to make the delay spread measurement was a pseudo-random noise (PN) channel probe, designed and built by the Institute for Telecommunication Sciences (ITS), Boulder, Colorado. The purpose of this paper is to summarize the data obtained by ITS.

The primary objective was to obtain propagation data, including measurements of delay spread and received signal level, in conjunction with measurements of digital transmission performance. The simultaneous collection of propagation and performance data over the same transmission channel can provide new insights into performance criteria and suggest adaptive techniques which may be valuable in planning and implementing future digital upgrades of other troposcatter links. It is also expected that the data will be useful in enhancing analytical models of troposcatter channels.

2. BACKGROUND

A common propagation problem in both line-of-sight and transhorizon radio links is caused by multipath, resulting from reflections or refraction/scatter in the transmission medium. Multipath can be more detrimental in the digital transmission mode than in its analog counterpart. A significant number of performance measurements have been reported that demonstrate the catastrophic effect multipath can have on digital transmission. Examples of specific measurements have been discussed by Dougherty and Hartman (1977), Anderson et al. (1979), Barnett (1978), and Hoffmeyer et al. (1986); a review of this field with extensive references has been given by Hubbard (1984). However, there are techniques that use the multipath to provide a form of in-band diversity improvement. Such is the case with the MD 918. The modem is designed to take advantage of the delay spread of the signal over a certain range. It is therefore important to know what values of delay spread are encountered in practice.

The primary purpose of ITS in the test and acceptance program for the Berlin/Bocksberg digital tropo link was to furnish the equipment necessary for the delay spread measurements. The PN channel

probe, described in Section 3, was interfaced to the host radio at the 70-MHz IF level. Details of the interface arrangement are discussed in Section 4.

The test signal was propagated over the path in the 4.5 to 5 GHz band. The path length is approximately 210 km. The path profile for the link, shown in Figure 1, indicates that the dominant propagation mechanism is expected to be troposcatter, but that the link may be diffractive under super-refractive conditions. The data presented in this paper were collected during the last two weeks of February 1986, when the signal was transmitted from Booksberg to Berlin.

3. MULTIPATH MEASUREMENT TECHNIQUE AND EQUIPMENT

Delay spread has been measured previously over a few selected troposcatter links using a system commonly known as a RAKE communication system (Price and Green, 1958; Barrow et al., 1969; Sherwood and Suyemoto, 1977). The RAKE system measures the value of a correlation function at the output of a finite number of taps along a tapped-delay line. The test signal uses a pseudo-random noise (PN) code, which is cross-correlated in the receiver with a locally generated replica of the PN code.

The instrumentation used in the ITS PN channel probe is similar to that of the RAKE system, with the exception of the correlation process. The ITS system uses a time-multiplex type correlation detector in the receiver, as opposed to the tapped-delay line used in the RAKE system. Delay between the received code and the locally generated replica is achieved by clocking the PN generator at a slightly slower rate in the receiver than in the transmitter. In this manner, delay is continuously varying, thereby enabling one to measure the correlation function (impulse response of the radio channel) as a function of time delay. The rate of delay change is variable, and the code length and clock rate are selectable over specified ranges to meet different transmission channel conditions. A detailed description of the theory and implementation of the ITS channel probe is given by Linfield et al. (1976). Delay spread measurements taken over troposcatter links with this probe have been discussed by Hubbard (1983).

The correlation process in the probe receiver takes advantage of time-bandwidth tradeoff, which permits the data to be recorded at a relatively low rate (small bandwidth), but with high equivalent time resolution. For example, the bit time for a PN code clocked at 10 MHz is 0.1μs. For a 511-bit code at this clock rate, a code word is 51.1μs in length. If a correlation function were developed for each code word, the bandwidth requirement for the data acquisition system would be quite broad. However, this data rate is not necessary if the dynamic changes in the transmission channel are much slower. In the PN channel probe receiver, the correlation process is slowed so that many code words are processed while one correlation function is developed. For example, the data rate for the tests described here was selected to be one correlation function per second. However, the range of time delays over which the correlation function is measured corresponds to the 51.1μs period of the PN code. Thus, 1 s of processing time in the receiver corresponds to 51.1μs in channel response time (a time-bandwidth factor of approximately 2×10^4).

A simplified block diagram of the probe is shown in Figure 2. For UHF band and troposcatter systems, an IF of 70 MHz and a PN clock rate of 10 MHz are used. These values were chosen to make the system compatible with existing communication systems that use a standard 70 MHz IF and to limit the PN test signal bandwidth to a value commensurate with the power amplifiers of those systems. In order to maintain frequency coherence between the tropo radio and the probe, the 10-MHz reference from the radio interface rack (LORAN C) was used as the probe reference signal in parallel with the tropo radio.

The receiver of the probe is configured for dual-channel operation, but only one channel is illustrated in Figure 2. The two independent channels allow data to be collected simultaneously from two diversity links. The probe receiver develops four signals from each channel. Two correlators are used to develop the in-phase and quadrature components of the equivalent low-pass impulse response of the transmission channel. Relative phases between multipath components can therefore be determined. The third signal is developed from the sum-of-the-squares processing of the in-phase and quadrature signals, which is the power impulse response of the channel. The fourth signal is the received signal level (RSL), measured as a power level in the IF amplifier stages. All of these signals were recorded on digital magnetic tape.

4. TEST CONFIGURATIONS AND DATA ACQUISITION SYSTEM

Digital performance was measured with an appropriate bit-error detector, using a predetermined digital test signal at the designated transmission rate. On one hand, the PN test signal requires the total baseband of the radio, and thus cannot be transmitted simultaneously with the data test signal. On the other hand, the troposcatter radio system uses quadruple diversity in a dual space/dual frequency configuration, so that probe data and digital performance data can be obtained simultaneously over the link if the radio is configured for dual diversity operation. In other words, one diversity pair can be used to receive the probe signal while the other diversity pair is receiving the digital performance test signal. This and the other configurations that were used in the test are listed in Table 1. The frequency diversity signals are transmitted with different polarizations (horizontal and vertical) and are identified by polarization rather than by frequency throughout this paper.

The control for the various configurations was provided at the transmitter terminal through the use of coaxial switches to change the input test signals. Command signals for the coaxial switches were sent via the service channel from the receive site to the transmit site. The test proceeded through the various configurations in a cyclic fashion, operating in a given configuration for a duration of 13 minutes before proceeding to the next configuration. At the transitions between configurations, the system was put into configuration 1 for a duration of approximately 2 minutes, during which time GTE

processed and recorded data. Thus, the test cycled through all four configurations over a period of 1 hour. The complete test configurations are shown in block diagram form in Figures 3 and 4.

The ITS acquired a total of 32 magnetic tapes of test data. Data were acquired in 1-second intervals (coincident with the errored-second performance monitoring instruments discussed below). The data were double-buffered at the input, compiled into a 5-second file, and recorded on the magnetic tape. One buffer was acquiring new data as the other buffer was being read to the tape.

Data were recorded onto magnetic tape only when digital errors were detected. However, in test configuration 4, only the PN probe signal was transmitted, so that the bit-error detector used by GTE generated continuous errors by comparing the probe signal to the digital test signal. Thus, data were recorded continuously in test configuration 4. The following signals were recorded:

1. In-phase and quadrature components of the impulse response and the power impulse response from each of the two channels of the PN probe receiver.

2. RSL (received signal level) of each tropo receiver and the two channels of the PN probe receiver.

3. Spectrum of the received signal in each diversity polarization. These data include both the probe and digital test signal in accord with the applicable test configuration discussed above.

4. Digital performance (error) data.

5. Test configuration number.

6. Time code.

The latter two signals were used in the data processing procedures discussed in Section 5.

Analog data inputs were sampled at different rates, commensurate with the Nyquist requirements for the various signals. For example, the impulse functions from the PN probe require the highest sampling rate for the necessary resolution. Therefore, these functions (a total of six signals) were sampled at a rate of 4 kHz. The response was measured once per second in the first 20 ms only, as this part of the function includes time delays to beyond 1 μs. Thus, each response was sampled 80 times. Four additional A/D channels were sampled at a 100-Hz rate. These were used to record the received signal spectra from the tropo receivers and the RSL of the two channels of the PN probe receiver. The remaining six A/D channels were sampled at a 10-Hz rate and were used to record the RSL of each of the four tropo receivers as well as the two signals used to determine the test configuration number.

The digital performance data were measured in the ITS system using a recording error analyzer operating in the external error mode. This instrument measures synchronous errored seconds and registers the number of bit errors in each errored second. The data source for the instrument was an error pulse train developed in the bit-error detector used by GTE to measure the radio performance. The bit-error detector monitored the error performance of one T1 bank in an FCC-99 multiplexer. The other five T1 banks were loaded with another PN code stream that was looped back and forth over the link to simulate full load conditions. At no time during the tests was the error performance of the full mission bit stream monitored.

The ITS provided additional support to the test and acceptance program by obtaining available meteorological data from the U.S. Air Force in Berlin. These consisted of radiosonde data that can be used to develop refractive index profiles for the link. The radiosonde launch sites were at Lindenberg, East Germany, Hanover, West Germany, and Berlin. Computer programs developed at ITS were used on-site to compute and plot these profiles during the tests. The objective was to correlate test results with features of these profiles.

5. DATA PROCESSING

The magnetic tape recordings and radiosonde data were returned to the ITS laboratories for processing and analysis. The ITS has developed a set of computer programs to perform a variety of analyses on the data described above, including the following:

1. Average impulse response.

2. Probability density functions (pdf) and cumulative distribution functions (cdf) of the impulse width.

3. Pdf and cdf of the time rate-of-change of the impulse width.

4. Computation of the two-sided rms width of the average power impulse response (2σ).

5. Average signal spectrum.

6. Pdf and cdf of RSL.

7. Cdf of 1-second BER.

8. Profiles of refractive index.

The individual impulse response functions that were used to compute the averages were first normalized so that each response had the same peak value. If the value of the average impulse power function at a time delay τ_i is denoted by $P(\tau_i)$, then σ is defined as

$$\sigma = \left[\frac{\sum_{i=1}^{N} P(\tau_i)\,(\tau_i - \bar{\tau})^2}{\sum_{i=1}^{N} P(\tau_i)} \right]^{1/2} ,$$

where N is the number of sample points (80) and $\bar{\tau}$ is the mean time delay:

$$\bar{\tau} = \frac{\sum_{i=1}^{N} P(\tau_i)\,\tau_i}{\sum_{i=1}^{N} P(\tau_i)} .$$

The impulse width is defined as the base width of an individual power impulse function, and the pulse width rate-of-change is computed as the difference between the pulse width of an impulse function and the pulse width of the previous (1 second earlier) impulse.

It should be noted that during the test configuration setup for Phase II (transmit from Berlin and receive at Booksberg), several changes to the equipment configuration were made. Both antennas at Booksberg were realigned, a baseband interface problem between the MD 918 modem and the KG-81 encryption unit (which caused intermittent burst errors) was discovered and fixed, and one antenna feedhorn at Booksberg was replaced. Any one or combinations of these changes could affect the absolute accuracy of the data analyses presented herein. The primary objective of the data analyses has been to identify those periods during which the radio system performed relatively poorly, and to relate the performance to propagation conditions in the transmission channel.

As discussed above, four different test configurations were used during the test and acceptance program. However, only during test configuration 4 were data collected on a continuous basis. For this reason, analyses of impulse response and RSL data were performed systematically only for this latter test configuration, in order to obtain results that are not biased by the error performance of the radio system. In test configuration 4, channels A and B of the probe were interfaced to tropo receiver 1 (horizontal polarization) and tropo receiver 4 (vertical polarization), respectively, thereby enabling the impulse response to be analyzed in both polarizations.

Examples of the average power impulse functions are shown in Figures 5 and 6. No scale appears on the vertical axes because the PN receiver does not have a local signal source, and thus the impulse response magnitude could not be calibrated; however, the impulse functions are plotted on a linear scale and relative power levels within a given impulse function can be determined accordingly. The legend in each plot gives the start and end times for the analysis and the value of 2σ. The statement "Mode-4" in each legend refers to test configuration 4.

The impulse functions corresponding to vertical polarization typically have a steep leading edge, followed by a tail with a relatively small amount of distortion corresponding to signal energy arriving at relatively large delay times (Figure 5). On the other hand, the impulse functions corresponding to horizontal polarization show a pronounced shoulder on the trailing edge and occasionally a distinct secondary peak, suggesting a mixed mode of propagation. An exception to this pattern can be seen in the impulse functions in Figure 6 corresponding to the time block on February 23, in which distinct shoulders appear on the leading and trailing edges for both horizontal and vertical polarization.

The digital performance data were processed by computing cumulative probability distributions of 1-second bit error ratios (BER) for test configurations 1, 2, and 3. As explained above, no performance data were provided during test configuration 4 because the PN probe signal was transmitted over both diversity pairs. The measurement resolution was determined by the bit rate of the T1 bank (1.544 Mbps) whose performance was monitored. Since one bit error is the smallest number of bit errors that can occur in any time interval, the smallest 1-second BER that could be measured was $1/(1.544 \times 10^6)$, or 6.48×10^{-7}.

The meteorological data consist of radiosonde messages that include values of atmospheric temperature, pressure, and dew-point departure at various heights. These data can be used to compute the atmospheric refractive index using the Smith-Weintraub relation (Smith and Weintraub, 1953), which expresses the refractive index in terms of temperature, pressure, and water vapor content. The radiosonde data were used to develop profiles of temperature, relative humidity, and index of refraction.

Examples of these profiles are shown in Figure 7. Each plot is labeled by time, date, and by the radiosonde launch site (Hanover, Lindenberg, or Berlin). Also, the elevations of the two ends of the link (Berlin and Booksberg) are shown on the plots. In addition to the profiles of temperature, relative humidity, and index of refraction (measured in N-units), each plot shows two other profiles labeled as "normal" and "ducting." These latter two profiles illustrate the refractivity gradients that correspond to a normal atmosphere (-40 N-units/km) and to ducting conditions (-157 N-units/km).

6. DISCUSSION OF RESULTS

In this section the results of the data analyses are summarized and discussed. Emphasis has been placed on the relationships between propagation parameters and radio performance. Then the measured values of delay spread are compared with theoretical values derived by applying ray theory to the Berlin/Bookaberg path profile. This analysis indicates that the measured values of delay spread are often larger than theoretical expectations and provides additional insight into the effects of propagation on radio performance.

6.1 Summary of Propagation and Performance Data

For ease of presentation, the results of the data analyses have been summarized in graphical form. Figures 8 through 12 are line plots of 2σ, pulse width, pulse width rate-of-change, and RSL versus time for the period February 24 through 26. In addition, each figure also contains line plots of BER over this same time period in order to facilitate comparing the propagation and performance data. The results shown in these figures embody only a small portion of all the data analyses that were performed, but are representative of the complete data base.

Each point is plotted at the time that corresponds to the center of the time block for that particular analysis. All times are given in Universal Time (UT); in Germany the local time is one hour ahead of UT. The time blocks used for these analyses vary from approximately 1 to 10 hours. The time blocks are not of equal length because the times during which data were collected were sometimes highly irregular, due to equipment failures and periodic RSL calibrations. Figure 8 shows the 2σ values for receivers 1 and 4 for test configuration 4. The 2σ values for receiver 4 (vertical polarization) vary from approximately 90 ns to 120 ns. For receiver 1 (horizontal polarization) the 2σ values are somewhat larger, varying from approximately 140 ns to 170 ns.

When interpreting delay-spread measurements, it should be recognized that the measured impulse response is actually the convolution of the impulse response of the transmission channel with the impulse response of the PN probe used to make the measurement. The probe impulse response is the autocorrelation function of the PN code, which is a triangular pulse whose base width is equal to two PN bit times (200 ns for a 10 Mbps clock rate). The power impulse response of the probe is therefore the square of the PN autocorrelation function. It is straightforward to calculate 2σ (twice the standard deviation) for such a pulse; the result is 63.2 ns. Thus, a nondispersive channel would have a measured 2σ equal to 63.2 ns. If one attributes the multipath dispersion of the transmission channel to the difference between the measured 2σ and the value of 2σ that would be measured for a nondispersive channel (63.2 ns), the results presented herein imply multipath dispersions that vary from less than 30 ns to greater than 100 ns. Expressed in terms of the symbol time T (200 ns), 2σ/T varies from approximately 0.15 to 0.5.

Figures 9 and 10 are line plots of the pulse widths for receivers 1 and 4, respectively. Each figure shows three plots, which correspond to the minimum, median, and maximum values of pulse width, obtained from the cumulative distributions. Although the maximum pulse widths are greater (by approximately 50 ns) for receiver 4 (vertical polarization), the median and minimum pulse widths are greater (by approximately 50 ns) for receiver 1 (horizontal polarization).

Line plots of the median pulse width rates-of-change for receivers 1 and 4 are shown in Figure 11. The median rates-of-change vary from approximately 20 ns/s to 200 ns/s and are greater for receiver 4. In view of the fact that median pulse widths are typically on the order of 400 ns, these results indicate that the troposcatter channel is quite dynamic over time scales on the order of or less than 1 second.

Figure 12 shows RSL plots for receiver 1. Each figure has three plots, corresponding to the minimum, median, and maximum values of RSL obtained from the cumulative distributions. Although RSL has not been converted to path loss, the median RSLs vary from approximately -45 dBm to -85 dBm, corresponding to a 40 dB variation in path loss. The trends are similar for all four receivers. However, receiver 1 had the highest RSLs. Receiver 2 was down from 1 by approximately 1 dB, receiver 3 was down from 1 by approximately 9 dB, and receiver 4 was down from 1 by approximately 5 dB. Thus, the horizontal diversity pair (receivers 1 and 2) had, on the average, approximately 7 dB greater RSL than did the vertical diversity pair.

The BER data for all three diversities are shown in the lower halves of Figures 8 through 12. The values plotted correspond to a probability of 0.9 in the cumulative distributions. A probability of 0.9 was chosen rather than 0.5 (corresponding to the median value) because the median value was often less than the measurement resolution (6.48×10^{-7}).

As expected, the quadruple diversity had lower BERs than either of the dual diversity configurations. However, the vertical diversity pair consistently had higher BERs than the horizontal diversity pair. Thus, the horizontal diversity pair had higher RSLs, larger delay spreads, and lower BERs than the vertical diversity. Since a higher RSL is expected to improve performance, whereas a larger delay spread is expected to degrade performance, it appears that the differences in RSL (between the two diversities) influenced performance more strongly than differences in delay spread.

Futhermore, comparing the BER data with the delay spread results in Figures 8 through 10, and the RSL data in Figure 12 indicates that within a given channel, variations in RSL correlate with performance more closely than variations in delay spread. For example, the periods of good performance on the mornings of February 24, 25, and 26 are accompanied by corresponding rises in RSL, whereas the 2σ and pulse width values are not particularly small at these times. However, it should be recognized that the adaptive equalization in the MD 918 is designed to compensate for multipath dispersion, which is consistent with the observation that delay spread and performance are not well correlated.

On the other hand, the gross variations in the pulse width rates-of-change in Figure 11 appear to track the variations in BER for both diversities. The fact that the rates-of-change were generally greater for receiver 4 (vertical) that for receiver 1 (horizontal) corroborates the view that greater rates-of-change are associated with higher BERs. This trend is also present in the results of other data analyses not shown in Figure 11 and suggests that substantial gains in performance could be realized by the implementation of adaptive equalization that takes channel dynamics into account.

The meteorological profiles (such as those in Figure 7) have been examined for features that correlate with periods of good and poor performance; however, no obvious trends have been noted. The surface refractivity showed little variation during the period February 14-28, and was close to 310 N-units. This value is consistent with other refractivity measurements in continental, temperate climates during the winter season (Bean et al., 1966; CCIR, 1978a).

The refractivity gradients were generally close to that of a standard atmosphere (-40 N-units/km), with a tendency to be slightly subrefractive (smaller gradients). Occasional discontinuities in the refractivity gradient (indicating the presence of atmospheric layers) appear in the refractivity profiles, and are often accompanied by temperature inversions. However, these inversions and/or layers do not appear to correlate in any obvious way with periods of good or poor performance. Similarly, no unusual features are apparent in the profiles during periods of unusually large or small delay spread.

It should be recognized that the radiosonde data are rather sparse; in fact, adjacent data points in the profiles are often separated by several hundred meters. Thus, the presence of thin reflecting/refracting layers would not generally appear in the profiles. Moreover, seasonal variations in refractivity could not be observed over the two-week period during which data were collected.

6.2 Comparison of Measured and Theoretical Values of Delay Spread

The values of delay spread reported herein are comparable to those found by previous measurements over other troposcatter paths. For example, Sherwood and Suyemoto (1977) reported values of 2σ which varied from 50 ns to 370 ns with a mean of 180 ns, and Hubbard (1983), who reported values of pulse width measured with the PN channel probe, found values ranging from less than 200 ns to greater than 1μs. However, Sherwood and Suyemoto pointed out that their measured values of 2σ were somewhat larger than those predicted by the Bello (1969) channel model.

The Bello model, and variations of it, use turbulent scattering theory to compute the differential scattering cross section in the common volume, thereby determining the amount of scattered energy received from each point in the common volume. Ray tracing is then used to compute the relative delay times from each point in the common volume, and the power impulse function is developed by integrating the received power over the common volume for each value of delay time. The delay spread can therefore be estimated by calculating the spread in arrival times of rays propagating from the transmitter to the receiver via scattering in the common volume.

The location of the common volume for the Berlin/Bocksberg link is illustrated with the path profile in Figure 1. The upper two rays correspond to the half-power beamwidths of the antenna patterns and the lower two rays correspond to the antenna boresites. The common volume is the region enclosed by these rays. The take-off angles of the rays were determined by positioning the boresites on the radio horizons. For 30-foot antennas operating in the 4.5-5.0 GHz band, the half-power beamwidths are approximately 0.5°. The rays corresponding to the half-power beamwidths therefore have take-off angles 0.25° above boresite. Using this construction, the positions of the extremities of the common volume (in the plane of the propagation path) can be obtained directly from the path profile in terms of elevation above sea level and lateral distance along the path.

The path lengths for the various rays were then calculated using the construction shown in Figure 13. The ray paths are assumed to be straight lines over an earth of effective radius R_e. For a standard atmosphere, R_e = 8497 km. The angle ϕ for a point in the common volume can be expressed in terms of its lateral distance d_0 along the path as $\phi = d_0/R_e$. Applying the law of sines to the triangle in Figure 13 implies that the ray path length d_θ is given by

$$d_\theta = (R_e+h)\sin\phi/\cos(\theta-\phi),$$

where h is the antenna elevation and θ is the ray takeoff angle measured downward from the horizontal.

It was found that the path length difference for rays propagating through the highest and lowest points in the common volume is only 1 m, implying a delay spread of only several ns. For the rays propagating through the two lateral extremes of the common volume (in the plane of the propagation path), the path length difference is 6 m, which translates into a delay spread of approximately 20 ns. Of course, this calculation does not take into account the lateral extent of the common volume transverse to the propagation path. However, it is easy to show that the delay spread due to lateral spreading of the beams is comparable to that due to spreading in the vertical dimension (≈ 1 ns). Thus, for pure troposcatter propagation one expects a measured value of 2σ which is approximately 20 ns greater than that measured for a nondispersive channel (53.2 ns), or approximately 85 ns.

This was occasionally observed for vertical polarization, in which case the power impulse function consists of a symmetric peak with very little distortion in either the leading or trailing edges. The fact that much larger values of 2σ were measured when shoulders appeared on the leading and/or trailing edges of the impulse functions suggests that these features were due to non-troposcatter modes of propagation. However, the ray tracing calculations discussed above imply that diffraction, foreground effects (if any are present), and/or reflections from atmospheric layers generate small (≈ 1 ns) contributions to delay spread, to be compared with discrepancies of tens of ns. If the large delay spreads are not attributed to non-troposcatter modes of propagation, then a possible explanation is that

the time of arrival of signal energy varies by tens of ns over the time interval during which the impulse response is measured. If this is the case, then the troposcatter channel is dynamic over time scales on the order of several ms.

The question remains as to why the horizontal diversity pair consistently had larger delay spreads and higher RSLs than the vertical diversity pair. However, as was pointed out in Section 5, several hardware problems with the radio system were discovered and fixed after the data discussed herein were obtained. Also, the horizontally and vertically polarized signals were transmitted from different antennas at Booksberg.

7. CONCLUSIONS

The primary objective of this work, to obtain delay spread measurements in conjunction with digital performance data over the Berlin/Booksberg tropo link, has been met. The PN channel probe proved to be quite valuable for this purpose; various propagation modes can readily be discerned from the impulse response data and dynamic changes in the transmission channel can be observed and analyzed.

The values of delay spread that were obtained over this link are comparable to those obtained from previous measurements over other troposcatter paths, and are often larger than the value expected for pure troposcatter propagation. In particular, the values of the two-sided rms width of the power impulse function, 2σ, varied from less than 90 ns to 170 ns, to be compared with a value of approximately 85 ns expected for pure troposcatter propagation in a stationary channel.

Variations in performance appeared to correlate well with variations in RSL, as expected. However, it was also observed that channel dynamics is related to radio performance; in particular, periods of poor performance were accompanied by large values (greater than 150 ns/s) of the pulse width rate-of-change. This portends the need to take into account channel dynamics in troposcatter models and in the design of adaptive equalization techniques. Such an approach could greatly enhance the capability to combat the effects of multipath dispersion on digital transmission systems.

8. REFERENCES

[1] Dougherty, H.T., and W.J. Hartman, "Performance of a 400 Mbit/s System Over a Line-of-Sight Path," IEEE Trans. Commun. COM-25, No. 4, Apr. 1977, pp. 427-432.

[2] Anderson, C.W., S. Barber, and R. Patel, "The Effect of Selective Fading on Digital Radio," 1978 Intl. Commun. Conf., Toronto, Ontario, Canada.

[3] Barnett, W.I., "Measured Performance of a High Capacity 6 GHz Digital Radio System," 1978 Intl. Commun. Conf., Toronto, Ontario, Canada.

[4] Hoffmeyer, J.A., L.E. Pratt, and T.J. Riley, "Performance Evaluation of LOS Microwave Radios Using a Channel Simulator," IEEE 1986 Military Commun. Conf., Monterey, CA, Paper No. 4.3.

[5] Hubbard, R.W., "A Review of Atmospheric Multipath Measurements and Digital System Performance," NATO AGARD Conf. Proc. No. 363, Propagation Influences on Digital Transmission Systems: Problems and Solutions, Athens, Greece, Paper No. 10, Jun. 1984.

[6] Price, R., and P.E. Green Jr., "A Communication Technique for Multipath Channels," Proc. IRE, Vol. 46, Mar. 1958, pp. 555-570.

[7] Barrow, B.B., F.G. Abraham, W.M. Cowan Jr., and R.M. Gallant, "Indirect Atmospheric Measurements Utilizing RAKE Troposcatter Techniques," Proc. IEEE, Vol. 57, Apr. 1969. pp. 537-551.

[8] Sherwood, A., and L. Suyemoto, "Multipath Measurements Over Troposcatter Paths," USAF/ESD, Report No. ESD TR-77-252, 1977.

[9] Linfield, R.F., R.W. Hubbard, and L.E. Pratt, "Transmission Channel Characterization by Impulse Response Measurements," OT Report 76-96, Aug. 1976.

[10] Hubbard, R.W., "Delay-Spread Measurements Over Troposcatter Links," NTIA Tech. Memo. 83-84, Mar. 1983.

[11] Smith, E.K., and S. Weintraub, "The Constants in the Equation for Atmospheric Refractive Index at Radio Frequencies," Proc. IRE, Vol. 41, Aug. 1953, pp. 1035-1037.

[12] Bean, B.R., B.A. Cahoon, C.A. Samson, and G.D. Thayer, A World Atlas of Atmospheric Radio Refractivity, ESSA Monograph 1, 1966.

[13] CCIR, "Radiometeorological Data," Report 563-1, Vol. V, Propagation in Non-ionized Media, Recommendations and Reports of the CCIR, 1978a, pp. 69-89.

[14] Bello, P.A. (1969), "A Troposcatter Channel Model," IEEE Trans. Comm. Technology, Vol. COM-17, Apr. 1969, pp. 130-137.

9. ACKNOWLEDGMENTS

The author wishes to acknowledge R. W. Hubbard for his many contributions and helpful suggestions throughout the course of this work. He also wishes to acknowledge the contributions of L. E. Pratt in developing the hardware for the channel probe and T. J. Riley for developing much of the necessary software for the data analyses. This work was supported by the U.S. Army.

Table 1. Test Configurations

Configuration Number (Mode Number)	Receivers Interfaced to PN Probe	Diversity Test Signals	
		Horizontal	Vertical
1	Receivers 1 and 4	MD 918 Data	MD 918 Data
2	Receivers 1 and 2	Probe Data	MD 918 Data
3	Receivers 3 and 4	MD 918 Data	Probe Data
4	Receivers 1 and 4	Probe Data	Probe Data

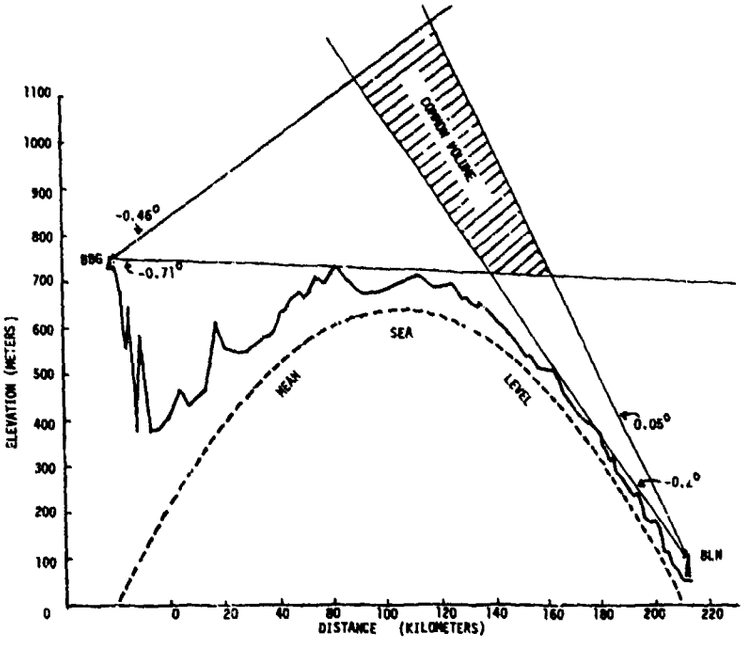


Fig. 1. Path profile from Bocksberg to Berlin.

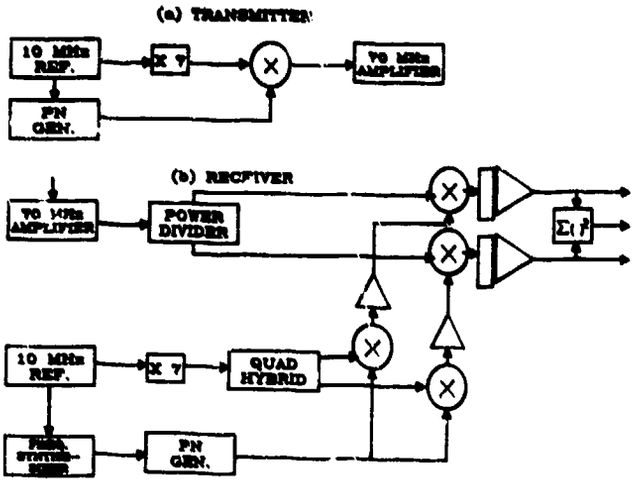


Fig. 2. PN probe block diagram.

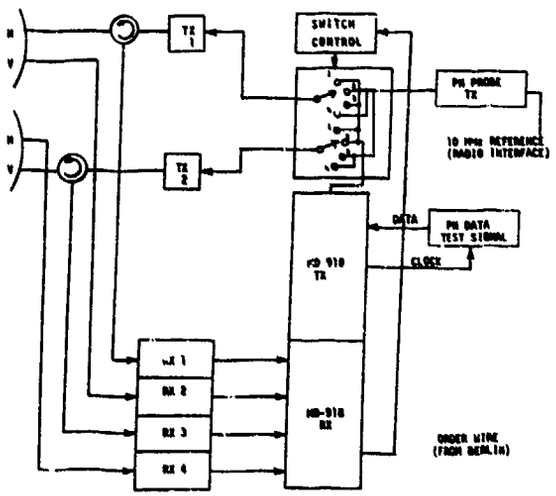


Fig. 3. Bocksberg site configuration (transmitter).

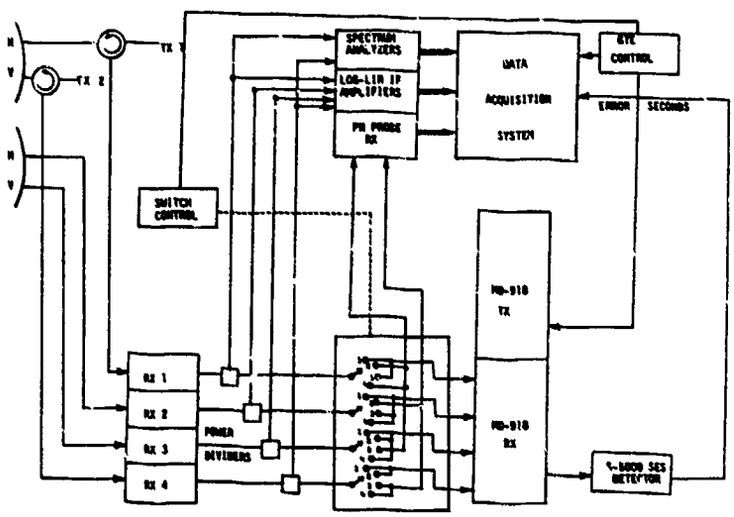


Fig. 4. Berlin site configuration (receiver).

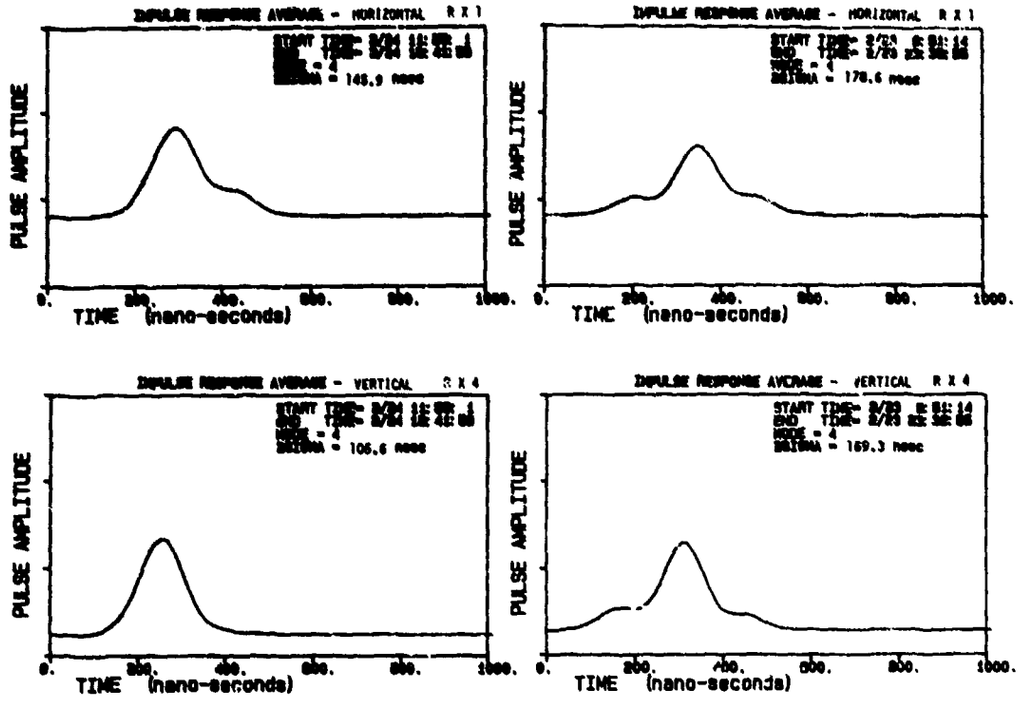


Fig. 5. Impulse power functions typical of those observed over the link.

Fig. 6. Unusual impulse power functions that suggest a mixed mode of propagation.

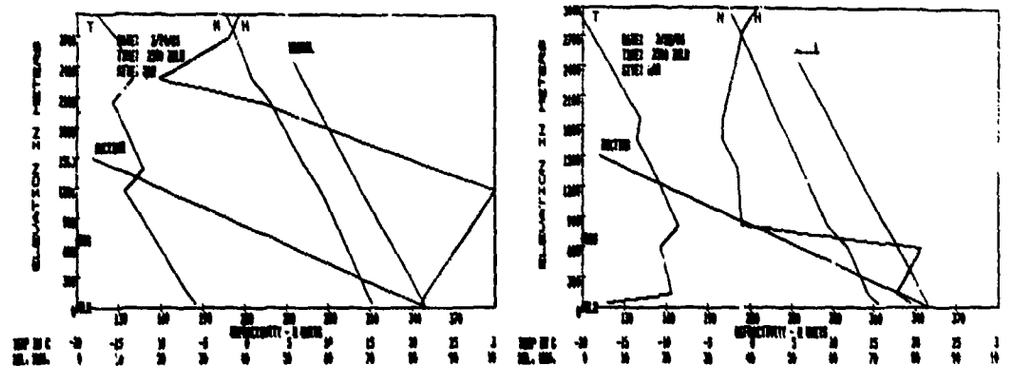


Fig. 7. Examples of meteorological profiles generated from radiosonde data.

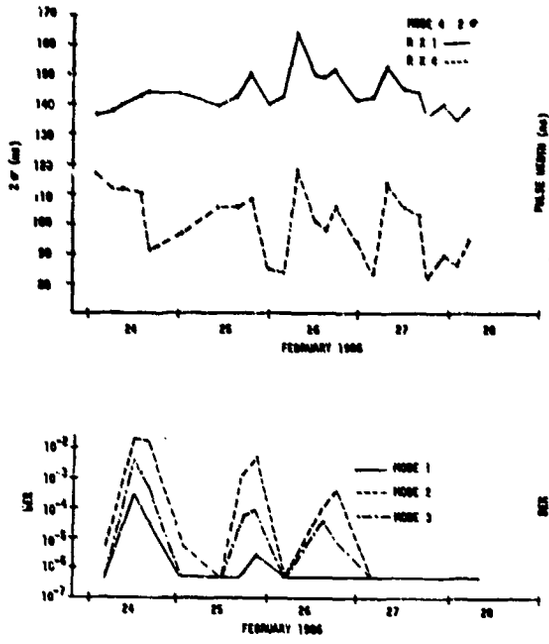


Fig. 8. Line plots of 2σ and BER.

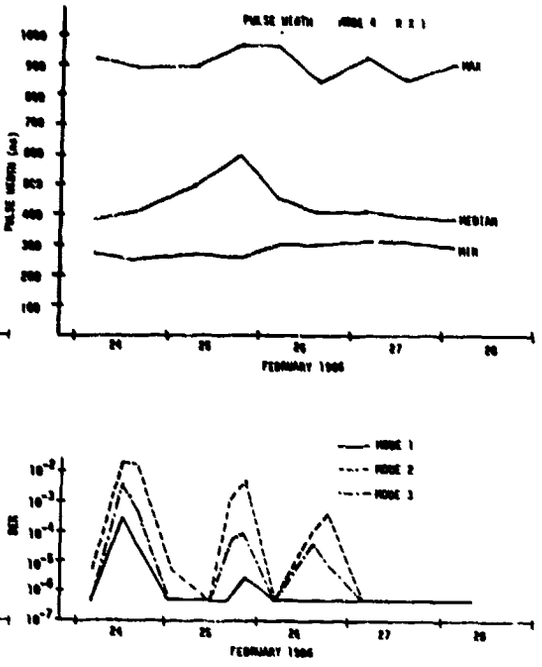


Fig. 9. Line plots of R X 1 pulse width and BER.

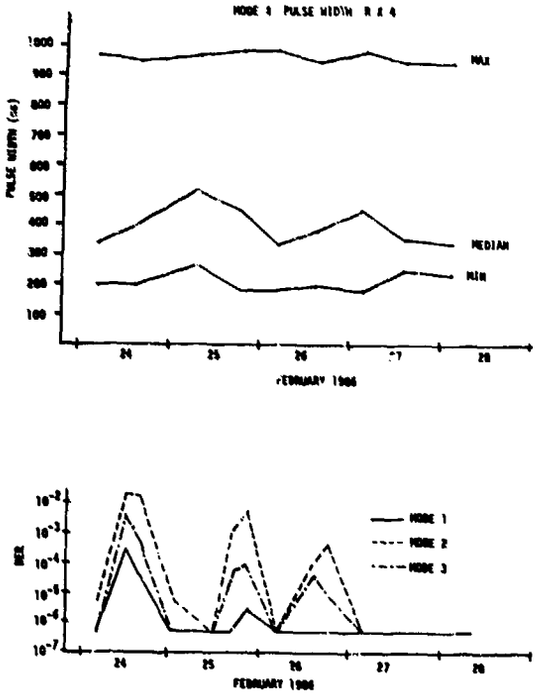


Fig. 10. Line plots of R X 4 pulse width and BER.

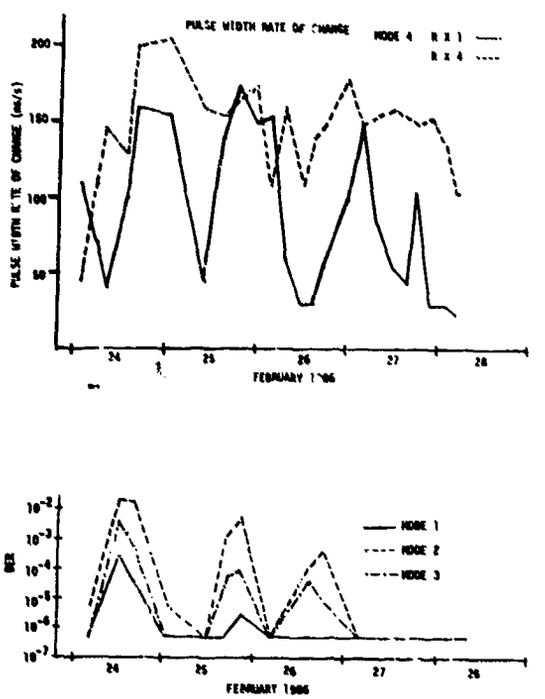


Fig. 11. Line plots of pulse width rate of change and BER.

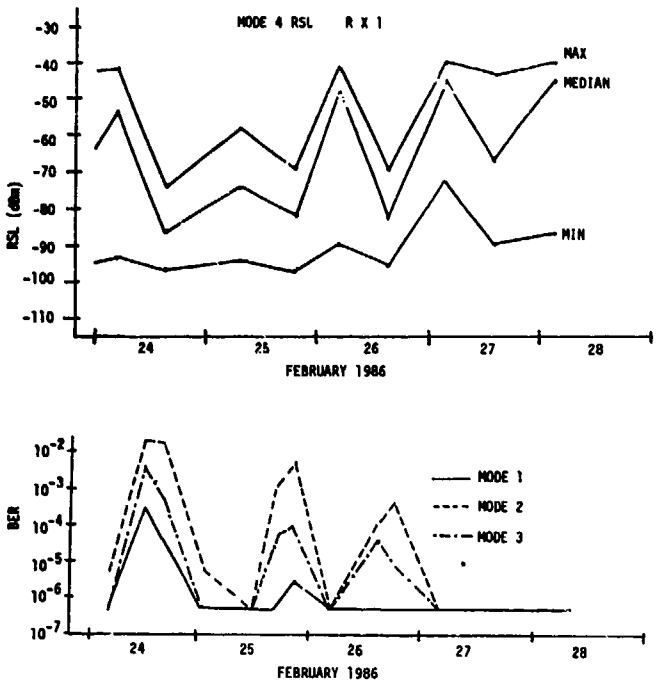


Fig. 12. Line plots of R X 1 RSL and BER.

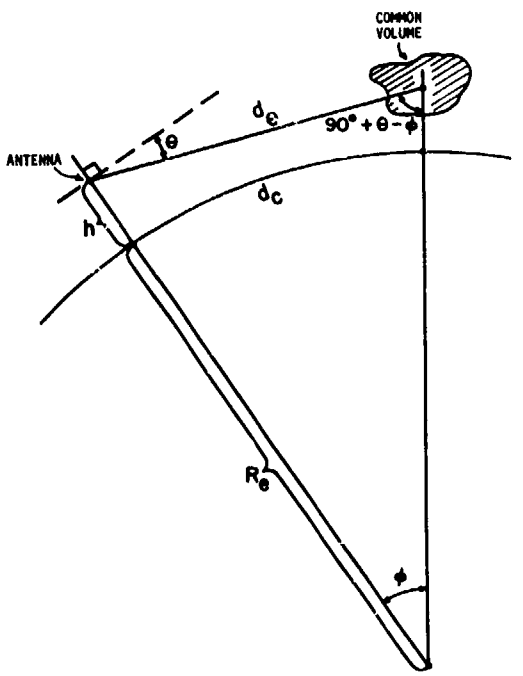


Fig. 13. Geometry for ray path-length calculation.

DISCUSSION

C. Goutelard, FR

English translation

Your lecture is very interesting. You introduce a new factor and suggest that it be taken into account in simulations. You gave results on the BER. Did you study the laws of distribution of errors in the function of the parameters? You know the importance of these parameters in correcting error problems.

Author's Reply

The BER results presented in this paper were obtained from cumulative probablility distribution functions of 1-second BERs and correspond to the BERs at a probability of 0.9. In this sense, the error distributions were studied as functions of various parameters, for example, pulse width rate-of-change. However, other features of the error distributions, such as error burst characteristics, have not been analyzed.

S. Silleni, IT

A question about your experimental technique. Was the refractivity (point 5.8 and Fig. 7) computed from ionosonde data or was it measured by airborne refractometer?

Author's Reply

The intended use of the radio system discussed in this paper is to carry operational traffic. However, the comparison of measured performance with military and/or CCIR standards was the responsibility of the prime contractor for the test and acceptance program (GTE Government Systems Corporation). The purpose of the analyses discussed here has been to identify those periods during which the radio system performed relatively poorly, and to attempt to correlate the performance with propagation conditions in the transmission channel.

R.J. Miller, UK

The technique used is pulse comparison in radars; much work has been done to establish pseudo-random sequences giving low sidelobe levels. Is it possible that "skirts" on one of your illustrations is due to very rapid fluctuations in the scattering medium?

Author's Reply

The PN sequence used in the channel probe is a maximal length shift register sequence, for which the autocorrelation function is a triangular pulse with no sidelobes. This is the primary reason that such a PN sequence was chosen for the channel probe. Yes, it seems possible that the "skirts" in the impulse functions are due to rapid fluctuations in the transmission medium. However, if this is the case, then these fluctuations must take place over time scales on the order of, or less than, several milliseconds, since this is the time scale over which a single impulse function is measured.

L. Boithias, FR

Is this equipment used for the transmission of information, and in this case, what is the performance obtained in comparison with military of CCIR standards?

Author's Reply

The refractivity has been computed from radiosonde data.

MEASUREMENT, MODELING, AND SIMULATION OF LOS MICROWAVE CHANNELS

James. A. Hoffmeyer and Lewis. E. Vogler
U. S. Department of Commerce
National Telecommunications and Information Administration
Institute for Telecommunication Sciences
325 Broadway
Boulder, CO 80303
USA

SUMMARY

This paper begins with a brief summary of prior work in the field of microwave line-of-sight (LOS) channel propagation measurements, channel models, and channel simulators. The objective of these efforts is the reliable prediction of digital microwave radio performance on any specified link. The ideal channel simulator is one that operates at rf, operates under computer control, is dynamic, simulates both minimum and nonminimum phase distortions, and has a dual channel capability for the comparative evaluation of space and frequency diversity radios. Significant parameters of this ideal simulator should be based on a model that has been validated through propagation measurements on different representative paths. Although much progress has been made, a number of issues remain. The work of the Institute for Telecommunication Sciences (ITS) in the area of channel simulation, propagation measurements, and modeling is described. Together with channel measurement programs currently under way by ITS, this work should be helpful in the resolution of many of the remaining issues.

1. INTRODUCTION

Many authors have reported that multipath fading, i.e., frequency-selective or dispersive fading, is the dominant reason for propagation-caused outages in wideband microwave digital radio systems [1-10]. Greenfield [8] found that dispersive fading was virtually the sole cause of outage on a long, 6-GHz path in the western United States. Frequency-selective fading has a much greater effect on digital radio performance than it does on analog radio performance [1]. In analog radio transmission, the major source of propagation-related outage is flat fading rather than frequency-selective fading. For analog systems, frequency-selective fading does cause intermodulation distortion, but this effect is secondary to flat fading. For digital radios, the effect of frequency-selective fading is much more severe. Unlike analog systems, digital radios are relatively insensitive to flat fading and are primarily affected by dispersive multipath fading [6].

In the last decade, numerous techniques have been devised to mitigate the effects of frequency-selective fading on digital microwave radios including: space diversity, frequency diversity, angle diversity, polarization diversity, adaptive equalizers, and more robust modulation schemes. Both vertical and horizontal [11] separation of space diversity antennas have been utilized. Several types of adaptive equalizers have been developed, including both slope (frequency domain) and transversal filter (time domain) equalizers. Many of these techniques are currently incorporated in commercially available digital radios.

The tasks of evaluating the relative effectiveness of the above techniques, comparing the performance of several digital radios, and predicting the performance of a specific radio on a specific link are very complex. In general, radio performance can be estimated theoretically, through field measurements, through the use of channel simulators, or through a selected combination of these three. Some of the advantages of channel simulator use are as follows [12, 13]: reduced cost, repeatability, accuracy, complete testing over a full range of channel conditions, and test bed availability. When considering a competitive procurement of off-the-shelf digital radios for use in military communications systems, the first two advantages are particularly strong arguments for the use of channel simulation. The comparative performance evaluation of several radios requires that the testing be conducted under identical test conditions. This can be done most economically in the laboratory using a channel simulator.

The results of digital radio tests that utilize a channel simulator are critically dependent upon the accuracy and completeness of the model that is the basis of the simulator. They are also dependent upon the methodology used in implementing that model in simulator hardware and software. Much progress has been made in the area of LOS channel modeling and simulation since the realization in the late 1970's of the vulnerability of digital microwave radios to multipath fading. Additional work is required, however. Evidence of the need for additional research is provided by Ranade [14] who found that estimates of outage seconds based on equipment fading signatures are an order of magnitude less than outage seconds observed in the field. Greenstein and Shafi [15] state that "outage calculation methods that include diversity effects lack completeness and maturity."

The ultimate objective of all this research is the accurate prediction of the outage probability of any specified radio on any specified link. It is the purpose of this paper to review briefly the progress that has been made toward the achievement of this objective. The review includes a short summary of measurements that have been made and channel models that have been developed. The ITS channel simulator is then described, along with results of digital radio tests with the simulator. The ITS channel propagation measurement data and the associated Multipath Analysis Software Package (MASP) are then presented. This is followed by a discussion of some of the remaining issues in LOS channel measurement, modeling, and simulation. The paper closes with a discussion of the application of MASP

data to these issues. The simulator and measurement programs conducted by ITS are viewed as steps toward the achievement of the ultimate objective of accurate prediction of digital radio outage.

2. LOS CHANNEL MEASUREMENTS AND MODELS--A HISTORICAL REVIEW

A simplified, geometrical optics representation of the transfer function of a point-to-point, n-path propagation channel is given by

$$H_n(\omega) = \rho_1 \exp(i\theta_1) + \rho_2 \exp(i\theta_2) + \ldots + \rho_n \exp(i\theta_n) \tag{1a}$$

$$= R_n \exp(i\sigma_n) = R_{n-1} \exp(i\sigma_{n-1}) + \rho_n \exp(i\theta_n), \tag{1b}$$

where

$$R_k = [R_{k-1}^2 + \rho_k^2 + 2R_{k-1}\rho_k \cos(\theta_k - \sigma_{k-1})]^{1/2}, \tag{2}$$

$$\sigma_k = \sigma_{k-1} + \tan^{-1}\left[\frac{\rho_k \sin(\theta_k - \sigma_{k-1})}{R_{k-1} + \rho_k \cos(\theta_k - \sigma_{k-1})}\right], \tag{3}$$

$$k = 1, 2, \ldots, n; \ (R_0, \sigma_0 = 0)$$

and $\rho_k \geq 0$, $\theta_k = \theta_k(\omega)$. In this description, the frequency variation, $\omega = 2\pi f$, is contained only in the phase terms under the assumption that the magnitudes ρ_k remain constant with frequency over the bandwidth of interest. Furthermore, it is usual to consider only the attenuation relative to some "principal path," in which case $\rho_1 = 1$ and $\theta_1 = 0$.

Of special concern to system performance are the regions near the amplitude nulls of the model, i.e., where the cosine in (2), for $k = n$, is negative. In actual measurements, a null can be classified into one of two types according to the group delay response $d\sigma_n/d\omega$. If we define $\theta_n - \sigma_{n-1} = \pi + \phi_n$, the group delay is given by

$$\frac{d\sigma_n}{d\omega} = \frac{\rho_n(\rho_n - R_{n-1}\cos\phi_n)}{R_n^2}\frac{d\phi_n}{d\omega} + \frac{\rho_n \sin\phi_n}{R_n^2}\frac{dR_{n-1}}{d\omega} + \frac{d\sigma_{n-1}}{d\omega}. \tag{4}$$

Near an amplitude null ($\phi_n \longrightarrow 2m\pi$), it can be seen that the factor multiplying $d\phi_n/d\omega$ will be positive or negative depending on whether ρ_n is greater or less than R_{n-1}. The two cases correspond, respectively, to the so-called nonminimum and minimum phase conditions.

Equations (1) through (4) provide a formal representation of the simplified n-path model and, in fact, (1b) indicates that any number of paths can be considered as a pseudo two-path model. This is perhaps one of the reasons why confusion sometimes arises as to whether a model is "really" two-path or three-path.

For instance, the Rummler model [16] can be obtained from (1b) by assuming $R_{n-1} = a$, $\rho_n = ab$, $\sigma_{n-1} = 0$, and $\theta_n = \pi + (\omega - \omega_0)\tau$:

$$H_n(\omega) = a[1 - b \exp\{i(\omega - \omega_0)\tau\}], \tag{5a}$$

$$|H_n(\omega)| = R_n = a[1 + b^2 - 2b\cos\{(\omega - \omega_0)\tau\}]^{1/2}, \tag{5b}$$

$$\frac{d\sigma_n}{d\omega} = \frac{b[b - \cos\{(\omega - \omega_0)\tau\}]\tau}{1 + b^2 - 2b\cos\{(\omega - \omega_0)\tau\}}. \tag{5c}$$

The same results can be obtained for $n = 3$ by letting $\rho_1 = 1$, $\rho_2 = a - 1$, and $\theta_1 = \theta_2 = 0$.

Notice that the condition $\sigma_{n-1} = 0$ severely restricts the descriptive capabilities of the model. This is best seen by assuming a simple linear frequency variation, $\sigma_{n-1} = (\omega - \omega_0)\tau_{n-1}$, and comparing plots of $d\sigma_n/d\omega$ from (4) for the two cases. The inclusion of a nonzero σ_{n-1} appears to characterize the delay offsets and different delay curve shapes, including the flat delay scans, noted by Balaban [17].

Most researchers have assumed either an effective two- or three-path attenuation model ($\rho_1 = 1$, $\theta_1 = 0$). Rummler's three-path model (5) presupposes a negligible time delay between the direct ray and the second path. The "a" parameter is actually the vector sum of the first two paths and "ab" is the amplitude of the third ray. The number of parameters is further reduced by giving "τ" a fixed value of 6.3 ns. This was done in order to fit the experimental data to the equation. Rummler has found that the parameter "b" is exponentially distributed with a mean of 3.8 dB, the parameter "a" depends on "b" and is lognormal, and ω_0 is a two-level function. A physical interpretation of (5) would lead one to conclude that ω_0 should be uniformly distributed. However, the model becomes nonphysical because of the assumption of a fixed value of τ of 6.3 ns.

The Rummler model parameter statistics were developed from a data base consisting of 25,000 measurements of received power vs frequency in a 25.3-MHz bandwidth. The measurements were made on a 42.3 km (26.4-mi) path in Georgia in June 1977. Power measurements were made at 24 frequencies spaced by 1.1 MHz.

Rummler developed an approach for predicting outage [18, 19] and developed an extension to the model for space and frequency diversity applications [20-23]. This work is summarized in [24].

Other authors have further extended the work of Rummler. Ranade and Greenfield [25] have devised a technique for characterizing the yearly variations of the relative amounts of dispersive and flat fading. Greenstein and Yeh [26] and Cartledge [27] have used the diversity model to investigate the

effect of both space diversity and adaptive equalization on the performance of digital radio systems. Balaban [17] generalized Rummler's model to include group delay or minimum/nonminimum phase. This was based on field measurements in Florida. Ranade [14] developed an improved method for the calculation of the dispersive fade margin. This method takes into consideration the fact that there is a performance hysteresis in adaptive equalizers.

The same data used by Rummler were also used by Greenstein and Czekaj [28] to develop a polynomial model of the channel transfer function. In a later paper [29], Wong and Greenstein state that the three-path model is preferable to the polynomial model. Subsequently, the polynomial model has received little attention. However, Sylvain and Lavergnal [30] report that both the Rummler and Greenstein models are in good agreement with their measured data.

A two-path model used by Meyers [31] and Greenstein and Prabhu [32] includes an additional phase term that represents the notch location of the null in the spectrum. Kolton [33] found that a two-path model is adequate 95.3 percent of the time based on data collected by ITS on a long (105 km) overwater path off the coast of California [34].

Numerous channel measurements have been made using the inband power distortion (IBPD) technique [8, 35]. IBPD is the power difference between the maximum and minimum attenuation of the received signal measured at several frequencies within the channel passband. Ranade [14] states that the severity of frequency-selective fading can be defined by this single parameter. Some performance prediction models are based on IBPD data (see [3] for example).

Greenstein and Shafi [15] state that a general three-path model may be more appropriate than the simplified three-path model for modeling of links having a terrain reflection. It has been demonstrated by Parl [36] that there will always be an odd number of rays (the direct and two refracted rays) from atmospheric refraction considerations alone. Siller [37] also notes the need for an odd number of rays whenever the receiver is situated within an appropriate atmospheric duct. Martin [38] states that group delay can be explained correctly only if one assumes that at least three rays arrive at the receiving antenna.

3. ITS APPROACH TO MEASUREMENTS, MODELING, AND SIMULATION

The Institute for Telecommunication Sciences has developed an LOS microwave channel simulator for testing digital radios. The Institute has also collected a substantial amount of propagation data useful to validate the LOS channel model. The statistical distributions of the parameters of a channel model are needed as part of the process of predicting digital radio performance. The propagation data collection and analysis tasks were conducted in parallel with the development of the channel simulator hardware and the simulator control software. The simulator hardware, as will be explained, has the capability to incorporate either the Rummler pseudo-three-path model or the general two-path model. As a result of the propagation data analysis effort, we believe that the most accurate model is the general three-path model. A simple modification of the simulator hardware will permit the inclusion of a second multipath signal. The propagation data acquisition and analysis systems provide a direct measurement of the multipath delays and amplitudes for both the first and second multipath rays. These data are required for the statistical distributions needed for estimating outage probability. The probabilities of occurrence of first and second multipath rays, minimum/nonminimum phase probabilities, and channel dynamics are among the data that can be gleaned from the propagation data obtained from the ITS channel probe. This will be explained in more detail in a later section. First we will discuss the ITS channel simulator as it is presently implemented.

Using the notation of Matsuura [39], the model is expressed as:

$$H(\omega) = a[1 + b \exp(i(\omega\tau + \phi))]. \qquad (6)$$

In equation (6), a represents flat fading, b represents the amplitude of the indirect path relative to the direct path, τ represents the relative delay between the two paths, ω represents the carrier frequency in the band of interest, and ϕ is an arbitrary phase. Although (6) is similar in form to Rummler's equation as given in (5), the parameters can be interpreted differently. Unlike Rummler, we do not restrict τ to a fixed value of 6.3 ns. As will be demonstrated, error performance of a digital radio is affected by changes in τ.

Because we have implemented the simulator at rf rather than at the fixed IF of 70 MHz, it was necessary to include the phase term ϕ. The 1 ns granularity for τ does not provide the flexibility to place notches anywhere within the rf passband of the radio. The ϕ parameter provides the needed vernier control of the location of the notch in the spectrum caused by frequency selective fading. In effect, $i(\omega\tau + \phi)$ exponent in (6) may be viewed as $i\omega(\tau + \Delta\tau)$.

We define the following quantities:

$$A = 20 \log_{10}(a),$$
$$B' = 20 \log_{10}(b), \text{ and}$$
$$B = 20 \log_{10}|1-b|.$$

These quantities will be used in our description of the ITS simulator and in the discussion of digital radio test results obtained with the simulator.

Description of Simulator

At the start of this project there were several objectives for the simulator: (1) the channel simulator must be implemented at rf; (2) the control of the simulator must be automated; (3) the simulator should permit variation in the delay parameter, τ; (4) the simulator must have dual channels

for testing dual diversity radios; and (5) the simulator should be made dynamic if possible. A dynamic simulator is one in which the simulator parameters can be changed on a continuous basis as opposed to a static simulator in which the parameters are changed in discrete steps. The first four objectives were totally met. The state-of-the-art microwave component technology did not permit meeting both the first and the last objectives simultaneously. Because of the importance placed on testing a complete radio, including all its rf components, we chose an implementation at rf even though this decision made it impossible, at that time, to meet the dynamic objective. However, new, improved phase shifters have now become available. They will permit this last objective to be met. Consequently, a modification to the existing simulator is planned.

Most of the LOS microwave channel simulators that have been developed are intermediate frequency (IF) implementations of Rummler's model. However, some have been implemented at rf [40-42]. The simulators reported in [40, 43] are dynamic simulators implemented at rf that have a fixed value of $\tau = 6.3$ ns.

Figure 1 is a functional block diagram of the ITS simulator. The relative delay, τ, between the direct and indirect paths is provided by switching in various lengths of semi-rigid coax lines in the switched delay sections. Five different lengths of cable can be switched into the circuit, either individually or in any combination. Any value of delay from 0 to 31 ns in 1-ns increments can be achieved. Variation of τ causes changes in both the location and shape of the notch in the spectrum created by the phasor addition of the direct and indirect path signals. The programable phase shifter, which has 256 steps of about 1.4° each, is used to move the notch across the spectrum. Thus, we can control both notch shape (through the parameter τ) and the notch location (through a combination of τ and ϕ). The programable attenuator in the indirect path represents the parameter b. The depth of the notch is controlled through this parameter. Both nonminimum phase and minimum phase conditions can be simulated by changing the sign of B'. The other programable attenuator represents the parameter a; i.e., the flat fading parameter. The manual attenuator at the input to the simulator reduces the signal level of the transmitter under test to levels that are compatible with the receiver section of the radio being tested.

One concern throughout this project has been to design the system such that changes in relative delay between the multipaths would not change the relative signal level between the multipaths and vice versa. That is, relative phase and relative amplitude of the paths must be independently controlled. Care was taken in the design and implementation of the system to ensure that this was accomplished. For this reason, a signal leveler is needed in the indirect path so that the signal level does not change when additional delay is placed in the indirect path by switching in the additional delay sections.

The purpose of the attenuator and line stretcher in the direct path is to make the delay and the attenuation of the indirect and direct paths equal when there is zero relative delay in the indirect path.

All of the parameters shown in Figure 1 (a, b, ϕ, and τ) can be controlled by a computer through an IEEE interface. The computer is also used to collect error information used in the generation of "m-curves." The simulator can be used at any frequency in the 4-12 GHz band.

Figure 2 is a picture of the simulator hardware. It occupies 13.3 cm (5.25 in) of vertical space in a standard 48.3-cm (19-in) rack.

Test Results

The channel simulator has been used to evaluate the performance of the DRAMA (Digital Radio and Multiplexer Acquisition) radio. This radio has been installed in portions of the Defense Communications System (DCS). The DRAMA radio is used in the U.S.-owned and operated Digital European Backbone (DEB) transmission network, which interfaces with NATO networks. Thomas et al. [44] describe the DRAMA radio in some detail.

The version of the radio tested combines two mission bit streams, each at 12.928 Mb/s, and utilizes quadrature partial response modulation. The radio does not have an adaptive equalizer, but it does have both space and frequency dual diversity versions.

Figure 3 depicts one of the test configurations. As seen in the figure, a test data stream is input into the transmit side of one DRAMA radio and detected at the output of the receive side of a second DRAMA radio. The ITS channel simulator was utilized to emulate distortion in the two simulated diversity channels. The simulator operates at rf frequencies; therefore, the entire DRAMA radio is tested in a realistic manner.

Two channel simulators are required for space diversity testing. As can be seen in Figure 3, the outputs of the two simulators are inputs to the rf sections of both the A and B sides of the DRAMA radio. After down conversion in the radio, the signal is demodulated and demultiplexed.

Figure 4 is a plot of the input signal to the DRAMA radio as seen on a spectrum analyzer. During this test, only one simulator and only one side of the DRAMA radio were active; therefore, the simulated link can be considered to be "unprotected" in the sense that the space diversity capability of the radio was not utilized. The ITS automated channel simulator was set up with the combination of parameters as indicated in the figure. For every given set of simulator parameters, a trace was stored in the spectrum analyzer before the parameters were changed. The three traces thus represent three different combinations of parameter settings. Of interest in the figure is the radio performance for each of the three settings of parameter conditions. The difference between the top and the bottom traces is 10 dB of attenuation. This represents an additional 10 dB of flat fading. For the top trace and the bottom trace, no errors occurred in the DRAMA radio. However, in the middle trace, additional distortion was put into the channel. One can see a very slight amount of flattening of the spectrum. This small amount of additional distortion was sufficient to cause the bit error ratio (BER) of the radio to

increase to 1 x 10^{-4}. In the figure one can clearly see that the radio is sensitive to very small amounts of signal distortion. This demonstrates the fact that significant errors can occur at received signal levels (rsl) well above the flat fade threshold of the radio. The reference level (RL) is given at the top of the figure.

Figure 5 further illustrates the sensitivity of the radio to amplitude distortion. A small amount of distortion was placed into the channel for the top two traces. The amount of distortion can be discerned subjectively by observing the asymmetry about the center frequency. Note that a small phase change causes the BER to drop off rapidly as seen in the top two traces. In this example a phase change of only 15.4° causes a change of three orders of magnitude in the BER. The bottom trace is an example of flat fading in which the signal level is near the flat fade margin (-74 dBm), which causes errors to occur. Note the symmetry of the signal for the bottom (flat fade) example.

Figures 6a and 6b are static m-curves for the unprotected (i.e., no equalizer and no diversity) DRAMA radio. The radio tested was the 26 Mb/s version with a quadrature partial response modem (QPR). The curves in Figure 6b are for the nonminimum fading case, which results from positive values of the B' parameter. This causes the indirect-path signal to be stronger than the direct-path signal. This situation can occur about 50 percent of the time for deep fades [6, 33]. The figures illustrate the effect of changes in τ on digital radio performance. Many authors [2, 13, 15, 24, 37, 39, 45-50] have used m-curves as a measure of radio performance. The m-curves were first used by Emshwiller [50]. They are not, however, directly applicable to the evaluation of dual-diversity radios.

Figures 4 and 5 have illustrated the sensitivity of the DRAMA radio to frequency-selective fading if there is no diversity. We shall now examine the radio's performance for a space-diversity configuration.

Figures 7 and 8 were obtained using both channel simulators as illustrated in Figure 3. First, in Figure 7 the DRAMA radio switching algorithm performs properly for the condition of flat fading in both channels. As can be seen in the figure, the upper trace (input to the A side of the radio) is well above the flat fading margin for the radio and no errors occur. In the lower trace, where the signal is near the flat fade threshold, the simulated flat fading is sufficient to cause errors; the BER is of the order of 10^{-3}. The space-diversity switching algorithm in the radio properly selected the A side of the radio.

Figure 8 illustrates the effects of selective fading in one channel (B) and flat fading in the second channel (A). In the upper trace, we had distorted the signal using the ITS automated channel simulator. The signal depicted by the upper trace was input to the B side of the radio and resulted in a BER of 1.6 x 10^{-5}. The signal shown as the lower trace was input to the A side of the DRAMA radio and resulted in no errors. However, the space-diversity switching algorithm erroneously selected the B side of the radio, even though errors were occurring in that side of the radio but not in the A side. The reason for this is that the switching algorithm is based primarily on the received signal level. Obviously, there are conditions where the stronger signal does not represent the best signal. That is, distortion of the signal can cause high error rates even at relatively high signal levels. Conversely, low error rates can be associated with low signal levels if there is no distortion of the signal. Many other authors have noted this characteristic of digital radio performance (see, for example, [2]).

The diversity-switching algorithm in the present DRAMA radio needs further explanation. At low error ratios (approximately 1 x 10^{-4}), the radio will switch to the side having the highest rsl. At error ratios greater than 1 x 10^{-4}, the excess-bit-error light on the front panel of the radio is illuminated and the radio will then switch to the other side. Thus, the switching algorithm may be appropriate for error ratios greater than 1 x 10^{-4}. It clearly does not always work properly for error ratios less than 1 x 10^{-4} as was demonstrated in Figure 8.

The figures described above serve to illustrate the following points: 1) the simulator is a useful device for simulating frequency-selective fading, and 2) unprotected digital radios are extremely sensitive to small distortions in the received signal. Link test data are needed to verify DRAMA radio performance in a frequency-selective fading channel. The data presented in these figures verify the contention of Barnett [51] that small amounts of signal distortion can cause unacceptable performance for an unprotected digital radio. Barnett found that distortion as little as 0.2 dB/MHz can cause unacceptable performance in a digital radio.

4. LOS CHANNEL PROPAGATION DATA ANALYSIS

The Institute has collected line-of-sight and troposcatter propagation data for many years using an instrument called a channel probe [34, 52, 53]. The channel probe is an instrument that measures delay spread in the impulse response function of the channel. (See [54] for a description of the channel probe.)

Kolton [33] has developed a set of computer programs useful for the analysis of this data. The information deduced from the channel probe measurement data by Kolton's software is very useful for the development of statistical distributions for LOS channel models. Some of the outputs of this software, referred to as the Multipath Analysis Software Package or MASP, are listed in Table 2.

A few example outputs are provided in Figure 9. These data are the result of channel probe measurements made on a 105-km over-water path from Point Mugu to San Nicolas Island in southern California. That coastal region is notorious for temperature inversions, especially during the summer time. The data summarize 152,979 seconds of measurements made in March 1984 and 47,427 seconds of measurements made in August of that same year. Measurements were not made for contiguous time intervals. Of the 152,979 seconds in March, 28 percent contained multipath; 96 percent of the August

data contained multipath. The channel probe has two channels, one for each of the space diversity antennas. Propagation data were recorded only when fading caused errors on a digital radio under test at the time.

Of the total time recorded, the probe channel associated with the upper antenna contained multipath 76 percent of the time. The probe channel associated with the lower antenna contained multipath 67 percent of the time. Misalignment of the lower antenna may have caused the asymmetry. Of interest is the fact that multipath occurred simultaneously in both channels more than half the time. This fact has an impact on the type of combiner being used. Greenfield [8] found that a bit combiner provided two to three times greater diversity improvement than an IF combiner on a long path that had a large amount of simultaneous multipath on the two space diversity paths. Thirty-five percent of the multipath fading was of the nonminimum phase type.

As noted earlier [36], a theoretical examination of multipath fading leads to the conclusion that the total number of atmospheric paths (including the direct path) must always be an odd number. Much of the time, however, the second multipath component is too weak to be observed. Table 3 provides statistics, obtained from MASP, on the occurrence of three-path propagation (i.e. two multipath components and a direct path). Of the data analyzed, 12.6 percent of the time in which multipath occurred, the second multipath component could be identified.

The data presented in Figure 9 and Table 3 are too limited to be used as the basis of any firm conclusions about multipath fading statistics. The figure and table are presented primarily to demonstrate a capability existing at ITS. The information that can be obtained from the Multipath Analysis Software Package is vitally important for the formulation and validation of several channel model statistical distributions. Of particular importance are

- distributions of multipath delay
- distributions of multipath power
- minimum phase/nonminimum phase statistics
- two-path vs three-path statistics
- space diversity statistics
- dynamics.

These data are needed in the continuing effort to develop and validate a realistic fading model on a LOS microwave channel.

5. ISSUES IN LOS MICROWAVE MEASUREMENTS, MODELING, AND SIMULATION

As stated earlier, the ultimate research objective of channel modeling and simulation is the development of techniques for reliably predicting the performance of any specified radio on any specified link. The outage prediction must consider dynamics of the propagation medium, as well as hysteresis in the performance of space diversity combiners and adaptive equalizers, minimum/nonminimum phase fades, etc. Greenstein and Shafi [15] state that each of the published outage prediction methods satisfies some of the requirements, but that none satisfy all of them.

Table 4 provides a list of some of the unresolved issues that must be addressed to achieve accurate outage prediction. Although computer models and Monte Carlo simulations can be useful tools in bounding the performance estimation problem, the need to include dynamics and imperfections in the implementation of digital radio hardware require that hardware channel simulators be used in the digital radio performance evaluation process. The requirements of the channel simulator include

- implementation of a channel model that realistically represents the actual LOS microwave fading channel
- computer control of the simulator
- implementation at rf
- dual channel for testing diversity radios
- simulation of both minimum and nonminimum phase fading
- three-ray fading simulation
- dynamic variation of simulator parameters.

The current ITS simulator possesses all of the above features except the last two. The last two features will be added later, based on data to be obtained from a channel propagation measurement project soon to be undertaken.

The requirement for simulation of the dynamics of the channel is a particularly important one. Hubbard [52] first recognized the importance of dynamic channel variations on radio system performance. Static m-curves have been widely used for digital radio performance characterization. Their usefulness is unquestionable. However, there is recent interest in the impact of dynamic channel variations on digital radio performance. Rummler et al. [24] note that the use of static channel models and simulators is based on the assumptions that 1) the channel response is much slower than the response of the radio equipment being tested, and 2) that there is no hysteresis in the radio performance. Leclert and Vandamme [4], however, question the classical assumption that the channel is slowly time varying in comparison with the symbol rate. Rummler et al. [24] note that dynamic considerations become more important as more complex modems and adaptive equalizers are used in digital radios.

Table 5 lists some of the dynamic multipath characteristics given in the recent literature. Clearly, more statistical data are needed to adequately describe a dynamic fading model. Data on channel dynamics and other channel statistical data to be collected in an upcoming measurement program at ITS are described in the next section.

Testing space-diversity radios with a channel simulator and predicting space-diversity outage performance are also important problems that need further work. All digital radios installed on links subjected to bad propagation conditions have required diversity to meet performance objectives [4]. Nondiversity m-curve measurements coupled with analytical techniques can be used to predict performance of space-diversity systems. A better approach may be to test the diversity radio performance using a dual-channel simulator. The general treatment of diversity in estimating digital radio outage needs further research [15].

6. APPLICATION OF FUTURE CHANNEL PROPAGATION MEASUREMENTS TO UNRESOLVED ISSUES

The Institute is currently undertaking two LOS microwave measurement programs that will result in a vast amount of data applicable to the unresolved modeling questions delineated in the previous section. Neither of these projects have as their primary purpose LOS microwave propagation research. The primary purpose is performance assessment of the digital radios and other equipment that are part of the Digital European Backbone. However, channel propagation data are being collected in support of the primary objective.

The first program (of three months duration) consists of measurements on a long LOS microwave link that crosses the English Channel. The terminals of this 88-km link are Dover, United Kingdom, and Houtem, Belgium. Both channel probe data and spectral distortion data are being collected.

The second program consists of end-to-end measurements on one segment of the DEB as depicted in Figure 10. Very detailed measurements will be made on the long (102-km) LOS link from Schwarzenborn to Feldberg, Germany. Data will be recorded for a period of 12 months. Both channel probe data and spectral distortion data will be collected on this link. The channel probe impulse response data will be collected every second if there is multipath on the link. Measurement of the channel impulse function once per second is sufficient for observing the dynamically changing channel. The probe has a bandwidth of 300 MHz.

Spectral distortion measurements will be made with two spectrum analyzers that will measure the IF spectrum of the two digital space diversity receivers used on the Schwarzenborn-Feldberg link. This will permit collection of data similar to the inband power difference (IBPD) measurements reported by Greenfield [8] and other researchers.

The data that will be collected will be useful for:

- validation of two-ray, general three-ray, and simplified three-ray models
- determination of parameter statistics for the above channel models (these will be joint probability statistics for a space diversity digital radio)
- quantification of channel dynamics using the MASP software
- probability of occurrence of three-path multipath
- minimum phase/nonminimum phase statistics
- validation of various outage prediction techniques
- empirical determination of space diversity improvement factor
- measurement of IBPD and determination of IBPD statistics
- measurement of multipath delay (τ) and its maximum value.

7. CONCLUSIONS

Substantial progress has been made during the past decade in modeling and simulation of LOS microwave channels and in the prediction of digital radio performance on fading channels. A number of issues remain, however. The Institute has developed a channel simulator, as well as channel propagation measurement and analysis techniques, that should be useful in addressing these issues. Data to be collected in the near future should add greatly to the body of knowledge on multipath fading and digital radio performance.

8. REFERENCES

[1] Smith, D.R., Digital Transmission Systems, Van Nostrand Reinhold Co., New York, 1985.

[2] Giger, A.J., and W.T. Barnett, "Effects of Multipath Propagation on Digital Radio," IEEE Trans. Commun., COM-29, No. 9, Sept. 1981, pp. 1345-1352.

[3] Serizawa, Y., and S. Takeshita, "A Simplified Method for Prediction of Multipath Fading Outage of Digital Radio," IEEE Trans. Commun., COM-31, No. 8, Aug. 1983, pp. 1017-1021.

[4] Leclert, A., and P. Vandamme, "Decision Feedback Equalization of Dispersive Radio Channels," IEEE Trans. Commun., COM-33, No. 7, Jul. 1985, pp. 676-684.

[5] Foschini, G.J., and J. Salz, "Digital Communications Over Fading Radio Channels," IEEE 1983 Intl. Conf. Commun., Boston, MA, Paper No. C8.1.

[6] Fenderson, G.L., M.H. Meyers, and M.A. Skinner, "Recent Advances in Multipath Propagation Countermeasures for High-Capacity Digital Radio Systems," IEEE 1985 Intl. Conf. Commun., Chicago, IL, Paper No. 39.2.

[7] Schiavone, J.A., "Meteorological Effects on Diurnal and Seasonal Fading Variations," IEEE 1983 Intl. Conf. Commun., Boston, MA, Paper No. C2.2.

[8] Greenfield, P.E., "Digital Radio Performance on a Long, Highly Dispersive Fading Path," IEEE 1984 Intl. Conf. Commun., Amsterdam, Holland, pp. 1451-1454.

[9] Yeh, Y.S., and L.J. Greenstein, "A New Approach to Space Diversity Combining in Microwave Digital Radio," AT&T Tech. J., 64, No. 4, Apr. 1985, pp. 885-905.

[10] Mayrargue, S., "Parametric Characterization of Channel Transfer Functions During Multipath Fading Events," IEEE 1984 Global Telecomm. Conf., Atlanta, GA, Paper No. 45.3.

[11] Gardina, M.F., and S.H. Lin, "Measured Performance of Horizontal Space Diversity on a Microwave Radio Path," IEEE 1985 Global Telecomm. Conf., New Orleans, LA, Paper No. 36.6.

[12] Hoffmeyer, J.A., and W. J. Hartman, "LOS Microwave Channel Simulation - A Survey of Models, Realizations and New Concepts," NATO AGARD Conf. Proc. No. 363, Propagation Influences on Digital Transmission Systems: Problems and Solutions, Athens, Greece, Jun. 1984, Paper No. 22.

[13] Hoffmeyer, J.A., L.E. Pratt, and T.J. Riley, "Performance Evaluation of LOS Microwave Radios Using a Channel Simulator," IEEE 1986 Military Commun. Conf., Monterey, CA, Paper No. 4.3.

[14] Ranade, A., "Statistics of the Time Dynamics of Dispersive Multipath Fading and its Effects on Digital Microwave Radios," IEEE 1985 Intl. Conf. Commun., Chicago, IL, Paper No. 47.7.

[15] Greenstein, L.J., and M. Shafi, "Outage Calculation Methods for Microwave Digital Radio," IEEE Commun. Mag., 25, No. 2, Feb. 1987, pp. 30-39.

[16] Rummler, W.D., "A New Selective Fading Model: Application to Propagation Data," Bell Syst. Tech. J., 58, No. 5, May-June 1979, pp. 1037-1071.

[17] Balaban, P., "Statistical Model for Amplitude and Delay of Selective Fading", AT&T Tech. J., 64, No. 10, Dec. 1985, pp. 2525-2550.

[18] Lundgren, C.W., and W.D. Rummler, "Digital Radio Outage Due to Selective Fading-Observation vs Prediction from Laboratory Simulation," Bell Syst. Tech. J., 58, No. 5, May-June 1979, pp. 1073-1100.

[19] Rummler, W.D., "A Simplified Method for the Laboratory Determination of Multipath Outage of Digital Radios in the Presence of Thermal Noise," IEEE Trans. Commun. COM-30, No. 3, Mar. 1982, pp. 487-494.

[20] Rummler, W.D., "A Statistical Model of Multipath Fading on a Space Diversity Radio Channel," Bell Syst. Tech. J., 61, No. 9, Nov. 1982, pp. 2185-2219.

[21] Rummler, W.D., "A Statistical Model of Multipath Fading on a Space Diversity Radio Channel," IEEE 1982 Intl. Conf. Commun., Philadelphia, PA, Paper No. 3B.5.

[22] Rummler, W.D., "Modeling the Diversity Performance of Digital Radios with Maximum Power Combiners," IEEE 1984 Intl. Conf. Commun., Amsterdam, pp. 657-660.

[23] Rummler, W.D., "A Rationalized Model for Space and Frequency Diversity Line-of-Sight Radio Channels," IEEE 1983 Intl. Conf. Commun., Boston, MA, Paper No. B2.7.

[24] Rummler, W.D., R.P. Coutts, and M. Liniger, "Multipath Fading Channel Models for Microwave Digital Radio," IEEE Commun. Mag., 24, No. 11, Nov. 1986, pp. 30-42.

[25] Ranade, A., and P.E. Greenfield, "An Improved Method of Digital Radio Characterization from Field Measurements," IEEE 1983 Intl. Conf. Commun., Boston, MA, Paper No. C2.6.

[26] Greenstein, L.J., and Y.S. Yeh, "A Simulation Study of Space Diversity and Adaptive Equalization in Microwave Digital Radio," AT&T Tech. J., 64, No. 4, Apr. 1985, pp. 907-935.

[27] Cartledge, J.C., "Outage Performance of QAM Digital Radio Using Adaptive Equalization and Switched Space Diversity," IEEE Trans. Commun., COM-35, No. 2, Feb. 1987, pp. 166-171.

[28] Greenstein, L.J., and B.A. Czekaj, "A Polynomial Model for Multipath Fading Channel Responses," Bell Syst. Tech. J., 59, No. 7, Sept. 1980, pp. 1197-1225.

[29] Wong, W.C., and L.J. Greenstein, "Multipath Fading Models and Adaptive Equalizers in Microwave Digital Radio," IEEE Trans. Commun., COM-32, No. 8, Aug. 1984, pp. 928-934.

[30] Sylvain, M., and J. Lavergnat, "Modelling the Transfer Function of a 55 MHz Wide Radio Channel During Multipath Propagation," IEEE 1985 Intl. Conf. Commun., Chicago, IL, Paper No. 47.8.

[31] Meyers, M.H., "Multipath Fading Characteristics of Broadband Radio Channels," IEEE 1984 Global Telecomm. Conf., Atlanta, GA, Paper No. 45.1.

[32] Greenstein, L.J., and V.K. Prabhu, "Analysis of Multipath Outage with Applications to 90-Mbit/s PSK Systems at 6 and 11 GHz," IEEE Trans. Commun., COM-27, No. 1, Jan. 1979, pp. 68-75.

[33] Kolton, E., "Results and Analysis of Static and Dynamic Multipath in a Severe Atmosperic Environment," NTIA Contractor Report 86-37, Sept. 1986 NTIS Order No. PB87-131165/AS.

[34] Hubbard, R.W., "Digital Microwave Transmission Tests at the Pacific Missile Test Center, Pt. Mugu, California," NTIA Report 83-126, Jun. 1983, NTIS Order No. PB83-251454.

[35] Liniger, M., and D. Vergeres, "Field Test Results for a 16-QAM and a 64-QAM Digital Radio, Compared with the Prediction Based on Sweep Measurements," IEEE 1986 Intl. Conf. Commun., Toronto, Canada, Paper No. 15.2.

[36] Parl, S.A., "Characterization of Multipath Parameters for Line-of-Sight Microwave Propagation," IEEE Trans. Ant. Prop., AP-31, No. 6., Nov. 1983, pp. 938-948.

[37] Siller, C.A., "Multipath Propagation," IEEE Commun. Mag., Feb. 1984, pp. 6-15.

[38] Martin, L., "Phase Distortions of Multipath Transfer Functions," IEEE 1984 Intl. Conf. Commun., Amsterdam, Holland, pp. 1437 1441.

[39] Matsuura, S.T. "Estimated Performance of a QPR Digital Microwave Radio in the Presence of Frequency Selective Fading," IEEE 1982 Intl. Conf. Commun., Philadelphia, PA, Paper No. 7B.2.

[40] Valentin, R., K. Metzger, and R. Sohneckenburger, "Performance Analysis of Diversity and Equalization Techniques Using a Selective Fading Simulator and Computer Modeling," IEEE 1985 Intl. Conf. Commun., Chicago, IL, Paper No. 39.3.

[41] Bessai, H.J., and W. Lorek, "Influence of Multipath Fading on the Multiplexing Factor of 140 Mbit/s 16-QAM Radio-relay Systems," IEEE 1984 Global Telecomm. Conf., Atlanta, GA, Paper No. 45.4.

[42] Bursztejn, J., "Influence de la Propagation Dans Les Faisceaux Hertziens Numeriques," NATO AGARD Conf. Proc. No. 363, Propagation Influences on Digital Transmission Systems: Problems and Solutions, Athens, Greece, June 1984, pp. 8-1 -- 8-17.

[43] Rustako, Jr., A.J., C.B. Woodworth, R.S. Roman, and H.H. Hoffman, "A Laboratory Simulation Facility for Multipath Fading Microwave Radio Channels," AT&T Tech. J., 64, No. 10, Dec. 1985, pp. 2281-2317.

[44] Thomas, C.M., J. E. Alexander, and E. W. Rahneberg, " A New Generation of Digital Microwave Radios for U.S. Military Telephone Networks," IEEE Trans. Commun., Vol. COM-27, No. 12, Dec. 1979, pp. 1916-1927.

[45] Noack, W., "Planning Considerations for High Capacity Digital Radio Relay Networks," 13th European Microwave Conference, Sept. 1983, pp. 599-604.

[46] Bates, C.P., and M.A. Skinner, "Impact of Technology on High-Capacity Digital Radio Systems", IEEE Intl. Conf. Commun., Chicago, IL, Paper No. F2.3.

[47] Kennard, P.A., J.D. McNicol, and M.D. Caskey, "Fading Dynamics in High Spectral Efficiency Digital Radio," IEEE 1986 Intl. Conf. Commun., Toronto, Canada, Paper No. 46.8.

[48] Hartmann, P.R., J.A. Crossett, and E.W. Allen, "Propagation and Countermeasures in Line of Sight Digital Transmission Systems," Tech. Bulletin 523-06090999-011A3J, Rockwell International Corp., pp. D3-1 -- D3-37.

[49] Fenderson, G.L., S.R. Shepard, and M.A. Skinner, "Adaptive Transversal Equalizer for 90-Mb/s 16-QAM Systems in the Presence of Multipath Propagation," IEEE 1983 Intl. Conf. Commun., Boston, MA, Paper No. C8.7.

[50] Emshwiller, M., "Characterization of the Performance of PSK Digital Radio Transmission in the Presence of Multipath Fading," IEEE 1978 Intl. Conf. Commun., Toronto, Canada, Paper No. 47.3.

[51] Barnett, W.T., "Multipath Fading Effects on Digital Radio," IEEE Trans. Commun., COM-27, No. 12, Dec. 1979, pp. 1842-1848.

[52] Hubbard, R.W., "A Review of Atmospheric Multipath Measurements and Digital System Performance," NATO AGARD Conf. Proc. No. 363, Propagation Influences on Digital Transmission Systems: Problems and Solutions, Athens, Greece, Jun. 1984, Paper No. 10.

[53] Hubbard, R.W., "Investigation of Digital Microwave Communications in a Strong Meteorological Ducting Environment," NTIS Report 79-24, Aug. 1979, NTIS Order No. PB301-212/AS.

[54] Linfield, R.F., R.W. Hubbard, and L.E. Pratt, "Transmission Channel Characterization by Impulse Response Measurements," OT Report 76-96, Aug. 1976, NTIS Order No. PB258-577.

[55] Gardina, M.F., and A. Vigants, "Measured Multipath Dispersion of Amplitude and Delay at 6 GHz in a 30 MHz Bandwidth," IEEE 1984 Intl. Conf. Commun., Amsterdam, Holland, pp. 1433-1436.

9. ACKNOWLEDGEMENTS

The authors would like to acknowledge the contributions of L. E. Pratt and T. J. Riley who developed the channel simulator hardware and software. We would also like to recognize R. F. Linfield for his many suggestions on the channel simulator and E. Kolton for his effort in developing the Multipath Analysis Software Package. Finally we would like to thank R. W. Hubbard for his many contributions over the years in the field of multipath fading measurements and analysis.

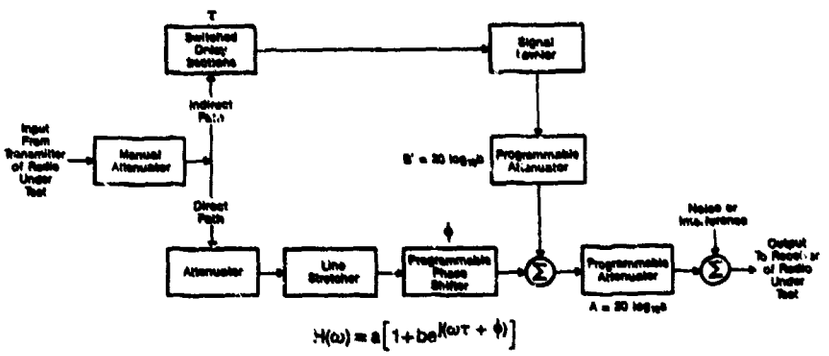


Figure 1. Simulator functional block diagram.

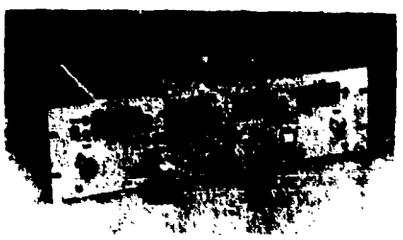


Figure 2. Simulator hardware.

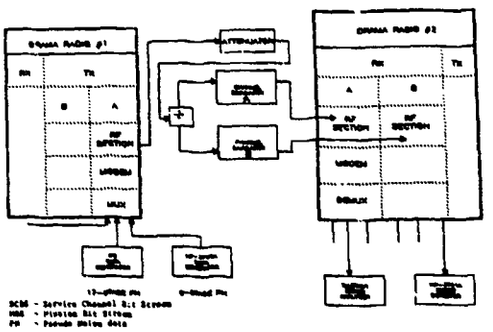


Figure 3. DRAMA radio test configuration.

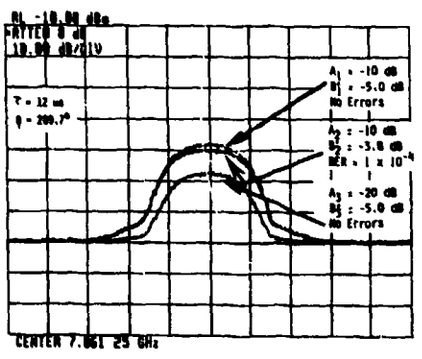


Figure 4. Simulator output (DRAMA radio input signal) and corresponding radio performance. Note the susceptibility of the DRAMA radio to small increases in distortion.

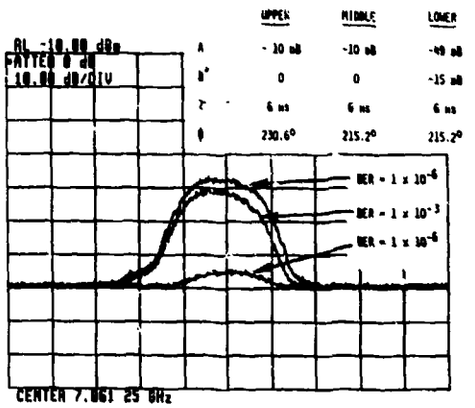


Figure 5. Simulator output (DRAMA radio input signal); low error rate for the top and bottom traces; high error rate for the middle trace due to signal distortion.

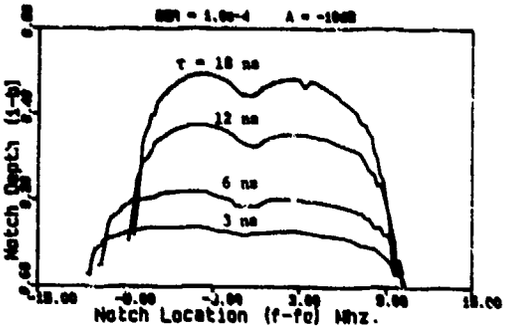


Figure 6a. M-curve for B'<0 (minimum phase).

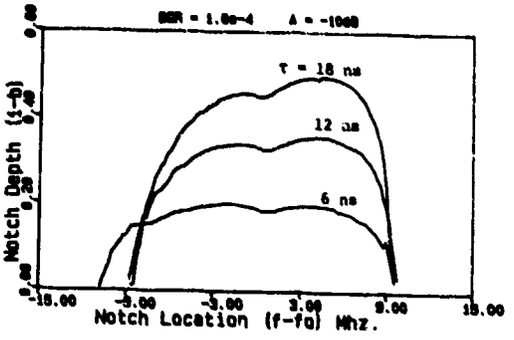


Figure 6b. M-curve for B'>0 (nonminimum phase).

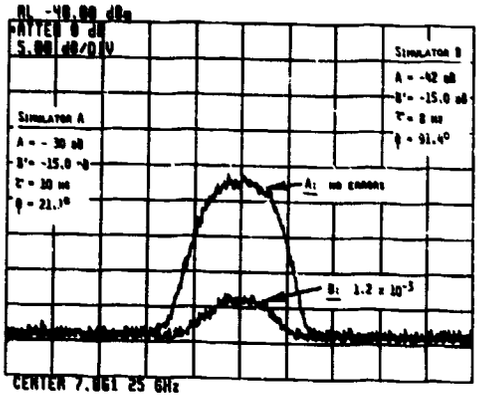


Figure 7. Example of correct DRAMA radio switching; flat fade in both sides of the radio.

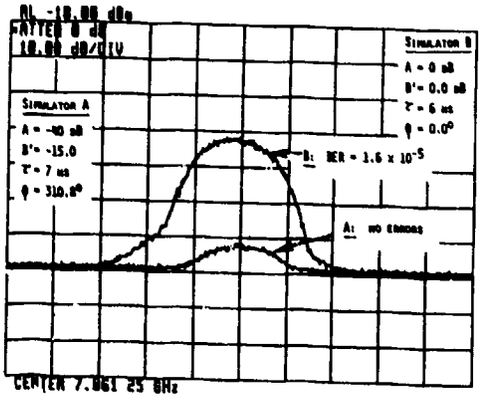
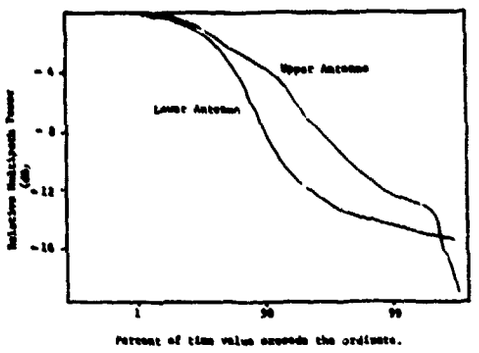
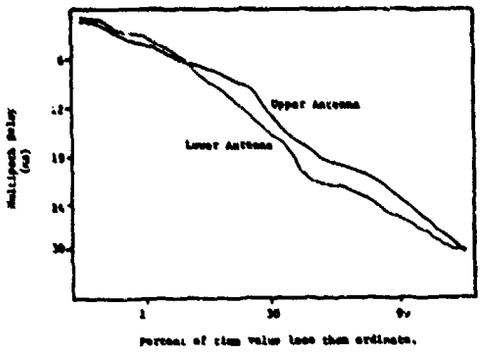


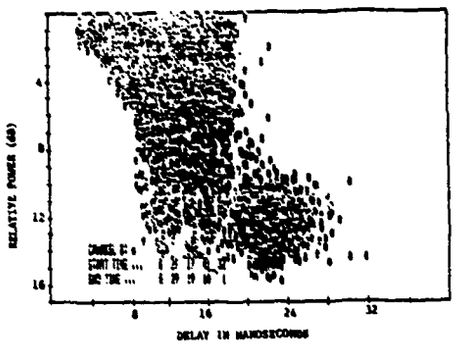
Figure 8. Example of incorrect DRAMA radio switching; the radio incorrectly switched to side B.



9a. Distributions of multipath power; 8/29/84.



9b. Distributions of multipath delay; 8/29/84.



9c. Scattergram of power vs. delay (lower antenna); 8/29/84.

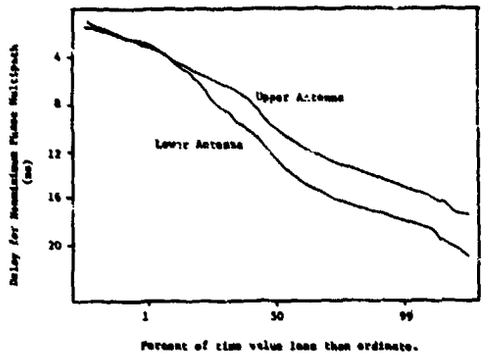
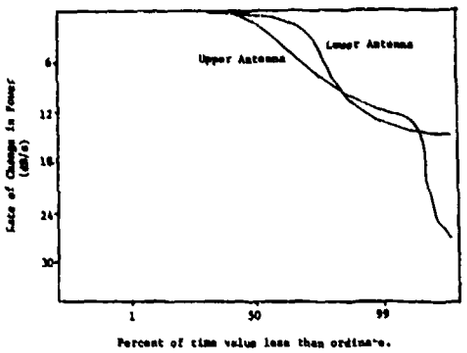
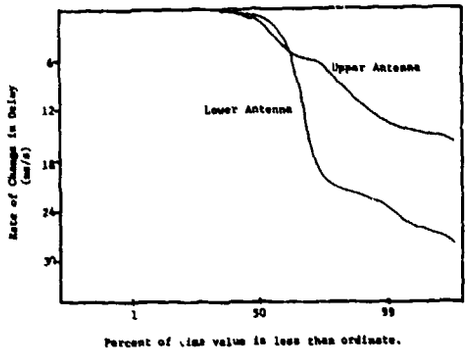


Figure 9d. Distributions of nonminimal phase delays; 8/29/84.



9e. Distributions of rate of power; 8/30/84.



9f. Distributions of rate of change in delay; 8/30/84.

Figure 9. Examples of MASP outputs.

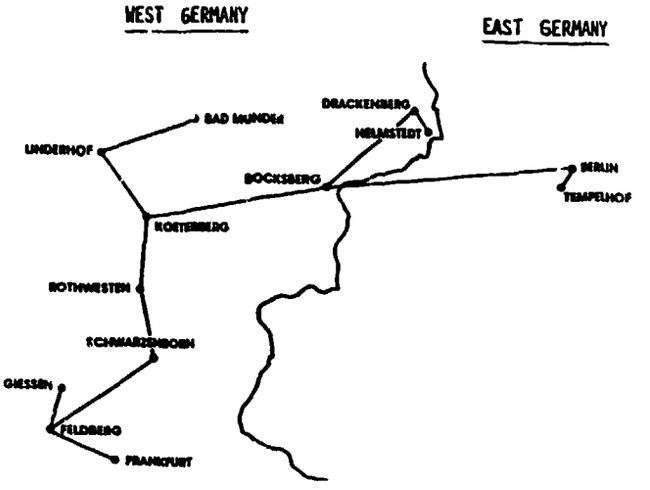


Figure 10. Frankfurt Phase I segment of DEB.

Table 1. Summary of Various Forms of Channel Function.

Model Type	Equation	Reference
General N-path	$H(\theta) = \rho_1 \cdot \exp(i\theta_1) + \rho_2 \cdot \exp(i\theta_2) + \cdots + \rho_N \cdot \exp(i\theta_N)$	
Simplified 3-path	$H(\omega) = a[1 - b \cdot \exp(-j(\omega - \omega_0)\tau)]$	Rummler [16]
3-path	$F(f) = a[1 - b \cdot \exp(j\phi) \cdot \exp(-j\omega\tau)]$	Wong and Greenstein [29]
Equivalent 2-path	$H(f) = a[1 + k \cdot \exp(-j2\pi f\tau) \cdot \exp(-j\theta)]$	Greenstein and Prabhu [32]
2-path	$H(f) = 1 - b \cdot \exp(-j2\pi(f - f_0)\tau)$	Meyers [31]
Polynomial model	$H(\omega) = A_0 + \sum (A_n + jB_n)(j\omega)^n$	Greenstein and Czekaj [28]

Table 2. Multipath Analysis Software Package Outputs.

- Cumulative distribution of multipath power relative to direct path power.
- Cumulative distribution of multipath delay relative to direct path.
- Scattergram of multipath delay vs multipath power.
- Cumulative distribution of multipath phase.
- Nonminimal fading statistics.
  - Frequency of occurrence of nonminimum phase fading.
  - Duration on nonminimum phase fading.
  - Cumulative distribution of multipath power relative to direct path.
  - Cumulative distribution of multipath delay relative to direct path.
- Statistics of multipath fading dynamics.
  - Cumulative distributions of rate of change of multipath power (dB/s).
  - Cumulative distributions of rate of change of multipath delay (ns/s).
  - Cumulative distributions of rate of change of multipath phase (rad/s).
  - Durations of coll pse and development of multipath.
- Two-path vs three-path fading statistics.

Table 3. Statistics of Existence of Two Multipath Component Impulse Responses.

Time Period	Total Experiment Time (s)	Total Number of Impulse Response Recorded	Total Number of Multipath Impulse Responses		Number of Two-Component Multipath			
			A	B	A	A(%)*	B	B(%)*
1. March 22 to 23	30,357	14,511	12,425	11,201	1,268	10.5	1,720	15.4
2. March 23 to 24	32,901	15,115	13,525	12,077	2,433	18.0	2,707	22.4
3. March 24 to 25	33,972	13,665	8,081	8,182	807	10.0	730	9.0
4. August 29	16,449	15,215	12,373	9,656	1,015	8.2	1,423	14.7
5. August 29 to 30	15,378	15,180	11,094	9,532	1,102	9.9	1,747	18.3
6. August 30	15,600	15,205	10,121	8,932	857	8.5	551	6.2

*Percent of multipath responses in the channel that have two components. Average percent of multipath that has been two components is 12.6%.

Table 4. Unresolved Issues in Microwave LOS Modeling, Measurements, and Simulation.

Issue	Source
Validation of channel model parameter statistical distributions	Institute for Telecommunication Sciences
Modeling and simulation of channel dynamics	Hubbard [52] Rummler, Coutts, and Liniger [24] Miller [37] Greenstein and Shafi [15] Leolert and Vandamme [4] Wong and Greenstein [29]
Minimum phase/ nonminimum phase statistics	Greenstein and Teh [26] Rummler, Coutts, and Liniger [24] Leolert and Vandamme [4]
Wideband (several GHz) measurements of delay and amplitude distortion; needed to identify physical parameters of multipath	Rummler, Coutts, and Liniger [24]
Effect of scintillation	Hoogward, Mehlhorn, and Casey [47] Hasnain [16] Greenstein and Shafi [15]
Outage calculation methodology that includes the effects of diversity; figure of merit for space diversity radio comparisons	Greenstein and Shafi [15]
Comparison of predicted and measured digital radio outage from multipath (i.e., validation of outage prediction methodologies)	Institute for Telecommunication Sciences

Table 5. Dynamic Multipath Characterization.

Source	Rate of Amplitude Change (dB/s)	Rate of Notch Frequency Change (MHz/s)
Leolert and Vandamme [4]	< 100 dB/s in 99% of cases	< 600 MHz/s in 99% of cases
Fenderson, Meyers, and Skinner [6]		< 20 MHz/s most of the time
Miller [37]	100 dB/s	50 MHz/s
Gardina and Vigants [55]	< 10 dB/s for 11% of fading time	< 15 MHz/s for 95% of fading time
Rummler, Coutts, and Liniger [24]	100 dB/s	100 MHz/s

DISCUSSION

L. Boithias, FR

I agree that modeling and simulation are very useful for comparison of digital radio performance, but I am not sure they may be useful for accurate outage predictions.

a) All the models include several parameters, the values of which have to be determined for the path under consideration -- how are these values determined?

b) It is not certain that all the actual situations are represented by the model.

c) Diversity reception and/or equalization are practically necessary in any case to meet the quality requirements. However their effects are generally not taken into account by the models. Moreover, for prediction purposes, it would be perhaps more efficient to use the concept of net margin.

Author's Reply

Many authors have used channel simulators to develop "m-curves" for a particular radio. These m-curves have then been used in the prediction of outages (see references [2] and [18] for example). I agree that the prediction of outage on a specific transmission path is a very difficult task. This can be accomplished only if channel models used in the outage prediction process accurately model multipath fading. The statistics of the model parameters are dependent both on path length and on climatic conditions which are unique to a specific path. One cannot realistically expect to have statistics of the channel model parameters for every path on which a digital radio is to be installed. However, it is possible to obtain multipath parameter values as a function of path length and climatological statistics which, together with m-curves, could be useful in placing a general bound on the outage prediction for a specific communications link.

a) We agree that statistical distributions are needed for each of the model parameters. Some information is available (see for example, Rummler [16]). The Institute for Telecommuncation Sciences expects to extend this data base in a 12-month measurement program discussed in the paper. Specifically, we will develop statistics on the multipath delay (τ in our model), relative signal strength of the multipath ray (b in our model), and the flat fading parameter (a in our model). In addition, we will collect data on the occurrence of a third path, rate of change of fading and path delay, i.e., fading dynamics, joint statistical distributions for the space diversity antenna received signals, and the probability of the occurrence of nonminimum phase fading.

b) We agree that models currently being used do not accurately model fading on line-of-sight microwave links. For this reason, we list several unresolved questions which can be answered only through additional research. It is hoped that the measurement program mentioned in the paper and referred to in (a) above will provide useful data in improving this model. We have already concluded that the model should be extended to a 3-ray model having a second multipath component and that the simulator should be made dynamic.

c) We agree that a model and the implementation of that model in a simulator must be capable of the evaluation of both adaptive equalization circuitry and diversity systems. Our current simulator has some of this capability. However, we need additional data on the

joint probability statistics for the accurate simulation of space diversity reception. These data will be obtained from the 12-month measurement program described in the paper.

The concept of net fade margin has been addressed by many authors in the field of performance predictions. This approach has the disadvantage that it requires measurements be made on a wide range of paths for various radio types.

STRUCTURES OF DENSITY AND VELOCITY FLUCTUATIONS IN THE AURORAL OVAL AND THEIR IMPACT ON COMMUNICATION AND RADAR SYSTEMS

Sunanda Basu[1], Santimay Basu[2], W.R. Coley[3], and N.C. Maynard[2]

1 Emmanuel College, Boston MA 02115
2 Air Force Geophysics Laboratory, Hanscom AFB MA 01731
3 University of Texas at Dallas, Richardson TX 75080

SUMMARY

A new class of ionospheric irregularities in the auroral oval associated with large structured plasma flows has been recently isolated with radar and satellite in-situ measurements. These density irregularities have large power spectral densities (psd) at short scale lengths (∿ hundreds to tens of meters). The paper characterizes the density and velocity spectra in such regions and discusses their impact on scintillation observations and radar performance. The structured plasma flows may occur in association with large (∿10 μA m^{-2}) or small (∿1 μA m^{-2}) field aligned currents. The velocity spectra have fairly shallow power spectral indices (∿-1.5) in regions of large field aligned currents and are steep (∿-3) in regions of small current flows. The density spectra, on the other hand, can be described by a power law index ∿-2 in both the large and small field aligned current regions. The temporal structure of scintillations will thus be dictated not only by the scattering strength but also by the large flow velocities encountered in the auroral oval. The density structures with large psd at short scale lengths are expected to introduce considerable ionospheric clutter in HF radar systems. The effect of E-region conductivity in modifying small-scale (<1 km) F-region structure and its implication for communication and radar systems is discussed.

INTRODUCTION

In recent years a concerted effort has been made to study high latitude F-region irregularities and their relationship to bulk plasma processes. Our understanding improved significantly when it was realized that km-scale irregularity structure was associated with the steep edges of convecting large scale plasma density enhancements both in the polar cap and auroral oval (see Weber et al., 1984; 1985; Klobuchar et al., 1986 and references therein). Since the blobs are large scale features on the order of 100 km, they have long lifetimes and can be tracked by incoherent scatter radars and have been found to be convecting with the ambient plasma (Vickrey et al., 1980). The generalized ExB instability was found to be a viable mechanism for the small scale structure associated with the blobs, with magnetic field aligned currents, neutral winds, plasma drifts and the large scale blob-associated density gradients all contributing to the structure formation (see Keskinen and Ossakow, 1983 for a review of the instability processes). If radio wave propagation techniques are used as diagnostics for the blob-related irregularities, then one would see scintillation structures maximizing on the edges of total electron content (TEC) enhancements (Basu et al., 1983).

More recently, another class of F-region irregularities has been isolated which is associated with large shears in the background convective plasma flows. The unique feature of this class of irregularities is that it is not associated with organized large scale gradients of plasma density (such as to be found at the edges of blobs), but rather with velocity shears with shear gradient scale lengths of 1-10 km (Basu et al., 1987a). These irregularities are also found to have large power spectral densities (psd) at small scales (<1 km). For this reason, it is possible, for instance, to find intense scintillations without any large perturbations in TEC (Basu et al., 1986).

It is the object of this paper to present simultaneously observed density and velocity spectra obtained in the vicinity of large sheared plasma flows. Lotova (1981) has discussed the effects of velocity turbulence on the modeling of scintillations from in-situ density structure. We shall compute UHF scintillations and HF backscatter expected from such density spectral forms in the presence of considerable velocity perturbations and discuss the effect of the large convective flows on the temporal structure of scintillations observed on the ground. For comparison, we shall also compute scintillations using observed density spectra in high conductivity regions. It is found that in such regions, for example, where energetic particle precipitation is observed as in the diffuse aurora, the density spectra are fairly steep with little power at the short scales (Basu et al., 1984; 1987a). The reduced power at such scales (<100 m) is attributed to the short lifetimes of F-region irregularities in the presence of underlying E-region conductivity (Vickrey and Kelley, 1981; Heelis et al., 1985).

OBSERVED DENSITY AND VELOCITY SPECTRAL FORMS

The DE-2 satellite (Hoffman and Schmerling, 1981) is an excellent source for obtaining high resolution F-region density and velocity data at high latitudes. This data base has recently been used to make the first simultaneous measurements of density ($\Delta N/N$) and electric field fluctuation (ΔE) spectra in the high latitude environment

(Basu et al., 1987a). It is to be noted that in low β plasma such as in the ionospheric F-region, velocity fluctuations are electrostatic and equivalent to electric field fluctuations (i.e., $\vec{v} = \vec{E} \times \vec{B}/B^2$). Thus, spectra of electric field fluctuations are to be considered equivalent to velocity fluctuation spectra.

In Figures 1(a,b) and 2(a,b) we reproduce 3 samples of 8s each density and electric field data and their respective spectra. The symbols S_H, S_G, and S_L on the data and their corresponding spectra represent samples taken from a uniformly high conductivity region (S_H), a region with sharp conductivity gradients (S_G), and a region of low conductivity (S_L). At the time the DE-2 data were taken, between 2149-2151 UT on May 26, 1982, the satellite was traversing the dawn sector of the auroral oval (0700 magnetic local time) between 70-75° invariant latitude in the southern hemisphere at an altitude of approximately 350 km. A detailed account of the particle precipitation character, small scale field aligned current intensities and ion and electron temperatures associated with these samples is given in Basu et al. (1987a).

If we confine our attention to the density and electric field data shown in Figures 1(a) and 2(a), we immediately notice the lack of high frequency structure in the high conductivity region. This is particularly noticeable in the electric field data. On the other hand, the conductivity gradient region (S_G) shows a very large amount of structure in both density and electric field, while the structure in the electric field is somewhat reduced in the low conductivity region (S_L). It is interesting to note that region S_G is associated with large field-aligned current intensities of tens of $\mu A\ m^{-2}$ in addition to the large velocity shears, whereas S_L is associated with weaker sheared flows and smaller field-aligned currents.

Before we discuss the ($\Delta N/N$) and ΔE spectra, it is important to recognize that we had to make the assumption that measurements of spatial structure in these quantities made on the satellite are Doppler shifted from zero to the frequency $f = kV_s/2\pi$, where V_s is the satellite velocity (approximately 8 km s^{-1}). In this paper whenever we refer to wavenumber k or wavelength $\lambda = 2\pi/k$, it is based upon this hypothesis. Fortunately, there is convincing evidence for this assumption of "zero-frequency turbulence" (see review by Kintner and Seyler, 1985 and references therein). Thus we feel that our assumptions concerning the spatial nature of the density and electric field variations are probably valid under most circumstances in the ULF frequency regime (Sugiura, 1984), except possibly when propagating waves such as ion cyclotron waves and Alfven waves are encountered over limited regions (Temerin, 1978; Gurnett et al., 1984).

The spectra of ($\Delta N/N$) and ΔE in the three different regimes are shown in Figures 1(b) and 2(b) respectively. Both ($\Delta N/N$) and ΔE spectra are fairly steep in the high conductivity region (S_H), while both are fairly shallow in the conductivity gradient region (S_G). Moreover, if one compares the power spectral density (psd) at 10 Hz (800 m) of the two density spectra, then one finds approximately 15 dB more power in the S_G sample than in S_H. In the ΔE spectra the separation in psd is much more dramatic with the S_G spectrum showing approximately 40 dB more power at 5 Hz (1.6 km). The density spectral forms and psd in the S_L and S_G regimes are almost identical with power law slopes of ~-2. However, the slopes of the ΔE spectra in the S_L and S_G regimes are quite different with the S_L spectral slope being -3 compared to the S_G slope of shallower than -2. In all 3 situations, the important point to note is that the electric field (i.e., velocity) spectra are either equal in slope or steeper than the corresponding density spectra. Thus following the arguments of Lotova (1981), it is expected that we should be able to model scintillations from in-situ density measurements. However, the large background velocities (100 mV m^{-1} is equivalent to 2 km s^{-1} convection velocities) would significantly alter the temporal structure of scintillations.

SCINTILLATION ESTIMATES

It is possible to estimate scintillations in the weak scatter formulation (Rino, 1979) if the irregularity amplitude, density spectral forms, background densities and irregularity layer thickness are known. It is the object of this paper to present several estimates of scintillations that may be observed under solar maximum or minimum conditions.

We use the density spectra observed in the velocity shear regions to estimate the scintillations to be expected with different levels of background ionization. We note from the top two panels of Figure 1b that the psd is -18 dB at a frequency of 1 Hz. Using the satellite velocity of 8 km s^{-1}, this frequency is equivalent to a scale length of 8 km. We use the measured psd and the observed one-dimensional density spectral slope of -2 to compute intensity scintillations at 413 MHz which is the UHF frequency transmitted by the orbiting HiLat satellite. We utilized the observed irregularity amplitude of approximately 20 percent and a thickness of 100 km for the irregularity layer. The latter seems to be a good estimate if contours of maximum density in the F-region are studied using latitude/altitude scans made by incoherent scatter radars at auroral latitudes (Basu et al., 1986). The weak-scatter formulation of Rino (1979) was used for the purpose. The equation for the S_4 index (Briggs and Parkin, 1963) is given by:

$$S_4^2 = (r_e\lambda)^2\ (L \sec\theta)\ C_S\ Z^{\nu-4}\ f(\nu)\ J$$

where r_e - classical radius of the electron
λ - the radio wavelength
L - the thickness of the irregularity layer

θ - the ionospheric zenith angle
C_S - strength of turbulence
z - $\lambda z_R \sec\theta/4\pi$, z_R is the range
ν - related to 1-D spectral index given by $2\nu-1$
J - geometrical parameter related to irregularity anisotropy
$f(\nu)$ - a function of the irregularity spectral index involving Γ-functions.

In this paper, we shall confine our computations to the S_4 index only as it is uniquely defined by the measurement of C_S and ν, the only major assumption being in regard to the irregularity anisotropy. The phase scintillation index, on the other hand, depends on the detrend filter characteristics and the effective velocity of the ray path. Since we will be primarily considering auroral observations, we will assume sheet-like irregularities aligned with the local L-shell (Rino et al., 1978). The best estimates of the shape is given by 8:4:1, with the largest anisotropy being along the magnetic field (Fremouw and Secan, 1984). The effect of the irregularity anisotropy on the S_4 index, in particular, is minimal except for regions of exact alignment.

In general, the greatest degree of variability is observed in C_S which is the strength of turbulence (Fremouw and Secan, 1984). The in-situ DE-2 data thus gives us an estimate of this important parameter for scintillation computations. As noted earlier the measured psd of -18 dB, the spectral index of -2, and irregularity amplitude of 20 percent translates to a value of $C_S = 4 \times 10^{-19}$ mks units using equations given by Rino (1979). This value of C_S translates to $S_4 = 0.25$ at 413 MHz for near overhead locations at an auroral station such as Tromso, Norway (magnetic dip = 78°). If field alignment is considered, then the S_4 index ≈ 0.5. Needless to say, at such times the S_4 index at 137 MHz will be saturated and cannot be estimated using this weak-scatter formulation.

It is gratifying to note, that these computations agree well with the HiLat observations at 413 MHz made at Tromso shown in Figure 3. The irregularities during this event were associated with velocity shears (Basu et al., 1986). Two significant structures were observed both giving rise to saturated VHF scintillations. However, the UHF S_4 index is slightly less than 0.3 for one and 0.4 for the other which is in the geometrical enhancement region. It is interesting to note that the background density at this time was 3×10^{11} m^{-3} as compared to 2×10^{11} m^{-3} used in the computations based on DE-2 data. This indicates that large irregularity amplitudes coupled with relatively shallow slopes can cause significant UHF scintillations in the auroral oval. Further, when the background density is larger by a factor of 3 or 4 during high sunspot conditions, if the same irregularity amplitude is preserved, it is possible to have a three to four-fold increase in the scintillation level. Thus saturated 413 MHz and even significant 1 GHz scintillation may be expected in the auroral oval in conjunction with velocity shears with particularly intense events being observed in the geometrical enhancement region.

EFFECT OF UNDERLYING E-REGION CONDUCTIVITY ON SCINTILLATIONS

The bottom panel of Figure 1a shows density data (S_H) obtained by DE-2 in the presence of diffuse auroral precipitation which creates high conductivity in the E-region. The field-line integrated Pedersen conductivity is 10 mhos and the Hall conductivity is 40 mhos (Basu et al., 1987a). The corresponding spectrum in Figure 1b shows the spectral slope to be -2.5. The electric field spectrum shown in Figure 2b is even steeper. Figure 4 shows spectral data in the auroral oval obtained from AE-D which exhibits a one-dimensional spectral slope of -3 in the scalelength range smaller than 1 km which is the region of interest for UHF scintillations (Basu et al., 1984). In order to emphasize the effect of a conducting E-region, we choose this experimentally observed slope of -3 in association with the large irregularity amplitude of 20 percent which was observed in conjunction with the velocity shears diacussed earlier. Using exactly the same background density and anisotropy parameters, we obtain $C_S = 8 \times 10^{-17}$ mks units and $S_4 = .05$ in the high conductivity region using a spectral index of -3. This is a fairly startling result which shows that scintillation is reduced by a factor of 5 for the same irregularity amplitude and F-region density merely by going into a region whose magnetic field lines terminate in a conducting E-region. Vickrey and Kelley (1982) and Heelis et al. (1985) have studied the effect of E-region conductivity on lifetimes of irregularities and we point out here how such factors can have a large impact on communication systems. The upshot is that it is difficult to observe significant UHF scintillations in regions of high E-region conductivity. This is an important factor to contend with in the auroral oval and polar cap, the former being the seat of the energetic auroral precipitation and the latter being illuminated by solar radiation continuously in the summer months. Indeed intensity scintillation measurements at Thule, Greenland in the polar cap conducted over half a solar cycle (1979 - 1984) have shown the enormous decrease of scintillation occurrence and magnitude during the local summer (Basu et al., 1987b).

EFFECT OF LARGE VELOCITIES ON SCINTILLATION STRUCTURE

Figure 2 gives examples of intense small scale velocity structure with 100 mV m^{-1} electric field giving rise to a velocity of 2 km s^{-1} in the high latitude environment. However, at other times fairly steady velocities on the order of 1 km s^{-1} may be observed in the anti-sunward direction in the polar cap and in the E-W direction in auroral latitudes (Weber et al., 1984; Basu et al., 1983). Such enhanced convection velocities have a noticeable effect on the temporal structure of scintillations as

manifested by measured decorrelation times, intensity spectral shapes and the intensity rate of scintillations. We present intensity scintillation data at 250 MHz in Figure 5 from two consecutive days as observed at Goose Bay within the auroral oval (Basu et al., 1985). Significant scintillations of the same level were observed on both days, but on March 7 the decorrelation time shown in dotted lines was found to be 2 s while that on March 8 was 0.4 s. Estimates of the velocity could be obtained from the intensity scintillation spectra at the 2 times denoted by arrows on Figure 5. These two spectra are shown in Figure 6. The spectrum on March 7 shows a Fresnel frequency (f_F) of 0.05 Hz while it is 0.3 Hz on March 8. Using the relationship $f_F = u/(2\lambda z)^{\frac{1}{2}}$ where u is the drift velocity perpendicular to the ray path (mostly E-W for this geometry), we determine this drift to be 65 m s^{-1} on March 7 and 390 m s^{-1} on March 8. Furthermore, we note that this velocity variation gives rise to widely different intensity rates. For the data sets shown in Figure 5 the intensity rate of 3 dB s^{-1} occurs in 0.1 percent of the total population on March 7; while the rate becomes 7 dB s^{-1} on March 8 for the same 0.1 percent level as shown in Figure 7 (Basu et al., 1987b). Again we find the variation of a magnetospheric parameter, namely its convection velocity, having a significant impact on propagation systems operating at high latitudes. Phase-scintillations were not discussed in this paper, but it was shown by Basu et al. (1985) that enhanced convection yields large values of phase scintillation when the source is a geostationary satellite. Thus convection not only affects second order quantities, such as decorrelation time, but even affects first order quantities, such as phase scintillation magnitude.

EFFECT OF UNDERLYING E-REGION CONDUCTIVITY ON F-REGION RADAR SYSTEM OPERATING AT HF

It was mentioned by Basu et al. (1987a) that one of the unique characteristics of velocity-shear-associated irregularities was the existence of high psd of ($\Delta N/N$) all the way up to approximately 10 m scalelength. In Figure 8 we show the psd at 125 m and 46.5 m observed in conjunction with the three categories of spectra displayed in Figures 1 and 2. We note from Figure 8 that the psd associated with S_H is almost three orders of magnitude less than that observed in the velocity shear region indicated by S_C and S_L. The filter output at 17 m, while not shown, indicates a similar variation of psd between the two categories, that in the high conductivity region being 10^{-11} Hz^{-1} whereas it is 10^{-8} Hz^{-1} in shear regions. Now, an HF radar operating at 10 MHz will be sensitive to a scalelength of 15 m. Since the background density variation through the region encompassing S_H, S_C and S_L in Figure 8 is insignificant, and since coherent radar backscatter is proportional to $(\Delta N)^2$ (Woodman and Basu, 1978), we can expect a 30 dB decrease in radar returns from the F-region at 10 MHz when the radar beam sweeps into the high conductivity region from the velocity shear region. Indeed Baker et al. (1986) have shown that HF radar backscatter has been significant from the cusp region which is a seat of large velocity shears and where E-region conductivity is low because of the soft particle precipitation. Thus, we find that underlying E-region conductivity controls, to a great extent, the evolution of F-region structure, and this in turn has significant impact on radar and communication systems operating in the high latitude environment.

REFERENCES

Baker, K.B., R.A. Greenwald, A.D.M. Walker, P.F. Bythrow, L.J. Zanetti, T.A. Potemra, D.A. Hardy, F.J. Rich, and C.L. Rino, A case study of plasma processes in the dayside cleft, J. Geophys. Res., 91, 3130, 1986.

Basu, Su., E. MacKenzie, S. Basu, H.C. Carlson, D.A. Hardy, F.J. Rich, and R.C. Livingston, Coordinated measurements of low-energy precipitation and scintillation/TEC in the auroral oval, Radio Sci., 18, 1151, 1983.

Basu, Su., S. Basu, E. MacKenzie, W.R. Coley, W.B. Hanson, and C.S. Lin, F-region electron density irregularity spectra near auroral acceleration and shear regions, J. Geophys. Res., 89, 5554, 1984.

Basu, Su., S. Basu, E. MacKenzie, and H.E. Whitney, Morphology of phase and intensity scintillations in the auroral oval and polar cap, Radio Sci., 20, 347, 1985.

Basu, Su., S. Basu, C. Senior, D. Weimer, E. Nielsen, and P.F. Fougere, Velocity shears and sub-km scale irregularities in the nighttime auroral F-region. Geophys. Res. Lett., 13, 101, 1986.

Basu, Su., S. Basu, E. MacKenzie, P.F. Fougere, W.R. Coley, N.C. Maynard, J.D. Winningham, M. Sugiura, W.B. Hanson, and W.R. Hoegy, Simultaneous density and electric field fluctuation spectra associated with velocity shears in the auroral oval, Submitted to J. Geophys. Res., 1987a.

Basu, S., E. MacKenzie, Su. Basu, E. Costa, P.F. Fougere, H.C. Carlson, and H.E. Whitney, 250 MHz/GHz scintillation parameters in the equatorial, polar and auroral environments, IEEE Journal on Selected Areas in Communications, SAC-5, 102, 1987b.

Briggs, B.H. and I.A. Parkins, On the variation of radio star and satellite scintillation with zenith angle, J. Atmos. Terr. Phys., 25, 339, 1963.

Fremouw, E.J. and J.A. Secan, Modeling and scientific application of scintillation results, Radio Sci., 19, 687, 1984.

Gurnett, D.A., R.L. Huff, J.D. Menietti, J. L. Burch, J.D. Winningham, and S.D. Shawhan, Correlated low-frequency electric and magnetic noise along the auroral field lines, J. Geophys. Res., 89, 8971, 1984.

Heelis, R.A., J.F. Vickrey, and N.B. Walker, Electrical coupling effects on the temporal evaluation of F-layer plasma structure, J. Geophys. Res., 90, 437, 1985.

Hoffman, R.A. and E.R. Schmerling, Dynamics Explorer program: an overview, Space Sci. Instr., 5, 345, 1981.

Keskinen, M.J. and J.L. Ossakow, Theories of high-latitude ionospheric irregularities: a review, Radio Sci., 18, 1077, 1983.

Kintner, P.M. and C.E. Seyler, The status of observations and theory of high latitude ionospheric and magnetospheric plasma turbulence, Space Sci. Rev., 41, 91, 1985.

Klobuchar, J.A., G.J. Bishop, and P.H. Doherty, Total electron content and L-band amplitude and phase scintillation measurements in the polar cap ionosphere, AGARD Conference Proceeding No. 382, Propagation Effects on Military Systems in the High Latitude Region, June 1985.

Lotova, N.A., Temporal scintillation spectra with allowance for the solar wind velocity distribution. Theory, Geomagnetism and Aeronomy, 21, 447, 1981.

Rino, C.L., A power-law phase screen model for ionospheric scintillation. (1) Weak scatter, Radio Sci., 14, 1135, 1979.

Rino, C.L., R.C. Livingston, and S.J. Matthews, Evidence for sheet-like auroral ionospheric irregularities, Geophys. Res. Lett., 5, 1039, 1978.

Sugiura, M., A fundamental magnetosphere-ionosphere coupling mode involving field-aligned currents as deduced from DE-2 observation, Geophys. Res. Lett., 11, 877, 1984.

Temerin, M., The polarization, frequency, and wavelengths of high-altitude turbulence, J. Geophys Res., 83, 2609, 1978.

Vickrey, J.F. and M.C. Kelley, The effects of a conducting E-layer on classical F-region cross-field plasma diffusion, J. Geophys. Res., 87, 4461, 1982.

Vickrey, J.F., C.L. Rino, and T.A. Potemra, Chatanika/TRIAD observations of unstable ionization enhancements in the auroral F-region, Geophys. Res. Lett., 7, 789, 1980.

Weber, E.J., J. Buchau, J.G. Moore, J.R. Sharber, R.C. Livingston, J.D. Winningham, and B.W. Reinisch, F-layer ionization patches in the polar cap, J. Geophys. Res., 89, 1683, 1984.

Weber, E.J., R.T. Tsunoda, J. Buchau, R.E. Sheehan, D.J. Strickland, W. Whiting, and J.G. Moore, Coordinated measurements of auroral zone plasma enhancements, J. Geophys. Res., 90, 6497, 1985.

Woodman, R.F. and Su. Basu, Comparison between in-situ spectral measurements of equatorial F-region irregularities and backscatter observations at 3m wavelength, Geophys. Res. Lett., 5, 669, 1978.

ACKNOWLEDGMENT

The work at Emmanuel College was supported by AFGL Contract F19628-86-K-0058.

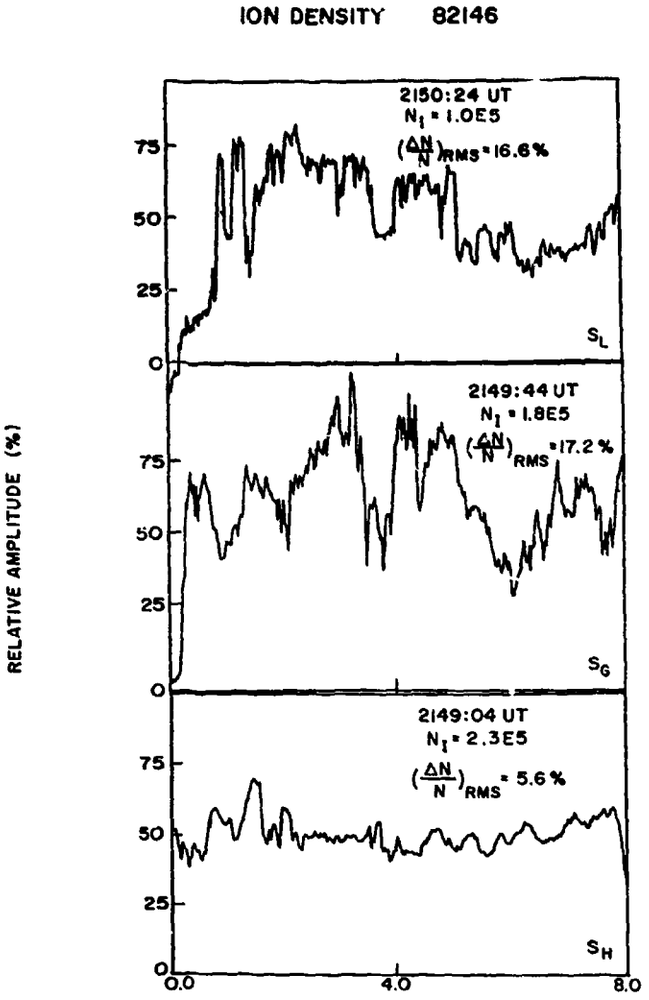


Figure 1a. Three 8-s samples of high resolution (64 Hz) density data from DE-2 from a high conductivity region (S_H), high gradient in the conductivity region (S_G) and low conductivity region (S_L). The irregularity amplitudes are indicated on the respective diagrams.

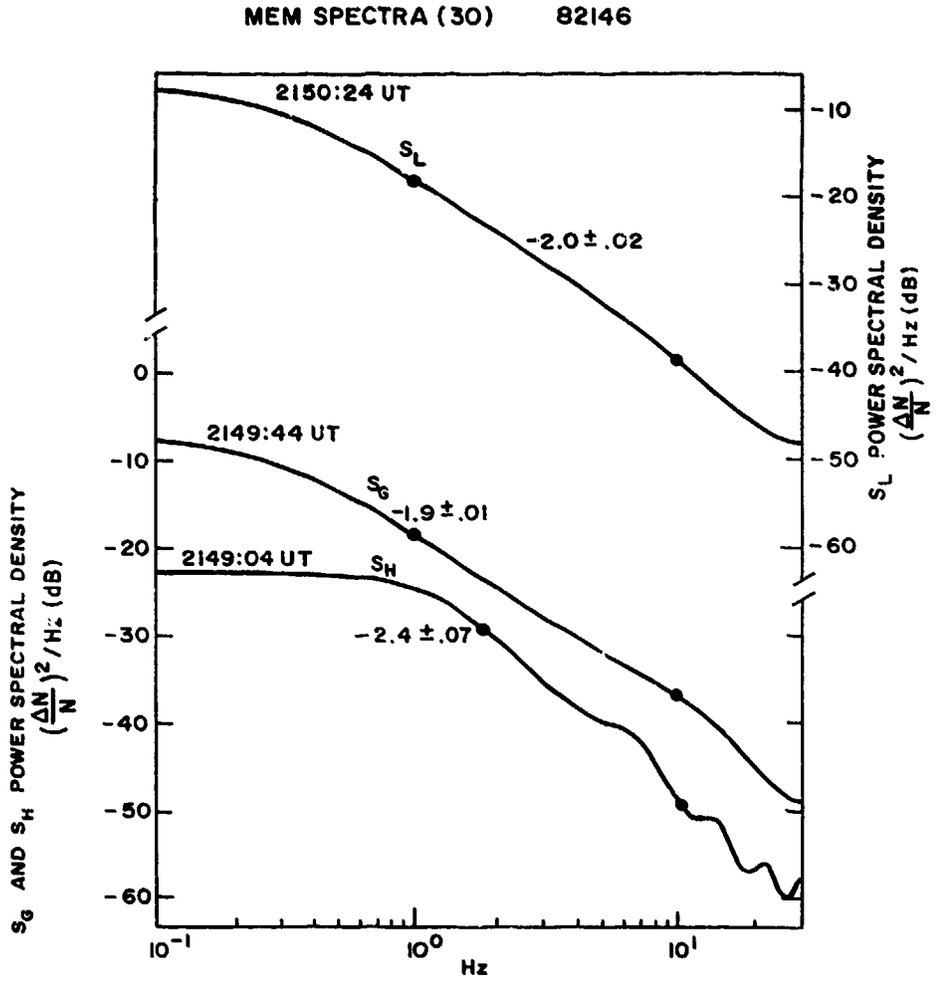


Figure 1b. Maximum entropy spectra corresponding to the three 8-s samples of density data shown in Figure 1a. The spectral indices are indicated on the respective diagrams.

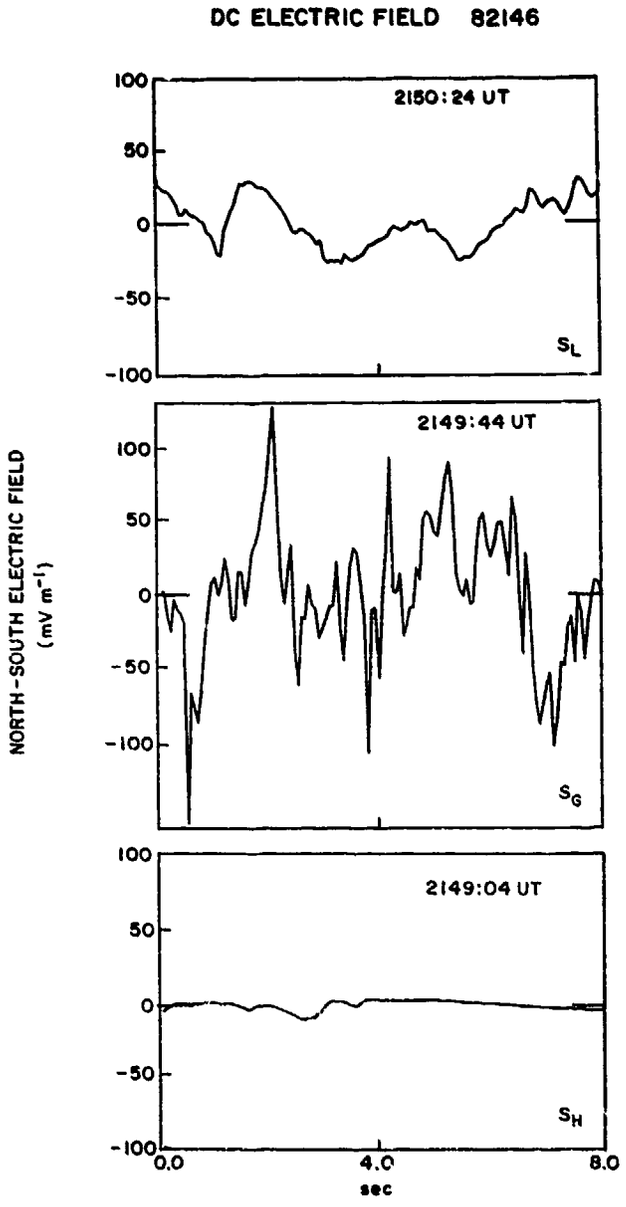


Figure 2a. Three 8-s samples of high resolution (16 Hz) dc electric field data from DE-2. The times are the same as those for Figures 1(a & b).

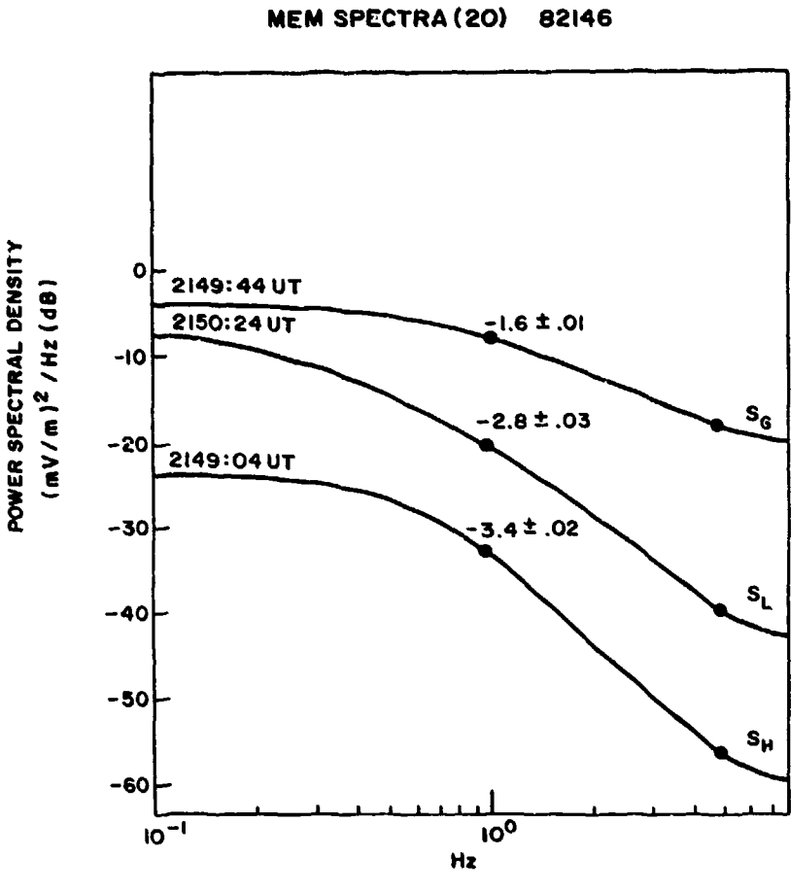


Figure 2b. Maximum entropy spectra corresponding to the three 8-s samples of dc electric field data shown in Figure 2a. The times are the same as those for Figures 1(a & b). Note that the spectrum for 2150:24 UT is shown in the middle panel.

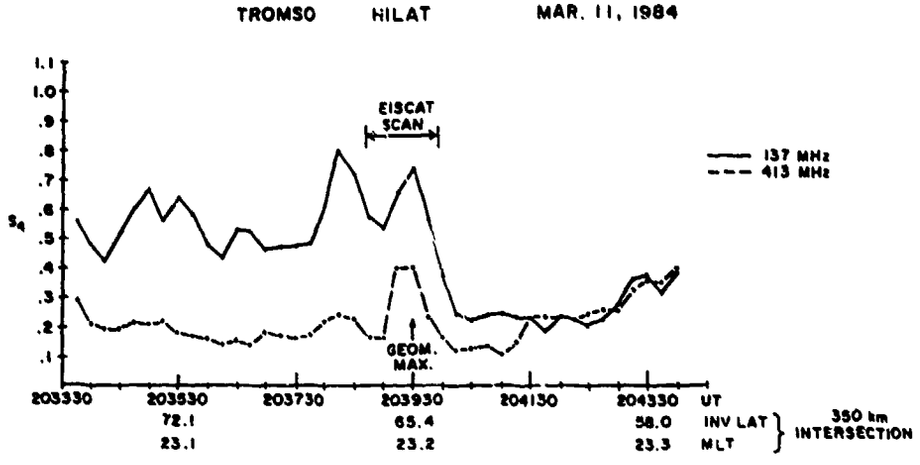


Figure 3. Intensity scintillation index S_4 at 137 and 413 MHz from HiLat pass at Tromso on March 11, 1984 between 2035-2042 UT. The invariant latitude and magnetic local time of 350 km intersection of the ray path are shown. The geometrical enhancement region is also indicated.

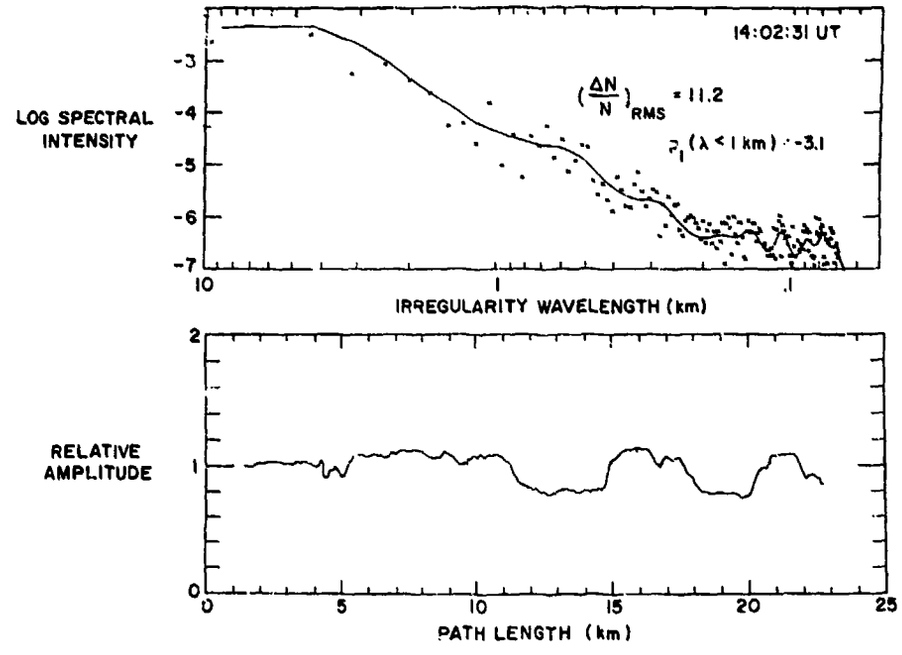


Figure 4. A 3-s sample of high resolution density data taken within a high conductivity region by AE-D (spatial resolution 35 m) on the lower panel and its spectra on the top panel. Note the steep spectrum with one-dimensional spectral index of -3.1 for scalelengths < 1 km.

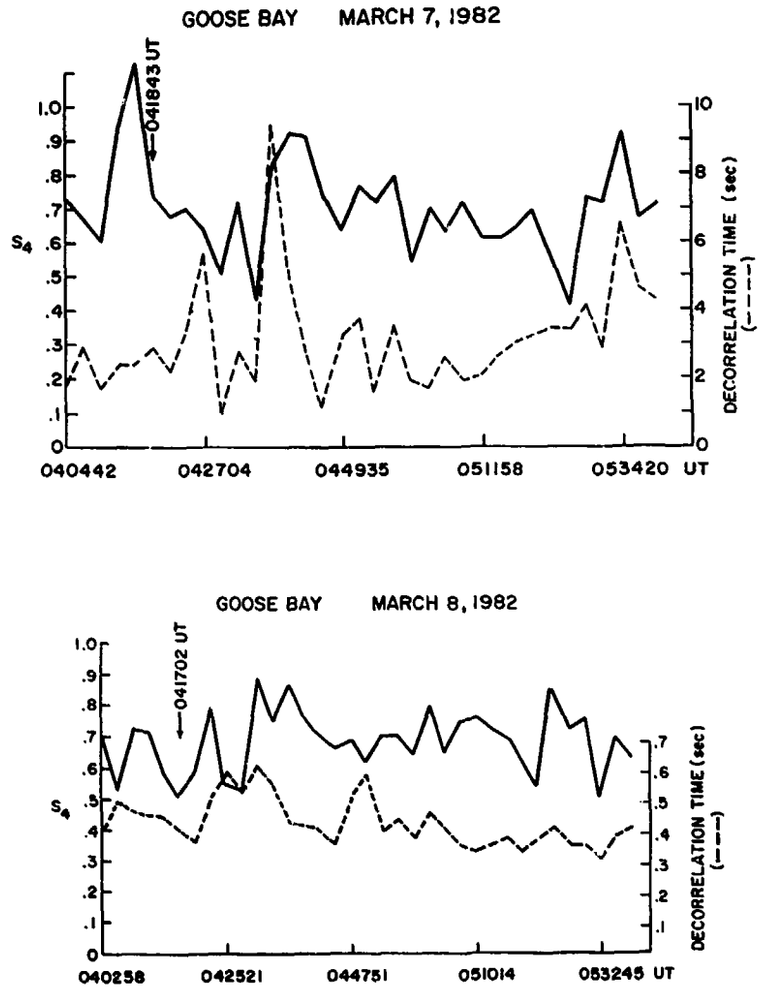
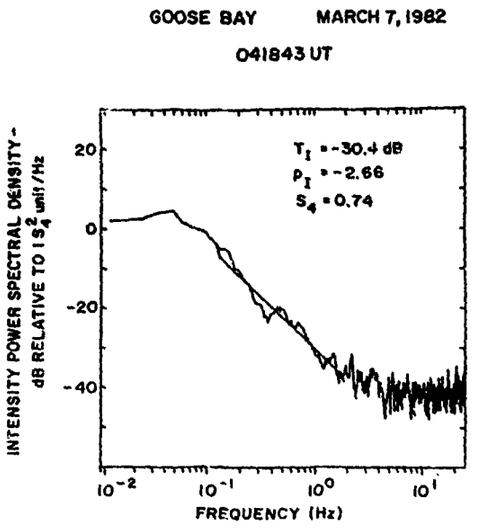


Figure 5. Intensity scintillation index S_4 at 250 MHz observed at Goose Bay on March 7 and March 8, 1982. Decorrelation times are also shown. Note the great variation in decorrelation time from one day to the next even though S_4 level in similar.



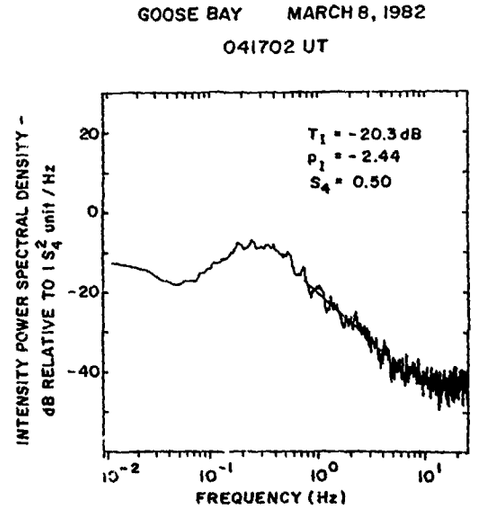


Figure 6. Intensity scintillation spectra observed on March 7 and March 8 at times denoted by arrows on Figure 5. Note the great variation in Fresnel frequency of these two spectra.

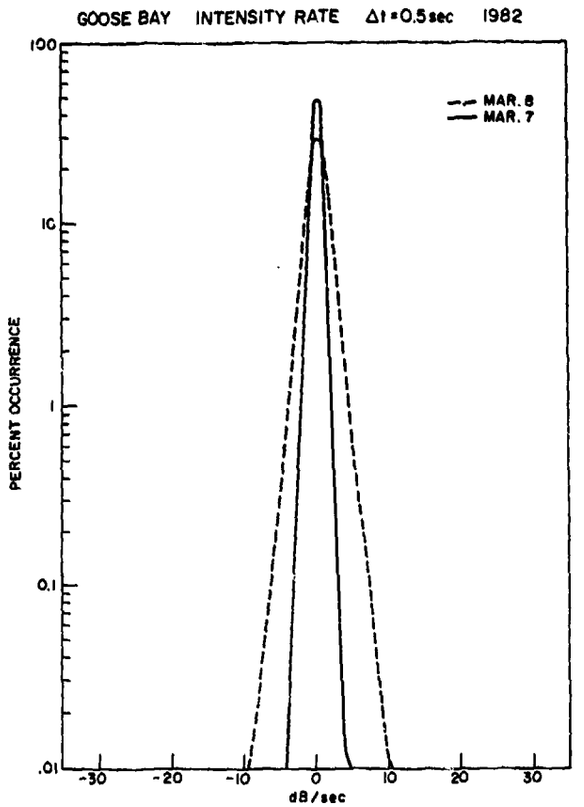


Figure 7. The distribution of intensity rate of scintillations for the data shown in Figure 5. The drift was six times larger on March 8 as compared to March 7.

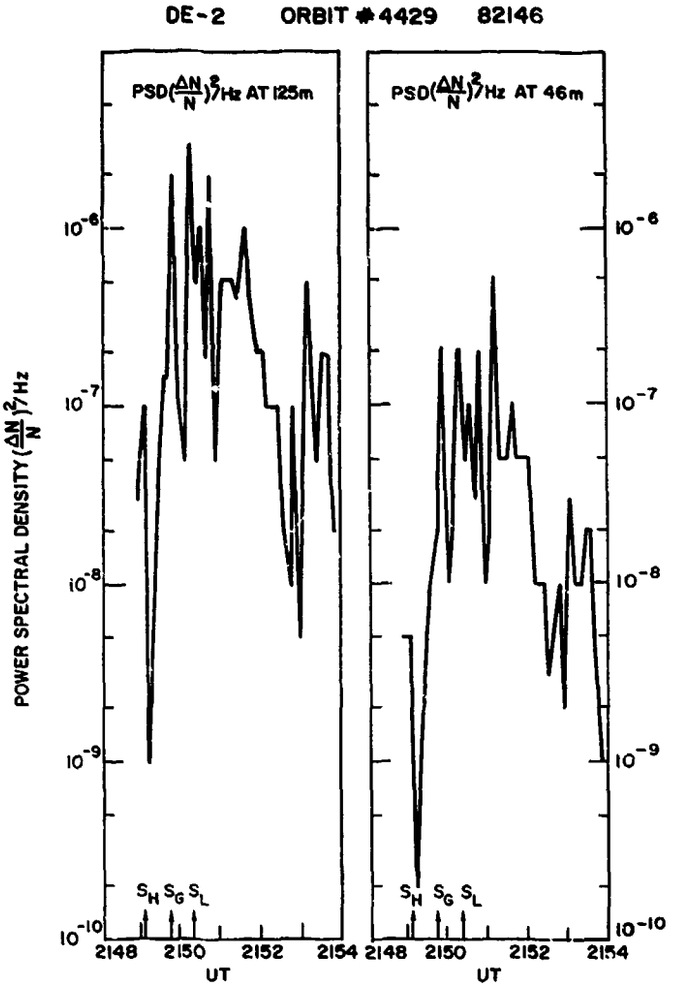


Figure 8. The power spectral density at 125 m and 46.5 m from DE-2 data. S_H, S_G and S_L have the same meaning as in Figures 1 and 2.

IMPULSE RESPONSE MEASUREMENTS AND CHARACTERIZATION OF WIDEBAND VHF RADIO LINKS

by
P. Lo Muzio G. Guidotti
Telettra S.p.A.
Chieti, Italy

N. Benvenuto S. Pupolin
Istituto di Elettrotecnica ed Elettronica
Università di Padova, Italy

SUMMARY

Results of an experiment to determine the characteristics of VHF radio links are presented. The experiment was conducted in a plain surrounded by mountains area with a system that allowed to measure the delay spread (difference between the maximum and minimum delay propagation paths) due to multipath propagation.
Various sites were explored with measurements being made at different carrier frequencies within the VHF band. In this environment, an interesting result was that delay spreads increase with the carrier frequency.

1. INTRODUCTION

Interest in using the VHF band in wideband ECCM systems requires an understanding of the propagation characteristics of radio frequency signals in various environments. Signal attenuation and the effects due to multipath are of particular interest.
In fact, one of the predominant characteristics of VHF radio propagation is the shadowing of the direct or line-of-sight propagation path by intervening obstacles and multipath due to scatter or reflection from buildings or mountains surrounding the radio.

A good description of the multipath characteristics of ECCM systems can be obtained by measuring the complex bandpass impulse response of a radio link at various sites of a mountain area.

These issues were addressed by a series of experiments conducted in the Navelli plain near L'Aquila, Italy. A simple and effective measuring system, whose original scheme is due to D. Cox [1], was built. This system is particularly attractive in radio environments when a wide bandwidth probing pulse is required [2].

This paper is divided into two parts. Section 2 describes the instrumentation that was used to make the measurements and Section 3 presents the radio links characterization results.

2. MEASURING SYSTEM

A technique for measuring the complex impulse response of a radio link is to transmit a carrier modulated with a pseudonoise waveform and crosscorrelate the received signal with the transmitted one [3][4]. This configuration is designed to produce the same effect as probing the radio link with a signal having a flat spectrum over the band of interest.

Since the signals of interest are of bandpass type, it is convenient to write the impulse response of the multipath medium b(t) as

$$b(t) = \mathrm{Re}[a(t)\ \exp(j2\pi f_c t)]\ , \qquad (1)$$

where Re [x] means the real part of x, f_c is the carrier frequency and a(t) is the so called complex envelope of b(t)[5].

A block diagram of the entire system to measure the impulse response of a radio link with unknown complex envelope a(t) is shown in Fig. 1. A shift register with feedback is used to generate repetitively a binary pseudonoise sequence (p_n), n=0, 1, ..., M-1; $p_n \in (-1,1)$ [6]. The most important property of these sequences is that their autocorrelation sequence

$$C_p(k) \triangleq 1/M \sum_{i=0}^{M-1} p_i\, p_{(i-k) \bmod M}\ , \qquad (2)$$

is like that of a white noise signal, namely:

$$C_p(k) = \begin{cases} 1 & \text{for } (k) \bmod N = 0 \\ 0 & \text{otherwise} \end{cases} . \qquad (3)$$

The output of the shift register goes into the mixer and the signal r(t) can be written as

$$r(t) = \sum_{i=0}^{+\infty} p_i \, g(t-iT) , \qquad (4)$$

F=1/T being the clock frequency of the shift register, (p_i) the periodic pseudonoise sequence ($p_i = p_i \bmod N$) and g(t) a pulse of the form *

$$g(t) = \text{rect}[(t-T/2)/T] . \qquad (5)$$

For later use, we derive the autocorrelation of r(t),

$$C_r(t) = 1/MT \int_{-MT/2}^{MT/2} r(v) \, r(v-t) \, dv . \qquad (6)$$

We note that $C_r(t)$ is a periodic function of period MT and its expression is given by [2]:

$$C_r(t) = -1/M + (1+1/M)(1-|t|/T) \, \text{rect}[t/2T] , \text{ for } |t| < MT/2 , \qquad (7)$$

A graphical description of equation (7) is reported in Fig. 2. $C_r(.)$ is also referred to as the probing pulse in the measuring system whose "width" is on the order of T. This will also be the time delay descrimination of the measuring system.

In the bandpass scheme of Fig. 1, the signal r(t) is frequency shifted up to radio-frequencies by phase modulating a carrier signal at frequency f_c with the pseudonoise signal. The result is a transmitted signal of the form:

$$S_t(t) = \text{Re}[r(t) \exp(j2\pi f_c t)] , \qquad (8)$$

where $f_c \in [30,88]$ MHz. Note that the mixer and the amplifier should have a half-power bandwidth of about F.

To discriminate two paths within a time delay of microseconds, the pseudonoise sequence is generated with a clock frequency of F = 500 KHz, i.e. T = 2 μsec. Moreover, an eight stages shift register is used to generate a sequence of N = 255 symbols [3] so that the time interval between two input pulses is MT = 510 μsec (see Fig. 2).

As far as the computation of the average power of the transmitting amplifier is concerned we have that by using antennas with an height of 2m, at a distance of 6 km from the transmitter we experience an attenuation of about 135 dB in the signal strength. Moreover, for a signal bandwidth of 1 MHz, the noise power at the receiver is about -114 dBmW. Thus, to guarantee a signal-to-noise of 24 dB at the receiver, the transmitted average power must be of 35 W.

Referring again to Fig. 1, let c(t) be the convolution of r(t) with the complex impulse response a(t), i.e.

$$c(t) = r(t) * a(t) . \qquad (9)$$

---

* The function rect (t-a)/b is equal to one for $a-b/2 \leq t \leq a+b/2$, zero elsewhere.

The received signal $S_2(t)$ can be written as +

$$S_2(t) = Re[c(t)\ exp(j2\pi f_C t)] \ . \qquad (10)$$

The first bandpass filter eliminates part of the input noise while the mixer is used to shift the signal to intermediate frequencies (here, f_I=21.4 MHz).
The second bandpass filter eliminates the signal components around the carrier $2f_C$-f_I producing a signal $S_3(t)$ of the form:

$$S_3(t) = Re[c(t)\ exp(j2\pi f_I t)] \ . \qquad (11)$$

This signal goes into a quadrature hybrid whose in-phase component $S_4(t)$ is similar to $S_3(t)$. The in-quadrature component $S_6(t)$ instead has a 90° phase shift with respect to $S_3(t)$, i.e.

$$S_6(t) = Re[c(t)\ exp(j(2\pi f_I t+\pi/2))] \ . \qquad (12)$$

Another mixer is used to down shift S_4 (t) to DC. This signal is then multiplied by a pseudorandom waveform that is identical to the transmitted sequence but it is produced by a different clock frequency F'=1/T'. F' is related to F by

$$F' = F-\Delta F \ , \qquad (13)$$

where

$$\Delta F = F/K \ , \qquad (14)$$

and K would be a parameter of our system.
Signals $S_5(t)$ and $S_7(t)$ are of the form:

$$S_5(t) = Re[c(t)\ r'(t)] + Re[c(t)\ r'(t)\ exp(j2\pi 2f_I t)] \qquad (15a)$$

and

$$S_7(t) = Im[c(t)\ r'(t)] + Im[c(t)\ r'(t)\ exp(j2\pi 2f_I t)] \ . \qquad (15b)$$

If the bandwidth of the lowpass filter with impulse response h(t) (also called correlator) is much smaller than f_I, the higher frequency components in (15) are eliminated by this filter. (The same result could have been obtained by using a low pass filter after the mixer).

Let d(t) denote the complex output of the correlators, i.e.

$$d(t) \triangleq i(t) + jq(t) \ . \qquad (16)$$

We have that

$$d(t) = h(t) * [c(t)\ r'(t)]$$

$$= \int_0^{+L} a(w)\left[\int_0^{+\infty} h(t-v)\ r(v-w)\ r'(v)\ dv\right]dw \ , \qquad (17)$$

upon substituting for c(t) the expression (9).

+ At the receiver, all signals are written unless a gain and phase factor.

A closed form expression for d(t) is easily derived when h(t) is the impulse response of an ideal integrate-and-dump filter, i.e. for

$$h(t) = 1/MT \; \mathrm{rect}[(t-MT/2)/MT] \; . \tag{18}$$

Consider the following crosscorrelation between r and r',

$$C_{r,r'}(\tau) \triangleq 1/MT \int_0^{MT} r(v-\tau) \; r'(v) \; dv \; , \tag{19}$$

where τ is the delay between the two pseudonoise sequences. In [2] it is shown that if K(see (14)) is large enough we can assume that

$$C_{r,r'}(t) \cong C_r(t) \; . \tag{20}$$

where $C_r(t)$ is given by (6).
On the other hand, at time t the delay between r' and r is $(t/T')(T'-T) = t/K$ and

$$1/MT \int_{t-MT}^{t} r(v-\tau) \; r'(v) \; dv = C_{r,r'}(\tau-(t-MT)/K) \; , \text{ for } t \geq MT \; . \tag{21}$$

Thus the output d(t) is given by

$$\begin{aligned} d(t) &= \int_0^{+\infty} a(w) \; C_{r,r'}(w-(t-MT)/K) \; dw \\ &\cong \int_0^{+\infty} a(w) \; C_r((t-MT)/K-w) \; dw \; , \end{aligned} \tag{22}$$

or

$$d(Kt+MT) = \int_0^{+\infty} a(w) \; C_r(t-w) \; dw \; . \tag{23}$$

From the above equation, $C_r(.)$ is referred to as the probing pulse in the measuring system. If the bandwidth of a(.) is much smaller than F, (23) simplifies into (see eq. (7)):

$$d(Kt+MT) \cong T \; a(t) \; , \tag{24}$$

i.e. the output of the measuring system coincides with a time scaled version of the impulse response of the radio link. Note that the bandwidth of d(.) is K times smaller than that of the probing pulse and a simple apparatus can be used to record the data.

Similar considerations hold true for an arbitrary lowpass filter h(t). In particular for a single pole filter with time constant RC [2]. However, the penalty of using such a simple filter with respect to the ideal integrate-and-dump filter is that an higher value of K must be used.

We summarize now the relationship among the various parameters when the correlator is a single pole RC filter. Suppose we want to measure reflections with a maximum delay t_R of 511 μsec and with a time discrimination on the order of microseconds (T=2 μsec). Moreover, the radio link is assumed to be time invariant for an interval t_W of 2.55 sec. It must be

$$\begin{aligned} &\text{(i)} && Mt &&\leq && t_W \\ &\text{(ii)} && MT &&> && t_R \\ &\text{(iii)} && RC/MT &&> && 1 \\ &\text{(iv)} && RC/KT &&< && 1 \ . \end{aligned} \qquad (25)$$

In fact, the first condition implies that the measurement is taken within an interval over which the channel can be considered time-invariant. From Fig. 2, the second condition allows to measure reflections with delays up to t_R seconds. The last two conditions are due to the fact that r' does not coincide with r and some distortion and additive noise are introduced in the probing pulse. However, the distortion is small if RC/(KT) is chosen small enough and the additive noise is negligible if RC/(MT) is chosen sufficiently large [2].

By selecting T = 2 μsec, M = 255, K = 5000 and RC = 2.8 μsec we satisfy the above costraints with RC/(MT) = 5.5 and RC/(KT) = 0.28. For these values an actual received probing signal in dB is like the second pulse shown in the fourth profile of Fig. 4.

To conclude the description of the measuring system, an automatic reset mechanism, based on energy detection, is used to position the observation window within the ambiguity window of 511 μsec. Thus, in actual path delay, the first echo is always set at zero seconds (t=0). For later processing, the complex output is stored in a computer after sampling the two outputs i(t) and q(t) with a frequency of 3.88 kHz and digitising them with two 8-bit A/D converters.

3. EXPERIMENTAL RESULTS

The equipment described in the previous section was used to measure the effects due to multipaths in the Navelli plain near L'Aquila, Italy. This plain is very narrow (2 km wide and 7 km long) and it is surrounded by mountains on all sides. Both the transmitter and receiver were placed in two vehicles and each one was connected to a two meter antenna. While the transmitter was set at a fixed place, the receiver instead was moved to different locations in the plain. Fig. 3 provides an artistic interpretation of the plain selected and its local surroundings. The numbers in the map refer to the mountain level at various points while a letter means a location selected for measurements.

Given the complex impulse response d(t), we are mainly interested on its envelope scaled in timeby K, i.e.

$$e(t) = |d(Kt)| = (i^2(Kt) + q^2(Kt))^{1/2} \ . \qquad (26)$$

In fact, e(t) provides the envelope delay profile for a radio link and represents the received signal as a function of path delay t referred to the minimum delay propagation path (t=0).

Incidentally, for a given path, the phase of the received signal turns out to be random with uniform distribution. Thus the phase of d(t), which can be considered as the composition of multiple random phases, is of scarce interest and will not be reported here.

Fig. 4 illustrates some extreme envelope delay profiles from Navelli plain. The horizontal axis is the propagation delay with the zero set at approximately the minimum propagation-path delay from transmitter to receiver. The vertical axis is e(t) in dB, normalized to a maximum value of about 0 dB. The first profile was taken by setting the transmitter and the reciver at points A and Q in the map respectively and for a carrier frequency of 50 MHz. The distance between the two points is about 4 km.
The longest excess delay (i.e. the delay spread) is over 7 μsec. For the computation of the delay spread we only take into account paths with a strength above -20 dB from the strongest path. The envelope delay profile changes dramatically if we increase the carrier frequency to 80 MHz (second profile of Fig. 4). The delay spread becomes 9 μsec. Moreover, we note that the strength of the direct path is lower than those of paths with longer delays. This is due to "fading" of the shorter delay profiles at this location.
The third profile of Fig. 4 has one of the worst delay spread (17 μsec) that was observed in the measurements. It was measured between the points T and E in the map and of a carrier frequency of 80 MHz. The fourth profile represents instead one of the deepest fading of the shorter delay paths that was measured. The minimum delay path has a strength of about 18 dB below that of the strongest path.

Fig. 5 is a set of six envelope delay profiles taken by setting the transmitter at point A and moving the receiver further away from the transmitter. The carrier frequency is of 30MHz. The delay spread is usually of 10 usec with a maximum of 14 μsec for the third profile (receiver at point M). No deep fading of the shorter delay paths was observed.

If we now repeat the above measurements but with an higher carrier frequency of 80 MHz two phenomena appear (see Fig. 6). The delay spread increases: up to 17 μsec for the second and sixth profile of Fig. 6. Furthermore, a fading of the lower delay profile is seen in the third and fourth profile.

Similar considerations were observed by setting the transmitter at point T in the map. Fig. 7 illustrates four envelope delay profiles with f_c = 34.8 MHz and two with f_c = 50 MHz. As above, delay spreads up to 13 μsec were measured with f_c = 80 MHz. Finally, in Fig. 8 we report envelope delay profiles at the same locations of Fig. 7 and changing f_c to 80 MHz. Again we measure an increase in the delay spread (up to 20 μsec for the first and second profile) and a fading for the shorter delay paths (see first profile).

4. CONCLUSIONS

In this paper we presented results of an experiment to determine the characteristics of radio links at VHF in a plain surrounded by mountains. The data from Navelli plain show that the envelope delay profile at a given location is time-invariant with a good approximation. On the other hand, the envelope delay profile may change substantially if we move the receiver of just 10 m. Obviously, the change depends on the area under consideration. However, the biggest change occurs by changing the carrier frequency. As a matter of fact, the delay spread generally increases as the carrier frequency is increased. Plots of envelope delay profiles show that for a carrier frequency of 30 MHz, for an example, the delay spread is generally 10 μsec with a maximum value of 14 μsec. However, for f_c = 80 MHz delay spreads of 17 and 20 μsec are not uncommon. Furthermore, fading of the minimum delay paths was observed only for higher values of the carrier frequency.

REFERENCES

[1] D.C. Cox, "Delay Doppler Characteristics of Multipath Propagation at 910 MHz in a Suburban Mobile Radio Environment", IEEE Trans. Antennas Propagat., vol. AP-20, pp. 625-635, Sept. 1972.

[2] N. Benvenuto, "Distortion Analysis on Measuring the Impulse Response of a System Using a Crosscorrelation Method", AT&T Bell Laboratories Technical Journal, vol. 63, pp. 2171-2192, Dec. 1984.

[3] J.D. Balcomb, H.B. Demuth, and E.P. Gyftopoulos, "A Cross-Correlation Method for Measuring the Impulse Response of Reactor Systems", Nuclear Sci. Eng., vol. II, pp. 159-166, Sept.-Dec. 1961.

[4] M.S. Gupta, "Applications of Electrical Noise", Proc. IEEE, vol. 63, pp. 996-1010, July 1975.

[5] L.E. Franks, Signal Theory, Englewood Cliffs, N.J.: Prentice Hall, 1969.

[6] S.W. Golomb, ed., Digital Communications With Space Applications, Englewood Cliffs, N.J.: Prentice Hall, 1964.

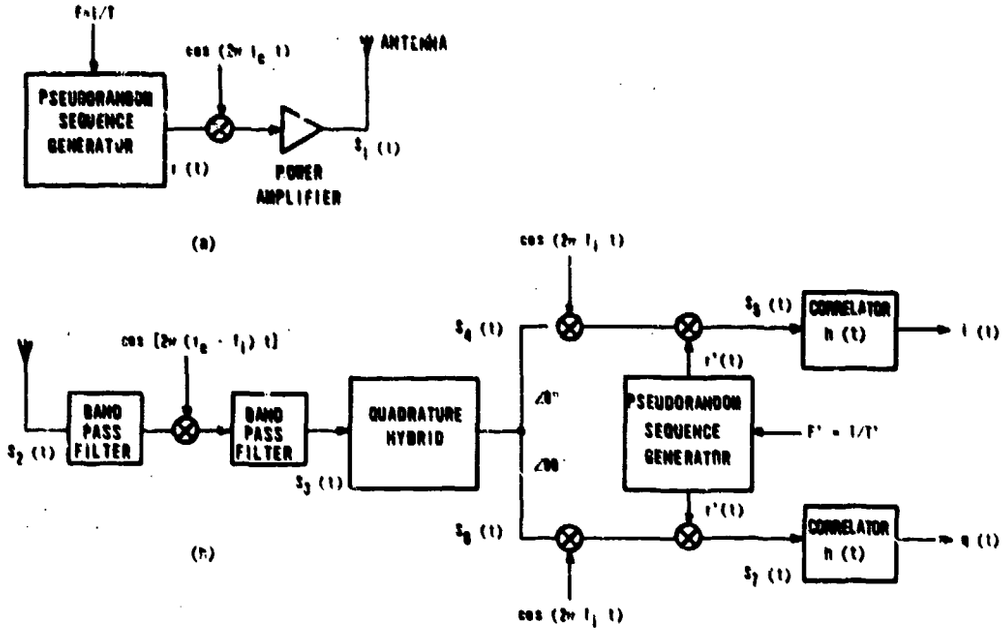


Fig. 1 Block diagram of the measuring system: a) transmitter, b) receiver.

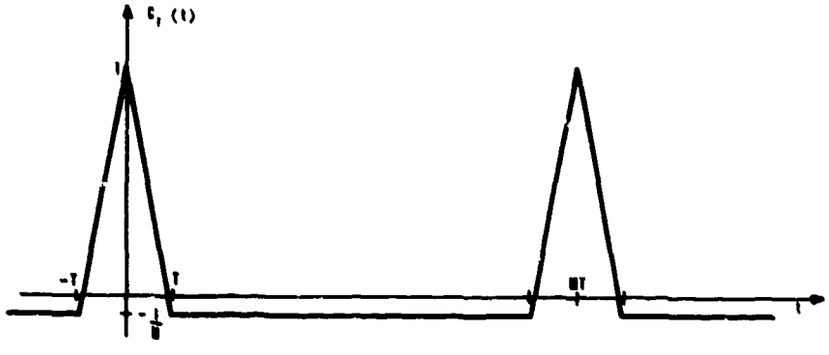


Fig. 2 Probing pulse in the measuring system.

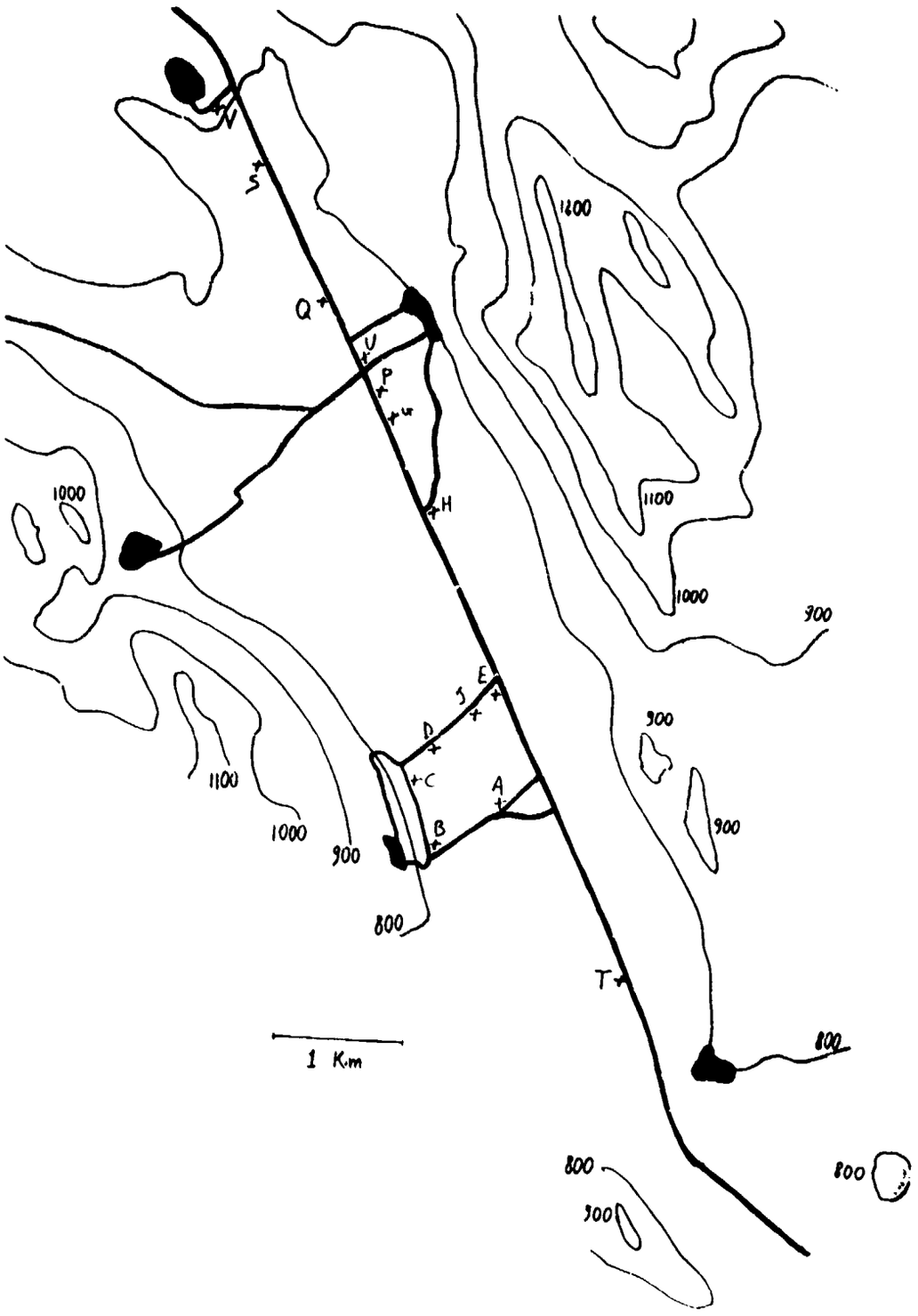


Fig. 3 Map of experimental area in Navelli plain near L'Aquila, Italy.

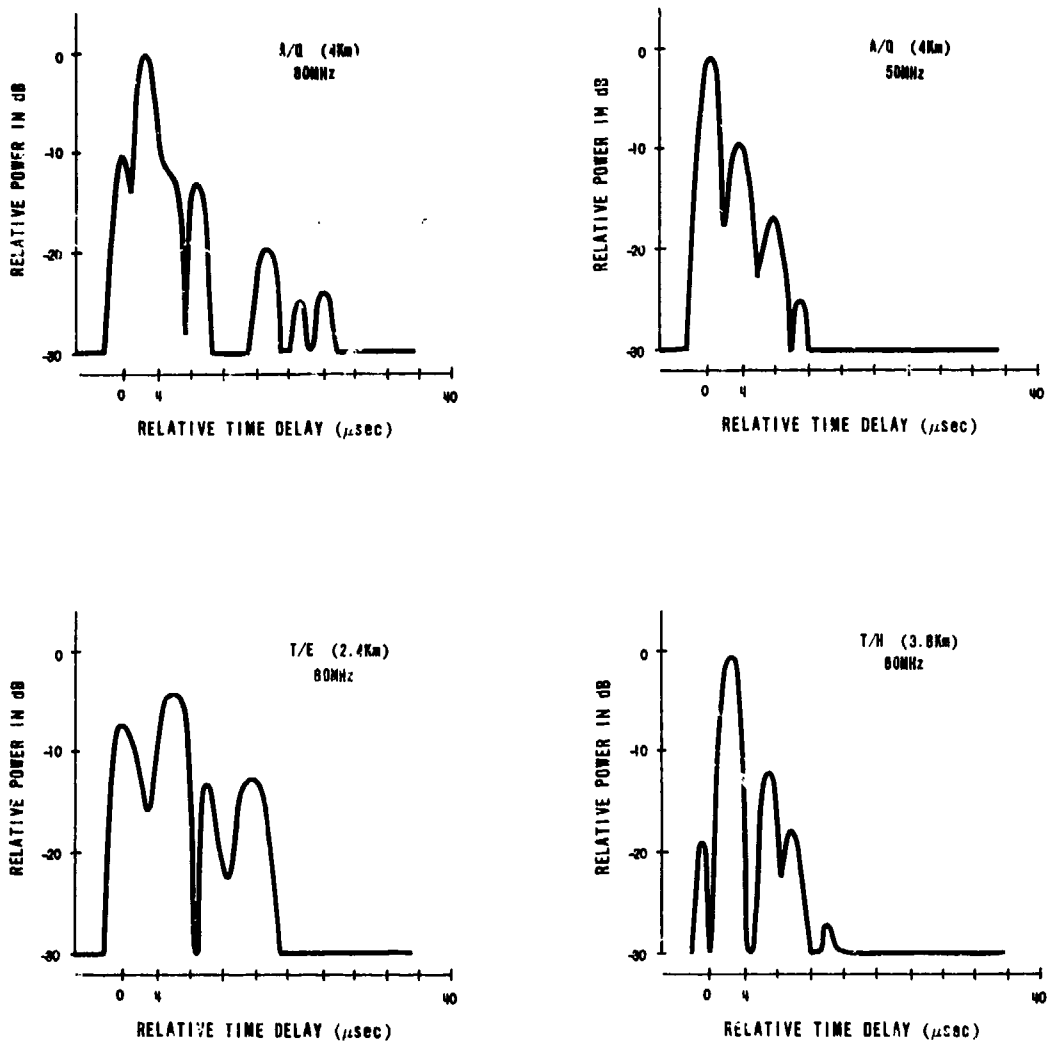


Fig. 4 Four envelope delay profiles taken from Navelli plain.

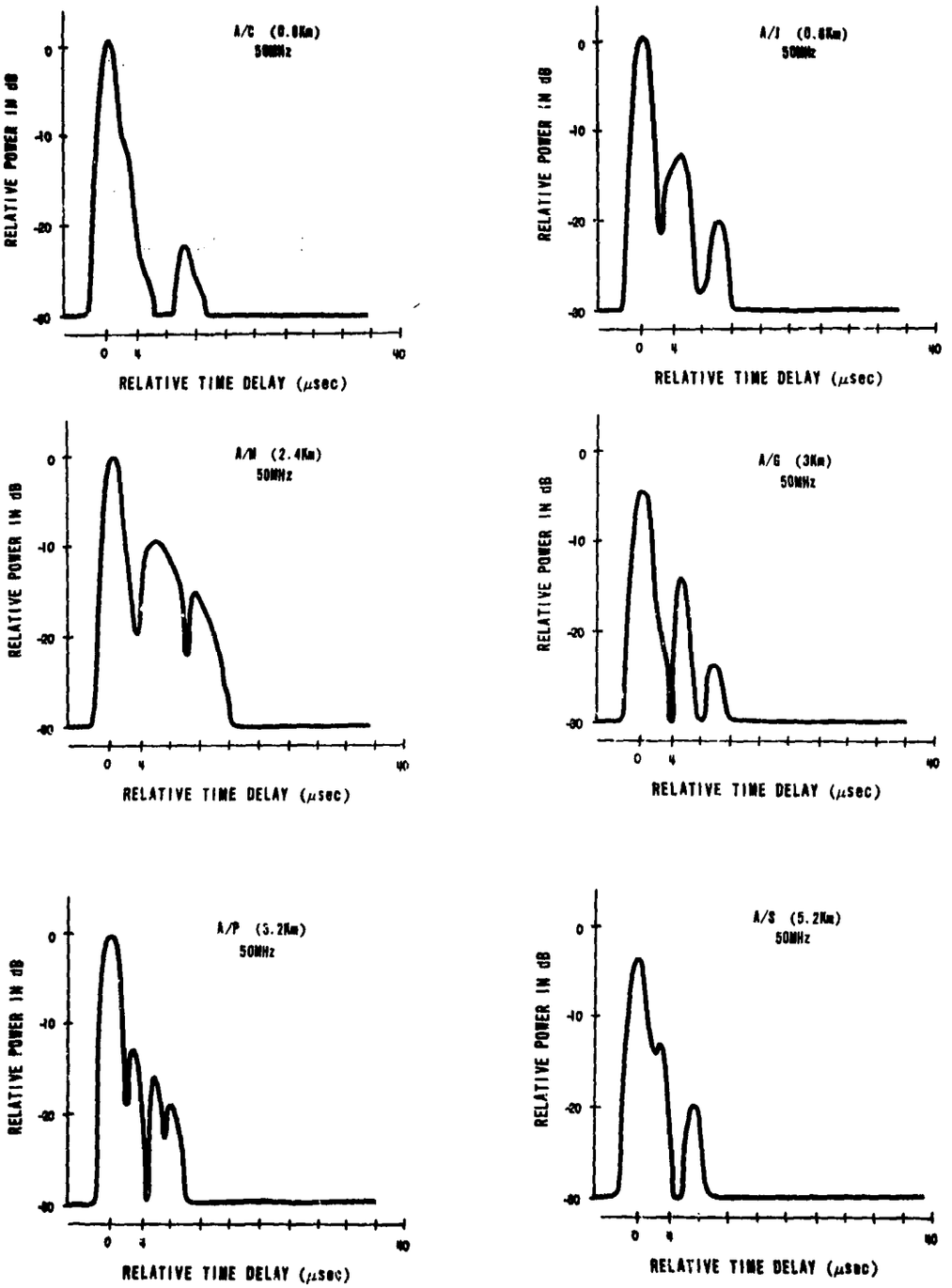


Fig. 5 Six envelope delay profiles taken from Navelli plain using a carrier frequency f_c = 50 MHz.

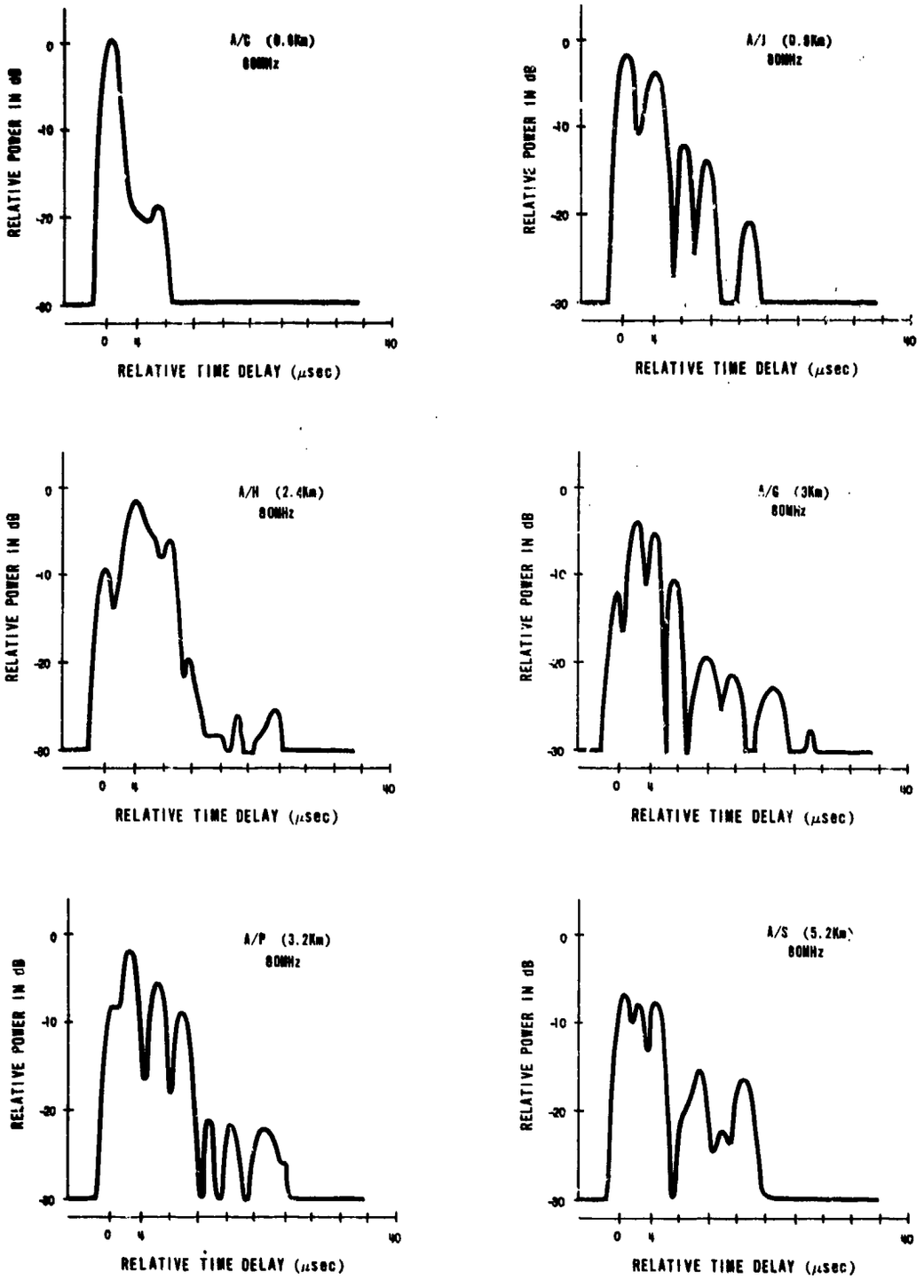


Fig. 6 Six envelope delay profiles taken from Navelli plain using a carrier frequency f_c = 80 MHz.

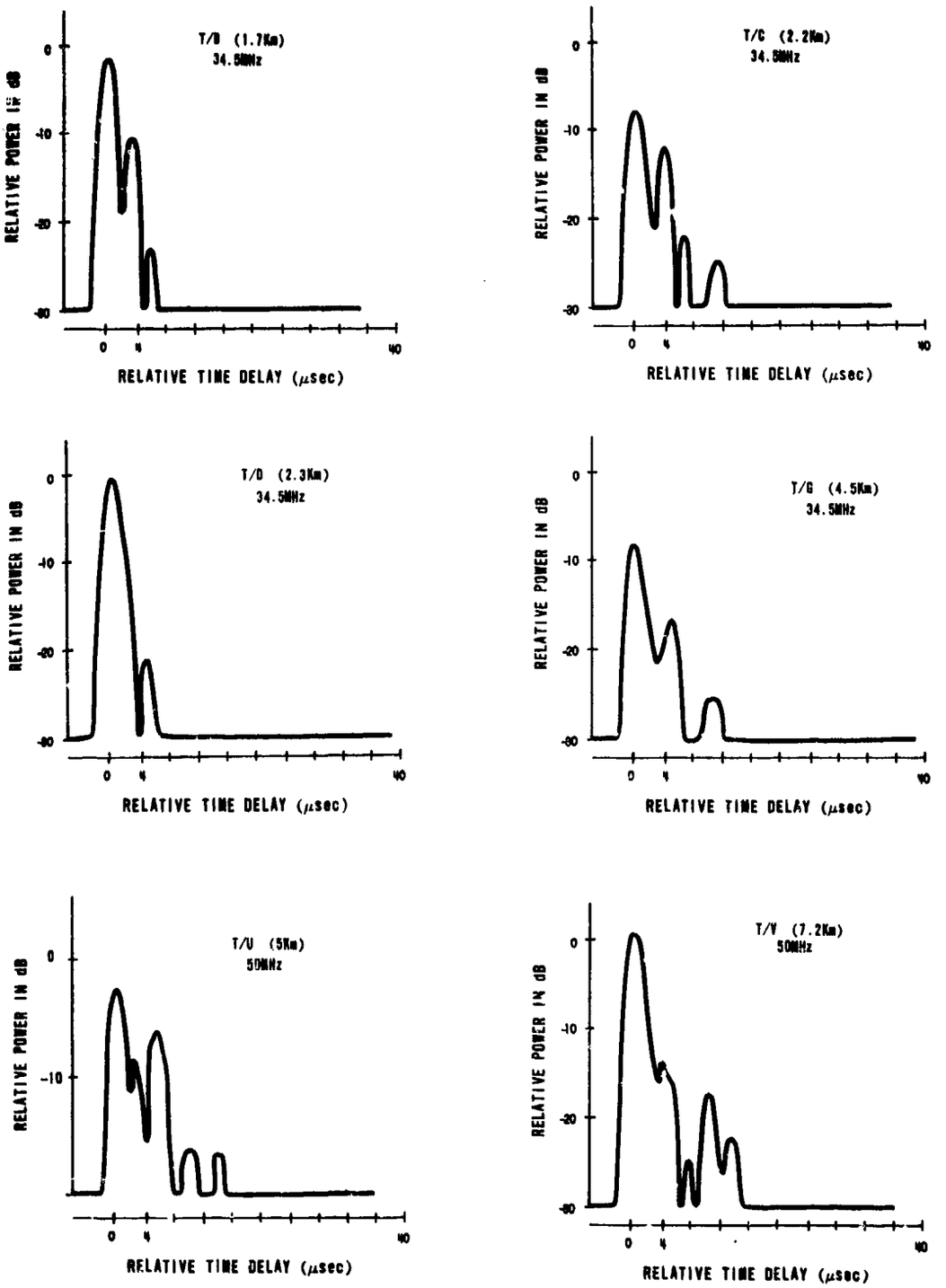


Fig. 7 Six envelope delay profiles from Navelli plain.

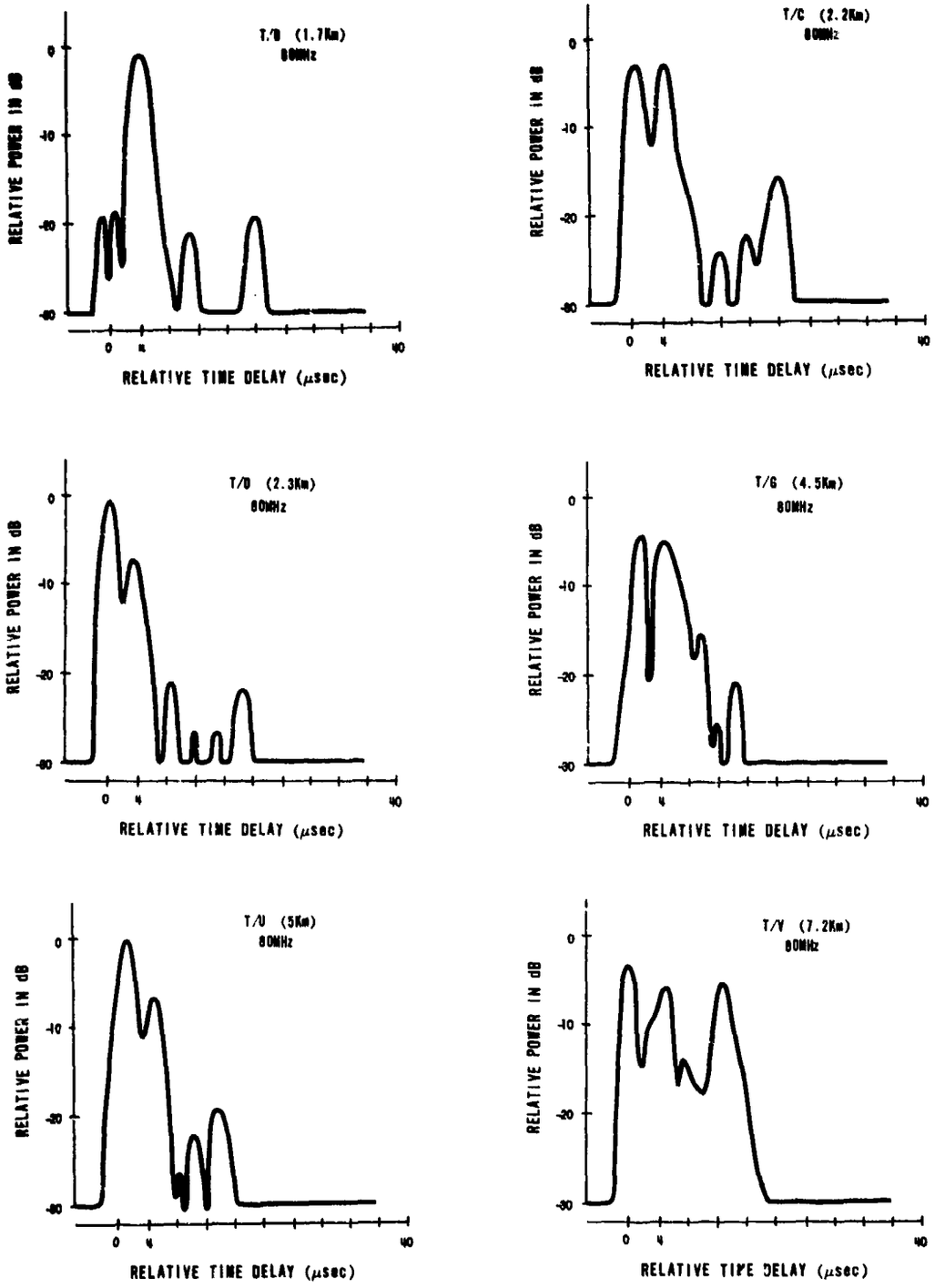


Fig. 8 Six envelope delay profiles from Navelli plain.

DISCUSSION

H. Vissinga, NE
Did you try to correlate the measured delays with typical features of the terrain?

Author's Reply
No, I didn't, because the measurements strongly depend on relative phases of the reflected signals.

C. Goutelard, Fr
English translation
Did you use a directive antenna for this experiment? This choice affects the form of the impulse response used.

Author's Reply
I've used only an isotropic antenna.

SUMMARY OF SESSION VII

THEORY

by

B.Crosignani, Session Chairman

There were six papers scheduled for presentation in this session, two of which, however, were not presented but are included in this final proceedings together with four other papers. The paper by O'Donnell was presented impromptu but is not included at the author's request.

In the first presentation, the author, S.J.Miller, examined the intensity fluctuations arising from diffractions when a nonmonochromatic wave was incident on a deeply modulating phase screen. By introducing the cross correlation between phase coherent waves of different wave numbers, it was possible to point out general features of the intensity fluctuations, not previously noted, concerning the far-field statistics.

In the second presentation, the authors, Y.Beniguel and B.Gibert, investigated the evolution of a signal crossing an ionized medium with strong fluctuations by dividing it into N homogeneous slabs each of which was considered as a weak phase screen, thus being able to calculate its amplitude, phase and scintillation rate.

The third presentation, by I.Besieris, dealt with the problem of transferring the better developed continuous scattering techniques to the study of discrete scattering, having in mind possible applications to remote sensing and propagation through snow and rain.

In the fourth presentation, by P.L.Chow, the method of functional integration for wave propagation through random media was presented and, in particular, applied to solving a random parabolic equation.

Finally, in the fifth presentation, by K.O'Donnell, light scattering from rough surfaces was investigated in the range of extreme conditions where usual theory does not work (e.g., large angles or corrugation scale shorter than the wavelength). Experimental work consisting of diffuse scattering properties was presented.

INTENSITY FLUCTUATIONS DUE TO MOVING POINT SOURCES

B.J. Uscinski, Ocean Acoustics Group,
Dept. of Applied Mathematics and Theoretical Physics,
Silver Street
Cambridge U.K. CB3 9EW

SUMMARY

An understanding of point sources in random media is essential if we are to deal with real sources, and effects such as source motion. Reliable theory now exists for the intensity fluctuations due to point sources in such media. Numerical simulations of such fluctuations agree with theoretical results. The intensity fluctuation theory and simulations have been extended to deal with the case of a moving source and observer. It is shown that as regards ensemble averaged quantities such as the intensity fluctuation spectra there is reciprocity between motion of the source and that of the observer. However, such reciprocity does not exist if we are dealing with the detailed individual fluctuation pattern arising in a particular realization of a random medium.

INTRODUCTION

During the last five years there have been a number of important advances in multiple scatter theory. As a result encouraging agreement was obtained between the new theory and previously unexplained experimental data. In particular, the time spectra of acoustic intensity fluctuations caused by ocean internal waves [1], which failed to agree with the results of Rytov theory and its modifications, now fitted the predictions of the new theory well [2], [3], [4].

These initial successes have led to many papers aimed at extending and refining the theory. Much effort has also been devoted to investigating the accuracy of the theoretical expressions. In this context numerical simulations of random propagation have been particularly useful. Not only have they provided a check on theoretical results but have also given us much insight into properties of the wave-field fluctuations that cannot be obtained from ensemble average expressions.

In what follows we shall outline the new developments in theory and also describe the accompanying advances in numerical simulations. The application to moving sources and observers will be discussed including the question of the reciprocity of these motions.

ADVANCES IN THEORY

The principal quantities associated with wave-field fluctuations in a random medium that have prospects of being derived theoretically are the second and fourth moments, m_2 and m_4. The following equations for these moments have long been known [5], [6]

$$\frac{\partial m_2}{\partial z} = \frac{i}{2k}\ (\nabla_1^2 - \nabla_2^2)m_2 - \beta(1 - f_{12})\ m_2 \tag{1}$$

$$\frac{\partial m_4}{\partial z} = \frac{i}{2k}\ (\nabla_1^2 - \nabla_2^2 + \nabla_3^2 - \nabla_4^2)m_4$$

$$-\beta\ (2 + f_{13} + f_{24} - f_{12} - f_{23} - f_{14} - f_{34})m_4 \tag{2}$$

where f_{ij} is the normalized two point autocorrelation function of refractive index fluctuations in the medium integrated in the direction of wave propagation z, k is the wave number of the radiation, ∇_i is the transverse Laplacian $\frac{\partial^2}{\partial x_i^2} + \frac{\partial^2}{\partial y_i^2}$, and β is the power attenuation coefficient of the random medium.

The second moment

The second moment m_2 describes the directional properties of the wave-field in the medium and also its mean intensity. Equation (1) for m_2 can be solved exactly for a number of useful cases including that of a point source. However, the introduction of a systematic refractive index profile in the medium leads to the appearance of curved ray paths and phenomena such as focussing, caustics and shadow zones. In this case the second moment equation cannot be solved exactly but various approximate methods such as eikonal series [7] and multi-scale expansions [8] have allowed these effects to be described with varying degrees of accuracy.

The fourth moment

The fourth moment m_4 describes the autocorrelation and variance of intensity fluctuations. The following solution of Eq. (2) was obtained in 1982 [9], for plane wave geometry, in the form of a multiple convolution for M, the Fourier transform of m_4

$$M(\nu,z) = \frac{1}{(2\pi)^N} \int\!\!\cdots\!\!\int \exp\{-\sum_{j=1}^{N} h(\xi_j,Q_j) + i\xi_j\ (\nu_j - \nu_{j-1})\}$$

$$d\nu_1 \ldots d\nu_{N-1}\ ,\ d\xi_1 \ldots d\xi_N \tag{3}$$

where

$$h(\xi,Q) = 1 - f(\xi) - f(Q) + \tfrac{1}{2}f(\xi + Q) + \tfrac{1}{2}f(\xi - Q),$$

$$Q_j = \left[\nu_M + \nu_{M-1} + \ldots + \nu_j\right] Z/M,$$

$$M = 2\Gamma Z = 2\beta z,$$

$$Z = z/kL^2 \quad \text{where } L \text{ is the transverse scale of the irregularities in the medium.}$$

This can be evaluated approximately to give the following useful expression

$$M_0(\nu,Z) = \frac{1}{2\pi} \int \exp\left\{-2\Gamma \int_0^Z h(\xi;\ \nu\left[\tfrac{1}{2} - Z'\right])\, dZ'\right\} \exp(-i\nu\xi)\, d\xi \ . \tag{4}$$

A similar solution for a point source [2] and a medium that varied in time allowed a satisfactory explanation to be given for the acoustic intensity fluctuations observed in the Cobb Seamount experiment [3]. Rytov theory had failed to account for these.

This initial success provided the impetus for extending and refining fourth moment solutions. The next major step was to find a better estimate of the multiple convolution Eq. (3). This was done in 1983 [10] and the improved result gave very good agreement with numerical simulations. (see Fig. 1)

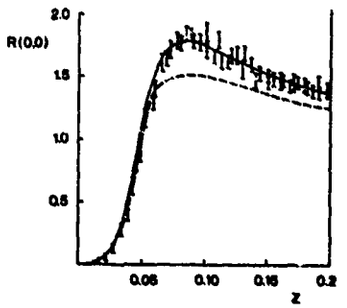


Fig. 1
Scintillation index for plane-wave geometry, $\Gamma = 1000$. The full curve gives the theoretical result and the points and error bars the results of numerical simulations.

Two-scale expansion

The original solution of the fourth moment equation was obtained by multiple convolution. However, other methods of solution were soon developed and it was encouraging to find that they yielded the same results as before, both as regards the fundamental approximation as well as the improved estimate. The first of the alternative methods used was that of the two scale expansion [10] which assumes that the required moment contains two distinct spatial scales. One of these is called the fast scale and the other the slow scale. Detailed investigations of the fourth moment solutions were carried out using the two scale method [11] and revealed much about the structure of the solutions.

Path integral methods

It had long been known that the various moments of the wave-field in a random medium can be written down in terms of the Feynman path integral [12]. This approach has the advantage that a medium with a deterministic refractive index profile can easily be dealt with, the ray paths arising naturally in the process of evaluation of the integral. This approach was used successfully to obtain the second moment m_2 [12]. It was subsequently used to find the fourth moment m_4 [13], giving results that were identical with those obtained by multiple convolution or two scale expansion. This extension of the fourth moment solution represents the most general and flexible form available at present. We shall now consider it in some detail.

General solution with profile

The general form of the fundamental approximation to the fourth moment in the case of a point source and an arbitrary deterministic refractive index profile is [13]

$$M_0(\nu,Z) = \frac{1}{(2\pi)^2} \iint \exp\left\{-2\Gamma \int_0^Z h(\underline{\nu}_1(Z');\ \underline{\nu}_2(Z'))\, dZ'\right\}$$
$$\exp\left\{-ik\left[\underline{\nu}_1'(Z)\ .\ \underline{\nu}_1(Z)\right]\right\} d\underline{\nu}_1(Z) \tag{5}$$

where $\underline{\nu}_1$ and $\underline{\nu}_2$ are the solutions of the equations

$$\underline{\nu}_1''(Z') = \underline{\nu}_1(Z')\ .\ \underline{\underline{W}} \tag{5a}$$

$$\underline{\nu}_2''(Z') = \underline{\nu}_2(Z')\ .\ \underline{\underline{W}} + \underline{\nu}k\delta(Z - Z') \tag{5b}$$

$\underline{\underline{W}}$ is a matrix of derivatives of n_0, the refractive index profile, along the ray path $\underline{S}$. Here $\underline{S}$ is the solution of the ray equation

$$\underline{\rho}''(Z') = \nabla n_c(\underline{\rho}(Z') \; ; \; Z') \tag{5c}$$

The following features of the general solutions are important:
(a) It describes a point source. In practice most sources are small and can be well approximated by a point.
(b) Because of the presence of the refractive index profile radiation from a point source follows the deterministic ray paths $\underline{\rho}(Z)$ in the absence of random irregularities. The $\underline{\rho}(Z)$ are found by solving the ray equation (5c). This is important in applications to ocean acoustics because of the sound speed profile that exists in all oceans. The solution (5) describes fluctuations due to scattering about a single ray path, but solutions can be combined to deal with convergence zones where several rays arrive along separate paths.
(c) The integration with respect to Z' in the exponent allows us to take into account variation in the scattering properties of the medium along the ray path. Such variations can occur in real situations and it is important to be able to deal with them.
(d) The ability to include curved ray paths allows us to deal with cases of foci and caustics.

Limitations of Cartesian coordinates

The obvious flexibility of the solution (5) means that it can be used in most cases encountered in practical ocean acoustics. A more accurate result can be achieved if necessary by the use of the next approximation which also handles points (a) - (d) above but has a more complicated structure. Certain serious objections have, however, been raised concerning the validity of the point source solutions described above. It has been suggested [14] that because the fourth moment was derived in a Cartesian system of coordinates the small departure from a truly circular wavefront encountered in this representation leads to a large cumulative error in the multiple scatter limit, and that the solution could be grossly in error.

Curvilinear coordinate systems

A recent major advance in scattering theory, relevant to the objection mentioned above, has been the formulation of the moment equations in general curvilinear coordinate systems rather than in Cartesian coordinates [15]. In this way wavefronts expanding from point sources can be dealt with exactly, while curved ray paths due to refractive index profiles can be made to coincide with the curvilinear coordinates and the limitations of small ray excursion and curvature can be removed. The only restriction now remaining is that the random irregularities in the medium should cause the radiation to depart by only small amounts from the deterministic ray paths.

The introduction of curvilinear coordinates has also enabled us to answer the question of the error arising when the wave-field from a point source is represented in Cartesian coordinates. The fourth moment equation, written in cylindrical coordinates, can be solved as a multiple convolution to give

$$M(\nu,Z) = \frac{1}{(2\pi)^N} \iint \exp\left\{\sum_{j=1}^{N} h(R_j \Psi_j \; ; \; R_j Q_j) + i\Psi_j (\nu_j - \nu_{j-1})\right\}' \; d\nu_1 \ldots d\nu_{N-1} \; d\Psi_1 \ldots d\Psi_N \tag{6}$$

where

$$Q_j = \frac{N}{R}\left[\nu_N \left(\frac{1}{N+1} - \frac{1}{N}\right) + \nu_{N-1}\left(\frac{1}{N} - \frac{1}{N-1}\right) + \ldots + \nu_j \left(\frac{1}{j+1} - \frac{1}{j}\right)\right]$$

and R is the scaled radial coordinate r.
Evaluation of Eq. (6) leads to results that are formally the same as those obtained when Cartesian coordinates are used, except that the z coordinate is replaced by the radial coordinate r.

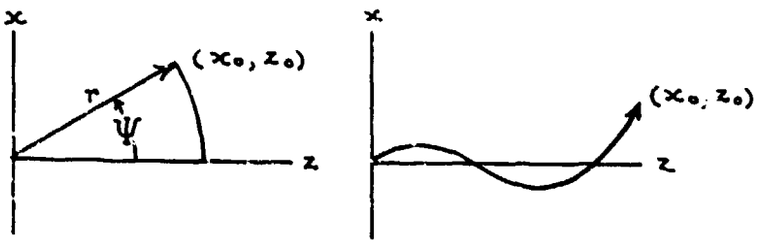


Fig. 2
(a) Cartesian and curvilinear coordinates for a point source with no refractive index profile
(b) Case of a general refractive index profile.

This implies that the Cartesian representation is accurate to the extent that r can be replaced by z. In other words the point of observation (x_o, z_o) must remain close to the z axis. The same result presumably also holds true even when the presence of a refractive index profile leads to curved ray paths. It is important to keep this in mind when using existing fourth moment solutions. The three methods of solution discussed above have been carried out using a Cartesian coordinate system and so the results should only be used provided that the ray paths do not depart much from the z axis (the ratio x_o, z_o should be small). Solutions found in curvilinear coordinates would be free from such restrictions. However, apart from the case given above, these solutions have not yet been found. They will be a logical

extension of the present work on fluctuation phenomena and will provide answers to some still unanswered questions in the field.

NUMERICAL SIMULATIONS

As a method for obtaining insight into fluctuation phenomena numerical simulations of random wave propagation area method that ranks equal in importance with the analytical approaches discussed above.

Plane wave geometry

Simulations have been used successfully to test the results of fourth moment theory in the case of plane wave geometry [16]. The principles of such numerical simulations are well-known and will not be described here. A typical example of the intensity fluctuations induced in a plane wave travelling in a random medium containing irregularities with a Gaussian autocorrelation function is given in Fig. 3. The variance of these intensity fluctuations estimated from many such numerical simulations is shown by the points with error bars in Fig. 1. This provided a check on the accuracy of the theoretical expression shown in the same figure.

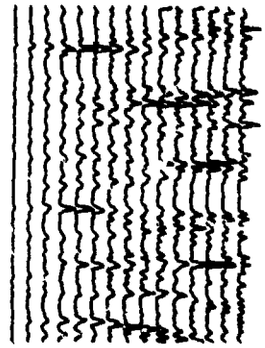


Fig. 3 Intensity fluctuations simulated for plane-wave geometry.

Point source

One method of checking the accuracy of the fourth moment solution in the case of a point source is by comparison with the results of numerical simulations, as was done in the case of plane wave geometry. However, numerical simulations involve considerable difficulties when we are dealing with a point source. This is because it is most convenient to represent the scattering medium in Cartesian coordinates. In such a coordinate system there are very rapid oscillations in the phase of the wave-field close to the source, and it is not possible to achieve the required resolution numerically. To overcome this a physically extended source [17] is used whose field approximates to that of a point source at ranges where the scattering effect is only just beginning to be important, and in a certain range of angles about the z axis. Simulations of intensity fluctuations using such a quasi-point source are shown in Fig. 4. The intensity fluctuation variance resulting from many such simulations is shown in Fig. 5 together with the theoretical variance obtained by solving the fourth moment equation for a point source. The agreement appears reasonable but there is a fairly large statistical scatter in the simulations. This is due to the fact that the intensity fluctuations are non-stationary transverse to the z direction and spatial averages cannot be used to substitute for ensemble averages. Thus the simulations must be repeated a much larger number of times in order to achieve a statistical average equivalent to that of the plane-wave case where spatial averages can also be used.

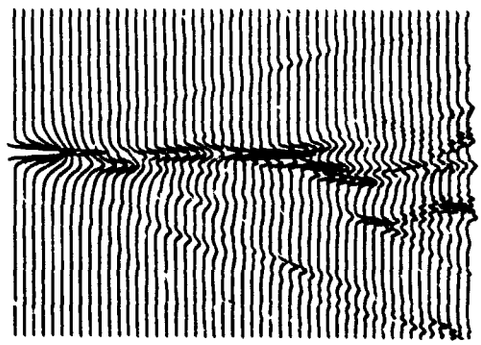


Fig. 4 Intensity fluctuations simulated with a quasi-point source.

Curvilinear coordinates can also be used in numerical simulations to avoid the problems associated with a point source [18]. Curved wave-fronts appear naturally in cylindrical coordinates and the rapid phase oscillations mentioned above are not encountered. Intensity fluctuations arising in the wave-field radiating from a point source are shown in Fig. 6.

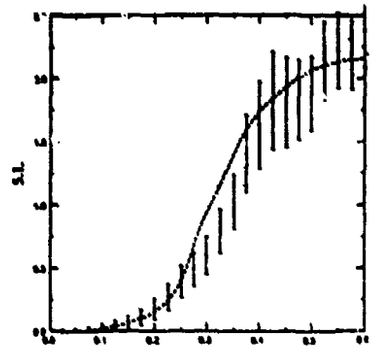


Fig. 5 Scintillation index from simulations with a quasi-point source. The full line gives the theoretical result.

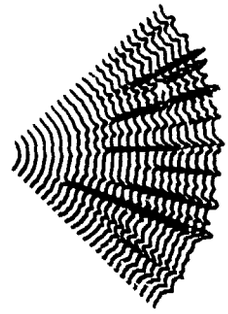


Fig. 6 Intensity fluctuations simulated with a true point source.

These fluctuations are now statistically stationary in the azimuthal direction and spatial averages can be used for ensemble averages. As a result better statistical averages can be obtained with fewer realizations. The variance of intensity fluctuations obtained by this method is shown in Fig. 7 together with the theoretical result, and the agreement is seen to be quite satisfactory.

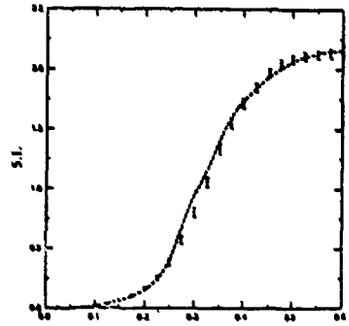


Fig. 7 Scintillation index from simulations with a true point source. The full line gives the theoretical result.

Thus numerical simulations have enabled us to verify the accuracy of our fourth moment solution in the case of a point source. We have additional confirmation of the conclusion, drawn above on theoretical grounds, that point sources can be adequately dealt with in Cartesian coordinate systems provided the observation point is not too far from the z axis.

MOTION OF SOURCE AND OBSERVER

The effects of motion of source and observer can now be studied since we have a theory for the intensity fluctuations due to a point source and can also simulate such propagation numerically.

Theory

Moving source

The spatial frequency spectrum of intensity fluctuations seen by a fixed observer when a point source moves in a direction transverse to the direction of wave propagation can be derived by any of the methods outlined above. The fundamental form of this spectrum is

$$M_0(\nu,Z) = \frac{1}{2\pi} \int \exp\left[-i \int_0^Z h[(\xi - \nu t)\, Z'/Z\,;\, \nu(Z - Z')]\, dZ'\right] \exp(-i\nu\xi)\, d\xi \,. \tag{7}$$

The source is assumed to be moving with a uniform velocity v in the positive x direction and t is the lag in observation times. When v is zero Eq. (7) reduces to the corresponding expression for a stationary source such as would be obtained from Eq. (5).

Moving observer

It is a simple matter to derive the spatial frequency spectrum of intensity fluctuations seen by a moving observer. The coodinate of the observer is written as a function of time using the velocity of the observer. For the case of an observer moving with a uniform velocity v in the positive x direction we have

$$M_0(\nu,Z) = \frac{1}{2\pi} \int \exp\left[-i \int_0^Z h[(\xi + \nu t)\, Z'/Z\,;\, \nu(Z - Z')]\, dZ'\right] \exp(-i\nu\xi)\, d\xi \,. \tag{8}$$

Comparison of Eqs. (7) and (8) shows that motion of the source and observer are equivalent as regards their effect on the ensemble averaged quantity $M_0(\nu,Z)$. The difference in signs between the factors $(\xi \pm \nu t)$ in the first exponential is due to the fact that positive x motion of the source is equivalent to a negative x motion of the observer. This result might have been expected on physical grounds, but it is satisfying to have proved that reciprocity exists as regards source and observer motion and their effect on the averaged spectrum $M(\nu,Z)$. However, when it comes to examining the specific intensity patterns recorded in the two cases of a moving source and a moving observer we find that this reciprocity does not hold.

Simulations

The intensity fluctuations due to a moving source and observer can be simulated using the techniques described above. We shall illustrate the main results using the quasi-point source. The pattern of intensity fluctuations seen by a moving observer is given by taking a cut through an intensity plot such as given in Fig. 4. We see that when the observer moves transverse to the direction of propagation both the main intensity peak due to the proximity of the source is encountered as well as additional peaks due to focussing by the medium.

The case of a stationary observer but a moving source can be simulate by using the same realization of the random medium but changing the position of the source by a small amount each time to obtain a continuous curve for the observed intensity at different distances from the moving point source. The intensity recorded by observers situated at different distances in a random medium when the source moves is shown in Fig. 6.

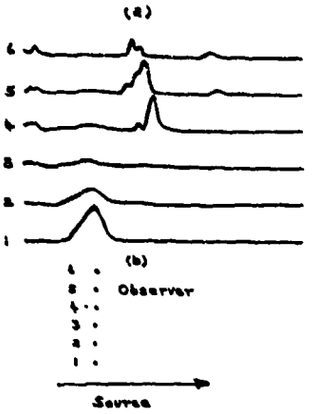


Fig. 6 (a) Intensity recorded by stationary observers at different distances in a random medium as the source moves from left to right.
(b) Positions of the observers and trajectory of the source.

The intensity records for the moving source, when compared with the corresponding records for the moving observer, show that there does not exist reciprocity between these two cases as regards the detailed intensity pattern observed. This is particularly well illustrated by the remarkable fact that for some fixed observer positions it is possible for the source to move completely across the field of view and for the observer to record no intensity peak. Not only do the observed fluctuations remain very low but also the large level of intensity due to the point source is not recorded. This is in contrast with the case of the moving observer. Here the observer always encounters both the main intensity peak due to the source as well as some subsidiary peaks due to the intensity fluctuations.

Conclusions

The necessary theory and numerical simulation techniques have been developed to allow us to represent a point source in a multiply scattering medium and treat the intensity fluctuations due to such a source.

The theory has allowed the main features of such intensity fluctuation patterns to be quantified and has enabled the simulation theory to be tested.

The question of the motion of source and observer has been treated using the above techniques and some of the main effects have been dealt with and described.

REFERENCES

[1] T.E. Ewart, "Acoustic fluctuations in the open ocean - A measurement using a fixed refracted path," J. Acoust. Soc. Am., Vol. 60, (1976), 46-59
[2] B.J. Uscinski, C. Macaskill, and T.E. Ewart, "Intensity fluctuations. Part I: Theory," J. Acoust. Soc. Am., Vol. 74, (1983), 1474-1483
[3] T.E. Ewart, C. Macaskill, and B.J. Uscinski, "Intensity fluctuations. Part II: Comparison with the Cobb Experiment," J. Acoust. Soc. Am., Vol.74, (1983), 1484-1499
[4] T.E. Ewart and S.A. Reynolds, "The Mid-Ocean Acoustic Transmission Experiment, MATE," J. Acoust. Soc. Am., Vol. 75, (1984), 785-80R
[5] L.S. Dolin, Izv. Vyssh. Ucheb. Zaved. Radiofizika, Vol. 7 (1964), 559
[6] V.I. Shishov, Izv. Vyssh. Ucheb. Zaved. Radiofizika, Vol. 11, (1968), 866
[7] C. Macaskill and B.J. Uscinski, "Propagation in waveguides containing random irregularities," Proc. R. Soc. Lond., Vol. A377, (1981), 79-98
[8] M.J. Beran, A.M. Whitman, and S. Frankenthal, J. Acoust. Soc. Am., Vol. 71, (1982), 1124
[9] B.J. Uscinski, "Intensity fluctuations in a multiple scattering medium. Solution of the fourth moment equation," Proc. R. Soc. Lond., Vol. A380, (1982), 137-169
[10] C. Macaskill, "An improved solution to the fourth moment equation for intensity fluctuations," Proc. R. Soc. Lond., Vol. A388, (1983), 461-471
[11] S. Frankenthal, A.M. Whitman, and M.J. Beran, "Two scale solutions for intensity fluctuations in strong scattering," J. Opt. Soc. Am., Vol. 1, (1984), 585
[12] R. Dashen, "Path integrals for waves in random media," J. Math. Phys., Vol 20, (1979), 894
[13] B.J. Uscinski, C. Macaskill, and M. Spivack, "Path integrals for wave intensity fluctuations in random media," J. Sound and Vibration, Vol. 106, (1986), 509-526
[14] R.J. Hill, "Comments on "Intensity fluctuations. Part I: Theory," J. Acoust. Soc. Am. (submitted)
[15] R.J. Hill, "Generalized parabolic wave equation and field moment equations for random media having spatial variations of mean refractive index," J. Acoust. Soc. Am., Vol. 77, (1985), 1742-1753
[16] C. Macaskill and T.E. Ewart, "Computer simulation of two-dimensional random wave propagation," IMA Journal of Applied Mathematics, Vol. 33, (1984), 1-15
[17] F.D. Tappert, "Wave propagation and underwater acoustics," in: Lecture Notes in Physics, Vol. 70, (1977) Berlin: Springer-Verlag, 224-287
[18] C. Macaskill, Private communication
[19] B.J. Uscinski and C. Macaskill, "Frequency cross-correlation of intensity fluctuations in multiple scattering," Optica Acta, Vol. 32, (1985), 71-89
[20] S.J. Miller and B.J. Uscinski, "Frequency cross-correlation of intensity fluctuations. Limitations of multiple scatter solutions," Optica Acta (submitted)

CROSS-FREQUENCY CORRELATION OF INTENSITY FLUCTUATIONS IN PHASE-CHANGING MEDIA

Sarah J. Miller Cambridge Ocean Acoustics Group
Dept. of Applied Mathematics and Theoretical Physics,
Silver Street, Cambridge U.K.

SUMMARY

The cross-correlation of intensity fluctuations at two different wave frequencies is a useful tool in remote sensing of sources and random phase changing media. The cross-spectrum of these fluctuations is investigated here for the model of a deeply modulated phase changing screen. An analytic expression is obtained for this spectrum and the effect of increasing frequency differences is demonstrated. Finally, the statistics of the wave fields in the far field are examined by comparing the second and fourth moments. It is shown that the relationship of these moments is consistent with the assumption that the statistics of a monochromatic field are normal in the far field, but inconsistent with wave fields of different frequencies having a joint normal distribution there.

INTRODUCTION

Observations of intensity fluctuations at two different wave frequencies are extremely useful in the remote sensing of random phase-changing media such as the ionosphere, atmospheric layers, the solar wind, and the rough surface of the ocean. If intensities only have to be recorded the method is much more robust and simple than in the case of complex amplitudes when the phases must also be measured. Cross-correlation of intensity fluctuations at two different frequencies provides some of the information obtainable from spaced observing stations, but offers the advantage that only a single station need be used.

This paper presents the theory of intensity cross-correlation for the model of a deeply modulated phase changing screen. Such a model has been long used successfully to treat most of the physical situations mentioned above ([2], [3], [4]). However, cross-frequency theory has existed only for screens with a weak phase modulation. This new extension of the theory exhibits some features of the intensity fluctuations not previously noted. Firstly, decorrelation of intensity fluctuations with distance beyond the screen is slow up to a certain distance, when it then proceeds much more rapidly. Secondly, there is a residual correlation even at quite large wave frequency differences that is surprisingly large. Thirdly, it can be demonstrated that at large distances beyond the screen the complex amplitudes of the wave field at different wave frequencies do not obey joint Gaussian statistics, contrary to what is usually believed.

These characteristics, and in particular the nature of the far field statistics of the fields, provide insight into the analogous, but more complicated, problem of the cross-correlation of intensity fluctuations produced by an extended scattering medium.

The theory presented allows cross-frequency techniques to be applied to real physical situations when the medium imposes large phase modulations on the wavefield . This should prove quite valuable and useful in diagonistic remote sensing of the ionosphere, atmosphere, solar wind, and rough ocean surface, where there is a large range of applications.

THE CROSS-SPECTRUM OF INTENSITY FLUCTUATIONS PRODUCED BY A DEEP-PHASE SCREEN

If a plane wave propagating in the positive z direction traverses a layer of medium with a randomly varying refractive index lying in the x-y plane, it will receive a phase modulation that is dependent on its wave number, k. If two phase coherent wavefields of different wave numbers k_1 and k_2 are incident on the layer they will receive different phase modulations so that as the fields propagate in free space beyond the layer, the fluctuations that develop in the intensity patterns are different for each field.

The joint intensity statistics of the fields are studied via the cross-correlation of intensity fluctuations. If the layer does not vary in the y direction this is

$$R(\xi) = \frac{\langle I_1 I_2 \rangle - \langle I_1 \rangle \langle I_2 \rangle}{\langle I_1 \rangle \langle I_2 \rangle}, \tag{1}$$

where $I_i = I(k_i, x_i, z)$ and $\xi = x_1 - x_2$. The Fourier transform of $R(\xi)$ is the cross-spectrum $F(\nu)$ which shows how the correlation is distributed over the different spatial frequencies, ν and how this is affected as the ratio of wave numbers $r = k_1/k_2$ is varied. For waves scattered by a layer of medium, which imposes a phase modulation of variance ϕ_0^2

$$F(\nu) = \frac{1}{2\pi} \int \{\exp[-\phi_0^2 h(\xi, \nu Z)] - \exp[-\phi_0^2 h(\infty, \nu Z)]\} e^{-i\nu\xi} \, d\xi, \tag{2}$$

where

$$h(\xi,\nu Z) = 1+r^{-2}-r^{-2}f(r\nu Z)-f(\nu Z)+r^{-1}[f(\xi+\tfrac{1}{2}[1+r]\nu Z) +f(\xi-\tfrac{1}{2}[1+r]\nu Z)]-r^{-1}[f(\xi+\tfrac{1}{2}[1-r]\nu Z)+f(\xi-\tfrac{1}{2}[1-r]\nu Z)]. \quad (3)$$

Here $f(\xi)$ is the normalized auto-correlation function of the phase modulation and Z is distance scaled with the Fresnel length.

When the layer imposes large phase modulations ($\phi_0^2 >> 1$), the spectrum can be evaluated [1] to give two approximate forms of $F(\nu)$; and $F_B(\nu)$ which is valid at large spatial frequencies and $F_A(\nu)$ valid at low frequencies. If the auto-correlation function is Gaussian, these large ϕ_0^2 approximations are

$$F_A(\nu) = \frac{1}{2\pi}\int \{\exp(-\phi_0^2[f''(\xi)-f''(0)][\nu Z]^2)-\exp(\ \phi_0^2 f''(0)[\nu Z]^2)\}e^{-i\xi\nu}\,d\xi, \quad \nu < Z^{-1} \quad (4)$$

and

$$F_B(\nu) = (4\pi\phi_0^2 r^{-2}|f''(0)|)^{-\frac{1}{2}}\exp\{-(1-r^{-1})^2\phi_0^2-\nu^2/\nu_w^2\}, \qquad (rZ)^{-1} < \nu$$

$$\nu_w = \begin{cases} 2\phi_0\{r^{-1}|f''(0)|\}^{\frac{1}{2}}, & Z < Z_0, \\ 2\{\phi_0 Z(1-r)\}^{-1}\{r^{-1}|f''(0)|\}^{-\frac{1}{2}}, & Z > Z_0 \end{cases} \quad (5)$$

$$Z_0 = [(1-r)r^{-1}|f''(0)|\phi_0^2]^{-1}.$$

Thus, at high frequencies, the spectrum decays like $\exp(-\nu^2/\nu_w^2)$ of width ν_w which is constant as the waves propagate away from the layer up to a distance Z_0. Beyond this, for $r < 1$, ν_w decreases and the correlation of the intensities is limited to smaller and smaller spatial frequencies as distance increases. This is illustrated in Figure 1 which shows cross-spectra for waves of acoustic frequency ratio r = 0.8 before and after $Z_0 = 0.02$ is reached.

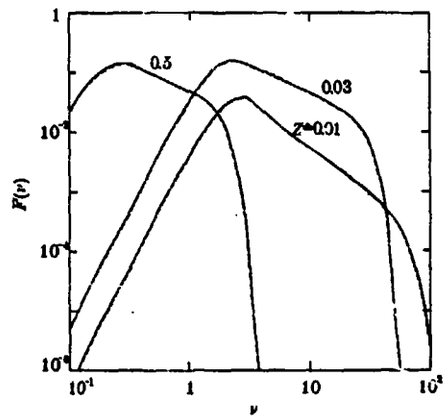


Figure 1
Cross-spectra of intensity fluctuations of acoustic frequency ratio r = 0.8.

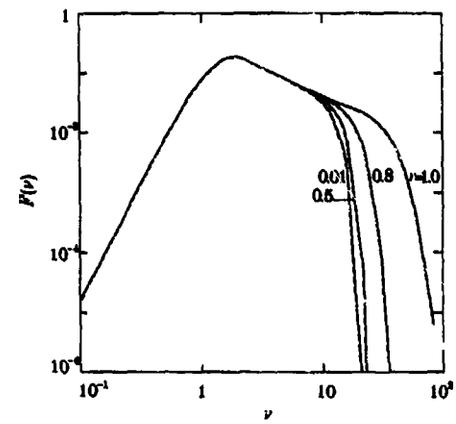


Figure 2
Cross-spectra of intensity fluctuations at scaled distance Z = 0.05.

The low frequency part of the spectrum $F_A(\nu)$ is independent of the ratio r and is therefore identical to the autospectrum which can be shown [4] to increase from the origin like ν^2 before passing through a maximum and decreasing like ν^{-4}. All the information about r is contained in $F_B(\nu)$ which becomes increasingly truncated at large ν as r decreases from one until, in the limit $r \to 0$, only $F_A(\nu)$ remains, (Figure 2). This corresponds to the fact that $F_B(\nu)$ represents the fine-detail features of the intensity fluctuations that become rapidly different as the intensity patterns arise from wavefields of increasingly different wave numbers. On the other hand, $F_A(\nu)$ corresponds to the very large features in the phase modulating layer, and hence in the intensity pattern, that retain their identity even when the incident fields have very different wave numbers.

LIMITATIONS OF GAUSSIAN STATISTICS IN THE FAR FIELD

The relation between different moments of the field beyond a random phase screen is of interest because it can yield important information about the probability distribution obeyed by the random field. It is

frequently assumed that in a random medium or beyond a deep phase screen for distances that are sufficiently large, the field has a normal distribution ([5], [6], [7]), and that, as a result, the second and fourth moments are connected in a simple manner. However, it can be shown [1] for a deep phase screen that this assumption may be valid in the case of a monochromatic wavefield but breaks down when waves of different frequencies are being considered.

If it is assumed that in the far field the complex fields $E(k_1)$ and $E(k_2)$ obey a joint normal distribution then in this region the cross-moments of intensity and those of the complex amplitude are related by

$$\langle I_1 I_2 \rangle = |\langle E_1 E_2^* \rangle|^2 + \langle I_1 \rangle \langle I_2 \rangle, \tag{6}$$

where $E_i = E(k_i, x_i, z)$. This is a relation between the cross-correlation $R(\xi)$ and the complex coherence $m(\xi) = \langle E_1 E_2^* \rangle$ and can be expressed in terms of spectra as

$$F(\nu) = \int M(\nu') M^*(\nu' - \nu)\, d\nu' \tag{7}$$

where $M(\nu)$ is the Fourier transform of $m(\xi)$ and for fields scattered by a deeply modulating screen is

$$M(\nu) = \exp\{-\tfrac{1}{2}\phi_0^2(1-r^{-1})^2 + \tfrac{1}{2}i\nu^2 Z(1-r)\} \times \frac{1}{2\pi}\int \exp\{-(\phi_0^2/r)[1-f(\xi)]\}\, e^{-i\xi\nu}\, d\xi. \tag{8}$$

If Eq. (7) were valid for all spatial frequencies ν, then its Fourier transform, Eq. (6), would be true, consistent with the joint normal assumption. However, it can be shown that Eq. (7) holds only for the part of the spectrum described by $F_B(\nu)$ and not for the part given by $F_A(\nu)$, $\nu < Z^{-1}$.

The implications of this are very different when the field is monochromatic ($r = 1$) from when r is less than one, and the two cases are illustrated in Figure 3. In the former case $F_B(\nu)$ has a width which is independent of Z, whereas the part of the spectrum described by $F_A(\nu)$ decreases as Z increases and eventually becomes a negligibly small part of the spectrum. At this point the relationship Eq. (7) can be considered to hold for all ν and its Fourier transform can be taken, giving Eq. (6), which is consistent with the assumption that the monochromatic complex field has a normal distribution at large distances from the scattering layer.

However, when the waves have distinct wave numbers, the width of $F_B(\nu)$ is constant only up to distance Z_*, beyond which it decreases at a rate comparable with the decrease in width of $F_A(\nu)$. The fraction of the spectrum described by $F_A(\nu)$ is constant as Z increases and can never be considered a negligibly small contribution. Since Eq. (7) does not hold for those frequencies described by $F_A(\nu)$, relation Eq. (6) cannot be recovered. The resulting inequality between the cross-correlation and the square of the complex coherence is incompatible with the fields having a joint normal distribution.

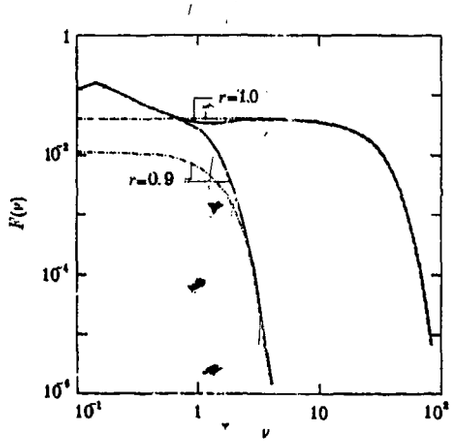


Figure 3
Auto-spectrum, r = 1, and cross-spectrum, r = 0.9, (continuous lines) at a large distance from a screen with a Gaussian autocorrelation function, and $\int M(\nu') M^*(\nu' - \nu)\, d\nu'$ (chain line); Z = 1.0.

CONCLUSION

Intensity fluctuations arising when a non-monochromatic wavefield is incident on a deeply modulating

phase-changing screen have been investigated. Examination of F(ν), the frequency cross-spectrum of the fluctuations produced by a screen with a Gaussian auto-correlation function has revealed certain general features of such intensity cross-spectra. A comparison of the complex coherence and the intensity correlation of the fields at a large distance from the screen, gives a result which is inconsistent with the assumption that the complex fields of waves with different frequencies obey a joint normal distribution.

REFERENCES

1. Miller, S.J. "Frequency cross-spectrum of intensity fluctuations produced by a deep-phase screen", Proc. R. Soc. Lond. A (to be published) 1987
2. Buckley, R. "Diffraction by a random phase screen with very large r.m.s. phase deviation", Aust. J. Phys. 24, 351, 373, 1971
3. Jakeman, E. "Fresnel scattering by a corrugated random surface with a random slope" J. Opt. Soc. Am. 72, 1034, 1982
4. Uscinski, B.J. & Macaskill, C. "Intensity fluctuations due to a deeply modulated phase screen", J. Atmos. Terr. Phys. 45, 607, 1983
5. Lee, L.C. & Jokipii, J.R. "Strong scintillations in Astrophysics: III", Astrophys. J. 202, 439, 1975
6. Lee, L.C. "Strong scintillations in Astrophysics: IV", Astrophys. J. 206, 744, 1976
7. Uscinski, B.J. & Macaskill, C. "Frequency cross-correlation of intensity fluctuations in multiple scattering", Optica Acta 32, 71, 1985

DISCUSSION

E. Jakeman, UK

Is the prediction of non-joint normal distortion at long distances a special feature of your screen problem or will it hold for other far-field speckle patterns?

Author's Reply

Non-joint Gaussian statistics is a result of two features present in the cross spectrum. 1) Decorrelation at high spatial frequencies of scattered fields of distinct wave frequencies. It is at these spatial frequencies where the individual fields obey Gaussian statistics.
2) Correlation at low spatial frequencies where each field is not normally distributed.
Provided the fields can be described in this way, the complex fields (summed over all spatial frequencies) will not obey joint Gaussian statistics. For example, this is a good description of multiply scattered fields in an extended (nondispersive) medium (Miller and Uscinski, 1936, Optica Acta 33).

A. Ishimaru, US

Are the phase fluctuations at the exit plane ($z = 0$) perfectly correlated at different frequencies?

Author's Reply

Yes, I'm assuming one of the following forms for the phase modulation (x) of a wave of frequency f. (Here c_o = speed of a wave in free space) either

a) $\phi(x) = \frac{2f}{c_o} h(x)$

Here the phase change is caused by scattering from an irregular surface of height h(x) (and with height and horizontal length scale such that this model is appropriate), or

b) The phase modulation is due to the wave passing through a thin layer of nondispersive refracting medium. Here, I'm assuming that the wave suffers no diffraction on passing through the layer and so it emerges with a pure phase change

$$(x) = \frac{2f}{c_o} (x)h$$

(x) = refractive index
h = width of layer

Modèle de propagation d'une onde électromagnétique dans un milieu ionisé à fortes fluctuations par la méthode des écrans de phase

Y. BENIGUEL, Laboratoire Central de Télécommunications
18-20 rue Grange Dame Rose - B.P.40
78141 Vélizy-Villacoublay Cedex

et B. GIBERT, Aérospatiale DEBS
Route de Verneuil - B.P. 96
78133 LES MUREAUX CEDEX
FRANCE

RESUME

Le milieu étudié (par exemple l'ionosphère aux altitudes élevées qui présente des irrégularités importantes) est défini de manière statistique par la valeur moyenne et la variance de la densité électronique et la densité spectrale des fluctuations de l'indice de propagation.

Ces données permettent de caractériser notamment la phase du signal considérée comme variable aléatoire à la traversée du milieu.

La distribution spatiale des irrégularités, liées à l'action du champ magnétique terrestre, rendant le milieu fortement anisotrope, le calcul de la propagation est difficile à effectuer si l'on spécifie simplement un profil de variation de la densité électronique moyenne dans celui-ci. La technique utilisée et exposée dans ce papier consiste à discrétiser le milieu en écrans de phase successifs de faible épaisseur, sur chacun desquels on sait calculer une solution.

La méthode de résolution sera explicitée.

Les résultats présentés porteront sur les calculs de l'amplitude du signal, de sa phase et du taux de scintillation de celui-ci.

1. INTRODUCTION

Le milieu atmosphérique présente, aux altitudes élevées (plusieurs centaines de kilomètres), des irrégularités de densité électronique causées vraisemblablement par les instabilités du plasma existant dans ces régions. L'action des champs électromagnétiques présents provoque sur les espèces du milieu des séparations de charges qui génèrent ces irrégularités.

Par exemple, dans les couches F de l'ionosphère, les inhomogénéités sont observées sous forme de bulles allongées le long des lignes de force du champ géomagnétique (latitudes équatoriales) ou de feuilles d'axe également aligné avec le champ (latitudes aurorales). Les irrégularités affectent la propagaiton des ondes électromagnétiques qui traversent ces zones ionisées créant notamment des effets de scintillation.

Si le milieu présente une structure à faibles fluctuations de densité électronique, le comportement des signaux peut être étudié par des méthodes de perturbations appliquées aux équations de propagation (méthodes globales). Dans le cas d'une structure à fortes fluctuations (par exemple perturbations ionosphériques faisant suite à une activité solaire importante) et à l'exception de quelques cas particuliers (cas d'une densité spectrale de l'indice du milieu de forme particulière), il n'existe pas de solution analytique. L'objet de cet article est de présenter une méthode numérique de résolution s'appliquant au cas général.

Ce modèle de propagation sera établi en discrétisant le milieu par la technique des écrans de phases successifs sur chacun desquels on sait calculer une solution.

Les paramètres du milieu (fluctuations de densité électronique, structure des inhomogénéités...) permettront de caractériser l'amplitude et la phase du signal qui sont assimilés ici à des variables aléatoires dont on étudiera les différents moments statistiques.

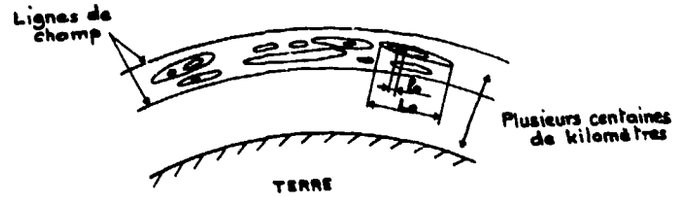
Comme exemple d'application des résultats obtenus, une comparaison intéressante est présentée avec les données expérimentales obtenues par une station sol située à Millstone Hill (USA) recevant, dans les bandes UHF-VHF, les signaux d'un satellite de poursuite (programme expérimental visant à étudier les inhomogénéités ionosphériques (années 1971-1973)).

2. DESCRIPTION DU MILIEU

Le milieu étudié contenant les inhomogénéités ionosphériques précédentes peut être défini de manière statistique à partir de la connaissance de la valeur moyenne $\langle N_e \rangle$ et de la variance $\langle \Delta N_e^2 \rangle$ de la densité électronique ainsi que de la densité spectrale spatiale de ses fluctuations $\gamma_{\Delta N_e}$.

En ce qui concerne $\gamma_{\Delta N_e}$,des travaux, type analyse des signeux transionosphériques, ont montré qu'elle dépendait principalement de deux grandeurs caractérisant le milieu, à savoir :

$q = 2\pi/\lambda$ définissant l'échelle des irrégularités du milieu (λ étant la dimension de ces irrégularités). En fait, on définit deux types d'inhomogénéités dont les dimensions et distributions sont difficiles à déterminer. Il y a des tâches de petites dimensions λ_o de l'ordre du kilomètre à une dizaine de kilomètres et des tourbillons (noyaux de surdensités) de plus grandes tailles, L_o , pouvant atteindre plusieurs dizaines, voire plusieurs centaines de kilomètres. Elles s'alignent sur le champ magnétique terrestre et peuvent se développer sur de vastes zones comme l'indique le schéma ci-après :

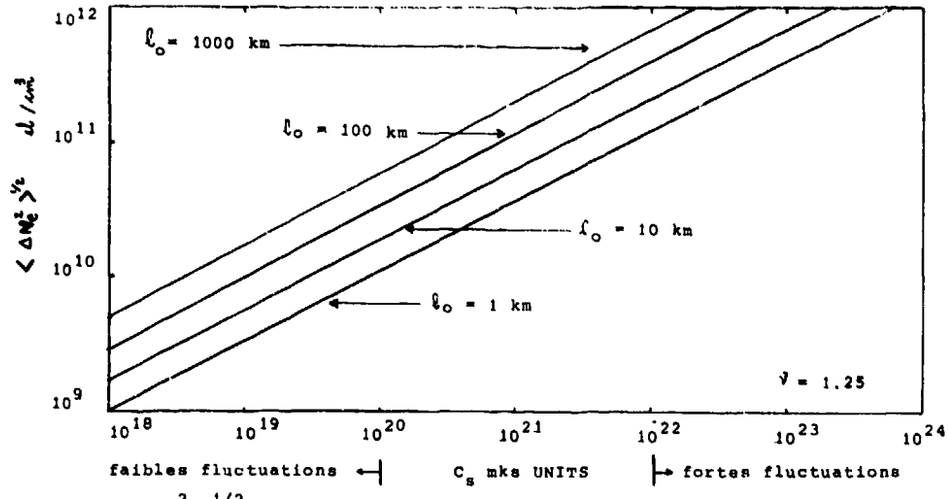


C_s caractérisant l'importance des turbulences et qui joue un rôle de constante de structure du milieu. Elle dépend des fluctuations de densité électronique $\langle \Delta N_e^2 \rangle$ et de l'échelle extérieure des irrégularités q_o ($2\pi/L_o$). Ce paramètre peut être mesuré par analyse spectrale sur un intervalle inférieur à L_o.

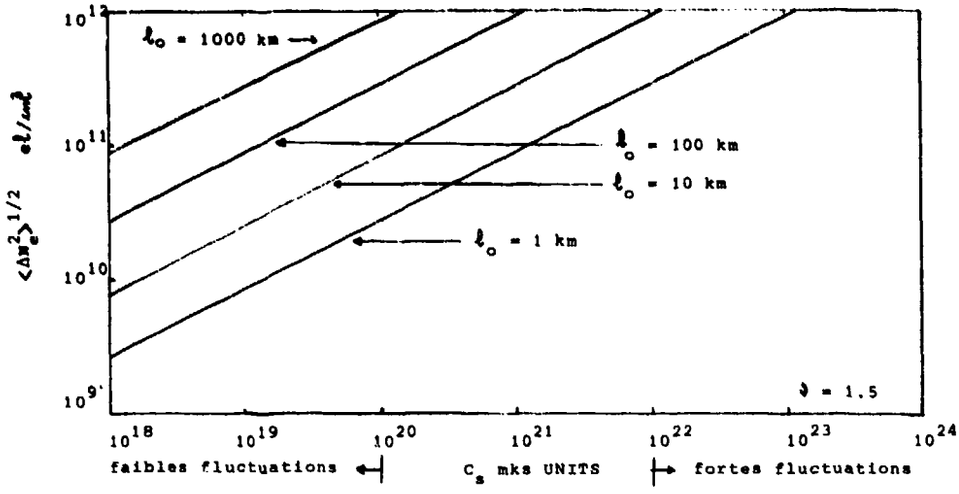
Ainsi la densité spectrale des fluctuations de densité électronique $\gamma_{\Delta N_e}$ peut être exprimée à l'aide de q et C_s par une loi en puissance.

L'exposant ν intervenant dans la loi qui est un paramètre critique du modèle varie avec l'intensité de la turbulence. Il décroit quand la turbulence augmente. Dans la plupart des cas, on prend $\nu = 1,5$.

Les figures ci-après donnent pour 2 valeurs de ν ($\nu = 1,25 - 1,5$) les fluctuations de densité électronique $\langle \Delta N_e^2 \rangle^{1/2}$ en fonction de C_s pour différentes valeurs de l'échelle extérieure des fluctuations L_o [1].



$\langle \Delta N_e^2 \rangle^{1/2}$ en fonction de C_s pour différentes valeurs de l'échelle extérieure des fluctuations $q_o = 2\pi/L_o$



$\langle \Delta N_e^2 \rangle^{1/2}$ en fonction de C_s pour différentes valeurs de l'échelle extérieure des fluctuations $q_o = 2\pi/L_o$

En général, les valeurs de C_s situées autour de 10^{10} correspondent aux faibles fluctuations alors que les valeurs atteignent 10^{12} - 10^{14} correspondent aux fortes fluctuations (par exemple une structure à fortes fluctuations dans l'ionosphère ($C_s = 10^{12}$) donne des fluctuations $\langle \Delta N_t^2 \rangle^{1/2}$ de l'ordre de 10^{11} eℓ/m^3 pour un L_o de l'ordre du kilomètre (c'est-à-dire $\langle \Delta N_e^2 \rangle^{1/2} / \langle \Delta N_e \rangle$ de l'ordre de 10% à 300 kilomètres d'altitude).

Il est intéressant de noter que dans les 2 cas de fluctuations (faibles et fortes) pour un milieu homogène et dans le cas d'une approche globale la variance de la phase du signal peut s'exprimer à l'aide des paramètres du milieu [2] c'est-à-dire :

$$\sigma_\phi^2 = 0{,}7817 \; C_n^2 \; k^2 \; L \; L_o^{5/3} \qquad (1)$$

où

C_n est la constante de structure liée à l'indice du milieu

L est l'épaisseur du milieu

k est le nombre d'ondes

Pour l'exemple précédent, $\dfrac{\langle \Delta N_e^2 \rangle^{1/2}}{\langle N_e \rangle} = 10\%$ $\qquad \sigma_\phi = 5$ rd

Ainsi les données nécessaires aux calculs relatifs aux écrans de phase, présentés dans la suite cet article sont :

f : fréquence du signal

ℓ_o : dimension des petites inhomogénéités

L_o : dimension des grandes inhomogénéités

$\langle \Delta N_e^2 \rangle$: fluctuations de densité électronique

ν : exposant de la loi en puissance de $\gamma_{\Delta N_e}$

Δz : épaisseur d'un écran de phase

3. TECHNIQUES DES ECRANS DE PHASE [illegible]

Dans le cas général, le milieu rencontré est dispersif, anisotrope et inhomogène. La technique proposée consiste à découper le milieu en N tranches homogènes qui peuvent être successives ou disjointes (écrans de phase) de faibles épaisseurs Δz. Les pertes peuvent être prises en compte de façon discrète d'un écran au suivant ainsi que l'anisotropie dans l'expression de la densité spectrale de l'indice du milieu.

Ainsi le modèle de propagation à travers l'ensemble du milieu sera construit à partir de la formulation établie sur un écran. Pour des raisons de simplicité dans la formulation, le modèle décrit dans cet article est bidimensionnel.

3.1 Formulation relative à l'écran

3.1.1 Propagation à l'intérieur d'un écran

3.1.1.1 Phase et valeur moyenne du champ en sortie de l'écran

Le calcul de la phase à la sortie de l'écran peut s'effectuer à partir des fluctuations du chemin optique à la traversée de celui-ci.

ρ étant la distance transverse par rapport à la direction z de propagation, la phase est :

$$\phi(\rho) = k \int_0^z n(\rho,z)dz \qquad (2)$$

et la fluctuation de celle-ci est :

$$\Delta\phi(\rho) = k \int_0^z \Delta n(\rho,z)dz \qquad (3)$$

Δn est la fluctuation de l'indice du milieu causée par les variations de la densité électronique ΔN_e. Δn se calcule de la façon suivante :

L'indice du milieu est donné par la relation :

$$n^2 = 1 - \frac{\omega_p^2}{\omega^2} = 1 - \frac{N_e e^2}{m\varepsilon_0\omega^2} \qquad (4)$$

où ω_p est la pulsation plasma.

Il en résulte :

$$\Delta n \# - \frac{\Delta N_e\, e^2}{2m\varepsilon_0\omega^2} \qquad (5)$$

et

$$\Delta\phi = - \frac{e^2 k}{2m\varepsilon_0\omega^2}\Delta N_T(\rho) = -\lambda r_e \Delta N_T(\rho) \quad (6)$$

avec

$$r_e = \frac{\mu_0 e^2}{4\pi m} = 2{,}82\ 10^{-15}\,m$$

$\Delta N_T = \int_0^z \Delta N_e(\rho,z)dz$ est la fluctuation totale de la densité électronique intégrée le long de la traversée de l'écran.

La largeur de l'écran est toujours grande par rapport à la longueur d'onde. Les irrégularités de l'indice engendrant les variations de phase pendant la traversée de l'écran sont multiples. Il en résulte qu'en sortie de l'écran, la phase est une variable aléatoire gaussienne centrée, ce qui permet d'écrire :

$$\langle e^{-j\phi}\rangle = e^{-\sigma_\phi^2/2} \qquad (7)$$

La variance de la phase σ se calcule à partir de la relation précédente :

$$\sigma_\phi^2 = \lambda^2 r_e^2 \; R_{\Delta N_T}(0) = 2\pi\Delta z \, \lambda^2 r_e^2 \int \gamma_{\Delta N}(K,0)dK \qquad (8)$$

où $R_{\Delta N_T}(\rho)$ est la fonction d'autocorrélation des fluctuations de densité électronique.

La valeur moyenne du signal à la sortie de l'écran de phase est par conséquent :

$$\langle E(\rho,o)\rangle = \langle E_o \; e^{-j\phi(\rho)}\rangle = E_o \; e^{-\sigma_\phi^2/2} \qquad (9)$$

Dès que l'écart type est supérieur à quelques radians, le signal présente un caractère diffus.

3.1.1.2 Synthèse de la phase

Le calcul de la phase à la sortie d'un écran est basé sur les techniques de filtrage linéaire.

On considère un filtre linéaire de réponse percussionnelle R(x) et de gain G (ν).

Si le signal à l'entrée de ce filtre est X (x), le signal en sortie Y (x), on a la relation de convolution :

$$Y(x) = R(x) * X(x) \qquad (10)$$

et

$$\gamma_Y(\nu) = |G(\nu)|^2 \; \gamma_X(\nu) \qquad (11)$$

Par conséquent, pour synthétiser un signal aléatoire de densité spectrale donnée, soit S(ν), il suffit de prendre pour signal d'entrée un signal de densité spectrale unité et de le convoluer avec un signal R(x) tel que sa transformée de Fourier (le gain du filtre) G(ν) soit donnée par la relation :

$$|G(\nu)| = [S(\nu)]^{1/2} \qquad (12)$$

Pratiquement, on dispose d'un générateur aléatoire dont les échantillons sont décorrélés et la densité spectrale est égale à 1.

S(ν) est donné par une formule analytique.

La réponse percussionnelle du filtre est la transformée de Fourier inverse de $[S(\nu)]^{1/2}$.

La phase du signal est obtenue en effectuant le produit de convolution du signal à l'entrée du filtre par la réponse percussionnelle de celui-ci

3.1.1.3 Densité spectrale du milieu

La densité spectrale de la phase s'exprime en fonction de la densité spectrale de la fluctuation de densité électronique sachant la relation (6) ou de celle de l'indice du milieu avec les équations (5) et (6). Ces trois fonctions sont identiques à un facteur près.

Deux alternatives sont habituellement retenues pour le choix de cette fonction :

- Densité spectrale de type Kolmogorov qui permet de prendre en compte les paramètres ℓ_o et L_o.

  Cette fonction a été approximée par Shkarofsky [3] à l'aide de fonctions K d'ordre fractionnaire. Le calcul de la transformée de Fourier de celle-ci (fonction d'autocorrélation de la phase) a également été effectué.

  Ce premier cas se prête mieux à une simulation numérique qu'à des développements analytiques.

- Densité spectrale approximée par une fonction puissance

  Si l'on écrit γ_ϕ sous la forme,

$$\gamma_\phi(q) = \frac{C_s}{(q_o^2 + q^2)^{\nu/2}} \qquad (13)$$

$$\text{avec } q_o = \frac{2\pi}{L_o} \qquad (14)$$

les calculs analytiques sont plus faciles à conduire dans ce cas [4].

Ces choix ne sont cependant pas équivalents vis à vis des fluctuations de phase engendrées. Le fait de prendre en compte la dimension L_o a pour effet de superposer des variations très rapides (hautes fréquences) aux variations initiales. Le résultat n'est pas identique si l'on calcule par exemple la valeur de la fonction de structure à la sortie du milieu.

3.1.1.4 Contraintes algorithmiques

Largeur de la fenêtre d'observation spatiale

Quel que soit le modèle retenu pour la densité spectrale du milieu, les fonctions correspondantes contiennent des termes en $q_x^2 + q^4$. Pour que ces fonctions soient approximées avec suffisamment de précision, il faut que q soit faible devant $1/L_o$

L'algorithme utilisé est un algorithme de FFT. La contrainte correspondante est :

$$L_f \gg L_o$$

où L_f est la largeur de la fenêtre. Il en résulte que L_f est également grand devant la largeur d'autocorrélation de la phase.

Pas spatial sur l'écran de phase

Pour un processus aléatoire gaussien, la densité des passages par zéro est :

$$\lambda_o = \frac{1}{\pi} \sqrt{\frac{-R_\phi''(0)}{R_\phi(0)}} \qquad (15)$$

La valeur moyenne du nombre de passages par zéro est :

$$\langle n_o \rangle = \frac{L_f}{2\pi} \sqrt{-\frac{R_\phi''(0)}{R_\phi(0)}} \qquad (16)$$

Pour un processus à valeur moyenne nulle, le nombre de tours de phase est environ :

$$\langle n_T \rangle = \frac{\langle n_o \rangle}{2} \frac{\sigma}{2\pi} \sqrt{2} = \frac{L_f}{8\pi^2} \sqrt{-2 R_\phi''(0)} \qquad (17)$$

Exemple : Densité spectrale de forme gaussienne.

La fonction d'autocorrélation est également de forme gaussienne, soit :

$$R_\phi(\rho) = \sigma^2 \; e^{-\rho^2/L_o^2} \qquad (18)$$

On en déduit :

$$\left(-2 R_\phi''(0) \right)^{1/2} = 2\sigma_\phi / L_o$$

$$\langle n_T \rangle = \frac{L_f \sigma_\phi}{4\pi^2 L_o} \qquad (19)$$

En prenant par exemple 4 points par période et tenant compte de la relation établie au paragraphe précédent, le nombre de points N de discrétisation doit respecter la condition :

$$N \geq \frac{\sigma_\phi}{2}$$

En choisissant une densité de type Kolmogorov, le nombre de passages par zéro de la phase est sensiblement plus grand.

3.1.2 Propagation en dehors d'un écran

Ce cas est étudié pour la propagation entre deux écrans successifs disjoints et la propagation en espace libre (diffraction).

3.1.2.1 Calcul de la diffraction

Le champ en sortie d'un écran de phase s'écrit sous la forme :

$$E(\rho,0) = E_0 \; e^{-j\phi(\rho)} \qquad (20)$$

Les pertes sont supposées nulles. Dans le cas contraire, il y aurait lieu de remplacer la constante E_0 par une fonction $E_0(\rho,\Delta z)$.

Le calcul du champ à la sortie d'un tel écran de phase peut s'effectuer en utilisant l'intégrale de Kirchhoff établie dans le cas de la diffraction de Fresnel (approximation des petits angles).

Cette intégrale a pour expression :

$$E(\rho,z) = e^{jkz} \frac{k}{2j\pi z} \int_{-\infty}^{\infty} d\rho' \; e^{jk\rho'^2/2z} E(\rho-\rho',0) \qquad (21)$$

Les simulations effectuées sur ordinateur pour le calcul de cette intégrale montrent que la convergence des résultats est très lente et qu'il faut mieux opérer une transformation de Fourier spatiale du champ à la sortie de l'écran de phase. La nouvelle intégrale à calculer est dans ce cas :

$$E(\rho,z) = e^{jkz} \int_{-\infty}^{\infty} \hat{E}(K,0) \; e^{\frac{jK^2 z}{2k} + jK\rho} dK \qquad (22)$$

où $\hat{E}(K,0)$ est la transformée de Fourier spatiale du champ à la sortie de l'écran.

L'algorithme correspondant a été validé en supposant une distribution de phase gaussienne en sortie de l'écran et en calculant le champ diffusé en différents plans transverses successifs. Ce cas équivalent à une lentille convergente a été étudié précédemment [5] et [6].

Le problème consiste par conséquent à calculer la phase en sortie de l'écran (cf. § 3.1.1.1).

3.1.2.2 Corrélation spatiale de signal

La fonction d'autocorrélation du signal,

$$\Gamma(z, \rho_1, \rho_2) = \langle E(z, \rho_1) \; E^*(z, \rho_2) \rangle$$

(où ρ_1, ρ_2 représentent les écarts entre 2 points courants et l'axe du faisceau incident dans un plan perpendiculaire à cet axe.)

peut être évaluée de plusieurs manières, par exemple à partir de l'équation de propagation dans le milieu.

Sa valeur est :

$$\Gamma(\rho) = e^{-1/2 D_\phi(z,\rho)} \qquad (23)$$

avec $\rho = \rho_1 - \rho_2$

$D_\phi(\rho)$ est la fonction de structure de la phase. Cette fonction est définie par la relation :

$$D_\phi(\beta) = \langle (\phi(\rho+\beta) - \phi(\rho))^2 \rangle \qquad (24)$$

$$= 2 [R_\phi(0) - R_\phi(\beta)] \qquad (25)$$

où $R_\phi(\beta)$ est la fonction d'autocorrélation de la phase.

La fonction D_ϕ joue un rôle important dans les calculs qui peuvent être effectués. Elle permet le calcul des moments statistiques du signal.

Son évaluation ne pose pas de problème numérique.

On en déduit notamment le rayon d'autocorrélation du signal. On peut définir celui-ci comme la distance à partir de laquelle l'affaiblissement est égal à e^{-1}.

Si R_A est cette distance, on aura simplement :

$$D_\phi(z, R_A) = 2$$

Cette fonction peut par ailleurs être majorée si l'on connait la valeur de la fonction d'autocorrélation en 0 sachant que pour un processus à bande limitée tel que $\gamma_\phi(K)$ soit nul pour $|K| > A$, on a la relation :

$$D_\phi(\rho) \leq A^2 \rho R(0) \qquad (26)$$

La constante A s'obtient à partir de la densité spectrale de la phase.

3.1.2.3 Taux de scintillation

Le taux de scintillation est défini par la relation :

$$S_4^2 = \frac{\langle I^4 \rangle - \langle I \rangle^4}{\langle I \rangle^4} \qquad (27)$$

La variance de l'intensité du signal s'obtient en intégrant la densité spectrale de celui-ci dont la valeur est :

$$\gamma_I(K_\perp) = \frac{1}{(2\pi)^2} \iint \exp\left(-g(\bar{\eta}_1, \bar{K}_\perp \frac{z}{k})\right) \exp\left(-j\bar{K}_\perp \cdot \bar{\eta}_1\right) d^2\eta \qquad (28)$$

avec

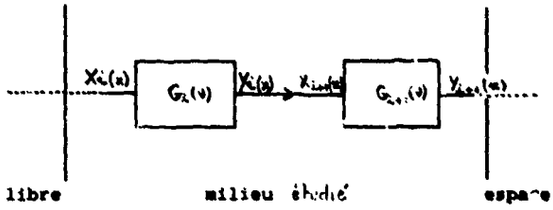
$$g(\bar{\eta}_1, \bar{\eta}_2) = D_\phi(\bar{\eta}_1) + D_\phi(\bar{\eta}_2) - 1/2\, D_\phi(\bar{\eta}_1 + \bar{\eta}_2) - 1/2\, D_\phi(\bar{\eta}_1 - \bar{\eta}_2) \qquad (29)$$

Connaissant la valeur de la fonction de structure en un point donné, les calculs de $\gamma_I(K_\perp)$ et par suite celui de S_4^2 s'effectuent sans difficultés.

3.2 Généralisation au cas de N écrans successifs

Comme il est indiqué aux paragraphes 2 et 3, les distributions des inhomogénéités conduisent à considérer plusieurs écrans disjoints ou non.

Pour effectuer le calcul des caractéristiques du signal après traversée complète du milieu, les étapes successives doivent être effectuées comme l'indique le diagramme suivant :



$X_i(x)$ et $Y_i(x)$ représentent les signaux à l'entrée et à la sortie de l'écran i de gain $G_i(\nu)$.

Propagation à l'intérieur du milieu ionisé

Les calculs suivants sont effectués à chaque étape :

- évaluation de la phase
- transformée de Fourier du champ (amplitude et phase) en sortie de chaque écran
- calcul de la diffraction (écrans disjoints)

Propagation en espace libre

La connaissance du champ en sortie du dernier écran permet celui du champ diffracté en un point quelconque de l'espace libre.

La connaissance de la phase en ce point permet donc d'évaluer les différents paramètres du signal (corrélation spatiale, taux de scintillation etc...)

Les pertes du milieu peuvent être prises en compte de façon discrète en modifiant l'amplitude du champ en sortie d'écran, si l'on connait la loi de répartition de l'énergie autour de l'axe de propagation. Il en résulte une modification du champ diffracté en espace libre.

Remarque

En fait les inhomogénéités du milieu ne sont en général pas stationnaires. La structure du milieu varie avec le temps. L'algorithme développé permet d'évaluer la corrélation temporelle du signal qui se déduit de la corrélation spatiale si on connait la vitesse de déplacement des irrégularités.

4. APPLICATION A UNE PROPAGATION SATELLITE-STATION SOL (expérience Millstone Hill)

Le milieu étudié correspond à l'ionosphère aux altitudes élevées (300 km, zone des inhomogénéités).

Les données sont les suivantes :

- épaisseur de la zone des inhomogénéités : 50 km
- taille des turbulences prises en compte : 1 km
- fréquence du signal 150 MHz
- $\langle N_e \rangle = 10^{12} e\ell/m^3$; $\sigma_{N_e} = 0.1 \langle N_e \rangle$

La densité spectrale de l'indice du milieu est de forme gaussienne.

En sortie de l'écran

Deux calculs analytiques peuvent être effectués :

- approche globale (formule (1) du paragraphe 2)
  Le résultat est $\sigma_\phi = 4.9$ radians.
- approche par la théorie des écrans développée dans cet article pour une propagation normale au champ magnétique (un seul écran).

On obtient : $$\sigma_\phi^2 = \sqrt{\pi}\ (r_e \lambda)^2\ L_\zeta\ \Delta z\ \langle \Delta N_e^2 \rangle \qquad (27)$$

$\sigma_\phi = 5.3$ radians

La figure 1 montre la variation de la phase du signal dans le plan tranverse à la direction de propagation.

L'écart type recalculé est égal à 5,4 radians. La fonction de structure qui s'en déduit est représentée sur la figure 2.

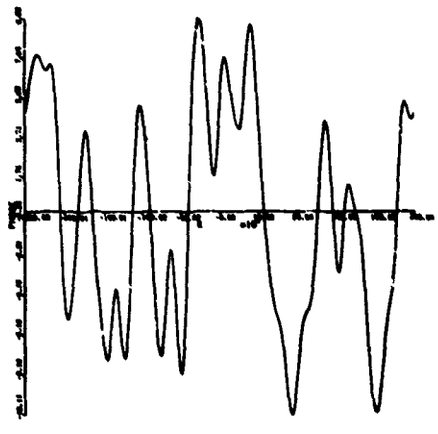


Figure 1
Phase du signal à la sortie de l'écran de phase

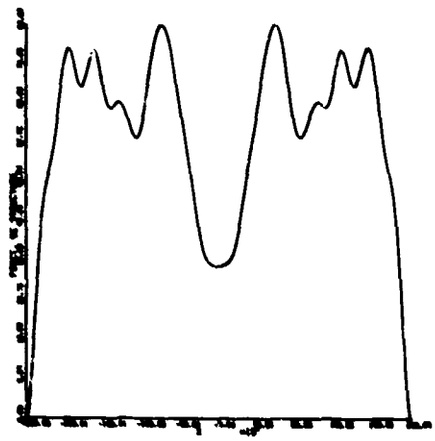


Figure 2
Fonction de structure à la sortie de l'écran de phase

Au niveau du sol

L'expérience effectuée à Millstone Hill a montré que l'écart type de la phase avait une valeur très proche de celle calculée en sortie de l'écran.
Ce résultat se retrouve analytiquement (hypothèse des faibles fluctuations). Dans cet exemple la scintillation mesurée est voisine de 1.2.

Les résultats correspondants obtenus par la technique des écrans de phase sont présentés sur les figures 3 à 5 (à savoir l'amplitude, la phase et la fonction de structure de la phase). L'écart type de la phase est également très proche de la valeur obtenue en sortie de l'écran et la scintillation est voisine de l'unité.

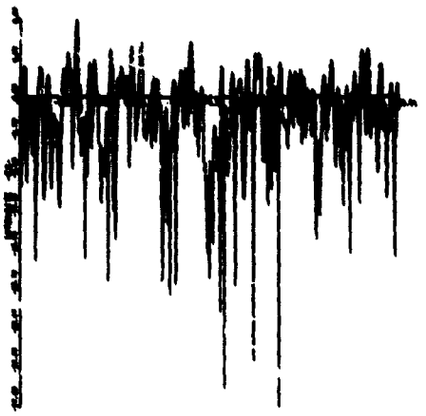


FIGURE 3
Amplitude du signal dans le plan d'observation

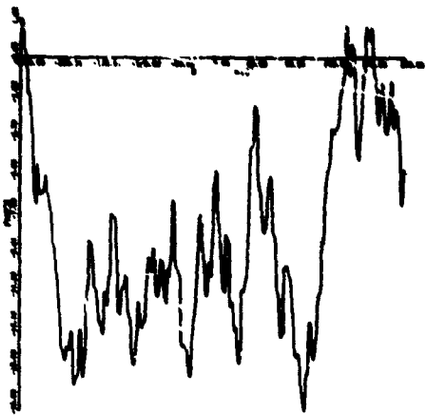


FIGURE 4
Phase du signal dans le plan d'observation

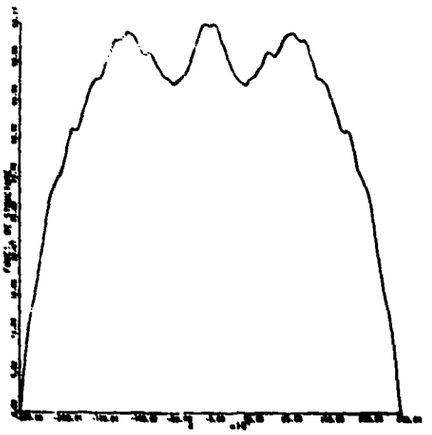


FIGURE 5
Fonction de structure dans le plan d'observation

5. CONCLUSION

La technique développée permet la calcul des caractéristiques d'un signal après propagation à l'intérieur d'un milieu aléatoire puis en espace libre. Elle tient compte par conséquent des deux aspects : diffusion à l'intérieur du milieu puis diffraction.

Certains recoupements ont été effectués avec des résultats de mesure publiés dans la littérature. Les ordres de grandeur obtenus sont comparables.

L'intérêt d'une telle méthode est double :

- elle permet notamment de prendre en compte le caractère inhomogène et anisotrope du milieu. Celui-ci est dans ce cas découpé en tranches homogènes et la technique indiquée s'applique successivement à chacune d'elles.

- elle permet le calcul des moments du signal diffracté en tout point de l'espace. Ceux-ci sont difficilement accessibles analytiquement, notamment dans le cas des fortes fluctuations.

6. BIBLIOGRAPHIE

[1] K.C. YEH, C.H. LIU "Statistical properties of transionospherically propagated radio signals under the intense scintillations conditions" AGARD C.P.284 Londres (1980).

[2] A. ISHIMARU "Wave Propagation and Scattering in Random Media". Academic Press (1978).

[3] I.P. SHKAROFSKY "Generalized turbulence space-correlation and wave-number spectrum function pairs" Canadian Journal of Physics. Vol 46 pp 2133-2153 (1968).

[4] C.L. RINO, V.H. GONZALEZ,A.R. HESSING "Coherence bandwidth loss in transionospheric radio propogation" Radio Science Mars-Avril 1981.

[5] R. BUCKLEY "Diffraction by a random phase-changing screen : a numerical experiment" Journal of Atmospherical and Terrestrial Physics. Vol 37 pp 1431-1446 (1975).

[6] D.L. KNEPP "Multiple Phase-screen Calculation of the temporal behavior of Stochastic waves" P.I.E.E.E. Juin 1983.

[7] J.V. EVANS Millstone Hill "Radar propagation studies. Scientific results" M.I.T. Lincoln Laboratories, Technical report 509 13/11/73.

ON THE APPLICABILITY OF CONTINUOUS SCATTERING METHODS TO DISCRETE SCATTERING PROBLEMS

by
Ioannis M. Besieris
Department of Electrical Engineering
Virginia Polytechnic Institute and State University
Blacksburg, Virginia 24061
U.S.A.

SUMMARY

The equivalence between continuous and discrete scattering modeling has been examined at two statistical levels: (1) the direct interaction/ladder approximation (continuous) - Twersky approach (discrete); (2) the first order smoothing approximation (continuous, discrete). Full first and second order moment equivalence has been established only at the level of the first order smoothing (or bilocal) approximation and, even then, for soft scatterers with weak transition operators.

1. INTRODUCTORY REMARKS

The discussion in the sequel will be restricted to scalar transverse electromagnetic or longitudinal acoustic cw propagation phenomena in a random channel; they are governed by the stochastic Helmholtz equations

$$\nabla^2 u(\vec{r};\alpha) + k^2 \epsilon_r(\vec{r};\alpha) u(\vec{r};\alpha) = 0, \tag{1}$$

$$\nabla^2 u(\vec{r};\alpha) + k^2 (1 - \sum_{i=1}^{N} V_i') u(\vec{r};\alpha) = 0 \tag{2}$$

for the continuous and the discrete case, respectively. Here, $u(\vec{r};\alpha)$ denotes the random wave field, k is a reference wavenumber and $\alpha \in A$, (A,F,P) being an underlying probability measure space. The quantity $\epsilon_r(\vec{r};\alpha)$ in Eq.(1) is the stochastic relative permittivity and the "operator" V_i' in Eq.(2) represents the effect of the ith scatterer.

Various techniques (widely diverging for the most part) have been developed for the study of continuous and discrete scattering. Since the continuous scattering problem is at present more fully developed (e.g., with respect to computation of higher order moments), the question arises whether techniques pertinent to the continuous scattering problem can be transfered to the discrete one; alternatively, whether a study is feasible of discrete random scattering by means of continuous medium modeling. An answer to this question would be important in connection to remote sensing applications [Tsang et al., 1985; Yang, 1987].

2. BASIC OBSERVATIONS

In principle, scattering of waves from a random distribution of correlated discrete scatterers can be studied by means of a continuous medium model provided that the full probabilistic structure of the "effective" permittivity "operator" $\epsilon_r(\vec{r};\alpha) = 1 - \Sigma V_i'$ is constructed from the specified distribution of discrete scatterers [Stratonovich, 1961; Barabanenkov, 1976]. Such a procedure has been used recently to examine the propagation of waves through Poisson-distributed aerosols [Barabanenkov and Ozrin, 1976; Svirkunov, 1977; Krutikov, 1980; Lukin, 1981].

Except for a few special cases, the study of continuous scattering is based on perturbative techniques [e.g., on the smallness of the fluctuating part of $\epsilon_r(\vec{r};\alpha)$]. When such techniques are transported uncritically to the discrete case, they may lead to significant errors since they presuppose a smallness in the potential operators V_i' (soft scatterers), while in an actual physical situation the smallness lies elsewhere, e.g., in the transition operator T_i' of the ith scatterer.

In realistic physical situations, an equivalence between continuous and discrete scattering models can be studied effectively only on the basis of the first and second moments. Whether such an equivalence exists or not depends on the actual physical parameters which, in turn, dictate the level of statistical analysis and the choice of particular statistical methods.

We have studied the feasibility of such an equivalence at two statistical levels: (1) the direct interaction/ladder approximation (continuous) - Twersky approach (discrete); (2) the first order smoothing approximation (continuous, discrete).

Our main conclusion is that although a first order moment equivalence is feasible at the direct interaction - Twersky level, albeit for soft scatterers, full first and second order moment equivalence is possible, in general, only at the level of the first order smoothing approximation and, even then, for scatterers which are soft and are characterized by weak transition operators.

3. CONTINUOUS MEDIUM MODELING OF DISCRETE SCATTERING WITHIN THE FRAMEWORK OF THE DIRECT INTERACTION/LADDER APPROXIMATION

It is well known that the first order smoothing approximation, when applied to discrete scattering

problems, fails to yield correct results regarding the damping of coherent waves. Correct results along these lines are obtained on the basis of the Foldy-Lax-Twersky formalism. This formalism, especially the Twersky approach, has been formally shown to correspond, at least at the level of the first moment and for weak scatterers, to Kraichnan's direct interaction approximation for continuous media characterized by strong statistical fluctuations or long range correlations. It is our specific intent in this section to discuss this correspondence in the first order coherence functions and to point out a distinct dissimilarity that exists in the second order coherence functions when the latter are derived by the ladder approximation for the continuous case and the Twersky approach for the discrete one.

First and Second Order Coherence Functions for Scalar Waves in a Random Continuum

The relative permittivity $\epsilon_r(\vec{r};\alpha)$ entering into Eq.(1) is decomposed into a deterministic (or regular) refraction part and a statistically varying term; specifically,

$$\epsilon_r(\vec{r};\alpha) = \epsilon_{rd}(\vec{r}) + \epsilon_{rf}(\vec{r};\alpha). \tag{3}$$

The fluctuating part is assumed to be a zero-mean Gaussian process with autocorrelation function

$$\langle \epsilon_{rf}(\vec{r}_2;\alpha)\epsilon_{rf}(\vec{r}_1;\alpha)\rangle = B(\vec{r}_2,\vec{r}_1). \tag{4}$$

The Dyson equation for the first moment $\langle u(\vec{r};\alpha)\rangle$ can be derived [Besieris and Kohler, 1981] using the Donsker-Furutsu-Novikov formula together with the ladder approximation:

$$[\nabla^2 + k^2\epsilon_{rd}(\vec{r})]\langle u(\vec{r};\alpha)\rangle = \int_{R^3} d\vec{r}'k^4\langle G(\vec{r},\vec{r}';\alpha)\rangle B(\vec{r},\vec{r}')\langle u(\vec{r}';\alpha)\rangle; \tag{5a}$$

$$[\nabla^2 + k^2\epsilon_{rd}(\vec{r})]\langle G(\vec{r},\vec{r}';\alpha)\rangle = \delta(\vec{r}-\vec{r}') + \int_{R^3} d\vec{r}''k^4\langle G(\vec{r},\vec{r}'';\alpha)\rangle B(\vec{r},\vec{r}'')\langle G(\vec{r}'',\vec{r}';\alpha)\rangle. \tag{5b}$$

The quantity $\langle G(\vec{r},\vec{r}';\alpha)\rangle$ is the ensemble average of the stochastic Green's function associated with the Helmholtz equation (1). In the framework described above [known as the Kraichnan direct interaction approximation (Frisch, 1968)], Eq.(5b) is a nonlinear integrodifferential expression for the mean Green's function. If, on the other hand, the mass operator in the kernel of Eq.(5b) is computed on the basis of the solution to the unperturbed problem

$$[\nabla^2 + k^2\epsilon_{rd}(\vec{r})]G_0(\vec{r},\vec{r}') = \delta(\vec{r}-\vec{r}'), \tag{6}$$

Eq.(5b) reduces to a linear equation for $\langle G(\vec{r},\vec{r}';\alpha)\rangle$, at a level of an approximation known as the first order smoothing [see Keller, 1964; Frisch, 1968].

The ladder approximation can be used to derive the Bethe-Salpeter equation for the mutual coherence function $\Gamma(\vec{r}_1;\vec{r}_2) = \langle u^*(\vec{r}_1;\alpha)u(\vec{r}_2;\alpha)\rangle$ [Besieris and Kohler, 1981]:

$$[(\nabla_1^2-\nabla_2^2) + k^2\epsilon_{rd}(\vec{r}_1) - k^2\epsilon_{rd}(\vec{r}_2)]\Gamma(\vec{r}_1,\vec{r}_2) = \int_{R^3} d\vec{r}'[-k^4B(\vec{r}_2,\vec{r}') + k^4B(\vec{r}_1,\vec{r}')]\langle G^*(\vec{r}_2,\vec{r}';\alpha)\rangle\Gamma(\vec{r}_1,\vec{r}') + \int_{R^3} d\vec{r}'[-k^4B(\vec{r}_2,\vec{r}') + k^4B(\vec{r}_1,\vec{r}')]\langle G(\vec{r}_1,\vec{r}';\alpha)\rangle\Gamma(\vec{r}',\vec{r}_2). \tag{7}$$

It should be noted that the second moment is coupled functionally to the first one via the mean Green's function and its complex conjugate.

First and Second Order Coherence Functions for Scalar Waves in a Random Distribution of Pair-Correlated Discrete Scatterers

The derivation of the Dyson equation for the mean field $\langle u(\vec{r};\alpha)\rangle$ and the Bethe-Salpeter equation for the mutual coherence function $\Gamma(\vec{r}_1,\vec{r}_2)$ associated with the discrete scattering problem [cf. Eq.(2)] is based on the Twersky [1964] procedure. The basic underlying assumptions are the following: (1) third order scattering by two scatterers, fourth order scattering by three scatterers, etc., is ignored (essentially the Twersky assumption); (2) all scatterers have the same shape, size and orientation distributions; (3) only pair correlations are considered; all contributions from higher order correlations are neglected; (4) the number N of scatterers in a volume is infinite; (5) the scattering channel is tenuous, i.e., the distance between two scatterers is much greater than a reference wavelength; (6) the Rayleigh-Debye condition holds, viz., $[\epsilon_{ri}(\vec{r}) - 1]kD_i \ll 1$, where D_i is a typical dimension of the ith scatterer, $\epsilon_{ri}(\vec{r})$ is the relative permittivity of the ith scatterer (assumed to be surrounded by free space), and k is a reference wavenumber; (7) anisotropic scattering effects are ignored.

Under the aforementioned conditions, the Dyson equation assumes the following form [Tsolakis et al., 1985]:

$$[\nabla^2 + k^2 + 4\pi f(k)\rho(\vec{r})]\langle u(\vec{r};\alpha)\rangle = -4\pi f(k)\int_{R^3} d\vec{r}'\langle\langle G(\vec{r},\vec{r}')\rangle\rangle B(\vec{r},\vec{r}')\langle u(\vec{r}';\alpha)\rangle; \tag{8a}$$

$$[\nabla^2 + k^2 + 4\pi f(k)\rho(\vec{r})]\langle\langle G(\vec{r},\vec{r}')\rangle\rangle = -4\pi f(k)\delta(\vec{r}-\vec{r}') - 4\pi f(k)\int_{R^3} d\vec{r}''\langle\langle G(\vec{r},\vec{r}'')\rangle\rangle B(\vec{r},\vec{r}')\langle\langle G(\vec{r}'',\vec{r}')\rangle\rangle. \tag{8b}$$

Here, $\langle\langle\cdot\rangle\rangle$ denotes configurational averaging (over size, shape and orientation distributions), $\rho(\vec{r})$ is the particle density function, $B(\vec{r}_2,\vec{r}_1)$ is the pair correlation function and $f(k)$ is a configurationally averaged scattering coefficient.

At the same order of approximation, the Bethe-Salpeter equation for the second moment can be written down as follows [Tsolakis et al., 1985]:

$$\begin{aligned}[(\nabla_1^2 - \nabla_2^2) + 4\pi f(k)\rho(\vec{r}_1) - 4\pi f^*(k)\rho(\vec{r}_2)]\Gamma(\vec{r}_1,\vec{r}_2) &= -4\pi[f(k)\rho(\vec{r}_1)\langle\langle G^*(\vec{r}_2,\vec{r}_1)\rangle\rangle\Gamma(\vec{r}_1,\vec{r}_1) \\ &\quad - f(k)\rho(\vec{r}_2)\langle\langle G(\vec{r}_1,\vec{r}_2)\rangle\rangle\Gamma(\vec{r}_2,\vec{r}_2)] \\ &\quad - 4\pi\int_{R^3} d\vec{r}'[f(k)B(\vec{r}_1,\vec{r}') - f^*(k)B(\vec{r}',\vec{r}_2)] \\ &\quad \times [\langle\langle G(\vec{r}_1,\vec{r}')\rangle\rangle\Gamma(\vec{r}',\vec{r}_2) + \langle\langle G^*(\vec{r}_2,\vec{r}')\rangle\rangle\Gamma(\vec{r}_1,\vec{r}')].\end{aligned} \tag{9}$$

An Important Remark

The functional form of the Dyson equation (8) is analogous to that derived earlier [cf. Eq.(5)] for scalar wave propagation in a continuous medium with fluctuations in the permittivity which are distributed according to a normal law and with a deterministic profile directly linked to the number of scatterers per unit volume. It is clear in this case that an equivalence between continuous and discrete scattering modeling can be achieved.

No counterpart to the first (collapsed) term on the right-hand side of the Bethe-Salpeter equation (9) exists in the analogous equation [cf. Eq.(7)] for the random continuous case. This severe dissimilarity precludes the possibility for a second moment equivalence between discrete and continuous scattering modeling at the level of the ladder/Twersky approximation.

4. CONTINUOUS MEDIUM MODELING OF DISCRETE SCATTERING WITHIN THE FRAMEWORK OF THE FIRST ORDER SMOOTHING APPROXIMATION

We shall show in this section that a complete first and second moment equivalence between continuous and discrete scattering can be established at the level of the first order smoothing approximation, albeit under very stringent assumptions. Toward this goal, we shall follow a procedure outlined by Keller [1964].

The Dyson and Bethe-Salpeter Equations for a Random Continuous Medium

We consider the following generalization of the stochastic equation (1):

$$M(\alpha;\varepsilon)u(\vec{r};\alpha;\varepsilon) = 0. \tag{10}$$

The quantities α and ε entering into the operator M are respectively the realization index defined earlier and a small dimensionless parameter.

The operator M is expanded next in powers of ε as follows:

$$M(\alpha;\varepsilon) = L + \varepsilon L_1(\alpha) + \varepsilon^2 L_2(\alpha) + O(\varepsilon^3). \tag{11}$$

L is the deterministic part of M and L_1, L_2 are statistically fluctuating operators. In this sense, the parameter ε is a measure of the strength of the random fluctuations of the medium.

Within the framework of the first order smoothing approximation, the coherent field $\langle u(\vec{r};\alpha;\varepsilon)\rangle$ satisfies the Dyson equation

$$\{L + \varepsilon\langle L_1\rangle + \varepsilon^2[\langle L_1\rangle L^{-1}\langle L_1\rangle - \langle L_1 L^{-1} L_1\rangle + \langle L_2\rangle]\}\langle u\rangle = 0 + O(\varepsilon^3), \tag{12}$$

where L^{-1} denotes the inverse of the background operator L. Similarly, the second order coherence

function $\Gamma(\vec{r}_1,\vec{r}_2;\varepsilon) = \langle u^*(\vec{r}_1;\alpha;\varepsilon)u(\vec{r}_2;\alpha;\varepsilon)\rangle$ obeys the Bethe-Salpeter equation

$$\langle u^*u\rangle = \langle u^*\rangle\langle u\rangle + \varepsilon^2\{\langle L^{-1}L_1L^{*-1}L_1^*\rangle - L^{-1}\langle L_1\rangle L^{*-1}\langle L_1^*\rangle\}\langle u^*u\rangle = 0 + O(\varepsilon^3). \tag{13}$$

In this expression, the conjugated quantities should be considered as functions of $\vec{r}_1$ and the unconjugated ones as functions of $\vec{r}_2$.

The Dyson and Bethe-Salpeter Equations for Discrete Scattering

Equation (2) is rewritten slighly as follows:

$$Lu - \sum_{i=1}^{N} \bar{V}_i' u = 0; \tag{14a}$$

$$L = \nabla^2 + k^2; \quad \bar{V}_i' = k^2 V_i'. \tag{14b}$$

A transition operator T_i' is also defined in terms of the field u^i incident on the ith scatterer:

$$T_i' u^i = \bar{V}_i' u; \tag{15a}$$

$$u^i = u - L^{-1}\bar{V}_i' u. \tag{15b}$$

Consider first the situation where the transition operator is "small" in the following sense:

$$T_i' = \varepsilon T_i. \tag{16}$$

Eq.(14) assumes then the form

$$[L - \varepsilon \sum_{i=1}^{N} T_i + \varepsilon^2 \sum_{i=1}^{N} T_i L^{-1} T_i + O(\varepsilon^3)]u(\vec{r};\alpha;\varepsilon) = 0. \tag{17}$$

By comparison with Eq.(11), the following associations can be made:

$$L_1 = -\sum_{i=1}^{N} T_i, \quad L_2 = \sum_{i=1}^{N} T_i L^{-1} T_i. \tag{18}$$

When all the transition operators T_i have the same mean and under the assumption that $\langle T_i L^{-1} T_j\rangle$ is independent of i and j when $i \neq j$ and independent of i when $i = j$, the application of the first order smoothing approximation yields the following equations for the first two moments:

$$\{L - \varepsilon N\langle T_1\rangle - (\varepsilon N)^2[(1 - N^{-1})\langle T_1 L^{-1} T_2\rangle - \langle T_1\rangle L^{-1}\langle T_1\rangle]\}\langle u\rangle = 0 + O(\varepsilon^3). \tag{19}$$

$$\langle u^*u\rangle = \langle u^*\rangle\langle u\rangle + \varepsilon^2\{N\langle L^{-1}T_1L^{*-1}T_1^*\rangle + N^2(1 - N^{-1})\langle L^{-1}T_1L^{*-1}T_2^*\rangle$$
$$- N^2 L^{-1}\langle T_1\rangle L^{*-1}\langle T_1^*\rangle\}\langle u^*u\rangle + O(\varepsilon^3). \tag{20}$$

Keller [1964] has shown that for uniformly distributed (ρ constant) and pair-correlated scatterers, the mean field $\langle u\rangle$ obeys an equation identical to the one based on the Twersky approach [cf. Eq.(8a)], except for the replacement in the latter of the configurationally averaged Green's function $\langle\langle G\rangle\rangle$ by the free space Green's function G_0. It is relatively simple to show that this statement applies also to the second moment; that is, Eq.(20) leads to Eq.(9), with $\langle\langle G\rangle\rangle$ replaced by G_0.

The application of the first order smoothing method to the discrete scattering problem under the assumption of weak transition operators has led us to a "partial" equivalence with the Twersky technique. Full first and second moment equivalence is achieved only in the absence of pair correlations.

In addition to the assumption of weak transition operators, let us further specify that the scatterers are soft, viz., $\bar{V}_i' = \varepsilon V_i$. It follows, then, that

$$T_i = V_i + \varepsilon V_i L^{-1} V_i + O(\varepsilon^2), \tag{21}$$

$$L_1 = \sum_{i=1}^{N} V_i, \quad L_2 = 0. \tag{22}$$

When the $\langle V_i\rangle$ is independent of i, while $\langle V_i L^{-1} V_j\rangle$ is independent of i and j for $i \neq j$ and is independent of i for $i = j$, the application of the first order smoothing approximation leads to the following equations for the first two moments:

$$\{L - \varepsilon N\langle V_1\rangle - (\varepsilon N)^2[\langle V_1 L^{-1} V_2\rangle - \langle V_1\rangle L^{-1}\langle V_1\rangle]\}\langle u\rangle = 0 + O(\varepsilon^3), \text{ N large}, \tag{23}$$

$$\langle u^*u\rangle = \langle u^*\rangle\langle u\rangle + \varepsilon^2\{N\langle L^{-1}V_1L^{*-1}V_1^*\rangle + N^2\langle L^{-1}V_1L^{*-1}V_2^*\rangle$$
$$- N^2 L^{-1}\langle V_1\rangle L^{*-1}\langle V_1^*\rangle\}\langle u^*u\rangle = 0 + O(\varepsilon^3), \text{ N large}. \tag{24}$$

These two expressions can be derived indirectly by substituting the transition operators T_i given in Eq.(21) into Eqs.(19) and (20), or directly by using Eq.(21) in conjunction with Eqs.(12) and (13). It is clear, then, that a full first and second order moment equivalence between continuous and discrete

scattering can be achieved at the level of the first order smoothing approximation provided that the scatterers are soft and have weak transition operators.

5. CONCLUDING REMARKS

Although a strict equivalence between continuous and discrete scattering modeling may not be feasible in an actual physical situation, one can use continuous scattering perturbative techniques to discrete scattering problems provided that small physical parameters can be identified. On the other hand, the observation that the Twersky approach corresponds loosely to the direct interaction/ladder formalism which was originally meant for strongly fluctuating continuous media, or nonlinear phenomena (e.g., Navier - Stokes equation, Vlasov plasmas, etc.,) points out the need for the generation of discrete scattering techniques which are distinct from those developed for continuous scattering.

6. REFERENCES

Barabanenkov, Yu. N., "Multiple scattering of waves by ensembles of particles and the radiation transport," Sov. Phys. - Usp., 18, 673-689 (1976).

Barabanenkov, Yu. N. and V. D. Ozrin, "Contribution to the statistical theory of the transfer of nonsteady radiation in a medium of variable scatterers," Izv. Vyssh. Uchebn. Zaved. Radiofiz., 20, 712-720 (1976).

Besieris, I. M. and W. E. Kohler, "Two-frequency radiative transfer equation for a statistically inhomogeneous and anisotropic absorptive medium," in Multiple Scattering and Waves in Random Media, edited by P. L. Chow, W. E. Kohler and G. C Papanicolaou (North-Holland, Amsterdam, 1981).

Frisch, U., "Wave propagation in random media," in Probabilistic Methods in Applied Mathematics, Vol. 1, edited by A. T. Bharucha-Reid (Academic Press, Orlando, FL, 1968).

Keller, J. B., "Stochastic equations and wave propagation in random media," Proc. Symp. Appl. Math., 16, 145-170 (1964).

Krutikov, V. A., "Calculation of the statistical characteristics of optical radiation in a medium with large-scale discrete inhomogeneities," Izv. Vyssh. Uchebn. Zaved. Radiofiz., 23, 1434-1446 (1980).

Lukin, I. P., "Random displacements of optical beams in an aerosal atmosphere," Izv. Vyssh. Uchebn. Zaved. Radiofiz., 24, 144-150 (1981).

Stratonovich, R. L., Selected Topics in the Theory of Fluctuations in Radiotechnology (Sov. Radio, M., 1961).

Svirkunov, P. N., "Propagation of electromagnetic radiation in a Poissonian randomly inhomogeneous medium," Izv. Vyssh. Uchebn. Zaved. Radiofiz., 20, 399-405 (1977).

Tsang, L., J. A. Kong and R. T. Shin, Theory of Microwave Remote Sensing (Wiley-Interscience, New York, 1985).

Tsolakis, A. I., I. M. Besieris and W. E. Kohler, "Two-frequency radiative transfer equation for scalar waves in a random distribution of discrete scatterers with pair correlations," Radio Sci., 20, 1037-1052 (1985).

Twersky, V., "On propagation in random media of discrete scatterers," Proc. Am. Math. Soc. Symp. Stochastic Processes Math. Phys. Eng., 16, 84-116 (1964).

Yang, C. C., "Scattering intensity from a turbulent medium with suspended particles," in Multiple Scattering of Waves in Random Media and Random Rough Surfaces, edited by V. V. Varadan and V. K. Varadan (The Pennsylvania State University Press, University Park, PA, 1987).

DISCUSSION

A. Ishimaru, US

In many practical situations, continuum often has large scale sizes while particle sizes can be comparable to wavelength. Could you comment on the importance of sizes.

Author's Reply

Multiscale problems, especially those involving an admixture of continuous and discrete scattering channels, cannot be handled easily by presently available statistical methods. Some progress has been made in connection with the problem of turbulence intermittences (two-scale continuous scattering situation); also, in the area of wave propagation through soft aerosols surrounded by a random continuum, especially in the case where the scales involved are large compared with wavelength. Much more work needs to be done in physical situations where some of the scale sizes are comparable to wavelength.

P. L. Chow, US

For discrete scattering problems, has anyone solved the Twersky's or the direct interaction approximation equation analytically?

Author's Reply

No analytical solutions are available in the presence of pair correlations. Reduced levels of approximation to the Bethe-Salpeter equation (e.g., radiative transfer theory) can be achieved, however, which are amenable to numerical computation.

ON FUNCTIONAL APPROACH TO RANDOM WAVE PROPAGATION PROBLEMS

P.L. Chow
Department of Mathematics, Wayne State University
Detroit, Michigan 48202, U.S.A.

SUMMARY

Method of functional integration for wave propagation through random media is presented. The method is applied to calculate the coherent and mutual coherent functions for a parabolic wave. It is shown that a correction to the parabolic - Markovian approximation can be easily made in this setting. Then the method is also applied to the random Helmholtz equation. It is possible to solve this problem by either Feynman's path integral or Wiener's integral. Asymptotic evaluation of such functional integrals is described. Examples and general remarks are provided.

1. INTRODUCTION

Functional approach to WPRM (wave propagation in random media) was introduced by the author (Chow, 1972). Up to that point in time, most problems had been treated by perturbation methods, such as Born's approximation, smoothing techniques etc, which are valid for the case of weak fluctuations. In wave propagation through a strongly turbulent medium, a drastically different method is needed. The functional approach seems to be one of most promising techniques available to date to deal with such problems. In view of recent research interest in strong fluctuation problems, it is fitting to give a breif review and to take a fresh look at the topical subject.

In WPRM, the problem is governed by a PDE (partial differential equation) with random function as its coefficient. The solution is therefore a functional of the random coefficient. From this point of view, the functional solution to such problem is natural one. Here, by functional approach we meant the analytical technique based a functional differential or integral calculus. Functional differential calculus has been used by KELLER (1964) to derive equations for some statistical functionals of the random wave function. However such equations are still intractable and have not yet produced any interesting results. On the other hand, the method of functional integration has found wider applications for its power and versatility. Therefore the functional integral approach will be our main concern here.

In the literature the term "functional integral" is usually refered to "Feynman's path integral" in proximity to quantum physics. However, in mathematics, one tends to regard it as "Wiener's functional integral". The basic idea in functional (integral) approach lies in expressing the solution, directly or indirectly, as a random functional integral of exponential type by the so-called "Feynman-Kac" formula. Then coherent, mutual coherent functions and higher moments can be written as single, double and multiple functional integrals. Although it is difficult to evaluate such integrals in general, like an ordinary integral representation, they often suggest novel analytical and numerical approximations, such as asymptotic expansions and Monte-Carlo techniques.

In this paper the functional integral and its application to solving a random parabolic equation will be presented in Section 2. This method is applied to calculate the moments of a parabolic wave function in Section 3. It is shown that a correction to the δ-correlated case can be easily made in the functional form. Even though, as indicated in our papers (Chow, 1972, 1980), the functional method can also be applied to the random Helmholtz equation, there has been little attention given to this fact. In Section 3 this point will be reiterated. In addition to Feynman's integral approach, the Wiener integral can also be used. The latter approach is amenable to a probabilistic treatment. Then an asymptotic evaluation of functional integrals by a stationary phase or Laplace method is described and applied to a Gaussian beam problem. In the last section, a few general remarks on the functional approach are given.

2. PRELIMINARIES

Let us first introduce the functional integral. Suppose $x(s)$ be a continuous vector-valued function for $0 \le s \le t$ in the d-dimensional space $R^d (d = 2 \text{ or } 3)$. Let $0 = t_0 < t_1 < t_2 < \ldots < t_n = t$ and set $x_k = x(t_k)$ for $k = 0, 1, 2, \ldots, n$. For a nice function $F_n(x_1, x_2, \ldots, x_n)$ of n variables, the following integral is well-defined

$$J_n(n, \Delta t) = \int_{R^d} \cdots \int_{R^d} F_n(x_1, \ldots, x_n) \{\Pi_{k=1}^n p_\alpha(\Delta t_k, x_k - x_{k-1})\} dx_1 \ldots dx_n \tag{1}$$

where $p_\alpha(t, x)$ is the Gaussian density with a complex variance parameter α,

$$p_\alpha(t, x) = \frac{1}{(2\alpha t)^{d/2}} e^{\frac{|x|^2}{2\alpha t}}, \tag{2}$$

and Δt is the maximum size of $\Delta t_k = (t_k - t_{k-1})$. Let $C_0 = C_0[0, t]$ denote the space of continuous paths $x_s = x(s)$ over $[0, t]$ with $x_0 = x$. Suppose that F_n is a discretized version of a smooth functional $F[x]$ on C_0. Then the functional integral of F over C_0 is defined as the sequential limit, if it exists, in the sense of CAMERON (1967)

$$J_\alpha = \lim_{\Delta t \to 0, n \to \infty} J_\alpha(n, \Delta t) \tag{3}$$

Since

$$\frac{|\,\mathbf{z}_k - \mathbf{z}_{k-1}\,|^2}{\Delta t_k} = \left|\,\frac{\mathbf{z}(t_k) - \mathbf{z}(t_{k-1})}{\Delta t_k}\,\right|^2 \Delta t_k,$$

in view of (1) and (2), the limit J_α may be written symbolically in an integral form

$$J_\alpha = \int_{C_0} F[\mathbf{z}]\, exp\,\{-\frac{1}{2\alpha}\int_0^t |\,\dot{\mathbf{z}}_s\,|^2\, ds\}\delta\mathbf{z} \tag{4}$$

It is a Feynman's path integral if α is imaginary while it is a Wiener's integral if α is real. In the latter case, J_α is just he mathematical expection of F

$$J_\alpha = E_x^\alpha\{F[\mathbf{z}]\} \tag{5}$$

over the Brownian motion with the variance α. For a short-hand notation, the expection symbol will be used in the case of complex α as well.

Consider the parabolic equation

$$\frac{\partial v}{\partial t} = \frac{\alpha}{2}\Delta v + \beta\eta(t,\mathbf{x})v, v(0,\mathbf{x}) = f(\mathbf{x}), \tag{6}$$

where α, β are complex constants and the functions f and η are given. Then, according to the Feynman-Kac formula (FEYNMAN, 1948; KAC 1949), the solution of (6) has a functional integral representation:

$$v(t,\mathbf{x}) = E_x^\alpha\{e^{\beta\int_0^t \eta(s,\mathbf{x}+\mathbf{z}_s-\mathbf{z}_t)ds} f(\mathbf{x}-\mathbf{z}_t)\} \tag{7}$$

Now let η be a random function $\eta(t,\mathbf{x},\omega)$ or a space-time random process. Its probability distribution is determined by the moment-generating functional

$$\Phi[\lambda] = E_\eta\, exp\,\{\beta\int_0^\infty\int_{R^d}\lambda(s,y)\eta(s,y)dsdy\} \tag{8}$$

where λ is a test function. It becomes the characteristic functional when $\beta = i$. Note that

$$\int_0^\infty\int_{R_d}\lambda(s,y)\eta(s,y)dsdy = \int_0^t \eta(s,\mathbf{x}+\mathbf{z}_s-\mathbf{z}_t)ds \tag{9}$$

if we set

$$\lambda = \lambda_1(s,y) = \beta h_t(s)\delta(y-\mathbf{x}-\mathbf{z}_s+\mathbf{z}_t) \tag{10}$$

where $h_t(s) = 1$ if $0 \le s \le t$; 0 otherwise, and δ is the delta function. For instance, if η is a Gaussian random function with mean and covariance functions given by

$$m(t,\mathbf{x}) = E\eta(t,\mathbf{x}), R(t,s;\mathbf{x},y) = E[\eta(t,\mathbf{x}) - m(t,\mathbf{x})][\eta(s,y) - m(s,y)] \tag{11}$$

then

$$\Phi[\lambda] = exp\,\{\beta\int\int m(s,y)\lambda(s,y)dsdy + \frac{1}{2}\beta^2\int\int\int\int R(s,s';y,y')\lambda(s',y')dsdyds'dy'\} \tag{12}$$

Thus, in view of (7), (10), the mean or the coherent function of v takes the form

$$\Gamma(t,\mathbf{x}) = E_\eta v(t,\mathbf{x}) = E_x^\alpha\{\Phi[\lambda_1]f(\mathbf{x}-\mathbf{z}_t)\} \tag{13}$$

which, for the Gaussian case (2.12), yields

$$\Gamma(t,\mathbf{x}) = E_x^\alpha\{f(\mathbf{x}-\mathbf{z}_t)\, exp\,[\beta\int_0^t m(s,\mathbf{x},\mathbf{z}_s-\mathbf{z}_t)ds + \frac{1}{2}\beta^2\int_0^t\int_0^t R(r,s;\mathbf{x}+\mathbf{z}_r-\mathbf{z}_t,\mathbf{x}+\mathbf{z}_s-\mathbf{z}_t)drds]\}. \tag{14}$$

Similarly, the second moment or the mutual coherent function is given by

$$\begin{aligned}\Gamma_2(t_1,\mathbf{x}_1,\mathbf{x}_2) = E_\eta\{v(t,\mathbf{x}_1,\bar{v}(t,\mathbf{x}_2)\} = E_{x_0}^\alpha\{f(\mathbf{x}_1-\mathbf{z}_1(t)\bar{f}(\mathbf{x}_2-\mathbf{z}_2(t))\, exp\,(\int_0^t[\beta m_1(s)+\bar{\beta}m_2(s)]ds \\ + \int_0^t\int_0^t[\frac{1}{2}\beta^2 R_{11}(r,s)+\beta\bar{\beta}R_{12}(r,s)+\frac{1}{2}\bar{\beta}^2 R_{22}(r,s)]drds)\},\end{aligned} \tag{15}$$

where $\sim$ means the complex conjugate and

$$m_i(s) = m[s,\mathbf{x}_i+\mathbf{z}_i(s)-\mathbf{z}_i(t)],$$

$$R_{ij}(r,s) = R[r,s;\mathbf{x}_i+\mathbf{z}_i(r)-\mathbf{z}_i(t),\mathbf{x}_j+\mathbf{z}_j(s)-\mathbf{z}_j(t)],$$

for $i,j = 1,2$. Derivation of this and higher moments can be found in (CHOW, 1972, 1980).

3. CORRECTION IN PARABOLIC EQUATION APPROXIMATION

In a forward scattering approximation, the Helmholtz equation is replaced by a "parabolic" equation

$$\frac{\partial v}{\partial t} = \frac{\alpha}{2}\Delta + \beta\eta(t,\underline{x},\omega)v, t > 0;\ v(0,\underline{x}) = f(\underline{x}), \tag{16}$$

where $t = x$ is actually the space variable in the direction of propagation, $\underline{x} = (x_1, x_2) = (y, z)$ is the transverse variable, and

$$\alpha = (ik)^{-1}, \beta = k/2i \text{ and } \eta(t,\underline{x}) = n^2(t,\underline{x}) - 1. \tag{17}$$

Further assume that the refractive index n^2 is Gaussian and transversely homogeneous so that η has the mean

$$E\eta(t,\underline{x}) = m(t) \tag{18}$$

and the covariance

$$R(t,s;\underline{x},\underline{y}) = \delta(t-s)\rho(t,\underline{x},\underline{y}) \tag{19}$$

Upon substituting (17) - (19) into the formulas (14) and (15) respectively, one gets immediately the coherent and the mutual coherent functions

$$\Gamma(t,\underline{x}) = (\frac{ik}{2\pi t}) \exp\{\frac{ik}{2}\int_0^t m(s)ds - \frac{k^2}{8}\int_0^t \rho(s,0)ds\} \times \int_{R^2} f(\underline{x}-\underline{y}) \exp ik\frac{|\underline{y}|^2}{2t}\}d\underline{y} \tag{20}$$

and

$$\Gamma_2(t,\underline{x}_1,\underline{r}_2) = E^n_{x_1}E^n_{x_2}\{f(\underline{x}_1 - \underline{x}_1(t))\bar{f}(\underline{x}_2 - \underline{x}_2(t)) \times \exp\left(-\frac{k^2}{4}\int_0^t[\rho(s,0) - \rho(s,\underline{x}_1(s) - \underline{x}_2(s))]ds\right)\} \tag{21}$$

which may be evaluated by a change of variables to yield

$$\Gamma_2(t,\underline{r}_1,\underline{r}_2) = \frac{k^2}{(2\pi t)^2}\int_{R^2}\int_{R^2}\Gamma_2(0,\underline{r}'_1,\underline{r}'_2)\exp\{\frac{ik}{t}(\underline{r}_1 - \underline{r}'_1)\cdot(\underline{r}_2 - \underline{r}'_2) - \frac{k^2}{4}\int_0^t[\rho(s,0) - \rho(s,\underline{r}'_2 + \frac{s}{t}(\underline{r}_2 - \underline{r}'_2))]\}d\underline{r}'_1 d\underline{r}'_2))]ds \tag{22}$$

where $\underline{r}_1 = \frac{1}{2}(\underline{x}_1 + \underline{x}_2), \underline{r}_2 = (\underline{x}_1 - \underline{x}_2)$ and

$$\Gamma_2(0,\underline{r}_1,\underline{r}_2) = f(\underline{r}_1 + \underline{r}_2/2)\bar{f}(\underline{r}_1 - \underline{r}_2/2).$$

Evaluation of higher moments would be difficult. But this can be done by solving the differential equations they satisfy, as done by KLYATSKIN and TATARSKI (1970), YEH, LIU and YOUAKIM (1975), among others.

The assumption (19) of δ-correlation, though resulting in a considerable simplification, seems too drastic in application. In reality it is only a first approximation to the case of short correlation-length. Here we wish to show that, by functional approach, it is easy to pick up the next order correction if so desired. To this end, one observes that, for a short correlation "time" (length), the covariance function $R(r,s;\underline{x},\underline{y})$ peaks at $r = s$ and then decays rapidly as $|r-s|$ increases. Thus we have the following expansion, for small $|r-s|$

$$R(r,s;\underline{x}_r - \underline{x}_s) \sim R_0(r,s) + \frac{1}{2}Q(r,s;\underline{x}_r - \underline{x}_s) \tag{23}$$

in which we have set $R_0(s,t) = R(s,t;0), \nabla R(s,t;0) = 0$, and
$Q(r,s;\underline{x}_s - \underline{x}_s) = \sum_{i,j=1}\frac{\partial^2}{\partial x_i \partial x_j}R(r,s;0)(x_r^i - x_s^i)(x_r^j - x_s^j)$.

If we substitute (3.4) and (3.9) into (2.14) with $\alpha = (ik)^{-1}$, it yields

$$\Gamma(t,\underline{x}) = E^n_{\underline{x}}\{f(\underline{x} - \underline{x}_t)\exp\left(-\frac{ik}{2}\int_0^t m(s)ds\right.$$

$$\left.-\frac{k^2}{8}\int_0^t\int_0^t[R_0(r,s) + \frac{1}{2}Q(r,s;\underline{x}_r - \underline{x}_s)]drds\right)\},$$

which involves a quadratic exponent in $\underline{x}$. This is similar to the case of a harmonic oscillator in quantum mechanics and can sometime be calculated by the method of integral equations. Another possible way of correction is to make use of the short wave asymptotic expansion. This will be discussed later in a more general situation.

4. FUNCTIONAL APPROACH TO RANDOM HELMHOLTZ EQUATION

In constract with the parabolic wave approximation, it seems less well-known that the functional method is also applicable to the random Helmholtz or reduced wave equation given by

$$\Delta u + k^2 n^2(\underline{x},\omega)u = f(\underline{x}) \tag{24}$$

in the free space or a half space (CHOW, 1972,1975) in three dimensions. The idea is based on the concept of imbedding by regarding the wave function u in (24) as a steady-state solution of a parabolic equation.

Let us consider the parabolic equation (16) which, by a Laplace transform, yields,

$$\frac{\alpha}{2}\Delta\hat{v} + (\beta\eta - \lambda)\hat{v} = f(\underline{x}), \tag{25}$$

where

$$\hat{v}(\lambda, x) = \int_0^\infty e^{-\lambda t} v(t, x) dt, \ Re\, \lambda > 0. \tag{26}$$

We shall give two different functional integral representations for the solution of the equation (24) as follows.

(a) Feynman integral approach.
If we let

$$\alpha = 2ik^{-1}, \beta = \frac{ik}{2}, \lambda = ik \text{ and } \eta = n^2 - 1, \tag{27}$$

then the solution u of (24) can be written as

$$u(x) = (ik)^{-1} \hat{v}(-ik, x) = (ik)^{-1} \int_0^\infty e^{-ikt} v(t, x) dt, \ Im\, k > 0, \tag{28}$$

Thus, according to (7), it becomes

$$u(x) = (ik)^{-1} \int_0^\infty e^{-ikt} E_x^w \{\exp\left[\frac{ik}{2} \int_0^t \eta(x + x_s - x_t) ds\right] f(x - x_t)\} dt \tag{29}$$

Since the variance parameter $\alpha = 2ik^{-1}$ is imaginery as $Im\, k = 0$, the above is a Feynman's path integral.

(b) Wiener integral approach.
Let $\lambda = \epsilon > 0$ be real and $0 \le a \le 2$. If we choose

$$\alpha = 2k^{-a}, \beta = k^{2-a} \text{ and } \eta = n^2, \tag{30}$$

then it is easy to see that, instead of (29), we get

$$u(x) = -k^{-a} \lim_{\epsilon \to 0} \int_0^\infty e^{ct} v(t, x) dt = -k^{-a} \lim_{\epsilon \to 0} \int_0^\infty e^{-ct} E_x^w \{\exp\left[k^{2-a} \int_0^t \eta(x + x_s - x_t) ds\right] f(x - x_t)\} dt. \tag{31}$$

Now the variance parameter $\alpha = 2k^{-a}$ is real as that the above expected functional is a Wiener integral.

In either case, as shown in Section 2, the moments of solution can be expressed in terms of multiple functional integrals involving the characteristic functional of the random medium. In contrast with the δ-correlation case, the evaluation of such integrals is much more difficult. However, at high frequencies, one can turn to the asymptotic method of evaluation, which will now be described.

To be definite, let us assume $\eta(x, \omega)$ be Gaussian with mean $m(x)$ and covariance $R(x, y)$. Suppose that we wish to evaluate the coherent function $\Gamma(t, x)$ for $v(t, x)$. Note that the equation (14) can be written as

$$\Gamma(t, x) = \int_{R^d} p_t(t, y) f(x - y) J(t, x, y) dy, \tag{32}$$

where, in functional form

$$J(t, x, y) = \int_{C_t(x,y)} \exp\left\{-\frac{1}{2\alpha} \int_0^t |\dot{x}_s|^2 ds + \beta \int_0^t m(x_s) ds + \frac{1}{2} \beta^2 \int_0^t \int_0^t R(x_r, x_s) dr ds\right\} \delta x, \tag{33}$$

and $C_t(x, y)$ denotes the class of continuous paths with $x_0 = x, x_t = y$.
For the case (a), noting (27), we have

$$J(t, x, y) = \int_{C_t(x,y)} F_t[x] e^{ik\theta_t[x]} \delta x \tag{34}$$

where

$$\theta_t[x] = \int_0^t |\dot{x}_s|^2 ds + \int_0^t m(x_s) ds \tag{35}$$

$$F_t[x] = \exp\left\{-\frac{k^2}{8} \int_0^t \int_0^t R(x_r, x_s) dr ds\right\} \tag{36}$$

If $k^2 R = 0(1)$, for large k, the main contributions to the integral (34) come from the neighbourhood of stationary paths x_* determined by the variational problem

$$\delta \theta_t[x] = 0 \tag{37}$$

In view of (36), it leads to Euler's equation

$$2 \frac{d^2 x_s}{ds^2} = \nabla m(x_s), x_0 = x, x_t = y. \tag{38}$$

For each stationary path x_*, the main contribution to the integral is given by

$$J \sim F_t[x_*] e^{ik\theta_t[x]} K_t(x, y), \tag{39}$$

where

$$K_1(z,y) = \int_{C_1(z,y)} \exp\{ik\int_0^t |\dot{z}_s|^2\,ds + Q_1(z_*,z)\}\delta z \tag{40}$$

and Q_1 is a quadratic functional obtained by a Taylor series expansion of the functional $\Phi_1[z] - \Phi_1[z_*]$ about z_* up to the quadratic term. In quantum mechanics, the above procedure corresponds to a semi-classical approximation. It is an extension of the method of stationary phase for an oscillatory integral (ALBEVERIO and KØEGH-KROHN, 1976).

For the Wiener integral case (b), the corresponding integral J in (32) takes the form

$$J(t,z,y) = \int_{C_1(z,y)} \exp\{-k^a\int_0^t |\dot{z}_s|^2\,ds + k^{b-a}\int_0^t m(z_s)ds + \frac{1}{2}k^{2(b-a)}\int_0^t\int_0^t R(z_r,z_s)drds\}\delta z. \tag{41}$$

which is a Laplace type of integral. For large k, by taking $a = 1$ with $k^2R = O(1)$, we can get an asymptotic expansion similar to the case (a). However there are other possibilities in this case. For instance, if $m \equiv 0$, one can choose $a = 4/3$ so that

$$J(t,z,y) = \int_{C_1(z,y)} \exp\{-k^{4/3}[\int_0^t |\dot{z}_s|^2\,ds + \int_0^t\int_0^t R(z_r,z_s)drds\}\delta z \tag{42}$$

The minimal paths z_* will be determined by the equation

$$\frac{d^2z_s}{ds^2} + \int_0^t \nabla R(z_r,z_s)dr = 0, z_0 = z, z_t = y. \tag{43}$$

Once the minimas z_* are found, the asymptotic evaluation is the same as before. Since $R = O(1)$ in this case, the result holds for strong fluctuation problems. Asymptotic evaluation of Wiener integrals has been studied by many authors, notably by DONSKER and VARADHAN (1975).

Let us consider a couple of simple examples by the method of stationary phase. For statistically homogenous media, $m = 1$ and $R(z,y) = R(z-y)$. From (38) we see that the ray is just a line segment

$$z_* = z + \frac{s}{t}(y-z), \quad 0 \le s \le t,$$

and

$$J(t,z,y) \sim K(t,z,y)\exp\{ik(t + \frac{|y-z|^2}{t}) - \frac{k^2}{8}\int_0^t\int_0^t R(\frac{r-s}{t}(y-z))drds\} \tag{44}$$

where

$$K(t,z,y) = \int_{C_1(z,y)} \exp\{ik\int_0^t |\dot{z}_s - \dot{z}_{s*}|^2\,ds\}\delta z. \tag{45}$$

Thus, for a radiation problem with $f(z) = \delta(z)$, the coherent function

$$\Gamma(z) \sim (ik)^{-1}\int_0^\infty p_n(t,z)K(t,z,y)\exp\{ik\frac{|y-z|^2}{t} - \frac{k^2}{8}\int_0^t\int_0^t R(\frac{r-s}{t}(z-y))drds\}dt \tag{46}$$

where K can be computed as in the quantum oscillator problem. As another example, let us consider the Gaussian beam propagation problem in the half-space $x_1 > 0$ with a prescribed aperture field

$$u_0^+(z) = A(z)e^{ik\phi(z)} \text{ at } x_1 = 0.$$

Then the cohesnce function has the asymptotic form

$$\Gamma^+(z) = 2ik^{-1}\frac{\partial}{\partial x}\int_{R^2}\int_0^\infty u_0^+(y)e^{-ikt}J(t,z,y)dtdy$$

where J has the asymptotic expansion (44). Thus Γ^+ can be calculated approximately but will not be done here. For details one is referred to our paper (CHOW, 1975). The procedure for asymptotic evaluation of second and higher moments, though more cumbersome, is quite similar. This is explained in our papers mentioned above.

5. GENERAL REMARKS

In this paper several aspects of functional integral method have been described. Most discussion has been confined to the coherent function for simiplicity. In fact, in contrast with other approaches, the procedure for calcutating higher moments at multi-points are as straightforward. It is believed that the present method is potentially useful in solving strong random scattering problems. In particular the Wiener integral approach to random Helmholtz equation is most promising and worth further study. The reason is as follows. To evaluate the functional integral asymptotically, it is possible to make use of certain analytical techniques in probability theory. In applications one is likely to appeal to a numerical approximation. In this respect the Wiener integral is much more robustic than Feynman's path integral, and its computational algorithm is readily available.

In closing we wish to point out that the Feynman integral had been used by DASHEN (1979) to calculate moments of the wave function under the parabolic equation approximation presented in Section 3. More recent references to the path

integral approach can be found in the interesting articles by FISHMAN and MCCOY (1984).

6. ACKNOWLEDGEMENT

This work was supported in part by the National Science Foundation under Grant DMS-01908.

REFERENCE

Albeverio, S. and R. Høegh-Krohn, Mathematical Theory of Feynman Path Integral, Lect. Notes in Math. 523, Springer-Verlag, Berlin, 1976.

Cameron, R.H., A family of integrals serving to connect the Wiener and Feynman integrals, J. Math. and phys., 39 (1987), 126.

Chow, P.L., Applications of function space integrals to wave propagation in random media, J. Math. phys. 13 (1972), 1324.

Chow, P.L., A functional phase-integral method and applications to the laser beam propagation in random media, J. Statist. phys. 12 (1975), 93.

Chow, P.L., Functional methods for waves in random media, in Multiple Scattering and Waves in Random Media, ed. by P.L. Chow, W.E. Kohler and G.C. Papanicolaou, North-Holland, Amsterdam, 1981.

Dashen, R., Path integrals for waves in random media, J. Math. phys., 20 (1979), 894.

Donsker, M.D. and S.R.S. Varadhan, Asymptotic evaluation of certain Wiener integrals for large time, in Functional Integration and Its Applications, ed. by A.M. Arthurs, Clarendon Press, Oxford, 1975.

Feynman, R.P., Space-time approach to nonrelativistic quantum mechanics, Rev. Modern phys. 20 (1948), 367.

Fishman, L. and J.J. McCoy, Derivation and application of extended parabolic wave theories I,II, J. Math. phys. 25 (1984), 285.

Kac, M., On distribution of certain Wiener functionals, Trans. Amer. Math. Soc. 65 (1949), 1.

Keller, J.B. Stochastic equations and wave propagation in random media, Proc. Symp. Appl. Math., 16 (1964), 145.

Klyatkin, V.I. and Tatarski, V.I., The parabolic equation approximation in a medium with random inhomogeneities, Sov. phys. JETP 31 (1970), 335.

Yeh, K.C., C.H. Liu and M.Y. Youakim, A theoretical study of the ionospheric scintillation behavior caused by multiple scattering. Radio Science, 10 (1975), 97.

NUMERICAL SIMULATION OF WAVE PROPAGATION IN RANDOM MEDIA

Mark Spivack
Dept. of Applied Mathematics & Theoretical Physics,
Silver Street, The University, Cambridge, CB3 9EW, ENGLAND

SUMMARY

Numerical simulation of random wave propagation has numerous applications. It enables us to examine individual features of the wave-field and to model actual experiments. Statistical quantities such as average power spectra of intensity fluctuations can also be obtained for comparison with theory.

This paper explains some of the techniques and uses of numerical simulation and describes some of the results which emerge.

1. INTRODUCTION

Wave propagation in random media has long been studied but the theory has been concerned mainly with averaged quantities, such as power spectra and moments of intensity fluctuations. Numerical simulation, however, enables us to study individual examples. This gives insight into features of the random wave-field that would otherwise be difficult to examine. Such effects include the long peaks of intensity which develop and the tendency of beams to wander from their equilibrium positions.

Simulation allows us to model actual experiments, and to compare results with theory. A variety of initial conditions and boundaries can be treated, together with deterministic conditions in the medium. It is also possible to investigate numerically some of the assumptions and approximations used in formulating the fundamental equations.

In the following sections the techniques of numerical simulation are explained, and some of the uses and results described.

2. MATHEMATICAL FORMULATION AND APPROXIMATIONS

The situation we consider is of a monochromatic wave incident on a half-space $z \geq 0$. We assume the wavelength k to be significantly shorter than the typical scale-size of irregularities and so scattering takes place mainly in a forward z-direction. The full elliptic wave equation can then be approximated by a parabolic form, in which z becomes a time-like direction of propagation. This expression is, in 2-dimensional Cartesian coordinates (x,z),

$$\frac{\partial E}{\partial z} = -i \frac{\partial^2 E}{\partial x^2} - i \frac{k}{z} (n^2 - 1) E \qquad (2.1)$$

where E is the complex wavefield, and n is the refractive index. We can write

$$n = 1 + n_d(x,z) + \mu W(x,z) \qquad (2.2)$$

where n_d is a deterministic departure from 1, and μW varies randomly with mean zero and standard deviation μ. Both n_d and μ are assumed to be small. (We have ignored variation in the third variable y. Time-dependence has also been excluded, since typically the wave-speed is very fast relative to changes in n. Both these restrictions are easily removed.)

For convenience we scale x and z by L and kL^2 respectively, where L is the correlation length of the medium in the x-direction. We thus put $Z = \frac{z}{kL^2}$, $X = \frac{x}{L}$, and we get approximately

$$\frac{\partial E}{\partial Z} = -\frac{i}{2} \frac{\partial^2 E}{\partial X^2} - \left(i \frac{k^2}{2} L^2 n_d + ik^2 L^2 \mu W \right) E \qquad (2.3)$$

The right hand side of 2.3 consists of a distance operator and scattering operator respectively. We denote by $\rho(\xi, \zeta)$ the normalised correlation function of refractive index fluctuations. Thus $\rho(\xi,\zeta) = \langle W(X,Z)\, W(X+\xi, Z+\zeta) \rangle$. W is assumed to have Gaussian statistics, but ρ is arbitrary.

In this way we can model, say, a plane wave or a narrow beamed (extended point) source, with arbitrary deterministic profile n_d. The wave propagating from a deep phase-changing screen $\phi(x)$ is also represented by 2.3. The initial condition is then, in effect, $E = e^{i\phi}$ and the scattering term is set to zero.

Although the extended point source accurately models many features of a true point source, we can model this directly in a similar way. The appropriate wave equation in polar coordinates can be transformed to Cartesian coordinates, and an expression similar to 2.3 is obtained. A typical simulation with this model is shown in Figure 1.

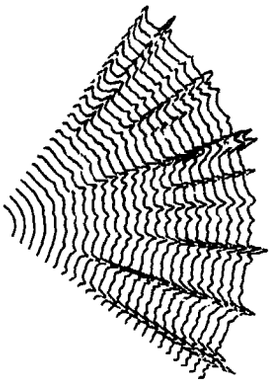


Figure 1. Intensity of cylindrically spreading wave due to point source.

Solution

The infinitesimal effect of scattering is to introduce pure phase variations in E. These gradually become focussed with distance, giving rise to intensity fluctuations. Thus over short distances ΔZ the solution of 2.3 is obtained approximately by solving first for one operator, and then applying the other. An accurate picture of E(X) as range increases is built up by repetition of this procedure (Mathematically this is equivalent to the fact that the two operators almost commute for small distances). The solution can be written formally as

$$\bar{E}(X) = E(X,Z) \exp\left[ik^2L^2\mu \int_Z^{Z+\Delta Z} W(X,Z')\,dZ'\right] \qquad (2.4)$$

and $$E(X, Z+\Delta Z) = \int_{-\infty}^{\infty} \bar{E}(X')\, e^{i\nu X'}\, e^{i\nu^2\Delta Z/2}\, e^{-i\nu X}\, dX'\, d\nu \qquad (2.5)$$

This solution closely parallels the theoretical solutions of the fourth moment equation by successive scatters (see Uscinski [1]).

It can be shown with simulation, in fact, that this approximation is extremely accurate (see §4).

3. NUMERICAL IMPLEMENTATION

We will describe here the representation on the computer of the random medium, and the numerical treatment of the diffraction effect.

As mentioned above, a step-length ΔZ is chosen such that, in that distance, the total phase-change imposed by the medium leads to only very small amplitude fluctuations.

Random medium

Given the statistics of the medium in terms of W(X,Z) we wish to construct a phase-screen U(X) to represent the total effect of W in the slice of medium (Z, Z+ΔZ). The (unnormalised) transverse correlation function ρ_1 of U is therefore

$$\rho_1(\xi) = \int_Z^{Z+\Delta Z} \rho(\xi,\zeta)\, dZ_1\, dZ_2 \qquad (3.1)$$

where $\zeta = Z_1 - Z_2$. In many cases of interest we can take ΔZ to be the horizontal scale-size L_0, and 3.1 simplifies. The individual screens U(X) can then be generated independently. It is often necessary, however, to generate the screens so that they are correlated.

The details of this procedure are given in Macaskill and Ewart [2] and follow a technique described in Jenkins and Watts [3]: The screens are generated in the frequency domain, using a random number generator. White noise is filtered by the spectral function corresponding to ρ_1, and the whole is transformed back to the spatial domain, using fast Fourier transforms, to give the required screens. We put

$\phi(X) = \sqrt{\Gamma\Delta Z}\ U(X)$, where $\Gamma = k^2\mu^2 L^2 L_g$ is the naturally arising "strength" parameter (see Uscinski [4]), and U(X) has variance 1.

The first part of the solution is then $\bar{E}(X) = E(X,Z)\exp[-i\phi(X)]$.

So far we have described the random medium for propagation of a linear wavefront. The considerations are similar for a point source, but the correlation functions of the screens are then range-dependent.

Diffraction effect

The formal solution (2.5) of the diffraction operator suggests solving by use of the fast Fourier transform (FFT). This technique was applied by Tappert and Hardin [5]. In it, the FFT of $\bar{E}(X)$ is taken, the individual Fourier components are propagated independently, and the inverse transform gives $E(X,Z+\Delta Z)$. The method is fast, and eliminates the need to deal with boundary conditions explicitly. Furthermore the accuracy is independent of ΔZ, and depends only on the discretisation itself. Thus in the particular case of propagation from a deep screen the step-lengths can be arbitrarily large.

The other method used in this work is that of finite differences. An implicit scheme is derived as follows: Equation 2.3 is discretised in X and Z, and the derivatives approximated by finite differences, using a Crank-Nicolson scheme. This yields an implicit system of linear equations of the form $AE_{l+1} = BE_l$ where A and B are tri-diagonal matrices, and the vector E_l corresponds to E(X) at range Z_l. A and B are constant with Z since the range-dependence has been included in the phase-screen. This system can then be solved using an efficient tri-diagonal matrix inversion algorithm. Explicit boundary conditions are taken into account in the definitions of the matrices A and B.

Note that numerical stability may require a finite difference step length smaller than ΔZ. The usual stability analysis must be replaced by a stochastic variant, because of the imposition at each step of a phase-screen.

Extremely close agreement with FFT results indicates the accuracy of both methods.

Wave-speed profiles

Deterministic variation $n_d(X,Z)$ in refractive index can be included without difficulty in the model. Typically this will be constant in Z. In the ocean, for example, such variation will result from temperature, pressure and salinity patterns.

4. RESULTS AND APPLICATIONS

We summarize a few applications of the model and the features which emerge.

A receiver may detect a strongly scintillating signal (with time, or movement of receiver) from a constant source. In the ocean an acoustic record with depth may be very weak except for occasional high peaks of intensity. These features show clearly in Figure 2, where long peaks of intensity build up with range and drift for some distance. A moving "observer" has a high probability of crossing these peaks.

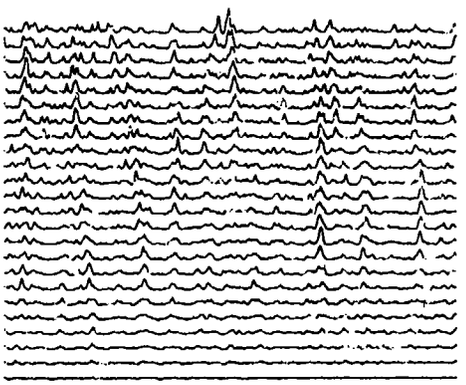


Figure 2. Simulation for medium with Gaussian correlation function, showing intensity I(X) changing with Z.

The field from a narrow beamed source is also frequently observed to wander from its equilibrium position. Such behaviour is evident in the simulation in Figure 3.

Three-dimensional simulations exhibit similar features. The long peaks of intensity occur, wandering now in a 2-dimensional path as range increases. (A moving observer in this case is likely, however, to miss the intensity peaks altogether.)

Linear and parabolic profiles n_d have a marked influence on propagation. Figure 4 shows the focussing effect of a parabolic profile on an extended source, in the absence of random variations. In this case a random medium will tend to diminish focussing.

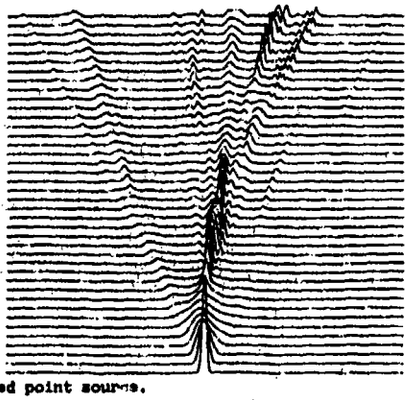


Figure 3. Simulation of extended point source.

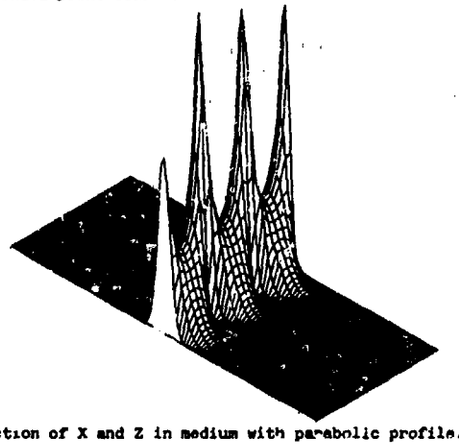


Figure 4. Intensity as function of X and Z in medium with parabolic profile.

Modelling of experiment

Environmental data collected during experiment can be incorporated in a computer simulation, and the experiment modelled in some detail. In recent ocean acoustics experiments, for example, the profile, n_d, and autocorrelation function, ρ, of the medium were measured in the region of the signal. In this way observed features of signal behaviour can be reproduced computationally, and can often be seen as part of a larger pattern not detected experimentally. Simulation can thus lead to the design of further experiments and measurements.

Theoretical solutions, of course, are also compared with experiment. The results of inverse theory (Uscinski [6]) can be applied, to yield more information about the random medium which can again be modelled in the simulation.

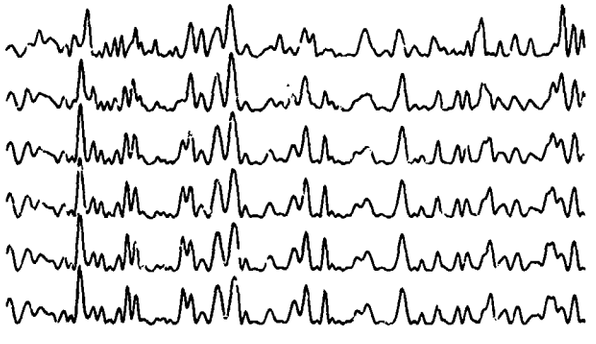


Figure 5. Intensities at fixed range compared for progressively finer screens, with the finest subdivision lowest.

Correlated screens

Several types of simulation can now be performed using screens correlated with range. Three-dimensional

and time-varying media both require this technique. We can examine the effect on propagation of elongation of the irregularities when the amount of scattering over small distances remains the same. In addition, by simulation we can progressively subdivide a medium into increasingly fine screens. This procedure has given a strong validation of these "split-step" methods and the fundamental approximations used. Figure 5 shows the intensity patterns after 8 correlation lengths into the medium for such a series of subdivisions, in which ΔZ is halved each time.

We have described mainly features of individual realisations of the random medium. By averaging many such results we can obtain such quantities as the fourth moment and power spectra of intensity fluctuations.

The use of numerical simulation thus interacts with theory and experiment to further our understanding of random wave propagation.

REFERENCES

1. B.J. Uscinski, Analytical solution of the fourth moment equation and interpretation as a set of phase screens, J. Opt. Soc. Am., 2, 2077-2091, 1985
2. C. Macaskill & T.E. Ewart, Computer simulation of two-dimensional random wave propagation, IMA Journal of Applied Math., 33, 1-15, 1984
3. G.M. Jenkins & D.G. Watts, Spectral analysis and its applications, San Francisco, Holden-Day, 1968
4. B.J. Uscinski, The elements of wave propagation in random media, New York, McGraw-Hill, 1977
5. F.D. Tappert & R.H. Hardin, Proceedings of the Eight International Congress on Acoustics, Vol. II, London, Goldcrest, p. 452, 1974
6. B.J. Uscinski, Acoustic scattering by ocean irregularities: aspects of the inverse problem, J. Acoust. Soc. Am., 64, 1460-1469, 1980

ACKNOWLEDGEMENTS

Much of the work shown here was carried out by Dr Nanette Freedman, whose contribtion is gratefully appreciated.

SUMMARY OF SESSION VIII

DISCRETE RANDOM MEDIA

by

W.A.Flood, Session Chairman

Six papers were presented in the session on discrete random media. Of these, three dealt with propagation and scattering in discrete random media, while a fourth reviewed the problems associated with the nonlinear interaction of a high powered laser beam with a discrete aerosol particle. The remaining two papers treated continuous random media. I propose to confine my remarks to the papers dealing with discrete particles with particular emphasis on the three papers treating propagation and scattering.

The three papers on propagation and scattering considered multiple scattering in increasing orders of complexity. They were (in ascending order of complexity):

1. Selective extinction of a dispersion of single and aggregated layered spheres, by F.Borghese et al.
2. Multiple scattering of waves in random media containing nonspherical scatterers, by V.V.Varadan et al.
3. Monte Carlo simulation of multiple scattering effects of microwaves from rain, by H.Jeske and P.H.Voss.

The paper by Borghese et al. considered extinction due to a sparse mono-disperse distribution of metal-coated spheres. The assumption of a sparse distribution was used to justify a single scatter (Born) calculation for the net extinction. Their model for a single sphere accounted for varying coating thickness and for the frequency variation of the complex refractive index of the metal itself. They showed how one could selectively control the frequency of peak extinction by varying the thickness of the metal coating and they further analyzed the effect on extinction if the particles formed binary aggregates. Within the constraints of a sparse distribution (single scatter), the calculations of these authors could be extended to poly-disperse distributions, albeit at the expense of significantly increased computational time.

The paper by the Varadans and Ma considered a dense random medium (the percentage of volume occupied by the scatterers was more than a few percent and was 20 percent in the numerical examples) such that in addition to multiple scattering, particle positional pair correlations must be considered. The paper offered a novel scheme for the computation of the incoherent intensity.

The authors used the coherent intensity as the exciting field for the incoherent intensity. As such, this is a single scatter formulation but with two important distinctions: (1) The exciting field, the coherent intensity is calculated by means of a full multiple scatter formulation (at least to the extent permitted by the Quasi Crystalline Approximation); (2) The presence of the other scatterers is partly accounted for by considering the effect of the pair correlation function. Consequently, this calculation differs significantly from those using a simple Born approximation. What is not clear is how much closer this result is to the true situation.

The paper by Jeske and Voss presented the results of a Monte Carlo numerical simulation of propagation through rain. For long paths, propagation at millimetre wavelengths may well require that multiple scatter be considered, but the volume fraction occupied by raindrops in a normal rainfall is not high enough to require the inclusion of pair correlations.

The three papers presented calculations with three different levels of accounting for multiple scatter. The paper by Borghese and his colleagues used the single scatter Born approximation appropriate for sparse distributions and optically thin media. The community is well aware of the fact that even for sparse distributions, if the optical depth is large enough and the albedo is high enough, multiple scattering solutions will be required. The paper by the Varadans and Ma postulated a dense medium and, therefore, knowledge of the pair correlation function was required in addition to multiple scattering solutions. The degree to which the particular treatment used in this paper reflects the truth for a medium with lossless scatterers remains to be demonstrated. Finally, the paper by Jeske and Voss treated the situation where the distribution of particles was sparse enough so that pair (and higher order) correlations could be neglected while higher orders of multiple scatter were calculated.

SELECTIVE EXTINCTION OF A DISPERSION OF SINGLE AND AGGREGATED LAYERED SPHERES

by
F. Borghese, P. Denti, R. Saija, G. Toscano
Università di Messina, Istituto di Struttura della Materia, 98100 Messina, Italy
and
O. I. Sindoni
Chemical Research Development and Engineering Center, Aberdeen P.G., 21010 Md, USA

Summary

The extinction coefficient for a low-density dispersion of small stratified spheres as well as for that of their binary aggregates has been calculated. We discuss the results for 50 Å spheres with a core of MgO and a coating of Al, a case in which a dramatic shift of the resonance peaks as a function of the thickness of the coating occurs. This suggests that a suitable choice of the thickness could produce selective extinction in a wide range of frequency, although this effect could be strongly weakened if a considerable percentage of spheres aggregate.

* * *

In this paper we describe and discuss some results from a series of calculations aimed to the study of the propagation of electromagnetic waves through a dispersion of small identical nonhomogeneous spheres as well as through the dispersion of their binary aggregates with random orientation. More specifically our purpose is to see how the extinction coefficient of a low-density dispersion of spherical scatterers is affected by their inhomogeneity; we want also to gain some information as to what extent the aggregation modify the effects due to the inhomogeneity of the scatterers.

The propagation through a dispersion of (possibly inhomogeneous) spherical objects is easily studied for, in the low-density limit we deal with, the extinction coefficient is given by the sum of the extinction cross-sections of the individual scatterers[1]. When the spheres aggregate, however, the resulting complex scatterers are intrinsically anysotropic so that their individual cross-sections depend on the orientations with respect to the incident wave. We describe elsewhere[2] in full detail how this difficulty can be overcome by a suitable extension of the multipole-field approach for complex scatterers built as aggregates of spheres we developed previously[3]. In summary, we used the transformation properties of the multipole fields under rotations[4] to cast the cross-section of an aggregate into a form that makes possible to perform analytically the sum over the orientations needed to calculate the extinction coefficient of the dispersion.

The inhomogeneous spherical scatterers we deal with were built as a sequence of concentric homogeneous shells of different dielectric properties. Between each pair of contiguous shells we introduced a thin transition layer within which the dielectric function varies in such a way as to ensure the continuity of ε and of $d\varepsilon/dr$ throughout the whole scatterer. Thanks to this choice we were able to calculate the field within each sphere by numerical integration of the appropriate radial equation - according to the technique of Wyatt[5] - rather than by using the customary boundary conditions at the surface separating shells of different dielectric properties. These latter were described by simple dielectric functions, viz. the Drude dielectric function for the metallic materials, and a damped-oscillator dielectric function for the insulating materials[6]; we were, in fact, interested in those properties that depend on the inhomogeneity of the scatterers rather than on the details of the dielectric function.

Our calculations were performed for several choices of the inhomoneneity of the scatterers and we report here one of the cases which gave significant results. We refer to a dispersion of spheres with radius of 50 Å composed of a dielectric core of MgO coated by a layer of Al. We also report the results for the random dispersion of the binary aggregates of these spheres. The quantities we actually drew are $g_{sp}=\gamma_{sp}/S$ and $g=\gamma/S$ as a function of $\nu=\omega/\omega_p$, γ_{sp} being the extinction coefficient of the dispersion of independent spheres and that of their binary aggregates; S is the sum of the geometrical cross-section of all the spheres in the dispersion and ω_p the plasma frequency of Al. We notice that the above mentioned normalization of γ_{sp} and of γ makes our results independent of the number density of the dispersion, provided it is sufficiently low as to render negligible the multiple scattering processes among different objects. In fig. 1 we drew g_{sp} (solid lines) and g (dashed lines) for four values of the thickness of the coating, viz. 4, 8, 16 and 32 Å. In figure 2 we report, for the sake of completeness, g_{sp} and g for spheres of aluminum only. An examination of figure 1 shows that, for any value of the thickness the spectrum of the extinction coefficient for the dispersion of (independent) spheres presents two resonance peaks, one at a lower and the other at a

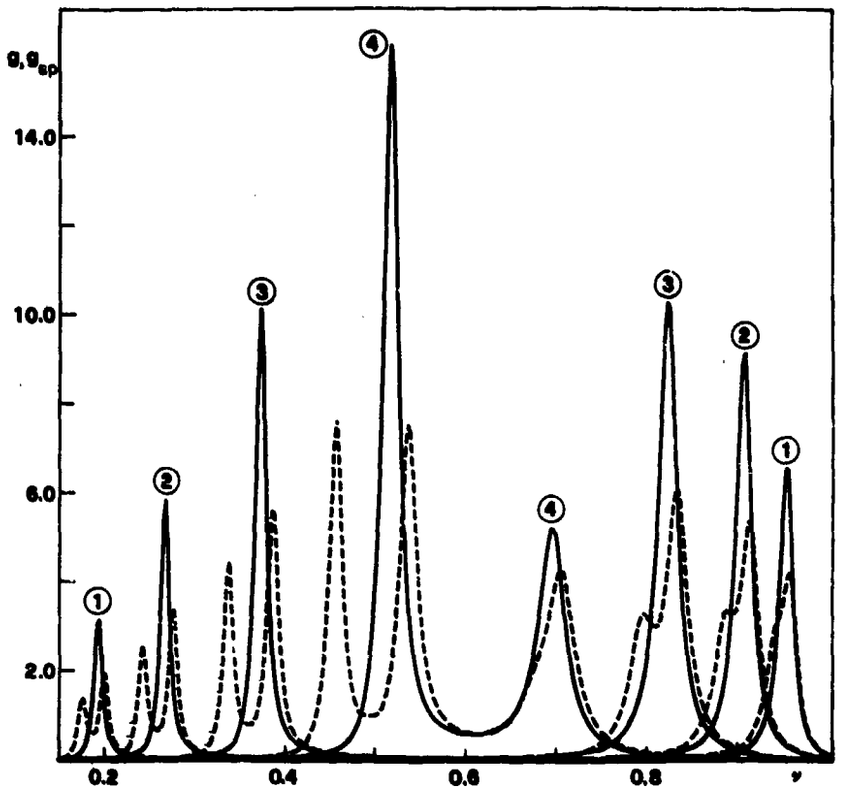


FIGURE 1 Extinction coefficient for spheres of MgO coated by Al with radius 50 Å. The encircled numbers refer to the thickness of the coating: ①=4 Å, ②=8 Å, ③=16 Å, ④=32 Å. The solid lines give g_{sp} , the normalized extinction coefficient of the dispersion of independent spheres, and the dashed lines give g, that of their binary aggregates. $\nu=\omega/\omega_p$.

higher frequency than that of the single peak at 0.57 ω_p which is characteristic of a 50 Å sphere of aluminum only (compare figure 2). Furthermore, when the thickness increases the resonance peaks tend to converge (at a decreasing rate) to the single peak of the only aluminum sphere. It is also worth noticing that the relative importance of the two peaks tends to exchange when the thickness increases. In fact, for small thickness the most important peak is that at higher frequency, while for large thickness the peak at lower frequency becomes the most important one. Thanks to the smallness of the spheres the frequency of the peaks reported in figure 1 is in fair agreement with that calculated from the surface resonance conditions of Fröhlich[7], written for the effective dielectric constant proposed by Van de Hulst to take account of the inhomogeneity of the scatterers[8]. This is shown in figure 3 where we drew the resonance frequency as a function of $\delta=t/\varrho$, t being the thickness of the coating and ϱ the radius of the spheres. Since far from resonance small spheres have a negligible extinction, scatterers of this kind could in principle be designed to produce selective extinction at any frequency within a wide range through a suitable choice of the thickness of the coating.

When we consider the extinction coefficient for the dispersion of binary aggregates (dashed curves in figure 1), the most evident feature is the duplication of the peaks as we already noticed in our previous work[3]. This duplication is particularly evident for the lower frequency peak of the independent spheres. As a consequence, if a considerable percentage of the spheres aggregate, any selective extinction they are designed to produce could be strongly weakened. We remark that we got a similar result by substituting the coating of aluminum with one of silver. The specific results are not reported for the

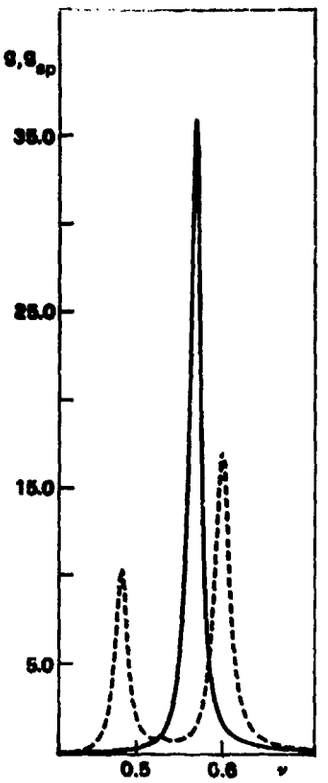


FIGURE 2 (left): Extinction coefficient for spheres of Al with radius of 50 Å. The solid lines give g_{sp} and the dashed lines give g. $\nu=\omega/\omega_p$.

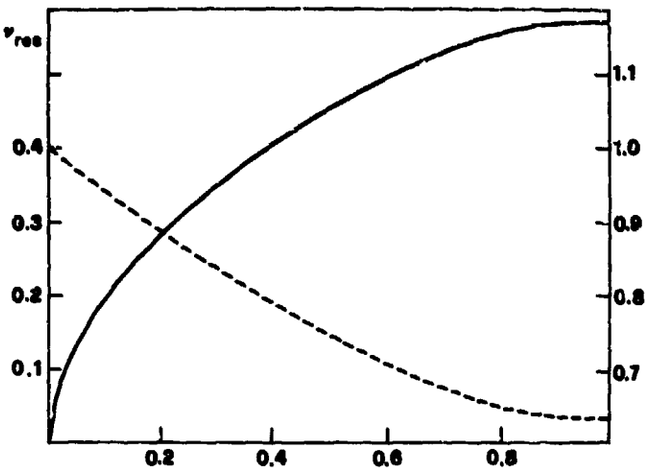


FIGURE 3: Frequency of the two resonance peaks, ν_{res}, expected for spheres of MgO with a coating of Al as a function of $\delta=t/\varrho$. The scale on the left refers to the solid line and that on the right to the dashed line.

spectrum of the extinction coefficient is not significantly different from that of fig.1. Anyway this proves that, as long as the Drude dielectric function can be effectively used to describe the behaviour of the metals, the extinction is only slightly affected by the choice of the parameters and specifically by the choice of ω_p.

The dramatic mobility of the peaks described above is not peculiar of the MgO-Al spheres as is clearly indicated by our preliminary results on the extinction of a dispersion of 50 Å spheres composed by a metal core coated by a different metal. In particular we found that the amount of shift of the peaks as a function of the thickness of the coating as well as the relative intensity of the peaks depend largely on the ratio of the plasma frequencies of the metals involved. A suitable choice of this ratio could ensure even in this case a selective extinction within a large range of frequency, although the aggregation should weaken the extinction just at the frequencies where the independent spheres present a maximum.

We did not investigate thoroughly the effect due to the aggregation of three or more inhomogeneous spheres: as it is easily understood, the geometry of the aggregation plays a fundamental role. According to our previous calculations on aggregates of homogeneous spheres[9], the spectrum of the extinction coefficient becomes more and more complicated with increasing complexity of the scatterers. Although this subject cannot be discussed in general terms any geometry of aggregation produces a system of peaks around the frequancy of those of the independent spheres. Ultimately, however, even an high degree of aggregation cannot produce a mobility of the extinction peaks as high as that due to the inhomogeneity of the spheres.

REFERENCES

1) R.G. Newton, "Scattering theory of waves and particles" (McGraw-Hill, New York, 1966).
2) F. Borghese, P. Denti, R.Saija, G. Toscano and O.I. Sindoni, "Macroscopic Optical constants of a cloud of randomly oriented nonspherical scatterers", Il Nuovo Cimento B 81, 29-50 (1984).
3) F. Borghese, P. Denti, R. Saija, G. Toscano and O.I. Sindoni, "Multiple electromagnetic scattering from a cluster of spheres. I. Theory", Aerosol Sci. Technol. 3, 227-235 (1984).
4) E.M. Rose, "Elementary theory of angular momentum", (Wiley, New York, 1957).
5) P.J. Wyatt, " Scattering of electromagnetic plane waves from inhomogeneous spherically symmetric objects", Phys. Rev. B 127, 1837-1843 (1962); erratum, Phys. Rev. 134, AB1 (1964).
6) F. Abeles, "Optical properties of solids", (North Holland, Amsterdam, 1972).
7) R. Ruppin, "Optical properties of small metal spheres", Phys. Rev. B 11, 2871-2876 (1975).
8) H.C. Van de Hulst, "Light scattering by small particles", (Wiley, New York, 1957).
9) F. Borghese, P. Denti, R. Saija, G. Toscano and O.I. Sindoni, "Effects of aggregation on the electromagnetic resonance scattering of dielectric spherical objects", Il Nuovo Cimento D 6, 545-558 (1985).

REFLECTIVITE ELECTROMAGNETIQUE D'UN MILIEU ALEATOIRE INHOMOGENE CONTINU A SYMETRIE CYLINDRIQUE

G. Muller, F. Molinet (*)

0 - INTRODUCTION

Pour le calcul de la réflectivité électromagnétique d'un milieu aléatoire l'usage est de séparer la réflectivité d'un milieu moyen de celle des fluctuations de ce milieu, qui se révèle prépondérante, et qui est donc souvent étudiée seule.

Dans le cas d'un milieu à pertes (plasma supposé sous-dense) et dans des études antérieures, il a été mis en évidence de fortes interactions entre le milieu moyen et les fluctuations. On s'est donc proposé dans l'étude actuelle d'évaluer la réflectivité des fluctuations du milieu en prenant pour champ incident le champ électromagnétique crée par les sources dans le milieu moyen exempt de fluctuations. Ceci équivaut à sommer tous les termes de la série de Born calculés avec le champ incident crée dans le vide et incluant une seule interaction avec le milieu aléatoire et un nombre quelconque d'interactions avec le milieu moyen.

1 - DESCRIPTION DU MILIEU ETUDIE

Ce milieu est un plasma ionisé lié à un écoulement fluide calculé dans l'hypothèse d'un mouvement moyen à symétrie axiale. Les écarts entre le mouvement réel ou les caractéristiques physiques effectives du milieu et les données fournies sont considérés comme aléatoires et appréhendés à travers plusieurs modèles de turbulence qui ont été ou seront testés. On suppose donc connues l'intensité et la loi de corrélation des fluctuations de vitesse et d'indice complexe en particulier sous une forme spectrale. Ce n'est pas l'objet du présent exposé.

Le plasma a des caractéristiques moyennes et aléatoires qui varient rapidement avec la distance à l'axe pour tendre vers celles de l'air ambiant, et lentement dans le sens longitudinal. Les calculs exposés sont faits localement et rapportés à l'unité de longueur de la configuration que l'on admet pour cela invariante longitudinalement.

2 - METHODE MATHEMATIQUE DE BASE

Les équations de Maxwell peuvent s'écrire sous la forme (équation de Helmoltz vectorielle)

$$\nabla \times \nabla \times \vec{E} - k_0^2 \varepsilon_r \vec{E} = 0 \qquad (1)$$

(On admettra dans la suite que la perméabilité relative μ_r est égale à l'unité).

Ou encore en introduisant une permittivité de référence ε_r°

$$\nabla \times \nabla \times \vec{E} - k_0^2 \varepsilon_r^\circ \vec{E} = k_0^2 (\varepsilon_r - \varepsilon_r^\circ) \vec{E} \qquad (2)$$

On définit une suite d'équations approchées (méthode de Born)

$$\nabla \times \nabla \times \vec{E}_0 - k_0^2 \varepsilon_r^\circ \vec{E}_0 = 0 \qquad (2)(o)$$

$$\nabla \times \nabla \times (\vec{E}_1 + \vec{E}_0) - k_0^2 \varepsilon_r^\circ (\vec{E}_1 + \vec{E}_0) = k_0^2 (\varepsilon_r - \varepsilon_r^\circ) \vec{E}_0 \qquad (2)(1)$$

$$\nabla \times \nabla \times (\vec{E}_n + \vec{E}_{n-1} + \cdots) - k_0^2 \varepsilon_r^\circ (\vec{E}_n + \vec{E}_{n-1} + \cdots) = k_0^2 (\varepsilon_r - \varepsilon_r^\circ)(\vec{E}_{n-1} + \cdots) \qquad (2)(n)$$

où $\vec{E}_0$, $\vec{E}_1$, ... $\vec{E}_n$ satisfont aux conditions aux limites sur la surface délimitant le plasma et à l'infini.

La limite des suites $\vec{S}_n = (\vec{E}_0 + \vec{E}_{0-1} + \cdots + \vec{E}_0)$ si elle existe est la solution cherchée. Le cas intéressant est le cas où la somme $(\vec{E}_1 + \vec{E}_0)$ est une bonne approximation, c'est-à-dire où les restes correspondants $(\vec{E}_n + \cdots + \vec{E}_n)$ sont négligeables quel que soit (n). En pratique on vérifie que $\vec{E}_n$ est d'un ordre de grandeur inférieur à $\vec{E}_1$.

2.1. Champ avec un milieu de référence homogène

Le cas le plus simple est celui où on prend (ε_r°) constant; dans ce cas l'équation d'ordre (o) admet les solutions particulièrement simples :

$$\vec{E}_0 = \nabla \times \left(\vec{A}\, e^{-j k_1 \vec{\ell} \cdot \vec{r}} \right)$$ (onde plane de direction $\hat{\ell}$)

(*) Société MOTHESIM, LA Bouraidière, RN 186, 92357 LE PLESSIS-ROBINSON, FRANCE

et $$\vec{E}_0 = \vec{\nabla} \times \left(\vec{A} \, \frac{e^{-jk_1 |\vec{r} - \vec{r}_0|}}{|\vec{r} - \vec{r}_0|} \right)$$ (onde sphérique de centre M_0)

avec $$k_1 = k\sqrt{\varepsilon_r}$$

D'autre part l'équation

(3) $$\nabla \times \nabla \times \vec{E} - k^2 \vec{E} = \delta(\vec{r} - \vec{r}_0)\vec{E}_0$$

admet la solution

$$\vec{\Pi} = \frac{e^{-jk|\vec{r} - \vec{r}_0|}}{4\pi |\vec{r} - \vec{r}_0|} \vec{E}_0 = G_0(r, r_0)\vec{E}_0$$

(4)

$$\vec{H} = -\frac{1}{j}\omega\varepsilon_0 \nabla \times \vec{\Pi}$$

$$\vec{E} = \nabla \times \nabla \times \vec{\Pi}$$

La fonction $G_0(r, r_0)$ est appelée fonction de Green. On en déduit la solution de l'équation d'ordre (1)

(5) $$\vec{E}_1 = \int \nabla \times \nabla \times (\varepsilon_0(r_0) - 1) \frac{e^{-jk|\vec{r} - \vec{r}_0|}}{4\pi |\vec{r} - \vec{r}_0|} \vec{E}_0 \, d^3\vec{r}_0$$

et dans le cas où $\varepsilon_1^* \neq 1$

(6) $$\vec{E}_1 = \int \nabla \times \nabla \times \frac{(\varepsilon_0(r_0) - \varepsilon_1^*)}{\varepsilon_1^*} \frac{e^{-jk_1|\vec{r} - \vec{r}_0|}}{4\pi |\vec{r} - \vec{r}_0|} \vec{E}_0 \, d^3\vec{r}_0$$

On peut également écrire (5) sous la forme

$$\vec{E}_1 = \vec{E}_1^m + \vec{E}_1^a = \frac{1}{4\pi} \int \nabla \times \nabla \times \left\{ \left[\varepsilon_1(\vec{r}_0) - \bar{\varepsilon}_1(r_0) \right] + \left[\bar{\varepsilon}_1(r_0) - 1 \right] \right\} \frac{e^{-jk|\vec{r} - \vec{r}_0|}}{|\vec{r} - \vec{r}_0|} \, d^3 r_0$$

de façon à séparer un terme moyen et un terme aléatoire. Pour celui-ci le résultat de l'intégration est nul en moyenne puisque la valeur moyenne

$$\langle \varepsilon_m(r_0) - \bar{\varepsilon}_m(r_0) \rangle$$ est par définition nulle

2.2. Section efficace avec un milieu de référence homogène

Admettons un champ $(\vec{E}_0)$ qu'on appelle champ incident et qui en fait correspond à une excitation imposée. Le champ total comprend en plus un champ diffracté $\vec{E}_d$ dont $\vec{E}_1$ est supposé une bonne approximation. $\vec{E}_0$ est de la forme :

$$\vec{E}_0 = \vec{A} \, e^{-j\vec{k}\cdot\vec{r}} \quad , \quad \vec{k} \cdot \vec{A} = 0$$

On définit la section efficace par l'égalité

$$\sigma_1 = \lim_{(r \to \infty)} \left\langle \left\{ 4\pi r^2 \int \left| \vec{E}_1(\vec{r}, \vec{r}') \, d^3\vec{r}' \right|^2 \right\} \right\rangle$$

que l'on écrit aussi :

$$\sigma_i = \underset{(\lambda \to \infty)}{\text{limite}} \left\langle \left\{ 4\pi\lambda^2 \int \vec{E}_i^{\circ}(\vec{\lambda}', \vec{\lambda}') \, d^3\lambda' \cdot \vec{E}_i^{*}(\vec{\lambda}'', \vec{\lambda}'') \, d^3\lambda'' \right\} \right\rangle$$

En remplaçant E_i par son expression on sépare l'intégrale en 4 termes dont 2 seulement ne sont pas nuls en moyenne

$$\sigma_i^{TT} = \underset{(\lambda \to \infty)}{\text{limite}} \left\langle 4\pi\lambda^2 \int d^3\vec{r}' d^3\vec{r}'' (\bar{\varepsilon}' - 1)(\bar{\varepsilon}'' - 1) \nabla \times \nabla \left(\vec{A} \frac{e^{-j(\vec{k}_i \cdot \vec{r}' + k|\vec{r}' \cdot \vec{r}|)}}{4\pi|\vec{\lambda}' - \vec{\lambda}'|} \right) \cdot \nabla \times \nabla \left(\vec{A}^* \frac{e^{j(\vec{k}_i \cdot \vec{r}'' + k|\vec{r}'' \cdot \vec{r}|)}}{4\pi|\vec{\lambda} - \vec{\lambda}''|} \right) \right\rangle$$

$$\sigma_i^{TT} = \underset{(\lambda \to \infty)}{\text{limite}} \left\langle 4\pi\lambda^2 \int d^3\vec{r}' d^3\vec{r}'' (\bar{\varepsilon}' - \bar{\varepsilon}_r)(\bar{\varepsilon}'' - \bar{\varepsilon}_r) \nabla \times \nabla \left(\vec{A} \frac{e^{-j(\vec{k}_i \cdot \vec{r}' + k|\vec{\lambda} - \vec{\lambda}'|)}}{4\pi|\vec{\lambda} - \vec{\lambda}'|} \right) \cdot \nabla \times \nabla \left(\vec{A}^* \frac{e^{j(\vec{k}_i \cdot \vec{r}'' + k|\vec{\lambda} - \vec{\lambda}''|)}}{4\pi|\vec{\lambda} - \vec{\lambda}''|} \right) \right\rangle$$

la première intégrale a une valeur exacte et c'est la contribution du milieu moyen négligeable d'après les calculs faits à ce jour. La seconde a une valeur aléatoire dont on calcule une valeur moyenne et c'est la contribution du milieu aléatoire.

Sous certaines conditions on peut définir les fonctions de corrélation

$$\int \left(\varepsilon(\vec{r}') - \bar{\varepsilon}(\vec{r}') \right) \left(\varepsilon(\vec{r}'') - \bar{\varepsilon}(\vec{r}'') \right)^* d^3(\vec{r}' - \vec{r}'') = B_\varepsilon(\vec{r}' - \vec{r}'')$$

et le spectre de corrélation

$$\phi_\varepsilon(k) = (2\pi)^3 \int B_\varepsilon(r) \, e^{jkr} \, d^3\vec{r}$$

Les conditions sont que les intégrales écrites tendent vers une limite dans un domaine

$$|\vec{r}| = |\vec{r}' - \vec{r}''| \ll \delta\lambda$$

$\delta\lambda$ étant tel que les propriétés moyennes et aléatoires du milieu puissent être considérées comme constantes dans ce domaine ou plus généralement que les valeurs des intégrales dépendent peu de l'extérieur de ce domaine.
Si on admet que l'observation se fait dans une direction $\hat{k}_i \# \widehat{r - r'} \# \widehat{r - r''}$, on a alors $k|\vec{r} - \vec{r}'| = \vec{k}_i \cdot (\vec{r} - \vec{r}')$ et en faisant le changement de variables

$$\Delta\vec{r} = \vec{r}' - \vec{r}'' \quad , \quad \vec{r}_m = \frac{1}{2}(\vec{r}' + \vec{r}'')$$

2.2.1. Si le milieu homogène est le vide

$$\sigma_T^{\circ} = \int 2\pi^2 \left| \vec{k}_i \times \vec{k}_i \times \vec{A} \right|^2 \phi_\varepsilon(\vec{k}_i - \vec{k}_i) \, d^3\vec{r}_m$$

compte tenu que le facteur

$$\frac{\lambda^2}{|\vec{r}' - \vec{r}||\vec{r}'' - \vec{r}|} \to 1$$

et que les termes provenant de la dérivation de $\left(\frac{1}{\lambda}\right)$ sont des infiniment petits d'ordre supérieur à l'expression retenue

2.2.2. Si le milieu de référence est homogène et le diélectrique à pertes

La surface efficace est une intégrale double de volume obtenus à partir du produit d'une intégrale de volume simple par l'intégrale des quantités conjuguées

La quantité conjuguée de :

$$e^{j\vec{k}_i \cdot \vec{r}''} = e^{j\vec{r}''(\vec{k}_i' + j\vec{k}_i'')}$$

n'est plus

$$e^{-j\vec{k}_i\vec{r}''}$$

mais

$$e^{(j\vec{k}_i\vec{r}'')^*} = e^{-j\vec{r}''(\vec{k}_i' - j\vec{k}_i'')}$$

de sorte qu'en posant $e^{j\vec{k}\cdot\vec{r}'} = e^{j\vec{k}\vec{r}_m} e^{j\vec{k}(\vec{r}' - \vec{r}_m)}$ on fait apparaître un facteur :

$$F = e^{\int d^3\vec{r}'(\vec{k}_i - \vec{k}_i)} \int d^3\vec{r}''(\vec{k}_i - \vec{k}_i)^* \cdot e^{\int (\vec{k}_i' - \vec{k}_i')(\vec{r}''-\vec{r}')} \cdot e^{-(\vec{k}_i'' + \vec{k}_i'')(\vec{r}'+\vec{r}''-2\vec{r}_m)}$$

L'intégration en $(\vec{r}' - \vec{r}'')$ fera donc apparaître la fonction spectrale de la partie réelle des nombres d'ondes :

$$\phi\left(\left|\vec{k}_i' - \vec{k}_i'\right|\right) = \phi\left(\left|\mathcal{R}e\left(\vec{k}_i - \vec{k}_i\right)\right|\right)$$

Dans l'intégration en $\vec{r}_m$ la deuxième partie du facteur F sera unitaire puisque l'exposant s'annule. D'où la transposition du cas où le milieu de référence était le vide.

Par ailleurs le potentiel de rediffusion n'est plus

$$\vec{\Pi} = \frac{1}{4\pi} \int \vec{E}_i \frac{e^{-jkr}}{r} (\varepsilon_r - 1)$$

mais

$$\Pi_1 = \frac{1}{4\pi} \int \vec{E}_i \frac{e^{-jkr}}{r} \left(\frac{\varepsilon_r - \bar{\varepsilon}_r}{\bar{\varepsilon}_r} \right)$$

2.3. Extension au cas d'un milieu hétérogène à pertes

On se place dans l'esprit de ce qui a été rappelé précédemment. Il s'agit de calculer le champ $(\vec{E}_0)$ et le champ $(\vec{E}_1)$ de la solution renormalisée par rapport au milieu moyen : ceci sera fait dans le cadre d'approximations numériques exposées plus loin (discrétisation du milieu), les équations de base étant :

2.3.1. Pour le champ E_0

Celui-ci doit satisfaire à

$$\nabla \times \nabla \times \vec{E}_0(r') - k_0^2 \bar{\varepsilon}_r(r') = 0$$

($\bar{\varepsilon}_r$ étant la permittivité moyenne locale), et se confondre à l'infini avec une onde plane donnée (E_0^i) dite " onde incidente à l'infini ".

2.3.2. Pour le champ E_1

Le champ $(\vec{E}_0 + \vec{E}_1)$ doit satisfaire à :

$$\nabla \times \nabla \times \left(\vec{E}_1 + \vec{E}_0\right) - k_0^2 \bar{\varepsilon}_r \left(\vec{E}_1 + \vec{E}_0\right) = k_0^2 \left(\varepsilon_r - \bar{\varepsilon}_r\right) \vec{E}_0$$

qui est l'approximation suivante du problème, et à la réduction à l'infini au champ $(\vec{E}_0^1)$.

Compte tenu de la linéarité du champ, si on définit des expressions

$$k_0^2 \varepsilon_r(r') \Delta \vec{E}_0$$

$\Delta \vec{E}_0$ étant un champ égal à $\vec{E}_0$ dans un petit volume $d^3\vec{r}'$ au voisinage de $\vec{r}'$ et nuls à l'extérieur, s'il y correspond des champs $\Delta \vec{E}_1$ continus dans tout l'espace et satisfaisant à

$$\nabla \times \nabla \times \left(\Delta \vec{E}_1(r, r')\right) - k_0^2 \bar{\varepsilon}_r \Delta \vec{E}_1(r, r') = k_0^2 \left[\varepsilon_r(r') - \bar{\varepsilon}_r(r')\right] \Delta \vec{E}_0$$

alors $$\vec{E}_1(\vec{r}, \vec{r}') = \sum \Delta \vec{E}_1(\vec{r}, \vec{r}')$$

ou si les champs $\Delta \vec{E}_1$ sont rapportés à des volumes unitaires

$$\vec{E}_1(\vec{r}, \vec{r}') = \int \Delta \vec{E}_1(\vec{r}, \vec{r}') d^3\vec{r}'$$

3 - CALCUL DES CHAMPS

3.1. Coordonnées cylindriques

Le calcul des champs sera mené en coordonnées cylindriques. On a choisi une méthode de discrétisation du milieu moyen en une série d'anneaux cylindriques homogènes, de sorte qu'on a introduit une interface entre deux milieux discrétisés successifs. Par contre, les caractéristiques turbulentes n'ont pas été discrétisées parallèlement.

On sait que tout champ peut être représenté comme dérivant d'un couple de potentiels axiaux : un potentiel TM(F) et un potentiel TE (G). Soit Z l'axe de symétrie, ρ la distance à l'axe, φ la coordonnée angulaire :

$$E_\rho = \frac{1}{j\omega\varepsilon}\frac{\partial^2 F}{\partial\rho\partial z} - \frac{1}{\rho}\frac{\partial G}{\partial\varphi}$$

$$E_\varphi = \frac{1}{j\omega\varepsilon\rho}\frac{\partial^2 F}{\partial\varphi\partial z} + \frac{\partial G}{\partial\rho}$$

$$E_z = \frac{1}{j\omega\varepsilon}\left(\frac{\partial^2}{\partial z^2} + k^2\right)F$$

$$H_\rho = \frac{1}{\rho}\frac{\partial F}{\partial\varphi} + \frac{1}{j\omega\mu}\frac{\partial^2 G}{\partial\rho\partial z}$$

$$H_\varphi = -\frac{\partial F}{\partial\rho} + \frac{1}{j\omega\mu\rho}\frac{\partial^2 G}{\partial\varphi\partial z}$$

$$H_z = \frac{1}{j\omega\mu}\left(\frac{\partial^2}{\partial z^2} + k^2\right)G$$

3.2. Calcul du champ E_0

Il se confond à l'infini avec le champ d'ondes planes.

$$\vec{E}_i^\infty \simeq \vec{E}_\infty e^{-j\vec{k}_i\cdot\vec{r}} = \vec{E}_\infty e^{jk_z z}\sum_{n=-\infty}^{+\infty} j^n J_n(k_\rho\rho)e^{jn\varphi}$$

$$H_i^\infty = -\frac{\nabla\times E_i^\infty}{j\omega\mu} = -j\frac{\hat{k}_i\times\vec{E}_i^\infty}{j\omega\mu}$$

avec

$$k_\rho = \sqrt{k^2 - k_z^2}$$

On cherche donc une solution dans chaque domaine homogène sous la forme

$$F^n = \sum_{n=-\infty}^{+\infty} F_{jn}^n J_n(k_\rho^n\rho)e^{jn\varphi} + F_{hn}^n H_n^{(2)}(k_\rho^n\rho)e^{jn\varphi}$$

$$G^n = \sum_{n=-\infty}^{+\infty} G_{jn}^n J_n(k_\rho^n\rho)e^{jn\varphi} + G_{hn}^n H_n^{(2)}(k_\rho^n\rho)e^{jn\varphi}$$

Les conditions à chaque interface sont la continuité des 4 composantes du champ (E_z, H_z, E_ρ, H_φ). La condition sur l'axe est que le champ est fini et ne contient que des fonctions J. La condition à l'infini est qu'il se réduise au champ donné, donc que les coefficients des fonctions J soient ceux relatifs à ce champ. Pour (i) interfaces, il y a (i+1) milieux et (4i) conditions pour (4i) coefficients inconnus. (Par des produits scalaires par $e^{-jn\varphi}$ et intégration on peut écrire ces équations pour chaque ordre (n)).

3.3. Calcul des champs E_1

Chaque élément de volume $d^3\vec{r}'$ sous l'influence d'un champ incident E_0 donne un potentiel

$$\vec{P} = \frac{\varepsilon_r - \bar{\varepsilon}_r}{4\pi\bar{\varepsilon}_r}\vec{E}_0 \; e\,\frac{-jk^n|r-r'|}{|r-r'|}$$

On omet le facteur $\frac{1}{4\pi}\left(\frac{\varepsilon_r}{\bar{\varepsilon}_r} - 1\right)$ dans ce qui suit. Ceci peut encore s'écrire en coordonnées cylindriques :

$$\vec{P} = \int d\vec{P} = \frac{1}{\varepsilon_f} \int dw\, \vec{E}_0 \sum_{-\infty}^{+\infty} H_n^{(2)}(\rho_> \sqrt{k^2-w^2})\, J_n(\rho_< \sqrt{k_1^2-w^2})\, e^{jn(\varphi-\varphi')+jwz}$$

Pour chaque valeur de $k_z = w$ et de $k_\rho^{(1)} = \sqrt{k_1^2-w^2}$ on se propose de déterminer un champ (F^{ext}, G^{ext}) qui soit équivalent en $(\vec{r}')$ au champ crée par le potentiel $d\vec{P}$.

En sommant tous ces champs, on obtiendra donc le champ $\Delta\vec{E}_{(w)}$ émis par la " source " $\vec{E}_0 \Delta^3 r'$ pour la valeur (w). La seule valeur de ce champ qui nous intéresse est la valeur à l'infini dans la direction d observation. Elle peut donc être évaluée par une expression asymptotique qui ne fait intervenir que les valeurs stationnaires de w. On peut montrer qu'il n'en intervient qu'une, à savoir

$$w_s = k_z$$

correspondant au point d'observation à l'infini.

Pour cette valeur, on affecte à chaque milieu un potentiel axial continu indéterminé (F^{ext}, G^{ext}) de la forme indiquée, et à ce champ on ajoute dans le domaine de la " source " celui qui est dérivé de $\vec{P}$ (ou de $d\vec{P}$). Les conditions aux interfaces permettent de déterminer tous les coefficients (le potentiel P n'intervient explicitement que sur les 2 interfaces voisines).

3.4. Expression du champ diffracté à l'infini

Dans le domaine discrétisé extérieur on a vu que le champ diffracté donc les potentiels ne contenaient que des fonctions H, soit

$$\begin{matrix} F^{ext} \\ G^{ext} \end{matrix}(\rho, \varphi, z) = \int \sum_n a_n^{ext}(w)\, H_n^{(2)}\left[\rho\sqrt{k^2-w^2}\right] e^{jn(\varphi-\varphi')+jw(z-z')}\, dw$$

Ces expressions sont asymptotiquement équivalentes à

$$\begin{matrix} F^{ext} \\ G^{ext} \end{matrix} \sim \sum a_n^{ext}(w) \sqrt{\frac{2\pi}{\pi\rho\sqrt{k^2-w^2}}}\, j^n\, e^{-j\rho\sqrt{k^2-w^2} - jn(\varphi'-\varphi)+jw(z-z')}$$

Si le point d'observation a les coordonnées r, θ, φ la phase est

$$\phi = r\left(-\sin\theta\sqrt{k^2-w^2} + w\cos\theta\right)$$

elle est donc stationnaire pour

$$\phi'_w = r\left(\frac{w\sin\theta}{\sqrt{k^2-w^2}} + \cos\theta\right) = 0$$

soit

$$w = -k\cos\theta$$

Pour cette valeur la dérivée seconde vaut

$$\phi''_{w^2} = \frac{r}{k\sin^3\theta}$$

L'évaluation asymptotique de l'intégrale est la valeur de l'intégrant pour cette valeur multipliée par

$$\sqrt{\frac{2\pi}{\phi''}}\; e^{\pm\pi/4}$$

Soit

$$F_{\varphi} \sim \sum_{n} a_n(-k\cos\theta)\, 2 j^{n+1}\, \frac{1}{r}\, e^{-jkr+jn(\varphi-\varphi')}$$

D'où :

$$E_\theta \sim \sum_{n} \frac{2 j^{n+1}}{j\omega\varepsilon}\, \frac{a_n^t}{r}\,(-k^2 \sin\theta\cos\theta)\, e^{-jkr+jn(\varphi-\varphi')}$$

$$E_\varphi \sim \sum_{n} \frac{2 j^{n+1}}{j\omega\varepsilon}\, \frac{a_n^c}{r}\,(-jk\sin\theta)\, e^{-jkr+jn(\varphi-\varphi')}$$

$$E_r \sim \sum_{n} \frac{2 j^{n+1}}{j\omega\varepsilon}\, \frac{a_n^z}{r}\, k^2 \tan^2\theta\, e^{-jkr+jn(\varphi-\varphi')}$$

Ces composantes peuvent être projetées sur les directions radiale (composante nulle) transversale méridienne et transversale perpendiculaire au plan méridien.

3.5. Calcul de la section efficace (observation à l'infini)

3.5.1. Expression de base

Le champ $\Delta\vec{E}_1$ peut être mis sous la forme

$$\Delta\vec{E}_1 = \frac{\varepsilon(r') - \bar{\varepsilon}(r')}{4\pi\,\bar{\varepsilon}(r')}\,\Delta\vec{E}'_1$$

ce qui permet de séparer un facteur aléatoire d'un facteur déterminé.

La section efficace s'écrit :

$$\sigma_1 = \lim_{(r\to\infty)} \left\langle \frac{r^2}{4\pi} \int \Delta\vec{E}'_1(r,r')\,\Delta\vec{E}'^{*}_1(r,r'') \left(\frac{\varepsilon(r')-\bar{\varepsilon}(r')}{\bar{\varepsilon}(r')}\right)\left(\frac{\varepsilon(r'')-\bar{\varepsilon}(r'')}{\bar{\varepsilon}(r'')}\right)^{*} d^3\vec{r}'\, d^3\vec{r}'' \right\rangle$$

Si on calculait cette expression avec une double intégration en volume, on ferait apparaître la fonction de corrélation spatiale

$$B_\varepsilon(\vec{r}',\vec{r}'') = \left\langle \left(\frac{\varepsilon(r')-\bar{\varepsilon}(r')}{\bar{\varepsilon}(r')}\right)\left(\frac{\varepsilon(r'')-\bar{\varepsilon}(r'')}{\bar{\varepsilon}(r'')}\right)^{*} \right\rangle$$

3.5.2. Expression simplifiée

Cependant on cherche à limiter le calcul à une seule intégration spatiale; pour ceci on fait une hypothèse sur le comportement du champ $E(\vec{r}, \vec{r}')$ au voisinage du point $\vec{r}'$, hypothèse bien entendu vérifiée lorsque le milieu est homogène. Ce comportement provient de 2 phénomènes qui se produisent quand on déplace le point $(\vec{r}')$:

- D'une part il y a le déplacement de ce point dans le champ fixe $\vec{E}_0$: celui-ci peut être considéré comme localement plan dans la plus grande partie de l'espace d'où la relation de voisinage :

$$\vec{E}_0(r') \simeq \vec{E}_0(\vec{r}'_m)\, e^{-j\vec{k}_i\cdot(\vec{r}'-\vec{r}'_m)}$$

Le vecteur d'onde $\vec{k}_i$ a l'intensité locale

$$k_i = k_1(r') = k_0\sqrt{\bar{\varepsilon}_r(r')}$$

et il est perpendiculaire aux surfaces d'onde de $\vec{E}_0$ et dirigé suivant le sens de propagation de ce champ.

- D'autre part quand $\vec{r}'$ se déplace en $\vec{r}'_m$, $\vec{E}_0$ étant inchangé, le champ correspondant $\Delta\vec{E}_1$ est remplacé par un autre champ et il faut postuler une relation analogue en $\Delta\vec{E}_1(\vec{r}, \vec{E}_0, \vec{r}')$ et $\Delta\vec{E}_1(\vec{r}, \vec{E}_0, \vec{r}'')$, la combinaison des deux phénomènes donnant :

$$\vec{E}_1(\vec{r},\vec{r}') \underset{(r\to\infty)}{\simeq} \vec{E}_1(\vec{r},\vec{r}'_m)\, e^{-j(\vec{k}_i-\vec{k}_i)(\vec{r}'-\vec{r}'_m)}$$

(qui est vérifiée pour un milieu homogène)

En introduisant cette formule dans l'expression de la section efficace, et en effectuant l'intégration en $(\vec{r}' - \vec{r}'')$ on obtient donc :

$$\sigma_1^T = \frac{4\pi}{(4\pi)^2} \underset{(r\to\infty)}{\text{limite}} \int \left| r \vec{E}_1 (\vec{r}, \vec{r}') \right|^2 \frac{(2\pi)^3}{|\varepsilon_r|^2} \Phi_\varepsilon \left(R_e |\vec{k}_i - \vec{k}_d| \right) d^3\vec{r}'$$

Φ_ε étant la fonction de corrélation spectrale des fluctuations de (ε_r).

En cas de rétrodiffusion, c'est-à-dire pour un point d'observation à l'infini $(\vec{r})$ dans la direction dont provient " l'onde incidente à l'infini ", les rayons incidents et diffractés vers (r) coïncident et

$$\vec{k}_d = -\vec{k}_i$$

$$|\vec{k}_i - \vec{k}_d| = 2 k_e(r')$$

3.5.3. Expressions algébriques

- Intégrations des sections efficaces locales :

L'expression de la section efficace est donc en rétrodiffusion

$$\sigma_1^T = \frac{4\pi}{(4\pi)^2} \int \left| r E_d(r, r') \right|^2 \frac{(2\pi)^3}{|\varepsilon_r|^2} \Phi_\varepsilon \left(2 R_e (k_e) \right) d^3 r'$$

La solution élaborée dans les axes cylindriques pour le domaine contenant le point d'observation est (forme asymptotique)

$$r_d E_d^i (r) = \sum a_n^i e^{-jkr + jn(\varphi - \varphi')}$$

L'indice (i) désignant la coordonnée spatiale envisagée. Dans le calcul de E on a trouvé

$$a_n^i = \sum A_{nm}^i e^{jm\varphi'} e^{jk_z z}$$

Or on peut obtenir les coefficients A_{mn}^i à condition de calculer le champ E_1 pour chacun des modes (m) du champ E_0.

Dans ces conditions

$$\sigma_1^T = 4\pi \int dz' \rho' d\rho' \delta_{ij} \sum_{i=1,3} \sum A_{nm}^i A_{n'm'}^{i\,*} e^{jm\varphi' + jn(\varphi - \varphi') - jn'\varphi' - jn'(\varphi - \varphi')} \frac{(2\pi)^3 \Phi_\varepsilon (2|k_1|) e}{(|\varepsilon_r|^2)}$$

- Intégration angulaire

Par convention on définit une section linéique locale. L'intégration en φ' est nulle pour les termes ne vérifiant pas

$$n + m = n' + m'$$

De sorte qu'il reste

$$(\sigma_1^T)_{\text{linéique}} = \frac{4\pi}{(4\pi)^2} \int 2\pi \rho \, d\rho \sum_i \sum_{\substack{m+n = \\ m'+n'}} A_{nm}^i A_{n'm'}^{i\,*} (2\pi)^3 \Phi_\varepsilon(\rho) / |\varepsilon(i)|^2$$

qu'on peut aussi écrire

$$(\sigma_1^T)_{\text{linéique}} = 4\pi^3 \int \rho \frac{d\rho}{|\vec{\varepsilon}|^2} \sum_{i=1}^{3} \sum_{\substack{n+m = \\ n'+m'}} R_e(A_{nm}^i) R_e(A_{n'm'}^i) + I_m(A_{nm}^i) I_m(A_{n'm'}^i)$$

Les fonctions R_e et I_m désignant les parties réelles et imaginaires de l'argument.

- Intégration radiale

Cette transformation des expressions limitant l'intégration numérique à l'intégration radiale en (ρ). En pratique un échantillonnage en (ρ) est défini dans chaque domaine discrétisé. Les caractéristiques " spectrales " n'ont pas besoin d'être discrétisées de la même façon que les caractéristiques de réfraction, de sorte que le coefficient local

$$F(r') = \frac{\Phi_2(\rho)\, 2 k_1(\rho')}{|\bar{\varepsilon}(\rho')|^2}$$

prend la valeur déterminée au point échantillonné sans modification.

4 - ANALYSE DES RESULTATS

4.1. Résultats globaux

On obtient d'une part les sections efficaces linéiques pour des conditions d'ionisation et de turbulence différentes, qui se rencontrent aux diverses positions longitudinales d'un même écoulement.

Avec le calcul ordinaire la rétrodiffusion turbulente est maximale aux niveaux d'ionisation et de turbulence les plus forts et diminue très nettement et fortement en même temps que ces paramètres.

Avec le calcul actuel " renormalisé " par rapport à un milieu moyen de rétrodiffusion aux niveaux d'ionisation et de turbulence élevée est plus basse que dans le cas précédent . Elle diminue moins avec ces paramètres pour rejoindre les valeurs de l'autre calcul lorsque les niveaux sont très faibles.

4.2. Résultats locaux

D'autre part on peut analyser les résultats partiels dans une même section correspondant à une même distance de l'axe (section efficace volumique moyennée angulairement) : ces résultats servent d'ailleurs au premier stade du calcul des décalages en fréquence (effet Doppler).

Du fait que dans le modèle de turbulence choisie, la valeur de la fonction spectrale est maximale sur l'axe, on constate dans le calcul classique que la réflectivité volumique est très élevée au centre et diminue continuellement quand le rayon ρ' croît.

Par contre dans le calcul " renormalisé " par rapport au milieu moyen, la réflectivité volumique est très faible sur l'axe et augmente continuellement quand ρ' croît, pour rejoindre à la périphérie des niveaux voisins des précédents, un peu inférieurs du fait qu'il s'agit d'une moyenne entre des rediffractions de zones situées du côté de la source et du point d'observation et d'autres zones placées derrière l'ensemble de l'écoulement.

4.3. Interprétation

Ceci s'interprète bien entendu par l'interception ou la réflexion d'une partie du rayonnement de la source par le milieu moyen conducteur, qui affaiblit la réémission locale, le rayonnement diffracté étant à son tour affaibli à la traversée des mêmes zones de ce milieu. Si les volumes dont on considère la diffraction sont placés à la périphérie de l'écoulement et du côté de la source et du point d'observation, ils sont peu affectés. Si au contraire ils se trouvent dans la zone axiale, ils le sont beaucoup.

4.4. Conclusion

Les résultats obtenus amènent à préciser les conclusions précédemment adoptées sur les zones de validité de la méthode de Born ordinaire concernant les écoulements considérés, et qui se fondaient sur l'évaluation de composantes des champs E dans ce cadre : ils montrent que le critère à retenir pour le rapport $|E_z / E_t|$ doit être relativement sévère.

On pense que dans tous les cas, un calcul du type de celui qui est défini ici peut donner une évaluation convenable de la réflectivité turbulente.

Les résultats détaillés et les graphiques correspondants seront fournis lors de la présentation orale.

5 - RESULTATS

5-1: Affaiblissement du rayonnement par absorption(effets cumulés du trajet incident et diffracté)
On extrait de l'intégrant des expressions de σ_t^i le facteur:

$$f(\ell) = \ell_0 \sum_{n,m,n',m'} Re\,(A^i_{nm})\,Re\,(A^i_{n'm'}) + Im\,(A^i_{nm})\,Im\,(A^i_{n'm'})$$

qui ne fait pas intervenir la réflectivité locale(ni donc l'expression du spectre de corrélation). ℓ_0 est choisi pour que $f(\ell)=1$ quand le milieu moyen est le vide.

La section choisie est à un niveau très ionisé et très turbulent(20 diamètres).Les coordonnées sont logarithmiques.

La figure 1) montre un très fort affaiblissement moyen dans la zone centrale.Les interfaces de discrétisation sont représentées en traits mixtes.

5-2: Effet Doppler

L'intégration en $(r'- r'')$ du § 3-5-2 fait apparaître une contribution de chaque volume élémentaire.Les points placés à la même distance ρ de l'axe ont une même vitesse moyenne V sensiblement parallèle à l'axe et une même intensité de fluctuations de vitesses σ_v.En première approximation la vitesse moyenne cause un décallage de fréquence:

$$\omega = -2k\,V\cos\theta$$

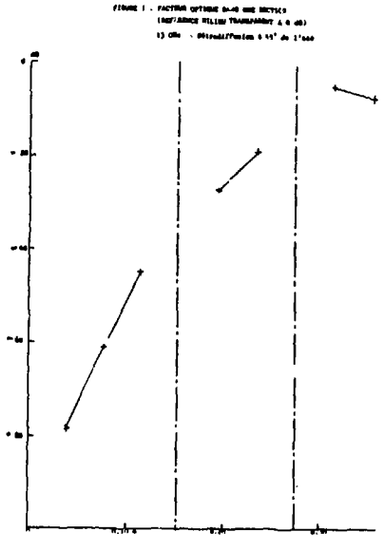
dont la contribution à la section efficace linéique est:

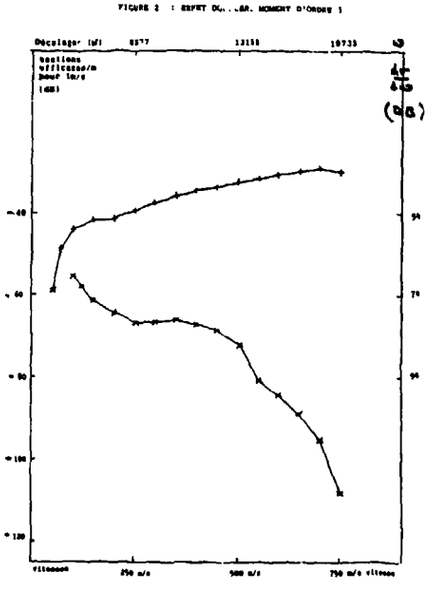
$$d\sigma_L^i = 2\pi^2 \sum_{\ell_v} \Phi_\varepsilon(\ell)\,\frac{d\left(\frac{\pi\rho^2}{dV}\right)}{dV}\,\frac{dV}{d\omega}\,d\omega$$

Cette formule de représentation de la densité de réflectivité linéique est reportée en figure 2) en fonction de V et ω .On saurait tenir compte des fluctuations de vitesses;on aboutirait à une sorte de lissage de la courbe peu sensible du fait que σ_v est "petit",et que la courbe est déjà continue.Par rapport à la figure 1)on a fait une transformation de coordonnées et tenu compte de la réflectivité locale.

La courbe supérieure représente les résultats classiques

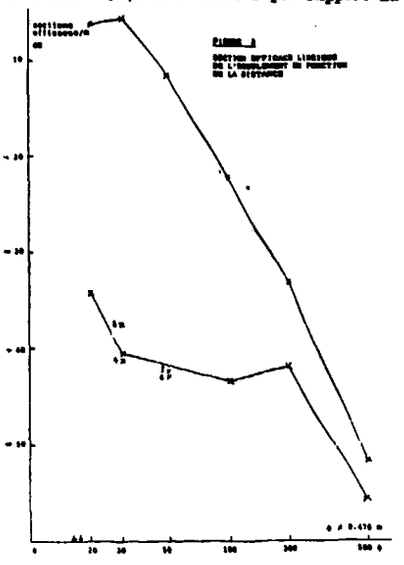
La courbe inférieure représente les résultats actuels.





5-3:Effet global à divers niveaux de l'écoulement:

Les sections efficaces linéiques calculées sont reportées sur la figure 3)en fonction de ladistance de cette section au début de l'écoulement.La courbe supérieure donne les anciens résultats (Born d'ordre 1 par rapport au vide) ,la courbe inférieure les résultats actuels:la différence est très sensible immédiatement après la zone de transition(flèches) et diminue peu à peu en même temps que l'ionisation et la turbulence.La courbe tracée est calculée avec 3 domaines(2interfaces).Des croix indiquent des résultats obtenus avec des discrétisations différentes



6-DISCUSSION

6-1:Hypothèse du champ localement plan,pour l'intégration locale.

Elle fait intervenir deux circonstances:

-Les variations d'indice faibles sur des distances de l'ordre de la longueur d'onde.Dans les calculs la longueur d'onde est de l'ordre du rayon utile de l'écoulement.Il y a donc une difficulté,qui serait plus forte si la variation continue était remplacée par une discontinuité physique franche.

-La zone des caustiques n'intervient pas:

Ici la seule différence optique retenue entre l'écoulement et l'environnement est la conductivité due à l'ionisation,suivant les formules adoptées:

$$\sigma = \frac{N_e e^2}{N_a \nu} \qquad \varepsilon_r = 1 + \frac{j\sigma}{\omega \varepsilon_0} \qquad n = \sqrt{\varepsilon_r}$$

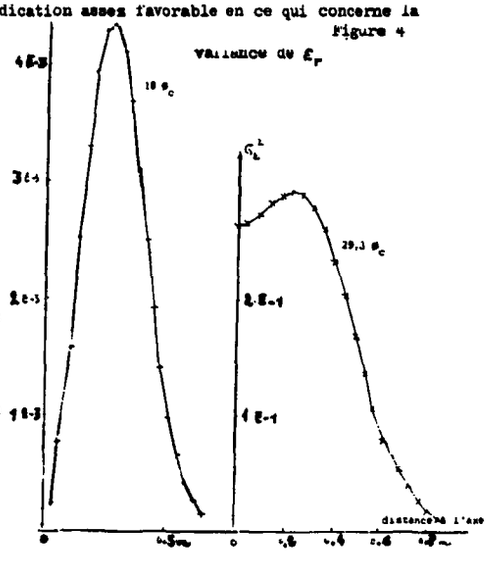
Où l'"absorption" Im(n) et la "réfringence" Re(n) sont étroitement liées.

On pourrait remarquer que le rayon moyen n'est coupé par le rayon infiniment voisin qu'au delà de l'axe.Donc,si l'ionisation est forte,au moins la pointe de la caustique a sa contribution très affaiblie par l'absorption. Si au contraire l'ionisation est très faible,cette pointe est en dehors de la zone active.

6-2 :Convergence de l'intégration en(r'-r")

Les estimations des échelles de turbulence d'après les formules classiques sont ici de l'ordre de 1 mm pour l et de 2 cm pour L au niveau du plus fort gradient.Ceci est une indication assez favorable en ce qui concerne la grandeur du domaine à considérer.

Figure 4



6-3 : Spectre de turbulence

On a affecté à l'expression de Von Karmann adoptée un coefficient Cn maximum sur l'axe.Ceci tient compte de résultats d'un calcul inspiré de modèles spécifiques concernant les écoulements envisagés.Sur la courbe 4 on voit que d'après ce calcul l'intensité des fluctuations comporte un minimum très accentué tout au début de la zone turbulente ,mais ce creux axial est pratiquement comblé à une faible distance(30 diamètres),du fait de la diffusion des fluctuations créés en amont dans les zones à fort gradient.

7 -DEVELOPPEMENTS ULTERIEURS

L'amélioration des résultats actuels dépend en premier lieu de nouvelles références de travaux théoriques concernant les propriétés aléatoires des écoulements étudiés..elles qui ont été utilisées sont déjà anciennes,et abordent la question de l'intensité des fluctuations d'indice,mais moins celle

des corrélations de ces fluctuations.

Il serait également intéressant de calculer les champs et les sections efficaces sans discrétisation d'espace. On trouve des indications en ce sens dans l'ouvrage de Barrick et Muck(L'impédance et l'admittance d'un milieu à symétrie cylindrique sont données par une équation de Riccati)

REFERENCES

Harrington R.: Time-Harmonic Electromagnetic Fields,McGrew-Hill Book Company 1961, New York,Toronto,London

Ishimaru A.: Wave Propagation and Scattering in Random Media,Academic Press 1978,New York,San Francisco,London

Tatarski V.I. :Wave Propagation in a turbulent medium,Dover Publications,Inc,New-York 1967

the effects of the turbulent atmosphere on wave propagation,Keter Press Jerusalem1971

,U.S Department of Commerce,National Technical Information Service

Gibson W.E.: Stochastic Model for turbulent reacting wakes,AIAA Journal,vol 4,n°11,Nov 1966

Rufine R.S. et D.A. de Wolf:Cross-Polarised Electromagnetic Backscatter from Turbulent Plasmas

Journal of Geophysical Research,vol 70,n°17,pp 4313-4321

D.A. de Wolf :Renormalisation of EM fields in application to large-angle scattering from randomly continuous media and sparse particle distributions,IEEE transactions on antennas and propagation vol AP-33,n°6,June 1985

MULTIPLE SCATTERING OF WAVES IN RANDOM MEDIA CONTAINING NON-SPHERICAL SCATTERERS

by
Vasundara V. Varadan, Vijay K. Varadan and Yushieh Ma
Center for the Engineering of Electronic and Acoustic Materials
and
Department of Engineering Science and Mechanics
The Pennsylvania State University
University Park, PA 16802
U.S.A.

SUMMARY

In this paper we wish to consider the effect of multiple scattering, scatterer geometry, statistics of the positional and orientational distribution functions on the propagation of time harmonic electromagnetic waves in a medium containing a random distribution of non-spherical scatterers. Some of the features that complicate the analysis are - (1) the size of the scatterers is comparable to the wavelength of the propagating wave; (2) the volume fraction occupied by the scatterers need not necessarily be small; (3) the impedance mismatch between the scatterers and the host medium need not necessarily be small. These in turn necessitate some of the effects we wish to focus on namely - detailed modeling of scatterer geometry and scatterer response, multiple scattering effects and the effect of correlations. We have already addressed many of these factors [1] and in our proposed talk we wish to present some recent results using non-spherical statistics for the second moment of the field.

In collaboration with Professor William A. Steele of Chemistry Department at Penn State, we have generated by Monte Carlo simulation the pair correlation function for spheroidal particles as a function of the distance between them and the direction of the vector joining their centers. At present we are generating the pair correlation function for randomly oriented spheroids and are also considering the effects of inter-particle forces as well as higher order correlation functions for clusters of particles. All of these have been incorporated into the multiple scattering calculations and compared with available experimental results. In contrast to previous work more attention will be focussed on the second moment of the field.

This paper will fit in very well with the scope of the symposium in the areas of mathematical methods for random media, characterization and modeling of random media and also interface quite well with some of the other papers in this area that we expect will be presented at the AGARD symposium.

1. PREFACE

The average or effective properties of a random medium containing inclusions of one material or voids distributed in some fashion in a second material called the host or matrix material can be conveniently studied by analyzing the propagation of plane waves in such materials and solving the resulting dispersion equations. Since waves propagating in such a two phase system will undergo multiple interactions with the scatterer phase, it becomes natural to consider multiple scattering theory and ensemble averaging techniques if the distribution of the inclusion phase is random. In this paper, a multiple scattering theory is presented that utilizes a T-matrix to describe the response of each scatterer to an incident field. The T matrix is simply a representation of the Green's function for a single scatterer in a basis of spherical functions. In this definition, it simply relates the expansion coefficients of the field that is incident on or excites a scatterer to the expansion coefficients of the field scattered when both fields are expanded in the same spherical wave basis [1]. In theory, the T-matrix is infinite, but in practice the T-matrix is truncated at some size that depends on the ratio of size of scatterer to the wavelength and the complexity of the geometry. Formally, the T-matrix includes a multipole description of the field scattered by the inclusion and this requires a propagator for multipole fields to describe the propagation from one scatterer to the next. Finally, the technique presented here is for a random distribution of scatterers which requires an ensemble average over the position of the scatterers and requires a knowledge of the positional correlation functions.

In previous studies [2,3] we relied on spherical statistics for hard spheres, generated by Monte Carlo simulation

or by the Percus–Yevick approximation even for non-spherical scatterers. Essentially, this increased the exclusion volume surrounding the non-spherical scatterer, and artificially restricted us to smaller concentrations in order to prevent the statistical spheres from overlapping. In the present study, these restrictions are removed by using a new Monte Carlo simulation developed by Steele [4] for non-spherical scatterers, that is based on expanding the two body correlation functions in Legendre polynomials. This permits us to consider the angular correlations that exist for non-spherical oriented scatterers. The final equation for the formalism is the dispersion equation which describes the propagation characteristics of the coherent or average filed in the effective medium. The numerical solution of this equation yields the effective complex, frequency dependent propagation number which is also a function of the size, geometry and distribution of the inclusion phase. The effective wavenumber is a function of the direction of propagation in the effective medium if the medium is effectively anisotropic. If, for example, the scatterers are spheres or if the non-spherical scatterers are randomly oriented, the effective medium will be isotropic, but if the medium contains aligned non-spherical scatterers the effective medium will be anisotropic. The effective wavenumber can be related to the effective material properties of the medium which are also complex and frequency dependent. For anisotropic materials, by solving the dispersion equation for different directions of propagation with respect to the aligned non-spherical scatterers, we can construct all components of the material property tensors of the effective medium such as the elastic stiffness tensor or the dielectric tensor, see [5].

In this paper, a systematic study is also made of first order contributions to the second moment or incoherent intensity of the wave field propagating in a discrete random medium. The second moment, which is traditionally defined as the correlation function of the component of the field fluctuations in any direction $\hat{u}$, is denoted by $I_u = <(\hat{u}\cdot\Delta E)(\hat{u}\cdot\Delta E)^*>$, where $\Delta E = E - <E>$ is the fluctuation of the field. Since the field fluctuations can be expanded in a multiple scattering series, each term of which contains sums on all possible scatterers, it is evident that we can divide the resulting terms into two sets; one involves considering only those terms in which the same scatterer contributes to a particular order term in each field fluctuation, and the other involves distinct scatterers. This latter set of terms will contribute to the incoherent intensity only if statistical correlations between scatterers are taken into account. The first category of terms are equivalent in spirit to radiative transfer theory since it is essentially the intensity of the field scattered by each scatterer that propagates from one site to another. Even for this set of terms, positional correlations between scatterers should be taken into account at volume fractions exceeding a few percentage, but these terms contribute to the incoherent intensity even if correlations are neglected.

Numerical results for aligned and randomly oriented oblate and prolate spheroids using the new correlation functions have been obtained and compared with previous calculations for spheroids that used spherical statistics. We foresee important applications of these new results to electromagnetic wave propagation through aerosols, which are non-spherical and often consist of aggregates and also in other cases where non-spherical scatterers are involved.

2. EFFECTIVE WAVENUMBER FOR THE AVERAGE FIELD IN A DISCRETE RANDOM MEDIUM

Let the random medium contain N scatterers in a volume V such that $N \to \infty$, $V \to \infty$, but $n_0 = N/V$ the number density of scatterers is finite. Let u, u^0, u^e_i, u^s_i be respectively the total field, the incident or primary plane, harmonic wave of frequency ω, the field incident or exciting the i-th scatterer and the field which is in turn scattered by the i-th scatterer. These fields are defined at a point r which is not occupied by any one of the scatterers. In general, these fields or potentials which can be used to describe them satisfy the scalar or vector wave equation. Let Re ϕ_n and Ou ϕ_n denote the basis of orthogonal functions which are eigenfunctions of the Helmholtz equation, see Morse and Feshbach [6]. As explained in the introduction the subscript 'n' is an abbreviated superindex and vector notation is implied. The qualifiers Re and Ou denote functions which are regular at the origin (Bessel functions) and outgoing at infinity (Hankel functions) which are respectively appropriate for expanding the field which is incident on a scatterer and that which it scatters. Thus, we can write the following set of self-consistent equations:

$$u = u^0 + \sum_{i=1}^{N} u^s_i = u^e_i + u^s_i = u^0 + \sum_{j\neq i} u^s_j + u^s_i \quad , \tag{1}$$

$$u^0(r) = p\exp(ikk_0\cdot r) = \Sigma_n\, a_n^i\, \mathrm{Re}\,\phi_n(r - r_i) \quad , \tag{2}$$

$$u^e_i = \Sigma_n\, \alpha_n^i\, \mathrm{Re}\,\phi_n(r - r_i);\ a < |r - r_i| < 2a \quad , \tag{3}$$

$$u^e_i = \Sigma_n\, f_n^i\, \mathrm{Ou}\,\phi_n(r - r_i);\quad |r - r_i| > a \quad , \tag{4}$$

where α_n^i and f_n^i are unknown expansion coefficients. We observe in Eqs. (3) and (4) that "a" is the radius of the

sphere circumscribing the scatterer and that all expansions are with respect to a coordinate origin located in a particular scatterer.

The T-matrix, by definition simply relates the expansion coefficients of u^0_i and u^s_i provided $u^0_i + u^s_i$ is the total field which is consistent with the definitions in Eq. (1). Thus [1],

$$f^i_n = \Sigma_{n'} T^i_{nn'} \alpha^i_{n'} , \tag{5}$$

and the following addition theorem for the basis functions is invoked:

$$Ru\, \phi_n (r - r_j) = \Sigma_{n'} \sigma_{nn'} (r_i - r_j)\, Re\, \phi_{n'} (r - r_i) . \tag{6}$$

Substituting Eqs. (2) - (5) in Eq. (1), and using the orthogonality of the basis functions we obtain

$$\alpha^i = a^i + \sum_{j \neq i} \sigma (r_i - r_j) T^j \alpha^j . \tag{7}$$

This is a set of coupled algebraic equations for the exciting field coefficients which can be iterated and leads to a multiple scattering series.

For randomly distributed scatterers, an ensemble average can be performed on Eq. (7) leading to

$$<\alpha^i>_i = a^i + <\sigma (r_i - r_j)\, T^j <\alpha^j>_{ij}>_i \tag{8}$$

where $< >_{ijk...}$ denotes a conditional average and Eq. (8) is an infinite hierarchy involving higher and higher conditional expectations of the exciting field coefficients. In actual engineering applications, a knowledge of higher order correlation functions is difficult to obtain, usually the hierarchy is truncated so that at most only the two body positional correlation function is required.

To achieve this simplification the Quasi-Crystalline Approximation (QCA), first introduced by Lax [7] is invoked, which is stated as

$$<\alpha^j>_{ij} \cong <\alpha^j>_j . \tag{9}$$

Then, Eq. (8) simplifies to

$$<\alpha^i>_i = a^i + <\sigma (r_i - r_j)\, T^j <\alpha^j>_j>_i ; \tag{10}$$

an integral equation for $<\alpha^i>_i$ which, in principle, can be solved. In particular, the homogeneous solution of Eq. (10) leads to a dispersion equation for the effective medium in the quasi-crystalline approximation. Defining the spatial Fourier transform of $<\alpha^i>_i$ as

$$<\alpha^i>_i = \int e^{iK \cdot r_i} C^i(K)\, dK \tag{11}$$

and substituting in Eq. (10), we obtain for the homogeneous solution

$$C^i(K) = \sum_{j \neq i} \int \sigma(r_i - r_j)\, T^j\, P(r_j|r_i)\, e^{i K \cdot (r_i - r_j)}\, dr_j\, C^j(K) . \tag{12}$$

If the scatterers are identical, then

$$C^i(K) = C^j(K) = C(K), \tag{13}$$

and thus for a non-trivial solution to $<\alpha^i>_i$, we require that

$$\left| I - \sum_{j \neq i} \int \sigma (r_i - r_j)\, T^j\, P(r_j|r_i)\, e^{i K \cdot (r_i - r_j)}\, dr_j \right| = 0 . \tag{14}$$

In Eqs. (12) and (14), $P(r_j|r_i)$ is the joint probability distribution function. In order to perform the integration in Eq. (14), we need a model for the pair correlation function. For non-spherical scatterers, the pair correlation function depends not only on the length of the vector connecting the centers of the scatterers, but also on the direction of this vector and the orientation of each scatterer. If the scatterers are spherical, then there is no dependence on direction and

orientation and the statistics are said to be spherical or isotropic. In both cases, the scatterers are not allowed to overlap, i.e. an infinite repulsive potential is assumed between scatterers.

For aligned spheroids which are rotationally symmetric, the dependence is only on the angle θ between the separation vector and the symmetry axis which is taken to be the z-axis of the coordinate system, as shown in Fig. 1. There is no dependence on the azimuthal angle ϕ. The joint probability distribution function is then written as

$$P(\mathbf{r}_j|\mathbf{r}_i) \quad \begin{cases} = 0; & |\mathbf{r}_i - \mathbf{r}_j| < R(\theta) \\ = G(\mathbf{x})/V; & |\mathbf{r}_i - \mathbf{r}_j| > R(\theta) \end{cases} \tag{15}$$

In the above equation, $G(\mathbf{x})$ is the pair correlation function for aligned spheroidal scatterers, $\mathbf{x} = \mathbf{r}_i - \mathbf{r}_j$, and $R(\theta)$ is the minimum center to center distance when the spheroids just touch one another at one point, such that the line joining their centers subtends an angle θ with the symmetry or z-axis of the spheroids. In this case the statistics are not isotropic but are a function of direction. Equation (14) can hence be simplified to

$$\left| I - n_0 \int \sigma(\mathbf{x})\, T\, G(\mathbf{x})\, e^{i\mathbf{K}\cdot\mathbf{x}}\, d\mathbf{x} \right| = 0 \tag{16}$$

where $(1/V)\sum_{j\neq i} = (N-1)/V \approx n_0$. The integral in Eq. (16) is simply the spatial Fourier transform of σTG. The zeroes of the determinant as expressed by Eq. (16), yield the allowed values of K as a function of the microstructure as determined by the T-matrix, the number density n_0 and the statistics of the distribution as determined by the pair correlation function. In general K, the effective wavenumber is complex and frequency dependent.

The dispersion equation as given in Eq. (16) is very well suited for computation. Using appropriate forms of the basic functions ϕ_n which are solutions of the field equations, the T-matrix of the single scatterer can be computed; for example, see Varadan and Varadan [1]. The translation matrix σ, although complicated in form for spherical functions, can nevertheless be computed in a straightforward manner. The spatial Fourier transform of σTG is fairly easy to compute because the integrand is well behaved for large values of the interparticle distance. In recent years, considerable progress has been made in Monte Carlo simulation to describe the statistics for non-spherical hard (impenetrable) particles by Steele. The joint probability functions have been expanded in a series of spherical harmonics and radial functions with unknown coefficients. The coefficients are evaluated directly in the Monte Carlo simulation. For aligned prolate and oblate spheroids, these results have just become available. The excluded volume for these geometries is also spheroidal. This has been implemented in calculations of the effective wavenumber in media containing random distributions of aligned spheroidal particles [8]. It can be seen that correct statistics conforming to the shape of the particle is needed to get correct results at volume fractions exceeding 5%.

2. INCOHERENT INTENSITY

The total scattered intensity is directly proportional to the second moment of the scattered field. It is known that the total scattered field is a combination of the average scattered field and the fluctuation of the field due to the random distribution of scatterers, i.e., $u = \langle u \rangle + u'$, the incoherent component of the scattered intensity can be obtained as

$$\langle u' u'^{*} \rangle = \langle u u^{*} \rangle - \langle u \rangle \langle u \rangle^{*}, \tag{17}$$

To first order, that is taking only the single scattering contribution to each scattered field, we obtain

$$\begin{aligned} \langle u' u'^{*} \rangle = \langle |u'|^2 \rangle &= \langle \Sigma u_j^{*} \Sigma u_k \rangle - \Sigma \langle u_j \rangle^{*} \Sigma \langle u_k \rangle \\ &= \sum_{j \neq k} \sum_{k} \langle u_j^{*} u_k \rangle + \sum_{j} \langle |u_j|^2 \rangle - \sum_{j} \sum_{k} \langle u_j \rangle^{*} \langle u_k \rangle. \end{aligned} \tag{18}$$

The ensemble averages in Eq. (18) can be written by integrating over the random positions $\mathbf{r}_j$, $\mathbf{r}_k$, etc. of the scatterers. Thus,

$$\begin{aligned} \langle |u'|^2 \rangle = n_0^2 \iint [((N-1)/N) \langle u_j^{*} u_k \rangle_{jk} - \langle u_j \rangle_j^{*} \langle u_k \rangle_k]\, d\mathbf{r}_j d\mathbf{r}_k \\ + n_0 \int \langle |u_j|^2 \rangle_j\, d\mathbf{r}_j . \end{aligned} \tag{19}$$

The second term in the above equation, which is proportional to n_0, is the ordinary single scattering approximation to the incoherent intensity and the magnitude of the incoherent intensity in any direction is proportional to the bistatic cross section of a single scatterer. The first term proportional to n_0^2 is due to the effect of positional correlations between pairs of scatterers.

For sparse concentrations, the scatterers are uncorrelated, and

$$\langle u_j^* u_k \rangle_{jk} = \langle u_j \rangle_j^* \langle u_k \rangle_k \tag{20}$$

and the first term of Eq. (19) vanishes.

In order to obtain the incoherent intensity for higher concentrations, the pair correlation function g(x) is taken into consideration. Recently Twersky [1983] has modified Eq. (19) for a dense distribution of scatterers in which the incoherent intensity has the form:

$$\langle |u'|^2 \rangle = n_0^2 \iint [G(r_j - r_k) - 1] \langle u_j \rangle_j^* \langle u_k \rangle_k \, dr_j \, dr_k + n_0 \int \langle |u_j|^2 \rangle_j \, dr_j \, . \tag{21}$$

Equation (21) is the final form used in our computation for the incoherent intensity up to the first order. However, the higher order contributions to the incoherent intensity become more and more important if the impedance mismatch between the scatterers and the host medium as well as the propagation distance are increasing. A detailed picture using the ladder diagrams in explaining the higher order multiple scattering processes can be found in our previous paper [9]. In the calculation, a knowledge of the coherent field is still required since the average scattered field $\langle u_j \rangle_j$ is involved in the formalism. The average scattered field $\langle u_j \rangle_j$ holding the j-th scatterer fixed can be expressed as, using Eq. (4),

$$\langle u_j \rangle_j = \Sigma_{n'} T_{nn'} \langle \alpha_n^j \rangle_j \phi_{n'}(r - r_j). \tag{22}$$

The exciting field coefficients α_n^j are initially unknown in Eq. (22). However, the average field $\langle \alpha_n^j \rangle_j$ exciting the j-th scatterer is known after defining an effective propagation constant K which is complex ($K = K_1 + iK_2$). Following this definition, the average or effective exciting field $\langle \alpha_n^j \rangle_j$ can be written as

$$\langle \alpha_n^j \rangle_j = A_n \, e^{iK \, k_0 \cdot r_j}, \tag{23}$$

where k_0 is the propagation direction of the incident wave. The unknown effective exciting amplitudes A_n, however, can be solved by invoking the extinction theorem.

If we substitute Eq. (22) in (21), we obtain

$$\langle |u'|^2 \rangle = n_0^2 \iint [G(r_j - r_k) - 1] \Sigma_{n'} T_{nn'} \langle \alpha_n^j \rangle_j \phi_{n'} \Sigma_{n''} T_{n''n'''}^* \langle \alpha_{n'''}^k \rangle_k^* \phi_{n'''} \, dr_j dr_k + n_0 \int | \Sigma T_{nn'} \langle \alpha_n^j \rangle_j \phi_{n'} |^2 \, dr_j. \tag{24}$$

We notice that in Eq. (24), the multiplication of the T-matrix and the effective exciting field is independent of the integral and the pair correlation function. In fact, the integral of the pair correlation function turns out to be the three dimensional spatial Fourier transform of the pair correlation function [G(x)-1]. In order to investigate the contribution of the incoherent intensity, we calculate the major normalized quantity which is defined as follows:

$$\langle I_u \rangle = (I_s/I_0)(kr)^2 (v/V) = 2c(\Sigma T_{nn'} A_{n'} Y_{n'})(\Sigma T_{n''n'''} A_{n'''} Y_{n'''})^* F(k_0, K, r) / [(K_2/k)(ka)^3 (Z/a)] \tag{25}$$

where $Y_{n'}$ are the normalized spherical harmonics, $\{Y_{lm\sigma}(\theta,\phi)\}$, Z is the distance of penetration of the incident wave, n'(n'' or n''') is the index representing l and m; r is the radial distance from the center of the scattering region to the observation point, v is the volume of a single scatterer and V is the whole scattering volume (region). The function F in Eq. (25) is given as

$$F = 1 + n_0 \int [G(x) - 1] \exp[i(Kk_0 - k\, r/r) \cdot x] \, dx \, . \tag{26}$$

For spheres, the radial distribution function depends only on the separation distance |x| and the integration in Eq. (26) is performed numerically using tabulated values of G(x) from Monte Carlo simulation or from the Percus Yevick integral equation for non-overlapping spheres. For non-spherical scatterers such as spheroids, we have nested integrations on orientation and distance and the integration is more time consuming. The statistics in this case are again obtained from Monte Carlo simulation.

3. RESULTS AND DISCUSSION

In order to study the characteristics of the incoherently scattered wave intensity, we choose electromagnetic waves as probing waves simply because there are a number of applications in remote sensing.

By sending plane electromagnetic waves through scatterers we intend to find, first, the angular dependence of the incoherent intensity and the influence of different polarizations, e.g., vertical and horizontal polarizations. If it is not specifically mentioned, scatterers are assumed to be spherical or spheroidal ice particles with a relative dielectric constant $\varepsilon = 3.168$ embedded in air. Fig. 2 presents the normalized incoherent intensity versus observation (scattering) angles. The forward scattering angle is, in our case 0° and therefore the backscattering direction is 180°. The nondimensional frequency considered is 0.6 which is equivalent to a physical frequency of about 14 GHz if a 2 mm particle is considered.

Taking a further look at Fig. 3, we can conclude that the vertical polarization gives more angular dependence of the incoherent intensity than the horizontal one. There is an extremely low intensity (i.e., a deep minimum in the curve) that occurs at 90° at a ka=0.6. This phenomenon happens again, however, at a higher observation angle of 125° when the frequency ka is raised to 2. There is no polarization difference at the forward and backscattering directions for the incoherent intensities.

In Fig. 4, we compare the backscattered intensity calculations with and without the effect of pair correlations. These results tell us that if the intensity is calculated without considering the pair correlation function when the concentration becomes even moderately high, i.e., 5%, one is able to see the difference in the magnitude particularly in the low frequency range.

Finally, we want to say something about the effect of the pair correlation function. In order to tell the importance of its effect on the final first order scattered intensity, we simply calculate the function F which appears in Eq. (25) and has been defined in Eq. (26). As can be seen from Eq. (26), it involves a Fourier transform of the pair correlation function and it contains an effective propagation constant K; hence it depends on the properties of the scatterers, the concentration, frequency and angle of observation. In Figs. 5 and 6, we can see that the Fourier transform of the pair correlation function dominates the scattering response particularly in the low frequency range and in the forward direction. In the high frequency range, it does not affect the scattered intensity much. Also, we observed that the intensity decreases after a volume fraction $c = 15\%$, which is also a fact pointed out in Kuga's experiments.

From Fig. 7, it is clear that the difference in obtaining the effective K is quite large if the spherical statistics is employed in approximating the nonspherical statistics. Therefore, for nonspherical scatterers of considerable concentrations, the incoherent intensity can be mistakenly estimated using Eqs. (22), (23) and (24) which all involve the effective wavenumber K. In addition, the pair correlation function G(x) in Eq. (26) may even contribute more to the difference depending on the concentration and the observation angle considered.

ACKNOWLEDGEMENT

The work reported here was supported in part by the U.S. Army Research Office through contract # DAAG29 - 84 - K - 0187 and DAAG29 - 85 - K - 0234 awarded to the Pennsylvania State University. The authors are grateful to Dr. Walter A. Flood for several helpful discussions and suggestions during the course of this work. They also wish to express their appreciation to Professor W. A. Steele who provided tabulated values of the pair statistics using Monte Carlo simulation

REFERENCES

(1) V.K. Varadan and V.V. Varadan, editors, Acoustic, Electromagnetic and Elastic Wave Scattering – Focus on the T-Matrix Method, Pergamon Press (1980).

(2) V. N. Bringi, V. V. Varadan and V. K. Varadan, "Effects of the Pair Correlation Function on Coherent Wave Attenuation in Discrete Random Media," IEEE Trans. AP-30, pp. 805 - 808 (1982).

(3) V. N. Bringi, V. K. Varadan and V. V. Varadan, "Average Dielectric Properties of Discrete Random Media Using Multiple Scattering Theory," IEEE Trans. AP-31, pp. 371 - 375 (1983).

(4) Y. D. Chen and W. A. Steele, J. Chem. Phys. 50, p. 1428 (1969).

(5) V.K. Varadan, Y. Ma and V.V. Varadan, "Multiple Scattering of Compressional and Shear Waves by Fiber Reinforced Composite Materials ", J. Acoust. Soc. Am. 80, 333 - 339 (1986).

(6) P. M. Morse and H. Feshbach, Methods of Theoretical Physics, Vol. II, p. 1865, McGraw-Hill (1953).

(7) M. Lax, "Multiple Scattering of Waves II. The Effective Field in Dense Systems," Phys. Rev. 85, pp. 621 - 629 (1952).

(8) V.V. Varadan, V.K. Varadan, Y. Ma and W.A. Steele, " Effects of Non-Spherical Statistics on EM Wave Propagation in Discrete Random Media," Radio Science, submitted (1987).

(9) V. V. Varadan, Y. Ma and V. K. Varadan, "Propagator Model including Multipole Fields for Discrete Random Media," J. Opt. Soc. Am. A2, pp. 2195 - 2201 (1985).

(10) V. Twersky, "Multiple Scattering of Sound by Correlated Monolayers," J. Accost. Soc. Am. 73, pp. 68 - 84 (1983).
(11) Y. Kuga and A. Ishimaru, "Retroreflectance from a Dense Distribution of Spherical Particles," J. Opt. Soc. Am. A1, pp. 831 - 835 (1984).

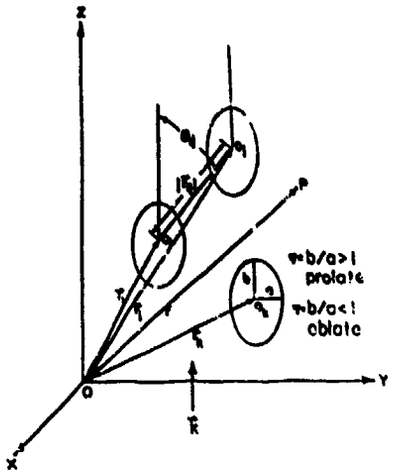


Figure 1 Multiple scattering of waves in discrete random media with positionally and orientationally correlated non-spherical scatterers.

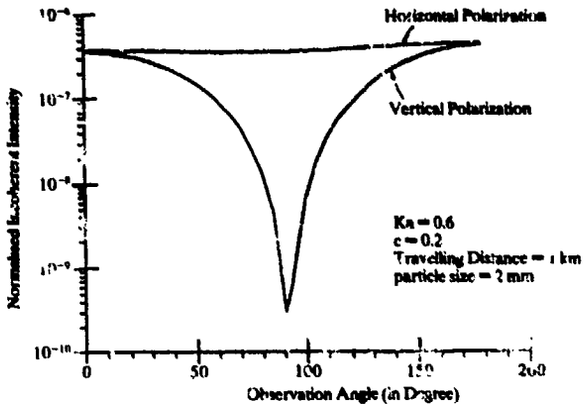


Figure 2 Normalized incoherent intensity vs. observation angle for ice particles (ka = 0.6).

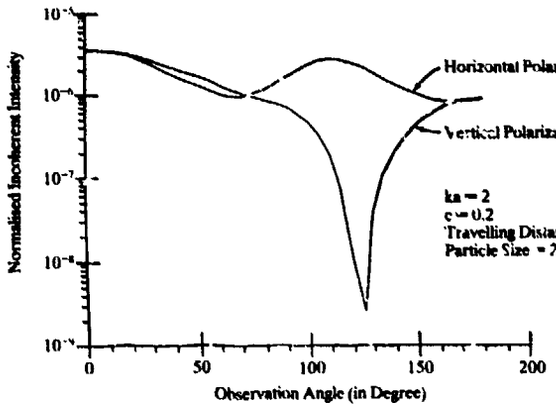


Figure 3 Same as Fig.2 except ka = 2.

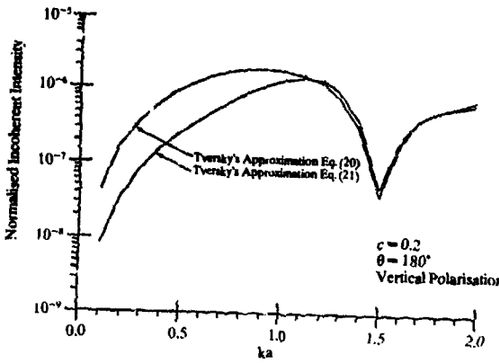


Figure 4 Normalized backscattered intensity vs. nondimensional frequency (c = 0.2).

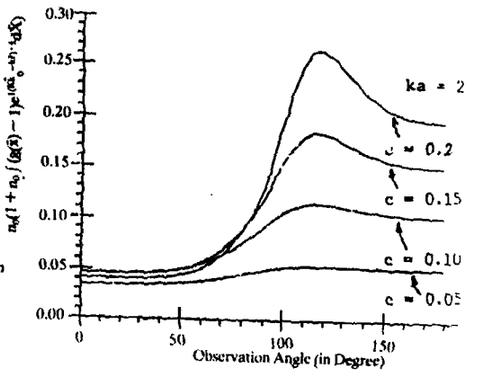


Figure 5 Effect of pair correlation function vs. observation angle.

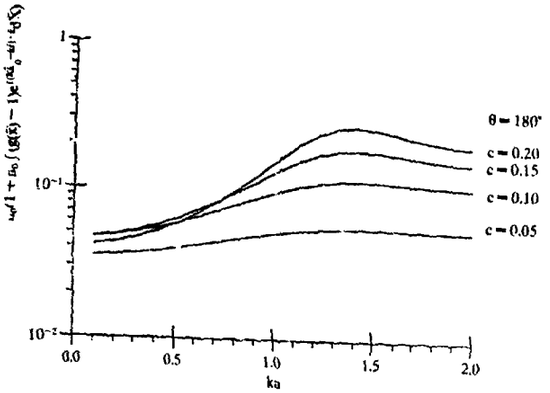


Figure 6 Effect of pair correlation function vs. nondimensional frequency ka.

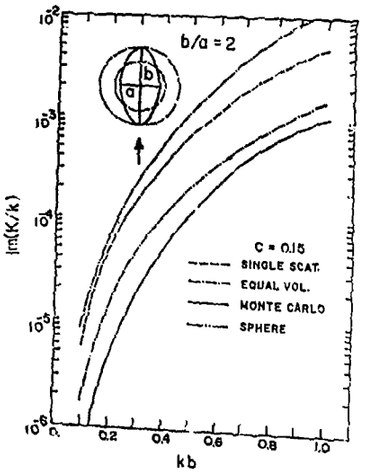


Figure 7 Imaginary part of effective wavenumber K vs. nondimensional frequency kb for prolate spheroids

Non-Linear Effects on the Atmospheric Transmission of High-Flux Electromagnetic Beams

by

R. L. Armstrong
Physics Department, New Mexico State University
Las Cruces, NM 88003, USA

The propagation of an intense beam of electromagnetic radiation through the atmosphere is accompanied by a host of interactions between the beam and atmospheric constituents present along the propagation path. These interactions may have a significant influence on the characteristics of the propagating beam. In this paper, we discuss aerosol-beam interactions which, in many cases of practical interest, are the dominant interactions between the atmosphere and the propagating beam. Theoretical analyses, numerical simulations, and experimental insights are reviewed in a survey of this complex problem.

When a high irradiance electromagentic beam propagates through the atmosphere, a variety of interactions occur with matter along the beam path. Both molecular and aerosol components of the atmosphere interact with the beam but, in many cases of interest, aerosol-beam interactions dominate. We consider this case in the present paper.

A complex group of aerosol-beam interactions must be accounted for at high beam irradiances. The aerosols absorb and scatter energy from the beam. The absorbed component heats the aerosols causing copious, perhaps explosive, vaporization. Hydrodynamic processes become significant, with internal and external shock waves responsible for droplet shattering, and for intense heating of the surrounding atmospheric medium. Electromagnetic interactions may result in the formation of an ionized plasma near the aerosol or, generally for liquid aerosol droplets, non-linear scattering processes and droplet lasing.

The propagating beam can be significantly influenced by these aerosol interactions. Since vaporization depends on the size of the aerosol particle (being proportional to the square of the droplet radius for spherical droplets), the beam propagates through aerosols progressively skewed towards a smaller size distribution. This results in significant spatio-temporal distortion of the beam. At higher irradiance levels, aerosol shattering and explosive vaporization effects can spontaneously (within a few acoustic times in the irradiated aerosol particle) liberate a large fraction of the aerosol mass as vapor into the surrounding medium. Scattering from these vapor aureoles, or from associated hydrodynamic (shock) disturbances may be significant. A companion process, which may occur at high irradiance levels, is aerosol-assisted plasma formation. Plasmoids may be formed near irradiated aerosols which significantly alter the absorption and scattering characteristics of the propagation path. Finally, more specialized effects may occur for spherical aerosols, such as stimulated Raman scattering, and lasing effects.

In this paper, we review progress made in understanding this complex problem. Aerosol interactions with intense electromagnetic beams may result in dramatic changes in the characteristics of the beam propagation path. These interactions include aerosol heating and vaporization,[1] explosive vaporization,[2,3] hydrodynamic effects,[4,5] plasma formation[2,6,7,8] and nonlinear optical phenomena.[9,10] The response of the propagating beam to these aerosol-beam interactions includes spatio-temporal distortion of the beam profile,[11,12,13] and possibly severe blockage of the beam due to the formation of a plasma.[14]

The temporal dependence of these interactions is of importance for the case of either singly or repetitively pulsed beams. Interactions occurring on a time scale long compared to the pulse width play only a minimal role in the beam dynamics.[1,2] For repetitively pulsed beams, both the pulse width and the inter-pulse period are significant. For example, droplet heating during the pulse, and cooling during the inter-pulse period, proceed with distinct time constants. It is characteristic of aerosol-beam interactions that they depend on the size of the aerosol particle, in addition to their dependence on other physical characteristics of the coupled aerosol-beam system. Therefore, in the propagation of a high intensity beam through a polydisperse distribution of aerosols, aerosol-beam interactions will generally vary across the size distribution,[1] as will the disturbance induced in the propagating beam.[12]

The study of aerosol-beam interactions has involved a combination of theoretical and experimental investigations. Although the theoretical aspects will be emphasized in the

present paper, it is instructive to review some of the recent experimental work in this subject. There have been a number of experimental studies of individual aerosol interactions with intense laser beams. Aerosol heating and vaporization has been investigated by observing changes in the Mie resonances.[15,16] Explosive aerosol vaporization has been observed directly using high-speed photographic techniques, and the associated shock-wave disturbances detected by a Schlieren system.[17,18] Plasma breakdown thresholds of aerosol-induced plasmas have been measured as a function of aerosol and beam parameters.[19,20] Both the spatial[7,8] and temporal[6,21] dependence of aerosol-induced plasmas have been measured. Finally, a variety of nonlinear processes associated with aerosols irradiated by intense light beams have been observed, including stimulated Raman scattering[22] and droplet lasing.[23]

Measurements of propagation effects on intense laser beams have also been made. For example, aerosol clearing,[24] the wavelength dependence of the atmospheric extinction coefficient following passage of a high power CO_2 laser beam,[25] plasma breakdown of the atmosphere after irradiation by a pulsed CO_2 beam[26], and Raman LIDAR excitation of stimulated Raman scattering from water aerosols in the atmosphere,[27] have probed the effect of aerosol-beam interactions on the pulsed beam. However, it should be noted that the comparison of these atmospheric propagation studies with detailed theoretical models of aerosol-beam interactions is not possible because of the lack of precise information concerning the aerosol size distribution.

In summary, interactions between atmospheric aerosols and an intense beam propagating along an atmospheric path will be reviewed. Numerical solutions to the complex dynamical equations will be described for cases of interest, and reference made to experimental studies where possible.

References

1. R. L. Armstrong, "Aerosol Heating and Vaporization by Pulsed Light Beams," Appl. Opt., Vol. 23, No. 1, 1 January, 1984, pp. 148-155.

2. R. L. Armstrong, "Interactions of Absorbing Aerosols with Intense Light Beams," J. Appl. Phys. Vol. 56, No. 7, 1 October, 1984, pp. 2142-2153.

3. S. Chitanvis, "Self-Similarity in Electrohydrodynamics" Physica Vol. 137 A, 1986, pp. 271-281.

4. R. L. Armstrong, P.J. O'Rourke, and A. Zardecki, "Vaporization of Irradiated Droplets," Phys. Fluids, Vol. 29, No. 11, November, 1986, pp. 3573-3581.

5. R. L. Armstrong and A. Zardecki, to be submitted to the Physics of Fluids.

6. A. Biswas, H. Latifi, P. Shah, L.J. Radziemski, and R.L. Armstrong, "Time-Resolved Spectroscopy of Plasmas Initiated on Single, Levitated Aerosol Droplets," Optics Letters (in press).

7. J. H. Eickmans, W. -F. Hsieh, and R.K. Chang, "Laser-Induced Explosion of H_2O Droplets: Spatially Resolved Spectra," Optics Letters (in press).

8. W. -F. Hsieh, J. H. Eickmans, and R. K. Chang, "Internal and External Laser-Induced Avalanche Breakdown of Single Droplets in an Argon Atmosphere," Optics Letters (in press).

9. R. K. Chang, S. -X, Qian, and J.H. Eickmans, "Stimulated Raman Scattering, Phase Modulation, and Coherent Anti-Stokes Raman Scattering from Single, Micrometer - Size Liquid Droplets," published in Proceeding of the Methods of Laser Spectroscopy Symposium Rehovot, Israel, 16-20 December, 1985.

10. J. A. Cooney and N.M. Khambatta, "CARS Scattering from Arbitrarily Sized Water Droplets," submitted to Appl. Opt.

11. R. L. Armstrong, S.A.W. Gerstl, and A. Zardecki, "Nonlinear Pulse Propagation in the Presence of Evaporating Aerosols," J. Opt. Soc. Am., Vol. A, No. 2, October, 1985, pp. 1739 - 1746.

12. S. C. Davies, and J.R. Brock," Laser Beam Propagation in an Evaporating Polydisperse Aerosol," Applied Optics (in press).

13. V. I. Bukatyi, Yu. D. Kopytin, and S.S. Khmelevtsov. "Thermal Defocusing of the Optical Radiation Traveling in an Absorbing Disperse Medium," Sov. J. Quant. Electron., Vol. 3, No. 1, July-August, 1973, pp. 37-39.

14. D. C. Smith, "Laser Radiation - Induced Air Breakdown and Plasma Shielding," Optical Eng., Vol. 20, No. 6, November/December, 1981, pp. 962-969.

15. T.R. Lettieri and E. Marx, "Resonance Light Scattering from a Liquid Suspension of Microspheres," Appl. Opt. Vol. 25, No. 23, 1 December, 1986, pp. 4325 - 4331.

16. J. F. Owen, R.K. Chang, and P.W. Barber, "Morphology-Dependent Resonances in Raman Scattering, Flouresecence Emission, and Elastic Scattering from Microparticles," Aerosol Sci. Technol., Vol. 1, 1982, pp. 293-302.

17. P. Kafalas and A.P. Ferdinand, Jr., "Fog Droplet Vaporization and Fragmentation by a 10.6μm Laser Pulse," Appl. Opt., Vol. 12, No. 1, January, 1973, pp. 29-33.

18. P. Kafalas and J. Herrmann, "Dynamics and Energetics of the Explosive Vaporization of Fog Droplets by a 10.6 μm Laser Pulse," Appl. Opt., Vol. 12, No. 4, April 1973, pp. 772-775.

19. P. Chylek, M. Jarzembski, N. Chou, and R. Pinnick, "Effect of Size and Material of Liquid Spherical Particles on Laser-Induced Breakdown," App. Phys. Lett., Vol. 49, 1986, pp. 1475-1477.

20. P. Chylek, M. Jarzembski, V. Srivastava, R. Pinnick, D. Pendleton, and J. Grunoleton, "Effect of Spherical Particles on Laser Induced Breakdown of Gases," Applied Optics (in press).

21. A. Biswas, H. Latifi, P. Shah, L. J. Radziemski, and R.L. Armstrong, to be submitted to Optics Letters.

22. J. B. Snow, S. -X. Qian, and R.K. Chang, "Stimulated Raman Scattering from Individual Water and Ethanol Droplets at Morphology-Department Resonances," Opt. Lett., Vol. 10, January, 1985, pp. 37-39.

23. H. -M. Tzeng, K. F. Wall, M.B. Long and R.K. Chang, "Laser Emission from Individual Droplets at Wavelengths Corresponding to Morphology-Dependence Resonances," Opt. Lett., Vol. 9, November, 1984, pp. 499-501.

24. A. V. Kuzikovskii, L.K. Chistyakova, and V. I. Kokhanov, "Pulsed Clearing of a Synthetic Aqueous Aerosol by CO_2 Laser Radiation," Sov. J. Quantum Electron, Vol. 11, No. 10, October, 1981, pp. 1277-1281.

25. M. C. Fowler, "Effect of a CO_2 Laser Pulse on Transmission through Fog at Visible and IR Wavelengths," Appl. Opt., Vol. 22, No. 19, 1 October, 1983, pp. 2960-2964.

26. M. Autric, J. P. Canessa, Ph. Bournot, D. Dufresne, and M. Sarazin, "Propagation of Pulsed Laser Energy through the Atmosphere," AIAA, Vol. 19, November, 1981, pp. 1415-1421.

27. U. Kh. Kopvillem, O.A. Bukin, V.M. Chudnovskii, S. Yu. Stolyarchuk, and V. A. Tyapkin, "Stimulated Raman Backscattering from a Water Aerosol in the Atmosphere," Opt. Spectrosc. Vol. 52, No. 2, August, 1985, pp. 184-187.

Acknowledgement

The author wishes to thank A. Zardecki for his collaboration on some of the work reported here.

A STATISTICAL ANALYSIS OF POLAR METEOR SCATTER PROPAGATION IN THE 45 - 104 MHz BAND

M.J. Sowa and J.N. Quinn
Applied Electromagnetics Division
Rome Air Development Center
Hanscom AFB, MA 01731
USA

J.E Rasmussen and P.A. Kossey
Ionospheric Physics Division
Air Force Geophysics Laboratory
Hanscom AFB, MA 01731
USA

J.C. Ostergaard
ElektronikCentralen
DK-2970 Horsholm
Denmark

SUMMARY

Data being acquired over a 1200 km path in northern Greenland, to characterize the polar meteor scatter channel, are described. The data include both propagation and projected communication statistics The propagation statistics include arrival rates and duty cycle as a function of frequency and received signal level. The communication statistics include estimates of the performance of a number of candidate systems in terms of throughput and message delivery time, as a function of frequency, time-of-day, season, data rate and modulation, for a specified bit-error-rate, message length and packet size.

1. INTRODUCTION

The need for reliable, over-the-horizon communications, coupled with recent advances in digital technology, have resulted in an increased interest in VHF meteor scatter propagation to support backup communications at high latitudes, where natural ionospheric disturbances can severely disrupt the more conventionally used HF band. Within the polar cap, Solar Proton Events (SPE's) produce ionospheric disturbances that can last for days, or even weeks, often resulting in extended periods of HF blackout. This is due to anomalous absorption caused by the increased ionization in the D-region (below about 90 km) that accompany SPE's.

Since VHF scatter from meteor trails occurs in the 90-110 km altitude range, the survivability of this mode of propagation is also controlled by the absorption effects associated with the disturbed D-region. Theoretical considerations [1] show that these effects, which can seriously degrade the performance of conventional meteor scatter systems operating around 40 MHz, can be reduced by operating at higher VHF frequencies This advantage is offset, since meteor-trail scattering efficiencies decrease significantly with increasing frequency. Thus, there is a need to quantify the trade-offs between these competing factors if one is to be able to project the performance of candidate meteor scatter systems under both normal and disturbed ionospheric conditions. To date, however, little experimental data have been available for this purpose. This paper describes a multi-frequency VHF meteor scatter diagnostic link [2,3], which was established in northern Greenland by the United States Air Force (USAF) to provide such needed data. In addition to discussing the current measurement program being carried out over the link, examples of propagation and communication statistics are given.

2. USAF HIGH LATITUDE METEOR SCATTER TEST-BED

The experimental link in northern Greenland was established by the Rome Air Development Center (RADC), and is now being operated by the Air Force Geophysics Laboratory (AFGL). It is providing data to address a number of questions concerning the potential performance of meteor burst communication systems in the polar region, including: the availability of useful meteor trails at very high latitudes; the potential communication capacity associated with those trails; the occurrence, persistence and effects of sporadic E-layers; and the effects of polar cap absorption events on the capacity of 45-104 MHz meteor scatter communication systems

Conventionally, the assessment of the communication capacities and bit-error-rates for meteor scatter systems are obtained by deploying a full duplex message handling system. The method has the advantage of providing precise (but limited) communication data; however, the information is relevant only to that particular system and provides little data on the specific propagation characteristics of the meteor scatter channel. In contrast, the USAF experimental approach exploits the concept that the meteor scatter channel can be considered as a transfer function. One aim of the experiment is to characterize the properties of the transfer function in as much detail as possible.

The link is located entirely within the polar cap, in northern Greenland between Sondrestrom Air Base (50° 39'W, 66o 59'N, elevation 330m) and Thule Air Base (47° 51'W, 76° 33'W, elevation 240m). The path is 1210 kilometers long and is shown in Figure 1. The transmitter at Sondrestrom Air Base and the receiver at Thule Air Base are not conventional communication system components. Rather, they were developed to investigate features of meteor scatter from a propagation point of view, as well as from a communication viewpoint. The efforts under this initial measurement program have been concentrated on characterising the time and frequency variations of the transfer function, including the variations in the instantaneous signal-to-noise ratios of each return from a meteor trail.

The transmitter at Sondrestrom AB, which is computer controlled, provides periodic transmissions at 45, 65, and 104 MHz. The first five minutes of each thirty minute time block are devoid of transmissions so that background noise measurements can be made at the receiver. Following the noise measurement, a CW signal is transmitted for twenty-five minutes. The system then steps to the next frequency 104 MHz is repeated bringing the total cycle time for all three frequencies to 2 hours. The cycle is repeated on a 24 hour per day basis. The Sondrestrom AB facility is shown in Figure 2 and a block diagram of the transmitting system is given in Figure 3. The transmitted power at all three frequencies can be varied. The transmitting antennas are Yagis, mounted so as to radiate horizontally polarized signals. The 45 and 65 MHz antennas are located at a height of 10 meters and the 104 MHz antenna is at 4.5 meters. The antenna gains are about 11 dBi and the beamwidths are approximately 55 degrees. During the operating period for which data is presented here, the transmitted power was approximately 600 watts at 45 MHz and 800 watts at 65 and 104 MHz. A 400 Hz FM modulation is imposed on the CW transmissions as a signature to identify the signals at the receiver.

The receiving facility at Thule AB is shown in Figure 4 and a block diagram of the receiving system is given in Figure 5. The receiver uses a waveform analyzer to capture the time history of each return. This data is recorded in digital form for later reduction and analysis. The receiving antennas are similar to those at the transmitting site with the 45, 65 and 104 MHz antennas mounted at heights of 12.5, 10 and 4.5 meters respectively. Because of the desire to quantify the effects of polar cap absorption events on the meteor scatter signals and the background noise, a special low noise receiver was built, having a noise temperature of 110° K, or a noise figure of 1.3 dB. The noise equivalent bandwidth is 30 KHz. The receiving system is controlled by a computer to cycle the receiver each half hour in accordance with the frequency selected at the transmitter. In addition, it controls the noise measurements that are made during the first five minutes of each half-hour time block, and a system calibration, which is performed once each day. Four-second data records of the envelope of the received CW signal are collected whenever the signal-to-noise ratio exceeds 4 dB and the 400 Hz signature tone is detected. The data are transferred to magnetic tape for storage and future processing.

3. DATA PROCESSING

The data processing sequence is shown in Figure 6. The raw data consist of voltage measurements of the received waveforms, background noise, and calibration signals. The voltage measurements are then calibrated to give received signal power. Examples of the calibrated trail returns are shown in Figure 7. A header, consisting of the date, time, noise level, transmitter power and frequency, is attached to each calibrated data record. A specially developed automatic technique [4] is employed to identify the dominant propagation mechanism (ionospheric or meteoric); and, if it is meteoric, the type (underdense or overdense). Those trails that cannot be automatically classified are identified and manually classified. After classification, data records are processed using a propagation/communication statistics program which creates a data base from the individual data records [5]. Propagation statistics, such as arrival rate, duration and duty cycle, can be obtained as a function of either Received Signal Level (RSL) or Signal-to-Noise Ratio (SNR). The communications analyses includes both fixed rate signaling and adaptive signaling, for which the instantaneous signaling speed is chosen, for any given modulation, to match the SNR in the channel. Information from the data base can then be accessed to determine the propagation and communication parameters given in Table 1.

1. Number of Arrivals Exceeding an RSL Threshold
2. Number of Arrivals Exceeding an SNR Threshold
3. Distribution of Time Above an RSL Threshold
4. Distribution of Time Above an SNR Threshold
5. Noise Level History
6. Distributions of Durations Above an RSL Threshold
7. Distributions of Durations Above an SNR Threshold
8. Distribution of Waiting Times for Trails Exceeding an RSL Threshold and Duration Threshold
9. Distribution of Waiting Times for Trails Exceeding an SNR Threshold and Duration Threshold
10. Capacity for Idealized Adaptive System for All Modes of Propagation
11. Capacity for Idealized Adaptive System for All Frequencies
12. Capacity for Realistic Fixed Rate System for All Frequencies
13. Capacity for Realistic Fixed Rate System for All Modes of Propagation
14. Waiting Time Required to Transmit a Message for a Fixed Rate System

Table 1. Parameter Options for Propagation and Communication Statistics Analysis

4. SAMPLES OF PROPAGATION AND COMMUNICATION STATISTICS

In this section examples are given to illustrate some of the propagation and communication statistics that can be derived from analyses of the returns from meteor trails received at Thule AB. The results are confined to May 1985 with the exception of an example given later to illustrate how the results can vary significantly from season-to-season. There were no significant ionospheric disturbances associated with any of the data described in this report

4.1 Propagation Statistics

4.1.1 Arrival Rates of Meteor Trails

Figure 8 gives meteor-trail arrival rates as a function of time-of-day and operating frequency, derived from returns having received signal levels (RSL's) exceeding -110 dBm. There was about a 3:1 diurnal variation in the arrival rates at all frequencies. The arrival rates for 45 MHz ranged from a maximum of three per minute to a minimum of one per minute, while at 65 MHz the rates varied over a range from about 0.8 per minute to 0.2 per minute. At 104 MHz the corresponding values were even lower, ranging from about 0.25 per minute to 0.08 per minute. The arrival rates were highest in the morning hours, between 0600-1200 local time (1000-1600 UT), and lowest in the evening between about 1800-2000 local time.

4.1.2 Return Durations and Duty Cycles

Average durations for returns with RSL's exceeding -110 dBm are shown in Figures 9, as a function of time-of-day and operating frequency. The durations are relatively constant as a function of time-of-day; however, they decrease significantly as the operating frequency is increased. At 45 MHz the average duration is nearly 0.4 seconds, while at 65 MHz and 104 MHz the average durations are about 0.3 seconds and 0.25 seconds, respectively.

Duty-cycles are determined simply from the product of arrival rates and durations. As shown in Figure 10, the duty cycles at 45 MHz ranged from a maximum of about 1.8% down to a minimum of about 0.6%. At 65 MHz the duty cycles were significantly less, ranging from about 0.5% to 0.1%. At 104 MHz the corresponding range was from about 0.12% to 0.03%. For all three frequencies the duty cycles have diurnal patterns that closely follow those of the arrival rates. This is in accordance with the near constancy of the durations of the returns, as described above.

4.2 Communication Statistics

4.2.1 Communication Capacity

Figure 11 presents communication capacity for a fixed data rate system, as a function of signaling speed and operating frequency. The data are for May 1985 and were calculated for BPSK modulation and a 10^{-4} Bit-Error-Rate (BER). In addition, a 100 bit packet size, an overhead of 16 bits and a 50 ms acquisition time were assumed. Only returns from underdense and overdense meteor trails were used in the computations (i.e., ionospheric scatter and returns from sporadic E layers were not included). The results given in Figure 11 indicate that as the signaling speed is increased, the projected communications capacity increases markedly, until the signaling speed gets to be several hundred thousand bits/s. This reflects the fact that over any extended period there tends to be some trails which can support very high data rates, and even though the number of such trails may be very small in terms of the total number of trails that provide returns in that period, they could provide the means for increasing the communications capacity for the period, if they can be exploited.

4.2.2 Message Delivery Time

This issue is further complicated, however, if one considers another communication's issue, message delivery time. As shown in Figure 12, for a given fixed-length message, there is a relatively well defined signaling rate which will minimize the delivery time. For a 1600 bit message that rate is about 10 kbits/s at an operating frequency of 45 MHz. At 65 MHz the optimum signalling speed is about 7 kbits/s, and at 104 MHz it is about 4 kbits/s.

4.2.3 Tradeoff Between Capacity and Delivery Time

Figures 11 and 12 illustrate that there may be a tradeoff to be considered depending upon whether the priority is minimum delivery time or maximum capacity. Stated in another way, if message delivery time is critical, it appears that one should use a relatively slow data rate, but use as many trails as possible; whereas, if capacity is the overriding factor, it would be better to increase the data rate substantially and wait for a particularly strong trail that will permit a very large amount of data to be transferred over the link.

4.2.4 Dependence of Capacity on Modulation Scheme

The capacity of a meteor scatter system also depends greatly on the modulation technique that is employed, as illustrated in Figures 13 and 14. Figure 13 gives computed capacities as a function of time-of-day and operating frequency, assuming a fixed data rate of 5 kbits/s and BPSK modulation and the same operating parameters used in developing Figures 11 and 12. At 45 MHz the capacity ranges from just under 50 bits/s to 165 bits/s with an average of about 100 bits/s. At 65 MHz the minimum capacity is 10 bits/s and the maximum is 60 bits/s, while at 104 MHz the range in capacity is from about 3 to 9 bits/s

Figure 14 shows the effects of changing the modulation from BPSK to noncoherent FSK. For the noncoherent FSK modulation, the maximum capacity at all operating frequencies is reduced by approximately 40%, compared to BPSK modulation.

4.2.5 Adaptive Signaling

Figure 15 illustrates that the potential capacity of a meteor burst communication system could be increased enormously if adaptive techniques can be used which will continuously match the signaling speed to the SNR. It is known from earlier experiments [6,7] that the maximum signaling rate which can be supported by a meteor trail is primarily limited by the SNR and not by the coherence bandwidth of the channel. The results given in Figure 15 correspond to a highly idealized BPSK adaptive system; specifically, no overhead bits or initialization delays were included and it was assumed that signaling speeds up to 250 kbits/s were possible, regardless of the SNR. Under these assumptions the computed average capacity at 45 MHz varies from about 2400 bits/sec to 700 bits/s, with the average being about 1400 bits/s. At 65 MHz the average is 475 bits/s with a maximum of nearly 1000 bits/s, while at 104 MHz the average capacity is 110 bits/s and the maximum is just over 200 bits/s. For comparison purposes, Figure 16 gives the results for a similarly idealized, fixed-rate system with BPSK modulation and a 5 kbits/s signaling rate. For the idealized fixed-rate system the average capacity at 45 MHz is 146 bits/s, or only 10% of the capacity available with an idealized adaptive system. At 65 MHz the fixed-rate system capacity is 40 bits/s, or only 8% of the adaptive capacity, while at 104 the average capacity is 8 bits/s, or about 7% of the adaptive system capability.

4.2.6 Seasonal Variations

The capacity of a meteor burst communication system also varies dramatically with time-of-year, or season, as illustrated in Figures 17 and 18, which were derived from data acquired during the months of February 1985 and July 1985, respectively. Along with the corresponding results for May 1985, already given in Figure 13, they provide a summary of the variations in system capacities from essentially winter conditions, through spring, and into summer at Thule. The data for February represent essentially the minimums observed over almost a year of observations, while those for July represent the maximum capacities observed during that period. Inspection of the Figures reveals that the capacity in July is a factor of two to three greater than in February, depending upon frequency. In addition, the times at which the relative maximum and minimum capacities occur over the February to July period are closely related to variations observed in the system (primarily cosmic) noise background. As shown in Figure 19, the peak of the system noise slides two hours per month, in accordance with sidereal time, as would be expected if the system was cosmic noise limited. For example, in February the peak occurs at approximately 1200 UT, while in May it is at 0600 UT and in July, at 0200 UT. Inspection of the fixed-rate system capacities given above for the same months (Figures 17, 13, and 18, respectively), reveal that the times at which the minimum capacities occur are very nearly the same as the times at which the cosmic noise is a maximum. This indicates that the variation in the cosmic-noise background is a more dominant factor than the variation in the arrival rate of the returns, in terms of the resulting diurnal pattern in the capacity of a meteor scatter system.

5. SUMMARY

The USAF Meteor Scatter Test-Bed has been established to investigate the potential performance of meteor scatter communications in the polar region, under a variety of normal and disturbed ionospheric conditions. The link is designed to obtain the data required to characterize a number of important propagation factors, including: The diurnal and seasonal variations in the availability of usable meteor trails at high latitudes, the effects of sporadic E and other (non meteor) scatter mechanisms, and the absorption associated with solar energetic particle events (PCA's). A primary goal of the research is to investigate and quantify how these factors vary with frequency over the 45-104 MHz band. In addition, emphasis is given to providing data that can be used to project the performance of candidate meteor scatter systems, which may employ both adaptive and fixed signaling rates as well as a number of different modulations.

Extensive software packages have been developed to reduce the large volume of data being acquired on the link. These packages automatically classify the recorded waveform in terms of its origin; i.e., whether it is from a meteor trail (underdense or overdense), from ionospheric scatter, or from a sporadic E layer. This classification allows the relative contribution of each of the scattering mechanisms to the overall system performance to be evaluated.

The data reveal that the contributions of overdense trails to the overall system capacities is nearly 50%, even though the number of overdense trails observed is less than 10%. This suggests that theoretical models describing meteor scatter propagation that only consider underdense trails (due to their preponderance) should be corrected to include the effects of overdense trails. The data being acquired over the Greenland link also show that sporadic E events can increase the system's throughput or capacity enormously. Indeed, the system's overall capacity for a month can be dominated by the capacity provided by a single sporadic E event. In the data described in this report, only the capacities provided by meteor trails have been included; however, in terms of estimating the true performance of a VHF "meteor burst" system, it may be important to include the effects of sporadic E. The multifrequency data being acquired over the Greenland link indicate that those effects are most pronounced at the lower VHF frequencies, and decrease significantly as the operating frequency increases.

Idealized calculations, using the experimental data being obtained in Greenland, indicate that the potential performance of candidate meteor burst systems can be substantially improved if multi-frequency and adaptive signaling techniques are employed. These will require much more complex equipment than conventional systems, so that "cost-effectiveness" may become an issue in the assessment of the desirability of employing such techniques to help achieve specified communication requirements.

It is difficult at this time to make direct comparisons of the performance of candidate meteor burst systems operating in the polar region with those operating at mid- or low latitudes. This is due to the fact that the performance of a meteor burst system can vary greatly with relatively small changes in such parameters as power, frequency, antenna gain, receiver thresholds, path length, etc. From the data being acquired over the Greenland link it appears that the overall performance of a given system at high latitudes may be less than what it would be at mid-latitudes (in accordance with such physical considerations as the orbits of the meteorites), but without truly comparable measurements, such statements cannot be quantified experimentally. It is anticipated that comprehensive physical models that are presently being developed in accordance with appropriate experimental data, such as that described by Brown [8], will provide a means by which such comparisons can be made.

REFERENCES

1. Crysdale, J.H., Analysis of the performance of the Edmonton-Yellowknife JANET circuit, IRE Trans., Com., March 1960.

2. Ostergaard, J.C., J.E. Rasmussen, M.J. Sowa, J.M. Quinn and P.A. Kossey, Characteristics of high latitude meteor scatter propagation over the 45 to 104 MHz band, AGARD Conf Proc., AGARD-CP-382, paper 9.2, 1985.

3. Ostergaard, J.C., J.E. Rasmussen, M.J. Sowa, J.M. Quinn and P.A. Kossey, The RADC High Latitude Meteor Scatter Test-Bed. Tech. Rep RADC-TR-86-74, Rome Air Development Center, July 1986.

4. Weitzen, J.A., and J. Tolman, A technique for automatic classification of meteor trails and other propagation mechanisms for the Air Force high latitude meteor burst test bed, Tech. Rep. RADC-TR-86-117, Rome Air Development Center, AD173133, 1986.

5. Weitzen, J.A., A data base approach to analysis of meteor burst data, Radio Science, Vol. 22, No. 1, pp 133-140, January-February 1987.

6. Akram, P., N.M. Sheikh, A. Jahved and M.D. Grossi, Impulse response of a meteor burst communication channel determined by raytracing, IREE Trans , Comm., 1977.

7. Weitzen, J.A., The multipath and fading profile of the high latitude meteor burst communication channel, Tech Rep. RADC-TR-86-166, Rome Air Development Center, AD174718, 1986.

8. Brown, D.W., A Physical Meteor Burst Model and Some Significant Results for Communications System Design, IEEE Journal on Selected Areas in Communications, Vol. SAC-3, No. 5, September 1985.

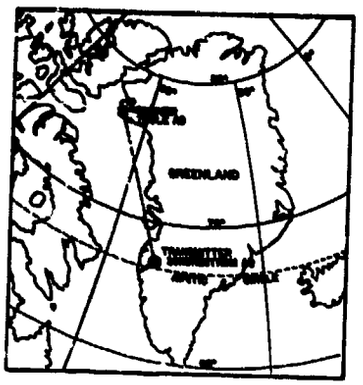


Fig. 1. Geometry of the experiment.

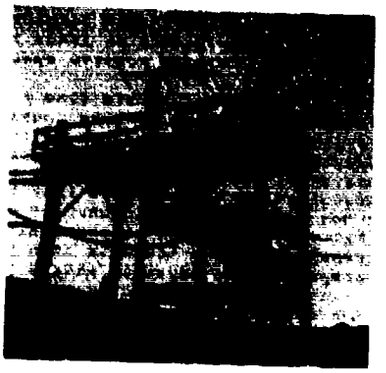


Fig. 2. Transmitter antenna tower at Sondrestrom AB.

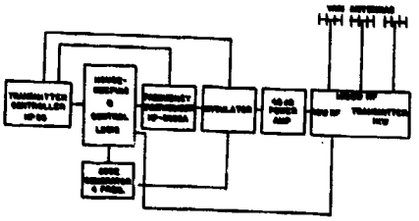


Fig. 3. Block diagram of the transmitter instrumentation.

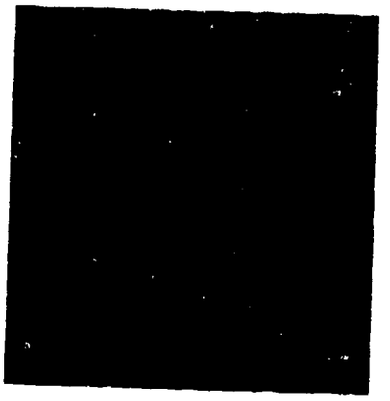


Fig. 4. Receiver building and antenna tower at Thule AB.

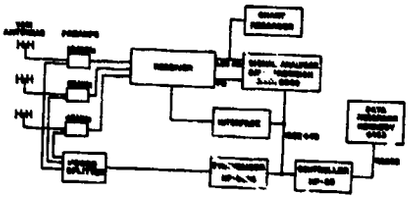


Fig. 5. Block diagram of the receiver instrumentation.

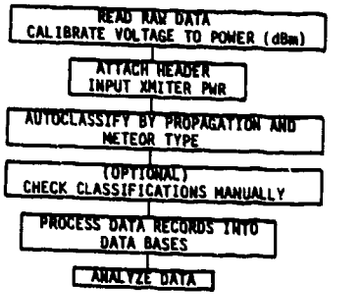
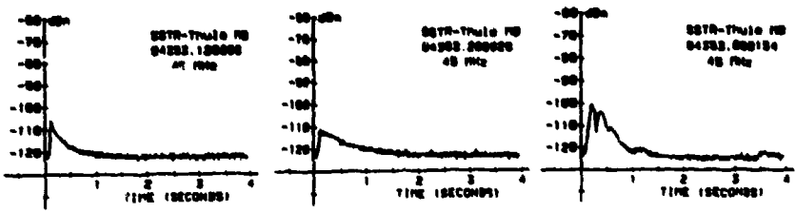
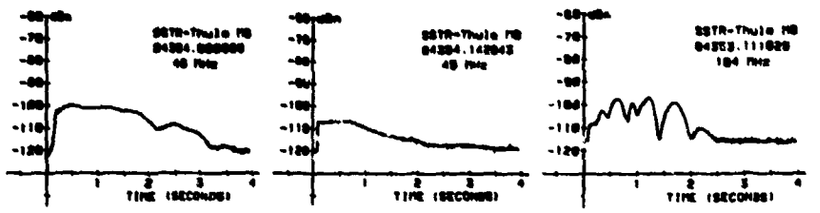


Fig. 6. Flow chart for the data reduction and analysis procedure.



(a) Underdense



(b) Overdense

Fig. 7. Examples of returns from underdense (a) and overdense (b) meteor trails.

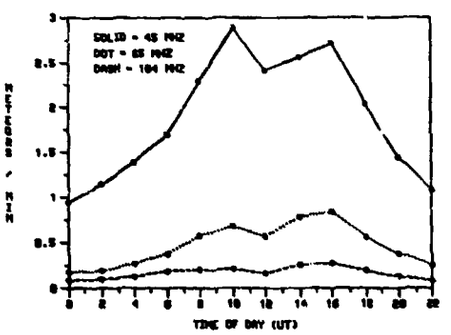


Fig. 8. Meteor return arrival rate as a function of time-of-day and frequency for signals from overdense and underdense trails which exceeded -110 dBm. May 1985.

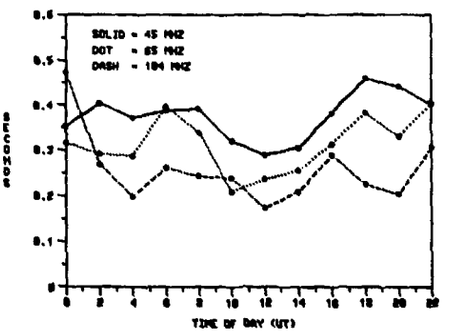


Fig. 9. Meteor return duration as a function of time-of-day and and frequency for signals from overdense and underdense trails which exceeded -110 dBm. May 1985.

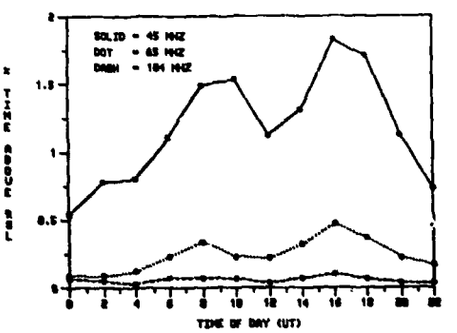


Fig. 10. Meteor return duty cycle as a function of time-of-day and operating frequency for signals from overdense and underdense trails exceeded -110 dBm. May 1985.

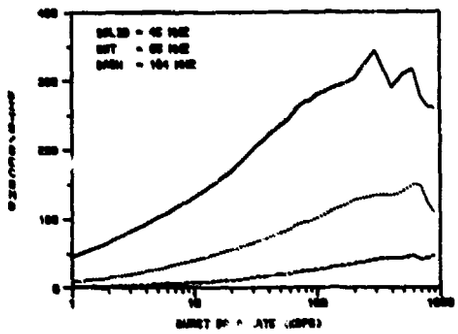


Fig. 11. Average capacity for a fixed signaling rate system as a function of signaling rate and operating frequency. Calculation based on May 1985 data, BPSK modulation, 1E-4 BER, underdense and overdense meteor trails, 100 bits/packet, 16 overhead bits and a 50 ms initialization time.

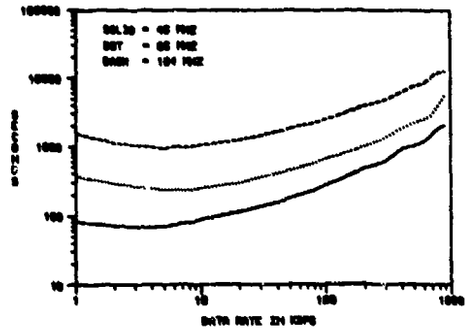


Fig. 12. Average message delivery time for a fixed signaling rate system as a function of signaling rate and operating frequency. Calculation based on May 1985 data, BPSK modulation, 1E-4 BER, underdense and overdense meteor trails, 100 bits/packet, 16 overhead bits and a 50 ms initialization time.

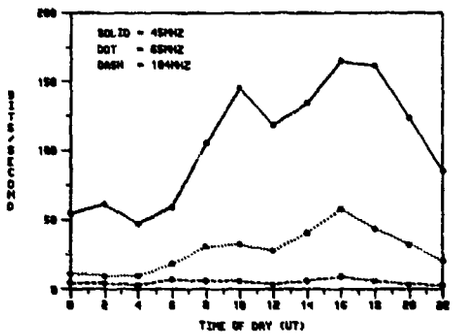


Fig. 13. Capacity for a fixed signaling rate system as a function of time-of-day and operating frequency. Calculation based on May 1985 data, a signaling rate of 5 kbit/s, BPSK modulation, 1E-4 BER, underdense and overdense meteor trails, 100 bits/packet, 16 overhead bits and a 50 ms initialization time.

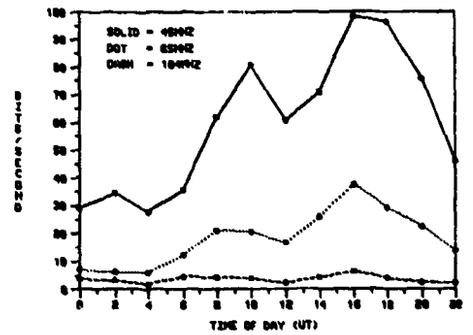


Fig. 14. Capacity for a fixed signaling rate system as a function of time-of-day and operating frequency. Calculation based on May 1985 data, a signaling rate of 5 kbit/s, Noncoherent FSK modulation, 1E-4 BER, underdense and overdense meteor trails, 100 bits/packet, 16 overhead bits and a 50 ms initialization time.

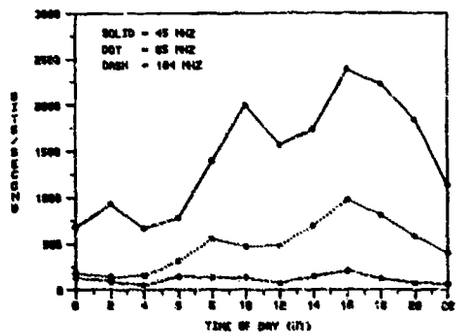


Fig. 15. Capacity for an idealized, fully adaptive system as a function of time-of-day and operating frequency. Calculation based on May 1985 data, BPSK modulation, 1E-4 BER, underdense and overdense meteor trails, no overhead and no initialization delay.

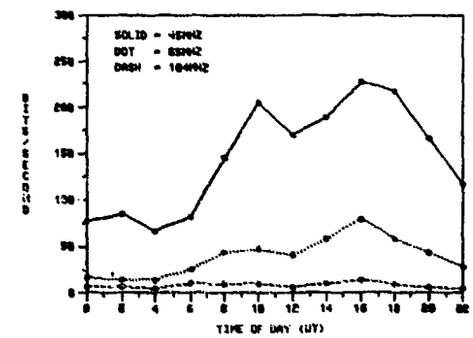


Fig. 16. Capacity for an idealized, fixed signaling rate system as a function of time-of-day and operating frequency. Calculation based on May 1985 data, a signaling rate of 5 kbits/s, BPSK modulation, 1E-4 BER, underdense and overdense meteor trails, no overhead bits and no initialization delay

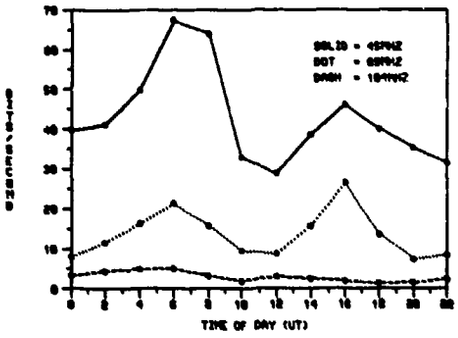


Fig. 17. Capacity for a fixed signaling rate system as a function of time-of-day and operating frequency. Calculation based on February 1985 data, a signaling rate of 5 kbits/s, BPSK modulation, 1E-4 BER, underdense and overdense meteor trails, 100 bits/packet, 16 overhead bits and a 50 ms initialization time.

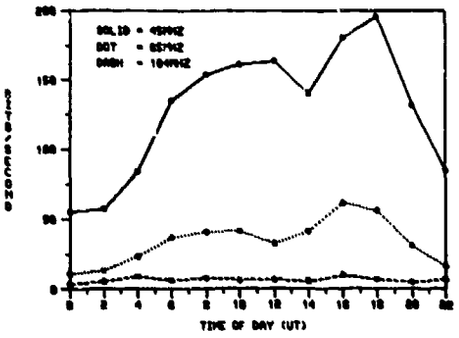
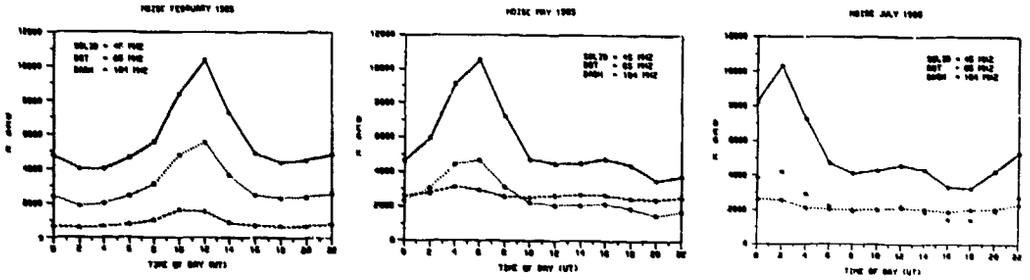


Fig. 18. Capacity for a fixed signaling rate system as a function of time-of-day and operating frequency. Calculation based on July data, a signaling rate of 5 kbits/packet, 16 overhead bits and a 50 ms initialization time.



a) February b) May c) July

Fig. 19. System noise for the Thule AB meteor scatter receiver for (a) February 1985, (b) May 1985, and (c) July 1985.

DISCUSSION

A. N. Ince, Tu

In a meteor-burst system called COMET (you called it a "classical system"), developed at SHAPE Technical Centre in the 1960s, we successfully demonstrated for the first time the value of diversity. What have you found in the high latitudes? Can you compare RAQ with FEC?

Author's Reply

We are well aware of your excellent results with space diversity reception in the COMET system. We have not, so far, investigated diversity reception techniques at high latitutdes. However, a frequency diversity experiment is contemplated.

As to the specific coding schemes to be used in a future high speed MB communication system, for which the propagation transit time could be comparable to packet length, it seems necessary to use several coding schemes, such as ARQ and FEC simultaneously.

MONTE CARLO SIMULATION OF MULTIPLE SCATTERING EFFECTS OF MILLIMETER WAVES FROM RAIN FOR A BISTATIC RADAR

by

P.-H.Voss* and H.Jeske
Meteorologisches Institut der Universität Hamburg
Bundesstrasse 55
D-2000 Hamburg 13
Federal Republic of Germany

Abstract

Within the scope of rain measurements with a bistatic dual-polarization radar, the influence of multiple scattering effects is discussed.

The determination of multiple scattering intensities (up to the sixth order) for frequencies of 33 and 94 GHz in dependence on rainfall rate, single scattering albedo, volume scattering coefficient, number of ground reflections, antenna beam widths, and dimension of the rain volume was done by the aid of an efficient Monte-Carlo algorithm.

The results show that multiple scattering cannot be neglected interpreting the scattered electromagnetic field on the basis of the normal radar equation. The portion to total scattering can become more than 5% for shorter microwaves and stronger rain rates (say 50 mm/h).

1. Introduction

As the operating frequencies of communication systems and remote sensing techniques move higher in the millimeter wave region, the scattering cross section of rain drops becomes comparable to the absorption cross section and herewith multiple scattering of rain clouds becomes more and more probable. Fig. 1 shows the single scattering albedo ω_o (ratio of volume scattering coefficient β_{sc} and the volume extinction coefficient β_{ext}) of rain clouds with rainfall rates of 10 mm/h and 50 mm/h as function of wavelength. It is confirmed that for wavelengths smaller than 5 mm the ω_o-values go to 0.5, e.g. the amount of scattering equals the amount of absorption.

In this paper calculations of multiple scattering effects at 33 and 94 GHz for a bistatic radar geometry will be presented. The experimental set-up considered is used for radar rain measurements with a dual polarization technique in which reflectivity is measured with two orthogonal polarizations. All interpretations of radar measuring techniques are - mostly exclusively - based on the well-known radar equation for single scattering, and so errors arising from multiple scattering are unavoidable.

To handle the three-dimensional multiple scattering problem the integro-differential equation of radiative transfer has to be solved. Several methods are known. In this paper an approach with an efficient Monte Carlo algorithm was undertaken (Voss, 1985). The scattering characteristics involved are calculated by the Mie-theory using a Marshall-Palmer drop size distribution (Marshall, Palmer, 1948).

Special studies of multiple scattering of rain on microwave propagation have been conducted, see e.g. Ishimaru et al. (1972-1982), Tsolakis et al. (1982), Oguchi (1980, 1981). It is suggested that multiple scattering for frequencies > 30 GHz and during heavy rain may become significant.

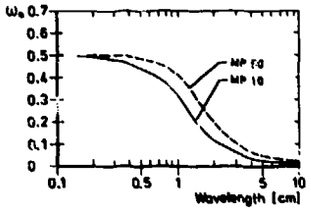


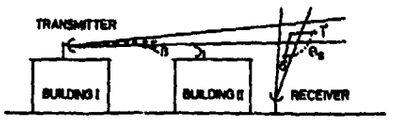
Fig. 1: Single scattering albedo ω_o as function of wavelength for rainfall rates of 10 mm/h and 50 mm/h. Drop size distribution after Marshall-Palmer. $\omega_o = \beta_{sc}/\beta_{ex}$; $\beta_{ex} = \beta_{sc} + \beta_{abs}$

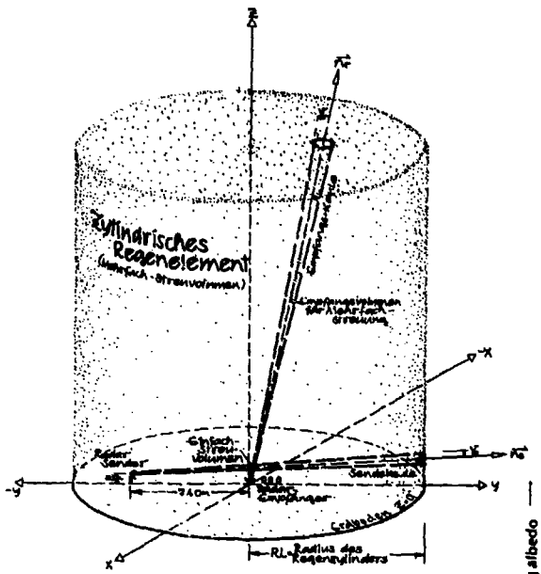
2. The Bistatic Radar Set-Up

The Meteorological Institute of Hamburg University made some rainfall rate measurements with a bistatic CW-radar at 33 GHz using the dual polarization technique (Dibbern, 1984, Dibbern et al., 1985). The geometry of the bistatic radar is given in Fig. 2a, b and the relevant geometrical and technical parameters of the experimental set-up are listed in Tab. 1. Transmitter and receiver of the bistatic CW-radar are equipped with antennas of half power beam

---

* Present Affiliation: GKSS-Forschungszentrum Geesthacht, FRG





Tab. 1: Geometrical and technical data of the bistatic radar experimental set-up.

Frequency	33.15	GHz
Wavelength	9.05	mm
Average power	0.25	W
Half beam width-transmitter	1°	
Half beam-receiver	2°	
Antenna gain-transmitter	44	dB
Antenna gain-receiver	38	dB
Antenna height (rel.)-transmitter	53	m
Antenna height (rel.)-receiver	0	m
Distance transmitter-receiver	740	m
Height of single scattering volume	100	m
Single scattering volume	136	m^3

Fig. 2a, b: Geometry of the bistatic radar measuring set-up, (a above): Overlook, (b below): Details with 3-dimensional rain volume cylinder.

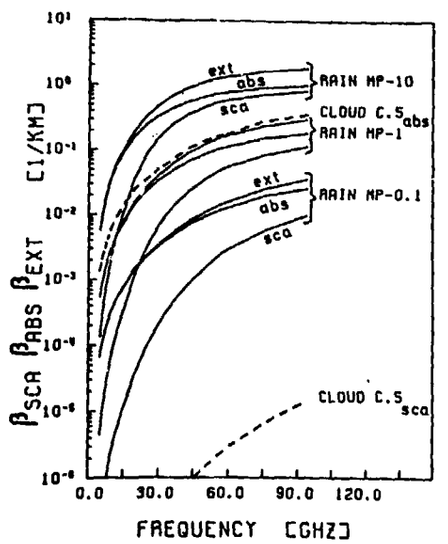


Fig. 3: Volume scattering - (β_{sc}), absorption - (β_{abs}), and extinction - (β_{ext}) coefficient (km^{-1}) as function of frequency for rainfall rates of 0.1, 1, 10 mm/h (Marshall-Palmer drop size distribution) and a cumulus congestus cloud (model C5 after Deirmendjian).

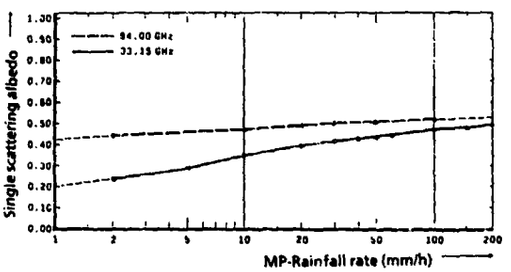


Fig. 4: Single scattering albedo as function of rainfall rate; frequencies are 33.15 GHz and 94 GHz.

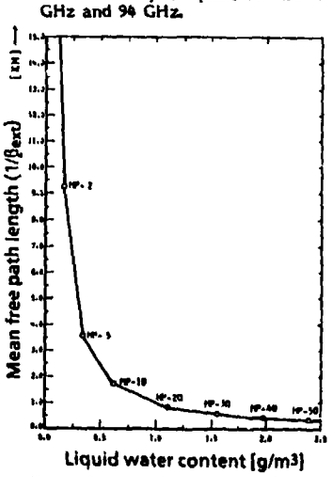


Fig. 5: Mean free path length ($1/\beta_{ext}$) as function of liquid water content (LWC); rainfall rates from 2 mm/h to 50 mm/h are marked at the curve.

widths of 1° and 2° for transmitting and receiving antennas, respectively. The transmitter is 53 m above the receiver and the distance between them is 740 m. The elevation angle of the transmitting antenna is assumed to be 3°, that of the receiving antenna 78°. The scattering plane is the plane through transmitter and receiver. the scattering angle for single scattering amouts to 105° (which gives an optimal sensitivity of the used experimental set-up (Dibbern, 1984)). The centre of the single scattering volume is in 100 m and the volume amounts to 136 m^3. In order to avoid direct radiation or disturbances of side lobes of the transmitting antenna, the radar receiving system will be shielded by a building.

The effective transmitted power was simulated by 600000 photons, radiated equally distributed over the antenna half beam width. The receiving antenna is characterized by an effective aperture of 0.049 m^2, corresponding to the antenna gain.

Additional model calculations take into consideration a frequency of 94 GHz and half beam widths of the 33 GHz antennas of 0.5° and 1° for the transmitting and receiving side, respectively. The radiation was - as a first attempt - assumed to be unpolarized. A cylindrical rain volume (height 4 km, radius variable 0.9-4.5 km) is assumed to be over the radar set-up (Fig. 2b).

3. The Relevant Optical Parameters

The optical parameters which control the radiative transfer including multiple scattering processes and which are input parameters for the model calculations may be shortly discussed.

The single scattering albedo ω_o as function of wavelength is given in Fig. 1 (for rainfall rates of 10 and 50 mm/h and a Marshall-Palmer drop size distribution). It is determined by the volume Mie coefficients for scattering β_{sc}, absorption β_{abs}, and extinction β_{ext} and may be interpreted as scattering probability of the photons. The probability of an absorption event is then given by $(1 - \omega_o)$. Fig. 3 presents the dependence of β_{sc}, β_{abs}, β_{ext} on frequency for some rainfall rates and a "cumulus-congestus"cloud model (C5 after Deirmendijan, 1975). The increasing influence of scattering against absorption at shorter wavelengths can be seen (as in Fig. 1). The increase of single scattering albedo as function of rainfall rate (for 33 and 94 GHz) is shown in Fig. 4.

The mean free path length $(1/\beta_{ext})$ as function of liquid water content (corresponding to rainfall) is represented in Fig. 5. This quantity is proportional to the distance between two interactions inside the rain volume.

The transmittance $\exp -\tau$, where τ is the optical thickness ($\tau = \beta_{ext} \cdot s$), is determined by the volume extinction coefficient β_{ext} and a distance s. The term $(1 - \exp -\tau)$ is the interaction probability within the distance s.
The discussed optical parameters (β_{ext}, $1/\beta_{ext}$, ω_o) are summarized in Tab. 2.

Fig. 6a shows the normalized scattering functions $P(\Theta)/4\pi$ for frequencies of 33 and 94 GHz and rainfall rates of 10 and 50 mm/h. Normalization means that

$$(1) \qquad (1/4\pi) \int_{\Omega} P(\Theta)\, d\Omega = 1$$

where $d\Omega$ is the solid angle element. The pronounced Mie-effect (foreward scattering) at 94 GHz becomes obvious. An example of a cumulative phase function $PP(\Theta)$ for a rainfall rate of 30 mm/h is given in Fig. 6b. $PP(\Theta)$ is determined by

$$(2) \qquad PP(\Theta) = 1/2 \int_{0}^{\Theta'} P(\Theta) \sin\Theta d\Theta.$$

It can be seen that scattering in foreward direction (scattering angle 0-90°) occurs for 94 GHz in 70% of cases and for 33 GHz in 50% of cases (Rayleigh scattering). $P(\Theta)$ and $PP(\Theta)$ are the basis for the determination of the scattering angles on the paths of the photons.

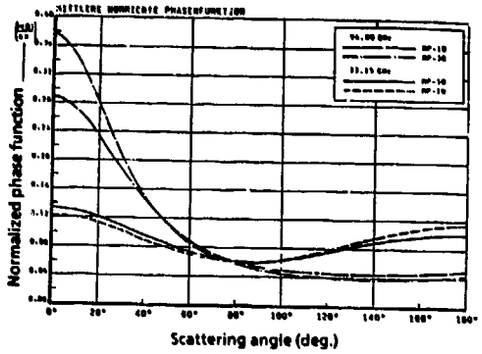


Fig. 6a: Normalized phase function $P(\Theta)/4\pi$ for different rainfall rates as function of the scattering angle Θ; frequencies are 33.15 GHz and 94 GHz, rainfall rates are 10 and 30 mm/h for 33.15 GHz and 10 and 30 mm/h for 94 GHz.

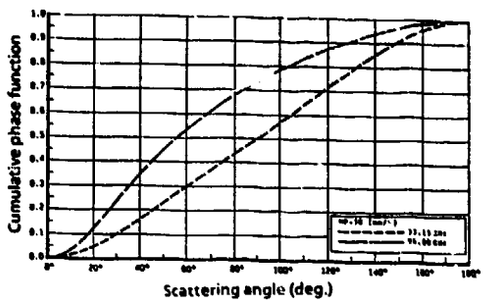


Fig. 6b: Cumulative phase function for a rainfall rate of 30 mm/h as function of the scattering angle Θ; frequencies 33.15 GHz and 94 GHz.

	ν GHz	t °C	β_{ext} km^{-1}	ω_0	LWC $g\,m^{-3}$	$1/\beta_{ext}$ km
CLOUD C.5	94.00	0	.3568	.41 E-03	.30	2.8027
CLOUD C.5	33.15	0	.6105 E-01	.72 E-04	.30	16.3800
CLOUD C.5	33.15	10	.4837 E-01	.92 E-04	.30	20.6749
RAIN MP- 1	94.00	0	.3048	.3850	.09	3.2808
RAIN MP- 1	33.15	10	.5098 E-01	.1960	.09	19.6155
RAIN MP- 10	94.00	10	1.881	.4773	.62	.5316
RAIN MP- 10	33.15	10	.5935	.3485	.62	1.6849
RAIN MP- 20	33.15	10	1.176	.3902	1.10	.8501
RAIN MP- 30	94.00	10	4.068	.5001	1.54	.2458
RAIN MP- 30	33.15	10	1.729	.4127	1.54	.5784
RAIN MP- 40	33.15	10	2.256	.4278	1.96	.4432
RAIN MP- 50	94.00	10	5.740	.5096	2.36	.1742
RAIN MP- 50	33.15	10	2.762	.4389	2.36	.3621
RAIN MP- 60	33.15	10	3.249	.4477	2.75	.3078
RAIN MP- 100	33.15	10	5.055	.4704	4.18	.1978
RAIN MP- 100	94.00	10	9.042	.5215	4.10	.1106
RAIN MP- 150	33.15	10	7.077	.4867	5.81	.1413
RAIN MP- 200	33.15	10	9.055	.4998	7.52	.1104

Tab. 2: Extinction parameters (β_{ext}, $1/\beta_{ext}$, ω_0) and liquid water content (LWC) of clouds with different rainfall rates for frequencies of 33.15 GHz and 94 GHz. For comparison, values of a C5 cloud (cumulo congestus) are given; temperature mostly 10°C.

The ground reflections are characterized by Fresnel reflection coefficients of 0.5 (33 GHz) and 0.35 (94 GHz), calculated for a water film (refractive index after Ray (1972): m = 4.73-2.72 i, temperature 10°C) covering the ground during moderate and heavy rain.

4. Monte Carlo Technique

The transfer of radiant energy through a given scattering and absorbing medium is considered as a photon transport problem, with the Monte Carlo model simulating the physics of the interactions of the photons with the medium. Since the photon transport is a stochastic process, so also is the Monte Carlo simulation (Marchuk et al., 1980, Cashwell et al., 1959).

4.1. The Monte Carlo Simulation

In Monte Carlo computations simulating radiative transfer one photon at a time is followed on its three-dimensional path through the scattering and absorbing rain medium. The various events which may happen to the photon on its way are defined by suitable probability distributions determined by the intrinsic radiative properties of the rain volume ω_o, β_{ext}, PP(Θ), P(Θ)/4π (s. Chapt. 3). A set of random numbers equal distributed between '0' and '1' is then used to make a particular choice for the result of each event. The averaged outcome of a large number of such photon-histories then provides an unbiased solution to the transfer problem under inclusion of multiple scattering.

When large optical depths are present, and computer time becomes prohibitiv, photons followed on their way are assigned a statistical weight W, which initially has the value '1' defining a fraction of the actual transmitting energy. The statistical weight may be reduced proportional to the probabilities of all the physical events occurring during simulation (Davies, 1976, Paltridge, Platt, 1976).

In our case of propagation through an isolated rain medium (cylinder) the only processes to be simulated without a weight reduction (direct simulation) are a) the emission at the antenna (emission angle), b) the distance travelled by the photon between two interactions and c) the change in direction caused by a scattering event.

a) The emission angle Θ_s inside the half beam width γ_s of the antenna can be simulated by a random number RN uniform distributed between '0' and '1' according to

(3) $$\cos \Theta_s = \cos (RN \gamma_s).$$

b) The simulation of the distance travelled by the photon is direct since the cumulative probability PR(s) that a photon travelling in a given direction will have had a collision within a distance s, is given by (Davies (1976), Paltridge, Platt (1976))

(4) $$PR(s) = 1 - \exp(-\beta_{ext} s) = 1 - \exp -\tau.$$

A random number with uniform distribution between '0' and '1', RN, is chosen for PR(s) and the distance s to the next collision is calculated from

(5) $$s = -(1/\beta_{ext}) \ln (1 - RN).$$

c) The change in direction caused by scasttering is governed by the single scattering phase function (s. Fig. 6a), P(Θ)/4π, which defines the angular distribution of the radiation following a scattering event. The scattering angle, Θ', is measured from the direction of propagation before the scattering to the direction after scattering. The normalized phase function (s. Equ. 1) is independent of the second angle needed to define the direction of propagation after scattering. This second angle, ϕ, is a rotation about the direction of propagation before interaction (scattering). ϕ is selected randomly between 0 and 2π.

To determine the scattering angle Θ' we need the probability of a photon being scattered between 0 and Θ', the cumulative phase function PP(Θ) (s.Equ. (2), Fig. 6b). From this the scattering angle Θ' is determined by choosing a random number RN between '0' and '1' for PP(Θ) and solving Equ. (2) for the upper integration limit (Davies, 1976).

4.2. Variance Reduction Methods in Monte Carlo Simulation

To make the Monte Carlo simulation more efficient some variance reduction methods are introduced where the photons are forced to perform interactions inside the rain volume until they deliver a non-negligible weight to the received signal up to a fixed number of scattering processes.

1. In an efficient Monte Carlo method a photon or its weight W is never terminated through absorption. At each collision the statistical weight W_{n-1} before collision is multipled by the single scattering albedo. This corrects for the absorption probability for the interaction. The photon then undergoes scattering and continues on its path.

2. The photons are not allowed to leave the rain volume through the top or the sides of the rain cylinder (Collins et al., 1972). If the photons extended path intersects the upper bound or the sides of the rain cylinder, a collision is forced to occur so that the photon never leaves the rain medium. The distance to the forced collision 'LR' inside the rain medium on the way from the last event to the border of the rain volume is chosen by a random number RN from a truncated density function

(6) $$LR = 1/\beta_{ext}) \ln (1 - RN (1 - \exp - \tau_B))$$

where τ_B is the optical depth along the path to the bound of the rain volume. Each time such a collision is forced to occur before the photon escapes the rain volume, the statistical weight W_{n-1} associated with a simulated photon is reduced by

(7) $$W_n = W_{n-1} (1 - \exp - \tau_B).$$

This removes the bias introduced by forcing the collision. The term $(1 - \exp - \tau_B)$ corresponds to the probability of a photon interaction along the way from the last (scattering) event to the bound of the rain volume.

3. If a direction to the ground and a distance greater than the distance along the path to the ground surface is selected, a reflection is forced at the point where the photon path intersects the ground surface. The weight parameter of the photon is then multipled by the ground reflection coefficient R. The correspondent absorption probability is given by $(1 - R)$.

4. If a scattering event occurs inside the receiving cone the photon is forced to scatter direct into the receiver (receiving aperture area) and the probability $PR = W_n$ of scatter directly into the receiver is calculated according to

(8) $$PR = W_n = W_{n-1} ((P(\tilde{\Theta}) \, d\Omega / 4\pi) \exp - \tau_R).$$

It gives the final weight of each photon reaching the receiver (Paltridge, Platt, 1976). "$P(\tilde{\Theta}) \, d\Omega / 4\pi$" is the probability of scattering directly into the receiver where $d\Omega$ is the very small solid angle subtended by the receiver aperture area at the point of scatter inside the receiving cone. The term "$\exp - \tau_R$" is the probability of direct transmission into the receiver, τ_R is the optical depth from the last point of scatter to the receiver and $P(\tilde{\Theta})$ is the value of the phase function at the angle $\tilde{\Theta}$ defining the direction of the receiver (centre) from the direction of travel before the last scattering event.

All the photons with their associated statistical weights arriving at the receiver during the simulation will be summed up, subdivided according to the order of scattering processes. A measure of multiple scattering is then given by the ratio of the sum of all photon weights after multiple scattering processes to the sum of single scattering photon weights.

5. Results

5.1 Different Order Scattering Effects

To show the contribution of different order multiple scattering k up to k = 6 to the total multiple scattering intensity in dependence of rainfall, frequency, and half beam width of the receiver antenna the dimensionless relation of different order received intensities to the total multiple intensity is presented in Tab. 3 (in percent). The calculations were done with 600000 photons and a radius of the rain volume cylinder of 2 km. The dominating part of multiple scattering results from second-order scattering with more than 80% and third order scattering with 6-13% for rainfall rates between 10 and 100 mm/h. Higher order scattering contribution for 33 GHz are mostly below 3% and for 94 GHz somewhat larger, and may be neglected for the given scenario.

It will be seen from Tab. 3 that the importance of second order scattering intensity in relation to higher order scattering intensity decreases with increasing rainfall rate and decreasing antenna beam width.

Order of scattering k	ν = 33.15 GHz					ν = 94 GHz	
	γ_s = 0.5° ; γ_r = 1.0°		γ_s = 1.0° ; γ_r = 2.0°			γ_s = 1.0° ; γ_r = 2.0°	
	MP - 10	MP - 30	MP - 10	MP - 30	MP - 100	MP - 10	MP - 30
k = 2	87.74 %	83.36 %	93.20 %	90.34 %	85.67 %	82.64 %	82.38 %
k = 3	11.62 %	14.29 %	5.91 %	7.94 %	10.59 %	15.38 %	11.44 %
k = 4	0.48 %	1.72 %	0.76 %	1.35 %	2.41 %	1.29 %	3.84 %
k = 5	0.13 %	0.54 %	0.11 %	0.29 %	1.05 %	0.65 %	1.59 %
k = 6	0.03 %	0.09 %	0.02 %	0.08 %	0.28 %	0.04 %	0.35 %

Tab. 3:
The relative significance of scattering of different order k (ratio of scattering of the k^{th} order to the total multiple scattering) in dependence of frequencies, rainfall rates, and half antenna beams.

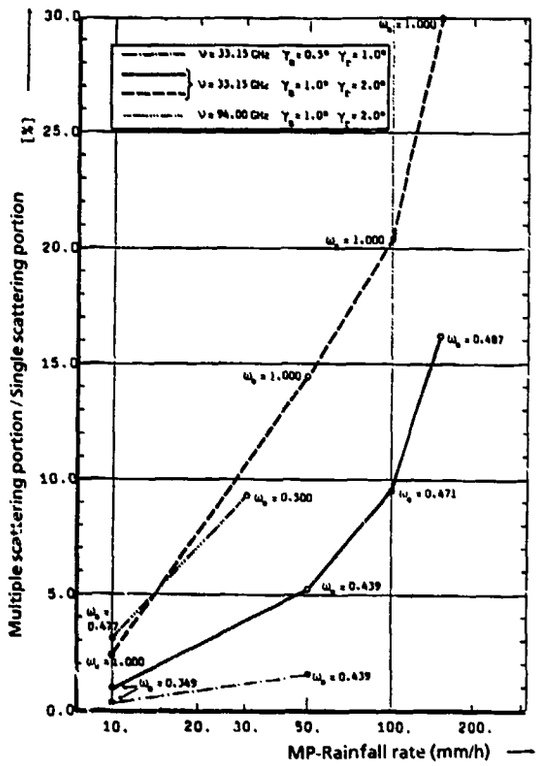


Fig. 7:
Ratio of multiple scattering intensity to single scattering intensity for the bistatic radar used as function of rainfall rate; frequencies 33.15 GHz and 94 GHz; half antenna beam widths 0.5° and 1° (transmitter) and 1° and 2° (receiver) for 33 GHz, 1° and 2° for 94 GHz; ω_o-values are marked at the curves.

5.2 Multiple Scattering as Function of Rainfall Rate and Frequency

The main results of the Monte Carlo Simulation are summarized in Fig. 7 showing the ratio of multiple scattering intensity to single scattering intensity (in percent) as function of rainfall rate. Marked at the curves are the different values of single scattering albedo for some rainfall rates and two frequencies (33 GHz and 94 GHz). The upper dashed curve gives the fictive case of scattering (33 GHz) by a rain of pure dielectric spheres without absorption (approximated by dry ice spheres or hail, $\omega_o = 1$ for all "rainfall rates"). The amount of multiple scattering increases from 2.4% at 10 mm/h to 20.4% at 100 mm/h. This curve presents an upper limit of multiple scattering effects. The more realistic case for rain and frequency of 33 GHz is given by the thick solid line. For 10 mm/h (ω_o = 0.35), multiple scattering amounts to 1%, increasing to 9.5% for a rainfall rate of 100 mm/h (ω_o = 0.47).

Calculations for a frequency of 94 GHz and rainfall rates of 10 mm/h (ω_o = 0.48) and 30 mm/h (ω_o = 0.50), as given in the - - - - curve of Fig. 7, show a distinct increase of multiple scattering up to 3.2% or 9.3% at rainfall rates of 10 mm/h and 30 mm/h, respectively.

The influence of single scattering albedo (inverse proportional to the mean free path length of photons $1/\beta_{ext}$, s. Tab. 2) is obvious.

5.3 The Influence of Antenna Beam Widths

The halvening of the antenna beam widths as considered for 33 GHz, see lower dot-dashed curve in Fig. 7, leads to a significant decrease of multiple scattering intensity. For half beam widths of 0.5° and 1° (transmitter and receiver) the amount of multiple scattering decreases for a rainfall rate of 10 mm/h to 0.3% (previously 1%) and for 30 mm/h to 1.7% (previously 5.2%). That means, with the possibility to have narrow antenna beams at higher microwave frequencies the influence of multiple scattering may be set down significantly.

6. Conclusion

Multiple scattering of millimeter waves, especially due to second and third order scattering, amounts for moderate and heavy rain to some percent and has to be noticed interpreting radar rain reflectivities. Using strongly bundeling antennas (half beam widths < 0.5°) the effect may be largely avoided. However, the case of high ω_o-values (ice-rain, hail) coupled with propagation of high frequencies (say 60 GHz) and heavy rainfall rates remain particularly critical in this connection. Not mentioned here are the other propagation effects as phase shifts or cross-polarization effects produced by a rain cloud.

7. Literature

1. CASHWELL, E.D., C.J. EVERETT, 1959: A manual of the Monte Carlo method for random walk problems. Pergamon Press, New York, 153 pp.
2. COLLINS, D.G., W.G. BRLATTNER, M.B. Wells, H.G. HORAK, 1972: Backward Monte Carlo calculations of the polarization characteristics of the radiation emerging from spherical-shell atmospheres. Appl. Opt., 11, (11), 2684-1696.
3. DAVIES, R., 1976: The three-dimensional transfer of solar radiation in clouds. Doctor-Thesis at the University of Wisconsin-Madison, 220 pp.
4. DEIRMENDJIAN, D., 1969: Electromagnetic scattering on spherical polydispersions. Elsevier, New York, 290 pp.
5. DEIRMENDJIAN, D., 1975: Far-infrared and submillimeter wave attenuation by clouds and rain. J. Appl. Meteor., 14, 1586-1593.
6. DIBBERN, J., 1984: Potential use of a bistatic dual polarization radar for measuring precipitation. Beitr. Phys. Atmosph., 57 (3), 346-356.
7. DIBBERN, J., H. JESKE, G. PUCHER, 1985: Der Einsatz eines bistatischen Dual-Polarisations-Radars zur Bestimmung von Niederschlagsparametern. Kleinheubacher Berichte, 28, Herausg. Fernmeldetech. Zentralamt d. Dt. Bundespost, Darmstadt.
8. ISHIMARU, A., J.C. LIN, 1972: Multiple scattering effect on wave propagation through air. Conf. on Telecommunication Aspects of Frequencies between 10 and 100 GHz, Adv. Group for Aeronaut. Res. and Dev., North Atl. Treaty Org., Gausdal, Norway, Sept. 18-21.
9. ISHIMARU, A., 1978: Wave propagation and scattering in random media. Vol. 1, Academic, New York.
10. ISHIMARU, A., R. WOO, J.W. ARMSTRONG, D.C. BLACKMAN, 1982: Multiple scattering calculations of rain effects. Radio Sci., 17 (6), 1425-1433.
11. KATTAWAR, G.W., G.N. PLASS, 1968: Monte Carlo calculations of light scattering from clouds. Appl. Opt., 7 (3), 415-419.
12. MARCHUK, G.I., G.A. MIKHAILOV, M.A. NAZARALTEV, R.A. DARBINJAN, B.A. KARGIN, B.S. ELEPOV, 1980: The Monte Carlo methods in atmospheric optics. Springer Verlag, Berlin-Heidelberg-New York, 207 pp.
13. MARSHALL, J.S., W. PALMER, 1948: The distribution of raindrops size. J. Met., 5, 165-166.
14. OGUCHI, T., 1980: Effect of incoherent scattering on attenuation and cross polarization of millimeter waves due to rain. Radio Res. Lab. Jpn., 27 (122/123), 1-51.
15. OGUCHI, T., 1981: Scattering from hydrometeors: A survey. Radio Sci., 16 (5), 691-730.
16. PALTRIDGE, G.W., C.M.R. PLATT, 1976: Radiative processes in meteorology and climatology. Elsevier, Amsterdam, 318 pp.
17. RAY, P.S., 1972: Broadband complex refractive indices of ice and water. Appl. Opt., 11 (8), 1836-1844.
18. TSOLAKIS, A., W.L. STUTZMAN, 1982: Multiple scattering of electromagnetic waves by rain. Radio Sci., 17 (6), 1492-1502.
19. VOSS, P.-H., 1985: Monte Carlo Simulation der Strahlungsübertragung in isolierten zylindrischen Regengebieten zur Untersuchung der Mehrfachstreuanteile des Empfangssignals eines bistatischen Radargerätes im Mikrowellenlängenbereich. Diplomarbeit, Fachbereich Geowissenschaften der Universität Hamburg.

DISCUSSION

A. Ishimaru

Please respond to comments made by Prof. Varadan on whether multiple scattering needs to be considered for rain because its volume density is low.

Author's Reply

Even if the volume density is small, multiple scattering cannot be neglected. The pair correlation can be neglected, but the multiple scattering due to independent scatterers is significant.

A. N. Ince, TU

Is there a physical explanation for the fact that at very small wavelengths and heavy rain β_{sc} and β_{abs} are almost equal?

Reply by A. Ishimaru

The absorption and scattering are 50% each in the high frequency limit because the total cross section approaches twice the geometric cross section and the absorption cross section approaches the geometric cross section in a high frequency limit.

SUMMARY OF SESSION IX

IONIZED MEDIUM

by

K.C.Yeh, Session Chairman

For over five decades, the ionosphere has been known to go turbulent quite frequently. When this happens, the electron density in the ionosphere is found to fluctuate with position and time. The effect created by these density fluctuations is to scatter radio waves. Such scattering can be manifested in different ways when probed by a radio wave. When the turbulent ionosphere is sounded by a radar, the returned echo is smeared to create what is commonly called the "spread-F" echo. On the other hand, when a radio signal passes through such a turbulent ionosphere, the signal is found to fluctuate or to scintillate. This session deals with the interaction of radio waves with the turbulent ionized medium and the use of this interaction for geophysical and astronomical interpretations.

The first paper, by A.Hewish, describes an experimental program that uses the scintillation technique to determine the shape and location of large-scale perturbations of interplanetary plasma. The observation shows that the source of solar transients is the open magnetic field regions known as coronal holes, in contradiction to the long-held theories in solar-terrestrial physics. The author further suggests that his observational program can be used to forecast the arrival of interplanetary shocks and hence the onset of geomagnetic storms.

In the second paper of this session, Aarons and Rodger use the scintillation and spread-F measurements to measure the presence of ionospheric irregularities. They suggest that during magnetic activities, the irregularities observed at the subauroral latitudes may be either convected from higher latitudes or created by the penetration of the electric field. They further suggest that the ring current may supply the energy needed to create irregularities during the recovery phase.

The effect of ionospheric irregularities on a radar signal is examined by G.S.Sales, the author of the third paper. He calculates the power scattered from irregularities elonged along the magnetic field when the incident ray is perpendicular to the magnetic field. The scattered power is observed by an over-the-horizon radar as ionospheric clutter.

In the last paper of this session, Basu et al. report their scintillation observations from the orbiting Hilat satellite. The most consistent and conspicuous feature of the scintillation phenomenon observed at an auroral oval station is the geometric enhancement when the propagation path is aligned with the local magnetic L-shell. Joint study of scintillation observations with the total electron content and other in-situ measurements provides insights of ionospheric coupling from the magnetosphere.

REMOTE SENSING OF INTERPLANETARY SHOCKS USING A SCINTILLATION METHOD

by
A. Hewish
Cavendish Laboratory
Madingley Road
Cambridge
CB3 0HE
UK

SUMMARY

Energetic interplanetary disturbances originating at the Sun cause geomagnetic storms when they reach the Earth. The disturbances affect radio-communications, damage electrical power grid networks, increase the atmospheric density and drag on satellites, and are accompanied by showers of energetic particles which present radiation hazards to manned spacecraft. This paper describes a new ground-based method for locating and tracking transients in interplanetary space long before they reach the Earth. Continuous observations of transients during a two year period near sunspot maximum have demonstrated the potential of the technique for predicting geomagnetic storms and given new information on the zones of the solar disk from which transients originate. The latter contradicts some widely held theories in solar-terrestrial physics and shows that a major revision of ideas is needed. Contrary to expectations, it has been found that open-magnetic field regions known as coronal holes are the dominant sources of the most powerful interplanetary shocks. This result conflicts with the solar flare theory of geomagnetic storms.

INTRODUCTION

A satisfactory study of solar-terrestrial relationships demands some means of continuously monitoring conditions in the interplanetary medium between the Sun and the Earth on a routine basis. Without such information the relation between events at the Earth and their causes on the Sun is clouded by uncertain knowledge of the transit-time, and also the region of origin on the Sun. The discovery, in 1964, that irregularities of plasma density in the solar wind caused certain radio galaxies and quasars to scintillate opened up the possibility that conditions along the line of sight could be monitored by ground-based radio telescopes. Initially the technique was used to measure the speed of the solar wind and to observe the passage past the Earth of long-lived compression regions associated with corotating streams (1, 2). Such work can be done by observing only a few radio sources with modest radio telescopes, but adequate mapping and tracking of short-lived disturbances demands continuous observations across a grid of many sources. This became possible with the completion of the 3.6 hectare phased array at Cambridge in 1978 which can observe 3,500 sources on a routine daily basis. Following careful calibration over a period of two years, during which many different disturbances near the Earth were mapped quantitatively, and then compared with in-situ observations of the same plasmas by spacecraft, it was found that scintillation provided a reliable means of determining the mean density along the line of sight to a radio source. The relevant portion of the line of sight extends for a length of about 0.5 to 1.0 AU, from the Earth so that major disturbances can be tracked over a range of roughly 0.5 to 1.5 AU. from the Sun.

This scintillation technique is currently the only method available for determining the shape and location of large-scale perturbations of plasma density in interplanetary space. Spot measurements by spacecraft at a few locations in deep space have, of course, been made, but so far they have been confined to the ecliptic plane and have given a very incomplete picture of the morphology of disturbances. Space-borne white-light coronagraphs have been used to map transients of enhanced density in the solar corona out to ten solar radii. This method is most sensitive to transients leaving the solar limb, in directions perpendicular to the Sun-Earth line, and is therefore not useful for locating disturbances on an Earth-bound course. Scintillation, on the other hand, is most sensitive to transients that intercept the Earth.

This paper outlines the essential features of the scintillation method and mentions some conclusions reached during a two year study of interplanetary disturbances during 1978-81. This period was close to the maximum of solar cycle 21 and included many geomagnetic disturbances. All significant magnetic storms and energetic particle events at the Earth were clearly associated with interplanetary disturbances that were mapped by scintillation. On the other hand some of the observed transients were travelling at too wide an angle to engulf the Earth and these did not generate terrestrial effects.

The utility of remote-sensing by scintillation for predicting geomagnetic storms and particle events was assessed from a study of 20 major disturbances. This showed that real-time data processing would have given at least 24 hours warning of the arrival of interplanetary shocks at the Earth in most cases, and sometimes considerably more. The ESA "cornerstone" programme for solar-terrestrial physics in the 1990's centres on the Solar High-Resolution Observatory (SOHO) to be located at approximately 1.5 Mkm from the Earth on the Sun-Earth line. In-situ observations of Earth-bound disturbances by SOHO will provide a warning of less than one hour, which underlines the advantage of remote-sensing by scintillation.

The ability to locate the origin on the solar disk of major interplanetary disturbances has given information of fundamental importance to solar-terrestrial physics. In addition, the combination of remote-sensing with spacecraft observations of the same disturbances has revealed an interesting new feature of interplanetary shocks. The energetic particles accelerated by shocks are observed to be strongly concentrated on the western sides of the shock fronts in the ecliptic as viewed from the Earth. This result can be readily understood in terms of a local acceleration mechanism in which the angle between the

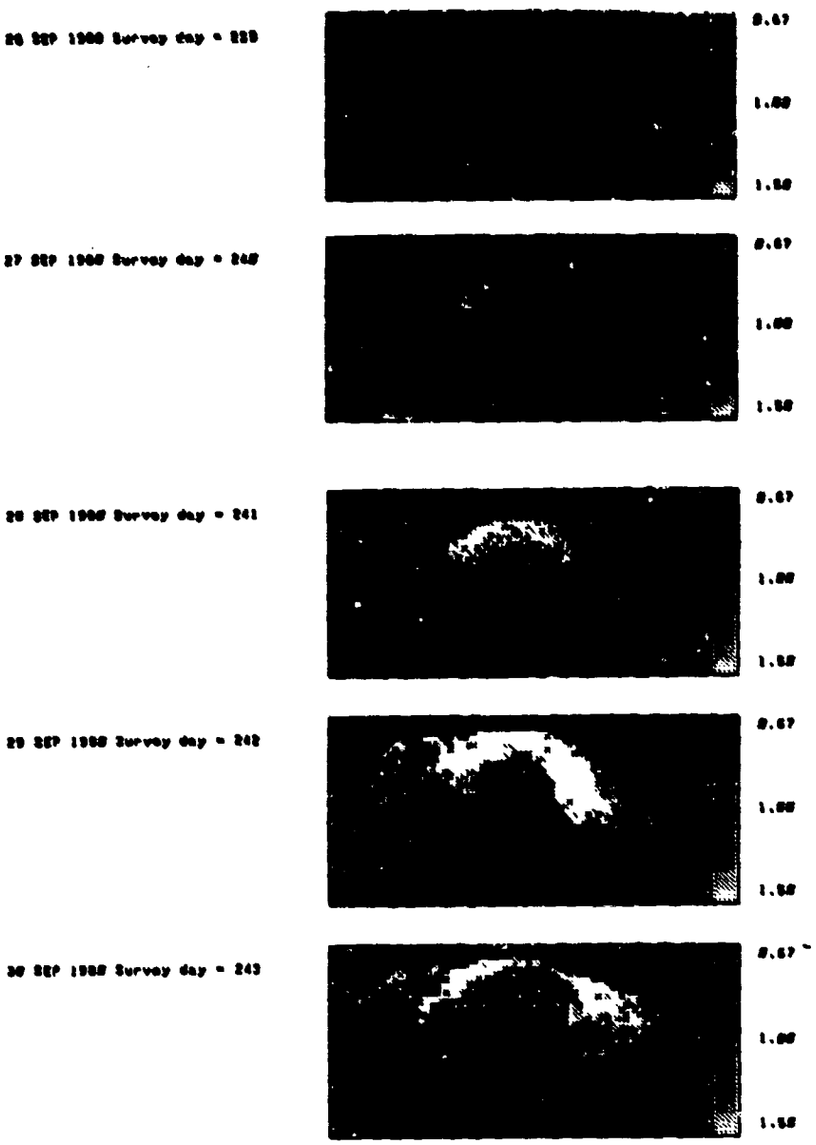


Figure 1. Sky maps of scintillation showing the development of a major interplanetary disturbance during September 26-30, 1980. The values of g correspond to the grey scale indicated and the map is plotted in ecliptic coordinates, with the Sun at the centre, using the Mollweide projection. This transient was centred above the ecliptic plane, although an increase of plasma density during its passage was recorded by near-Earth spacecraft.

interplanetary magnetic field ahead of the shock and the shock-normal is a dominant factor. It is likely that future projects in space science would be similarly enhanced if knowledge of the overall morphology of disturbances in the space environment in which the local observations are made were available.

THE METHOD OF REMOTE SENSING

The 3.6 hectare phased-array operates at 81.5 MHz and allows sources to be observed at meridian transit in 16 declination bands simultaneously. Scintillation is caused by microturbulence in the solar wind on a scale of 100-1000 km which typically generates fluctuations of some intensity at 0.1 - 3.0 Hz. The primary data consist of measurements of ΔB^2 integrated over 0.1-3 Hz and sampled at 10s intervals, where ΔB is the instantaneous fluctuation of intensity (B) of a source from its mean intensity.

Initial calibration involves the determination for each radio source of the function $\Delta B_0(\epsilon)$, which represents the long-term averaged RMS scintillation for that source as a function of its solar elongation. Curves of $\Delta B_0(\epsilon)$ initially rise as ϵ decreases, corresponding to the increased plasma density nearer the Sun, but fall steeply for $\epsilon<35°$ owing to blurring of scintillation by the source diameter. Perturbations of density about the mean are then computed according to $g = \Delta B_\epsilon / \Delta B_0(\epsilon)$. Observations of g for up to 2,000 sources may be obtained on a routine basis each day. By comparing values of g with simultaneous near-Earth spacecraft measurements of local plasma density N it was found that $g \propto (N\ cm^{-3}/8)^{0.5}$. The result establishes that scintillation provides a reasonably accurate measure of the average plasma density along the line of sight (3).

To map disturbances it is necessary to select a suitable grid of sources and to plot their g-values over the sky. This gives a map of the two-dimensional projection of disturbances which immediately provides much information on their location and distance from the Sun. More detailed information can be obtained by a model-fitting process in which the scintillation is computed for assumed models of the disturbances. In practice the transients have simple shapes and occur sufficiently infrequently that interpretations of the maps are not usually confused by superposed disturbances. Examples of model-fitting have been described (4,5,).

To illustrate the method a series of g-maps showing the development of a major transient is presented in Figure 1. These maps were constructed from observations of 2,500 sources and average g-values were computed for 5° x 5° pixels (8) which contained several sources. Other forms of data presentation where g-values were colour-coded have proved to be somewhat easier to interpret than the grey scale in Figure 1.

A convenient feature of the data-reduction is that it automatically compensates for the systematic increase of plasma density with decrease of distance from the Sun. At 81.5 MHz disturbances are not detected within 0.5 AU. This may be due to blurring of scintillation caused by the finite angular diameters of the sources, or by the radial development of the disturbances themselves. Observations at a higher frequency are required to decide between these possibilities.

THE ORIGIN OF MAJOR TRANSIENTS

A day to day study of interplanetary disturbances was carried out during August 1978 - September 1979 from g-maps obtained using a grid of 900 sources (7). 96 disturbances occurred during this period of high solar activity and no significant interplanetary shock or geomagnetically active transient escaped detection. Some of the disturbances were corotating sectors of increased density associated with compression zones generated by moderately long-lived high-speed streams. The most frequent transients, however, were roughly spherical shells of enhanced density followed by outflows of high speed and reduced density, and often characterised by shocks at their outer boundaries. The angular spread was found to be roughly 90° and the disturbances were detectable when they were centred within ~70° of the Sun-Earth line. A typical g-map of a transient of this kind is shown in Figure 2.

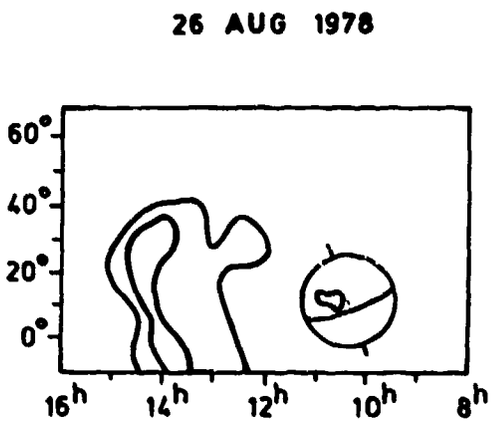


Figure 2. Sky map for August 26, 1978 showing contours of enhanced scintillation (g = 1.25, 1.5) denoting the compression zone at the front of a strong transient which caused a major geomagnetic storm on August 28. The coronal hole source is shown on the much-enlarged sketch of the solar disk.

It has long been thought that energetic transients not associated with corotating streams are caused by solar flares or filament eruptions. In contrast to this view, back-projection to the Sun along the directions obtained from scintillation mapping, which could be done to an accuracy of about ± 25°, showed that, in fact, the sources coincided with coronal holes (8). This new finding is not surprising, bearing in mind that stable coronal holes are already known to be the sources of long-lived high-speed streams. Thus it is natural that unstable coronal holes, typically observed during the rise to solar maximum, should be the sources of short-lived streams, which erupt suddenly, and often persist for only a few days. Some solar flares "confidently" assumed by other workers to be the sources of a number of the transients that were mapped are clearly disconnected events far from the actual site of the eruption on the Sun (9). It is not impossible, however, that eruptions from coronal holes could trigger flares and filament activity as peripheral phenomena.

In the past, the absence of a visible flare prior to the arrival of a major shock and geomagnetic storm has often been ascribed to the occurrence of a flare behind the limb of the Sun. There is no longer any need for such assumptions as g-maps have not yet failed to point to a suitably positioned coronal hole. The statistical significance of the coronal hole associations has, or course, been demonstrated (8).

FORECASTING GEOMAGNETIC ACTIVITY AND PROTON EVENTS

The utility of remote-sensing by scintillation-mapping for predicting geomagnetic storms can only be confirmed operationally. So far this has not been attempted. A useful assessment is, however, possible from the observations during 1978-79. As previously explained, no important event occurred in the absence of an associated transient on the g-maps. A check of what should be achieved with daily g-maps available in real time has been made (10) by selecting all geomagnetic storms of disturbance index Ap≥40 and all alpha particle events when the flux in the energy band 9-70 MeV exceeded 10^{-2} cm^{-2}s^{-1}sr^{-1}MeV^{-1}. There were 29 such occasions, 7 of which satisfied both criteria. The delay in hours between first detecting a transient on the g-maps, and its subsequent arrival at the Earth (as given by spacecraft or the geomagnetic sudden commencement) is

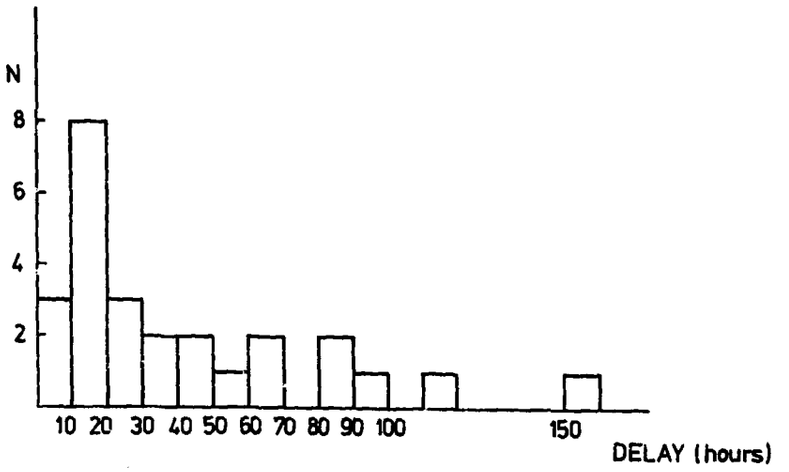


Figure 3. Histogram of delays between the first detection of transients which caused magnetic storms or energetic particle events, and their arrival at the Earth.

shown in Figure 3. From a site at latitude 52°N it is not always possible to map transients adequately when they are centred beneath the ecliptic. Improved forecasts could also be made by incorporating sites at more than one longitude.

REFERENCES

1. P.A. Dennison and A. Hewish; The solar wind outside the plane of the ecliptic. Nature, 213, 1967, 343-346.

2. Z. Houminer and A. Hewish; Long-lived sectors of enhanced density irregularities in the solar wind. Planet. Space Sci., 20, 1972, 1703-1716.

3. S.J. Tappin; Interplanetary scintillation and plasma density. Planet. Space Sci., 34, 1986, 93-97.

4. S.J. Tappin, A. Hewish and G.R. Gapper; Tracking a major interplanetary disturbance. Planet. Space Sci., 31, 1983, 1171-1178.

5. S.J. Tappin, A. Hewish and G.R. Gapper; Tracking a high-latitude corotating stream for more than half a solar rotation. Planet. Space Sci., 32, 1984, 1273-1281.

6. S.J. Tappin; Numerical modelling of scintillation variations from interplanetary disturbances. Planet. Space Sci. 1987, in the press.

7. G.R. Gapper, A. Hewish, A. Purvis and P.J. Duffett-Smith: Observing interplanetary disturbances from the ground. Nature, 296, 1982, 633-636.

8. A. Hewish and S. Bravo: The sources of large-scale heliospheric disturbances. Solar Phys. 106. 1986, 185-200.

9. A Hewish, S.J. Tappin and G.R. Gapper: The origin of strong interplanetary shocks. Nature, 314, 1985, 137-140.

10. A Hewish and P.J. Duffett-Smith: A new method of forecasting geomagnetic activity and proton showers. Planet. Space Sci., 1987, in the press.

DISCUSSION

J. S. Belrose, CA

Since you are reporting on data observed during the past solar cycle maximum, and since you say that most of your work has been published, your startling conclusions (for me) perhaps reveal that it is a number of years since I have been working in the area of STP relations. However, I must say that my past experience has lead me to believe that solar proton events are associated with large solar flares. Certainly most geomagnetic storms are not so directly related to solar flares and your observations certainly provide a different insight into these phenomena. Solar proton events are prompt events (20 minutes to several hours travel times), and so their positive identification with the causative solar proton flare is easy. Could you comment?

Author's Reply

Positive identification with solar flares is never easy when the sun-earth transit time is obtained by guesswork! The so-called "prompt" proton events often raise difficulties. Particle flux profiles similar to "prompt" events often involve long delays and are not prompt. The concept of particle "storage" was invented to solve this problem but is now not believed. Again, prompt events have been identified with flares near the east limb of the sun when propagation along "well-connected" magnetic field lines is impossible. New evidence from space measurements shows that the particle flux increases with distance from the sun and usually peaks near the shock. This is explained simply if the particles are accelerated locally (and continuously) at the shock front.

Our IPS observations show that the proton flux is strongly concentrated toward the western sides of the spherically expanding shocks which supports the shock-acceleration theory. Of course, solar flares may sometimes be triggered by coronal hole eruptions as peripheral sideshows.

K. C. Yeh, US

In one slide you showed the time delays between the observation of compression and the occurrence of geomagnetic storms. The histogram shows the time delay extending from tens of minutes to several days. You mentioned that by making observations at several stations on the earth, it is possible to have a reliable technique for forecasting storms. Would you comment on that?

Author's Reply

The earliest warnings are made when disturbances are detected as near to the sun as possible. When radio sources are observed at meridian transit, this implies having data taken within ± 6 hours from local noon. Several sites are needed to achieve this. Even with a fully scanned antenna there is a dead time during the night.

G. S. Sales, US

1. Have you been able to continue these measurements into the period of solar minimum activity when the character of these events are known to change?
2. With what resolution are you able to trace these propagating events back to the surface of the sun?

Author's Reply

1. No, the observations ceased in 1981. During 1978-81 we mapped a number of recurrent enhancements due to long-lived corotating streams and I am sure that these would constitute the dominant distrubances during the decline from solar maximum.
2. Model fitting gives an accuracy of about $\pm 20^{\circ}$ in most cases. Backtracking involves a further uncertainty since we do not detect transients inside 0.5 AU and must assume a speed of departure from the sun. Overall, the accuracy is about $\pm 25^{\circ}$ in solar latitude and longitude.

J. Aarons, US

Proton spectra have been determined and verified by radio observations (microwave and meter wavelength) of solar outbursts.

Author's Reply

The type II radio outbursts associated with solar flares have traditionally been identified with coronal shocks, but recent work has shown that meter wave and microwave type IIs are not associated with kilometric (interplanetary) type IIs which correlate with proton events.

MAGNETIC STORM EFFECTS ON F LAYER IRREGULARITIES NEAR THE AURORAL OVAL

Jules Aarons
Department of Astronomy
Boston University
Boston, MA USA 02215

Alan S. Rodger
British Antarctic Survey
Cambridge, U.K. CB3 0ET

SUMMARY

The effect of F layer irregularities on trans-ionospheric transmissions and fading at HF at equatorial, auroral, and polar latitudes has been documented. Little has been done on morphology and physics of irregularities noted at sub-auroral latitudes, in the vicinity of the plasmapause. The intensities of the irregularities are considerably less than those observed at equatorial and high latitude regions. The scatterers in this region are at times correlated with magnetic activity and at other times present during periods of low magnetic activity, including the recovery phase of magnetic storms.

A study was made of F layer irregularities for the month of October 1981 using a series of scintillation and spread F measurements between 0° and 71° W. This included F layer intersections at sub-auroral as well as auroral latitudes. In the data set a comparison was made of scintillation on one propagation path, in the Northern Hemisphere, and spread F data at a Southern Hemisphere conjugate position, the Argentine Islands. The 350 km points were roughly conjugate within 6° of longitude and 4° of latitude. Correlation was obtained on those nights when scattering was noted over several hours. There were some nights when one path was active and the conjugate path quiet. Usually these occurred when irregularities were observed over periods less than two hours and with the active path showing low intensity activity.

We have separated the major irregularity activity periods into the following:
a. Irregularities either created during magnetically disturbed periods at sub-auroral latitudes in the vicinity of plasmapause latitudes or convected to these latitudes (auroral latitudes are also disturbed at these times); and
b. Lower latitude (sub-auroral) irregularities not associated with magnetic activity as denoted by local magnetograms or by Kp indices. These are not accompanied by intense F layer irregularities at auroral latitudes. At times during these periods of low magnetic activity there is moderate irregularity intensity at auroral latitudes. The sub-auroral irregularities have been noted during SAR arcs as well as during other periods of magnetic quiet.

The separation of irregularity occurrence at sub-auroral latitudes into cases associated with magnetic activity and cases when magnetic activity was quiet does not allow for simple modeling or statistical ordering. Ordering by Dst rather than Ap yields the best statistical results.

During magnetic activity, the irregularities may be convected from higher latitudes or created by penetration of the electric field to lower latitudes. During the recovery phase it is proposed that ring current energies supply the ultimate source of the irregularity production at F layer heights.

INTRODUCTION

The effect of F layer irregularities on trans-ionospheric transmissions and fading at HF at equatorial, auroral, and polar latitudes has been documented. Little has been done on morphology and physics of irregularities noted at sub-auroral latitudes near the plasmapause. The intensities of the irregularities are considerably less than those observed at equatorial and high latitude regions. The scatterers in this region are at times correlated with magnetic activity and at other times present during periods of low magnetic activity, including the recovery phase of magnetic storms (Basu, 1974; Aarons, 1986).

From the scientific viewpoint the total development of magnetic variations is of importance in attempting to determine the origin of F layer irregularities at sub-auroral and auroral latitudes. It is clear that at auroral and polar latitudes there are phenomena correlated with irregularities including precipitation (Basu et al.,

1983), sheer effects (Basu et al., 1984), convection of plasma containing irregularities (Weber et al., 1985) as well as other factors in instability processes (Hudson and Kelley, 1976, Keskinen and Ossakow, 1983).

OBSERVATIONS

A study of F layer irregularities was made in October 1981, a period of both high solar flux and considerable magnetic activity, by a series of scintillation and spread F measurements between 0° and 71° West Longitude. This included F layer intersections at sub-auroral as well as auroral latitudes. One site was located in the Southern Hemisphere at Argentine Islands; the rest were in the Northern Hemisphere. The Argentine Islands site was approximately conjugate with a propagation path from the Boston area to the satellite ATS-5. The 350 km points were roughly conjugate within 6° of longitude and 4° of latitude. Station positions in the case of sounders are given in Table 1 along with 350 km propagation intersections for the satellite observations. Corrected Geomagnetic Latitude is given for the observations.

TABLE 1	LATITUDE	LONGITUDE	CGL
Goose Bay, Canada (ATS-5)	48° N	62° W	61°
S. Uist, U.K.	57° N	7° W	58°
Sagamore Hill, MA. USA	39° N	71° W	53°
Slough, U.K.	52° N	.5° W	51°
Argentine Islands	65° S	64° W	49°

A map with geographic and invariant latitude ticks is shown in Figure 1.

THE DATA

A comparison of two sub-auroral observations with similar longitudes from the conjugate positions is shown in Figure 2. A glance at the figure indicates that during periods of irregularity activity both stations showed relatively high levels of scintillation index or spread. Excellent correlation was obtained on those nights when scattering was noted over several hours. However some nights were noted with one path active and the conjugate path quiet. Days do appear when scintillation was more readily seen at the 53° CGL intersection than at the 48° CGL intersection. Days of one sensor noting activity and the other failing to note activity occur for the most part with low values of irregularity intensity and for less than two hours. Additional data for other months is to be shown in a future publication being prepared by the authors. The same general trends were noted in these sets of data taken in 1981.

The aim of this paper is to examine in detail a portion of the data set, setting out the magnetic conditions surrounding the development of irregularities at F layer heights. The hypothesis developed is that irregularity activity periods should be separated into the following:

a. During magnetically disturbed periods irregularities are either created near plasmapause latitudes or convected to sub-auroral latitudes; auroral and other latitudes are also disturbed at these times.

b. Lower latitude irregularities not associated with magnetic activity or with F layer irregularities at auroral latitudes are at times noted during periods of little local magnetic activity quiet. During these tines auroral F layer irregularity activity displays quiet magnetic activity levels. These cases appear to be the result of stored energy available in the recovery phases of magnetic storms; the mechanism for production in these cases cannot be convection since there are no strong irregularities at the higher latitudes. Other cases appear when both auroral and sub-auroral irregularities are intense but with little local magnetic activity. This too is an example of stored energy producing the irregularities.

If this approach is valid, the parameter Dst, would appear to be better for correlation with sub-auroral F layer irregularities than K_p since Dst levels are indicative of the storage levels of the ring current. In order to test this hypothesis, normalised values of spread F over Argentine Islands for 0-12 UT were correlated with the average Dst (Rodger and Aarons, 1987). The correlation with Dst is 0.65, which is significant at better than the .01% level, while with the use of the Ap value of the day, the correlation coefficient was found to be 0.13.

QUIET AND DISTURBED MAGNETIC CONDITIONS

The basic concept to be presented is as follows: the source of energy producing the necessary conditions for the generation of irregularities at both auroral and sub-auroral latitudes would have to be a source with long term storage that is modulated or filled during strong magnetic activity. The source, in all likelihood the ring current, has its effect on the ionosphere as a function of local time. The modulation of the source or the filling of the ring current varies, depending on the conditions in the ring current when the modulation or filling began (Smith and Hoffman, 1973; Arnoldy, 1983; Williams, 1986).

The period of October 10-14 is illustrative of the concepts stated. In Figure 3 a plot of Dst values for the period is given. Dst gives a picture of the storage of energy and its dissipation. On an instantaneous level, however, magnetograms indicate localised activity particularly in a longitudinal region. In this case we have reproduced magnetograms from the AFGL Magnetometer Network (Knecht, 1985) with observations from 70° W to longitudes west of the Boston area. The data represent a variety of magnetic conditions. The first day analysed, Oct. 10, is one of moderate magnetic activity. It is followed by a very disturbed day, Oct. 11, and a moderately disturbed early portion of the UT day of Oct.12. From 1000 on Oct. 12 to 0800 on Oct. 13, very quiet magnetic conditions existed. On Oct. 13 at 2230 a magnetic storm started. A substantial deviation in the magnetic field occurred at 0220 UT on Oct. 14 at the primary longitude of interest.

IRREGULARITY DATA

The scintillation data is taken from two sets of observations, both of 137 MHz scintillations of ATS-5. The lower latitude propagation path intersected 53° CGL and the higher latitude intersection was 61° CGL. The sounder data was reduced according to standard techniques of data reduction. The comparison of observations in the following figure is to study occurrence patterns. The data sets have differing measurements of intensity. The data are presented in Universal Time.

Figure 4a shows the usual irregularity activity for a moderately disturbed day, Oct. 10. The higher latitude sites, Goose Bay and S. Uist, showed more activity than the lower latitudes. The stations are ordered in the diagrams in longitude so that correspondence in time can be studied at sites located near the same longitudes.

Oct. 11, Figure 4b. At local times of 02 to 03 (07 UT) the Sagamore Hill path and the Argentine Islands overhead ionosphere, both in the 60-75° West region, were affected by the magnetic storm. Slough with the storm starting at a local time of 06 and with its low invariant latitude was just barely affected, although S. Uist shows relatively high levels for that local time. The magnetic activity appears to have its maximum effect on lower latitude sub-auroral F layer irregularities when close to the midnight time period.

Oct 12, Fig. 4c. Scintillation activity was strong at the higher latitude stations of Goose Bay and S. Uist from 2300 UT on the 11th to at least 1000 UT on the 12th. On the path from Sagamore Hill only a burst of scintillation activity was noted at 2200 UT on the 53° intersection. As the night progressed however with local time for both Argentine Island and Sagamore Hill approaching midnight, irregularity activity commenced increasing to well after midnight. Through either convection of the patches of irregularities or due to the energy sources penetrating their lowest diurnal latitudes, irregularity activity increased during the midnight local time period.

Oct 13, Fig. 4d. From 1100 UT on the 12th to 08 UT on the 13th the magnetograms show little activity. On this magnetically quiet night both auroral and sub-auroral latitudes showed considerable irregularity activity. The Goose Bay propagation path and the S. Uist sounder showed high irregularity intensity levels from 1800 and 2000 UT on Oct. 12. Activity on the Sagamore Hill path started at 0500 with Argentine Island indicating particle E data from 0200 on. With the magnetic activity for this period extremely low, irregularities were relatively intense at Sagamore Hill and in all likelihood at the Argentine Islands. The indications are that the storage of energy had taken place earlier. The result was the discharge of considerable energy in this period of time in the sub-auroral region and in the auroral oval.

On Oct. 14, Figure 4e, a classical magnetic storm developed. While the magnetic displacement started at 2300 on the 13th, effects at the lower latitude stations occurred later, from 0230 UT or 2130-2230 LT on.

DISCUSSION

The effect of magnetic activity on auroral irregularities has been known for a long time. The effect can be noted on local magnetograms more readily than studying the Kp levels. The extension of auroral effects on F layer irregularities into lower latitudes has also been documented. However, the study of irregularities at the sub-auroral latitudes appears to have halted with statistical approaches. In the auroral oval statistical approaches work for forecasting and for evaluation of irregularity problems in communications (examples are given in Aarons and Allen, 1971 and in Rino and Matthews, 1980), but in the sub-auroral region near the plasmapause when both magnetic activity and magnetic quiet show F layer irregularities, the dynamic approach to understanding the phenomenon should be used. The ring current parameter, Dst, would appear to be a better means of approaching irregularity development in the lower latitude regions. The case illustrated is one of many cases where high intensity F layer irregularities have appeared during periods of magnetic quiet.

We have avoided stating that various effects take place at plasmapause latitudes since independently we have not shown that the latitudes where irregularities appear is precisely at plasmapause latitudes; they are in the general vicinity of that region but it may be that plasmapause latitudes like trough latitudes differ as a function of the parameter being measured.

Monitoring the ring current dynamics, the F layer convection pattern (Blanc, 1983) and the energies involved would appear to be the next step in tracking ring current energies and F layer irregularities at both auroral and sub-auroral latitudes.

CONCLUSIONS

The separation of irregularity occurrence into cases associated with magnetic activity and cases when magnetic activity was quiet does not allow for simple modeling or statistical ordering particularly in the region near plasmapause latitudes.

During magnetic activity, the irregularities may be convected from higher latitudes or created by penetration of the electric field to lower latitudes. In the case illustrated both auroral and sub-auroral latitudes show irregularity effects during a period of magnetic quiet. During other periods (Aarons, 1987) only sub-auroral latitudes show intense irregularities. In work in progress by the authors, the dynamic development and the creation of irregularities of the "pure" lower latitude cases is being studied during what may be termed a sub-auroral storm near plasmapause latitudes. Low energy precipitation has been associated with the irregularities (Gurgiolo et al., 1982); the origin of these irregularities may lie in the storage mechanism of the ring current. The general behavior of ring current ions fits the morphology of high latitude irregularities during the development of a magnetic storm in its various phases. The ring current ion energy may be converted into ion cyclotron waves which may in turn produce the heating and precipitation. Such a two step process taking place has been suggested and summarised by Williams et al., 1986.

ACKNOWLEDGEMENTS: The authors would like to thank the technical staff of the observatories for the care in taking the records. We would also like to thank S. Basu and J. Klobuchar of AFGL for supplying the scintillation records. J. Aarons was supported by the Office of Naval Research USA, A.S. Rodger by the National Environment Research Council UK.

BIBLIOGRAPHY

Aarons, J. and R. S. Allen (1971), Scintillation boundary during quiet and disturbed magnetic conditions, J. Geophys. Res., 76, 170-177, 1971.
Aarons, J. (1987), F-layer irregularity observations of the SAR arc event of March 5-6, 1981, Radio Science, 22, 100-110.
Arnoldy, R.L. and T.E. Moore (1983), Longitudinal structure of sub-storm injections at synchronous orbit, J. Geophys. Res., 88, A8, 6213-6220.

Basu, Sun. (1974), VHF ionospheric scintillations at L=2.8 and formation of stable auroral red arcs by magnetospheric heat conduction, J. Geophys. Res., 79, 3155-3160.
Basu, Sun., E. MacKensie, S. Basu, H.C. Carlson, D.A. Hardy, F.J. Rich and R.C. Livingston (1983), Coordinated measurements of low energy electron precipitation and scintillations/TEC in the auroral oval, Radio Sci., 18, 1151.
Basu, Su., S. Basu, E. MacKensie, W. R. Coley, W. R. Hanson, and C. S. Lin (1984), F region electron density irregularity spectra near auroral acceleration and shear regions, J. Geophys. Res., 89, 5554.

Blanc, M. (1983), Magnetospheric convection effects at mid-latitudes 1. Saint Santin observations, J. Geophys. Res., 88, 211-223.
Gurgiolo, D., D.W. Slater, J. D. Winningham, J. L. Burch (1982), Observation of a heated elctron population associated with the 6300 A SAR Arc emission, Geo. Res. Let., 9, 965-968.
Hudson, M K. and M.C. Kelley (1976), The temperature gradient drift instability at the equatorward edge of the ionospheric plasma trough, J. Geophys. Res., 81, 3913, 1976.
Keskinen, M.J. and S.L. Ossakow (1983), Theories of high-latitude ionospheric irregularities: a review, Radio Sci., 18, 1077.
Knecht, D.J. (1985), Daily Magnetograms for 1981 from the AFGL network AFGL, Hanscom AFB, MA. AFGL-TR-85-0030 #246.
Rino, C. L. and S.J. Matthews (1980), On the morphology of auroral zone radio wave scintillation, J. Geophys. Res., 85, 4139.
Rodger, A.S. (1976), The simultaneous occurrence of spread F at magnetically conjugate points, J. Atmos. Terr. Phys., 1365-1368.
Rodger, A.R., and J. Aarons (1987), Studies of ionospheric F-layer irregularities from geomagnetic middle latitude conjugate regions, submitted to J. Atmos. and Terr. Phys.
Smith, P.H. and R.A. Hoffman (1973), Ring current particle distribution during the magnetic storms of Dec. 16-18, 1971, J. Geophys. Res., 78, 4731.
Weber, E.J. , R.T. Tsunoda, J. Buchau, R.E. Sheehan, D.J. Strickland, W. Whiting, and J.G. Moore (1985). Coordinated measurements of auroral zone plasma enhancements.
Williams, D.J. (1983), The earth's ring current: present situation and future thrusts: Review paper at Sixth International Symposium on Solar-Terrestrial Physics, Toulouse, France.
Williams, D. J., W. Lennartsson, and L.A. Frank (1986), Low energy ions at low equatorial altitudes, Johns Hopkins report May 1986.

Figure 1. A map of invariant latitudes at 300 km and the positions of the intersections from each of the observing sites. The intersections are overhead for the sounder observations and through the ionosphere at 300 km for the satellite beacon recordings.

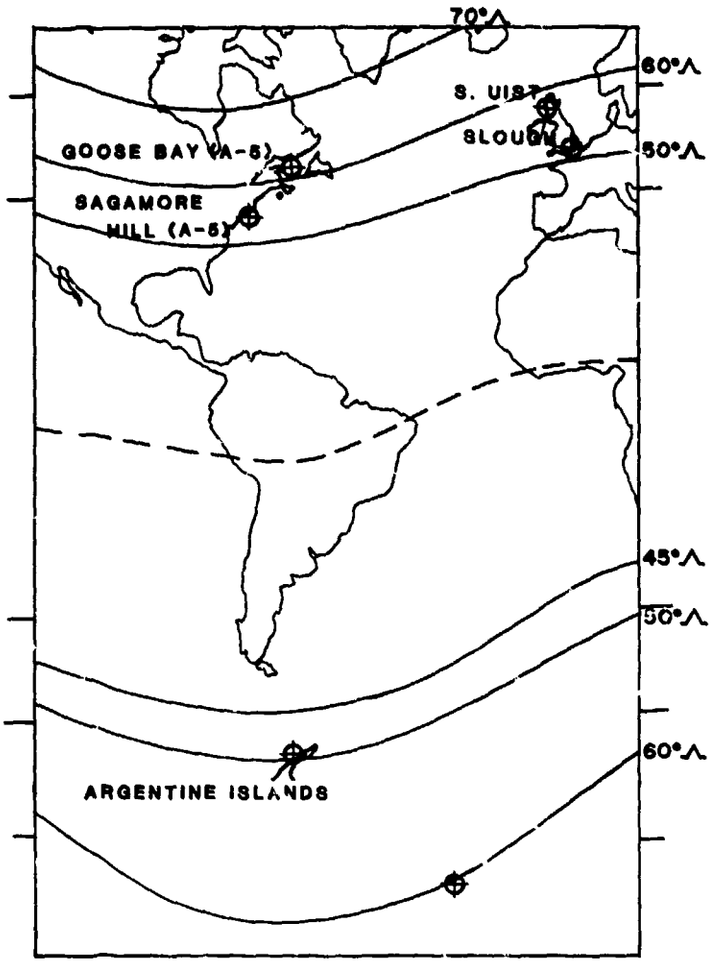


Figure 2. For the month of October 1981 spread F data from the Argentine Islands and scintillation indices in dB excursions are plotted. Filled in areas are scintillation data from 0-20 dB. Cross hatched are overlap times. Slash marks are spread F data.

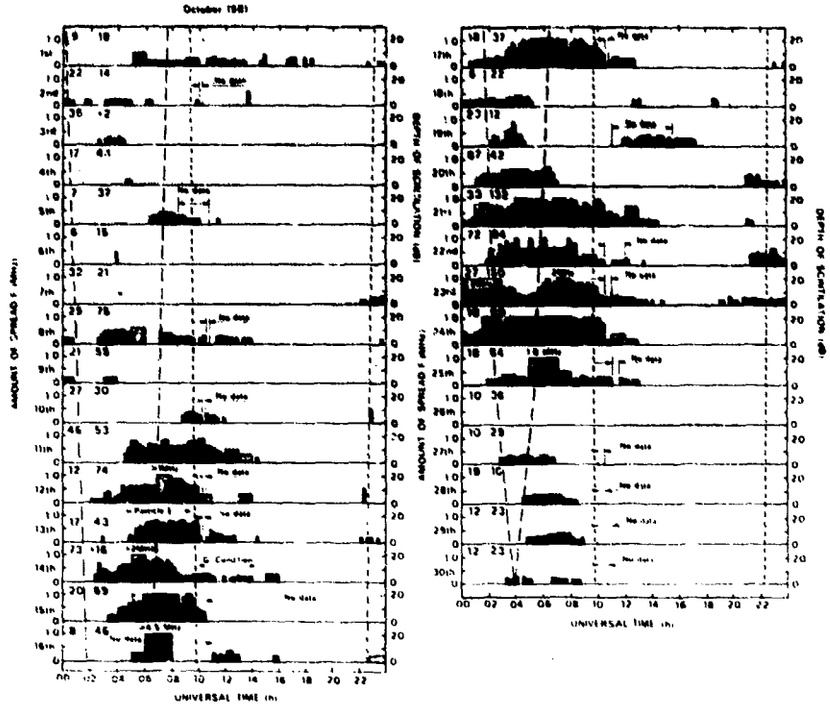


Figure 2

Figure 3. Dst for the period Oct. 9-15, 1981

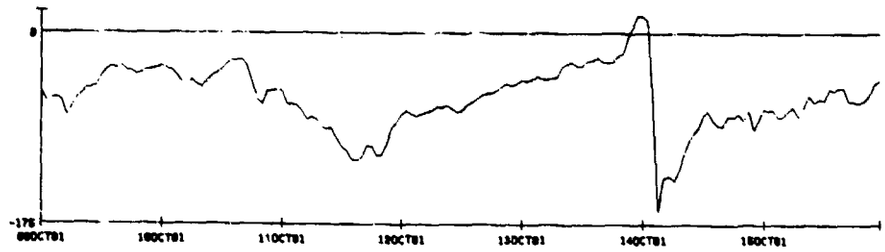
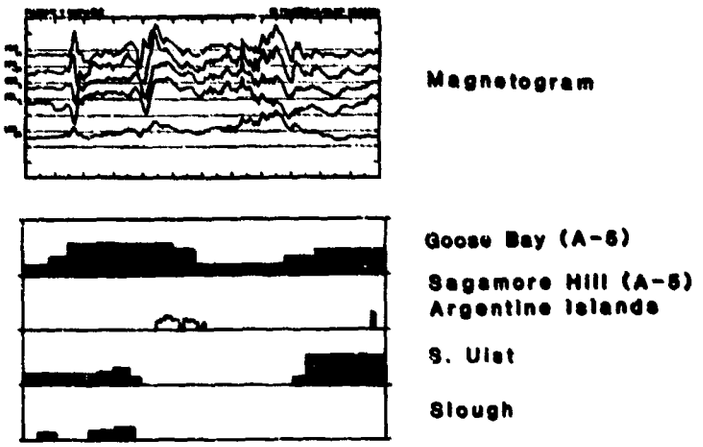


FIG. 3: Dst for October 1981

Figure 4. Data for the period of Oct. 10-14, 1981 is graphed in detail. At the top of each graph is the APGL magnetogram. The other data is placed close in longitude in order to note the effect of various magnetic changes as a function of local time. The Argentine Islands data are given by dashed lines; the Sagamore Hill data are graphed in solid lines.

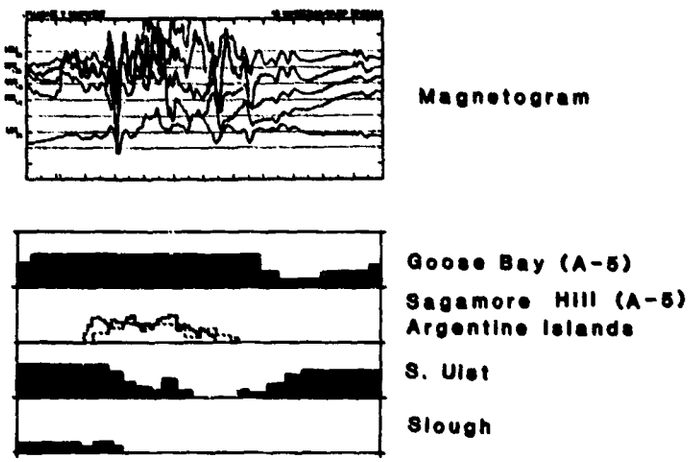
4a. October 10, a moderately disturbed day.



OCT 10

Figure 4a

4b. October 11, a very disturbed day magnetically.



OCT 11

Figure 4b

4c. From 1000 UT on Oct. 12 to 0800 on Oct. 13, very quiet magnetic conditions.

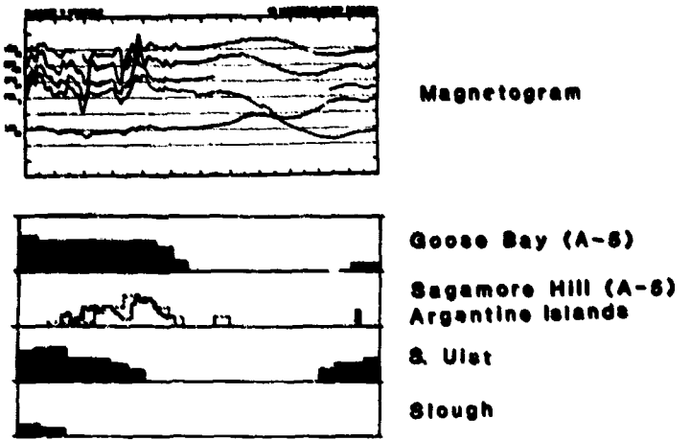


Figure 4c

4d. October 13 At 2230 on Oct. 13 a magnetic storm commenced with a substantial deviation in the magnetic field at 0220 UT.

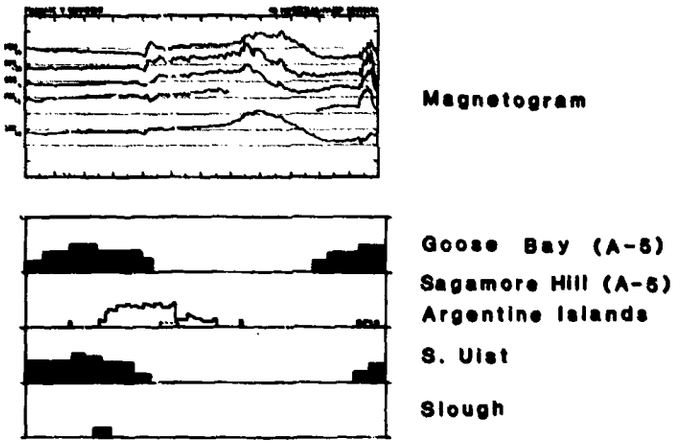


Figure 4d

4e. October 14 - Magnetic storm activity for the night of October 13-14 for the longitudes of interest.

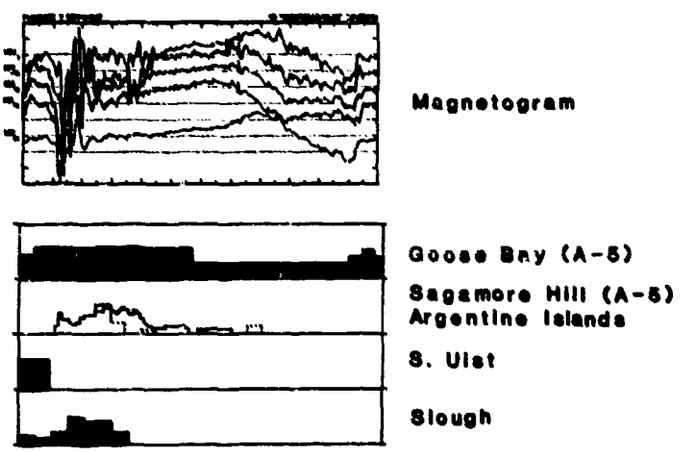


Figure 4e

SPECULAR SCATTER: A NEW MECHANISM FOR IONOSPHERIC BACKSCATTER

Gary S. Sales
University of Lowell Center for Atmospheric Research
450 Aiken Street
Lowell, MA 01854, USA

1. INTRODUCTION

Recent investigation into backscatter from ionospheric irregularities at high frequencies (3 to 30 MHz) has indicated that the usual scatter mechanism requiring orthogonality with the field-aligned irregularities in the E and F region of the ionosphere is not sufficient to explain all the observations. Particularly the range dependence of ionospheric clutter as seen by an OTH radar system looking into or near the auroral region poses a major problem. Assuming field-aligned electron density irregularities, ray tracing shows that clutter originates in the region where the ray becomes perpendicular to the earth's magnetic field lines within the ionosphere. The intensity of these irregularities can be described in terms of $\Delta N/N$, the fractional deviation from the ambient electron density. The actual distribution of electron density fluctuations is described using a power law spectrum with an exponent of $n = 2$. As will be shown in Section 2, the orthogonality condition can always be satisfied in the F region of the ionosphere at mid and high latitudes near the reflecting point where the rays have become near-horizontal.

A simple ray tracing, as shown in Figure 1 for a horizontally stratified ionosphere using an operating frequency f equal to 2.2 times the layer critical frequency, indicates that the orthogonalities occur near the mid-point of the ray path from the OTH radar to the ground coverage area. In this case, while the ground range coverage extends from approximately 2000 to 3000 km, one area of orthogonality occurs near the 1/2 hop region at ranges of 1000 to 1500 km and the other, the 1-1/2 hop orthogonality extends from 3000 to beyond 4500 km. A large gap in the occurrence of orthogonal clutter appears to exist at the ranges of the ground clutter. This does not agree with the many radar observations that show auroral type clutter coincident with the ground range backscatter.

The orthogonal clutter mechanism is restricted to F-region altitudes near the reflection point for obliquely propagating HF signals. In the auroral ionosphere, in addition, the E-region irregularities are expected to be intense and, as will be shown later, can contribute to the overall ionospheric clutter through the mechanism of specular scatter. This scattering mechanism had not been considered before and we will describe it here in detail. At this point it is sufficient to indicate that specular scatter can produce ionospheric backscatter clutter at all ranges including the ranges associated with ground coverage. Finally the specular scatter mechanism permits effective scatter at a wide range of altitudes throughout the F and E regions of the ionosphere.

2. SPECULAR SCATTER MECHANISM

Specular scatter is a relatively simple mechanism that is best described using Figure 2. This figure depicts a field-aligned irregularity with an overall ellipsoidal shape. A wave incident at an angle θ_i with respect to the long axis of the irregularity (the direction of the earth's magnetic field at that point), scatters at an equal angle (specular) in the plane of propagation. It is clear that orthogonal scatter is a special case of specular scatter, that is where $\theta_i = 90$ degrees.

In Section 3 the scattered power and its dependence on location, azimuth and radar parameters including pulse width and frequency will be calculated. Here we will show that the conditions for specular scatter can be met using a reasonable ionospheric model and that its relationship to the range of the ground coverage is significantly different than for orthogonal scatter.

The approach used here is to determine how often and to what degree these conditions can be met with a set of rays obtained using a basic 3-D ray tracing program such as Jones-Stephenson. The ionospheric model used for this preliminary study is limited to a one-dimensional variation, that is electron density vs. height; the same profile being repeated down range to provide the required 2-D electron density model. For the ray tracing, rays are launched with 0.5 degree steps from 0° elevation angle to 30° elevation angle. The ray tracing program includes a spherical harmonic model of the earth's magnetic field. For this study an azimuth of magnetic north was selected for the propagation direction; the operating frequency is expressed in terms of the ratio f/foF2.

As shown in Figures 2 and 3, each potential scattering point requires two rays, one for the outgoing path and one for the return path. Each intersection of these two rays is examined to determine whether the specularity condition $\theta_i = \theta_s$ is met with respect to the local geomagnetic field. The adopted procedure was to examine each interaction for the set of 61 rays. These 61 rays produce 1830 intersections at the 1/2 hop region, another 1830 intersections near the ground coverage region and another 1830 intersections at the 1-1/2 hop region (Figure 3).

These three regions, in terms of their range coverage, are also distinguished from each other by the number of ground reflections involved in the two propagation paths. For the first region neither ray forming the intersection has a ground reflection on the outward or return leg of the path. This region has been designated as containing the Type I intersections. Type II intersections involve only one ground reflection on either the outgoing or return leg of the path but not both. Finally the Type III intersection involves a ground reflection for both legs of the path. This set of rays and the three different intersection types are illustrated in Figure 3. The distinction between outgoing and return leg is arbitrary since the paths are completely reciprocal and both configurations must be considered.

By this procedure we have insured that the two rays involved at each intersection are legitimate rays in terms of ionospheric propagation and that they both originate at the radar site. All of these intersections are then examined to determine whether the specular condition is satisfied; that is that the angle of incidence is equal to the scattered angle within a specified tolerance. The criteria for the limits on deviation from specularity depends on the scattering process and in particular the aspect sensitivity of the scatterer. This is, of course, a function of the wave length of the radio wave relative to the mean dimensions of the irregular fluctuations.

The results of this ray tracing calculation are presented in Figure 4 showing the location of the three types of intersections meeting the specular condition. In addition, the location of the orthogonal intersections are also indicated. For the orthogonal scatter locations the two rays, outgoing and return, have merged into a single path.

Several important characteristics of specular scatter become apparent as a result of these calculations.

1. Within the specified tolerance, the scattering centers exist at all altitudes from the F-region to below the E-region.

2. There is a clear range and altitude dependence associated with each scattering type. Types I and III meet the specularity condition at F-region altitudes and are associated with the 1/2 hop and 1-1/2 hop ranges, while the Type II specular scatter condition is clearly met in the E-region and at ranges that closely correspond to the ground range coverage.

3. The orthogonal scatter points form an upper boundary to the specular scatter for Types I and III. In general there are no orthogonalities associated with the Type II.

The importance of the Type I and Type III scatterers comes from the fact that the area of the ionosphere contributing to the backscattered energy is much larger than would be estimated on the basis of considering only the orthogonal scatter. As will be shown in the next section, the specular scatter cross-section is as large and, in fact, somewhat larger than the orthogonal scattering cross-section and cannot be ignored without serious error. The above ray tracing was used to determine the distribution of angles θ that contribute to the specular condition. Typically these angles range from 90° degrees (orthogonal) to about 75 degrees. This indicates that the two rays associated with a specular scatter intersection are relatively close in takeoff angle and also close to the rays associated with orthogonal scatter and the absorption losses and ground reflection losses will differ from orthogonal scatter by only a small amount.

In the next section a quantitative approach will be developed to estimate the scattered power using the radar equation.

3. BACKSCATTERED POWER

To estimate the backscattered power from ionospheric irregularities causing specular scatter we use the radar equation and estimate the appropriate parameters associated with the scatter mechanism.

The specular scatter contribution to the backscattered power is determined by developing a specular scattering cross-section $\sigma_i(m^2)$; where $\sigma_i = \rho_i \cdot V$, and $\rho_i(m^{-1})$ is the volumetric scattering coefficient and V is the volume in the ionosphere that contributes to a single time delay (range gate) measurement. For this study it is assumed that, using an effective pulse width τ, directly related to the reciprocal RF bandwidth W, a volume can be defined within which all scattering points lie within a spatial distance of $\pm\ \tau/2$ from each other in the vertical plane and within the receive antenna beam width at a range R in the horizontal plane.

Simple geometry for a spherical earth yields for the volume element, V;

$$V = \left(\frac{c}{2W}\right) \cos E \{R_e \arccos\left[\cos^2\left(\frac{R}{R_e}\right) + \sin^2\left(\frac{R}{R_e}\right) \cos\phi_0\right]\} H$$

where W = radio frequency bandwidth

$c = 3 \times 10^8$ m/s

E = mean elevation angle for the two specular rays

R_e = 6370 × 10^3 m (radius of the earth)

R = range to the volume element

ϕ_0 = half power receive antenna beamwidth

and H is the height range over which the contribution of scatters must be integrated for a constant time delay. In general H >> c/2W and this integration will be carried out over all altitudes where the ray tracing shows that the specular condition is satisfied for the selected time delay (see Figure 3).

The volumetric scattering coefficient ρ_i is obtained using the methods of Ishimaru as modified by Yukon for scattering from a spectrum of irregularity sizes in the ionosphere and assuming, for field-aligned irregularities, a power law spectrum in both the transverse direction and in the direction along the magnetic field.

Using the results of Ishimaru, the specular scattering from field-aligned irregularities gives for the volumetric cross-section $\rho_i = 2\pi k^4 \Phi_n(k)$ where $k = 2\pi/\lambda$ (the magnitude of the wave vector) and $\Phi_n(k)$ is the scattering wavenumber spectral density function. For an anisotropic random medium, we have assumed a power law spectrum of the form,

$$\Phi_n(k) = \frac{0.033\ C_n^2\ (L_\perp^2\ L_\parallel)^{11/6}}{[1 + k_\perp^2\ L_\perp^2 + k_z^2\ L_\parallel^2]^2}$$

where $L_\perp$ and $L_\parallel$ are the outer scale sizes of the irregular medium perpendicular and parallel to the earth's magnetic field, $k_\perp$ and k_z are the projection of the wave vector perpendicular and parallel, respectively, to the earth's magnetic field and C_n^2 is explained below.

Assuming the propagation plane is in the direction of the magnetic meridian and only the scattering in the specular direction $\theta_s = \theta_i$ is considered, Ishimaru has shown that the structure constant C_n^2 describing the intensity of the fluctuations is given by,

$$C_n^2 = \frac{1.91\ \langle(\Delta n)^2\rangle}{(L_\perp\ L_\parallel)^{1/3}}$$

where $\langle\Delta n^2\rangle$ is the mean square fluctuation in the refractive index of the medium.

Before putting all of these terms together to obtain an expression for the volumetric scattering coefficient, it is useful to convert the mean square refractive index fluctuation into a mean square electron density fluctuation. This can only be done approximately using a Taylor expansion and the following relationship is used here:

$$\langle(\Delta n)^2\rangle \simeq \left(\frac{f_p}{f}\right)^4 \langle\left(\frac{\Delta N}{N}\right)^2\rangle$$

where f_p is the mean local plasma frequency, f the radar frequency and $\langle(\Delta N/N)^2\rangle$ is the mean squared value of the fluctuation in electron density.

The final result then for the volumetric specular scattering, where the scattered angle θ_s equals the incident angles θ_i and $k^2 = k_\perp^2 + k_z^2$;

$$\rho_i = \frac{0.4\ k^4\ \left(\frac{f_p}{f}\right)^4 \langle\left(\frac{\Delta N}{N}\right)^2\rangle\ (L_\perp^2\ L_\parallel)}{[1 + k^2\ (L_\perp^2 \sin^2\theta_i + L_\parallel^2 \cos^2\theta_i)]^2}\ .$$

In order to better utilize the above equation it is necessary to examine the magnitude of some of the terms. The outer scale sizes $L_\perp$ and $L_\parallel$ are assumed to be of the order of 1000 m with a ratio $L_\parallel/L_\perp$, depending on location, vary between 2 and 5. These are generally consistent with observations in the E and F-regions of the ionosphere.

Using ray tracing to simulate the radar operation, for ground coverage range of 2000 to 3000 km, we find that the ratio of the operating frequency to the maximum plasma frequency in the F region (we always assume F-mode propagation) is typically 2.5. This means using radar frequencies of approximately 6 MHz at night and 15 MHz during the day. The same ray tracing results in a typical θ_i varying from 90 to 75° (90° corresponds to orthogonality).

Putting all these factors together, in the denominator term in the equation for ρ_i, we find that,

$$k^2\ (L_\perp^2 \sin\theta_i + L_\parallel^2 \cos^2\theta_i) >> 1$$

and the equation then becomes,

$$\rho_i = \frac{0.4 \left(\frac{f_p}{f}\right)^4 \langle \left(\frac{\Delta N}{N}\right)^2 \rangle}{\gamma^2 L_u \left(\frac{\sin^2 \theta_i}{\gamma^2} + \cos^2 \theta_i\right)^2}$$

where $\gamma = L_u / L_\perp$.

For the special case of $\theta_i = 90°$ a very simple form appears as

$$\rho_i = 0.4 \left(\frac{f_p}{f}\right)^4 < \left(\frac{\Delta N}{N}\right)^2 > \frac{\gamma^2}{L_u} .$$

Using the form of the equation for ρ_i that involves θ_i we have computed the backscatter coefficient for three different values of the irregularity scale term L_u/γ^2 which is the same as $L_\perp/\gamma$. In Figure 5, in the graph for ρ_i, the volumetric scattering coefficient, the abscissa is the ratio of the operating frequency to the local mean plasma frequency in which the irregularities are embedded and we have assumed a fluctuation intensity $\langle (\Delta N/N) \rangle_{RMS} = 0.1$ corresponding to an auroral region condition. Since ρ_i is proportional to the square of the root mean square fluctuation intensity it is relatively simple to estimate the clutter power level under other ionospheric conditions. In Figure 5 we see a decrease in scattered power as f/fp and the scale size of the irregularities increases.

Finally, as a test case for backscattered power, a nighttime ionosphere was chosen when auroral clutter is most likely to occur. The selected parameters are $\theta_i = 80°$, L_u = 1.6 km and $L_\perp$ = 0.4 km. In this case, a range of fluctuation intensities $(\Delta N/N)_{rms}$ are considered, from 0.1 for intense auroral activity to a value of 10^{-4} for a very quiet ionosphere. Ultimately the appropriate values must be determined from independent measurements.

These data can now be applied to the radar equation. The model OTH radar considered here has the following system parameters

$P_T = 10^6$ W

G_T = 20 dB

G_R = 24 dB

f = 9 MHz

λ = 33.3 m

and a ground range of 2200 km.

The ray tracing results indicate a typical elevation angle of 15 degrees and a specular angle around 80 degrees. The cross-section results are not very sensitive to the assumed outer scale sizes for the spectrum of irregularities $L_\perp$ and L_u. All of these values are substituted into the radar equation to determine the received backscattered power.

The radar equation has the form:

$$P_R = \frac{P_T G_T G_R \lambda^2 \sigma_i}{(4\pi)^3 R^4 L^2} .$$

The choice for σ_i will depend on the particular type of clutter; for the specular scatter $\sigma_i = \rho_i V$.

For comparison purposes the ground clutter and a typical target return are also calculated. For the ground clutter, the illuminated backscatter area is computed using the same expression derived for the volume scattering except for the height integration term H. The effective area is obtained by multiplying this illuminated area on the ground by a factor which takes into account the backscatter reflectivity from a rough sea, i.e. -23 dB. Finally for the target calculation a constant cross-section of 25 dBsm is used.

The signal-to-noise ratio (SNR) is defined as the ratio of the received power from any source, i.e. ionospheric clutter, sea clutter or target signal to the atmospheric noise level at the selected frequency. These results for signal and noise power are presented in Figure 6 using a value for the atmospheric noise of -160 dBW in a 1 Hz post processing bandwidth. The received power is computed for a value of f/fp = 6, i.e. the mean plasma frequency in the auroral E-layer was assumed to be 1.5 MHz. The abscissa is the variation of $\Delta N/N$ from 10^{-1} to 10^{-4}.

4. CONCLUSIONS

Although the curves presented in Figure 6 depend on the system parameters selected, it is clear that as the intensity of the fluctuations in electron density increases, the multiplicative noise level associated with specular scatter increases until it exceeds target signals at the range of the targets.

An OTH radar system with narrow beamwidths and pulse widths can reduce the magnitude of specular clutter and improve the target-to-noise ratio over a wide range of the level of irregularity intensity.

Any experiments aimed at the study of auroral backscatter must also include these specular scatter processes in order to correctly interpret the cross-section associated with these irregularities. Consideration of this new scattering process has resulted in a wider distribution, in range and altitude of HF backscatter clutter, wider than is permitted when only orthogonality clutter is considered. This new model has resulted in scattering characteristics that agree better with radar observations. It can be used to estimate the performance of any HF radar system under a variety of ionospheric conditions from intense auroral irregularities to a relatively quiet, smooth ionosphere. It is easy to show that the optimum radar design reduces the multiplicative noise caused by specular scatter to a level at or near the atmospheric noise level. Certainly higher transmitter power does not solve the problem of detection in the presence of multiplicative noise once this specular clutter noise reaches the level of the atmospheric noise.

Further measurements are required to estimate the actual level of electron density fluctuation associated with the typical mid-latitude and high latitude ionospheres under quiet and disturbed conditions.

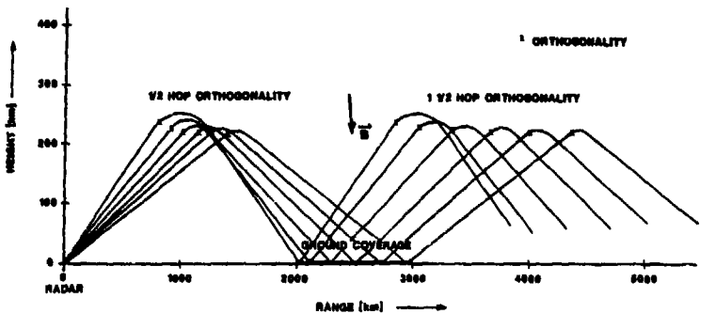


FIGURE 1

2-D ray tracing showing ground coverage, 1/2 hop and 1-1/2 hop orthogonality.

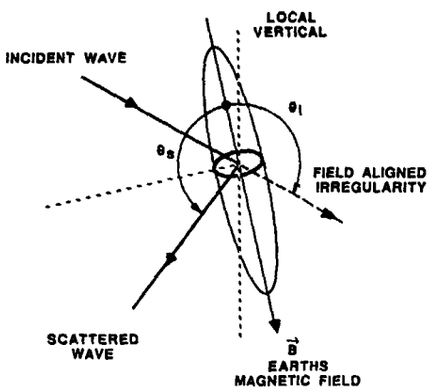


FIGURE 2

Geometry of specular scatter from a field-aligned ellipsoidal irregularity.

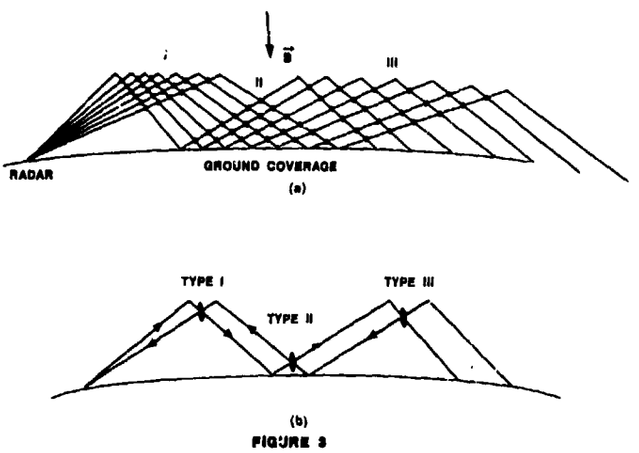


FIGURE 3

Schematic diagram showing Type I, II and III specular scatter regions.

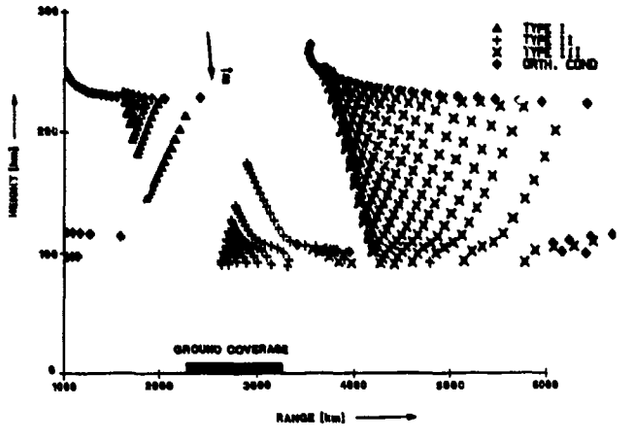


FIGURE 4

Location of specular scatter points using 2-D ray tracing.

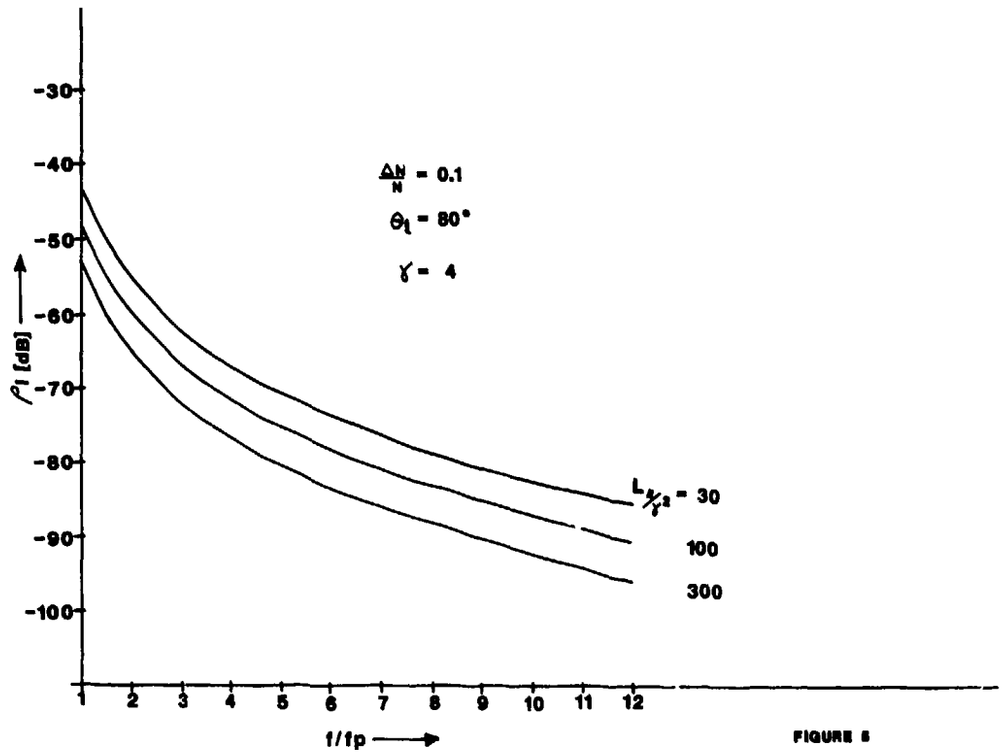


FIGURE 5

Volumetric scattering coefficient as a function of radar frequency relative to the local plasma frequency.

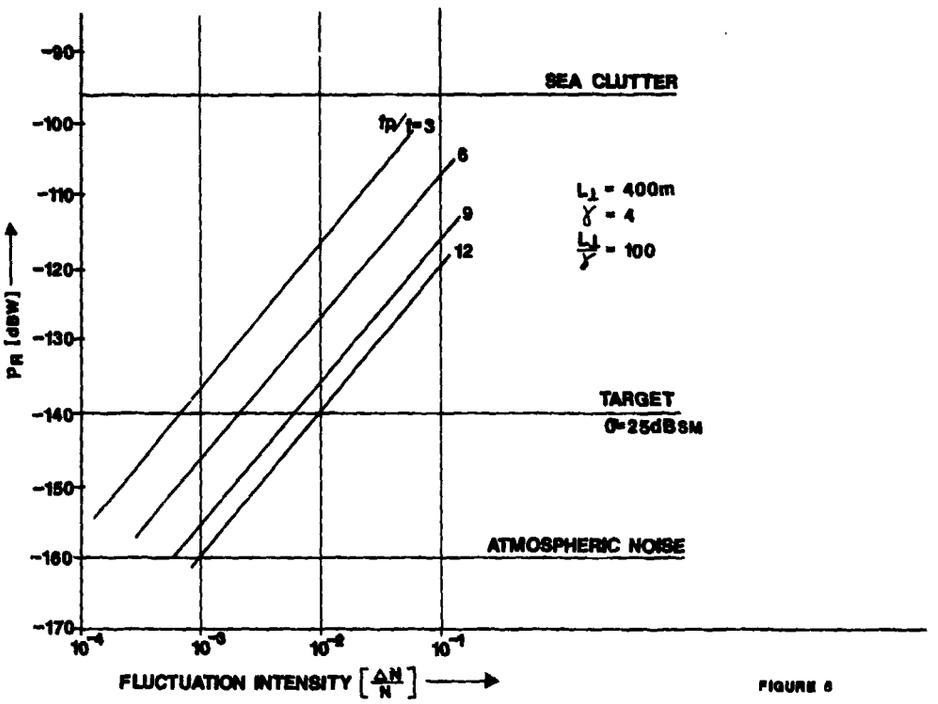


FIGURE 8

Scattered power as a function of fluctuation intensity ΔN/N. Sea surface and target scattered powers are also indicated.

IONOSPHERIC SCINTILLATIONS AND IN-SITU MEASUREMENTS AT AN AURORAL LOCATION IN THE EUROPEAN SECTOR

Santimay Basu
Air Force Geophysics Laboratory
Hanscom AFB MA 01731

Sunanda Basu and Eileen MacKenzie
Emmanuel College
Boston MA 02115

Dan Weimer
Regis College
Weston MA 02193

SUMMARY

The orbiting HiLat satellite launched by the Defense Nuclear Agency in 1983 offered a unique opportunity for studying the ionospheric scintillation parameters in relation to the in-situ measurements of ionization density, drift velocity, field-aligned current, and particle precipitation during the sunspot minimum period. This paper discusses the results of such a morphological study performed by the Air Force Geophysics Laboratory based on their observations at the auroral oval station of Tromso, Norway. The dynamics of the spatial and temporal extent of this region are illustrated in the invariant latitude/magnetic local time grid. The geometrical enhancement of scintillations observed during the alignment of the propagation path with the local magnetic L-shell is shown to be the most consistent and conspicuous feature of scintillations in the nighttime auroral oval. The steepening of phase spectral slope in this region is indicative of the presence of L-shell aligned sheet-like irregularities at long scale lengths. The seasonal variation of total electron content (TEC) determined from the differential Doppler measurements of HiLat transmissions is discussed in relation to the in-situ density measurements at 830 km. The results are also utilized to illustrate the dependence of ionospheric structure parameters on short-term variability of solar activity during the sunspot minimum period. Special effort is made to illustrate that the joint study of scintillation/TEC and in-situ parameters provides an insight into the nature of magnetospheric coupling with the high latitude ionosphere.

INTRODUCTION

A wide variety of C^3I systems suffers degradation in performance due to phase and intensity scintillations imposed by the ionospheric irregularities of electron density. There is a great deal of interest in understanding the development of such irregularities at high latitudes where the ionosphere is often strongly coupled with the magnetosphere. In such an environment the distant magnetosphere serves to activate different sources of free energy, e.g., electron precipitation, field aligned currents, electric fields, etc., that control the formation of ionospheric irregularities. No longer is it possible to pursue a study of the irregularity development in the local ionospheric environment without considering the coupling between the ionosphere and the magnetosphere. This approach is particularly useful in extrapolating our knowledge of the natural ionospheric irregularity structures to problems related to the structuring of artificially injected plasma clouds in the high latitude ionosphere.

In an effort to pursue a study of plasma structuring in the above context, the Defense Nuclear Agency (DNA) launched, on 27 June 1983, the HiLat satellite in a circular 830-km orbit at 82^0 inclination (Fremouw et al., 1985). The satellite transmits coherent signals at 137, 390, 413, and 436 MHz and the phase reference signal at 1239 MHz to measure complex signal scintillation and total electron content (TEC). It also carries a variety of in-situ probes providing measurements of ion density, ion drift, energetic electron precipitation, field aligned currents, and emissions at two visible wavelengths. All instruments except the Langmuir probe, the vacuum-ultraviolet imager and a part of the magnetometer continue to operate reliably. The major objective of the HiLat satellite program is to provide a quantitative specificiation of high latitude scintillation strength and, in particular, the temporal and spatial spectra of intensity and phase fluctuations and the shape of the irregularity structures. These parameters provided by the radio beacon experiments are supported by the simultaneous in-situ data that define the background ionospheric processes. The morphology of ionospheric structures and magnetospheric control thereof derived primarily from HiLat observations at Sondrestrom, Greenland have been enumerated by Vickrey et al. (1985).

In this paper we shall concentrate on the HiLat satellite observations performed by the Air Force Geophysics Laboratory at Tromso, Norway during the 1984-1985 period. The station is located in the central part of the auroral oval during the nighttime under magnetically quiet conditions as defined by the planetary magnetic index $Kp < 3.5$. We shall study the strength and the structure specifications of complex signal scintillations in the spatial and temporal frames of invariant latitude and magnetic local time. These distributions will then be examined in the context of in-situ plasma structures observed by the HiLat satellite in this environment and the

theoretical predictions of structures that characteristically develop in this region through gradient drift and Kelvin Helmholtz instability processes.

RESULTS

In this section we shall first illustrate the space time variations of the statistical parameters that define the complex scintillation magnitudes and their structure. In order to avoid the effects of multipath propagation, the data acquired above a satellite elevation angle of 20^0 were used in the study. This provided a maximum latitude coverage of about 17^0 at an ionospheric height of 350 km around the station. Due to precession of the HiLat orbit to earlier times each day, a full coverage in local time is also obtained over a season (i.e., 3 months) when the ascending and descending node passes are combined.

The top and bottom panels of Figure 1(a) illustrate the rms phase deviation of 137 MHz scintillation for winter 1983 (start of observations in December 1983 to January 1984) and summer 1984 (May-July, 1984) respectively for Kp < 3.5. The rms phase deviation is computed over a 30-second data interval. Since the projected scan velocity of the satellite is 3 km/sec at 350 km, the data interval covers irregularity scale sizes as large as 90 km. The data are binned in 2.5^0 latitude and 1 hour time intervals and the median values for each bin are indicated in the diagram. Each bin contains at least ten data points. The tic marks along the noon-midnight and the dawn-dusk meridians indicate 10^0 intervals between 50^0-90^0 invariant latitudes (to be denoted as Λ). The sharp increase in rms phase deviation exceeding 5 radians over a narrow latitude swath (65^0-$67.5^0\Lambda$) between the pre-midnight and dawn periods is the most conspicuous feature of both diagrams. This region of enhancement corresponds to the location where the alignment of the ray path with the magnetic L-shell occurs (Rino et al., 1978). This region also coincides with the location of the diffuse aurora which is the seat of density irregularities. As we shall show later the region has enhanced total electron content (TEC) on a statistical basis due to the occurrence of plasma density blobs. Thus a combination of high irregularity amplitude, increased TEC and geometrical factors contribute to the pronounced increase of phase scintillations. Comparing the top and bottom panels of Figure 1(a) the magnitude of phase scintillations during winter is found to be larger than summer. This may appear to be somewhat intriguing because the TEC (to be shown later) was higher in summer. This leads us to conclude that the irregularities are probably less preponderant during summer in the presence of enhanced ionization of the underlying E-region.

The top and bottom panels of Figure 1(b) show the behavior of rms phase deviation at 137 MHz during February-April and August-October, 1984. The nighttime enhancement of phase deviation between 65^0-$67.5^0\Lambda$ is again observed. The larger phase deviation observed during the vernal equinox can be related to increased solar activity during this period as will be shown in a subsequent diagram.

The remaining results will be presented in a different format and will indicate the variations of the statistical parameters with invariant latitude in the midnight and noon time periods only. These are basically obtained from a noon-midnight cut through the dial plots shown in Figures 1(a) and 1(b). When the number of data points in a particular bin over the noon-midnight sector fall below ten, the values are extrapolated from an adjacent time sector. Figure 2 shows such a plot for rms phase deviation obtained during 1984 and 1985. This figure illustrates an overall decrease of scintillations in 1985 due to decreased solar activity.

The intensity scintillation magnitudes have been expressed in terms of the standard S_4 index, defined as the normalized variance of signal intensity (Briggs and Parkin, 1963). Figure 3 shows the variation of S_4 index at 137 MHz with invariant latitude during noon and midnight observed during 1984 and 1985. The nighttime enhancements of S_4 index in the region of alignment of the ray path with the magnetic L-shell (65^0-$67.5^0\Lambda$) is observed to be much less pronounced when it is compared to σ_ϕ enhancements shown in Figure 2. This indicates that the L-shell alignment of km-scale irregularities causing intensity scintillations is considerably less than the irregularities in the tens of kilometers scale that control the σ_ϕ values. The nighttime scintillation magnitudes during February-April, 1984 are again higher than that during August-October, 1984 due to enhanced solar activity.

In Figure 4, we show the behavior of power law spectral index, p_ϕ, for phase scintillations at 137 MHz during 1984 and 1985. A linear least square fit to the phase spectrum indicating the variation of the logarithm of power spectral density (psd) with the logarithm of frequency is obtained over the frequency interval of 0.2 Hz to 10 Hz. The best-fit line provides p_ϕ as it defines the dependence of psd on frequency f as psd $\propto f^{p_\phi}$. Considering the scan velocity of the ray path through the F-region, the fit range 0.2 Hz to 10 Hz corresponds to the scale size regime of about 15 km to 300 m. This regime encompasses the dominant structures that cause phase and intensity scintillations at VHF and UHF over the observing data interval. From Figure 4, it may be noted that the phase spectral index is least affected by the propagation geometry and does not show significant variations with season and solar activity in contrast to the behavior of S_4 and σ_ϕ. There exists, however, a tendency for p_ϕ to increase around $65^0\Lambda$, during the nighttime. Since this location corresponds to the average location of the diffuse aurora, the associated E-region conductivity may account for damping the short scale irregularities and causing the phase spectrum to steepen (Vickrey and Kelley, 1982). This steepening may also arise from increased psd at larger scales in the geometrical enhancement region due to better L-shell alignment of large scale irregularities as noted in connection with the increased σ_ϕ in comparison with S_4. The enhancements of p_ϕ are, however, smooth and distributed in contrast to the sharp geometrical enhancements of σ_ϕ. Probably, the spectral steepening arises from an interplay of both geophysical and geometrical effects.

The comb of three UHF transmissions from HiLat is used to derive the total electron content of the ionosphere up to the satellite altitude of 830 km by the differential Doppler technique (Fremouw et al., 1978). Figure 5 shows the latitude variation of median TEC values during the noon and midnight for different seasons. The next diagram, Figure 6, shows the observed variation of noontime TEC in relation to the sunspot number. The effects of the solar activity and season on TEC appear to be coupled. At high latitudes, owing to the near vertical orientation of the earth's magnetic field, the ionospheric irregularities of electron density at F-region height are usually extended in altitude. The integrated effect of the irregularities on radio wave propagation, such as scintillation, is therefore, weighted by the total electron content of the ionosphere. Thus measurements of irregularity amplitude, $\Delta N/N$ (ΔN being the rms electron density fluctuation and N the background density), and total electron content may form the basis for a modeling of scintillation magnitudes.

Among the various in-situ parameters probed by the satellite borne sensors, the in-situ ion-density measurement is an important parameter. In the F-region, due to charge neutrality, the electron and ion densities are equal. Figure 7 shows the variation of this parameter with latitude in the noon-midnight time frame as a function of season in 1984 and 1985 during magnetically quiet conditions. The ion density at 830 km is observed to follow closely the pattern of TEC variations shown earlier in Figure 5. The ion density variations are also controlled by both solar activity and season.

Although we did not illustrate the variation of scintillations and background ionospheric parameters with magnetic activity, it should be emphasized that the magnetic activity in addition to sunspot number exerts overwhelming control of scintillations at high latitudes (Basu and Aarons, 1980; Basu et al., 1985). Our HiLat observations indicate that during magnetically active conditions scintillation magnitudes are enhanced during the nighttime and the region of enhanced activity extends both in the poleward and the equatorward directions. Irrespective of the level of solar activity, scintillations are enhanced during magnetic disturbances.

DISCUSSIONS

We have shown that the most notable feature in the observed scintillation morphology at this auroral station even under magnetically quiet to moderate conditions is the enhancement of scintillations over a narrow latitude interval centered at 65°A in the nighttime sector. This narrow band increase of scintillations coincides with the expected region of geometrical enhancement due to the alignment of the ray path with the magnetic L-shell oriented irregularities. It is interesting to note that the boundary blobs which signify plasma density enhancements also occur in this region (Rino et al., 1983). The spatial configuration of the blobs is controlled by the high latitude convection pattern which is mostly E-W in the auroral region (Heelis et al., 1982). Robinson et al. (1985) have shown with the help of simulation studies that even a primarily circular patch of ionization being convected in from the polar cap would assume a narrow in latitude and elongated in longitude shape. These blobs can also develop small scale irregularities on their trailing edges through $\vec{E}x\vec{B}$ instability mechanisms. In general, the plasma blobs transported from distant regions get continually structured in the convection field and contribute a major source of nighttime auroral scintillations.

The other notable finding related to the scintillation structure is the steep phase spectral slopes observed in the region of geometrical enhancement. This region coincides with the central part of the diffuse aurora under magnetically quiet conditions as has been recently shown by Hardy et al., (1985) from DMSP satellite observations. Unlike the limited HiLat satellite data base of particle precipitation the DMSP satellites have provided a very large amount of data which have been organized by Hardy et al. to show the characteristic variations of particle precipitation with magnetic activity. The average energy of the particle precipitation in the diffuse auroral region is on the order of a few keV which is sufficient to produce a conducting E-region. This could reduce the lifetime of small scale irregularities (~100 m) and contribute to the observed steepening of the phase spectral indices. Basu et al. (1984) have illustrated such steepening of in-situ density spectra in regions of energetic auroral particle precipitation.

The structures present in the in-situ ion density probed by the HiLat satellite have recently been investigated (Weimer 1987). This study indicates that plasma density blobs at 830 km are concentrated over a fairly narrow latitude interval. This region when mapped down the magnetic field line corresponds approximately with the region of enhanced scintillations. These results indicate that, on a statistical basis, the blobs in addition to their E-W extent are also extended along the magnetic field lines to the topside ionosphere. The altitude profiles of the blobs have been published earlier using incoherent scatter radar measurements (Vickrey et al., 1980).

The extension of blobs to altitudes as high as 830 km indicates that magnetospheric coupling effects need to be included in the analysis of high latitude F-layer instabilities. The inclusion of ion-inertia in the $\vec{E}x\vec{B}$ instability theories results in a reduction of growth rates and generation of irregularities with spectral isotropy (Mitchell et al., 1985). In the non-inertial domain the irregularity spectra become anisotropic in the north-south and the east-west directions. Thus, the irregularity spectral indices are expected to be different in the north-south and east-west directions in the non-inertial case and identical for the inertial case. At Tromso, in addition to making HiLat observations that provide a north-south scan through the ionosphere, we have performed scintillation observations with near-stationary polar beacon satellites which provide an east-west scan controlled by ionospheric motion. The spectral indices of both sets of measurements are found to be

approximately equal indicating that the inertial effects are important in the generation of kilometer scale irregularities at high latitudes which cause VHF scintillations.

Another type of auroral irregularity not associated with large scale organized density gradients (such as to be found on the edges of blobs) but associated with velocity shears with shear gradient scale lengths ~10 km has been identified from HiLat observations (Basu et al., 1986). These irregularities, having considerable pad at the shorter scales, can cause intense VHF scintillations at the edges of auroral arcs in association with upward field aligned currents. In view of the well-known temporal and spatial variability of auroral arcs, the signature of such velocity shears will be difficult to identify in a statistical study of auroral scintillations.

REFERENCES

Basu, Su. and J. Aarons, The morphology of high-latitude VHF scintillation near 70°W, Radio Sci., 15, 59, 1980.

Basu, Su., S. Basu, E. MacKenzie, W.R. Coley, W.B. Hanson, and C.S. Lin, F-region electron density irregularity spectra near auroral acceleration and shear regions, J. Geophys. Res., 89, 5554, 1984.

Basu, Su., S. Basu, E. MacKenzie, and H.E. Whitney, Morphology of phase and intensity scintillations in the auroral oval and polar cap, Radio, Sci., 20, 347, 1985.

Basu, Su., S. Basu, C. Senior, D. Weimer, E. Nielsen, and P.F. Fougere, Velocity shears and sub-km scale irregularities in the nighttime auroral F-region, Geophys. Res. Lett., 13, 101, 1986.

Briggs, B.H. and I.A. Parkin, On the variation of radio star and satellite scintillation with zenith angle, J. Atmos. Terr. Phys., 25, 339, 1963.

Fremouw, E.J., R.L. Leadabrand, R.C. Livingston, M.D. Cousins, C.L. Rino, B.C. Fair, and R.A. Long, Early results from the DNA Wideband satellite experiment: Complex-signal scintillation, Radio Sci., 13, 167, 1978.

Fremouw, E.J., H.C. Carlson, T.A. Potemra, P.F. Bythrow, C.L. Rino, J.F. Vickrey, R.C. Livingston, R.E. Huffman, C.-I. Meng, D.A. Hardy, F.J. Rich, R.A. Heelis, W.B. Hanson, and L.A. Wittwer, The HiLat mission, Radio Sci., 20, 416, 1985.

Hardy, D.A., M.S. Gussenhoven, and E. Holeman, A statistical model of auroral electron precipitation, J. Geophys. Res., 90, 4229, 1985.

Heelis, R.A., J.K. Lowell, and R.W. Spiro, A model of the high-latitude ionospheric convection pattern, J. Geophys. Res., 87, 6339, 1982.

Mitchell, H.G., Jr., J.A. Fedder, M.J. Keskinen, and S.T. Zalesak, A simulation of high latitude F-layer instabilities in the presence of magnetosphere-ionosphere coupling, Geophys. Res. Lett., 12, 283, 1985.

Rino, C.L., R.C. Livingston, and S.J. Matthews, Evidence for sheet-like auroral ionospheric irregularities, Geophys. Res. Lett., 5, 1039, 1978.

Rino, C.L., R.C. Livingston, R.T. Tsunoda, R.M. Robinson, J.F. Vickrey, C. Senior, M.D. Cousins, J. Owen, and J.A. Klobuchar, Recent studies of th structure and morphology of auroral zone F-region irregularities, Radio Sci., 18, 1167, 1983.

Robinson, R.M., R.T. Tsunoda, J.F. Vickrey, and L. Guerin, Source of F-region ionization enhancements in the nighttime auroral zone, J. Geophys. Res., 90, 7533, 1985.

Vickrey, J.F. and M.C. Kelley, The effects of a conducting E-layer on classical F-region cross-field plasma diffusion, J.Geophys. Res., 87, 4461, 1982.

Vickrey, J.F., C.L. Rino, and T.A. Potemra, Chatanika/TRIAD observations of unstable ionization enhancements in the auroral F-region, Geophys. Res. Lett., 7, 789, 1980.

Vickrey, J.F., R.C. Livingston, R.T. Tsunoda, C.L. Rino, N.B. Walker, T.M. Dabbs, R.M. Robinson, and R.A. Heelis, The SRI ionospheric plasma structure and dynamics program - 1985 results, Final Technical Report, SRI International, June 1985.

Weimer, D.R., Large-scale plasma density fluctuations measured with the HiLat satellite at 830 km altitude, AFGL Technical Rpt., Hanscom AFB, MA, 1987.

ACKNOWLEDGMENT

This work was supported by AFGL Contract F19628-86-K-0038 with Emmanuel College and by the Defense Nuclear Agency. The authors thank L. Wittwer, H.C. Carlson, and F.J. Rich for their interest and support.

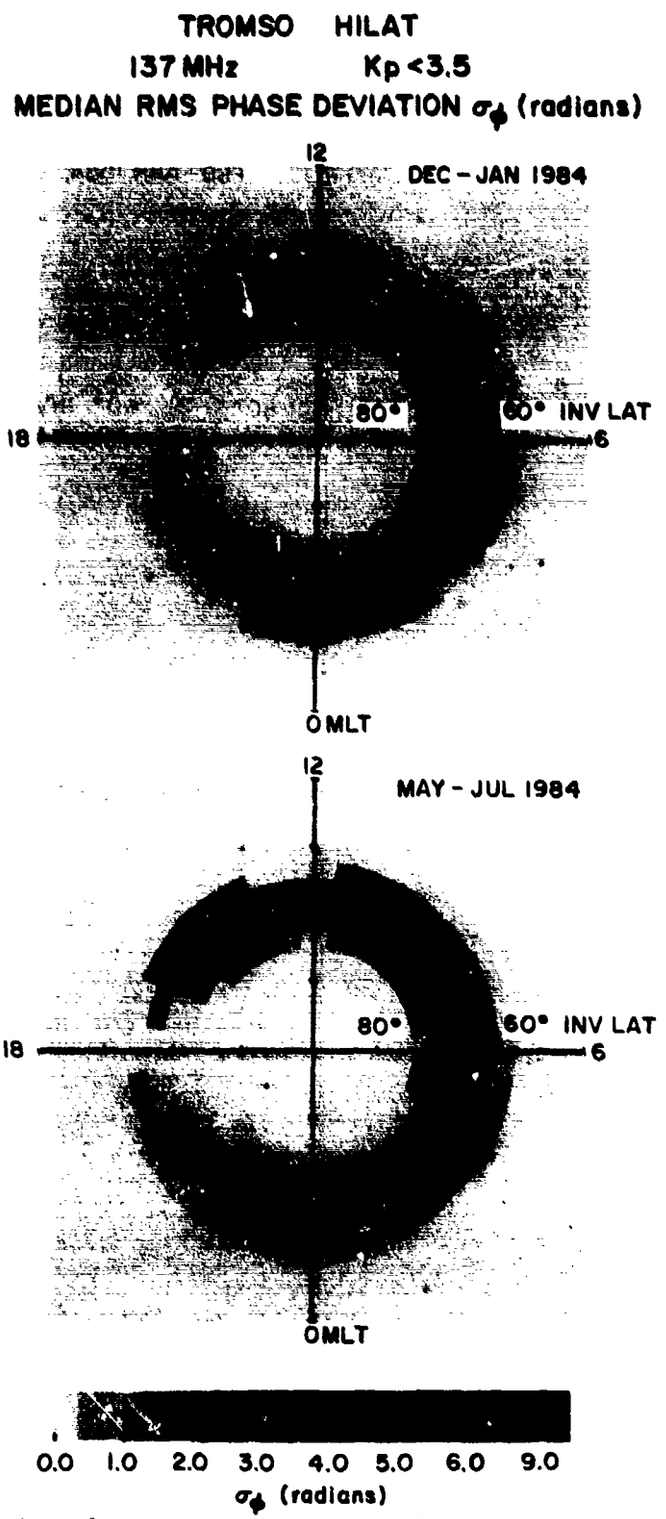


Figure 1a. Variations of rms phase deviation at 137 MHz with invariant latitude and magnetic local time during winter and summer.

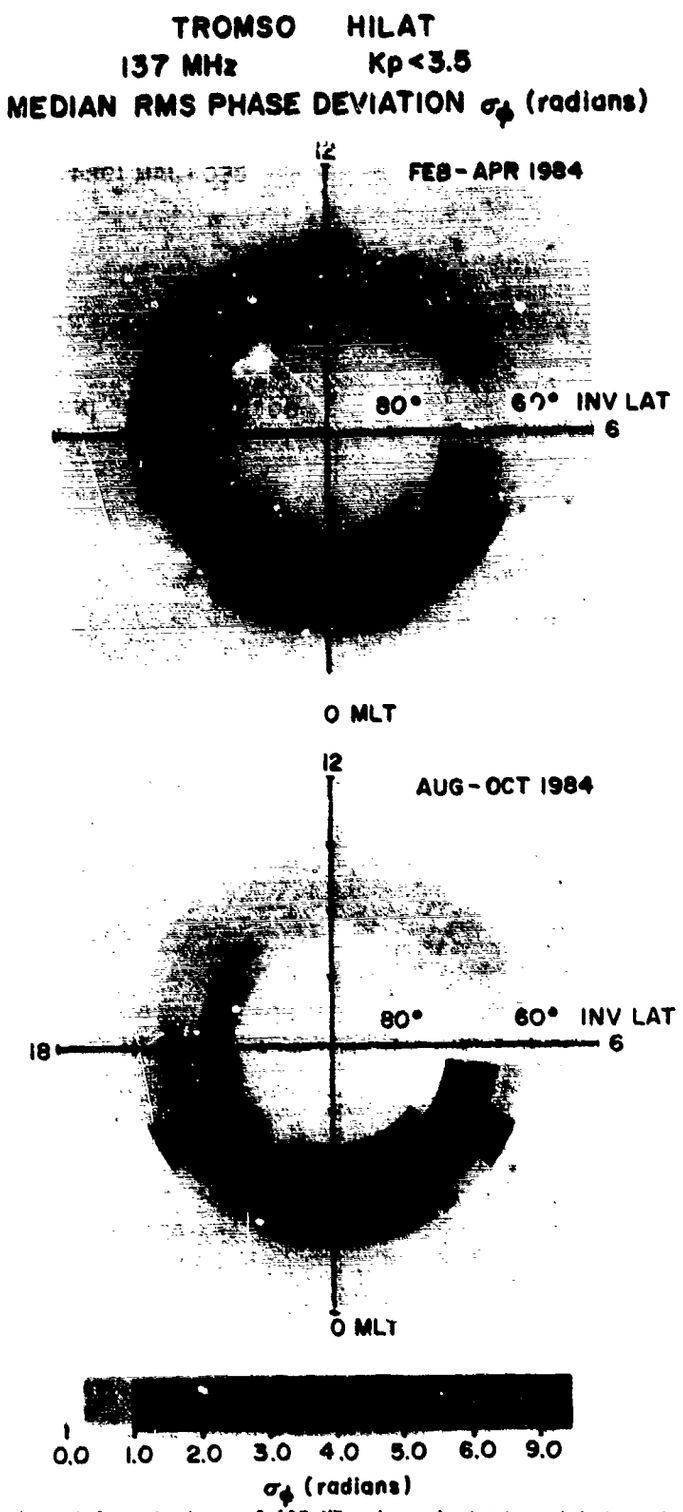


Figure 1b. Equinoctial variations of 137 MHz phase deviation with invariant latitude and magnetic local time.

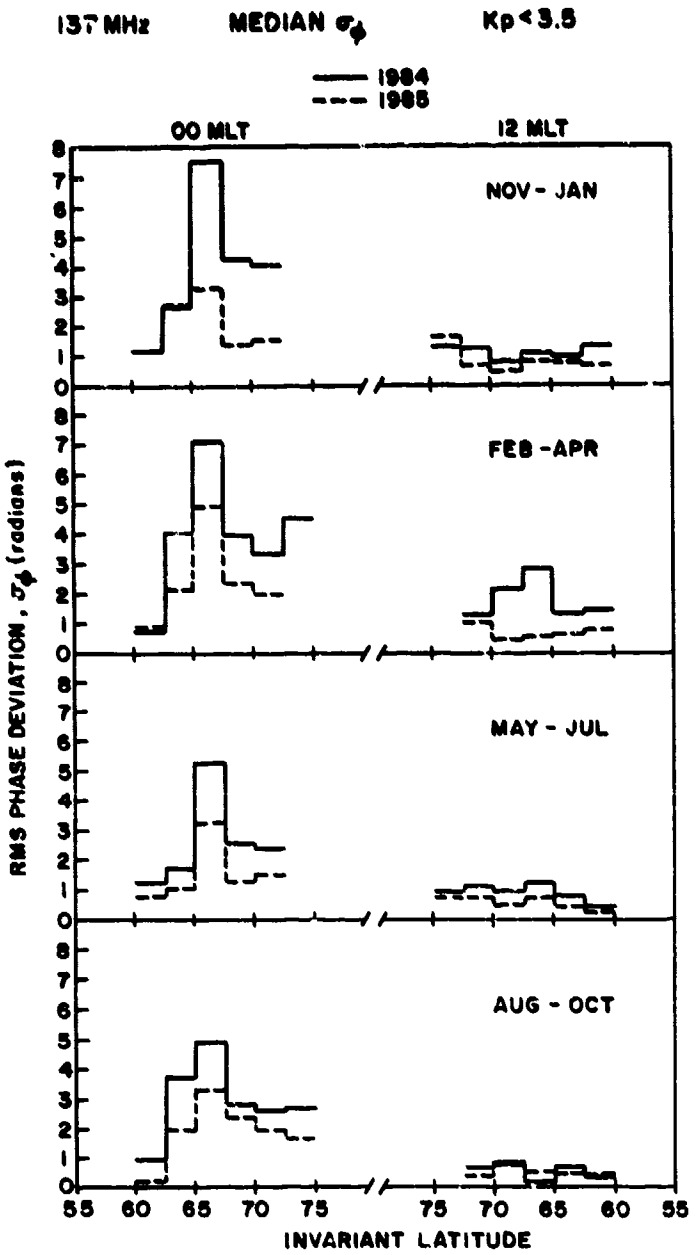


Figure 2. Seasonal variations of rms phase deviation at 137 MHz with invariant latitude along the noon-midnight meridian in 1984 and 1985.

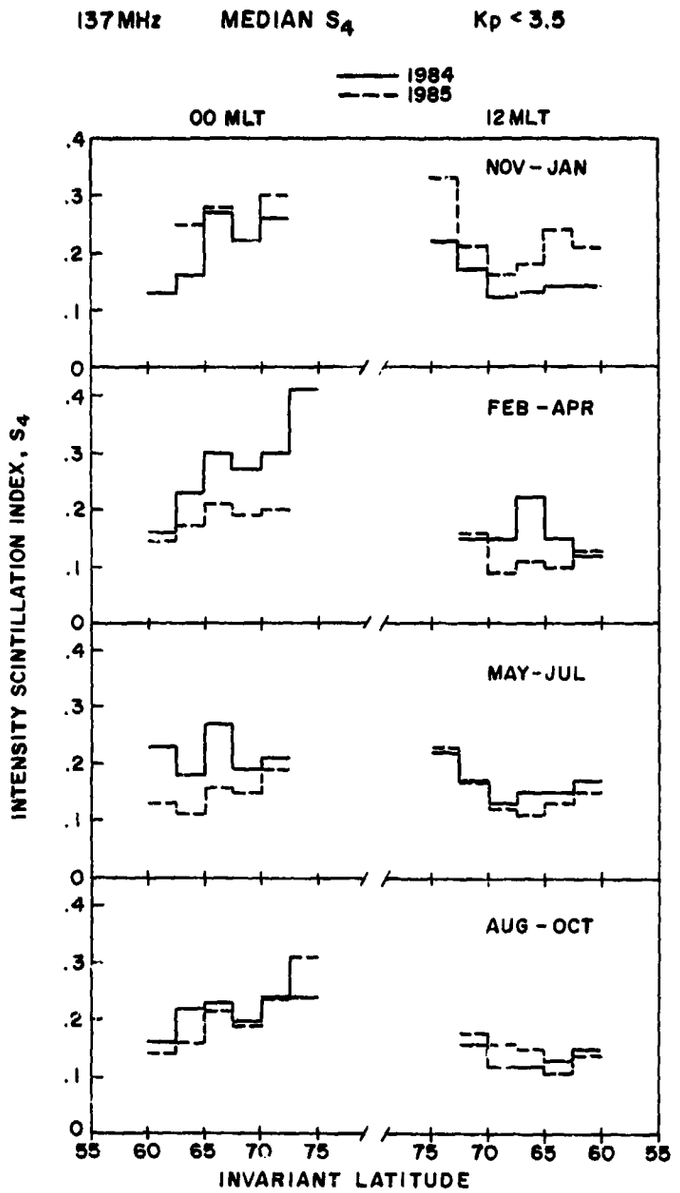


Figure 3. Seasonal variations of intensity scintillation index at 137 MHz along the noon-midnight meridian in 1984 and 1985.

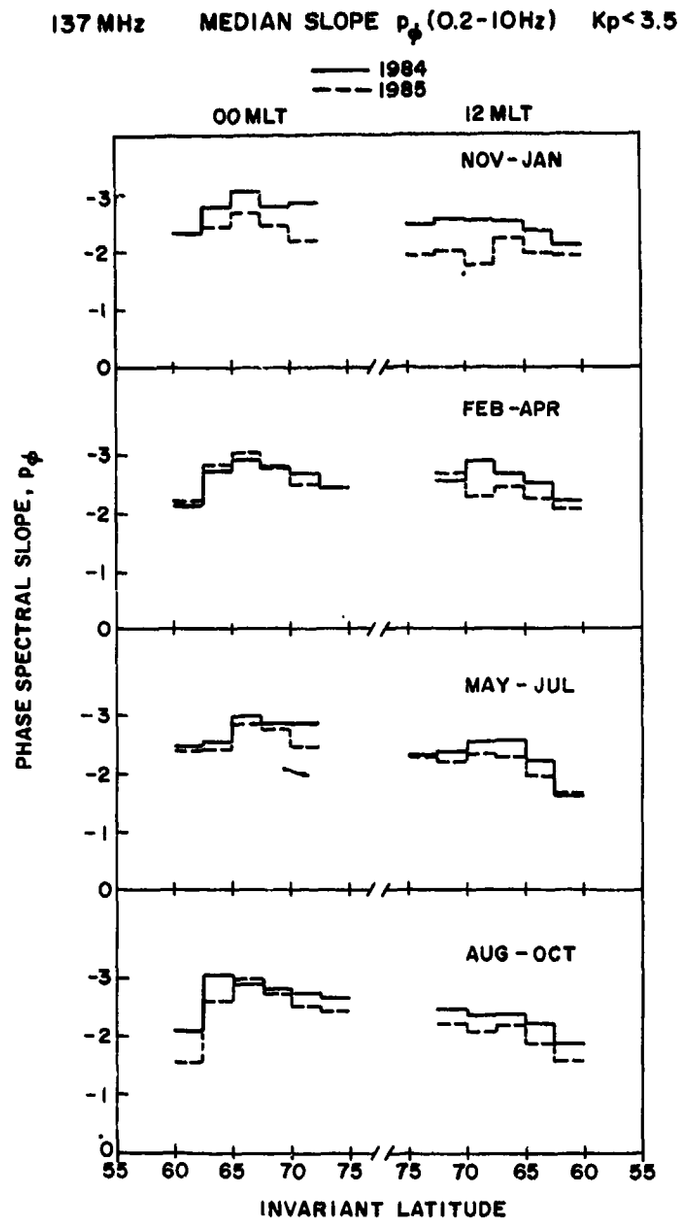


Figure 4. Seasonal variations of the slope of 137 MHz phase scintillation spectra along the interval of 0.2-10 Hz along the noon-midnight meridian in 1984 and 1985.

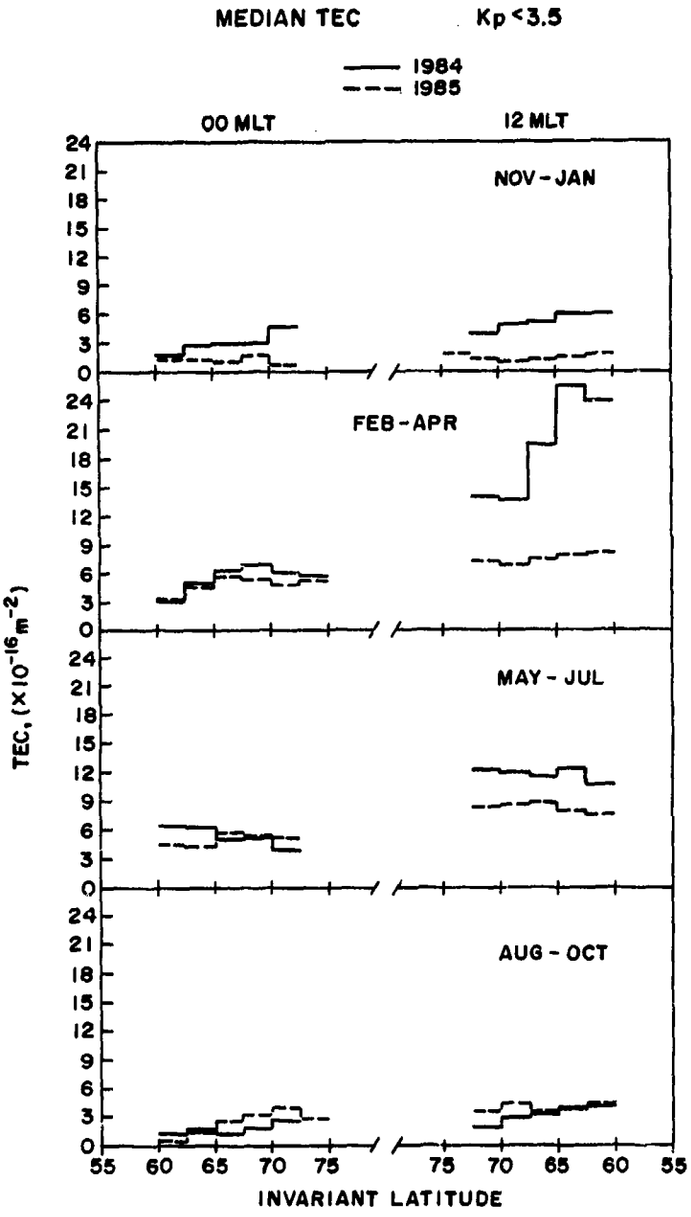


Figure 5. Seasonal variations of total electron content variations along the noon-midnight meridian in 1984 and 1985.

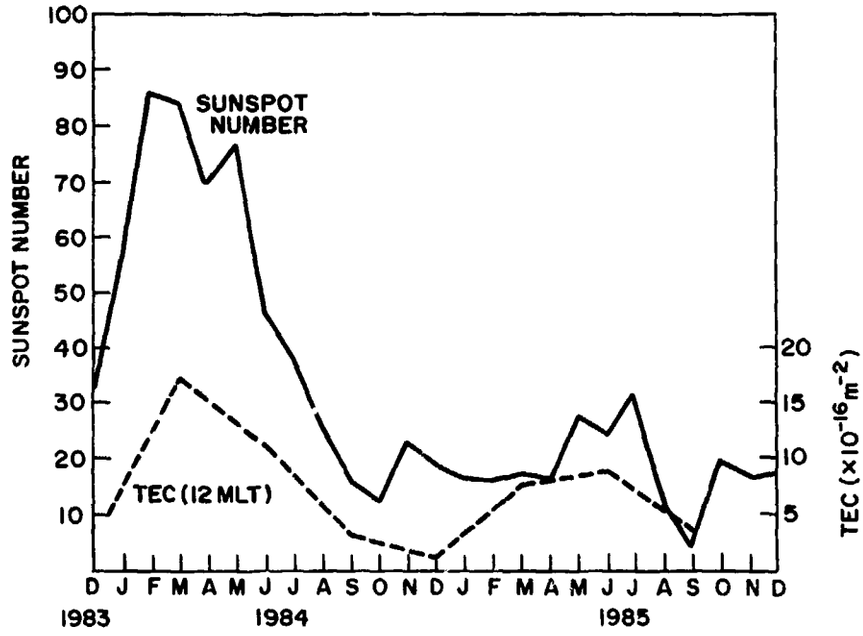


Figure 6. Illustrates the correspondence between the variations of total electron content and sunspot number.

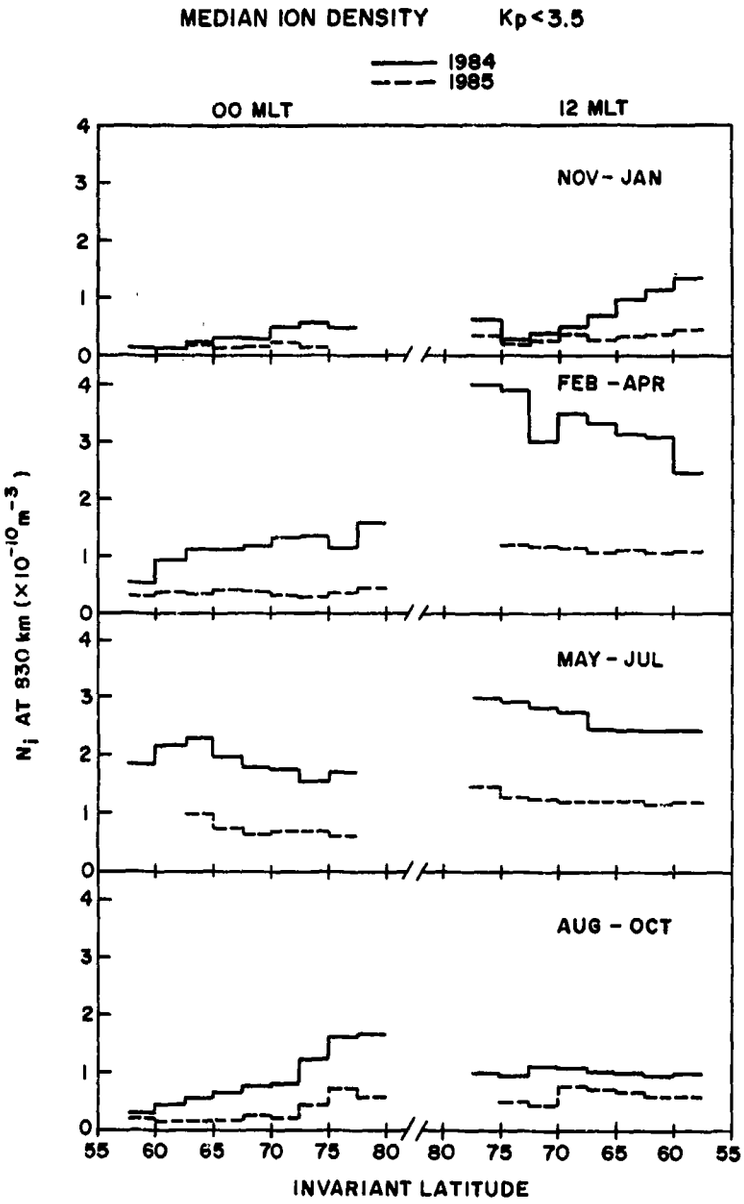


Figure 7. Seasonal variations of ion density at the satellite altitude of 830 km along the noon-midnight meridian in 1984 and 1985.

ROUND TABLE DISCUSSION

The participants were given the following questions to think about beforehand and were asked to bring their thoughts to the Round Table Discussion.

1. The study of wave propagation in random media can generally be classified into three kinds: random continuum, rough surface scattering and random discrete scatter. Over the years, each class has been developed more or less independently. Among these three classes of problems, what are the similarities and differences either in theoretical methods or analysis or observed physical phenomena?
2. What is the current status of theoretical development in this area?
   (a) Should we be satisfied with the correlation analysis? Are there needs to go to higher moments? How about distribution functions?
   (b) What are the relative advantages and disadvantages of analytic methods, numerical methods and Monte Carlo simulations?
   (c) How would you compare a theory based on first principals vs. one developed phenomenologically?
3. What experiments should be conducted?
   (a) Under laboratory controlled conditions?
   (b) Multisensors under natural conditions?
   (c) Applications and inverse problems?
4. System considerations.
   (a) Characterization and modeling of fading channels.
   (b) What is the role of simulators?
   (c) What is the impact on system design?
5. Future directions.

In about one hour allocated to this part of the program, comments were made by a number of people, including: I. M. Besieris, L. Boithias, J. A. DeSanto, W. A. Flood, C. Goutelard, A. Ishimaru, R. Miller, K. A. O'Donnell, J. F. Patricio, etc. These comments were expressed individually; they do not necessarily reflect the collective sentiments of all the participants at the meeting.

- The three classes of random media: random continuum, rough surface and discrete scatterers, require the development of specific techniques to deal with them separately.
- In treating continuous random media, promises have been shown in using path integral techniques when applied to large fluctuations and self-similar thechniques when applied to a deep screen.
- In the study of discrete scattering, more work is needed on backscattering enhancement, especially in higher moments and on multiscale problems especially when the fluctuation scale is of the order of a wavelength.
- Further studies are needed in dealing with a medium which is a mixture of the three kinds just described. One example is a medium consisting of particles in a turbulence; another is a rough surface created by the boundary of discrete scatterers.
- In radar applications, e.g., ground clutter, there is need to know the higher moments, such as intensity fluctuations. The distribution function is also of interest, although details cannot be determined uniquely in general, by a few moments. Here models may be useful. Use has been made of K-distributions or any other models generated by self-similar arguments.
- In certain applications, the statistical properties of the medium are neither homogeneous nor stationary. In a weakly inhomogeneous or weakly nonstationary medium, the structure function has been found useful. For some problems, the inhomogeneity can be characterized by

a structure constant as a product of two functions: one depending on the center of gravity coordinates and one depending on the difference coordinates.

- The mm-wave experiments carried out at Flatville, Illinois, were very unique because of the availability of radio data and atmospheric data. Currently, the data base is being used in turbulence studies and boundary layer meteorology. It appears that mm-waves at 95 GHz can offer path-averaged measurements for estimating the momentum transfer in a boundary layer. The data base is available to anyone wishing to use it by writing to S. F. Clifford, Wave Propagation Laboratory, NOAA, Boulder, CO 80303, USA.
- In spite of limitations and difficulties in characterizing rough surfaces in a laboratory setup, laboratory-controlled experiments are far better for checking the accuracy of theoretical models. At the present time, there seems to exist a wide gap, in some cases, between theory and observations. It is important to know in what direction we must go in order to bring them into agreement.

LIST OF PARTICIPANTS

Aarons, Dr J.	Dept. of Astronomy Boston University 725 Commonwealth Ave Boston, MA 02215 United States
Albrecht, Dr Ing. H-J	FGAN Neuenahrer Str. 20 D-5307 Wachtberg-Werthhoven Federal Republic of Germany
Allen, Mr K.C.	NTIA/ITS S3 325 Broadway Boulder, CO 80303 United States
Altmann, Dr K.	Messerschmitt-Bölkow-Blohm GmbH Abt ZTA11 Postfach 80 11 09 8000 München 80 Federal Republic of Germany
Arkwright, Mr J.H.	Staff Officer, R & D NDHQ/DRDCS-4 National Defence Headquarters 11CBN 101 Colonel By Drive, Ottawa Canada
Armstrong, Prof. R.L.	Physics Department, Box 3D New Mexico State University Las Cruces. NM 88003 United States
Bahar, Prof. E.	Elect. Engr. Dept., WESC 209N University of Nebraska Lincoln, NE 68588-0511 United States
Baker, Mr C.J.	R.S.R.E. Saint Andrews Road Malvern, Worcs WR14 3PS United Kingdom
Basili, Prof. P.	c/o Aeronautica Militare Ufficio del Delegato Nazionale all'AGARD Piazzale K.Adenauer, 3 00144 Roma/EUR Italy
Belrose, Dr J.	Communications Research Center P.O. Box 11490 Station H Ottawa, Ontario K2H 8S2 Canada
Beniguel, Mr	Lab. Central de Télécommunications 18,20 Rue Grange Dame Rose 78141 Velizy-Villacoublay
Besieris, Prof. I.M.	Dept. of EE Virginia Polytechnic University Blackburg, VA 24061 United States
Bishop, Mr G.J.	British Aerospace Naval Weapons Division FPC [illegible] ilton B[illegible]12 7QW United Kingdom

Boithias, Mr L.	CNET 38—40, rue du Général Leclerc 92131 Issy les Moulineaux France
Bossy, Prof. L.	174, Ave Winston Churchill 1180 Bruxelles Belgium
Burgess, Dr B.	Head R & N Dept. Royal Aircraft Establishment Farnborough Hants, GU14 6TD United Kingdom
Carel, Mr C.	Nuclétudes SA Av. du Hoggar — ZA de Courtaboeuf BP 117 91944 Les Ulis Cedex France
Cassara, Ltc. A.	Aeronautica Militare Div. Aera Studi, Ricerche e Sperim. Rep. Armamenonnto 00040 Pratica di Mare Italy
Chow, Prof. P.L.	Dept of Mathematics Wayne State University Detroit, MI 48202 United States
Christophe, Mr F.	ONERA—CERT BP 4025 31055 Toulouse Cedex France
Ciattaglia, Lt. Col.	Aeroporto Vigna di Valle Director Meteorological Station 00062 Vigna Di Valle (Roma) Italy
Clifford, Mr S.F.	NOAA/FRL/Wave Propagation Lab. 325 Broadway Boulder, CO 80303 United States
Colin, Dr Lawrence	Chief, Space Science Div. NASA Ames Research Center MS 245-1 Moffet Field, CA 94035 United States
Consortini, Prof. A.	Universita de Firenze Dipartimento di Fisica Via S.Marta 3 50139 Firenze Italy
Cook, Michael C.	Marconi Maritime Applied Research Laboratory Unit 33 Cambridge Science Park Milton Road, Cambridge, CB4 4FX United Kingdom
Crosignani, Prof. B.	Fondazione "Ugo Bordoni" c/o ISPT Viale Europa 160 00153 Roma Italy
Cucinotta, Dr G.	Elmer Industrie per lo Spazio e le Communicazioni Viale dell'Industria 4 00040 Pomezia (RM) Italy

Cutolo, Prof. M.	Universita di Napoli Istituto di Fisica Via Monteoliveto 3 80134 Napoli Italy
De Franceschi, Dr G.	Via di Villa Ricotti 42 Roma Italy
Denti, Prof. P.	Istituto di Struttura della Materia Universita di Messina 98100 Messina Italy
DeSanto, Dr J.A.	Center for Wave Phenomenon Math Dept. Colorado School of Mines Golden, CO 80401 United States
Di Porto, Prof. P.	Universita di Roma Dipartimento di Fisica Piazzale A.Moro 2 00185 Roma Italy
Felsen, Prof. L.B.	Dept. of EE and Computer Science Weber Research Institute Polytechnic University Farmingdale, NY 11735 United States
Flood, Dr Walter A.	Geoscience Division US A.R.O., P.O. Box 12211 Research Triangle Park NC 27709 United States
Fournier, Mr M.	Lab. Central de Télécommunications 18—20 rue Grange Dame Rose 78141 Velizy-Villacoublay France
Frank, Mr S.J.	EE University of Illinois 1406 W.Green St Urbana , IL 61801 United States
Fuchs, Dr H.H.	FGAN-FHP/GA Neuenahrer Str. 20 D-5307 Wachtberg-Werthhoven Federal Republic of Germany
Fung, Prof. A.K.	Wave Scattering Research Ctr Dept. of EE, Room 316 Box 19016 Arlington, TX 76019 United States
Gibert, Ing. B.	Aérospatiale route de Verneuil 78130 Les Mureaux France
Gill, Dr R.S.	Marconi Research Centre West Hanningfield Rd Chelmsford, Essex United Kingdom
Goncalves, Mr C.A.	Instituto Nacional de Meteo, Geofis. Rua C Aeroporto 1700 Lisboa Portugal

Goutelard, Prof. C.	L.E.T.T.I. 9 Avenue de la Division Leclerc 92230 Cachan France
Hewish, Prof. A.	Cavendish Labs Madingley Road Cambridge, CB3 0HE United Kingdom
Heynisch, Dipl. Ing. B.	AEG Aktiengesellschaft Geschäftsbereich Hochfrequenztechnik Sedanstr. 10 D-7900 Ulm Donau Federal Republic of Germany
Hoffmeyer, Mr J.A.	US Dept. of Commerce NTIA/ITS 325 Broadway Boulder, CO 80303 United States
Hurtaud, Mr Y.	Lab. Antennes & Micro-Electronique C.N.R.S. Université de Rennes I Avenue du Général Leclerc 35042 Rennes Cedex France
Ince, Prof. Doc. A.Nejat	Tubitak Ataturk Blv No 221 Ankara Turkey
Ishimaru, Prof. A.	Dept. of UU, ST-10 University of Washington Seattle, WA 98195 United States
Jakeman, Prof. E.	R.S.R.E. Saint Andrews Road Malvern, Worcs WR14 3PS United Kingdom
Jefferson, Dr J.H.	R.S.R.E. Room KE008 Saint Andrews Road Malvern, Worcs WR14 3PS United Kingdom
Jeske, Mr H.	Meteorol. Institut der Universität Hamburg Bundesstrasse 55 D-2000 Hamburg 13 Federal Republic of Germany
Katelouzos, Ltc D.	HAFGS/C3 Holargos, Athens Greece
Kelly, Mr F.J.	Naval Research Lab. E.O. Hulbert Ctr for Space Research Ionospheric Effects Branch Washington, DC 20375-5000 United States
Lange-Hesse, Dr G.	Max-Planck-Institut für Aeronomie D-3411 Katlenburg-Lindau 3 Federal Republic of Germany
Langot, Ing. L.	DRET 26 Bd Victor 75996 Paris Armées France
Lemmon, Dr J.J.	US Dept of Commerce NTIA/ITS 325 Broadway Boulder, CO 80303 United States

Ligthart, Dr Ing. L.P.	Delft University of Technology Mekelweg 2628 CD Delft Netherlands
Lo Melo, Mr	c/o Aeronautica Militare Ufficio del Delegato Nazionale all'AGARD Piazzale K.Adenauer, 3 Roma/EUR Italy
Lo Muzio, Ing. P.	Tellettra SPA Via Piaggio 71 66013 Chieti Scalo Italy
Luttrell, Dr S.P.	R.S.R.E. Saint Andrews Road Malvern, Worcs WR14 3PS United Kingdom
Matera, Lten. F.	Commando Corpo Tecnico Esercito Via della Batteria Momentana 51 Roma Italy
Mazar, Dr R.	Dept. of Electr. Engineering and Computer Science Route 110 Farmingdale, NY 11735 United States
Miller, Miss S.	Dept. of Applied Math. Cambridge University Silver Street Cambridge, CB3 9EW United Kingdom
Miller, Mr R.J.	Marconi Research Centre West Hanningfield Road, Great Baddow Chelmsford, Essex United Kingdom
Molinet, Mr et Mme.	Direction Société Mothesim Centre de la Boursidière, RN 186 92357 le Plessis Robinson France
Muller, Mr G.	Société Mothesim La Boursidière RN 186 92357 le Plessis Robinson France
Nesenberg, Mr M.	US Dept. of Commerce NTIA/ITS 325 Broadway Boulder, CO 80303 United States
O'Donnell, Dr K.A.	Universita degli Studi Fisica Sup. Dipartimento di Fisica Via S. Marta, 3 50139 Firenze Italy
Ochs, Mr Alfred	Forschungsinstitut der DBP beim FTZ Postfach 5000 D-6100 Darmstadt Federal Republic of Germany
Oliver, Dr C.J.	R.S.R.E Saint Andrews Road Malvern, Worcs WR14 3PS United Kingdom

Ostergaard, Mr J.
Dept. of Telecom. Engr.
Elektronik Centralen
Ved Lighedsvej 4
DK-2870 Horsholm
Denmark

Papa, Mr R.J.
Electromagnetic Sciences Division
RADC/EEC
Hanscom AFB, MA 01731
United States

Patricio, Mr J.F.
Direcçao Geral De Telecomunicaçoes
Av. Fonte Pereira de Melo, 40
1089 Lisboa Cedex
Portugal

Pianigiani, Lt. R.
c/o Aeronautica Militare
Ufficio del Delegato Nazionale all'AGARD
Piazzale K.Adenauer, 3
Roma/EUR
Italy

Rasmussen, Mr J.E.
Chief, Ionosph. Interactions Branch
Air Force Geophys. Laboratory
Hanscom AFB, MA 01731
United States

Rauch, Dr D.
Istituto di Acustica
Via Cassia 1216
00189 Roma
Italy

Reeve, Mr Dominic
Marconi Maritime Applied Research
Laboratory Unit 33--35, Science Park
Milton Road, Cambridge, CB4 4FX
United Kingdom

Rice, Mr David E.
Marconi Research Centre
West Hanningfield Road, Great Baddow
Chelmsford, Essex
United Kingdom

Richter, Dr J.H.
Code 54
N.O.S.C.
San Diego, CA 92152-5000
United States

Risitano, Mr A.
Aeritalia
C. Marche 41
Torino
Italy

Rother, Dr Ing. D.
SEL Pforzheim
Ostendstr. 3
D-7530 Pforzheim
Federal Republic of Germany

Rousset, Dr Gerard
ONERA
29 Avenue de la Div. Leclerc
B.P. 72
92322 Châtillon Cedex
France

Saija, Dr R.
Universita di Messina
Istituto di Struttura della Materia
Via dei Verdi
98100 Messina
Italy

Sales, Dr G.
University of Lowell
Ctr for Atmospheric Research
450 Aiken St.
Lowell, MA 01854
United States

Santimay Basu, Dr	AFGL/LIS Hanscom AFB, MA-01731-5000 United States
Schimpf, Dr Hartmut M.	Research Scientist FGAN-FHP/GA Neuenahrer Str. 20 D-5307 Wachtberg-Werthhoven Federal Republic of Germany
Schmiedel, Dr Ing. H.	Forschungsinstitut der DBP beim Fernmeldetechnischen Zentralamt Postfach 5000 D-6100 Darmstadt Federal Republic of Germany
Sezgin, Capt. A.	Eskisehir Ikmal Bakim Merkezi Komutanligi Arge Mudurlugu Eskisehir Ankara Turkey
Sinttruyen, Ir. J.S.Van	Technische Universiteit Mekelweg 4 2628 CD Delft Netherlands
Soicher, Dr H.	Center for COMM/ADP US Army Communications-Electronics Command, Attn AMSEL-COM-TA-1 Fort Monmouth, N.J. 07703-5202 United States
Sprenkels, Col. C.	Etat Major de la Force Aérienne Section Communication et Elect. Quartier Reine Elisabeth B-1140 Bruxelles Belgium
Sunanda Basu, Dr	Emmanuel College Physics Research Division Boston, MA 02115 United States
Taagholt, Mr J.	Danish Scientific Liaison Officer for Greenland 10 Oester Voldgade DK 1350 Copenhagen K Denmark
Tacconi, Prof. G.	Universita di Genova Dip. Ingegneria Bifisica et Ellettr. Via dell'o Pera Pia 11A 16145 Genova Italy
Van der Geest, Prof. P.C.	P.O. Box 90154 4800 R G Breda Netherlands
Vasundra V.Vara, Prof.	227, Hammond Bldg Pennsylvania State University University Park, PA 16802 United States
Vijay, Dr	Prof. Engineering Science 149 Hammond Bldg Pennsylvania State University University Park, PA 16802 United States
Vissingo, Ir. H.	F.E.L.T.N.O. P.O. Box 96864 2509 J.G. The Hague Netherlands

Walsh, Dr J.
Faculty of Engr. & Appl. Science
Memorial U. of N.F.
St Johns, Newfoundland A1B 3X5
Canada

Yeh, Prof. K.C.
EE University of Illinois
1406 W. Green St
Urbana, IL 61801
United States

Zolesi, Dr B.
Istituto Nazionale di Geofisica
Via di Villa Ricotti 42
Roma
Italy

REPORT DOCUMENTATION PAGE			
1. Recipient's Reference	**2. Originator's Reference**	**3. Further Reference**	**4. Security Classification of Document**
	AGARD-CP-419	ISBN 92-835-0444-5	UNCLASSIFIED

5. Originator Advisory Group for Aerospace Research and Development
North Atlantic Treaty Organization
7 rue Ancelle, 92200 Neuilly sur Seine, France

6. Title

SCATTERING AND PROPAGATION IN RANDOM MEDIA

7. Presented at

the Electromagnetic Wave Propagation Panel Specialists' Meeting held in Rome, Italy, 18—22 May 1987.

8. Author(s)/Editor(s)	**9. Date**
Various	March 1988
10. Author's/Editor's Address	**11. Pages**
Various	562

12. Distribution Statement This document is distributed in accordance with AGARD policies and regulations, which are outlined on the Outside Back Covers of all AGARD publications.

13. Keywords/Descriptors

Scattering
Propagation
Random media
Radiation
Electromagnetic waves
Spectrum

14. Abstract

The topic of scattering and propagation in random media is one that has implications for the design, development and operation of most military systems that radiate energy as a means of accomplishing their function. Primary emphasis is on scattering and transmission in the atmosphere; however, other related random medium effects are not excluded.

Modern methods of characterizing random media, mathematical methods and their applicability, effects on electromagnetic waves and the interpretation of these effects to specific system applications are described.

The region of the spectrum considered is essentially unlimited and ranges from very long waves to optics.

The performance of existing surveillance communication and navigation systems as well as the design of future systems is influenced by the propagation of energy via random media. An understanding of the nature of the medium and its impact on system design and performance is essential to the NATO community.

Modern methods of characterizing random media, mathematical methods and their applicability, effects on electromagnetic waves and the interpretation of these effects to specific system applications are described.

The region of the spectrum considered is essentially unlimited and ranges from very long waves to optics.

The performance of existing surveillance communication and navigation systems as well as the design of future systems is influenced by the propagation of energy via random media. An understanding of the nature of the medium and its impact on system design and performance is essential to the NATO community.

Papers presented at the Electromagnetic Wave Propagation Panel Specialists' Meeting held in Rome, Italy, 18—22 May 1987.

ISBN 92-835-0444-5

Modern methods of characterizing random media, mathematical methods and their applicability, effects on electromagnetic waves and the interpretation of these effects to specific system applications are described.

The region of the spectrum considered is essentially unlimited and ranges from very long waves to optics.

The performance of existing surveillance communication and navigation systems as well as the design of future systems is influenced by the propagation of energy via random media. An understanding of the nature of the medium and its impact on system design and performance is essential to the NATO community.

Papers presented at the Electromagnetic Wave Propagation Panel Specialists' Meeting held in Rome, Italy, 18—22 May 1987.

ISBN 92-835-0444-5

Modern methods of characterizing random media, mathematical methods and their applicability, effects on electromagnetic waves and the interpretation of these effects to specific system applications are described.

The region of the spectrum considered is essentially unlimited and ranges from very long waves to optics.

The performance of existing surveillance communication and navigation systems as well as the design of future systems is influenced by the propagation of energy via random media. An understanding of the nature of the medium and its impact on system design and performance is essential to the NATO community.

Papers presented at the Electromagnetic Wave Propagation Panel Specialists' Meeting held in Rome, Italy, 18—22 May 1987.

ISBN 92-835-0444-5

Modern methods of characterizing random media, mathematical methods and their applicability, effects on electromagnetic waves and the interpretation of these effects to specific system applications are described.

The region of the spectrum considered is essentially unlimited and ranges from very long waves to optics.

The performance of existing surveillance communication and navigation systems as well as the design of future systems is influenced by the propagation of energy via random media. An understanding of the nature of the medium and its impact on system design and performance is essential to the NATO community.

Papers presented at the Electromagnetic Wave Propagation Panel Specialists' Meeting held in Rome, Italy, 18—22 May 1987.

ISBN 92-835-0444-5

AGARD Conference Proceedings No.419 Advisory Group for Aerospace Research and Development, NATO SCATTERING AND PROPAGATION IN RANDOM MEDIA Published March 1988 562 pages The topic of scattering and propagation in random media is one that has implications for the design, development and operation of most military systems that radiate energy as a means of accomplishing their function. Primary emphasis is on scattering and transmission in the atmosphere; however, other related random medium effects are not excluded. P.T.O	AGARD-CP-419 Scattering Propagation Random media Radiation Electromagnetic waves Spectrum	AGARD Conference Proceedings No.419 Advisory Group for Aerospace Research and Development, NATO SCATTERING AND PROPAGATION IN RANDOM MEDIA Published March 1988 562 pages The topic of scattering and propagation in random media is one that has implications for the design, development and operation of most military systems that radiate energy as a means of accomplishing their function. Primary emphasis is on scattering and transmission in the atmosphere; however, other related random medium effects are not excluded. P.T.O	AGARD-CP-419 Scattering Propagation Random media Radiation Electromagnetic waves Spectrum
AGARD Conference Proceedings No.419 Advisory Group for Aerospace Research and Development, NATO SCATTERING AND PROPAGATION IN RANDOM MEDIA Published March 1988 562 pages The topic of scattering and propagation in random media is one that has implications for the design, development and operation of most military systems that radiate energy as a means of accomplishing their function. Primary emphasis is on scattering and transmission in the atmosphere; however, other related random medium effects are not excluded. P.T.O	AGARD-CP-419 Scattering Propagation Random media Radiation Electromagnetic waves Spectrum	AGARD Conference Proceedings No.419 Advisory Group for Aerospace Research and Development, NATO SCATTERING AND PROPAGATION IN RANDOM MEDIA Published March 1988 562 pages The topic of scattering and propagation in random media is one that has implications for the design, development and operation of most military systems that radiate energy as a means of accomplishing their function. Primary emphasis is on scattering and transmission in the atmosphere; however, other related random medium effects are not excluded. P.T.O	AGARD-CP-419 Scattering Propagation Random media Radiation Electromagnetic waves Spectrum

AGARD
NATO OTAN
7 rue Ancelle · 92200 NEUILLY-SUR-SEINE
FRANCE
Telephone (1)47.38.57.00 · Telex 610 176

DISTRIBUTION OF UNCLASSIFIED AGARD PUBLICATIONS

AGARD does NOT hold stocks of AGARD publications at the above address for general distribution. Initial distribution of AGARD publications is made to AGARD Member Nations through the following National Distribution Centres. Further copies are sometimes available from these Centres, but if not may be purchased in Microfiche or Photocopy form from the Purchase Agencies listed below.

NATIONAL DISTRIBUTION CENTRES

BELGIUM
Coordonnateur AGARD — VSL
Etat-Major de la Force Aérienne
Quartier Reine Elisabeth
Rue d'Evere, 1140 Bruxelles

CANADA
Director Scientific Information Services
Dept of National Defence
Ottawa, Ontario K1A 0K2

DENMARK
Danish Defence Research Board
Ved Idraetsparken 4
2100 Copenhagen Ø

FRANCE
O.N.E.R.A. (Direction)
29 Avenue de la Division Leclerc
92320 Châtillon

GERMANY
Fachinformationszentrum Energie,
Physik, Mathematik GmbH
Karlsruhe
D-7514 Eggenstein-Leopoldshafen 2

GREECE
Hellenic Air Force General Staff
Aircraft Support Equipment Directorate
Department of Research and Development
Holargos, Athens, 15500

ICELAND
Director of Aviation
c/o Flugrad
Reyjavik

ITALY
Aeronautica Militare
Ufficio del Delegato Nazionale all'AGARD
3 Piazzale Adenauer
00144 Roma/EUR

LUXEMBOURG
See Belgium

NETHERLANDS
Netherlands Delegation to AGARD
National Aerospace Laboratory, NLR
P.O. Box 126
2600 AC Delft

NORWAY
Norwegian Defence Research Establishment
Attn: Biblioteket
P.O. Box 25
N-2007 Kjeller

PORTUGAL
Portuguese National Coordinator to AGARD
Gabinete de Estudos e Programas
CLAFA
Base de Alfragide
Alfragide
2700 Amadora

TURKEY
Milli Savunma Bakanlığı (MSB)
ARGE Daire Başkanlığı (ARGE)
Ankara

UNITED KINGDOM
Defence Research Information Centre
Kentigern House
65 Brown Street
Glasgow G2 8EX

UNITED STATES
National Aeronautics and Space Administration (NASA)
Langley Research Center
M/S 180
Hampton, Virginia 23665

THE UNITED STATES NATIONAL DISTRIBUTION CENTRE (NASA) DOES NOT HOLD STOCKS OF AGARD PUBLICATIONS, AND APPLICATIONS FOR COPIES SHOULD BE MADE DIRECT TO THE NATIONAL TECHNICAL INFORMATION SERVICE (NTIS) AT THE ADDRESS BELOW.

PURCHASE AGENCIES

National Technical
Information Service (NTIS)
5285 Port Royal Road
Springfield
Virginia 22161, USA

ESA/Information Retrieval Service
European Space Agency
10, rue Mario Nikis
75015 Paris, France

The British Library
Document Supply Division
Boston Spa, Wetherby
West Yorkshire LS23 7BQ
England

Requests for microfiche or photocopies of AGARD documents should include the AGARD serial number, title, author or editor, and publication date. Requests to NTIS should include the NASA accession report number. Full bibliographical references and abstracts of AGARD publications are given in the following journals:

Scientific and Technical Aerospace Reports (STAR)
published by NASA Scientific and Technical
Information Branch
NASA Headquarters (NIT-40)
Washington D.C. 20546, USA

Government Reports Announcements (GRA)
published by the National Technical
Information Services, Springfield
Virginia 22161, USA



Printed by Specialised Printing Services Limited
40 Chigwell Lane, Loughton, Essex IG10 3TZ

ISBN 92-835-0444-5